ITALIAN PHYSICAL SOCIETY ASI-NATO

PROCEEDINGS
OF THE
INTERNATIONAL SCHOOL OF PHYSICS
«ENRICO FERMI»

COURSE XCVII

edited by G. CICCOTTI and W. G. HOOVER
Directors of the Course

VARENNA ON LAKE COMO
VILLA MONASTERO
23 July - 2 August 1985

Molecular-Dynamics Simulation of Statistical-Mechanical Systems

1986

NORTH-HOLLAND
AMSTERDAM - OXFORD - NEW YORK - TOKYO

Copyright © 1986, by Società Italiana di Fisica

All rights reserved. No part of this publication may be reproduced, stored in a retrieval system, or transmitted, in any form or by any means, electronic, mechanical, photocopying, recording or otherwise, without the prior permission of the copyright owner.

PUBLISHED BY:

North-Holland Physics Publishing
a division of
Elsevier Science Publishers B.V.
P.O. Box 103
1000 AC Amsterdam
The Netherlands

SOLE DISTRIBUTORS FOR THE USA AND CANADA:

Elsevier Science Publishing Company Inc.
52, Vanderbilt Avenue
New York, N.Y. 10017
U.S.A.

Technical Editor
P. Papali

Library of Congress Cataloging-in-Publication Data

International School of Physics "Enrico Fermi" (1985 : Varenna, Italy)
Molecular-dynamics simulation of statistical-mechanical systems.

(Proceedings of the International School of Physics "Enrico Fermi" ; course 97)
At head of title: Italian Physical Society.
Includes added t.p. in Italian.
Includes index.
1. Statistical mechanics--Mathematical models--Congresses. 2. Statistical mechanics--Data processing--Congresses. 3. Molecular dynamics--Mathematical models--Congresses. 4. Molecular dynamics--Data processing--Congresses. I. Ciccotti, Giovanni. II. Hoover, William G. (William Graham), 1936- . III. Società italiana di fisica. IV. Title. V. Series: International School of Physics "Enrico Fermi." Proceedings of the International School of Physics "Enrico Fermi" ; course 97.
QC174.7.I55 1985 530.1'3 86-31078
ISBN 0-444-87033-4

Proprietà Letteraria Riservata
Printed in Italy

INDICE

G. Ciccotti and W. G. Hoover – Foreword . . . . . pag. xv

Gruppo fotografico dei partecipanti al Corso fuori testo

Part I – History and fundamentals

W. W. Wood – Early history of computer simulations in statistical mechanics . . . . . » 3

G. Benettin – Ordered and chaotic motions in dynamical systems with many degrees of freedom.

1. Introduction . . . . . » 15
2. The Fermi-Pasta-Ulam problem . . . . . » 16
3. Theoretical background . . . . . » 23
4. Applications to statistical mechanics . . . . . » 27

Part II – Equilibrium molecular dynamics

H. J. C. Berendsen and W. F. van Gunsteren – Practical algorithms for dynamic simulations.

1. Introduction . . . . . » 43
2. The computation of forces . . . . . » 45
3. Algorithms for molecular dynamics . . . . . » 47
   3·1. Integration methods . . . . . » 47
   3·2. Euler's methods . . . . . » 51
   3·3. Gear algorithms . . . . . » 52
   3·4. The Verlet, leap-frog and Beeman algorithms . . . . » 55
   3·5. Algorithms for complex systems . . . . . » 58

4. Incorporation of constraints . . . . . pag. 60
5. Modifications in the equations of motion . . . . . » 61
6. Stochastic dynamics . . . . . » 63
7. Conclusions . . . . . » 64

B. J. ALDER – Molecular-dynamics simulations.

1. Introduction . . . . . » 66
2. Hydrodynamic tail . . . . . » 67
3. Molasses tail . . . . . » 69
4. Lorentz tails . . . . . » 70
5. Generalized hydrodynamics . . . . . » 76

M. D. FEIT and B. J. ALDER – Reaction rate calculations via transmission coefficients.

1. Introduction . . . . . » 81
2. Formalism . . . . . » 82
3. Numerical example. The Eckart barrier . . . . . » 85

J.-P. HANSEN – Molecular-dynamics simulation of Coulomb systems in two and three dimensions.

I. – Simulation of Coulomb systems: how to cope with long-range forces . . . . . » 89

1. Introduction . . . . . » 89
2. The problem of long-range forces . . . . . » 92
3. Ewald summations . . . . . » 94
4. Particle-mesh simulations . . . . . » 99
5. Specific methods in two dimensions . . . . . » 100

II. – Strongly coupled plasmas . . . . . » 101

6. General considerations . . . . . » 101
7. The one-component plasma . . . . . » 103
8. Binary ionic mixtures . . . . . » 105
9. Two-component plasmas . . . . . » 107

III. – Coulomb systems in condensed-matter physics . . . . . » 111

10. Ionic liquids and solids . . . . . » 111
11. Molten salts . . . . . » 112
12. Superionic conductors . . . . . » 116

IV. – Two-dimensional Coulomb systems . . . . . » 120

13. The two-dimensional electron gas . . . . . » 120
14. The two-dimensional one-component plasma . . . . . » 121
15. The two-component plasma in two dimensions and the Kosterlitz-Thouless transition . . . . . » 122

F. F. ABRAHAM – Computer simulations of two- and quasi–two-dimensional atomic systems.

1. Two-dimensional melting of a simple atomic system . . . . pag. 130
2. Quasi-two-dimensional physisorbed films . . . . . » 135
   2'1. Melting of submonolayer rare-gas solid films on graphite » 135
   2'2. The incommensurate phase of krypton on graphite . . » 141
      2'2.1. Structure of the incommensurate phase . . . . » 142
      2'2.2. Energetics of the incommensurate phase . . . . » 145

PART III – Free-energy computations and new equilibrium molecular dynamics

D. FRENKEL – Free-energy computation and first-order phase transitions.

1. Introduction . . . . . » 151
2. Methods to compute free energies . . . . . » 154
   2'1. Preliminary remarks . . . . . » 154
   2'2. Direct methods . . . . . » 154
   2'3. Particle insertion and related methods. . . . . » 156
   2'4. Grand canonical ensemble . . . . . » 159
   2'5. Overlapping distributions and related methods . . . . » 161
   2'6. Umbrella sampling. . . . . » 167
   2'7. Thermodynamic integration . . . . . » 169
3. First-order phase transitions . . . . . » 173
   3'1. Preliminary remarks . . . . . » 173
   3'2. Liquid-vapour transition . . . . . » 173
   3'3. Free energy of solids. . . . . » 174
4. Free energy of fluctuations . . . . . » 178
5. Conclusions . . . . . » 180

Appendix A. . . . . » 181

Appendix B. . . . . » 183

G. JACUCCI – Defect calculations beyond the harmonic model.

1. Introduction . . . . . » 189
2. Machine calculations on point defects . . . . . » 190
3. LD formula . . . . . » 191
4. Finding extrema . . . . . » 193
5. LD for the perfect LJ crystal. . . . . » 194
6. LD for the LJ crystal containing a lattice vacancy . . . . » 196
7. Test of common approximations . . . . . » 197
8. Comparison with MC results. . . . . » 199

9. Vacancy migration: rate theory formulae . . . . . pag. 200
10. Anharmonic contributions to thermodynamics . . . . . » 201
11. Rapid dynamical events . . . . . » 201

M. PARRINELLO – Molecular-dynamics study of crystal structure transformations.

1. Introduction . . . . . » 204
2. Periodic boundary conditions . . . . . » 205
3. Molecular dynamics at constant pressure . . . . . » 206
4. MD with a variable cell . . . . . » 207
5. MD at constant external stress . . . . . » 210
6. Applications of the new MD . . . . . » 212
6'1. Polymorphic transition in KCl under applied hydrostatic pressure . . . . . » 212
6'2. Superionic AgI . . . . . » 214
6'3. Ni under uniaxial [100] stress . . . . . » 216

PART IV – Nonequilibrium molecular dynamics, kinetic theory and rigorous results

D. J. EVANS – Nonequilibrium molecular dynamics.

1. Introduction . . . . . » 221
2. Liouville space . . . . . » 221
3. Isothermal response theory . . . . . » 225
4. Comparison of susceptibilities . . . . . » 229
5. Nonequilibrium molecular-dynamics algorithms . . . . . » 230
6. Planar Couette flow . . . . . » 236

B. L. HOLIAN – Simulations of vibrational relaxation in dense molecular fluids.

1. Introduction . . . . . » 241
2. Methods . . . . . » 246
2'1. Adiabatic relaxation . . . . . » 248
2'2. Isokinetic thermostatting . . . . . » 251
2'3. Andersen stochastic thermostatting . . . . . » 252
2'4. The Nosé-Hoover thermostat . . . . . » 254
3. Results . . . . . » 255
4. Conclusions . . . . . » 258
Appendix. - Potentials . . . . . » 258

J. R. DORFMAN and T. R. KIRKPATRICK – Recent results in the kinetic theory of hard-sphere systems.

1. Introduction . . . . . pag. 260
2. From kinetic theory to mode-coupling theory . . . . . » 263
3. Mode-coupling theory and extended modes . . . . . » 274
4. Neutron scattering and mode-coupling theory . . . . . » 277
5. Large long-time tails in the shear viscosity . . . . . » 280
6. The glass transition . . . . . » 284
7. Conclusion . . . . . » 289

Appendix. - The ring operator with static corrections . . . . . » 290

J. W. DUFTY, J. J. BREY and A. SANTOS – Some theoretical aspects of nonequilibrium simulation methods.

1. Introduction . . . . . » 294
2. Nonequilibrium statistical mechanics . . . . . » 295
3. Constant-temperature shear viscosity . . . . . » 299
4. Discussion . . . . . » 301

H. SPOHN – Exact results in kinetic theory.

1. Introduction . . . . . » 304
2. Derivation of the Boltzmann equation . . . . . » 306
3. The motion of a tagged particle (self-diffusion) . . . . . » 309
4. Some results for systems at finite density . . . . . » 312

H. J. M. HANLEY – Round-table: perspectives in nonequilibrium molecular dynamics.

General remarks (H. J. M. HANLEY) . . . . . » 317
Remarks (J. W. DUFTY) . . . . . » 321
Remarks (D. J. EVANS) . . . . . » 323
Remarks (J. P. RYCKAERT) . . . . . » 323
Contribution from the floor . . . . . » 324

PART V – Molecular systems

J. P. RYCKAERT – The method of constraints in molecular dynamics. General aspects and application to chain molecules

1. Introduction . . . . . » 329
2. The imposition of geometrical constraints . . . . . » 331

3. The equations of motion . . . . . pag. 334
4. An iterative method treating individual constraints in succession . . . . . » 337
5. Application to a crystal of partially rigid paraffins . . . . » 338

I. R. McDonald – Molecular liquids: orientational order and dielectric properties.

1. Introduction . . . . . » 341
1·1. A little history . . . . . » 341
1·2. Models . . . . . » 343
1·3. Algorithms . . . . . » 344
2. Structure and orientational order . . . . . » 345
2·1. The molecular-pair distribution function . . . . . » 345
2·2. Expansions of $g(1, 2)$ . . . . . » 347
2·3. Site-site distribution functions. . . . . » 350
2·4. The calculation of G_2 . . . . . » 354
3. Dielectric properties . . . . . » 355
3·1. The static dielectric constant . . . . . » 356
3·2. Dielectric relaxation . . . . . » 363
Appendix. - Derivation of eq. (3.50) . . . . . » 368

P. A. Madden – Simulation of properties of spectroscopic interest.

1. Introduction . . . . . » 371
2. On relating experimental and simulation results . . . . . » 375
2·1. Interaction-induced effects in the Raman spectrum . . » 375
2·2. The Raman and n.m.r. reorientation times . . . . . » 379
3. Detailed studies of short-time effects . . . . . » 381
3·1. The diffusion coefficient and the velocity correlation function . . . . . » 381
3·2. The orientational and angular-velocity correlation functions . . . . . » 384
4. Probing the intermolecular encounters . . . . . » 387
4·1. Cages, rebounds, etc.. . . . . » 388
4·2. Why do the torques appear Gaussian?. . . . . » 390
5. Other liquids . . . . . » 394
6. Other topics . . . . . » 395
6·1. Collective *vs.* single-particle motion . . . . . » 395
6·2. Interaction-induced spectra . . . . . » 397
6·3. Vibrational dynamics. . . . . » 397

R. W. IMPEY – Computer simulation of water and ionic solutions: what can we learn?

1. Introduction . . . . . pag. 401
2. Molecular-dynamics calculations . . . . . » 402
3. Structure . . . . . » 403
   3·1. Partial radial distribution functions . . . . . » 405
   3·2. Co-ordination numbers . . . . . » 407
   3·3. Conformation of the ion-water complex . . . . . » 408
   3·4. Neutron-weighted distribution functions . . . . . » 409
4. Residence times and hydration numbers . . . . . » 412
5. Conclusions . . . . . » 415

K. WATANABE and H. C. ANDERSEN – Molecular-dynamics study of several atomic solutes in water.

1. Introduction . . . . . » 418
2. Intermolecular forces and simulation method . . . . . » 419
3. Simulation of several solutes in water . . . . . » 420
4. Summary and discussion . . . . . » 422

M. L. KLEIN – Structure and dynamics of molecular crystals.

Part I: Structure of rotator phases . . . . . » 424

1. Introduction . . . . . » 424
2. Characterization of orientational disorder by neutron scattering . . . . . » 426
3. Order parameters . . . . . » 431
4. Molecular-dynamics calculations . . . . . » 434
   4·1. Mixed crystal $(KCN)_x(KBr)_{1-x}$ . . . . . » 434
   4·2. Lithium sulphate . . . . . » 435
   4·3. Solid nitrogen . . . . . » 437

Part II: Dynamical properties of rotator phases . . . . . » 439

1. Introduction . . . . . » 439
2. Relaxation of the order parameters . . . . . » 440
   2·1. Potassium cyanide . . . . . » 440
   2·2. Lithium sulphate . . . . . » 442
   2·3. Ammonium bromide . . . . . » 443
3. Single-particle dynamics . . . . . » 446
   3·1. Velocity autocorrelation functions . . . . . » 446
4. Collective modes. The dynamical structure factor . . . . . » 449
   4·1. Potassium cyanide . . . . . » 452
   4·2. Sodium nitrite . . . . . » 454
   4·3. Ammonium bromide . . . . . » 454

Part III: Structural transformations . . . . . pag. 455

1. Introduction . . . . . » 455
2. Extended-system methods . . . . . » 457
   2·1. Canonical-ensemble molecular dynamics . . . . . » 457
   2·2. Constant-pressure molecular dynamics . . . . . » 460
   2·3. Constant-temperature and constant-pressure molecular dynamics . . . . . » 461
3. Phase transitions in molecular solids . . . . . » 462
4. Examples of simulated transitions . . . . . » 463
   4·1. Solid carbon tetrafluoride . . . . . » 463
   4·2. Solid nitrogen at high pressure . . . . . » 464
   4·3. Bicyclo octane . . . . . » 466
   4·4. Phase diagram of potassium cyanide . . . . . » 468
5. Conclusions . . . . . » 474

M. MEYER – Molecular-dynamics study of orientational order in a plastic crystal. High-temperature phase of adamantane.

1. Introduction . . . . . » 477
2. Structural properties of adamantane . . . . . » 478
3. Model and computation . . . . . » 480
4. Orientational order . . . . . » 482
   4·1. Determination of the orientational probability density function . . . . . » 482
   4·2. Cubic-harmonics analysis . . . . . » 482
   4·3. Ideal orientations . . . . . » 487
5. Applications of the orientational probability density function » 489
   5·1. Librational amplitude . . . . . » 489
   5·2. Rotational motion . . . . . » 490
6. Conclusions . . . . . » 491

Appendix A. - Symmetry elements, symmetry operations of adamantane (high-temperature phase) . . . . . » 491
Appendix B . . . . . » 492
Appendix C. - Subroutine of forces . . . . . » 492
Appendix D. - Cubic harmonics . . . . . » 493
Appendix E. - Calculation of ${}_1K_4$ . . . . . » 494

H. J. C. BERENDSEN – Biological molecules and membranes.

1. Introduction . . . . . » 496
2. MD of proteins . . . . . » 498
   2·1. Potentials and methods . . . . . » 498
   2·2. Protein structure in solution . . . . . » 500
   2·3. Functional role of protein dynamics . . . . . » 502

3. Free-energy considerations . . . . . pag. 504
3·1. The determination of binding constants . . . . . » 504
3·2. The determination of entropies of conformational states » 505
4. Membrane simulations . . . . . » 509
4·1. Biological membranes and their models . . . . . » 509
4·2. A simple membrane simulation . . . . . » 511
4·3. An all-atom membrane simulation . . . . . » 515

PART VI – Materials science

S. YIP – Atomistic simulations in materials science.

1. Introduction . . . . . » 523
2. Molecular-dynamics and Monte Carlo simulations . . . . . » 524
3. Structural and dynamical properties of grain boundary solids » 526
3·1. Bicrystal models . . . . . » 527
3·2. Coupled sliding and migration . . . . . » 530
3·3. Structural transition and melting . . . . . » 534
3·4. Vacancy migration and atomic diffusion . . . . . » 536
4. Thermal ignition in self-heating fluids . . . . . » 542
4·1. Continuum theory . . . . . » 542
4·2. Molecular-dynamics simulation . . . . . » 545
4·3. Results . . . . . » 547
4·4. Discussion . . . . . » 550
5. Stress-induced structural transformations in crystalline solids » 552
6. Concluding remarks . . . . . » 556

V. PONTIKIS – Round-table: perspectives in materials science.

Introductory remarks . . . . . » 562
Summary of contributed discussion . . . . . » 564

PART VII – Quantum problems and new computers

D. M. CEPERLEY – The simulation of liquid helium.

1. Introduction . . . . . » 571
2. The density matrix . . . . . » 572
3. The Monte Carlo method . . . . . » 574
4. Results . . . . . » 576

E. MARINARI – A numerical approach to the theory of strong interactions.

1. Introduction . . . . . pag. 583
2. The role of gauge invariance . . . . . » 584
3. Path integral quantization. . . . . » 586
4. Quantum chromodynamics. . . . . » 588
5. Renormalization group and continuum limit . . . . . » 589
6. The lattice theory . . . . . » 591
7. Numerical methods . . . . . » 593
8. Observables and results . . . . . » 594
9. Statistical and systematic error . . . . . » 598

C. MOSER – Round-table: perspectives in computations.

New computers for molecular dynamics (C. MOSER) . . . . . » 600
Computation for molecular dynamics . . . . . » 602

PART VIII – Conclusions

A. BELLEMANS – Synopsis of the school and final remarks . . » 607

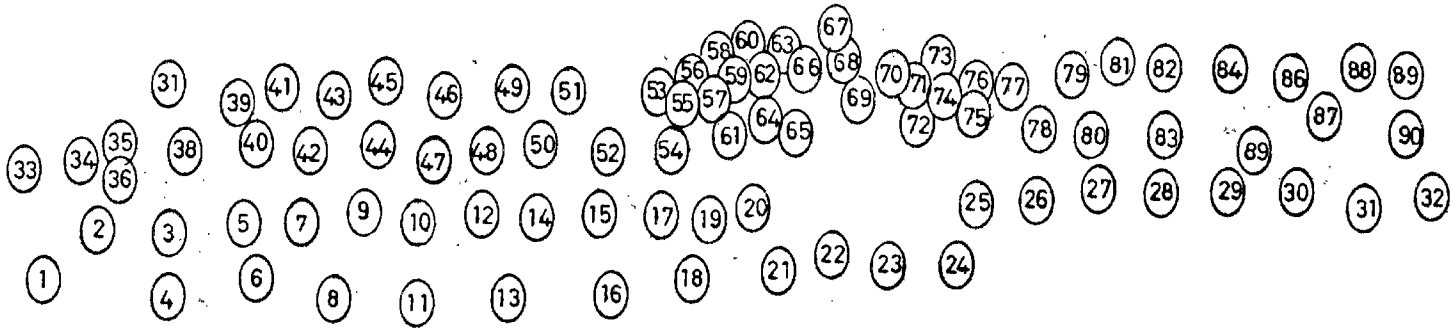

1. R. W. Impey
2. G. Benettin
3. B. J. Alder
4. H. J. C. Berendsen
5. H. Hanley
6. M. A. Moller
7. S. Yip
8. J.-P. Ryckaert
9. G. M. Van Waveren
10. J. H. J. Van Opheusden
11. J. F. Lutsko
12. W. G. Hoover
13. B. Holian
14. E. Mazzi
15. G. Ciccotti
16. W. Wood
17. G. V. Paolini
18. R. Le Sar
19. E. Memeo
20. M. Hayoun
21. D. Evans
22. J. Dufty
23. M. Coti Zelati
24. W. Smith
25. M. Haughney
26. J. Carter
27. J. Johansson
28. G. Torrie
29. F. Abraham
30. J. Valleau
31. P. Maselli
32. M. Zoppi
33. G. Cardini
34. N. Motta
35. A. Campa
36. M. C. Abramo
37. G. Giunta
38. F. Buda
39. S. Quartieri
40. P. Madden
41. M. Marechal
42. D. Frenkel
43. R. Dorfman
44. J. Board
45. D. Mac Gowan
46. G. Morriss
47. M. Meyer
48. Y. Hiwatari
49. F. Baras
50. P. V. Giaquinta
51. G. Chiarotti
52. B. Moran
53. J. Brey
54. M. Ferrario
55. A. Pavlovitch
56. C. Moser
57. A. Branka
58. G. Chabrier
59. A. Bellemans
60. W. L. Morgan
61. A. Tani
62. P. Turq
63. B. Piller
64. G. Marechal
65. I. R. Mc Donald
66. V. Pontikis
67. M. Ernst
68. D. Rapaport
69. J. Clerouin
70. V. Rosato
71. M. Schoen
72. M. Guillope
73. C. Caccamo
74. M. G. Betti
75. S. Morante
76. P. Letardi
77. J.-P. Hansen
78. D. Ceperley
79. C. Pierleoni
80. G. De Lorenzi
81. C. Massobrio
82. Z. Kotler
83. J. A. Padro
84. H. Suhl
85. A. M. Martin
86. G. Suffritti
87. D. Heyes
88. R. Fazio
89. D. Rocca
90. M. Winterhalter

SOCIETÀ ITALIANA DI FISICA

SCUOLA INTERNAZIONALE DI FISICA «E. FERMI»

XCVII CORSO - VARENNA SUL LAGO DI COMO - VILLA MONASTERO - 23 Luglio - 2 Agosto 1985

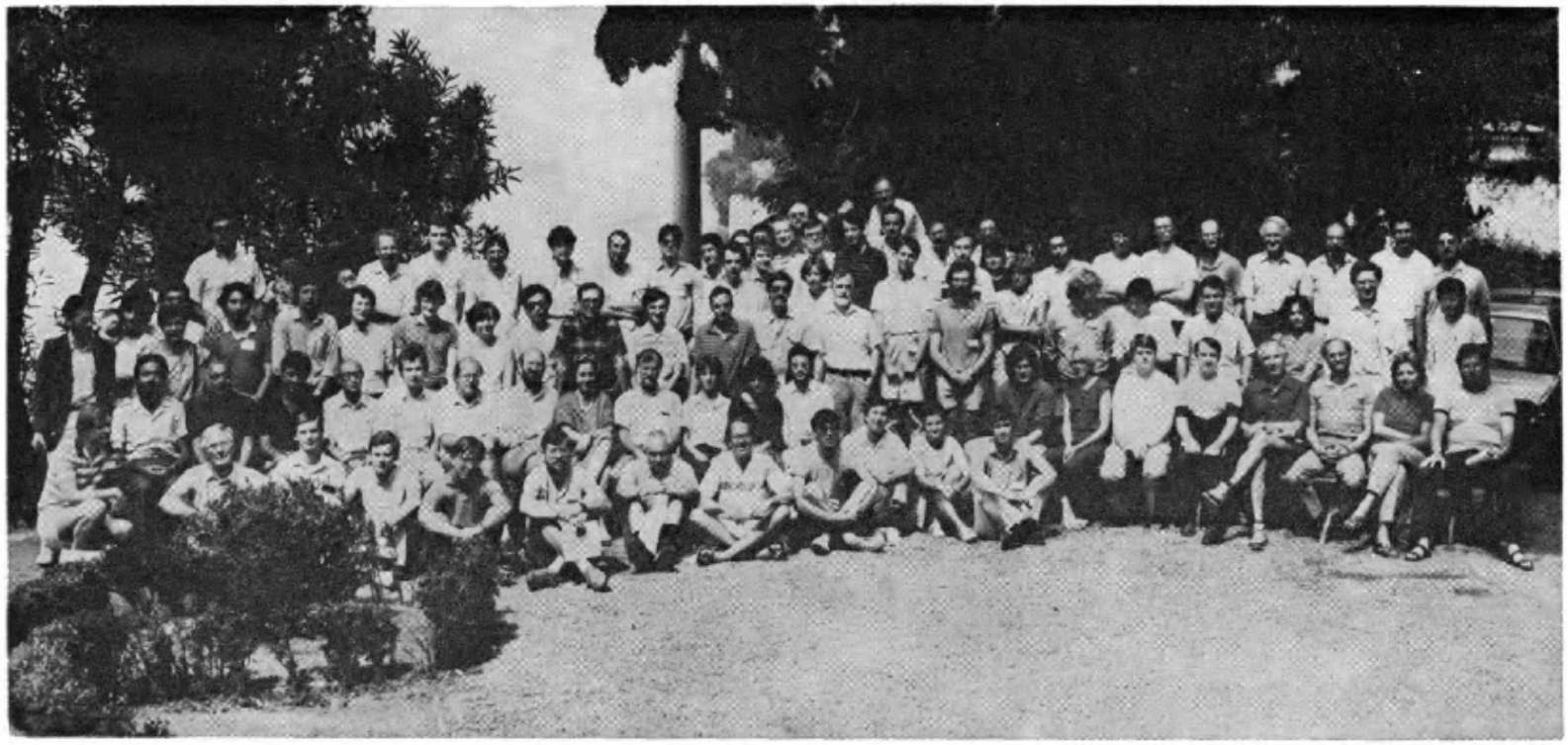

Foreword.

We were in Paris in August 1983 to attend one of Carl Moser's CECAM workshops on « Solid State Diffusion ». Two recent IUPAP conferences, Edmonton in 1980 and Edinburgh in 1983, were in our minds. These international conferences on « Statistical Mechanics » seemed to us to be primarily devoted to elaborations of the Ising model that ONSAGER worked out in the 1940's. The present Varenna School was sketched out, over ice-cream, at a small restaurant on the « rive droite » in front of Ile-Saint-Louis. Our basic recipe for a school on « Simulation of Statistical Mechanical Systems » was to scrupulously avoid the Ising model. To help insure the prohibition, « Molecular Dynamics » was later added to the title.

In the fall and winter we began inquiries seeking participation and support. The responses were prompt, positive and enduring. In November 1984 a stimulating meeting held at the Argonne National Laboratory to celebrate the twentieth anniversary of Anees Rahman's paper on liquid Lennard-Jones dynamics confirmed the validity of our choice. We regret very much that Anees was not able to contribute to this school.

Three of the original Varenna pioneers of the 1957 IUPAP Meeting at Varenna « Condensed States of Simple Systems », Berni ALDER, André BELLEMANS and Bill WOOD, agreed to return in 1985 to share their perspectives and sense of progress with us. We were specially pleased to have Berni ALDER with us, just short of his sixtieth birthday, a traditional time for reminiscence and celebration in physics.

While we were forced, for mysterious reasons, to refuse Jerry Percus' direct request to attend, it was a special pleasure to discover during the school that two stimulating unexpected guests had successfully slipped in, Matthew ERNST and Philippe CHOQUARD, the latter also a 1957 veteran. ALDER, BELLEMANS and WOOD were officially joined by 25 lecturers and seminar speakers and 66 students and observers in the delightful Villa Monastero. Many more scientists wanted to come but could not be admitted officially due to lack of space. Some of these materialized successfully, nevertheless.

NATO, NSF, IBM, the French Embassy in Rome through the kindness of Prof. Daniel GABAY, and the Italian Foreign Ministry, the Science Faculty of Rome University, through the kindness of Prof. Giorgio TECCE, joined the Italian Physical Society in supporting this Enrico Fermi school and seminar.

In all we raised about $ 50 000 to support the meeting and the dissemination of its proceedings.

One of the returning pioneers, Bill WOOD, a cognac fan, persuaded to forsake fishing in Montana, assured us that the basic appeal of Varenna remained much the same. Kirkwood's 1957 favorite, grappa, still abounds but would probably still lose its appeal if it were exported from Italy to California. Lake Como and its villas, the roads—the mountain trails—are more heavily used today. There are many more motorcycles and power boats, but also windsurfers. But WOOD noted that the comfortable, slightly chaotic and bucolic atmosphere conducive to conversation is little changed from 1957.

After this school, we see very clearly the broadening of interest from fundamentals to include more applications of molecular dynamics. At the 1957 meeting Kirkwood's students Berni ALDER and Bill WOOD reported strong evidence for the first-order freezing transition in a hard-sphere fluid. This conclusion was preceded by thousands of hours of computer time and tens of hours devoted to convincing KIRKWOOD that the cumbersome calculations of fluid properties based on his « superposition » approximation were inferior to the results of Metropolis' « Monte Carlo » sampling scheme, and even to the prediction of the crude one-particle cell model.

In 1957 physicists and chemists had developed many approximate schemes for understanding many-body problems: the virial expansion, integral equations, cell models, ... In 1985 these methods are largely out of date. Simulation can be used, instead, to model directly both the static and dynamic equilibrium and nonequilibrium properties of atomic and molecular systems. With realistic simulations replacing cruder approximations it has become possible to treat a much broader range of physical problems.

Today the methods described in 1957 have led to detailed understanding not only of melting, but also a host of polymorphic, rotational and electronic phase transformations. In this book Mike KLEIN and Daan FRENKEL survey these developments. The big change in simulation is the graphic real-time visualization of dynamical processes. Mike's two-dimensional fourteen-quadrupole model, illuminated and projected by a viewgraph machine, and Farid Abraham's movies of the dynamics of 161 604 « krypton » atoms bound to a « graphite » substrate illustrate co-operative phenomena directly.

The theoretical analysis of nonequilibrium phenomena remains primitive, with some of the basic properties of two- and three-body nonequilibrium systems still unknown. The emerging field of nonequilibrium molecular dynamics is evolving rapidly, as did equilibrium theory in the 1960's and 1970's. André BELLEMANS emphasized the regrettable but understandable tendency of « pure » Newtonian theoreticians, of which Bob DORFMAN is prototypical, to ignore the problems and results of the pragmatic practitioners of nonequilibrium molecular dynamics. We believe that this school has been instrumental in bringing these heterogeneous groups closer together and will persuade

increasing numbers of theoreticians to study the problems involved in simulating and analysing properties far from equilibrium.

The basis of equilibrium theory seems to be less secure than it was in 1957, when the KAM theorem was known to only a few. The condensation of bundles of trajectories of Hamiltonian systems within attractors, possibly with fractal dimension, appears to violate Liouville's theorem. Such apparent violations could explain why formal results—such as constancy of entropy in an ensemble of isolated systems—can be misleading or wrong. The mathematical analysis assisted by computers on systems composed of small numbers of particles is adding to our ability to reconcile the second law of thermodynamics with reversible and deterministic equations of motion. Perhaps the next Varenna school on simulation will mark a more generally agreed upon understanding of time's arrow in mechanics. Work linking the linear response regime to nonlinear simulations and Lyapunov instability is headed in this direction.

The school was useful in providing an advanced but well-documented survey of the simulation possibilities from the fundamental problems described by Giancarlo BENETTIN to the drug simulation physics of Hermann BERENDSEN. The diligence of the speakers in clarifying their ideas on paper (*) made it possible to capture, long after the lectures, the gist of occasionally inscrutable, densely packed, viewgraphs described in a sometimes unfamiliar accent. This individual study, the only reliable route to knowledge, is now available thanks to the help of our friends and colleagues. We thank them again and the many institutions supporting the school for making this collaboration a success.

At Christmas time Daan FRENKEL concocted a miraculous information form which successfully extracted information from the speakers which our own carefully composed letters had failed to dislodge. We specially thank Paolo GIAQUINTA, the scientific secretary, for his near round-the-clock help with all the scientific, social, technical and gastronomic activities carried on at and near the school. Paolo found more support for the school, at IBM Italia, and was also a master at soothing the bruised egos of scientists and students injured in their battles with the various rules imposed on the school by its sponsors. Angela DI SILVESTRO remained kind and efficient, throughout the onerous typing chores engendered by the school.

G. CICCOTTI and W. G. HOOVER, Marseille, August 1985

(*) The proceedings contain also the paper prepared for the school by H. C. ANDERSEN despite the fact that he could not join the school.

Part I

HISTORY AND FUNDAMENTALS

Early History of Computer Simulations in Statistical Mechanics.

W. W. WOOD

Carroll College - Helena, MT 59625
Los Alamos National Laboratory - Los Alamos, NM 87545

H. N. V. TEMPERLEY, in his introductory chapter to the book edited by himself, ROWLINSON and RUSHBROOKE [1], remarks « A key year for liquid state physics was 1957 ». He then refers to two simultaneously published letters to the editor in the *Journal of Chemical Physics* on the hard-sphere equation of state, one by ALDER and WAINWRIGHT [2] using the molecular-dynamics method, the other by WOOD and JACOBSON [3] using the Monte Carlo method. Not mentioned by TEMPERLEY, but of equal importance is the 1957 Monte Carlo paper of Wood and Parker [4]. The quick notoriety attained by these three papers was due in no small part to the fact that much of their material was also presented at the IUPAP conference « Condensed States of Simple Systems » held at this same beatiful location in September 1957, and published in its proceedings in *Nuovo Cimento* [5, 6].

The organizers of this course in the International School of Physics « Enrico Fermi », in their wisdom, have asked me to tell you something of the early history of computer simulations in statistical mechanics. In doing so they have conveniently ignored the fact that the subject of the course is molecular-dynamics simulations, whereas my own early work was entirely on Monte Carlo simulations of equilibrium properties. And even in that area, I was not involved in the original work of Metropolis, Rosenbluth, Rosenbluth, Teller and Teller [7], although I was at Los Alamos at the time. I only learned about it when Marshall ROSENBLUTH gave me a preprint at the time of submission of the paper for publication. Nevertheless, tempted by the opportunity to renew so many old friendships, I have agreed to tell you what I personally know about the subject, and also to share with you some information gained by talking with colleagues and acquaintances since accepting the kind invitation of Drs. CICCOTTI and HOOVER.

The genesis of the Metropolis Monte Carlo method lies in the early use of stochastic numerical methods on neutron diffusion problems at Los Alamos by VON NEUMANN, ULAM and METROPOLIS, with the calculations being done on the ENIAC, then at Aberdeen, Maryland. Previously, while the ENIAC

was still at the University of Pennsylvania, VON NEUMANN, METROPOLIS and FRANKEL had carried out an early thermonuclear calculation on the machine. At a conference in Los Alamos in April 1946, they described their results and the capabilities of the machine. It was at that time that ULAM realized that the speed of such machines would make possible large-scale use of statistical sampling techniques on physical and mathematical problems. However, the ideas are much older. SEGRÈ [8] relates «... I know that FERMI had invented, but of course not named, the present Monte Carlo method when he was studying the moderation of neutrons in Rome. He did not publish anything on the subject, but he used the method to solve many problems with whatever calculating facilities he had, chiefly a small mechanical adding machine». In fact, in 1947 when the ENIAC was unavailable during its transfer from Philadelphia to Aberdeen, FERMI invented, and with L. D. P. KING constructed, a small mechanical device (in effect, an analog computer) for neutron diffusion calculations [9]. As regards the name «Monte Carlo», Nick METROPOLIS [10] recalls that he first thought of it in a conversation with Stan ULAM in 1947, when ULAM was proposing the use of stochastic techniques in connection with neutron diffusion. The term appears in the title of a 1949 paper by METROPOLIS and ULAM [11].

The idea of statistical sampling applied to numerical calculations has, of course, a much longer history, of which HAMMERSLEY and HANDSCOMB [12] give several instances. Perhaps most interestingly for our purposes, they cite an article by Lord KELVIN [13], in which random sampling techniques were used to initialize trajectories of particles undergoing elastic collisions with the walls of variously shaped containers. This was in connection with the turn-of-the-century disputes about the failures of the equipartition law and the foundations of statistical mechanics. Lord KELVIN expresses his debt to his secretary and assistant, Mr. William ANDERSON, for performing the calculations for more than 5000 collisions!

When the Los Alamos MANIAC computer became operational in March 1952, METROPOLIS was interested in having as broad a spectrum of problems as possible tried on the machine, in order to evaluate its logical structure and to demonstrate the capabilities of the machine. The classical statistical mechanical N-body problem via Monte Carlo techiques was one of these first problems, done by METROPOLIS in collaboration with the TELLERS and the ROSENBLUTHS, and led to the development of what is now known as the Metropolis Monte Carlo method. METROPOLIS also recalls that J. E. MAYER had frequently urged the importance of this problem, and the general idea of a computational approach, in conversations at Chicago.

My own involvement with the Monte Carlo method began with my receipt of the Metropolis *et al.* preprint in the spring of 1953, which led to me mentioning it briefly in a 3 March letter to Prof. John G. KIRKWOOD. It is, however, quite possible that KIRKWOOD would have heard something about

it the previous summer during his regular consulting visit to Los Alamos. It was largely due to his consulting connection that I had joined the Los Alamos staff in the fall of 1950, after finishing my doctoral work with him at Cal Tech. Because of the importance of obtaining better methods of estimating the equation of state of the products behind a detonation wave, we were working on various approaches to that problem, notably the generalization of the Lennard-Jones-Devonshire (« free volume ») theory to mixtures of reacting species, and the Kirkwood-Salsburg integral equation (nothing useful ever resulted from our work on the latter). It was not immediately clear that I should become involved with the Metropolis method, as the ROSENBLUTHS were still actively working on their investigation of three-dimensional hard spheres [14], which was submitted for publication in September, 1953. During his visit that summer, however, KIRKWOOD learned a good bit more about the work from direct contact with METROPOLIS and the ROSENBLUTHS. It had also become apparent that the pressure of other, more urgent, problems would prevent the original investigators from immediately pursuing further work in the statistical mechanics of fluids. KIRKWOOD had immediately recognized the potential of the method, and evidently was able to persuade METROPOLIS and the ROSENBLUTHS that we (that is, my computational assistant for many years, Frederick R. PARKER, and myself) could be trusted to continue the work in reliable fashion. So it was at his urging that we did so, and until his untimely death in 1959, he was a most valuable source of advice, comment and criticism, as well as promoting my attendance at important meetings, and drawing the attention of his wide circle of colleagues and acquaintances to our work. J. O. HIRSCHFELDER and Z. W. SALSBURG were also similarly helpful.

I, of course, began the work in the belief that METROPOLIS *et al.* and the ROSENBLUTHS had published the last word on the equation of state of hard spheres. For that reason, and because of our applied interest in more realistic models of the intermolecular potential, the obvious next problem to investigate was the equation of state of three-dimensional « Lennard-Jones (6, 12) » molecules. PARKER and I had already had quite a bit of experience in programming other problems (in assembly language, of course; there was no FORTRAN in those days) on the IBM-701, so it was natural for us to begin the work on that machine rather than on the MANIAC.

We did not, of course, lay aside the other problems with which we were engaged, and it is not until July, 1954, that one of my surviving notebooks (much of the original record of this work did not survive the subsequent zeal of various bureaucrats to reduce the amount of material on file) records that the code was then ready for intensive use. However, this was not due only to work on other problems. Kirkwood's initial enthusiasm for the Monte Carlo method had temporarily waned. It had become evident from the Rosenbluths' results for hard spheres that at high density (the case of most interest for shocks and detonations) the Monte Carlo method gave much better agreement with

the simple free-volume theory than with the results from the Born-Green-Kirkwood-Yvon integral equation under the superposition approximation. Several of Kirkwood's students had devoted substantial parts of their theses to this numerical problem, which was very nontrivial with the then available computing equipment, so it is easy to understand his skepticism. My correspondence files (fortunately preserved from the bureaucrats) contain a letter of 16 November 1953 in which he mentioned having seen Marshall ROSENBLUTH at a meeting in Japan, and that he was now convinced that the Monte Carlo method was wrong.

In order to see the nature of his objection, it will be necessary to recall briefly the essentials of the Metropolis method for the estimation of canonical averages. As you know, it corresponds to carrying out a random walk in the configuration space of the system. In describing the method, one usually approximates that space as a finite set of states, say M in number. The random walk is a realization of a Markov chain, which is completely specified by its single-step transition probability matrix $p(i, j)$, giving the conditional probability that, if the system is in state i on the n-th step, it will then be in state j on the $(n+1)$-th step. Suppose that one wishes to estimate the ensemble average

$$\langle f \rangle = (1/Q) \sum_{i=1}^{M} f(i) \exp[-\beta E(i)] , \qquad Q = \sum_{i=1}^{M} \exp[-\beta E(i)] , \tag{1}$$

of some state function $f(i)$.

The Monte Carlo estimate is the realization average

$$\bar{f}^{(m)} = (1/m) \sum_{n=1}^{m} f(i(n)) \tag{2}$$

over some large number m of steps, $i(n)$ being the state of the system realized on the n-th step of the random walk. Aside from important requirements with respect to the ergodic structure of the chain, a sufficient condition for the stochastic convergence with increasing m of $\bar{f}^{(m)}$ to the ensemble average $\langle f \rangle$ is that $p(i, j)$ satisfies the condition of microscopic reversibility

$$p(i, j) \exp[-\beta E(i)] = p(j, i) \exp[-\beta E(j)] . \tag{3}$$

In practice this is usually done by taking

$$p(i, j) = A(i, j)\, q(i, j) , \qquad j \neq i, \tag{4}$$

in which $A(i, j)$ is a symmetric stochastic matrix satisfying the normalization conditions

$$\sum_{j=1}^{M} A(i, j) = 1 , \qquad i = 1, 2, \ldots, M, \tag{5}$$

and with

$$q(i,j) = \begin{cases} 1 & \text{for } E(j) \leqslant E(i)\,, \quad (6a) \\ \exp\left[-\beta(E(j)-E(i))\right] & \text{for } E(j) > E(i)\,. \quad (6b) \end{cases}$$

The necessary normalization condition is then satisfied simply by letting

$$p(i,i) = 1 - \sum_{j \neq 1} p(i,j)\,. \tag{7}$$

In the standard implementations matrix $A(i,j)$ corresponds to the selection of the « trial state » j uniformly over some set of neighbor states of state i, while eq. (6*a*) specifies the unconditional move into the trial state j if the energy decreases. If the energy increases, the trial state is accepted with a probability less than unity, as given by eq. (6*b*). The essential normalization condition eq. (7) then mandates the « count state i again » procedure, *i. e.* the event $i(n+1) = i(n)$, with the conditional probability $1 - q(i,j)$.

It was this last part of the procedure, the repeated counting of state i when the trial state is rejected, to which KIRKWOOD first objected. He was certainly not the last to do so. He indicated in his 16 November 1953 letter that one should not count the state $i(n)$ again, but rather should simply select a new trial state until a successful move was found. In that letter he in fact attributed such a procedure to FRANKEL and LEWINSON, but in this he may have been mistaken. There then ensued a lively correspondence between KIRKWOOD and me, and also between KIRKWOOD and Marshall ROSENBLUTH, whom I had, of course, kept informed. Marshall wrote up a new and more detailed proof of the validity of the method (it was still not based on the central-limit theorem for Markov chains; as far as I know, it was never published). The ROSENBLUTHS carried out a Monte Carlo calculation for one-dimensional hard spheres (hard rods) using the Metropolis procedure, showing that it gave good agreement with the exact theoretical (Tonks) equation of state. I did a similar calculation both analytically and numerically for the simple case of a single hard rod confined to a line segment by « hard walls ». All this activity, principally Marshall's proof, temporarily convinced KIRKWOOD, as in a letter written on 21 December 1953 he mentioned receiving Marshall's proof, and that he now believed the method to be correct. He said that he had previously understood the procedure to involve repeated displacements of the same particle until it was successfully moved, with recounting of the parent configuration on every failure.

Our satisfaction at this turn of events was not long-lived, however, as during a visit I made to New Haven in January, 1954, he was again objecting to one of the procedural details of the method. His objection was now to the preferential treatment given to a transition to a state of lower energy by the

$q(i, j)$ matrix in eq. (6). He advocated instead what he referred to as the « Kahn rule », namely

$$q(i, j) = \frac{\exp[-\beta E(j)]}{\exp[-\beta E(i)] + \exp[-\beta E(j)]}. \tag{8}$$

Both Marshall and I were quite willing to agree that eq. (8) was valid, but we also were certain that eq. (6) was correct, and intuitively we thought it was better. Further correspondence ensued, until on 12 April 1954 KIRKWOOD wrote to me « I was finally able to find the time to devote a weekend to thinking about the Monte Carlo problem ». He went on to say that he now agreed that eq. (6) was « one of the correct » ones. But not to let us off too easily, he continued by saying that « Marshall's arguments were at no time helpful », and that « your [WWW, presumably] modes of exposition were opaque ». From this point on, as I have already indicated, he was an active proponent of the importance of the work. He visited Los Alamos for a week or so nearly every summer, and we provided him with copies of our monthly reports.

During his visit in the summer of 1954, KIRKWOOD received a preprint of the paper by ALDER, FRANKEL and LEWINSON [15] in which they used Monte Carlo techniques to calculate the radial distribution function $g(r)$ for hard spheres. In the first of their methods they repeatedly added particles to a periodic box, rejecting the particle and trying again if the particle overlapped any previously added particle. WIDOM [16] subsequently showed that this procedure is inconsistent with the canonical ensemble. In addition, they indicated that they had independently discovered the Metropolis method, and used it to calculate $g(r)$ for a system of 80 hard spheres at $V/V_0 = 1.383$ (V_0 = f.c.c. close-packed volume) from a very short run, averaging over only 5 configurations per particle. At this density the system is now known to be in the solid phase, and their $g(r)$ does indeed look quite solidlike. But it is now clear that the run was much too short to give a reliable estimate of the equilibrium $g(r)$. Prior to KIRKWOOD telling me about this preprint, I had heard something about Alder's attempts with the first method, but nothing about the second.

The Monte Carlo calculations for Lennard-Jones molecules then proceeded rather rapidly through their first phase. By October 1954 we had preliminary results for the $kT/\varepsilon^* = 2.74$ (argon at 328 K) isotherm throughout the fluid region ($V/V^* \geqslant 0.95$, $V^* = \frac{1}{2}\sqrt{2}\,Nr^{*3}$, ε^* = well depth of the LJ(6, 12) potential, r^* = radius of the well), with comparisons with Michel's and Bridgman's experimental pVT data. Preliminary results for higher temperatures had also been obtained for use in the shock and detonation regions. By February 1955 the first evidence for the liquid-solid phase transition, in the form of the subsequently familiar two-level stucture of the pressure *vs.* Markov chain « time » plots, had been noticed. Most of these early runs were made with $N = 32$ particle systems, and we were very aware of the need to correct the results

for the long-range interactions which are omitted or distorted in these small systems. Work on this aspect of the problem, and other unrelated work, as well as the task of transferring the code to the IBM-704, the first of which arrived in early 1956, occupied us through most of that year. The monthly reports of this period make frequent reference to the preparation of the results for publication, a task which KIRKWOOD was continually urging on us.

The publication of the paper by me and PARKER [4] suffered a slight further delay when it became apparent that it would be necessary to repeat the hard-sphere calculations of the Rosenbluths. This came about in the following way. In early 1955 we had been contemplating the addition of another person to our small group, and KIRKWOOD mentioned that he had heard that Berni ALDER was thinking of leaving Berkeley. So in a letter dated 14 April 1955 I wrote to Berni inviting him to consider coming to Los Alamos. On 28 April 1955 he responded, saying that he was accepting an appointment at Livermore that would allow him to continue on a part-time basis at Berkeley. He mentioned also that he had heard from Marshall that I was working with the Monte Carlo method, and asked whether I had obtained any precise radial distribution functions for the hard-sphere system. He also described briefly work he had underway to evaluate numerically the transport properties of fluids. This was the first time that I heard of what was soon to become known as the molecular-dynamics method. I replied on 25 May 1955 that we were working on Lennard-Jones systems, not hard spheres.

In August 1956, ALDER and WAINWRIGHT [17] participated in a symposium on transport processes in Brussels. I did not attend, and the proceedings were not published until 1958. In the published paper they report the serious discrepancy between their molecular-dynamics results for hard spheres, compared to the Rosenbluths' results, in what would subsequently become known as the transition region. This paper also contains, as far as I know, the first published molecular-dynamics results for a transport process, namely, the velocity autocorrelation function and the self-diffusion coefficient for hard spheres. There are also some calculations showing the approach of the one-particle velocity distribution function to equilibrium from an initially nonequilibrium distribution. As far as the long-time behavior of the velocity autocorrelation function is concerned, this paper emphasizes the fairly good agreement at $V/V_0 = 2$ at short and intermediate times, with the then-expected exponential decay. In retrospect, looking at their fig. 9, one can perhaps see a hint of the famous long-time tail that would be reported by them much later.

That fall, unaware of this work, I learned from a Los Alamos colleague who had met Berni in Scotland during the summer, that Berni was planning to visit Los Alamos. My colleague had only a vague understanding of Berni's work, but realized that it resembled ours in some respects, and urged me to write to him. I did so, on 2 October 1956, describing in some detail our cur-

rent and planned Monte Carlo work. One of the things on which I was hoping to work, but never did, was mixtures of hard spheres, which was clearly a possibility also for the molecular-dynamics method. So my letter emphasized my desire to avoid duplication of any work which Berni might have underway, and urged him to see us if he did indeed come to Los Alamos. Berni's response, on 8 October 1956, described the molecular-dynamics method (although he did not yet use that term), and emphasized that there was no current duplication of problems. Most importantly, he described briefly the disagreement between their hard-sphere results and those of the Rosenbluths.

ALDER and WAINWRIGHT visited Los Alamos in mid-November 1956, and it was agreed that my Los Alamos colleagues and I would repeat the hard-sphere Monte Carlo calculations in the vicinity of $V/V_0 = 1.6$, where the disagreement was most pronounced. I was quite sure, as soon as the discrepancy was called to my attention, that it was due simply to the early random walks not being long enough. I had already noticed that, in order to obtain reliable results for LJ systems, we had to extend the calculations to at least several thousand configurations per particle, compared to the few hundred used by the ROSENBLUTHS. And, as already mentioned, we had previously seen the two-level structure suggesting the solid-liquid transition near $kT/\varepsilon^* = 2.74$, $V/V^* = 0.95$, for the Lennard-Jones case. It was also, of course, a very easy task to modify the Lennard-Jones code to handle hard spheres, although the resulting code was not very efficient for the larger systems ($N > 32$) since it examined all $N - 1$ interactions with the displaced particle. Thus for the most part I postponed Monte Carlo calculations for the larger systems until a more efficient program could be written. The latter is described in nauseating detail in [18]. So at first we concentrated on a series of Monte Carlo runs in the vicinity of $V/V_0 = 1.6$ with $N = 32$ hard spheres.

By mid-December 1956, we had made Monte Carlo runs at three densities, $V/V_0 = 1.5$, 1.6 and 1.7, and observed the transient « melting » of the initial lattice configuration at $V/V_0 = 1.6$ in both $N = 32$ and $N = 108$ systems, interpreting it in terms of a probable solid-liquid transition in the hard-sphere system. These results were communicated to ALDER and WAINWRIGHT in letters of 4 December 1956 and 4 January 1957, and, of course, also to KIRKWOOD. He was delighted, since such a transition in hard spheres had been predicted by him [19] much earlier, a prediction quite contrary to the intuition of many. In January 1957, a symposium on the many-body problem was held at the Stevens Institute of Technology. I did not attend, but KIRKWOOD presented many of our then current results, and argued in favor of the phase transition interpretation of them. The proceedings of this symposium were not published until 1963 [20], but the transcripts of two round-table discussions which are reproduced therein make interesting reading, in that at that time Berni was disputing our (Kirkwood and my) phase transition interpretation of our results. By the time the paper of Alder and Wainwright [20] which

appears in the proceedings was written, however, further results from both methods led them to write « ... but it is clear that some transition is occurring in that region, presumably a first-order one from a fluid to a solid phase ».

As can be seen from this temporary disagreement, although Berni and I were quickly able to come to agreement that the early Monte Carlo results were wrong in the transition region, agreement between our new results and the molecular-dynamics results was not immediately forthcoming. In part this was due to our strategy of emphasizing runs with a small number ($N = 32$) of particles, compared to Alder and Wainwright's emphasis on larger systems. In the latter case, the disordering of the initial lattice takes more calculator time, so that unless adequately long runs were used the results tended to give too small and quite N-dependent results for the pressure. Thus for a while the Monte Carlo results for the « fluid branch » pressure appeared to be higher than the molecular-dynamics values, whereas, when adequately long runs for systems of the same size were finally made using both methods, the Monte Carlo results were found to be consistently lower. The latter behavior was eventually explained by HOOVER and ALDER [21] on the basis of the difference in finite-system effects between the canonical ensemble used in the Monte Carlo calculations and the « molecular-dynamics ensemble ».

The period between the Stevens Institute symposium and the Varenna meeting in 1957 was one of intense collaboration between the Livermore and Los Alamos groups. Our January 1957 monthly report contains a summary of the Monte Carlo results, with all runs except one being for 32-particle systems. When the realizations were started from the usual f.c.c. lattice, all runs with $V/V_0 \leqslant 1.55$ gave pressures on the « solid branch » of the equation of state, while those with $V/V_0 \geqslant 1.5625$ eventually stabilized on the « fluid branch », after various transient behaviors more or less suggestive of pressures typical of an extension to lower density of the solid branch. One realization, at $V/V_0 = 1.575$, showed a very-well-defined residence in the solid state followed by a distinct jump into the fluid state, where it then remained. Our next report, for February 1957, contains additional results, including our first observation of a return to the solid branch after once entering the fluid states. This occurred in a run at $V/V_0 = 1.55$ in which the initial configuration was a regular lattice, but squeezed slightly into one corner of the periodic unit cell. By this time we at Los Alamos had examined the structure of the systems on the two branches of the equation of state, noting the preservation of relatively ordered arrangements on the solid branch, with relatively little diffusion of particles with respect to their neighbors, as contrasted with destruction of the lattice order and relatively free diffusion in the fluid states. This, of course, increased our confidence in our conjecture that the general behavior was symptomatic of the « expected » (depending upon one's prejudices) phase transition. However, the very low frequency of the interclass transitions soon brought home to us the impracticality of establishing the overall equilibrium equation of state

in the transition region, and, therefore, the likelihood that we would not be able to « prove » the existence of a first-order transition.

By early March 1957 the Monte Carlo and molecular-dynamics results for $N = 32$ and $V/V_0 = 1.6$ were still in serious disagreement, the Monte Carlo pressure being notably higher. Neither group was sure of the reason for this, and perhaps each of us secretly distrusted the other code, though I was pretty sure that the molecular-dynamics runs were simply not long enough. Berni suggested, in a letter of 1 March 1957, that we send him our « final » configuration from the Monte Carlo realization, to be used as the initial configuration for a molecular-dynamics run. In my response on 7 March 1957, I accepted the proposal, and suggested that he reciprocate by sending us the final positions from the previous molecular-dynamics run, from which we would start a Monte Carlo run. In the same letter I also urged the Livermore group to check their molecular-dynamics configuration to see whether it was disordered, telling them that we knew that our Monte Carlo configuration was disordered. The next day I sent them our $N = 32$, $V/V_0 = 1.6$ « final » positions. On 20 March 1957, Berni sent us the molecular-dynamics positions, saying that they had not yet started their run from the Monte Carlo positions, due to a shortage of time on the Livermore UNIVAC, on which they were running the $N = 32$ problems in spite of its slowness compared to the IBM-704. He also reported that they had not yet examined their « final » configuration with respect to disordering. At the end of March WAINWRIGHT made a brief visit to Los Alamos, following which I wrote to Berni on 2 April 1957 recording the various steps on which we had agreed in order to resolve the discrepancies which were puzzling us. I also reported that the Monte Carlo run at $V/V_0 = 1.6$ starting from the molecular-dynamics positions had been run to some 500 000 configurations (or roughly 15 600 configurations per particle). The pressures were typical of the solid branch, and somewhat lower than their previous molecular-dynamics value, over the first one-third of the run, but then a sudden jump occurred to pressures actually somewhat larger than our previous Monte Carlo value on the fluid branch. In the same letter I also invited Berni to consider seriously an extended visit to Los Alamos during the forthcoming summer (a possibility we had been discussing for some time), suggesting that he bring a molecular-dynamics program for the IBM-704 capable of running 32-particle hard-sphere systems, in view of the shortage of machine time at Livermore.

Berni replied on 10 April, reporting that their molecular-dynamics run starting from the Monte Carlo positions was giving pressures in fair agreement with the Monte Carlo value for the fluid branch. He also noted that they had now found that their previous molecular-dynamics run at this density had not succeeded in disordering the initial lattice, which explained their lower (solid branch) pressure. More importantly, he accepted the invitation to visit Los Alamos and did so from early June 1957 until early August, using some

178 hours of 704 time during that period. At the conclusion of this visit we prepared our short letters for simultaneous publication in the *Journal of Chemical Physics* [2, 3] and presentation at Varenna [5, 6].

By this time both groups were persuaded that we had jointly done about as much as could be expected with that generation of computing machinery on systems of three-dimensional hard spheres. The two groups agreed to try both methods on two-dimensional hard spheres (hard disks) in the hope that the reduced interfacial effects in the lower-dimensional system might permit a more definitive demonstration of a first-order phase transition. We continued to collaborate closely, with frequent exchanges of results and comments. With the aid of faster computing equipment ALDER and WAINWRIGHT [22] were eventually successful in generating a plausible « Van der Waals loop » for a system of 870 hard disks. The parallel Monte Carlo effort eventually concentrated on adapting the Metropolis method to the isothermal-isobaric (NpT) ensemble [23] and obtained some confirmatory evidence for the phase transition.

* * *

I am deeply indebted to Dr. N. METROPOLIS for his recollections of the early development of the Monte Carlo method at Los Alamos. I also thank Dr. M. ROSENBLUTH for a recent conversation regarding the development of the Metropolis method, and Dr. J. J. ERPENBECK for a critical reading of this paper.

REFERENCES

[1] H. N. V. TEMPERLEY, J. S. ROWLINSON and G. S. RUSHBROOKE: *Physics of Simple Liquids* (Wiley, New York, N. Y., 1968), p. 7.
[2] B. J. ALDER and T. E. WAINWRIGHT: *J. Chem. Phys.*, **27**, 1208 (1957).
[3] W. W. WOOD and J. D. JACOBSON: *J. Chem. Phys.*, **27**, 1207 (1957).
[4] W. W. WOOD and F. R. PARKER: *J. Chem. Phys.*, **27**, 720 (1957).
[5] T. E. WAINWRIGHT and B. J. ALDER: *Suppl. Nuovo Cimento*, **9**, 116 (1958).
[6] W. W. WOOD, F. R. PARKER and J. D. JACOBSON: *Suppl. Nuovo Cimento*, **9**, 133 (1958).
[7] N. METROPOLIS, A. W. ROSENBLUTH, M. N. ROSENBLUTH, A. H. TELLER and E. TELLER: *J. Chem. Phys.*, **21**, 1087 (1953).
[8] E. SEGRÈ: *From X-rays to Quarks* (W. H. Freeman, San Francisco, Cal., 1980), p. 221.
[9] Unsigned news item in the *Atom*, October 1966 (Los Alamos National Laboratory), p. 7. The device is on display in the Los Alamos Science Museum.
[10] N. METROPOLIS: private communication (June 1985).
[11] N. METROPOLIS and S. ULAM: *J. Am. Stat. Assoc.*, **44**, 335 (1949).
[12] J. M. HAMMERSLEY and D. C. HANDSCOMB: *Monte Carlo Methods* (Chapman and Hall, London, 1964), p. 1.

[13] Lord KELVIN: *Philos. Mag.*, (6)**2**, 1 (1901).
[14] M. N. ROSENBLUTH and A. W. ROSENBLUTH: *J. Chem. Phys.*, **22**, 881 (1954).
[15] B. J. ALDER, S. P. FRANKEL and V. A. LEWINSON: *J. Chem. Phys.*, **23**, 417 (1955).
[16] B. WIDOM: *J. Chem. Phys.*, **44**, 3888 (1966).
[17] B. J. ALDER and T. E. WAINWRIGHT: in *International Symposium on Statistical Mechanical Theory of Transport Processes, Brussels 1956*, edited by I. PRIGOGINE (Interscience, New York, N. Y., 1958).
[18] W. W. WOOD and J. D. JACOBSON: in *Proceedings of the Western Joint Computer Conference* (San Francisco, Cal., 1959), p. 261.
[19] J. G. KIRKWOOD: in *Phase Transformations in Solids*, edited by R. SMOLUCHOWSKI, J. E. MAYER and W. A. WEYL (Wiley, New York, N. Y., 1951), p. 67.
[20] J. K. PERCUS, Editor: *The Many-Body Problem* (Interscience, New York, N. Y., 1963); see p. 380-382 and p. 497-501 for the relevant parts of the round-table discussions, p. 511-522 for the contribution of Alder and Wainwright, and p. 523 for a summary (written by me after the event) of our results.
[21] W. G. HOOVER and B. J. ALDER: *J. Chem. Phys.*, **46**, 686 (1967); see also J. J. ERPENBECK and W. W. WOOD: in *Statistical Mechanics*, Part B, edited by B. J. BERNE (Plenum, New York, N. Y., 1977), p. 1.
[22] B. J. ALDER and T. E. WAINWRIGHT: *Phys. Rev.*, **127**, 359 (1962).
[23] W. W. WOOD: *J. Chem. Phys.*, **48**, 415 (1968); **52**, 729 (1970); also, H. N. V. TEMPERLEY, J. S. ROWLINSON and G. S. RUSHBROOKE: *Physics of Simple Liquids* (Wiley, New York, N. Y., 1968), p. 115.

Ordered and Chaotic Motions in Dynamical Systems with Many Degrees of Freedom.

G. BENETTIN

Dipartimento di Fisica dell'Università - Padova, Italia
Centro Interuniversitario di Struttura della Materia - Via Marzolo, 8 - Padova, Italia

1. – Introduction.

One of the fields where molecular-dynamics simulation (or, more generally, computer simulation of dynamical sytems) has been extensively and successfully employed is ergodic theory. This type of study is in fact as old as computers are: indeed, the pioneering work by FERMI, PASTA and ULAM [1], where for the first time numerical simulation was used in order to test the ergodic assumptions of classical statistical mechanics, was carried out on the Los Alamos MANIAC I in 1954.

The ergodic problem, *i.e.* the problem of the dynamical foundation of classical statistical mechanics, is a difficult one: not only because it is hard to solve it, but also because it is not so easy to formulate it properly. Of course, different ergodic properties, more or less strong, are easily defined (for example, the so-called metric indecomposability, or the mixing property, or the K-property [2, 3]), however, no one can at the moment say which assumption is appropriate to support a statistical mechanical approach.

According to the traditional attitude, one desires that a system, no matter how prepared, relaxes on a reasonable time scale towards a statistical equilibrium; in turn this equilibrium, for an isolated system, should be characterized by the microcanonical probability, for physically significant observable quantities. Such a behaviour requires two basic properties: the absence of physically significant integrals of motion other than energy and a sufficiently rapid decay of time correlations; for the microscopic dynamics, this means that a typical orbit in the phase space, representing the microscopic state of the system as a function of time, must wander more or less randomly, or irregularly, throughout the whole energy surface; if one desires that correlations decay and that the memory of the initial state is to be rapidly lost, one requires that any two orbits, which at a given time are very close each other, are rapidly separated

by the dynamics, losing on a reasonable time scale any reciprocal relation (« sensitive dependence on initial conditions »).

These properties are the basic attributes of what is presently called « chaos », as opposed to ordered dynamics, which is characterized by essentially opposite properties: presence of integrals of motion, no decay of correlations, very regular (quasi-periodic) turning of orbits in the phase space. All of these ideas could be easily made formal and mathematically precise. However, to proceed formally we would need to spend much of our time on mathematical rigour. Instead, in my opinion, the spirit of this school on molecular dynamics is better served if we proceed in a more intuitive way, and try to introduce a few basic ideas through examples.

The first section will be entirely devoted to the numerical experiment by FERMI, PASTA and ULAM; some recent studies on the same model will be also included. In the second section we will shortly introduce a few basic mathematical concepts and results from classical perturbation theory. Finally, in the last section, we will be concerned with other numerical examples, and also with the difficult problem of the physical interpretation of numerical and theoretical results. As we will see, it is not easy to draw conclusions: indeed, in spite of their age and of their physical relevance, many questions still remain open. However, great efforts from physicists and mathematicians are presently devoted to this problem, so that the situation might change significantly in the near future; this is at least what I warmly hope.

Let me finally say that these lectures are very far from being an even partially complete review: indeed, we will be always confined to a very small subset of dynamical-system theory, as we will be only concerned with classical, Hamiltonian, nearly integrable dynamical systems, with special attention to systems with many degrees of freedom. And even within this subset, our discussion will be necessarily quite limited. A much wider introduction to the subject can be found, for example, in ref. [4-8]; in particular, ref. [8] contains an excellent bibliography, and a basic collection of reprints.

I am indebted to L. GALGANI for many discussions, and for having kindly reviewed the manuscript.

2. – The Fermi-Pasta-Ulam problem.

As is well known, the Fermi-Pasta-Ulam (FPU) model [1] is a chain of $n+2$ equal particles, connected in the simplest possible way by nonlinear springs; the two particles at the end of the chain are fixed. Let us denote by $p_1, \ldots, p_n$ the momenta of the n moving particles, and by $q_1, \ldots, q_n$ their displacements from the equilibrium positions; the co-ordinates $q_0 = q_{n+1} = 0$ are also introduced for the end particles. The Hamiltonian of the model is

written

$$(2.1)\qquad H(p_1, \ldots, p_n, q_1, \ldots, q_n) = \sum_{j=1}^{n} \frac{p_j^2}{2m} + \sum_{j=0}^{n} \left[\frac{K}{2}(q_{j+1} - q_j)^2 + \frac{\alpha}{r}(q_{j+1} - q_j)^r\right],$$

with $r = 3$ or $r = 4$. The mass m of the particles and the elastic constant K are conventionally equal to one. At fixed energy E, the parameter α gives the nonlinearity; alternatively, one can keep α fixed, and vary the energy: indeed, as is well known, by a rescaling of co-ordinates and momenta one immediately sees that the dynamics at given α and E, or $\tilde{\alpha}$ and $\tilde{E}$, are exactly similar, if one has $\alpha E^{r/2-1} = \tilde{\alpha}\tilde{E}^{r/2-1}$.

For small nonlinearity it is convenient to introduce the harmonic normal modes, namely

$$(2.2)\qquad a_k = \left(\frac{2}{n+1}\right)^{\frac{1}{2}} \sum_{j=1}^{n} q_j \sin\frac{jk\pi}{n+1}, \qquad k = 1, \ldots, n,$$

with the corresponding angular frequencies and harmonic energies

$$(2.3)\qquad \begin{cases} \omega_k = 2\sin\dfrac{k\pi}{2(n+1)}, \\ E_k = \dfrac{1}{2}(\dot{a}_k^2 + \omega_k^2 a_k^2), \end{cases} \qquad k = 1, \ldots, n.$$

The equations of motion, for the variables a_k, $k = 1, \ldots, n$, take the form

$$(2.4)\qquad \ddot{a}_k + \omega_k^2 a_k = \alpha f_k(a_1, \ldots, a_n), \qquad k = 1, \ldots, n,$$

where $f(a_1, \ldots, a_n)$ is a complicated polynomial of degree $r - 1$; thus, for vanishing nonlinearity, the harmonic energies $E_1, \ldots, E_n$ turn out to be n independent integrals of motion.

FERMI, PASTA and ULAM used the MANIAC I to solve numerically the equations of motion corresponding to Hamiltonian (2.1), with n up to 64. They gave initially the whole energy to one or few modes of low k, and expected to observe a sensible energy flow from the lower to the higher normal modes. Everything went instead in a completely different way, as the authors stressed:

« *Let us say here that the results of our computations were, from the beginning, surprising us. Instead of a continuous flow of energy from the first mode to the higher modes, all of the problems show an entirely different behavior. ... Instead of a gradual increase of all the higher modes, the energy is exchanged, essentially, among only a certain few. It is, therefore, very hard to observe the rate of "thermalization" or mixing in our problem, and this was the initial purpose of the calculation.* »

The failure of energy equipartition is evident from the time averages of the energies of the normal modes

$$\bar{E}_k(T) = \frac{1}{T}\int_0^T E_k(t)\,\mathrm{d}t\,, \qquad k = 1, \ldots, n. \tag{2.5}$$

For example, fig. 1 (*), which refers to the FPU model with $r = 3$, $n = 32$, $\alpha = 0.1$ and specific energy $\mathscr{E} \equiv E/n \simeq 0.07$, shows $\bar{E}_k(T)$ *vs.* T (on a logarithmic scale) for $k = 1, \ldots, 4$ (solid lines, top to bottom); the lowest dashed line represents instead the sum $\sum_{k=5}^{32} \bar{E}_k(T)$. As the figure shows, the whole energy was initially given to the first normal mode. Figure 1 shows no trend towards equipartition: most energy is shared by just few modes, and not to the same extent.

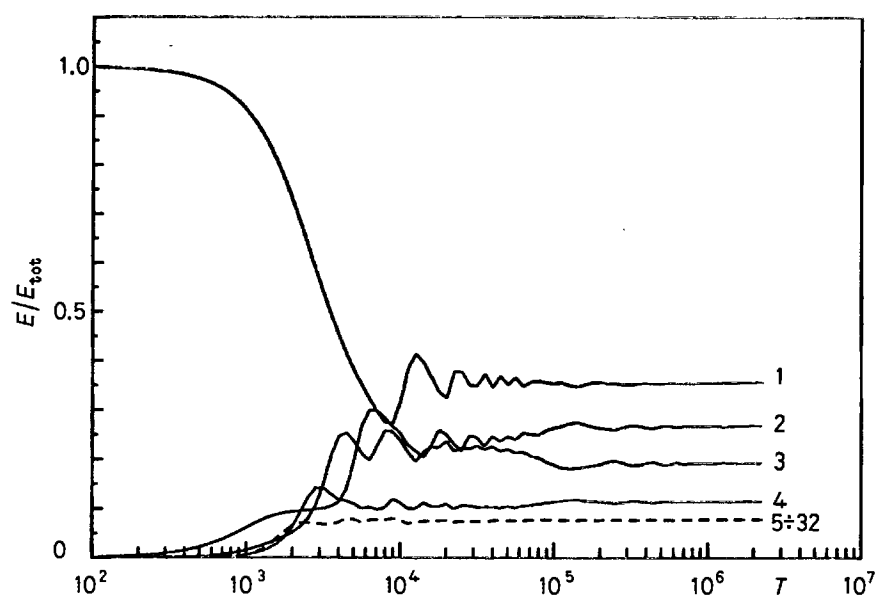

Fig. 1. – Time averages $\bar{E}_1(T), \ldots, \bar{E}_4(T)$ (solid lines, top to bottom), and $\sum_{k=5}^{32} \bar{E}_k(T)$ (dashed line), for the 32-particle FPU model with $r = 3$, $\alpha = 0.1$ and $\mathscr{E} \simeq 0.07$. First mode initially excited.

What is happening can be understood by looking at the time behaviour of the energies $E(t)$ (without averaging). Figure 2 represents $E_k(t)$ *vs.* t, for $k = 1, 2$ and 3 (solid, dashed and dotted lines, respectively). The presence of recurrences, with long-range order in the dynamics, is evident. The recur-

(*) This and the following figures are not the original figures appearing in the paper by FERMI, PASTA and ULAM, but recent ones; in particular, the integration times are much longer.

rence is not perfect. In fig. 2 the main peaks of mode one, at $t \simeq 10^4$ and $t \simeq 2 \cdot 10^4$, are slightly lower with respect to the initial peak at $t = 0$. This is because there are recurrences on even longer times, as in evident in fig. 3, which shows $E_1(t)$ as a function of t on a ($\simeq 20$ times larger) time scale. This longer recurrence has been observed by TUCK and MENZEL [9].

Considering the FPU model with $r = 4$, or modifying the initial condition, does not introduce any significant difference: for small nonlinearity the results do not support classical statistical mechanics.

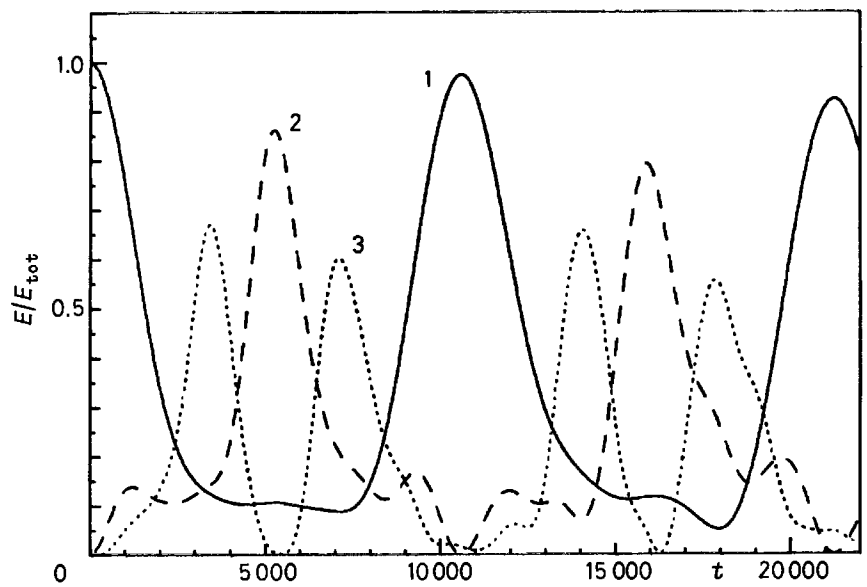

Fig. 2. – $E_1(t)$, $E_2(t)$ and $E_3(t)$ (solid, dashed and dotted lines, respectively), for the same conditions of fig. 1.

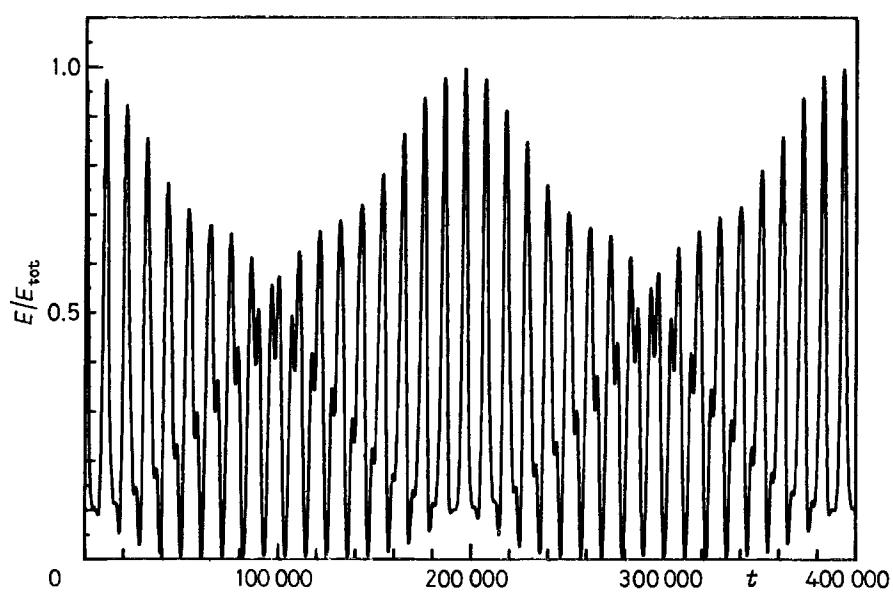

Fig. 3. – $E_1(t)$, for the same conditions as fig. 1 and 2.

For higher nonlinearity, the situation changes drastically, as noticed in 1966 by IZRAILEV and CHIRIKOV [10, 11]. Figure 4 shows $\bar{E}_k(T)$ *vs.* T for $k = 1, \ldots, n$ for the 32-particle FPU model with $r = 3$, at $\alpha = 0.1$ and $\mathscr{E} \simeq 1.2$; here too only the first mode was initially excited. Now an intense energy sharing among all modes takes place, leading to energy equipartition, as required by the ordinary formulation of classical statistical mechanics.

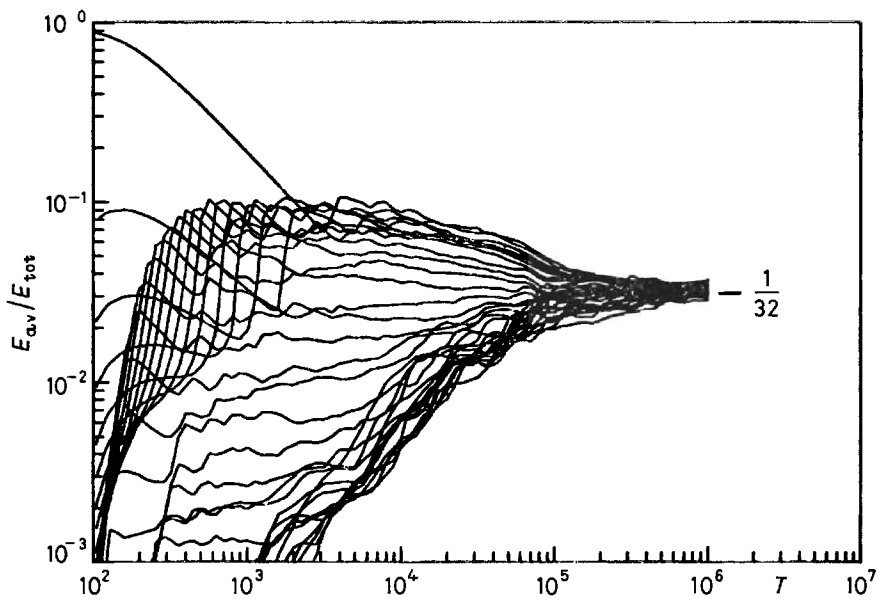

Fig. 4. – Time averages $\bar{E}_k(T)$, $k = 1, \ldots, 32$, for the 32-particle FPU model, with $r = 3$, $\alpha = 0.1$ and higher specific energy $\mathscr{E} = 1.2$.

There are several problems which, at this point, need to be discussed, in order to be sure that the phenomena of Fermi, Pasta and Ulam are physically relevant. First of all, one should wonder whether these phenomena are peculiar to the FPU model, or are they found in a wider class of physically interesting models? This point is today quite clear. A lot of numerical experiments show essentially the same behaviour for many different models, in one [12-17] and two dimensions [18-21]. In particular, essentially all systems representing (as the FPU model) weakly coupled harmonic oscillators (normal modes) exhibit ordered motions at low enough energy, with chaotic motions found only at a higher energy. A relevant point is that the transition region from ordered to chaotic motions falls in a physically significant energy range: for example, in a two-dimensional Lennard-Jones system of 64 particles [20, 21], with the physical parameters of argon, one finds the transition region at energies equivalent to temperatures of about 5 K.

A second, more important question concerns the dependence of these phenomena on the number n of degrees of freedom. In fact, when the results by FERMI, PASTA and ULAM became known, the first natural idea was to

hope that the lack of ergodic behaviour might disappear in the thermodynamic limit, and thus disappear from statistical physics. Against this widespread opinion, a small group of people—among them, CERCIGNANI, GALGANI and SCOTTI—tried to produce evidence that ordered motions persist even at large n. Excellent results have been recently obtained by LIVI *et al.* [22, 23], for the FPU models. We can describe here these results only very briefly; the interested reader should consult the original papers.

In these works the authors introduce a basic quantity, called *spectral entropy*, defined by

$$h(t) = -\sum_{k=1}^{n} P_k(t) \log P_k(t) , \tag{2.6}$$

where $P_k(t) = E_k(t) \Big/ \sum_{l=1}^{n} E_l(t)$. h ranges from zero, whenever a single mode is excited, to $\log n$, for equipartition. Numerical experiments on the FPU models (*), with n from 64 to 512 and $r = 3$ or 4, show that at sufficiently low specific energy (α is kept fixed to 0.1) $h(t)$ remains close to the initial value h_0, while for higher values of $\mathscr{E}$ the entropy $h(t)$ reaches asymptotically a limit value h_∞, between zero and $\log n$. The parameter

$$\eta = \frac{\log n - h_\infty}{\log n - h_0} \tag{2.7}$$

is then a promising candidate to investigate the behaviour of these models at different values of n. Concerning the initial conditions, these were fixed by initially exciting (to the same extent) all the modes with k/n in a given range, with different choices of this range.

The most relevant result, for the model with $r = 3$, is reported in fig. 5, where η is plotted *vs.* $\mathscr{E}$, for n from 64 to 256. Clearly, a limit curve $\eta_\infty(\mathscr{E})$ seems to exist, indicating that equipartition is not reached even in the limit $n \to \infty$.

Such a result is, in my opinion, impressive, and possibly far-reaching; of course, being numerical, it is not as conclusive as a theorem would be, but it is hard to believe that fig. 5 is produced by computer errors. Moreover, let us recall that the above result is certainly not an isolated one: on the contrary, it is only the last of a sequence of results, based as this one on the energy sharing among modes [12-15, 20], or on the sensitive dependence on the initial data [16, 17, 20], which indicate the general existence of

(*) These results refer to models with periodic rather than fixed-end boundary conditions; this is not important.

energy thresholds for chaotic behaviour, which are practically independent of n (for not too low n).

As a final comment, let us stress that the possible existence of order in the low-energy dynamics of physically relevant systems gives rise to a paradoxical situation, which is not easily solved. Lack of energy equipartition and infinite-time memory of initial data are serious difficulties if one wants to sup-

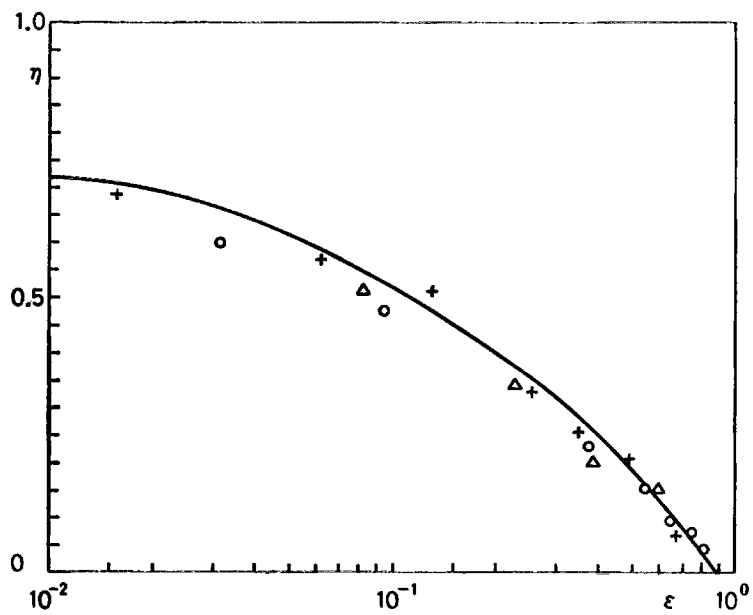

Fig. 5. – Equipartition parameter η *vs.* specific energy $\mathscr{E}$, for the FPU model with $r = 3$, $\alpha = 0.1$ and $n = 64$ (circles), $n = 128$ (crosses), $n = 256$ (triangles); modes with k up to $(1/16)n$ were initially excited (from ref. [23]).

port dynamically the approach to the microcanonical equilibrium in an isolated dynamical system. Recall that half a century before FERMI, PASTA and ULAM, the faith in the equipartition principle was so strong among physicists that the lack of energy equipartition observed in the black-body radiation, or in other examples where « freezing » of degrees of freedom occurs, was considered the best evidence of the failure of classical mechanics to explain microscopic phenomena.

There is third question which should be discussed, the problem of the time scales on which the energy sharing among modes is expected: clearly, all of the above results could be explained if these time scales become extremely long for small energy. This point will be considered later, after having introduced, in the next section, a few basic theoretical tools.

3. – Theoretical background.

It is curious fact that, while ergodicity and chaotic dynamics please people interested in statistical mechanics, instead people working in celestial mechanics are quite interested in situations of ordered dynamics, long-time memory of initial conditions and not too sensitive dependence on initial data: indeed, these features not only allow one to make accurate predictions, but they also provide an explanation for some regular structures which are often found in astronomical systems, like planetary or ring systems, or spiral galaxies.

Consider our solar system. If we disregard the mass of the planets with respect to the solar mass, then the dynamics becomes trivial; in particular, there are as many integrals of motion as the number of degrees of freedom. For each planet, the energy, the total angular momentum and, say, its z-component are conserved quantities. Notice that these integrals of motion « commute », *i.e.* have vanishing mutual Poisson brackets. Every time a dynamical system with n degrees of freedom admits n « commuting » integrals of motion, and (as a consequence of these conservation laws) has bounded motion, one can introduce canonical action-angle co-ordinates (I, φ), with $I = (I_1, \ldots, I_n) \in \mathscr{B} \subset \boldsymbol{R}^n$ and $\varphi = (\varphi_1, \ldots, \varphi_n) \in \boldsymbol{T}^n$ ($\mathscr{B}$ is here an open subset of $\boldsymbol{R}^n$, while $\boldsymbol{T}^n$ denotes the n-dimensional torus) such that the Hamiltonian is independent of the angles, *i.e.* one has

$$H(I, \varphi) = H_0(I) \,. \tag{3.1}$$

Such a statement (with a few more details) is the Liouville-Arnold theorem [2, 24]. Let us remark that also the FPU model with zero α, *i.e.* a system of uncoupled harmonic oscillators (normal modes), has this property; the transformation to action-angle co-ordinates is given, in this case, by $a_k = \sqrt{2}I_k/\omega_k \cos\varphi$, $\dot{a}_k = \sqrt{2\omega_k I_k} \sin\varphi$, so that one has $E_k = \omega_k I_k$, and the angle-independent Hamiltonian turns out to be $H_0(I) = \omega \cdot I \equiv \sum_{k=1}^{n} \omega_k I_k$.

By means of action-angle co-ordinates, the dynamics is immediately seen to be trivial: one has

$$I(t) = I(0) \,, \qquad \varphi(t) = \varphi(0) + \omega(I(0))\, t \,, \tag{3.2}$$

where $\omega = (\omega_1, \ldots, \omega_n) = \partial H_0/\partial I$ is the angular frequency. Thus the phase space $\mathscr{B} \times \boldsymbol{T}^n$ is « foliated » into invariant tori $\{I\} \times \boldsymbol{T}^n$, $I \in \mathscr{B}$ (an orbit starting on a torus remains there forever). Systems having this property are called *integrable dynamical systems*; they are the most regular, or « least ergodic » systems.

If now one takes into consideration the small attraction between planets, then in place of Hamiltonian (3.1) one obtains a perturbed Hamiltonian of the form

$$H(I, \varphi, \varepsilon) = H_0(I) + \varepsilon H_1(I, \varphi) + \varepsilon^2 \dots , \tag{3.3}$$

where ε is the ratio of the largest planet mass to the solar mass ($\varepsilon \simeq 10^{-3}$ for the solar system).

A natural question then arises. Is the dynamics of the perturbed system (3.3), for small ε, in some sense close to the unperturbed dynamics, or are instead essentially new features produced by the perturbation? This is not a new question, being a generalization of the question of ergodicity we posed in the last section in connection with the FPU model: indeed for that model, with nonvanishing α, the above substitution clearly gives a Hamiltonian of the form (3.3), with α in place of ε. Thus we see that we have just arrived at the same question from the other side.

POINCARÉ considered understanding the general behaviour of Hamiltonian systems of the form (3.3) to be the most relevant problem of dynamics. One should not be surprised by this. Recall, on the one hand, that the extraordinary success of Newtonian mechanics was based on the application of perturbation theory to Lagrangian systems, equivalent to Hamiltonian systems of the form (3.3); while, on the other hand, the dispute over the possible ergodicity of the black-body, and the difficulties of classical physics, was particularly vivid at Poincaré's time.

In spite of the great achievements obtained by classical perturbation theory in the last thirty years, Poincaré's problem still remains open: the general behaviour of Hamiltonian dynamical systems like (3.3) is not completely clear if one is interested in systems with infinitely many degrees of freedom, that is, in statistical mechanics. A lot of work is presently being devoted to this delicate question. Necessarily, we will restrict ourselves to describe two basic results, the KAM theorem [25-27] (from KOLMOGOROV, ARNOLD and MOSER), which goes back to 1954, and the more recent theorem by NEKHOROSHEV [28], which appeared in 1977.

Let us consider again Hamiltonian (3.3). The goal of classical perturbation theory would be to find (for small ε) a canonical change of variables $(I, \varphi) = \mathscr{C}_\varepsilon(I', \varphi')$, such that the new Hamiltonian $H'(I', \varphi', \varepsilon) \equiv H(\mathscr{C}_\varepsilon(I', \varphi'), \varepsilon)$ still has the integrable form

$$H'(I', \varphi', \varepsilon) = H'_0(I', \varepsilon) . \tag{3.4}$$

In that case the perturbed system would be essentially the image of the unperturbed one: one would have quasi-periodic motions everywhere in the phase space, and no statistics at all.

Such a possibility is out, as proved by POINCARÉ himself: according to his theorem on the nonexistence of integrals of motion in nearly integrable Hamiltonian systems [29], some essential modifications must appear in the dynamics of these systems, for small ε. However, as proved later for small ε, with quite mild assumptions, one has that

i) the qualitative differences between perturbed and unperturbed systems are confined to a subset of the phase space of small measure (although open and dense),

ii) even inside that subset, the actions behave as approximate integrals of the motion for extremely long times.

These vague statements are made precise by the KAM and Nekhoroshev theorems, respectively. Concerning the KAM theorem, we follow the recent formulation by POESCHEL [30] and by CHIERCHIA and GALLAVOTTI [31]:

Theorem 1 (KAM). *Consider a nearly integrable Hamiltonian system*

$$H(I, \varphi, \varepsilon) = H_0(I) + \varepsilon H_1(I, \varphi, \varepsilon) , \tag{3.5}$$

and assume

i) *H is analytic in a neighbourhood of $\mathscr{B} \times \boldsymbol{T}^n$;*

ii) $\det\left(\dfrac{\partial^2 H}{\partial I \partial I}\right) \geqslant d > 0 , \qquad \forall I \in \mathscr{B};$

iii) *ε is smaller than a threshold ε_0 (depending on the number of degrees of freedom, as well as on d and on other details of the Hamiltonian).*

Then there exists a canonical transformation $(I, \varphi) = \mathscr{C}_\varepsilon(I', \varphi')$, ε-close to the identity, and an integrable dynamical system $H_0'(I', \varepsilon)$, both infinitely differentiable in $\mathscr{B} \times \boldsymbol{T}^n$, such that the new Hamiltonian $H'(I', \varphi', \varepsilon) \equiv H(\mathscr{C}_\varepsilon(I', \varphi'), \varepsilon)$ satisfies the relation

$$H'(I', \varphi', \varepsilon) \overset{\mathscr{B}_\varepsilon}{=} H_0'(I', \varepsilon) , \tag{3.6}$$

where $\mathscr{B}_\varepsilon$ is a closed subset of $\mathscr{B}$, whose measure is ε-close to the measure of $\mathscr{B}$, and the symbol $\overset{\mathscr{B}_\varepsilon}{=}$ denotes equality of the two members, as well as of their derivatives, for $I' \in \mathscr{B}_\varepsilon$.

Remark. In agreement with Poincaré's theorem, the set $\mathscr{B}_\varepsilon$, although large in measure, has empty interior; its complement is open and dense in $\mathscr{B}$.

From (3.6) it follows that $I_1', \ldots, I_n'$ are integrals of motion (and correspondingly the orbit regularly turns on an invariant torus) if the initial datum

belongs to $\mathscr{B}_\varepsilon$. Correspondingly the old actions are approximate integrals of motion, *i.e.* one has, for any t, $|I_k(t) - I_k(0)| = \mathcal{O}(\varepsilon)$. The perturbed system remains similar *in measure* to the unperturbed one, and in particular no statistical approach is possible, except in the complement of $\mathscr{B}_\varepsilon$.

For $n = 2$ the situation is peculiar: invariant tori are two-dimensional surfaces, embedded in a three-dimensional energy surface; consequently, in each energy surface the complement of $\mathscr{B}_\varepsilon$ is separated by tori into disjoint thin strips; orbits inside a strip at $t = 0$ are trapped there forever, and the actions $I_1, \ldots, I_n$ are almost-integrals of motion even inside $\mathscr{B}_\varepsilon$. For $n > 2$ one has instead

$$\dim(\text{constant-energy surface}) - \dim(\text{tori}) > 1\,, \tag{3.7}$$

so that the complement of $\mathscr{B}_\varepsilon$ is not only open and dense, but is also connected. Thus the possibility is left open of having a dense set of orbits wandering, perhaps randomly, throughout an energy surface.

This phenomenon, called *Arnold diffusion*, can be proven to effectively take place in some simple examples [2, 32], and is probably a general feature of nearly integrable dynamical systems with at least three degrees of freedom. This phenomenon, however, turns out to be extremely slow, according to the following

Theorem 2 (NEKHOROSHEV). *Consider the Hamiltonian*

$$H(I, \varphi, \varepsilon) = H_0(I) + \varepsilon H_1(I, \varphi)\,, \tag{3.8}$$

defined for $(I, \varphi) \in \mathscr{B} \times \boldsymbol{T}^n$, *and assume*

i) H *is analytic in a neighbourhood of* $\mathscr{B} \times \boldsymbol{T}^n$,

ii) $\dfrac{\partial^2 H}{\partial I \partial I}$ *is positive definite in* $\mathscr{B}$,

iii) ε *is smaller than a convenient threshold* ε_0.

Then there exist constants A, B, α, β, *such that any motion* $(I(t), \varphi(t))$ *satisfies the estimate*

$$|I_k(t) - I_k(0)| < A\varepsilon^\alpha\,, \qquad k = 1, \ldots, n, \tag{3.9}$$

for

$$|t| \leqslant B \exp\left[\left(\frac{1}{\varepsilon}\right)^\beta\right]. \tag{3.10}$$

The proof of Nekhoroshev theorem can be found, in the original paper,

or in ref. [24, 33, 34]. In ref. [24, 34] it is shown that assumption ii) can be replaced by the assumption of having harmonic oscillators, *i.e.* $H_0 = \sum_{k=1}^{n} \omega_k I_k$, with nonresonant (« diophantine ») angular frequencies. The KAM theorem can aldo be extended to harmonic oscillators, although in a less direct way.

From the Nekhoroshev theorem it follows that any evolution in the actions of a nearly integrable Hamiltonian system requires extremely long times, longer than any negative power of ε. Up to these long times, as shown in ref. [33, 34], chaotic motions in the complement of KAM tori are possible, but are bounded, and, moreover, they involve only some of the degrees of freedom, the remaining ones being essentially uncoupled. More precisely, for each finite ε the action space $\mathscr{B}$ can be divided into a finite number of regions (according to the resonance properties of $\omega(I)$), and in each region one can introduce « adapted » canonical co-ordinates (I', φ'), which give the Hamiltonian the following form:

$$H'(I', \varphi', \varepsilon) = H^{(1)}(I'_1, \ldots, I'_n, \varphi'_1, \ldots, \varphi'_r, \varepsilon) + \exp\left[-\left(\frac{1}{\varepsilon}\right)^{\beta}\right] H^{(2)}(I', \varphi', \varepsilon)\,. \tag{3.11}$$

$H^{(1)}$ gives bounded but possibly chaotic motions for the first r degrees of freedom; $I'_{r+1}, \ldots, I'_r$ behave there as parameters. $H^{(2)}$ provides an interaction, which is sensible only on an exponentially long time scale.

4. – Applications to statistical mechanics.

The possible relevance of KAM theorem and Nekhoroshev theorem for statistical mechanics is still open. One would like to have the thresholds ε_0, as well as the exponents α and β, independent of n (a logarithmic dependence could also be accepted). Unfortunately, all of the present general proofs lead to a wild n-dependence: while α is independent of n [24, 34], instead β decreases at least as n^{-1}, and ε_0 as n^{-n}.

However, the real situation is certainly much better: for example, for a class of systems with short-range coupling, WAYNE [35] was able to construct a n-independent perturbation theory very close to the Nekhoroshev theorem, while some n-independent KAM-like results (*) have been very recently obtained

(*) One could see that it is not possible to have a KAM theorem as formulated in sect. **3**, for $n = \infty$ and finite specific energy. One must either consider systems with finite total energy (this is very appropriate, for example, for a classical black-body), or modify somehow the statement, for example by requiring that H_0 is not integrable, but has, say, a number of degrees of freedom of order n. The results here quoted refer to the first possibility.

by VITTOT [36] and by FROELICH *et al.* [37]. If one believes the numerical results, or the long-time stability of some many-particle astronomical structures, one should conclude that regular motions do not necessarily disappear for large n. Of course, according to the Nekhoroshev theorem, regular motions could be confined to a long but finite time scale.

This problem of the time scales was considered to be a highly relevant one at the turn of the century by BOLTZMANN [38], who tried to provide a classical dynamical explanation of the « freezing » of degrees of freedom, observed, for example, in the specific heats of polyatomic gases at ordinary temperatures, or in the black-body spectrum. The idea is as follows: consider, as a model example (*), a system of N perfectly smooth hard spheres in a smooth box, and assume the gas is initially in thermal equilibrium, the translational and rotational degrees of freedom having the same average energy $\frac{1}{2}kT$ per degree of freedom. Then, try to raise the gas temperature, by adiabatically compressing it. Clearly, in the absence of friction, no energy can flow from translational to rotational degrees of freedom, so the gas will appear in the experiment as having only $3N$ degrees of freedom, the remaining $3N$ being dynamically frozen. Now, let us introduce a very small friction. An energy flow from the translational to the rotational degrees of freedom is now possible, so that energy equipartition will eventually occur; of course, this phenomenon will require a typical time $\mathscr{T}$ which gets longer for smaller friction. This typical time must be compared with the time scale of our experiment: if $\mathscr{T}$ is shorter, then we will also see the contribution to the specific heat of the $3N$ rotational degrees of freedom (*i.e.* thermodynamic internal energy and mechanical energy of the molecules will coincide); instead, if $\mathscr{T}$ is much larger than the experimental time scale, then the rotational degrees of freedom will still appear to be frozen (thermodynamic and mechanical microscopic energy no longer coincide).

The basic idea of BOLTZMANN was that, in physical systems like polyatomic gases or a radiation cavity, different typical relaxation times were associated with different degrees of freedom, in order they be significantly involved into energy sharing. In particular, high-frequency degrees of freedom should be characterized (at ordinary temperatures) by relaxation times « of days or years », and thus should not be taken into consideration in ordinary experiments.

Unfortunately, this beautiful and ingenious idea of BOLTZMANN (supported also by RAYLEIGH and JEANS, at the 1912 Solvay Conference) was no longer investigated after the advent of quantum mechanics. Only recently was the Boltzmann conjecture seriously reconsidered [39-43], in connection with the Nekhoroshev theorem, where long time scales appear in the dynamics [42, 43].

(*) This example goes back to BOLTZMANN.

As explained in these references, the point of view of BOLTZMANN could also lead to the introduction of quantumlike features in classical statistical physics, and to a removal of the ultraviolet catastrophe.

Numerical evidence can be obtained for the existence of very long characteristic times in nearly integrable Hamiltonian systems. As an example, let us consider the one-dimensional model of a radiation cavity introduced by BOCCHIERI *et al.* [44] (see also ref. [45-47]). This model represents the electromagnetic field between two infinitely extended parallel mirrors; the coupling between the normal modes of the electromagnetic field is provided (quite artificially)

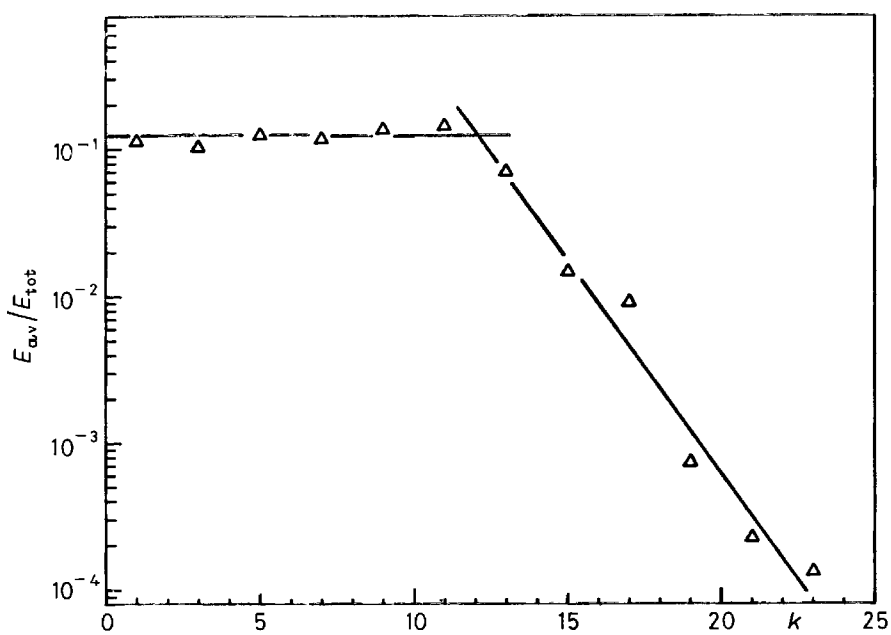

Fig. 6. – Energy distribution among normal modes for the one-dimensional model of a radiation cavity, after a sufficiently long time (from ref. [46]).

by a macroscopic uniformly charged plane, placed midway between the mirrors, which is free to move only parallel to the mirrors, and is subject, beside the electromagnetic forces, also to a mechanical nonlinear force. Because of the geometry of the model, the only relevant variables are the component of the vector potential orthogonal to the plane, say $A(x, t)$, and an abscissa z for the plane. If l denotes the half-distance between the mirrors, and c is the velocity of light, the normal modes of the field are given by

$$A(x, t) = 2c\sqrt{\frac{\pi}{l}} \sum_{k \text{ odd}} a_n(t) \cos \frac{\omega_k x}{c} \tag{4.1}$$

(because of the symmetry of the model, only odd modes occur), with $\omega_k =$

$= k\pi c/2l$. The equations of motions are then

$$
(4.2) \qquad \begin{cases} \ddot{a}_k + \omega_k^2 a_k^2 = 2\sqrt{\dfrac{\pi}{l}}\,\sigma\dot{z}\,, \\ \ddot{z} = F(z) - 2\sqrt{\dfrac{\pi}{l}}\,\dfrac{\sigma}{\mu}\sum\limits_{k\ \mathrm{odd}} \dot{a}_k\,, \end{cases}
$$

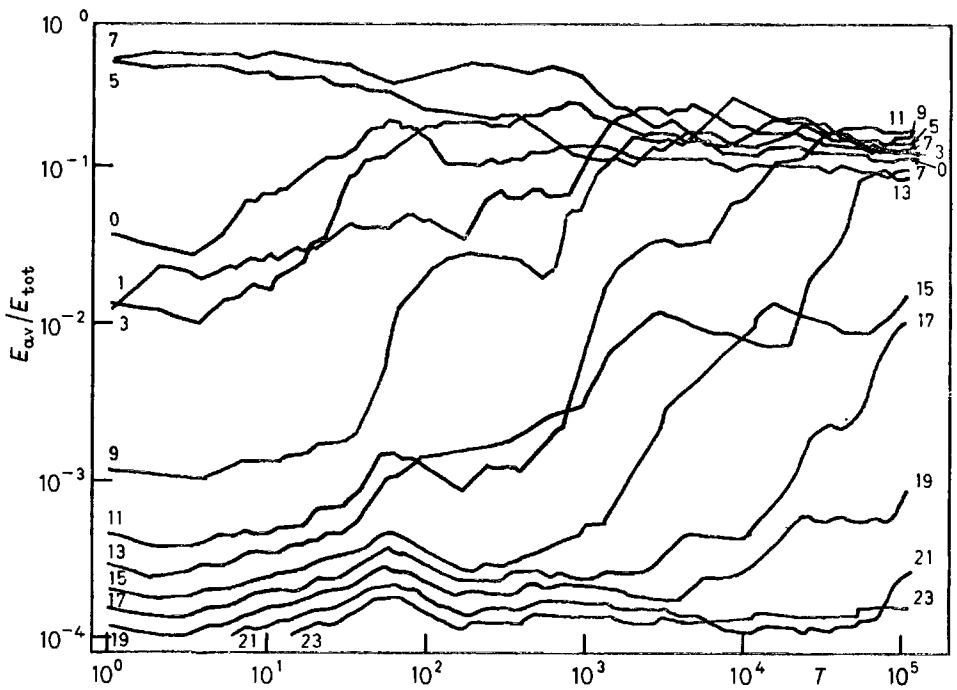

Fig. 7. – Average energies $\bar{E}_k(T)$ *vs.* T, for k up to 23, in the one-dimensional model of a radiation cavity (from ref. [46]).

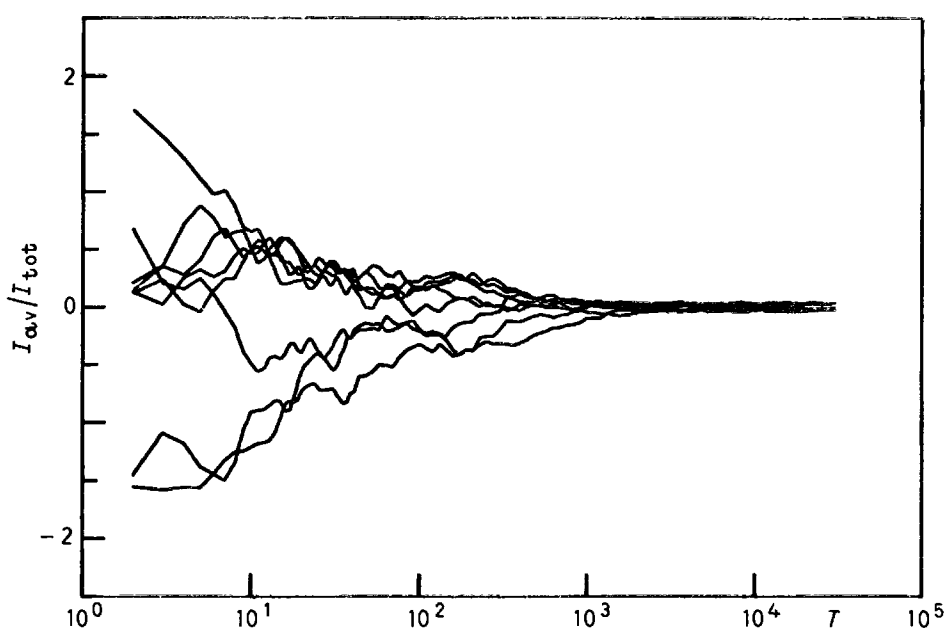

Fig. 8. – Average actions $\bar{I}_j(T)$, $j = 1, \ldots, 8$, for the 8-rotator model with $\varepsilon = 0.9$ (from ref. [48]).

where σ and μ are, respectively, the charge and mass of the plane per unit area, while $F(z) = -\alpha z^3$ is the mechanical nonlinear restoring force. For details on how to work with this system of infinitely many equations, see ref. [45, 46].

The result which is more interesting from our point of view is the following [46]: for suitable values of the parameters, if one gives initially all of the energy to a few normal modes of low frequency, then one observes a progressive energy sharing with other modes, which gives rise, after a certain time, to the energy spectrum represented in fig. 6, that is, to a *plateau*, followed by an exponential queue. After such a situation has been reached, the exponential cut-off appears to move slowly to the right, taking longer and longer times to advance towards the higher frequencies. The presence of time scales increasing rapidly with the frequency is clear in fig. 7, where the average energies of the normal modes $\bar{E}_k(T)$ are plotted *vs.* the averaging time T, on a logarithmic scale: clearly, modes of high frequency take longer and longer times to be in-

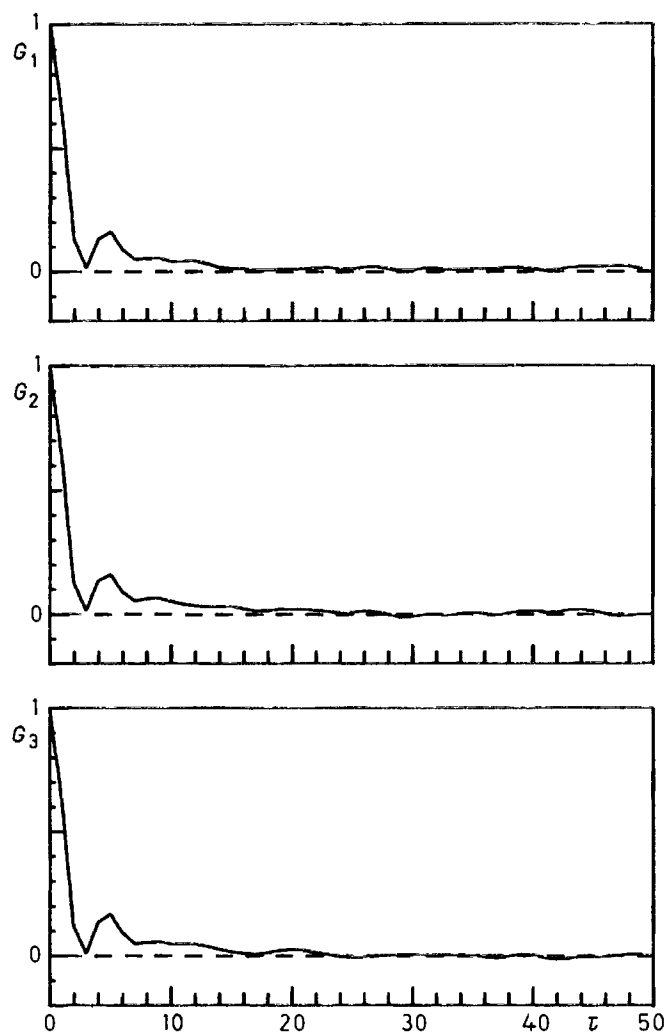

Fig. 9. – Correlation functions $G_j(r)$, for $j = 1$, 2 and 3, in the 8-rotator model, with the same conditions as in fig. 8 (from ref. [48]).

volved into the energy sharing; in fact, on the logarithmic scale, these characteristic times are roughly regularly spaced, indicating an exponential dependence of characteristic times on frequency.

The coexistence, for long times, of intense energy sharing among some degrees of freedom, with no significant interaction with other degrees of freedom, can be clearly visualized in a simple example, a chain of n weakly coupled rotators. The Hamiltonian is

$$H(I, \varphi) = \sum_{j=1}^{n} \frac{I_j^2}{2} - \varepsilon \sum_{j=1}^{n} \cos(\varphi_j - \varphi_{j-1}) , \qquad \varphi_0 \equiv \varphi_n ; \tag{4.3}$$

the main difference, with respect to the FPU model, or other nonlinear spring models, is that here the actions are local (not collective) variables, coupled by a finite-range interaction; notice also that here actions and angular velocities coincide. This model has been numerically studied in ref. [48], as an illustration of classical perturbation theory [49], which for this model is par-

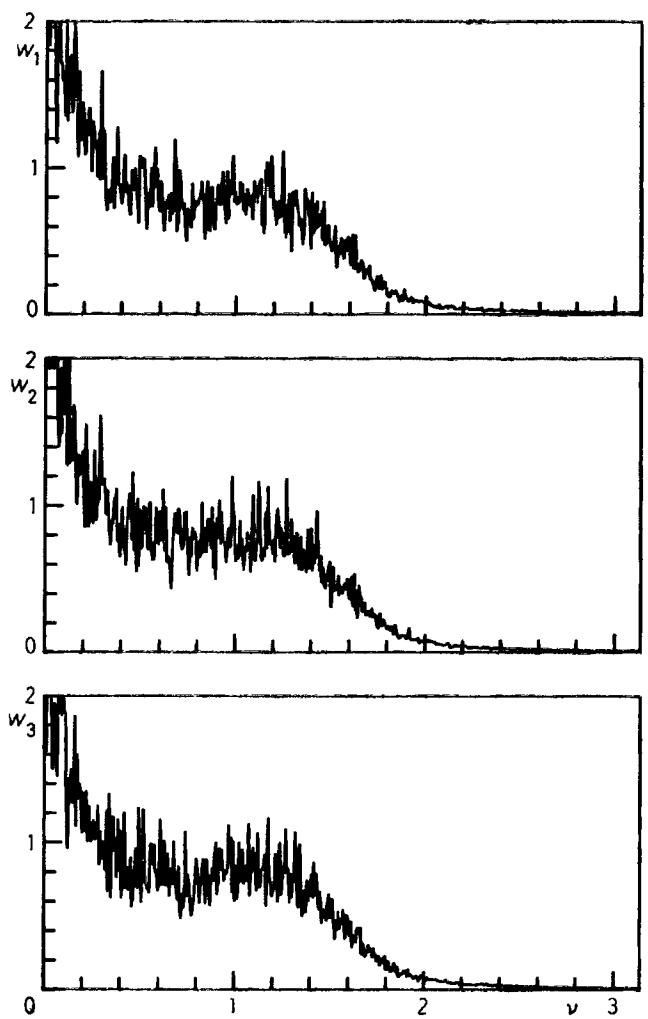

Fig. 10. – Power spectra $w_j(\nu)$, for $j = 1$, 2 and 3, in the 8-rotator model, with the same conditions as in fig. 8 and 9 (from ref. [48]).

ticularly simple. This dynamical system is also the simplest example of the class of systems for which WAYNE [35], as already remarked, was able to construct a n-independent perturbation theory.

We present here some results from ref. [48], which refer to a chain of 8 rotators, at specific energy $E/n = 1$. For ε of order one, the rotators are strongly coupled; no perturbation theory is possible, and the model seems to have all of the properties one needs for a statistical mechanical approach. Figure 8 represents the average actions

$$\bar{I}_j(T) = \frac{1}{T}\int_0^T I_j(t)\,\mathrm{d}t\,, \qquad j = 1, \ldots, n, \tag{4.4}$$

as functions of the averaging time T, for T up to the maximal integration time T_M. Here it is $\varepsilon = 0.9$. The existence of an intensive energy sharing among all the degrees of freedom is evident.

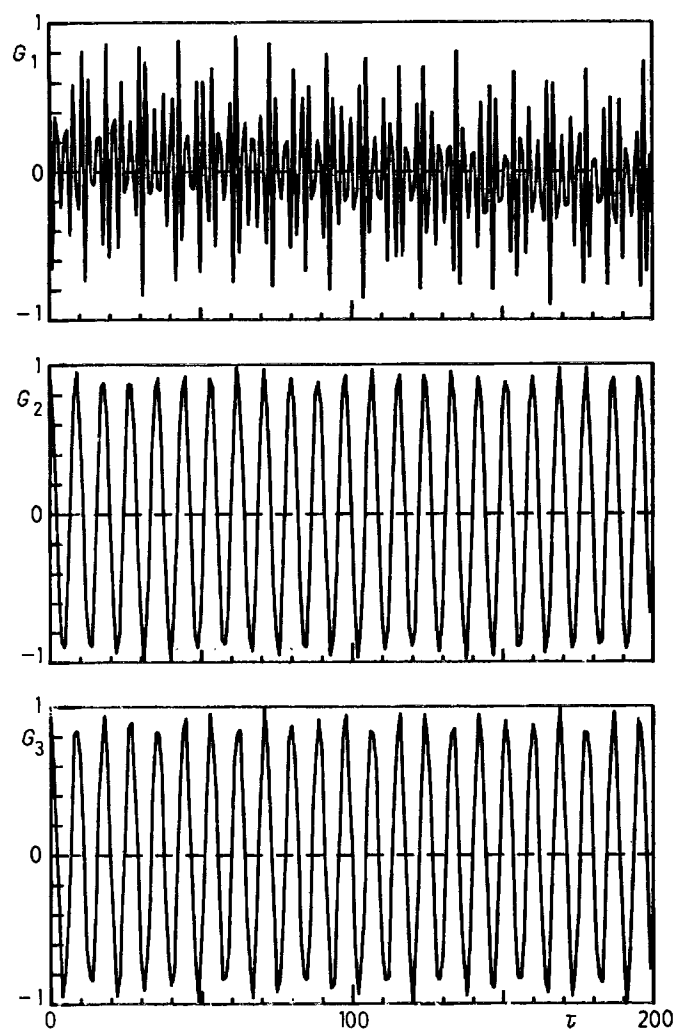

Fig. 11. – Correlation functions $G_j(\tau)$, for $j = 1$, 2 and 3, in the 8-rotator model, at lower $\varepsilon = 0.03$ (from ref. [48]).

The time scale for the energy sharing is quite small: for example, one can compute the autocorrelation functions

$$G_j(\tau) = \frac{\overline{I_j(t+\tau)I_j(t)} - [\bar{I}_j(T_M)]^2}{\sigma_j^2}, \qquad j = 1, \ldots, n, \tag{4.5}$$

where the first bar denotes averaging on t up to T_M, and σ_j denotes the variance of I_j. The behaviour of $G_j(\tau)$ for $j = 1, 2$ and 3 is illustrated in fig. 9; a very rapid correlation decay is evident. The irregular character of motions is also clear from the power spectrum $w_j(\nu)$, which is defined as follows:

$$\begin{cases} I_j(t) = \dfrac{1}{\sqrt{T_M}} \sum_k \hat{I}_j(k) \exp\left[\dfrac{2\pi i k t}{T_M}\right], \\ w_j(\nu) = |\hat{I}_j(k)|^2, \qquad \nu = \dfrac{2\pi k}{T_M}. \end{cases} \tag{4.6}$$

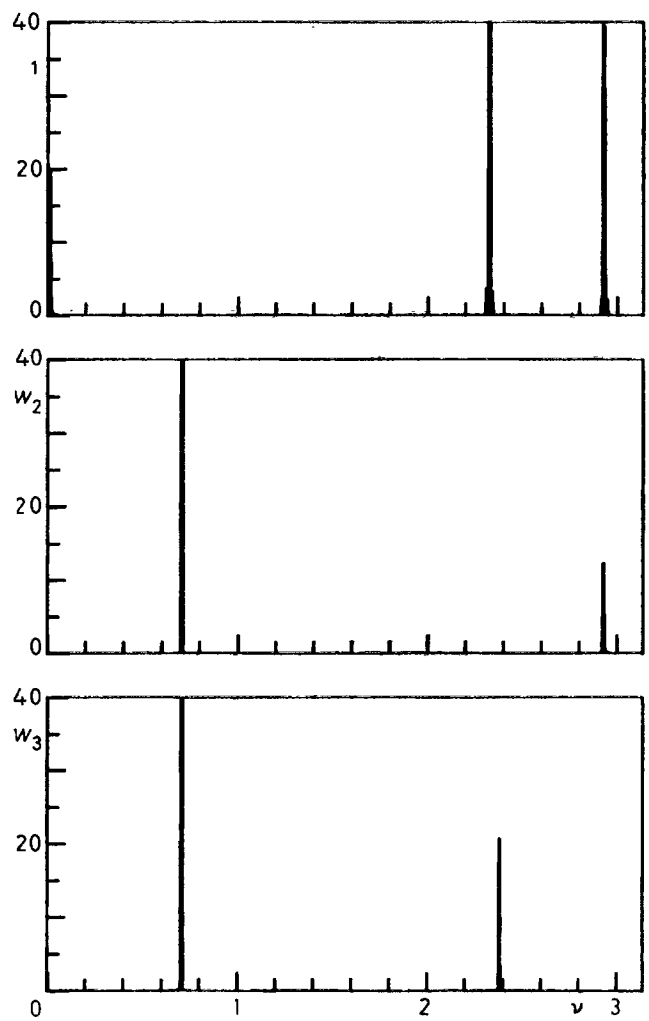

Fig. 12. – Power spectra $w_j(\nu)$, for $j = 1$, 2 and 3, in the 8-rotator model, with the same conditions as in fig. 11 (from ref. [48]).

Figure 10 shows that, at this high value of ε, the power spectrum has the form of a more or less continuous band (*).

For small ε, there are essentially two possibilities (which are very well understood within classical perturbation theory). The first one occurs when there are no « resonances »; for the present model this means that no neighbouring rotators turn with the same angular velocity, within a tolerance of order $\sqrt{\varepsilon}$. In this case the motion is highly ordered: the actions are almost constant, and their small fluctuations, which turn out to be of order ε, exhibit a long-time correlation. This behaviour can be seen in fig. 11 and 12, where $G_j(\tau)$ and, respectively, $w_j(\nu)$ are reported, for $\varepsilon = 0.03$. The difference with respect to the previous situation is remarkable; clearly, no randomness is present, and no statistical approach seems appropriate.

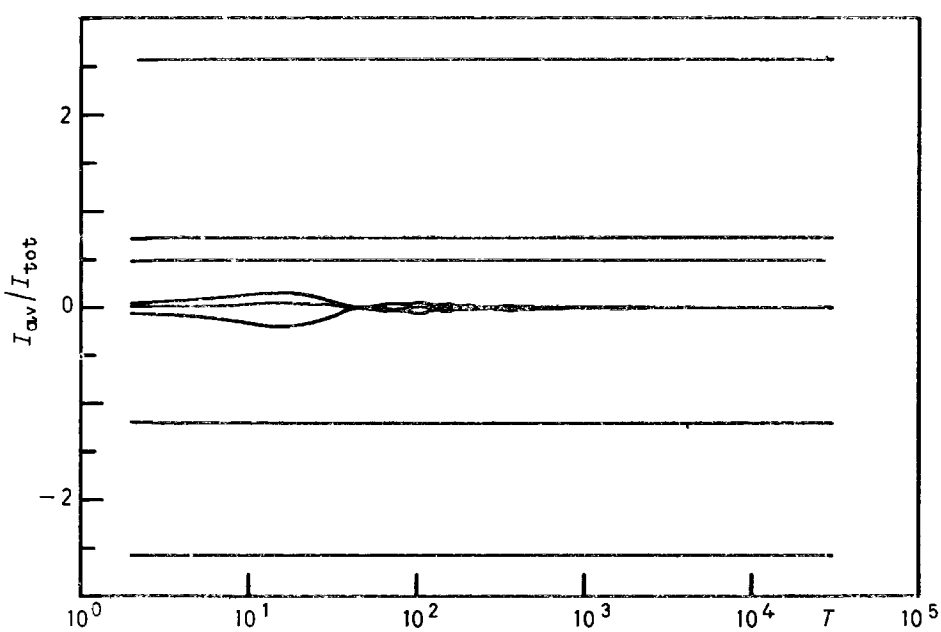

Fig. 13. – Average actions $\bar{I}_j(T)$, $j = 1, \ldots, 8$, for the 8-rotator model at $\varepsilon = 0.03$, with 3 strongly interacting rotators and 5 almost free ones (from ref. [48]).

A second possibility is that, within the chain, there is a « droplet » of rotators turning with close frequencies (within $\simeq \sqrt{\varepsilon}$). In this case, for no matter how small ε, rotators within the droplet behave as strongly coupled ones, so that chaotic motions can occur. However, they remain essentially uncoupled from the rest of the chain, giving rise to the situation illustrated by fig. 13-15, which show average actions, correlations and, respectively, power spectra of rotators 1, 2 and 3, which are initially given close angular velocities and exhibit chaotic motions, and rotators 4 and 5, which at the same time turn

(*) A smoothing procedure has been applied.

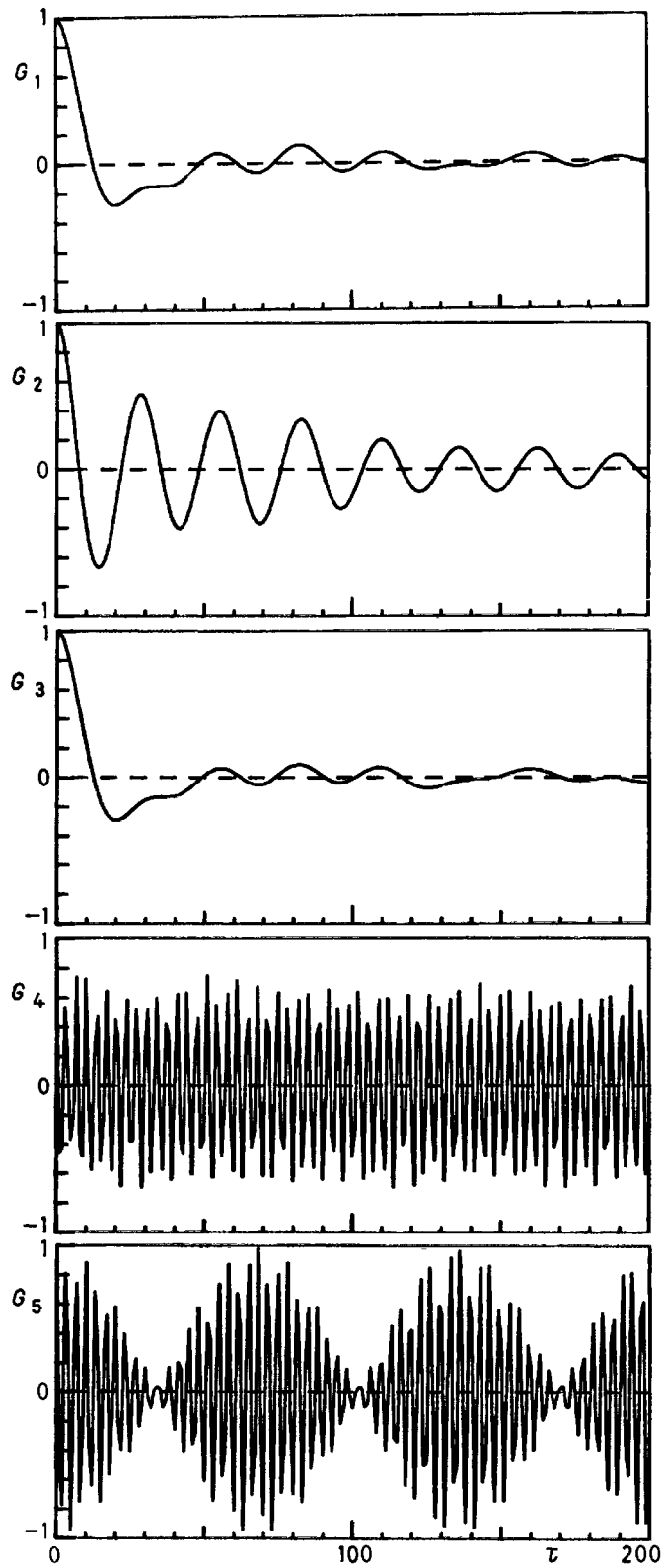

Fig. 14. – Correlation functions $G_j(\tau)$, $j = 1, \ldots, 5$ for the 8-rotator model, with the same conditions as in fig. 13 (from ref. [48]).

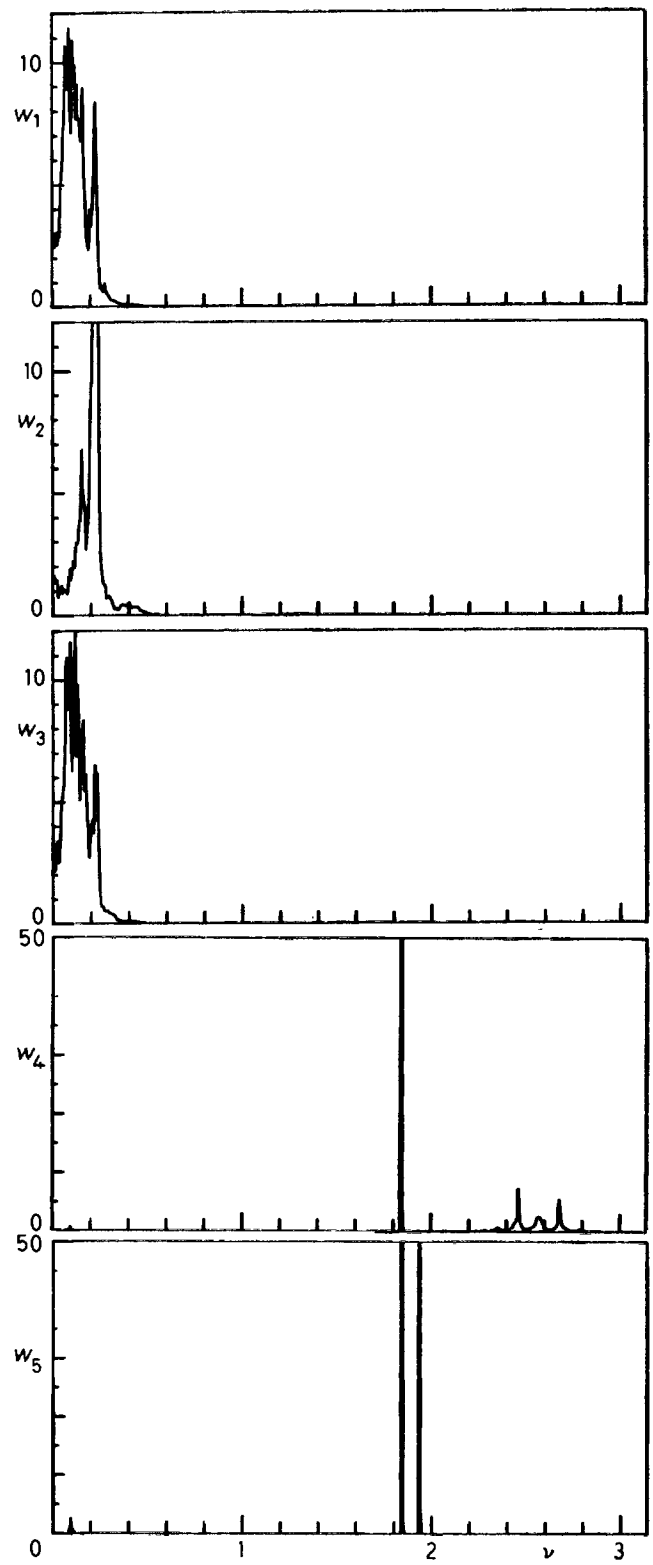

Fig. 15. – Power spectra $w_j(\nu)$, $j = 1, \ldots, 5$, for the 8-rotator model, with the same conditions as in fig. 13 and 14 (from ref. [48]).

regularly (*). What we learn from this example is that chaos and order are not always global properties of a dynamical system, but can also refer to subsets of dynamical variables, and coexist for very long times. This behaviour is in agreement with the Nekhoroshev theorem: indeed, in this simple model, because of the short-range interaction between actions, the local chaotic motions of that theorem are localized in the chain. A numerical indication has also been obtained that on longer time scales, according to the Nekhoroshev theorem, the situation evolves slowly (something like the growing or disappearing of chaotic droplets can occur). However, the precise behaviour is not yet clear.

I close this last section by stressing once more the basic point of this discussion concerning the physical interpretation of ordered motions at low energy, the problem of the time scales associated with the energy sharing among the degres of freedom of different frequency. This is a type of problem which can be studied by molecular-dynamics simulation; in particular, very interesting results have been reported by HOLIAN, in his contribution to this shool [50]. The expression HOLIAN proposes for relaxation times is something like $\exp[a\omega/E]$, with $E = kT$: such a behaviour, if confirmed in general for weakly interacting systems, could support Boltzmann's conjecture, as for high frequencies and low temperatures one easily obtains times of « days or years », as BOLTZMANN claimed. Let me also point out that the constant a inserted above in the exponential for dimensional reasons is an action: this could mean that each classical model has a typical action, and that significant energy exchanges happen (in a reasonable time) only if $kT > a\omega$.

REFERENCES

[1] E. FERMI, J. PASTA and S. ULAM: Los Alamos Report No. LA-1940 (1955), later published in E. FERMI: *Collected Papers* (Chicago, Ill., 1965); *Lect. Appl. Math.*, **15**, 143 (1974).

[2] V. I. ARNOLD and A. AVEZ: *Ergodic Problems of Classical Mechanics* (Benjamin, New York, N. Y., 1968).

[3] I. P. CORNFELD, S. V. FOMIN and YA. G. SINAI: *Ergordic Theory* (Springer, New York, N. Y., 1982).

[4] R. H. G. HELLEMAN: in *Fundamental Problems in Statistical Mechanics V*, edited by E. G. D. COHEN (North-Holland, Amsterdam, 1980), p. 420.

[5] A. J. LICHTEMBERG and M. A. LIEBERMAN: *Applications in Mathematical Science*, No. 38 (Springer, Berlin, 1982).

(*) Elementary scaling predicts that the width of the spectrum's continuous band must be proportional to $\sqrt{\varepsilon}$; this explains the difference between fig. 15 and fig. 10. Correspondingly, correlation times increase as $1/\sqrt{\varepsilon}$, and the amplitude of chaotic motions of the strongly interacting rotators is proportional to $\sqrt{\varepsilon}$. Here it was $\varepsilon = 0.03$.

[6] G. Iooss, R. H. G. Helleman and R. Stora, Editors: *Chaotic Behavior of Deterministic Systems, Les Houches Summer School 1981* (North-Holland, Amsterdam, 1983).
[7] J.-P. Eckman and D. Ruelle: *Rev. Mod. Phys.*, **57**, 617 (1985).
[8] H. Bai-Lin: *Chaos* (World Scientific, Singapore, 1984).
[9] J. L. Tuck: Los Alamos Report No. LA-3990 (1968), published in *Adv. Math.*, **9**, 399 (1972).
[10] F. M. Izrailev and B. V. Chirikov: *Sov. Phys. Dokl.*, **11**, 30 (1966).
[11] B. V. Chirikov, F. M. Izrailev and V. A. Tayursky: *Comput. Phys. Commun.*, **5**, 11 (1973).
[12] P. Bocchieri, A. Scotti, B. Bearzi and A. Loinger: *Phys. Rev. A*, **2**, 2013 (1970).
[13] M. C. Carotta, C. Ferrario, G. Galgani and G. Lo Vecchio: *Phys. Rev. A*, **17**, 786 (1978).
[14] L. Galgani and G. Lo Vecchio: *Nuovo Cimento B*, **52**, 1 (1979).
[15] B. Callegari, M. C. Carotta, C. Ferrario, G. Lo Vecchio and G. Galgani: *Nuovo Cimento B*, **54**, 463 (1979).
[16] E. Diana, L. Galgani, M. Casartelli, G. Casati and A. Scotti: *Teor. Mat. Fiz.*, **29**, 213 (1976) (English translation: *Theor. Math. Phys.*, **29**, 1022 (1976)).
[17] M. Casartelli, E. Diana, L. Galgani and A. Scotti: *Phys. Rev. A*, **13**, 1921 (1976).
[18] H. Hirooka and N. Saito: *J. Phys. Soc. Jpn.*, **26**, 624 (1968).
[19] P. Bocchieri and F. Valz-Gris: *Phys. Rev. A*, **9**, 1252 (1974).
[20] G. Benettin, G. Lo Vecchio and A. Tenenbaum: *Phys. Rev. A*, **9**, 1252 (1979).
[21] G. Benettin and A. Tenenbaum: *Phys. Rev. A*, **28**, 3020 (1983).
[22] R. Livi, M. Pettini, S. Ruffo, M. Sparpaglione and A. Vulpiani: *Phys. Rev. A*, **31**, 1039 (1985).
[23] R. Livi, M. Pettini, S. Ruffo and A. Vulpiani: *Phys. Rev. A*, **31**, 2740 (1985).
[24] G. Gallavotti: lectures given at *The 1984 Les Houches Summer School*, to be published.
[25] A. N. Kolmogorov: *Dokl. Akad. Nauk SSSR*, **98**, 527 (1954); English translation in G. Casati and G. Ford, Editors: *Lectures Notes in Physics*, No. 93 (Springer-Verlag, Berlin, 1979). Reprinted also in ref. [8].
[26] V. I. Arnold: *Usp. Mat. Nauk*, **18**, 13 (1963) (English translation: *Russ. Math. Surv.*, **18**, 9 (1963)); *Usp. Mat. Nauk*, **18**, 91 (1963) (English translation: *Russ. Math. Surv.*, **18**, 85 (1963)).
[27] J. Moser: *Nachr. Akad. Wiss. Gottingen, Math.-Phys. Kl.*, **2**, 1 (1962).
[28] N. N. Nekhoroshev: *Usp. Mat. Nauk*, **32**, 5 (1977) (English translation: *Russ. Math. Surv.*, **32**, 1 (1977)); *Trudy Sem. Petrows.*, No. 5, 5 (1979).
[29] H. Poincaré: *Les méthodes nouvelles de la méchanique céleste*, Vol. **3** (Gauthier-Villars, Paris, 1899).
[30] J. Poeschel: *Commun. Pure Appl. Math.*, **35**, 653 (1982); *Celest. Mech.*, **28**, 133 (1982).
[31] L. Chierchia and G. Gallavotti: *Nuovo Cimento B*, **67**, 277 (1982).
[32] V. I. Arnold: *Dokl. Akad. Nauk SSSR*, **156**, 9 (1964) (English translation: *Sov. Math. Dokl.*, **6**, 581 (1964)).
[33] G. Benettin, L. Galgani and A. Giorgilli: *Celest. Mech.*, **37**, 1 (1985).
[34] G. Benettin and G. Gallavotti: *Exponential estimates for the stability times in nearly integrable Hamiltonian systems*, to appear in *J. Stat. Phys.*
[35] C. E. Wayne: *Commun. Math. Phys.*, **104**, 21 (1986).
[36] M. Vittot: *Théorème* KAM *et grand nombres de degrés de liberté*, preprint 1985.

[37] J. FROELICH, T. SPENCER and C. E. WAYNE: *The existence of an invariant torus in a Hamiltonian system with infinitely many degrees of freedom*, preprint 1985.
[38] L. BOLTZMANN: *Nature (London)*, **51**, 413 (1895).
[39] L. GALGANI: *Nuovo Cimento B*, **62**, 306 (1981).
[40] L. GALGANI: *Lett. Nuovo Cimento*, **31**, 65 (1981).
[41] L. GALGANI and G. BENETTIN: *Lett. Nuovo Cimento*, **35**, 93 (1982).
[42] G. BENETTIN, L. GALGANI and A. GIORGILLI: *Nature (London)*, **311**, 444 (1984).
[43] G. BENETTIN, L. GALGANI and A. GIORGILLI: *On the persistence of ordered motions in Hamiltonian systems and the problem of energy partition*, to appear in *Dynamical Systems: a Renewal of Mechanicism*, edited by S. DINER and G. LOCHAK (Springer-Verlag, Berlin).
[44] P. BOCCHIERI, A. CROTTI and A. LOINGER: *Lett. Nuovo Cimento*, **4**, 341 (1972).
[45] G. CASATI, I. GUARNERI and F. VALZ-GRIS: *Phys. Rev. A*, **16**, 1273 (1977).
[46] G. BENETTIN and L. GALGANI: *J. Stat. Phys.*, **27**, 153 (1982).
[47] G. CASATI, I. GUARNERI and F. VALZ-GRIS: *J. Stat. Phys.*, **30**, 195 (1983).
[48] G. BENETTIN, L. GALGANI and A. GIORGILLI: *Nuovo Cimento B*, **89**, 103 (1985).
[49] G. BENETTIN, L. GALGANI and A. GIORGILLI: *Nuovo Cimento B*, **89**, 89 (1985).
[50] B. L. HOLIAN: this volume, p. 241.

Part II

EQUILIBRIUM MOLECULAR DYNAMICS

Practical Algorithms for Dynamic Simulations.

H. J. C. BERENDSEN and W. F. VAN GUNSTEREN

Laboratory of Physical Chemistry, University of Groningen
Nijenborgh 16 - 9747 *AG Groningen, The Netherlands*

1. – Introduction.

Classical molecular dynamics solves Hamilton's equation of motion for a set of (generalized) co-ordinates q_i and momenta p_i:

$$\dot{q}_i = \frac{\partial H}{\partial p_i} \text{ and } \dot{p}_i = -\frac{\partial H}{\partial q_i} . \tag{1.1}$$

In many cases the potential is conservative and Cartesian co-ordinates x_i and velocities $v_i = p_i/m_i$ are used, for which the Hamiltonian reads

$$H(\{p_i, x_i\}) = \sum_i p_i^2/2m_i + V(\{x_i\}) . \tag{1.2}$$

We now obtain Newton's equations of motion:

$$\dot{x}_i = v_i , \tag{1.3}$$

$$m_i \dot{v}_i = F_i , \tag{1.4}$$

where F_i, for conservative force fields, is a function of the co-ordinates only:

$$F_i = -\frac{\partial}{\partial x_i} V(\{x_i\}) . \tag{1.5}$$

Note that the computation of velocities in this case is not essential, because eqs. (1.3), (1.4) are equivalent to a set of second-order differential equations

$$m_i \ddot{x}_i = F_i(\{x_i\}) . \tag{1.6}$$

The first question is how the *forces* are calculated. This is quite straight-

forward, unless long-range interactions or nonpair-additive potentials are used. We will consider these questions in sect. **2**.

The next question concerns *algorithms* to solve eqs. (1.3), (1.4) numerically in an efficient and accurate way. There are many standard methods, but only a few have survived in practice. The details will be treated in sect. **3**.

In many cases (particularly when covalently bonded molecules are considered) some of the degrees of freedom are treated as *constraints*. This poses various problems that will be treated separately in this school by RYCKAERT. The consequences for algorithms will be considered briefly in sect. **4**.

Modifications of the equations of motion are often considered, especially when nonequilibrium systems are treated which are driven by external forces or coupled to external degrees of freedom. Also when it is desired to introduce nonphysical constraints in order keep certain properties of the system constant (temperature, pressure, velocity gradients), modified Hamiltonians are used. These cases will also be considered in detail in this school by others. Only a special case of coupling to an external bath will be treated in sect. **5**.

When it is desired to reduce the number of degrees of freedom in the system because the details of the behaviour of certain particles (numbered α) are not relevant, these particles can be omitted from the detailed simulation. However, the forces they exert on the other particles (numbered i) must be represented as faithfully as possible. This means that correlations of such forces with positions and velocities of particles i must be incorporated, while uncorrelated contributions can be represented by random forces. We are now in the realm of *stochastic dynamics*. If the potential field $V(\{x_i, x_\alpha\})$ is averaged over an equilibrium ensemble of α-particles, a potential of mean force is obtained:

$$\langle V(\{x_i, x_\alpha\})\rangle_\alpha = V_m(\{x_i\}) \,. \tag{1.7}$$

This really is a free energy with respect to the α-particles. We shall not consider here how such potentials of mean force can be obtained. They modify the potential functions, but have no influence on the algorithm. But the velocity-correlated and random parts of the forces modify the equations of motion. Because of the velocity dependence the forces are not conservative any longer, and the equations of motion must contain the velocities explicitly. The random forces are related to the velocity-dependent friction forces by the second fluctuation dissipation theorem.

The simplest case is a random force with white-noise character, uncorrelated between the various degrees of freedom, corresponding to a friction force proportional to the velocity of the same particle to which the force applies:

$$x_i = \dot{v}_i \,, \tag{1.8}$$

$$m_i \dot{v}_i = F_i(\{x_i\}) - m_i \gamma_i v_i + R_i(t) \,, \tag{1.9}$$

where $R_i(t)$ is a zero-mean Gaussian-distributed random force with properties

$$\begin{cases} \langle R_i(0)\, R_j(t)\rangle = 2m_i\gamma_i kT\,\delta(t)\,\delta_{ij}\,, \\ \langle v_i(0)\, R_j(t)\rangle = 0 \qquad\qquad \text{for } t\geqslant 0\,. \end{cases} \tag{1.10}$$

This a called the simple Langevin equation. In sect. **6** we will consider efficient algorithms to solve this equation numerically.

Considering algorithms choices must be made. The choices made here are based on our experience and may not always coincide with the preference of others. We have placed simplicity, efficiency, accuracy, stability and reliability high on the list of priorities. An important additional consideration is that only algorithms should be chosen that allow vectorization on modern supercomputers as the Cray or Cyber-205. Such algorithms will often (but not always) be suitable for computers with highly parallel architecture that will undoubtedly emerge as important future tools for large-scale simulations. The main consideration for vectorizable algorithms is that a large number of similar operations can be carried out on long vector operands, before the results of these operations are needed in another operation. This may often require vector storage space that would not be needed in a sequential machine where certain intermediate variables can be kept local in an inner loop of a repetitive operation. The operands should preferentially be of such a kind that they can be stored contiguously in memory, *i.e.* operations on vectors should be sequential without requiring computations on their indices. Such considerations are always important when an algorithm is coded, but the possibility to implement such requirements often depends also on the choice of algorithm.

2. – The computation of forces.

It is not the place here to consider details of force calculations and we shall only give a few general remarks. In most cases forces are derived from pair interactions and the problem lies in the reduction of the number of pairs to consider. For short-ranged interactions a simple cut-off can be used at a radius that does not incorporate more than some hundred neighbours. The use of a cut-off radius produces truncation errors that manifest themselves as noise in the forces and extra fluctuation and/or drift in the total energy of the system. One may also modify the potential $V(r)$ in such a way that both potential and force vanish at the cut-off radius [1, 2]

$$V_{\text{mod}}(r) = V(r) - V(r_c) - \left(\frac{\partial V}{\partial r}\right)_{r_c}(r - r_c)\,. \tag{2.1}$$

Here V_{mod} is the modified potential and r_c is the cut-off radius. The integration algorithm will now be more precise, but we are really simulating a system with interactions that differ from what we intended. The effect of such a perturbation of the potential can be evaluated by perturbation methods.

Instead of using the modification mentioned above (which has the disadvantage that the derivative of the force is discontinuous at the cut-off), one may also introduce a smooth decay to zero by multiplying the potential with a smooth switching function that reduces the potential and its derivatives to zero at r_c. Again, the physics of the system is modified and one may be misled by the accurate functioning of the integration algorithm and thus not be aware of the errors in the results. We prefer to use a simple cut-off, because errors are then immediately apparent in the noise or drift the algorithm produces and one is at least warned.

The method to search for neighbours depends on the computer one uses [3]. In vector computers one can go quickly over all possible pairs, but, if a force calculation is to be carried out over a small fraction of all neighbours, this calculation becomes inefficient. The Cyber-205 has the possibility to control vector computations by a logical bitvector, but, if this control vector is sparse, efficiency becomes poor because the pipeline processor needs a clock cycle whether an operation is suppressed or not. One can then compress the vector first, producing a new vector that is operated on in full. With a very large number of particles it is more efficient to produce a neighbour list once every so many steps (10 to 20) and use this list for force calculation for all steps in between updates of the neighbour list. The neighbour list must at least contain all particles within the cut-off radius. This can automatically be taken care of if an interaction range for the construction of the neighbour list is chosen somewhat larger than r_c (*e.g.*, 10% larger), while in every step the maximum particle displacement is monitored. As soon as this maximum displacement exceeds the difference between the range used for the neighbour list and r_c, the list is updated.

When interactions are intrinsically long range, the use of a neighbour list becomes impractical. There are two possible solutions:

i) One uses infinite-summation methods, such as the Ewald summation [4, 5], or Fourier methods [6]. Especially the latter are quite efficient, but also complicated.

ii) One uses two interaction ranges, a short one and a long one. While making up the neighbour list for the short range, the forces due to particles in the shell between the short and the long range are evaluated and stored per particle. This requires only one extra storage vector. This long-range part is kept unchanged between updates of the neighbour list.

The long-range interaction can be refined more if we not only store the force, but also its derivatives. When the central particle moves, it experiences

a changing field that can then be calculated. The disadvantage of that method is that not only one storage vector ($3N$ words) but an extra $5N$ words are required for the derivative tensor. The advantage is that rotations of central dipolar particles (which may be significant between updates) are treated with more accuracy.

Complications arise when forces are not pair-additive. For example, if 3-body forces are included, the number of triples becomes very large and a small cut-off radius must be used for these forces. Another example of nonpair-additive forces is the inclusion of atomic or molecular polarizability in the potential-energy function. The induced dipoles depend on the field produced by themselves and an iterative procedure is necessary. Alternatively, the induced dipoles can be found by matrix inversion methods, but for large systems this is not feasible. In a dynamics simulation the iterative scheme is quite efficient because the configuration at the previous step is already very close to the solution. We found, using a polarizable model for water, that it suffices to include one extra iteration per step, thereby roughly doubling the time to compute the forces [7].

3. – Algorithms for molecular dynamics.

3·1. *Integration methods.* – Numerical methods to solve sets of differential equations can be found in almost any general textbook on applied mathematics [8, 9] and a number of more specialized books [10-12]. All methods are based on finite differences and solve the equations step by step in time. Often the step size is taken to be constant. One requirement for molecular dynamics immediately invalidates a number of methods. The computation of the force is extremely laborious compared to any manipulation involved in updating the variables to take one step forward in time. This means that any method that involves more than one force evaluation per step cannot be a method of choice. This rules out the well-known Runge-Kutta method and its variants, requiring 4 force evaluations per step in its usual version. Another requirement is that an algorithm should behave well for the type of force that one encounters in molecular dynamics. Normally molecular dynamics produces a trajectory in the valley regions of a potential field that has a very mountainous character. In the valley regions the second derivatives of the potential with respect to most co-ordinates are positive (although the small and negative ones are the most interesting ones to open new vistas!). This means that the second spatial derivatives of the potential have a systematic sign and the algorithm should at least incorporate the proper treatment of the first derivative of the forces to avoid accumulating errors and instability of the solution. This means that the *order* of the algorithm, defined as the highest order of the time step h included in the equation for the

solution of the co-ordinates, should be at least 3. Higher orders correspond to higher than first derivatives of the forces. It is expected that these have a more erratic and nonsystematic behaviour. In complex systems that also involve cut-off errors in the forces, it is generally not very advantageous to go beyond third or fourth order.

In order to judge the algorithms for our purpose, let us try them out on a very simple case: the harmonic oscillator

$$x'' = -x \tag{3.1}$$

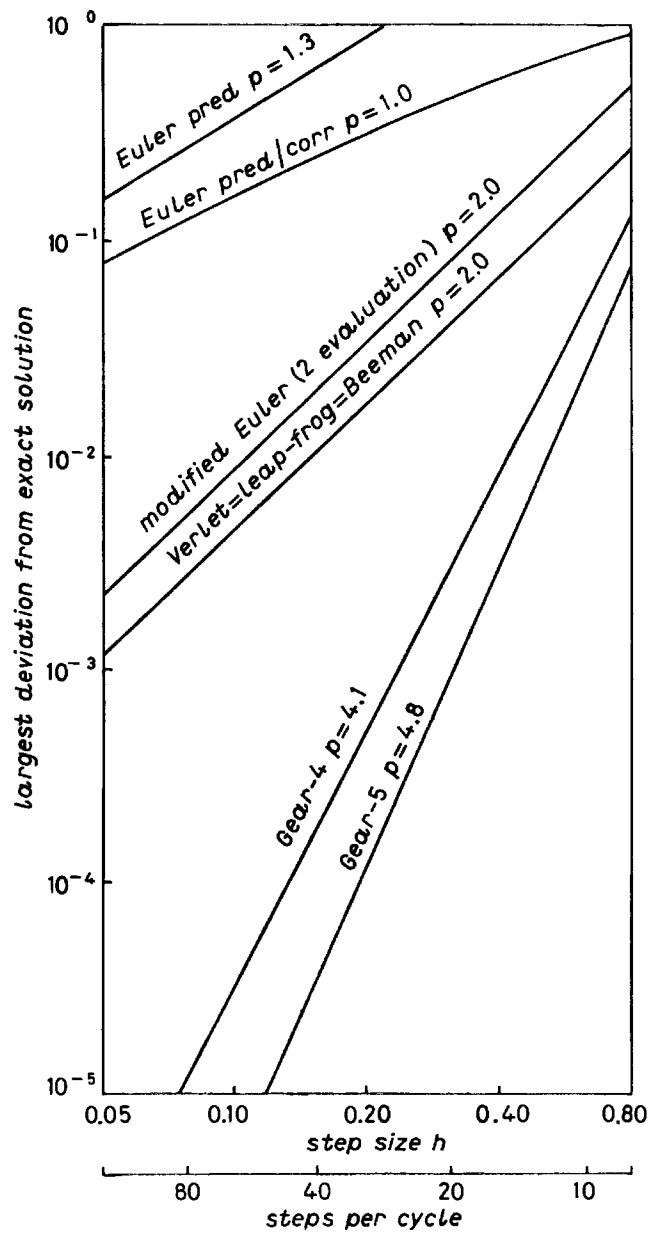

Fig. 1. – Largest deviation in x from exact solution of harmonic oscillator during first two periods of the oscillation, as a function of step size. The oscillator amplitude is 1 and the oscillator period is 2π. The quantity p denotes the « apparent order » defined as the slope of the curves on a double logarithmic scale.

or, in terms of first-order differential equations,

$$x' = v\,, \qquad v' = -x\,. \tag{3.2}$$

Primes will denote derivatives with time. We shall choose initial conditions

$$x_0 = 1\,, \qquad v_0 = 0\,, \tag{3.3}$$

which correspond to the exact solution

$$x(t) = \cos t\,, \qquad v(t) = -\sin t \tag{3.4}$$

representing an oscillation with period 2π.

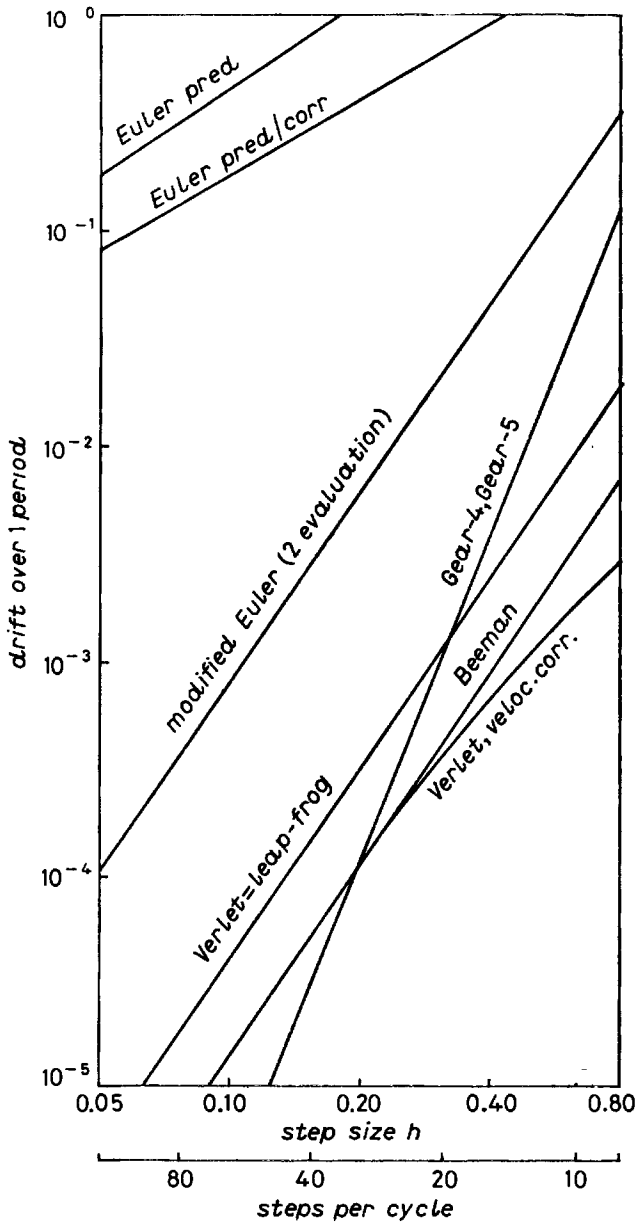

Fig. 2. – Drift in the « energy » $x^2 + v^2$ of the harmonic oscillator, per period of oscillation. The « conserved » value of this energy is 1.

We shall carry out simulations over 2 cycles ($t = 4\pi$) and record, as a measure of *accuracy*, the largest deviation of x from the exact solution (fig. 1). We shall also judge the behaviour of the solution by monitoring the quantity

$$E(t) = x^2(t) + v^2(t) \tag{3.5}$$

that we will call the « energy » and that should be a conserved quantity. In real MD simulations we do not have the opportunity to compare with the exact trajectory, but we can monitor the total energy that should be conserved. We shall analyse $E(t)$ by a linear regression, performing a least-squares fit of $E(t)$ to a straight line. The slope, expressed as the change per cycle (*i.e.*

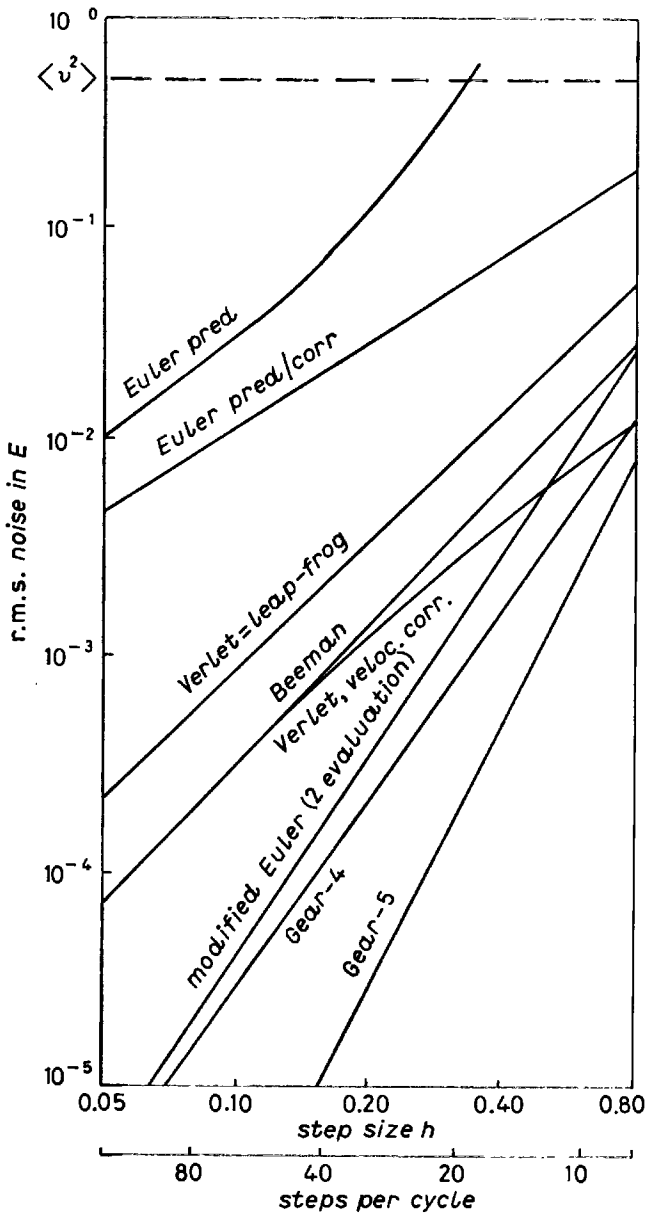

Fig. 3. – Noise or r.m.s. deviation from the linear regression line of the « energy » $x^2 + v^2$ of the harmonic oscillator.

per time interval of 2π), will be called the *drift* (fig. 2), and the r.m.s. deviation from the regression line the *noise* (fig. 3).

The general form of the second-order differential equation is

$$x''(t) = f(x)\,, \tag{3.6}$$

$x(t)$ represents a vector of all $3N$ co-ordinates, but for clarity we omit the vector notation. We shall use *step-by-step* methods with step size h:

$$t_n = nh\,. \tag{3.7}$$

There are two types of methods:

i) *Open* or *predictor* methods that predict x_{n+1} exclusively in terms of quantities already known or found in previous steps (we assume that we have found a way to start). This will include forces up to and including $f_n = f(x_n)$.

ii) *Closed* or *predictor-corrector* methods that first predict a value y_{n+1} with a predictor formula and then use $f(y_{n+1})$ to correct the predicted value y_{n+1} to obtain x_{n+1}. The prediction-correction procedure can be repeated and iterated until the correction becomes as small as desired, but such an iteration requires more than one force evaluation per step and is thus discarded for our purpose. Predictor-corrector methods with only one force evaluation per step are often referred to as *Gear algorithms*, named for GEAR [12] who developed this method systematically.

3·2. *Euler's methods.* – The simplest and most straightforward but very inaccurate method is a Taylor expansion for x and v:

$$x_{n+1} = x_n + hv_n + \tfrac{1}{2}h^2 f_n\,, \tag{3.8}$$

$$v_{n+1} = v_n + hf_n\,, \tag{3.9}$$

where $f_n = f(x_n)$.

The behaviour of this method (fig. 1-3: Euler pred) is extremely bad. It does not contain the force derivatives!

A better method is to evaluate the force again at x_{n+1} and then recalculate (3.8), (3.9) using the average of the forces f_n and $f(x_{n+1})$. This is the *modified Euler* method, which really is a predictor-corrector method:

$$\text{pred:} \quad y_{n+1} = x_n + hv_n + \tfrac{1}{2}h^2 f_n\,, \tag{3.10}$$

$$f^* = \tfrac{1}{2}\big(f_n + f(y_{n+1})\big)\,; \tag{3.11}$$

$$\text{corr:} \quad x_{n+1} = x_n + hv_n + \tfrac{1}{2}h^2 f^* , \tag{3.12}$$

$$= y_{n+1} + \tfrac{1}{4}\big(f(y_{n+1}) - f_n\big) , \tag{3.13}$$

$$v_{n+1} = v_n + hf^* ; \tag{3.14}$$

$$\text{force:} \quad f_{n+1} = f(x_{n+1}) . \tag{3.15}$$

This method behaves much better (fig. 1-3: modified Euler) but requires two force evaluations per step. If we reduce the number of force evaluations to one by omitting eq. (3.15) and putting

$$f_{n+1} = f(y_{n+1}) , \tag{3.16}$$

then the behaviour again becomes very bad (see fig. 1-3: Euler pred/corr).

3·3. *Gear algorithms* [12, 13]. – For a systematic notation of general predictor-corrector algorithms we will now turn to a vector notation of the quantities kept and updated per step. There are a variety of ways to keep information. For example, one may keep several derivatives and the column vector $\boldsymbol{x}_n$ (the elements of which are themselves vectors of length $3N$) is then defined as

$$\boldsymbol{x}_n = \big(x_n, hx'_n, \tfrac{1}{2}h^2 x''_n, \tfrac{1}{6}h^3 x'''_n\big)^{\mathrm{T}} . \tag{3.17}$$

In this example three derivatives of x are kept, and since a total of 4 values are retained, the resulting algorithm is a 4-*value* type. It is also a 1-*step* type because only values at t_n are stored. This representation, expressed in higher derivatives of the co-ordinates, is called a Nordsieck or *N-representation*, named for NORDSIECK [14]. It is a particularly convenient representation if one wishes to change the step size h. Alternatively, one may keep co-ordinates only, from previous steps. For example,

$$\boldsymbol{x}_n = (x_n, x_{n-1}, x_{n-2})^{\mathrm{T}} \tag{3.18}$$

yields a 3-value, 3-step method. We call this a co-ordinate or *C-representation*. A convenient representation uses co-ordinates and velocities of one step and forces at previous steps, because the forces have been directly evaluated. For example,

$$\boldsymbol{x}_n = \big(x_n, hx'_n, \tfrac{1}{2}h^2 x''_n, \tfrac{1}{2}h^2 x''_{n-1}, \tfrac{1}{2}h^2 x''_{n-2}\big)^{\mathrm{T}} \tag{3.19}$$

gives a 5-value, 3-step method in the force or *F-representation*. The various representations can be transformed into each other by matrix transformations as GEAR [12] has pointed out.

The vectors $\boldsymbol{x}_n$ in a k-value method are vectors in the space of all polynomials of degree $k-1$. Transformation of representation R_1 into another R_2 is really a linear co-ordinate transformation $\boldsymbol{T}$ in that space

$$\boldsymbol{x}_n(R_2) = \boldsymbol{T}\boldsymbol{x}_n(R_1)\,. \tag{3.20}$$

$\boldsymbol{T}$ can be found easily by considering that the transformation is exact if $x(t)$ represents a polynomial of degree $k-1$. For example: derive a 3-value C-representation from a 3-value N-representation:

$$\begin{pmatrix} x_n \\ x_{n-1} \\ x_{n-2} \end{pmatrix} = \begin{pmatrix} 1 & 0 & 0 \\ 1 & -1 & 1 \\ 1 & -2 & 4 \end{pmatrix} \begin{pmatrix} x_n \\ hx_n' \\ \frac{1}{2}h^2 x_n'' \end{pmatrix}. \tag{3.21}$$

This follows immediately from Taylor expansions:

$$x_{n-1} = x_n - hx_n' + \tfrac{1}{2}h^2 x_n''\,, \tag{3.22}$$

$$x_{n-2} = x_n - 2hx_n' + 2h^2 x_n''\,. \tag{3.23}$$

Similarly, a 4-value F-representation follows from a 4-value N-representation:

$$\begin{pmatrix} x_n \\ hx_n' \\ \frac{1}{2}h^2 x_n'' \\ \frac{1}{2}h^2 x_{n-1}'' \end{pmatrix} = \begin{pmatrix} 1 & 0 & 0 & 0 \\ 0 & 1 & 0 & 0 \\ 0 & 0 & 1 & 0 \\ 0 & 0 & 1 & -3 \end{pmatrix} \begin{pmatrix} x_n \\ hx_n' \\ \frac{1}{2}h^2 x_n'' \\ \frac{1}{6}h^3 x_n''' \end{pmatrix} \tag{3.24}$$

because $x_{n-1}'' = x_n'' - hx_n'''$. The transformation matrices from N- to F-representation up to 8-value dimension and their inverses are given in ref. [15].

The predictor step can be contracted to a matrix multiplication

$$\boldsymbol{y}_{n+1} = \boldsymbol{A}\boldsymbol{x}_n\,. \tag{3.25}$$

Transformation $\boldsymbol{T}$ into another representation (from R_1 into R_2) yields

$$\boldsymbol{A}(R_2) = \boldsymbol{T}\boldsymbol{A}(R_1)\boldsymbol{T}^{-1}\,, \tag{3.26}$$

which follows from the fact that both x_n and y_{n+1} transform as

$$\boldsymbol{x}(R_2) = \boldsymbol{T}\boldsymbol{x}(R_1)\,. \tag{3.27}$$

For the predictor $\boldsymbol{A}$ a Taylor expansion is used, which is most easily expressed in the N-representation:

$$\boldsymbol{A}(N) = \begin{pmatrix} 1 & 1 & 1 & 1 & 1 \ldots \\ 0 & 1 & 2 & 3 & 4 \\ 0 & 0 & 1 & 3 & 6 \\ 0 & 0 & 0 & 1 & 4 \\ 0 & 0 & 0 & 0 & 1 \\ \ldots & \ldots & \ldots & \ldots & \ldots \end{pmatrix}. \tag{3.28}$$

One recognizes the binomial coefficients in the columns.

It is now easy to find prediction matrices in other representations by applying (3.26). For example, in a 4-value F-representation the prediction matrix is

$$\begin{pmatrix} 1 & 0 & 0 & 0 \\ 0 & 1 & 0 & 0 \\ 0 & 0 & 1 & 0 \\ 0 & 1 & 1 & -3 \end{pmatrix} \begin{pmatrix} 1 & 1 & 1 & 1 \\ 0 & 1 & 2 & 3 \\ 0 & 0 & 1 & 3 \\ 0 & 0 & 0 & 1 \end{pmatrix} \begin{pmatrix} 1 & 0 & 0 & 0 \\ 0 & 1 & 0 & 0 \\ 0 & 0 & 1 & 0 \\ 0 & 0 & \frac{1}{3} & -\frac{1}{3} \end{pmatrix} = \tag{3.29}$$

$$= \begin{pmatrix} 1 & 1 & \frac{4}{3} & -\frac{1}{3} \\ 0 & 1 & 3 & -1 \\ 0 & 0 & 2 & -1 \\ 0 & 0 & 1 & 0 \end{pmatrix},$$

where the third matrix is the inverse of the first matrix, which is given in (3.24).

Prediction matrices for the N-representation up to 8-value dimension are given in ref. [15].

The next step is the calculation of the force at the predicted position $f(y_{n+1})$, which can be compared with y''_{n+1}. The difference is then used in a correction:

$$\boldsymbol{x}_{n+1} = \boldsymbol{y}_{n+1} + \boldsymbol{a}\,\tfrac{1}{2}h^2\big(f(y_{n+1}) - y''_{n+1}\big)\,. \tag{3.30}$$

The correction vector $\boldsymbol{a}$ must be chosen on the basis of accuracy and stability requirements. There is no unique choice and different algorithms with different correction vectors are in use. One requirement is that the coefficients for $\frac{1}{2}h^2 x''_n$ must be 1 to update the second derivative correctly. GEAR [12] has derived the correction vectors given in table I in the N-representation (see also ref. [15]).

Transformation from representation R_1 to R_2 is again straightforward

$$\boldsymbol{a}(R_2) = \boldsymbol{T}\boldsymbol{a}(R_1)\,. \tag{3.31}$$

For example, for the 4-value F-representation

$$a(F) = \begin{pmatrix} 1 & 0 & 0 & 0 \\ 0 & 1 & 0 & 0 \\ 0 & 0 & 1 & 0 \\ 0 & 0 & 0 & -3 \end{pmatrix} \begin{pmatrix} \frac{1}{6} \\ \frac{5}{6} \\ 1 \\ \frac{1}{3} \end{pmatrix} = \begin{pmatrix} \frac{1}{6} \\ \frac{5}{6} \\ 1 \\ 0 \end{pmatrix}. \tag{3.32}$$

It turns out that in the F-representation for any value the first three elements are the same as in the N-representation (table I), while all higher elements are zero. Thus the correction has a particularly simple form in the F-representation. This is to be expected since all second derivatives at previous positions are already equal to the correct forces and they cannot be improved by later updating.

TABLE I. – *Predictor vectors for the N-representation according to Gear* [12], *up to* 8-*valued methods.*

Values	a_0	a_1	a_2	a_3	a_4	a_5	a_6	a_7
4	1/6	5/6	1	1/3				
5	19/120	3/4	1	1/2	1/12			
6	3/20	251/360	1	11/18	1/6	1/60		
7	863/6048	665/1008	1	25/36	35/144	1/24	1/360	
8	275/2016	19087/30240	1	137/180	5/16	17/240	1/120	1/2520

The behaviour of 4- and 5-value Gear algorithms for the harmonic oscillator is given in fig. 1-3. We see that the algorithms are highly accurate and that also the fluctuations are small. The drift is not quite negligible unless a very small time step is chosen, and this does not seem to improve for higher order of the algorithm. When the error in the trajectory is found to be proportional to h^p, p is called the « apparent order » (indicated in fig. 1).

The Gear algorithms need to be started, if only x_0 and v_0 are given. This can be done by taking a small step at the available accuracy, deriving the next higher derivative of x at x_0 from a force evaluation at the new position and repeating this procedure until the required order is obtained. It is also possible to use a Runge-Kutta procedure first. In the F-representation one can increase the order per step by using the generated forces.

In *summary* we give the formulae for 4-, 5- and 6-value Gear algorithms in both N- and F-representation [15] in table II.

3·4. *The Verlet, leap-frog and Beeman algorithms.* – Three open methods that do not use a corrector on the co-ordinates are widely used in molecular dynamics. Although they are less accurate than higher-order Gear algorithms,

they are much easier to use and require less storage. The three methods produce exactly the same trajectory and are thus equivalent. They have the important advantage that they are time-reversible, which implies that they will have essentially no drift.

VERLET [16] proposed the following simple scheme

$$x_{n+1} = 2x_n - x_{n-1} + h^2 f(x_n) \tag{3.33}$$

TABLE II. – *Formulae for Gear algorithms.*

Vector definition:

N-repr. $\quad \boldsymbol{x}_n = \left(x_n,\ hx'_n,\ \frac{1}{2}h^2 x''_n,\ \frac{1}{3!}h^3 x'''_n,\ \frac{1}{4!}h^4 x^{\mathrm{iv}}_n, \ldots\right)$

F-repr. $\quad \boldsymbol{x}_n = \left(x_n,\ hx'_n,\ \frac{1}{2}h^2 x''_n,\ \frac{1}{2}h^2 x''_{n-1},\ \frac{1}{2}h^2 x''_{n-2}, \ldots\right)$

Algorithm:

predictor $\quad \boldsymbol{y}_n = \boldsymbol{A}\boldsymbol{x}_{n+1}$

corrector $\quad \boldsymbol{x}_{n+1} + \boldsymbol{a}\frac{1}{2}h^2(f(y_{n+1}) - (y''_{n+1}))$

$k = 4$ $\quad N$-repr.

$$\boldsymbol{A} = \begin{pmatrix} 1 & 1 & 1 & 1 \\ 0 & 1 & 2 & 3 \\ 0 & 0 & 1 & 3 \\ 0 & 0 & 0 & 1 \end{pmatrix} \qquad \boldsymbol{a} = \begin{pmatrix} \frac{1}{6} \\ \frac{5}{6} \\ 1 \\ \frac{1}{3} \end{pmatrix}$$

$k = 4$ $\quad F$-repr.

$$\boldsymbol{A} = \begin{pmatrix} 1 & 1 & \frac{4}{3} & -\frac{1}{3} \\ 0 & 1 & 3 & -1 \\ 0 & 0 & 2 & -1 \\ 0 & 0 & 1 & 0 \end{pmatrix} \qquad \boldsymbol{a} = \begin{pmatrix} \frac{1}{6} \\ \frac{5}{6} \\ 1 \\ 0 \end{pmatrix}$$

$k = 5$ $\quad N$-repr.

$$\boldsymbol{A} = \begin{pmatrix} 1 & 1 & 1 & 1 & 1 \\ 0 & 1 & 2 & 3 & 4 \\ 0 & 0 & 1 & 3 & 6 \\ 0 & 0 & 0 & 1 & 4 \\ 0 & 0 & 0 & 0 & 1 \end{pmatrix} \qquad \boldsymbol{a} = \begin{pmatrix} \frac{19}{120} \\ \frac{3}{4} \\ 1 \\ \frac{1}{2} \\ \frac{1}{12} \end{pmatrix}$$

$k = 5$ $\quad F$-repr.

$$\boldsymbol{A} = \begin{pmatrix} 1 & 1 & \frac{19}{12} & -\frac{5}{6} & \frac{1}{4} \\ 0 & 1 & \frac{23}{6} & -\frac{8}{3} & \frac{5}{6} \\ 0 & 0 & 3 & -3 & 1 \\ 0 & 0 & 1 & 0 & 0 \\ 0 & 0 & 0 & 1 & 0 \end{pmatrix} \qquad \boldsymbol{a} = \begin{pmatrix} \frac{19}{120} \\ \frac{3}{4} \\ 1 \\ 0 \\ 0 \end{pmatrix}$$

TABLE II (*continued*)

$k = 6$ N-repr.

$$\boldsymbol{A} = \begin{pmatrix} 1 & 1 & 1 & 1 & 1 & 1 \\ 0 & 1 & 2 & 3 & 4 & 5 \\ 0 & 0 & 1 & 3 & 6 & 10 \\ 0 & 0 & 0 & 1 & 4 & 10 \\ 0 & 0 & 0 & 0 & 1 & 5 \\ 0 & 0 & 0 & 0 & 0 & 1 \end{pmatrix} \qquad \boldsymbol{a} = \begin{pmatrix} \frac{3}{20} \\ \frac{251}{360} \\ 1 \\ \frac{11}{18} \\ \frac{1}{6} \\ \frac{1}{60} \end{pmatrix}$$

$k = 6$ F-repr.

$$\boldsymbol{A} = \begin{pmatrix} 1 & 1 & \frac{323}{180} & -\frac{22}{15} & \frac{53}{60} & -\frac{19}{90} \\ 0 & 1 & \frac{55}{12} & -\frac{59}{12} & \frac{27}{12} & -\frac{3}{4} \\ 0 & 0 & 4 & -6 & 4 & -1 \\ 0 & 0 & 1 & 0 & 0 & 0 \\ 0 & 0 & 0 & 1 & 0 & 0 \\ 0 & 0 & 0 & 0 & 1 & 0 \end{pmatrix} \qquad \boldsymbol{a} = \begin{pmatrix} \frac{3}{20} \\ \frac{251}{360} \\ 1 \\ 0 \\ 0 \\ 0 \end{pmatrix}$$

which is a Taylor predictor, as we see by adding eqs. (3.34) and (3.35)

$$x_{n+1} = x_n + hx_n' + \tfrac{1}{2}h^2 x_n'' + \tfrac{1}{6}h^3 x_n''' + O(x_n^{\mathrm{iv}}) , \tag{3.34}$$

$$x_{n-1} = x_n - hx_n' + \tfrac{1}{2}h^2 x_n'' - \tfrac{1}{6}h^3 x_n''' + O(x_n^{\mathrm{iv}}) . \tag{3.35}$$

This algorithm contains no explicit velocities, and we see that also the third derivative cancels. If velocities are needed, they can be approximated by

$$v_n = (x_{n+1} - x_{n-1})/2h . \tag{3.36}$$

The algorithm can be started if two successive steps are known, but, if x_n and v_n according to (3.36) are stored, x_{n+1} can be exactly retrieved from

$$x_{n+1} = x_n + hv_n + \tfrac{1}{2}h^2 f(x_n) . \tag{3.37}$$

The Verlet algorithm is not as accurate as Gear-4 (fig. 1); it has the apparent order p of only 2. The drift is smaller than the noise and thus insignificant.

Another formulation of the same algorithm is the *leap-frog* scheme [6]

$$v_{n+\frac{1}{2}} = v_{n-\frac{1}{2}} + hf(x_n) , \tag{3.38}$$

$$x_{n+1} = x_n + hv_{n+\frac{1}{2}} . \tag{3.39}$$

The equivalence with (3.33) is apparent if we substitute $(x_n - x_{n-1})/h$ for $v_{n+\frac{1}{2}}$ in (3.39). It also follows that the velocity

$$v_n = \tfrac{1}{2}(v_{n-\frac{1}{2}} + v_{n+\frac{1}{2}}) \tag{3.40}$$

is equivalent to v_n according to (3.36). So all properties of the leap-frog and Verlet algorithms are equal.

The *Beeman* algorithm [17] looks very different:

$$x_{n+1} = x_n + hv_n + \tfrac{2}{3}h^2 f_n - \tfrac{1}{6}h^2 f_{n-1}\,, \tag{3.41}$$

$$v_{n+1} = v_n + \tfrac{1}{3}hf_{n+1} + \tfrac{5}{6}hf_n - \tfrac{1}{6}hf_{n-1}\,, \tag{3.42}$$

where $f_n = f(x_n)$. This is a regular predictor for x_{n+1} in the F-representation (see table II), but no corrector is used on x. It has only recently been realized [18, 19] that this algorithm is actually equivalent to the Verlet scheme. We see this by applying (3.41) to one step earlier which yields

$$hv_{n-1} = x_n - x_{n-1} - \tfrac{1}{6}h^2(4f_{n-1} - f_{n-2})\,. \tag{3.43}$$

Now applying (3.42) to one step earlier and substituting v_{n-1} from (3.43) yields

$$hv_n = x_n - x_{n-1} + \tfrac{1}{3}h^2 f_n + \tfrac{1}{6}h^2 f_{n-1}\,. \tag{3.44}$$

If we substitute this in (3.41), we recover the Verlet equation (3.33).

The accuracy of the Beeman algorithm is, of course, the same as Verlet's (fig. 1). Slight differences may arise from slightly different starting conditions. But the drift and noise seem to be better (fig. 2 and 3)! The reason is that the Beeman velocity is more accurate than eq. (3.36) or (3.40), although it plays no role in the trajectory.

We can also modify the Verlet or leap-frog velocities. We can even do better than Beeman velocities by observing the time reversal symmetry (the Beeman velocities do not obey time reversal symmetry). The improved velocities are

$$v_n = \frac{1}{2}(v_{-\frac{1}{2}} + v_{\frac{1}{2}}) + \frac{h}{12}(f_{n-1} - f_{n+1})\,. \tag{3.45}$$

With these velocities the noise decreases by a factor of at least two and even drops below Beeman's values for larger time steps (fig. 3).

Since the Beeman algorithm is more complicated and uses more memory, there seem to be no good reasons for its use.

3·5. *Algorithms for complex systems.* – The evaluation of algorithms for molecular dynamics of complex systems is not so straightforward as for the harmonic oscillator. When the system has a very large number of degrees of freedom (tens of thousands), the memory storage required may be a matter of concern. The most favourable algorithm in this respect is the leap-frog scheme, requiring 3 storage vectors, while k-value Gear algorithms require storage of $k + 1$ vectors. But more important are the fluctuations and inac-

curacies in the forces due to truncation at the cut-off radius. In simulations of real systems such fluctuations cannot be avoided and they will cause the forces to be more erratic and unpredictable. This makes the use of higher-order algorithms less desirable, because higher-order systematic differences in the forces will be swamped by unpredictable fluctuations. Moreover, the cut-off noise will add to the algorithmic noise and the improvement on going to higher-order algorithms will be less apparent.

We have compared the Verlet scheme with higher-order Gear algorithms for a small protein (BPTI: basic pancreatic trypsin inhibitor), made up of 458 nonhydrogen atoms [15]. The CPU time was 1.2 s for Verlet, and 1.3 to 1.5 s for 4- to 8-valued Gear. The results (fig. 4) show that Gear algorithms are better if high accuracy is required, but that for low accuracy Verlet does better. The Verlet algorithm is also more stable for large steps. For any step size we find that the accuracy is not further improved above $k = 7$. It is worth noticing that $k = 5$ does not give much improvement above $k = 4$,

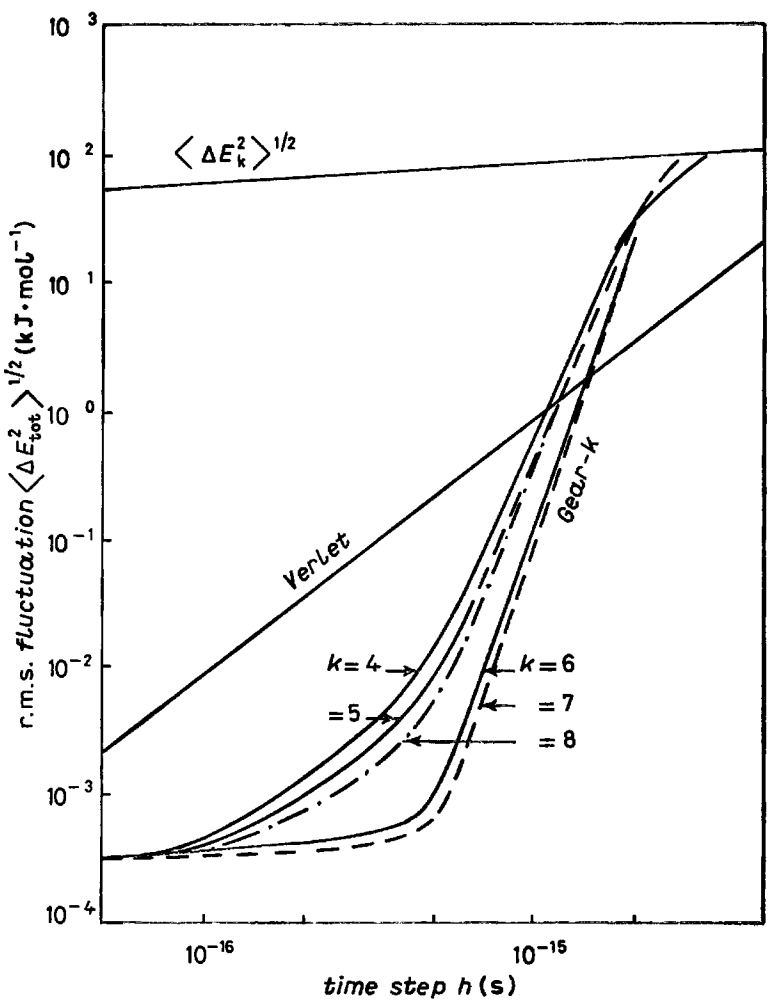

Fig. 4. – R.m.s. fluctuation of the total energy over 100 steps in a molecular-dynamics simulation of the protein BPTI (458 atoms). Verlet and Gear algorithms are compared. The fluctuation in the total kinetic energy is indicated as a reference (from ref. [15]).

but $k = 6$ improves significantly above $k = 5$. We conclude that Gear algorithms perform better than the Verlet scheme does.

In this example bond-stretching frequencies are the highest frequencies occurring in the system. The model used for bond vibrations is harmonic. That means that the behaviour of the algorithm will be much like its behaviour on a harmonic system. Comparing fig. 3 and 4 we see that the behaviour is very similar. The slope of the Verlet noise (on a logarithmic scale) corresponds to an exponent of 2.0 in the harmonic oscillator and 1.9 in the protein. In the h.o. a noise of 0.001 with respect to the « kinetic-energy » fluctuation is obtained for a step size of 0.075 (84 steps per cycle); in the protein this noise is observed for a time step of $2.6 \cdot 10^{-16}$ s. With 84 steps per cycle this would correspond to a highest frequency of $4.5 \cdot 10^{13}$, or 1500 cm^{-1}, indeed very close to the highest bond-stretching frequencies in the system.

How accurate a simulation has to be in order to provide reliable statistical results is still a matter of debate. The purpose is never to produce reliable trajectories. Whatever accuracy the forces and the algorithms have, significant deviations from the exact solution will inevitably occur. Also in the real physical world individual trajectories have no meaning: in a quantum-mechanical sense they do not exist and even classically they become unpredictable in the long run due to the nonisolated character of any real system. So what counts are statistical averages. It seems that very little systematic evaluation of algorithms has been done with this in mind. We have the impression (from nonsystematic experience) that a noise as high as 10 % of the kinetic-energy fluctuation is still acceptable, although the accuracy of fluctuations may not be sufficient to obtain thermodynamic data from them. With such a level of inaccuracy the Verlet or leap-frog algorithm is always to be preferred.

4. – Incorporation of constraints.

Treatment of certain stiff degrees of freedom in a molecular system as constraints removes high frequencies from the simulation and allows for a much larger time step. The way to treat such constraints is considered more extensively in this school. Also for rigid molecules the use of constraints is advantageous because Cartesian co-ordinates can be retained, without the need to write equations of motion in terms of quaternions [20, 21]. Let it suffice to say here that we prefer to use the procedure SHAKE [22, 23], which allows the time step to be increased by a factor of 4 in proteins, without affecting the physics of the system when only bond lengths are constrained [15]. The procedure boils down to taking an unconstrained step and then applying the resetting procedure SHAKE to satisfy the constraints. For the Verlet or leap-frog algorithm this requires only one application of SHAKE per step.

For Gear algorithms, however, two applications are necessary, because SHAKE must also be applied to velocities. The prediction-correction procedure by itself does conserve approximate constraints, but it does not prevent the propagation of constraint errors through the velocity terms. This makes any algorithm with explicit velocities unstable unless SHAKE is applied twice per step.

Applying Gear algorithms to constrained dynamics [15], we found that k-values higher than 4 give no improvement, and that the Verlet algorithm is superior unless very high accuracies are required (fig. 5). This obviously results from the fact that high-frequency harmonic (and hence predictable) modes are removed from the system; the remaining forces have a less predictable character. So for dynamic simulations with constraints the Verlet (leap-frog) algorithm is to be preferred.

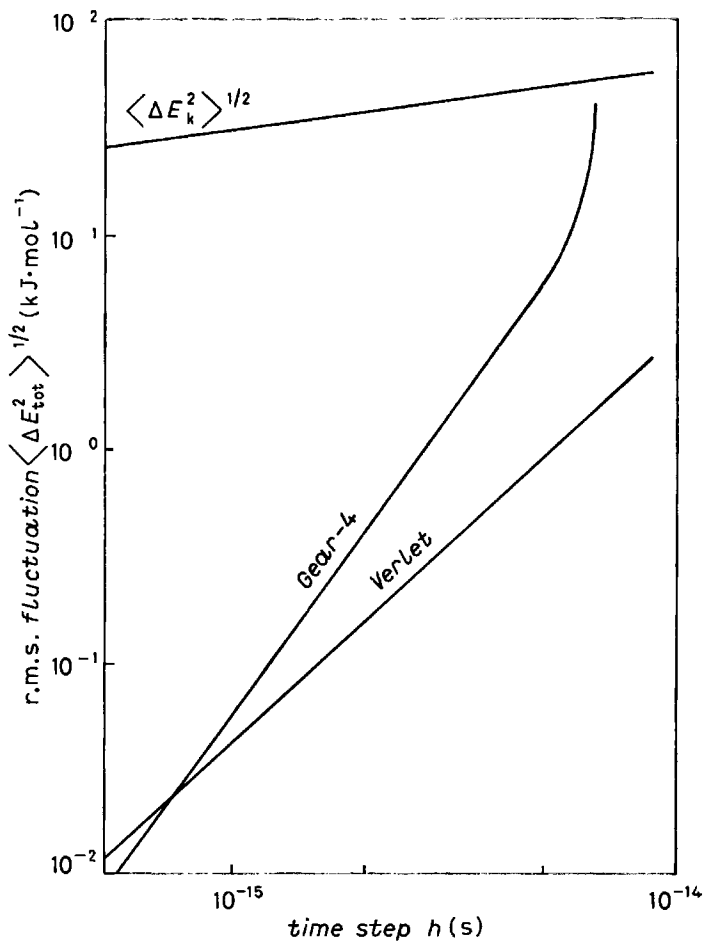

Fig. 5. – R.m.s. fluctuation in the total energy over 100 steps in a simulation of BPTI, using the SHAKE method to constrain covalent bond lengths (from ref. [15])

5. – Modifications in the equations of motion.

There are numerous examples of modified equations of motion, either to represent modified Hamiltonians [24-26], or to include coupling to an external

bath [27]. The former cases will be treated more extensively in this school, and the methods to solve the new equations are essentially the same as described in sect. **3**. The latter do modify the equations of motions in such a way that they cannot be derived from a Hamiltonian (for example, there is no longer a conserved quantity that can be monitored to judge the behaviour of the algorithm) and we will consider this case briefly.

Weak coupling to an external bath of constant temperature and pressure has the purpose to make the total temperature T and pressure P decay slowly to an external reference temperature T_0 and pressure P_0:

$$\frac{\mathrm{d}T}{\mathrm{d}t} = \frac{T_0 - T}{\tau_\mathrm{T}} \tag{5.1}$$

and

$$\frac{\mathrm{d}P}{\mathrm{d}t} = \frac{P_0 - P}{\tau_\mathrm{P}}, \tag{5.2}$$

where τ_T and τ_P are time constants of the coupling, representing the strength of the coupling, which can be chosen at will. This can be accomplished by the following modification of the equations of motion [27]:

$$\dot{x}_i = v_i - \beta(P_0 - P)/3\tau_\mathrm{P}, \tag{5.3}$$

$$\dot{v}_i = F_i/m_i - \left(\frac{T_0}{T} - 1\right) v_i/2\tau_\mathrm{T}, \tag{5.4}$$

where β is the isothermal compressibility.

Although it should be possible to solve such equations using Gear algorithms, the application of the leap-frog scheme is quite easy and straighforward. Two modifications are made: velocities are scaled each step with a factor λ

$$\lambda = \left(1 + \frac{h}{\tau_\mathrm{T}}\left(\frac{T_0}{T} - 1\right)\right)^{\frac{1}{2}} \tag{5.5}$$

and co-ordinates (as well as the size of the computational box) are scaled each step with a factor μ

$$\mu = \left(1 + \frac{h}{\tau_\mathrm{P}}\beta(P - P_0)\right)^{\frac{1}{3}}. \tag{5.6}$$

It is not necessary to compute equal-time velocities; the shifted leap-frog velocities can be scaled directly, using temperature data of the previous step. This is because the time constant in the coupling is much larger than the time step and no inaccuracies result from this procedure. The incorporation of these couplings into constrained dynamics is also straightforward using the leap-frog scheme. For details we refer to ref. [27].

The equations no longer conserve total energy and hence monitoring that quantity is not useful to judge the behaviour of the algorithm. However, when the coupling time constants are made very large, the original Hamiltonian equations are recovered and the total-energy conservation is again a valid criterion. Thus at any time a check is possible.

The conclusion is that equations of motion can most readily be modified in the leap-frog scheme, which is one more reason to prefer this simple, stable and elegant algorithm for complex systems.

6. – Stochastic dynamics.

Solution of the simple Langevin equation (1.9) requires a completely different approach because of the random term in the force. This naturally makes the force more unpredictable than in normal molecular dynamics. One would suppose that a very-low-order algorithm would suffice, but this is not so. The same argument, given in sect. **3**, that the potential functions have consistently positive second derivatives requiring a third- or higher-order algorithm, still applies. When comparing a second-order algorithm with a third-order algorithm in a stochastic simulation of butane and decane, we found that the third-order algorithm behaves very much better than a second-order one [28]. Unfortunately a third-order algorithm, based on the Verlet or leap-frog scheme, is rather complicated.

The point to make here is that the time step and accuracy of the algorithm are entirely determined by the systematic force in the simulation and not by the random force. Without the systematic force the Langevin equation is exactly solvable by integration of the force to obtain the velocity and subsequent integration of the velocity to obtain the co-ordinates. These steps involve integration of random variables, multiplied by certain functions of time, over a time interval. Such integrals are again stochastic variables, the statistical properties of which can be calculated. That means that these integral quantities can be sampled directly from random variables and do not have to be constructed by summation. A complication arises from the fact that more than one integral appears, with correlated statistical properties. Therefore, sampling of two correlated random variables from a Gaussian distribution is necessary. But these problems have been solved [28-30].

In the case of second-order algorithms, the force is assumed to be constant over the time interval and integration is quite straightforward [31]. In the case of third-order algorithms the derivative of the force must be taken into account, thus complicating the algorithm. We refer to the original literature for details: ERMAK and BUCKHOLTZ [32] originated work on stochastic integration algorithms, we [31] described a second-order algorithm, ALLEN [29] described a stochastic integration in the Beeman algorithm and we [28] con-

structed a Verlet-type stochastic algorithm. ALLEN [18] pointed out that these two algorithms are essentially equivalent. In ref. [28] the applicability of constraints is also considered. Formulation in terms of a leap-frog scheme is in preparation. VESELY [30] has given an algorithm for the more general case of nonwhite random forces. CICCOTTI and RYCKAERT also simulated the generalized Langevin equations [33].

7. – Conclusions.

We conclude that for many purposes the leap-frog algorithm is the most suitable for molecular dynamics (and also stochastic dynamics), because it is simple, efficient, stable and reasonably accurate. It can also be easily modified for different equations of motion. However, for accurate dynamics it will not be the best algorithm: Gear algorithms of order 4 or 6 are to be preferred. This makes only sense if the forces are determined with high accuracy and no random terms are included.

REFERENCES

[1] W. B. STREETT, D. J. TILDESLEY and G. SAVILLE: *Mol. Phys.*, **35**, 639 (1978).
[2] J. J. NICOLAS, K. E. GUBBINS, W. B. STREETT and D. J. TILDESLEY: *Mol. Phys.*, **37**, 1429 (1979).
[3] W. F. VAN GUNSTEREN, H. J. C. BERENDSEN, F. COLONNA, D. PERAHIA, J. P. HOLLENBERG and D. LELLOUCH: *J. Comput. Chem.*, **5**, 272 (1984).
[4] P. P. EWALD: *Ann. Phys. (Leipzig)*, **64**, 253 (1921).
[5] C. KITTEL: Appendix A in *Introduction to Solid State Physics* (New York, N. Y., 1956).
[6] R. W. HOCKNEY and J. W. EASTWOOD: *Computer Simulation using Particles* (New York, N. Y., 1981).
[7] H. J. C. BERENDSEN and G. A. VAN DER VELDE: Report of CECAM Workshop *MC and MC of Water* (Centre Europeén de Calcul Atomique et Moléculaire, Orsay, France, 1972).
[8] E. KREISZIG: *Advanced Engineering Mathematics* (New York, N. Y., 1962, fifth edition, 1983).
[9] C. RAY WYLIE: *Advanced Engineering Mathematics* (New York, N. Y., 1951; Tokyo, 1961).
[10] G. DAHLQUIST and Å. BJÖRCK: *Numerical Methods* (Englewood Cliffs, N.J., 1974).
[11] L. LAPIDUS and J. H. SEINFELD: *Numerical Solution of Ordinary Differential Equations* (New York, N. Y., 1971).
[12] C. W. GEAR: *Numerical Initial Value Problems in Ordinary Differential Equations* (Englewood Cliffs, N. J., 1971).
[13] C. W. GEAR: Report ANL-7126, Argonne National Laboratory (1966).
[14] A. NORDSIECK: *Math. Comput.*, **16**, 22 (1962).
[15] W. F. VAN GUNSTEREN and H. J. C. BERENDSEN: *Mol. Phys.*, **34**, 1311 (1977).

[16] L. VERLET: *Phys. Rev.*, **159**, 98 (1967).
[17] D. BEEMAN: *J. Comput. Phys.*, **20**, 130 (1976).
[18] M. P. ALLEN: *Mol. Phys.*, **47**, 599 (1982).
[19] J. ÅQVIST, W. F. VAN GUNSTEREN, M. LEIJONMARCK and O. TAPIA: *J. Mol. Biol.*, **183**, 461 (1985).
[20] D. J. EVANS and S. MURAD: *Mol. Phys.*, **34**, 327 (1977).
[21] H. GOLDSTEIN: *Classical Mechanics*, second edition (Reading, Mass., 1980).
[22] J. P. RYCKAERT, G. CICCOTTI and H. J. C. BERENDSEN: *J. Comput. Phys.*, **23**, 327 (1977).
[23] H. J. C. BERENDSEN and W. F. VAN GUNSTEREN: in *The Physics of Superionic Conductors and Electrode Materials*, edited by J. W. PERRAM, NATO ASI Series B **92** (New York, N. Y., 1983), p. 241.
[24] H. C. ANDERSEN: *J. Chem. Phys.*, **72**, 2384 (1980).
[25] S. NOSÉ: *Mol. Phys.*, **52**, 255 (1984).
[26] S. NOSÉ: *J. Chem. Phys.*, **81**, 511 (1984).
[27] H. J. C. BERENDSEN, J. P. M. POSTMA, W. F. VAN GUNSTEREN, A. DINOLA and J. R. HAAK: *J. Chem. Phys.*, **81**, 3684 (1984).
[28] W. F. VAN GUNSTEREN and H. J. C. BERENDSEN: *Mol. Phys.*, **45**, 637 (1982).
[29] M. P. ALLEN: *Mol. Phys.*, **40**, 1073 (1980).
[30] F. J. VESELY: *Mol. Phys.*, **53**, 505 (1984).
[31] W. F. VAN GUNSTEREN and H. J. C. BERENDSEN: in *The Physics of Superionic Conductors and Electrode Materials*, edited by J. W. PERRAM, NATO ASI Series B **92** (New York, N. Y., 1983), p. 221.
[32] D. L. ERMAK and H. BUCKHOLTZ: *J. Comput. Phys.*, **35**, 169 (1980).
[33] G. CICCOTTI and J.-P. RYCKAERT: *Mol. Phys.*, **40**, 141 (1980); **46**, 875 (1982).

Molecular-Dynamics Simulations.

B. J. ALDER

Lawrence Livermore National Laboratory, University of California
Livermore, CA 94550

1. – Introduction.

The single most important fundamental discovery for the dynamic properties of interacting particles by computer simulation is that the molecular-chaos approximation is generally not valid. In fact, the molecular-chaos approximation, which implies that a particle after a sufficiently long time forgets its past, or, equivalently, that correlations decay exponentially, is not valid for even the simplest models, such as a dilute gas or a Lorentz gas. This approximation was originally introduced because it seemed physically reasonable and because it led to a great mathematical simplification, namely that dynamic processes could be described by Markov processes. By computer simulation, before real experiments such as neutron diffraction studies, it was possible to investigate the decay of correlations with sufficient resolution to show that the decay had a long-time tail, corresponding to a power law fall-off with time [1]. This discovery caused a fundamental change in the mathematical structure with which to describe transport properties. For example, the Boltzmann equation and the Chapman-Enskog expansion used in its solution can be shown not to be valid for a finite-density gas. This discovery, however, also initiated a stampede that ascribed all tails that have been subsequently discovered to the same mechanism. The primary focus of this lecture is to demonstrate the differences between various tails.

For that purpose, the tails of the Lorentz gas will be discussed, since that is the simplest model for which such tails might be analyzed, because only the motion of a single point particle among randomly arranged fixed scatterers is involved. In order to contrast the tails of the Lorentz gas with that of others that occur in fluids, however, a brief review of their characteristics will be given. At least one of these other tails, that for the diffusion coefficient of fluids, is due to collective phenomena; that is, due to the co-operative motion of the particles in the medium, which by the very nature of the Lorentz model cannot occur in that system. The nature of the collective mode in the dif-

fusion case can be identified with great confidence since a hydrodynamic model confirmed by molecular-dynamics results yielded quantitative agreement [2]. The only other important collective effect that was discovered by molecular dynamics in fluid transport phenomena was in the slow decay of the stress autocorrelation function that determines the viscosity [3]. That tail, called the molasses tail to distingush it from the hydrodynamic tail for diffusion, has also been analyzed by the same methods as for diffusion with far from quantitative success. As shall be seen, the employment of a hydrodynamic-type analysis for all tails including that for the Lorentz gas is of doubtful validity.

2. – Hydrodynamic tail.

The decay of the velocity autocorrelation function

$$\varrho(t) = \langle v(0)\, v(t)\rangle / \langle v^2(0)\rangle \tag{2.1}$$

at intermediate fluid densities is illustrated in fig. 1*a*). The velocity autocorrelation function, whose integral is the diffusion coefficient, shows a positive persistence of velocity that can observed for some 100 collisions. That positive tail can be quantitatively accounted for by a hydrodynamic model in which a sphere, surrounded by a continuum fluid, characterized by a compressibility and a viscosity, is given an initial velocity or momentum [1]. Those initial conditions lead to a positive pressure in the fluid ahead of the sphere that generates a sound wave and a corresponding rarefaction wave behind. In addition, the positive pressure in front and the negative pressure behind can equalize by creating a double-vortex structure around the sphere. This phenomenon is vividly verified by investigating the velocity field $= \left\langle \sum_{j=1}^{n} V_i(0) V_j(t) \right\rangle$ surrounding the sphere by molecular dynamics [2]. The velocity field is the correlation between the original velocity of the sphere, i, and the net velocity of all the particles, j, in a surrounding volume element at some time, t, later. The agreement between this molecular dynamically determined velocity field and the corresponding hydrodynamic one is quantitative after some 10 collisions, or about 10^{-13} s. The remarkable validity of hydrodynamics at this time scale and distance scale of only a few molecular diameters will be referred to again later.

A dimensional analysis of the hydrodynamic model leads to a quantitative description of the tail. After first observing that at long times only the vortex mode contributes since it spreads diffusively, as the square root of νt, while the sound wave spreads faster, namely to further distances as ct, where ν is the kinematic viscosity (the shear viscosity divided by the density) and c is the speed of sound. Since momentum (mass times velocity $= mv$) is conserved,

$m\int v\,\mathrm{d}\tau$ must be a constant, where τ is the volume element, which must be integrated over the entire space to account for all the momentum. Since τ spreads as $(\nu t)^{d/2}$, where d in the dimensionality of the space, v must decay as $(\nu t)^{-d/2}$ to keep the momentum constant. The more difficult but readily doable task is to determine the coefficient A in the power law decay of the velocity, $A/(\nu t)^{d/2}$, since that requires knowing how much of the momentum is carried away by the sound wave and how much of the rest is fed back via

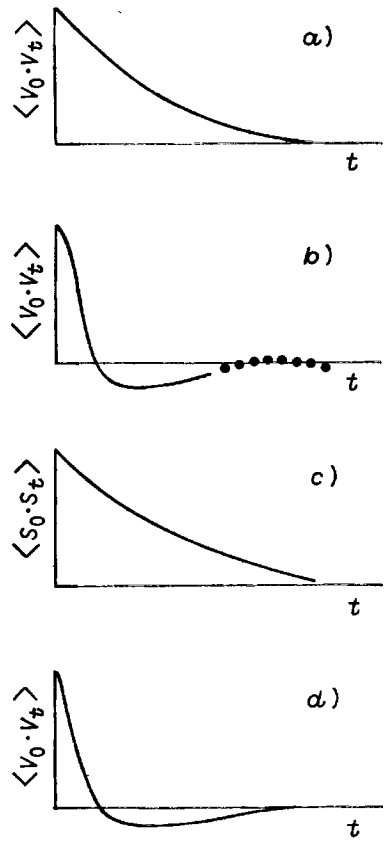

Fig. 1. – Schematic diagrams for different tails: *a*) the velocity autocorrelation function for fluids at intermediate densities leading to a hydrodynamic tail, *b*) the velocity autocorrelation function for fluids near solidification, *c*) the stress autocorrelation function for fluids near solidification leading to a molasses tail, *d*) the velocity autocorrelation function for the Lorentz gas with a geometry-dependent tail.

the medium to the moving sphere. This same power law has also been derived by graph-theoretical methods involving summation of ring diagrams [4] that have intuitively close correspondence to vortex rings. Other derivations by mode-coupling theories [5] also have their origin in hydrodynamic arguments. Finally, a derivation by renormalization theory has also been carried out. Not surprisingly, renormalization theory applies since the exponent is universal, namely, it does not depend on any of the detailed molecular properties of the system.

3. – Molasses tail.

The velocity autocorrelation function at higher density, near normal liquid density, is shown in fig. 1*b*). In that case, the positive tail has not been observed because it is overpowered by a negative feature in the velocity autocorrelation function near solid densities caused by a reversal of the velocity of a typical particle by backscattering. This effect can only be accounted for hydrodynamically by introducing viscoelastic effects, as shall be seen later. These significant viscoelastic effects are a reflection of the slow decay of the stress autocorrelation function, shown in fig. 1*c*), dubbed the molasses tail. For the molasses tail, the hydrodynamic, or graph-theoretical analysis [6] again leads to a tail of the form $A'/t^{d/2}$, but the molecular-dynamics results have only established the appropriateness of the power law over a very limited time domain and with a value of A' which is at least an order of magnitude larger than the theoretically predicted one [7]. We believe that this theoretical prediction is appropriate only for the kinetic part of the viscosity. A considerable effort to observe this tail for the kinetic part of the viscosity failed, however, because the numerical resolution was not high enough [8].

An investigation as to the origin of the molasses tail is underway. Just as the diffusion coefficient can be calculated by $D = \langle \Delta X^2 \rangle / 2t = \int_0^\infty \langle \dot{X}(0) \dot{X}(t) \rangle \, \mathrm{d}t$, so can the viscosity from $\eta = \langle \Delta G^2 \rangle / 2t = \int_0^\infty \langle \dot{G}(0) \, \dot{G}(t) \rangle \, \mathrm{d}t$, where G is the dynamic variable $G = \sum_i x_i \dot{y}_i$ and $\Delta G = \int_0^\infty \dot{G} \, \mathrm{d}t$, the potential part of which is $\sum x_{ij} \Delta \dot{y}_{ij}$, where the dot indicates differentiation with respect to time and the subscripts ij indicate that the two hard-sphere particles i and j are in collision. Upon differentiating G, two terms arise. The first one involves $\dot{x}\dot{y}$ and leads to the kinetic term discussed above, whose tail was found to be unobservable. The second, or potential term, involves $x\ddot{y}$ or xV', where the acceleration has been replaced by the force, or derivative of the potential. It is that term that develops the molasses tail but only near solidification densities. It appears to be connected with a slow structural adjustment in the presence of a shear. A likely mechanism for this structural rearrangement is a slight ordering or layering of the spheres parallel to the plane of the shear so as to reduce the resistance to flow. It is analogous to the ordering of asymmetric molecules in the presence of a velocity gradient in such a way that the long axis is preferentially parallel to the flow. For spherical particles structural effects have been observed for colloidal suspension in fluids and by nonequilibrium molecular-dynamics calculations in the presence of an enormous, externally imposed, shear [9]. For these spherical particles the manifestations are a decrease in the viscosity with shear rate, called shear thinning, which, with sufficiently high shear rate, dramatically results in shear-induced ordering or solidification.

The likely cause for the slowness of the response is that this partial ordering process involves, at high density, a large number of particles, namely all those within the correlation length (the distance beyond which the radial distribution function becomes constant). The long correlation is not likely to be between successive magnitudes of the velocity changes upon collision, $|\Delta\dot{y}_{ij}|$, in the expression for $\langle\Delta G^2\rangle$ since the absolute values of velocities were found to equilibrate fast even at high density. The hypothesis that is being tested is that successive angles between collisions are correlated. Formally, that means one would like to show that at long times the autocorrelations of $\sum x_{ij}y_{ij}$ and of $\sum x_{ij}\ddot{y}_{ij}$ for colliding particles have the same behavior. Certainly, $\sum x_{ij}y_{ij}$ will have an infinitely ranged correlation in the solid phase in as much as the angle between any pair of successive collisions will stay fixed on the average even if the pairs are separated by very large distances. This is then consistent with the known infinite viscosity in the solid phase. Furthermore, such slow decays of correlations have been observed already in a very similar autocorrelation function, namely the one for dipolar density fluctuation $\sum_{i<j} x_{ij}y_{ij}/r_{ij}^5$ appropriate to depolarized light scattering calculations [10], where the sum is now over all pairs in the system, not just those in collision. In fact, that autocorrelation was observed to decay even slower than that of the stress which can be explained by noting that the dipole autocorrelation function is more long ranged. In the dipolar case, the calculation was broken down into its three components corresponding to correlations between the same pair of particles, two different pairs sharing one particle in common and two totally different pairs. A similar breakdown in the stress case would help identify the contributor to the slow decay.

Hopefully, these studies will ultimately lead to a model for the molasses tail, but it is unlikely to be of simple hydrodynamic origin. Such a model is of particular interest in the theory of glass formation. A proper dynamical theory of the glass transition identifies the stable amorphous state as the point at which the viscosity becomes infinite along the metastable fluid branch [11]. However, to predict the cooling rate necessary to prevent crystallization requires knowledge of the rate of growth of the molasses tail for a cluster the size of a critical solid nucleus compared to the rate of formation of that critical sized nucleus. That is, one needs to know the rate of decay of the molasses tail for the viscosity at the appropriate wave vector, so than it can be compared to the rate at which the system tries to crystallize.

4. – Lorentz tails.

The tails in the Lorentz gas are of a still different nature than the ones discussed so far. They are illustrated in fig. 1*d*) and are characterized by a slow decay in the negative region of the velocity autocorrelation function

and can be observed at all densities of the random scatterers, even when the diffusion coefficient vanishes, and for all sorts of different types and arrangements of the scatterers. We shall confine our discussion to two-dimensional systems since these are the most interesting in the sense that sometimes they behave like one-dimensional systems that have zero diffusion coefficients even in the low-density limit and sometimes they imitate three-dimensional systems with vanishing diffusion coefficients only at high density, above a percolation density. The class in which the gas falls depends on the restriction on the degree of freedom of motion that is imposed in the model. We shall also confine our discussion primarily to hard-square and hard-disk scatterers in various random arrangements such as overlapping and nonoverlapping. For squares we shall also consider various random arrangements of the squares on a chessboard and, furthermore, not only impenetrable squares. The latter is of interest as a model for scattering of electrons in a two-dimensional metallic fluid as proposed by ANDERSON, and hence we also discuss the quantum-mechanical version of the Lorentz gas. In the Anderson model, the question again concerns whether or not it falls in the one-dimensional class, that is, whether the resistance of a fluid metal film never vanishes.

The negative tails in the Ehrenfest wind tree model can be ascribed to the higher than random probability of return of the particle (the wind) to its point of origin [12]. The trees in that model are squares placed with their diagonals along either the x or y axis. The particles are also started off moving in only the x or y direction and because of the geometry will subsequently confine their motion to these two directions only. In the overlapping version of the Ehrenfest model it can then be shown by graph-theoretical methods that the diffusion coefficient vanishes even in the low-density limit with a power law tail whose exponent is a known function of density. The vanishing of the diffusion coefficient arises because sooner or later a particle will exactly collide at the intersection of two overlapping squares, whereupon it must exactly retrace its path back to the origin. This graph-theoretical prediction was confirmed by computer simulation [13]. This restricted motion model hence falls in the one-dimensional class.

In the case of nonoverlapping squares in the Ehrenfest model, the analysis yields a nonvanishing diffusion coefficient with a tail of the same type as in the overlapping case but with different constants in the functional density dependence. Also in the case of overlapping disks, the diffusion coefficient is finite below the percolation density, again with a tail of the same form with still different constants both above and below the percolation density. In all these cases, whether the particle is trapped or not, there are negative tails caused by the higher than random probability of return paths, but the power law that describes the tail is first of all not universal since it depends on the density of the fixed random scatterers and secondly differs in detail in the constants depending on the shape of the objects that do the scattering or on

the intermolecular potential. This is to be contrasted with the hydrodynamic tail where a universal mechanism determines the power law with a power that depends only on the dimensionality.

The graph-theoretical arguments so far have only been able to predict the power law constant in the disk case in the low-density limit [12]. The mode-coupling or hydrodynamiclike models predict that this low-density power law constant holds universally at all densities and for all shapes of scatterers. This ignores the known difference in the constant between squares and disks even in the low-density limit. Furthermore, this disagrees with computer simulation results which show a decided density dependence in the power law behavior at long enough times where the lack of a density dependence should have become apparent. It thus appears that the power law decay of the tail depends on the topological details and that hydrodynamic scaling or renormalization arguments cannot be applied. Such arguments have also been used for the quantum Lorentz gas and the conclusions, therefore, are suspect.

Rigorous mathematical analyses of the disk Lorentz gas are, in fact, of topological origin, but, so far, only very limited in scope. The only relevant proof is that in periodic space the tail is exponential in character [14]. In periodic spaces you do not have random scatterers and, indeed, as fig. 2 shows

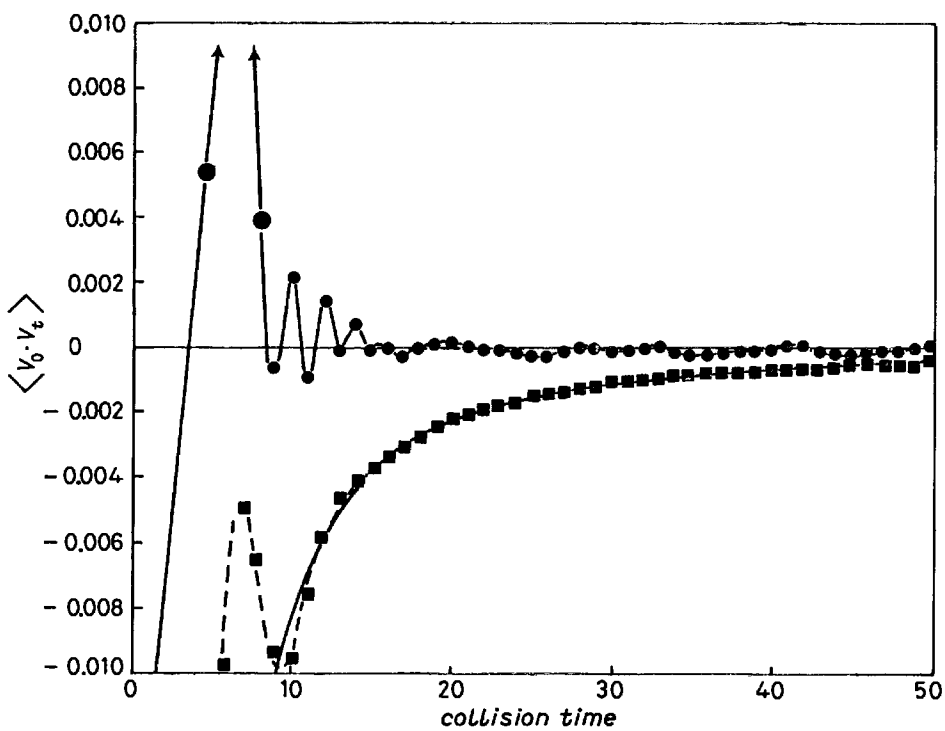

Fig. 2. – The velocity autocorrelation function for an ordered disk Lorentz gas (circles) contrasted with the one for a disordered nonoverlapping solid (squares) at the same density, $A/A_0 = 1.1$, where A_0 is the area at close packing. The solid line is an empirical power law fit to the disordered case. The velocity autocorrelation function is normalized to unity at zero time and time is given in terms of collision times.

in the case of an ordered high-density solid consisting of disks, the envelope of the oscillating velocity autocorrelation function is of exponential character. This is to be contrasted with the disordered nonoverlapping disk solid where the velocity autocorrelation function after a few oscillations has a power law tail.

We now return to the question of when a diffusion constant exists. Rigorous arguments in favor of the existence of a diffusion constant have been made for the Lorentz gas but unfortunately only under the restriction of the Boltzmann-Grad limit [15]. In that limit, long retracing trajectories are eliminated by a finite free-path cut-off. Hence, this theorem cannot distinguish between the overlapping square and disk model. In the latter, because particles can move in all directions, the probability of exactly colliding at the intersection of two disks is much lower (zero measure), so that the diffusion coefficient exists, but, nevertheless, the probability of returning is sufficiently high to produce a long tail. Thus the disk case falls into the three-dimensional class. There are variations of the square model that fall in between the Ehrenfest and disk case that are presently under investigation to determine in which category they belong. One such variation is randomly occupied squares on a chessboard where the particle can start off in any direction. A variation on that is that the randomly blocked squares can only be among the black squares of the chessboard, so that squares can only touch occasionally at their corners.

These square models are artificial. However, if scaling were to work, that would not matter. In the band theory of metals such square models are a natural extension to two dimensions of the repeated square-well square-mound potential used in one-dimensional versions. It can be shown in one dimension that if the potential is regular, that is the height and width of the square wells and square mounds are repeatedly the same, a metallic conduction band results. On the other hand, it can be shown that, if the depth of the square well and the height of the square mound are randomly selected between bounds, then the diffusion coefficient vanishes and the particle is bound no matter what its energy is relative to the mound. ANDERSON has argued that the two-dimensional version of this, where the squares on a chessboard have random heights and depths between bounds, behaves as the one-dimensional model [16]. Although the proof in one dimension is rigorous, the one in two dimensions assumes the validity of scaling. It is just this scaling that has been questioned for classical Lorentz gases.

I have, therefore, started to investigate two aspects of the Anderson model. The first one is the classical limit of that model to test whether it follows scaling and whether it conforms to the Anderson prediction of localization no matter what the energy of the particle is. The preliminary results are presented in fig. 3 and are negative on both counts. Given the Bohr correspondence principle one could still argue that ANDERSON might be right if

the limit of Planck's constant going to zero is not approached uniformly. There are precedents for the limiting process and the limit being different, particularly for discontinous potentials. In the classical limit of the Anderson model, three different regimes can be recognized. When the energy of the particle is less than half the maximum possible mound height or depth, the particle appears to be trapped, leading to an oscillating and rapidly decaying velocity autocorrelation function. If the energy of the particle is in between half and the mound maximum value, the particle diffuses with a long negative power law tail, while, with an energy above the mound, the diffusion coefficient is enormous due to a positive power law tail. The power law of the tail appears to be energy dependent, thus making scaling inoperative.

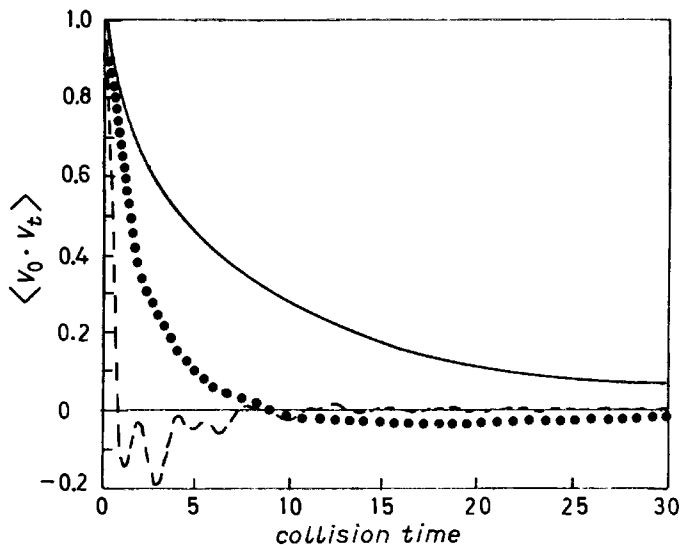

Fig. 3. – Comparison of the velocity autocorrelation function for the classical version of the two-dimensional Anderson model at three different energies relative to the maximum scattering potential. The solid lines represent the case for 1.1, the dotted line for 0.9, and the dashed line for 0.4.

The second aspect of the Anderson model investigated is its dynamical aspects. That is, we solved the time-dependent Schrödinger equation for a particle propagating through a random arrangement of overlapping disks in order to confirm a conjecture; namely, that at long times such a quantum-mechanical system has the same behavior as a classical system provided the particle is not trapped. A loose argument in favor of this is that letting $\hbar$ go to zero is equivalent to letting time go to infinity. A slightly more serious argument is to write the time-dependent Schrödinger equation in terms of an amplitude A and a phase S, that is

$$i\hbar \frac{\partial \varphi}{\partial t} = -\hbar^2/2m\nabla^2\varphi + V\varphi \tag{4.1}$$

and $\varphi = A \exp[iS/\hbar]$, so that under this Madelung transformation

$$\frac{\partial A}{\partial t} + \nabla\cdot(A^2\,\nabla S/m) = 0\,, \tag{4.2}$$

$$\frac{\partial S}{\partial t} + \frac{(\nabla S)^2}{2m} + V = \frac{\hbar^2}{2m}\frac{\nabla^2 A}{A}\,. \tag{4.3}$$

If $\hbar$ is set to zero in these two equations, we recognize that they reduce to the classical Hamilton-Jacobi equations if $\nabla S/m$ is interpreted as a velocity. The question then is under what circumstances does $\nabla^2 A/A$ vanish, so that the condition under which a single-particle quantum system behaves classically can be specified. If we make the reasonable assumption that the probability distribution, $\psi^*\psi = A^2$, is Gaussian at long times, that is $\psi^*\psi = c\cdot\exp[-x^2/\langle x^2\rangle]$, with a half width $\langle x^2\rangle = \int\psi^* x^2\psi\,\mathrm{d}\tau = Bt^\alpha$ which has a long-time tail with a positive power α, then $\nabla^2 A/A = -1/Bt^\alpha$. Thus the $\nabla^2 A/A$ term vanishes in the long-time limit unless $\alpha = 0$, in which case the particle is trapped since $\langle x^2\rangle$ is bounded. Note that, even if α is between zero and unity and hence the diffusion coefficient $\langle x^2\rangle/t$ vanishes, the conjecture still holds because the wave function is still spreading.

The weakest point in the above argument is that $\psi^*\psi$ is a smooth Gaussian. For any individual experiment the wave function is locally not smooth, for example near a scatterer. However, for an ensemble average, the assumption is likely to be valid. Thus we have committed the crime of interchanging differentiation and ensemble averages, but we are in good company. Linear fluctuation theory only holds for an average velocity autocorrelation function, any individual velocity changes upon collisions can be enormous. We thus believe that the tails in the quantum and classical velocity autocorrelation functions have the same power law. The numerical evidence given in fig. 4 is as yet too crude to say this with confidence. If it proves to be correct, an enormous amount of computer time could be saved in the investigation of tails in the quantum case, since the equivalent classical systems run orders of magnitude faster.

There are two more points to be made with respect to quantum calculations. One is that in the following lecture we present another conjecture that would be very useful in chemical-rate calculations; namely, that, in steady-state calculations, the long-time behavior of the probability density is the same in real- and imaginary-time calculations. The latter are very much easier to implement. The other point is that very convincing numerical quantum-mechanical calculations have been made that confirm Anderson's localization prediction in two dimensions [17]. The criticism that can be leveled at these calculations is that they are quasi-one-dimensional, because, in the narrow strips they investigated, the correlation length near a possible critical point exceeded the width of the system. A proper extrapolation to large two-dimen-

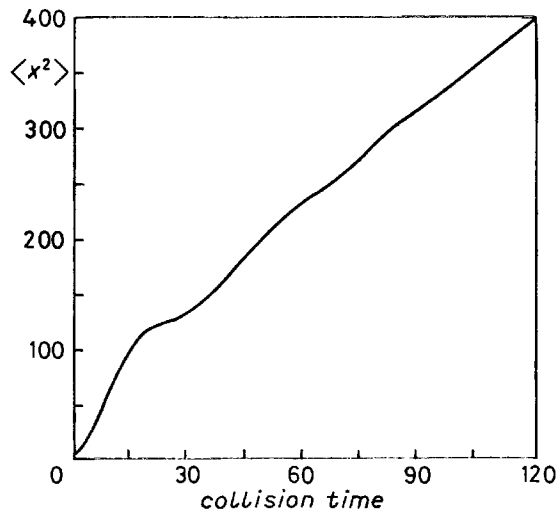

Fig. 4. – The mean square distance in units of the disk radius, r, traveled for a quantum particle in the two-dimensional overlapping Lorentz model as a function of collision time at a density of $nr^2 = 0.24$, where n is the number density of scatterers, and at an energy of 10 in $\hbar/mr$ units. The slope at long times corresponds to the diffusion coefficient, which is comparable to the classical one.

sional systems requires that in that process the width-to-correlation-length ratio be kept constant.

5. – Generalized hydrodynamics.

One of the consequences of the long-time tails is that none of the Taylor series expansions of the transport coefficients, such as in density, temperature, wavelength, frequency, gradients, etc., exists. As an illustration of the divergences, the linear Burnett coefficients for diffusion for the Lorentz gas will be discussed, because this is the only case for which the expansion could be re-expressed so that it is convergent. The reason for the divergences is that, because of the long-time memories which the tail represents, the distribution of distances a particle travels in a given time is not Gaussian except in the infinite-time limit. In that limit, the second moment of that Gaussian, or the half width, determines the diffusion coefficient. However, the next moment or cumulant, which is the first Burnett coefficient, $[\langle \Delta x^4 \rangle - 3 \langle \Delta x^2 \rangle^2]/t$, exists only if the distribution approaches the Gaussian as a Gaussian, which, because of the long-memory effects, is not the case [18]. Another way to see the divergence is to utilize the dimensional arguments by which the tail for the diffusion coefficient was analyzed. If $\langle \Delta x^2 \rangle / t$ had a tail of $t^{-\alpha}$, then $\langle \Delta x^4 \rangle / t$ must have a tail one power of t higher, namely $t^{-\alpha+1}$. Indeed, the computer results for the Lorentz gas confirmed that each successive Burnett coefficient has a tail one power of t higher than the previous one and thus sooner or later the higher ones will diverge.

The Burnett coefficients measure the dependence of the transport coefficients on the size of the relevant gradient, that is, on the wavelength of the fluctuation. The Burnett coefficients are also the coefficients that appear in the Chapman-Enskog expansion for the Boltzmann equation and in the higher-order corrections to Fick's law for diffusion

$$\frac{\partial f(x,t)}{\partial t} = D\frac{\partial^2 f}{\partial x^2} + B\frac{\partial^4 f}{\partial x^4} + \dots, \tag{5.1}$$

where f is the distribution function, and B the first linear Burnett coefficient. The proper generalization of Fick's law that leads to a redefinition of the Burnett coefficients which is well behaved is shown both by computer simulation [18] and graph-theoretical analysis to be

$$\frac{\partial f(x,t)}{\partial t} = \int_0^t \varrho(t-t')\frac{\partial^2 f}{\partial x^2}\,\mathrm{d}t' + \frac{B}{D}\int_0^t \varrho(t-t')\frac{\partial^4 f}{\partial x^4}\,\mathrm{d}t' + \dots. \tag{5.2}$$

If the velocity autocorrelation function, ϱ, is short ranged, then the expression reduces to the older theory. If that is not the case, a nonlocal in time memory function, ϱ, generalizes Fick's law into an integral differential equation. For fluids a memory function that is both nonlocal in time as well as in space must be introduced to obtain a convergent series. That memory function has not been firmly established. In the Lorentz gas with stationary scatterers such nonlocal spatial correlations cannot develop. Another simplification in the Lorentz gas is that all the higher Burnett coefficients have the same memory function, which may not be the case in fluids. For the nonlinear Burnett coefficients, namely coefficients of the form of $(\partial^2 f/\partial x^2)^2$, even the appropriate fluctuation dissipation expression of the Kubo form has not yet been formulated, although it too is expected to diverge.

Even though the dependence of the generalized transport coefficients on the wavelength, the frequency and the amplitude of the fluctuations is not analytic, there exists fluctuating hydrodynamic formulations for these generalized coefficients that are amenable to calculation by molecular dynamics [19] and which determine the value of the transport coefficients for specific values of the wavelength and the frequency, but, as mentioned above, this is not the case for the amplitude. The latter formulation is being worked on, and thus we can only discuss generalized linear-transport theory. The purpose of generating these generalized linear-transport coefficients is to replace the constant transport coefficients in the Navier-Stokes equations by them, so as to introduce a length and time scale into the hydrodynamic equations. From that it is possible to learn to what small-distance and short-time scales hydrodynamics can be pushed. We already know from the hydrodynamic

model for the tail that hydrodynamics applies on a submicroscopic scale and at less than picosecond times. We also know that in order to explain the negative feature in the velocity autocorrelation function near solidification densities by a hydrodynamic model a nonlocal wavelength- and frequency-dependent viscosity is required. The primary cause of this nonlocality in time of the viscosity is the molasses tail. We furthermore know that such a viscosity is required to explain shear mode propagation observed in the fluid phase near solidification in the neutron scattering function.

The only hydrodynamic problem actually solved so far with generalized transport coefficients is the Stokes problem of an infinitely massive sphere falling in a fluid, in order to find out what the corrections to Stokes law would be if the sphere was of atomic dimensions [19]. Indeed, it was found that the corrections were small, only about 30 % for the friction coefficient compared to the macroscopic sized sphere. In general, it is extremely difficult to solve the Navier-Stokes equation with nonlocal transport coefficients. It is hard enough to solve the ordinary Navier-Stokes equation with constant coefficients even when the nonlinear (in the square of the velocity) term that leads to hydrodynamic instabilities, such as turbulence, is left out. Usually, further simplifications such as incompressiblity or inviscidness have to be introduced to simplify the mathematics. Yet, frequently the physical situation is even more complex, particularly in those leading to hydrodynamic instabilities. Then, the fluid often contains regions where the gradients are steep. However, even the equations to describe that situation are not yet formulated, let alone numerically tractable.

There now emerges a possibility to circumvent, at least for some physical situations, this complex program of calculating the linear and nonlinear generalized transport coefficients and introducing them into the conservation laws, leading to Navier-Stokes type of equations that are computationally difficult to solve. That scheme takes advantage of the earlier observations that hydrodynamics works on an atomic scale; namely, it suggests to simulate via molecular dynamics directly the hydrodynamic problem. Thus, instead of solving the Navier-Stokes equations, solve the Liouville equation for perhaps 100 000 particles for initial conditions which mock up the physical situation. Encouraging results in that direction have recently been obtained for a plate representing a satellite entering the Earth's atmosphere near sound speed velocities [20]. Using 40 000 particles to represent the three-dimensional medium allowed the system to be some one hundred mean free paths wide. The solid-plate width was a substantial fraction of the width of the system. The velocity field and streamlines that were calculated by molecular dynamics showed clear evidence of the alternate vortex-shedding phenomenon leading to realistically looking wakes behind the plate. The comparable hydrodynamic problem has yet to be solved. It appears that, as computers can handle bigger and bigger molecular-dynamics systems for longer and longer times, the direct

simulation of complex hydrodynamic phenomena is a practical possibility. In the above problem it would have been possible to represent the plate and hence the solid-fluid boundary conditions more realistically by having the solid plate made up of particles as well. What may ultimately be most effective is to solve the hydrodynamic problem on a molecular scale until the nonlinear and memory effects have disappeared and then feed that molecular-dynamics solution as an input to the Navier-Stokes equation to pursue the problem to macroscopic distance and time scales.

In this connection it is worthwhile to briefly summarize under what circumstances one needs to use what form of linearized, generalized hydrodynamics, and where one only needs ordinary hydrodynamics; that is, where ordinary ($k = 0$, $w = 0$) transport coefficients suffice. For orientational purposes $k\sigma = 2\pi$ or $1/k\sigma \sim 0.15$ represents the atomic spacing and $V/V_0 = 5$ corresponds roughly to the liquid-gas critical-point volume of a fluid, while $V/V_0 = 1.5$ is the fluid-solid coexistence volume. As can be seen from fig. 5, ordinary hydrodynamics works beyond some 20 intermolecular spacings or some 100 Å at all densities. For smaller distances, the hydrodynamic relaxation time, $(\nu k^2)^{-1}$, is not long compared to the molasses tail relaxation time and viscoelastic effects appear and a time- or frequency-dependent viscosity needs to be used. At lower densities, however, where there is no significant molasses tail, such a region never appears nor does there appear a region where both nonlocality in space

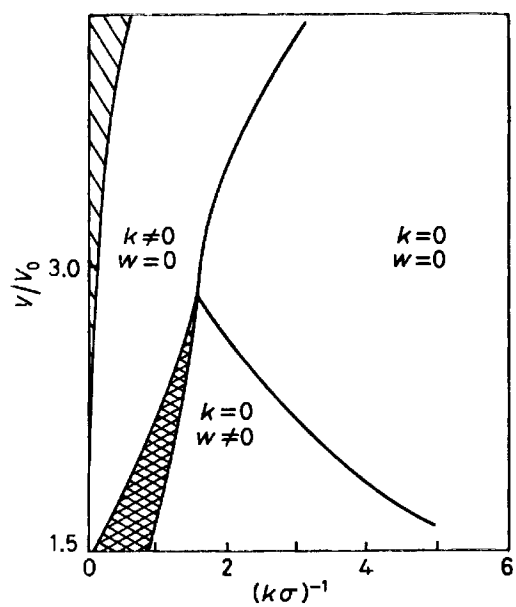

Fig. 5. – Schematic diagram denoting the various regimes of validity of different forms of generalized hydrodynamics for hard-sphere fluids depending on the density, V/V_0, given as the volume, V, relative to the close packed volume V_0, *vs.* the reciprocal wave number, k, times the hard-sphere diameter σ. In the singly hatched region hydrodynamics is not applicable because the mean free path is too large. In the double hatched region neither $k = 0$ nor $w = 0$ is applicable, thus fully generalized hydrodynamics must be used.

and time has to be taken into account. However, when the wave number gets to be such that wavelengths less than an intermolecular spacing are considered, the continuum approximation of hydrodynamics starts to break down. On the other hand, kinetic theory becomes valid and hydrodynamics can be converted to kinetic theory by the device of using wavelength-dependent transport coefficients. However, when the distances to be considered are smaller than a mean free path, the whole approach breaks down.

* * *

I want to thank E. ALLEY and S. FUTRAL for their significant contributions to this lecture. Work performed under the auspices of the U. S. Department of Energy by the Lawrence Livermore National Laboratory under contract number W-7405-ENG-48.

REFERENCES

[1] B. J. ALDER and T. E. WAINWRIGHT: *Phys. Rev. A*, **1**, 18 (1970).
[2] B. J. ALDER and T. E. WAINWRIGHT: *J. Phys. Soc. Jpn.*, **26**, 267 (1969).
[3] B. J. ALDER, D. M. GASS and T. E. WAINWRIGHT: *J. Chem. Phys.*, **53**, 3813 (1970).
[4] J. R. DORFMAN and E. G. D. COHEN: *Phys. Rev. Lett.*, **25**, 1257 (1970).
[5] H. H. H. H. YUAN and I. OPPENHEIM: *Physica (Utrecht) A*, **90**, 561 (1978).
[6] D. J. EVANS: in *Nonlinear Fluid Behavior*, edited by H. J. M. HANLEY (North-Holland, Amsterdam, 1983), p. 51.
[7] B. L. HOLIAN and D. J. EVANS: *J. Chem. Phys.*, **78**, 5147 (1983).
[8] B. J. ALDER, T. E. WAINWRIGHT and D. M. GASS: *Phys. Rev. A*, **4**, 233 (1971).
[9] J. ERPENBECK: *Phys. Rev. Lett.*, **52**, 1333 (1984).
[10] B. J. ALDER, H. L. STRAUSS and J. J. WEIS: *J. Chem. Phys.*, **59**, 1002 (1973).
[11] E. LEUTHEUSSER: *Phys. Rev. A*, **29**, 2765 (1984).
[12] E. H. HAUGE and E. G. D. COHEN: *J. Math. Phys. (N. Y.)*, **10**, 379 (1969).
[13] W. W. WOOD and F. LADO: *J. Chem. Phys.*, **7**, 528 (1971).
[14] L. A. BUNIMOVICH and Y. SINAI: *Commun. Math. Phys.*, **78**, 479 (1981).
[15] J. L. LEBOVITZ and H. SPOON: *J. Stat. Phys.*, **19**, 633 (1978).
[16] E. ABRAHAMS, P. W. ANDERSON, D. C. LICCIARDELLO and T. V. RAMAKRISHNAN: *Phys. Rev. Lett.*, **42**, 673 (1979).
[17] A. MACKINNON and B. KRAMER: *Phys. Rev. Lett.*, **49**, 695 (1982).
[18] B. J. ALDER and W. E. ALLEY: in *Perspective in Statistical Physics*, edited by H. RAVECHE (North-Holland, Amsterdam, 1981), p. 3.
[19] W. E. ALLEY and B. J. ALDER: *Phys. Rev.*, **27**, 3158 (1983).
[20] E. MEIBURG: *Phys. Fluids*, to appear, October 1986.

Reaction Rate Calculations via Transmission Coefficients.

M. D. FEIT and B. J. ALDER

Lawrence Livermore National Laboratory, University of California
Livermore, CA 94550

1. – Introduction.

The calculation of thermal average reaction rates is a formidable task, requiring, in principle, the solution of a time-dependent quantum many-body problem involving nuclei and electrons. Such calculations are completely intractable in a practical sense. The theory is simplified by tacitly ignoring all dynamical correlations between the reacting atoms and introducing a Born-Oppenheimer potential surface to describe the motion of the nuclei in the average field of the electrons. This itself entails the solution of an equilibrium quantum many-body problem in which the nuclei are held fixed. Assuming the validity of such an adiabatic potential surface (despite the fact that the best-known potentials contain the light element hydrogen for which the approximation is least applicable), the rate problem can be formulated in terms of an S-matrix linking the reactant and product states. The rate calculation via the S-matrix is still an extremely difficult calculation; furthermore all the detailed information about intermediate states is finally thrown away when the thermal averaging is carried out.

The simple reaction rate theory [1] eliminates the need for such time-dependent calculations by assuming equilibration along the reaction path. This assumption reduces the time-dependent aspect of the rate calculation to a determination, for the given physical situation, of how many reactants attempt to scale the potential barrier per unit time or the flux of such particles. This flux is then related to the reactive flux across the barrier by a Boltzmann factor.

The final step in completing a rate calculation in this model is the determination of the relative probabilities of the system ending up in the reactant or various product channels given that the initial flux was crossing the phase space surface dividing reactants from products. From these probabilities, the so-called conversion coefficient or transmission coefficient can be calculated.

The essential point we wish to make here is that this conversion coefficient,

which accounts for multiple crossings of the dividing surface and tunneling, need not be obtained from a dynamic calculation. It should be obtainable from a steady-state quantum Monte Carlo calculation. Not only are such calculations easier than time-dependent calculations, they can readily be extended to multidimensional situations.

The physical reason steady-state calculations should suffice is simply that at long times the relative probabilities in the various channels are time independent. After the reaction is over, the products and reactants are far removed from the potential barrier and can be considered as « free » particles. With increasing time, their wave functions spread and become more plane-wave-like as the particle moves down a channel; however, the net probability in a given channel remains invariant.

The method proposed here is analogous to the well-established classical picture of reaction rates. In that picture, a particle confined to the top of the barrier, selected from an equilibrium distribution, is released and monitored to determine where it ends up. Starting such particles at the top of the barrier overcomes the difficulty of looking for rare events. An average over many initial releases determines the conversion coefficient.

Alternatively, one could have dynamically followed a particle at the top of the barrier with an initial velocity selected from a thermal distribution and calculated a velocity-velocity autocorrelation function by averaging over many different initial velocities. The time integral of the autocorrelation function directly measures the conversion factor since it is proportional to the probability of ending up in a given channel. Calculations of such time-dependent flux-flux autocorrelation functions quantum mechanically in many-dimensional systems have not been possible. Recently such flux autocorrelation functions have, however, been calculated numerically in « imaginary time » since that involves only an equilibrium calculation [2]. To obtain the real-time autocorrelation function, one is then faced with an uncertain extrapolation from imaginary- to real-time behavior, *i.e.* numerical analytic continuation. The present lecture shows that this analytic continuation is unnecessary. The equivalence of a real-time dynamic calculation with a steady-state calculation of the flux is demonstrated in a one-dimensional example.

2. – Formalism.

The formal equivalence of these different approaches is easily demonstrated from the definition of the transmission coefficient as the temporal integral of the probability flux into the product space normalized by the total probability. It is from the direct calculation of the probability flux according to the above definition that we obtain the transmission coefficient. The connection between such a real-time calculation of the probability flux

and the corresponding imaginary-time one will be made by noting that at long times the behavior in both cases is dominated by small energy splittings. The connection is made quantitative by accounting for the nonconservation of probability in imaginary-time calculations by scaling the steady-state calculation by a factor corresponding to the weight of the outgoing final state present in the initial wave packet.

To define the transmission coefficient, consider a simple wave packet initially located on the transition surface and having an initial velocity v along the reaction co-ordinate. The transition surface is defined here as passing through the saddle point, and otherwise being everywhere normal to equipotentials. In the case of multiple product channels, we assume the product space can be divided into parts associated with each product separately. This should cause no practical difficulty. The transmission coefficient is calculated directly by integrating the Schrödinger equation of motion

$$i\hbar \frac{\partial \psi}{\partial t} = -\frac{\hbar^2}{2m} \nabla^2 \psi + V\psi \tag{2.1}$$

until there is no longer any change in the division of probability between the reactant and product channels. The probability density $\varrho = \psi^* \psi$ obeys the continuity equation

$$\frac{\partial \varrho}{\partial t} + \nabla \cdot \boldsymbol{J} = 0 \,, \tag{2.2}$$

where the probability current density $\boldsymbol{J}$ is given by

$$\boldsymbol{J} = \frac{\hbar}{2im} (\psi^* \nabla \psi - \psi \nabla \psi^*) \,. \tag{2.3}$$

If we call f the amount of probability in the product space (p.s.), it follows that

$$\frac{\mathrm{d}f}{\mathrm{d}t} = \int_{\text{p.s.}} \frac{\partial \varrho}{\partial t} \, \mathrm{d}V = -\int_{\text{p.s.}} \nabla \cdot J \, \mathrm{d}V = -\int_{n} J \mathrm{d}A \equiv F(t) \,, \tag{2.4}$$

where the first two forms are integrated over the entire product space volume V. Green's theorem allows the volume integral to be transformed into a surface integral over the transition surface A. We define the flux $F(t)$ as the probabilty per unit time flowing across the transition surface into the product space, noting that f changes because of this probability flow. The transmission coefficient τ is defined as the normalized increase of probability in the product space in the long-time limit , *i.e.*

$$\tau = f(t) - f(0) = \int_0^t F(t') \, \mathrm{d}t' \,. \tag{2.5}$$

A wave packet with initial flux $F(0)$ then contributes $\tau F(0)$ to the reactive flux $\mathscr{F}$. The rate k equals the thermal average reactive flux $\langle\mathscr{F}\rangle$ times a Boltzmann factor $\exp[-V_0/kT]$, where V_0 is the barrier height. The equivalence between the flux autocorrelation function expression for the rate and the transmission coefficient expression used in the present lecture is shown by writing the reactive flux as

$$\langle\mathscr{F}\rangle = \langle\tau F(0)\rangle = \int_0^t \mathrm{d}t' \langle F(t')F(0)\rangle\,, \tag{2.6}$$

where we have interchanged the temporal and ensemble averagings, which is permitted at equilibrium. Thus the thermal average of the net reactive flux, taken as the initial flux times a transmission coefficient, can be rewritten as the temporal integral of a thermally averaged flux-flux autocorrelation function.

The equivalence between real- and imaginary-time calculations of the transmission coefficient is established by first noting that at long times the probability in each channel becomes time independent. Then it is shown that the ultimate steady-state division of probability between the channels depends, in both real and imaginary time, on the energy splitting of the lowest-energy states.

In practice, the system can be considered to be confined to a « box » of side L and the steady-state result is reached when the wave packets are well removed from the potential barrier, but have not reached the boundaries of the box. The use of wave packets in a finite-size « box » should be acceptable provided the box is large compared to the scale size of the potential barrier. It can be shown that the total flux is independent of L since the flux is proportional to the energy splitting, which varies as $1/L$ as the box gets larger, while the number of contributing states is proportional to the density of states $L/2\pi$, so the product is independent of L. The final asymptotic steady state can be considered to consist of plane waves $\exp[\pm ikx]/\sqrt{L}$ of wave number $k = 2\pi n/L$. The long-time division of probability will be shown to depend on the energy splitting between these lowest-energy plane-wave states. This situation is entirely analogous to the transfer of probability between two states coupled through a potential-energy barrier [3]; the rate of transfer is proportional to the energy splitting between the states and the amount transferred depends on an overlap integral. The main difference is that in the double potential well an equilibrium distribution is established, while here a steady state is reached.

The flux across the potential barrier in a box can be written in terms of energy differences by expressing ψ as a linear combination of eigenstates u_l

$$\psi = \sum_l A_l\, U_l(r) \exp[-iE_l\, t/\hbar]\,, \tag{2.7}$$

with expansion coefficients A_l. We use the definition of the flux $F(t)$ given in

eq. (2.4), and substitute $H\psi$ for $i\hbar\,\mathrm{d}\psi/\mathrm{d}t$ to find

$$F(t) = \int_{\text{D.S.}} \frac{\partial}{\partial t}(\psi^*\psi)\,\mathrm{d}V = \frac{1}{i\hbar}\int_{\text{D.S.}} (\psi^* H\psi - \psi H\psi^*)\,\mathrm{d}V\,, \tag{2.8}$$

with H the Hamiltonian operator of eq. (2.1). Thus the eigenfunction expansion yields

$$F(t) = \sum_{l,m} A_l^* A_m \left[\int_{\text{D.S.}} U_l^* U_m\,\mathrm{d}V\right] \frac{E_m - E_l}{i\hbar} \exp\left[-i[E_m - E_l]\,t/\hbar\right]. \tag{2.9}$$

This expresses the flux as a sum of terms, each of which is proportional to an overlap integral over the product space and to an energy difference. At long times, the different cosine and sine terms representing the exponential of imaginary argument dephase from each other and $F(t)$ vanishes. Thus the total probability, given by the time integral of $F(t)$ in the product space, becomes time independent:

$$\int_0^t F(t')\,\mathrm{d}t' = \sum_{l,m} A_l^* A_m \left[\int_{\text{D.S.}} U_l^* U_m\,\mathrm{d}V\right] \exp\left[-i[E_m - E_l]t/\hbar - 1\right]. \tag{2.10}$$

At long times, the dominant contribution to the sum comes from the state with the smallest energy splitting (the longest dephasing time).

The crucial point is that, in the imaginary-time solution of the Schrödinger equation, the same eigenstates are involved as for the real-time solution. The main difference is that the sinusoidal real-time dependence of $\exp[-iEt/\hbar]$ is replaced by the decaying exponential $\exp[-Et/\hbar]$ in imaginary time. Again only the lowest-energy states contribute at long times, all higher-energy states decay faster. As a consequence of this decay, rather than cancellation, a change in normalization of the wave function must be taken into account by projecting the final surviving state onto the initial wave packet. That is, since only the lowest-energy state survives to long times, the normalization is relative to the weight of the final state in the initial wave paket.

3. – Numerical example. The Eckart barrier.

As a simple test of the ideas expressed here, we have carried out both real-time and imaginary-time calculations of the transmission coefficient for a one-dimensional Eckart barrier potential

$$V(x) = V_0\left[\operatorname{sech}^2(x/a) + e\,\operatorname{tgh}(x/a)\right]. \tag{3.1}$$

Here a is the width of the barrier, V_0 its height, and e is a parameter that determines the degree of asymmetry in the barrier. Both real- and imaginary-time solutions of the Schrödinger equation were found numerically using a split-operator fast-Fourier-transform method [4] of demonstrated accuracy.

The initial wave packet for the real-time calculations consisted of a minimum-uncertainty (Gaussian) wave packet of form $\exp[-(x/\sqrt{2}s)^2]\exp[imvx/\hbar]$. The width of the wave packet was chosen so that the momentum distribution was thermal, *i.e.* $2s^2 = h^2/mkT$, and the initial velocity across the barrier was v. The long-time fraction of probability on the product side was found from the real-time solution of the Schrödinger equation with these initial conditions by using the definition of f given in eq. (2.4). Since, by symmetry, $f(-v) = 1 - f(v)$ for the symmetric barrier ($e = 0$), we report the net transmission coefficient $f(v) - f(-v) = 2f(v) - 1$ in the results for the symmetric barrier below. The corresponding initial wave packet for imaginary-time calculations is of the form $\exp[-(x/\sqrt{2}s)^2]\exp[-mvx/\hbar]$, *i.e.* with v changed to iv, which has an initial probability gradient proportional to v.

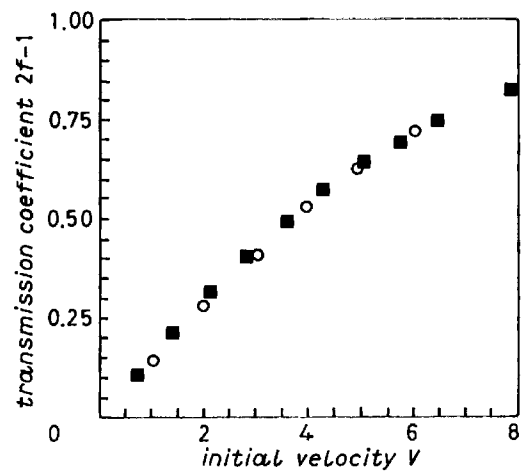

Fig. 1. – Comparison of the real-time and imaginary-time calculations of the transmission coefficient $2f - 1$ as a function of the initial wave packet velocity along the reaction co-ordinate for a symmetric Eckart potential barrier. ○ real-time calculations, ■ imaginary-time calculations. The velocity is given in units of $\hbar/ma$.

A comparison of the real- and imaginary-time determinations of the transmission coefficients for a symmetric barrier is given in fig. 1 for a set of initial velocities and at a temperature of $kT/V_0 = 0.01$. In accordance with the formal discussion, the velocity axis for the imaginary-time calculation has to be scaled or renormalized by the number of plane-wave states (Fourier components) present in the initial state relative to the single final state. In a box of side L, the plane-wave states have wave numbers separated by $2\pi/L$. Our initial Gaussian wave packet of half-width s has k-space r.m.s. half-width $1/\sqrt{2}s$. The scaling factor is thus $2(1/\sqrt{2}s)/(2\pi/L)$ or $L/\sqrt{2}\pi s$ which equals 14.405 in the present case. This scaling was tested for several values of the parameters.

For an asymmetric barrier, account has to be taken of the fact that in the imaginary-time calculation probability decays faster at long times on one side of the barrier than on the other because of the different plateau energies on the two sides. The long-time probability is given by $P_L \exp[-E_L t]$ to the left and by $P_R \exp[-E_R t]$ to the right. Hence an additional renormalization of the right-hand side probability relative to the left of $\exp[T(E_R - E_L)]$ must be applied at time T. It is also necessary to account for the fact that the initial wave function is slightly displaced from the saddle point. The very small shift in the saddle position due to the asymmetric term in the potential is numerically unimportant in the present case. However, the velocity-dependent shift due to the form of the imaginary-time initial wave packet is significant. Unimportant for the symmetric barrier, this shift enters now because of the asymmetry in probability decay rates. The wave packet can be considered as having started at some earlier (later) time or equivalently as starting with enhanced (decreased) probability for displacement of the initial wave packet to the right (left). The enhanced probability is easily calculated from the fractional increase in initial probability of the displaced Gaussian $smv/\hbar\sqrt{\pi}$ and applied as a multiplicative factor for the right-hand side probability. In the present example, this adjustement is much smaller than the factor correcting for the different plateau energies. The overall adjustment amounts to multiplying the final right-hand side probability by a factor of $30 \div 100$ in the cases shown in fig. 2. These corrections are in addition to the velocity renormalization of $L/\sqrt{2}\pi s$ which still is necessary. Results for an asymmetric barrier with $e = 0.001$ are shown in fig. 2. Again, there is a clear correspondence between real- and imaginary-time results.

From the correspondence demonstrated here between real-time and imaginary-time determinations of the transmission coefficient, we conclude that

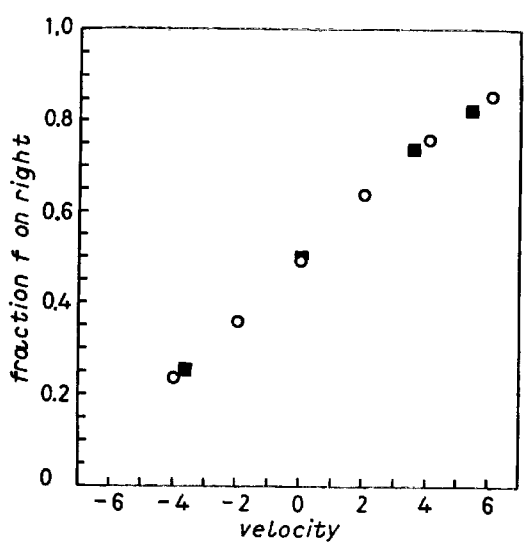

Fig. 2. – Comparison of real-time and imaginary-time calculations of f for an asymmetric Eckart barrier.

it is possible to calculate rates without recourse to time-dependent computations. The correspondence found here should be extendable to higher dimensionality. In this case, one can still pick a minimum-uncertainty wave packet along the reaction co-ordinate, and sample the transverse co-ordinates from a thermal distribution. As a practical matter, such many-dimensional calculations will be feasible only with a quantum Monte Carlo technique [5].

* * *

Work performed under the auspices of the U.S. Department of Energy by Lawrence Livermore National Laboratory under contract #W-7405-Eng-48.

REFERENCES

[1] For a recent review see P. PECHUKAS: *Annu. Rev. Phys. Chem.*, **32**, 159 (1981).
[2] W. H. MILLER, S. D. SCHWARTZ and S. W. TRUMP: *J. Chem. Phys.*, **79**, 4889 (1983).
[3] D. H. THOULESS: *Proc. Phys. Soc.*, **86**, 893 (1965).
[4] M. D. FEIT and J. A. FLECK jr.: *J. Comput. Phys.*, **47**, 412 (1982).
[5] D. M. CEPERLY and B. J. ALDER: *J. Chem. Phys.*, **81**, 5833 (1984).

Molecular-Dynamics Simulation of Coulomb Systems in Two and Three Dimensions.

J.-P. HANSEN

Laboratoire de Physique Théorique des Liquides (*)
Université Pierre et Marie Curie - 75230 *Paris* 05
Ecole Normale Supérieure de Saint-Cloud - 92211 *Saint-Cloud, France*

I. – Simulation of Coulomb Systems: How to Cope with Long-Range Forces.

1. – Introduction.

The electrostatic potential at a point $\boldsymbol{r} \in \mathscr{R}^d$ due to a charge q placed at the origin is the solution of Poisson's equation

$$\nabla^2 \varphi(r) = - C_d q \delta(\boldsymbol{r}) , \tag{1.1}$$

where $r = |\boldsymbol{r}|$, $C_d = 2,\ 2\pi,\ 4\pi$ in $d = 1, 2, 3$ dimensions.

The solutions are

$$\varphi(r) = - qr \qquad (d = 1) , \tag{1.2a}$$

$$\varphi(r) = - q \log (r/L) \qquad (d = 2) , \tag{1.2b}$$

$$\varphi(r) = \frac{q}{r} \qquad (d = 3) . \tag{1.2c}$$

While the functional form of $\varphi(r)$ depends on dimensionality, its Fourier transform exhibits the characteristic k^{-2} behaviour, which follows directly from Poisson's equation (1.1), for all d:

$$\hat{\varphi}(k) = \int \exp [i\boldsymbol{k} \cdot \boldsymbol{r}] \varphi(r) \, \mathrm{d}^d r = \frac{C_d q}{k^2} . \tag{1.3}$$

In any many-particle Coulombic system, the fundamental requirement is that

(*) Equipe associée au CNRS.

of global charge neutrality. Let $n = N_\alpha/|\Lambda|$ be the number of particles of species α, carrying an electric charge $q_\alpha = Z_\alpha e$, in a d-dimensional domain Λ of measure $|\Lambda|$; then

$$\sum_{\alpha=1}^{\nu} q_\alpha n_\alpha = 0 , \tag{1.4}$$

where ν is the total number of species. Since we are interested in classical dynamics, stability against the collapse of pairs of oppositely charged particles (a special case of H-stability) requires that the corresponding pair potential contain a short-range « regularization » of the attractive Coulumb singularity in $d > 2$ dimensions (the case $d = 2$ is special and will be discussed in part IV). The pair potentials will hence always be of the general form

$$v_{\alpha\beta}(r) = v^{s}_{\alpha\beta}(r) + v^{c}_{\alpha\beta}(r) = v^{s}_{\alpha\beta}(r) + q_\alpha q_\beta \psi(r) , \tag{1.5}$$

where $v^{s}_{\alpha\beta}(r)$ is the short-range part of the potential, and $\psi(r) = \varphi_\alpha(r)/q_\alpha = \varphi_\beta(r)/q_\beta$ if φ_α denotes the electrostatic potential (1.2) around a charge q_α. The origin of $v^{s}_{\alpha\beta}$ depends on the physical system under consideration. We shall be mainly concerned with two very different classes of Coulomb systems:

a) Fully ionized matter (or plasmas) made up of point ions (nuclei) and electrons. In that case quantum effects are never completely negligible and the short-range potentials arise from « quantum smearing » originating in the Heisenberg uncertainty principle.

b) Ionic liquids and solids of condensed-matter physics. The $v^{s}_{\alpha\beta}$ then describe the strong short-range repulsion occurring when ionic cores overlap.

Whatever their physical origin, the short-range potentials introduce a characteristic length, σ say, which sets the length scale of the problem; σ can be the ionic radius in condensed matter or the electronic de Broglie thermal wavelength in plasmas. In the following we shall almost exclusively restrict ourselves to two-component Coulomb systems ($\nu = 2$). In that case the relative proportions of positive and negative charges are fixed by eq. (1.4), and an equilibrium state of the system is characterized by two variables, temperature T and total number density $n = n_1 + n_2$. It is convenient to work with dimensionless (reduced) variables, and we shall use

$$n^* = n\sigma^d , \qquad \gamma = \frac{e^2}{k_B T \sigma^{d-2}} = \frac{1}{T^*} , \tag{1.6}$$

where e is the elementary charge. Note that v^s determines n^* (through σ), while γ is independent of σ for $d = 2$. γ can be looked upon as a Coulomb coupling constant equal to the ratio of the Coulomb potential energy of two particles at contact over the thermal energy.

A second characteristic length of the problem is independent of the interactions between particles, and defined to be the radius of the domain containing on average one particle, *i.e.* $a \sim n^{-1/d}$, so that $n^* \sim (\sigma/a)^d$; a is a measure of the interparticle spacing.

The collective behaviour of a system of charged particles is characterized by the Debye screening length λ_D, roughly equal to the range at which an external charge is shielded by the « polarization cloud » which it induces. The simple mean-field argument of Debye and Hückel leads to the expression

$$\lambda_D^{-2} = \sum_{\alpha=1}^{\nu} \lambda_{D\alpha}^{-2} = C_d \sum_{\alpha=1}^{\nu} \frac{n_\alpha q_\alpha^2}{k_B T} . \tag{1.7}$$

λ_D occurs quite naturally in the perfect-screening (or second Stillinger-Lovett) sum rule obeyed by the partial pair correlation functions $h_{\alpha\beta}(r) = g_{\alpha\beta}(r) - 1$, which follows directly from a linear-response argument [1] and can even be derived rigorously from the Yvon-Born-Green hierarchy [2]:

$$\frac{\sum_\alpha \sum_\beta x_\alpha z_\alpha x_\beta z_\beta n \int h_{\alpha\beta}(r)\, r^2\, \mathrm{d}\boldsymbol{r}}{\sum_\alpha x_\alpha z_\alpha^2} = -2d\lambda_D^2 . \tag{1.8b}$$

The corresponding first Stillinger-Lovett sum rule is merely an expression of local charge neutrality:

$$\sum_\beta x_\beta z_\beta n \int h_{\alpha\beta}(r)\, \mathrm{d}\boldsymbol{r} = -z_\alpha , \qquad 1 \leqslant \alpha \leqslant \nu . \tag{1.8a}$$

Dynamical screening is governed by the plasma frequency built from the partial Debye wave numbers $k_{D\alpha} = \lambda_{D\alpha}^{-1}$ and the thermal velocities $v_{0\alpha} = (k_B T/m_\alpha)^{\frac{1}{2}}$:

$$\omega_p^2 = \sum_\alpha \omega_{p\alpha}^2 = \sum_\alpha k_{D\alpha}^2 v_{0\alpha}^2 = C_d \sum_\alpha \frac{n_\alpha q_\alpha^2}{m_\alpha} . \tag{1.9}$$

A dimensionless parameter which plays an important role in plasma physics is the so-called « graniness » g equal to the reciprocal of the mean number of particles in a domain of size λ_D:

$$g = \frac{1}{n\lambda_D^d} . \tag{1.10}$$

If we make the transformation $n \to 2n$, $m \to m/2$, $q \to q/2$, $v \to v$ (and hence $T \to T/2$), v_0, λ_D and ω_p are invariant, but g is divided by 2. In this way it is clear that $g \to 0$ corresponds to a continuum limit where the individual character of the particles plays a negligible role in the collective behaviour, because there is a large number of particles in a Debye domain. This limit coincides

with the weak-coupling regime where the time scale set by ω_p^{-1} is much shorter than the mean collision time (collisionless regime). In ionic liquids the opposite is true, and the screening length λ_D, which becomes shorter than the interparticle spacing a, loses its physical meaning ($g > 1$).

The present lecture is devoted to a review of molecular-dynamics simulations of equilibrium structure, microscopic dynamics and linear transport of classical Coulomb systems; it is organized as follows:

The first part examines the technical problem of dealing with long-range forces.

The second part is devoted to strongly coupled plasmas.

Ionic liquids and solids, including molten salts and superionic conductors will be the topic of part III. Ionic solutions will not be included in this brief survey, because the solvent (*e.g.*, water) introduces additional complications.

The last part describes some recent simulation work on two-dimensional Coulomb systems; the main emphasis will be on the two-component Coulomb gas which exhibits an interesting « metal-insulator » (or Kosterlitz-Thouless) transition.

2. – The problem of long-range forces.

The usual procedure for simulating bulk properties and minimizing surface effects in molecular-dynamics (MD) « experiments » on small ($N = 10^2 \div 10^3$) samples is to use periodic boundary conditions (PBC). This must, however, be supplemented by a prescription of how to handle the interactions between particle images belonging to different periodic replicas of the basic simulation cell. If the interatomic forces are of short range (as in a Lennard-Jones fluid), one of two conventions is used:

a) Spherical cut-off: the force between two particles is truncated beyond a cut-off radius r_c. This procedure is totally inapplicable in the case of slowly decaying ($\sim r^{1-d}$) Coulomb forces, for two reasons. Firstly, it introduces large discontinuities at the distance of truncation; secondly, it tends to violate local charge neutrality, because a charged particle will tend to expel equally charged particles, and to attract oppositely charged particles situated near the boundary of its interaction sphere, in order to lower the total potential energy. For that reason highly unphysical behaviour is observed if a spherical cut-off is applied to Coulomb systems [3].

In some instances the spherical-cut-off convention can be maintained for Coulomb systems, provided the pair potential is divided into short-range (*e.g.*, a screened Coulomb potential) and long-range parts:

$$v_{\alpha\beta}(r) = v_{\alpha\beta}^{(0)}(r) + v_{\alpha\beta}^{(1)}(r) \,. \tag{2.1}$$

The « reference » system of particles interacting via $v^{(0)}_{\alpha\beta}(r)$ may then be simulated with the spherical–cut-off convention, provided $v^{(0)}_{\alpha\beta}(r)$ is negligibly small for $r = r_c$, while the « tail » $v^{(1)}_{\alpha\beta}(r)$ can be treated by perturbation theory, *e.g.* by a generalized random-phase approximation. This idea has been successfully applied to the calculation of static properties (like the structure factors) of ionic fluids [4, 5], but it cannot be extended to the calculation of dynamical properties (like time-dependent correlation functions) since the latter are much more sensitive to details of the interactions than the static properties. In fact, thermodynamic perturbation theory, in powers of the perturbation Hamiltonian $H^{(1)}$, is known to be rapidly convergent in dense fluids [6], but a similar expansion in powers of the associated Liouville operator $\mathscr{L}^{(1)}$ is bound to fail because the particle trajectories depend strongly on the force law (exponential divergence of trajectories).

b) Minimum-image (or nearest-image) convention. This standard procedure has the advantage of maintaining strictly local charge neutrality when applied to systems of charged particles. A necessary (but far from sufficient) condition for success is that the linear dimension of the system (*i.e.* the box size) exceed the range of static correlations (*i.e.* the Debye length in the weak-coupling limit). Under these conditions, the miminum-image convention has been shown to yield reasonable, weakly N-dependent, results for the thermodynamic properties and the pair structure of plasmas [7] and electrolytes [8] characterized by a graniness parameter $g \leqslant 1$. In practice, several runs for increasing sample sizes N must be carried out, and the results plotted *vs.* $1/N$ to be extrapolated to the thermodynamic limit ($1/N = 0$). However, the minimum-image rule fails again badly when it is used to compute dynamical correlation functions, even when the coupling is relatively weak ($g \leqslant 1$) [9]. An example will be given in part II. The situation might be improved by the use of simulation cells that are more spherical in shape than the usual d-dimensional cube (like the truncated octahedron in 3d [10]), but this has not yet been checked in the case of dynamical properties. Because of the failure of the spherical-truncation and nearest-image schemes in the case of Coulombic systems, the generally accepted procedure (at least in 3d!) is to replace the bare Coulomb force between two particles in the simulation cell by an effective one obtained by summing the interactions between *all* the periodic images of these particles. To implement this procedure, two complementary points of view may be adopted. The first one focuses on the pair forces (« action at a distance » formulation) and makes use of well-established Ewald summation techniques [11] familiar from the calculation of Madelung constants in solid-state physics. The second point of view is that generally adopted in the particle codes of plasma physics, and amounts to a solution of Maxwell's field equations for a strictly periodic system, using a time-space grid (« force at a point » formulation).

3. – Ewald summations.

Consider a system of N charges $\{q_i\}$ satisfying condition (1.4), enclosed in a d-dimensional cube of edge L, together with the infinite array of periodic replicas. The total Coulomb energy of the system is

$$V_N^{\mathrm{C}} = \tfrac{1}{2} \sum_{\boldsymbol{n}} \sum_i \sum_j{}' \, q_i q_j \psi(|\boldsymbol{r}_{ij} + L\boldsymbol{n}|) \,, \tag{3.1}$$

where $\boldsymbol{r}_{ij} = \boldsymbol{r}_i - \boldsymbol{r}_j$, the first sum is over all vectors of integer components, and the primed summation implies $i \neq j$ if $\boldsymbol{n} = \boldsymbol{0}$. Now, while the simulation cell is electrically neutral, it carries, for any instantaneous configuration of the N charges, a total dipole moment

$$\boldsymbol{M}_N = \sum_{i=1}^{N} q_i \boldsymbol{r}_i \,. \tag{3.2}$$

Each periodic image of the basic ($\boldsymbol{n} = \boldsymbol{0}$) cell carries an identical dipole moment. For sufficiently large $|\boldsymbol{n}|$, the electrostatic energy of interaction between the basic cell and its image $\boldsymbol{n}$ can be calculated by a multipole expansion, of which the leading term is the dipole-dipole interaction $\boldsymbol{M}_N \boldsymbol{M}_N : \nabla\nabla\psi(\boldsymbol{r})|_{\boldsymbol{r}=L\boldsymbol{n}}$ which is $O(|\boldsymbol{n}|^{-d})$. Consequently the lattice sum in eq. (3.1) is *conditionally* convergent, *i.e.* it depends on the order in which the summation over $\boldsymbol{n}$ is taken [12]. In other words, the electrostatic energy (3.1) depends on the shape of the infinite array of periodic replicas of the basic cell because of the polarization (surface charge) of the infinitely remote boundary. The problem has been examined in detail by DE LEEUW *et al.* [12-14], who used convergence factors, of the form $\exp[-sL^2|\boldsymbol{n}|^2]$, to sum (3.1) over concentric spherical shells, taking the limit $s \to 0$ at the end of the calculation. An alternative, more general formulation has been worked out by PILLER [15]; here we follow closely his derivation.

Consider a basic simulation cell of measure $|\Lambda|$ (*e.g.*, a cube) and its periodic replicas, positioned at $\boldsymbol{R}$, inside a domain of arbitrary shape D; the domain is enlarged by multiplying its « radius » $|D|^{1/d}$ by a scale factor ξ which will tend to ∞ at the end of the Ewald transformation of

$$V_N(D_\xi) = \tfrac{1}{2} \sum_{\boldsymbol{R} \in D_\xi} \sum_i \sum_j{}' \, q_i q_j \psi(|\boldsymbol{r}_{ij} + \boldsymbol{R}|) \,. \tag{3.3}$$

$\psi(\boldsymbol{r})$ is the solution of the d-dimensional Poisson equation (1.1). We introduce an auxiliary « smeared » charge distribution $\varrho(\boldsymbol{r})$ and the associated potential $\psi_r(\boldsymbol{r})$, which is regular at the origin:

$$\nabla^2 \psi_r(\boldsymbol{r}) = - C_d \varrho(\boldsymbol{r}) \,. \tag{3.4}$$

Equation (3.3) can now be rewritten as

$$V_N = V_N^{(0)} + V_N'^{(1)}, \tag{3.5}$$

where the short-range and long-range parts are, respectively,

$$V_N^{(0)} = \tfrac{1}{2} \sum_{\boldsymbol{R}\in D_\xi} \sum_i \sum_j{}' q_i q_j [\psi(|\boldsymbol{r}_{ij} + \boldsymbol{R}|) - \psi_r(|\boldsymbol{r}_{ij} + \boldsymbol{R}|)], \tag{3.6a}$$

$$V_N'^{(1)} = \tfrac{1}{2} \sum_{\boldsymbol{R}\in D_\xi} \sum_i \sum_j{}' q_i q_j \psi_r(|\boldsymbol{r}_{ij} + \boldsymbol{R}|) . \tag{3.6b}$$

$V_N^{(0)}$ is short-ranged if $\varrho(\boldsymbol{r})$ is chosen such that $\psi(\boldsymbol{r}) - \psi_r(\boldsymbol{r})$ is integrable, *i.e.* decays more rapidly than r^{-d}. In practical MD simulations, $\varrho(\boldsymbol{r})$ is chosen such that $\psi(\boldsymbol{r}) - \psi_r(\boldsymbol{r})$ is negligible outside the basic simulation cell, and the minimum-image convention can be used to calculate (3.6*a*). To calculate $V_N'^{(1)}$ we first add and subtract the term $\boldsymbol{R} = 0$, $i = j$:

$$V_N'^{(1)} = \frac{1}{2} \sum_{\boldsymbol{R}\in D_\xi} \sum_i \sum_j q_i q_j \psi_r(|\boldsymbol{r}_{ij} + \boldsymbol{R}|) - \frac{1}{2} \sum_i q_i^2 \psi_r(r = 0) = \\ = V_N^{(1)} - \frac{\psi_r(r = 0)}{2} \sum_i q_i^2 . \tag{3.7}$$

Next we rewrite $V_N^{(1)}$ by introducing the characteristic function $f_\xi(\boldsymbol{r})$ of the domain D_ξ:

$$V_N^{(1)} = \tfrac{1}{2} \sum_{\boldsymbol{R}\in\mathscr{R}^d} \sum_i \sum_j q_i q_j \psi_r(|\boldsymbol{r}_{ij} + \boldsymbol{R}|) f_\xi(\boldsymbol{R}) = \\ = \tfrac{1}{2} \sum_{\boldsymbol{R}} \int \mathrm{d}\boldsymbol{r}\, \delta(\boldsymbol{r} - \boldsymbol{R}) f_\xi(\boldsymbol{r}) \sum_i \sum_j q_i q_j \psi(|\boldsymbol{r}_{ij} + \boldsymbol{r}|) . \tag{3.8}$$

Upon introduction of the Fourier transforms $\hat{f}_\xi(\boldsymbol{k})$ and $\hat{\psi}_r(\boldsymbol{k})$ of $f_\xi(\boldsymbol{r})$ and $\psi_r(\boldsymbol{r})$, and inverting the order of summations, (3.8) can be cast in the form

$$V_N^{(1)} = \frac{1}{2} \frac{1}{(2\pi)^{2d}} \int \mathrm{d}\boldsymbol{k}\, \hat{f}_\xi(\boldsymbol{k}) \int \mathrm{d}\boldsymbol{k}'\, \hat{\psi}_r(\boldsymbol{k}') \sum_i \sum_j q_i q_j \cdot \\ \cdot \exp[i\boldsymbol{k}'\cdot\boldsymbol{r}_{ij}] \sum_{\boldsymbol{R}} \int \mathrm{d}\boldsymbol{r}\, \delta(\boldsymbol{r} - \boldsymbol{R}) \exp[i\boldsymbol{r}\cdot(\boldsymbol{k} + \boldsymbol{k}')] . \tag{3.9}$$

Next we make use of the identity

$$\sum_{\boldsymbol{R}} \exp[i\boldsymbol{R}\cdot(\boldsymbol{k} + \boldsymbol{k}')] = \frac{(2\pi)^d}{|\Lambda|} \sum_{\boldsymbol{G}} \delta(\boldsymbol{k} + \boldsymbol{k}' - \boldsymbol{G}) , \tag{3.10}$$

where the $\boldsymbol{G}$ are reciprocal-lattice vectors; then

$$V_N^{(1)} = \frac{1}{2|\Lambda|} \frac{1}{(2\pi)^d} \int \mathrm{d}\boldsymbol{k}\, \hat{f}_\xi(\boldsymbol{k}) \sum_{\boldsymbol{G}} \hat{\psi}_r(\boldsymbol{G} - \boldsymbol{k}) \sum_i \sum_j q_i q_j \exp[i\boldsymbol{r}_{ij}\cdot(\boldsymbol{G} - \boldsymbol{k})] . \tag{3.11}$$

Now

$$\lim_{\xi\to\infty} \hat{f}_\xi(\boldsymbol{k}) = (2\pi)^d\, \delta(\boldsymbol{k}) \tag{3.12}$$

and, according to Poisson's equation (3.4),

$$\hat{\psi}_r(k) = \frac{C_d}{k^2}\, \hat{\varrho}(k)\ . \tag{3.13}$$

Hence it is clear that only the term $\boldsymbol{G} = \boldsymbol{0}$ in eq. (3.11) will pose a problem in the limit $\xi \to \infty$. We separate off this term, labelled V_N^{pol} for reasons to become clear below, and write

$$\lim_{\xi\to\infty} V_N^{(1)} = \frac{1}{2|\Lambda|} \sum_{\boldsymbol{G}\neq\boldsymbol{0}} \hat{\psi}_r(\boldsymbol{G}) |\varrho_{\boldsymbol{G}z}|^2 + V_N^{\text{pol}}\,, \tag{3.14}$$

where

$$\varrho_{\boldsymbol{G}z} = \sum_i q_i \exp\left[i\boldsymbol{G}\cdot\boldsymbol{r}_i\right] \tag{3.15}$$

is a Fourier component of the microscopic charge density of the sample. Moreover,

$$\begin{aligned}
V_N^{\text{pol}} &= \lim_{\xi\to\infty} \frac{1}{2|\Lambda|} \frac{1}{(2\pi)^d} \int \mathrm{d}\boldsymbol{k}\, \hat{f}_\xi(\boldsymbol{k})\, \psi_r(k) \sum_i \sum_j q_i q_j \exp\left[-i\boldsymbol{k}\cdot\boldsymbol{r}_{ij}\right] = \\
&= \lim_{\xi\to\infty} \frac{1}{2|\Lambda|} \frac{1}{(2\pi)^d} \int \mathrm{d}\boldsymbol{k} \int_{D_\xi} \mathrm{d}\boldsymbol{r} \exp\left[-i\boldsymbol{k}\cdot\boldsymbol{r}\right] \hat{\psi}_r(k) \sum_i \sum_j q_i q_j \exp\left[-i\boldsymbol{k}\cdot\boldsymbol{r}_{ij}\right] = \\
&= \lim_{\xi\to\infty} \frac{1}{2|\Lambda|} \int_{D_\xi} \mathrm{d}\boldsymbol{r} \sum_i \sum_j q_i q_j \psi_r(-\boldsymbol{r} - \boldsymbol{r}_{ij}) = \\
&= \lim_{\xi\to\infty} \left\{ \frac{1}{2|\Lambda|} \int_{D_\xi} \mathrm{d}\boldsymbol{r} \sum_i \sum_j q_i q_j [\psi_r(\boldsymbol{r} + \boldsymbol{r}_{ij}) - \psi(\boldsymbol{r} + \boldsymbol{r}_{ij})] + \right. \\
&\qquad\qquad \left. + \frac{1}{2|\Lambda|} \int_{D_\xi} \mathrm{d}\boldsymbol{r} \sum_i \sum_j q_i q_j \psi(\boldsymbol{r} + \boldsymbol{r}_{ij}) \right\}.
\end{aligned} \tag{3.16}$$

Since $\psi_r(r) - \psi(r)$ is integrable, the first term in the last line of (3.16) vanishes, due to charge neutrality. To evaluate the second term, we scale the variable $\boldsymbol{r}: \boldsymbol{r} \to \xi\boldsymbol{r}$:

$$\begin{aligned}
V_N^{\text{pol}} &= \lim_{\xi\to\infty} \frac{1}{2|\Lambda|}\, \xi^{d-(d-2)} \int_D \mathrm{d}\boldsymbol{r} \sum_i \sum_j q_i q_j \psi\left(\boldsymbol{r} + \frac{\boldsymbol{r}_{ij}}{\xi}\right) = \\
&= \lim_{\xi\to\infty} \frac{1}{2|\Lambda|}\, \xi^2 \int_D \mathrm{d}\boldsymbol{r} \sum_i \sum_j q_i q_j \left[\psi(\boldsymbol{r}) + \frac{\boldsymbol{r}_{ij}}{\xi}\cdot\nabla\psi(r) + \frac{1}{2}\, \frac{\boldsymbol{r}_{ij}\boldsymbol{r}_{ij}}{\xi^2} : \nabla\nabla\psi(r) + O\left(\frac{1}{\xi^3}\right)\right].
\end{aligned} \tag{3.17}$$

The first term in the integrand vanishes because of charge neutrality, the second term vanishes because $\boldsymbol{r}_{ij} = -\boldsymbol{r}_{ji}$; we are then left with

$$V_N^{\text{pol}} = \frac{1}{2|\Lambda|}\int_D \mathrm{d}\boldsymbol{r}\,\frac{1}{2}\,\boldsymbol{\nabla}\boldsymbol{\nabla}\psi(r):\sum_i\sum_j \boldsymbol{r}_{ij}\boldsymbol{r}_{ij}q_iq_j = \tag{3.18}$$

$$= -\frac{1}{2|\Lambda|}\sum_i\sum_j q_iq_j\boldsymbol{r}_i\boldsymbol{r}_j:\int_D \mathrm{d}\boldsymbol{r}\,\boldsymbol{\nabla}\boldsymbol{\nabla}\psi(r) = \frac{1}{2|\Lambda|}\overleftrightarrow{T}:\boldsymbol{M}_N\boldsymbol{M}_N\,,$$

where $\overleftrightarrow{T}$ is the depolarization tensor, which depends only on the *shape* of the domain D:

$$\overleftrightarrow{T} = -\int_D \mathrm{d}\boldsymbol{r}\,\boldsymbol{\nabla}\boldsymbol{\nabla}\,\psi(\boldsymbol{r})\,, \tag{3.19}$$

and $\boldsymbol{M}_N$ is the total dipole moment (3.2). $\overleftrightarrow{T} = \pi\overleftrightarrow{I}$ for a disk or a square (2d) and $T = (4\pi/3)\overleftrightarrow{I}$ for a sphere (3d), where $\overleftrightarrow{I}$ is the unit tensor. Gathering results, we arrive at the final expression

$$V_N = \frac{1}{2}\sum_{\boldsymbol{R}}\sum_i\sum_j{}' q_iq_j[\psi(\boldsymbol{r}_{ij}+\boldsymbol{R}) - \psi_r(\boldsymbol{r}_{ij}+\boldsymbol{R})] + \tag{3.20}$$

$$+\frac{1}{2|\Lambda|}\sum_{\boldsymbol{G}\neq 0}\hat{\psi}_r(\boldsymbol{G})|\varrho_{\boldsymbol{G}z}|^2 - \frac{\psi_r(r=0)}{2}\sum_i q_i^2 + \frac{1}{2|\Lambda|}\overleftrightarrow{T}:\boldsymbol{M}_N\boldsymbol{M}_N\,.$$

In practice $\varrho(r)$ is chosen to be a Gaussian charge distribution:

$$\varrho(r) = \frac{\alpha^d}{\pi^{d/2}}\exp[-\alpha^2r^2]\,. \tag{3.21}$$

In 2d the resulting separation of the Coulomb potential into short range and long range is [14]

$$\psi(r) = -\frac{1}{2}\ln r^2 = \frac{1}{2}\int_0^\infty [\exp[-tr^2] - \exp[-t]]\,\frac{\mathrm{d}t}{t} = \tag{3.22}$$

$$= \frac{1}{2}\int_0^{\alpha^2}\ldots + \frac{1}{2}\int_{\alpha^2}^\infty\ldots = \psi(r) - \psi_r(r) + \psi_r(r)\,.$$

The resulting expression for V_N is

$$V_N^{d=2} = \frac{1}{4}\sum_{\boldsymbol{R}}\sum_i\sum_j{}' q_iq_jE_i[\alpha^2(\boldsymbol{r}_{ij}+\boldsymbol{R})^2] + \tag{3.23}$$

$$+\frac{\pi}{S}\sum_{\boldsymbol{G}\neq 0}\frac{\exp[-G^2/4\alpha^2]}{G^2}|\varrho_{\boldsymbol{G}z}|^2 - \frac{1}{4}(\gamma + \ln\alpha^2)\sum_i q_i^2 + \frac{1}{2S}\overleftrightarrow{T}:\boldsymbol{M}_N\boldsymbol{M}_N\,,$$

where S is the area of the sample, γ is Euler's constant and E_i denotes the exponential integral. In 3d,

$$\psi_r(r) = \frac{\operatorname{erf}(\alpha r)}{r}, \tag{3.24}$$

so that

$$V_N^{d=3} = \frac{1}{2}\sum_{i\neq j}\sum q_i q_j \psi_{\text{eff}}(\boldsymbol{r}_{ij}) - \frac{\psi_r(r=0)}{2}\sum_i q_i^2 + \frac{1}{2V}\overleftrightarrow{T}:\boldsymbol{M}_N\boldsymbol{M}_N, \tag{3.24a}$$

where the *effective* potential between particles i and j is given by

$$\psi_{\text{eff}}(\boldsymbol{r}_{ij}) = \sum_{\boldsymbol{R}} \frac{\operatorname{erfc}(\alpha|\boldsymbol{r}_{ij}+\boldsymbol{R}|)}{|\boldsymbol{r}_{ij}+\boldsymbol{R}|} + \frac{2\pi}{V}\sum_{\boldsymbol{G}\neq\boldsymbol{0}} \frac{\exp[-G^2/4\alpha^2]}{G^2}\exp[i\boldsymbol{G}\cdot\boldsymbol{r}_{ij}]. \tag{3.24b}$$

In these expression V is the volume of the simulated sample, $\operatorname{erf}(x)$ denotes the error function and $\operatorname{erfc}(x)$ its complement. Note that $\psi_{\text{eff}}(\boldsymbol{r})$ is *not* spherically symmetric, but reflects the symmetry (*e.g.*, cubic) of the simulation cell. A similar effective potential can be written down in 2d, to re-express $V_N^{d=2}$ in a form entirely analogous to (3.24*a*). In practical MD simulations, α is chosen sufficiently large so that the sum over $\boldsymbol{R}$ can be limited to the term $\boldsymbol{R}=\boldsymbol{0}$ (nearest-image convention). The sum over reciprocal vectors must be typically carried over the first $N_G \simeq 10^2$ vectors $\boldsymbol{G}$ in 3d. Note that in the calculation of the N forces for a given time step this involves of the order of $N\times N_G$ operations (and not $N^2\times N_G$!), since the quantity

$$\sum_{\boldsymbol{G}\neq\boldsymbol{0}} \hat{\psi}_r(\boldsymbol{G})\,\varrho_{\boldsymbol{G}z} = \sum_{\boldsymbol{G}\neq\boldsymbol{0}} \hat{\psi}_r(\boldsymbol{G})\sum_j q_j \exp[i\boldsymbol{G}\cdot\boldsymbol{r}_j]$$

is calculated only once [16]. Thus the time spent in computing the reciprocal lattice sum is comparable to the time spent for the calculation of the short-range contribution. The alternative procedure is to tabulate $\psi_{\text{eff}}(\boldsymbol{r})$ on a d-dimensional grid, taking full advantage of the symmetry of the simulation cell, and make interpolations, but this method is demanding on computer memory and hard to vectorize.

The polarization term in eq. (3.20) is missing in careless applications of Ewald's procedure. However, if the domain D is assumed to be surrounded by a medium of dielectric constant $\varepsilon'\neq 1$, the expression for V_N^{pol}, in the case of a 3d spherical domain, must be replaced by [12]

$$V_N^{\text{pol}} = \frac{2\pi}{2\varepsilon'+1}|\boldsymbol{M}_N|^2. \tag{3.25}$$

For finite values of ε', V_N^{pol} leads to a restoring force which prevents charge diffusion and hence electrical conduction [13]. To obtain nonzero values of the

conductivity (closed circuit!), the domain D must be surrounded by a conducting medium ($\varepsilon' = \infty$), and then V_N^{pol} vanishes. This is precisely the Hamiltonian which has been used in the great majority of simulations of Coulomb systems.

4. – Particle-mesh simulations.

Another way of handling Coulombic systems is to consider strictly periodic (toroidal) systems and construct the corresponding potential by solving Poisson's equation, for a given charge distribution, in a cell with periodic boundaries. The resulting V_N can then be cast in the general form (3.20) with the polarization term V_N^{pol} missing [15].

For the sake of completeness we briefly mention the « particle-mesh » algoritms which are widely used in plasma simulation work [17]. In the purely electrostatic versions of the « particle-mesh » scheme, the electrostatic potential is computed from a finite-mesh solution of Poisson's equation on a periodic grid. A standard algorithm is an iteration of four basic steps [17]:

a) Charge assignment. Starting from a given charge density $\varrho(\boldsymbol{r})$, the distribution of electric charges at each mesh point of a d-dimensional grid is determined via a given weighting function.

b) Solution of Poisson's equation on the mesh. The Laplacian is replaced by a finite-difference approximation. The simplest example in 2d is a five-point formula

$$\frac{\varphi(i-1,j)-2\varphi(i,j)+\varphi(i+1,j)}{(\Delta x)^2}+\frac{\varphi(i,j-1)-2\varphi(i,j)+\varphi(i,j+1)}{(\Delta y)^2}= \\ =-4\pi\varrho(i,j)\,, \qquad 1\leqslant i\leqslant N_x\,,\ 1\leqslant j\leqslant N_y\,, \tag{4.1}$$

where N_x and N_y are the numbers of grid points in the x and y directions, and Δx, Δy are the corresponding grid spacings. Equations such as (4.1) are conveniently solved by fast-Fourier-transform techniques.

c) Force interpolation. The forces are computed from the mesh-defined potential φ and then interpolated at particle positions.

d) Particle displacement. Particle positions are redefined according to the applied forces, as in MD codes.

For large systems (N up to 10^6 particles!) the particle-mesh codes are much more efficient than MD codes which require of the order of N^2 operations at each time step, but this gain of efficiency is at the cost of resolution of potential and force fields; close collisions are not correctly accounted for, so that the

particle-mesh codes are applicable only to systems of very low graniness ($g \ll 1$), such as hot (collisionless) plasmas and galaxies.

5. – Specific methods in two dimensions.

For d-dimensional systems, boundaries can be avoided from the start, by confining the sample to a closed surface in $(d+1)$-dimensional space, *e.g.* the surface of a $(d+1)$-dimensional sphere. This method has been successfully applied to the simulation of two-dimensional Coulomb systems confined to the surface of a 3d sphere [18-20]. The position of each particle on the sphere is determined by two polar angles, or equivalently by a radial unit vector $\boldsymbol{u}$.

The equations of motion of N interacting particles on a sphere are equivalent to those of N coupled, rigid, three-dimensional rotators. The distance between particles i and j is measured along the great circle, according to

$$R\psi_{ij} = R \operatorname{arcos}(\boldsymbol{u}_i \cdot \boldsymbol{u}_j) ,$$

where R is the radius of the sphere. The Coulomb potential on the sphere is taken to be [19]

$$v^{(C)}_{\alpha\beta}(\psi_{ij}) = - q_\alpha q_\beta \ln(r_{ij}/L) , \tag{5.1}$$

where r_{ij} is the length of the chord joining particles i and j:

$$r_{ij} = 2R \sin(\psi_{ij}/2) . \tag{5.2}$$

The reliability of this method will be illustrated in sect. **13** and **14**. Among the many advantages of the method, two deserve special mention. The total dipole moment $\boldsymbol{M}_N$ of a sample of charged particles is defined without any ambiguity on the sphere. The static structure factor can be determined from the calculated pair distribution function, without any truncation error, according to [18]

$$S(q) = 1 + 2r^2 \int_0^\pi [g(r\theta) - 1] \sin\theta \, J_0(r\theta q) \, \mathrm{d}\theta , \tag{5.3}$$

where $q = ka$ is a dimensionelss wave number, $r = R/a$ and J_0 denotes the zeroth-order Bessel function.

To conclude the first part, I would like to attract attention to the vast body of 1d simulations of Coulomb systems, which are particularly attractive because of the simplicity of the force law (see eq. (1.2a)) [21, 22].

II. – Strongly Coupled Plasmas.

6. – General considerations.

The plasma state, which is the exception under terrestrial conditions, is in fact the most common in the Universe. Plasmas span an extremely wide range of densities and temperatures, as can be seen from table I which lists several representative examples with the corresponding Fermi degeneracy temperatures and the values of the graniness parameter g. An alternative dimensionless coupling parameter, which is widely used to characterize the strength of Coulomb correlations, is the ratio of the Coulomb energy of two elementary charges separated by the mean interparticle spacing $a = (3/4\pi n)^{\frac{1}{3}}$ (or « ion sphere radius ») over the thermal energy $k_B T$:

$$\Gamma = \frac{l}{a} = \frac{e^2}{a k_B T} = \gamma \frac{\sigma}{a} \sim g^{\frac{2}{3}}, \tag{6.1}$$

where l denotes the Landau length (or classical distance of closest approach).

TABLE I. – *Characteristics of some typical astrophysical and terrestrial plasmas.* T_F is the degeneracy temperature of the electrons. When $T_F > T$, the graniness parameter applies to the nondegenerate ionic plasma.

Plasma	n (electrons/cm^3)	T (K)	T_F (K)	$g = (n\lambda_D^3)^{-1}$
gaseous nebula	10^2	10^4	10^{-9}	$3\cdot 10^{-8}$
ionosphere (F layer)	10^6	10^3	10^{-7}	10^{-4}
solar corona	10^6	10^6	10^{-7}	$3\cdot 10^{-9}$
nonneutral electron plasma	10^{10}	10^0	10^{-4}	10^2
electric discharge	10^{13}	$10^4 \div 10^5$	10^{-2}	10^{-3}
solar atmosphere	10^{14}	10^4	10^{-1}	$3\cdot 10^{-2}$
Tokamak plasma	10^{16}	10^8	1	$3\cdot 10^{-7}$
electron gas in a metal	10^{23}	10^2	10^5	10^6
Jovian interior	10^{25}	10^4	10^6	10^4
stellar interior inertial-confinement plasma	10^{26}	$> 10^7$	10^7	1
white-dwarf interior	10^{30}	10^8	10^{10}	3

Another important ratio is that of a suitably defined collision frequency ν_c over the plasma frequency $\nu_p = \omega_p/2\pi$. The electron-electron collision frequency can be estimated from the Rutherford differential cross-section:

$$\sigma(\chi, w) = \frac{1}{4}\left(\frac{e^2}{\mu w^2}\right)^2 \frac{1}{\sin^4(\chi/2)}, \tag{6.2}$$

where w is the relative velocity, and χ the scattering angle, with the result [23]

$$\nu_c = \left(\frac{\pi}{2}\right)^{\frac{3}{2}} \frac{ne^4}{m^{\frac{1}{2}}(k_B T)^{\frac{3}{2}}} \ln \Lambda . \tag{6.3}$$

The « Coulomb logarithm », $\ln \Lambda$, accounts for the cut-offs in the divergent integral over scattering angles, both at large distances (small angles) and short distances (large angles). For $g \ll 1$, the standard result is

$$\ln \Lambda = \ln \frac{3\lambda_D}{l} . \tag{6.4}$$

When $g \geqslant 1$, $\lambda_D \leqslant l$ and the Coulomb logarithm (which would become negative!) must be replaced by a more rigorous expression [24] which turns out to be numerically of the order of unity. The required ratio is finally

$$\frac{\nu_c}{\nu_p} = \frac{(2\pi)^{\frac{1}{2}}}{32} g \ln \Lambda . \tag{6.5}$$

When $g \ll 1$, ν_c is negligibly small compared to ν_p, and the corresponding collisionless plasma is well described by the nonlinear Vlasov equation; such plasmas are generally far from local thermodynamic equilibrium, and give rise to numerous instabilities and turbulent behaviour, which are simulated by particle-mesh codes of the type described in sect. **4**. In the opposite limit $g \gg 1$, the plasma is in a collision-dominated regime which is *a priori* well suited for MD simulations. However, since close collisions play now an essential role, the problem of quantum degeneracy effects at short distances becomes crucial. Let $\lambda\!\!\!^{-}_e$ denote the de Broglie thermal length $\hbar/(2\pi m_e k_B T)^{\frac{1}{2}}$ of the electrons and $\lambda\!\!\!^{-}_i$ the corresponding (much shorter) length of the ions. Two clearly distinct regimes will be considered:

a) $\lambda\!\!\!^{-}_i \ll a \ll \lambda\!\!\!^{-}_e$. The first inequality means that the ions behave classically (ionic quantum effects can be treated as small corrections); the second inequality is equivalent to the requirement $T \ll T_F$, so that the electron gas is highly degenerate. If, moreover, the density is sufficiently high, such that the Thomas-Fermi screening length $\lambda_{TF} = (\pi/12)^{\frac{1}{3}}(\hbar^2/me^2)^{\frac{1}{2}} a^{\frac{1}{2}}$ of the degenerate electron gas greatly exceeds the mean interionic spacing a, the electrons can be regarded,

to a good approximation, as a uniformly « smeared-out » neutralizing background in which the classical ions move. If the latter belong to a single species, the relevant model is the « one-component plasma » (OCP), one of the most widely studied models of statistical mechanics [9], which will be the subject of sect. **7**. Its extension to two ionic components, the so-called « binary ionic mixture » (BIM), will be considered in sect. **8**.

b) $\lambda\!\!\!^{-}_{\mathrm{i}} \ll \lambda\!\!\!^{-}_{\mathrm{e}} \lesssim a$. This corresponds to a situation where $T \gtrsim T_{\mathrm{F}}$: the electrons are only weakly degenerate and the ion-electron plasma must be treated as a genuine two-component plasma (TCP), with effective pair potentials to account for quantum « smearing »; this case will be discussed in sect. **9**.

7. – The one-component plasma.

This is the simplest model of an ionic fluid in which one of two oppositely charged species (the electrons) is replaced by a structureless neutralizing background. The potential energy for N point ions of charge q in this background is, in d dimensions,

$$V_N = \frac{1}{2|\Lambda|} \sum_{\boldsymbol{k}}{}' \hat{v}(k)[\varrho_{\boldsymbol{k}}\varrho_{-\boldsymbol{k}} - N]\,, \tag{7.1a}$$

$$\hat{v}(k) = \frac{C_d q^2}{k^2}\,, \tag{7.1b}$$

$$\varrho_{\boldsymbol{k}} = \sum_{i=1}^{N} \exp\,[i\boldsymbol{k}\cdot\boldsymbol{r}_i]\,, \tag{7.1c}$$

where the prime in the summation over wave vectors compatible with the periodic boundary conditions indicates that the $k = 0$ component is cancelled by the background contributions. Note that, since the interaction is purely Coulombic, there is no length scale characteristic of a short-range interaction v^{s}, so that $\sigma = 0$ and there is only one dimensionless thermodynamic variable, which we choose to be Γ, as defined in eq. (6.1) (with $q = e$).

The OCP is a very usufel starting point in the study of very dense, degenerate stellar matter (Jovian interior, white dwarfs and neutron star crusts), of simple liquid metals and of charge-stabilized colloid suspensions. Its static and dynamic equilibrium properties have been extensively studied by Monte Carlo and MD simulations [9]. The most salient results are the following:

a) The isothermal compressibility χ_{T} becomes negative for $\Gamma \gtrsim 3$ [25], but the OCP remains stable against density fluctuations, due to the electrostatic restoring force [26]. Concurrently the ionic pair distribution function changes from a monotonous, Debye-like, to an oscillatory behaviour characteristic of short-range order [7, 25].

b) The OCP crystallizes into a b.c.c. lattice when $\Gamma \simeq 170$ [27] with zero volume change [28] but a finite latent heat.

c) Due to conservation of momentum, the plasma oscillation mode is undamped in the long-wavelength ($k \to 0$) limit. The dispersion of the plasmon, $d\omega/dk$, becomes *negative* for $\Gamma \geqslant 10$ [28]. The intensity of the diffusive entropy fluctuation mode is k^2 times smaller than that of the propagating plasmon mode [26, 29]. Landau damping of the plasmon is dominant for $\Gamma < 1$, whereas collisional damping takes over for $\Gamma \geqslant 1$. The sensitivity of this collective mode to a cut-off of the Coulomb force is illustrated by the simulations of ref. [29] at $\Gamma = 1$: the nearest-image convention leads to a 10 % increase of the plasmon frequency at the smallest wave number compatible with the sample size ($N = 128$ and hence $ak \simeq 0.62$), compared to the correct result obtained with the full Ewald boundary conditions. The discrepancy would be worse for stronger coupling.

d) The velocity autocorrelation function $Z(t)$ exhibits pronounced oscillations at roughly the plasma frequency, for $\Gamma \geqslant 10$ [29]. The damping of these oscillations weakens as Γ increases; they can be attributed to the coupling of the single-particle motion to the plasma oscillations [30]. A rough argument shows why the oscillations are not observed in MD « experiments » for $\Gamma \leqslant 10$, at least at short times.

It is reasonable to assume that the long-time behaviour of $Z(t)$ is essentially determined by the coupling to short-wavelength plasmons, *i.e.* $k \simeq 2\pi/a$ (for shorter wavelengths, the plasmon is overdamped). An ion having the thermal velocity $v_0 = (k_B T/m)^{\frac{1}{2}}$ can be « trapped » in such a plasma wave only if $v_0 k < \omega_p$, implying $\Gamma \geqslant 12$.

e) The OCP exhibits shear wave propagation near crystallization, as signaled by a well-defined peak at nonzero frequency in the spectrum of the transverse current autocorrelation function [29]. The peak is observed to split before vanishing at $ka \simeq 2\pi$.

f) The various transport coefficients have been computed via the Green-Kubo formulae. The correlation functions associated with the thermal conductivity $\varkappa$ and with the bulk viscosity ζ are observed to oscillate at roughly the plasma frequency and twice that frequency, respectively [31]. When plotted *vs.* Γ, the reduced shear viscosity and thermal conductivity go through a minimum (around $\Gamma \simeq 10$), while the bulk viscosity is only a small fraction ($\simeq 1$ %) of the shear viscosity [26, 31, 32].

g) The velocity autocorrelation function and the self-diffusion of the OCP in a strong, constant, external magnetic field $\boldsymbol{B}$ has been studied by BERNU [33]. The equations of motion now involve the velocity-dependent

Lorentz force

$$\boldsymbol{v}_i = \dot{\boldsymbol{r}}_i\,, \tag{7.2a}$$

$$\dot{\boldsymbol{v}}_i = \frac{q}{m}\boldsymbol{E}_i + \boldsymbol{v}_i \wedge \boldsymbol{\Omega}_B\,, \tag{7.2b}$$

where $\boldsymbol{\Omega}_B = q\boldsymbol{B}/mc$ is the cyclotron frequency. A time-reversible Lorentz force integrator similar to the usual Verlet (or leapfrog) algorithm is readily written down:

$$\boldsymbol{r}_i^{(n+1)} - 2\boldsymbol{r}_i^{(n)} + \boldsymbol{r}_i^{(n-1)} = (\Delta t)^2\left[\frac{q}{m}\boldsymbol{E}_i(\{\boldsymbol{r}_j^{(n)}\}) + \boldsymbol{v}_i^{(n)} \wedge \boldsymbol{\Omega}_B\right], \tag{7.3a}$$

$$\boldsymbol{v}_i^{(n)} = \frac{1}{2\,\Delta t}[\boldsymbol{r}_i^{(n+1)} - \boldsymbol{r}_i^{(n-1)}]\,. \tag{7.3b}$$

These equations are implicit in the velocity, but this poses no problem, since the Lorentz force is linear in the velocity. With $\boldsymbol{\Omega}_B$ chosen along Oz, it is clear that the algorithm is identical to the standard Verlet algorithm in that direction. Along Ox and Oy the equations read

$$x_i^{(n+1)} - 2x_i^{(n)} + x_i^{(n-1)} = (\Delta t)^2\left[\frac{q}{m}E_{ix}^{(n)} - \Omega v_{iy}^{(n)}\right], \tag{7.4a}$$

$$y_i^{(n+1)} - 2y_i^{(n)} + y_i^{(n-1)} = (\Delta t)^2\left[\frac{q}{m}E_{iy}^{(n)} + \Omega v_{ix}^{(n)}\right], \tag{7.4b}$$

$$v_{ix}^{(n)} = \frac{1}{2\,\Delta t}[x_i^{(n+1)} - x_i^{(n-1)}]\,, \tag{7.4c}$$

$$v_{iy}^{(n)} = \frac{1}{2\,\Delta t}[y_i^{(n+1)} - y_i^{(n-1)}]\,. \tag{7.4d}$$

This linear system is easily solved for the four unknowns $x_i^{(n+1)}$, $y_i^{(n+1)}$, $v_{ix}^{(n)}$, $v_{iy}^{(n)}$. In the simulations the magnetic field was chosen sufficiently strong for the Lorentz forces to be of the same order of magnitude as the Coulomb forces, *i.e.* $\Omega_B/\omega_p \simeq 1$ [33].

As expected, the diffusion constants parallel and perpendicular to $\boldsymbol{B}$, Dz and Dx, differ considerably, with $Dx < Dz$. The greatest surprise is that, for strong coupling ($\Gamma \geqslant 10$), Dz is strongly reduced by the magnetic field, while it is practically independent of B for weaker coupling ($\Gamma \simeq 1$). Moreover, the plasmon resonance in the spectrum $\hat{Z}_z(\omega)$ of $Z_z(t)$ disappears for $\Omega_B/\omega_p \simeq 1$ in the strong-coupling regime.

8. – Binary ionic mixtures.

The BIM model is the natural extension of the OCP to the situation where two ionic species, carrying charges $q_1 = Z_1 e$ and $q_2 = Z_2 e$ (> 0), move in a

uniform neutralizing background. The interactions are still purely Coulombic, with an expression for the total potential energy generalizing eq. (7.1):

$$V_N = \frac{1}{2|\Omega|} \sum_{\boldsymbol{k}}' \hat{v}(k)[\varrho_{\boldsymbol{k}Z}\varrho_{-\boldsymbol{k}Z} - N\overline{Z^2}] , \tag{8.1a}$$

$$\varrho_{\boldsymbol{k}Z} = \sum_{i=1}^{N} Z_i \exp[i\boldsymbol{k}\cdot\boldsymbol{r}_i] = Z_1\varrho_{\boldsymbol{k}1} + Z_2\varrho_{\boldsymbol{k}2} , \tag{8.1b}$$

where $\overline{Z^2} = x_1 Z_1^2 + x_2 Z_2^2$ and $x_\alpha = N_\alpha/N$. An equilibrium state is characterized by two variables, Γ (as defined in (6.1)) and x_1. Compared to the OCP, the essential, qualitatively new feature is the mutual diffusion of the two ionic species, which leads to a finite resistivity (binary collisions between ions conserve momentum, but not electric current) and collisional damping of the plasmon mode, even in the long-wavelength limit [34, 35]. More unexpectedly, the MD simulations also reveal a shift of the infinite-wavelength ($k \to 0$) frequency of the plasmon mode *above* its weak-coupling, kinetic limit:

$$\Omega_{\mathrm{p}} = (\omega_{\mathrm{p}1}^2 + \omega_{\mathrm{p}2}^2)^{\frac{1}{2}} = \left(\frac{4\pi Z_1^2 e^2 n_1}{m_1} + \frac{4\pi Z_2^2 e^2 n_2}{m_2}\right)^{\frac{1}{2}} . \tag{8.2}$$

The frequency shift and damping of the plasmon mode at $k = 0$ increase with Γ; the former reaches about 5 % in an equimolar H^+-He^{++} mixture at $\Gamma = 40$ [36].

The relation between the interdiffusion coefficient D_{12} and the electrical conductivity σ follows directly from the standard Kubo formulae, if it is noticed that the fluctuating electric current relative to the centre-of-mass motion is proportional to the interdiffusion current $\boldsymbol{j}_c(t)$:

$$\boldsymbol{j}_Z'(t) = \boldsymbol{j}_Z(t) - \frac{\overline{Z}}{\overline{m}}\boldsymbol{j}_M(t) \equiv \frac{Z_1 m_2 - Z_2 m_1}{\overline{m}}\boldsymbol{j}_c(t) , \tag{8.3}$$

where

$$\boldsymbol{j}_Z(t) = Z_1\boldsymbol{j}_1(t) + Z_2\boldsymbol{j}_2(t) , \tag{8.4a}$$

$$\boldsymbol{j}_M(t) = m_1\boldsymbol{j}_1(t) + m_2\boldsymbol{j}_2(t) , \tag{8.4b}$$

$$\boldsymbol{j}_c(t) = x_2\boldsymbol{j}_1(t) - x_1\boldsymbol{j}_2(t) , \tag{8.4c}$$

$$\boldsymbol{j}_\alpha(t) = \sum_{i=1}^{N_\alpha} \boldsymbol{v}_{i\alpha}(t) , \qquad \alpha = 1, 2 . \tag{8.4d}$$

The result is

$$\sigma = \frac{ne^2}{k_{\mathrm{B}}T} x_1 x_2 \left(\frac{Z_1 m_2 - Z_2 m_1}{\overline{m}}\right)^2 D_{12} \tag{8.5}$$

if account is taken of the fact that the BIM is practically an ideal mixture for all couplings and concentrations. Under these conditions D_{12} is given by

$$D_{12} = \frac{k_B T \overline{m}}{m_1 m_2} \int_0^\infty J(t)\, dt\,, \tag{8.6}$$

where $J(t)$ is the normalized autocorrelation function of $\boldsymbol{j}_c(t)$. If cross-correlations between the velocities of different ions are neglected for any time displacement, $J(t)$ is a simple linear combination of the normalized velocity autocorrelation functions of the two species:

$$J(t) \simeq x_2 \frac{m_2}{\overline{m}} Z_1(t) + x_1 \frac{m_1}{\overline{m}} Z_2(t)\,. \tag{8.7}$$

Due to the purely Coulombic nature of the interactions, equality (8.7) is exact to order t^2 in the BIM. In fact, extensive MD simulations for several couplings and concentrations show that it is very well verified at all times despite the complicated oscillatory behaviour of the three functions in the strong-coupling limit [36]. Under these conditions D_{12} is very well approximated by the following simple linear combination of the self-diffusion constants of the two species:

$$D_{12} \simeq x_2 D_1 + x_1 D_2\,. \tag{8.8}$$

A similar approximate relation for σ follows from combination of eqs. (8.5) and (8.8). It is interesting to note from eq. (8.5) that σ vanishes not only in the one-component (OCP) limit (*i.e.* when $x_1 = 0$ or 1), but also for mixtures such that

$$\frac{Z_1}{Z_2} = \frac{m_1}{m_2}\,. \tag{8.9}$$

With the exception of mixtures involving protons, this condition is practically satisfied by most mixtures of fully stripped ions (*i.e.* nuclei)!

9. – Two-component plasmas.

The situation which we consider next is characterized by $\lambda\!\!\!^{-}_1 \ll \lambda\!\!\!^{-}_e \lesssim a$: the electrons are only weakly degenerate, and must be treated on the same footing as the ions in a semi-classical description involving effective pair potentials which differ from a purely Coulombic potential at short distances. Due to the Heisenberg uncertainty principle, the electron charge can be considered as being « smeared out » over a sphere of radius $\simeq \lambda\!\!\!^{-}_e$, leading to a « regularization » of the singular Coulomb attraction between point charges of opposite signs [37].

Moreover, since electrons are fermions, symmetry effects, due to the Pauli exclusion principle, come into play between parallel-spin electrons. For sufficiently high temperatures, the contribution of bound states becomes negligible, and diffraction and symmetry effects can be approximately accounted for by the set of effective pair potentials worked out by DEUTSCH and collaborators [38]:

$$v_{\alpha\beta}(r) = \frac{Z_\alpha Z_\beta e^2}{r}\left[1 - \exp\left[-r/R_{\alpha\beta}\right]\right] + \delta_{\alpha 2}\,\delta_{\beta 2}\,v_{22}^{(S)}(r)\,, \tag{9.1}$$

where the index 1 refers to the ions and 2 to the electrons, and

$$R_{\alpha\beta}^2 = \lambda\!\!\!^{-2}_{\alpha} + \lambda\!\!\!^{-2}_{\beta}\,. \tag{9.2}$$

The second term on the r.h.s. of eq. (9.1) accounts for electron symmetry effects [38]:

$$v_{22}^{(S)} = k_B T \ln 2 \exp\left[-\frac{1}{\pi \ln 2}\left(\frac{r}{R_{22}}\right)^2\right]. \tag{9.3}$$

These effective potentials have been used in conjunction with the classical equations of motion in MD simulations of a dense hydrogen (electron-proton) plasma [39-41]. The relevant dimensionless parameters are the coupling constant Γ and the ratio $r_S = a/a_0$ of the ion sphere radius a divided by the Bohr radius a_0. Note that

$$\frac{\lambda\!\!\!^{-}_{e}}{a} = \left(\frac{\Gamma}{2\pi r_S}\right)^{\frac{1}{2}}, \qquad k_B T = \frac{2}{\Gamma r_S}\,\mathrm{Ryd}\,. \tag{9.4}$$

Due to the contradictory requirements of complete ionization ($k_B T > 1$ Ryd $= e^2/2a_0 = 13.6$ eV), weak degeneracy ($\lambda\!\!\!^{-}_{e}/a < 1$) and strong coupling ($\Gamma \gtrsim 1$, in order for MD to be efficient), the domain of the temperature-density plane which can be usefully explored by MD is relatively restricted (see fig. 1). All simulations have been carried out for $\Gamma \simeq 1$, $r_S \simeq 1$, which are typical of the initial stages of an imploding pellet in inertial-confinement experiments.

One of the main difficulties of these simulations is that two very different time scales are involved, since the ratio of the electronic and ionic plasma frequencies scales as $(m_i/m_e)^{\frac{1}{2}} \simeq 43$. The MD time step must, of course, be adapted to the fast electronic motion. This means that little or no information will be gained concerning the much slower ionic motion and the dynamical properties associated with it, like the shear viscosity of the plasma. Fortunately the fast electronic motion dominates electrical and thermal conduction and the wave-number- and frequency-dependent dielectric function $\varepsilon(k, \omega)$, which determines in particular the dispersion and damping of the plasmon mode. Among

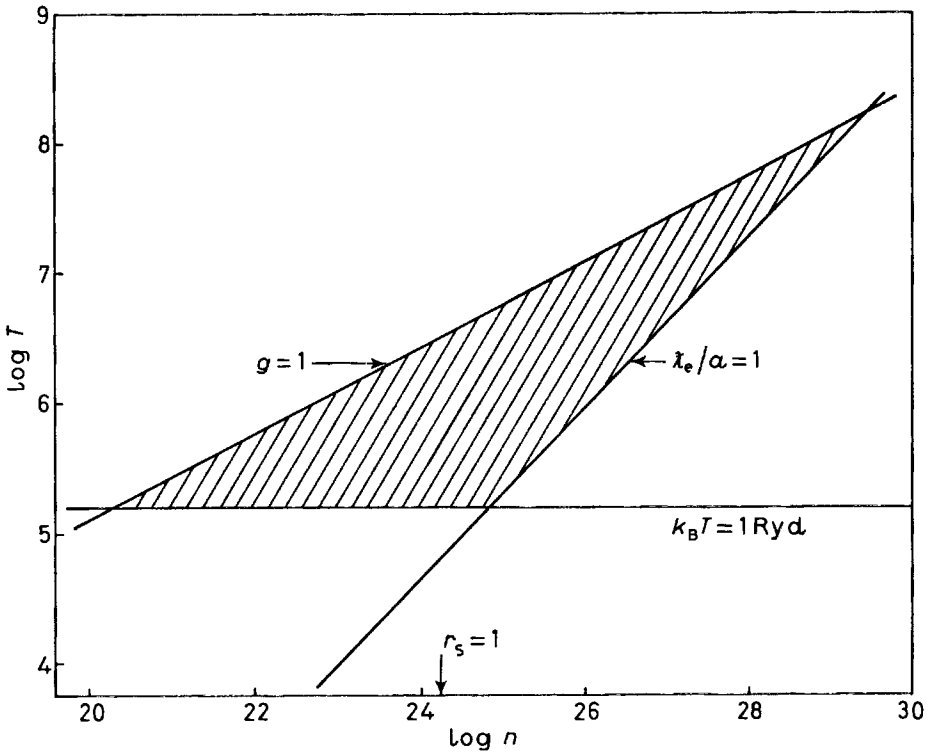

Fig. 1. – Range of validity of the semi-classical description of the strongly coupled hydrogen (ion-electron) plasma in the $\log n$ (n is the electron density in cm^{-3})-$\log T$ plane. The plasma is fully ionized for $k_B T > 1$ Ryd or for $r_S > 1$ (pressure ionization); it is weakly degenerate above the line $\lambda\!\!\!^{-}_e = a$ and strongly coupled below the line g (graniness parameter) $= 1$; classical MD simulations are applicable in the shaded triangle.

the many revelations gleaned from the MD experiments we summarize here the following:

a) The autocorrelation function $J(t)$ of the electric current (8.4*a*) decays considerably more slowly that the electron velocity autocorrelation function $Z_2(t)$ (see fig. 2), so that the equivalent of the approximate relation (8.8), *i.e.* (since D_1 is negligible compared to D_2)

$$\sigma \simeq \omega_{p2}^2 \frac{m_2}{k_B T} D_2 , \tag{9.5}$$

is violated by as much as a factor of 3. This can be understood in view of the fact that electron-electron collisions conserve the electric current, but not individual electron velocities. A reasonably accurate kinetic theory for $J(t)$ and σ is by now available [24, 40].

b) The heat conductivity $\varkappa$ is, as usual, defined under conditions of zero electric current [41]. This means that it is not directly expressible in terms of the autocorrelation function of a suitably defined heat current (as

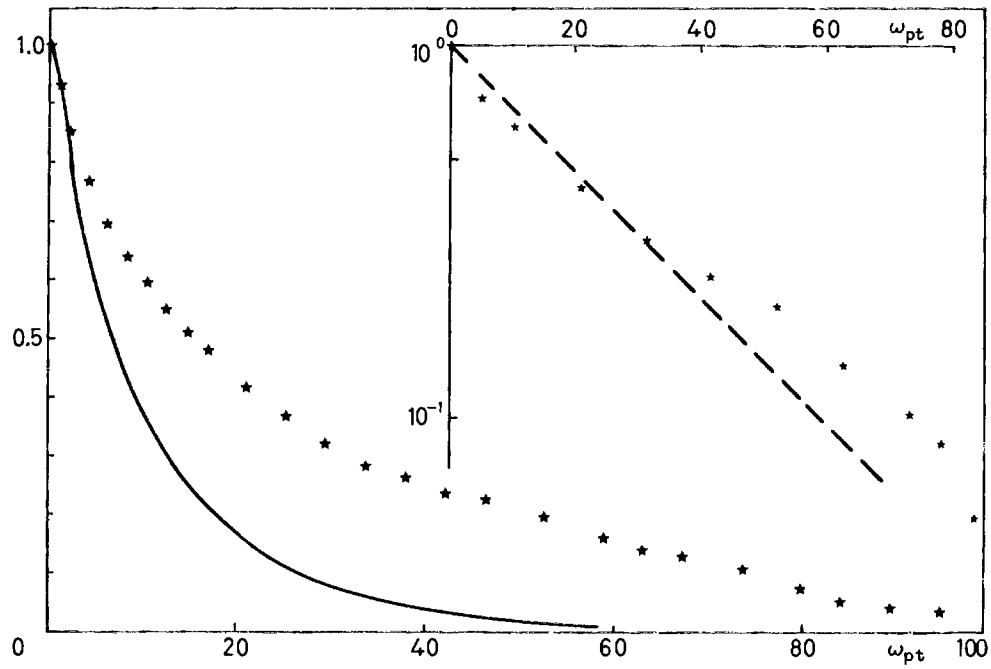

Fig. 2. – Electron velocity (full line) and electric-current (stars) autocorrelation functions *vs.* reduced time. The insert shows the logarithm of the latter function (stars), to stress the nonexponential character of this function; the straight line, corresponding to an exponential least-squares fit, is merely a visual guide.

in a one-component system), but $\varkappa$ is defined by a combination of three coefficients related to the correlation functions of the electric current and of the heat current. Since the latter has a large component parallel to the former, the heat current must be redefined by subtracting a suitably defined « average » projection in practical MD calculations [42]. This redefined heat current decays on the same time scale as the individual electron velocity, *i.e.* much faster than the electric current, so that no simple Wiedemann-Franz relation holds for the hydrogen plasma [41].

c) Due to electron-electron and electron-ion collisions, the plasmon resonance in the charge-charge dynamical structure factor

$$S_{zz}(k, \omega) = \frac{1}{2\pi} \int_{-\infty}^{+\infty} \langle \varrho_{kz}(t) \varrho_{-kz} \rangle \exp[i\omega t] \, \mathrm{d}t \tag{9.6}$$

is considerably shifted and broadened, compared to the mean-field (collisionless) Vlasov result [39]. In the long-wavelength limit, the frequency of the plasmon resonance is shifted by a few percent *above* the electron plasma frequency ω_{p2} at $\Gamma \simeq 1$ [43]; the effect appears to be much larger that in the BIM, where it becomes sizable only when $\Gamma \gg 1$ [36].

d) While the MD simulations have revealed considerable deviations of the transport coefficients from their weak-coupling Landau-Spitzer estimates [23],

based on the collision frequency (6.3), (6.4), the rate at which a «two-temperature» plasma (where ion and electron temperatures T_1 and T_2 are initially very different) relaxes towards overall thermodynamic equilibrium appears to be surprisingly well described by Landau-Spitzer theory [44]; the latter estimates the rate of (kinetic) energy transfer between the two species to be governed by the relaxation time

$$\tau = \frac{3\pi}{32}\frac{m_1}{m_2}\nu_c^{-1} . \tag{9.7}$$

This time is long because of the large ion-electron mass ratio which inhibits the transfer of kinetic energy during collisions. This slow decay renders a MD simulation of thermal relaxation very difficult [44], but the observed rates are well reproduced by formulae (9.7) and (6.3), provided the large-angle cut-off in the Coulomb logarithm is determined by $R_{12} \simeq \lambda\!\!\!^{-}_2$, rather than by the Landau length, so that

$$\ln \Lambda = \ln \frac{\lambda_{D2}}{\lambda\!\!\!^{-}_2} . \tag{9.8}$$

As a by-product of the thermal relaxation simulations [44], the electron self-diffusion coefficient D_2 was estimated for the two-temperature plasma, by extending the standard Green-Kubo formula to this case, *i.e.*

$$D_2^* = \frac{D_2}{a^2\omega_{p2}} = \frac{1}{3}T_2^*\int_0^\infty Z_2(t^*)\,\mathrm{d}t^* , \tag{9.9}$$

where $T^* = k_B T/(e^2/a)$ and $t^* = \omega_{p2}t$. Equation (9.9) is strictly valid only in thermodynamic equilibrium (where $T_1 = T_2 = T$), but it may be expected to apply also in quasi-stationary nonequilibrium situations, provided the characteristic decay time of $Z_2(t)$ is much shorter than the thermal relaxation time τ. This is true in the present situation, since it was found that $Z_2(t)$ decays to zero on a time scale over which T_2 scarcely changes. The MD results show that the diffusion coefficient in the two-temperature plasma is consistently 10 to 20% lower than in the corresponding equilibrium calculation, carried out at the same density (r_S) and at a temperature $T = T_2 = T_1$. The difference can be traced back to the faster decay of $Z_2(t)$ in the nonequilibrium (two-temperature) case.

III. – Coulomb Systems in Condensed-Matter Physics.

10. – Ionic liquids and solids.

Under terrestrial conditions, ionic systems are less common than under the very high temperatures, and very high or low densities prevalent in stellar

and interstellar matter. *Metals* can be regarded as cold electron-ion plasmas, and a very successful description of liquid alkali metals in terms of OCP reference systems has been put forward [45]. However, in view of the quantum nature of the degenerate gas of conduction electrons, and of the large ratio of time scales, existing MD simulations take advantage of the adiabatic approximation and of the pseudoatom concept to describe the ionic dynamics in liquid metals [46]. The simulation of *ionic* and *macroionic solutions* is complicated by the presence of solvent (generally water) molecules, and few attempts have been made to simulate realistic models of such multicomponent systems. In the so-called « Brownian dynamics » simulations, the effect of the solvent on the ions is modelled by a friction force and a random force, so that the solution can be looked upon as a system of interacting Brownian particles [47].

The most typical examples of Coulomb systems in condensed-matter physics are *ionic crystals* and *molten salts*. Ionic crystals have been extensively studied over many decades, in particular through lattice dynamics calculations, and their collective modes of acoustic (sound) and optic (plasmon) character are well understood. KLEIN will describe the results of recent MD simulations of *molecular ionic crystals*, formed by alkali ions and molecular anions, like Li_2SO_4, $NaNO_2$ and KCN [48]. In this part we shall concentrate on molten salts and on a very interesting class of ionic solids, the so-called superionic conductors.

11. – Molten salts.

At first sight, molten salts, made up of two species of oppositely charged ions, have much in common with two-component ion-electron plasmas, with the ionic core repulsion replacing the quantum regularization of the Coulomb potential at short distances. There are, however, several important differences, chief among which is the mass ratio m_1/m_2 which is of the order of 1 in molten salts, while it is 2000 or larger in ion-electron plasmas. On the other hand, while the densities may be comparable, the melting temperature of most salts ($\simeq 10^3$ K) is such that the Coulomb coupling constant $\Gamma \simeq \gamma$ (since $\sigma \simeq a$, because ions touch) is much larger in a molten salt (typically of the order of 50) than in semi-classical two-component plasmas.

Since the pioneering Monte Carlo work of Woodcock and Singer [49] on KCl, molten alkali halides have been the subject of intense computer simulation work. Both rigid- and polarizable-ion models have been considered [50]. Rigid-ion models generally use the Born-Huggins-Mayer pair potentials:

$$v_{\alpha\beta}(r) = A_{\alpha\beta}\exp[-r/\varrho_{\alpha\beta}] - C_{\alpha\beta}\left(\frac{r_0}{r}\right)^6 - D_{\alpha\beta}\left(\frac{r_0}{r}\right)^8 + \frac{Z_\alpha Z_\beta e^2}{r} \tag{11.1}$$

with potential parameters determined from solid-state data [51]. An even

simpler, symmetric potential model, which retains only the core overlap repulsion and Coulomb interaction, is capable of yielding a reasonable description of most alkali halides [52]:

$$v_{\alpha\beta}(r) = \frac{e^2}{\sigma}\left[\frac{1}{n}\left(\frac{\sigma}{r}\right)^n + Z_\alpha Z_\beta\left(\frac{\sigma}{r}\right)\right]. \tag{11.2}$$

In the limit $n \to \infty$, the model reduces to the restricted primitive model of electrolytes (oppositely charged hard spheres of equal diameter). A « realistic » choice of the exponent is $n = 9$. If moreover the masses of anions and cations are equal ($m_+ = m_-$), the model is fully symmetric under charge conjugation, and is sometimes referred to as the « simple molten salt » (SMS). Invariance under charge conjugation implies, in particular, that number (or mass) and charge density fluctuations are completely decoupled at all wave numbers and all times [53], a property which is true for nonsymmetric molten salts in the long-wavelength limit only [42, 54]. It has been the object of the first extensive MD simulation of the collective dynamical behaviour of molten salts [53]. The most salient results of that simulation can be summarized as follows:

a) The like- and unlike-pair distribution functions, $g_{++}(r) \equiv g_{--}(r)$ and $g_{+-}(r)$, oscillate with exactly opposite phases, a striking manifestation of « charge ordering » which arises from a competition between local charge neutrality and excluded-volume effects [49]. Correspondingly the number pair distribution function

$$g_{NN}(r) = \tfrac{1}{4}[g_{++}(r) + g_{--}(r) + 2g_{+-}(r)] \tag{11.3}$$

is a rather flat, structureless function of r, while, on the contrary, the charge pair distribution function

$$g_{ZZ}(r) = \tfrac{1}{4}[g_{++}(r) + g_{--}(r) - 2g_{+-}(r)] \tag{11.4}$$

exhibits long-lived oscillations. The resulting number structure factor $S_{ZZ}(k)$ exhibits a very sharp main peak. It is worth stressing that the hypernetted-chain (HNC) integral equation reproduces the MD results rather well, except that it leads to a strong over-estimation of the isothermal compressibility, *i.e.* of the $k \to 0$ limit of $S_{NN}(k)$.

b) The two identical velocity autocorrelation functions $Z_+(t) \equiv Z_-(t)$ exhibit backscattering effects. The autocorrelation function of the electric current, $J(t)$, decays only slightly faster, so that the electrical conductivity and the self-diffusion constants $D_+ \equiv D_-$ are well correlated by the Nernst-Einstein relation similar to eqs. (8.8) or (9.5), *i.e.*

$$\sigma = \frac{ne^2}{k_B T}\frac{D_+ + D_-}{2} f, \tag{11.5}$$

where the correlation factor f (which deviates from 1 due to the cross-correlations between velocities of different ions) is typically of the order of 0.8, in good agreement with experimental findings. This behaviour contrasts sharply with the situation in the electron-proton plasma, where $f \geqslant 2$ (see sect. **9**).

c) The longitudinal collective modes reveal themselves in the number and charge dynamical structure factors $S_{NN}(k, \omega)$ and $S_{zz}(k, \omega)$. For sufficiently small k, $S_{NN}(k, \omega)$ is expected to exhibit a Rayleigh-Brillouin structure associated with heat diffusion and sound waves. No trace of a Brillouin side peak was found in the simulations of the SMS, presumably because the small system size (216 ions) did not allow the investigation of sufficiently small wave numbers. $S_{zz}(k, \omega)$, on the other hand, exhibits a well-defined plasmon resonance, reminiscent of the optic mode of ionic crystals. The $k \to 0$ limit of the normalized charge fluctuation spectrum can also be extracted from the MD experiments, since a simple hydrodynamic argument shows that the electric-current autocorrelation function $J(t)$ is precisely the memory function for this spectrum *i.e.* [36, 42, 55]

$$\lim_{k\to 0} \frac{S_{zz}(k, \omega)}{S_{zz}(k)} = \frac{1}{\pi} \mathscr{R} \frac{1}{-i\omega + 4\pi\sigma(\omega)}, \tag{11.6}$$

where $\sigma(\omega)$ is the complex frequency-dependent conductivity

$$\sigma(\omega) = \frac{\omega_p^2}{4\pi} \int_0^\infty J(t) \exp[i\omega t]\, dt \tag{11.7}$$

and $\omega_p^2 = \omega_{p1}^2 + \omega_{p2}^2$. The real and imaginary parts of $\sigma(\omega)$ lead to a shift of the plasmon frequency above ω_p (by about 25 %) and to damping of the charge oscillation mode; the effects are much larger than in the two-component plasma, because of the much stronger coupling.

As k increases, the plasmon frequency shifts to lower frequencies (negative dispersion), but, very surprisingly, the plasmon width (damping) decreases slightly at first; the plasmon resonance disappears from $S_{zz}(k, \omega)$ at a wavelenght roughly equal to twice the interionic spacing. This unexpected behaviour is qualitatively reproduced by a mode-coupling calculation [56], but there is apparently no simple physical interpretation of this observation.

The results for the SMS are qualitatively reproduced by MD simulations of more realistic models of alkali halides, based on the pair potentials (11.1) and natural mass ratios m_+/m_-. Extensive results are available for longitudinal and transverse collective modes in RbBr [57], NaCl [58], NaI [59] and KCl [60]. These simulations have also revealed the existence of a resonance in the transverse electric-current autocorrelation function which is associated with transverse optic mode, familiar from ionic crystals. As is the case for the latter, the

frequency of this mode differs by ω_p from the corresponding longitudinal optic mode in the long-wavelength limit (Lyddane-Sachs-Teller sum rule); the dispersion of this mode, $d\omega/dk$, is practically zero. The validity of the Nernst-Einstein relation (11.5) (with $f \simeq 1$) has been checked for several alkali halides within the rigid-ion model (11.1) [61]. Self-diffusion has also been examined in MD simulations of the LiCl-KCl mixture [62] and in molten $SrCl_2$ [63]. The former calculations have revealed a significant decrease of the mobility of Li^+ ions when the concentration of K^+ ions increases. A recent rigid-ion MD calculation of the shear viscosity and of the thermal conductivity of molten KCl, at two different temperatures, shows excellent agreement with available experimental data [60]; the calculated bulk viscosity (for which no experiment is as yet available) is only slightly smaller than the shear viscosity, in sharp contrast to the case of the OCP discussed in sect. 7.

If the ions are highly polarizable (typically electronic polarizabilities $\alpha > 1$ Å^3), as is generally the case for the anions, induction forces can no longer be neglected. Polarization effects have been effectively incorporated into MD simulations of molten salts via the so-called shell model [50, 59, 64]. In this model the total charge of a polarizable ion is assumed to be divided between a core (of charge $Z^* e = (Z - \zeta)\, e$) and a massless shell (of charge ζe), the latter being bound to the core by a harmonic potential of spring constant k. In addition, the short-range repulsive forces are assumed to act through the shells. If the vector joining the core to the shell of the i-th ion is denoted by $\boldsymbol{s}_i$, the total potential energy of the polarizable-ion model reads

$$V_N = \frac{1}{2}\sum_i k_i s_i^2 + \sum_{i<j}\sum [A_{ij} \exp[-|\boldsymbol{r}_{ij} + \boldsymbol{s}_{ij}|/\varrho_{ij}] - \\ - C_{ij}\left(\frac{r_0}{r_{ij}}\right)^6 - D_{ij}\left(\frac{r_0}{r_{ij}}\right)^8 + \frac{Z_i^* Z_j^* e^2}{r_{ij}} + \frac{Z_i^* \zeta_j e^2}{|\boldsymbol{r}_{ij} - \boldsymbol{s}_j|} + \frac{\zeta_i Z_j^* e^2}{|\boldsymbol{r}_{ij} + \boldsymbol{s}_i|} + \frac{\zeta_i \zeta_j e^2}{|\boldsymbol{r}_{ij} + \boldsymbol{s}_{ij}|}. \tag{11.8}$$

In this model the polarization of the ions corresponds to a bodily shift of the shell (representing the electron cloud) relative to the core (representing the nucleus). The shells, being of zero mass, are assumed to adjust themselves instantaneously in such a way as to satisfy the equilibrium condition $\nabla_s V_N = 0$. In practice, V_N is expanded to second order in the shell displacements $\boldsymbol{s}_i$, and a rapidly convergent iterative method must be used to obtain the $\boldsymbol{s}_i$ from the equilibrium condition [64].

Ion polarizability has nonnegligible effects on various quantities measured in MD experiments, compared to the predictions of rigid-ion models. The most striking changes are the following [59, 64]:

a) Phonon dispersion curves of ionic crystals are brought into good agreement with experimental data; the optic frequencies are lowered significantly while the acoustic modes are less affected.

b) The partial pair distribution functions are slightly less structured, and the difference between the « like » functions $g_{++}(r)$ and $g_{--}(r)$ (which is generally small with rigid-ion models) is enhanced.

c) The oscillatory nature of the velocity autocorrelation functions is less pronounced with the polarizable-ion models, and the resulting diffusion constants, particularly D_+, increase significantly (by more than 50 % for the K^+ ions in the presence of the highly polarizable I^- ions).

d) Among the transport coefficients, the electrical conductivity σ does not change (within statistical errors) in going from a rigid- to a polarizable-ion model, but the shear viscosity is significantly reduced.

e) The frequency of the longitudinal optic (plasmon) mode decreases significantly (typically by 10 %), while the damping increases when ion polarization is included in the simulations, as in the case of ionic crystals. The effect of polarization on the transverse optic mode is, however, negligible, an observation which is intimately related to the lack of sensitivity of the electrical conductivity σ to ion polarizability.

These various observations indicate that polarizable molten (as well as crystalline) salts are somewhat more « sluggish » than their rigid-ion pictures, because local charge neutrality is more easily achieved through ionic shell displacements, which leads to somewhat weaker correlations, and enhanced damping of spontaneous charge fluctuations.

12. – Superionic conductors.

Superionic conductors are ionic solids which, over an extended range of temperatures, below their melting point, exhibit electrical conductivities characteristic of the molten phase, indicative of a high degree of mobility of one of the ionic species. Schematically speaking, this can be interpreted in terms of a high degree of disorder (« melting ») of one of the ionic sublattices, the opposite species retaining a well-defined crystalline long-range order. A first class of superionic conductors is such that the transition to the superionic state can be associated with a structural phase change; the most prominent member of this class is AgI, which is a normal ionic crystal in its low-temperature β-phase; at a temperature roughly equal to half the melting temperature, AgI undergoes a first-order structural transition to the α-phase, and at the same time the electrical conductivity σ increases by many orders of magnitude to values typical of a molten salt. In the second class of superionic conductors, the transition is more diffuse and no thermodynamic phase transition can be associated with the rapid (but continuous) increase in conductivity, although the specific heat goes through a pronounced maximum. Examples of this class are the alkaline-

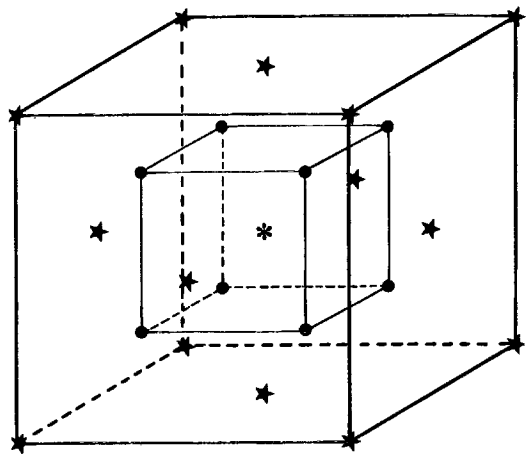

Fig. 3. – Fluorite structure (CaF_2 crystal). The Ca^{++} cations (stars) occupy the sites of a f.c.c. lattice (outer cube), while the vertices of the inner cube are occupied by F^- anions (full circles), half-way between the vertices of the f.c.c. cell and the centre of that cell, which is an octahedral site of the fluorite structure (asterisk). Note that each anion has four cation nearest neighbours (tetrahedral symmetry). The octahedral site plays the role of a (temporary) interstitial site in the superionic phase.

earth halides CaF_2 and $SrCl_2$, as well as PbF_2, all of which have the familiar fluorite structure (see fig. 3).

The four examples of superionic (or fast ion) conductors mentioned above have been extensively studied by MD and Monte Carlo computer experiments, and it is fair to say that these simulations have been instrumental in gaining a correct microscopic view of the phenomenon. AgI has been examined by VASHITA and RAHMAN (MD) [65] and by HIWATARI and UEDA [66]. Despite the uncertainties concerning the pair potentials (the system exhibits charge transfer between the two ionic species and a certain amount of covalent bonding), these authors report semi-quantitative agreement with experimental findings. In α-AgI the small Ag^+ cations (of diameter $\sigma_+ \simeq 1.26$ Å) become disordered above the transition temperature at which the I^- lattice changes from f.c.c.-like to b.c.c.

Rahman's pioneering work on superionic conductors dealt with CaF_2, which is fully ionic and has the fluorite structure [67]; his work was extended by DIXON and GILLAN [68] and by JACUCCI and RAHMAN [69]. The most extensive MD study, including a detailed study of temperature dependence, was devoted to another fluorite structure superionic conductor, $SrCl_2$ [70]; a very similar study dealt with PbF_2 [71]. The main characteristics of these various investigations are the following:

a) Most simulations were carried out for samples of 108 cations and 216 anions; rigid-ion potentials were used throughout.

b) Below the melting temperature, the cations always form a thermally agitated f.c.c. lattice; their motion is harmonic, to a good approximation, as

can be seen from the essentially Gaussian (Debye-Waller) behaviour of the corresponding elastic structure factor $F_+(\boldsymbol{G})$, defined as the Fourier transform of the periodic mean ion density $\varrho_+(\boldsymbol{r})$:

$$\varrho_\alpha(\boldsymbol{r}) = \frac{1}{n_\alpha}\left\langle \sum_{i=1}^{N_\alpha} \delta(\boldsymbol{r}-\boldsymbol{r}_{i\alpha})\right\rangle, \tag{12.1a}$$

$$F_\alpha(\boldsymbol{G}) = \int \varrho_\alpha(\boldsymbol{r}) \exp[i\boldsymbol{G}\cdot\boldsymbol{r}]\,\mathrm{d}\boldsymbol{r} = \left\langle \sum_{i=1}^{N_\alpha} \exp[i\boldsymbol{G}\cdot\boldsymbol{r}_{i\alpha}]\right\rangle, \qquad \alpha = 1, 2, \tag{12.1b}$$

$$F_+(\boldsymbol{G}) \simeq \exp\left[-\frac{1}{6}G^2\langle u_+^2\rangle\right], \tag{12.1c}$$

where $\boldsymbol{G}$ is reciprocal-lattice vector, and $\langle u_\alpha^2\rangle$ the mean square vibrational displacement of species α.

c) Above a diffuse transition temperature, the anions show diffusive motion, with a diffusion constant D_- which increases rapidly with temperature and reaches liquidlike values ($\geqslant 10^{-5}$ cm^2 s^{-1}) long before melting. But contrarily to the situation in a liquid, the diffusive motion is non-Gaussian; this can be seen as follows. Let $\langle r_\alpha^2(t)\rangle$ denote the time-dependent mean square displacement of species α; its MD estimate is

$$\langle r_\alpha^2(t)\rangle \simeq \frac{1}{N_t}\sum_{n=1}^{N_t}\frac{1}{N_\alpha}\sum_{i=1}^{N_\alpha}[\boldsymbol{r}_{i\alpha}(t+n\,\Delta t)-\boldsymbol{r}_{i\alpha}(n\,\Delta t)]^2, \tag{12.2}$$

where N_t is the number of time origins and Δt the time step ($\simeq 10^{-14}$ s in most simulations). In the long-time limit,

$$\langle r_\alpha^2(t)\rangle = B_\alpha + 6D_\alpha t\,. \tag{12.3}$$

For the cations, $D_+ = 0$ and $B_+ = 2\langle u_+^2\rangle$. In the Gaussian approximation [6], the Van Hove self-correlation function is given by

$$G_S^\alpha(r,t) = \frac{1}{N_\alpha}\sum_{i=1}^{N_\alpha}\langle\delta(\boldsymbol{r}+\boldsymbol{r}_{i\alpha}(t)-\boldsymbol{r}_{i\alpha}(0))\rangle \simeq \simeq \left[\frac{2\pi}{3}\langle r_\alpha(t)^2\rangle\right]^{-1}\exp\left[-\frac{3}{2}\frac{r^2}{\langle r_\alpha^2(t)\rangle}\right], \tag{12.4}$$

which is exact in the long-time limit. The Gaussian approximation implies that

$$P_\alpha(t) = \frac{3\langle r_\alpha^4(t)\rangle}{5\langle r_\alpha^2(t)\rangle} = 1\,, \tag{12.5}$$

where

$$\langle r_\alpha^{2n}(t)\rangle = \int r^{2n}\, G_S^{(\alpha)}(r, t)\, \mathrm{d}\boldsymbol{r}\,. \tag{12.6}$$

While (12.5) is well satisfied, at all times, for the cations at all temperatures (below melting) and for the anions below the superionic transition temperature, large deviations (of up to 60 % after 1 ps) are observed for the latter above the transition.

d) While the partial pair distribution functions $g_{++}(r)$ and $g_{+-}(r)$ exhibit typical crystalline features, $g_{--}(r)$ is much less structured and liquidlike, indicating a relatively high degree of disorder.

e) Projections of $\varrho_-(\boldsymbol{r})$ unto high-symmetry crystalline planes (density contour plots) clearly show that the anions are mainly concentrated around their regular (simple cubic) lattice sites, although with a relatively broad and nonspherical distribution, which is noticeably distorted along the lines joining nearest-neighbour anion sites. Contrarily to a generally held belief, they do not occupy, to any appreciable extent, the octahedral (cube-centred) interstitial sites (see fig. 3); in particular, the distribution of anions around these sites exhibits a (nearly zero) minimum, rather than a maximum. The concentration of defects of the anion lattice amounts to only a few percent of vacancies per regular site, above the transition temperature.

f) The above observations, and in particular the high anion mobility, can be interpreted in terms of a jump diffusion picture: the anions diffuse by discrete « hops » between regular (cubic) lattice sites, the residence time of the ions being an order of magnitude longer than the flight time. A detailed « hopping catalogue » shows that jumps are highly correlated, and are mainly along the (100)-direction (*i.e.* between nearest-neighbour sites); they can be interpreted in terms of the motion of vacancies and interstitials, the total numbers of defects of both types being the same at each instant of time. The large diffusion constant of the anions is a simple consequence of the high mobility of defects which do not reside on any site for more than a few vibration periods.

g) The peak in the specific heat near the transition arises from a significant increase of the internal energy above its harmonic value (by roughly 5 kJ/mol in $SrCl_2$).

h) The partial dynamical structure factor $S_{--}(k)$ exhibits a pronounced central peak in superionic $SrCl_2$ (at 1484 K), which is absent below the transition (at 938 K), over a range of wave vectors along the (100)-direction, in agreement with the findings of quasi-elastic neutron scattering experiments.

It appears clearly from the above discussion that MD simulations have led to a very coherent microscopic picture of fast ion conduction.

IV. – Two-Dimensional Coulomb Systems.

13. – The two-dimensional electron gas.

A clear distinction must be made between genuine 2d Coulomb systems, where the charges interact by the logarithmic potential (1.2*b*), and systems of particles confined to a surface (monolayers), which interact through the 3d Coulomb potential (1.2*c*). A practical realization of the first category would be a system of very long, parallel charged rods (*e.g.*, the lyotropic nematic phase of charged rods such as the tobacco mosaic virus). Layers of electrons trapped at the surface of liquid helium are a good example of the second category, which has been widely studied in the laboratory [72]. We shall start our discussion of 2d Coulomb systems with the 2d electron gas, since it has been the subject of a number of MD simulations [18, 73-75]. Electron layers on liquid helium have typical areal densities $n = (10^8 \div 10^9)\,\mathrm{cm}^{-2}$; with a temperature of 1 K, the de Broglie thermal length λ_e ($\simeq 100$ Å) is negligible compared to the mean interelectronic spacing $a = (\pi n)^{-\frac{1}{2}} \simeq 1\ \mu\mathrm{m}$, so that the system is accurately described by classical statistical mechanics. It is the equivalent of the 3d OCP, confined to a plane. The coupling constant $\Gamma = e^2/ak_B T$ is of the order of 10 or larger. In fact, by lowering the temperature, GRIMES and ADAMS [72] were able to observe the crystallization of the layer unto a triangular lattice, for $\Gamma \simeq 130$. This value is remarkably well reproduced by MC and MD simulations of the 2d electron gas in a uniform background [75, 76]. The single-particle and collective dynamics of the model are particularly interesting. The dimensionless 2d Fourier transform of the 3d Coulomb potential is

$$\frac{n\hat{v}(k)}{k_B T} = \frac{k_D}{k}\,, \tag{13.1}$$

where $k_D = (2\pi n e^2/k_B T)^{\frac{1}{2}}$ is the 2d Debye wave number. Assuming that the direct correlation function $c(r)$ behaves as $-v(r)/k_B T$ at large r, we conclude immediately from the Ornstein-Zernike relation that the structure factor $S(k)$ behaves for small k as

$$S(k) \underset{k\to 0}{\simeq} \frac{k}{k_D}\,. \tag{13.2}$$

The long-wavelength limit of the characteristic frequency of the longitudinal collective mode can be estimated from a simple sum rule argument as

$$\omega_l(k) \simeq \left[\frac{\int_{-\infty}^{+\infty} \omega^2 S(k,\omega)\,\mathrm{d}\omega}{S(k)}\right]^{\frac{1}{2}} \underset{k\to 0}{=} \left[\frac{v_0^2 k^2}{k/k_D}\right]^{\frac{1}{2}} = v_0 k_D \left(\frac{k}{k_D}\right)^{\frac{1}{2}}, \tag{13.3}$$

showing the charecteristic $k^{\frac{1}{2}}$ behaviour of the « plasma frequency » for this system ($v_0 = (k_B T/m)^{\frac{1}{2}}$ is the thermal velocity). In fact, an exact hydrodynamic analysis leads to the following long-wavelength dispersion relation [77]:

$$\omega(k) = \omega_1(k)\left[1 + \delta\frac{k}{k_D} + \ldots\right] \tag{13.4}$$

with $\delta = (1/2)(C_p/C_v)(\chi_T^{(0)}/\chi_T)$, where C_p/C_v and $\chi_T/\chi_T^{(0)}$ denote the ratio of the specific heats and the isothermal compressibility relative to its perfect-gas value. As in the case of the 3d OCP, χ_T changes sign for $\Gamma \simeq 3$, so that the dispersion of the longitudinal mode changes from positive to negative. The dispersion relation for larger k can be determined by MD calculations of the dynamical structure factor $S(k, \omega)$ [73, 74]; $\omega(k)$ is identified with the position of the peak in $S(k, \omega)$, which is well resolved, up to $ka \simeq 2$. In the strong-coupling limit $\Gamma \gg 1$, the dispersion curve is found to flatten out beyond $ka \simeq 1$ at a frequency $\omega \simeq \omega(ka \simeq 1) \simeq 1.2\,\tau^{-1}$, where $\tau = (ma^3/e^2)^{\frac{1}{2}}$ is the « natural » time unit. This flattening of the dispersion curve is probably responsible for the well-defined, long-lived oscillations which had been observed earlier [18] in the velocity autocorrelation function of the 2d electron gas. The frequency of these oscillations had been found to be precisely equal to $1.2\,\tau^{-1}$ and to be the same for $\Gamma = 36$ and $\Gamma = 90$, thus supporting the view that the oscillations are a consequence of the coupling of the individual motion of electrons to relatively short-wavelength « plasma » oscillations.

In ref. [18] it was argued that these oscillations in $Z(t)$ may also be responsible for the existence of a diffusion constant for this 2d system, because they may override the slow $1/t$ decay of $Z(t)$ characteristic of 2d systems with short-range forces [78]. Indeed the simulations, which were carried out for systems of 104 and 400 electrons on the surface of a sphere (see sect. **5**), showed no indication of an N-dependence of D, similar to that observed in the hard-disk fluid [79]. Another argument in favour of the existence of a well-defined diffusion constant for the 2d electron gas is the fact that D is found to be independent of an applied magnetic field perpendicular to the surface, even for cyclotron frequencies as large as $\omega_c\tau = 3$. Note that this behaviour contrasts sharply with the behaviour of $D_\perp$ in the 3d OCP (see sect. **7**).

14. – The two-dimensional one-component plasma.

The exact two-dimensional equivalent of the 3d OCP is a system of identical point particles of charge q interacting through the 2d Coulomb potential (1.2*b*) and immersed in a uniform neutralizing background. We shall reserve the name of « 2d OCP » for this system; its total potential energy is given by eq. (7.1). All excess properties are characterized by the single dimensionless coupling

constant (see eq. (1.6))

$$\Gamma = \frac{e^2}{k_B T} \tag{14.1}$$

which is independent of density; a direct consequence of this peculiarity is that a trivial scaling argument yields the exact equation of state, which is simply [80]

$$\frac{P}{nk_B T} = 1 - \frac{\Gamma}{4}. \tag{14.2}$$

Moreover, by a mathematical accident, all equilibrium static properties can be calculated exactly for $\Gamma = 2$ [81], thus providing a stringent test for simulation results.

Extensive MC and MD simulations of the model underline the (not unexpected) striking similarity of the static and dynamic behaviour of the OCP in 2 and 3 dimensions [19, 82, 83]. The three sets of available simulation data are particularly instructive, because they use three types of boundary conditions: between 104 and 256 particles confined to the surface of a sphere (as described in sect. **5**) in ref. [19], periodic boundary conditions with Ewald summations in ref. [82], 511 particles in a disk with free boundaries in ref. [83]. All three yield very similar energies and predict melting to occur at $\Gamma \simeq 135$. The simulations of ref. [82] clearly exhibit hysteresis in the fluid-solid transition region (with metastable supercooled fluid and superheated solid states), while solid-fluid coexistence was observed in ref. [83], so that the transition appears to be clearly first order, with a finite entropy change ($\Delta S/Nk_B \simeq 0.3$) and no change in density [28]. Moreover, the free-boundary simulations of ref. [83] have revealed very interesting premelting phenomena, which are co-operative, cyclic permutations of six or more particles.

As regards time-displaced correlations, the MD simulations of ref. [82] have shown that, for sufficiently strong coupling ($\Gamma \gg 1$), the velocity autocorrelation function $Z(t)$ exhibits well-defined oscillations at a frequency slightly below ω_p, very similar to those observed in the 3d OCP and in the 2d electron gas.

15. – The two-component plasma in two dimensions and the Kosterlitz-Thouless transition.

The classical two-component plasma has a behaviour which depends strongly on dimensionality. In 1d it is always a dielectric made up of bound pairs of oppositely charged particles. In 3d it is unstable against collapse of oppositely charged particles at all temperatures, unless the Coulomb attraction is cut at short distances by a hard core or quantum « smearing »; such stable two-

component plasmas form then a conducting phase, under all conditions, except when they crystallize (ionic solids). The 2d case is the most interesting. A two-component plasma of point particles ($\sigma = 0$) is thermodynamically stable for $T > q^2/2k_B$ ($\Gamma < 2$) since the Boltzmann factor for a pair of opposite charges

$$\exp\left[-\frac{q^2}{k_B T}\ln(r/L)\right] = \left(\frac{r}{L}\right)^{-\Gamma} \tag{15.1}$$

is integrable in 2d for $\Gamma < 2$. Below $\Gamma = 2$, the equation of state is given exactly by (14.2); as $\Gamma \to 2$ the internal energy diverges as $(2-\Gamma)^{-1}$ and the specific heat c_s as $(2-\Gamma)^{-2}$ [80]. Above $\Gamma = 2$, the two-component plasma is stable in the presence of a hard-core repulsion between opposite charges. This system, which can be shown to be isomorphous to the 2d XY model, undergoes a Kosterlitz-Thouless (KT) transition between a low-temperature dielectric phase (where opposite charges are bound in pairs as in 1d) and a high-temperature conducting (plasma) phase (as in 3d) [84, 85]. A mean-field argument shows that in the limit of low density ($n^* = n\sigma^2 \to 0$), the transition should occur at $\Gamma = 4$ [84].

The KT transition has recently been studied by MC simulations of a system of oppositely charged hard disks confined to the surface of a sphere (see sect. **5**) [20]. The potential model

$$v_{\alpha\beta}(r) = \begin{cases} \infty\,, & r < \sigma\,, \\ -q_\alpha q_\beta \ln\dfrac{r}{L}\,, & r > \sigma\,,\ q_\alpha, q_\beta = \pm q\,, \end{cases} \tag{15.2}$$

is the exact 2d counterpart of the 3d « restricted primitive model » of electrolytes. The two dimensionless parameters which characterize an equilibrium state of the system are the packing fraction $\eta = \pi n\sigma^2/4 = \pi n^*/4$ and Γ. At sufficiently low temperatures ($\Gamma \geqslant 12$), the $P(\eta)$ isotherms exhibit van der Waals loops in the NVT ensemble simulations, while the distribution of volumes becomes bimodal in the NPT calculations, thus indicating the existence of a « liquid-gas » phase separation very similar to the corresponding phase transition in the 3d « restricted primitive model ». The critical parameters are estimated to be $\eta_c \simeq 0.11$ and $\Gamma_c \simeq 12$. Above this temperature, MC simulations have been carried out in the one-phase region to detect the KT (dielectric-plasma) transition. The main « diagnostic » used to detect the transition was the fluctuation of the total dipole moment (3.2), which is related to the external dielectric susceptibility χ, which measures the response per unit area to a homogeneous external electric field

$$\frac{1}{S}\langle \boldsymbol{M}\rangle = \chi \boldsymbol{E}_0 \tag{15.3}$$

via the standard linear-response relation

$$\chi = \frac{1}{2k_B T} \frac{\langle |\boldsymbol{M}|^2 \rangle}{S} . \tag{15.4}$$

In the low-density ($\sigma \to 0$), low-temperature limit, the system behaves as a collection of N independent pairs, so that

$$\langle |\boldsymbol{M}|^2 \rangle = \langle \sum_i \sum_j \boldsymbol{m}_i \cdot \boldsymbol{m}_j \rangle \simeq N \langle |\boldsymbol{m}|^2 \rangle = N q^2 \langle r^2 \rangle , \tag{15.5}$$

where r is the (variable) length of a dipole, *i.e.* the distance between the two charges in a pair. The mean square length of a pair is easily calculated for an isolated pair, with the result (see eq. (15.1))

$$\langle r^2 \rangle = \frac{2\pi \int_\sigma^\infty r^{-\Gamma} r^2 r \, \mathrm{d}r}{2\pi \int_\sigma^\infty r^{-\Gamma} r \, \mathrm{d}r} = \sigma^2 \frac{\Gamma - 2}{\Gamma - 4} , \qquad \Gamma > 4 , \tag{15.6}$$

so that

$$\frac{1}{S} \langle |\boldsymbol{M}|^2 \rangle = \frac{n}{2} q^2 \sigma^2 \frac{\Gamma - 2}{\Gamma - 4} , \tag{15.7}$$

and the corresponding susceptibility (15.4) diverges in the limit $\Gamma \to 4+$ [84]. At finite densities, the interaction between dipoles cannot be neglected anymore; the Coulomb attraction between the two charges of a pair is weakened by the dielectric constant due to surrounding pairs, and the transition is expected to take place at lower temperatures. $\langle |\boldsymbol{M}|^2 \rangle$ is also easily calculated in the conducting phase, where pairs are broken:

$$\begin{aligned} \frac{1}{S} \langle |\boldsymbol{M}|^2 \rangle &= \frac{1}{S} \left\langle \sum_i \sum_j q_i q_j \boldsymbol{r}_i \cdot \boldsymbol{r}_j \right\rangle = \frac{1}{S} \left\langle \sum_{i \neq j} \sum q_i q_j |\boldsymbol{r}_i - \boldsymbol{r}_j|^2 \right\rangle = \\ &= -\frac{1}{2} \sum_\alpha \sum_\beta n_\alpha n_\beta q_\alpha q_\beta \int g_{\alpha\beta}(r) r^2 \, \mathrm{d}^2 r = \frac{k_B T}{\pi} , \end{aligned} \tag{15.8}$$

where the perfect-screening sum rule (1.8*b*) has been used. When the system becomes a conductor, the mean square dipole is expected to change discontinuously from a value of the order of the estimate (15.7) to the value (15.8). This is confirmed by the MC simulations of Caillol and Levesque [20], although, for a finite system, the variation of $\langle |\boldsymbol{M}|^2 \rangle$ with Γ (for a given η) is « rounded ». The transition is accompanied by a pronounced peak in the specific heat. Due to the continuous variation of $\langle |\boldsymbol{M}|^2 \rangle$ with Γ in the simulations, the location Γ_c of the transition is somewhat « fuzzy », but Γ_c increases steadily with η,

with Γ_c close to 4 for $\eta = 10^{-3}$ and $\Gamma \simeq 10$ for $\eta = 5 \cdot 10^{-2}$. The KT transition line may intersect the « liquid-gas » coexistence curve at the critical point.

In parallel with this MC study, the KT transition has also been studied by MD simulations of a simplified model, in which charges of one species (the positive « ions », say) were fixed on the sites of a triangular lattice, while the opposite charges (the negative « electrons », say) move in the periodic field of the fixed ions [86]. In this way the KT transitions is mapped onto a « delocalization » transition corresponding to the onset of electron diffusion and electrical conductivity. While the electrons interact via the bare Coulomb potential (1.2*b*), the ion-electron interaction includes a « soft core », *i.e.*

$$v_{+-}(r) = q^2 \left[\left(\frac{\sigma}{r} \right)^n + \ln \frac{r}{L} \right], \tag{15.9}$$

where n was chosen equal to 10. This particular two-component plasma can also be looked upon as a one-component plasma of classical electrons in a periodic (rather than uniform) neutralizing ionic field.

In the MD simulations the basic cell was chosen to be a hexagon containing $N = 75$, 108 or 192 ions and as many electrons, with periodic boundary conditions, and the nearest-image convention was adopted [86]; some preliminary simulations were also carried out for a periodic rectangular system with Ewald summations [87]. The choice of time step is dictated by the characteristic frequencies of the system. In the high-temperature plasma phase ($\Gamma < 4$) the dynamics are expected to be dominated by the electron plasma frequency $\omega_p = (2\pi n q^2/m)^{\frac{1}{2}}$, while in the low-temperature dielectric phase the characteristic frequencies are those associated with the individual rotational and vibrational motion of each electron in the field of the ion with which it is paired. The vibrations have the higher frequency, and an elementary calculation yields an estimate of $\omega_v \simeq 10\omega_p$, so that a time step $\Delta t \simeq 0.005\omega_p^{-1}$ was chosen to ensure good conservation of the total energy. MD runs of a total length of $(10^2 \div 10^3)\,\omega_p^{-1}$ were carried out to cover the range $20 \gtrsim \Gamma \gtrsim 1$, with particular emphasis on the vicinity of $\Gamma = 4$, where the KT transition is expected to take place. The most extensive calculations were done for a density such that $\sigma/a = 0.1$, but subsequent calculations covered the densities $\sigma/a = 0.2$, 0.05, 0.02 and 0.005.

The key diagnostic in these MD simulations is the onset of electron diffusion and electrical conductivity. Graphical display of the electron trajectories shows that these are strongly localized for $\Gamma > \Gamma_1$; delocalization of the electrons occurs gradually for $\Gamma < \Gamma_1$. At first tightly bound ion-electron pairs are observed to coexist with delocalized electrons which appear to be exchanged between ions; this « hopping » diffusion is reminiscent of similar mechanism in superionic conductors (see sect. **12**). For still higher temperatures, the electronic trajectories become more and more space filling. These observations

can be expressed in a more quantitative way by computimg the electron velocity autocorrelation function $Z(t)$ and the electric-current autocorrelation function $J(t)$, from which the diffusion constant D and the electrical conductivity σ can be derived via the usual Green-Kubo relations. While $Z(t)$ and $J(t)$ are identical, within statistical errors, for $\Gamma \gtrsim \Gamma_1$, and show much structure associated with the individual rotational and vibrational motions in that region, these functions decay monotonically in the high-temperature limit ($\Gamma \ll \Gamma_1$); the relaxation time of $J(t)$ is about twice as large as that associated with $Z(t)$ in that limit, a situation reminiscent of our earlier observations for the 3d electron-proton plasma [39] (see fig. 2). D and σ take nonzero values for Γ less than the threshold coupling Γ_1, which depends on density. The MD results are compatible with the low-density limit

$$\lim_{\sigma/a \to 0} \Gamma_1 = 2 \tag{15.10}$$

which is precisely the coupling for which the two-component plasma of *point*

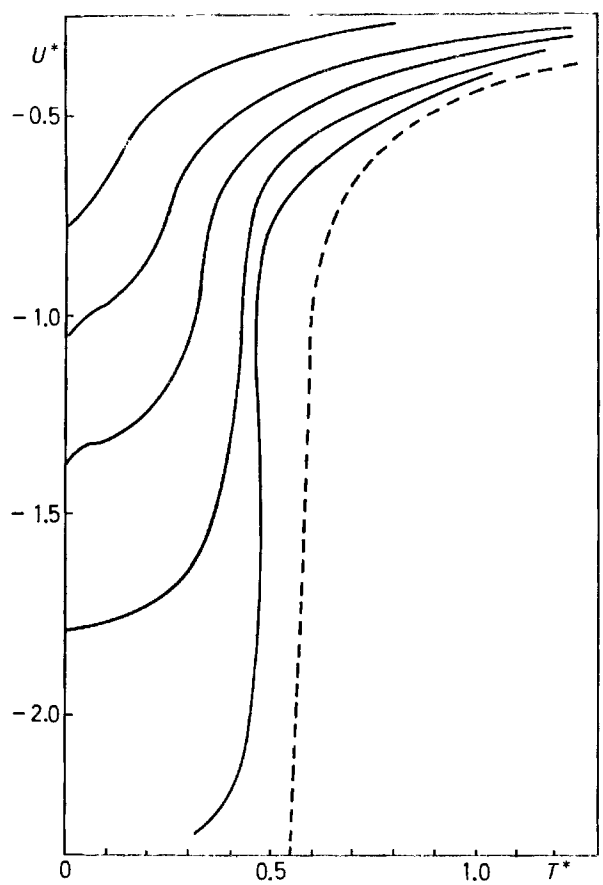

Fig. 4. – Reduced excess internal energy per particle ($U^* = U/2Nq^2$) of the two-dimensional two-component plasma, with ions of one species fixed on a triangular lattice, *vs.* reduced temperature $T^* = k_B T/q^2 = 1/\Gamma$. The full curves are for various densities, corresponding, from top to bottom, to $\sigma/a = 0.2$, 0.1, 0.05, 0.02 and 0.01. The dashed curve is the corresponding energy for point particles ($\sigma \equiv 0$), which diverges as $T^* \to 0.5$.

charges collapses. This low-density limit differs by a factor of two from the KT limit for a two-component plasma where both species are mobile [20, 84].

A plot of the internal energy *vs.* reduced temperature $T^* = 1/\Gamma$ shows a sharp rise around the « critical » temperature $T_1^* = 1/\Gamma_1$; correspondingly the specific heat exhibits a pronounced peak at a temperature T_2^* slightly higher than T_1^*. The temperatures T_1^* and T_2^* appear to tend to the common low-density limit (15.10), as can be seen from fig. 4. In the same limit, the specific heat appears to diverge. The energy and specific-heat values show no significant N-dependence and the nearest-image and Ewald summation results agree closely in the transition region. Significant differences appear only at very low temperatures where the nearest-image convention does not correctly describe the correlations between the dipoles formed by the tightly bound ion-electron pairs [87].

The main problem which remains to be solved is to determine the law according to which D vanishes as $T^* \to T_1^*$; this goal appears to be achievable if the repulsive core in the potential (15.9) is replaced by a harmonic regularization of the divergent Coulomb attraction, reminiscent of the « quantum smearing » used in the study of strongly coupled plasmas (see sect. **9**); the corresponding electron-ion vibration frequency ω_v is much lower than with the potential (15.9), thus allowing a substantial increase of the time step and hence much longer trajectories.

* * *

I am indebted to B. PILLER for his help in preparing part I, and to him and J. CLÉROUIN for their stimulating collaboration on our recent, partly unpublished work on the Coulomb gas in two dimensions.

REFERENCES

[1] F. H. STILLINGER and R. LOVETT: *J. Chem. Phys.*, **49**, 1991 (1968).
[2] PH. A. MARTIN and CH. GRUBER: *J. Stat. Phys.*, **31**, 691 (1983).
[3] J. P. VALLEAU: in *NRCC Proceedings* No. 9, edited by D. CEPERLEY (1980), p. 3.
[4] D. M. CEPERLEY and G. V. CHESTER: *Phys. Rev. A*, **15**, 755 (1977).
[5] B. LARSEN and B. ROGDE: *J. Chem. Phys.*, **72**, 2578 (1980).
[6] J. P. HANSEN and I. R. MCDONALD: *Theory of Simple Liquids* (Academic Press, London, 1976).
[7] S. G. BRUSH, H. L. SAHLIN and E. TELLER: *J. Chem. Phys.*, **45**, 2102 (1966).
[8] D. N. CARD and J. P. VALLEAU: *J. Chem. Phys.*, **52**, 6232 (1970).
[9] M. BAUS and J. P. HANSEN: *Phys. Rep.*, **59**, 1 (1980).
[10] D. J. ADAMS: *Chem. Phys. Lett.*, **62**, 329 (1979).
[11] P. P. EWALD: *Ann. Phys. (Leipzig)*, **64**, 253 (1921).
[12] S. W. DE LEEUW, J. W. PERRAM and E. R. SMITH: *Proc. R. Soc. London, Ser. A*, **373**, 27, 57 (1980).

[13] S. W. DE LEEUW and J. W. PERRAM: *Physica (Utrecht) A*, **107**, 179 (1981).
[14] J. W. PERRAM and S. W. DE LEEUW: *Physica (Utrecht) A*, **109**, 237 (1981).
[15] B. PILLER: private communication.
[16] D. J. ADAMS and I. R. MCDONALD: *J. Phys. C*, **7**, 2761 (1974).
[17] R. W. HOCKNEY and J. W. EASTWOOD: *Computer Simulation Using Particles* (McGraw-Hill, New York, N. Y., 1981).
[18] J. P. HANSEN, D. LEVESQUE and J. J. WEIS: *Phys. Rev. Lett.*, **43**, 979 (1979).
[19] J. M. CAILLOL, D. LEVESQUE, J. J. WEIS and J. P. HANSEN: *J. Stat. Phys.*, **28**, 325 (1982).
[20] J. M. CAILLOL and D. LEVESQUE: *Phys. Rev. B*, **33**, 499 (1986).
[21] M. FEIX: in *Strongly Coupled Plasmas*, edited by G. KALMAN and P. CARINI (Plenum Press, New York, N. Y., 1978), p. 499.
[22] M. DAWSON: *Phys. Fluids*, **5**, 445 (1962).
[23] L. SPITZER: *Physics of Fully Ionized Gases* (Interscience, New York, N. Y., 1956).
[24] M. BAUS, J. P. HANSEN and L. SJÖGREN: *Phys. Lett. A*, **82**, 180 (1981).
[25] J. P. HANSEN: *Phys. Rev. A*, **8**, 3096 (1973).
[26] P. VIEILLEFOSSE and J. P. HANSEN: *Phys. Rev. A*, **12**, 2048 (1975).
[27] W. L. SLATTERY, G. D. DOOLEN and H. E. DE WITT: *Phys. Rev. A*, **21**, 2087 (1980); **26**, 2255 (1982).
[28] J. D. WEEKS: *Phys. Rev. B*, **24**, 1530 (1981).
[29] J. P. HANSEN, I. R. MCDONALD and E. L. POLLOCK: *Phys. Rev. A*, **11**, 1025 (1975).
[30] H. GOULD and G. F. MAZENKO: *Phys. Rev. A*, **15**, 1274 (1977). T. GASKELL: *J. Phys. C*, **15**, 1601 (1982); M. C. MARCHETTI and T. R. KIRKPATRICK: to be published.
[31] B. BERNU and P. VIEILLEFOSSE: *Phys. Rev. A*, **18**, 2345 (1978).
[32] J. WALLENBORN and M. BAUS: *Phys. Rev. A*, **18**, 1737 (1978).
[33] B. BERNU: *J. Phys. (Paris)*, **42**, L253 (1981).
[34] M. BAUS: *Physica (Utrecht) A*, **88**, 319, 336, 591 (1977).
[35] J. P. HANSEN, I. R. MCDONALD and P. VIEILLEFOSSE: *Phys. Rev. A*, **20**, 2590 (1979).
[36] J. P. HANSEN, F. JOLY and I. R. MCDONALD: *Physica (Utrecht) A*, **132**, 472 (1985).
[37] T. MORITA: *Prog. Theor. Phys.*, **22**, 757 (1959).
[38] C. DEUTSCH: *Phys. Lett. A*, **60**, 317 (1977); H. MINOO, M. M. GOMBERT and C. DEUTSCH: *Phys. Rev. A*, **23**, 924 (1981).
[39] J. P. HANSEN and I. R. MCDONALD: *Phys. Rev. A*, **23**, 2041 (1981).
[40] L. SJÖGREN, J. P. HANSEN and E. L. POLLOCK: *Phys. Rev. A*, **24**, 1544 (1982).
[41] B. BERNU and J. P. HANSEN: *Phys. Rev. Lett.*, **48**, 1375 (1982).
[42] B. BERNU: *Physica (Utrecht) A*, **122**, 130 (1983).
[43] J. P. HANSEN and L. SJÖGREN: *Phys. Fluids*, **25**, 617 (1982).
[44] J. P. HANSEN and I. R. MCDONALD: *Phys. Lett. A*, **97**, 42 (1983).
[45] M. P. TOSI: in *Electron Correlations*, edited by J. T. DEVREESE and F. BROSENS (Plenum Press, New York, N. Y., 1983), p. 235.
[46] A. RAHMAN: *Phys. Rev. Lett.*, **32**, 52 (1974).
[47] P. TURQ, F. LANTELME and H. L. FRIEDMAN: *J. Chem. Phys.*, **66**, 3039 (1977).
[48] M. L. KLEIN and I. R. MCDONALD: *J. Chem. Phys.*, **79**, 2333 (1983).
[49] L. V. WOODCOCK and K. SINGER: *Trans. Faraday Soc.*, **67**, 12 (1971).
[50] M. J. SANGSTER and M. DIXON: *Adv. Phys.*, **25**, 247 (1976).
[51] M. P. TOSI and F. G. FUMI: *J. Phys. Chem. Solids*, **25**, 45 (1964).
[52] D. J. ADAMS and I. R. MCDONALD: *Physica (Utrecht) B*, **79**, 159 (1975).
[53] J. P. HANSEN and I. R. MCDONALD: *Phys. Rev. A*, **11**, 2111 (1975).
[54] P. V. GIAQUINTA, M. PARRINELLO and M. P. TOSI: *Phys. Chem. Liq.*, **5**, 305 (1976).

[55] M. PARRINELLO and M. P. TOSI: *Riv. Nuovo Cimento*, **2**, 1 (1979).
[56] J. BOSSE and T. MUNAKATA: *Phys. Rev. A*, **25**, 2743 (1982).
[57] J. R. D. COPLEY and A. RAHMAN: *Phys. Rev. A*, **13**, 2276 (1976).
[58] E. M. ADAMS, I. R. MCDONALD and K. SINGER: *Proc. R. Soc. London, Ser. A*, **357**, 37 (1977).
[59] M. DIXON: *Philos. Mag. B*, **47**, 509, 531 (1983); **48**, 13 (1983).
[60] B. BERNU: to be published.
[61] G. CICCOTTI, G. JACUCCI and I. R. MCDONALD: *Phys. Rev. A*, **13**, 426 (1976).
[62] F. LANTELME and P. TURQ: *J. Chem. Phys.*, **77**, 3177 (1982).
[63] S. W. DE LEEUW: *Mol. Phys.*, **36**, 765 (1978).
[64] G. JACUCCI, I. R. MCDONALD and A. RAHMAN: *Phys. Rev. A*, **13**, 1581 (1976).
[65] P. VASHISHTA and A. RAHMAN: *Phys. Rev. Lett.*, **40**, 1337 (1978).
[66] Y. HIWATARI and A. UEDA: *J. Phys. Soc. Jpn.*, **48**, 766 (1980).
[67] A. RAHMAN: *J. Chem. Phys.*, **65**, 4845 (1976).
[68] M. DIXON and M. J. GILLAN: *J. Phys. C*, **11**, L165 (1978).
[69] G. JACUCCI and A. RAHMAN: *J. Chem. Phys.*, **69**, 4117 (1978).
[70] M. J. GILLAN and M. DIXON: *J. Phys. C*, **13**, 1901, 1919, L835 (1980).
[71] A. B. WALKER, M. DIXON and M. J. GILLAN: *J. Phys. C*, **15**, 4061 (1982).
[72] C. C. GRIMES and G. ADAMS: *Phys. Rev. Lett.*, **42**, 795 (1979).
[73] H. TOTSUJI and H. KAKEYA: *Phys. Rev. A*, **22**, 1220 (1980).
[74] R. K. KALIA, P. VASHISHTA, S. W. DE LEEUW and A. RAHMAN: *J. Phys. C*, **14**, L991 (1981).
[75] R. K. KALIA, P. VASHISHTA and S. W. DE LEEUW: *Phys. Rev. B*, **23**, 4794 (1981).
[76] R. C. GANN, S. CHAKRAVARTY and G. V. CHESTER: *Phys. Rev. B*, **20**, 326 (1979).
[77] M. BAUS: *J. Stat. Phys.*, **19**, 163 (1978).
[78] B. J. ALDER and T. E. WAINWRIGHT: *Phys. Rev. A*, **1**, 18 (1970).
[79] W. W. WOOD: in *Fundamental Problems in Statistical Mechanics*, Vol. **3**, edited by E. G. D. COHEN (North-Holland, Amsterdam, 1975), p. 331.
[80] E. H. HAUGE and P. C. HEMMER: *Phys. Norv.*, **5**, 209 (1971).
[81] A. ALASTUEY and J. JANCOVICI: *J. Phys. (Paris)*, **42**, 1 (1981).
[82] S. W. DE LEEUW and J. W. PERRAM: *Physica (Utrecht) A*, **113**, 546 (1982).
[83] PH. CHOQUARD and J. CLÉROUIN: *Phys. Rev. Lett.*, **50**, 2086 (1983).
[84] J. M. KOSTERLITZ and D. J. THOULESS: *J. Phys. C*, **6**, 1181 (1973).
[85] J. FRÖHLICH and T. SPENCER: *Phys. Rev. Lett.*, **46**, 1006 (1981).
[86] J. CLÉROUIN and J. P. HANSEN: *Phys. Rev. Lett.*, **54**, 2277 (1985).
[87] B. PILLER: unpublished results.

Computer Simulations of Two- and Quasi–Two-Dimensional Atomic Systems.

FARID F. ABRAHAM

IBM Almaden Research Center - San Jose, CA 95120

1. – Two-dimensional melting of a simple atomic system.

During the last decade, the study of phase transitions in two-dimensional systems has gained the attention of a large number of experimentalists and theorists in the physics and chemistry communities. We have witnessed numerous significant innovations in experimental surface science, resulting in the discovery of a vast richness of novel adsorption phenomena at solid surfaces. This has, in turn, stimulated a great deal of theoretical activity, challenged by the need to explain these novel phenomena which may owe their existence to the lower dimensionality of the system and encouraged by the belief that the theoretical analysis in two-dimensional geometry should be significantly simpler and more familiar than in three-dimensional geometry. One recent example has been the study of melting in two and quasi-two dimensions.

KOSTERLITZ and THOULESS [1], and independently FEYNMAN [2], pioneered the application of the dislocation model of melting for a two-dimensional crystal. From this theory of melting, the Kosterlitz-Thouless-Feynman criterion for the stability of a solid phase against the formation of isolated dislocations was obtained and reads

$$K \equiv \frac{4a^2}{kT_m}\frac{\mu(\mu+\lambda)}{2\mu+\lambda} = 16\pi\,, \tag{1.1}$$

where T_m is the Kosterlitz-Thouless-Feynman melting transition temperature, a is the lattice constant and μ, λ are the Lamé elastic coefficients [3]. Hence, this theory predicts that K shows a universal discontinuity at the melting transition of 16π. Furthermore, if one accepts the model that the mechanism for melting is the unbinding of a dilute gas of dislocation pairs, then this phase transition should not depend on the type of interatomic interaction.

Expanding on the studies of Kosterlitz, Thouless and Feynman, HALPERIN and NELSON [4, 5] have developed a detailed theory of defect-mediated melting

for a two-dimensional crystal. This entailed the assumption that a « liquid » close to its freezing point has a structure similar to that of a solid, but that its equilibrium configuration has some concentration of defects (dislocations and/or disclinations) to give the state liquidlike properties, *i.e.*, in order to extend the predictions of the earlier studies, HALPERIN and NELSON modelled the equilibrium liquid state as a solid with particular types of topological defects.

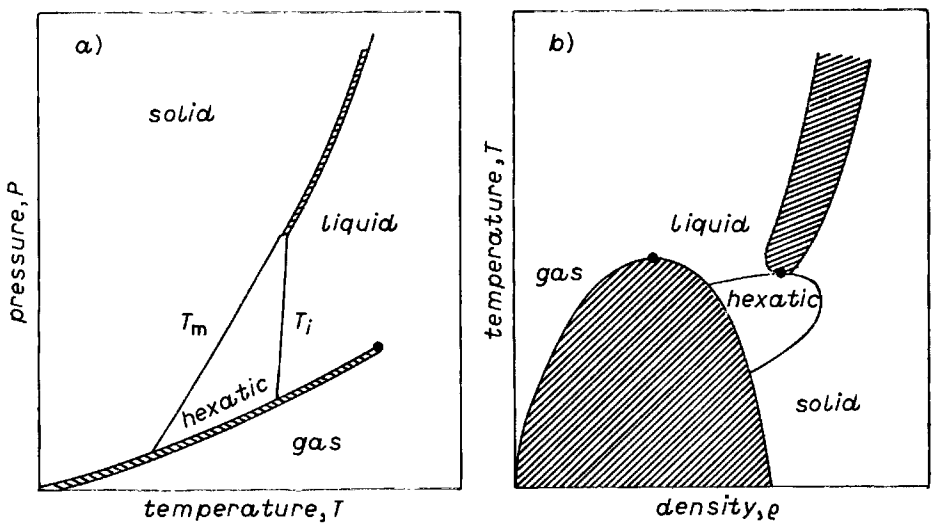

Fig. 1. – *a*) The Halperin-Nelson pressure-temperature phase diagram for a two-dimensional atomic system represented by an interatomic interaction bearing an attractive potential with a repulsive core. Solid, liquid, gas and hexatic phases are shown, together with heavy hatched lines of first-order transitions. The loci of higher-order dislocation and disclination unbinding transitions are shown as light lines. *b*) The corresponding temperature-density phase diagram from the Halperin-Nelson theory. The hatched areas represent two-phase coexistence.

One important feature of the Halperin-Nelson theory is the possibility that the transition from a two-dimensional solid to a two-dimensional liquid takes place by two continuous transitions with increasing temperature (see fig. 1). At some temperature T_m given by eq. (1.1), dissociation of dislocation pairs gives rise to a continuous transition from a solid phase, with algebraic decay of transitional order and long-range orientational order, to a *liquid-crystal* (*hexatic*) phase, with exponential decay of translational order but algebraic decay of sixfold orientational order. At a higher temperature, $T_i > T_m$, dissociation of dislocations into disclinations gives rise to another continuous phase transition from the hexatic phase to the isotropic fluid phase. HALPERIN and NELSON do emphasize that this particular melting mechanism is only one possibility. They cannot rule out the possibility of a first-order melting transition.

Direct experimental verification of the Halperin-Nelson theory for two-dimensional melting is difficult because several possible mechanisms are involved in real systems which might conceivably influence the apparent order of the

transition, *e.g.*, epitaxy, second-layer promotion and heterogeneity, as well as the details of the adatom and substrate interactions. In order to circumvent the uncertainties and limitations of current laboratory experiments, a *computer experiment* may be performed on the well-defined model systems constrained to remain two-dimensional, and we will present the outcome of some such experiments. An extensive survey is provided in ref. [6].

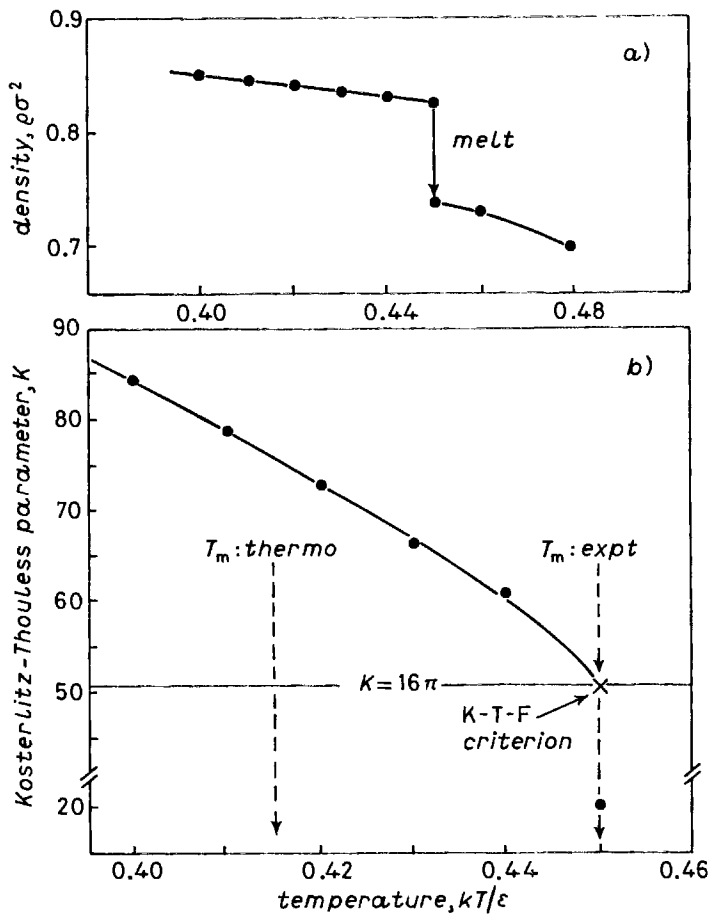

Fig. 2. – *a*) The equilibrium density as a function of temperature for the 529 Lennard-Jones atom system at a fixed pressure $P^* = 0.05$ near the triple-point pressure. *b*) The Kosterlitz-Thouless parameter K as a function of temperature for the 529 Lennard-Jones atom system at fixed temperatures and densities corresponding to an average pressure of $P^* = 0.05$.

In fig. 2*a*), we present the equilibrium density ϱ^* for the Lennard-Jones system of 529 atoms as a function of temperature T^* and for a fixed pressure $P^* = 0.05$ [7]. At $T^* = 0.45$, the solid melts into a liquid after $\sim 5 \cdot 10^6$ configurations with a dramatic decrease in equilibrium density. For the 529 Lennard-Jones atom system at fixed temperatures and densities corresponding to an average pressure of $P^* = 0.05$, we have calculated the Lamé coefficients. From the measured Lamé coefficients and eq. (1.1), the Kosterlitz-Thouless parameter K was obtained and is presented as a function of temperature in

fig. 2*b*). We note that, at the observed instability temperature $T_m^* = 0.45$, K has approached, by extrapolation, the approximate value of 16π, while at the neighboring temperature of 0.44 the K of the solid is significantly above 16π. Using the experimental elastic-constant data for the temperature below 0.45, we estimate that the instability temperature based on the Kosterlitz-Thouless-Feynman criterion is 0.45 ± 0.005. The measured value of K at the observed melting temperature is significantly lower than 16π because of defect formation in the solid constrained to remain at a solid density. We conclude that this experimentally observed melting temperature is consistent with the Kosterlitz-Thouless-Feynman instability criterion and that the transition at this temperature is consistent with a first-order phase change. This first-order behavior contradicts the prediction based on the application of renormalization group arguments to the dislocation theory for melting where it is predicted that the two-dimensional melting transition is continuous.

The detailed free-energy analyses yielding the phase diagram of the two-dimensional Lennard-Jones system find that the *thermodynamic melting temperature is approximately* 0.415 [6]. This is in sharp contrast to the finding that computer experiment and the Kosterlitz-Thouless-Feynman theory give a melting temperature of ~ 0.45. However, this may be resolved by the following argument. The dislocation theory of melting only describes the stability of the solid state in terms of the improbable existence of solid-state defects (*e.g.*, dislocations, disclinations) in its equilibrium solid structure. At the Kosterlitz-Thouless-Feynman instability temperature, a dilute concentration of defects becomes likely and the solid may then readily transform to the lowest free-energy phase, the liquid state. Certainly, the defect solid with a low concentration of dislocations is not a proper model for a liquid and must be in a higher free-energy state relative to the equilibrium liquid state. However, the defect solid state is an effective *precursor* for melting to the liquid state. In the laboratory, atomic solids do not melt at this stability limit to defect formation, but melt at, or very near to, their thermodynamic melting temperature. This is because of the necessary existence of a solid surface. In fig. 3, this is demonstrated by Monte Carlo simulations of a two-dimensional strip of 512 Lennard-Jones atoms at a temperature (0.40) slightly below and at a temperature (0.42) slightly above the thermodynamic melting temperature of 0.415 and initialized at the appropriate low-pressure, solid-state densities for the respective temperatures. Periodic boundary conditions exist at the strip's horizontal boundaries, while the two vertical boundaries are free surfaces in contact with a vapor-phase region. The trajectory plots are generated from $5 \cdot 10^6$ consecutive configurations and are typical of the equilibrium atomic behavior of the strip over a continuous simulation of $\sim 50 \cdot 10^6$ configurations for each temperature. The simulations clearly demonstrate a stable crystal phase with premelted surfaces at $T^* = 0.40$ (fig. 3*a*)) and a stable liquid phase at $T^* = 0.42$ (fig. 3*b*)). The results in fig. 3 also provided nice confirmation that the estimate of the

thermodynamic melting temperature from free-energy considerations is valid. In the computer experiments, it is easy (actually, too easy) to exclude the presence of surfaces by imposing periodic conditions at all boundaries of the computational cell and to effectively constrain the solid to superheat well beyond the thermodynamic melting temperature.

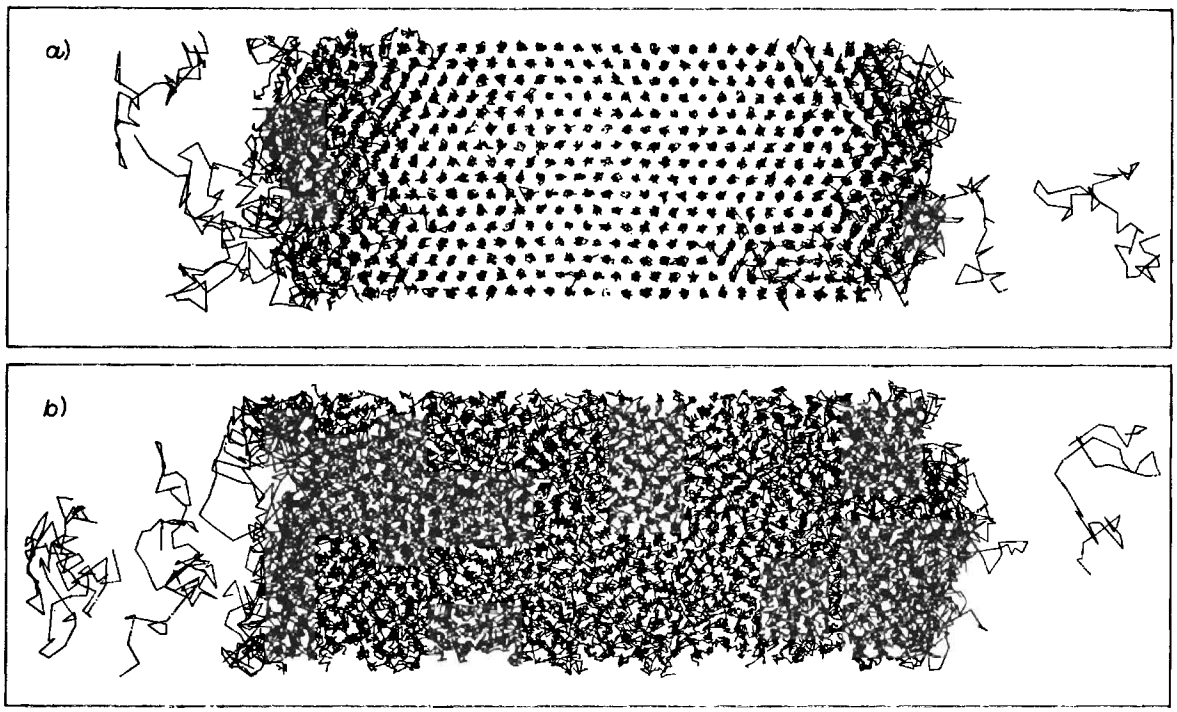

Fig. 3. – Atomic trajectory pictures of a two-dimensional Lennard-Jones system of 512 atoms with two free surfaces for a temperature 0.40 slightly below (*a*)) and a temperature 0.42 slightly above (*b*)) the thermodynamic melting point of 0.415.

In summary, the dislocation-unbinding model for two-dimensional melting leads to a theoretical instability temperature that is consistent with the experimentally observed instability temperature of the solid phase. However, this melting temperature is not the *thermodynamic* melting temperature, this being much lower; it is a temperature corresponding to an upper limit for the stability of the *metastable*, two-dimensional solid with no free surfaces. Also, the renormalization group arguments applied to the Kosterlitz-Thouless-Feynman model predict that the melting transition is continuous, in sharp contrast to the first-order character observed in the computer experiments. We conclude that the dislocation-unbinding theory for melting does not give a correct thermodynamic theory of melting. The *thermodynamic* melting temperature is significantly lower than the temperature for which the solid becomes unstable to dislocation pair dissociation (the Kosterlitz-Thouless-Feynman temperature), and the *thermodynamic* phase transition is first order.

2. – Quasi-two-dimensional physisorbed films.

Phase transformation phenomena for quasi-two-dimensional phases adsorbed on solid surfaces has become an area of intense research activity over the last several years, the challenge being both experimental and theoretical. The systems of interest range from rare-gas atoms physisorbed on graphite and electrons confined to the liquid-helium surface, to polystyrene spheres trapped at the air-water interface. We will consider some particular aspects of this quasi-two-dimensional world.

2·1. *Melting of submonolayer rare-gas solid films on graphite.* – In a recent X-ray scattering experiment, McTAGUE *et al.* [8] examined the melting of xenon, krypton and argon films on the (001) basal plane of ZYX graphite at submonolayer coverages and found the melting behavior to differ markedly be-

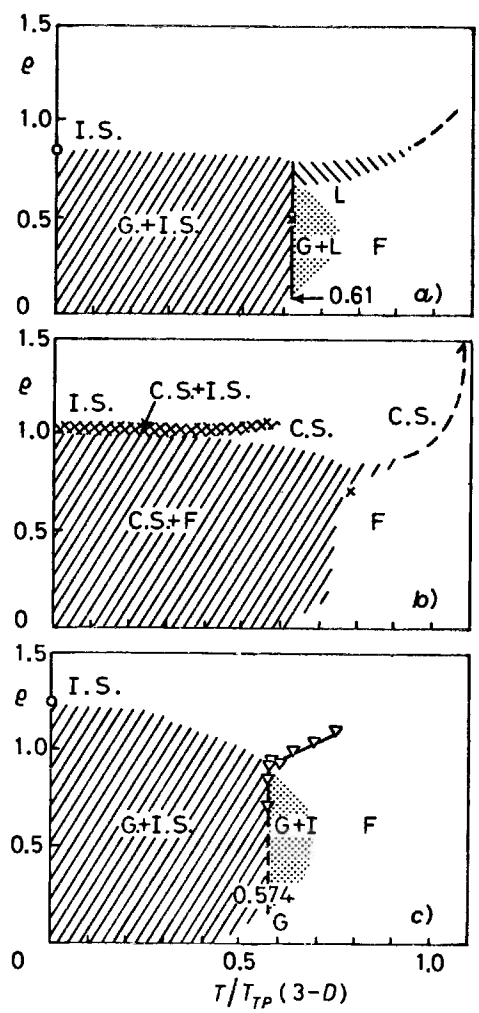

Fig. 4. – The phase diagram for Xe, Kr and Ar films on graphite [8]: *a*) Xe on graphite, *b*) Kr on graphite, *c*) Ar on graphite.

tween the various rare-gas films. The phase diagrams for Xe, Kr and Ar films on graphite are given in fig. 4. Comparison of all three systems under the same experimental conditions is a significant advance in clarifying the complexities of substrate-influenced melting and provided the stimulus to carry out a similar program employing computer simulation experiments. Using the molecular-dynamics simulation technique, we have studied the melting of submonolayer xenon, krypton and argon films on graphite [9], observing first-order melting of xenon which mimics the melting of an idealized two-dimensional film, first-order melting of krypton with the existence of an « incipient triple point » [10] and continuous melting of argon over a temperature interval of approximately 7 K. All of these findings are consistent with the experiment of McTague *et al.* [8].

The Lennard-Jones pair potentials were chosen to represent the interaction between the various atoms of the rare-gas atom/graphite system. The Xe-Xe, Kr-Kr and Ar-Ar parameters are taken to be $\varepsilon/k = 236$, 170 and 120 K and $\sigma = 3.92$, 3.60 and 3.38 Å, respectively. The Xe-C, Kr-C and Ar-C parameters are taken to be $\varepsilon/k = 76.38$, 64.83 and 54.46 K and $\sigma = 3.38$, 3.22 and 3.11 Å, respectively (C denotes carbon). Simple pairwise additivity of the atomic interactions was assumed, and the carbon atoms defining the semi-infinite graphite solid are fixed at their lattice sites. The atomic positions of the graphite surface define the basal plane of the computational box, this being a parallelogram compatible with the triangular lattice of a close-packed, registered adatom crystal. Periodic boundary conditions are imposed at the four faces of the computational cell which pass through the sides of the basal parallelogram at normal incidence to the surface. The basal plane of the computational box must be compatible with the graphite structure, otherwise periodic replication creates unphysical size dependences. A reflecting wall is placed at the top of the computational box at a 9 Å height, but an adatom reaches this normal extent very infrequently at the studied temperatures. Conventional molecular dynamics was employed. At the lowest temperature of 0.36 (in reduced units), the rare-gas system's initial configuration is a two-dimensional strip spanning the x-dimension with the appropriate solid-state density and with a coverage corresponding to a mean reduced density of 0.6. The number of rare-gas atoms for the Xe, Kr, Ar films are 1175, 1323, 1680, respectively, and this corresponds to a cell dimension of approximately 200 Å. The presentation of the simulation results will be expressed as a function of reduced temperature, *since this will clearly demonstrate variations from the idealized two-dimensional picture where the film properties of the three rare-gas systems would be identical.*

A series of simulations has been performed at reduced temperatures spanning the melting regime of the various films. The total simulation time for each temperature needed to be very long in the case of Ar film melting, where over 100 000 time steps were executed in order to obtain reasonable statistics. The adatom energy per atom as a function of temperature is presented in fig. 5 (top)

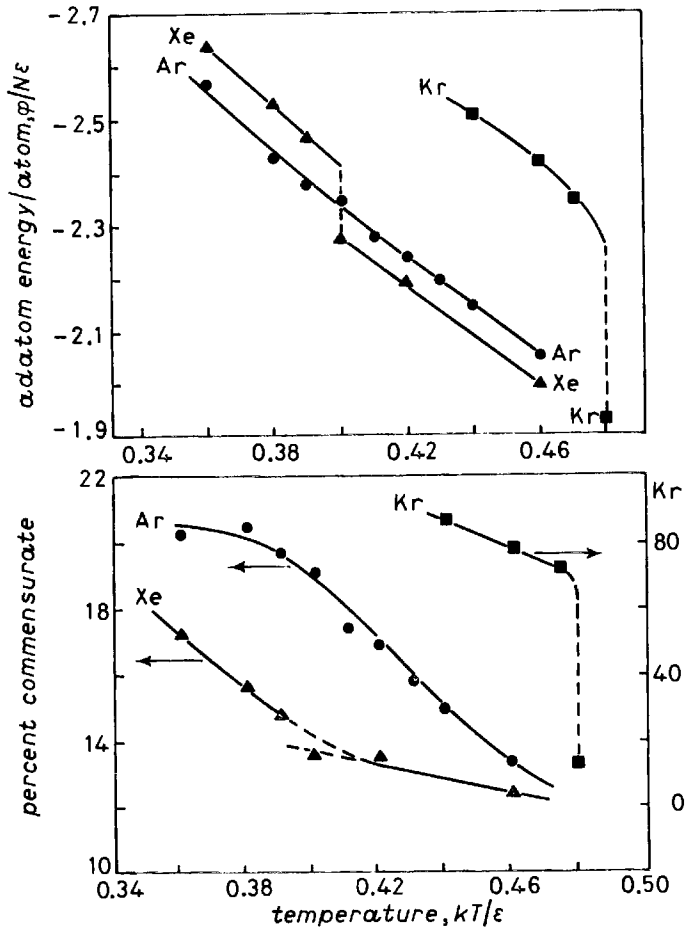

Fig. 5. – Adatom energy per atom (top) and percent commensurate with respect to the graphite substrate (bottom) as a function of reduced temperature T^* for the Xe, Kr and Ar.

for the Xe, Kr and Ar films. While we note a discontinuous change in the energy at the melting temperature of 0.40 for Xe and of 0.48 for Kr, the energy variation for the Ar film is continuous (to within the experimental error) over the entire temperature region. The Xe melting temperature of 0.40 agrees very well with the two-dimensional melting temperature of 0.41. Of course, any deviation from 0.41 is a consequence of the substrate interaction and deviation from strictly two-dimensional behavior. The deviation is especially large for the Kr and Ar films. All of the adatom energies converge to a common high-temperature fluid film trend. In fig. 5 (bottom), the percentage of adatoms that are commensurate with the graphite substrate is shown as a function of temperature, where commensurability is arbitrarily defined as an adatom being displaced from a graphite adsorption site by an amount that is less than two-tenths of a graphite lattice constant. Because of the size of a rare-gas atom relative the graphite adsorption size spacing, it is expected that Kr will be commensurate and Ar, Xe will be incommensurate. Until the film melts, the Kr atoms are highly commensurate. Actually, it is the « premelted » surface atoms

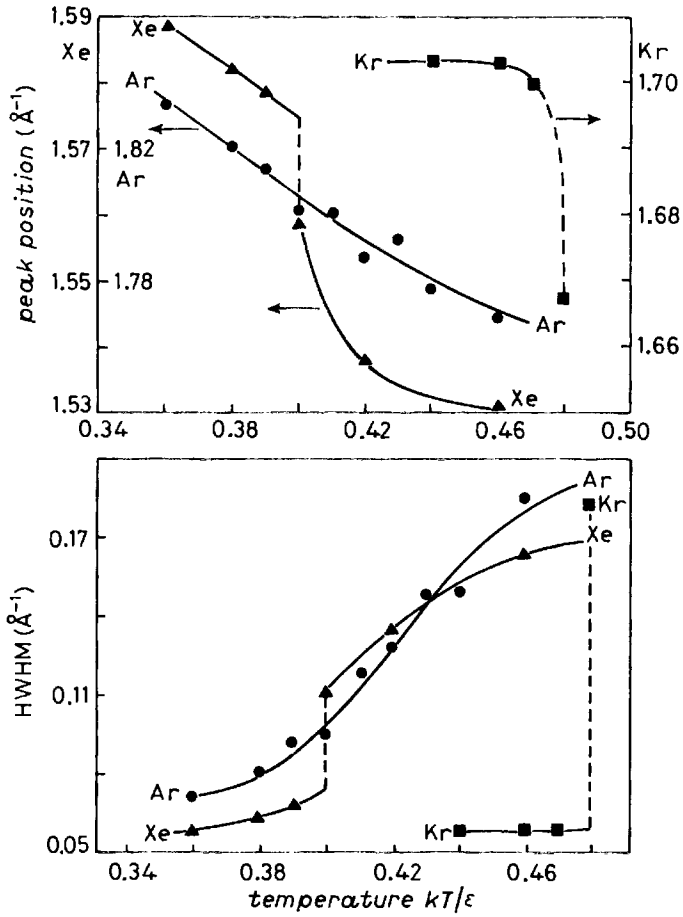

Fig. 6. – Peak position (top) and half width at half maximum (bottom) of the structure factor as a function of reduced temperature T^* for the Xe, Kr and Ar films.

that are incommensurate and all of the solid Kr atoms remain commensurate until melting; that is why the percent commensurate is not more nearly 100 %. The commensurability decreases continuously with increasing temperature, all films converging to a common high-temperature fluid-film trend. There might be a discontinuity in the Xe curve at melting, but it is small if it exists. In fig. 6, structure factor properties as a function of temperature are presented for the various rare-gas films. Both for the peak position and the half width at half maximum of the first Bragg peak, the temperature dependence is consistent with the temperature dependence of the adatom energy for the various films. The Xe and Kr films melt by first-order transitions at their respective melting temperatures, while the Ar melting is apparently continuous.

The character of the melting of the various films can be best appreciated from the trajectory pictures of « typical » states of the Xe, Kr and Ar films as a function of temperature as shown in fig. 7 and 8. For the Xe film at $T^* = 0.38$, we see a solid strip with premelted surfaces and coexisting low-density vapor. At $T^* = 0.4$ and greater, the film is liquid with density decreasing with increasing temperature and coexisting with a low-density vapor. Going to fig. 8, we note that the Kr film remains solid with premelted surfaces and coexisting

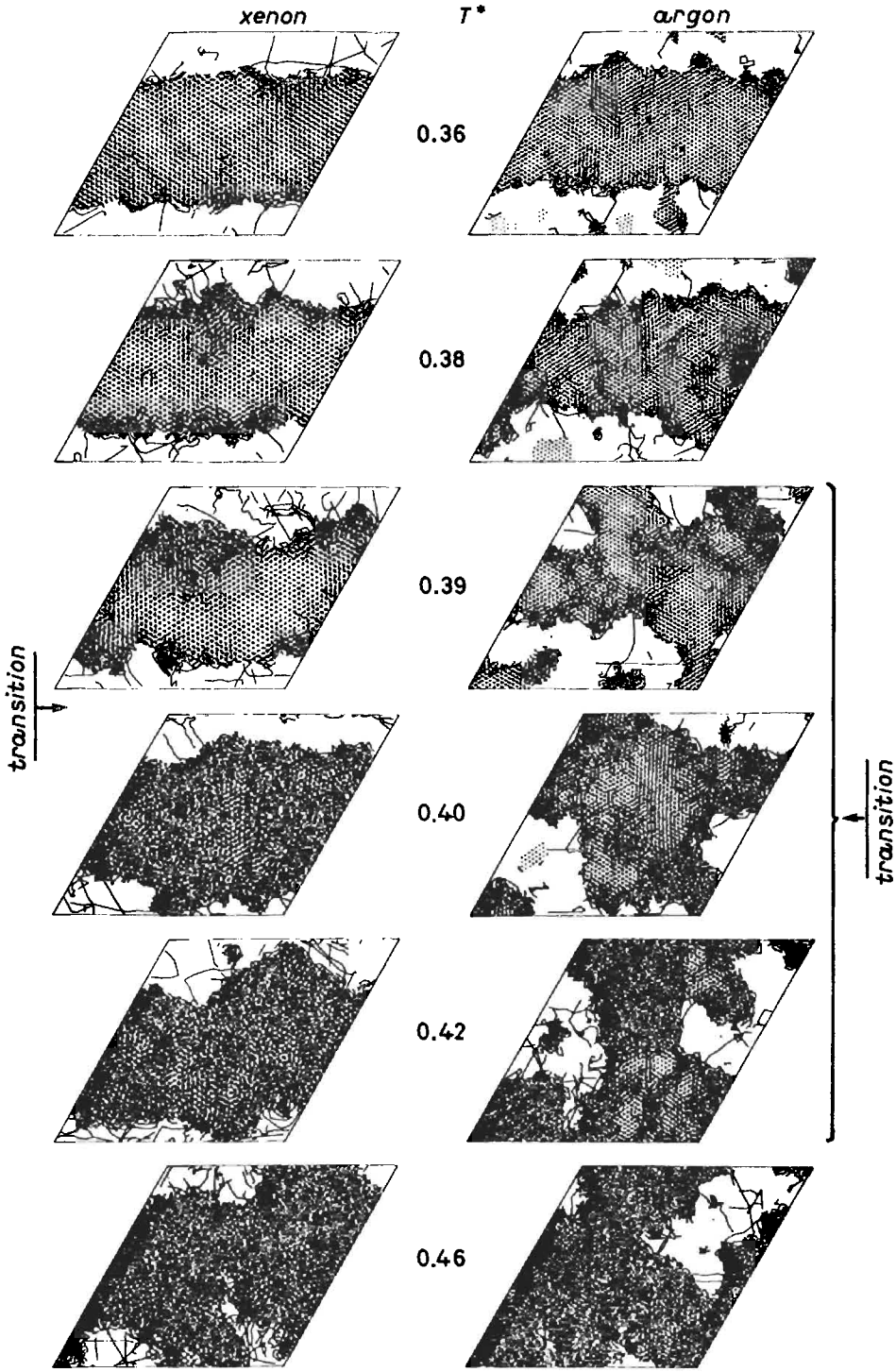

Fig. 7. – Trajectory analysis of the adatom motions for the Xe and Ar films as a function of reduced temperature T^*.

vapor until a temperature of 0.48 is reached, when it becomes a homogeneous fluid! From the phase diagrams in fig. 4, an estimate of the critical temperature gives approximately 0.48. Hence, the Kr film melts in the neighborhood of the critical temperature for this system. This simulation finding is in agreement with the «incipient triple point» picture of Butler *et al.* [10]. It

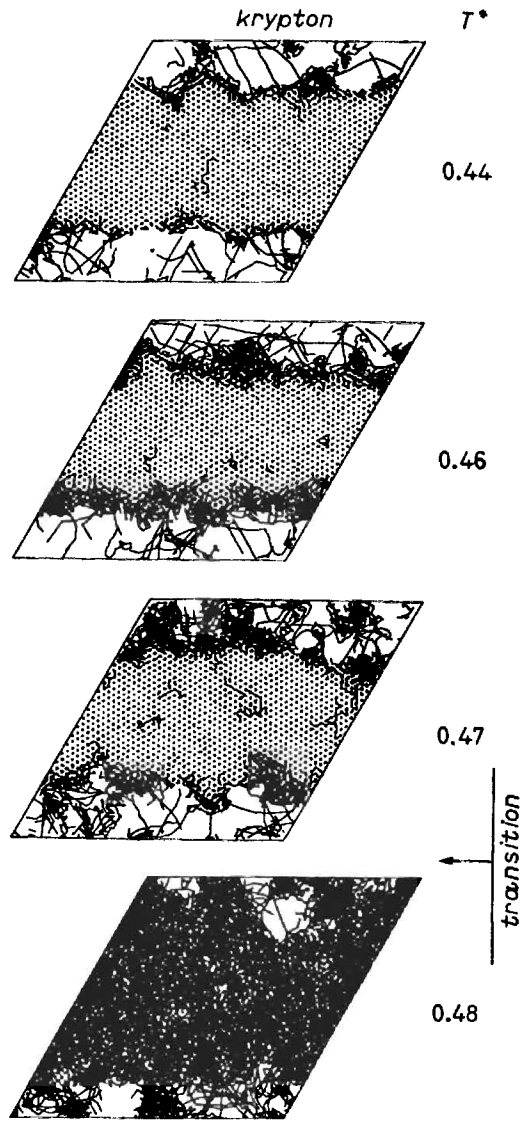

Fig. 8. – Trajectory analysis of the adatom motions for the Kr film as a function of reduced temperature T^*.

is in fig. 7 that we note the different character of the Ar film's state as a functions of temperature that suggests an explanation of the continuous nature of the melting process. Through the Ar melting regime of 0.39 to 0.44, we note an apparent coexistence of liquidlike and solidlike regions, this being shown by the atomic mobility of the respective regions in the film. With increasing temperature, the dominance of the liquidlike regions increases continuously until the film is entirely liquid around $T^* = 0.44$.

The origin of these substrate-mediated features can best be appreciated by noting the following facts. The barrier to translation of a single adatom on the graphite surface from one site to another is essentially the same for Xe, Kr and Ar atoms and is approximately 50 K, while the melting temperatures of Xe, Kr and Ar are 95 K, 82 K and 47 K, respectively. Also, the

reduced densities for the Xe, Kr and Ar solid films to be commensurate with the graphite substrate are 0.978, 0.820 and 0.727, respectively, while the reduced densities for an incommensurate Lennard-Jones solid and liquid at melting are 0.83 and 0.73, respectively. Hence, the incommensurate Xe solid melts to an incommensurate liquid with a lateral atomic mobility weakly influenced by the underlying substrate. For Kr, the solid density corresponds to a commensurate structure relative to the graphite substrate which provides a greater stability and, hence, a higher melting temperature. At melting, the Kr liquid is incommensurate and at a temperature comparable to the critical temperature of an incommensurate fluid; this is the origin of the «incipient triple point». Also, the Kr fluid temperature is sufficiently high that the lateral atomic mobility is weakly influenced by the underlying substrate. Ar is a further step up in the hierarchy of complexity. The incommensurate Ar solid melts to a liquid at a reduced temperature comparable to that of Xe, but the liquid Ar density is approximately that required for an Ar solid film to be commensurate with the graphite substrate. Furthermore, the lateral atomic mobility is *strongly* influenced by the underlying substrate since the melting temperature and the energy barrier between graphite sites are essentially equal. Hence, the configurations of the condensed-phase Ar film upon melting are strongly influenced by its interaction with the graphite substrate, resulting in a continuous melting transition over an approximate 7 K temperature window and manifesting a solidlike and liquidlike character in coexistence during the molecular-dynamics simulation. At a sufficiently high reduced temperature, all of the liquid films converge to like properties.

2·2. *The incommensurate phase of krypton on graphite.* – A high-density surface layer of krypton physisorbed on graphite is a good model system to study the properties of the commensurate-incommensurate (C-IC) transition. The krypton-carbon interaction favors regularly spaced adsorption sites at the graphite surface and it is well known from experiment [11] that monolayer krypton on graphite forms a solid in registry with the underlying substrate. As a consequence of the size of the krypton atom, only one-third of the adsorption sites are occupied, and there exist three energetically degenerate commensurate sublattices (see fig. 9). With increasing coverage, it is no longer possible for all of the krypton atoms to occupy adsorption sites, and the system becomes more and more incommensurate, approaching a lattice constant representative of bulk krypton. However, in the transition region, the krypton solid is significantly modulated due to the krypton-graphite interaction. The details of this transition are being extensively studied experimentally [11-18], theoretically [19-27] and by computer simulation techniques [28-32]. Despite the extensive research, such basic features as the nature of the C-IC transition are still controversial.

The nature of the incommensurate phase of krypton on graphite and its

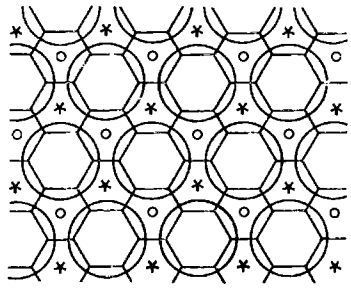

Fig. 9. – Krypton monolayer on graphite registered phase. The centers of the adatom (circles) occupy the A sites. Dots denote the B sites and stars are the C sites. There exist three energetically degenerate commensurate sublattices (A, B, C) as a consequence of the size of the krypton atom (from ref. [26]).

transition to the $\sqrt{3}\times\sqrt{3}R30°$ commensurate phase are being extensively investigated. Theories have been developed for the incommensurate phase at zero temperature which are based on the model of incommensurate domain walls separating large commensurate regions such that the distance between domain walls is large compared to the width of the walls. For Kr on graphite, the domain walls may be in three different directions because of the hexagonal substrate structure. If wall intersections are energetically unfavorable, a *striped* phase might be expected where walls are only in one direction. However, VILLAIN has noted that a *honeycomb* array of walls has a degeneracy in which the hexagons of the array can expand or contract without changing the total wall length or the number of nodes (*i.e.* wall crossings) [21]. Hence VILLAIN argues that this additional contribution to the entropy stabilizes the honeycomb phase relative to the striped phase.

2·2.1. Structure of the incommensurate phase. We describe the structure of the incommensurate phase of krypton on graphite as a function of temperature and coverage using the molecular-dynamics simulation technique for systems of 103 041 and 161 604 krypton atoms [31]. Hence graphite substrate dimensions up to 1700 Å are realized and are essentially identical to present-day laboratory capabilities [17]. We observe that the incommensurate phase consists of commensurate islands separated by an interconnecting network of incommensurate domain walls, the structure of this network being a sensitive function of temperature and coverage. At low temperature, the honeycomb network of domain walls is observed for all coverages. An incommensurate striped phase is not seen. With increasing temperature, distortions from the perfect honeycomb structure become more prevalent. At high temperatures, the individual domain walls fluctuate significantly from the symmetry directions while possessing boundary roughness and a greater wall thickness.

Similar to previous section, we use the Lennard-Jones pair potential to represent the interaction between the various atoms of the krypton/graphite

system. Simple pairwise additivity of the atomic interactions is assumed, and the carbon atoms defining the semi-infinite solid are fixed at their lattice sites. In order to reduce the computer memory requirement, we constrain the movement of the krypton atoms to a plane parallel to the graphite surface. The 161 604 Kr atom system required approximately 13 megabytes of memory and executes 110 time steps per CPU hour on the IBM/370 3081 computer. The external field of the graphite is reproduced to a very good approximation by the expression

$$\varphi_{\text{Kr-G}} = -V_g[\cos 2\pi s_1 + \cos 2\pi s_2 + \cos 2\pi(s_1 + s_2)]\,, \tag{2.1}$$

where $V_g = 0.08\varepsilon_{\text{Kr-Kr}}$ and s_1, s_2 are the basis vectors of the graphite unit cell.

Figure 10 shows the principal results of our simulations for the 103 041 atom

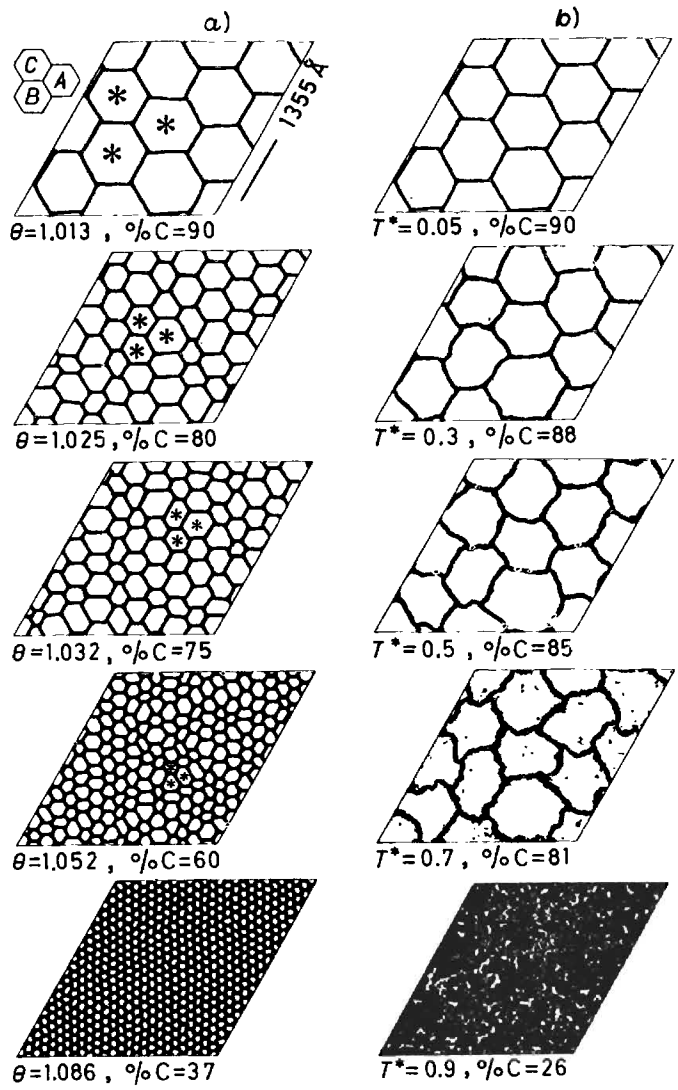

Fig. 10. – Pictures of the domain wall network for an equilibrium configuration of the incommensurate phase as a function of coverage θ at fixed temperature $T^* = 0.05$ and as a function of temperature at a fixed coverage $\theta = 1.013$; 103 041 krypton atoms on graphite.

system. The incommensurate and commensurate regions are shown as solid black and solid white areas, respectively; in actual fact, we plotted the incommensurate atoms as points, but the lack of graphical resolution merged the points to make a solid region. We first consider the case in which the temperature is fixed at the low value of 0.05 and the coverage is varied. We note that for all coverages a honeycomb network of domain walls is established, the network consisting of straight walls with smooth boundaries which are aligned to the three symmetry directions of the graphite substrate. The commensurate regions form an array of honeycomb domains, the individual hexagons not being identical in size and shape. This honeycomb domain structure with *breathing* freedom is direct confirmation of Villain's picture of the incommensurate phase, and this is the first direct observation of this structure. At fixed temperature, the percentage Kr atoms that are commensurate (% C) decreases linearly with increasing coverage (90 %, 80 %, 75 %, 60 % and 37 %, respectively), while the domain wall thickness remains essentially constant at 18 Å. This % C decrease is associated with an increase of the total length of domain walls, and this gives rise to smaller and more numerous commensurate domains. We simulated as large a system as we felt was practical within the constraint of our computer resources—a 161 604 Kr atom system. The temperature and coverage are 0.05 and 1.005, respectively. In fig. 11, we again see the incommensurate honeycomb structure at this low temperature. Furthermore, we do not observe the *striped* phase or two-phase coexistence between the commensurate and incommensurate phases, which would be indicative of a first-order transition when the total coverage is held constant in the two-phase region.

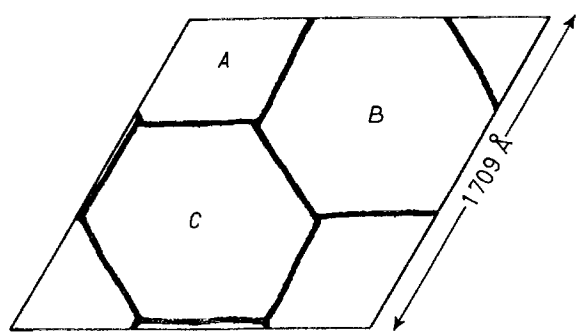

Fig. 11. – A picture of the domain wall network for an equilibrium configuration of the incommensurate phase simulated using 161 604 Kr atoms on graphite at a coverage $\theta = 1.005$ and temperature $T^* = 0.05$. The percentage of commensurate atoms % C is 96.

Returning to fig. 10, we now consider the series of simulations where the coverage was held fixed at 1.013. With increasing temperature, the overall appearance of the incommensurate phase remains that of the domain wall network which becomes increasingly distorted, the walls becoming broader and

the wall boundaries roughening considerably. Also, we note the marked increase in the wall thickness with increasing temperature, the wall thickness at $T^* = 0.7$ being approximately twice the wall thickness at $T^* = 0.05$. This is consistent with the gradual decrease of percentage of commensurate atoms (90%, 88%, 85%, 81%, respectively). At the highest temperature, the system is mainly incommensurate since it is principally a liquid.

To classify the domain walls for krypton on graphite, one can distinguish between two configurationally distinct types of walls, which we call heavy (h) and light (l) walls [24]. (In some other references, *e.g.* ref. [25], these walls are labelled « super heavy » and « heavy » walls, respectively.) The classification is determined by the orientation of the particular wall and by the two different sublattices separated by this wall. Analyzing the pictures in fig. 10, we find only heavy walls. This feature does not change, as we consecutively heat our system. As long as the domain walls are more or less aligned to the three symmetry directions, *i.e* roughly up to a value of $T^* = 0.5$, we observe heavy walls only. However, with increasing temperature, the overall appearance of the system changes gradually. The domain wall network gets more and more distorted, the walls become broader and their surface roughens considerably.

2·2.2. Energetics of the incommensurate phase. To study the energetics of the weakly incommensurate phase, we simulated a *quasi-two-dimensional* system of 20 736 krypton atoms on a graphite substrate. We have chosen a recently proposed krypton-graphite potential which gives the commensurate phase as the lowest-energy state at zero temperature [33]. The lateral variation of this potential is of order twice the value normally adopted [34]. However, we have found that for temperatures greater than $\simeq 0.1$, the lowest free-energy state using the Steele potential is also the commensurate state.

The remarkable invariance of the wall features with respect to changes in the coverage and the indications for a breathing freedom of the honeycomb array suggest a phenomenological expression for the energy increase $\Delta\varepsilon$ of the weakly incommensurate phase in terms of these walls. Such an expression should contain a term proportional to the total wall length Lb, but it should also contain a term proportional to the number, 2ν, of wall intersections [19]:

$$\Delta\varepsilon = \tfrac{2}{3}\xi L + 2\nu\Lambda + \omega_0 N l^{\alpha-2} \exp[-kl]\,. \tag{2.2}$$

It has been suggested in the literature that the energy should also contain an elastic interaction between the walls mediated through the domains which can be described qualitatively [26] by the third term in eq. (2.2). This interaction is expected to decay exponentially when the mean distance $lb/2$ between wall intersections increases.

Since only heavy walls are found in the simulations, the topology of the honeycomb array is completely determined by the number of hexagons, ν. Thus it is possible to evaluate the total wall length Lb using ν idealized identical cells. The size of a cell is determined by the average number, $n_\nu = l/2 + 1$, of particles per side of a hexagon, which is related to the average number of particles per commensurate region, N/ν:

$$N/\nu = 3n_\nu^2 - 3n_\nu + 1 \,. \tag{2.3}$$

We find a wall length $6(lb/2 + b/3)$ per hexagon, and, since each wall part is shared by two hexagons, the total wall length Lb is given by

$$L = (\nu/2)(3l + 2) \,. \tag{2.4}$$

Figure 12 shows that we find no pronounced influence of the elastic wall interaction for the quasi-2D results. This repulsive interaction between walls would increase the potential energy per particle with decreasing l (increasing θ),

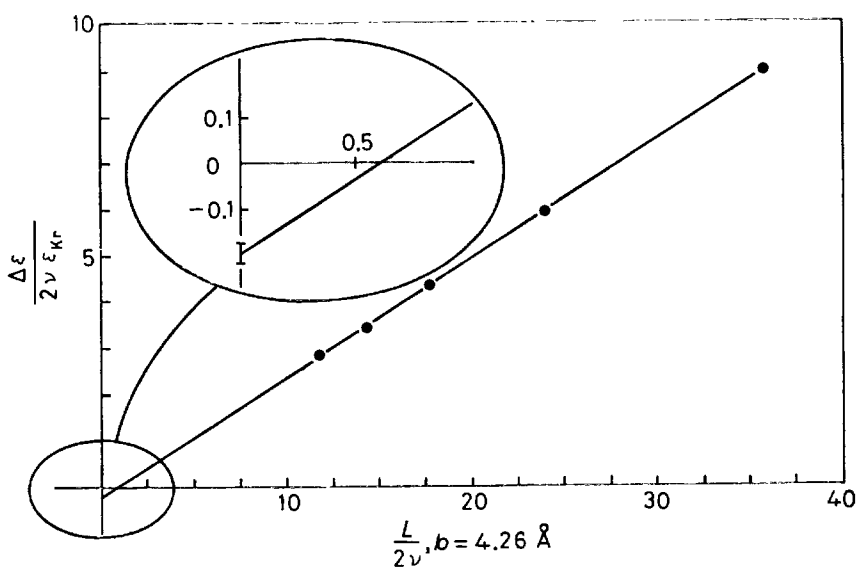

Fig. 12. – Quasi-two-dimensional system: energy increase of IC phase per wall intersection plotted as a function of the total wall length per wall intersection; $\Delta\varepsilon/2\nu = (2/3)\,\xi(L/2\nu) + \Lambda$, $(2/3)\,\xi = (0.254 \pm 0.001)\,\varepsilon_{Kr}$, $\Lambda = (-0.197 \pm 0.02)\,\varepsilon_{Kr}$.

resulting in an upward curvature of $\Delta\varepsilon 2/\nu$ for small values of $L/2\nu$. Instead, the results are in excellent agreement with the form given by the first two terms of the right-hand side of eq. (2.2). This fact enables us to determine the wall energy per unit length, $2\xi/3 = (0.254 \pm 0.001)\,\varepsilon_{Kr}$, and the energy associated with each wall intersection, $\Lambda = (-0.197 \pm 0.02)\,\varepsilon_{Kr}$, although the finite size of the computational cell determines an upper limit for $L/2\nu$ and the mean distance between wall intersections (a lower limit for $\theta - 1$), re-

spectively. Note that the absolute values of ξ and Λ are of the same order of magnitude and Λ is significantly negative. For $\Lambda < 0$, the transition is first order and the hexagonal symmetry is preserved [26] in the IC phase.

Since we found a significantly negative value of Λ, the transition is expected to be first order independent of temperature, in contrast to experimental findings. It will be of interest to obtain an estimate of the critical size of the transition in order to investigate the influence of finite-size effects. To obtain a reasonable estimate, it is necessary to have a quantitative description of the elastic wall repulsion, which, unfortunately, is not available yet. As a further step, the influence of dislocations [23] on the C-IC transition remains to be addressed.

REFERENCES

[1] J. M. Kosterlitz and D. J. Thouless: *J. Phys. C*, **5**, L124 (1972); **6**, 1181 (1973).

[2] R. P. Feynman: unpublished. An outline of this theory is given by R. L. Elgin and D. L. Goodstein: *Phys. Rev. A*, **9**, 2657 (1974).

[3] L. D. Landau and E. M. Lifshitz: *Theory of Elasticity* (Pergamon Press, Oxford, 1970).

[4] B. I. Halperin and D. R. Nelson: *Phys. Rev. Lett.*, **41**, 121, 519(E) (1978).

[5] D. R. Nelson and B. I. Halperin: *Phys. Rev. B*, **19**, 2457 (1979).

[6] F. F. Abraham: *Phys. Rep.*, **80**, 339 (1981).

[7] F. F. Abraham: *Phys. Rev. B*, **23**, 6145 (1981).

[8] J. P. McTague, J. Als-Nielsen, J. Bohr and M. Nielsen: *Phys. Rev. B*, **25**, 7765 (1982).

[9] F. F. Abraham: *Phys. Rev. B*, **28**, 7338 (1983).

[10] D. M. Butler, J. A. Litzinger, G. A. Steward and R. B. Griffiths: *Phys. Rev. Lett.*, **42**, 1289 (1979).

[11] See, *e.g.*, the following review articles: O. E. Vilches: *Annu. Rev. Phys. Chem.*, **31**, 463 (1980); A. Thomy, X. Duval and J. Regnier: *Surf. Sci. Rep.*, **1**, 1 (1981).

[12] M. Nielsen, J. Als-Nielsen, J. Bohr and J. P. McTague: *Phys. Rev. Lett.*, **47**, 582 (1981).

[13] M. D. Chinn and S. C. Fain: *Phys. Rev. Lett.*, **39**, 146 (1977).

[14] C. Fain, M. D. Chinn and R. D. Diehl: *Phys. Rev. B*, **21**, 4170 (1980).

[15] P. W. Stephens, P. Heiney, R. J. Birgeneau and P. M. Horn: *Phys. Rev. Lett.*, **43**, 47 (1979).

[16] R. J. Birgeneau, E. M. Hammonds, P. Heiney, P. W. Stephens and P. A. Horn: in *Ordering in Two Dimensions*, edited by S. K. Sinha (Plenum Press, New York, N. Y., 1980), p. 29.

[17] D. E. Moncton, P. W. Stephens, R. J. Birgeneau, P. M. Horn and G. S. Brown: *Phys. Rev. Lett.*, **46**, 1533 (1981).

[18] P. W. Stephens, P. A. Heiney, R. J. Birgeneau, P. M. Horn, D. R. Moncton and G. S. Brown: *Phys. Rev. B*, **29**, 3512 (1984).

[19] P. Bak, D. Mukamel, J. Villain and K. Wentkowska: *Phys. Rev. B*, **19**, 1610 (1979).

[20] H. SHIBA: *J. Phys. Soc. Jpn.*, **46**, 1852 (1979); **48**, 211 (1980).
[21] J. VILLAIN: in *Ordering in Strongly Fluctuating Condensed Matter Systems*, edited by T. RISTE (Plenum Press, New York, N. Y., 1980), p. 221.
[22] P. BAK: *Rep. Prog. Theor. Phys.*, **45**, 587 (1982).
[23] S. N. COPPERSMITH, D. S. FISHER, B. I. HALPERIN, P. A. LEE and W. F. BRINKMAN: *Phys. Rev. Lett.*, **46**, 549 (1981); *Phys. Rev. B*, **25**, 349 (1982).
[24] D. A. HUSE and M. E. FISHER: *Phys. Rev. Lett.*, **49**, 793 (1982).
[25] M. KARDAR and A. N. BERKER: *Phys. Rev. Lett.*, **48**, 1552 (1982).
[26] For the most recent review of theory including comparison with experiment, see J. VILLAIN and M. B. GORDON: *Surf. Sci.*, **125**, 1 (1983).
[27] M. SCHOEBINGER and S. W. KOCH: *Z. Phys. B*, **53**, 233 (1983).
[28] F. HANSON and J. P. MCTAGUE: *J. Chem. Phys.*, **72**, 6363 (1980).
[29] F. F. ABRAHAM, S. W. KOCH and W. E. RUDGE: *Phys. Rev. Lett.*, **49**, 1830 (1982).
[30] S. W. KOCH and F. F. ABRAHAM: *Helv. Phys. Acta*, **56**, 755 (1983).
[31] F. F. ABRAHAM, W. E. RUDGE, D. J. AUERBACH and S. W. KOCH: *Phys. Rev. Lett.*, **52**, 445 (1984).
[32] S. W. KOCH, W. E. RUDGE and F. F. ABRAHAM: *Surf. Sci.*, **145**, 329 (1984).
[33] G. VIDALI and M. W. COLE: *Phys. Rev. B*, **29**, 6736 (1984).
[34] W. A. STEELE: *Surf. Sci.*, **36**, 317 (1983).

Part III

FREE-ENERGY COMPUTATIONS AND NEW EQUILIBRIUM MOLECULAR DYNAMICS

Free-Energy Computation and First-Order Phase Transitions.

D. FRENKEL

Physical Laboratory, Rijksuniversiteit Utrecht
P.O. Box 80000, 3508 TA *Utrecht, The Netherlands*

1. – Introduction.

The usual molecular-dynamics and Monte Carlo simulations yield statistical information about the « mechanical » properties of the system under consideration. The term mechanical property is reserved for explicit functions of the phase-space co-ordinates of a system. Examples are the potential energy of a given configuration, $U(\boldsymbol{q}^N)$, where $\boldsymbol{q}^N$ stands for all (generalized) co-ordinates, or the virial $V(\boldsymbol{q}^N) = \sum_{i=1}^{N} \boldsymbol{r}_i \cdot \boldsymbol{F}_i$, where $\boldsymbol{r}_i$ is the centre-of-mass co-ordinate of the i-th particle and $\boldsymbol{F}_i$ the force on molecule i due to all other molecules. Knowledge of the ensemble or time average of such mechanical properties enables us to compute a number of important thermodynamic properties such as the internal energy E of a system, its pressure P and its heat capacity C_V (or C_P). In contrast, it is not possible to obtain from a computer simulation direct information about « thermal » properties. Here the expression thermal properties is used to designate all properties whose value depends on the total volume of phase space that is accessible to the system under consideration. Typical examples are the entropy S of a system, its free energy F (here, and in what follows, I reserve the term free energy for the *Helmholtz* free energy; the Gibbs free energy, or free enthalpy, is denoted by G) and the chemical potential μ_α of component α in a mixture. The rest of this lecture will be concerned with computational techniques that enable us to compute thermal quantities. First, however, we have to answer two questions. The first question is: why can thermal properties not be obtained in the same way as mechanical properties? The second is: under what circumstances should one take the trouble of computing, say, the free energy of a system?

To answer the first question, let us consider a typical Monte Carlo (MC) simulation of a canonical ensemble. The present argument can be extended to other ensembles with minor modifications. In the canonical ensemble the

probability of finding a system of N particles, volume V and temperature T in a (hyper) volume $\mathrm{d}\boldsymbol{q}^N$ around a point $\boldsymbol{q}^N$ in configuration space is given by

$$P(\boldsymbol{q}^N)\,\mathrm{d}\boldsymbol{q}^N = \exp\left[-\beta U(\boldsymbol{q}^N)\right]\mathrm{d}\boldsymbol{q}^N/Q_{NVT}\,. \tag{1}$$

Here $\beta = 1/kT$ and Q_{NVT} is the configurational part of the partition function. Q_{NVT} is related to the free energy of the system by

$$F_{NVT} = -kT\ln\left(Q_{NVT}/N!\,\Lambda^{3N}\right) \tag{2}$$

with $\Lambda = (h^2/2\pi mkT)^{\frac{1}{2}}$. In a Monte Carlo simulation with Metropolis (importance) sampling [1] the system performs a random walk through configuration space such that the probability of visiting a point $\boldsymbol{q}^N$ is *proportional* to $P(\boldsymbol{q}^N)$ but (unless one performs astronomically long runs) the constant of proportionality is unknown. To visualize this problem, it is helpful to think of the equivalent of the Monte Carlo method to measure the average depth $\langle d\rangle$ of a river, a « mechanical » property, and its surface area A, a « thermal » property. Metropolis sampling in this case corresponds to taking a random step in the water and rejecting it if it takes you on to the riverbank but accepting it otherwise (see fig. 1). After every attempted step the depth d_i is recorded.

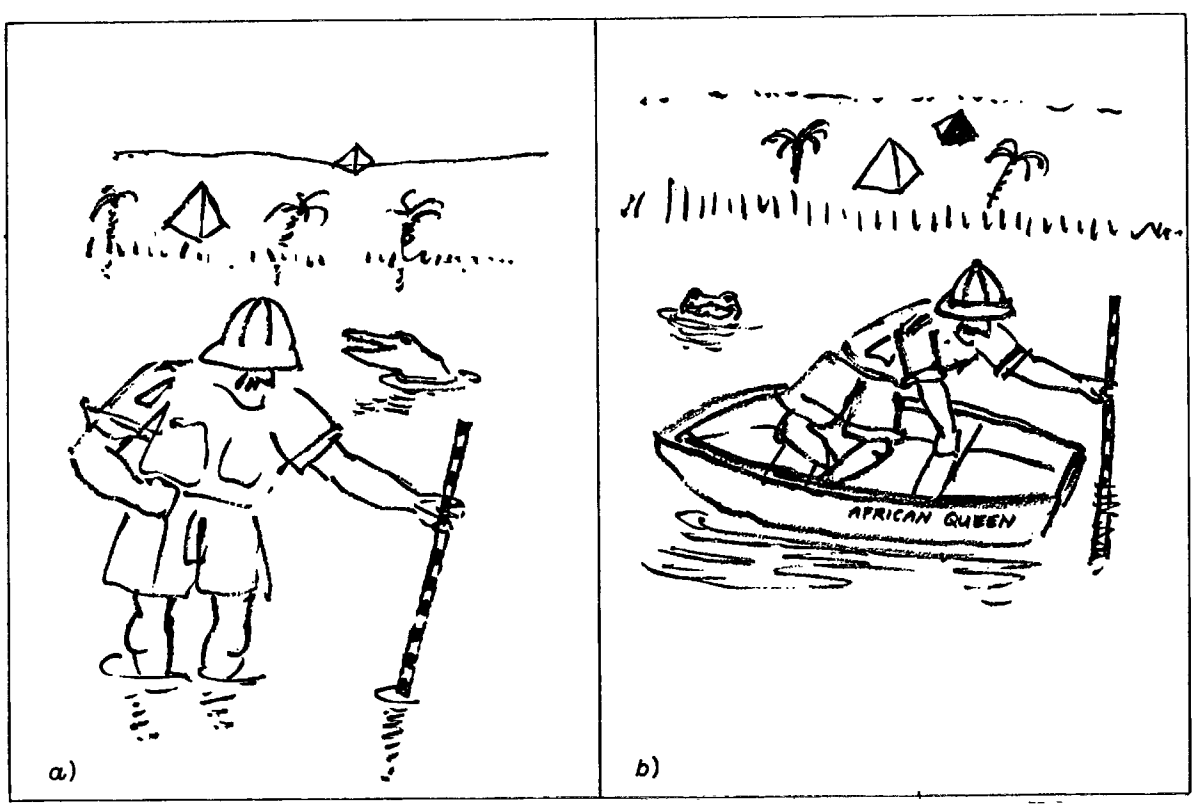

Fig. 1. – Measurement of the average depth of a river by the equivalents of importance sampling (a)) and molecular-dynamics simulation (b)). Note that neither method provides direct information about the area of the river. However, the frequency with which any known area of water is visited can be used to compute the total area [2].

The average depth of the river is obtained from

$$\langle d \rangle = \lim_{N \to \infty} \frac{1}{N} \sum_{i=1}^{N} d_i \,. \tag{3}$$

In practice the condition $N \to \infty$ is replaced by the condition that N be sufficiently large that a representative (even if infinitesimal) fraction of all points in the river is visited. In contrast, no such procedure can be used to measure the surface area of the river, because A is not a « local » quantity like d. And the probability distribution does not help much either because, to take an extreme example, if only *one* point of area $\mathrm{d}A$ is sampled, one obtains a normalized probability 1 to be at that point; this result is indeed proportional to the correct probability $\mathrm{d}A/A$, but that does not help much.

The only way to measure the area in this kind of Monte Carlo experiment is to determine the mean *recurrence* time, *i.e.* the number of steps that separate, on average, two visits to the same area $\mathrm{d}A$. In statistical mechanical model systems this time, the Monte Carlo equivalent of the Poincaré time, is truly astronomical for all but the smallest systems. In fact, in a molecular-dynamics (MD) determination of the accessible volume of phase space the relevant time would indeed be the Poincaré time (see, however, subsect. **2**·2 and ref. [2]). Having indicated that the computation of thermal properties must involve additional effort, it is useful to consider the second question formulated above: under what circumstances should one bother to compute thermal properties.

Apart from the obvious possibility that one may be interested in thermal properties for their own sake, *e.g.* to compare predictions of perturbation theories with computer experiments, there are situations where one has little choice but to compute thermal properties. The most important examples are phase equilibria and chemical equilibria. We recall that the condition for the coexistence of n phases at constant temperature and pressure is that the chemical potential μ_α of each molecular species has the same value in all phases, while the condition for chemical equilibrium at constant T and P is of the form $\sum \nu_\alpha \mu_\alpha = 0$, where the ν_α are the stoichiometric coefficients [3].

Of course, the fact that such equilibria put certain restrictions on the chemical potentials does not necessarily imply that one should explicitly calculate these quantities. After all, the great charm of computer simulation is that, given a sufficiently large system and a sufficiently long run, the system will find out for itself which phase and/or which chemical composition it prefers. The problem is that for most systems (though not all; see subsect **3**·1) sufficiently large is too large and sufficiently long is too long for the average computing budget. More importantly, techniques exist which do the job at a lower price.

In the remainder of this lecture we will discuss a number of such techniques.

For general background information the reader is referred to [4-8] and, of course, to other lectures in the present volume.

2. – Methods to compute free energies.

2·1. *Preliminary remarks.* – In this section we discuss a number of computational techniques to compute absolute free energies and free-energy differences. Actually, there is no sharp distinction between the two because in the end almost all free-energy computations reduce to the evaluation of the free-energy *difference* between two states. Therefore, we reserve the term « absolute free-energy calculation » for cases where one of the two states under consideration is sufficiently simple that its absolute free energy can be evaluated analytically. In the examples to be discussed below we shall switch back and forth between free-energy computations and determinations of the chemical potential. For a one-compound system these computations are equivalent because all relevant thermal quantities are simply related ($F = E - TS$, $G = F + PV$, $\mu = G/N$). However, for a multicomponent system it is really μ_α, the chemical potential of the α-th species, that we are interested in.

2·2. *Direct methods.* – The free energy F of a system is related to its partition function Z by

$$F = -kT \ln Z \,, \tag{4}$$

which for a classical system reduces to

$$F = -kT \ln (Q/N!\Lambda^{3N}) \,. \tag{2}$$

Hence in order to compute F we need to determine Q_{NVT}:

$$Q = \int \mathrm{d}\boldsymbol{q}^N \exp[-\beta U(\boldsymbol{q}^N)] \,, \tag{5}$$

where the notation is as in eq. (1).

The first point to note is that a direct numerical integration of eq. (5) is out of the question for all but the smallest systems. Consider, for instance, a « fluid » of $N = 4$ hard spheres at a density of $\frac{2}{3}\varrho_0$, where ϱ_0 is the density of regular close packing. If we use Simpson's method to evaluate the integral in eq. (5) with 10 points in all $3(N-1)$ independent co-ordinates, then of the 10^9 evaluations of the integrand only ~ 5 will yield a nonvanishing result. The situation gets much worse as one goes to larger systems.

Very close to the direct sampling method is the importance sampling technique devised by SALSBURG *et al.* [9] to determine the configurational integral of a 2D lattice gas. The method is based on the observation that V^N/Q can be written as

$$V^N/Q = \int \exp[\beta U] \exp[-\beta U] \mathrm{d}\boldsymbol{q}^N \Big/ \int \exp[-\beta U] \mathrm{d}\boldsymbol{q}^N \,, \tag{6a}$$

or

$$V^N/Q = \langle \exp[\beta U] \rangle , \tag{6b}$$

where the angular brackets stand for a canonical average. Note that Q has now been related to the average of a *mechanical* quantity and can, therefore, in principle, be obtained by importance sampling. The problem with this method, at least when applied to typical fluids and solids, is that large contributions to the average of $\exp[\beta U]$ come from regions in configuration space where the sampling probability (*i.e.* $\exp[-\beta U]$) is vanishingly small. Hence, unless all states including those with high energy are adequately sampled during a run, the method will give incorrect results. But such sampling involves at least as much work as sampling the whole of configuration space uniformly. Hence this method is of no practical use for classical fluids. For hard-core fluids the method even fails in principle. For further details see [6, 10-13].

A method that may be of some use for hard-core systems was devised by COLDWELL [14, 15]. This technique is based on the observation that the configurational integral of a system of N hard-core particles may be written as

$$Q_N = V \cdot \langle V_2 \rangle_1 \cdot \langle V_3 \rangle_{1,2} \cdot \ldots \cdot \langle V_N \rangle_{1,2,\ldots,N-1} , \tag{7}$$

where $\langle V_N \rangle_{1,\ldots,N-1}$ stands for the average volume available to particle N in the presence of particles 1 through $N-1$. This approach is very similar in spirit to the early work of Byckling [16] (although apparently developed independently), but, because of the sophisticated bookkeeping of the volume available to the next particle to be added, it is more efficient. Coldwell's method was tried on 16 hard discs [14] and 25 $(2+\frac{1}{2})$-dimensional spherocylinders [15], and it appears to work satisfactorily up to rather high densities.

The main drawback of the method is that errors are introduced because all co-ordinates are discretized. In addition, the sheer complexity of the programming may discourage others from applying it to anything but the simplest systems.

A completely different method designed to evaluate the configurational integral of dense solids was developed by KRATKY [17]. In this approach the uniform sampling of configuration space used in a brute-force evaluation of Q is replaced by a nonuniform sampling. The weighting function is concentrated around the lattice positions of the individual particles and this restricts Kratky's method to systems with perfect translational order. The form of the weighting functions is optimized in an iterative fashion. Results were obtained in ref. [17] for hard-sphere crystals near close packing.

A final example of a direct method to compute a thermal average directly is the technique used by EDHOLM *et al.* [18] to evaluate the conformational entropy of a chain molecule. The approach is based on the expression for the

configurational entropy S_c:

$$S_c = -k\int P(\boldsymbol{q}^N)\ln P(\boldsymbol{q}^N)\,\mathrm{d}\boldsymbol{q}^N\,, \tag{8}$$

where $P(\boldsymbol{q}^N)$ is defined as in eq. (1).

In ref. [18] a discretized version of eq. (8) is used to obtain an estimate for conformational entropy of a chain molecule. The success of the method depends on the fact that at least a number of conformations are sampled sufficiently frequently to yield a reliable estimate of the probability of their occurrence. A very similar method was proposed earlier by MA [2].

2·3. *Particle insertion and related methods.* – We now turn to a number of more general and, on the whole, more powerful techniques to compute the chemical potential of a fluid. First among these is the so-called « particle insertion method », usually associated with the name of Widom, who formulated the general principles upon which this method is based [19], although actually a similar technique had first been employed by BYCKLING several years earlier [16]. The idea behind the particle insertion method is the following. Consider the expression for the chemical potential:

$$\mu = \left(\frac{\partial F}{\partial N}\right)_{V,T} = \lim_{\substack{N\to\infty\\ V\to\infty\\ N/V=\varrho}} -kT\ln\left(\frac{Q_N}{Q_{N-1}}\Big/\Lambda^3 N\right), \tag{9}$$

where we have used eq. (2). In the limit $N/V\to 0$ the ratio $Q_N/Q_{N-1}\to V$ and μ reduces to the ideal-gas chemical potential:

$$\mu_{\mathrm{id}} = kT\ln(\varrho\Lambda^3)\,, \tag{10}$$

where we have introduced the number density $\varrho = N/V$. In (10) we have assumed the gas to be monatomic. Generalization to molecular systems is straightforward. Upon inserting (10) in (9) we obtain

$$\mu^{\mathrm{ex}} \equiv \mu - \mu_{\mathrm{id}} = -kT\ln(Q_N/VQ_{N-1})\,. \tag{11}$$

Hence the computation of the excess chemical potential μ^{ex} is equivalent to the calculation of $Q_N/Q_{N-1}V$. The latter quantity can be cast in a form that can be evaluated by Monte Carlo sampling:

$$Q_N/Q_{N-1}V = \frac{1}{V}\,\frac{\int\exp[-\beta U(\boldsymbol{q}^{N-1})]\exp[-\beta V(\boldsymbol{q}_N;\boldsymbol{q}^{N-1})]\,\mathrm{d}\boldsymbol{q}^N}{\int\exp[-\beta U(\boldsymbol{q}^{N-1})]\,\mathrm{d}\boldsymbol{q}^{N-1}}\,. \tag{12}$$

In eq. (12) $U(\boldsymbol{q}^{N-1})$ is the potential-energy function of the $N-1$ particles,

while $V(\boldsymbol{q}_N; \boldsymbol{q}^{N-1})$ represents the interaction of the N-th particle with all the others. Equation (12) can be written as the canonical average of a mechanical quantity:

$$Q_N/Q_{N-1}\, V = \frac{1}{V}\int \mathrm{d}\boldsymbol{q}_N \langle \exp[-\beta V]\rangle_{N-1}\,. \tag{13}$$

Note that eq. (13) contains an average over $\boldsymbol{q}^{N-1}$ co-ordinates which can be evaluated by importance sampling, and an integral over the N-th co-ordinate $\boldsymbol{q}_N$ which must be sampled uniformly. In words: $\exp[-\beta\mu_{\mathrm{ex}}]$ is equal to the ensemble average of $\exp[-\beta V_A]$, where V_A is the interaction energy of the $N-1$ particles with an extra particle added at a random position in the system.

In a hard-core fluid eq. (13) just gives the probability of acceptance of a Monte Carlo move consisting of the addition of an N-th particle at a random position in a system of $N-1$ particles. Note that the particle insertion method is in no way limited to one-component systems. The particle insertion method as formulated by WIDOM has been used by several authors to study the thermal properties of atomic [20] and molecular [21, 22] fluids. An example is shown in fig. 2. An advantage of this technique is that it is very simple to insert in

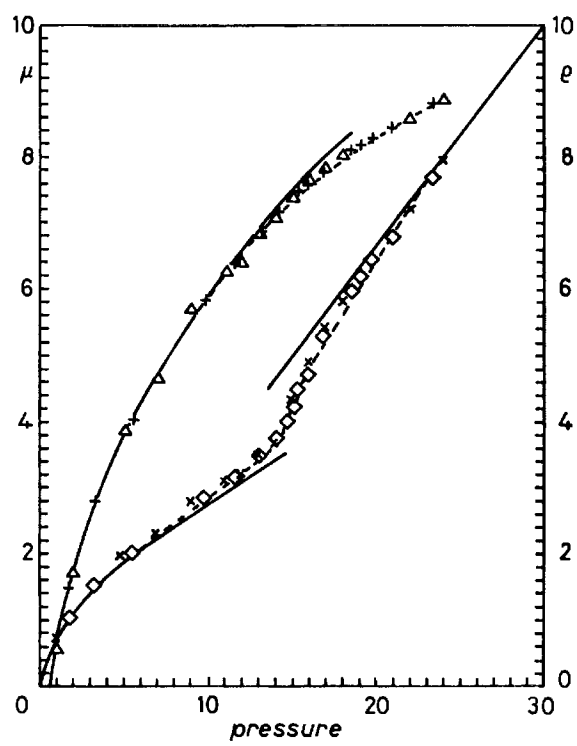

Fig. 2. – Chemical potential μ of infinitely thin hard platelets of diameter σ [23] (pluses and triangles) determined by Widom's particle insertion method. The drawn curve through the data points was computed using the first five virial coefficients of hard platelets. The dashed curve was obtained by integration of the equation of state (squares and crosses) from low densities, using the Gibbs-Duhem relation. All quantities in reduced units, $\sigma = 1$, $kT = 1$.

existing Monte Carlo programs (including isobaric MC); with microcanonical simulations the situation is slightly more complicated (see appendix A). A problem with the Widom method is that the statistics become very poor as the density of the fluid under consideration is increased to the solidification point (for crystalline solids the method fails completely).

Several authors have developed techniques to extend the range of applicability of the particle insertion method. In a number of cases this was achieved by carrying out biased sampling, in the sense that the test particle is no longer inserted at random, but preferentially at « cavities » where it is most likely to be accepted [23-25]. As all these authors use either consciously or unconsciously « umbrella sampling », we will defer discussion to subsect. **2·6**.

One rather different technique to compute μ_{ex} in a dense 2D hard-disk fluid was developed by ZOLLWEG [26]. This author actually explicitly computes the fraction of the total area available for an additional disk in a fluid of N disks. This fraction is, of course, equal to the probability of acceptance of the insertion of the additional particle for a particular configuration.

This method works well even in the solid phase. However, the programming effort appears appreciable and no one has, as yet, found the courage (or the time) to extend Zollweg's method to continuous potentials or three-dimensional fluids.

Another extension of the particle insertion method is due to SHING and GUBBINS [27, 28]. Their approach is based upon the observation that μ_{ex} could, in principle, also be obtained by considering the random ***removal*** of one particle from an N-particle system. In a way completely analogous the eqs. (11)-(13) above one may then derive that

$$\beta\mu_{ex} = \ln \langle \exp [+\beta V_R] \rangle_N \,, \tag{14}$$

where V_R is the interaction energy of the particle to be removed with the $N-1$ others. Actually, eq. (14) itself is not used by SHING and GUBBINS, as it leads to systematic underestimates of μ_{ex}. This point has been investigated in some detail by POWLES and coworkers [29, 30]. The reason why eq. (14) taken at face value is misleading stems from the same cause that makes the Salsburg method unreliable. For example, for a hard-core fluid eq. (14) would always yield $\mu_{ex} = 0$, unlike the Widom method. The method that SHING and GUBBINS use to obtain a reliable estimate of μ_{ex} does not use $\langle \exp [\beta V_R] \rangle$ or $\langle \exp [-\beta V_A] \rangle$ but rather the probability distributions of V_R and V_A. As this method turns out to be identical to Bennett's overlapping-distribution method [31], we postpone the discussion to subsect. **2·5**.

A method closely related to the particle insertion method is the cavity distribution method described in the same paper of Widom [19]. It was first formulated by HOOVER and POIRIER [32] and later extended by MEERON and SIEGERT [33].

The gist of the method is that one may show that the cavity function $y(r)$ is related to the correlation function of $\exp[-\beta V_A]$:

$$y(r) \equiv \exp[\beta\varphi(r)]g(r) = \exp[2\beta\mu_{ex}]\langle\exp[-\beta V_A(0)]\exp[-\beta V_A(r)]\rangle\,, \tag{15}$$

where $\varphi(r)$ is the intermolecular potential, $g(r)$ the radial distribution function and $V_A(\boldsymbol{r})$, as before, the interaction of a test particle at $\boldsymbol{r}$ with the molecules already present. For hard-core particles, in the limit $r \to 0$, eq. (15) reduces to

$$y(0) = \exp[\beta\mu_{ex}]\,. \tag{16}$$

This indicates that μ_{ex} can be determined by measuring the cavity distribution function down to $r = 0$. An example of such a computation can be found in ref. [34]. The cavity method runs into the same problems at high densities as the particle insertion method. Moreover, it is less simple to program. It seems unlikely that the cavity method will prove a powerful computational tool to measure free energies of simple fluids.

2·4. *Grand canonical ensemble.* – Rather similar in implementation, though different in spirit than the particle insertion and extraction methods of the previous subsection is the grand canonical (GC) ensemble method. This method, first introduced by NORMAN and FILINOV [35], was later extended and improved by a number of workers [20, 36-43]. Here we shall sketch the approach suggested by ADAMS [20, 36-38], but modified for didactical reasons.

In the grand canonical ensemble T, V and μ are held fixed, while E, P and N may fluctuate. The basic idea behind grand canonical Monte Carlo (GCMC) is that μ is known *a priori*, because it is imposed, and the simulation then yields values for $\langle N\rangle$ etc. It is convenient to consider the GC ensemble as a system of volume V which can exchange heat and particles with a very large reservoir which contains an ideal gas of the same particles. The volume of the reservoir is $V' \gg V$. The total number of particles is M. The partition function for this joint system is given by

$$\frac{Q_M(V, V'; T)}{M!} = \sum_{N=0}^{M} \frac{Q_N(V)}{N!}\,\frac{Q_{M-N}(V')}{(M-N)!}\,, \tag{17}$$

where it is understood that $M \to \infty$, $V' \to \infty$, $M/V' \to \Lambda^{-3}\exp[\beta\mu]$ (remember, in V' we have an ideal gas). Now we could follow the usual procedure, *i.e.* to divide (17) by $Q_M(V')/M!$ and obtain the GC partition function for the small system V, but this is not what we shall do. We just ask ourselves: what is the probability of finding N particles in a volume of $\mathrm{d}\boldsymbol{q}^N$ around $\boldsymbol{q}^N$ in V and $M-N$ particles in a volume $\mathrm{d}\boldsymbol{q}^{M-N}$ around $\boldsymbol{q}^{M-N}$ in V'? Clearly, this probability

is given by

$$P(\boldsymbol{q}^M)\,\mathrm{d}\boldsymbol{q}^M = Q_M^{-1}(V, V'; T)\exp[-\beta U(\boldsymbol{q}^N)]\,\mathrm{d}\boldsymbol{q}^N\,\mathrm{d}\boldsymbol{q}^{M-N}\,\frac{M!}{N!(M-N)!}\,. \tag{18a}$$

Now it is convenient to switch to reduced co-ordinates $\boldsymbol{\tau}$, such that both in V and in V' all components of τ range from 0 to 1: $\boldsymbol{\tau}^N = \boldsymbol{q}^N/V^N$ and $\boldsymbol{\tau}^{M-N} = \boldsymbol{q}^{M-N}/V'^{(M-N)}$. This constitutes a one-to-one mapping of reduced co-ordinates in V and V'. In terms of $\boldsymbol{\tau}^M$,

$$P(\boldsymbol{\tau}^M)\,V^N\,V'^{(M-N)}\,\mathrm{d}\boldsymbol{\tau}^M = Q_M^{-1}(V, V'; T)\,\frac{V^N\,V'^{(M-N)}\,M!}{N!(M-N)!}\exp[-\beta U(\boldsymbol{\tau}^N)]\,\mathrm{d}\boldsymbol{\tau}^M\,. \tag{18b}$$

Now we can ask for the ratio R of probability (18*b*) to the probability where one particle has been moved from V' to the same reduced position in V.

It is easy to see that this ratio must be

$$R_{N+1,N} = \frac{V}{N+1}\,\frac{M-N}{V'}\exp\left[-\beta\left(U(\boldsymbol{\tau}^{N+1}) - U(\boldsymbol{\tau}^N)\right)\right] \tag{19}$$

or, keeping in mind that $M \gg N$ and $M/V' = \Lambda^{-3}\exp[\beta\mu]$,

$$R_{N+1,N} = \frac{V}{N+1}\,\Lambda^{-3}\exp[\beta(\mu - \Delta U)]\,, \tag{20}$$

where we have written ΔU for $U(\boldsymbol{\tau}^{N+1}) - U(\boldsymbol{\tau}^N)$. Similarly, the corresponding ratio of probabilities where one particle is moved from V to V' is given by

$$R_{N-1,N} = \frac{N}{V}\,\Lambda^3\exp\left[-\beta\left(\mu - U(\boldsymbol{\tau}^N) + U(\boldsymbol{\tau}^{N-1})\right)\right]. \tag{21}$$

Hence, we can sample a GC as long as the relative probability with which particles are added or removed obeys eqs. (20) and (21). One method to achieve this is to use the conventional Metropolis sampling for the probability of acceptance of particle insertions and removals:

$$\begin{cases} P_{\mathrm{acc}}(N+1, N) = \min[1, R_{N+1,N}]\,, \\ P_{\mathrm{acc}}(N-1, N) = \min[1, R_{N-1,N}]\,. \end{cases} \tag{22}$$

In eq. (22) it is assumed that the numbers of *attempts* to add or remove a particle are equal. In addition to particle-number-changing moves one performs normal MC sampling at constant N. One final remark on eqs. (20), (21). Note that, if we denote the, *a priori* unknown, average density in V by $\varrho = \langle N\rangle/V$, then $\beta\mu_{\mathrm{id}}(\varrho) = \ln(\langle N\rangle\Lambda^3/V)$. Inserting this in (20), (21) results in the slightly

simpler expressions

$$(23)\qquad \begin{cases} R_{N+1,N} = \exp\left[\beta(\mu_{ex} + \beta^{-1}\ln\langle N\rangle - \Delta U)\right]/(N+1)\,, \\ R_{N-1,N} = \exp\left[-\beta(\mu_{ex} + \beta^{-1}\ln\langle N\rangle + \Delta' U)\right]N\,. \end{cases}$$

In a simulation the quantity $B = \beta\mu_{ex} + \ln\langle N\rangle$ is the control variable.

At the end of the run μ_{ex} is computed using the value of $\langle N\rangle$ obtained during the simulation. The GCMC method has the attractive feature that it is possible to carry out simulation at a particularly interesting value of μ, *e.g.* at a phase transition. GCMC is easy to extend to multicomponent systems, and has been generalized to ionic systems [42, 43] where particles can only be inserted or removed in neutral groups.

There are several problems with the GCMC method that should be mentioned.

The first is easily eliminated if one is aware of it. It was noted [36] that the results of the GCMC are very sensitive to the quality of the random-number generator used. The second is actually the same problem that limited the applicability of particle insertion methods at high densities (see subsect. 2·3). At typical liquid densities the acceptance of particle-number-changing moves becomes very low. As a consequence it may be impossible to reach the correct equilibrium density in a reasonable time. MEZEI [41] has succeeded in improving the efficiency of the GCMC at high densities by preferentially inserting particles in « cavities ». It is, however, not obvious that this method really results in a dramatic saving of computing time.

The final point to note is that the results for μ_{ex} obtained by the GCMC show a pronounced system size dependence [20]. This may well be due to the fact that, for most systems, the thermal properties exhibit a $\ln N/N$ dependence. Usually one can eliminate this problem by computing excess properties (*e.g.* μ_{ex}) with respect to a reference system *with the same number of particles.*

However, in the conventional GCMC method the reference system is the *infinite* ideal gas. (The same holds, by the way, for the Widom method.) Hints that this is indeed at the root of the problem came from the work of Yao *et al.* [40] who carried out the GCMC on a system with an upper limit on the total number of particles that could be inserted. These authors found no evidence for system size dependence of μ.

To my knowledge no one has tried to perform a truly finite-size GCMC, starting from eq. (18*b*), with M chosen such that $\langle N\rangle \approx M - \langle N\rangle$.

2·5. *Overlapping distributions and related methods.* – Suppose we have, in one way or another, obtained the free energy F_0 of a system with potential-energy function U_0 at temperature $T = (k\beta)^{-1}$ and volume V.

We wish to know the free energy of a closely related system with potential-energy function $U_1 = U_0 + \Delta U$, or of the same system but at a different temperature T'. Let us, for simplicity, concentrate on the first case. The

free-energy difference between systems 1 and 0 is given by

$$F_1 - F_0 = -kT \ln (Q_1/Q_0) \,. \tag{24}$$

But Q_1/Q_0 can be written as an expectation value of $\exp[-\beta\Delta U]$:

$$Q_1/Q_0 = \frac{\int \exp[-\beta(U_0 + \Delta U)]\,\mathrm{d}\boldsymbol{q}^N}{\int \exp[-\beta U_0]\,\mathrm{d}\boldsymbol{q}^N} = \langle \exp[-\beta\Delta U]\rangle_0 \tag{25}$$

and hence

$$F_1 - F_0 = -kT \ln \langle \exp[-\beta\Delta U]\rangle_0 \,. \tag{26}$$

It is convenient to discuss eq. (26) in terms of the potential-energy density function $\gamma_0(U)$, first introduced by McDonald and Singer [44-46].

$\gamma_0(U)$ is defined as

$$\gamma_0(X) = V^{-N} \int \delta(X - U_0(\boldsymbol{q}^N))\,\mathrm{d}\boldsymbol{q}^N \,. \tag{27}$$

The probability of finding the system 0 at inverse temperature β in a range $\mathrm{d}U$ around U is given by

$$f_0^T(U)\,\mathrm{d}U = \frac{\gamma_0(U)\, V^N \exp[-\beta U]\,\mathrm{d}U}{Q_0(T)} \,. \tag{28}$$

Now whereas $\gamma_0(U)$ is a very rapidly increasing function of U, $f_0^T(U)$ is sharply peaked around a value U', such that $(\partial \ln \gamma_0/\partial U)_{U'} = \beta$. Now suppose we wish to use eq. (25) to determine the free-energy difference between two state points of the same system at temperatures T and T'.

Then, from eqs. (25) and (28) we have

$$Q(T')/Q(T) = \frac{\int \gamma_0(U) \exp[-\beta' U]\,\mathrm{d}U}{\int \gamma_0(U) \exp[-\beta U]\,\mathrm{d}U} \,. \tag{29}$$

From eq. (29) it follows that, if one knows the (unnormalized) $\gamma_0(U)$ over a wide range of U's, one can compute free-energy differences over a wide range of temperatures. This is precisely what McDonald and Singer did. Unfortunately, computing $\gamma_0(U)$ is not easy, and the way it was obtained in ref. [45] resembles later multistage and umbrella sampling methods (see below). It is much easier to obtain $f_0(U)$. In terms of $f_0^T(U)$, the ratio $Q(T')/Q(T)$ is given by

$$Q(T')/Q(T) = \int f_0(U) \exp[-\beta\Delta U]\,\mathrm{d}U \,. \tag{30}$$

Equation (30) follows directly from eq. (28), with $\Delta U = U(\beta'/\beta - 1)$. Note that the (normalized) distribution $f_0(U)$ can be obtained directly in a normal

(Metropolis) MC run. The applicability of eq. (30) is limited by the fact that, as the difference between β' and β increases, the maximum of $f_0(U)\exp[-\beta\Delta U]$ shifts to values of U where $f_0(U)$ itself is very small and hence inadequately sampled during a normal Monte Carlo run. When this occurs eq. (30) and hence eqs. (25), (26) cease to be useful. Examples of the direct application of eq. (26) can be found in ref. [47, 48]. Several methods have been devised to extend the applicability of eqs. (25), (26). The most straightforward of these is the so-called multistage sampling technique [6, 11, 49, 50]. This method is basically aimed at obtaining information about $\gamma_0(U)$ over a wide range of U's by sampling $f_0^T(U)$ over a range of temperatures. The idea is that, as $\gamma_0(U) \sim \sim \exp[\beta U] f_0^T(U)$, $\gamma_0(U)$ can be obtained over a range of energies by computing $f_0^T(U)$ for several different temperatures. These temperatures should be chosen sufficiently differently that they all probe a different range of U's, yet sufficiently close that there is a substantial range of U's where the successive $f_0^T(U)$ overlap. This latter requirement guarantees that the unnormalized function $\exp[\beta U] f_0^T(U)$ can be joined smoothly to $\exp[\beta' U] f_0^{T'}(U)$; in this way one obtains an unnormalized function $C\gamma_0(U)$ from which free-energy differences can be computed using eq. (29).

BENNETT [31] has presented a more general framework in which to discuss the relation between free-energy differences and potential-energy distributions. Consider two N-particle systems 0 and 1 with potential-energy function $U_0(\boldsymbol{q}^N)$ and $U_1(\boldsymbol{q}^N)$. During a simulation on system 0 one may accumulate a histogram of $p_0(\Delta U)$ which measures the probability density of observing a potential-energy difference $\Delta U = U_1 - U_0$. Conversely, during a simulation on system 1 one may obtain the corresponding probability density $p_1(\Delta U)$. Both p_0 and p_1 are normalized to 1, which equals the probability to observe *any* potential-energy difference. p_0 and p_1 can be written as normal canonical averages:

$$p_1(\Delta U) = Q_1^{-1}\int \exp[-\beta(U_0 + \Delta U)]\,\delta(U_1 - U_0 - \Delta U)\mathrm{d}\boldsymbol{q}^N = \\ = (Q_0/Q_1)\exp[-\beta\Delta U]p_0(\Delta U)\,, \tag{31}$$

or

$$p_1(\Delta U)/p_0(\Delta U) = \exp[\beta(\Delta F - \Delta U)]\,, \tag{32}$$

where $\Delta F = F_1 - F_0$ is the free-energy difference between 1 and 0. What eq. (30) says is that, wherever p_0 and p_1 overlap, the ratio of the two can be used to compute the free-energy difference ΔF. For hard-core systems one need only keep track of the values of p_0 and p_1 at $\Delta U = 0$. The ratio $p_1(0)/p_0(0)$ then measures the fraction of the configuration space of 1 that is accessible to 0, divided by the fraction of configuration space of 0 that is accessible to 1. In this case eq. (32) can be given a simple geometric interpretation (see fig. 3). It should be added that, although eq. (33) expresses a relation between the free

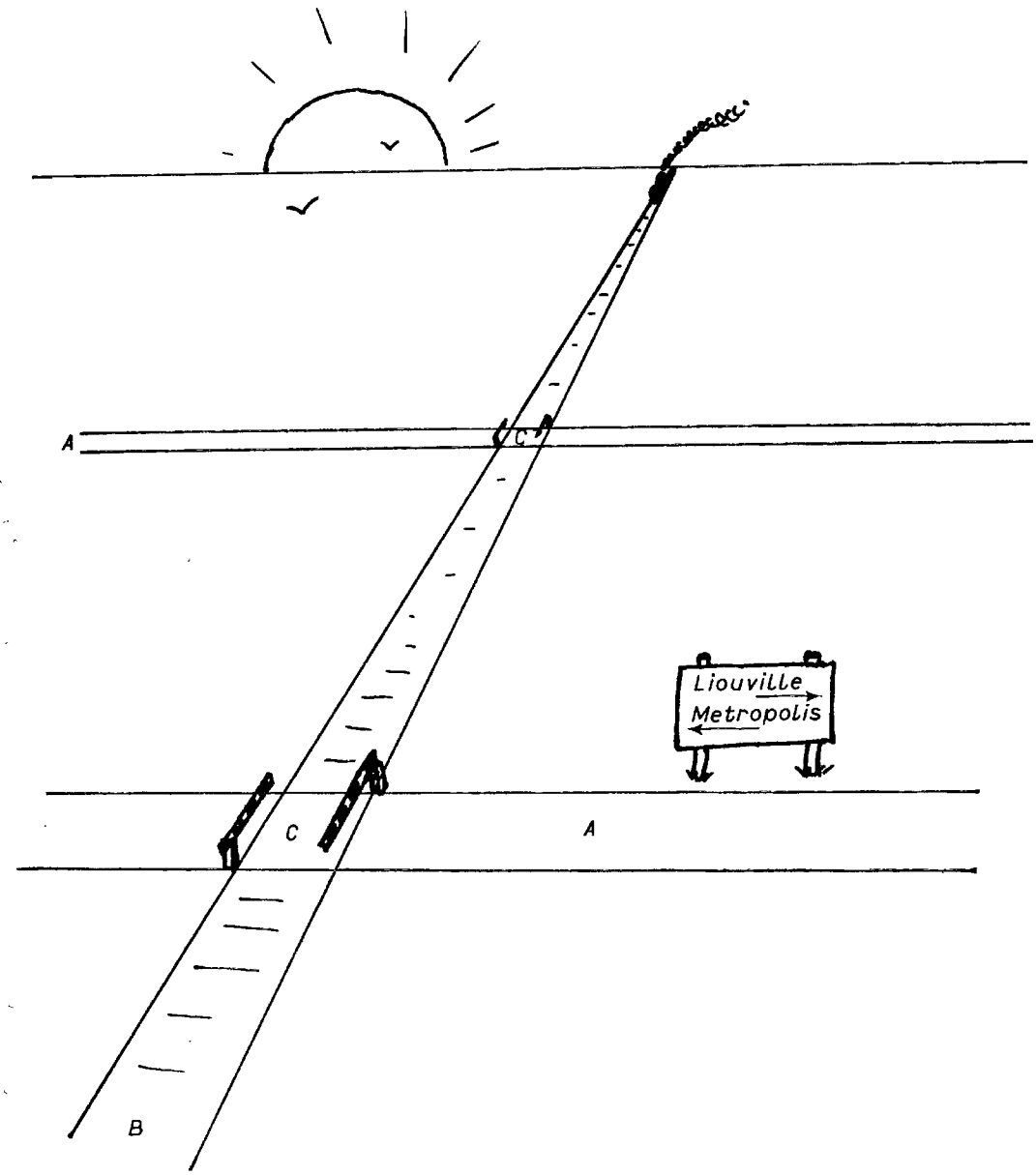

Fig. 3. – Consider two subvolumes of phase space, volume A (« roads ») and volume B (« railroads »). The intersection of A and B is C (« level crossings »). If the level crossings account for 1% of the area of all railroads and for 0.1 % for the total road area, then the area of all roads is ten times the area of all railroads.

energy of two N-particle systems, one or more of the particles in either system may be « fictitious » in the sense that they do not interact with any of the other particles. In particular, one may use eqs. (30)-(32) to derive the Shing-Gubbins expression for the chemical potential (see subsect. 2·3).

To this end consider an N-particle system 1, and system 0 consisting of $N-1$ interacting particles and one fictitious particle. In that case it is easy to show that

$$p_1(\Delta U)/p_0(\Delta U) = \exp\left[\beta(\mu_{ex} - \Delta U)\right]. \tag{33}$$

This is the expression used in ref. [27-29] to compute μ_{ex}. BENNETT [31] argues that in order to obtain ΔF it is often not even necessary to have p_1 and p_0 overlap at all, as long as both are reasonably smooth functions of ΔU and the gap between them is not too wide. The procedure suggested by BENNETT is to plot

$$f_1(\Delta U) \equiv \ln p_1(\Delta U) + \tfrac{1}{2}\beta\Delta U \quad \text{and} \quad f_0(\Delta U) \equiv \ln p_0(\Delta U) - \tfrac{1}{2}\beta\Delta U$$

vs. ΔU. From eq. (32) it follows that

$$f_1(\Delta U) = f_0(\Delta U) + \beta\Delta F\,. \tag{34}$$

Hence one can obtain ΔF by fitting f_0 to a polynomial $P(\Delta U)$ and fitting f_1 to the same polynomial plus a constant offset X; the value of X that yields the best fit is the best estimate for $\beta\Delta F$. If the gap between p_0 and p_1 is so wide that straightforward interpolation is not sufficiently accurate, eq. (32) may be combined with multistage sampling in which one carries out a number of simulations on systems with potential-energy function intermediate between U_0 and U_1, *e.g.* $U(\lambda) = \lambda U_1 + (1-\lambda)U_0$. By choosing a sufficient number of intermediate λ-values one can always guarantee that the successive distributions will indeed overlap (see fig. 4). Examples of applications of the overlapping-distribution method can be found in ref. [51-53], while the extension to quantum systems is discussed in ref. [54]. A second method to compute free-energy differences is also due to BENNETT [31]. This method is usually referred to as the acceptance ratio method. The starting point here is the identity

$$Q_0/Q_1 = (Q_0/Q_1)\,\frac{\int W(\boldsymbol{q}^N)\exp[-\beta(U_0+U_1)]\,\mathrm{d}\boldsymbol{q}^N}{\int W(\boldsymbol{q}^N)\exp[-\beta(U_0+U_1)]\,\mathrm{d}\boldsymbol{q}^N}\,, \tag{35}$$

where $W(\boldsymbol{q}^N)$ is an, as yet unspecified, weight function. Equation (35) can be rewritten as

$$\exp[\beta(F_1-F_0)] = \langle W\exp[-\beta U_0]\rangle_1/\langle W\exp[-\beta U_1]\rangle_0\,. \tag{36}$$

BENNETT then proceeds to show that the choice of W that leads to the best estimate of $\Delta F = F_1 - F_0$ is of the form

$$W(\boldsymbol{q}^N) = C(Q_0/n_0\exp[-\beta U_1] + Q_1/n_1\exp[-\beta U_0])^{-1}\,. \tag{37}$$

In eq. (37) n_0 (n_1) stands for the number of statistically independent samples in system 0 (1) on which the expectation values of $\langle W\exp[-\beta U_1]\rangle_0$ and $\langle W\exp[-\beta U_0]\rangle_1$ are based. Of course, Q_0 and Q_1 are not known *a priori* and it might seem, therefore, that eq. (37) is of little use. However, inserting eq. (37)

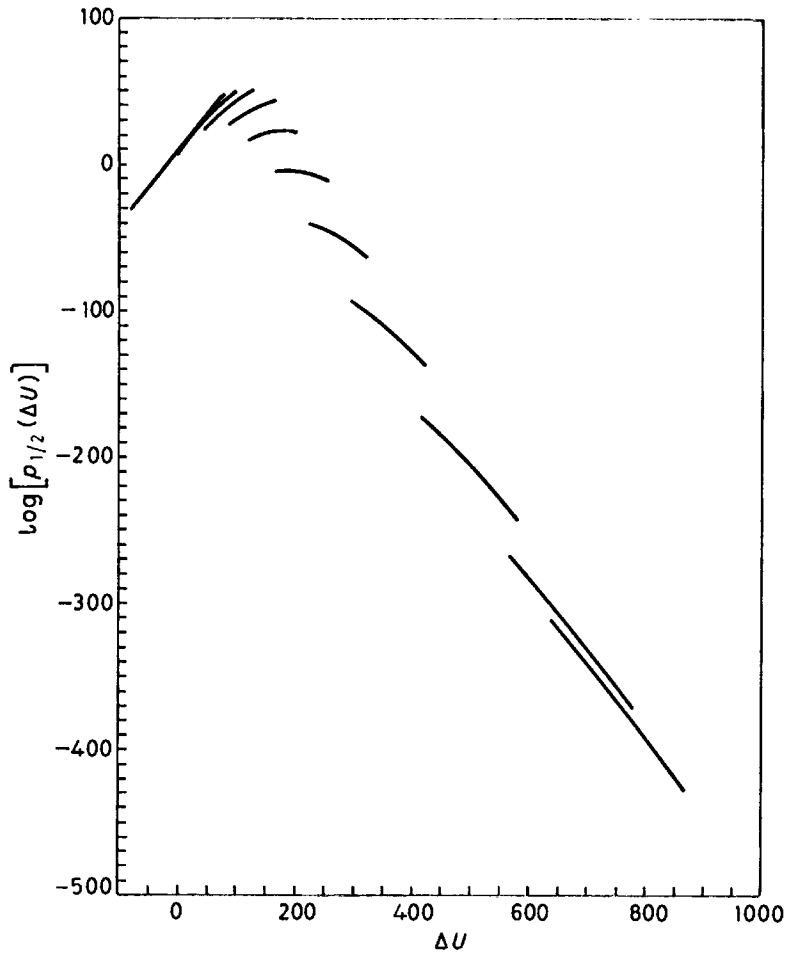

Fig. 4. – Multistage overlapping-distribution method to determine the free-energy difference between f.c.c. « helium » crystal (see ref. [55]) and a corresponding Einstein crystal. The plot shows $\ln(p_\lambda(\Delta U)) + \beta\,\Delta U$, where ΔU is the potential-energy difference between a system with potential energy $U(\lambda)$ and a system with $\lambda = \frac{1}{2}$. The sum of the discontinuities between successive curves yields $(F_{\text{f.c.c.}} - F_{\text{Einstein}})/NkT = 0.8640$, which is within the estimated error of the thermodynamic-integration value $\Delta F = 0.8638$ (see subsect. **3**'3).

in (36) we obtain

$$\exp[\beta\Delta F] = \frac{\langle f(\beta(U_0 - U_1) + C\rangle_1}{\langle f(\beta(U_1 - U_0) - C\rangle_0} \exp[C]\,, \tag{38}$$

where $f(X)$ is the Fermi function $1/(1+\exp[X])$ and $C = \ln(Q_0 n_1/Q_1 n_0)$. Note that, as eq. (36) is valid for *any* W, eq. (38) is valid for any C. The value of C given below eq. (38) is, however, the one consistent with the optimal choice for W (eq. (37)). In practical calculations the value of C is determined graphically.

Writing

$$\langle f(\beta(U_0 - U_1) + C)\rangle_1 = n_1^{-1}\,\Sigma_1\, f(\beta(U_0 - U_1) + C) \tag{39}$$

and the corresponding expression for $\langle f(\beta(U_1 - U_0) - C)\rangle_0$, we obtain from (38)

$$\beta\Delta F = \ln \frac{\Sigma_1 f(\beta(U_0 - U_1) + C)}{\Sigma_0 f(\beta(U_1 - U_0) - C)} + C - \ln(n_1/n_0)\,, \tag{40a}$$

while the condition for the optimal choice of C can be written as

$$\beta\,\Delta F = C - \ln\,(n_1/n_0)\,. \tag{40b}$$

The best estimate for ΔF is obtained by choosing C such that (40*a*) and (40*b*) are satisfied simultaneously, which occurs for a value of C, and that

$$\Sigma_1 f(\beta(U_0 - U_1) + C) = \Sigma_0 f(\beta(U_1 - U_0) - C)\,. \tag{41}$$

Because the optimum value of C is not known *a priori*, it is useful either to compute Σ_1 and Σ_0 for a range of C values during the simulation, or, more conveniently, to store a histogram of potential-energy differences, *i.e.* the functions $p_0(\Delta U)$ and $p_1(\Delta U)$ mentioned above, and carry out the solution for the optimal value of C afterwards. For more details the reader is strongly urged to consult Bennett's very lucid paper [31]. In appendix B we show how the acceptance ratio and overlapping-distribution methods can be generalized to microcanonical simulations.

The acceptance ratio method has been applied by a number of authors [51, 53, 56, 57] and its extension to quantum systems has been discussed by JACUCCI [54].

A few general remarks on the acceptance ratio and overlapping-distribution methods are in place. First of all, both methods can be used simultaneously using the accumulated histrograms $p_0(\Delta U)$ and $p_1(\Delta U)$. RAHMAN and JACUCCI [53] have observed that the acceptance ratio method tends to be the more accurate method of the two. Secondly, both methods become less efficient as the number of particles in the system is increased. Large systems must be studied by multistage sampling techniques. The feature that larger is not necessarily better is typical of all techniques discussed in this subsection.

In subsect. 2·7 we shall argue that, for large systems and a fixed number of stages in the multistage sampling, the overlapping-distribution method becomes equivalent to thermodynamic integration.

Finally it is worth pointing out that the acceptance ratio method should provide a better estimate of the chemical potential than Widom's method (subsect. 2·3).

To my knowledge Bennett's acceptance ratio method has not yet been applied to the computation of chemical potentials.

2·6. *Umbrella sampling.* – We mentioned in the previous subsection that, although free-energy differences can in principle be evaluated using an expression

of the form

$$Q_1 = Q_0 \langle \exp[-\beta(U_1 - U_0)] \rangle_0 , \tag{25}$$

the applicability of this approach is limited by the fact that, whenever U_0 and U_1 are not very similar, the probability $f_0(U)$ of sampling a point in the configuration space of system 0 for which $\exp[-\beta(U_1 - U_0)]$ is appreciable tends to be very small. TORRIE and VALLEAU [6, 58-61] have devised a method to improve the sampling of part of configuration space where the product $f_0^T(U) \exp[-\beta \Delta U]$ is large by carrying out a biased (non-Boltzmann) sampling.

The basic idea behind this Monte Carlo scheme is that the relative probability to sample a point $\boldsymbol{q}^N$ in configuration space is no longer proportional to $\exp[-\beta U_0(\boldsymbol{q}^N)]$, but to $w(\boldsymbol{q}^N) \exp[-\beta U_0(\boldsymbol{q}^N)]$, where the weighting function w is chosen such that both the region where $f_0^T(U)$ is large and the region where $\exp[-\beta \Delta U] f_0^T(U)$ has its maximum are adequately sampled. The relation between the desired average (eq. (25)) and the average obtained by using the biased sampling is given by

$$\langle \exp[-\beta \Delta U] \rangle_0 = \frac{\int \mathrm{d}\boldsymbol{q}^N (\exp[-\beta U_0] w) w^{-1} \exp[-\beta \Delta U]}{\int \mathrm{d}\boldsymbol{q}^N (\exp[-\beta U_0] w) w^{-1}} \tag{42a}$$

$$= \frac{\langle \exp[-\beta \Delta U]/w \rangle_w}{\langle 1/w \rangle_w} , \tag{42b}$$

where the angular brackets with subscript w indicate an average over the biased random walk. Equation (42*b*) can be written in a slightly different form, namely

$$\langle \exp[-\beta \Delta U] \rangle_0 = \langle \exp[-\beta \Delta U]/w \rangle_w \langle w \rangle_0 . \tag{42c}$$

The latter equation shows most clearly that in order to get reliable results w should be chosen such that $w \exp[-\beta U_0]$ is reasonably large in the region of configuration space accessible to system 1 (otherwise the first term on the right-hand side of eq. (42*c*) vanishes), but w should also have an appreciable value wherever $\exp[-\beta U_0]$ is large (otherwise the second right-hand term in (42*c*) vanishes). The fact that $w \exp[-\beta U_0]$ is designed to cover both $f_0^T(U)$ and $f_1^T(U)$ explains the name « umbrella sampling ». This introduction to umbrella sampling is, of course, incomplete without giving the recipe for the weighting function w. Unfortunately, no general prescription can be given.

Sometimes w is determined by trial and error, in other cases the function $w \exp[-\beta U_0]$ corresponds to some intermediate value of the potential-energy function (*e.g.*, $w \exp[-\beta U_0] = \exp[-\beta(U_0 + U_1)/2]$) and in other cases still physical intuition about $\gamma_0(U)$ (eq. (27)), the density of states in configuration space as a function of U_0, is used to choose a form for w which guarantees as uniform a sampling of the relevant part of configuration space as possible. As the system size becomes larger, it becomes increasingly difficult to find a

weighting function that does the job. In such cases umbrella sampling is combined with multistage sampling. Umbrella sampling (US), or very similar techniques, has been used by a number of authors [24, 25, 44, 45, 58-65]. Umbrella sampling has some advantages and some disadvantages as well. To begin with the latter: US is usually carried out with a « nonphysical » weighting function, as a consequence setting up a US run implies modifying a normal Monte Carlo program. As humans are fallible, this always entails more risks than just gathering some extra statistics in the course of a normal simulation. A second disadvantage, certainly for the less experienced, is the fact the success of the method depends on the choice of w.

In some cases the choice may be obvious, but often it requires some groping-around in configuration space. On the other hand, there are several advantages associated with the use of umbrella sampling. First of all, given a reasonable choice for w, free-energy differences (or, for that matter, mechanical quantities) can be obtained for a range of different Hamiltonians and/or temperatures. This was the incentive behind the early work of McDonald and Singer [44-46].

A second advantage is that the US method is actually far more general than suggested by eq. (42). Instead of $\exp[-\beta\Delta U]$ any other function $A(\boldsymbol{q}^N)$ may be probed [58]. Let us, for instance, consider the case that we are interested in the probability that the quantity $A(\boldsymbol{q}^N)$ has its value in an interval $\mathrm{d}X$ around X. We assume that this value of A is very unlikely in the original ensemble, it could, for instance, correspond to an improbable molecular conformation or a large fluctuation of some order parameter. In that case, simple Boltzmann sampling will yield very poor statistics on the desired probability.

However, with umbrella sampling the weighting function w can be chosen such that the relevant region of configuration space is adequately sampled.

The probability density to observe A around X is then given by

$$P_A(X) = \frac{\langle \delta(A - X)/w \rangle_w}{\langle 1/w \rangle_w} . \tag{43}$$

In this way umbrella sampling can be used to estimate the probability of rare events, or to construct the Landau free energy associated with a particular type of order parameter fluctuations (see sect. 4).

2·7. *Thermodynamic integration.* – Thermodynamic integration (TI) is undoubtedly the method most widely used to compute absolute free energies and free-energy differences. The reason is that, although it may be more time consuming than some of the sophisticated methods described above, it is straightforward, accurate and does not run into special problems at high densities or for large system sizes. Moreover, it is closest to the way free-energy differences are measured in the real world. The simplest TI methods rely on

the fact that the system under study can be expanded, compressed, heated or cooled to a system of known free energy, henceforth referred to as the reference system. The thermodynamic relations used in simple thermodynamic integrations are

$$(\partial F/\partial V)_{N,T} = -P \tag{44a}$$

and

$$(\partial(F/T)/\partial T^{-1})_{N,V} = E\,. \tag{44b}$$

For example, if one wishes to compute the free energy of a dense fluid, the ideal gas is often taken as the reference state. Using eq. (44*a*), the free energy of the fluid at a volume V is written as

$$F(V) = F(V_0) - \int_{V_0}^{V} P(V')\,\mathrm{d}V'\,, \tag{45}$$

where V_0 is a volume sufficiently large that $F(V_0)$ may be replaced by $F_{\mathrm{id}}(V_0)$, the free energy of an ideal gas at the same density. Equation (45) can be cast in a form that is computationally more convenient. Using $\mathrm{d}V = -N/\varrho^2\,\mathrm{d}\varrho$ and the ideal-gas law $P_{\mathrm{id}} = \varrho kT$, eq. (45) becomes

$$\frac{F(\varrho)}{NkT} = \frac{F_{\mathrm{id}}(\varrho)}{NkT} + \int_0^{\varrho} ((P/\varrho' kT - 1)/\varrho')\,\mathrm{d}\varrho'\,. \tag{46}$$

The advantage of eq. (46) over eq. (45) is that the former contains two logarithmically diverging contributions which cancel, while the latter contains only well-behaved terms. Note that at low densities the integrand in eq. (46) can be expanded:

$$(P/\varrho' kT - 1)/\varrho' = B_2 + B_3\varrho' + \dots\,, \tag{47}$$

where B_n is the n-th virial coefficient.

In order to obtain reliable estimates of $F(\varrho)$ from eq. (46), knowledge of B_2 is essential. Knowledge of higher virial coefficients is useful if they happen to be available. (The literature abounds with applications of eq. (46).)

Thermodynamic integration using eq. (44*b*) is employed in two rather different cases. The first is when the system approaches the reference system as $T \to \infty$. Examples are a hard-core fluid with bounded continuous interaction such as hard spheres with an added soft interaction, or the Lennard-Jones fluid which approaches the soft-sphere (r^{-12}) fluid as $T \to \infty$. In either case the free energy at temperature T of the system under consideration can be

expressed as

$$\frac{F(T)}{T} = \frac{F_{\text{ref}}(T)}{T} - \int_0^{1/T} \left(E_{\text{ref}}(T') - E(T')\right) \mathrm{d}1/T' . \tag{48}$$

Examples of applications of eq. (48) can be found in [49, 66].

The second application of eq. (45*b*) takes the reference state at $T = 0$. This method is often employed to compute the free energy of crystalline solids.

The reference state is the harmonic solid. The free-energy integration proceeds as in eq. (48) but for the fact that it is convenient to use T' instead of $1/T'$ as integration variable over the range $0 \leqslant T' \leqslant T$. The harmonic-lattice method was first introduced in this context by HOOVER *et al.* [67, 68]. Other examples of applications can be found in [69-71].

The thermodynamic-integration methods mentioned thus far are all « natural » techniques, in the sense that they can also be carried out in the real world.

In addition to these natural TI methods there is a wide class of « artificial » TI techniques. For the latter the integration variable is a quantity such as the strength of intermolecular interaction that is not normally under the control of the experimentalist. Let us denote this control parameter by λ.

The Hamiltonian of the system under study is now a function $H(\lambda)$ of λ. As a consequence the free energy also depends on λ:

$$F(\lambda) = -kT \ln\left(\frac{1}{\Lambda^{3N} N!} \int \exp\left[-\beta U(\lambda)\right] \mathrm{d}\boldsymbol{q}^N\right). \tag{49}$$

In eq. (49) we have limited ourselves to the case that only the potential energy depends on λ. Parametrizations of the kinetic energy can be handled analytically and are anyway of little interest. The usual procedure is to choose a form for $U(\lambda)$ such that $F(\lambda = 0)$ is known, while $F(\lambda = 1)$ is the free energy we wish to determine. Then, using the fact that

$$\frac{\partial F(\lambda)}{\partial \lambda} = \frac{\int (\partial U(\lambda)/\partial \lambda) \exp\left[-\beta U(\lambda)\right] \mathrm{d}\boldsymbol{q}^N}{\int \exp\left[-\beta U(\lambda)\right] \mathrm{d}\boldsymbol{q}^N} = \left\langle \frac{\partial U(\lambda)}{\partial \lambda} \right\rangle_\lambda , \tag{50}$$

we may obtain $F(\lambda = 1)$ from

$$F(\lambda = 1) = F(\lambda = 0) + \int_0^1 \mathrm{d}\lambda' \left\langle \frac{\partial U(\lambda')}{\partial \lambda'} \right\rangle_{\lambda'} . \tag{51a}$$

Note that $\langle \partial U/\partial \lambda \rangle_\lambda$, the canonical average of a mechanical quantity $\partial U/\partial \lambda$ for a system with Hamiltonian $H(\lambda)$, can be obtained by computer simulation.

A typical example of eqs. (50), (51) is the situation where F is known for

a system with potential-energy function U_0 (*e.g.*, a hard-sphere fluid), while we wish to know F for a potential-energy function $U_0 + U_1$. A possible parametrization in this case would be $U(\lambda) = U_0 + \lambda U_1$, and eq. (51) would simplify to

$$F(\lambda = 1) = F(\lambda = 0) + \int \mathrm{d}\lambda' \langle U_1 \rangle_{\lambda'} . \tag{51b}$$

In practice the thermodynamic integration in eqs. (51*a*) and (51*b*) is best performed using an n-point Gauss-Legendre quadrature [72], with n typically 5 to 10.

The parametrization of $U(\lambda)$ will be chosen such that the integrand is a reasonably smooth function of λ. Typical examples of such free-energy calculations can be found in ref. [12, 73-75]. Most other applications will be discussed in the next section on phase transitions. It is interesting to compare thermodynamic integration with Bennett's method of multistage sampling of the potential-energy difference. Suppose that at each quadrature point λ_i of our thermodynamic integration (eq. (51*b*)) we also compute the distribution function $p_{\lambda_i}(U_1)$. Then we can see that the Bennett distribution contains information not just about $\langle U_1 \rangle_\lambda$, but also about $\langle U_1^2 \rangle_\lambda - \langle U_1 \rangle_\lambda^2$ and higher moments, *i.e.* of higher derivatives $\partial^n F(\lambda)/\partial\lambda^n$. It might, therefore, seem that Bennett's method is always preferable. This is, however, not necessarily true.

First of all, during a TI run these higher moments could also be computed at no extra cost. But more importantly, as the system size grows, the distribution $p_{\lambda_i}(U_1)$ tends to become rather narrow. In that case it is to a good approximation a Gaussian which is completely specified by $\langle U_1 \rangle_\lambda$ and $\langle U_1^2 \rangle_\lambda - \langle U_1 \rangle_\lambda^2$. Still it might seem that this contains more information than is used in the integration of eq. (51*b*). After all, if n points and n derivatives of $\partial F/\partial\lambda$ are given, we can construct a polynomial of degree $2n - 1$ which fits these data exactly. In contrast, the straightforward thermodynamic integration uses only n function values. Nevertheless the two methods are equivalent in this limit as long as the λ_i are chosen according to the Gauss-Legendre prescription because an n-point Gauss-Legendre quadrature integrates any polynomial of degree $2n - 1$ or less *exactly*. It should be added that almost all other procedures mentioned in the previous subsections do worse than TI for large N. A notable exception is Widom's particle insertion method and the related GCMC method. However, these techniques tend to become less efficient at high densities. As mentioned at the beginning of this subsection, thermodynamic integration suffers from neither of these drawbacks. Finally it should be added that thermodynamic integration is not limited to the canonical ensemble. It has been applied to the NPT-ensemble (see next section) in which case one obtains $(\partial G/\partial\lambda)_{P,T}$. It could be applied to the grand canonical ensemble, but this is less useful and has, to my knowledge, not been tried. Nor do I know of applications in the microcanonical ensemble in which case the quantity of interest would be

$(\partial S/\partial\lambda)_{E,V}$. Using the same reasoning as in appendix A, one can show that $\partial S/\partial\lambda$ is related to a microcanonical ensemble average:

$$(\partial S/\partial\lambda)_{E,V} = -\langle(\partial U/\partial\lambda)/T^*\rangle_{\mathrm{MC}}\,, \tag{52}$$

where T^* is (but for a term of $O(1/N)$) equal to the instantaneous temperature.

3. – First-order phase transitions.

3·1. *Preliminary remarks.* – One of the most important applications of free-energy calculations is the location of first-order phase transitions. First-order phase transitions are not easily observed directly in computer simulations because, for the small system sizes concerned, the free energy required to form an interface is nonnegligible. As a consequence it is often possible to overheat or supercool a phase well beyond its point of thermodynamic stability. In fact, to prepare two coexisting phases in a computer simulation requires a considerable amount of time and effort [76-82]. Hence most computer simulations of first-order phase transitions are designed to obtain the temperature, pressure and chemical potential of the pure phases.

The coexistence point is then located by searching for the point where T, P and μ of the two phases are equal. In this section we shall briefly discuss the liquid-vapour transition and then proceed to consider first-order transitions involving solids.

3·2. *Liquid-vapour transition.* – To locate the liquid-vapour coexistence point at a given temperature T, we want to know the pressure and chemical potential along the corresponding liquid and vapour isotherms. The determination of the chemical potential or, equivalently, free energy of the vapour is no problem because, once we know the vapour isotherm, we can use eq. (46) to determine the excess free energy at a density ϱ. Computing the free energy of the liquid is less straightforward. Equation (46) cannot be employed because the integration path from $\varrho = 0$ crosses the two-phase region. Because equilibration times are very long in a two-phase system, it is difficult to obtain accurate values for the pressure. One method to circumvent this problem was devised by HANSEN and VERLET [83]. These authors artificially constrain density fluctuations in the two-phase region. As a consequence full-scale phase separation is suppressed and equilibration is relatively rapid. It is then possible to use eq. (46) to compute the free energy of the liquid phase. In this way the liquid-vapour coexistence curve for a Lennard-Jones system was first mapped out. Other methods have also been used to locate the liquid-vapour coexistence curve. The vapour-liquid coexistence has been investigated using Widom's particle insertion method for the LJ system [29] and for liquid Br_2 and Cl_2 [22]. Grand can-

onical MC has been applied to the LJ system [36, 37, 39]. And umbrella sampling was used to investigate both the LJ fluid [58] and a fluid of dipolar hard spheres [60]. In principle the free energy of the dense liquid could also have been determined by performing thermodynamic integration around the critical point. To our knowledge, this has not been done. However, for a different problem integration around a critical point has been carried out, namely in the case of the transition from isotropic fluid to nematic liquid crystal [84]. The isotropic-nematic transition which is normally first order can be suppressed in a strong magnetic field. Hence the free energy of the nematic phase can be computed by performing thermodynamic integration along a path which consists of compression from the dilute gas in a strong field followed by slowly switching off the field at a typical nematic density.

3·3. *Free energy of solids.* – The free energy of the fluid phase can always be obtained by constructing a reversible path to the dilute-gas reference state. In contrast, a dilute gas cannot be compressed or cooled reversibly to form a crystalline solid because in computer simulation the crystalline phase nucleates irreversibly, if at all, from the metastable fluid. Several methods have been developed to link the solid phase by a reversible path to a reference state of known free energy. The most natural method, already mentioned in the previous section, is to take the low-temperature (or high-pressure) harmonic solid as the reference state and use eq. (44*b*) (or (44*a*)) to obtain the free energy of the solid at the desired temperature and density. This method was first applied by HOOVER *et al.* [67, 68] to 3D fluids with a repulsive r^{-n} potential ($n = 12, 9, 6, 4$). Later authors applied the harmonic-lattice method to the 3D one-component plasma [85], pseudopotential « sodium » [70] and the 2D one-component plasma [86], Lennard-Jones system [69] and r^{-6} system [71]. There are several factors limiting the applicability of the harmonic-lattice method. First of all, its use is restricted to solid phases that can be cooled down or compressed to a harmonic state. This rules out all solids of particles with hard-core interactions, which are never harmonic. Moreover, it cannot be applied to solids that are only stable under conditions where the harmonic description fails (*e.g.*, plastic crystals). It should be emphasized, however, that it is not necessary to prepare the solid under consideration in a thermodynamically stable harmonic state; mechanical stability suffices. A second factor limiting the use of the harmonic-lattice method is of a more mundane nature. Although the amount of work involved in computing the free energy of a harmonic lattice of atoms or ions should not defer anyone from attempting the calculation, the same cannot be said of an arbitrary molecular solid. A more generally applicable method to compute the free energy of solids is the so-called single-occupancy-cell (SOC) method of Hoover and Ree [87]. In the SOC method an artificial reversible path is constructed from the solid phase to the dilute-gas phase. The reference state is in this case not the ideal gas, but a lattice gas with every particle con-

strained to one cell. The cells form a regular lattice with the same symmetry as the solid under consideration. At high densities the centre of every cell coincides with the lattice position of the particle it is designed to hold. In the dense solid phase the presence of the artificial walls is unimportant because the atoms are kept in their place through interaction with their neighbours. But as the SOC solid is expanded, the walls take over and prevent the atoms from diffusing. As a consequence, the SOC solid does not melt. It can be expanded reversibly to low densities where its partition function is known analytically. The SOC method was used by HOOVER and REE to compute the free energy and hence the melting point of the hard-sphere and hard-disk solids [88]. The same method has also been used to find the melting point of 3D systems with a repulsive r^{-n} potential ($n = 12$) [67, 89, 90], ($n = 9, 6, 4$) [68], the 3D [83] and 2D [91] Lennard-Jones system. The free energy of the SOC hard-sphere system has also been determined by umbrella sampling [59], but the method does not appear to offer any advantages over straightforward thermodynamic integration.

Although the SOC method is quite flexible and easy to use, it does have a few peculiarities which require some care. First of all, at low densities the equation of state of the SOC gas is a nonanalytic function of density:

$$(P_{\text{SOC}} - \varrho kT)/\varrho^2 = b_2 \varrho^\alpha + \ldots \tag{53}$$

with $\alpha = 1/D$ for a D-dimensional space-filling lattice of cells [87] and $\alpha = (D+1)/D$ for a lattice of touching spherical cells [68]; b_2 plays the role of an effective « second virial coefficient ». Its value depends on the intermolecular potential and the nature of the lattice of cells [83]. A second and potentially more serious feature of the SOC method, at least in 3D, is that, at the point where the hard-cell walls take over from the intermolecular forces in stabilizing the lattice, the SOC pressure shows a change of slope [67, 88] and possibly even a discontinuity [90]. In other words, the 3D SOC system goes through a second-order or weakly first-order transition. This implies that long simulation runs are needed to obtain reliable values for the pressure near this point because close to an (almost) 2nd-order transition fluctuations in the thermodynamic properties of the system decay slowly. Moreover, the presence of a cusp in the SOC pressure makes it essential to compute the pressure at a fairly large number of state points because the accuracy of most numerical integration procedures deteriorates if the integrand is not smooth. Another approach to compute the free energy of solid phases by thermodynamic integration along an artificial path was recently proposed by FRENKEL and LADD [92]. In this method the Hamiltonian of the solid under consideration is changed reversibly to that of an Einstein crystal with the same structure. The advantage of this particular reference system is that, as it has the same structure and density as the original solid, there is no reason to expect a phase transition

along the integration path. For hard-core systems the parametrization of the Hamiltonian takes the form

$$H(\lambda) = H_{\text{h.c.}} + \lambda k_{\max} \sum_{i=1}^{N} (\boldsymbol{r}_i - \boldsymbol{r}_i^0)^2 , \tag{54}$$

where $H_{\text{h.c.}}$ is the Hamiltonian of the unperturbed hard-core system, $\boldsymbol{r}_i - \boldsymbol{r}_i^0$ is the displacement of particle i from its lattice site $\boldsymbol{r}_i^0$, and $k_{\max}$ is the spring constant tying the particles to their lattice sites in the Einstein crystal. $k_{\max}$ must be chosen sufficiently large that for $\lambda = 1$ the free energy of the system approaches that of a true Einstein crystal. The advantage of the method is that it is simple to use and that, with moderate expenditure of computer time, the estimated error in the excess free energy of the solid can be reduced to $\sim 0.002\, NkT$. In ref. [92] the method is applied to the h.c.p. and f.c.c. phases of hard spheres. The Einstein crystal method has been extended to molecular hard-core systems [84]. The only difference is that in addition to the spring constants fixing the molecular centre-of-mass positions there are now also springs fixing the molecular orientation. Using this approach it has proved possible to determine the melting point of hard ellipsoids of revolution over a wide range of length-to-breadth ratios [84] (see fig. 5). The generalization to systems with a continuous intermolecular potential is straightforward. The

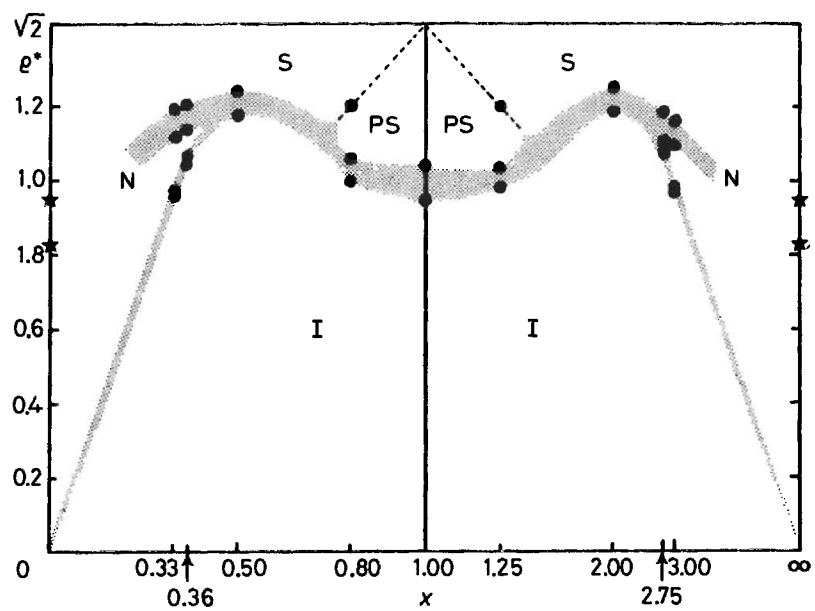

Fig. 5. – Phase diagram of hard ellipsoids of revolution as a function of the length-to-breadth ratio X. The maximum density $\sigma = \sqrt{2}$ corresponds to regular close packing. I = isotropic fluid, N = nematic fluid, S = ordered solid and PS = plastic (orientationally disordered) solid. The shaded area is the two-phase region. All points are coexistence points that follow from absolute free-energy computations of the solid and fluid phases (see ref. [84]).

parametrized potential-energy function now becomes

$$V(\lambda) = V_0 + (1-\lambda)(V_s(\boldsymbol{q}^N) - V_0) + \lambda k_{\max} \Sigma(\boldsymbol{r}_i - \boldsymbol{r}_i^0)^2 , \tag{55}$$

where V_0 is the static lattice energy of the solid and $V_s(\boldsymbol{q}^N)$ the potential energy of a given lattice configuration. It is advisable to choose $k_{\max}$ such that the mean square displacement of the particles varies little as λ is changed. As an example we apply this method to the relative stability of the f.c.c. and b.c.c. phases of a model for helium [55, 93]. In fig. 6 we show the value of $\langle \partial H(\lambda)/\partial\lambda \rangle_\lambda$

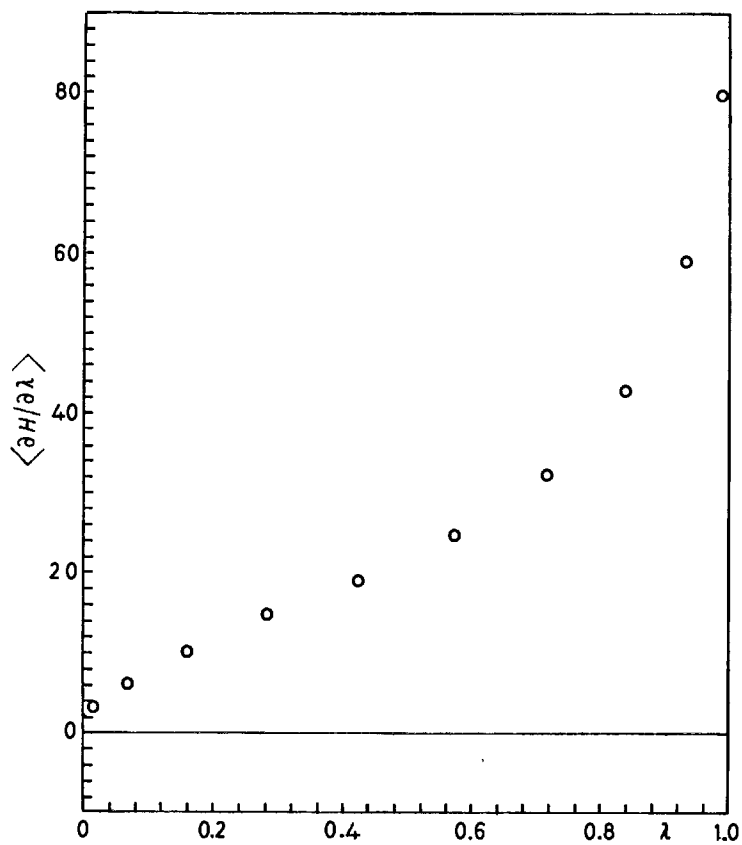

Fig. 6. – Integrand in the free-energy integration from f.c.c. « helium » (see text) to the corresponding Einstein crystal, as a function of the coupling parameter λ. The integrand was evaluated at values of λ corresponding to a 10-point Gauss-Legendre quadrature.

for a number of λ values, for both f.c.c. and b.c.c. « helium » at a reduced temperature of $T^* = 32$ (in units $\varepsilon_{LJ} = 10.22\ k$) and a reduced density $\varrho^* = 2.41$. At this density and temperature the f.c.c. phase is still marginally more stable than the b.c.c. phase $(\Delta F = (F_{\text{b.c.c.}} - F_{\text{f.c.c.}})/N_k T = 0.0087 \pm 0.0018)$. For more details on the Einstein crystal method we refer the reader to [94]. We wish to remind the reader that thermodynamic integration and multistage

sampling are closely related. An example of the application of multistage sampling to compute the free-energy difference of the f.c.c. and b.c.c. phases for a number of model potentials can be found in [53].

4. – Free energy of fluctuations.

Thus far we have been concerned with the computation of the free energy of bulk phases. Now we wish to make a few remarks about the free energy associated with fluctuations. Consider a mechanical quantity $S(\boldsymbol{q}^N)$ which in principle may be anything, but in cases of practical interest usually is some kind of order parameter. The probability of observing an equilibrium fluctuation such that O is in a range ΔO around O is

$$P(S)\Delta S = \frac{\int_{\Delta S} \exp[-\beta H]\,\mathrm{d}\boldsymbol{q}^N}{\int \exp[-\beta H]\,\mathrm{d}\boldsymbol{q}^N} \equiv \exp[-\beta F(S)]\Delta S\,, \tag{56}$$

where the subscript ΔS in the integral in the numerator restricts the integral to that part of phase space were O is within the specified range.

The second expression on the right in eq. (56) defines the free-energy density $F(S)$. From eq. (56) we see that the free-energy density associated with a particular fluctuation of S can be obtained from the probability density of finding a certain value for S:

$$F(S) = -\,kT \ln (P(S))\,. \tag{57}$$

A classical example of the relation between $F(S)$ and $P(S)$ can be found in the work of Wood [95] on density fluctuations in the isobaric ensemble.

In this case the probability density of finding a particular value of V, if the applied pressure is P_0, is given by

$$P(V) = c \exp[-\beta(P_0 V + F(V))]\,, \tag{58}$$

where c is a normalizing constant. The term $P_0 V + F(V)$ plays the role of the free enthalphy $G(V)$ associated with a given fluctuation of V. We see that G has its minimum if

$$-(\partial F/\partial V) = P_0\,. \tag{59}$$

Equation (59) expresses just the condition for mechanical equilibrium. Wood observed that eq. (58) offers the possibility of probing the equation of state at densities around the equilibrium density given by eq. (59). A similar relation exists between the probability density of potential-energy fluctuations in the canonical ensemble and the dependence of U on T.

PARRINELLO [96] has recently pointed out that the probability density of the scaling parameter s in Nosé's canonical MD [97] contains comparable information. An interesting feature of eq. (58) is the fact that, in principle, at a first-order phase transition $P(V)$ becomes double peaked.

The pressure for which the two peaks of $P(V)$ have equal height is the coexistence pressure because at that point two different volumes V_1 and V_2 satisfy the relation $\partial F/\partial V = -P_0$ and $G(V_1) = G(V_2)$. Unfortunately, this property of $P(V)$ can only be exploited for very small systems. For larger systems configuration space is not adequately sampled on the time scale of a simulation and hence we do not obtain the correct $P(V)$. However, in other situations, in particular near weakly first-order or higher-order phase transitions eq. (57) may be extremely useful to study precursor effects of the transition. One way of analysing such precursor effects is in terms of the Landau free energy, the expansion of the free-energy density in integer powers of the order

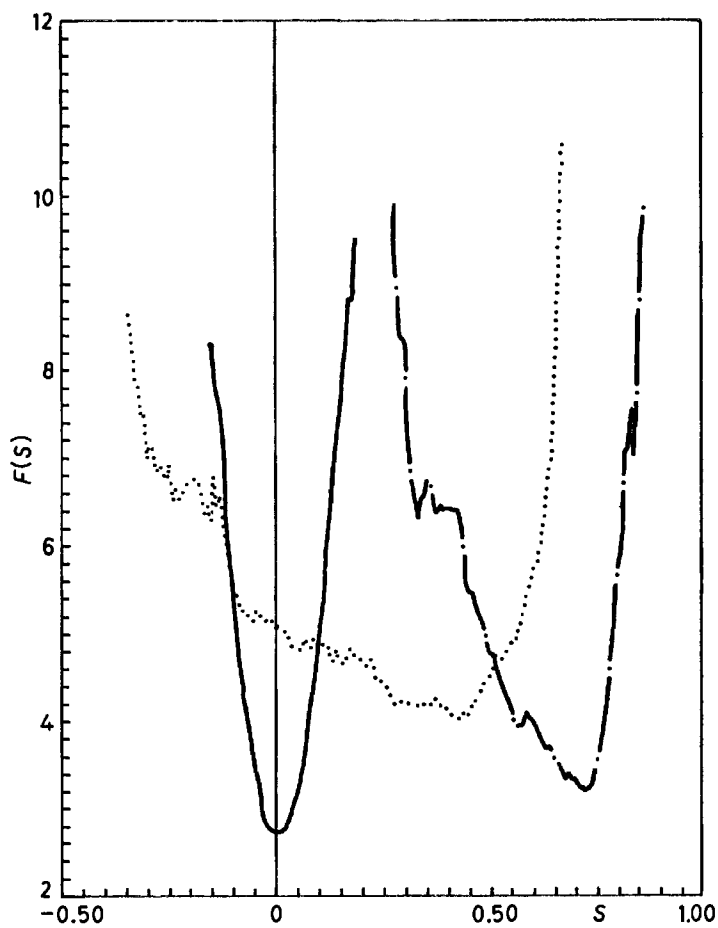

Fig. 7. – The Landau free energy (in units kT) associated with fluctuations of the nematic order parameter S in a system of 100 hard platelets of diameter σ (ref. [23]). Drawn curve: low density, well into the isotropic fluid phase. Dotted curve: higher density, just beyond the isotropic nematic transition; note that the most probable value of S has moved to a nonzero value. Dash-dotted curve: high density, well inside the nematic phase; only small fluctuations around a nonzero order parameter are possible.

parameter:

$$F(S) = F_0 + aS^2 + bS^3 + cS^4 + \dots . \tag{60}$$

Of course, an expansion of this type need not be correct and indeed, close to phase transitions, the simple Landau picture often fails. The important point we wish to stress here is that the Landau free energy is not just an abstract concept that may or may not be useful. Using eq. (57) the Landau free energy can be « measured » in a computer simulation. As an example, fig. 7 shows the Landau free energy associated with fluctuations of the orientational order parameter S close to the (weakly first-order) transition from isotropic liquid to nematic liquid crystal. The fact that $P(S)$ in fig. 7 develops a double-peaked structure confirms the first-order nature of the transition. Actually, in this particular case the Landau expansion eq. (60) appears to run into trouble. For further details see ref. [23].

One basic problem with the use of eq. (57) is that $P(S)$ becomes very narrow for larger system sizes, until eventually the only information one obtains is the average value of O and its variance. However, as already indicated in subsect. 2·5 (eq. (43)), one could still probe the wings of the distribution, and thereby higher-order terms in the Landau expansion, by using umbrella sampling. To my knowledge this has not been attempted.

5. – Conclusions.

After this fairly exhaustive review of free-energy computation techniques I wish to end by given specific recommendations to the newcomer who is considering carrying out such calculations. This section has inevitably a personal bias and I apologize to all those who feel I am giving bad advice.

First of all a general point: always look for the simplest method available even if you feel that other methods are more sophisticated. In general a problem can be tackled with several methods of which at least one is « simple ». Other methods may appear cheaper, but in the end, after all the hours spent programming, debugging and discovering hidden subtleties you may wish you had started with the « more time consuming » simple method. Of course, once you are more skilled, you may go for the « smart » methods.

What are the simple methods? First of all the « natural » thermodynamic-integration methods, compression, expansion, heating or cooling, Remember, if you have a working MD or MC program, you can do it. Of these the methods that have the harmonic lattice as their reference point are less favoured unless the harmonic-crystal free energy can easily be calculated. For solids, the Einstein crystal method (personal bias!) is simplest, directly followed by the single-occupancy-cell method. Note that the free-energy difference between two solids can be computed by thermodynamic integration or by Bennett's

acceptance ratio or overlapping-distribution method. All three are easy. The best is to accumulate a histogram of potential-energy differences during the simulations, and use it to try out all three methods. Note that for thermodynamic integration it is advisable to choose values of the coupling parameter λ according to a Gauss-Legendre or similar quadrature. For Bennett's method there is no need to choose the number of points in advance. Start with simulations for $\lambda = 0$ and $\lambda = 1$ and keep on doing simulations at intermediate values of λ until you find you have reached the desired accuracy.

If you are studying multicomponent mixtures at low densities use Bennett's modification of the Widom/Shing-Gubbins method or grand canonical MC (but watch your random-number generator!). At higher densities multicomponent systems become difficult and you will probably need one of the « smart » methods. Of the smart methods umbrella sampling seems the most powerful. This method requires some skill, so use it only where the simpler methods will not do. It turns out that there remains a large class of problems where such biased sampling is the only tool available.

* * *

Most of this manuscript was written during my stay at the Department of Molecular Physics of the Katholieke Universiteit Leuven. I wish to express my gratitude to all members of the Molecular Physics Group for their hospitality.

Figure 1 was drawn by N. D'OLVEYRA. I am grateful for her artwork.

APPENDIX A

It has been suggested in the literature [29] that the particle insertion method may also be used in microcanonical simulation using

$$\beta\mu_{ex} = -\ln\langle\exp[-V_A/kT']\rangle\,, \tag{A.1}$$

where V_A is, as before, the interaction of a randomly placed test particle with the other molecules, and T' is the *running average* of the temperature during microcanonical simulation. We argue that, although this recipe may work satisfactorily in practice, it is not correct in principle. Moreover, the correct recipe is simple to implement. We start from the relation

$$\mathrm{d}S = \mathrm{d}E/T + (P/T)\,\mathrm{d}V - (\mu/T)\,\mathrm{d}N \tag{A.2}$$

from which is follows that

$$-(\mu/T) = \left(\frac{\partial S}{\partial N}\right)_{E,V}. \tag{A.3}$$

The classical expression for $S(E, V, N) = k \ln \omega(E)$ is

$$S = k \ln\left(\frac{1}{h^{3N} N!} \int \delta(H_N - E)\, \mathrm{d}\boldsymbol{p}^N \mathrm{d}\boldsymbol{q}^N\right), \tag{A.4}$$

where $H_N(\boldsymbol{p}^N, \boldsymbol{q}^N) = V(\boldsymbol{q}^N) + K(\boldsymbol{p}^N)$ is the Hamiltonian of the system. For simplicity we have assumed that we are dealing with atoms. Generalization to molecules is straightforward. We now write $(\partial S/\partial N)_{E,V}$ as

$$(\partial S/\partial N)_{E,V} \underset{N\to\infty}{=} k \ln\left(\omega_N(E)/\omega_{N-1}(E)\right). \tag{A.5}$$

Or, introducing ε_N, the kinetic energy of the test particle, and V_A, its interaction with the rest of the system,

$$\frac{\omega_N(E)}{\omega_{N-1}(E)} = \frac{1}{h^3 N} \frac{\int \delta(H_{N-1} + V_A + \varepsilon_N - E)\, \mathrm{d}\boldsymbol{p}^N \mathrm{d}\boldsymbol{q}^N}{\int \delta(H_{N-1} - E)\, \mathrm{d}\boldsymbol{p}^{N-1} \mathrm{d}\boldsymbol{q}^{N-1}}. \tag{A.6}$$

Using the fact that

$$\mathrm{d}\boldsymbol{p}^N = \left\{(2\pi m)^{3/2(N-1)}/\Gamma\big(3/2(N-1)\big)\right\} K^{3/2(N-1)-1}\, \mathrm{d}K \tag{A.7}$$

(for a systen that does not conserve linear momentum, all $N-1$ should be replaced by N), we can readily perform the integrations over the momenta in eq. (A.6):

$$\omega_N(E)/\omega_{N-1}(E) = \frac{1}{h^3 N} \frac{\int (E - V_{N-1} - V_A)^{3/2(N-1)-1} (2\pi m)^{\frac{3}{2}} \big(3/2(N-2)\big)^{-\frac{3}{2}}\, \mathrm{d}q^N}{\int (E - V_{N-1})^{3/2(N-2)-1}\, \mathrm{d}q^{N-1}}. \tag{A.8}$$

Noting that $E - V_{N-1} = K_{N-1}$, the kinetic energy in the $N-1$ particle system, we obtain

$$\omega_N(E)/\omega_{N-1}(E) = \left(\frac{2\pi m}{h^2}\right)^{\frac{3}{2}} \cdot \frac{\int (1 - V_A/K_{N-1})^{3/2(N-1)-1} \big(K_{N-1}/3/2(N-2)\big)^{\frac{3}{2}} K_{N-1}^{3/2(N-2)-1}\, \mathrm{d}q^N}{\int (E - V_{N-1})^{3/2(N-2)-1}\, \mathrm{d}q^{N-1}}. \tag{A.8'}$$

Equation (A.8′) can be expressed as a microcanonical expectation value:

$$\frac{\omega_N(E)}{\omega_{N-1}(E)} = \left(\frac{2\pi m}{h^2}\right)^{\frac{3}{2}} \frac{V}{N} \frac{1}{V} \int \mathrm{d}\boldsymbol{q}_N \left\langle (1 - V_A/K_{N-1})^{3/2(N-1)-1} \big(K_{N-1}/3/2(N-2)\big)^{\frac{3}{2}} \right\rangle_{\mathrm{MC}}. \tag{A.9}$$

For sufficiently large N we can write $(1 - V_A/K_{N-1})^{3/2(N-1)-1}$ as

$$\exp\left[-V_A\Big/\Big(K_{N-1}/\big(3/2(N-2) + \tfrac{1}{2}\big)\Big)\right].$$

With the conventional definition of the instantaneous temperature T_i

$$T_i = K_{N-1}/\big(3/2(N-2)\,k\big) \tag{A.10}$$

and neglecting corrections of order N^{-1} to T_1, we obtain

$$\text{(A.11)} \qquad \omega_N(E)/\omega_{N-1}(E) = (\varrho\Lambda^3)^{-1}\langle T\rangle^{-\frac{3}{2}}\frac{1}{V}\int \mathrm{d}\boldsymbol{q}_N\,\langle \exp[-V_A/kT_1]T_1^{\frac{3}{2}}\rangle_{\mathrm{MC}}$$

and finally

$$\text{(A.12)} \qquad \beta\mu_{\mathrm{ex}} = -\ln\{\langle T\rangle^{-\frac{3}{2}}\langle \exp[-V_A/kT_1]\,T_1^{\frac{3}{2}}\rangle\}\,.$$

The angular brackets now stand for microcanonical averaging over the phase space co-ordinates of the $N-1$ particles in the original system for random positions of the test particle. Note that eq. (A.11) can easily be implemented in a molecular-dynamics program because the instantaneous temperature is always well defined. Note also that, because of the convexity of $\exp[-V_A/T_1]T_1^{\frac{3}{2}}$, eq. (A.11) must lead to a *lower* estimate of μ_{ex} than is obtained by the method of ref. [29]. This may be serious for small systems or for systems with a large heat capacity (large T fluctuations). Note that the μ's in ref. [29] tend to be marginally higher than earlier data. For molecular systems the $(T_1/\langle T\rangle)^{\frac{3}{2}}$ is replaced by some other power of $T_1/\langle T\rangle$, *e.g.* 5/2 for linear molecules.

Appendix B

Bennett's acceptance ratio method and the method of overlapping distributions can be generalized to the microcanonical ensemble. In the literature it has thus far been assumed [53] that Bennett's canonical expressions can be used without modification in microcanonical simulations. Here we argue that, although such an approach may yield reasonable answers for large systems, it is not correct. This is important because free-energy difference calculations are often carried out on rather small systems where the choice of the ensemble does make a difference.

As in appendix A, the central quantity to be computed in a microcanonical simulation is the entropy difference between two systems. The expression for the entropy of a classical N-particle system with total energy E is

$$\text{(B.1)} \qquad S = k\ln(\omega(E)) = k\ln\left\{(h^{3N}N!)^{-1}\int\delta(H_N - E)\,\mathrm{d}\boldsymbol{p}^N\,\mathrm{d}\boldsymbol{q}^N\right\}.$$

Performing the integration over momenta, we obtain

$$\text{(B.2)} \qquad \omega(E) = c\int\left(E - U(\boldsymbol{q}^N)\right)^{(3N-5)/2}\mathrm{d}\boldsymbol{q}^N\,,$$

with $c = \{(2\pi m)^{(3N-5)/2}/\Gamma((3N-3)/2)\}/h^{3N}N!$. As in appendix A we have assumed that we are dealing with an atomic system and that linear momentum is conserved. The entropy difference between two N-particle systems 0 and 1 is given by

$$\text{(B.3)} \qquad \Delta S = k\ln(\omega_1(E_1)/\omega_0(E_0)) = k\ln\frac{\int(E_1 - U_1(\boldsymbol{q}^N))^{(3N-5)/2}\mathrm{d}\boldsymbol{q}^N}{\int(E_0 - U_0(\boldsymbol{q}^N))^{(3N-5)/2}\mathrm{d}\boldsymbol{q}^N}\,.$$

Starting from eq. (B.3), we can easily derive the microcanonical equivalent of the overlapping-distribution and acceptance ratio methods.

I) *Overlapping-distribution method.* Let us denote the kinetic energy of systems 0 and 1 by $K_0 = E_0 - U_0(\boldsymbol{q}^N)$ and $K_1 = E_1 - U_1(\boldsymbol{q}^N)$. Note that K_0 and K_1 are explicit functions of the particle co-ordinates $\boldsymbol{q}^N$. Consider the probability of observing the quantity $x = \big((3N-5)/2\big)\ln(K_1/K_0)$ in a range $\mathrm{d}x$ around x. If microcanonical sampling is carried out in system 0, the expression for the probability density $p_0(x)$ of x is

$$p_0(x) = \frac{\int \delta\{((3N-5)/2)\ln(K_1/K_0) - x\}\, K_0^{(3N-5)/2}\,\mathrm{d}\boldsymbol{q}^N}{\int K_0^{(3N-5)/2}\,\mathrm{d}\boldsymbol{q}^N}\,. \tag{B.4}$$

Using eq. (B.3), (B.4) can be rewritten as

$$p_0(x) = \exp[\Delta S/k]\,\frac{\int \delta\{((3N-5)/2)\ln(K_1/K_0) - x\}\exp[-x]\,K_1^{(3N-5)/2}\,\mathrm{d}\boldsymbol{q}^N}{\int K_1^{(3N-5)/2}\,\mathrm{d}\boldsymbol{q}^N} \tag{B.5}$$

or

$$p_0(x) = \exp[\Delta S/k]\exp[-x]\,p_1(x)\,. \tag{B.6}$$

Note that eq. (B.6) is of the same form as eq. (32). For $|K_1 - K_0| \ll K_0$ we can write

$$\big((3N-5)/2\big)\ln(K_1/K_0) \simeq (\Delta E - \Delta U)/kT_0^*\,, \tag{B.7}$$

where T_0^* is the *instantaneous* temperature of system 0. In the special case that the average temperatures of 0 and 1 are equal we can combine (B.6) and (B.7) to yield

$$\begin{aligned} p_0\big((\Delta E - \Delta U)/kT_0^* = x\big) &= \\ &= \exp[\Delta S/k]\exp[-x]\,p_1\big((\Delta E - \Delta U)/kT_1^* = x\big)\,, \end{aligned} \tag{B.8}$$

or, with $x' = x - \Delta E/kT$, where T is the average of T_1^* and T_0^*,

$$\begin{aligned} p_0\big(\{\Delta E(1/kT_0^* - 1/kT) - \Delta U/kT_0^*\} = x'\big) &= \\ = \exp[-\Delta F/kT]\exp[-x']\,p_1\big(\{\Delta E(1/kT_1^* - 1/kT) - \Delta U/kT_1^*\} = x'\big)\,. \end{aligned} \tag{B.9}$$

Note that eq. (B.9) is similar, but not identical, to eq. (32). The difference is due to the effect of temperature fluctuations in the microcanonical ensemble. Of course, in the thermodynamic limit this effect disappears, but in that same limit the overlapping-distribution method loses its advantage over thermodynamic integration.

II) *Acceptance ratio method.* To arrive at the microcanonical equivalent of Bennett's acceptance ratio method we start, once more, from eq. (B.3).

We begin with the identity

$$\text{(B.10)} \qquad \frac{\omega_1(E_1)}{\omega_0(E_0)} = \frac{\omega_1(E_1)}{\omega_0(E_0)} \frac{\int W(\boldsymbol{q}^N)(K_1 K_0)^{(3N-5)/2} \mathrm{d}\boldsymbol{q}^N}{\int W(\boldsymbol{q}^N)(K_1 K_0)^{(3N-5)/2} \mathrm{d}\boldsymbol{q}^N},$$

where $W(\boldsymbol{q}^N)$ is an as yet still arbitrary function. Proceeding exactly as in ref. [31] it is easy to show that the estimated error in ΔS is minimized for the following choice of $W(\boldsymbol{q}^N)$:

$$\text{(B.11)} \quad W(\boldsymbol{q}^N) = \text{const} \cdot X \left\{ (\omega_0(E_0)/n_0) K_1^{(3N-5)/2} + (\omega_1(E_1)/n_1) K_0^{(3N-5)/2} \right\}^{-1} .$$

Here n_0 and n_1 are the numbers of independent configurations sampled in a microcanonical simulation of systems 0 and 1, respectively. Defining, as in eq. (B.4), a quantity x by

$$\text{(B.12)} \qquad x = \{(3N-5)/2\} \ln (K_1/K_0) ,$$

we can combine eqs. (B.10) and (B.11) to yield

$$\text{(B.13)} \qquad \frac{\omega_1}{\omega_0} = \frac{\langle f(-x+C)\rangle_0}{\langle f(+x-C)\rangle_1} \exp [C] ,$$

where the angular brackets stand for a microcanonical average in system 0 or 1, $f(y) \equiv (1 + \exp [y])^{-1}$ is the Fermi function, and C is a constant. Although eq. (B.13) is in principle valid for any value of C, the best estimate for ΔS results for the choice

$$\text{(B.14)} \qquad C = \ln \{(\omega_1/n_1)(n_0/\omega_0)\} .$$

If $|K_1 - K_0| \ll K_0$ we can, as in eq. (B.7), replace x by $(\Delta E - \Delta U)/kT^*$, with T^* the instantaneous temperature. In the special case that $\langle T_1^* \rangle = \langle T_0^* \rangle = T$, we can rewrite eq. (B.13) as

$$\text{(B.15)} \quad \exp [-\Delta F/kT] = \frac{\langle f(-\Delta E(1/kT_0^* - 1/kT) + \Delta U/kT_0^* + C')\rangle_0}{\langle f(+\Delta E(1/kT_1^* - 1/kT) - \Delta U/kT_1^* - C')\rangle_1} \exp [C'],$$

with $C' = C - \Delta E/kT$. Note that eq. (B.15) is similar to the canonical expression (eq. (38)), but, as with the overlapping-distribution case, the microcanonical term is changed due to temperature fluctuations.

It should be stressed that the microcanonical methods described above are just as easily implemented in a normal MD program as the less appropriate canonical expressions. The best approach is to accumulate a histogram of $\ln \{(E_1 - U_1)/(E_0 - U_0)\}$ during simulations of systems 0 and 1. The analysis required to solve eq. (B.6) or eqs. (B.13) and (B.14) then proceeds exactly as with the original Bennett methods and can be carried out afterwards. Extension of the microcanonical methods to multistage sampling is straightforward.

REFERENCES

[1] N. METROPOLIS, A. W. ROSENBLUTH, M. N. ROSENBLUTH, A. H. TELLER and E. TELLER: *J. Chem. Phys.*, **21**, 1087 (1953).
[2] S. K. MA: *J. Stat. Phys.*, **62**, 221 (1981).
[3] C. J. ATKINS: *Equilibrium Thermodynamics* (McGraw-Hill, London, 1968).
[4] J. P. HANSEN and I. R. MCDONALD: *Theory of Simple Liquids* (Academic Press, London, 1976).
[5] J. P. VALLEAU and S. G. WHITTINGTON: in *Modern Theoretical Chemistry*, Vol. **5**, edited by B. J. BERNE (Plenum Press, New York, N. Y., 1977), p. 137.
[6] J. P. VALLEAU and G. M. TORRIE: in *Modern Theoretical Chemistry*, Vol. **5**, edited by B. J. BERNE (Plenum Press, New York, N. Y., 1977), p. 169.
[7] D. LEVESQUE, J. J. WEIS and J. P. HANSEN: in *Applications of the Monte Carlo Method*, edited by K. BINDER (Springer, Berlin, 1984), p. 37.
[8] O. G. MOURITSEN: *Computer Studies of Phase Transitions and Critical Phenomena* (Springer, Berlin, 1985).
[9] Z. W. SALSBURG, J. D. JACOBSON, W. FICKETT and W. W. WOOD: *J. Chem. Phys.*, **30**, 65 (1959).
[10] W. W. WOOD: in *Physics of Simple Liquids*, edited by H. N. V. TEMPERLEY, G. S. RUSHBROOKE and J. S. ROWLINSON (North-Holland, Amsterdam, 1968), p. 116.
[11] J. P. VALLEAU and D. N. CARD: *J. Chem. Phys.*, **57**, 5457 (1972).
[12] J. C. OWICKI and H. A. SCHERAGA: *J. Am. Chem. Soc.*, **99**, 7403 (1977).
[13] M. MEZEI: *Mol. Phys.*, **47**, 1307 (1982).
[14] R. L. COLDWELL: *Phys. Rev. A*, **7**, 270 (1973).
[15] R. L. COLDWELL, T. P. HENRY and C.-W. WOO: *Phys. Rev. A*, **10**, 897 (1974).
[16] E. BYCKLING: *Physica (Utrecht)*, **27**, 1030 (1961).
[17] K. W. KRATKY: *Chem. Phys.*, **57**, 167 (1981).
[18] O. EDHOLM, H. J. C. BERENDSEN and P. VAN DER PLOEG: *Mol. Phys.*, **48**, 379 (1983); O. EDHOLM and H. J. C. BERENDSEN: *Mol. Phys.*, **51**, 1011 (1984).
[19] B. WIDOM: *J. Chem. Phys.*, **39**, 2808 (1963).
[20] D. J. ADAMS: *Mol. Phys.*, **28**, 1241 (1974).
[21] S. ROMANO and K. SINGER: *Mol. Phys.*, **37**, 1765 (1979).
[22] S. G. POWLES: *Mol. Phys.*, **41**, 715 (1980).
[23] R. EPPENGA and D. FRENKEL: *Mol. Phys.*, **52**, 1303 (1984).
[24] K. S. SHING and K. E. GUBBINS: *Mol. Phys.*, **43**, 717 (1981).
[25] M. FIXMAN: *J. Chem. Phys.*, **78**, 4223 (1983).
[26] J. A. ZOLLWEG: *J. Chem. Phys.*, **72**, 6712 (1980).
[27] K. S. SHING and K. E. GUBBINS: *Mol. Phys.*, **46**, 1109 (1982).
[28] K. S. SHING and K. E. GUBBINS: *Mol. Phys.*, **49**, 1121 (1983).
[29] J. G. POWLES, W. A. B. EVANS and N. QUIRKE: *Mol. Phys.*, **46**, 1347 (1982).
[30] J. G. POWLES: *Chem. Phys. Lett.*, **86**, 335 (1982).
[31] C. H. BENNETT: *J. Comput. Phys.*, **22**, 245 (1976).
[32] W. G. HOOVER and J. C. POIRIER: *J. Chem. Phys.*, **37**, 1041 (1962).
[33] E. MEERON and A. J. F. SIEGERT: *J. Chem. Phys.*, **48**, 3139 (1968).
[34] J. A. BALLANCE and R. J. SPEEDY: *Mol. Phys.*, **54**, 1035 (1985).
[35] G. E. NORMAN and V. S. FILINOV: *High Temp. Res. USSR*, **7**, 216 (1969).
[36] D. J. ADAMS: *Mol. Phys.*, **29**, 307 (1975).
[37] D. J. ADAMS: *Mol. Phys.*, **32**, 647 (1976).

[38] D. J. ADAMS: *Mol. Phys.*, **37**, 211 (1979).
[39] L. A. ROWLEY, D. NICHOLSON and N. G. PARSONAGE: *J. Comput. Phys.*, **17**, 401 (1975).
[40] J. YAO, R. A. GREENKORN and K. C. CHAO: *Mol. Phys.*, **46**, 587 (1982).
[41] M. MEZEI: *Mol. Phys.*, **40**, 901 (1980).
[42] J. P. VALLEAU and K. L. COHEN: *J. Chem. Phys.*, **72**, 5935 (1980).
[43] W. VAN MEEGEN and I. SNOOK: *J. Chem. Phys.*, **73**, 4656 (1980).
[44] I. R. MCDONALD and K. S. SINGER: *Discuss. Faraday Soc.*, **43**, 40 (1967).
[45] I. R. MCDONALD and K. S. SINGER: *J. Chem. Phys.*, **47**, 4766 (1967).
[46] I. R. MCDONALD and K. S. SINGER: *J. Chem. Phys.*, **50**, 2308 (1969).
[47] E. L. POLLOCK: *J. Phys. C*, **9**, 1129 (1976).
[48] S. M. DE LEEUW and M. J. GILLAN: *J. Phys. C*, **15**, 5161 (1982).
[49] G. N. PATEY and J. P. VALLEAU: *Chem. Phys. Lett.*, **21**, 297 (1973); G. N. PATEY, G. M. TORRIE and J. P. VALLEAU: *J. Chem. Phys.*, **71**, 96 (1979).
[50] K. S. SHING and K. E. GUBBINS: *Mol. Phys.*, **45**, 129 (1982).
[51] N. QUIRKE and G. JACUCCI: *Mol. Phys.*, **45**, 823 (1982).
[52] G. MARTIN, A. PERINI and G. JACUCCI: in *Point Defects in Metals* (University of Tokyo Press, Tokyo, 1982), p. 718.
[53] A. RAHMAN and G. JACUCCI: *Nuovo Cimento D*, **4**, 357 (1984).
[54] G. JACUCCI: in *Monte Carlo Methods in Quantum Problems*, edited by M. KALOS (D. Reidel, Dordrecht, 1984), p. 117.
[55] D. LEVESQUE, J. J. WEIS and M. L. KLEIN: *Phys. Rev. Lett.*, **51**, 670 (1983).
[56] J. JACUCCI and N. QUIRKE: *Phys. Lett. A*, **98**, 269 (1983).
[57] A. T. CLARK and M. LAL: *J. Phys. A*, **11**, L11 (1978).
[58] G. M. TORRIE and J. P. VALLEAU: *Chem. Phys. Lett.*, **28**, 578 (1974).
[59] G. M. TORRIE, J. P. VALLEAU and A. BAIN: *J. Chem. Phys.*, **58**, 5479 (1973).
[60] K. C. NG, J. P. VALLEAU and G. M. TORRIE: *Mol. Phys.*, **38**, 781 (1979).
[61] G. M. TORRIE and J. P. VALLEAU: *J. Comput. Phys.*, **23**, 187 (1977).
[62] S. OKAZAKI, K. NAKANISHI, H. TOUHARA and Y. ADACHI: *J. Chem. Phys.*, **71**, 2421 (1979).
[63] C. Y. LEE and H. L. SCOTT: *J. Chem. Phys.*, **73**, 4591 (1980).
[64] G. JACUCCI and N. QUIRKE: *Mol. Phys.*, **40**, 1005 (1980).
[65] K. NAKANISHI, S. OKAZAKI, K. IKARI, T. HIGUCHI and H. TANAKA: *J. Chem. Phys.*, **76**, 629 (1982).
[66] B. L. HOLIAN, G. K. STRAUB, R. E. SWANSON and D. C. WALLACE: *Phys. Rev. B*, **27**, 2873 (1983).
[67] W. G. HOOVER, M. ROSS, D. HENDERSON, J. A. BARKER and B. C. BROWN: *J. Chem. Phys.*, **52**, 4931 (1970).
[68] W. G. HOOVER, S. G. GRAY and K. W. JOHNSON: *J. Chem. Phys.*, **55**, 1128 (1971).
[69] J. A. BARKER, D. HENDERSON and F. F. ABRAHAM: *Physica (Utrecht) A*, **106**, 226 (1981).
[70] R. E. SWANSON, G. K. STRAUB, B. L. HOLIAN and D. C. WALLACE: *Phys. Rev. B*, **25**, 7807 (1982).
[71] M. P. ALLEN, D. FRENKEL, W. GIGNAC and J. P. MCTAGUE: *J. Chem. Phys.*, **78**, 4206 (1983).
[72] M. ABRAMOWITZ and I. A. STEGUN: *Handbook of Mathematical Functions* (Dover, New York, N. Y., 1970).
[73] M. R. MRUZIK, F. F. ABRAHAM and D. E. SCHREIBER: *J. Chem. Phys.*, **64**, 481 (1976).
[74] G. N. PATEY and J. P. VALLEAU: *J. Chem. Phys.*, **64**, 170 (1976).
[75] M. MEZEI, S. SWAMINATHAN and D. L. BEVERIDGE: *J. Am. Chem. Soc.*, **100**, 3255 (1978).

[76] B. J. ALDER and T. E. WAINWRIGHT: *Phys. Rev.*, **127**, 359 (1962).
[77] S. TOXVAERD and E. PRAESTGAARD: *J. Chem. Phys.*, **67**, 5291 (1977).
[78] Y. HIWATARI, E. STOLL and T. SCHNEIDER: *J. Chem. Phys.*, **68**, 3401 (1978).
[79] A. J. C. LADD and L. V. WOODCOCK: *Mol. Phys.*, **36**, 611 (1978).
[80] A. J. C. LADD and L. V. WOODCOCK: *J. Phys. C*, **11**, 3565 (1978).
[81] J. N. CAPE and L. V. WOODCOCK: *Chem. Phys. Lett.*, **59**, 271 (1978).
[82] A. UEDA, J. TAKADA and Y. HIWATARI: *J. Phys. Soc. Jpn.*, **50**, 307 (1981).
[83] J. P. HANSEN and L. VERLET: *Phys. Rev.*, **84**, 151 (1969).
[84] D. FRENKEL, B. M. MULDER and J. P. MCTAGUE: *Mol. Cryst. Liq. Cryst.*, **123**, 119 (1985).
[85] E. L. POLLOCK and J. P. HANSEN: *Phys. Rev. A*, **8**, 3110 (1973). See also W. L. SLATTERY, G. D. DOOLEN and H. E. DEWITT: *Phys. Rev. A*, **26**, 2255 (1982).
[86] R. C. GANN, S. CHAKRAVARTY and G. V. CHESTER: *Phys. Rev. B*, **20**, 326 (1979).
[87] W. G. HOOVER and F. H. REE: *J. Chem. Phys.*, **47**, 4873 (1967).
[88] W. G. HOOVER and F. H. REE: *J. Chem. Phys.*, **49**, 3609 (1968).
[89] J. P. HANSEN: *Phys. Rev. A*, **2**, 221 (1970).
[90] H. OGURA, H. MATSUDA, T. OGAWA, N. OGITA and A. UEDA: *Prog. Theor. Phys.*, **58**, 419 (1977).
[91] S. TOXVAERD: *J. Chem. Phys.*, **69**, 4750 (1978).
[92] D. FRENKEL and A. J. C. LADD: *J. Chem. Phys.*, **81**, 3188 (1984).
[93] D. FRENKEL: *Phys. Rev. Lett.*, **56**, 858 (1986).
[94] M. L. KLEIN *et al.*: CECAM report, to be published.
[95] W. W. WOOD: *J. Chem. Phys.*, **48**, 415 (1968).
[96] M. PARRINELLO: ISAS preprint 52/84/C.M.
[97] S. NOSÉ: *Mol. Phys.*, **52**, 255 (1984).

Defect Calculations beyond the Harmonic Model.

G. JACUCCI

Centro del Consiglio Nazionale delle Ricerche e
Dipartimento di Fisica dell'Università di Trento - 38050 *Povo, Italia*
Department of Physics and Materials Research Laboratory
University of Illinois at Urbana-Champaign - *Urbana,* IL 61801

1. – Introduction.

Advances in the theory of atomic diffusion in crystals due to thermal generation and migration of point defects rely upon both an accurate knowledge of the interaction potential energy of the crystal as a function of atomic positions and a precise calculation of the consequences of the N-body potential-energy surface on thermodynamic and dynamic properties expressed as thermal averages. In this seminar we shall concentrate on the latter statistical mechanical aspect, and we shall consider model crystals in which atoms of given mass interact by specifically chosen force laws.

The ability of modern electronic computers to handle large dynamical matrices in a reasonably short time has allowed exact treatments of structural relaxation and of vibrational energy and entropy. As a result, theoretical treatments based on equilibrium statistical mechanics and transition state theory have provided the path to the evaluation and comparison with experiments of important factors in solid-state diffusion like defect concentration, jump frequency, isotope effect, all in the harmonic approximation and assuming memory randomization.

However, the effect of anharmonicity on canonical averages and the role of crystal memory in subsequent defect jumps, all phenomena lying beyond the reach of the assumptions and approximations mentioned above, entail fundamental questions as the origin of curvature of Arrhenius plots, high-temperature deviations from rate theory predictions and anomalous isotope effects.

Computer simulation techniques have brought about the conditions for a change of this situation. These methods and their applications to point defects [1, 2] have permitted to precisely assess the shortcomings of the harmonic model and to test the adequacy of analytical treatments of anharmonicity in solid-state diffusion. Perhaps the latter point is the most important outcome

of Monte Carlo and molecular-dynamics studies, *i.e.* the necessity for increased emphasis on the detailed analytical investigation of the N-body potential-energy surface.

2. – Machine calculations on point defects.

Consider a crystal consisting of N interacting atoms disposed either in a regular lattice or in a lattice containing a defect. Place it in contact with a heat bath at a given temperature and pressure. The exact evaluation of the energy, entropy and volume of this system from knowledge of the interaction potential is a formidable computational task even for pair additive forces and $N \sim 100$.

Computer simulation techniques, or, better, should we say machine calculations, like Monte Carlo (MC) and molecular dynamics (MD), have been used extensively to this end for liquids and more recently for high-temperature solids. These sampling techniques are needed to evaluate the $3N$-dimensional configurational integrals related to the desired thermodynamic quantities in classical statistical mechanics. No sufficiently accurate analytical treatment is available for such highly disordered systems.

A quite different case are crystals below the Debye temperature, whether consisting of regular, or defected, lattices. Here the disorder can be subjected to analytical treatment. Terms beyond quadratic in the Taylor expansion of the potential energy in powers at the atomic displacements about static equilibrium configurations can be neglected, the quadratic form diagonalized, and the integrals over normal co-ordinates analytically carried out to obtain precise expressions of the energy, entropy and pressure as a function of temperature and volume. The computational task is reduced to the determination of the crystal static energy Φ and of the vibrational eigenfrequencies ω_α in the relaxed equilibrium configuration, as functions of the crystal volume. This task still requires the solution of an N-body problem. However, it can be carried out on modern machines for N up to ~ 100 using standard computer routines performing function minimization and matrix diagonalization. The results are, of course, affected by zero variance, these procedures being analytical, and not statistical, in character. These calculations are called lattice dynamics (LD).

At temperatures at which atomic diffusion is important, terms beyond quadratic in the expansion of the crystal energy are not negligible. As a result, anharmonic contributions to the thermodynamics of lattice defects are to be expected. Machine calculations of the type mentioned above, *i.e.* MC and MD, are, of course, exact in this respect. They properly include in the results the effect of all features of a given interaction potential. The reason that existing calculations of this kind are so scarce is that point defects contribute

only terms of the order of $1/N$ to the total crystal properties. As a consequence, the sought result is buried in the statistical noise in standard calculations. One must revert to sophisticated, if available, difference techniques. Apart from its use as a means of sampling configuration space to perform thermal averages, the method of MD is the primary tool to investigate in full the dynamics of a classical many-particle system. Trajectories of the representative point of the system in $6N$-dimensional phase space can be generated and analyzed. Jump frequencies can be measured in a simple way, at least when the residence time of the defect is not much longer than a picosecond. The actual path taken in the jump process can be monitored. All questions connected with crystal memory and persistence in the direction of motion of the defect, multiple jumps and anharmonic isotope effects are open to direct observation.

In short, there exist two essentially different ways to exploit the knowledge of the N-body potential-energy surface Φ. One was just mentioned, *i.e.* sampling configurations from a thermal ensemble using the potential energy as statistical weight in MC or MD calculations to evaluate thermal averages related to free energies, and jump frequencies. Alternatively, one can investigate the shape of the surface Φ directly and make use of the information thus gained in the framework of an analytical theory. This is the strategy used in LD. From knowledge of Φ and ω_α at special points, thermodynamic parameters of point defects are calculated with the quasi-harmonic theory of lattice vibrations, and jump frequencies are derived with the help of transition state theory.

One can take the latter point of view and extend the Taylor-expansion approach beyond harmonicity. While the harmonic treatment truncates the Taylor expansion of the energy surface to second order, the third-order terms can be calculated as a next step. Lowest-order anharmonic contributions to the free energy can be evaluated in this way as well as lowest-order dynamical corrections to rate theory in the form of the occurrence of immediate return jumps or deviations from harmonic isotope effects.

3. – LD formula.

Let us lay down the expressions of relevant thermodynamic quantities in LD. The Helmholtz free energy F of a vibrating crystal is expressed in terms of the potential energy Φ_0 and the normal-mode frequencies ω_α calculated at the relevant minimum R_0 in $3N$-dimensional configurational space; it reduces at high temperatures (*i.e.* $h\omega/k_B T \ll 1$) to the classical approximation (see [3])

$$F = \Phi_0 + k_B T \sum_{\alpha}^{3N-3} \ln (h\omega_\alpha/k_B T) . \tag{1}$$

The three translational degrees of freedom of the center of mass have been excluded from the sums. For pair potentials the potential energy is written as

$$\Phi_0 = \sum_{i<j=1}^{N} v(r_{ij}) + \Phi_c\,, \tag{2}$$

the term Φ_c containing the correction due to long-range cut-off of pair contributions excluded from the sum for $r_{ij} > r_c$. The normal-mode frequencies ω_α are simply related to the eigenvalues λ_α of the dynamical matrix $\|\Phi_{lm}\|$:

$$\omega_\alpha = \sqrt{\lambda_\alpha}/m\,, \tag{3}$$

m being the mass of the particles, here taken to be the same for all. Other relevant quantities are the internal energy U, the entropy $S = (U - F)/T$ and the pressure $P = -(\partial F/\partial V)_T$:

$$U = \Phi_0 + 3Nk_B T\,, \tag{4}$$

$$S = -k_B \left\{ \sum^{3N-3} [\ln (\hbar\omega_\alpha/k_B T) - 1] \right\}, \tag{5}$$

$$P = P_\Phi + P_\omega(T) \quad \text{with } P_\Phi = -\frac{\partial \Phi_0}{\partial V} \text{ and } P_\omega(T) = -\left(\frac{\partial(F - \Phi_0)}{\partial V}\right)_T. \tag{6}$$

When allowing for changes of the crystal volume V, the parameters of the quasi-harmonic description, *i.e.* Φ_0 and the ω_α, must change. Otherwise the featureless exactly harmonic description will be recovered, where there is no internal pressure. Given the interaction potential law, Φ_0 and ω_α will be determined for the different equilibrium configurations corresponding to different values of the crystal volume V. And quite naturally they will depend on V. The internal pressure is then fixed by eq. (6).

Thermal volume expansion is automatically included in this description. This is because P from eq. (6) depends on the temperature at a given V. Fixing the value of the external pressure P_{ex} and letting T vary produces the LD equation of state for the crystal, *i.e.* the volume V for which P from eq. (6) equals P_{ex} at a chosen T. The thermal expansion of the crystal volume being one of the effects of anharmonicity of lattice vibrations, LD is also called a quasi-harmonic treatment. It cannot be overemphasized that a thermodynamically consistent implementation of LD requires that, when thermal volume expansion is considered and Φ_0 recalculated at different values of V corresponding to values of T derived from some equation of state (not necessarily the LD one), the variations of ω_α should also be considered, together with the resulting variations of S and P.

We see from eq. (6) that P is the sum of two terms, one coming from

variations of Φ with V, and the other from variations of ω_α with V. The first term is easily treatable analytically, giving the virial expression

$$P_\Phi = -\frac{N}{3V}\sum_{i<j}^{3N-3}\frac{\partial v(r_{ij})}{\partial r_{ij}}r_{ij} + P_c\,, \tag{7}$$

P_c indicating the correction due to long-range cut-off. On the contrary, P_ω is best evaluated numerically using incremental ratios built from recalculations of the ω_α at two closely spaced values of V.

It is important to realize that the virial formula in eq. (7) differs from the usual formula based on the thermal average of the virial sum precisely by the term $P_\omega(T)$:

$$P = -\left(\frac{\partial F}{\partial V}\right)_T = -\frac{N}{3V}\left\langle\sum_{i<j}^{3N-3}\frac{\partial v(r_{ij})}{\partial r_{ij}}r_{ij}\right\rangle_T + P_c = P_\Phi + P_\omega(T)\,. \tag{8}$$

As a result the substitution of the thermal average of the virial sum with the value of the sum calculated in the most probable configuration, *i.e.* the equilibrium configuration R_0, may lead to disastrous results, because it essentially consists in using P_Φ alone disregarding the volume dependence of the ω_α. This is only correct at $T = 0$ and in the classical approximation.

Fixing the volume is a more or less imposed choice in LD. In the static lattice, with thermal vibrations frozen out, the pressure as read by the virial formula does not contain $P_\omega(T)$. This term, of course, can be evaluated separately and added on to get P from eq. (6). A numerical iteration procedure is, however, necessary to precisely determine V at given P_{ex} and T.

4. – Finding extrema.

We have illustrated how LD calculations are based on the determination of the static equilibrium configuration R_0 of the crystal. R_0 is defined at volume fixed. The atomic positions correspond to a fully relaxed configuration, *i.e.* all forces are zero: $\nabla\Phi(R_0) = 0$. In regular crystals having a high degree of symmetry (*e.g.*, s.c., f.c.c., b.c.c.) the configuration R_0 is obvious. In defect formation calculations R_0 denotes also the relaxed configuration of the crystal containing the defect. In defect migration studies, transition state theory requires use of the thermodynamic quantities given by eqs. (1)-(7) evaluated at the saddle point R_s for the $(3N-1)$-dimensional space normal to the eigenvector with negative eigenvalue, *i.e.* obtained by letting the reaction co-ordinate ξ equal zero, in order to estimate the jump frequency. In both cases one needs to locate an extremum of Φ, R_0 or R_s (R_0 being also a minimum). The location of one of these points is done with the help of one of many function minimization

routines applied to $|\nabla\Phi|^2$, or even to Φ itself for R_0, starting the search from guess configurations [4]. The procedure chosen has no relevance to the final result if one makes sure that the right extremum has been exactly determined within the numerical precision available. This is easily checked because, fortunately, the property of an extremum is a local property: $\nabla\Phi(R_0) = 0$. The neighborhoods of R_0 are first attained with routines that converge rather slowly but have a large radius of convergence. Then a few iterations of the extremely fast first-order Taylor expansion of the gradient bring the system exactly at R_0 within the precision of the computer:

$$\Delta\Phi(\boldsymbol{R})\cdot(\boldsymbol{R} - \boldsymbol{R}_0) = \nabla\Phi(\boldsymbol{R}) \; ; \tag{9}$$

this, of course, requires matrix inversion, but the time involved is negligible with respect to that for the matrix diagonalization to follow.

5. – LD for the perfect LJ crystal.

We shall discuss in some detail results of a recent LD study [5] of vacancy formation and migration in a simple model for rare-gas crystals: the Lennard-Jones (6-12) pair potential.

The most striking features of the results refer to the pressure data. Four state points have been chosen on the equation of state of crystalline argon at vapor pressure, *i.e.* $P \ll 1$ in units of ε/σ^3. Therefore, LD values of $|P| \ll 1$ would indicate that

i) the LJ model provides a satisfactory description of the equation of state,

ii) the values of σ and ε employed in converting V and T to reduced units have been chosen satisfactorily,

iii) quantum effects are either small (both $|P|$ and $|P_Q| \ll 1$) or satisfactorily taken into account (only $|P_Q| \ll 1$),

iv) the residual anharmonicity of lattice vibrations, after the volume dependence of the ω_α has been taken into account, contributes only a small term to the free energy of the crystal; this contribution should be small at low T and vanish for $T = 0$ in classical mechanics.

In fact, the results shown that

a) P_Q is quite close to zero at small and intermediate temperatures,

b) P is close to zero only at intermediate temperatures,

c) P_Φ is large and negative everywhere, but much more so at high T.

Observations *a*) and *b*) indicate that points i) and ii) are satisfied, *i.e.* the model is not bad. Furthermore, quantum effects are rather large in argon. They are never really negligible in the pressure, the deviation from the classical value exceeding 0.5 ε/σ^3 below ~ 40 K.

Observation *c*) indicates that the contributions of thermal vibrations to the pressure have a huge effect on the equation of state. We may expect in general that LD calculations neglecting P_ω can meet with disaster at high T.

When the volume dependence of Φ_0 and the ω_α are correctly included in the calculation of the pressure by adding P_Φ and P_ω, much of the anharmonicity of Φ is accounted for in these quasi-harmonic calculations. This can be argued from the fact that the LD equation of state does not depart too much from that of the real crystal. In particular P is less than one-fifth of P_Φ for the state point of argon close to melting.

The residual anharmonicity quoted in iv) is, of course, not taken into account by LD. This fact is most probably causing the positive deviations of P_Q and P from zero that grow towards high T. In fact, these deviations can be taken as a measure of the residual anharmonicity. A direct comparison of LD and MC data on the same model would definitely confirm this interpretation. The comparison indeed exists: it had been carefully carried out by HOLT, HOOVER, GRAY and SHORTLE [6].

From the results reported by HOLT *et al.* [6] we see that the effect of residual anharmonicity is to lower the value of P in MC with respect to P in LD by about -0.17, -0.45 and -0.91 in units of ε/σ^3, at $T \sim 40$ K, 60 K and 80 K, respectively. The deviations of $(U-\Phi_0)/Nk_B T$ from the classical value of 3 in LD are also negative in MC. The measured values of this quantity at the same state point as previously specified are 2.89, 2.85 and 2.79. The effect on the values of U/N is to lower them from -7.49, -6.92 and -6.22 to -7.53, -6.99 and -6.36 in units of ε. If we correct the quantum-mechanical value of P_Q with the deviation $P_{MC}-P_{LD}$ measured by HOLT *et al.* [6], we get the gratifyingly small values of -0.04, $+0.01$ and $+0.06$ at $T \sim 40$ K, 60 K and 80 K, *i.e.* a good description of the argon crystal.

The LD values for the crystal entropy per particle are also a fair estimate of the properties of natural argon. The LD values can be transformed into excess entropies S_e/Nk_B with respect to the classical ideal gas at the same density and temperature. The values obtained for $T \sim 60$ K and 80 K are -5.62 and -4.89, *i.e.* about 0.19 and 0.35 high with respect to experiment for Ar, and 0.29 and 0.43 high for Kr [7]. Note that these LD values do not include the correction term $-\ln(2\pi N)^{\frac{1}{2}} \sim -0.030$ from Stirling's formula. Furthermore, they are probably affected by small crystal corrections of order $(\ln N)/N$.

Whether the observed deviations from experiment are due to the neglect by LD of anharmonic terms can be checked using MC data. RAHMAN and JACUCCI [8] have measured the free-energy difference between the f.c.c. LJ

crystal, at $T \sim 60$ K for Ar, and the corresponding harmonic solid (*i.e.* the LD approximation). MC calculations based on the acceptance ratio method [4] and graphical display gave $(F_{LJ} - F_{LD})/Nk_B T = 0.143 \pm 0.002$ for a 54-particle system. Previously quoted MC energy values gave $(U_{LJ} - U_{LD})/Nk_B T = -0.15$ at this temperature. As a result, we have $(S_{LJ} - S_{LD})/Nk_B = -0.29$, or $S_{LJ}/Nk_B = -5.62 - 0.29 = -5.91$, that compares favorably with the experimental values of -5.81 (Ar) and -5.91 (Kr). (Note that anharmonic contributions lower the energy, but lower the entropy twice as much, so that the effect on the free energy is a net increase.)

6. – LD for the LJ crystal containing a lattice vacancy.

Results for vacancy formation may be obtained by comparing properties relative to the regular-lattice crystal C_0 containing N atoms with those relative to a crystal C_v containing $N-1$ atoms and one vacant site, both systems being subjected to periodic boundary conditions. Extensive properties of the regular lattice must be reduced by the factor $(N-1)/N$ before taking differences, *e.g.*

$$\Delta U = U(N-1, v) - U(N, 0)(N-1)/N\,,$$

$$\Delta S = S(N-1, v) - S(N, 0)(N-1)/N\,;$$

this is because an extra bulk atom results upon forming the vacancy in a lattice.

The vacancy formation process can be investigated in three different thermodynamic conditions: at constant lattice parameter (CL), at constant atomic volume (CΩ), at constant external pressure (CP). In the CΩ calculation the lattice of C_v is squeezed so that its total volume V be reduced by the factor $(N-1)/N$ to leave the atomic volume $\Omega = V/N$ unaltered. In the CP calculation the lattice parameter of C_v is varied until the reading of the pressure coincides with that of C_0. Relevant vacancy parameters are identified as limiting values obtained with these procedures for $N \to \infty$.

We shall now briefly discuss the results of De Lorenzi, Jacucci and Ronchetti [5], perform a thermodynamic check to their internal consistency, and verify quantitatively whether certain approximations often encountered in evaluations of defect properties are indeed acceptable.

As a first observation we note that the formation volume at constant pressure is predicted to be always within about 10% of unity. As a consequence CL values are much closer to CP value than to CΩ ones. The obtained CΩ values are indeed remarkable: $(\Delta S)_\Omega$ is large and negative (see [3]), and $(\Delta U)_L$ decreases roughly linearly with temperature, so that in $\Delta F = \Delta U - T\Delta S$ the temperature variation of the energy and entropy terms cancels to a large extent. CL and CP values for ΔU are much less dependent on T, and ΔS is

much smaller and positive in those cases; as a consequence ΔF is again only moderately dependent on T.

Secondly $(\Delta U)_L$ at $T = 0$ is not too different from $-U/N$. As T increases, however, $-U/N$ decreases, while $(\Delta U)_L$ remains remarkably constant. A similar comparison for $(\Delta F)_L$ and $-F/N$ shows that $-F/N$ increases with temperature, while $(\Delta F)_L$ decreases. In conclusion, the formation energy of the vacancy is not accurately described by the opposite of the energy per particle, relative deviations of about one-third being observed close to the melting temperature.

Thirdly, $(\Delta F)_\Omega$ and $(\Delta G)_P$ are always only a few percent apart. This is a gratifying result and it constitutes the first indication that the thermodynamics of the vacancy formation process are correctly described. It is in fact a general result [3] that in thermodynamic transformations involving volume changes one has that

$$(\Delta F)_\Omega = (\Delta G)_P \tag{10}$$

to order $\Delta V/V$, or $1/N$ in this case. This result conveys the information that energy and entropy changes in the transformations with and without lattice dilatation balance out. Only a thermodynamically consistent description can, therefore, reproduce it.

7. – Test of common approximations.

The basic approximation to be encountered in this type of calculation is the static model, *i.e.* the neglect of entropy and related contribution, resulting from lack of knowledge of the ω_α. The only quantity entering the description is, therefore, Φ_0. However, since the contributions related to entropy are invariably multiplied by the factor T, this description becomes exact at $T = 0$ in classical mechanics, the expected errors growing with T. One simple check of the magnitude of these errors can be performed on the mentioned equality $(\Delta G)_P = (\Delta F)_\Omega$ (to order $1/N$), that can also be written as

$$(\Delta H)_P = (\Delta U)_\Omega + T[(\Delta S)_P - (\Delta S)_\Omega]\,. \tag{11}$$

This relation is particularly useful whenever CΩ calculations are to be preferred, *e.g.* for metals described with the pseudopotential model [9]. $(\Delta U)_\Omega$ is the outcome of these calculations, and $(\Delta H)_P$ is the sought result, being the slope of experimental Arrhenius plots. The neglect of the entropy term in argon at high temperature brings disaster: $(\Delta U)_\Omega$ is only about one-third of $(\Delta H)_P$. It has become customary in these cases to evaluate separately the entropy

term using a value for the thermal-expansion coefficient α_P independently available (often from experiment) and the approximate relation [3, 9]

$$T(\Delta S_P - \Delta S_\Omega) \simeq T\Delta\Omega_P\alpha_P/K_T\,, \tag{12}$$

based on the evaluation of the entropy change upon expansion of the regular lattice C_0. It is indeed found that the estimate of eq. (12) provides the desired value of the entropy difference term within the LD model to order $1/N$. However, in the model argon being investigated MC values of $T\Delta\Omega_P\alpha_P/K_T \equiv P_\omega$ are some 15% lower than LD values at $T \sim 80$ K (see pressure comparisons for the perfect lattice reported above; the discrepancy would be even larger were it not for a partial cancellation of differences in α_P and K_T). As a result, the value of $T(\Delta S_P - \Delta S_\Omega)$ at high temperature predicted in this way is accordingly lower than what it would be using LD consistently.

Another feature of the static approximation is to neglect the entropy-related term P_ω in the pressure. We already noted that the size of this term is by no means negligible for the external pressure of the regular crystal. Let us see what the value is of $(\Delta P_\Phi)_L$ and compare it with the sum $(\Delta P_\Phi)_L + (\Delta P_\omega)_L = (\Delta P)_L$. It is found [5] that $(\Delta P_\Phi)_L$ is 0.0567, 0.0828, 0.1136 at $T \sim 40$ K, 60 K, 80 K, instead of the values of $(\Delta P)_L$ 0.0064, 0.0014, $-$ 0.0182. This means that the formation volume $(\Delta V)_P$ predicted using $(\Delta F_\Phi)_L$, or $(\Delta P_\Phi)_\Omega$, comes out to be much too large. In fact, in the static approximation it is found $(\Delta V)_P = 1.24\Omega$ and 1.50Ω at $T \sim 60$ K and 80 K instead of 1.00, 0.92! Even the sign of the relaxation volume is wrong. This huge discrepancy of the static approximation to $(\Delta V)_P$ from the LD value is probably the most noticeable effect of neglecting P_ω and represents a very important discovery in the work of De Lorenzi *et al.* [5]. Although argon (and its models) is expected to be badly behaved in this respect because of the relatively high value of its Grüneisen parameter, from now on the effect of P_ω on defect properties cannot be disregarded light-heartedly.

The results of the static treatment are thermodynamically consistent only if read at $P_{ex} = P_\Phi$ and $T = 0$, where they are also exact in the classical framework. Values corresponding to different lattice parameters will then refer to different external pressures at $T = 0$. Attempts to interpret the data in terms of different temperatures assuming thermal volume expansion are bound to meet with inconsistencies, because of the neglect of the contribution of S to F, or of $\partial S/\partial V$ to P, or both. For instance, eq. (11) holds exactly at $T = 0$ in the classical static model, with $P \equiv P_\Phi$ given by eq. (7), for any given lattice parameter:

$$(\Delta U)_{P_\Phi} + P_\Phi(\Delta V)_{P_\Phi} = (\Delta U)_\Omega\,. \tag{13}$$

If one now desires to use the same data, obtained from knowledge of Φ_0, Φ_v

and their volume derivatives, to exploit or check eq. (11) in full, *i.e.* at finite temperature T, he must alter both sides to include entropy contributions. In the l.h.s., $P = P_\Phi + P_\omega$ will replace P_Φ throughout, and in the r.h.s. the term $T(\Delta S_P - \Delta S_\Omega)$ will be added. Performing only one of such modifications will, of course, unbalance eq. (13). An approximate treatment consistently neglecting P_ω but properly including S produces $(\Delta F)_\Omega \simeq 8.06$ and $(\Delta G)_P \simeq -1.86$ at $T \simeq 80$ K in complete disregard of eq. (10) and grave prejudice of the stability of the lattice held at constant external pressure!

8. – Comparison with MC results.

The free energy of formation of lattice vacancies in LJ crystals was first measured by SQUIRE and HOOVER [7] using MC and a path integration method. The calculation was repeated by JACUCCI and RONCHETTI [10] using the acceptance ratio method, and has been recently extended to include the evaluation of the formation volume [5]. In these calculations one measures the free energy Δf associated with reversibly removing a particle from a perfect crystal, keeping the lattice parameter constant. The free-energy contribution G/N of reintroducing the particle in the bulk of the system must be accounted for separately. This is commonly done using MC energies and pressures, and experimental excess entropies. Eventually, the excess free energy should also be measured by MC in the model system.

The formation Gibbs free energy is obtained as [5, 7]

$$(\Delta G)_P = \Delta f + G/N\,. \tag{14}$$

The formation volume is evaluated as a finite-difference derivative of Δf with respect to volume.

The LD value of the quantity $(\Delta G)_P - P\Omega$ exceeds the MC one by 6% at 60 K and 10% at 80 K (these deviations double if the term $P\Omega$ is not subtracted). Since the difference in the Helmholtz free energy per particle (~ 0.07 at 60 K, see above) is only one-fifth of this, almost all the large explicit anharmonic contribution to $(\Delta G)_P$ comes from Δf, *i.e.* from the lattice relaxation around the defect. This conclusion is easily checked by a direct comparison of Δf values. The effect of anharmonicity is to lower the free energy of formation, with an increase by a factor ~ 4 of the number of lattice vacancies at 80 K in Ar.

An interesting result of the work of De Lorenzi *et al.* [5] is that the MC value of the formation volume, $\Delta\Omega_P/\Omega = 1.21 \pm 0.05$ for $T \sim (60 \div 80)$ K, is intermediate between LD and LS values, LD being too low, and LS too high, by over 20%.

9. – Vacancy migration: rate theory formulae.

In the limit of classical mechanics rate theory is used to calculate the vacancy jump frequency. Calling S the saddle surface, or « watershed », separating the regions τ and τ' in configuration space corresponding to the defect being located at two neighboring lattice sites, one writes the jump rate as [11]

$$\Gamma = \frac{k_B T}{2\pi} \frac{\int_S \exp[-\Phi/k_B T]\, dS}{\int_\tau \exp[-\Phi/k_B T]\, d\tau} . \tag{15}$$

The integral in the denominator extends over one of the two equivalent regions. In using eq. (15), it is assumed that no memory of previous jumps is kept, so that the equilibrium distribution is established before each jump, and that no recrossings occur, *i.e.* that the surface S is crossed only once during the jump event. In the quasi-harmonic approximation Γ is written as [11]

$$\Gamma_0 = \frac{1}{2\pi} \frac{\prod_\alpha^{3N-3} \omega_\alpha}{\prod_\alpha^{3N-4} \omega_{s\alpha}} \exp[-(\Phi_s - \Phi_v)/k_B T] , \tag{16}$$

where again the center-of-mass motion has been excluded. The $\omega_{s\alpha}$ are the normal-mode frequencies at the saddle point, and $\alpha = 3N - 3$ is the index of the imaginary frequency relative to the reaction co-ordinate, that has been left out from the product at the denominator. In this approximation S is replaced by the hyperplane S_0 tangent to S at the saddle point.

We choose to rewrite eq. (16) as

$$\Gamma_0 = \frac{\bar{\omega}}{2\pi} \exp[\Delta S/k_B] \exp[-\Delta U/k_B T] \tag{17}$$

with

$$(\bar{\omega})^{3N-3} = \prod_\alpha^{3N-3} \omega_\alpha , \qquad \Delta S = k_B \sum_\alpha^{3N-4} \ln \frac{\bar{\omega}}{\omega_{s\alpha}} \qquad \text{and} \qquad \Delta U = \Phi_s - \Phi_v .$$

Values of ΔU, ΔS and $\bar{\omega}$ can be calculated by LD in the quasi-harmonic approximation, as for vacancy formation quantities. Results obtained in the reported investigation [5] are discussed below.

The calculations are done at constant Ω and at constant P. These conditions refer to the saddle point configuration with respect to the equilibrium one, *i.e.* they are chosen to be at values of P and Ω appropriate to the formation of the defect at constant pressure. Building $(\Delta G)_P$ and $(\Delta F)_\Omega$ from ΔU, ΔS and $(\Delta U)_P$, eq. (10) is seen to be again rather well obeyed.

10. – Anharmonic contributions to thermodynamics.

The calculation of Γ in eq. (15) is essentially a free-energy difference problem. It can, therefore, be approached using methods based on sampling of the type encountered earlier for the calculation of the free energy of formation of defects. In fact BENNETT [1] has invented one such method to evaluate Γ. For LJ at $T \sim 60$ K and 80 K he finds $\ln [\Gamma(m\sigma^2/\varepsilon)^{\frac{1}{2}}] = -7.5 \pm 1.0$ and -5.0 ± 0.5. The LD estimates are -9.2 and -6.1, showing a rather large discrepancy between the quasi-harmonic approximation and fully anharmonic rate theory predictions. Because in Bennett's work direct jump frequency measurements were also made and gave the value of -5.3 ± 0.2 for the logarithm of the jump frequency at $T \sim 80$ K, in agreement with his anharmonic rate theory prediction, we conclude that i) rate theory is reliable, while ii) LD evaluations at high temperature may not be. In this case LD predictions are low by a factor anywhere from 2 to 15.

It should be noted that previous evaluations of Γ_0 using lattice statics values of $(\Delta U)_\Omega$ and an effective attack frequency ν^* in the place of the LD factor $(\bar{\omega}/2\pi) \exp [(\Delta S)_\Omega]$ accidentally yielded better agreement with anharmonic jump rates [1]. The LD value for $(\Delta S)_\Omega/k_B$ is larger than unity in modulus and negative in sign. This somewhat unexpected fact lowers the value of the LD prediction for Γ below estimates, thus destroying the apparent agreement between static predictions and dynamical results.

11. – Rapid dynamical events.

While the methods of calculation of defect formation properties are now well in hand, at the present time there is no exact theory of jump rates for defects in model crystals. The theoretical framework for algorithms by which jump rates can be evaluated is still not fully established [12]. The dynamical behavior of migrating defects differs from static properties in that it involves the system memory. Correlations in the positions particles occupy at two successive times cannot be described in terms of single-time distribution functions, like the ones involved in the calculation of free energy and related thermodynamic properties.

Simple theories of the jump process neglect this difficulty. The crystal is assumed to randomize immediately, so that single-time distribution functions can be employed. In Vineyard treatment, for example, the jump rate is evaluated from the total flux through the dividing hypersurface S in configuration space, neglecting dynamical correlation and the possibility of immediate recrossings of S.

Bennett's pioneering computer simulation studies have provided clear

evidence for the existence of dynamical correlation between subsequent jump events, and also of dynamical fluctuations causing multiple crossings of the dividing saddle hyperplane. FLYNN [13] has pointed out that curved « watershed » saddle surfaces provide a mechanism for fast dynamical events: trajectories which are almost parallel to the boundary can cut it twice in rapid succession if the boundary surface is curved.

It can be argued [14] that the crystal randomizes so rapidly that the dynamical consequences of a previous jump exert an appreciable effect only for a fraction of a Debye period. With this assumption, the dynamical events of concern involve relatively small movements of the atoms close to the jumping particle. One is, therefore, led to investigate the possibility of describing correlated dynamical events in terms of analytical properties of the potential-energy function in a diffuse locality about the saddle point.

The notion of an activation barrier and harmonic vibrations, as in Vineyard treatment, is usually a good zeroth-order approximation. One is then faced by the task of taking into account anharmonicities in such a way as to formulate an augmented rate theory (ART) that takes into account rapid dynamical events. The resulting formulation includes short-time memory (SM) [15] effects and it can deal with anharmonicities that cause the saddle surface to become curved. A consequence is that momentum co-ordinates no longer factor out in the ratio of two partition functions expressing the classical rate. These functions retain the form of integrals over phase space

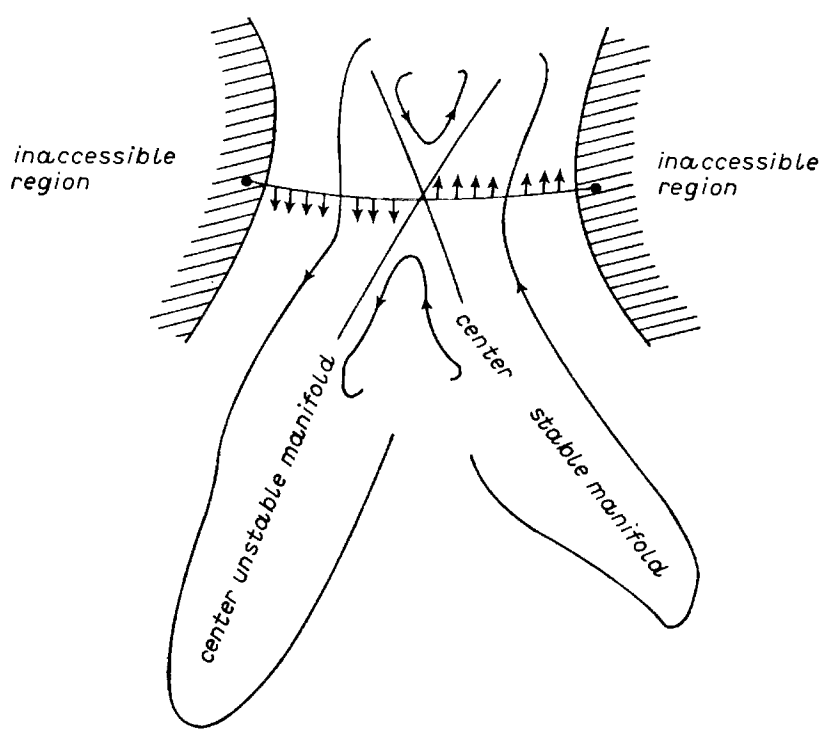

Fig. 1. – Sketch of flow in phase space showing the center stable and unstable manifolds and their intersection at the center manifold. The latter divides the flow field into parts respectively associated with flow in the two alternative senses.

rather than configuration space. This fact is related to the generalization of the jump criterion to take into account the known flow behavior of conservative systems through their trajectories in phase space in the neighborhood of a singular point. It turns out that certain invariant manifolds, used in the discussion of the properties of dynamical systems, constitute the appropriate generalizations of the saddle surface concept in the SM-ART theory (see fig. 1). These are called center manifolds. Dynamically correct predictions within the SM-ART theory have been obtained for model potentials, including up to fourth-order terms in the series expansion in terms of displacements from the saddle point [15]. These new advances show how anharmonicity and phase-space analysis become interrelated concepts in the study of jump rates.

REFERENCES

[1] C. H. Bennett: in *Diffusion in Solids: Recent Developments*, edited by A. S. Nowick and J. J. Burton (Academic Press, New York, N. Y., 1975), Chapt. 2.

[2] G. Jacucci: in *Diffusion in Crystalline Solids*, edited by G. E. Murch and A. S. Nowick (Academic Press, New York, N. Y., 1984), Chapt. 8.

[3] C. P. Flynn: *Point Defects and Diffusion* (Oxford University Press, New York, N. Y., 1972).

[4] C. H. Bennett: *J. Comput. Phys.*, **22**, 245 (1976).

[5] G. De Lorenzi, G. Jacucci and M. Ronchetti: to be published.

[6] A. C. Holt, W. G. Hoover, S. G. Gray and D. R. Shortle: *Physics (N. Y.)*, **49**, 61 (1970).

[7] D. R. Squire and W. G. Hoover: *J. Chem. Phys.*, **50**, 701 (1969).

[8] A. Rahman and G. Jacucci: *Nuovo Cimento D*, **4**, 357 (1984).

[9] G. Jacucci and R. Taylor: *J. Phys. F*, **9**, 1489 (1979).

[10] G. Jacucci and M. Ronchetti: *Solid State Commun.*, **33**, 35 (1980).

[11] G. H. Vineyard: *J. Phys. Chem. Solids*, **3**, 121 (1957).

[12] G. De Lorenzi, C. P. Flynn and G. Jacucci: *Phys. Rev. B*, **30**, 5430 (1984).

[13] C. P. Flynn: *Phys. Rev. Lett.*, **35**, 1721 (1975).

[14] C. P. Flynn and G. Jacucci: *Phys. Rev. B*, **10**, 6225 (1982).

[15] M. Toller, G. Jacucci, G. De Lorenzi and C. P. Flynn: *Phys. Rev. B*, **32**, 2082 (1985).

Molecular-Dynamics Study of Crystal Structure Transformations.

M. PARRINELLO

Dipartimento di Fisica Teorica - Trieste, Italia
International School for Advanced Studies - Trieste, Italy

1. – Introduction.

A major issue in solid-state theory is the study of the mechanical behaviour of solids under various conditions of temperature and stress. At low temperatures traditional solid-state theories, based on the harmonic approximation, give a rather good account of the observed properties. However, a large number of systems are so much affected by anharmonicity that the harmonic approach is bound to fail. Under such circumstances molecular dynamics (MD) is expected to be of invaluable help [1]. Crystal structure transformations are a clear example of a highly anharmonic phenomenon and as such a natural candidate for MD studies. However, until very recently such studies were believed to be impossible. This was a consequence of the periodic boundary conditions (pbc) that in MD one is forced to assume in order to minimize boundary effects. The reason for this difficulty lies in the fact that structural transformations are often associated with changes in the shape of the crystal. Fixed pbc prevent shape fluctuations and inhibit the occurrence of structural changes. If the number of particles is very large, the effect of the boundary becomes irrelevant since, by forming appropriate defects, the system will eventually crystallize in the structure of lowest free energy. However, even with modern computers one is restricted to small systems, especially for complex molecular crystals.

Recently, however, new and powerful techniques have been developed that allow variations in the shape of the MD cell [2] under conditions of constant stress or hydrostatic pressure. The usefulness of this approach has been demonstrated in a large variety of cases, leading to a deeper understanding of the mechanism underlying the transition and of the details of the associated kinetics.

In these notes the theoretical foundations of these new MD methods will be reviewed and several applications will be discussed.

2. – Periodic boundary conditions.

In MD the number of particles that one can simulate is very often rather small; thus it is very important to choose boundary conditions that minimize small-size effects. If one is interested in the study of bulk properties, the most convenient choice is to introduce pbc, which automatically eliminate unwanted surface effects. Pbc are usually implemented as follows. One takes a cubic cell of length L containing N particles. By rigid translations in the three orthogonal directions the cell is repeated so as to fill the whole space. This operation obviously removes to infinity all free surfaces. By construction any particle of co-ordinate r will have an infinite number of images at position $\boldsymbol{r}' = \boldsymbol{r} + \boldsymbol{L}(l, m, n)$, where l, m and n are arbitrary positive or negative integers.

In principle each particle interacts with any other particle in the same cell and with all the other images including its own. Considerable simplifications occur if the range of the forces is smaller than $L/2$, since interactions with the closest images need to be considered. In the case of long-range forces this procedure is not permissible and interactions with all the images are to be taken into account.

From the above discussion it is apparent that in the simulation of bulk properties pbc are an essential ingredient of any MD procedure and cannot be eliminated without introducing undesired spurious effects. As discussed above, pbc are implemented in conventional MD by keeping the size and shape of the MD cell fixed. That serves to maintain the cell of cubic shape and to keep L fixed. This procedure is not of major consequence when dealing with isotropic systems such as liquids. However, the use of a MD cell which is fixed in shape may severely affect the MD study of anisotropic solid systems. This remark can be substantiated as follows.

Let us consider a b.c.c. lattice in a cube whose side is of length a (fig. 1). The plane $ABCD$ perpendicular to a face diagonal is a rectangle of sides a

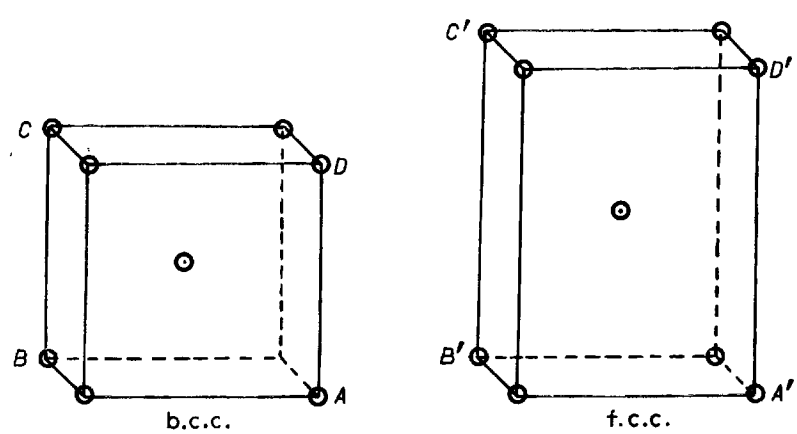

Fig. 1. – Showing the change in the unit cell shape which transforms a b.c.c. into a f.c.c. structure and *vice versa*; see text.

and $\sqrt{2}\,a$. If we stretch the b.c.c. cube along the edge BC so as to make $A'B' = B'C'$, we can easily recognize in the diagonal $A'B'C'D'$ of the tetragonal body-centred cell one of the cubic faces of the f.c.c. lattice. The reverse is also true since by compressing a f.c.c. lattice it is possible to generate a b.c.c. structure. This kind of transformation involves shape changes which are strongly inhibited in standard MD.

3. – Molecular dynamics at constant pressure.

Although the new MD methods can be formulated in a Hamiltonian formalism, it is somewhat more transparent to use a Lagrangian formulation. For future reference we recall here that Newton's equations can be derived from the Lagrangian

$$\mathscr{L} = \sum_{i=1}^{N} \tfrac{1}{2} m_i \dot{\boldsymbol{r}}_i^2 - V(\boldsymbol{r}_1, \ldots, \boldsymbol{r}_N)\,, \tag{1}$$

where $V(\boldsymbol{r}_1, \ldots, \boldsymbol{r}_N)$ is the interaction potential of the N particles of mass m that compose the system. The total energy of the system

$$E = \sum_{i=1}^{N} \tfrac{1}{2} m_i \dot{\boldsymbol{r}}_i^2 + V(\boldsymbol{r}_1, \ldots, \boldsymbol{r}_N) \tag{2}$$

is conserved by the Lagrangian in eq. (1).

If we are dealing with a cubic cell of length L, we can introduce a set of scaled co-ordinates $\boldsymbol{s}_i$, with $0 < s_i^x, s_i^y, s_i^z < 1$ related to the real co-ordinates $\boldsymbol{r}$ by

$$\boldsymbol{r}_i = L\boldsymbol{s}_i = \Omega^{\frac{1}{3}} \boldsymbol{s}_i\,, \tag{3}$$

where $\Omega = L^3$ is the volume of the cell and the image positions are then obtained by letting $\boldsymbol{s}_i \to \boldsymbol{s}_i + (l, m, n)$ in eq. (3). In terms of these scaled co-ordinates $\mathscr{L}$ can obviously be written as

$$\mathscr{L} = \sum_{i=1}^{N} \tfrac{1}{2} m_i (L\dot{\boldsymbol{s}}_i)^2 - V(\boldsymbol{r}_1, \ldots, \boldsymbol{r}_N)\,. \tag{4}$$

Using the fact that $L = \Omega^3$ ANDERSEN [3] has proposed the use of the following Lagrangian to generate the particle trajectories in MD calculations:

$$\mathscr{L} = \sum_{i=1}^{N} \tfrac{1}{2} m_i (\Omega^{\frac{1}{3}}(t)\,\dot{\boldsymbol{s}}_i)^2 - V(\boldsymbol{r}_1, \ldots, \boldsymbol{r}_N) + \tfrac{1}{2} W \dot{\Omega}^2(t) - p\Omega(t)\,, \tag{5}$$

where W is a constant of appropriate units whose role will be discussed later and p the pressure that we want to impose on the system. The important dif-

ference between eqs. (4) and (5) is that in eq. (5) a new dynamical variable, the volume Ω, has been added and two new terms, $(1/2)W\dot{\Omega}^2$ and $p\Omega$, have been introduced. The first is related to the inertial effects associated with the variations in Ω, while the second term gives the familiar thermodynamic work $p\Omega$. As ANDERSEN has shown, the temporal averages over the trajectories generated by the Lagrangian of eq. (5) have a precise statistical mechanical meaning. They are in fact equivalent in the thermodynamical limit to the Gibbs averages in the (H, p, N) ensemble. Namely, an ensemble in which the enthalpy $H = E + p\Omega$, the pressure and the number of particles N are kept constant. This is to be contrasted with ordinary MD where the ensemble generated is of the (E, Ω, N) type. We shall postpone to a following section the discussion of the role of the constant W. ANDERSEN invention of the Lagrangian in eq. (5) has certainly been a major advancement in the field of MD and his seminal paper is at the origin of many recent developments. However, Andersen's Lagrangian allows only volume fluctuations. In order to study crystal structure transformations where shape changes play a major role, further elaboration is needed.

4. – MD with a variable cell.

We generalize here Andersen ideas so as to include the possibility of shape changes. To this end we assume a MD cell which has the form of a generic parallelepiped. We can describe the edges of the parallelepiped by three linearly independent vectors $\boldsymbol{a}$, $\boldsymbol{b}$ and $\boldsymbol{c}$. As in ordinary MD the content of the cell is repeated to fill the whole space. We introduce, as in Andersen case, scaled co-ordinates $\boldsymbol{s}$. However, the relation between real and scaled co-ordinates is more complicated than eq. (3) and reads

$$\boldsymbol{r}_i = \boldsymbol{a}s_i^x + \boldsymbol{b}s_i^y + \boldsymbol{c}s_i^z . \tag{6}$$

Introducing the matrix $\boldsymbol{h} = (\boldsymbol{a}, \boldsymbol{b}, \boldsymbol{c})$ whose columns are in the order the components of the vectors $\boldsymbol{a}$, $\boldsymbol{b}$, $\boldsymbol{c}$, we can rewrite eq. (6) in the compact form

$$\boldsymbol{r}_i = \boldsymbol{h}\boldsymbol{s}_i , \tag{7}$$

which conveniently generalizes eq. (3) whose validity is restricted to isotropic volume fluctuations. The distance between two particles of co-ordinates $\boldsymbol{r}_i = \boldsymbol{h}\boldsymbol{s}_i$ and $\boldsymbol{r}_j = \boldsymbol{h}\boldsymbol{s}_j$ is calculated as

$$(\boldsymbol{r}_i - \boldsymbol{r}_j)^2 = (\boldsymbol{s}_i - \boldsymbol{s}_j)^{\mathrm{T}} \boldsymbol{h}^{\mathrm{T}} \boldsymbol{h}(\boldsymbol{s}_i - \boldsymbol{s}_j) = (\boldsymbol{s}_i - \boldsymbol{s}_j)^{\mathrm{T}} \boldsymbol{G}(\boldsymbol{s}_i - \boldsymbol{s}_j) , \tag{8}$$

where the superscript T denotes the transpose of a tensor or vector and $\boldsymbol{G} = \boldsymbol{h}^{\mathrm{T}}\boldsymbol{h}$ is the metric tensor. The volume of the MD cell is $\Omega = \boldsymbol{a}\cdot(\boldsymbol{b}\wedge\boldsymbol{c}) = \det \boldsymbol{h}$ and

the reciprocal space is spanned by the vectors

$$\boldsymbol{k}_1 = \frac{2\pi}{\Omega}(\boldsymbol{b}\wedge\boldsymbol{c}), \quad \boldsymbol{k}_2 = \frac{2\pi}{\Omega}(\boldsymbol{c}\wedge\boldsymbol{a}), \quad \boldsymbol{k}_3 = \frac{2\pi}{\Omega}(\boldsymbol{b}\wedge\boldsymbol{c}). \tag{9}$$

The matrix $\boldsymbol{\sigma} = (\boldsymbol{b}\wedge\boldsymbol{c}, \boldsymbol{c}\wedge\boldsymbol{a}, \boldsymbol{a}\wedge\boldsymbol{b})$ describes the size and orientation of the MD cell faces. Since we want the MD cell to vary in time, we have to prescribe an appropriate law for the change in time of the $\boldsymbol{h}$ matrix. This is obtained from the following Lagrangian:

$$\mathscr{L} = \tfrac{1}{2}\sum_{i=1}^{N} m_i(\dot{\boldsymbol{s}}_i^{\mathrm{T}}\boldsymbol{G}\dot{\boldsymbol{s}}_i) - V(\boldsymbol{r}_1, \ldots, \boldsymbol{r}_N) + \tfrac{1}{2}W\,\mathrm{Tr}\,\dot{\boldsymbol{h}}^{\mathrm{T}}\dot{\boldsymbol{h}} - p\Omega. \tag{10}$$

The constant W has the dimension of a mass and p is the pressure that we want to impose on the system. Whether such a Lagrangian can be derived from first principles is a question for further investigation. Its validity, at present, can be judged only from the physical meaning of the equations of motion it generates and from its connection to some well-defined statistical mechanical ensembles.

The equations of motion that result from the Lagrangian in eq. (10) are

$$\frac{\mathrm{d}\boldsymbol{p}_i}{\mathrm{d}t} = \boldsymbol{F}_i - \boldsymbol{h}^{\mathrm{T}^{-1}}\dot{\boldsymbol{h}}^{\mathrm{T}}\boldsymbol{p}_i, \tag{11}$$

$$W\ddot{\boldsymbol{h}} = (\boldsymbol{\pi} - p)\boldsymbol{\sigma}, \tag{12}$$

where, using the dyadic notation,

$$\boldsymbol{p}_i = m_i\boldsymbol{h}\dot{\boldsymbol{s}}_i, \tag{13}$$

$$\boldsymbol{F}_i = -\frac{\partial V(\boldsymbol{r}_1, \ldots, \boldsymbol{r}_N)}{\partial \boldsymbol{r}_i}, \tag{14}$$

$$\Omega\boldsymbol{\pi} = \sum_{i=1}^{N}\left(\frac{\boldsymbol{p}_i\otimes\boldsymbol{p}_i}{m_i} + \boldsymbol{r}_i\otimes\boldsymbol{F}_i\right). \tag{15}$$

Interpreting $\boldsymbol{p}_i$ as the momentum of particle i, it follows that $\boldsymbol{\pi}$ is the internal stress tensor. Thus the physical content of eq. (12) is that the time variation of $\boldsymbol{h}$ is determined by the imbalance between the externally applied pressure and the instantaneous value of the internal stress, this imbalance acts across the faces $\boldsymbol{\sigma}$ of the MD cell.

As to the meaning of eq. (11), we note first that it reduces to the ordinary Newton's equations in the case of fixed boundary conditions, $\boldsymbol{h} = \text{const}$. If $\dot{\boldsymbol{h}} \neq 0$, we can interpret $\boldsymbol{h}^{\mathrm{T}^{-1}}\dot{\boldsymbol{h}}^{\mathrm{T}}$ as the strain rate tensor and eq. (11) becomes identical to the equations given by HOOVER *et al.* [4] in order to describe the

effect of an imposed strain rate. However, in the approach of these authors the strain rate tensor is made to vary in a preassigned fashion. Instead here we let it vary so as to establish the equilibrium between external pressure and internal stress.

The case discussed by ANDERSEN is that of a cubic MD cell that fluctuates in volume but not in shape. In such a case,

$$h_{ij} = \delta_{ij}\Omega^{\frac{1}{3}} . \tag{16}$$

Inserting this expression into eq. (11) and eq. (12), we find that the first reduces to the corresponding equation given by ANDERSEN, while the second does not. RAY [5] has proposed to modify the kinetic term $\frac{1}{2}W \operatorname{Tr} \dot{\boldsymbol{h}}^{\mathrm{T}} \dot{\boldsymbol{h}}$ into $\frac{1}{2}W \operatorname{Tr} \dot{\boldsymbol{h}}^{\mathrm{T}} \boldsymbol{G}^2 \dot{\boldsymbol{h}}$. With this modification the equation of motion for $\boldsymbol{h}$ reduces to that of Andersen in the isotropic limit $\boldsymbol{h}_{ij} = \delta_{ij}\Omega^{\frac{1}{3}}$. However, in the general anisotropic case the physical interpretation of Ray's equation for $\boldsymbol{h}$ does not appear to be simple.

A conserved quantity for $\mathscr{L}$ is

$$\mathscr{H} = \sum_i \frac{\boldsymbol{p}_i^2}{2m_i} + V(\boldsymbol{r}_1, \ldots, \boldsymbol{r}_N) + p\Omega + \frac{1}{2} W \operatorname{Tr} \dot{\boldsymbol{h}}^{\mathrm{T}} \dot{\boldsymbol{h}} . \tag{17}$$

This is but for the last term the enthalphy of the system:

$$H = E + p\Omega . \tag{18}$$

At equilibrium

$$\langle \mathscr{H} \rangle = \langle H \rangle + \tfrac{1}{2} W \langle \operatorname{Tr} \dot{\boldsymbol{h}}^{\mathrm{T}} \dot{\boldsymbol{h}} \rangle = \langle H \rangle + \tfrac{9}{2} k_{\mathrm{B}} T . \tag{19}$$

For large N, $9k_{\mathrm{B}}T/2$ is negligible as compared to $\langle H \rangle$, whose leading term grows as N. Thus to order $1/N$ the entalpy is a conserved quantity. This point can be refined along lines parallel to those of Andersen and one can show that the Lagrangian in eq. (10) leads to a (H, p, N) ensemble.

Finally it is worth dwelling on the choice of W, which in the present scheme plays the role of a mass. As such the values of W have no influence on the evaluation of static properties, since in a classical system the equilibrium properties do not depend on the mass of the constituents. In contrast W will play a relevant role in determining the dynamical properties of the system. ANDERSEN has provided a physically attractive criterion for the choice of W. One can imagine that the MD cell is a portion of a much larger system. The relaxation time τ of the volume of this small subsystem when disturbed by local imbalances in the pressure is of the order of $\tau \sim L/c$, where c is the sound velocity. By properly tuning W it is possible to obtain a relaxation time of the MD cell which is close to τ. This choice of W clearly adds an element of

realism to the MD experiment and makes the calculation of dynamical properties meaningful.

From a slightly different point of view one can estimate the frequency of vibration of the MD cell linearizing eq. (12). This leads to the estimate for the period of isotropic oscillations $(4\pi^2\chi W/3L)^{\frac{1}{2}}$, where χ is the compressibility of the system. Equating this estimate to the time needed for a sound wave to cross the cell, L/c, one is led to the prescription $W = 3\sum_i m_i/4\pi^2$. However, explicit calculations have shown that some dynamical properties are not greatly affected by the choice of W, provided that W is varied within reasonable limits.

5. – MD at constant external stress.

The formulation of MD presented in the previous section lends itself naturally to the introduction of nonisotropic external stress [6]. In fact, in the theory of elasticity [7] the notion of strain is connected to the variations of the metric tensor and $\boldsymbol{G}$ is a natural constituent of the present MD scheme.

In order to make this remark practicable, we have to introduce a reference state relative to which the strain is defined. In the language introduced in the previous section this can be described in terms of its matrix $\boldsymbol{h}_0$ and volume $\Omega_0 = \det \boldsymbol{h}_0$. In this reference state a point in space of scaled co-ordinate $\boldsymbol{s}_0$ is in real space at the position

$$\boldsymbol{r}_0 = \boldsymbol{h}\boldsymbol{s}_0 . \tag{20}$$

Homogeneous distortion of the system changes $\boldsymbol{h}_0$ to $\boldsymbol{h}$ and $\boldsymbol{r}_0$ to $\boldsymbol{r}$ with

$$\boldsymbol{r} = \boldsymbol{h}\boldsymbol{s}_0 = \boldsymbol{h}\boldsymbol{h}_0^{-1}\boldsymbol{r}_0 \tag{21}$$

producing a displacement

$$\boldsymbol{u} = \boldsymbol{r} - \boldsymbol{r}_0 = (\boldsymbol{h} - \boldsymbol{h}_0)\boldsymbol{h}_0^{-1}\boldsymbol{r}_0 . \tag{22}$$

Connection to the strain tensor is made through [7]

$$\varepsilon_{\lambda\mu} = \frac{1}{2}\left(\frac{\partial u_\lambda}{\partial x_\mu} + \frac{\partial u_\mu}{\partial x_\lambda} + \sum_\nu \frac{\partial u_\nu}{\partial x_\mu}\frac{\partial u_\nu}{\partial x_\lambda}\right), \tag{23}$$

where x_λ is the λ component of $\boldsymbol{r}$. Inserting eq. (22) into eq. (23), we find

$$\boldsymbol{\varepsilon} = \tfrac{1}{2}(\boldsymbol{h}_0^{\mathrm{T}^{-1}}\boldsymbol{G}\boldsymbol{h}_0^{-1} - 1) . \tag{24}$$

Having identified the strain, we write for the elastic energy the expression

$$V_{el} = p(\Omega - \Omega_0) - \Omega_0 \operatorname{Tr} (\boldsymbol{S} + p)\boldsymbol{\varepsilon}\,, \tag{25}$$

where $\boldsymbol{S}$ is the external stress. In the case of an isotropic stress p,

$$S_{ij} = -\,\delta_{ij} p \tag{26}$$

and

$$V_{el} = p(\Omega - \Omega_0)\,, \tag{27}$$

which differs from the $p\Omega$ term introduced in eq. (4) by an inessential constant term $p\Omega_0$.

In the limit of small strain,

$$\operatorname{Tr} \boldsymbol{\varepsilon} = (\Omega - \Omega_0)/\Omega_0 \tag{28}$$

and eq. (25) reduces to

$$V_{el} = -\,\Omega_0 \operatorname{Tr} \boldsymbol{S}\boldsymbol{\varepsilon}\,, \tag{29}$$

which is commonly employed in the theory of infinitesimal elasticity.

Next step is to replace $p\Omega$ in eq. (10) by the more general expression in eq. (25). This leads, dropping inessential constants and using the invariance of the trace to cyclical permutations, to a new Lagrangian

$$\mathscr{L}_s = \mathscr{L} - \tfrac{1}{2} \operatorname{Tr} \boldsymbol{\Sigma}\boldsymbol{G}\,, \tag{30}$$

where $\boldsymbol{\Sigma}$ is a symmetric tensor related to the stress by

$$\boldsymbol{\Sigma} = \boldsymbol{h}_0^{-1}(\boldsymbol{S} + p)\,\boldsymbol{h}_0^{\mathrm{T}^{-1}}\Omega_0\,. \tag{31}$$

Using $\mathscr{L}_s$, we find that eq. (11) remains inaltered but eq. (12) is modified as follows:

$$W\ddot{\boldsymbol{h}} = (\boldsymbol{\pi} - p)\boldsymbol{\sigma} - \boldsymbol{h}\boldsymbol{\Sigma}\,. \tag{32}$$

It can be easily proved [8] that the statistical mechanical ensemble generated by $\mathscr{L}_s$ is a $(H, \boldsymbol{S}, N)$ ensemble where

$$H_s = E + V_{el} \tag{33}$$

conveniently generalizes the notion of enthalpy.

In the above discussion it has been assumed that the external stress is so small that the theory of infinitesimal elasticity can be safely applied. This

can be done in many cases; however, if the deformations are large, the theory of finite elasticity has to be used; for a discussion of this point we refer the reader to ref. [6].

6. – Applications of the new MD.

Before going into the details it will be useful to illustrate with a simple example the role played by changes in shape of the repeating MD cell in permitting or inhibiting a structural phase transition.

In one of the first applications of the method a system of 500 atoms was arranged to form a f.c.c. lattice in a cubic MD cell. The interaction potential was taken as the one suitable for the study of atomic motions in rubidium metal [9]. Under the action of the new Lagrangian the MD cell spontaneously evolved from a cube into a shape that, within small fluctuations, was a parallelepiped with edges in the ratio $\sqrt{2}:\sqrt{2}:1$. Microscopic analysis of the particle positions showed that the pair correlation which at the beginning of the calculation had, by construction, a f.c.c. character with a co-ordination number of 12 became in the final stable state b.c.c.-like with a co-ordination number of 14; this co-ordination occurs because the first co-ordination shell of 8 and the second of 6 remain unresolved at the ambient temperature. (See ref. [2] for details.) This result, that a potential suitable for the study of rubidium favours the b.c.c. and not the f.c.c. structure, is in agreement with the experimental fact that Rb crystallizes as a b.c.c. structure.

Since that first application [2] several other structural phase transitions have been studied in greater detail.

6·1. *Polymorphic transition in* KCl *under applied hydrostatic pressure.* – The study of the transition from the NaCl into the CsCl structure that occurs in most of the alkali halides has attracted considerable attention in the past [10] and it is still a subject of considerable interest.

Recently BOYER [11] has made extensive calculations of the critical pressure for the rocksalt to CsCl structural transition using the harmonic approximation. Clearly, the MD methods described above go beyond the harmonic approximation and can give considerable insight into the kinetics of the transformation; this is an aspect of the transition which, at the microscopic level, cannot be investigated by other means. For this reason we have started a series of calculations on the KCl polymorphic transition. We present here only one of the many calculations performed [12].

A rocksalt KCl system of 500 ions was equilibrated at zero pressure and 300 K. The pressure was then suddenly increased to 44 kb within one MD integration step. The resulting changes in temperature and density are depicted in fig. 2.

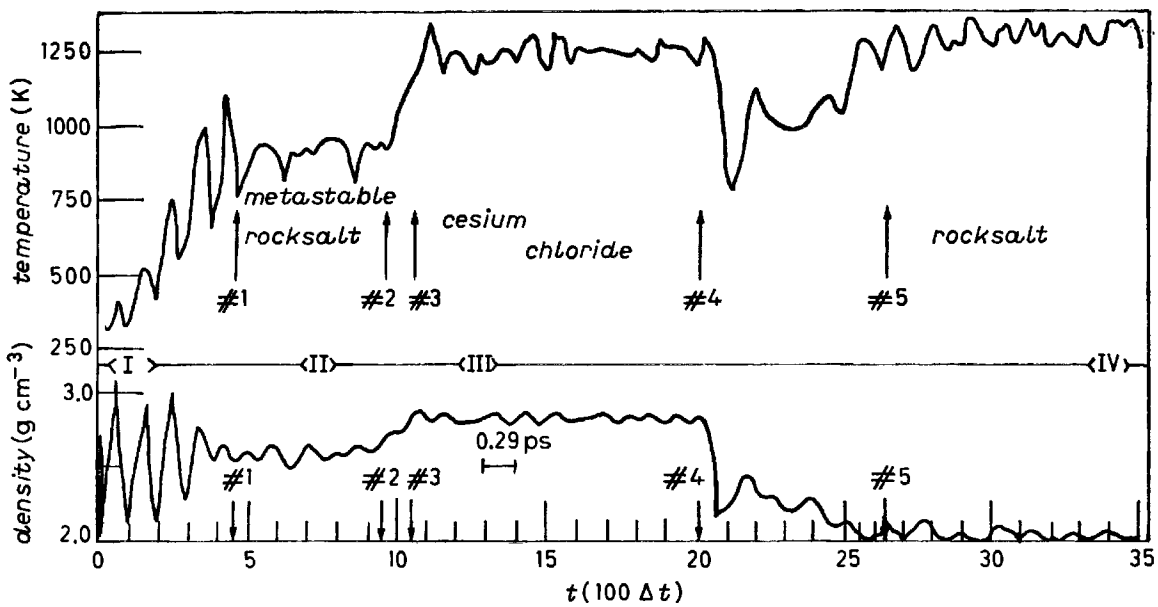

Fig. 2. – Time history of a compression and decompression molecular-dynamics run on KCl. Points plotted are 25 Δt apart, hence the nonsmooth appearance. In regions I to IV the pair correlations were monitored; these have not been shown in this lecture. Significance of the numbered vertical arrows is discussed in the text.

One can observe that in about 1.3 ps the system acquires a new state at 925 K and 2.6 g/cm³. This turns out to be a metastable state that lasts for 1.5 ps; this is marked in fig. 2 by arrows #2 and #1. After a short interval of rapid changes, between arrows # 2 and # 3, the system acquires a final equilibrium state which was analysed in a variety of ways to investigate the internal structure. The analysis of the pair correlations in the time intervals indicated by Roman numerals II and III showed that during interval II the system was rocksalt and it was CsCl during interval III. At the time indicated by arrow # 4 the pressure was dropped to zero. This caused new changes in the system between arrows # 4 and # 5. At the end of this process a new equilibrium state was reached. This final state is again a rocksalt structure although at a much higher temperature than the original one.

A novel feature of this calculation is the light it sheds on the manner in which the rocksalt structure transforms into a CsCl one. This is illustrated in fig. 3; diagram marked A shows a body-centred tetragonal lattice of lattice vectors $\boldsymbol{a}$, $\boldsymbol{b}$, $\boldsymbol{c}$ of lengths a, a, $\sqrt{2}a$. The atoms of one sublattice are indicated by ●; they form a f.c.c. lattice. The other species shown by ∘ completes the rocksalt structure. The transformation can be depicted as having occurred in two steps.

Step 1 is a uniform dilatation of amount $\sqrt{2}$ in the direction of $\boldsymbol{a}$ making $a' = \sqrt{2}\,a$. This is indicated by the thick arrow on the left of diagram A. This dilatation makes diagram A change into B which consists of a body-centred tetragonal structure of each of the two species.

Step 2 is a translation of amount $a/2$, shown as thin arrows in diagram B, of particles situated in alternate planes perpendicular to the c direction. This gives the final result shown in diagram C of fig. 3.

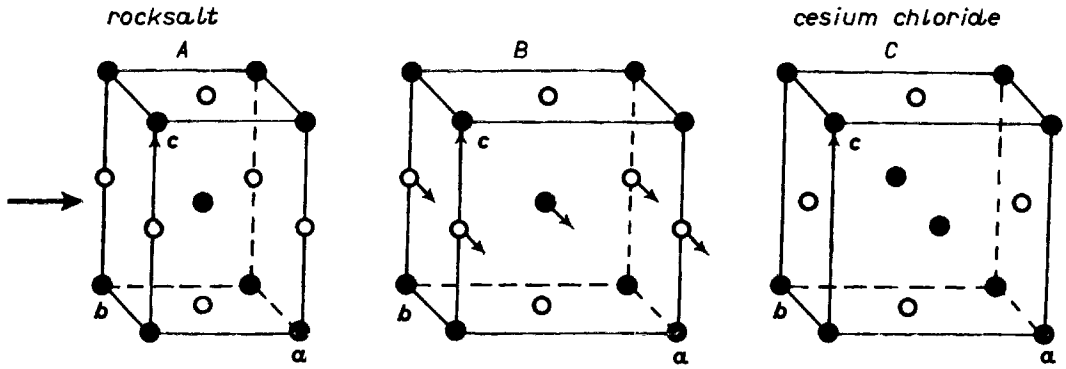

Fig. 3. – Detail of rocksalt to cesium chloride change found to occur in the MD calculation. Thick arrow in A indicates a dilatation resulting in B. Fine arrows in B indicate displacements of particles with a common c direction co-ordinate, resulting in the final structure C. A is rocksalt, C is cesium chloride (see text).

An examination of diagram C of fig. 3 shows that the like ions form simple cubic structures. The two put together form a CsCl structure.

The geometrical description, of course, does *not* imply that the above are two distinct temporal events during the polymorphic transition.

This description of the transition is at variance with previous speculations in the literature [13]. For more details see ref. [10].

6·2. *Superionic* AgI. – Superionic conductors have attracted considerable attention in recent years [14] and have provided a challenging field of application for MD methods. A prototype superionic conductor is AgI. A detailed study of AgI with the new MD methods has given many interesting results. These will be given elsewhere [15]. Here we shall only give a brief summary.

AgI has a rather complicated phase diagram as a function of temperature and pressure. At low temperature AgI has the zincblende structure, *i.e.* I^- forms a f.c.c. lattice and the cations are tetrahedrally co-ordinated to I^-. The low-temperature phase is called the γ-phase. As the temperature is raised, there is a transformation from γ to β phase which has the Wurtzite structure in which I^- is an h.c.p. lattice and the cations continue to be tetrahedrally co-ordinated to I^-. In the laboratory the α and β phases are invariably found to be mixed together.

In AgI at 420 K there is a crystal structure transformation to the α-phase; this transition is characterized by a sudden increase in the d.c. conductivity; the conductivity is a consequence of large Ag^+ mobility. In α-AgI the I^- form instead a b.c.c. lattice. Even though the Ag^+ are mobile, the Ag^+-I^- still maintain a co-ordination of four.

Another interesting feature of the AgI phase diagram is that an increase in the external pressure transforms α-AgI into a rocksalt structure.

In the MD calculation [15] the pair interaction potentials are taken to be of the form

$$\varphi_{ij} = A_{ij}(\sigma_i + \sigma_j)^{n_{ij}}/r^{n_{ij}} + z_i z_j e^2/r - \tfrac{1}{2}(\alpha_i z_j^2 + \alpha_j z_i^2)/r^2 - w_{ij}/r^6 , \tag{34}$$

where α_i are the electronic polarizabilities. A choice of parameters that reproduces the properties of the low-temperature phase of AgI is

$$\begin{cases} \varphi_{AgAg}(r) = H_{AgAg}/r^{11} + 0.36/r , \\ \varphi_{AgI}(r) \;\; = H_{AgI}/r^9 - 0.36/r - 1.1736/r^4 , \\ \varphi_{II}(r) \;\; = H_{II}/r^7 + 0.36/r - 2.3472/r^4 - 6.9331/r^6 , \end{cases} \tag{35}$$

where

$$\begin{cases} H_{AgAg} = A(\sigma_{Ag} + \sigma_{Ag})^{11} = 0.014\,804 , \\ H_{AgI} \;\; = A(\sigma_{Ag} + \sigma_{I})^9 = 114.48 , \\ H_{II} \;\; = A(\sigma_{I} + \sigma_{I})^7 = 446.64 , \\ A \;\; = 0.010\,248 . \end{cases} \tag{36}$$

The lengths are measured in A and the energy in $e^2/A = 14.39$ eV.

The starting point of the calculations was an α-AgI configuration with 500 ions in a cubic MD cell at $T = 700$ K. For a calculation extending over $5 \cdot 10^{-11}$ s (2500 integration steps of MD) we found a system with normal α-AgI-like behaviour [16]. The I^- form a stable b.c.c. lattice with an apparent n.n. co-ordination of 14. The Ag^+ show a high mobility with a constant of self-diffusion $D_{Ag} = 4 \cdot 10^{-5}$ cm^2 s^{-1}. The pair correlation function for Ag^+-I^- shows a n.n. co-ordination of 4.

At this point the well-equilibrated α-AgI system at 700 K was rapidly cooled down to 350 K; in the standard fashion structural and dynamical behaviour of I^- and Ag^+ was monitored in the course of the calculation.

Only 1000 steps ($2 \cdot 10^{-11}$ s) after quenching it became clear than the shape of the MD cell was starting to get modified; in addition, the n.n. (I^--I^-) co-ordination was changing from 14 to 12 neighbours indicating a change in the I^- lattice from b.c.c. to a close-packed structure (f.c.c. or h.c.p.). At the same time the n.n. (Ag^+-I^-) co-ordination remained constant at 4. The system was observed for additional 2500 time steps ($5 \cdot 10^{-11}$ s) and no further changes in the co-ordinations occurred. The diffusion constants of Ag^+ and I^- became zero indicating a transition to a nonsuperionic state. In order to discriminate between the zincblende and the Wurtzite structure, an analysis of the (I^--I^-) pair correlation beyond the n.n. co-ordination shell was needed. The detailed de-

scription of the shape of the MD cell and of the pair correlations is given in ref. [17]. The conclusion was inescapable that indeed the system had transformed from α-AgI into the nonconducting β-AgI polymorph with a Wurtzite structure.

By heating the β-AgI thus obtained to 495 K further transformations occurred and after equilibration an analysis of the pair correlations and of the diffusive behaviour of the Ag^+ ions showed that the system had reverted back to the α-AgI conducting polymorph. With repeated MD calculations several $\alpha \to \beta$ and $\beta \to \alpha$ transformations were obtained. Using the temperatures at which these runs were made it was concluded that the transition temperature for $\alpha \to \beta$, in our model, lies between 472 K and 495 K. This is in satisfactory agreement with the experimental value of 420 K.

6·3. Ni *under uniaxial* [100] *stress*. – Recently a theoretical study has been made of the behaviour of a model of Ni under conditions of uniform externally applied stress [18]. In this calculation the pairwise Ni interaction potential was taken to be

$$\varphi(r) = D\{\exp[-2\alpha(r - r_0)] - 2\exp[-\alpha(r - r_0)]\}\,, \tag{37}$$

where the constants D, α, r_0 were fixed by a fit to the elastic constants and to the lattice spacing a_0 of f.c.c. Ni [19]. The calculation was made assuming initially a perfect f.c.c. lattice. The system was then allowed to deform under the action of a uniform tensile and compressive [100] load [18]. However, only homogeneous orthorhombic distortions were considered and thermal vibrations were not permitted.

From the point of view of the present discussion the most relevant conclusions of these static calculations [18] were as follows.

In traction a rather unusual behaviour was predicted. For small deformations the stress-strain relation was of the normal kind; the three edges of the cell a_1, a_2, a_3, which under zero stress were all equal $a_1 = a_2 = a_3 = a_0$, became $a_1 > a_2 = a_3$, where 1 is the direction of the tensile load. However, at a certain value of the deformation a bifurcation point was reached in the stress-strain diagram; beyond this point, *i.e.* on the new branch emanating at that point, the tetragonal symmetry was broken with $a_1 > a_2 > a_3$; along the new stress-strain path, starting at the bifurcation point, with further decrease in the tensile load a_2 increased and rapidly enough to catch up with a_1 and eventually at zero load satisfied $a_1 = a_2 = \sqrt{2}\,a_3$, which is a b.c.c. state.

Under compression no unexpected behaviour was predicted. First the system deformed elastically with $a_1 < a_2 = a_3$; beyond a certain compressive load it became mechanically unstable.

The MD method presented here clearly provides the means of checking the validity of these results once the restricting hypotheses of zero temperature and of allowing only a limited range of crystal deformations are lifted [6]. The

results of our calculations made at a temperature of 350 K were in complete agreement with the predictions of ref. [18], in the region of stress where a normal elastic behaviour was predicted, but differed considerably elsewhere. These findings are described briefly below.

Under tensile load our calculations showed that the system breaks down before the bifurcation point predicted on the basis of static calculations is reached. The mechanical failure appears in our calculation as an unbounded increase of the MD cell edge in the direction of loading, with a sharp decrease in density to nonsolidlike values and a breakdown of the crystalline order. Any attempt to produce an orthorhombic lattice which occurs in static calculations failed because the system spontaneously evolved into a tetragonal state or failed if the applied tensile stress was too large.

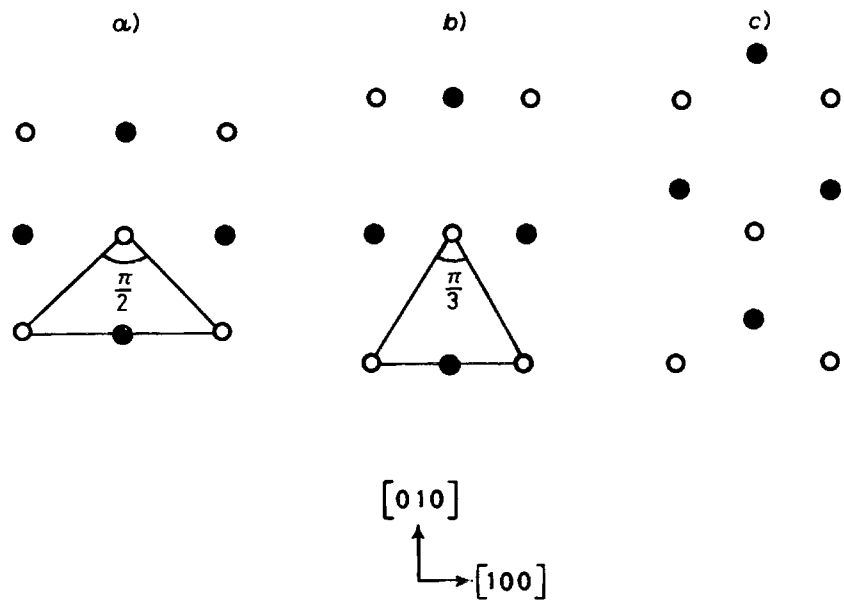

Fig. 4. – Two planes of a f.c.c. structure perpendicular to [001] are shown by ○ and ●, respectively. *a*)-*b*) shows how the face-centred square structure changes to a triangular lattice on suitable compression in the [100] direction. *b*)-*c*) shows the necessary translation of the ● planes to achieve h.c.p. ordering. At the same time spacing between ○ and ● planes has to correspond to the « c/a » value of an h.c.p. arrangement, namely $\sqrt{8/3}$.

The behaviour of the system under a compressive load showed unexpected and interesting features. At small value of the load the behaviour was elastic and in agreement with ref. [18]. However, when the limit of mechanical instability predicted in ref. [18] was approached, the crystalline arrangement changed spontaneously from f.c.c. to h.c.p. The path in configuration space that provides the link between the two crystalline arrangements is illustrated in fig. 4. For clarity it can be described as having occurred as a two-step process. In the first step the [100] square centred planes of the original f.c.c. lattice became rectangles whose edges were in the ratio $\sqrt{3}:1$; this is necessary to

obtain a hexagonal arrangement of particles in these planes. In the second step alternate planes were shifted in the direction of the long edge of the rectangle mentioned above in order to obtain the proper h.c.p. stacking, while at the same time the distance between successive planes took on the appropriate value corresponding to the « c/a » of an h.c.p. structure.

REFERENCES

[1] E. R. Cowley, G. Jacucci, M. L. Klein and I. R. McDonald: *Phys. Rev. B*, **14**, 1758 (1976).
[2] M. Parrinello and A. Rahman: *Phys. Rev. Lett.*, **45**, 1196 (1958).
[3] H. C. Andersen: *J. Chem. Phys.*, **72**, 2384 (1980).
[4] W. G. Hoover, D. J. Evans, R. B. Hickman, A. J. C. Ladd, W. T. Ashurst and B. Moran: *Phys. Rev. A*, **22**, 1690 (1980).
[5] J. R. Ray: *J. Chem. Phys.*, **79**, 5128 (1983).
[6] M. Parrinello and A. Rahman: *J. Appl. Phys.*, **52**, 7158 (1981).
[7] L. D. Landau and E. M. Lifshitz: *Theory of Elasticity* (Pergamon Press, Oxford, 1959).
[8] J. R. Ray and A. Rahman: *J. Chem. Phys.*, **80**, 4423 (1984).
[9] D. L. Price: *Phys. Rev. A*, **4**, 358 (1971); D. L. Price, K. S. Singwi and M. P. Tosi: *Phys. Rev. B*, **2**, 2983 (1970).
[10] M. P. Tosi and T. Arai: in *Advances in High Pressure Research*, Vol. **1**, edited by R. S. Bradley (Academic Press, New York, N. Y., 1966).
[11] L. L. Boyer: *Phys. Rev. B*, **23**, 3673 (1981).
[12] M. Parrinello and A. Rahman: *J. Phys. (Paris)*, *C***6**, 511 (1981).
[13] M. J. Buerger: in *Phase Transformations of Solids*, edited by R. Smoluchowski, J. E. Meyer and W. A. Weyl (John Wiley, New York, N. Y., 1951), p. 183.
[14] P. Vashishta, J. N. Mundy and G. K. Shenoy, Editors: *Fast Ion Transport in Solids* (Elsevier North-Holland, New York, N. Y., 1979).
[15] M. Parrinello, A. Rahman and P. Vashishta: *Phys. Rev. Lett.*, **50**, 1073 (1983).
[16] P. Vashishta and A. Rahman: *Phys. Rev. Lett.*, **40**, 1337 (1978).
[17] A. Rahman and P. Vashishta: in *The Physics of Superionic Conductors and Electrode Materials*, edited by J. W. Perram (Plenum Press, New York, N. Y., 1980).
[18] F. Milstein and B. Farber: *Phys. Rev. Lett.*, **44**, 277 (1980).
[19] F. Milstein: *J. Appl. Phys.*, **44**, 3825 (1973).

Part IV

NONEQUILIBRIUM MOLECULAR DYNAMICS, KINETIC THEORY AND RIGOROUS RESULTS

Nonequilibrium Molecular Dynamics.

DENIS J. EVANS

Research School of Chemistry, Australian National University
G.P.O. Box 4, Canberra, A.C.T. 2601, Australia

1. – Introduction.

In this short course of lectures we aim to provide a pedagogical introduction to the theory of nonequilibrium molecular dynamics. Thus the emphasis will lie with the physical justification of algorithms rather than with either an examination of numerical analysis or the particular results that have been obtained for the multitude of systems which have been studied to date [1]. We hope that, after reading these lecture notes, the reader will be able to understand the design of any of the commonly used nonequilibrium molecular-dynamics (NEMD) algorithms and if necessary be able to construct correct NEMD algorithms for new problems which he may encounter.

Because of space limitations we will assume that the reader is aware of the Green-Kubo relations for the Navier-Stokes transport coefficients [2]. This will be a common starting point for algorithm design.

2. – Liouville space.

Consider an N-particle system evolving under the following dynamics

$$\dot{\boldsymbol{q}}_i = \frac{\boldsymbol{p}_i}{m} + \boldsymbol{C}_i F_e(t)\,, \tag{2.1}$$

$$\dot{\boldsymbol{p}}_i = \boldsymbol{F}_i + \boldsymbol{D}_i F_e(t) - \alpha \boldsymbol{p}_i\,. \tag{2.2}$$

In these equations F_e represents a scalar external field and the phase variables $\boldsymbol{C}_i(\boldsymbol{\Gamma})$ and $\boldsymbol{D}_i(\boldsymbol{\Gamma})$ describe the coupling of the field to the system. The generalization to vector or tensor fields is straightforward. The term $-\alpha \boldsymbol{p}_i$ couples the system to a thermostat and we shall usually take

$$\alpha = \alpha_0 + \alpha_1 F_e = \frac{\sum \boldsymbol{F}_i \cdot \boldsymbol{p}_i}{\sum p_i^2} + \frac{\sum \boldsymbol{p}_i \cdot \boldsymbol{D}_i}{\sum p_i^2} F_e\,. \tag{2.3}$$

Such a system is described as being Gaussian isothermal since the kinetic energy

$$K = \sum \frac{p_i^2}{2m} \tag{2.4}$$

is a constant of the motion [3]. We assume that, in cases in which the field F_e may cause convection, the $\boldsymbol{p}_i$ defined by (2.1) and (2.2) are measured with respect to the local streaming velocity $\boldsymbol{u}$. If this is the case, then the canonical kinetic energy K will be a measure of the temperature T. Thus in a three-dimensional system

$$\frac{3N}{2} k_B T = K . \tag{2.5}$$

In this case,

$$H_0 = \sum \frac{p_i^2}{2m} + \Phi(q) \tag{2.6}$$

is the correct phase variable for the internal energy. In the absence of the external field and the thermostat, H_0 is, of course, a constant of the motion.

Let $f(\boldsymbol{\Gamma}, t)$ be the N-particle distribution function describing the evolution of an ensemble of systems in $6N$-dimensional phase space. Since the number of members of the ensemble is clearly fixed, the only way that the number of systems in an arbitrary volume of phase space V can change is by systems flowing out of the enclosing surface S:

$$\frac{\mathrm{d}}{\mathrm{d}t} N = \int_V \mathrm{d}\boldsymbol{\Gamma} \frac{\partial f}{\partial t} = -\int_S \mathrm{d}\boldsymbol{S} \cdot \dot{\boldsymbol{\Gamma}} f . \tag{2.7}$$

In this equation $\mathrm{d}\boldsymbol{S}$ is the usual vector surface area element of S. Since the initial choice of the volume V was arbitrary, we find that

$$\frac{\partial f}{\partial t} = -\frac{\partial}{\partial \boldsymbol{\Gamma}} \cdot (\dot{\boldsymbol{\Gamma}} f) = -\dot{\boldsymbol{\Gamma}} \cdot \frac{\partial f}{\partial \boldsymbol{\Gamma}} - f \frac{\partial}{\partial \boldsymbol{\Gamma}} \cdot \dot{\boldsymbol{\Gamma}} . \tag{2.8}$$

Equation (2.8) is the so-called non-Liouville equation [4]. For adiabatic systems ($\alpha = 0$) in which the equations of motion (2.1) and (2.2) can be derived from a Hamiltonian, (2.8) reduces to the usual Liouville equation since in that case $(\partial/\partial \boldsymbol{\Gamma}) \cdot \dot{\boldsymbol{\Gamma}} = 0$. This circumstance is *never* met in the treatment of isothermal systems and is sometimes not satisfied even in adiabatic systems. The physical interpretation of the non-Liouville equation is that the density of systems in phase space evolves like a *compressible* $6N$-dimensional fluid. In the adiabatic Hamiltonian case where the usual Liouville theorem is valid the density evolves like a $6N$-dimensional *incompressible* fluid.

Consequently we call Λ,

$$\Lambda = \frac{\partial}{\partial \mathbf{\Gamma}} \cdot \dot{\mathbf{\Gamma}} = -\frac{1}{f}\frac{\mathrm{d}f}{\mathrm{d}t}, \tag{2.9}$$

the phase space compression factor.

It is convenient to write the Liouville equation in operator form

$$\frac{\partial f}{\partial t} = -il(t)f = -iL(t)f - f\Lambda(t) = -\frac{\partial}{\partial \mathbf{\Gamma}} \cdot (\dot{\mathbf{\Gamma}} f) . \tag{2.10}$$

The operator $il(t)$ is called the f-Liouvillean and $iL(t)$ is called the p or phase-Liouvillean. The explicit time dependence is required because the external field F_e is, in general, time dependent.

The formal solution of the non-Liouville equation is

$$f(t) = \exp_{\mathrm{L}}\left[-\int_0^t \mathrm{d}s\, il(s)\right] f = U_{\mathrm{L}}(t) f . \tag{2.11}$$

This is easily checked by substitution into (2.10). The « $\exp_{\mathrm{L}}$ » denotes the time-ordered exponential with the latest times in the power series expansion appearing to the left. $U_{\mathrm{L}}(t)$ is known as an f-propagator since its action upon distribution functions advances time by an amount t.

Ensemble averages of arbitrary phase variables $B(\mathbf{\Gamma})$ are taken in the usual way

$$\langle B(t) \rangle = \int \mathrm{d}\mathbf{\Gamma}\, B(\mathbf{\Gamma}) f(\mathbf{\Gamma}, t) . \tag{2.12}$$

This is the Schrödinger picture for a time average.

We can transform to the Heisenberg [5] picture by using integrations by parts:

$$-\int \mathrm{d}\mathbf{\Gamma}\, B(\mathbf{\Gamma})\, il(t) f = \int \mathrm{d}\mathbf{\Gamma}\, B(\mathbf{\Gamma}) \left[-\dot{\mathbf{\Gamma}} \cdot \frac{\partial f}{\partial \mathbf{\Gamma}} - f \frac{\partial}{\partial \mathbf{\Gamma}} \cdot \dot{\mathbf{\Gamma}}\right] =$$

$$= \int \mathrm{d}\mathbf{\Gamma} \left[f\left(\frac{\partial}{\partial \mathbf{\Gamma}} \cdot \dot{\mathbf{\Gamma}} B\right) - Bf \frac{\partial}{\partial \mathbf{\Gamma}} \cdot \dot{\mathbf{\Gamma}}\right] = \tag{2.13}$$

$$= \int \mathrm{d}\mathbf{\Gamma}\, f iL(t) B . \tag{2.14}$$

Thus in the Heisenberg picture

$$\langle B(t) \rangle = \int \mathrm{d}\mathbf{\Gamma} f(\mathbf{\Gamma}, 0) \exp_{\mathrm{R}}\left[\int_0^t \mathrm{d}s\, iL(s)\right] B . \tag{2.15}$$

Note that the integration by parts reverses the time ordering in the exponential. Symbolically we can write that

$$B(t) = \exp_{\mathrm{R}}\left[\int_0^t \mathrm{d}s\, iL(s)\right] B = U_{\mathrm{R}}(t)\, B\,. \tag{2.16}$$

This result can be checked by differentiation leading to the correct result that

$$\dot{B}(t) = U_{\mathrm{R}}(t)\, iL(t)\, B\,. \tag{2.17}$$

The equivalence of the Heisenberg and Schrödinger pictures is known as the transitivity of averages [4], since in the Heisenberg picture the average is taken over the initial ensemble, while in the Schrödinger picture the average is taken with respect to the distribution function at time t.

Another result which we will make much use of is the Dyson decomposition of propagators [4]. Suppose we wish to compare two propagators $U_{\mathrm{R}}(t)$, $U_{\mathrm{R0}}(t)$. Typically $U_{\mathrm{R0}}(t)$ may be an approximation to $U_{\mathrm{R}}(t)$. We assume that the p-Liouvillean associated with $U_{\mathrm{R0}}(t)$, namely $iL_0(t)$, in fact has no explicit time dependence.

The Dyson decomposition is

$$U_{\mathrm{R}}(t) = U_{\mathrm{R0}}(t) + \int_0^t \mathrm{d}s\, U_{\mathrm{R}}(s)\big(iL(s) - iL_0\big)\, U_{\mathrm{R0}}(t-s)\,. \tag{2.18}$$

One can prove the correctness of this equation by first noting that at $t = 0$ it is an identity and second by differentiating both sides with respect to t. This leads to

$$\frac{\partial U_{\mathrm{R}}(t)}{\partial t} = U_{\mathrm{R}}(t)\, iL(t)\,. \tag{2.19}$$

That this is the correct equation of motion for the right propagator is easily seen from (2.16) above.

The corresponding equations for left-ordered f-propagators are [5]

$$U_{\mathrm{L}}(t) = U_{\mathrm{L0}}(t) - \int_0^t \mathrm{d}s\, U_{\mathrm{L0}}(t-s)\big(il(s) - il_0\big)\, U_{\mathrm{L}}(s) \tag{2.20}$$

and

$$\frac{\partial U_{\mathrm{L}}(t)}{\partial t} = -\, il(t)\, U_{\mathrm{L}}(t)\,. \tag{2.21}$$

It is handy to use a graphical shorthand [4] for the Dyson equation. Equations

(2.18) and (2.19) become, respectively,

(2.22) $\rightarrow = \ominus + \rightarrow (\cdot - \circ) \ominus$

and

(2.23) $\leftarrow = \ominus - \ominus (\cdot - \circ) \leftarrow .$

The dot and circles denote the Liouvilleans associated with the propagators $U_R(t)$ or $U_L(t)$ and $U_{R0}(t)$ or $U_{L0}(t)$, respectively. Arrow chains denote convolutions.

3. – Isothermal response theory [6].

We are now in a position to analyse the time-dependent response of a system to an external field which we assume is applied to an ensemble of equilibrium systems at time zero. The initial ensemble characterized by the N-particle distribution function f_0 should be such that, in the absence of the applied field $F_e(t)$,

$$\frac{\partial f_0}{\partial t} = -il_0 f_0 = 0 . \tag{3.1}$$

This still does not uniquely define the initial ensemble. For example, both the canonical distribution f_c

$$f_c = \frac{\exp[-\beta H_0]}{\int d\Gamma \exp[-\beta H_0]} \tag{3.2}$$

and the so-called isothermal distribution function f_T [7]

$$f_T = \frac{\delta(K - K_0)\exp[-\beta\Phi]}{\int d\Gamma\, \delta(K - K_0)\exp[-\beta\Phi]}, \tag{3.3}$$

where $\beta = 3N/2K_0$, are stationary solutions of the field-free isothermal equations of motion (2.1) and (2.2) and, therefore, both satisfy (3.1).

Assuming the system is ergodic, the isothermal distribution, however, is the only distribution over which time averages taken over a single phase space trajectory (2.1) and (2.2) will be equivalent to ensemble averages.

Consider a phase variable $B(\Gamma)$ whose mean value at equilibrium is zero:

$$\langle B\rangle_0 = \int d\Gamma\, f_0(\Gamma) B(\Gamma) = 0 . \tag{3.4}$$

If at $t = 0$ we subject an equilibrium ensemble f_0 to an isothermally applied external field $F_e(t)$ (2.1) and (2.2), then the time-dependent response of B is

$$\langle B(t)\rangle = \langle U_R(t) B\rangle_0 . \tag{3.5}$$

We can transform the full field-dependent propagator appearing in (3.5) into the field-free Gaussian isothermal propagator $U_{R0}(t)$ using the Dyson equation. Assuming the equilibrium average of B vanishes,

$$(3.6)\quad \langle B(t)\rangle = \langle \rightarrow (\cdot - \circ) \ominus B\rangle_0 = \langle \ominus (\cdot - \circ) \ominus B\rangle_0 + O(F_e^2)\,.$$

Integrating by parts, we find that

$$(3.7)\qquad \langle B(t)\rangle = \int \mathrm{d}\boldsymbol{\Gamma}\,(f_0 \ominus)\big((\cdot - \circ) \ominus B\big) + O(F_e^2)\,.$$

From the fact that the equilibrium distribution f_0 is preserved by the Liouvillean il_0, we see that

$$(3.8)\qquad \langle B(t)\rangle = -\int_0^t \mathrm{d}s \int \mathrm{d}\boldsymbol{\Gamma}\,\big((il(s) - il_0)\,f_0\big)\,U_{R0}(t-s)\,B + O(F_e^2)\,.$$

If f_0 is taken to be either the canonical or isothermal ensemble, then

$$(3.9)\qquad i\,\Delta l(s)\,f_0 = \big(il(s) - il_0\big)\,f_0 = -\,\beta f_0\big(i\,\Delta L(s)\,\boldsymbol{H}_0\big) + f_0\,\Delta\Lambda(s)\,.$$

We assume that in the absence of a thermostat $\Lambda = (\partial/\partial\boldsymbol{\Gamma})\cdot\dot{\boldsymbol{\Gamma}} = 0$. This condition is known as the adiabatic incompressibility of phase space ($AI\Gamma$). Of course, it is possible to pursue the analysis without $AI\Gamma$, however it seems unnecessary to do so. In every case so far studied equations of motion can be found which satisfy $AI\Gamma$.

Using this assumption

$$(3.10)\qquad \Lambda(s) = -\,3N\alpha + O\,(1)\,.$$

Now using our equations of motion (2.1) and (2.2)

$$(3.11)\quad i\,\Delta L(s)\,H_0 - kT\,\Delta\Lambda(s) = F_e(s)\left[\sum_i \boldsymbol{D}_i\cdot\frac{\boldsymbol{p}_i}{m} - \boldsymbol{C}_i\cdot\boldsymbol{F}_i\right] = \dot{H}_0^{\mathrm{ad}}(s) = +\,J(\boldsymbol{\Gamma})\,F_e(s)\,.$$

In this equation $\dot{H}_0^{\mathrm{ad}}$ denotes the adiabatic derivative of the internal energy in the presence of the external field. $J(\boldsymbol{\Gamma})$ is known as the dissipative flux. In circumstances where one can express the adiabatic coupling of the external field of the system through a Hamiltonian H, $H = H_0 - A(\boldsymbol{\Gamma})F_e$, one finds that $J(\Gamma) = \dot{A}$. In general J is not a perfect differential. We do not need to specify whether the time derivative is taken with respect to the perturbed or unperturbed Hamiltonian since

$$(3.12)\qquad \dot{A} = \{A, H\} = \{A, H_0\}\,.$$

Substituting (3.11) into (3.8), (3.9), we derive the basic result for the isothermal linear response of $B(\Gamma)$

$$\langle B(t)\rangle = \int_0^t \mathrm{d}s \int \mathrm{d}\Gamma\, \beta f_0 J(\Gamma)\, U_{\mathrm{R}0}(t-s)\, B F_e(s) + O(F_e^2)\,. \tag{3.13}$$

This result can be written more compactly as

$$\langle B(t)\rangle = \int_0^t \mathrm{d}s\, \chi(t-s) F_e(s) + O(F_e^2) \tag{3.14}$$

with the isothermal susceptibility expressed as an equilibrium time correlation function whose time dependence is governed by the field-free isothermal propagator $U_{\mathrm{R}0}$,

$$\chi(t) = \beta \int \mathrm{d}\Gamma\, f_0 J U_{\mathrm{R}0}(t) B = \beta \langle J B(t_0)\rangle_0\,. \tag{3.15}$$

We use the expression $B(t_0)$ to denote time propagation with the field-free Gaussian isothermal propagator $U_{\mathrm{R}0}(t)$.

In the standard textbook treatment of the adiabatic linear response [8] the final expression for the susceptibility uses the normal adiabatic, field-free Newtonian propagator. Conventional adiabatic treatments of linear response theory are ergodically inconsistent because time averaging along a single Newtonian trajectory cannot generate either the isothermal or canonical distribution functions. Even for the microcanonical distribution function there are severe formal difficulties with the standard theory [9].

By contrast, if f_0 is chosen to be the isothermal distribution, time averages and ensemble averages are consistent. It seems likely that ergodic consistency in linear response theory can only be achieved if explicit account is taken of the thermostat.

In these lectures we only deal with isothermal response of either the canonical or the isothermal ensemble. It is, however, possible to design equations of motion which have other constants of the motion such as the internal energy or the enthalpy. These equations have been described in a recent review by EVANS and MORRISS [10]. We show in table I the susceptibilities obtained by carrying out linear response theory using these different equations of motion.

It should be noted that one cannot mix equations of motion and initial ensembles at random and expect that the susceptibility will always take the form $\chi = \beta\,\langle JB(t)\rangle$. For example, KUBO [9] has recently shown that, if one considers the adiabatic response of an initial cumulative microcanonical ensemble (all states less than a specified energy), then the susceptibility involves a Newtonian, equilibrium time correlation function of the usual microcanonical

ensemble (all states of a given energy) [9]. In this case the initial ensemble and the susceptibility ensemble are not the same!

In table I we also show the linear response for a system of dynamics proposed by NOSÉ [11]. At equilibrium Nosé dynamics generates the true canonical ensemble rather than the isothermal ensemble. Proof of (T.5) can be found in [12].

TABLE I. – *Linear susceptibilities* [10]

Adiabatic response of canonical ensemble

(T.1) $$\chi = \beta\langle JB(t_N)\rangle_c \,.$$

Isothermal response of canonical or isothermal ensemble

(T.2) $$\chi = \beta\langle JB(t_0)\rangle_{c,T} \,.$$

Iso-energetic response of canonical or microcanonical ensembles [10]

(T.3) $$\begin{cases} \chi = \langle\beta(\Gamma)\, JB(t_N)\rangle_{C,E} = \beta\langle JB(t_N)\rangle_{C,E} + O(1)\,, \\ \beta(\Gamma)^{-1} = \sum p^2/3Nm \qquad\qquad (t_E = t_N \text{ if } F_e = 0)\,. \end{cases}$$

Iso-enthalpic response of iso-enthalpic ensemble

(T.4) $$\begin{cases} \chi = \beta\langle JB(t_I)\rangle_I\,, \\ JF_e = \dot{I}\,, \qquad \text{iso-enthalpic dynamics defined in [10]}\,. \end{cases}$$

Nosé dynamics of the canonical ensemble

(T.5) $$\chi = \beta\langle JB(t_c)\rangle_c \,.$$

Nosé dynamics is described in [11] and this expression for the susceptibility is derived in [12].

The iso-energetic response (T.3) is interesting because it leads to the result [10]

(3.16) $$\chi = \langle\beta(\Gamma)\, J(\Gamma)\, B(\Gamma, t_E)\rangle_E$$

which is not of the standard form because of the presence inside the average of $\beta(\Gamma)$ defined in table I. However, it is straightforward to show that in the thermodynamic limit it reduces to the standard form since

(3.17) $$\chi = \left\langle\left[\frac{JB(t_N)}{\langle\beta\rangle^{-1} + \Delta\beta^{-1}}\right]\right\rangle_E = \langle\beta\rangle\langle JB(t_N)\rangle_E - \langle\beta\rangle^2\langle J\Delta\beta^{-1}B(t_N)\rangle_E + O(\Delta^2)\,.$$

Now if J, B are extensive and average to zero at equilibrium, then the first term in (3.20) is $O(N)$ while the second is $O(1)$. This is seen by realizing that, if U, V, W are extensive local phase variables that individually average to zero at equilibrium, then

(3.18) $$\langle UVW\rangle = O(N)\,.$$

4. – Comparison of susceptibilities.

We shall now address the important question of how the various linear susceptibilities described in table I relate to one another. For simplicity let us assume that the initial unperturbed ensemble is canonical. In this case the only difference among the adiabatic (T.1), the isothermal (T.2), the isoenergetic (T.3) and the Nosé (T.5) susceptibilities is via the respective field-free propagators used to generate the equilibrium time correlation functions.

We will now discuss the differences between the adiabatic and isothermal responses, however the analysis of the other cases involves virtually the same arguments. We shall assume that the dissipative flux J and the response phase variable B are both extensive and have mean values which vanish at equilibrium. The susceptibility is of order N.

The only difference between (T.1) and (T.2) is in the time propagation

$$B(t_0) = U_{\mathrm{R}0}(t)B(\Gamma) = \exp[iL_0 t]B\,, \tag{4.1}$$

$$B(t_N) = U_{\mathrm{R}N}(t)B(\Gamma) = \exp[iL_N t]B\,. \tag{4.2}$$

In (4.1) and (4.2) the Liouvillean $iL_N = \dot{\boldsymbol{\Gamma}}\cdot\partial/\partial\boldsymbol{\Gamma}$ is the Newtonian Liouvillean. iL_0 is defined by the isothermal equations of motion

$$\dot{\boldsymbol{q}}_i = \boldsymbol{p}_i/m\,, \tag{4.3}$$

$$\dot{\boldsymbol{p}}_i = \boldsymbol{F}_i - \alpha\boldsymbol{p}_i\,, \tag{4.4}$$

$$\alpha = \sum \boldsymbol{F}_i\cdot\boldsymbol{p}_i/\sum p_i^2\,. \tag{4.5}$$

In both cases there is no explicit time dependence.

We can now use the Dyson equation to calculate the difference between the isothermal and adiabatic susceptibilities of the canonical ensemble. If $\rightarrow$ denotes the isothermal propagator and $\overset{\ominus}{\rightarrow}$ the Newtonian, the difference between the two relevant equilibrium time correlation functions is

$$\beta\langle J \rightarrow B\rangle - \beta\langle J \overset{\ominus}{\rightarrow} B\rangle = \beta\langle J \rightarrow \Delta \overset{\ominus}{\rightarrow} B\rangle = \beta\,\delta\langle J \rightarrow B\rangle\,, \tag{4.6}$$

where we have used eq. (2.22).

Now

$$\Delta = \Delta\dot{\boldsymbol{\Gamma}}\cdot\partial/\partial\boldsymbol{\Gamma} = \frac{-\sum \boldsymbol{F}_j\cdot\boldsymbol{p}_j}{\sum p_j^2}\sum \boldsymbol{p}_i\cdot\frac{\partial}{\partial\boldsymbol{p}_i}\,. \tag{4.7}$$

Thus

$$\beta\,\delta\langle J \rightarrow B\rangle = -\int_0^t \mathrm{d}s\,\beta\left\langle J\exp[iL_0 s]\,\alpha\sum \boldsymbol{p}_i\cdot\frac{\partial}{\partial\boldsymbol{p}_i}\exp[iL_N(t-s)]B\right\rangle, \tag{4.8}$$

where α is the field-free Lagrange multiplier appearing in the isothermal equation of motion. Provided that B is an analytic function of the momenta, (4.8) can be rewritten as

$$\beta\delta\langle J \to B\rangle = -\int_0^t \mathrm{d}s\,\beta\langle J \exp[iL_0 s]\alpha \exp[iL_N(t-s)]B'\rangle\,, \tag{4.9}$$

where B' is extensive. This is because $\sum \boldsymbol{p}_i\cdot\partial/\partial\boldsymbol{p}_i$ is, apart from combinatorial factors, an identity operator. Since α is intensive, (3.18) shows that the difference between the two time correlation functions is of $O(1)$ and can, therefore, be disregarded in the thermodynamic limit. This means that in that limit the adiabatic and isothermal susceptibilities are equivalent. The same arguments can be also be used to show the thermodynamic equivalence of the iso-energetic and Nosé susceptibilities as well. It is pleasing to be able to prove that the mechanical response is independent of the thermostating *mechanism* and so only depends upon the thermodynamic *state* of the system.

5. – Nonequilibrium molecular-dynamics algorithms.

We will now show how the theory of the mechanical response of many-body systems can be used to calculate transport coefficients. There are two types of transport coefficients: mechanical and thermal. The calculation of mechanical transport coefficients is essentially a trivial application of the response theory we have outlined in sect. **3** and **4**. In this case the system is driven by a real external field $\boldsymbol{F}_e$ and the equations of motion are essentially given by (2.1) and (2.2).

In Nature a mechanical system may respond adiabatically or, depending upon circumstances, it may be approximately isothermal. In the latter situation the heat may be radiated or conducted away to an external resevoir. In the pseudo-isothermal case the transfer of heat can only take place if there is a gradient in the temperature. This implies that the system cannot be truly homogeneus or « isothermal ». However, we expect, provided the characteristic length scales of these inhomogeneities are macroscopic rather than microscopic, that the system can be treated locally as if it were truly isothermal.

Furthermore in view of the robustness of the results described in sect. **3**, **4** to the precise methods used to thermostat steady states, we might expect that in many experimental systems the thermostats may be modelled either by our Gaussian isothermal or iso-energetic equations of motion. For linear transport close to equilibrium, our theory shows the thermodynamic equivalence of the adiabatic, isothermal and iso-energetic responses.

Because of the fundamental relations between the linear response and equilibrium time-dependent fluctuations (table I) we have two ways of cal-

culating the susceptibilities. We could perform an equilibrium simulation ($F_e = 0$) and simply calculate the appropriate equilibrium time correlation functions. The principal advantage of this method is that all possible transport coefficients can be calculated from a single molecular-dynamics run. This approach is, however, very expensive in computer time with very poor signal-to-noise ratios and results that depend strongly and nonmonotically upon the size of the system being simulated.

A much better approach is to perform a nonequilibrium simulation $F_e \neq 0$, and to calculate

$$L = \int_0^\infty \mathrm{d}t\, \chi(t) = \lim_{F_e \to 0} \lim_{t \to \infty} \frac{\langle B(t) \rangle_{F_e}}{F_e} . \tag{5.1}$$

The use of eq. (5.1) necessitates a thermostat, since otherwise the expression diverges. This method is known as nonequilibrium molecular dynamics (NEMD). NEMD has the added advantage that it can be used to calculate nonlinear as well as linear transport coefficients. They can be calculated as a function of external field strength, frequency or wave vector. The most efficient, number-independent way to calculate mechanical transport coefficients is to ignore the beautiful results of response theory and to duplicate transport processes, essentially as they occur in Nature.

Thermal transport processes are much more difficult to duplicate on the computer. A thermal transport process is one which is driven by boundary conditions rather than by mechanical fields. In thermal processes we cannot perform time-dependent perturbation theory because there is no external field appearing in the Hamiltonian which could be used as a perturbation variable.

In spite of this difference, susceptibilities for thermal processes show many similarities with their mechanical counterparts. If J is the flux of some conserved quantity (mass, momentum or energy) and if X is a gradient in the density of that conserved quantity, then a Navier-Stokes transport coefficient is defined by a constitutive relation

$$J = LX . \tag{5.2}$$

For example, the heat flux $\boldsymbol{J}_q$, the diffusive energy flux, is related to the temperature gradient by Fourier's law

$$\boldsymbol{J}_q = -\lambda \nabla T . \tag{5.3}$$

To put Fourier's law in more mechanical language, the heat flux vector is the diffusive energy flux, computed in a comoving co-ordinate frame. The temperature gradient is the Galilei-invariant, thermodynamic gradient of the energy density.

It is well known that the Navier-Stokes transport coefficients are related to equilibrium fluctuations by Green-Kubo relations [2]. These relations are set out in table II. Remarkably Navier-Stokes thermal transport coefficients are related to equilibrium time correlation functions in essentially the same way as the mechanical transport coefficients. We must stress, however, that this close formal similarity between thermal and mechanical transport coefficients only applies to Navier-Stokes thermal transport processes. If non-conserved variables are involved, then Green-Kubo relations must be generalized [13].

TABLE II [2, 8]. – *Green-Kubo relations for Navier-Stokes transport coefficients.*

(T.6)	$D_s = \frac{1}{3}\int_0^\infty \mathrm{d}t\,\langle \boldsymbol{v}_i(t)\cdot\boldsymbol{v}_i(0)\rangle$	self-diffusion .
(T.7)	$\lambda = \frac{V}{3k_B T^2}\int_0^\infty \mathrm{d}t\,\langle \boldsymbol{J}_q(t)\cdot\boldsymbol{J}_q(0)\rangle$	thermal conductivity .
(T.8)	$\eta = \frac{V}{k_B T}\int_0^\infty \mathrm{d}t\,\langle P_{xy}(t)\,P_{xy}(0)\rangle$	shear viscosity .
(T.9)	$\varkappa = \frac{1}{Vk_B T}\int_0^\infty \mathrm{d}t\,\langle (p(t)\,V(t)-\langle pV\rangle)\,(p(0)\,V(0)-\langle pV\rangle)\rangle$	bulk viscosity .

$\boldsymbol{v}_i(t)$ is the velocity of particle i at time t.
P_{xy} is the xy element of the pressure tensor.

The ensemble averages employed in table II are usually taken to be canonical, while the time dependence is adiabatic or Newtonian. Using Dyson techniques, however, we can prove that isothermal dynamics can also be used to generate the time dependence.

To calculate thermal transport coefficients using computer simulation we have the same two options that were available to us in the mechanical case. We could use inefficient equilibrium molecular dynamics or we could mimic experiment as closely as possible and calculate the transport coefficients from their defining constitutive relations. The first technique to be used was equilibrium molecular dynamics. Later the more efficient nonequilibrium approach was pioneered by HOOVER and ASHURST [14].

Although the realistic nonequilibrium approach proved more efficient than using equilibrium molecular dynamics, it was still found to be far from ideal. This is because for thermal transport processes appropriate boundary conditions are needed to drive the system—moving walls or walls maintained at different temperatures. These boundary conditions necessarily make the system

inhomogeneous. This gives rise to significant number dependence and interpretive difficulties [14, 15].

The most effective way to calculate thermal transport coefficients makes use of the formal similarities of the time correlation functions appearing in the susceptibilities of both thermal and mechanical transport coefficients. The general procedure is outlined in table III.

TABLE III. – *Synthetic* NEMD.

1) For the transport coefficient of interest L, $J_1 = LX$, identify its Green-Kubo relation:

$$L = \beta \int_0^\infty \mathrm{d}t \, \langle J_1(t) J_2(0) \rangle \, .$$

2) Invent a fictitious field F_e and its coupling to the system such that the dissipative flux $J = J_2$.

3) Check $AI\Gamma$ and periodicity of equations of motion.

4) Couple F_e to the system isothermally or iso-energetically and compute the steady-state average $\langle J_1(t) \rangle_{ss}$. Linear response theory then proves

$$L = \lim_{F_e \to 0} \lim_{t \to \infty} \frac{\langle J_1(t) \rangle}{F_e} \, .$$

With regard to step 3) in table III, it is not absolutely necessary to invent equations of motion which satisfy $AI\Gamma$. One could generalize response theory so that $AI\Gamma$ was not required. However, it is simpler and more convenient to require $AI\Gamma$ and thus far it *always* proved possible to generate algorithms which satisfy $AI\Gamma$ [10].

Although $AI\Gamma$ is satisfied, most sets of equations of motion used in synthetic NEMD are *not* derivable from a Hamiltonian. The favoured algorithms for thermal conductivity and shear viscosity are not derivable from Hamiltonians. In the case of thermal conductivity the Hamiltonian approach must be abandoned because of conflicts with the periodic-boundary convention used in simulations. For shear viscosity the breakdown of the Hamiltonian approach occurs for deeper reasons (see sect. **6** below).

Equations of motion generated by this procedure are not unique, and it is usually not possible *a priori* to predict which particular algorithm will be most efficient. It is important to realize that the algorithms generated by this procedure are only guaranteed to lead to the correct *linear* ($\lim F_e \to 0$) transport coefficient. We have said nothing so far about generating the correct nonlinear response. It may be that the nonuniqueness mentioned above would be removed if a satisfactory nonlinear response theory could be developed. It is likely, however, that in cases such as thermal conductivity the nonlinear

response necessarily requires the abandonment of homogeneity. If this is the case, then one may as well use « realistic » NEMD [14, 15].

The general scheme outlined in table III can, of course, be generalized to treat non-Navier-Stokes transport. It can also be generalized to handle frequency and wave-vector-dependent disturbances [16, 17].

We will now give a list of some of the synthetic NEMD algorithms that have been used to calculate Navier-Stokes transport coefficients. Each of the

TABLE IV.

Self-diffusion [18].

$$\text{(T.10)} \qquad \begin{cases} \dot{\boldsymbol{r}}_i = \boldsymbol{p}_i/m\,, \\ \dot{\boldsymbol{p}}_i = \boldsymbol{F}_i + (-1)^i \boldsymbol{F}_e\,, \\ D_s = \dfrac{(N-1)}{N^2}\dfrac{Vk_B T}{} \lim \dfrac{\left\langle \sum_i (-1)^i \boldsymbol{v}_i \right\rangle \cdot \boldsymbol{F}_e}{F_e^2}\,. \end{cases}$$

These equations can be transformed to the Norton ensemble.

Thermal conductivity [19, 20].

$$\text{(T.11)} \qquad \begin{cases} \dot{\boldsymbol{r}}_i = \boldsymbol{p}_i/m\,, \\ \dot{\boldsymbol{p}}_i = \boldsymbol{F}_i + (E_i - \bar{E})\boldsymbol{F}_e - \dfrac{1}{2}\sum_j \boldsymbol{F}_{ij}(\boldsymbol{r}_{ij}\cdot\boldsymbol{F}_e) + \dfrac{1}{2N}\sum_{jk} \boldsymbol{F}_{jk}(\boldsymbol{r}_{jk}\cdot\boldsymbol{F}_e)\,, \\ \lambda = \dfrac{1}{T}\lim \dfrac{\langle \boldsymbol{J}_Q\rangle\cdot\boldsymbol{F}_e}{F_e^2}\,. \end{cases}$$

Shear viscosity, Doll's tensor [21].

$$\text{(T.12)} \qquad \begin{cases} \dot{\boldsymbol{r}}_i = \dfrac{\boldsymbol{p}_i}{m} + \boldsymbol{r}_i\cdot\boldsymbol{F}_e\,, & \boldsymbol{F}_e = \nabla\boldsymbol{u}\,, \\ \dot{\boldsymbol{p}}_i = \boldsymbol{F}_i - \boldsymbol{F}_e\cdot\boldsymbol{p}_i\,, & F_{e\alpha\beta} = \begin{cases} F_e\,, & \alpha = x,\ \beta = y\,, \\ 0, & \text{otherwise}\,, \end{cases} \\ \eta = -\lim\limits_{F_e\to 0} \langle \boldsymbol{P}\rangle^{0s} : \boldsymbol{F}_e/F_e : \boldsymbol{F}_e\,. \end{cases}$$

Shear viscosity, S'llod [22].

$$\text{(T.13)} \qquad \begin{cases} \dot{\boldsymbol{r}}_i = \dfrac{\boldsymbol{p}_i}{m} + \boldsymbol{r}_i\cdot\boldsymbol{F}_e\,, & \boldsymbol{F}_e = \nabla\boldsymbol{u}\,, \\ \dot{\boldsymbol{p}}_i = \boldsymbol{F}_i - \boldsymbol{p}_i\cdot\boldsymbol{F}_e\,, & F_{e\alpha\beta} = \begin{cases} F_e\,, & \alpha = x,\ \beta = y\,, \\ 0, & \text{otherwise}\,. \end{cases} \end{cases}$$

Notes:

a) lim denotes $\lim F_e \to 0$.

b) The S'llod/Doll's algorithms can be generalized to calculate either bulk viscosity or longitudinal viscosity etc.

c) Of all the algorithms listed in this table S'llod is the only one known to correctly generate the nonlinear response.

algorithms listed in table IV satisfies $AI\Gamma$ and is consistent with periodic boundary conditions. The reader should consult the references for discussion on this point.

The algorithm for self-diffusion (T.10) can be modified for mutual and thermal diffusion coefficients. It has also been tested in the Norton, nonequilibrium ensemble in which the flux rather than the external field is the independent driving variable [23]. Both the diffusion and thermal-conductivity algorithms are used with ordinary periodic boundary conditions. In both cases the synthetic external field *replaces* the thermodynamic gradients present in real experiments. The algorithms are truly homogeneous and they succeed in calculating their respective transport coefficients in the absence of either concentration or temperature gradients.

The two viscosity algorithms discussed here are *not* consistent with fixed periodic boundary conditions. Instead they must be used with time varying shearing periodic boundary conditions. The strain rate tensor $\nabla \boldsymbol{u}$ describing the lattice deformation is

$$\nabla \boldsymbol{u} = \boldsymbol{F}_e \,. \tag{5.4}$$

Details describing how those boundary conditions are implemented are given in ref. [10].

Although both the Doll's tensor and S'llod algorithms both give the correct *linear* behaviour, the Doll's tensor algorithm begins to yield incorrect results at quadratic order in the strain rate. These errors show up as errors in the normal stress differences. The pressure and shear stress are apparently correct arbitrarily far from equilibrium. EVANS and MORRISS [22] have recently proved that the S'llod algorithm gives an exact description of shear flow arbitrarily far from equilibrium.

For irrotational flows $(\nabla \boldsymbol{u} = (\nabla \boldsymbol{u})^{\mathrm{T}})$ the S'llod and Doll's tensor methods become one and the same algorithm, as can easily be seen from their equations of motion. By treating the strain rate tensor field as a Lagrange multiplier one can use the S'llod algorithm to derive equilibrium molecular-dynamics algorithms for constant pressure or enthalpy simulations.

Only two of the algorithms described in table IV are derivable from Hamiltonians. The colour current equations of motion are derivable from the colour Hamiltonian

$$\boldsymbol{H} = \boldsymbol{H}_0 - \sum_i (-1)^i \boldsymbol{r}_i \cdot \boldsymbol{F}_e \,. \tag{5.5}$$

The Doll's tensor equations of motion can be derived from the Doll's tensor Hamiltonian

$$H = H_0 + \sum_i \boldsymbol{r}_i \boldsymbol{p}_i : (\nabla \boldsymbol{u})^{\mathrm{T}} \,. \tag{5.6}$$

As has been mentioned earlier, the existence of a generating Hamiltonian is sufficient but not necessary for the $AI\Gamma$ condition to be satisfied.

6. – Planar Couette flow.

In this section we will examine algorithms for shear flow in more detail. Our analysis of NEMD algorithms has been based on *linear* response theory and the linear Green-Kubo relations for the respective thermal transport coefficients. We have alluded to the fact that, for the diffusion and thermal-conductivity algorithms (table IV), the fictitious external fields F_e actually *replace* the thermodynamic forces responsible for mass flow and heat flow in the corresponding thermal transport processes. For these algorithms one can actually calculate the diffusion coefficient and the thermal conductivity in the absence of either chemical-potential gradients or temperature gradients. Indeed this replacement is essential to the homogeneity property of the algorithms.

As mentioned in sect. **5**, both of the viscosity algorithms, although homogeneous, are inconsistent with fixed, orthogonal periodic boundary conditions. If they are implemented with these boundaries, the equations of motion will be discontinuous whenever particles move outside the primitive simulation cell, replaced by their respective images.

To gain a better understanding of the viscosity algorithms consider a canonical ensemble of systems

$$f_c = \exp[-\beta H_0]/\int \mathrm{d}\mathbf{\Gamma} \exp[-\beta H_0]\,, \tag{6.1}$$

where $H_0 = \sum p^2/2m + \Phi$, suddenly subject to an imposed linear velocity profile. This can be achieved by mapping each of the initial x-velocities $\dot{x}_i(0^-)$ onto a new velocity $\dot{x}(0^+)$ where

$$\dot{x}_i(0^+) = \dot{x}_i(0^-) + \gamma y_i\,. \tag{6.2}$$

The Jacobian for the transformation $\mathbf{\Gamma}^- \to \mathbf{\Gamma}^+$ is easily seen to be unity. The resulting N-particle distribution function will, of course, be the local equilibrium distribution function with a local streaming x-velocity u_x, proportional to the y co-ordinate via a strain rate γ

$$u_x = \gamma y\,. \tag{6.3}$$

We denote the distribution function arising from this instantaneous transformation as f_l. It is the local equilibrium distribution function for planar Couette flow.

If the subsequent dynamics is generated by the adiabatic, field-free Newtonian equations of motion, the system will respond to the imposed initial shear rate as in an experiment. If the system is viewed as being essentially infinite in extent, the imposed zero-wave-vector velocity profile can never

decay. The system will undergo adiabatic Couette flow for ever. If the shear rate is large, the resulting long-time velocity profile may develop superimposed eddies or vortices, but the underlying $k = 0$ strain rate will not change.

If we let the strain rate take the form

$$\gamma(t) = \gamma\theta(t)\,, \tag{6.4}$$

where $\theta(t)$ is the Heaviside step function, we can write down equations which will precisely duplicate this transformation:

$$\ddot{x}_i = \frac{F_{xi}}{m} + \dot{\gamma}(t)\,y_i\,, \qquad \ddot{y}_i = \frac{F_{yi}}{m}\,, \qquad \ddot{z}_i = \frac{F_{zi}}{m}\,. \tag{6.5}$$

Integrating these equations over an infinitesimal time interval about zero shows that they accomplish the transformation (6.2). Furthermore for $t > 0$ these equations are the usual field-free Newtonian equations of motion.

If we write down a formally equivalent set of first-order equations of motion through the introduction of peculiar momenta $\boldsymbol{p}_i$, we find

$$\begin{cases} \dot{x}_i = \dfrac{p_{xi}}{m} + \gamma(t)\,y_i\,, \qquad \dot{y}_i = \dfrac{p_{yi}}{m}\,, \qquad \dot{z}_i = \dfrac{p_{zi}}{m}\,, \\ \dot{p}_{xi} = F_{xi} - \gamma(t)\,p_{yi}\,, \qquad \dot{p}_{yi} = F_{yi}\,, \qquad \dot{p}_{zi} = F_{xi}\,. \end{cases} \tag{6.6}$$

The equivalence of (6.6) and (6.5) can be easily checked by differentiation of (6.6) and elimination of the momenta. It is important to remember that the momenta are peculiar, only with respect to the imposed $k = 0$ velocity profile. If the velocity profile subsequently develops eddies (*i.e.* becomes turbulent), then the $\{\boldsymbol{p}_i\}$ cannot be used to calculate properties like the temperature through equations such as $3NkT/2 = \sum p^2/2m$. The use of such equations must rely on the subsequent observation that under appropriate conditions the profile remains planar.

In writing down eqs. (6.6) we have succeeded in transforming a boundary condition (the initial linear velocity profile) into the form of an external mechanical field. These equations are in fact the S'llod equations of motion that we have already met (table IV). It is, therefore, not surprising that the mechanical linear response to the « external field » $\gamma(t)$ is precisely the same as the Green-Kubo expression for shear viscosity. Indeed we could now reverse the argument and apply mechanical linear response theory to (6.6) to *derive* the correct equilibrium time correlation function expression for shear viscosity.

For viscous flow there is, therefore, an obvious plurality between the thermal and the mechanical response. This plurality means that we can go further and can derive formal expressions for the nonlinear response.

If we denote the Newtonian propagator by $\exp[iL_0t]$ and the S'llod propagator by $\exp[iLt]$, then this plurality can be expressed mathematically as

$$f(t) = \begin{cases} \exp[-iL_0t]f_i\,, & t > 0\,, \\ \exp[-iLt]f_c\,, & t \geqslant 0\,. \end{cases} \tag{6.7}$$

Remembering that, although no Hamiltonian can be found to generate the Sllod equations, they nevertheless satisfy AII'. We know that the respective f and p propagators are simply Hermitian conjugates. Substituting (6.1) into the second form of (6.7), we see that

$$f(t) = \frac{\exp[-\beta\tilde{H}_0(-t)]}{\int \mathrm{d}\Gamma \exp[-\beta H_0]}\,, \tag{6.8}$$

where the tilde serves to remind us that time propagation is via the S'llod rather than the Newtonian propagator. If we substitute (6.8) into the Liouville equation, we find that

$$\frac{\partial f(t)}{\partial t} = -\beta\gamma V\tilde{P}_{xy}(-t)f(t)\,. \tag{6.9}$$

In deriving this equation we have used the fact that

$$iLH_0 = -\gamma VP_{xy}\,. \tag{6.10}$$

Now eq. (6.9) may be integrated to yield a compact form for the nonlinear N-particle distribution function:

$$f(t) = \exp\left[-\beta\gamma V\int_0^t \mathrm{d}s\,\tilde{P}_{xy}(-s)\right]f_c\,. \tag{6.11}$$

This equation was first derived using very different methods by KAWASAKI and YAMADA [24]. It is important to remember that, if one expands this equation to form a power series representation of the nonlinear response, terms involving γ arise from two sources. Firstly they arise from the prefactor in the exponential and secondly they arise from the γ-dependent Sllod propagator used to generate $\tilde{P}_{xy}(-s)$. Such an expansion was used by EVANS and MORRISS [22] to show that the Doll's tensor method first introduces errors at second order in γ and then only in normal stress differences and not in either the shear stress or in the hydrostatic pressure [22].

Thus far we have only been discussing the adiabatic nonlinear response. However, we have recently shown that the nonlinear response in thermostatted systems can still be written in Kawasaki form. In general one finds

that the N-particle distribution function is given by [12, 25]

$$f(t) = \exp\left[\int_0^t \mathrm{d}s\, \tilde{J}(-s) F_e\right] f_0\,, \tag{6.12}$$

where we imagine that, as in the linear case, at time zero an ensemble characterized by the equilibrium distibution f_0 is subject to an external force F_e. In deriving (6.12) we assume as usual that AII is satisfied. The field-dependent *thermostatted* equations of motion are used to calculate $\tilde{J}(-s)$. Response equations take this form regardless of whether the thermostatting is carried out using Nosé [11] or Gaussian thermostats [25]. There are many unresolved questions associated with nonlinear response theory. At the present time it is a very active field of research.

* * *

Much of the work described in these lectures is the result of collaboration between the author and a number of colleagues. In particular, it is a pleasure to thank Dr. G. P. MORRIS, Dr. B. L. HOLIAN and Prof. W. G. HOOVER. Without their interest, stimulation and criticism our progress in this field would certainly have been much slower.

REFERENCES

[1] A number of such surveys already exist. See the special issue on *Non-Equilibrium Fluids, Phys. Today*, **37** (1984); *Nonlinear Fluid Behaviour*, edited by H. J. M. HANLEY (North-Holland, Amsterdam, 1983); W. G. HOOVER: *Annu. Rev. Phys. Chem.*, **34**, 103 (1983).

[2] Standard texts for the derivation of Green-Kubo relations are J. P. HANSEN and I. R. MCDONALD: *Theory of Simple Liquids* (Academic Press, New York, N. Y., 1976); chapter 5 of *Statistical Mechanics, B*, edited by B. J. BERNE (Plenum Press, New York, N. Y., 1977).

[3] Gaussian isothermal equations of motion were first proposed by HOOVER and EVANS: W. G. HOOVER, A. J. C. LADD and B. MORAN: *Phys. Rev. Lett.*, **48**, 1818 (1982); D. J. EVANS: *J. Chem. Phys.*, **78**, 3297 (1983).

[4] D. J. EVANS and G. P. MORRISS: *Chem. Phys.*, **87**, 451 (1984).

[5] B. L. HOLIAN and D. J. EVANS: *J. Chem. Phys.*, **83**, 3560 (1985).

[6] G. P. MORRISS and D. J. EVANS: *Mol. Phys.*, **54**, 629 (1985).

[7] D. J. EVANS and G. P. MORRISS: *Phys. Lett. A*, **98**, 433 (1983).

[8] D. A. MCQUARRIE: *Statistical Mechanics* (Harper and Row, New York, N. Y., 1976).

[9] R. KUBO: *Int. J. Quantum Chem.*, **16**, 25 (1982).

[10] D. J. EVANS and G. P. MORRISS: *Comput. Phys. Rep.*, **1**, 297 (1984).

[11] S. NOSÉ: *J. Chem. Phys.*, **81**, 511 (1984); *Mol. Phys.*, **52**, 255 (1984).

[12] D. J. EVANS and B. L. HOLIAN: *J. Chem. Phys.*, **83**, 4069 (1985).
[13] D. J. EVANS and H. J. M. HANLEY: *Phys. Rev. A*, **25**, 1771 (1982); D. J. EVANS: *Phys. Rev. A*, **23**, 2622 (1981).
[14] W. G. HOOVER and W. T. ASHURST: *Theor. Chem. Adv. Perspect.*, **1**, 1 (1975).
[15] G. CICCOTTI and A. TENENBAUM: *J. Stat. Phys.*, **23**, 767 (1980); C. TROZZI and G. CICCOTTI: *Phys. Rev. A*, **29**, 916 (1984).
[16] D. J. EVANS: *Phys. Rev. A*, **23**, 2622 (1981).
[17] D. J. EVANS: *Mol. Phys.*, **47**, 1165 (1982).
[18] D. J. EVANS, W. G. HOOVER, B. H. FAILOR, B. MORAN and A. J. C. LADD: *Phys. Rev. A*, **28**, 1016 (1983).
[19] D. J. EVANS: *Phys. Lett. A*, **91**, 457 (1982).
[20] M. J. GILLAN and M. DIXON: *J. Phys. C*, **16**, 869 (1983).
[21] W. G. HOOVER, D. J. EVANS, R. B. HICKMAN, A. J. C. LADD, W. T. ASHURST and B. MORAN: *Phys. Rev. A*, **22**, 1690 (1980).
[22] D. J. EVANS and G. P. MORRISS: *Phys. Rev. A*, **30**, 1528 (1984).
[23] D. J. EVANS and G. P. MORRISS: *Phys. Rev. A*, **31**, 3817 (1985).
[24] T. YAMADA and K. KAWASAKI: *Prog. Theor. Phys.*, **38**, 1031 (1967).
[25] G. P. MORRISS and D. J. EVANS: *Mol. Phys.*, **54**, 629 (1985).

Simulations of Vibrational Relaxation in Dense Molecular Fluids.

B. L. HOLIAN (*)

Los Alamos National Laboratory - Los Alamos, NM 87545

1. – Introduction.

The phenomena of energy sharing among center-of-mass translational degrees of freedom and internal (rotational and vibrational) degrees of freedom in dense, hot molecular fluids are crucial to the understanding of a variety of chemical explosive properties. We shall illustrate, in a highly simplified way, the processes occurring in the passage of a steady detonation wave in a condensed (fluid or solid) high explosive. First, as we sit on some typical explosive (that is, chemically unstable) molecule, a compressive shock wave arrives in the form of collisions from neighboring molecules. Center-of-mass separations shrink, causing the density to rise sharply, along with the « temperature » in the shock propagation direction. The « temperature » in the transverse direction is cold at first, until sideways collisions cause translational kinetic energy in the longitudinal direction to be fed into transverse (shearing) motion. Within one or two mean collision times, all center-of-mass kinetic energies equilibrate, so that, in the sense of local equilibrium, we may speak more correctly about temperature. Soon thereafter, rotational motions of the molecules also equilibrate, leaving only internal vibrations of the molecules relatively « cold ». If the molecule is fairly complex, there will exist lower-frequency bond-bending modes that are more easily excited than the high-frequency bond compression modes. The closer two frequencies are, the easier it is for them to « talk » to each other, *i.e.* to transfer energy; this resonance phenomenon occurs both classically and quantum-mechanically. Thus a sequence of energy transfers will occur, climbing a ladder in the frequency domain: the lowest-frequency modes to be equilibrated are translational, followed roughly by rotations, bond-bending and finally bond-stretching vibrations.

The latter vibrational temperature may take a long time to equilibrate.

(*) Work performed under the auspices of the U. S. Department of Energy.

Our aim is to understand the time (and, also, the mechanisms) it takes for energy from a shock front to be transferred into molecules, in order to prepare them for the highly excited vibrational states necessary for electronic rearrangement (chemical reaction) to occur. Once electronic states are significantly perturbed through vibrations, chemical energy in unstable bonds can be released, which drives the detonation—in effect, providing the piston for the shock wave. Of course, this is undoubtedly a terribly oversimplified picture of the time scales in high-explosive detonations. (We have said nothing about the effect of inhomogeneities, for example.) Nevertheless, the statistical process of energy transfer form center-of-mass collisions at high density up through the frequency ladder into internal vibrations must be understood before we will have even a rudimentary understanding of the kinetics of explosive chemical reactions.

Because of the high densities involved in this picture of detonations in condensed explosives, we are forced to consider many-body effects—there are no isolated binary collisions between molecules. Because of the high temperatures involved, we suppose that, even if binary collisions were appropriate, the most efficient energy transfer would occur when the relative kinetic energy of a colliding pair of molecules is several times kT; therefore, at these temperarures, it is plausible that quantum effects on vibrational relaxation are small. The method of molecular dynamics (MD), where the classical many-body problem is solved numerically, is the only tool available for studying vibrational relaxation in dense, hot molecular fluids.

MD has been successfully applied to equilibrium problems, even though it is intrinsically a time-dependent method, as distinct from Monte Carlo, where configurations are generated so as to sample from a canonical ensemble. The principal limitation to MD in equilibrium problems has been the smallness of systems considered, $N \sim 100$ to 1000 molecules. At normal fluid densities, such a small sample would not possess properties at all close to bulk values. With the surface skin depth given by the range of interatomic forces, if 100 to 1000 particles were placed in a box with rigid walls, the walls would dominate the results—everything would be surface; there would be no bulk to speak of. Periodic boundary conditions, where the « box » of N particles in volume V is surrounded by an infinite periodic array, or checkerboard, of such systems, remove this surface problem to such an extent that corrections to equilibrium properties are of relative order $1/N$. In nonequilibrium molecular dynamics (NEMD), where, for example, a fluid is sheared by moving two parallel walls in opposite directions, similar wall or surface effects are seen. The shear viscosity is given by the shear stress averaged over time, divided by the steady shear rate. If, instead of moving walls, homogeneous external forces are applied to particles throughout the fluid, the resulting shear viscosity (in three dimensions) is noticeably more independent of system size. Thus both equilibrium and steady-state time averages are reliably obtained by

MD or NEMD. What is not as clear, however, is whether truly time-dependent properties, such as a relaxation time (or its inverse, the relaxation rate), can be reliably obtained. In equilibrium systems, fluctuations about equilibrium yield time correlation functions, where the influence of periodic boundary conditions can affect the result for times longer than that for a sound wave to cross the system. In nonequilibrium systems, not only are the correlations between periodic cells of concern, but also the effect upon rates due to external forces must be taken into account. One of the aims of this lecture is to show just how such problems in NEMD can be carefully resolved in order to obtain believable results for nonequilibrium rate processes.

In this lecture, we will concentrate on a relatively simple problem. We will study the rate of energy transfer from translational and rotational degrees of freedom into bond vibration in a hot, dense diatomic molecular fluid. We have chosen a potential-energy surface (see appendix) that is a reasonable approximation to nitrogen (N_2). In addition to temperature and density, we can vary the bond vibrational frequency to study its effect on the rate of relaxation. Typically, we are concerned with N_2 at 2 to 3 times normal fluid density ($\sim 2\ \mathrm{g/cm^3}$), temperatures of $(2000 \div 4000)$ K and pressures of $(200 \div 300)$ kbar, that is, states like those achieved behind detonations of high explosives. For the purposes of this study, we will assume that our idealized diatomic molecular fluid is dense but isotropic, that is, if a shock wave has passed through, the shear stress has been relieved by viscous flow, and that the temperatures in the 3 translational and 2 rotational degrees of freedom have equilibrated to a high value, while the vibrational temperature is at the low ambient value, *i.e.* room temperature (300 K). The process whereby the temperature in the bond-vibrational and the 5 other « external » modes, or reservoirs, comes to equilibrium isoenergetically will be referred to as « adiabatic ». The most important issue to be considered in adiabatic relaxation is whether it is correct to suppose that the vibrational temperature T_{vib} relaxes exponentially from its cold initial temperature T_0 to the final equilibrium temperature T with some characteristic relaxation time τ_{vib}:

$$T_{\mathrm{vib}}(t) = T - (T - T_0)\exp[-t/\tau_{\mathrm{vib}}]\,. \tag{1}$$

The vibrational-relaxation rate ν_{vib} is then obtainable from the initial temperature increase

$$\nu_{\mathrm{vib}} = \tau_{\mathrm{vib}}^{-1} = \frac{\dot{T}_{\mathrm{vib}}(0)}{T - T_0}\,. \tag{2}$$

Equation (1) can only make sense if the vibrational mode equilibrates with the external reservoir at fixed temperature T, which in the adiabatic case is both the final temperature and the average, neglecting potential-energy redis-

tribution:

$$5T_x(t) + T_{\text{vib}}(t) \simeq 6T\,.$$

One could argue that eq. (1) is, therefore, not valid for adiabatic relaxation, since the vibrational reservoir does not equilibrate with itself, even insofar as its contribution to the average temperature T, but rather with a continuous sequence of external-mode temperatures from $T_x(0)$ down to T. Equation (2) would then have to be replaced by

$$\nu_{\text{vib}}[T_x(t)] = \frac{\dot{T}_{\text{vib}}(t)}{T_x(t) - T_{\text{vib}}(t)}\,, \tag{2a}$$

which describes a complex multitemperature relaxation process. An unambiguous rate could then be obtained only at $t = 0$. (See fig. 1 for an illustration of totally adiabatic response of the vibrational and external reservoirs.)

Since the adiabatic response gives only the initial rate in a straightforward

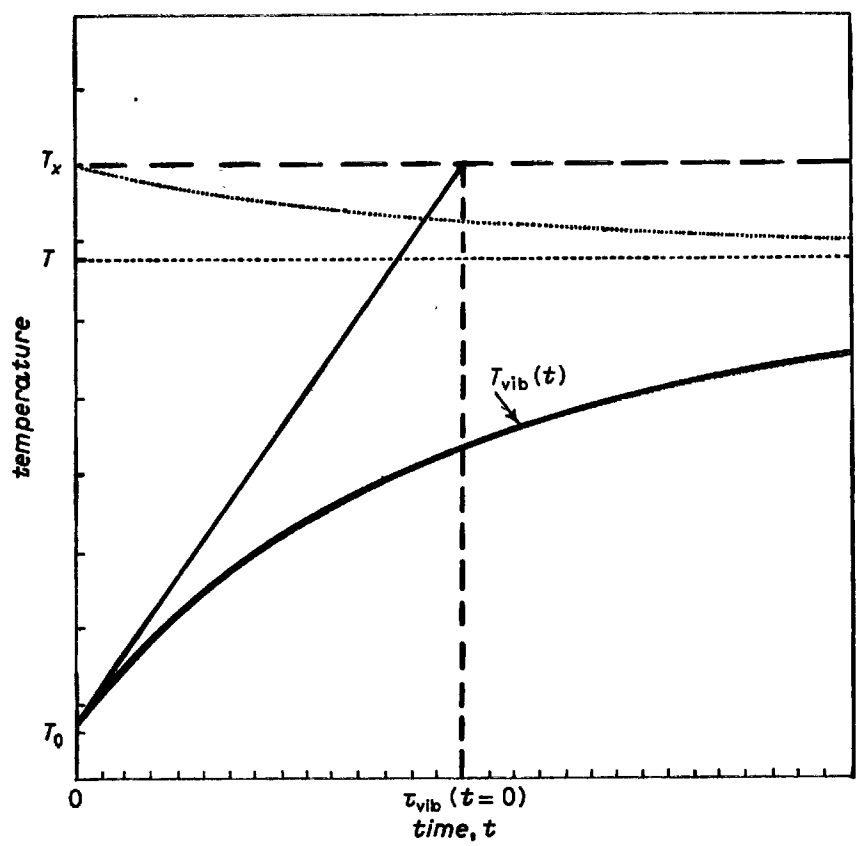

Fig. 1. – Total adiabatic response of the vibrational temperature T_{vib} as a function of time t. The external degrees of freedom begin the equilibration having been thermostatted at a high temperature T_x, while the vibrational degree of freedom has been thermostatted at a low temperature T_0. At $t = 0$, thermostatting is stopped and all degrees of freedom relax toward the final temperature T, where $6T \sim 5T_x + T_0$. The initial relaxation time τ_{vib} is shown.

manner, some of the ambiguity can be eliminated by thermostatting the external reservoir at temperature $T_x = T$, leaving the vibrational temperature to rise from T_0 to T in a partially adiabatic manner. (See fig. 2 for an illustration of partial adiabatic response of the vibrational reservoir to a fixed external-reservoir temperature.)

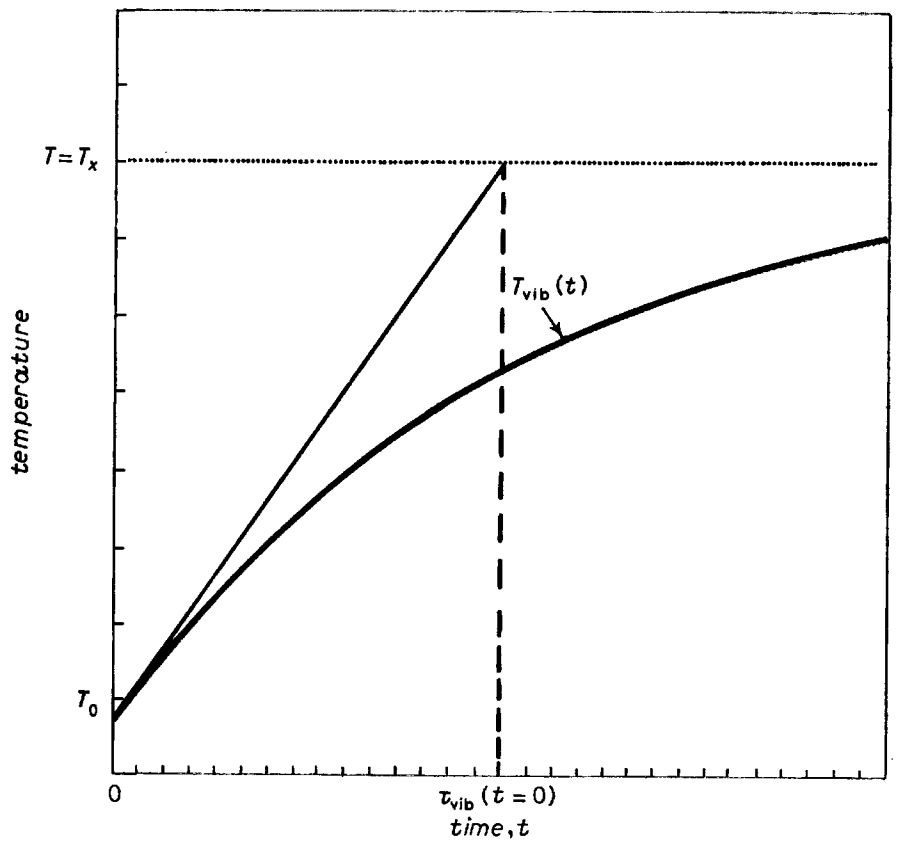

Fig. 2. – Partial adiabatic response shown as exponential vibrational-relaxation process, $T_{vib}(t)$. (See eq. (1) in text.) The external degrees of freedom continue to be thermostatted with the vibrational thermostat turned off at $t = 0$ (compare with fig. 1).

A reservoir can be fixed at constant temperature $T_x = T$ by several means: isokinetic thermostatting (either by Gaussian constrained dynamics [1*a*, *b*] or its equivalent for small time steps, velocity scaling [1*c*], to achieve a perfectly constant kinetic energy in the external reservoirs), Andersen stochastic thermostatting [2] (where velocities are randomly reset from a Maxwell-Boltzmann distribution), or Nosé-Hoover feedback thermostatting [3] (where the equation of motion of an extra degree of freedom—the thermostatting coefficient ξ—is included in the dynamics).

By completely thermostatting the vibrational degree of freedom at the low temperature T_0 and the other degrees of freedom at the high temperature T, we eliminate the ambiguities of multitemperature rates mentioned above, and the problem is reduced to measuring $\dot{T}_{vib}(0)$ in eq. (2) as a time average of the appropriate quantities, depending on thermostatting mecha-

nisms, over long enough times in a steady-state nonequilibrium system. In the following sections, we will discuss each of the methods outlined above and present results for our idealized dense, hot molecular fluid.

We can already point out some qualitative features of vibrational relaxation in these systems: the rate ν_{vib} decreases exponentially with the vibrational ω_e of the bond, ν_{vib} increases faster than linearly with density; ν_{vib} increases with temperature qualitatively like an Arrhenius law, namely an exponential of minus the inverse temperature. We emphasize that our interest is in dense, hot fluids where we suppose that quantum effects are small (that is, the collisional velocities that transfer energy most efficiently correspond to several times kT, or, in other words, sample the wings of the Maxwell-Boltzmann velocity distribution) and that isolated binary collisions are inappropriate at these high densities to account for the relaxation phenomenon Nevertheless, the techniques developed here may be applicable in other regimes as well. Finally, we show that the Nosé-Hoover thermostat possesses superior characteristics for measuring rate processes, including the capability of extrapolating out its effect altogether, compared to Andersen's stochastic thermostat or the Gaussian isokinetic thermostat.

2. – Methods.

In this section we describe the NEMD methods we have developed for studying vibrational relaxation. First, the common element to all these approaches is the absolute necessity for transforming from the six Cartesian atomic co-ordinates $(\boldsymbol{r}_1, \boldsymbol{r}_2)$ of each diatomic molecule to three center-of-mass $(\boldsymbol{R})$ and three relative $(\boldsymbol{r})$ molecular co-ordinates:

$$\boldsymbol{MR} = m_1 \boldsymbol{r}_1 + m_2 \boldsymbol{r}_2 , \qquad \boldsymbol{r} = \boldsymbol{r}_2 - \boldsymbol{r}_1 ,$$

where the atomic masses (m_1, m_2) are related to the total molecular mass by $M = m_1 + m_2$ and to the reduced mass by $\mu = m_1 m_2 / M$. The kinetic energy of the system can then be partitioned into $3(N-1)$ translational (total linear momentum $N\boldsymbol{p}_0 = \sum \boldsymbol{p} = 0$), $2N$ rotational and N vibrational degrees of freedom:

$$K = \sum_{i=1}^{N} \sum_{a=1}^{2} \tfrac{1}{2} m_a |\dot{\boldsymbol{r}}_{ia}|^2 = \sum_{i=1}^{N} \left(\tfrac{1}{2} M |\dot{\boldsymbol{R}}_i|^2 + \tfrac{1}{2} \mu |\dot{\boldsymbol{r}}_i|^2 \right) = K_{\text{trans}} + K_{\text{rot}} + K_{\text{vib}} ,$$

where in the thermostatted steady state the time averages $\langle \ldots \rangle_{ss}$ of kinetic energies are related to the temperatures by

$$\langle K_{\text{trans}} \rangle_{ss} = \tfrac{3}{2} (N-1) kT , \qquad \langle K_{\text{rot}} \rangle_{ss} = NkT , \qquad \langle K_{\text{vib}} \rangle_{ss} = \tfrac{1}{2} NkT_0 .$$

It is essential to partition kinetic energy into these natural molecular reservoirs in order to thermostat the vibrational temperature at the lower value T_0 and the external temperatures (translational and rotational) at the higher value T. The atomic Cartesian reservoirs simply will not control the temperatures, even for the relatively simple case $T_0 = T$; the vibrational temperature for reasonable bond force constants (much larger than intermolecular) stubbornly refuses to equilibrate. The center-of-mass and relative forces (dropping molecular index i) are then

$$\boldsymbol{F} = M\ddot{\boldsymbol{R}} = m_1\ddot{\boldsymbol{r}}_1 + m_2\ddot{\boldsymbol{r}}_2 = \boldsymbol{F}_1 + \boldsymbol{F}_2 ,$$

$$\boldsymbol{f} = \mu\ddot{\boldsymbol{r}} = \frac{m_1}{M} m_2\ddot{\boldsymbol{r}}_2 - \frac{m_2}{M} m_1\ddot{\boldsymbol{r}}_1 = \frac{m_1}{M}\boldsymbol{F}_2 - \frac{m_2}{M}\boldsymbol{F}_1 .$$

The relative velocities and forces can be further decomposed into components parallel and perpendicular to the bond, where the unit vector along the bond is $\hat{\boldsymbol{r}} = \boldsymbol{r}/|\boldsymbol{r}|$, *e.g.*,

$$\dot{\boldsymbol{r}}^{\parallel} = (\dot{\boldsymbol{r}}\cdot\hat{\boldsymbol{r}})\hat{\boldsymbol{r}} , \qquad \dot{\boldsymbol{r}}^{\perp} = \dot{\boldsymbol{r}} - \dot{\boldsymbol{r}}^{\parallel} ,$$

the vibrational and rotational velocities, respectively.

The physical process of thermostatting in the real world occurs by surface contact of the system of interest with a large thermal reservoir: molecules near the surface of the system collide with the walls of the heat bath and diffuse back into the bulk of the system, carrying the news of the outside world like thermal messengers. In NEMD, we simulate the effect of the thermal reservoir by homogeneous alterations of the equations of motion. By homogeneous, we mean that the contact with the « reservoir » occurs throughout the volume V of our system. If the alterations to the equations of motion are in the nature of feedback, then all N molecules are affected in some small way all of the time. By feedback, we mean that some collective property of the system, such as kinetic energy of a particular mode, is monitored, and information is fed back into the equations of motion so that, for example, the time average of the property is equal to a preset value, or so that the property itself is a constant of the motion. (If the alterations to the equations of motion are homogeneous but stochastic, then all N molecules are equally susceptible to being chosen for application of the random force.)

The homogeneous feedback equations of motion for thermostatting each reservoir can be written in the form

$$\dot{q} = \frac{p}{m} , \qquad \dot{p} = F - \xi p , \tag{3}$$

where the co-ordinate is q and momentum is p; F is the force, which in our model is assumed to arise from atom-atom intermolecular interactions plus

an atom-atom bond potential (see appendix for details). The thermostatting coefficient ξ_{vib} is related to the relaxation rate ν_{vib} ($= \tau_{\text{vib}}^{-1}$) by noting that

$$\dot{K} = \sum \frac{p}{m}\dot{p} = \sum \frac{p}{m}(F - \xi p) = \sum F\dot{q} - 2K\xi\,. \tag{4}$$

At the thermostatted steady state

$$\langle \dot{K} \rangle_{ss} = 0 = \langle \sum F\dot{q} \rangle_{ss} - 2\langle K\xi \rangle_{ss} = \langle \dot{K}(0) \rangle_{ss} - 2K_0 \langle \xi \rangle_{ss}\,,$$

where we have made the identification that the initial adiabatic ($\xi \equiv 0$) rate is

$$\dot{K}(0) = \sum F\dot{q} = \tfrac{1}{2} gk\dot{T}(0)$$

(g is the number of degrees of freedom, *e.g.*, $g = N =$ number of molecules, for vibration), so that

$$\langle \dot{K}(0) \rangle_{ss} = \langle F\dot{q} \rangle_{ss}\,.$$

Then,

$$\langle \dot{T}(0) \rangle_{ss} = 2T_0 \langle \xi \rangle_{ss}\,,$$

which, with eq. (2), gives

$$\nu_{\text{vib}} = \frac{2\langle \xi_{\text{vib}} \rangle_{ss}}{T/T_0 - 1}\,. \tag{5}$$

We use this equation for both the Gaussian isokinetic and Nosé-Hoover isothermal methods. The physical interpretation is that, for the lower vibrational temperature $T_0 < T$, the thermostatting coefficient is positive, $\langle \xi \rangle_{ss} > 0$. Collisions tend to drive the vibrational kinetic energy up, on the average, $\langle F\dot{q} \rangle > 0$, while the thermostat bleeds vibrational kinetic energy away, much like linear viscous damping. Of course, the small systems we study have large fluctuations, so that, at times, ξ behaves like viscous « *un*damping. » Thermostatting is essential, even for preparing the initial state for adiabatic-response methods, but we begin by discussing adiabatic-relaxation methods, followed by the isokinetic method of thermostatting, Andersen stochastic thermostatting and finally Nosé-Hoover feedback thermostatting.

2·1. *Adiabatic relaxation.* – The method for measuring adiabatic relaxation is to select a state from a constrained nonequilibrium simulation, as described in the next three subsections for example, as an initial condition for standard MD (Newton's equations of motion). With the thermostatting constraints entirely removed, so that the vibrational temperature can rise to T from T_0 and the external temperature can drop to T from T_x, the typical

adiabatic response is shown in fig. 3. Also shown is the difference in response that occurs when only the vibrational thermostat is turned off (labeled partial in fig. 3). The partial adiabatic realization was obtained, as was the former, from a Nosé-Hoover NEMD experiment (see subsect. 2·4) with thermostatting rates $\nu_T t_0 = 10$ in the external reservoirs as well as in the vibrational mode; the external-reservoir temperature was set and maintained at $T_x = 4000$ K, while the vibrational temperature was set at $T_0 = 300$ K; at the beginning of the partial adiabatic run, only the vibrational thermostatting rate was set to zero, while, in the total adiabatic run, all thermostatting was turned off.

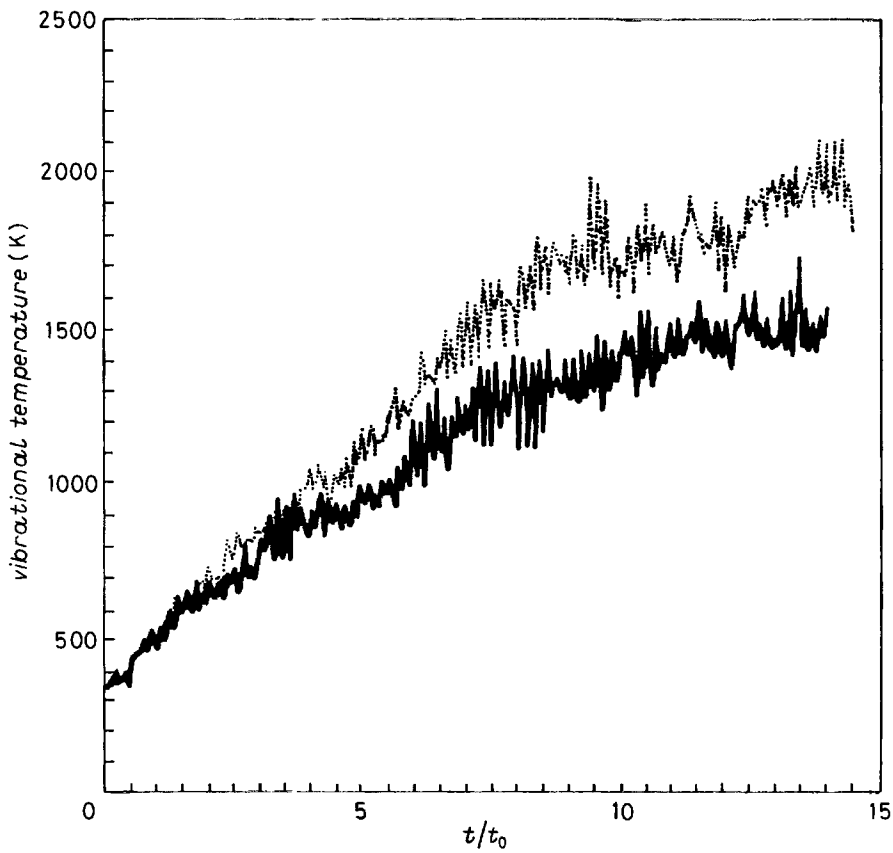

Fig. 3. – Adiabatic relaxation from the thermostatted initial state: partial, *i.e.* translation and rotation thermostatted (– – –), total, *i.e.* no thermostatting (— — —). Fluctuations have been reduced by coarse-graining into bins of $20\,\Delta t$ ($\Delta t = 0.0025\,t_0$, $t_0 = 0.13$ ps).

Initially, for both realizations, the vibrational temperature is identical, with detectable differences appearing after $(0.1 \div 0.2)t_0$. After approximately one relaxation time, the partial adiabatic response has clearly risen well beyond the fluctuation level above the total adiabatic response, the latter having slowed down by virtue of the drop in the external temperature (initially, $T_x = 4000$ K, finally $T = 3400$ K). If the vibrational-relaxation rate exhibits

an Arrhenius behavior appropriate to a thermal activation mechanism,

$$\nu_{\text{vib}}(T_x) = \nu_{\text{vib}}(\infty) \exp[-\theta/T_x],$$

where T_x is the external temperature, then the difference in the two curves in fig. 3 can be reconciled if the activation temperature θ is roughly 18 000 K and the vibrational relaxation in the partial adiabatic case is simple exponential (no dependence on T_{vib}). This estimate is a reasonable one in view of a body of calculations we have done at different temperatures. Thus we can answer the question, ν_{vib} is a function of what temperature?—the external temperature (translation and rotation).

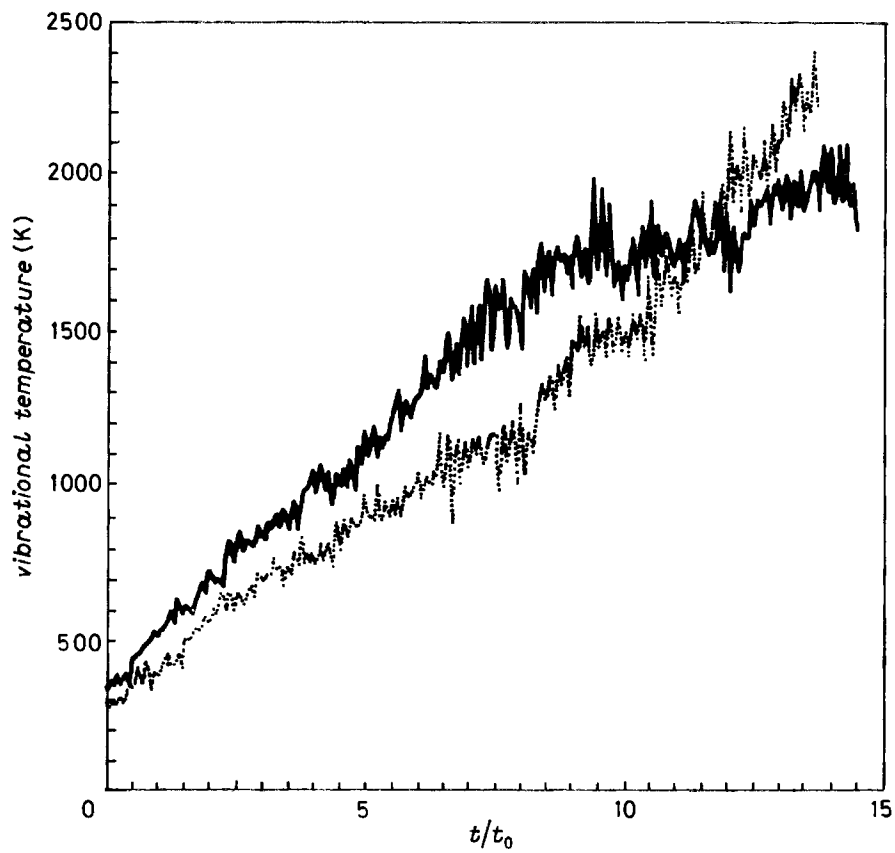

Fig. 4. – Difference in partial adiabatic relaxation due to initial conditions: initial phase chosen from Nosé-Hoover run at $t = 40\,t_0$ (——), initial phase at $t = 39\,t_0$ (– – –). Fluctuations reduced by coarse-graining (see fig. 3).

The main practical difficulty of measuring the vibrational-relaxation rate by the partial adiabatic method, which, at least, is a one-temperature process as we have just seen, is illustrated in fig. 4. The two curves shown differ only in the initial phase, chosen from a Nosé-Hoover thermostatting run: in one case, the vibrational thermostat was turned off at $t = 40\,t_0$; in the second, $t = 39\,t_0$. It is clear that one must average over an ensemble of starting times in order to sort out the considerable effects of fluctuations on the measured

rate of vibrational relaxation. Even the curvatures of these two traces are different, the latter being concave upward rather than downward, as would be appropriate for exponential relaxation. We are thus led to the thermostatted methods of the following subsections for reliable measurements. The motivation for these methods is to replace an ensemble average over starting points with a time average over a continuously restarted steady-state experiment.

2·2. *Isokinetic thermostatting.* – There are two forms of isokinetic thermostatting, where the kinetic energies of each of the reservoirs—translational, rotational and vibrational—are kept constant. Historically, the first method to appear was velocity scaling [1*c*]. In finite-central-difference form, Newton's equations of motion are written

$$\Delta q_+ = \Delta q_- + F\Delta t^2/m\,,$$

with displacements evaluated half-way between time steps $\Delta q_\pm = \Delta q(t \pm \frac{1}{2}\Delta t)$ and the co-ordinates given by $q(t+\Delta t) = q(t) + \Delta q(t + \frac{1}{2}\Delta t)$; the force is evaluated at time t. In velocity rescaling, the displacement Δq_+ is scaled so as to fix the total kinetic energy for a given reservoir:

$$\Delta q'_+ = \alpha\,\Delta q_+\,,$$

where α is the velocity scaling factor. At time $t + \frac{1}{2}\Delta t$, the kinetic energy is equal to the preset value K_0, just as it was at time $t - \frac{1}{2}\Delta t$:

$$K = \sum \frac{1}{2}\, m\, \frac{\Delta q'^2_+}{\Delta t^2} = \alpha^2 \sum \frac{1}{2}\, m\, \frac{\Delta q^2_+}{\Delta t^2} = \alpha^2 \left(\sum \frac{1}{2}\, m\, \frac{\Delta q^2_-}{\Delta t^2} + \sum F\Delta q_- + \ldots \right) =$$
$$= \alpha^2 (K_0 + \sum F\Delta q_- + \ldots) = K_0\,,$$

whence

$$\alpha = 1 - \frac{\sum F\Delta q_-}{2K_0} + \ldots = 1 - \Delta t\, \frac{\sum F\dot{q}_-}{2K_0} + \ldots\,.$$

The Gaussian feedback equations of motion [1*a*, *b*] are embodied in eq. (3). In finite-difference form, with $\dot{q}(t) = \Delta q/\Delta t$ and $\Delta q = \frac{1}{2}(\Delta q_+ + \Delta q_-)$,

$$\Delta q_+ = \Delta q_- + F\Delta t^2/m - \xi\,\Delta q\,\Delta t = \frac{(1 - \frac{1}{2}\xi\Delta t)\,\Delta q_- + F\Delta t^2/m}{1 + \frac{1}{2}\xi\Delta t}\,. \tag{6}$$

Since $K = K_0$ is the fixed value of the kinetic energy, we may set $\dot{K} = 0$ in eq. (4) to get the thermostatting coefficient

$$\xi_G = \frac{\sum F\dot{q}}{2K_0}\,.$$

Clearly, for small time steps, the Gaussian feedback and velocity scaling methods are identical, with the velocity scaling factor given by $\alpha = 1 - \xi_G \Delta t + \ldots$. Since velocity scaling is a somewhat simpler scheme to implement, we evaluate the vibrational-relaxation rate by the equivalent form of eq. (5):

$$\nu_{\text{vib}} = \frac{\alpha^{-2} - 1}{\Delta t(T/T_0 - 1)} .$$

The adiabatic methods for our small ($N = 108$) systems are quite noisy, as we have seen in the last subsection, but the isokinetic rate as computed from the above equation is almost a factor of two higher. The flaw in the isokinetic-thermostatting method is that it is impossible to separate out the effects of thermostatting on rate processes. That is, the measured rate of vibrational relaxation could very well be the sum of two terms: the underlying, unthermostatted (adiabatic) rate, plus a contribution from the thermostatting process itself. The homogeneous intrusion into the dynamics, small though it may be, alters the velocity distribution function. If the alteration affects the high-velocity wings of the distribution (as it most surely does), then the rate is also affected, since high-velocity collisions provide the most efficient means of energy transfer. The following thermostatting schemes have this same limitation, but their degree of intrusion into the usual dynamics can be varied, unlike the isokinetic methods.

2·3. *Andersen stochastic thermostatting.* – In a landmark paper, ANDERSEN [2] showed how velocities in MD could be altered in a stochastic way, so that time averages along an equilibrium « trajectory » give the same values as the canonical (NVT) ensemble, rather than the usual MD ensemble (NVE, $N\boldsymbol{p}_0 = 0$) values. The stochastic prescription is to select particles at random at a thermostatting rate $\nu_T = 1/\tau_T$, such that a fraction of particles $\nu_T \Delta t = \Delta N/N$ per time step Δt have their velocities reset from a Maxwell-Boltzmann velocity distribution with temperature T_0; *i.e.*, if random number η_i ($i = 1, 2, \ldots, N$) uniformly distributed between 0 and 1 satifies $\eta_i \tau_T < \Delta t$, then reset the displacement by the Box-Muller transformation [4] (uniform- to Gaussian-distributed random variables)

$$\Delta q'_+ = \lambda(-\ln \eta')^{\frac{1}{2}} \cdot \begin{cases} \cos 2\pi\eta'' , \\ \sin 2\pi\eta'' , \end{cases}$$

where η' and η'' are a pair of random numbers uniform on the interval [0, 1] and $\lambda = \Delta t(2kT_0/m)^{\frac{1}{2}}$ ensures that the long-time average of K is $\frac{1}{2} gkT_0$:

$$\langle K \rangle = \sum \frac{1}{2} m \frac{\langle \Delta q'^2_+ \rangle}{\Delta t^2} = g \frac{m\lambda^2}{2\,\Delta t^2} \langle -\ln \eta' \rangle \frac{1}{2} \langle \cos^2 2\pi\eta'' + \sin^2 2\pi\eta'' \rangle = \frac{1}{2} gkT_0 ,$$

since $\langle -\ln \eta \rangle = 1$.

There are three serious objections to this method of thermostatting. First, if the rate of thermostatting ν_T far exceeds any natural rates, such as the collision rate, particles will simply jiggle furiously about their current positions, diffusing very slowly in configuration space, while executing the expected canonical fluctuations in momentum space. Since *all* of phase space must be accessible at equilibrium, it will take a very long time to obtain canonical-ensemble averages as trajectory time averages in the limit $\nu_T \to \infty$. Second, if ν_T is too slow compared to the collision rate, an inordinate amount of time may be spent waiting for momentum-space transients to settle down, especially in the nonequilibrium case. Even though ANDERSEN proved that his procedure would give correct canonical-ensemble results, he did not guarantee that it could be done in less than infinite time—an explicit statement of ergodicity problems in the either limit $\nu_T \to 0$ or $\nu_T \to \infty$. The infinite time required to achieve either equilibrium or a nonequilibrium steady state is a serious practical limitation. These ergodicity difficulties can be overcome by choosing ν_T to be not too far from the collision rate, avoiding both $\nu_T = 0$ and $\nu_T = \infty$ limits.

The third, and perhaps most serious objection to the Andersen thermostatting procedure is illustrated in fig. 5. In a nonequilibrium experiment,

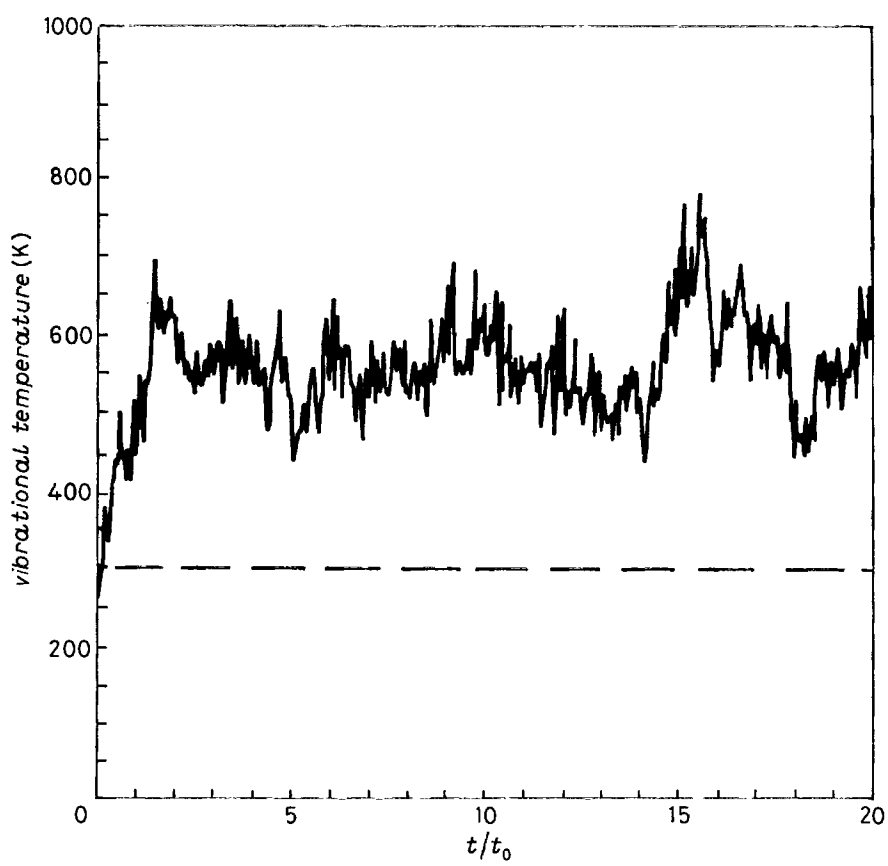

Fig. 5. – Inability of the Andersen thermostat to fix the vibrational temperature at $T_0 = 300$ K ($T_{trans} = T_{rot} = 4000$ K) in a nonequilibrium simulation ($\tau_T = \nu_T^{-1} = 0.5\,t_0$).

the Andersen thermostat fails to maintain the vibrational temperature at its preset value T_0. (Berendsen's deterministic scheme [5] also has this shortcoming.) The problem is not simply one of waiting long enough for a transient to settle down, since the temperature has fairly quickly (*i.e.* on the order of τ_T) reached a steady-state value $T_0' > T_0$. The relaxation rate $\nu_{vib}(T, \nu_T)$ is given then by

$$\frac{1}{2} gk(T - T_0')\nu_{vib} = \langle \dot{K}_{vib}(0)\rangle_{ss} = \frac{\langle \Delta K_{vib}\rangle_{ss}}{\Delta t},$$

where $\Delta K_{vib} = \sum \frac{1}{2}\mu(\Delta q_+^2 - \Delta q_+'^2)/\Delta t^2$ is the change in kinetic energy due to resetting the displacements from Δq_+ to $\Delta q_+'$. However, if higher-order effects make ν_{vib} also dependent upon T_0' in this example, or if one had hoped to characterize the nonequilibrium steady state before, rather than after the fact, then the Andersen thermostat is inadequate to the task. In the next subsection, we present a deterministic (feedback) method which overcomes this last objection.

2·4. *The Nosé-Hoover thermostat.* – Following Andersen's work, NOSÉ [3*a*] derived a deterministic method of generating isothermal trajectories. He proposed a Hamiltonian internal-energy function involving an extra co-ordinate and conjugate momentum, whereby time averages over the remaining co-ordinates and momenta (those of the usual N-molecule many-body system) yield canonical-ensemble averages and fluctuations. In a further simplification, HOOVER [3*b*] showed that only a single extra variable, the thermostatting coefficient ξ that appears in the equations of motion (eq. (3)), is necessary, along with the assumption of a canonical distribution function and its stationarity at equilibrium. The resulting equation of motion for ξ is then shown to be

$$\dot{\xi} = \nu_T^2(K/K_0 - 1)\,. \tag{7}$$

The thermostatting rate is ν_T, analogous to the Andersen stochastic procedure. We have aready derived an expression for the vibrational-relaxation rate, given the steady-state nonequilibrium value of ξ_{vib}, namely eq. (5).

It is clear from eq. (7) that at the steady state $\langle \dot{\xi}_{vib}\rangle_{ss} = 0$, so that $\langle K_{vib}\rangle_{ss} = K_0$. In other words, the deterministic thermostat of Nosé and Hoover is able to maintain the temperature at its preset value. This is illustrated in fig. 6 for a situation very closely parallel to the example of the Andersen thermostat in fig. 5. Note that, when the thermostatting time constant has been switched from $\tau_T = 0.1$ to 0.5 at $t = 0$, there is a transient response that settles out in a few times τ_T.

Again, as in the Andersen method, the limits $\nu_T \to 0$ or $\nu_T \to \infty$ pose ergodic hazards to the computation of the vibration-relaxation time by this homo-

geneous method. Spurious results can be obtained when the thermalization rate is too much higher than collision frequencies ($\nu_T \to \infty$) [6]. At the other extreme, one must average over very long times, both to be sure that transients have died out and to compensate for larger characteristic times, despite the smaller fluctuations in ξ: at equilibrium, since ξ is Gaussian-distributed, one can show that $\langle \xi^2 \rangle - \langle \xi \rangle^2 = 1/g\tau_T^2$. This is also true, to a good approximation, away from equilibrium, where $\langle \xi \rangle \neq 0$. Nevertheless, over a certain range of thermostatting rates, we expect that the vibrational-relaxation rate determined by our method can be represented by a linear relation:

$$\nu_{vib}(\nu_T) \simeq \nu_{vib}(0) + a\nu_T \,. \tag{8}$$

That means that the effect of the thermostat on the intrinsic rate process can be extrapolated away.

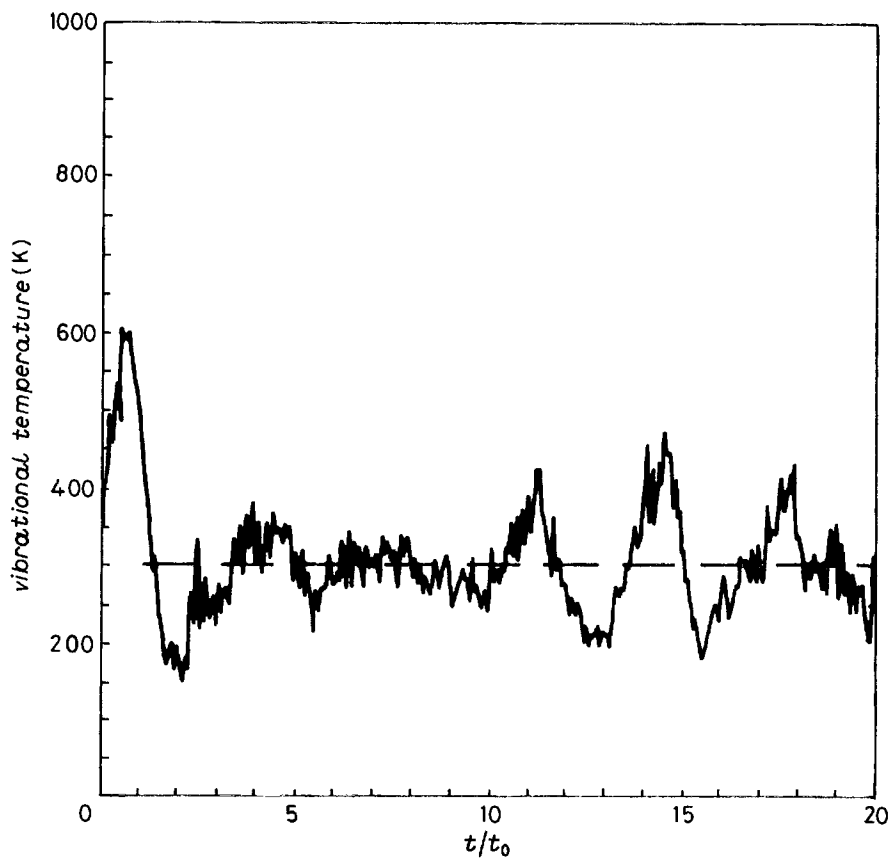

Fig. 6. – Ability of the Nosé-Hoover thermostat to fix vibrational temperature at $T_0 = 300$ K ($T_{trans} = T_{rot} = 4000$ K) in a nonequilibrium simulation (at $t = 0$, $\tau_T = \nu_T^{-1} = 0.5t_0$; for $t < 0$, $\tau_T = 0.1t_0$).

3. – Results.

In the previous section, we have presented some qualitative results for each of the NEMD methods presented. In this section, we compare methods

and use them to discuss certain physical features of vibrational relaxation in dense molecular fluids.

In fig. 7, we show the dependence of the vibrational-relaxation rate on thermostatting rate for the Andersen stochastic and Nosé-Hoover deterministic thermostatting schemes. Also shown at zero thermostatting rate are the results for adiabatic response and Gaussian isothermal methods (of course, the lat-

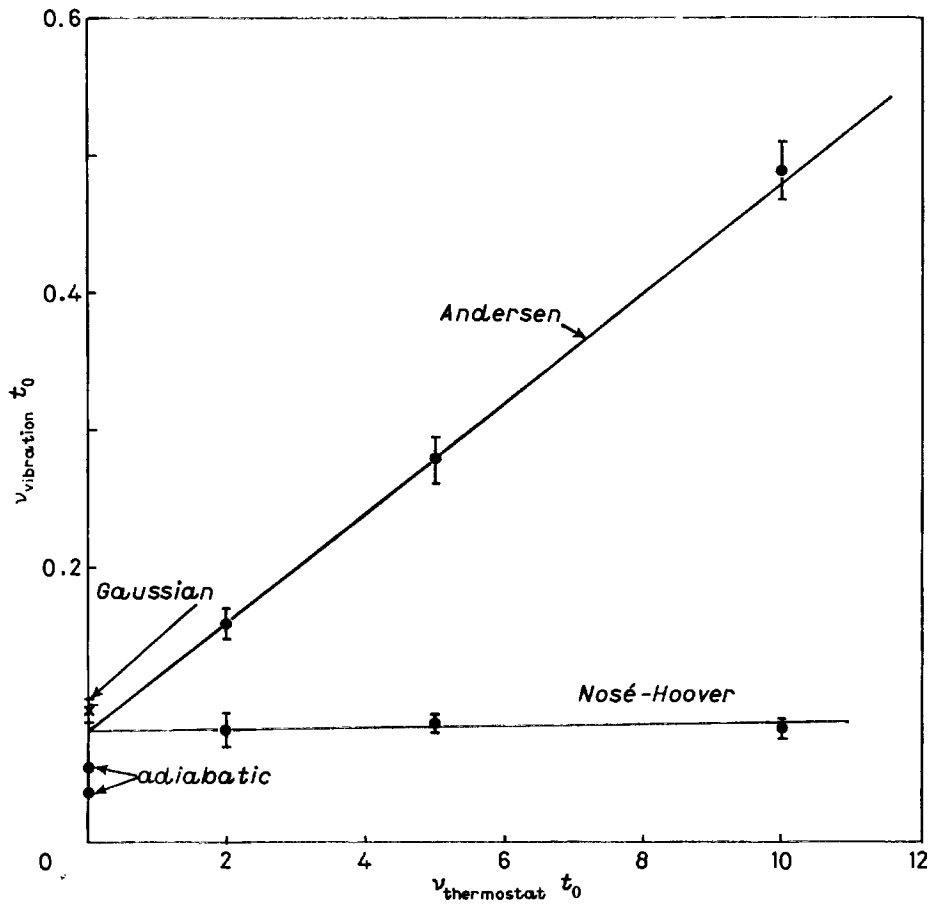

Fig. 7. – Vibrational relaxation rate $\nu_{\text{vibration}}$ as a function of thermostatting rate $\nu_{\text{thermostat}}$ for Andersen stochastic and Nosé-Hoover feedback thermostatting. Also shown are the Gaussian isokinetic feedback and adiabatic results; $\varrho = 2.3\ \text{g/cm}^3$, $T = 4000$ K, $T_0 = 300$ K, $\omega_e = 322$ THz, $t_0 = 0.13$ ps.

ter is really an infinite-rate rather than zero-rate procedure). Notice that, in agreement with eq. (8), both Andersen and Nosé-Hoover thermostattings appear to extrapolate to the same value of vibrational-relaxation rate in the adiabatic (zero thermostatting rate) limit, though the slopes differ dramatically, with the slope in the Andersen method 40 times that of the almost flat Nosé-Hoover method. The reason for this dramatic difference in slopes is almost surely due to the difference in smoothness of the trajectories: the Andersen method arbitrarily and abruptly resets velocities, often as not ramming molecules into one another in a way inherently far less gentle than the gradual effect of feed-

back in the Nosé-Hoover method. It is nevertheless comforting that the two methods give the same adiabatic limit, since at equilibrium they generate the same long-time averages, namely, canonical averages. This limiting value is somewhat above the two adiabatic NEMD results; however, it is doubtful that the discrepancy is statistically significant. In order to convince oneself of the significance, an ensemble of adiabatic experiments, rather than only two, would need to be performed. The Gaussian isokinetic result is, however, significantly higher than that of the adiabatic experiments, by almost a factor of two, and is also higher than any of the Nosé-Hoover realizations, as might be supposed from the relative « stiffness » of the two feedback methods. That is, the Gaussian method rigidly clamps the kinetic energy at a fixed value, with no fluctuations allowed, while the Nosé-Hoover method allows the value to fluctuate about the set value for characteristic times of the order of the thermostatting time constant. Nevertheless, the Gaussian method, being deterministic, is gentler than the stochastic method and gives a lower measured vibrational-relaxation rate than the Andersen procedure.

These results demonstrate that the Nosé-Hoover method gives essentially the adiabatic vibrational-relaxation rate without need for extrapolation to zero thermostatting rate, while it is absolutely essential to perform such an extrapolation with the Andersen procedure. The Gaussian method, on the other hand, affords no clue as to the underlying adiabatic rate except to overestimate it. As long as the Nosé-Hoover thermostatting rate is neither too large compared to the vibrational frequency, nor too small compared to the collision frequency, it is the method of choice among the thermostatting procedures presented here. The total-adiabatic-response method gives a rate that decays with temperature, so that its main utility is to show that the one-temperature partial adiabatic method gives the correct initial rate. Unfortunately, the severe dependence on initial conditions for these small systems ($N = 108$ molecules) makes it necessary to perform an impractically large ensemble of partial adiabatic experiments in order to glean the true adiabatic vibrational-relaxation rate by this NEMD method. It is comforting to note (at these densities at least) that the results for $N = 32$ are not noticeably different.

In the remainder of this lecture, we will discuss the qualitative features obtained from several adiabatic-response experiments. As indicated above, the absolute values of relaxation rates may be suspect, but the trends we will point out are nevertheless valid. First of all, our calculations indicate that the rate of vibrational relaxation drops exponentially as the frequency ω_e of the bond vibration increases. For example, at the state point examined in the previous examples ($\varrho = 2.3$ g/cm^3, $T = 4000$ K, $T_0 = 300$ K), the rate for $\omega_e = 322$ THz was $\sim 0.05 t_0^{-1}$, while at $\omega_e = 444$ THz (appropriate to N_2) the rate is an order of magnitude smaller. This exponential dependence of energy transfer upon frequency is typical of resonance phenomena. Second,

the temperature dependence of vibrational relaxation is approximately Arrhenius. This is not to say that the rate is sufficiently accurate to rule out a Landau-Teller [7] $(\exp[-(\theta/T)^{\frac{1}{3}}])$ or some other prediction of temperature dependence. Third, the density dependence of the Arrhenius activation temperature is well approximated by a quadratic function of inverse density. The density dependence is far from linear, that is, isolated binary collisions provide an inadequate description of vibrational relaxation in dense molecular fluids. In future publications, more details of numerical results will be presented.

4. – Conclusions.

Vibrational relaxation in dense molecular fluids can be best studied by homogeneously thermostatted nonequilibrium molecular dynamics, using the deterministic Nosé-Hoover equations of motion. For thermostatting rates lower than the collision rate, the intrusion of the thermostat on vibrational-relaxation rates is linear. Andersen's stochastic method of thermostatting, like the Nosé-Hoover method, allows one to extrapolate away the effects of thermostatting upon nonequilibrium rate processes, though the stochastic intrusion is much more dramatic, but Andersen's method does not maintain the temperature at a predetermined value. Gaussian isokinetic thermostatting is not useful for determining vibrational-relaxation rates, since there is no straightforward way to separate out the effects of thermostatting. For small systems that are practical for molecular-dynamics studies, total adiabatic relaxation is complicated by the fact that the rate is temperature- and, therefore, time-dependent. When all but the vibrational temperature is thermostatted (partial adiabatic relaxation), the rate is time-independent, but difficult to measure because of the inherent noisiness (fluctuations) and strong dependence on initial conditions in these small systems. Qualitative features of vibrational relaxation in dense molecular fluids, to be described in more detail in future work, have nevertheless been pinpointed, namely, the exponential dependence of rate on vibrational frequency, the nonlinearity of the density dependence and the approximate Arrhenius behavior, suggesting a thermally activated mechanism.

Appendix

Potentials.

The potential energy of the system of N molecules is assumed to be represented by

$$\Phi = \tfrac{1}{2}\sum_{i=1}^{N}\sum_{j\neq i}\sum_{a=1}^{2}\sum_{b=1}^{2}\varphi_{ab}(r_{ia,jb}) + \sum_{i=1}^{N}\varphi(r_{i1,i2})\,,$$

where

$$r_{ia,jb} = |\boldsymbol{r}_{ia} - \boldsymbol{r}_{jb}|$$

are atom-atom distances, φ_{ab} is the unbounded atom-atom intermolecular potential of the exponential-six form

$$\varphi_{ab}(r) = \frac{\varepsilon}{\alpha - 6}\left\{6 \exp\left[\alpha\left(1 - \frac{r}{r_0}\right)\right] - \alpha\left(\frac{r_0}{r}\right)^6\right\},$$

with $\varepsilon/k = 27.28$ K, $r_0 = 3.842$ Å and $\alpha = 13.16$ (these parameters fit configuration interaction calculations [8] for N_2, except that ε is scaled by 0.8 so as to fit experimental shock wave data; the equilibrium bond length is $r_e = 1.098$ Å) and φ is the intramolecular (bond) potential of the Morse form

$$\varphi(r) = D_e\left\{1 - \exp\left[\xi\left(1 - \frac{r}{r_e}\right)\right]\right\}^2,$$

with $D_e/k = 114\,950$ K and $\xi = 2.952$ (these parameters fit spectroscopic data [9] for N_2). By varying D_e and fixing r_e and ξ, we are able to alter the effective frequency of the bond from the N_2 value $\omega_e = 444$ THz by the relation ($\mu = 7.00335$ a.m.u. is the N_2 reduced mass)

$$\omega_e = (2D_e\xi^2/\mu r_e^2)^{\frac{1}{2}}.$$

REFERENCES

[1] *a*) W. G. Hoover, A. J. C. Ladd and B. Moran: *Phys. Rev. Lett.*, **48**, 1818 (1982); *b*) D. J. Evans: *J. Chem. Phys.*, **78**, 3297 (1983); *c*) W. T. Ashurst and W. G. Hoover: *Phys. Rev. Lett.*, **31**, 206 (1972).

[2] H. C. Andersen: *J. Chem. Phys.*, **72**, 2384 (1980).

[3] *a*) S. Nosé: *J. Chem. Phys.*, **81**, 511 (1984); *b*) W. G. Hoover: *Phys. Rev. A*, **31**, 1695 (1985).

[4] B. Jansson: *Random Number Generators* (Pattersons, Stockholm, 1966).

[5] H. J. C. Berendsen, J. P. M. Postma, W. F. van Gunsteren, A. DiNola and J. R. Haak: *J. Chem. Phys.*, **81**, 3684 (1984).

[6] D. J. Evans and B. L. Holian: *J. Chem. Phys.*, **83**, 4069 (1985).

[7] L. Landau and E. Teller: *Phys. Z. Sowietunion*, **10**, 34 (1936).

[8] P. J. Hay, R. T. Pack and R. L. Martin: *J. Chem. Phys.*, **81**, 1360 (1984).

[9] K. P. Huber and G. Herzberg: *Molecular Spectra and Molecular Structure*, Vol. **4** (van Nostrand Reinhold, New York, N. Y., 1979), p. 412.

Recent Results in the Kinetic Theory of Hard-Sphere Systems.

J. R. DORFMAN and T. R. KIRKPATRICK

Institute for Physical Science and Technology and
Department of Physics and Astronomy, University of Maryland
College Park, MD 20742

1. – Introduction.

In these lectures we will outline some of the main techniques used to describe nonequilibrium processes in hard-sphere fluids, and then discuss some interesting recent results for such fluids. The central focus of the first lecture will be to outline the microscopic foundation for mode-coupling theory [1]. The second lecture will be devoted to the application of the theory. There we will discuss *a*) nonanalytic dispersion relations for hydrodynamic modes of fluids [2, 3], such relations having been recently observed in neutron scattering experiments [4]; *b*) the theory [5, 6] for the « anomalous long-time tails » seen in computer simulations [7, 8] of the equilibrium stress tensor autocorrelation function and the theory [5, 9, 10] for the shear-rate-dependent shear viscosity observed in computer simulations of nonequilibrium fluids [11-14], and *c*) the theory of the dynamical phase transition of hard-sphere fluids at high densities to a glasslike state [15-18].

At first sight the theory of nonequilibrium processes in hard-sphere systems would seem to be a very simple one to develop. After all, only two hard spheres can collide at a time, their collisions are instantaneous, and they can never interpenetrate. While these points do represent important simplifications of the complicated dynamics of particles that interact with softer potentials, the proper mathematical description of the dynamics of N hard spheres has proved to be quite intricate. Since only two spheres can collide at a time, a representation of the dynamics in terms of binary collisions—the binary-collision expansion (BCE)—is appropriate. However, it took some time to work out the correct representation of the binary-collision operators that appear in the BCE. All of the complications in the BCE [19] have to do with the problem of overlapping configurations of hard-sphere particles. If one has initially, say, a physically allowed configuration of hard spheres (*i.e.* no overlaps), then the

BCE should not contain any nonzero contributions where overlaps appear. Since every term in the BCE has contributions from overlapping configurations, it is important to be certain that the binary-collision operators are properly defined so that all contributions from overlapping configurations cancel, and that the dynamics so described is the motion from one allowed configuration to another in proper accord with mechanics. We will discuss these operators in sect. **2**.

After the binary-collision operators and the BCE have been defined, we will turn to a discussion of equilibrium time correlation functions of microscopic momentum and density fluctuations in the system. These correlation functions are of critical interest for transport theory since one can use them to determine the frequency- and wave-number-dependent transport coefficients needed for a general hydrodynamic description of transport in the fluid [20]. The Green-Kubo formulae are typical examples of the relation between equilibrium time correlation functions and transport coefficients.

For a sufficiently dilute gas these functions can be expressed in terms of a function which is the solution of a linearized inhomogeneous Boltzmann equation. As one considers higher densities, one encounters two types of corrections to this equation, roughly characterized by the terms static and dynamic [21]. The static corrections take excluded-volume effects into account, that is, particles cannot collide in a region of space already occupied by one or more other particles. Dynamic corrections to the Boltzmann equation take into account binary-collision sequences where there exists some sort of dynamical correlation between the first and last collision in the sequence. In general, a correction to the Boltzmann equation will contain both static and dynamic contributions. Of the various dynamic corrections, the most important for our discussion here are due to the so-called ring events. These events consist of correlated sequences of l binary collisions among l particles and have been discussed in considerable detail elsewhere [22]. These ring events plus static corrections to them are responsible for the mode-coupling terms in the kinetic equation, and thus provide the microscopic basis of the mode-coupling theory. This derivation of the mode-coupling theory will be outlined in sect. **2** and **3** below. In sect. **2** we will outline the derivation of the mode-coupling theory for low-density systems. In sect. **3** we will discuss the important additional features that occur at high densities [23]. Of particular importance will be the wave number dependence of the mode frequencies at high densities.

In sect. **4**, **5** and **6** we will present three applications of mode-coupling theory of some interest for the interpretation of data from neutron scattering experiments and from computer-simulated molecular dynamics. These are, respectively, *a*) the derivation of nonanalytic dispersion relations for sound propagation in fluids, *b*) the mode-coupling explanation of large long-time tails for the equilibrium stress tensor autocorrelation function at high fluid density, and the theory for the shear-rate-dependent shear viscosity observed in com-

puter simulations of nonequilibrium fluids, and *c*) the theory of the glass transition in hard-sphere fluids at high densities. The dispersion relations discussed in sect. **4** determine the (complex) sound mode frequencies, $\omega_\pm(k)$, as functions of the wave number k. The usual sound dispersion relation of hydrodynamics is given by [1, 2]

$$\omega_\pm = \pm ikc + \Gamma k^2/2 + O(k^3)\,, \tag{1.1}$$

where c is the adiabatic velocity of sound and Γ is the sound damping constant that can be expressed in terms of the coefficients of kinematic and bulk viscosity and of thermal conductivity. Mode-coupling effects produce important corrections to these hydrodynamic relations for three-dimensional systems (*) of the form $a_\pm k^{\frac{5}{2}}$ [2, 3]. As recently reported by DE SCHEPPER *et al.* [4], these $k^{\frac{5}{2}}$ terms may have been detected in recent experiments at Delft.

One of the important consequences of the mode-coupling theory is the appearance of « long-time tail » contributions to transport coefficients such as the coefficient of shear viscosity [7, 8]. Theoretical calculations of the time correlation functions that determine the transport coefficients in the Green-Kubo formulae show that these functions decay as $t^{-d/2}$ for long time t. Here d is the number of dimensions of the system [2]. The coefficient of the $t^{-d/2}$ term in the coefficient of shear viscosity can be computed for hard spheres (or disks for $d = 2$), and the result can be compared with the computer simulations of the time correlation functions of the microscopic current in the system [8]. The point of our discussion here is that, although the results of computer simulations are consistent with the $t^{-d/2}$ decay predicted by mode-coupling theory for the long-time tails, the strength of this decay appears to be several hundred times larger in the computer experiments than that predicted by theory. Recently, VAN BEIJEREN [6] and KIRKPATRICK [5] have presented a resolution of this discrepancy which we will discuss in sect. **5**.

Section **6** will be devoted to a discussion of the dynamical phase transition that hard spheres undergo to a glasslike state. The theory for the phase transition can be based on mode-coupling theory, but it requires an extension of the theory discussed in sect. **2** and **3** to include nonlinear effects [15-17]. The original calculation was by LEUTHEUSSER [15]. Here we will discuss a slightly different approach given by KIRKPATRICK [17] that provides a quantitative self-consistent theory for this phase transition.

Finally in sect. **7** we will discuss some general features of the calculations presented here. In particular, we will indicate how far the results obtained here can be extended from hard-sphere particles to those that interact with more realistic potentials.

(*) For two-dimensional systems, mode-coupling effects render the transport coefficients in the Navier-Stokes equations nonanalytic functions of the gradients.

2. – From kinetic theory to mode-coupling theory.

The main focus of our work here will be a calculation of equilibrium time correlation functions of microscopic density and momentum fluctuation in hard-sphere systems (*). Such correlation functions are all defined in terms of a basic correlation function $C_{\mu\mu}(x, x', t)$ given by

$$C_{\mu\mu}(x, x', t) = \frac{1}{V}\langle \delta\mu(x, t)\, \delta\mu(x')\rangle\,, \tag{2.1}$$

where

$$\delta\mu(x') = \sum_{i=1}^{N} \delta(\boldsymbol{v}_i - \boldsymbol{v}')\, \delta(\boldsymbol{r}_i - \boldsymbol{r}') - n\varphi_0(v')\,, \tag{2.2a}$$

$$\delta\mu(x, t) = \sum_{i=1}^{N} \delta(\boldsymbol{v}_i(t) - \boldsymbol{v})\, \delta(\boldsymbol{r}_i(t) - \boldsymbol{r}) - n\varphi_0(v)\,. \tag{2.2b}$$

Here $x = (\boldsymbol{r}, \boldsymbol{v})$, $x' = (\boldsymbol{r}', \boldsymbol{v}')$, while $\{\boldsymbol{r}_i, \boldsymbol{v}_i\}$ denote the positions and velocities of the particles of the system, $\{\boldsymbol{r}_i(t), \boldsymbol{v}_i(t)\}$ denote positions and velocities at time t, and the angular brackets denote an equilibrium grand-canonical-ensemble average for a system confined to a volume V. In eqs. (2.2a) and (2.2b), $n = \langle N\rangle/V$, where $\langle N\rangle$ is the average number of particles, and $\varphi_0(v)$ denotes an equilibrium Maxwell-Boltzmann velocity distribution function. Due to the spatial isotropy of the equilibrium average, we can replace the computation of $C_{\mu\mu}(x, x', t)$ by an equivalent computation of its Fourier transform $C_{\boldsymbol{k}}(\boldsymbol{v}, \boldsymbol{v}', t)$ defined by ($\boldsymbol{k} \neq 0$)

$$C_{\boldsymbol{k}}(\boldsymbol{v}, \boldsymbol{v}', t) = \frac{1}{V}\langle g_{\boldsymbol{k}}(\boldsymbol{v}, t)\, g_{-\boldsymbol{k}}(\boldsymbol{v}')\rangle\,, \tag{2.3}$$

where

$$g_{-\boldsymbol{k}}(\boldsymbol{v}') = \sum_{i=1}^{N} \delta(\boldsymbol{v}_i - \boldsymbol{v}') \exp[-i\boldsymbol{k}\cdot\boldsymbol{r}_i] \tag{2.4a}$$

and

$$g_{\boldsymbol{k}}(\boldsymbol{v}, t) = \sum_{i=1}^{N} \delta(\boldsymbol{v}_i(t) - \boldsymbol{v}) \exp[i\boldsymbol{k}\cdot\boldsymbol{r}_i(t)]\,. \tag{2.4b}$$

Here $\boldsymbol{k}$ is a Fourier wave vector. Almost all of the quantities of interest to us below can then be expressed as velocity integrals of $C_{\boldsymbol{k}}(\boldsymbol{v}, \boldsymbol{v}', t)$. For example, the transverse-momentum autocorrelation function $C_\perp(\boldsymbol{k}, \omega)$, to be discussed

(*) We will usually formulate our calculations so as to apply to d-dimensional spheres where $d = 2, 3$.

later on, is given by

$$C_\perp(\boldsymbol{k}, \omega) = \mathrm{Re}\int_0^\infty \mathrm{d}t \int \mathrm{d}\boldsymbol{v} \int \mathrm{d}\boldsymbol{v}' \left(\beta \frac{m}{n}\right) \exp[i\omega t]\, (\hat{\boldsymbol{k}}_\perp^{(1)}\cdot\boldsymbol{v})(\hat{\boldsymbol{k}}_\perp^{(1)}\cdot\boldsymbol{v}')\, C_{\boldsymbol{k}}(\boldsymbol{v}, \boldsymbol{v}', t)\,. \tag{2.5}$$

Here $\beta = (k_B T)^{-1}$, where k_B is Boltzmann's constant and T the thermodynamic temperature, Re denotes the real part, $\hat{\boldsymbol{k}}_\perp^{(1)}$ is one of the unit vectors orthogonal to $\boldsymbol{k}$, and m is the mass of the particle. For later reference we note here the relation between $C_\perp(\boldsymbol{k}, \omega)$ and the wave-number- and frequency-dependent kinematic viscosity $\nu(k, \omega)$ given by [20]

$$C_\perp(\boldsymbol{k}, \omega) = \mathrm{Re}[-i\omega + k^2\nu(\boldsymbol{k}, \omega)]^{-1}\,. \tag{2.6}$$

The remainder of this section will be devoted to outlining the derivation of the mode-coupling expression for $C_{\boldsymbol{k}}(\boldsymbol{v}, \boldsymbol{v}', t)$, or equivalently for the generalized transport coefficients like $\nu(\boldsymbol{k}, \omega)$.

The time dependence of $C_{\boldsymbol{k}}(\boldsymbol{v}, \boldsymbol{v}', t)$ can be formally represented in terms of an N-particle streaming operator $S_t(x^N)$ which replaces the phases of N particles $x^N = \{\boldsymbol{r}_1, \boldsymbol{v}_1, \ldots, \boldsymbol{r}_N, \boldsymbol{v}_N\}$ by their phases $x^N(t) = \{\boldsymbol{r}_1(t), \boldsymbol{v}_1(t), \ldots, \boldsymbol{r}_N(t), \boldsymbol{v}_N(t)\}$ at a time t later following the dynamical motion of the system of N particles. Thus $C_{\boldsymbol{k}}(\boldsymbol{v}, \boldsymbol{v}', t)$ can be written

$$C_{\boldsymbol{k}}(\boldsymbol{v}, \boldsymbol{v}', t) = \frac{1}{V}\langle g_{-\boldsymbol{k}}(\boldsymbol{v}')\, S_t(x^N)\, g_{\boldsymbol{k}}(\boldsymbol{v})\rangle\,. \tag{2.7}$$

Due to the special properties of hard-sphere systems mentioned in the introduction, the explicit representation of $S_t(x^N)$ has two properties: *a*) $S_t(x^N)$ should be defined in such a way that unphysical configurations of the hard spheres are never generated during the course of the dynamical motion generated by this representation and *b*) $S_t(x^N)$ should be written in terms of binary-collision operators since hard-sphere dynamics is a succession of instantaneous binary collisions. Both of these properties are ensured by the following representation of $S_t(x^N)$ [19]: Consider the operator $S_t(x^N)$ in combination with the equilibrium distribution function $\exp[-\beta H_N] = \exp[-\beta H_N^0]\, W(\boldsymbol{r}^N)$, where

$$H_N^0 = \sum_{i=1}^N \frac{m v_i^2}{2} \tag{2.8a}$$

and

$$W(\boldsymbol{r}^N) = \exp\Big[-\beta \sum_{i<j} \varphi(r_{ij})\Big] \tag{2.8b}$$

with $\varphi(r_{ij})$ the hard-sphere potential

$$\varphi(r_{ij}) = \begin{cases} \infty & \text{for } r_{ij} < \sigma, \\ 0 & \text{for } r_{ij} \geqslant \sigma, \end{cases} \tag{2.8c}$$

where $r_{ij} = |\boldsymbol{r}_i - \boldsymbol{r}_j|$ and σ is the diameter of the hard spheres. Then $S_t(x^N)$ has two different representations depending on whether $W(\boldsymbol{r}^N)$ appears to the right or left of it.

1) $W(\boldsymbol{r}^N)$ to the left. Then

$$W(\boldsymbol{r}^N) S_t(x^N) = W(\boldsymbol{r}^N) \exp[tL_+] = W(\boldsymbol{r}^N) \exp\Big[tL_N^0 + \sum_{i<j} T_+(i,j)\Big]. \tag{2.9}$$

Here

$$L_N^0 = \sum_{i=1}^N \boldsymbol{v}_i \cdot \frac{\partial}{\partial \boldsymbol{r}_i} \tag{2.10a}$$

and $T_+(i,j)$ is a binary-collision operator defined by

$$T_+(i,j) = \sigma^{d-1} \int \mathrm{d}\hat{\boldsymbol{\sigma}}\, \theta(-\boldsymbol{v}_{ij}\cdot\hat{\boldsymbol{\sigma}}) |\boldsymbol{v}_{ij}\cdot\hat{\boldsymbol{\sigma}}|\, \delta(\boldsymbol{r}_{ij} - \sigma\hat{\boldsymbol{\sigma}})(b_\sigma(i,j) - 1). \tag{2.10b}$$

Here $\theta(x)$ is the step function $\theta(x) = 1$ if $x > 0$, and is zero otherwise, $\hat{\boldsymbol{\sigma}}$ is a unit vector describing the line between the center of particles i and j at the instant of their collision, $\boldsymbol{v}_{ij} = \boldsymbol{v}_i - \boldsymbol{v}_j$, and $b_\sigma(i,j)$ is a velocity replacement operator with

$$b_\sigma \boldsymbol{v}_i = \boldsymbol{v}_i - (\boldsymbol{v}_{ij}\cdot\hat{\boldsymbol{\sigma}})\hat{\boldsymbol{\sigma}}, \tag{2.11a}$$

$$b_\sigma \boldsymbol{v}_j = \boldsymbol{v}_j + (\boldsymbol{v}_{ij}\cdot\hat{\boldsymbol{\sigma}})\hat{\boldsymbol{\sigma}}. \tag{2.11b}$$

The representation given by (2.9) is appropriate for ensuring that, if the system starts from a nonoverlapping configuration—guaranteed by the presence of $W(\boldsymbol{r}^N)$ on the left—, then its development in time will never lead to an overlapping configuration. The other representation is appropriate for

2) $W(\boldsymbol{r}^N)$ to the right. Then

$$S_t(x^N) W(\boldsymbol{r}^N) = \exp[t\bar{L}_+] W(\boldsymbol{r}^N) = \exp\Big[tL_N^0 + \sum_{i<j} \bar{T}_+(i,j)\Big] W(\boldsymbol{r}^N), \tag{2.12}$$

where

$$\bar{T}_+(i,j) = \sigma^{d-1} \int \mathrm{d}\hat{\boldsymbol{\sigma}}\, |\boldsymbol{v}_{ij}\cdot\hat{\boldsymbol{\sigma}}|\, \delta(\boldsymbol{r}_{ij} - \sigma\hat{\boldsymbol{\sigma}})[\theta(-\boldsymbol{v}_{ij}\cdot\hat{\boldsymbol{\sigma}}) b_\sigma - \theta(\boldsymbol{v}_{ij}\cdot\hat{\boldsymbol{\sigma}})]. \tag{2.13}$$

The representation given by eq. (2.12) ensures that $S_t(x^N)W(\boldsymbol{r}^N)$ vanishes for any initial configuration of the N particles that contains overlapping spheres, and that the dynamics is correctly described for the nonoverlapping situations.

An essential ingredient for the use of these two representations of the Liouville operator is the binary-collision expansion given by

$$\exp[tL_+] = S_t^0(x^N) + \sum_\alpha \int_0^t \mathrm{d}\tau\, S^0_{(t-\tau)}(x^N)\, T_+(\alpha)\, S^0_\tau(x^N) + \tag{2.14}$$

$$+ \sum_\alpha \sum_\beta \int_0^t \mathrm{d}\tau_1 \int_0^{\tau_1} \mathrm{d}\tau_2\, S^0_{(t-\tau_1)}(x^N)\, T_+(\alpha)\, S^0_{(\tau_1-\tau_2)}(x^N)\, T_+(\beta)\, S^0_{\tau_2}(x^N) + \ldots$$

with a similar expansion for $\exp[t\bar{L}_+]$ with the $T_+(\alpha)$ replaced by $\bar{T}_+(\alpha)$. Here α denotes a particular pair of particles and $S_t^0(x^N) = \exp[tL_N^0]$. Then binary-collision expansions in conjunction with the appropriate $W(\boldsymbol{r}^N)$ give the correct representation of hard-sphere dynamics in terms of successive binary collisions.

Returning now to the main quantity of interest for us $C_{\boldsymbol{k}}(\boldsymbol{v}, \boldsymbol{v}', t)$, we see that it can be written in terms of a single-particle correlation function $\Phi_{\boldsymbol{k}}(\boldsymbol{v}_1, \boldsymbol{v}, t)$ as

$$C_{\boldsymbol{k}}(\boldsymbol{v}, \boldsymbol{v}', t) = n\int \mathrm{d}\boldsymbol{v}_1\, \delta(\boldsymbol{v}' - \boldsymbol{v}_1)\varphi_0(v_1)\, \Phi_{\boldsymbol{k}}(\boldsymbol{v}_1, \boldsymbol{v}, t)\,, \tag{2.15}$$

where φ_0 is defined above eq. (2.3) and

$$n\varphi_0(v_1)\, \Phi_{\boldsymbol{k}}(\boldsymbol{v}_1, \boldsymbol{v}, t) = \frac{1}{V\Xi} \sum_{N=0}^{\infty} \frac{\varkappa^N}{(N-1)!} \int \mathrm{d}\boldsymbol{r}_1 \int \mathrm{d}^{N-1}x \exp[-i\boldsymbol{k}\cdot\boldsymbol{r}_1]\cdot \tag{2.16}$$

$$\cdot \exp[t\bar{L}_+] \exp[-\beta H_N]\, g_{\boldsymbol{k}}(\boldsymbol{v})\,.$$

Here Ξ is the grand canonical partition function and $\varkappa$ is the fugacity.

Several authors have shown that the computation of $\Phi_{\boldsymbol{k}}$ can be reduced to the solution of a linearized kinetic equation. Various methods have been devised for derivation of the kinetic equation for $\Phi_{\boldsymbol{k}}$ [21, 22, 24, 25]. Elsewhere we have given a derivation based on the B.B.G.K.Y. hierarchy equations together with cluster expansions of the many-particle correlation functions which are used to truncate the hierarchy equations at various levels of approximation [2]. Probably the most extensive discussion of the kinetic equation of $\Phi_{\boldsymbol{k}}$ was given by VAN BEIJEREN and ERNST [21]. Their method is based on a diagrammatic expansion of $\Phi_{\boldsymbol{k}}$ in terms of the BCE of $\exp[tL_+]$ and on the Mayer f-expansion of the equilibrium spatial distribution function $W(\boldsymbol{r}^N)$. Here we will quote the main results of this analysis and explain the dynamical origin of the terms of interest to us here. It is worth mentioning, though, that any systematic analysis of $\Phi_{\boldsymbol{k}}$ will, of course, lead to the same result as that presented below.

VAN BEIJEREN and ERNST consider the Laplace transform of $\Phi_k(\boldsymbol{v}_1, \boldsymbol{v}, t)$ with Laplace variable z, and show that this quantity, $\Phi_{kz}(\boldsymbol{v}_1, \boldsymbol{v})$, is given by

$$\Phi_{kz}(\boldsymbol{v}_1, \boldsymbol{v}) = \left[1 + nh(k)\int \mathrm{d}\boldsymbol{v}_2 \varphi_0(v_2) P_{12}\right][z - i\boldsymbol{k}\cdot\boldsymbol{v}_1 - B_{kz}(\boldsymbol{v}_1)]^{-1}\delta(\boldsymbol{v}_1 - \boldsymbol{v}) . \tag{2.17}$$

Here $h(k)$ is the Fourier transform of the equilibrium two-body correlation function, P_{12} is a permutation operator that interchanges indices for particles 1 and 2, $B_{kz}(\boldsymbol{v}_1)$ is a kinetic operator that takes into account dynamical processes in the system, as well as static corrections to these dynamical effects. The term involving $h(k)$ takes into account static correlations in the initial state of the system. The operator $B_{kz}(\boldsymbol{v}_1)$ can, in principle, be expanded as a power series in the density. However, due to well-known divergence difficulties in this expansion [22] which appear as the Laplace variable $z \to 0$, a resummation of the terms in the density expansion is necessary in order to obtain results that should be more well behaved as $z \to 0$. Here we will present the expression for $B_{kz}(\boldsymbol{v}_1)$ when the resummation is already carried out. The contributions to B_{kz} can be roughly divided into two parts [21, 24]: 1) a random or « bare » part that describes the effect on Φ_{kz} due to uncorrelated collision sequences, and 2) a « memory preserving » part that takes into account correlated collision sequences (*) among the particles.

The bare part of the collision operator, denoted by $B_{kz,\mathrm{E}}(\boldsymbol{v}_1)$, is given by

$$B_{kz,\mathrm{E}}(\boldsymbol{v}_1) = n\chi(\sigma)\Lambda_k(\boldsymbol{v}_1) - nA_k(\boldsymbol{v}_1) \tag{2.18a}$$

with $\Lambda_k(\boldsymbol{v}_1)$ acting on any functions of $\boldsymbol{v}_1$, $h(\boldsymbol{v}_1)$, say, given by

$$\Lambda_k(\boldsymbol{v}_1)h(\boldsymbol{v}_1) = \int \mathrm{d}\boldsymbol{v}_2 \varphi_0(v_2)\sigma^2 \int \mathrm{d}\hat{\boldsymbol{\sigma}}\, \theta(-\boldsymbol{v}_{12}\cdot\hat{\boldsymbol{\sigma}})|\boldsymbol{v}_{12}\cdot\hat{\boldsymbol{\sigma}}|\cdot \\ \cdot[(b_\sigma - 1) + \exp[-i\boldsymbol{k}\cdot\hat{\boldsymbol{\sigma}}\sigma](b_\sigma - 1)P_{12}]h(\boldsymbol{v}_1) \tag{2.18b}$$

and $A_k(\boldsymbol{v}_1)h(\boldsymbol{v}_1)$ is given by

$$A_k(\boldsymbol{v}_1)h(\boldsymbol{v}_1) = [C(k) - \chi(\sigma)C_0(k)]\, i\int \mathrm{d}\boldsymbol{v}_2 \varphi_0(v_2)\, \boldsymbol{k}\cdot\boldsymbol{v}_2 h(\boldsymbol{v}_2) . \tag{2.18c}$$

Here $\chi(\sigma)$ is the equilibrium pair distribution function evaluated for two hard spheres at contact, $C(k)$ is the Fourier transform of the direct correlation function, and $C_0(k)$ is the lowest-order term in the density expansion of $C(k)$. The subscript E for the bare part of B_{kz} refers to ENSKOG who gave the first theory for density corrections to the Boltzmann equation for hard-sphere systems [26].

(*) Although one can give careful definitions of uncorrelated and correlated collision sequences, we will simply illustrate the difference by means of examples given below.

To understand the dynamical processes that contribute to $B_{kz,\mathrm{E}}(\boldsymbol{v}_1)$, we first consider the low-density and small-wave-number limit of this operator, $B_{00\mathrm{E}}(\boldsymbol{v}_1) = n\Lambda_0(\boldsymbol{v}_1)$, where Λ_0 is the linearized Boltzmann collision operator obtained by setting $\chi(\sigma) = 1$ and $\boldsymbol{k} = 0$ in eq. (2.18*b*). Then it is helpful to revert to the time representation and to note that to lowest order in the density $\Phi_{\boldsymbol{k}}(\boldsymbol{v}_1, \boldsymbol{v}, t)$ is given by

$$\Phi_{\boldsymbol{k},0}(\boldsymbol{v}_1, \boldsymbol{v}, t) = \exp\left[t(i\boldsymbol{k}\cdot\boldsymbol{v}_1 + n\Lambda_0(\boldsymbol{v}_1)\right]\delta(\boldsymbol{v}_1 - \boldsymbol{v})\,. \tag{2.19}$$

This contribution to $\Phi_{\boldsymbol{k}}(t)$ is due to binary-collision sequences where each collision is unrelated physically with any collision that preceded it, and to free particle motion between the collisions. In eq. (2.19), the free particle motion is responsible for the factor $i\boldsymbol{k}\cdot\boldsymbol{v}_1$ in the exponential, while the binary collisions are responsible for the operator $n\Lambda_0(\boldsymbol{v}_1)$. This operator describes collisions of two particles where either of the particles continues to participate in at least part of the subsequent collision sequence. A typical collision sequence of this type is illustrated in fig. 1*a*).

The higher-order density contributions to $B_{kz,\mathrm{E}}$ are all static corrections to the low-density result. The factor of $\exp[-i\boldsymbol{k}\cdot\hat{\boldsymbol{\sigma}}\sigma]$ in $\Lambda_{\boldsymbol{k}}$ takes into account the separation of the two hard spheres by a distance σ when they collide. The factor $\chi(\sigma)$ that multiplies $\Lambda_{\boldsymbol{k}}$ in eq. (2.18*b*) incorporates excluded-volume effects whereby the colliding particles cannot occupy a region of space where another particle is located. In graphical terms the first density correction to χ, for example, is a configuration of three particles in which a field particle is simultaneously overlapping both particles of the colliding pairs, as illustrated in fig. 1*b*). It is also possible to imagine situations in which one of the field particles in an overlapping configuration for one collision is the participant in the next collision in the collision sequence as illustrated in fig. 1*c*). This type of collision is described by the term $A_{\boldsymbol{k}}$ given by eq. (2.18*c*).

Therefore, if one includes only the « bare » part of the collision operator, one obtains an expression for $\Phi_{kz}(\boldsymbol{v}_1, \boldsymbol{v})$ or, equivalently, for $\Phi_{\boldsymbol{k}}(\boldsymbol{v}_1, \boldsymbol{v}, t)$ denoted by $\Phi_{kz,\mathrm{E}}(\boldsymbol{v}_1, \boldsymbol{v})$ or $\Phi_{\boldsymbol{k},\mathrm{E}}(\boldsymbol{v}_1, \boldsymbol{v}, t)$, respectively, where

$$\Phi_{\boldsymbol{k},\mathrm{E}}(\boldsymbol{v}_1, \boldsymbol{v}, t) = \left[1 + nh(k)\int \mathrm{d}\boldsymbol{v}_2\varphi_0(v_2)P_{12}\right]\exp\left[tL_{\boldsymbol{k},\mathrm{E}}(\boldsymbol{v}_1)\right]\delta(\boldsymbol{v}_1 - \boldsymbol{v})\,, \tag{2.20a}$$

where

$$L_{\boldsymbol{k},\mathrm{E}}(\boldsymbol{v}_1) = i\boldsymbol{k}\cdot\boldsymbol{v}_1 + n\chi(\sigma)\Lambda_{\boldsymbol{k}}(\boldsymbol{v}_1) - nA_{\boldsymbol{k}}(\boldsymbol{v}_1) \tag{2.20b}$$

and $\Phi_{kz,\mathrm{E}}(\boldsymbol{v}_1, \boldsymbol{v})$ is its Laplace transform. The factor multiplying the exponential on the right-hand side of eq. (2.20) is due to equilibrium correlations contained in $\Phi_{\boldsymbol{k}}$ at the initial time $t = 0$, and consequently contribute to the dynamical evolution of this quantity. For low densities, eq. (2.20*a*) reduces to eq. (2.19) and provides a good description of $\Phi_{\boldsymbol{k}}$ for all times.

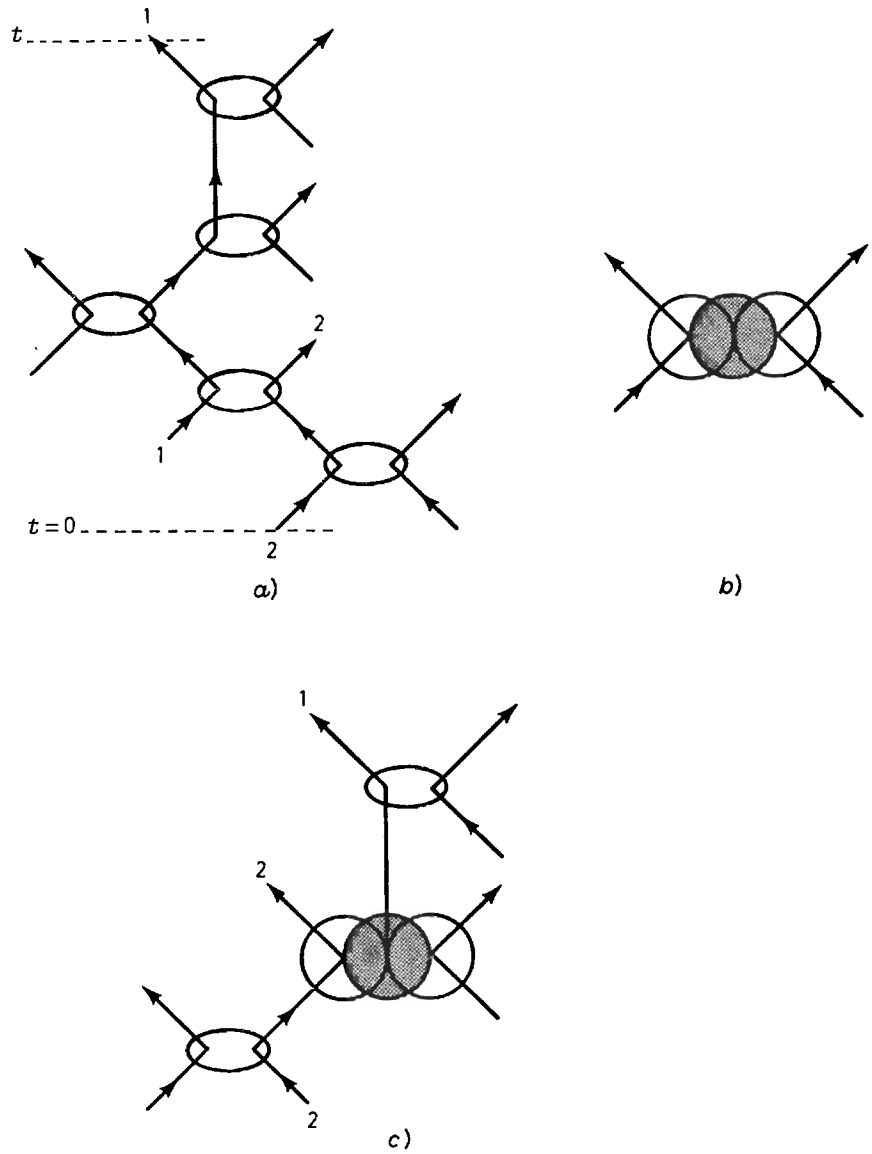

Fig. 1. – *a*) A typical binary-collision sequence that contributes to $\Phi_{k,0}(\boldsymbol{v}_1, \boldsymbol{v}, t)$, *b*) an overlapping configuration that contributes to the density corrections incorporated in the factor χ in eq. (2.18*a*), *c*) a typical dynamical sequence that contributes to the operator A_k in eq. (2.18*c*).

For systems at high densities, $n\sigma^3 > 0.85$ or so, the quantity $\Phi_{k,\mathrm{E}}(\boldsymbol{v}_1, \boldsymbol{v}, t)$ given above leads to a good description of the correlation function $C_k(\boldsymbol{v}_1, \boldsymbol{v}, t)$ only for very short times, on the order of one or two mean free times. For times longer than this, memory-preserving effects not included in $L_{k,\mathrm{E}}(\boldsymbol{v}_1)$ need to be taken into account. The simplest type of memory-preserving collision sequences are the ring collision events, which if considered separately in each order of the density are responsible for the divergences in the virial expansion of the transport coefficients, for example. It is the resummation of the contributions from ring events to each order of the density $B_{kz}(\boldsymbol{v}_1)$ that leads to the mode-coupling contributions to the time correlation functions and to the trans-

port coefficients [1, 24]. For our purpose here (*) the ring events consist of sequences of l collisions among l particles for $l \geqslant 3$, and in addition « static » density corrections to these collisions, similar to those discussed above, whereby excluded-volume and finite-size effects are taken into account. Examples of three- and four-body ring events are illustrated in fig. 2*a*) and *b*), respectively. If we retain the bare contribution to $B_{ks}(\boldsymbol{v}_1)$ as well as the ring contribution,

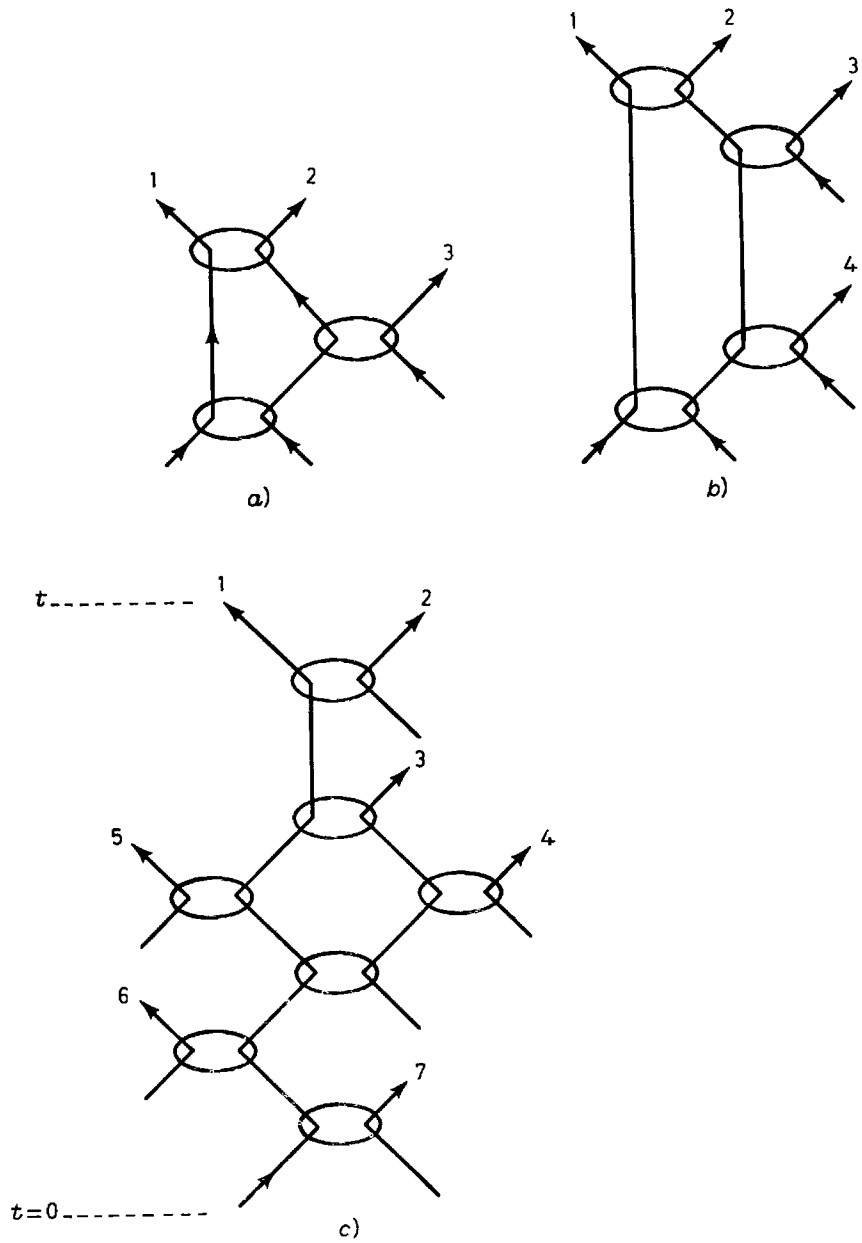

Fig. 2. – *a*) A three-body ring event, *b*) a four-body ring event, *c*) a typical collision sequence consisting of uncorrelated binary-collision and ring events.

(*) We will consider here not only the basic ring events of l binary collisions among l particles but also static corrections to them. See, for example, the two papers by DORFMAN and COHEN [24].

we have an expression for this kinetic operator of the form

$$B_{kz}(\boldsymbol{v}_1) = B_{kz,\mathrm{E}}(\boldsymbol{v}_1) + R_{kz}(\boldsymbol{v}_1)\,, \tag{2.21}$$

where $B_{kz,\mathrm{E}}(\boldsymbol{v}_1)$ is given by eq. (2.18) and $R_{kz}(\boldsymbol{v}_1)$ is the ring contribution with static corrections. The full form of $R_{kz}(v_1)$ is too elaborate to give here. Instead, we give the full expression in appendix A. In order to illustrate the essential features of the ring contribution to $\Phi_{kz}(\boldsymbol{v}_1)$, we first consider only the low-density form of the operator where finite-size and static effects are ignored. In this approximation $R_{kz}(\boldsymbol{v}_1)$ is denoted by $R^0_{kz}(\boldsymbol{v}_1)$ given by [2, 24]

$$R^0_{kz}(\boldsymbol{v}_1)\,h(\boldsymbol{v}_1) = n\int \mathrm{d}\boldsymbol{v}_2 \int \frac{\mathrm{d}\boldsymbol{q}}{(2\pi)^d}\, T_0(12) G^0_{q,l,z}\, T_0(1+P_{12})\,h(\boldsymbol{v}_1)\,, \tag{2.22a}$$

where $\boldsymbol{l} = \boldsymbol{k} - \boldsymbol{q}$,

$$T_0(12) = \sigma^{d-1}\int \mathrm{d}\hat{\boldsymbol{\sigma}}\,|\boldsymbol{v}_{12}\cdot\hat{\boldsymbol{\sigma}}|\,\theta(-\boldsymbol{v}_{12}\cdot\hat{\boldsymbol{\sigma}})(b_\sigma - 1) \tag{2.22b}$$

and

$$G^0_{q,l,z} = [z - L_{q,0}(\boldsymbol{v}_1) - L_{l,0}(\boldsymbol{v}_2)]^{-1}\,. \tag{2.22c}$$

Here $L_{q,0}(\boldsymbol{v}_1)$ is the low-density limit of $L_{q,\mathrm{E}}(\boldsymbol{v}_1)$ defined by eq. (2.20*b*) and is

$$L_{q,0}(\boldsymbol{v}_1) = i\boldsymbol{q}\cdot\boldsymbol{v}_1 + n\Lambda_0(\boldsymbol{v}_1)\,. \tag{2.23}$$

Therefore, if we take into account *a*) uncorrelated binary collisions and *b*) three-, four-, ... body ring events, all without static corrections and all with finite-size effects ignored, we obtain an expression for $\Phi_{kz}(\boldsymbol{v}_1, \boldsymbol{v})$ as

$$\Phi_{kz}(\boldsymbol{v}_1, \boldsymbol{v}) = [z - L_{k,0}(\boldsymbol{v}_1) - R^0_k(\boldsymbol{v}_1)]^{-1}\,\delta(\boldsymbol{v}_1 - \boldsymbol{v})\,. \tag{2.24}$$

A typical dynamical event that contributes to this expression for Φ_{kz} is illustrated in fig. 2*c*). This particular event consists of some uncorrelated binary collisions, before and after a four-body ring event. One can see that in general contributions to $\Phi_{kz}(\boldsymbol{v}_1, \boldsymbol{v})$ given by eq. (2.24) consist of all possible combinations of uncorrelated binary-collision sequences and ring events.

Next we examine the method used to analyze the ring collision operator $R^0_{kz}(\boldsymbol{v}_1)$. The essential idea is to express this operator in terms of the eigenvalues and eigenfunctions of the operators $L_{q,0}(\boldsymbol{v}_1)$ and $L_{l,0}(\boldsymbol{v}_2)$ [1]. Clearly the most interesting contributions to $R^0_{kz}(\boldsymbol{v}_1)$ will come from the eigenfunctions of L_q and L_l, $\theta_\alpha(\boldsymbol{v}_1, \boldsymbol{q})$, $\theta_\beta(\boldsymbol{v}_2, \boldsymbol{l})$, with the smallest eigenvalues, $-\omega_\alpha(q)$ and $-\omega_\beta(l)$. These are the so-called hydrodynamic modes of these operators. The hydrodynamic modes of $L_q(\boldsymbol{v}_1)$ have eigenvalues that go to zero as $|\boldsymbol{q}| \to 0$, and have eigenfunctions which to lowest order in q are conserved quantities in a binary

collision, *i.e.* linear combinations of 1, $\boldsymbol{v}_1$ and v_1^2. There are $d+2$ hydrodynamic modes—one heat mode, two longitudinal sound modes, and $d-1$ transverse shear modes. For small q the corresponding eigenvalues are

$$\omega_{\mathrm{H}}(q) = D_{\mathrm{T}}^{(\mathrm{B})} q^2 + \dots , \qquad \text{heat mode,} \tag{2.25a}$$

$$\omega_{\pm}(q) = \pm\, iqc^0 + \Gamma^{(\mathrm{B})} q^2/2 + \dots , \qquad \text{sound modes,} \tag{2.25b}$$

$$\omega_{\nu}(q) = \nu^{(\mathrm{B})} q^2 + \dots , \quad i = 1, \dots, d-1, \qquad \text{shear modes.} \tag{2.25c}$$

Here $D_{\mathrm{T}}^{(\mathrm{B})}$ is the Boltzmann equation value for the coefficient of thermal diffusivity, $\Gamma^{(\mathrm{B})}$ the sound damping constant and $\nu^{(\mathrm{B})}$ the kinematic viscosity and c^0 is the ideal-gas sound velocity. The ellipses in eqs. (2.25*a*)-(2.25*c*) denote higher-order terms in a power series in q, which converges (*) for $q \leqslant l^{-1}$, where l is the mean free path [27]. Thus we write

$$R_{\boldsymbol{k}z}^0(\boldsymbol{v}_1) = \sum_{\alpha,\beta} n \int \mathrm{d}\boldsymbol{v}_2 \int' \frac{\mathrm{d}\boldsymbol{q}}{(2\pi)^d} \cdot \frac{T_0(12)|\theta_\alpha(\boldsymbol{v}_1, \boldsymbol{q})\theta_\beta(\boldsymbol{v}_2, \boldsymbol{l})\rangle\langle\theta_\alpha(\boldsymbol{v}_1, \boldsymbol{q})\theta_\beta(\boldsymbol{v}_2, \boldsymbol{l})|T_0(12)(1+P_{12})}{z + \omega_\alpha(q) + \omega_\beta(l)} + R_{\perp,\boldsymbol{k}z}^{(0)}(\boldsymbol{v}_1) . \tag{2.26}$$

Here the summations over α and β include only the hydrodynamic modes, the $\boldsymbol{q}$ integral is restricted to the range $|\boldsymbol{q}| < l^{-1}$, $|\theta_\alpha\rangle$ and $\langle\theta_\alpha|$ represent right and left eigenfunctions of $L_{\boldsymbol{q}}(\boldsymbol{v}_1)$ respectively, we use an obvious inner-product notation, and all other contributions to $R_{\boldsymbol{k}z}^0(\boldsymbol{v}_1)$ are lumped together in $R_{\perp\boldsymbol{k}z}^0(\boldsymbol{v}_1)$. The operator $R_\perp^0$ contains short-distance effects $(|\boldsymbol{q}| > l^{-1})$ and the effects of kinetic rather than hydrodynamic modes. It is customary to assume that $R_\perp^0$ is small in comparison with the dominant kinetic contribution given by $L_{\boldsymbol{k},0}(\boldsymbol{v}_1)$ in eq. (2.24). However, a careful verification of this assumption would be helpful.

To illustrate the use of eq. (2.24), and to motivate our work in the next sections, we compute the low-density ring contributions to the correlation function $C_{\boldsymbol{k}z}(\boldsymbol{v}, \boldsymbol{v}')$. Using the approximate value of $\Phi_{\boldsymbol{k}z}(\boldsymbol{v}_1, \boldsymbol{v})$ given by eq. (2.24), we find

$$C_{\boldsymbol{k}z}(\boldsymbol{v}, \boldsymbol{v}') = \int \mathrm{d}\boldsymbol{v}_1 \varphi_0(v_1)\, \delta(\boldsymbol{v}_1 - \boldsymbol{v}')[z - L_{\boldsymbol{k},0}(\boldsymbol{v}_1) - R_{\boldsymbol{k}z}^0(\boldsymbol{v}_1)]^{-1} \delta(\boldsymbol{v}_1 - \boldsymbol{v}) . \tag{2.27}$$

Imagine now that we can compute right and left eigenfunctions of the operator $-\left(L_{\boldsymbol{k},0}(\boldsymbol{v}_1) + R_{\boldsymbol{k}z}^0(\boldsymbol{v}_1)\right)$ and their corresponding eigenvalues, so that

$$-\left(L_{\boldsymbol{k}0}(\boldsymbol{v}_1) + R_{\boldsymbol{k}z}^0(\boldsymbol{v}_1)\right)|\varphi_{\boldsymbol{k}z,0}^{(\alpha)}(\boldsymbol{v}_1)\rangle = \Omega_{\alpha,0}(\boldsymbol{k}, z)|\varphi_{\boldsymbol{k}z,0}^{(\alpha)}(\boldsymbol{v}_1)\rangle \tag{2.28a}$$

(*) For hard spheres at least.

and

$$\langle\varphi^{(\alpha)}_{\boldsymbol{k}z,0}(v_1)|[-(L_{\boldsymbol{k},0}(\boldsymbol{v}_1)+R^0_{\boldsymbol{k}z}(\boldsymbol{v}_1))]=\langle\varphi^{(\alpha)}_{\boldsymbol{k}z,0}(\boldsymbol{v}_1)|\Omega_{\alpha,0}(\boldsymbol{k},z)\,. \tag{2.28b}$$

Here the subscript 0 on the eigenfunctions and eigenvalues indicates that we are simply looking at the lowest-density contributions to the bare and the ring kinetic operators. If we can construct these quantities, then $C_{\boldsymbol{k}z}(\boldsymbol{v},\boldsymbol{v}')$ can be written

$$C_{\boldsymbol{k}z}(\boldsymbol{v},\boldsymbol{v}')=\sum_\alpha\frac{\langle\delta(\boldsymbol{v}_1-\boldsymbol{v}')|\varphi^{(\alpha)}_{\boldsymbol{k}z,0}(\boldsymbol{v}_1)\rangle\langle\varphi^{(\alpha)}_{\boldsymbol{k}z,0}(\boldsymbol{v}_1)|\delta(\boldsymbol{v}_1-\boldsymbol{v})\rangle}{z+\Omega_{\alpha,0}(\boldsymbol{k},z)}\,. \tag{2.29}$$

Next we treat the ring operator as a small perturbation to the Boltzmann collision operator. One can justify this in two ways: *a*) we can regard the ring operator as a small, density-dependent correction to the linearized Boltzmann collision operator; or *b*) we can, for general density, regard the ring operator as a small correction to the Enskog operator (*). Using, then, the ring operator as a small approximation, we find that

$$C_{\boldsymbol{k}z}(\boldsymbol{v},\boldsymbol{v}')=\sum_\alpha\langle\delta(\boldsymbol{v}_1-\boldsymbol{v}')|\theta_\alpha(\boldsymbol{v}_1,\boldsymbol{k})\rangle\langle\theta_\alpha(\boldsymbol{v}_1,\boldsymbol{k})|\delta(\boldsymbol{v}_1-\boldsymbol{v})\rangle\cdot \cdot[z+\omega_\alpha(k)+\omega^{(\alpha)}_{\text{m.c.}}(k,z)]^{-1}\,. \tag{2.30}$$

Here $-\omega_\alpha(\boldsymbol{k})$ is the eigenvalue of $L_{\boldsymbol{k},0}(\boldsymbol{v}_1)$ with corresponding eigenfunction $\theta_\alpha(\boldsymbol{v}_1,\boldsymbol{k})$, and $\omega^{(\alpha)}_{\text{m.c.}}(\boldsymbol{k},z)$ is the ring or «mode coupling» correction to the Boltzmann result given by

$$\omega^{(\alpha)}_{\text{m.c.}}(\boldsymbol{k},z)=\frac{k^2}{2n}\sum_{\mu,\nu}\int'\frac{\mathrm{d}\boldsymbol{q}}{(2\pi)^d}\langle\theta_\nu(\boldsymbol{v}_1,\boldsymbol{q})\theta_\mu(\boldsymbol{v}_1,\boldsymbol{l})P_\perp(\hat{\boldsymbol{k}}\cdot\boldsymbol{v}_1)\theta_\alpha(\boldsymbol{v}_1,\boldsymbol{k})\rangle\cdot \cdot\langle\theta_\nu(\boldsymbol{v}_1,\boldsymbol{q})\theta_\mu(\boldsymbol{v}_1,\boldsymbol{l})P_\perp(\hat{\boldsymbol{k}}\cdot\boldsymbol{v}_1)\theta_\alpha(\boldsymbol{v}_1,\boldsymbol{k})\rangle\,[z+\omega_\nu(q)+\omega_\mu(l)]^{-1}\,. \tag{2.31}$$

In eq. (2.31), the operator $P_\perp$ is a projection operator that projects onto the space of functions orthogonal to the conserved quantities 1, $\boldsymbol{v}_1$ and v_1^2. Further all eigenfunctions in this expression are to be replaced by their components in the direction of the conserved quantities.

Equation (2.31) is the low-density form of the well-known mode-coupling formula [1]. If we apply it, say, to a calculation of the transverse-momentum correlation function defined by eq. (2.5), we obtain an expression for the low-density mode-coupling contribution to kinematic viscosity as

$$\nu_{\text{m.c.}}(k,z)=\frac{1}{2n}\sum_{\alpha,\beta}\int'\frac{\mathrm{d}\boldsymbol{q}}{(2\pi)^d}\frac{|\langle\theta_\alpha(\boldsymbol{v}_1,\boldsymbol{q})\theta_\beta(\boldsymbol{v}_1,\boldsymbol{l})P_\perp(\boldsymbol{k}\cdot\boldsymbol{v}_1)(\hat{\boldsymbol{k}}^{(1)}_\perp\cdot\boldsymbol{v}_1)\rangle|^2}{z+\omega_\alpha(q)+\omega_\beta(l)}\,.$$

(*) When the ring contribution to some quantity becomes of the same order as the Enskog terms, one should begin to take into account other contributions in addition to the ring terms.

This result leads to the $t^{-d/2}$ long-time tail contribution to the shear viscosity [1, 2, 22, 24].

For dilute gases the mode-coupling contributions to the transport coefficients lead to interesting small-z or large-time effects, but their contributions to the transport coefficients are of $O(n^2)$ compared to the Boltzmann equation values. For systems at high densities, the mode-coupling contributions to the time correlation functions and the transport coefficient can be quite large [5, 6, 28]. This is due to a combination of three effects: *a*) hydrodynamic eigenvalues still vanish at small wave numbers, as in the low-density region; *b*) the matrix elements in the integrands may become large (*), and *c*) the effective range of the wave number increases dramatically at high densities. To see this, note that for high densities $l \ll \sigma$, *i.e.* the mean free path is smaller than a molecular size. Thus the wave number integral includes wave numbers that are on the order of inverse molecular size. As we will see later, it is this region of the $\boldsymbol{q}$ integration that leads to large contributions to the time correlation functions. Of course, when the mode-coupling terms are large, the argument for expressions like eq. (2.31) must be carefully re-examined.

In the next section we will consider the extension of (2.31) to higher densities and then consider the application of these theoretical developments to neutron scattering experiments.

3. – Mode-coupling theory and extended modes.

The main point of the previous section was to introduce the ring collision operator $R_{kz}(\boldsymbol{v}_1)$ and to outline the analysis of the hydrodynamic-mode contribution to this operator. In this section we will discuss the features of this hydrodynamic-mode decomposition that are important for the transport theory of hard-sphere fluids at high density, *i.e.* for densities of order $n\sigma^3 \geqslant 0.85$ or so.

In our previous discussion of the low-density ring operator $R^0_{kz}(\boldsymbol{v}_1)$ given by eq. (2.22) we argued that the most interesting contribution to the operator came from the small-wave-number region of the $\boldsymbol{q}$ integral for $q < l^{-1}$. Further, we argued that in this region the hydrodynamic-mode parts gave the largest contribution. Consider now the high-density case. Then we need to determine the hydrodynamic-mode contribution to the operator

$$G_{q,l,z} = [z - L_{q,\mathrm{E}}(\boldsymbol{v}_1) - L_{l,\mathrm{E}}(\boldsymbol{v}_2)]^{-1}\,, \tag{3.1}$$

where $L_{q,\mathrm{E}}(\boldsymbol{v}_1)$, $L_{l,\mathrm{E}}(\boldsymbol{v}_2)$ are given by eq. (2.20*b*). Such a hydrodynamic-mode decomposition will be valid in the small-wave-number region $ql_{\mathrm{E}} \lesssim 1$, where

(*) The growth of the mode-coupling matrix elements is responsible for the singularities in the transport coefficients near the critical point of a phase transition.

l_E is the mean free path for the hard spheres at high densities (*), since the mean free path sets the length scale for hydrodynamic or collective transport processes in a fluid.

There is yet another length scale characterizing the fluid, namely σ, the diameter of the spheres. For low densities the mean free path is much larger than σ. However, for high enough densities the mean free path can be a small fraction of the sphere diameter. This fact has as an important consequence that the hydrodynamic eigenvalues have a much more complicated dependence on the wave number at high densities than they do at low densities. To see this, consider the operator $L_{\boldsymbol{k},E}(\boldsymbol{v}_1)$, eq. (2.20*b*). This operator is characterized by two dimensionless parameters $k\sigma$ and kl_E. For low densities $k\sigma \ll 1$ for the entire range of k, $0 \leqslant kl \lesssim 1$, but for high enough densities $k\sigma$ can range from 0 to 20 or so over the range $0 \leqslant kl_E \lesssim 1$. The behavior of the hydrodynamic-mode eigenfunctions and eigenvalues of $L_{\boldsymbol{k},E}(\boldsymbol{v}_1)$ at high densities has been studied in some detail by DE SCHEPPER and COHEN [23], and here we will summarize their main results (**):

1) For $k\sigma \gg 1$,

$$L_{\boldsymbol{k},E}(\boldsymbol{v}_1) \approx L^s_{\boldsymbol{k},E}(\boldsymbol{v}_1)\,,$$

where $L^s_{\boldsymbol{k},E}$ is the Enskog-Lorentz operator that describes self-diffusion. It is given by

$$L^s_{\boldsymbol{k},E}(\boldsymbol{v}_1) = -\,i\boldsymbol{k}\cdot\boldsymbol{v}_1 + n\chi\Lambda^s(\boldsymbol{v}_1) \tag{3.2a}$$

and

$$\Lambda^s(\boldsymbol{v}_1) = \sigma^{d-1}\int \mathrm{d}\boldsymbol{v}_2\varphi_0(v_2)\int \mathrm{d}\hat{\boldsymbol{\sigma}}\,\theta(-\,\boldsymbol{v}_{12}\cdot\hat{\boldsymbol{\sigma}})|\boldsymbol{v}_{12}\cdot\hat{\boldsymbol{\sigma}}|(b_\sigma - 1)\,. \tag{3.2b}$$

This follows from eqs. (2.18*b*) and (2.18*c*) since for large $k\sigma$ the exponential factor on the right-hand side of eq. (2.18*b*) is effectively damped, and the correlation functions $C(k)$ and $C_0(k)$ approach zero as $k\sigma \gg 1$. The operator $L^s_{\boldsymbol{k},E}$ describes the motion of a single particle in the fluid. It has only one hydrodynamic mode corresponding to the one « zero » eigenfunction of the operator $\Lambda^s(\boldsymbol{v}_1)$ which only conserves particle number. The corresponding hydrodynamic eigenvalue of $L^s_{\boldsymbol{k},E}(\boldsymbol{v}_1)$ is $-\,\omega_D(k)$, given by

$$\omega_D(k) \approx D_E k^2 + O\big((kl_E)^4\big) \tag{3.3}$$

when D_E is the Enskog value for the coefficient of self-diffusion.

(*) In fact, using the Enskog theory, one can easily show that $l_E = [\pi n\chi(\sigma)\sqrt{2}]^{-1}$.
(**) It should be mentioned that there are alternate approaches to the wave-number-dependent hydrodynamic modes that lead to basically the same conclusions as some of those presented here [28-30].

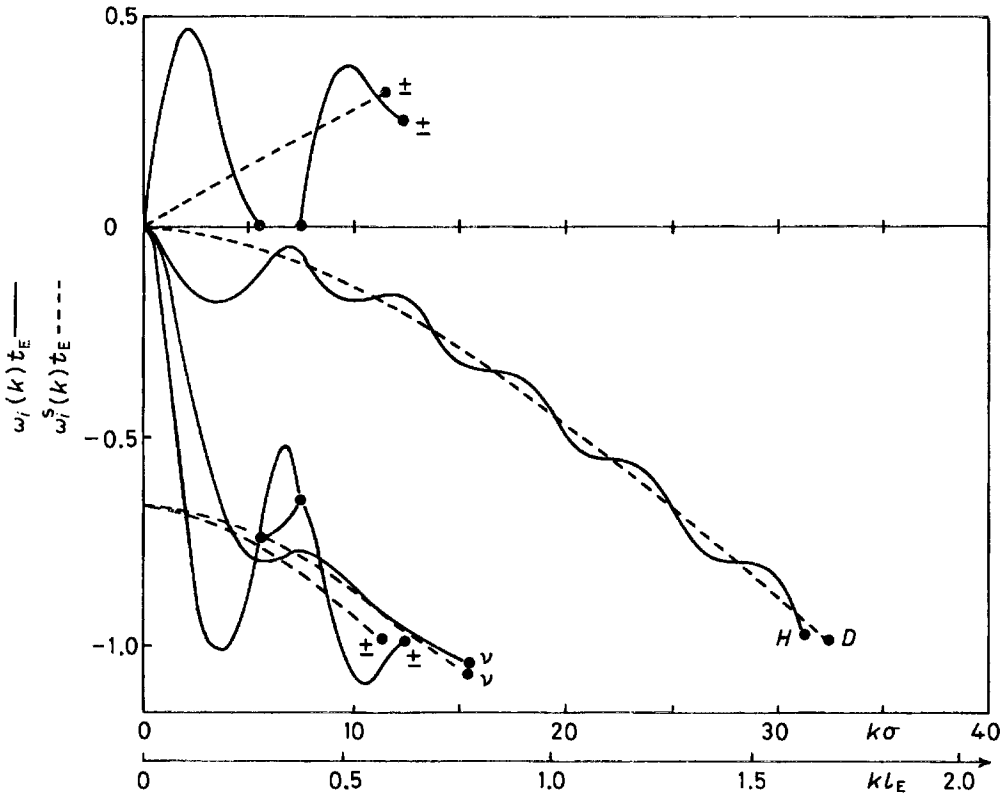

Fig. 3. – Eigenvalues of $L_{\boldsymbol{k},\mathrm{E}}(\boldsymbol{v}_1)$, $\omega_i(k)$ (full lines) and of $L^s_{\boldsymbol{k},\mathrm{E}}(\boldsymbol{v}_1)$, $\omega^s_i(k)$ (dotted lines) as functions of $k\sigma$ and kl_E for hard-sphere fluid at a density of $n\sigma^3 = 0.884$. Here t_E is the Enskog mean free time. Positive values refer to the absolute value of the imaginary parts of ω_i and ω^s_i, negative values refer to real parts. In addition to the hydrodynamic eigenvalue ω_D, two nonhydrodynamic-mode eigenvalues of $L^s_{\boldsymbol{k},\mathrm{E}}$ are also plotted. This figure is taken from ref. [23].

2) The hydrodynamic eigenvalues of $L_{\boldsymbol{k},\mathrm{E}}$ are plotted in fig. 3 for hard spheres at a density of $n\sigma^3 = 0.884$. At this density $l_\mathrm{E} = 0.052\sigma$, so that $k\sigma = 19.32\, kl_\mathrm{E}$. In addition, fig. 3 also exhibits the hydrodynamic eigenvalue, ω_D, and two nonhydrodynamic eigenvalues of the operator $L^s_{\boldsymbol{k},\mathrm{E}}(\boldsymbol{v}_1)$.

Several features of these results are worth comment:

a) For small $k\sigma$, the hydrodynamic eigenvalues are similar to the low-density results, *i.e.* ω_H, $\omega_\nu \sim k^2$, while $\omega_\pm = \pm ikc + \Gamma k^2/2$. For larger values of $k\sigma$ the eigenvalues are no longer monotonic functions of k.

b) For $k\sigma \gtrsim 1$, the heat mode eigenvalue softens (*) considerably, and then oscillates around the self-diffusion eigenvalue ω_D.

c) The shear mode eigenvalue softens and approaches one of the nonhydrodynamic eigenvalues of the operator L^s_k for $k\sigma > 1$.

(*) That is, its value gets smaller and comes close to zero.

d) The imaginary part of the sound mode eigenvalue vanishes for a range of $k\sigma$. This indicates the absence of propagating sound modes in the fluid for this range of $k\sigma$. Instead, over this range there are two strongly damped diffusive modes which become propagating again for larger values of $k\sigma$.

These results for the eigenvalues of $L_{k,\mathrm{E}}$ and $L^{s}_{k,\mathrm{E}}$ were obtained by DE SCHEPPER and COHEN using kinetic models for Λ_k and Λ^{s}_k that are similar to the BGK models of the linearized Boltzmann collision operator commonly used in kinetic theory. Another approach leading to qualitatively similar results has been given by KIRKPATRICK using wave-number-dependent generalized hydrodynamic equations for hard-sphere potentials [30].

In the work to be described in the following sections, the softening of the heat mode at high densities and for $k\sigma \approx 1$ will play an important role. It will then be necessary to have a useful expression for $\omega_{\mathrm{H}}(k)$ as a function of kl and $k\sigma$. This is provided by [23, 30]

$$\omega_{\mathrm{H}}(k) \simeq \frac{D_{\mathrm{E}}k^2}{S(k)}\, d(k) + O\big((kl_{\mathrm{E}})^4\big) \qquad \text{for } k\sigma > 1\,, \tag{3.4a}$$

where

$$d(k) = [1 - j_0(k\sigma) + 2j_2(k\sigma)]^{-1}\,. \tag{3.4b}$$

Here $S(k)$ is the static structure factor, $j_l(k\sigma)$ is the spherical Bessel function of order l, and D_{E} is the coefficient of self-diffusion as given by the Enskog theory for hard spheres.

4. – Neutron scattering and mode-coupling theory.

As our first application of the methods of the two previous sections, we consider the calculation of the dynamic structure factor $S(\boldsymbol{k}, \omega)$. This quantity is of interest because it can be measured by means of neutron scattering experiments [4, 23, 31] as well as by computer-simulated molecular dynamics [28, 32, 33]. As usually defined $S(\boldsymbol{k}, \omega)$ is

$$S(\boldsymbol{k}, \omega) = \frac{1}{2\pi}\int_{-\infty}^{\infty} \mathrm{d}t \exp[i\omega t]\, F(\boldsymbol{k}, t)\,, \tag{4.1a}$$

where $F(\boldsymbol{k}, t)$ is the intermediate scattering function

$$F(\boldsymbol{k}, t) = \frac{1}{nV}\Big\langle \sum_i \sum_j \exp[i\boldsymbol{k}\cdot(\boldsymbol{r}_i(t) - \boldsymbol{r}_j)]\Big\rangle = \frac{1}{n}\int \mathrm{d}\boldsymbol{v}\int \mathrm{d}\boldsymbol{v}'\, C_{\boldsymbol{k}}(\boldsymbol{v}, \boldsymbol{v}', t)\,, \tag{4.1b}$$

where $C_{\boldsymbol{k}}(\boldsymbol{v}, \boldsymbol{v}', t)$ is defined by eqs. (2.3) and (2.4). Using our general expression for $C_{\boldsymbol{k}}(\boldsymbol{v}, \boldsymbol{v}', t)$ given by eqs. (2.15) and (2.17), we find that $S(\boldsymbol{k}, \omega)$ can be written as

$$S(\boldsymbol{k}, \omega) = \int \mathrm{d}\boldsymbol{v}_1 \varphi_0(v_1) \Big[1 + nh(k) \int \mathrm{d}\boldsymbol{v}_2 \varphi_0(v_2)\, P_{12}\Big] \cdot \cdot [-i\omega - i\boldsymbol{k}\cdot\boldsymbol{v}_1 - B_{\boldsymbol{k},-i\omega}(\boldsymbol{v}_1)]^{-1} 1 \,, \tag{4.2}$$

where we have explicitly indicated that the inverse operator acts on the unit function. For $kl_{\mathrm{E}} \lesssim 1$ and for small enough frequencies (roughly $\omega\tau_{\mathrm{E}} \lesssim 1$, where τ_{E} is the mean free time between collisions), the dominant contribution to $S(\boldsymbol{k}, \omega)$ comes from the hydrodynamic modes of the total collision operator [4, 23, 31] $i\boldsymbol{k}\cdot\boldsymbol{v}_1 + B_{\boldsymbol{k},-i\omega}(\boldsymbol{v}_1)$. Of these modes, the two sound and the heat modes are the most important, so that a good approximation for $S(\boldsymbol{k}, \omega)$ is

$$S(\boldsymbol{k}, \omega) = \frac{1}{\pi} \sum_{j=-1}^{1} \mathrm{Re}\, \frac{A_j(\boldsymbol{k})}{-i\omega + \Omega_j(\boldsymbol{k}, \omega)} \,, \tag{4.3}$$

where $j = \pm 1, 0$ denotes the sound mode and heat mode contributions, respectively, A_j are the k-dependent matrix elements, similar to those given by eq. (2.29), and $-\Omega_j(\boldsymbol{k}, \omega)$ are the, possibly extended, hydrodynamic eigenvalues of the operator $[i\boldsymbol{k}\cdot\boldsymbol{v}_1 + B_{\boldsymbol{k},-i\omega}(\boldsymbol{v}_1)]$. In the approximation that $B_{\boldsymbol{k},-i\omega}(\boldsymbol{v}_1)$ is replaced by its Enskog and ring contributions, eq. (2.21), the eigenvalues $\Omega_j(\boldsymbol{k}, \omega)$ can be computed in some detail. Using this approximation for $B_{\boldsymbol{k},-i\omega}$, we can express $\Omega_j(\boldsymbol{k}, \omega)$ as

$$\Omega_j(\boldsymbol{k}, \omega) = \omega_j(k) + \omega_j^{(\mathrm{m.c.})}(\boldsymbol{k}, \omega) \,, \tag{4.4}$$

where $\omega_j(k)$ are the extended hydrodynamic eigenvalues of the operator $-L_{\boldsymbol{k},\mathrm{E}}$ discussed in sect. **3**, and $\omega_j^{(\mathrm{m.c.})}(\boldsymbol{k}, \omega)$ are the mode-coupling corrections to them.

The use of the extended eigenvalues $\omega_j(k)$ in discussing neutron scattering results has been discussed in some detail by DE SCHEPPER *et al.* [4, 23, 31]. Apart from the usual difficulties of fitting hard-sphere theories to experimental data by picking an appropriate (but fixed) hard-sphere diameter for the real system, the fit of the extended hydrodynamic-mode description to $S(\boldsymbol{k}, \omega)$ is quite good. Moreover, there is evidence that prediction of the vanishing of the sound frequency over a limited range of values of $k\sigma$ is correct.

Here, we want to consider the corrections to the $\omega_j(k)$ due to mode-coupling effects. Based on our analysis of the mode-coupling contribution to the eigenvalues in sect. **2**, and appendix A, we can see that the quantities $\omega_j^{(\mathrm{m.c.})}(\boldsymbol{k}, \omega)$ will have the form

$$\omega_j^{(\mathrm{m.c.})}(\boldsymbol{k}, \omega) = k^2 \sum_{(\mu,\nu)} \int_{q<l_{\mathrm{E}}^{-1}} \frac{\mathrm{d}\boldsymbol{q}}{(2\pi)^d} \frac{S_j^{(\mu,\nu)}(\boldsymbol{q}, \boldsymbol{l})}{-i\omega + \omega_\mu(q) + \omega_\nu(l)} \,. \tag{4.5}$$

Here $S_j^{(\mu,\nu)}(\boldsymbol{q}, \boldsymbol{l})$ is a mode-coupling amplitude, (μ, ν) denote combinations of two hydrodynamic modes of $L_{\boldsymbol{q},\mathrm{E}}$ and $L_{\boldsymbol{l},\mathrm{E}}$ with eigenvalues $-\omega_\mu(q)$, $-\omega_\nu(l)$, respectively. We are going to consider here only the mode-coupling contributions to the ordinary hydrodynamic-mode frequencies. The mode-coupling corrections to the extended mode frequencies have not yet been calculated. Under this condition, $\omega \sim O(k)$ in the region where the sound modes contribute to $S(\boldsymbol{k}, \omega)$ or of $O(k^2)$ where the heat modes contribute. For ω in either of these regions, the dominant contributions to $\omega_j^{(\mathrm{m.c.})}$ come from two sound modes ($\sigma = \pm 1$) such that [2, 3]

$$\omega_\sigma(q) + \omega_{-\sigma}(l) = i\sigma c\hat{\boldsymbol{q}}\cdot\boldsymbol{k} + \Gamma q^2 + \dots . \tag{4.6}$$

For small k the imaginary part of this sum nearly vanishes. In fact, one can easily demonstrate that combinations of this type appearing in the denominator in the right-hand side of eq. (4.5) lead to terms of order $k^{\frac{5}{2}}$. To see this, look at the sound mode contribution to $\omega_{\pm 1}^{(\mathrm{m.c.})}(\boldsymbol{k}, \omega)$ for $\omega \approx ick\sigma'$. Then one has, using eq. (4.6), integrals of the form (for $d = 3$)

$$\int_0^{l_\mathrm{E}^{-1}} \mathrm{d}q \frac{q^2}{ikc(\sigma\hat{\boldsymbol{q}}\cdot\hat{\boldsymbol{k}} - \sigma') + \Gamma q^2} = \frac{1}{\Gamma} l_\mathrm{E}^{-1} - k\int_0^{l_\mathrm{E}^{-1}} \frac{\mathrm{d}q(i\alpha(\hat{\boldsymbol{q}}))}{ikc(\sigma\hat{\boldsymbol{q}}\cdot\hat{\boldsymbol{k}} - \sigma') + \Gamma q^2}$$

which for small enough k consists of a finite part plus a term of order $k^{\frac{1}{2}}$. A similar result holds for $\omega^{(\mathrm{m.c.})}(\boldsymbol{k}, \omega)$ for $\omega \approx O(k^2)$. Thus

$$\omega_j^{(\mathrm{m.c.})}(\boldsymbol{k}, \omega \sim O(k) \text{ or } O(k^2)) = \alpha_j^{(\mathrm{m.c.})}k^2 + a_j^{(\mathrm{m.c.})}k^{\frac{5}{2}} . \tag{4.7}$$

The term $\alpha_j^{(\mathrm{m.c.})}k^2$ can be absorbed in $\omega_j(k)$, to give an improved value for the transport coefficient, while the main mode-coupling contribution is of order $k^{\frac{5}{2}}$.

Returning now to the expression for $S(\boldsymbol{k}, \omega)$ given by eq. (4.1), we can see that for a given value of k the sound mode contributions will be peaked at $\omega = \pm (ck + a_\mathrm{s}k^{\frac{3}{2}})$—the two Brillouin peaks—with a width proportional to $k^2 + b_\mathrm{s}k^{\frac{5}{2}}$. The heat mode contribution—the Rayleigh peak—will be centered at $\omega = 0$, with a width proportional to $k^2 + b_\mathrm{H}k^{\frac{5}{2}}$. The various coefficients of the $k^{\frac{5}{2}}$ terms have been computed by ERNST and DORFMAN [2].

In fig. 4, we show a plot given by DE SCHEPPER *et al.* [4, 31] for the sound mode frequency $\omega_\mathrm{s}(k)$ as a function of wave number k, obtained by neutron scattering experiments on liquid argon at $T = 120$ K. The sound mode frequency is obtained experimentally by fitting the spectra to a combination of three Lorentzians, two for the Brillouin lines and one for the Rayleigh line. The theoretical value is obtained from eqs. (4.4), (4.5) and (4.7). The dashed curve in fig. 4 shows the theoretical result for $\omega_\mathrm{s}(k)$. As one can see, the data are in reasonably good agreement with the theory for $k \leqslant 0.8$ Å^{-1}. The data

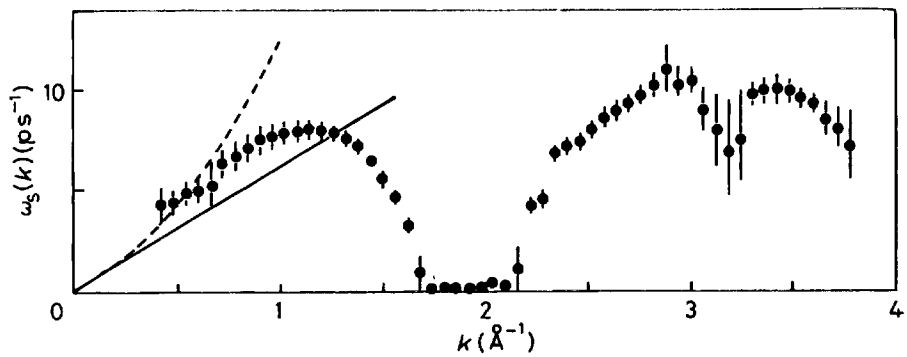

Fig. 4. – The absolute value of the imaginary part of the sound mode frequency as a function of k for liquid argon at $T = 120$ K and $P = 20$ bar. The dashed line represents the results of mode-coupling theory with the $k^{\frac{5}{2}}$ terms. The solid line is the hydrodynamic value $\omega_s = ck$. This figure is taken from ref. [4].

further indicate the existence of a range of k for which the sound modes do not propagate.

These experimental results are the most convincing ones available for confirming the prediction of the $k^{\frac{5}{2}}$ terms in the sound mode eigenvalues.

5. – Large long-time tails in the shear viscosity.

Over the past several years the mode-coupling analysis of equilibrium time correlation functions has been called into question by the results of computer-simulated molecular dynamics. Both hard-sphere and Lennard-Jones molecule simulations indicated that the stress tensor autocorrelation function that determines the coefficient of shear viscosity decays as $t^{-d/2}$ for d dimensions. However, if the fluid density is sufficiently high ($n\sigma^3 \gtrsim 0.85$), the measured coefficients of the $t^{-d/2}$ decay were several hundred times larger than those predicted by mode-coupling theory for the asymptotic $t^{-d/2}$ decay [7, 8]. A similar anomalous result was obtained for the coefficient of the nonanalytic terms in the shear-rate-dependent shear viscosity, where computer results were again several hundred times larger than theoretical predictions based on a nonequilibrium extension of mode-coupling theory [11-14].

A consideration of the computer data led most theorists to conclude that the measurements were not seeing the real asymptotic decay of the shear viscosity correlation function, but rather some sort of intermediate-time effect that exhibited the same $t^{-d/2}$ decay as that predicted for the asymptotic region. However, in the absence of a theoretical calculation that would reproduce the computer results the intermediate-time argument was not very convincing. Recently the situation has clarified considerably due to the work of van Beijeren [6] and Kirkpatrick [5], and we will present some features of their analysis here.

To set the argument properly, we need to consider the function calculated in the computer simulations and the time scale over which this function is studied. The quantity of interest is the stress tensor autocorrelation function $C_\eta(t)$ which is related to the frequency-dependent kinematic shear viscosity at zero wave number $\nu(k = 0, \omega)$, defined in eq. (2.6), by

$$\nu(k = 0, \omega) = \int_0^\infty \mathrm{d}t \exp[i\omega t] C_\eta(t) \tag{5.1}$$

and

$$C_\eta(t) = \frac{1}{V} \langle J_{xy}(t) J_{xy}(0) \rangle , \tag{5.2}$$

where $J_{xy}(t)$ is the x-y component of the microscopic stress at time t. The computer results for $C_\eta(t)$ at high densities can be described as follows [8]: For short times $0 \leqslant t \lesssim 2t_E$, where t_E is the Enskog mean free time, $C_\eta(t)$ decays approximately exponentially. For the region $2t_E \lesssim t \lesssim 10t_E$, C_η has a complicated behavior. Then for $10t_E \leqslant t \lesssim 50t_\eta$, $C_\eta(t)$ appears to decay as $t^{-d/2}$. For low fluid densities the coefficient of the $t^{-d/2}$ decay is roughly in agreement with mode-coupling theory, but for high enough densities the experimental coefficient is about 500 times larger than predicted for the asymptotically long $t^{-d/2}$ decay.

One important problem with mode-coupling theory is that it does not give a clear indication of the time scale on which the asymptotic $t^{-d/2}$ decay should be found. However, at the high densities studied, and over the relevant time scale, a simpler correlation function, the velocity autocorrelation function, has clearly not reached its asymptotic value. This suggests that the shear stress autocorrelation function may also not be in its asymptotic region on the time scales covered by the computer experiment. The fact that the anomalous $t^{-d/2}$ behavior only occurs at high densities also suggests that effects due to the slow structural relaxation of the fluid on a molecular-length scale may be important. Thus it seems natural to consider the role played by the extended hydrodynamic modes, and in particular the extended heat mode, in the stress autocorrelation function (*). Because the wave number integration in the mode-coupling formula includes regions where the extended heat mode is very soft, there is a mechanism *within mode-coupling theory* which could describe a slow hydrodynamiclike relaxation of the fluid, but which would not be the true asymptotic decay seen at very long times.

By following a generalization (to higher density) of the argument leading

(*) It is important to note that extended heat mode softens and approaches the self-diffusion mode at wave numbers on the order of a few σ^{-1}. Thus the slow relaxation is basically one of particle diffusion through the fluid.

to eq. (2.31) and by setting $k = 0$ in the frequency- and wave-number-dependent kinematic viscosity, we can obtain an expression for $C_\eta^{(\mathrm{m.c.})}(t)$ of the form (for $d = 3$)

$$C_\eta^{(\mathrm{m.c.})}(t) = \sum_{\mu,\nu} \int_{q<l_\mathrm{E}^{-1}} \frac{\mathrm{d}\boldsymbol{q}}{(2\pi)^3} S_\eta^{(\mu,\nu)}(\boldsymbol{q}, -\boldsymbol{q}) \exp\left[-\left(\omega_\nu(q) + \omega_\mu(q)\right)t\right]. \tag{5.3}$$

Here $S_\eta^{(\mu,\nu)}(\boldsymbol{q}, -\boldsymbol{q})$ is a mode-coupling amplitude and $\omega_\nu(q)$, $\omega_\mu(q)$ are the mode eigenvalues considered to be general functions of q. Now the dominant contribution to this integral over the range of the $\boldsymbol{q}$ integration comes from the extended heat modes. There is still some uncertainty in the proper definition of the mode-coupling amplitude for this calculation, since the usual derivation of the mode-coupling formula assumes that only the asymptotic region $t \to \infty$ (or $\omega \to 0$) is being described [5, 34, 35]. A very careful theory for the two-mode contribution is currently being developed by VAN BEIJEREN and co-workers.

A reasonably good approximation for $S_\eta^{(\mathrm{H,H})}(\boldsymbol{q}, -\boldsymbol{q})$ can be obtained by neglecting terms of $O(ql_\mathrm{E})$ in the hydrodynamic modes, and this leads to the expression [5]

$$S_\eta^{(\mathrm{H,H})}(\boldsymbol{q}, -\boldsymbol{q}) = \frac{1}{30\beta^2}\left[\frac{qS'(q)}{S(q)}\right]^2, \tag{5.4}$$

where $S(q)$ is the static structure factor, $S'(q)$ is its wave number derivative, and $\beta = (k_\mathrm{B}T)^{-1}$. For the extended-heat-mode eigenvalues one can use eq. (3.4*b*) for $\omega_\mathrm{H}(q)$ and then compute the integral numerically. The result for $C_\eta(t)$ is plotted in fig. 5, and compared with computer results [8] over the range $12\,t_\mathrm{E} < t < 50\,t_\mathrm{E}$. Note that the theoretical result for the heat mode contribution to $C_\eta(t)$ appears to decay as $t^{-\frac{3}{2}}$ over this time interval, even though for

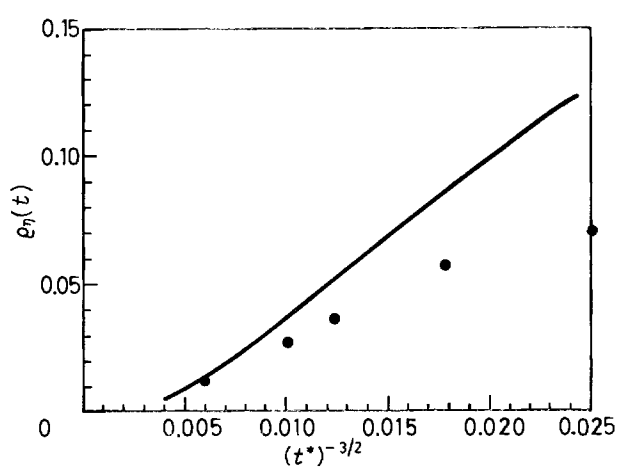

Fig. 5. – A plot of the normalized stress tensor autocorrelation function as a function of $(t^*)^{-\frac{3}{2}}$, with $t^* = t/t_\mathrm{E}$, and $\varrho(t) = \beta t_0 C_\eta(t)/\eta_\mathrm{E}$. Here t_0 is the Boltzmann mean free time and η_E is the Enskog value of the cofficient of shear viscosity. The data points are taken from ref. [8] for hard spheres at $n\sigma^3 = 0.88$.

$t \to \infty$ this integral does decay faster than $t^{-\frac{3}{2}}$. Further the slope is only off by a factor of two or so rather than by the factor of 500 for the asymptotic $t^{-\frac{3}{2}}$ result. The discrepancy of the factor of two is probably due to the use of the above form for $S_\eta^{(\mathrm{H},\mathrm{H})}(\boldsymbol{q}, -\boldsymbol{q})$, as well as to contributions from three and higher modes.

A similar line of argument [5] also serves to resolve a related discrepancy between mode-coupling theory and the results of computer simulations. For this case one considers the shear-rate-dependent coefficient of shear viscosity. Imagine a steady shear flow imposed on a fluid at constant temperature and density, such that the local fluid velocity $\boldsymbol{u}$ has the profile given by $\boldsymbol{u} = \varepsilon x \hat{\boldsymbol{y}}$, where ε is the shear rate, $\hat{\boldsymbol{y}}$ is a unit vector in the y direction. Then the pressure tensor element P_{xy} has the general form [2]

$$P_{xy} = -\eta(\varepsilon)\,\varepsilon\,. \tag{5.5}$$

Then, for small ε, mode-coupling theory predicts that $\eta(\varepsilon)$ has the form [9, 10]

$$\eta(\varepsilon) = \eta(0) + a|\varepsilon|^{\frac{1}{2}} + \ldots \quad \text{for } d = 3, \qquad \text{and} \qquad \eta(\varepsilon) = b \log|\varepsilon| + \ldots \quad \text{for } d = 2\,,$$

as $\varepsilon \to 0$. Here again these forms are confirmed by computer experiments [11-14], but with coefficients several hundred times larger than those predicted by the theory. This discrepancy can be resolved by including the extended heat modes in the mode-coupling description of $\eta(\varepsilon)$, in parallel to the way it was done for $C_\eta(t)$. Again one obtains an integral that must be computed numerically. In fig. 6 we plot the resulting expression for the heat mode contribution to $\eta(\varepsilon)$, for $d = 3$, as a function of $\varepsilon^{\frac{1}{2}}$. One can see that, over a range of ε, this expression for $\eta(\varepsilon)$ appears to vary linearly with $\varepsilon^{\frac{1}{2}}$, but, for small ε, this contribu-

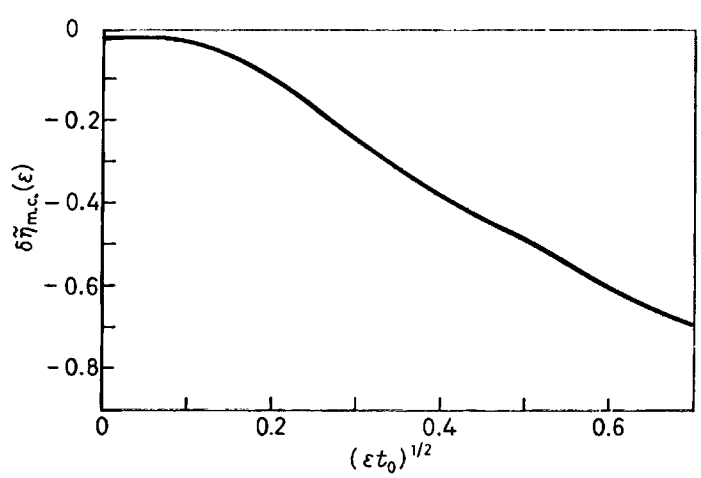

Fig. 6. – A plot of the nonequilibrium mode-coupling contribution, $\delta\tilde{\eta}_{\mathrm{m.c.}}(\varepsilon)$, to the shear-rate-dependent coefficient of shear viscosity defined in eq. (5.5), as a function of $(\varepsilon t_0)^{\frac{1}{2}}$.

tion is actually proportional to ε^2. The slope of the $\varepsilon^{\frac{1}{2}}$ behavior is in qualitative agreement with the computer results but is a factor of two too large. The $\varepsilon^{\frac{1}{2}}$ prediction of mode-coupling theory is correct, too, but only for very small ε, smaller than those used in the simulations.

In summary, the anomalous long-time tails in the stress tensor autocorrelation function and the anomalous $\varepsilon^{\frac{1}{2}}$ terms in the shear-rate-dependent viscosity (all at high densities) can be explained by incorporating the extended heat modes into the calculation. The softening of the heat mode provides a slow structural relaxation that mimics the true asymptotic $t \to \infty$, or $\varepsilon \to 0$ limits. However, in neither case is the computer seeing an asymptotic result, but rather an « intermediate » time or shear rate result, dominated by exponential relaxation, but with a very long lifetime. It would be interesting to look at an analogous simulation for the long-time tail in the bulk viscosity correlation function. Here one expects both the asymptotic long-time tail, as well as the extended-heat-mode « tail » to be large.

It should be remarked that the apparent long-time tail on $C_\eta(t)$ is more than of just academic interest at and above these densities. Computer experiments [36] indicate that at $n\sigma^3 = 0.88$ the true shear viscosity is given by $\eta \simeq 1.52\eta_E$, *i.e.* the Enskog theory is only very approximate. This increase in η over its Enskog value can be explained as being due to the large long-time tails discussed above. As the density increases more, the apparent long-time tails become even more important and soon dominate the Enskog contribution. In the next section these ideas are made more precise by constructing a theory of the approach to the glass transition where $\eta \to \infty$.

Finally, we mention that a calculation closely related to that given here also accounts for the existence of propagating shear waves in dense, hard-sphere fluids [5, 34].

6. – The glass transition.

Perhaps the most striking recent extension and application of mode-coupling theory is to a description of the glass transition in supercooled liquids. It is found, both experimentally and through computer simulations, that liquids can be rapidly cooled far below their freezing temperature or compressed beyond their freezing density, and remain in a glassy state for long periods of time (*). If the density of the supercooled liquid is high enough, the liquid forms a glass [15-17, 37], and, for a fixed temperature, T, of the fluid, there is a density, $n_g(T)$, below which the supercooled fluid is a liquid and above which, a glass (**).

(*) In real systems, the lifetime of glasses can be centuries.

(**) Thus for a fixed density there may be a temperature T_g below which a supercooled liquid is a glass.

The characteristic features of the glass are: 1) The coefficient of self-diffusion for a particle in the glass is essentially zero, and 2) the coefficient of shear viscosity of the glass is many orders of magnitude larger than that of the liquid. For the special case of hard-sphere systems one can show that n_g does not depend on temperature, so that here we will simply concentrate on the effect of density variation in a compressed hard-sphere fluid.

The quantity we are going to consider in describing the mode-coupling theory of the glass transition is the wave-number-dependent density-density correlation function Φ_{kz} defined by

$$\Phi_{kz} = \frac{1}{S(k)} \int_0^\infty \mathrm{d}t \exp[-zt] F(\boldsymbol{k}, t) , \tag{6.1}$$

where $F(\boldsymbol{k}, t)$ is the intermediate scattering function defined in eq. (4.16), and $S(k)$ is the static structure factor introduced here for normalization. This quantity is of interest here since for a dense fluid the dynamics on a molecular scale ($k \sim \sigma^{-1}$) will be very slow due to the slow structural rearrangement in the fluid. We know also from our previous discussion that at small wavelengths the decay of $F(\boldsymbol{k}, t)$ will be mainly due to self-diffusion. Thus, since the onset of the glass transition should be signaled by the vanishing of the coefficient of self-diffusion, $F(\boldsymbol{k}, t)$ should not decay at all for $n > n_g$, or equivalently Φ_{kz} should be proportional to z^{-1} in this region (*). We know that even when mode-coupling effects are not taken into account $F(\boldsymbol{k}, t)$ decays slowly at these wave numbers due to the softening of the heat mode, so that, if mode-coupling effects are included, the decay of $F(\boldsymbol{k}, t)$ should be even slower. The important point here is that mode-coupling theory takes into account at least some of the collective effects in the system that are responsible either for maintaining or for relaxing the short-range structure in the fluid. Now since the mode-coupling effects themselves depend on the density-density correlation function, there is a nonlinearity that can lead to the glass transition where the dynamical processes become frozen. This mechanism was first suggested by LEUTHEUSSER [15], and further developed by others [16, 18], there we follow the work of Kirkpatrick [17]. Although we do not expect the simple mode-coupling of theory to account for all the quantitative details of this transition, we do expect that the basic qualitative features should appear in such a calculation.

To proceed with the mode-coupling theory [17], we first consider that the fluid is at very high density and that we are interested in effects on a molecular-length scale so that temperature fluctuations can be neglected [39]. Then

(*) Thus $F(\boldsymbol{k}, t)$ acts like the order parameter of the glass transition. As $t \to \infty$, $F(\boldsymbol{k}, t) \to 0$ for the liquid, and to a nonzero constant for the glass. This is similar to the Edwards-Anderson order parameter for a spin glass [38].

Φ_{kz} can be written

$$\Phi_{kz} = \frac{1}{z + \Omega(\boldsymbol{k}, z)}, \tag{6.2}$$

where $\Omega(\boldsymbol{k}, z)$ is a generalized hydrodynamic eigenvalue. In our discussion in sect. **3** and **4**, we considered that $\Omega(\boldsymbol{k}, z)$ could be written as a « bare » contribution plus a mode-coupling term. The « bare » part is the extended-heat-mode eigenvalue, $\omega_{\mathrm{H}}(k)$, given by eq. (3.4). The mode-coupling analysis is facilitated if one uses a memory function formulation [20] and writes

$$\Omega(\boldsymbol{k}, z) = \frac{k^2}{\beta m S(k)\, \Gamma(\boldsymbol{k}, z)} \tag{6.3a}$$

with

$$\Gamma(\boldsymbol{k}, z) = \gamma(k) + \Sigma(\boldsymbol{k}, z)\,. \tag{6.3b}$$

The bare part of $\Gamma(\boldsymbol{k}, z)$, given by eq. (3.4), is

$$\gamma = \frac{2}{3t_{\mathrm{E}}}\left(1 - j_0(k\sigma) + 2j_2(k\sigma)\right), \tag{6.4}$$

where $t_{\mathrm{E}} = 2\beta m D_{\mathrm{E}}/3$ is the Enskog mean free time. Of course, the central issue here is to derive an equation for $\Sigma(\boldsymbol{k}, z)$. To do this one uses again the fact that on a short distance scale the only obvious slowly varying dynamical variable is the microscopic density, since neither momentum nor energy is going to be conserved on this scale. Thus the dominant mode contributions to $\Sigma(\boldsymbol{k}, z)$ are going to be density modes. We assume, then, that $\Sigma(\boldsymbol{k}, z)$ is determined by the two-density mode contribution and also that the decay of the microscopic density modes with wave number $\boldsymbol{q}$ is, in turn, determined by $F(\boldsymbol{q}, t)$. Thus one would expect that the mode-coupling expression for $\Sigma(\boldsymbol{k}, z)$ has the form

$$\Sigma(\boldsymbol{k}, z) = \int \frac{\mathrm{d}\boldsymbol{q}}{(2\pi)^3} \int_0^\infty \mathrm{d}t \exp[-zt]\, S_{nn}^{(\Sigma)}(\boldsymbol{q}, \boldsymbol{k}-\boldsymbol{q})\, \Phi(\boldsymbol{q}, t)\, \Phi(\boldsymbol{k}-\boldsymbol{q}, t)\,. \tag{6.5}$$

Here $S_{nn}^{(\Sigma)}(\boldsymbol{q}, \boldsymbol{k}-\boldsymbol{q})$ is a mode-coupling amplitude, determined by equilibrium-like correlations in the fluid (*). In the two-density mode case $S_{nn}^{(\Sigma)}(\boldsymbol{q}, \boldsymbol{k}-\boldsymbol{q})$ can be expressed in terms of Fourier transforms of the two-particle and direct correlation function, and the three-particle direct correlation function. When this expression for $\Sigma(\boldsymbol{k}, z)$ is inserted on the right-hand side of eq. (6.3*a*), a

(*) Remember that we are really describing a metastable state of the system. The stable state is a crystalline solid.

highly nonlinear equation for Φ_{kz} is obtained. This equation can be simplified with some reasonable approximations, the most important of which involves expansions of the static structure factor and other related quantities about their values at a point $k = k_0$ where k_0 is the location of the first maximum of $S(k)$. Then one finds the following results [17]:

1) There exists a density n_g above which the compressed system is a glass and below which it is a liquid.

2) Above this transition density $\Gamma(\boldsymbol{k}, z)$ in eq. (6.3) has the form

$$\Gamma(\boldsymbol{k}, z) = \frac{a}{z} + \Gamma_v(z)\,, \qquad \text{with } a \neq 0\,, \text{ and } z\Gamma_v(z) \to 0 \text{ as } z \to 0\,, \tag{6.6}$$

indicating that the density-density correlation function does not decay in time.

3) For densities close to, but below the transition density, the coefficient of self-diffusion, D, as well as the coefficient of shear viscosity, η, are finite. However, as n approaches n_g, $D \to 0$ and $\eta \to \infty$ as

$$D \sim (n_g - n)^{1.89} \tag{6.7a}$$

and

$$\eta \sim (n_g - n)^{-1.89}\,. \tag{6.7b}$$

It is these results that indicate that the theory is describing a glass transition, since, as mentioned earlier, the vanishing of D and the divergence of η are the indicators of the transition (*). In fig. 7 we plot the theoretical result for D, eq. (6.7a), as a function of n near the transition density n_g, and compare with computer data obtained by WOODCOCK [40]. The value of n_g used in this plot is obtained by a best fit of the data rather than from the theory, although the « experimental » and the theoretical value are in reasonable agreement. We should also mention here that the computer experiments cannot accurately probe the real experimental glass transition region since for a real glass the relaxation time is very much longer (on the order of seconds) than that accessible by computer simulations (on the order of picoseconds). It is not even known whether or not hard spheres can form a glass with such long relaxation times.

The prediction that $\Gamma(\boldsymbol{k}, z) \to 0$ as $z \to 0$ at the glass transition leads to two further results that are consistent with neutron scattering experiments or with computer simulations. One is that the width of the central peak of $S(\boldsymbol{k}, \omega)$ as measured by neutron scattering should vanish as one approaches

(*) In real experiments η does not diverge at T_g but it is 15 orders of magnitude larger than its liquid-state value.

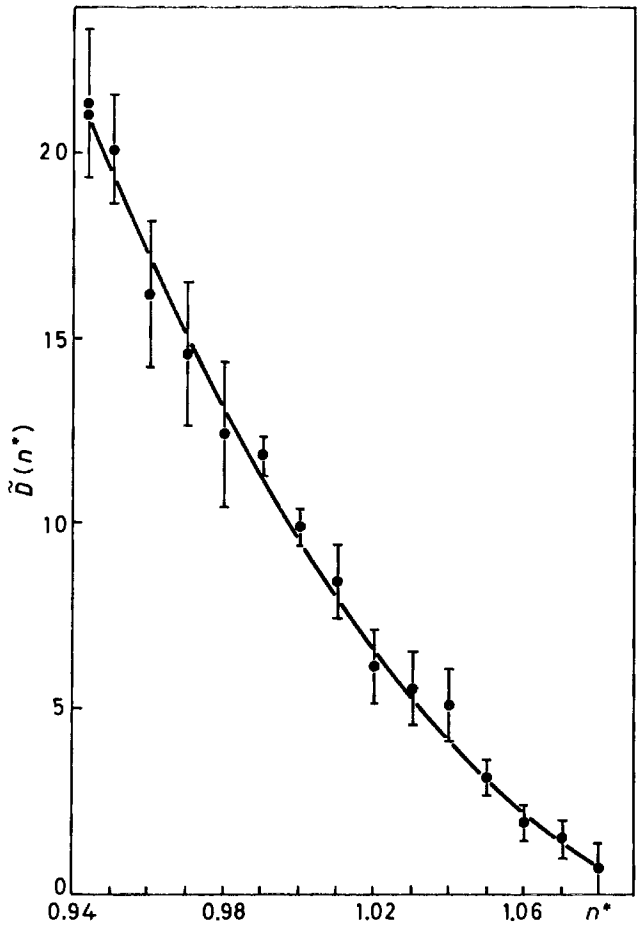

Fig. 7. – A plot of the coefficient of a self-diffusion for a compressed hard-sphere system for densities below the glass transition density n_g. Here D is measured in units of $10^3(\beta m)^{\frac{1}{2}}/\sigma$ and $n^* = n\sigma^3$. The solid line represents eq. (6.7*a*) and the data are taken from ref. [40].

the glass transition. The other prediction, roughly confirmed by computer simulation, is that

$$\lim_{t\to\infty} \frac{F(\boldsymbol{k}, t)}{S(k)} = \frac{2}{3} \qquad \text{at } n = n_g \tag{6.8}$$

at $k = k_0$. This indicates that the limiting value of $F(\boldsymbol{k}, t)$ plays the role of an order parameter in the glass transition.

Although these and similar results are very encouraging that an important start has been made in understanding the transition, there are quite a number of points to straighten out. Foremost among these are the following:

a) The mode-coupling theory presented here takes into account some of, but by no means all of, the collective effects necessary for a good quantitative theory of the glass transition. In particular, the theory outlined above does not take into account very co-operative motion among many particles which is probably the last type of motion possible in a supercooled or compressed

fluid. One expects that a correct theory for η would lead to a divergence in $\eta \sim \exp[A/(n_g - n)]$ as $n \to n_g$ as seen in experiments on real glasses [34, 37].

b) Insofar as it is correct, the theory presented here applies only to simple liquids which usually do not form glasses in the laboratory. For such liquids it is assumed that translational diffusion plays the dominant role. In real-glass-forming liquids, one expects that orientational motion is more important than translational motion. It is of considerable interest to try to develop a mode-coupling theory for more complicated fluids that form glasses.

7. – Conclusion.

In these lectures we have summarized the microscopic foundations for the mode-coupling contributions to time correlation functions for hard-sphere fluids and considered a number of applications. Here we want to summarize and elaborate on some of the central points.

1) Mode-coupling effects are due to dynamical correlations in the fluid. Essentially, these correlations are established by the ring collision sequences, which introduce a mechanism whereby dynamical correlations extend over many mean free paths and over many mean free times in the fluid. Since these collision sequences are by no means restricted to hard-sphere fluids, we expect essentially the same results for any system of particles that interact with short-ranged, central forces.

2) The central theme of these lectures has been the study of mode-coupling effects for fluids at high densities. We have seen that, for simple fluids, the main physical effect is the slow relaxation of the short-range fluid structure due to the diffusion of particles. In the language of mode-coupling theory, for wave numbers on the order of an inverse molecular diameter the only quantity that satisfies a hydrodynamic conservation law is the fluid density. There is no reason to believe that this is special for hard spheres, so we can expect that for general fluids the heat mode and self-diffusion mode become identical at large enough wave numbers [29].

3) The validity of hydrodynamics even at wave numbers on the order of an inverse diameter is assured, at high densities, by the fact that the mean free path is much smaller than the diameter of a molecule. Since hydrodynamics applies for wave numbers up to an inverse mean free path, it certainly applies for wave numbers on the order of σ^{-1}.

4) Since the results described here appear to be applicable to more general systems than hard spheres, one might wonder if the main result could be derived from a more general standpoint. In fact, all the results here can be

obtained from a much more phenomenological mode-coupling theory as initiated by KADANOFF and SWIFT, and extended by many other workers [2]. Even such results as the softening of the heat mode can be discussed from the point of view of generalized hydrodynamics [29, 30].

5) Here we have used the simplest form of mode-coupling theory in that we have considered two-mode contributions, and, for the glass transition, a self-consistent generalization of the two-mode terms. Except for the asymptotic long-time, or small-z, behavior, this restrictive form is unjustified. Therefore, it is important to examine the higher-mode contributions as well as corrections to the two-mode coupling amplitudes used here in order to make quantitative improvements on these results. It is important to stress that most of the computer results do not pertain to the asymptotic region where two-mode theory is correct but rather to an intermediate-time region where other effects may be important.

The glass transition is only one of a number of transitions in which the order parameter is a dynamical quantity. A partial listing of such transitions would include *a*) the Anderson localization transition for electrons in amorphous solids [41], *b*) the phonon localization transition [42], *c*) the percolation transition for a classical particle moving in an overlapping configuration of hard disks or spheres [43] and *d*) the spin-glass transition [38]. In each case the order parameter is a quantity like the diffusion coefficient or electrical conductivity that is nonzero on one side of the transition and vanishes on the other.

It is an interesting question to discuss the appropriate definition of a « dynamical » phase transition and to distinguish one from a « static » transition. Is such a distinction possible? and if so, under what circumstances?

* * *

This work was supported in part by National Science Foundation Grant DMR 83-09449.

APPENDIX

The ring operator with static corrections.

In this appendix we write out the ring collision operator $R_z(\boldsymbol{r}_1, \boldsymbol{v}_1)$ appearing in eq. (2.21) in which all relevant static corrections to the basic low-density ring event have been taken into account [21, 44]. For simplicity we present the operator as a function of the real-space variable $\boldsymbol{r}_1$, and $R_{\boldsymbol{k}z}(\boldsymbol{v}_1)$ is obtained from this by taking the Fourier transform with respect to $\boldsymbol{r}_1$.

We define the following functions:

a) $H(\boldsymbol{r}_1, \boldsymbol{r}_2) = g(\boldsymbol{r}_1, \boldsymbol{r}_2) - 1$ is the pair correlation function, represented by the usual set of Mayer graphs.

b) $H(\boldsymbol{r}_1, \boldsymbol{r}_2|\boldsymbol{r}_3)$ is the set of all Mayer graphs which can be obtained by replacing one field point by a root point in the Mayer graphs for $g(\boldsymbol{r}_1, \boldsymbol{r}_2)\cdot \cdot\exp[\beta\varphi(\boldsymbol{r}_1, \boldsymbol{r}_2)]$, where $\varphi(\boldsymbol{r}_1, \boldsymbol{r}_2)$ is the hard-sphere potential.

c) $H(\boldsymbol{r}_1, \boldsymbol{r}_2|\boldsymbol{r}_3, \boldsymbol{r}_4)$ is the set of all Mayer graphs which can be obtained by replacing two field points by two root points.

d) $$\tilde{G}_z(1,2) = \left[1 + \int \mathrm{d}3\, \varphi_0(v_3) H(\boldsymbol{r}_1, \boldsymbol{r}_3) P_{13}\right]\cdot \cdot\left[1 + \int \mathrm{d}4\, \varphi_0(v_4) H(\boldsymbol{r}_2, \boldsymbol{r}_4) P_{24}\right] G_z(1,2)\,,$$

where $1 \equiv (\boldsymbol{r}_1, \boldsymbol{v}_1)$ and $\mathrm{d}1 = \mathrm{d}\boldsymbol{r}_1\,\mathrm{d}\boldsymbol{v}_1$, and

$$G_z(1,2) = [z - L_{\mathrm{E}}(1) - L_{\mathrm{E}}(2)]^{-1}$$

and L_{E} is the inverse Fourier transform of $L_{\boldsymbol{k},\mathrm{E}}$ given by eq. (2.20*b*). Then [44],

$$\begin{aligned}
R_z(1)F(1) = {} & \int \mathrm{d}2\, \varphi_0(v_2) \overline{T}(1,2)\,(1 + H(\boldsymbol{r}_1, \boldsymbol{r}_2))\,\tilde{G}_z(1,2)\,(1 + H(\boldsymbol{r}_1, \boldsymbol{r}_2))\,T(1,2)\cdot \\
& \cdot(1 + P_{12})F(1) + \int \mathrm{d}2 \int \mathrm{d}3\, \varphi_0(v_2)\varphi_0(v_3)\overline{T}(1,2) H(\boldsymbol{r}_1, \boldsymbol{r}_2|\boldsymbol{r}_3)(1 + P_{12})\tilde{G}_z(1,3)\cdot \\
& \cdot(1 + H(\boldsymbol{r}_2, \boldsymbol{r}_3))\,T(1,3)(1 + P_{13})F(1) + \tfrac{1}{2}\int \mathrm{d}2 \int \mathrm{d}3 \int \mathrm{d}4\, \varphi_0(v_2)\varphi_0(v_3)\cdot \\
& \cdot\varphi(v_4)\overline{T}(1,2) H(\boldsymbol{r}_1, \boldsymbol{r}_2|\boldsymbol{r}_3, \boldsymbol{r}_4)\tilde{G}_z(3,4)(1 + H(\boldsymbol{r}_3, \boldsymbol{r}_4))\,T(3,4)(1 + P_{34})F(3) + \\
& + \int \mathrm{d}2 \int \mathrm{d}3\, \varphi_0(v_2)\varphi_0(v_3)\overline{T}(1,2)\,(1 + H(\boldsymbol{r}_1, \boldsymbol{r}_2))\,\tilde{G}_z(1,2)(1 + P_{12})\cdot \\
& \cdot H(\boldsymbol{r}_1, \boldsymbol{r}_3|\boldsymbol{r}_2)\,T(1,3)(1 + P_{13})F(1) + \int \mathrm{d}2 \int \mathrm{d}3 \int \mathrm{d}4\, \varphi_0(v_2)\varphi_0(v_3)\varphi_0(v_4)\cdot \\
& \cdot\overline{T}(1,2) H(\boldsymbol{r}_1, \boldsymbol{r}_2|\boldsymbol{r}_3)(1 + P_{12})\tilde{G}_z(1,3)(1 + P_{13}) H(\boldsymbol{r}_1, \boldsymbol{r}_4|\boldsymbol{r}_3)\,T(1,4)\cdot \\
& \cdot(1 + P_{14})F(1) + \tfrac{1}{2}\int \mathrm{d}2 \int \mathrm{d}3 \int \mathrm{d}4 \int \mathrm{d}5\, \varphi_0(v_2)\varphi(v_3)\varphi_0(v_4)\varphi_0(v_5)\overline{T}(1,2)\cdot \\
& \cdot H(\boldsymbol{r}_1, \boldsymbol{r}_2|\boldsymbol{r}_3, \boldsymbol{r}_4)\tilde{G}_z(3,4)(1 + P_{34}) H(\boldsymbol{r}_3, \boldsymbol{r}_5|\boldsymbol{r}_4)\,T(3,5)(1 + P_{35})F(3) + \\
& + \tfrac{1}{2}\int \mathrm{d}2 \int \mathrm{d}3 \int \mathrm{d}4\, \varphi_0(v_2)\varphi_0(v_3)\varphi_0(v_4)\,T(1,2)\,(1 + H(\boldsymbol{r}_1, \boldsymbol{r}_2))\,\tilde{G}_z(1,2)\cdot \\
& \cdot H(\boldsymbol{r}_3, \boldsymbol{r}_4|\boldsymbol{r}_1, \boldsymbol{r}_2)\,T(3,4)(1 + P_{34})F(3) + \tfrac{1}{2}\int \mathrm{d}2 \int \mathrm{d}3 \int \mathrm{d}4 \int \mathrm{d}5\, \varphi_0(v_2)\varphi_0(v_3)\cdot \\
& \cdot\varphi(v_4)\varphi(v_5)\overline{T}(1,2) H(\boldsymbol{r}_1, \boldsymbol{r}_2|\boldsymbol{r}_3)(1 + P_{12})\tilde{G}_z(1,3) H(\boldsymbol{r}_4, \boldsymbol{r}_5|\boldsymbol{r}_1, \boldsymbol{r}_2)\cdot \\
& \cdot T(4,5)(1 + P_{45})F(4) + \tfrac{1}{4}\int \mathrm{d}2 \int \mathrm{d}3 \int \mathrm{d}4 \int \mathrm{d}5 \int \mathrm{d}6 \prod_{i=2}^{6} \varphi_0(v_i)\overline{T}(1,2)\cdot \\
& \cdot H(\boldsymbol{r}_1, \boldsymbol{r}_2|\boldsymbol{r}_3, \boldsymbol{r}_4)\tilde{G}_z(3,4) H(\boldsymbol{r}_5, \boldsymbol{r}_6|\boldsymbol{r}_3, \boldsymbol{r}_4)\,T(5,6)(1 + P_{56})F(5)\,.
\end{aligned}$$

REFERENCES

[1] Cf. M. H. ERNST, E. H. HAUGE and J. M. J. VAN LEEUWEN: *J. Stat. Phys.*, **15**, 7 (1976); Y. POMEAU and P. RESIBOIS: *Phys. Rep. C*, **19**, 63 (1975).

[2] M. H. ERNST and J. R. DORFMAN: *Physica (Utrecht)*, **61**, 157 (1972); *J. Stat. Phys.*, **12**, 311 (1975).

[3] Y. POMEAU: *Phys. Rev. A*, **5**, 2569 (1970); **7**, 1134 (1973).

[4] I. M. DE SCHEPPER, P. VERKERK, A. A. VAN WELL and L. A. DE GREFF: *Phys. Rev. Lett.*, **50**, 974 (1983).

[5] T. R. KIRKPATRICK: *Phys. Rev. Lett.*, **53**, 1735 (1984); *J. Non-Cryst. Solids*, **75**, 437 (1985); T. R. KIRKPATRICK and J. NIEUWONDT: *Phys. Rev. A*, **33**, 2651, 2658 (1986).

[6] H. VAN BEIJEREN: *Phys. Lett. A*, **105**, 191 (1984).

[7] D. J. EVANS: *J. Stat. Phys.*, **22**, 81 (1980).

[8] J. J. ERPENBECK and W. W. WOOD: *J. Stat. Phys.*, **24**, 455 (1981).

[9] K. KAWASAKI and J. D. GUNTON: *Phys. Rev. A*, **8**, 2058 (1973); T. YAMADA and K. KAWASAKI: *Prog. Theor. Phys.*, **52**, 111 (1975).

[10] M. H. ERNST, B. CICHOCKI, J. R. DORFMAN, J. SHARMA and H. VAN BEIJEREN: *J. Stat. Phys.*, **18**, 237 (1978).

[11] T. NAITOH and S. ONO: *Phys. Lett. A*, **57**, 448 (1976); *J. Chem. Phys.*, **69**, 125 (1978); **70**, 4515 (1979).

[12] D. J. EVANS: *Phys. Lett. A*, **75**, 229 (1979); *Phys. Rev. A*, **23**, 1988 (1981).

[13] W. G. HOOVER, D. J. EVANS, R. B. HICKMAN, A. J. C. LADD, W. T. ASHURST and B. MORAN: *Phys. Rev. A*, **22**, 1690 (1980).

[14] J. J. ERPENBECK: *Phys. Rev. Lett.*, **52**, 1333 (1984).

[15] E. LEUTHEUSSER: *Phys. Rev. A*, **24**, 2765 (1984); *Z. Phys. B*, **55**, 235 (1984).

[16] U. BENGTZELIUS, W. GÖETZE and A. SJÖLANDER: *J. Phys. C*, **17**, 5915 (1984).

[17] T. R. KIRKPATRICK: *Phys. Rev. A*, **31**, 939 (1985).

[18] S. P. DAS, G. F. MAZENKO, S. RAMASWAMY and J. J. TONER: *Phys. Rev. Lett.*, **54**, 118 (1985).

[19] M. H. ERNST, J. R. DORFMAN, W. HOEGY and J. M. J. VAN LEEUWEN: *Physica (Utrecht)*, **45**, 127 (1969).

[20] Cf. J. P. BOON and S. YIP: *Molecular Hydrodynamics* (New York, N. Y., 1980).

[21] For a systematic study see H. VAN BEIJEREN: Ph.D. Thesis, Nijmegen (1974); H. VAN BEIJEREN and M. H. ERNST: *J. Stat. Phys.*, **21**, 125 (1979).

[22] For a review see J. R. DORFMAN and H. VAN BEIJEREN: in *Statistical Mechanics*, Part B, edited by B. J. BERNE (New York, N. Y., 1978), p. 65.

[23] I. M. DE SCHEPPER and E. G. D. COHEN: *J. Stat. Phys.*, **27**, 223 (1982).

[24] J. R. DORFMAN and E. G. D. COHEN: *Phys. Rev. A*, **6**, 776 (1972); **12**, 292 (1975).

[25] M. H. ERNST and E. G. D. COHEN: *J. Stat. Phys.*, **25**, 153 (1981).

[26] Cf. S. CHAPMAN and T. G. COWLING: *The Mathematical Theory of Non-Uniforu Gases* (London, 1970).

[27] J. A. MCLENNAN: *Phys. Fluids*, **8**, 1580 (1985).

[28] W. E. ALLEY and B. J. ALDER: *Phys. Rev. A*, **27**, 3158 (1983).

[29] T. MUNAKATA: *J. Phys. Soc. Jpn.*, **43**, 1723 (1977).

[30] T. KIRKPATRICK: *Phys. Rev. A*, **32**, 3130 (1985).

[31] I. M. DE SCHEPPER, E. G. D. COHEN and M. J. ZUILHOF: *Phys. Lett. A*, **101**, 399 (1984); **103**, 120 (1984); *Physica (Utrecht) B*, **127**, 282 (1984).

[32] I. M. DE SCHEPPER, J. C. VAN RIJS, A. A. VAN WELL, P. VERKERK, L. A. DE GRAAF and C. BRUIN: *Phys. Rev. A*, **29**, 1602 (1984).
[33] W. E. ALLEY, B. J. ALDER and S. YIP: *Phys. Rev. A*, **27**, 3174 (1983).
[34] E. LEUTHEUSSER: *J. Phys. C*, **15**, 280 (1982).
[35] See also J. BOSSE, W. GÖETZE and M. LÜCKE: *Phys. Rev. A*, **17**, 434 (1978).
[36] B. J. ALDER, D. M. GASS and T. E. WAINWRIGHT: *J. Chem. Phys.*, **53**, 3813 (1970).
[37] Some recent papers with extensive references are S. BRAWER: *J. Chem. Phys.*, **81**, 954 (1984); Y. SINGH, J. P. STOESSEL and P. G. WOLYNES: *Phys. Rev. Lett.*, **54**, 1059 (1985); J. J. ULLO and S. YIP: *Phys. Rev. Lett.*, **54**, 1509 (1985).
[38] Cf. A. P. YOUNG: *J. Stat. Phys.*, **34**, 871 (1984).
[39] N. K. AILAWADI, A. RAHMAN and R. ZWANZIG: *Phys. Rev. A*, **4**, 1616 (1971).
[40] L. V. WOODCOCK: *Ann. N. Y. Acad. Sci.*, **371**, 274 (1981); see also D. FRENKEL and J. P. MCTAGUE: *Annu. Rev. Phys. Chem.*, **31**, 491 (1980); C. A. ANGELL, J. H. R. CLARKE and L. V. WOODCOCK: *Adv. Chem. Phys.*, **48**, 398 (1981).
[41] For a review see T. R. KIRKPATRICK and J. R. DORFMAN: in *Fundamental Problems in Statistical Mechanics*, Vol. **6**, edited by E. G. D. COHEN (Amsterdam, 1985), p. 365.
[42] T. R. KIRKPATRICK: *Phys. Rev. B*, **31**, 5746 (1985).
[43] Cf. T. OHTSUKI and T. KEYES: *Phys. Rev. Lett.*, **52**, 1177 (1984); H. E. STANLEY: *J. Stat. Phys.*, **36**, 843 (1984); J. NIEUWOUDT and S. MUKAMEL: *J. Stat. Phys.*, **36**, 677 (1984).
[44] T. R. KIRKPATRICK: unpublished.

Some Theoretical Aspects of Nonequilibrium Simulation Methods.

J. W. DUFTY (*), J. J. BREY and A. SANTOS

Departamento de Física Teórica, Universidad de Sevilla - 41080 *Sevilla, Spain*

1. – Introduction.

Many recent developments for systems far from equilibrium have resulted from novel methods for nonequilibrium computer simulation [1]. However, a direct comparison with theoretical predictions or experimental results has often been inconclusive, due to an imprecise correspondence to the numerical algorithms [2]. For example, the transport properties of a fluid under shear have been studied using standard molecular-dynamics techniques, except with periodic boundary conditions imposed in the Lagrangian frame for uniform shear flow. These are the Lees-Edwards boundary conditions [3], and they result in the desired macroscopic nonequilibrium flow field. However, in contrast to a real fluid sheared by mechanical contact with moving surfaces, the system heats up monotonically at spatially constant temperature and density. Thus, although the macroscopic velocity field is the same as that expected in an experimental situation, the other hydrodynamic fields differ and it is possible that the transport properties would also be different. In addition, external nonconservative forces can be used in the computer simulations to compensate for the viscous heating. This has the advantage of allowing for a stationary state, but it further complicates the relationship of transport properties obtained from such simulations to either experimental properties or those computed from theoretical models. The objective here is to summarize briefly a theoretical formulation of the Lees-Edwards type of simulation method and some results comparing shear viscosities for systems with and without viscous heating.

(*) Permanent address: Department of Physics, University of Florida, Gainesville, FL 32611.

2. – Nonequilibrium statistical mechanics.

A simple fluid of N particles in a cube of volume $V = (2l)^3$ is considered. The state of the system is characterized by a distribution function, $\varrho(\Gamma, t)$, defined over this region, where the phase point, $\Gamma = \{\boldsymbol{q}_\alpha, \boldsymbol{p}_\alpha\}$, denotes the positions and momenta in an inertial frame (the laboratory frame). The average of an observable, $A(\Gamma)$, is defined by

$$\langle A; t\rangle = \int \mathrm{d}\Gamma A(\Gamma)\varrho(\Gamma, t)\,. \tag{1}$$

The time dependence of the distribution function is calculated from the Liouville equation,

$$\left(\frac{\partial}{\partial t} + L\right)\varrho(\Gamma, t) + \sum_\alpha \nabla_{\boldsymbol{p}_\alpha}\cdot(\boldsymbol{f}_\alpha\varrho) = 0\,, \tag{2}$$

where L is the Liouville operator associated with the Hamiltonian, H, for the N particles,

$$L = \sum_\alpha \left[\frac{\boldsymbol{p}_\alpha}{m}\cdot\nabla_{\boldsymbol{q}_\alpha} + \sum_{\beta\neq\alpha}\boldsymbol{F}(\boldsymbol{q}_{\alpha\beta})\cdot\nabla_{\boldsymbol{p}_\alpha}\right], \tag{3}$$

and $\boldsymbol{F}(\boldsymbol{q}_{\alpha\beta})$ is the force on the α-th particle due to the β-th particle (assumed to depend only on their relative separation, $\boldsymbol{q}_{\alpha\beta} = \boldsymbol{q}_\alpha - \boldsymbol{q}_\beta$). The last term on the left-hand side of eq. (2) represents the effects of a nonconservative force, $\boldsymbol{f}_\alpha$, which in general is a function of the momenta. Equation (2) must be supplemented with suitable initial and boundary conditions. A general class of boundary conditions for the Liouville equation has the homogeneous form [4]

$$[\varrho(\Gamma, t)]_{\substack{\boldsymbol{q}_\alpha\in\Sigma\\ \boldsymbol{p}_\alpha\cdot\hat{n}>0}} = \int_{\substack{\boldsymbol{q}'_\alpha\in\Sigma\\ \boldsymbol{p}'_\alpha\cdot\hat{n}'<0}} \mathrm{d}\Gamma' W(\Gamma, \Gamma'; t)\varrho(\Gamma', t)\,, \tag{4}$$

where Σ is the surface for the volume and $\hat{n}$ is a unit vector normal to the surface, directed inward. The function $W(\Gamma, \Gamma'; t)$ characterizes the distribution of particles entering the system in terms of those incident on the surface.

The system to be modelled is a fluid with equal but opposite average flow velocity at the surfaces $y = \pm l$. The average velocity field, $\boldsymbol{U}(\boldsymbol{r})$, is expected to be linear between these surfaces, and directed along the x-axis, *i.e.*

$$U_i(\boldsymbol{r}) = a_{ij}r\,, \qquad a_{ij} = a\,\delta_{ix}\delta_{jy}\,. \tag{5}$$

Here, $a = \partial U_x/\partial y$ is the magnitude of the shear rate. For such a macroscopic flow it is useful to refer the positions and momenta of all particles to a frame of reference that is locally at rest with respect to the average flow. This is accomplished by a local Galilean transformation

$$\tilde{q}_{\alpha i} = \Lambda_{ij}(t)\, q_{\alpha j}\,, \qquad \tilde{p}_{\alpha i} = p_{\alpha i} - m U_i(\boldsymbol{q}_\alpha)\,, \qquad \Lambda_{ij}(t) = \delta_{ij} - a_{ij} t\,. \tag{6}$$

The co-ordinate transformation is that for the Lagrangian variables of the flow. The Lees-Edwards boundary conditions are easily stated in terms of these variables: a particle incident on a surface at position $\tilde{\boldsymbol{q}}_\alpha$ with momentum $\tilde{\boldsymbol{p}}_\alpha$ is replaced by a particle on the opposite surface with the same momentum and same values for the co-ordinates within the surface. This prescription is consistent with a periodic extension of the original volume, and this extension is also part of the Lees-Edwards conditions. It is clear that these are the usual periodic boundary conditions for equilibrium simulations, except that they are applied in the rest frame.

The above can be translated into corresponding boundary conditions for the Liouville equation. Using the notation $\tilde{G}(\tilde{\Gamma}) = G(\Gamma)$ for the transformation of an arbitrary function, G, under (6) (where $\tilde{\Gamma} = \{\tilde{\boldsymbol{q}}_\alpha, \tilde{\boldsymbol{p}}_\alpha\}$), the Lees-Edwards boundary conditions in terms of eq. (4) are

$$\begin{aligned} \tilde{W}(\tilde{\Gamma}, \tilde{\Gamma}') = {} & \delta(\tilde{\boldsymbol{p}}_\alpha - \tilde{\boldsymbol{p}}'_\alpha)\,\delta(\tilde{q}_{\alpha x} + \tilde{q}'_{\alpha x})\,\delta(\tilde{q}_{\alpha y} - \tilde{q}'_{\alpha y})\,\delta(\tilde{q}_{\alpha z} - \tilde{q}'_{\alpha z})\cdot \\ & \cdot \prod_{\beta\neq\alpha} \delta(\tilde{\boldsymbol{q}}_\beta - \tilde{\boldsymbol{q}}'_\beta)\,\delta(\tilde{\boldsymbol{p}}_\beta - \tilde{\boldsymbol{p}}'_\beta)\,, \end{aligned} \tag{7}$$

for $\tilde{q}_{\alpha x} = \pm l$ and $\tilde{\boldsymbol{q}}_\beta \notin \Sigma$ for $\beta \neq \alpha$. Similar expressions apply for $\tilde{q}_{\alpha y} = \pm l$ and $\tilde{q}_{\alpha z} = \pm l$, and the generalization to many particles simultaneously on the surface is straightforward. Equations (6) and (7) lead to the simpler condition

$$[\tilde{\varrho}(\tilde{\Gamma}, t)]_{\tilde{q}_{\alpha i}=l} = [\tilde{\varrho}(\tilde{\Gamma}, t)]_{\tilde{q}_{\alpha i}=l}\,, \tag{8}$$

so that the distribution function on opposite surfaces must be the same. Equation (8) is also compatible with a periodic extension of the original volume, but it is necessary to show that the Liouville equation will admit such periodic solutions. In the rest frame variables eqs. (2) and (3) become

$$\begin{cases} \left(\dfrac{\partial}{\partial t} + \mathscr{L}\right)\tilde{\varrho} + \displaystyle\sum_\alpha \nabla_{\tilde{\boldsymbol{p}}_\alpha}\cdot(\tilde{\boldsymbol{f}}_\alpha \tilde{\varrho}) = 0\,, \\ \mathscr{L} = \displaystyle\sum_\alpha \left[\Lambda_{ij}(t)\frac{\tilde{p}_{\alpha j}}{m}\frac{\partial}{\partial \tilde{q}_{\alpha i}} - a_{ij}\tilde{p}_{\alpha j}\frac{\partial}{\partial \tilde{p}_{\alpha i}} + \sum_{\beta\neq\alpha} \tilde{\boldsymbol{F}}(\bar{\bar{\Lambda}}(-t)\cdot\tilde{\boldsymbol{q}}_{\alpha\beta})\cdot\nabla_{\tilde{\boldsymbol{p}}_\alpha}\right]. \end{cases} \tag{9}$$

The Liouville equation in these variables is, therefore, invariant under co-ordinate translations, if the nonconservative force is invariant. A sufficient condi-

tion for periodic solutions is a periodic representation of the conservative and nonconservative forces, and the boundary condition (8). For self-consistency, the class of observables in (1) should also be given a periodic extension. Equations (1), (8) and (9) constitute the statistical mechanical formulation of the Lees-Edwards boundary-value problem.

A class of homogeneous solutions to (9) results for initial conditions, $\tilde{\varrho}(\tilde{\Gamma}, t = 0)$, that are translationally invariant functions. In that case the macroscopic conservation laws are satisfied by an average number density, momentum density and energy density given by

$$\begin{cases} \langle n(\boldsymbol{r}); t\rangle = n_0 , \quad \langle \boldsymbol{p}(\boldsymbol{r}); t\rangle = n_0 m \boldsymbol{U}(\boldsymbol{r}) , \\ \langle u(\boldsymbol{r}); t\rangle = \frac{1}{2} m n_0 \boldsymbol{U}^2(\boldsymbol{r}) + \varepsilon(t) . \end{cases} \tag{10}$$

Here, m is the mass, $\boldsymbol{U}(\boldsymbol{r})$ is the flow field (5), n_0 is the constant density, and $\varepsilon(t)$ is the internal energy, whose time evolution is governed by

$$\frac{\partial}{\partial t}\varepsilon(t) = - a_{ij} P_{ij} + V^{-1}\langle \sum_\alpha \boldsymbol{f}_\alpha \cdot \boldsymbol{p}_\alpha ; t\rangle , \tag{11}$$

where P_{ij} is the average pressure tensor (defined below). Equations (10) and (11) include the additional constraints of zero average nonconservative force and initial momentum. The macroscopic hydrodynamic equations, therefore, have exactly the flow field desired, and spatially uniform internal energy and density. Interestingly, these results are exact for all $\boldsymbol{r}$ and t; there are no boundary layers, and all initial transients occur only through $\varepsilon(t)$. This is a very special feature of the Lees-Edwards boundary conditions.

The transport properties characterize the pressure tensor as a function of the shear rate and $\varepsilon(t)$. At small shear rates Newton's viscosity law is expected to hold, $P_{ij} = p\delta_{ij} - \eta_0(a_{ij} + a_{ji})$, where p is the hydrostatic pressure and η_0 is the shear viscosity. More generally, it follows from the symmetry of the problem that the pressure tensor has the form

$$\begin{aligned} P_{ij} = \left[p + \frac{a^2}{3}\left(\psi_1(a) + 2\psi_2(a)\right)\right]\delta_{ij} - \eta(a)(a_{ij} + a_{ji}) - \\ - \psi_1(a) a_{ik} a_{jk} - \psi_2(a)(a_{ik} a_{jk} + a_{ki} a_{kj}) . \end{aligned} \tag{12}$$

The three scalar functions are the nonlinear shear viscosity, $\eta(a)$, and the first and second viscometric functions, $\psi_1(a)$ and $\psi_2(a)$, respectively. The pressure tensor can be calculated from

$$\begin{cases} P_{ij} = V^{-1}\langle T'_{ij}; t\rangle , \\ T'_{ij} = \sum_\alpha \left[\frac{1}{m}\tilde{p}_{\alpha i}\tilde{p}_{\alpha j} + \frac{1}{2}\sum_{\beta\neq\alpha} q_{\alpha\beta i} F_j(\boldsymbol{q}_{\alpha\beta})\right] . \end{cases} \tag{13}$$

(The phase function, T'_{ij}, is that part of the microscopic stress tensor excluding convection by the macroscopic flow.)

The objective now is to obtain useful representations of the pressure tensor from formal solutions to the Liouville equation. The transport properties vanish in the local equilibrium ensemble, so it is useful to represent formal solutions in terms of the deviation from this ensemble,

$$\tilde{\varrho}(t) = \tilde{\varrho}_{\mathrm{L}}(t) + \tilde{\Delta}(t)\,, \qquad \tilde{\varrho}_{\mathrm{L}}(t) = \exp\left[-\beta(t)\tilde{H}'\right]\Big/\int \mathrm{d}\tilde{\Gamma}\exp\left[-\beta(t)\tilde{H}'\right], \tag{14}$$

where $H' = H(\{\boldsymbol{q}_\alpha, \tilde{\boldsymbol{p}}_\alpha\})$, *i.e.* it is the Hamiltonian for the system, but with the laboratory momentum replaced by the rest frame momentum. This simple form of the local equilibirum ensemble is another special aspect of the hydrodynamic field (10), resulting from the Lees-Edwards boundary conditions. The parameter $\beta(t)$ is defined by the requirement

$$\langle H'; t\rangle = \langle H'\rangle_{\beta(t)} \equiv \int \mathrm{d}\tilde{\Gamma}\,\tilde{\varrho}_{\mathrm{L}}(t)\,\tilde{H}'\,. \tag{15}$$

It follows that $T(t) = (k_{\mathrm{B}}\beta(t))^{-1}$ is a nonequilibrium temperature whose functional relationship to the internal energy is the same as that in equilibrium. This is distinguished from the kinetic temperature, $T_{\mathrm{k}}(t) = 2\langle K'; t\rangle/3k_{\mathrm{B}}N$, where $K' \equiv \sum_\alpha (\tilde{p}_\alpha^2/2m)$ is the kinetic energy relative to the flow. A formal expression for $\tilde{\Delta}(t)$ is obtained from the Liouville equation (with $\tilde{\Delta}(t=0) = 0$),

$$\left\{\begin{aligned} \tilde{\Delta}(t) &= -\int_0^t \mathrm{d}\tau\, \tilde{\mathscr{U}}(t,\tau)\, S(\tau)\, \tilde{\varrho}_{\mathrm{L}}(\tau)\,, \\ S(t) &= \beta(t)\, a_{ij}\, T'_{ij} - \frac{\partial\beta(t)}{\partial t}\left(\tilde{H}' - \langle\tilde{H}'\rangle_{\beta(t)}\right) - \sum_\alpha\left(\beta(t)\tilde{\boldsymbol{f}}_\alpha\cdot\frac{\tilde{\boldsymbol{p}}_\alpha}{m} - \nabla_{\tilde{\boldsymbol{p}}_\alpha}\cdot\tilde{\boldsymbol{f}}_\alpha\right), \end{aligned}\right. \tag{16}$$

where $\tilde{\mathscr{U}}(t, z)$ is the solution operator for the Liouville equation,

$$\left(\frac{\partial}{\partial t} + \mathscr{L}\right)\tilde{\mathscr{U}}(t,\tau) + \sum_\alpha \nabla_{\tilde{\boldsymbol{p}}_\alpha}\cdot\boldsymbol{f}_\alpha\,\tilde{\mathscr{U}}(t,\tau) = 0\,, \qquad \tilde{\mathscr{U}}(\tau,\tau) = 1\,. \tag{17}$$

The function $S(t)$ represents three types of sources for the nonequilibrium state. The first arises from the inertial forces due to the Lees-Edwards boundary conditions imposed in a noninertial frame. The second term is an effect of the viscous heating, and the third is entirely associated with the nonconservative force.

In the following, attention will be restricted to the shear viscosity. From

eqs. (12)-(16), this is given by

$$a\eta(a, t) = \int_0^t \mathrm{d}\tau\, V^{-1} \langle T'_{xy}(t, \tau)\, S(\tau) \rangle_\beta \,, \tag{18}$$

where the time dependence has been shifted to $T'_{ij}(t, \tau) = \tilde{\mathscr{U}}^\dagger(t, \tau)\, T'_{ij}$, and $\tilde{\mathscr{U}}^\dagger$ denotes the adjoint of $\tilde{\mathscr{U}}$. In the next section this expression is considered in more detail for two specific choices for the nonconservative force.

3. – Constant-temperature shear viscosity.

One important reason for introducing the nonconservative force is to control viscous heating. As mentioned in the introduction, it is not clear what other effects are induced in the system when such forces are effective. Here, the shear viscosity at constant temperature is compared with that for a system with only the conservative Newtonian force. It should be noted at the outset that the nonconservative force used to hold the temperature constant is not unique, and a choice of convenience is made here to allow for a rather detailed analysis in the low-density limit. Further comment on this point is made in the discussion section.

The form for the nonconservative force commonly used in computer simulations is a « drag » force,

$$\tilde{f}_\alpha = -\lambda \tilde{p}_\alpha \,, \tag{19}$$

where λ can be selected to control the temperature $T(t)$ (or some other property of the system). For constant temperature the condition is

$$\frac{\partial \varepsilon(t)}{\partial t} = -V^{-1} \langle [2\lambda K' + a_{ij} T'_{ij}]; t \rangle = 0 \,, \tag{20}$$

which is satisfied by

$$\lambda = -a_{ij} \langle T'_{ij}; t \rangle / \langle 2K'; t \rangle = a^2 \eta(a, t) / 2\varepsilon_{\mathrm{k}}(t) \,. \tag{21}$$

The second equality follows from the definition of the shear viscosity in eqs. (12) and (13), and $\varepsilon_{\mathrm{k}}(t) = V^{-1} \langle K'; t \rangle$. The formal expressions for the nonlinear shear viscosities with and without nonconservative forces can now be compared. These viscosities are denoted by $\eta^{(i)}(a, t)$, with $i = 1$ for the case of viscous heating ($\lambda = 0$) and $i = 2$ for constant temperature (λ given by eq. (21)). From (18) a common form for the expressions is obtained,

$$\eta^{(i)}(a, t) = \int_0^t \mathrm{d}\tau \left[C(t, \tau | \beta(\tau)) - a\eta^{(i)}(a, \tau)\, D^{(i)}(t, \tau | \beta(\tau)) \right] , \tag{22}$$

where $C(t, \tau|\beta(\tau))$ and $D^{(i)}(t, \tau|\beta(\tau))$ are the correlation functions,

$$
(23)\qquad \begin{cases} C(t,\tau|\beta(\tau)) & \equiv \beta(\tau)\, V^{-1}\langle T'_{xy}(t,\tau)\, T'_{xy}\rangle_{\beta(\tau)}\,, \\ D^{(1)}(t,\tau|\beta(\tau)) & \equiv \dfrac{\partial\beta(\tau)}{\partial\varepsilon(\tau)}\, V^{-1}\langle T'_{xy}(t,\tau)\,[\tilde{H}' - \langle\tilde{H}'\rangle_{\beta(\tau)}]\rangle_{\beta(\tau)}\,, \\ D^{(2)}(t,\tau|\beta) & \equiv \dfrac{\partial\beta_{\mathbf{k}}(\tau)}{\partial\varepsilon_{\mathbf{k}}(\tau)}\, V^{-1}\left\langle T'_{xy}(t,\tau)\left[\dfrac{\beta}{\beta_{\mathbf{k}}(\tau)}\,\tilde{K}' - \langle\tilde{K}';\tau\rangle\right]\right\rangle_{\beta}\,. \end{cases}
$$

It is understood here that the time dependence of $T'_{ij}(t, \tau)$ in these expressions is calculated using the appropriate λ for each case.

The forms of the shear viscosities for the two cases are seen to be quite similar. In the first, $T(t)$ varies in time, while, in the second, $T(t)$ is constant but $T_{\mathbf{k}}(t)$ varies. Further considerations show that $D^{(2)}$ differs in form from $D^{(1)}$ only by fluctuations in the potential energy. Consequently, the structure of the shear viscosities is the same in the low-density limit, with only $T(t)$ and λ being different. Also, since $T_{\mathbf{k}}(t) \to T(t) =$ const at low density in case 2, a stationary value for $\eta^{(2)}(a, t)$ may be expected. At finite density a stationary value is apparently not obtained, even though the hydrodynamic state variables are constant in time. In the Navier-Stokes limit the second term in the brackets of eq. (22) vanishes, the temperature becomes constant, and the time evolution of $T'_{xy}(t, \tau)$ is Newtonian with periodic boundary conditions in the laboratory frame. Consequently, both cases 1 and 2 agree with the Green-Kubo result in this limit.

Equations (22) are highly nonlocal and nonlinear. Nevertheless, a closed description of the transport properties at the macroscopic level is obtained once the correlation functions have been determined, which may prove useful for approximations at large shear rates. For example, at low density it can be shown [5] that the correlation functions are determined from a bilinear kinetic equation related to the nonlinear Boltzmann equation (the method of ref. [5] extends in a straightforward way to include the nonconservative force chosen here). The resulting shear viscosities are also equivalent to those obtained directly from the kinetic-theory pressure tensor,

$$
(24)\qquad P_{ij}(t) = \int \mathrm{d}\tilde{\boldsymbol{p}}\, \frac{1}{m}\, \tilde{p}_i \tilde{p}_j \tilde{f}\,,
$$

where $\tilde{f}$ is the homogeneous solution to the nonlinear Boltzmann equation in the local rest frame,

$$
(25)\qquad \left[\frac{\partial}{\partial t} - a_{ij}\, \tilde{p}_j \frac{\partial}{\partial \tilde{p}_i} - \lambda \nabla_{\tilde{\boldsymbol{p}}}\cdot\tilde{\boldsymbol{p}}\right]\tilde{f} = J[\tilde{f}, \tilde{f}]\,.
$$

Use has been made of Lees-Edwards boundary conditions at low density [6]

and invariance of the collision operator under transformation to the rest frame. Finally, λ in (25) is given by the low-density limit of (21) for case 2, or zero for case 1. In the latter case, IKENBERRY and TRUESDELL [7] have calculated the exact nonlinear shear viscosity from (24) and (25) for Maxwell molecules ($\boldsymbol{F}(q) \sim q^{-5}$). The method can be applied to case 2 as well, so that the shear viscosities are known in detail for all values of the shear rate at low densitites. To state the result, a dimensionless shear rate, $\bar{a} = a/\nu$, and shear viscosity, $\bar{\eta}(\bar{a}) = \eta(a)\nu/p$, are introduced. Here ν is a constant associated with an eigenvalue of the collision operator. The result for Maxwell molecules is then

$$\bar{\eta}^{(1)}(\bar{a}) = \bar{\eta}^{(2)}(\bar{a}) \,. \tag{26}$$

This equivalence of constant-temperature and viscous-heating states extends to all other transport properties as well [6].

This is an encouraging result to support the view that the nonconservative forces are « passive », *i.e.* that the temperature can be controlled without affecting the transport properties. However, the exact equivalence for Maxwell molecules probably holds only at low density, and cannot be extended to other force laws even in this limit. To support this latter statement, the shear viscosity has been determined for a class of force laws, $\boldsymbol{F} \sim q^{-n}$, for a model of the nonlinear Boltzmann equation (the BGK model) [8]. For $n = 5$ the model gives the same viscosities as the Boltzmann equation and (26) is regained. For $n \neq 5$ the equality in (26) fails, so that different transport properties are obtained when the viscous heating is controlled. In the case of hard spheres ($n \to \infty$) the coefficients of order $\bar{a}^2$ in the shear viscosity (super Burnett coefficients) differ by about 30 %. However, the functions $\bar{\eta}^{(1)}(\bar{a})$ and $\bar{\eta}^{(2)}(\bar{a})$ are quite similar over the whole range of shear rates, with a maximum difference of about 16 %.

4. – Discussion.

Two main topics have been addressed here: a suitable formulation of the Lees-Edwards boundary-value problem and the influence of nonconservative forces on transport properties. Regarding the first, the Liouville equation (9) with periodic boundary conditions, (8), is appropriate for the calculation of transport and other properties (*e.g.*, structure factors, fluctuations) for both homogeneous and inhomogeneous states. It is also the form suitable for comparison with a class of computer simulations. The effects of nonconservative forces on transport properties are somewhat difficult to predict *a priori*. The example given here shows that it is possible to control the temperature by such forces without changing the qualitative behaviour of transport in the system, although it also indicates that quantitative differences are to be expected. Some additional points not addressed here should be noted:

a) The Lees-Edwards boundary conditions are nonlocal, relating the distribution on one surface to that on the opposite surface. As a consequence, there are no boundary layers or spatial variations in the temperature. At best it is an idealized representation of the bulk properties of real fluids. Some care is required in comparison with other computer simulation methods that are more realistic (*e.g.*, stochastic boundary condition methods [9]).

b) The periodic boundary conditions are applied in a noninertial frame, and there are « inertial forces » in the corresponding Newtonian equations of motion. The latter are equivalent to one of the « non-Newtonian » methods used in computer simulation (the Doll's tensor form [10] is apparently incorrect). Such methods are interpreted here as Newtonian, but expressed in the frame of reference for which the boundary conditions are simplest.

c) The nonconservative force chosen in sect. **3** is not unique. A stronger constraint is to hold the total microscopic energy constant in time. In that case the parameter λ becomes a phase function

$$\lambda = -a_{ij} T'_{ij}/2K' , \tag{27}$$

and the nonlinear shear viscosity is found to be

$$\eta(a) = \int_0^t \mathrm{d}\tau \, V^{-1} \langle T'_{xy}(t, \tau)(3N/2K') \, T'_{xy} \rangle_\beta \, . \tag{28}$$

This is a particularly simple form, similar to the Green-Kubo result of linear response. However, in contrast to the force of sect. **3**, eq. (27) implies an inherently many-body, nonlocal force. It does not appear possible to describe this case by kinetic theory, even in the low-density limit. While it is possible to show that the shear viscosity in the Navier-Stokes limit agrees with the Green-Kubo result (to order N^{-1}), no further connection with real fluids has been established.

d) A local form for λ can be found, consistent with constant microscopic energy, that avoids the theoretical problems of (27). However, the result differs from the Green-Kubo result even at Navier-Stokes order ($\sim 100\,\%$ at low density). This illustrates the need for a detailed analysis of each method chosen to control heating.

e) An alternative to controlling the total energy is to require constant kinetic energy. This is the usual method for nonequilibrium computer simulations. In this case, even the results at zero shear rate are uncertain (although the correct thermodymanics is obtained). Preliminary considerations indicate

that the Navier-Stokes order results are quite close to the Green-Kubo results [11].

* * *

This research was supported by National Science Foundation grant CHE 8411932, the U.S.-Spain Co-operation Program and by the Alianza España-Florida.

REFERENCES

[1] Two reviews with references are W. G. HOOVER: *Annu. Rev. Phys. Chem.*, **34**, 103 (1983); D. J. EVANS and G. P. MORRISS: *Comput. Phys. Rep.*, **1**, 299 (1984).
[2] See, for example, *Nonlinear Fluid Dynamics*, edited by H. M. HANLEY (North-Holland Publ. Co., Amsterdam, 1983).
[3] A. LEES and S. F. EDWARDS: *J. Phys. C*, **5**, 1921 (1972).
[4] J. R. DORFMAN and H. VAN BEIJEREN: in *Statistical Mechanics*, Part B, edited by B. J. BERNE (Plenum Press, New York, N. Y., 1977), p. 65.
[5] J. W. DUFTY and M. LINDENFELD: *J. Stat. Phys.*, **20**, 259 (1979).
[6] J. W. DUFTY, A. SANTOS, J. J. BREY and R. F. RODRÍGUEZ: *Phys. Rev. A*, **33** 459 (1986).
[7] E. IKENBERRY and C. TRUESDELL: *J. Rat. Mech. Anal.*, **5**, 55 (1956).
[8] R. ZWANZIG: *J. Chem. Phys.*, **71**, 4416 (1979).
[9] C. TROZZI and G. CICCOTTI: *Phys. Rev. A*, **29**, 916 (1984).
[10] W. G. HOOVER, D. J. EVANS, R. HICKMAN, A. J. C. LADD, W. T. ASHURST and B. MORAN: *Phys. Rev. A*, **22**, 1690 (1980).
[11] D. J. EVANS: *J. Chem. Phys.*, **78**, 3297 (1983); J. M. HAILE and S. GUPTA: *J. Chem. Phys.*, **79**, 3067 (1984).

Exact Results in Kinetic Theory.

H. SPOHN

Ludwig-Maximilians-Universität München, Theoretische Physik
Theresienstrasse 37 - 8000 *München* 2, *B. R. D.*

1. – Introduction.

In physics the notion « exact result » usually means that the solution of a complicated problem is obtained in terms of a fairly simple analytical expression. One of the most famous examples is Onsager's solution of the two-dimensional Ising model. Because, in the critical region, the exact solution did not agree with current theories, it triggered a far-reaching development. Another example, more recent and more close to the subject discussed here, are exact solutions of the nonlinear Boltzmann equation as initiated by KROOK and WU [1] and BOBYLEV [2] (cf. [3] for a review). These solutions depend only on the energy. Still, they teach us how equilibrium is approached.

It is a historical fact that mathematical physics in its modern form has mostly abandoned emphasis on exact results. This may be regretted, but is easily understood. To avoid a general discussion let me illustrate the motivation with the help of an example which at the same time serves as an introduction. Let us consider the problem of self-diffusion for a hard-sphere fluid/solid. The hard-sphere system is in thermal equilibrium and one particle is tagged. The position of the tagged particle at time t is denoted by $q(t)$; $q(0) = 0$. There is no hope to ever compute exactly, in closed form, the distribution, $\varrho_t(q)$, of $q(t)$. This distribution is just too complicated. Still we might be able to prove that for sufficiently large times, on the appropriate spatial scale, $\varrho_t(q) \simeq (4\pi Dt)^{-\frac{3}{2}} \exp[-q^2/4Dt]$ with D the self-diffusion coefficient, more precisely (in three dimensions)

$$\lim_{\varepsilon\to 0} \varepsilon^{-3} \varrho_{\varepsilon^{-2}t}(\varepsilon^{-1}q) = (4\pi Dt)^{-\frac{3}{2}} \exp[-q^2/4Dt]\,, \tag{1.1}$$

as required by the scale invariance of the diffusion equation. More modestly, one might try to prove that

$$\lim_{t\to\infty} \frac{1}{6t} \langle q(t)^2 \rangle = \lim_{t\to\infty} \frac{1}{6t} \int \mathrm{d}q\, \varrho_t(q)\, q^2 = D \tag{1.2}$$

for some D with $0 < D < \infty$. Physically, such a result is greeted with disappointment. It asserts something we were certain of anyhow. Only the existence of a D with no specific numerical value is assured. In good cases a rough estimate of D is provided. But a small-scale molecular-dynamics simulation could do better.

Why bother with exact results? First of all there is the conceptual component. Self-diffusion is a common physical phenomenon. At least in some models we want to be sure then that it is a strict consequence of Newtonian dynamics (together with the above-mentioned assumption on the statistical distribution of the initial data). Secondly (1.1), (1.2) constitute a difficult and, therefore, challenging mathematical-physics problem. The distribution $\varrho_t(q)$ is defined indirectly through a complicated dynamical and averaging prescription. Nevertheless it has a simple asymptotic behaviour. If $v(t)$ denotes the velocity of the tagged particle at time t, then

$$\frac{1}{\sqrt{t}}\, q(t) = \frac{1}{\sqrt{t}} \int_0^t \mathrm{d}s\, v(s). \tag{1.3}$$

$v(t)$ is a stationary stochastic process (this means $\langle v(t_1 + \tau) \dots v(t_n + \tau)\rangle = \langle v(t_1) \dots v(t_n)\rangle$). From (1.3) we conclude that (1.1) is nothing else than the central-limit theorem for $v(t)$. If $v(t)$ would be a Markov process, we know very well how to prove a central-limit theorem even in cases where the velocity autocorrelation function, $\langle v(0)\, v(t)\rangle$, decays slowly but still integrably. However, $v(t)$ as defined is non-Markovian. One has to understand the memory effects inherent in $v(t)$. Why do they not conspire as to render (1.1) invalid (in fact, in two dimensions we believe they do)? So the eventual goal is a qualitative understanding of the statistical properties of $v(t)$, good enough to ensure (1.1). I am using many words to emphasize that some people consider it *intrinsically* interesting to contemplate such matters.

I want to summarize here exact results in kinetic theory, *i.e.* the behaviour of a system of many particles at low density. It is not surprising that this is the best-understood regime. I restrict myself to classical structureless particles governed by Newton's equation of motion. Section **2** deals with the derivation of the nonlinear Boltzmann equation and related results on time correlations. Section **3** deals with the motion of a tagged particle, *i.e.* self-diffusion at low density. Also the dynamics of a heavy particle and of a particle weakly scattered by impurities are mentioned. In the final section I will briefly discuss a few results of the Euler equation for hard rods, tracer diffusion and the Lorentz gas with a periodic scatterer configuration. The periodic Lorentz gas is equivalent to the Sinai billiard and, therefore, links up with the ergodic theory of mechanical systems with a few degrees of freedom.

2. – Derivation of the Boltzmann equation.

For simplicity we consider a system of hard spheres in three dimensions. They have mass m and diameter σ. The proof holds for an arbitrary spatial dimension. The case of a positive pair potential of finite range has been worked out in [4]. With some effort a more general class of potentials could be covered, presumably. However, the condition of finite range, *i.e.* $V(q) = 0$ for $|q| > R$ with some R, is essential. For notational simplicity no boundary conditions are imposed. But if desired, periodic, reflecting, or stochastic boundary conditions could be included.

As discussed in [5], low density means $N\sigma^3 \to 0$ but $N\sigma^2 \to$ finite, where N denotes the number of particles. It is convenient to introduce a dimensionless scaling parameter, ε, $\varepsilon \to 0$, such that

$$\text{(2.1)} \qquad \begin{cases} \text{diameter} = \varepsilon\sigma\,, \\ \text{number of particles} \simeq \varepsilon^{-2}\,. \end{cases}$$

Let $\{\varrho_n^\varepsilon(q_1, p_1, \ldots, q_n, p_n) | n = 0, 1, \ldots\}$ be the initial ($t = 0$) correlation functions of the hard-sphere system with diameter $\varepsilon\sigma$. The condition on the number of particles is formalized as

(C2) There exist continuous functions $\{r_n | n = 0, 1, \ldots\}$ such that

$$\text{(2.2)} \qquad \lim_{\varepsilon\to 0} \varepsilon^{2n} \varrho_n^\varepsilon(q_1, p_1, \ldots, q_n, p_n) = r_n(q_1, p_1, \ldots, q_n, p_n)\,, \quad n = 0, 1, \ldots\,.$$

At coinciding spatial points $\varrho_n^\varepsilon = 0$ independently of ε. Therefore, we require that (2.2) holds uniformly on compact sets of $\{q_1, p_1, \ldots, q_n, p_n | q_i \neq q_j,\ i, j = 1, \ldots, n,\ i \neq j\}$. Secondly, the initial correlation functions should not be too singular, in the sense

(C1) Let h_β be the normalized Maxwellian at inverse temperature β. Then there exist constants z, β and M such that

$$\text{(2.3)} \qquad \varepsilon^{2n} \varrho_n^\varepsilon(q_1, p_1, \ldots, q_n, p_n) \leqslant M \prod_{j=1}^{n} z h_\beta(p_j)\,.$$

(C1) and (C2) are conditions on the statistical distribution of the *initial* data.

We now evolve these correlation functions according to the rules of the hard-sphere dynamics. The correlation functions at time t are denoted by $\varrho_n^\varepsilon(q_1, p_1, \ldots, q_n, p_n, t)$. The ε-dependence comes from both the initial data and the dynamics (the hard-sphere diameter is $\varepsilon\sigma$).

Before stating the main result let me introduce the *Boltzmann hierarchy*.

It is the set of linear equations

$$(2.4)\qquad \frac{\partial}{\partial t} r_n(q_1, p_1, \ldots, q_n, p_n, t) + \sum_{j=1}^{n} \frac{1}{m} p_j \frac{\partial}{\partial q_j} r_n(q_1, p_1, \ldots, q_n, p_n, t) =$$

$$= \sum_{j=1}^{n} \sigma^2 \int\limits_{\hat{\omega}\cdot(p_{n+1}-p_j)\geqslant 0} \mathrm{d}p_{n+1}\, \mathrm{d}\hat{\omega}\, \frac{1}{m}\, \hat{\omega}\cdot(p_{n+1}-p_j)\cdot$$

$$\cdot\big(r_{n+1}(q_1, p_1, \ldots, q_j, p'_j, \ldots, q_j, p'_{n+1}, t) - r_{n+1}(q_1, p_1, \ldots, q_j, p_j, \ldots, q_j, p_{n+1}, t)\big)\,,$$

$t \geqslant 0$, $n = 1, 2, \ldots$. Here (p'_n, p'_{n+1}) is a pair of incoming momenta with outgoing momenta (p_j, p_{n+1}) and momentum transfer in the direction of $\hat{\omega}$. $\hat{\omega}$ is a unit vector and $\mathrm{d}\hat{\omega}$ the integration over the unit sphere. In essence, the Boltzmann hierarchy corresponds to statistical solutions of the Boltzmann equation [6]. In particular, the hierarchy is not invariant under time reversal.

Theorem 1 [7, 8]. Let the initial state satisfy (C1) and (C2). Let $0 \leqslant t < t_0(z, \beta) = 0.2\sqrt{3\beta}/\pi z = 0.2$ (mean free time). Then

$$(2.5)\qquad \lim_{\varepsilon\to 0} \varepsilon^{2n} \varrho_n^{\varepsilon}(q_1, p_1, \ldots, q_n, p_n, t) = r_n(q_1, p_1, \ldots, q_n, p_n, t)$$

exists with the exception of a set of $\mathrm{d}q_1\,\mathrm{d}p_1 \ldots \mathrm{d}q_n\,\mathrm{d}p_n$-measure zero, $n = 1, 2, \ldots$, and $\{r_n(t) | n = 1, 2, \ldots\}$ are the solution of the Boltzmann hierarchy with initial data $\{r_n | n = 1, 2, \ldots\}$.

This is the basic theorem. From it and its proof a number of interesting consequences can be deduced, some with a little, and others with considerable, effort. The main drawback of the theorem is its restriction to short times. The origin is that the convergence of a certain perturbation series, which is related to the binary-collision expansion, can be controlled only for short times. This constitutes one of the basic technical problems in the field, reflected also by the fact that the existence of solutions of the Boltzmann equation for a large class of initial data has been established only for short times.

If the *initial* conditions satisfy asymptotically (*i.e.* as $\varepsilon \to 0$) the condition of molecular chaos

$$(2.6)\qquad r_n(q_1, p_1, \ldots, q_n, p_n) = \prod_{j=1}^{n} f(q_j, p_j)\,,$$

then it is satisfied also at all later times,

$$(2.7)\qquad r_n(q_1, p_1, \ldots, q_n, p_n, t) = \prod_{j=1}^{n} f(q_j, p_j, t)$$

and $f(q, p, t)$ is the solution of the Boltzmann equation

$$(2.8)\qquad \frac{\partial}{\partial t} f(q, p, t) + \frac{1}{m} p\cdot\frac{\partial}{\partial q} f(q, p, t) =$$

$$= \sigma^2 \int\limits_{\hat{\omega}\cdot(p-p_1)\geqslant 0} \mathrm{d}p_1\, \mathrm{d}\hat{\omega}\, \frac{1}{m}\, \hat{\omega}\cdot(p-p_1)[f(q, p'_1, t)\, f(q, p', t) - f(q, p_1, t) f(q, p, t)]\,.$$

Therefore, at least for short times, we have derived an irreversible equation on the basis of strictly reversible Newtonian dynamics. Why do we not run into mathematical contradictions? The answer is somewhat subtle: The convergence, as $\varepsilon \to 0$, of the correlation functions at time $t = 0$ is stronger than at a later time. Imagine that at time $\tau > 0$, $\tau < t_0$, we reverse all velocities. Then after reversal the correlation functions satisfy (C1), but not (C2). Therefore, we cannot conclude (fortunately) that the initial correlation functions manufactured through velocity reversal at time τ evolve according to the Boltzmann equation in the limit $\varepsilon \to 0$. An improved version of theorem 1 shows that one can go forward in time (*i.e.* $\tau, 2\tau, 3\tau, \ldots$ as long as (C1) holds) but cannot backtrack. Also, theorem 1 holds for $t < 0$ provided the sign of the collision operator is reversed.

If molecular chaos at the initial time holds, then the statement about correlation functions can be cast in a more physical and intuitive form. For ε sufficiently small the phase space may be divided into a set of « good » phase and « bad » phase points. The bad phase points have small measure with respect to the initial state as defined by the correlation functions $\{\varrho_n^\varepsilon | n = 0, 1, \ldots\}$. The set of good phase points has almost measure one and every configuration in the one-particle phase space constructed from a good phase point follows in the course of time the solution of the Boltzmann equation up to a small error. Therefore, the Boltzmann equation governs the actual, not only the average, number of particles in a small cell of the one-particle phase space. However, the set of good phase points has a complicated structure and can be characterized only statistically.

If the initial correlation functions are sufficiently small, if there are no boundary conditions and if the spatial dimension is two, then the validity of the Boltzmann equation (in the above sense) is proved without any restriction on the length of time [9]. Physically, the gas evaporates into free space and after a while collisions become very unlikely. This mechanism controls the convergence of the perturbation expansion for arbitrary times.

An instructive example is the dynamics of hard cubes at low density. The cubes are oriented at 45 degrees ($\equiv$ diamonds). There are only six allowed velocities pointing along the co-ordinate axis. The speed is unity. Elastic collisions are defined in the obvious way with the constraint to preserve the discrete structure of the velocity space. The usual nonrigorous derivations suggest the validity of the Boltzmann equation where the collision operator is modified such that $(p, p_1) \to (p', p_1')$ runs over the discrete set of possible collisions only. A more careful analysis [10] reveals long-lasting dynamical correlations which do not disappear at low density. For hard spheres recollisions are of the order (density)^2. For hard cubes, because of the discrete velocity space, some recollisions have a weight proportional to the density and are, therefore, of the same order as uncorrelated collisions. Therefore, the limit $\varepsilon \to 0$ of (2.5) exists. But the limiting correlation functions, even

assuming initial molecular chaos, do not satisfy the Boltzmann equation. Out of curiosity it may be of interest to understand the transport properties of hard cubes at low density.

We turn to equilibrium time correlation functions at low density. The hard-sphere system is assumed to be in thermal equilibrium at inverse temperature β and fugacity $\varepsilon^{-2}z$. The equilibrium state denoted by $\langle\,\rangle_\varepsilon$, where the ε-dependence comes from scaling both the fugacity and the hard-sphere diameter. For a one-particle function g we define

$$\xi^\varepsilon(g, t) = \varepsilon\left[\sum_j g(q_j^\varepsilon(t), p_j^\varepsilon(t)) - \int \mathrm{d}q\,\mathrm{d}p\, g(q, p)\, \varrho_1^\varepsilon h_\beta(p)\right]. \tag{2.9}$$

$\xi^\varepsilon(g, t)$ measures the deviation from equilibrium. Therefore, $\{\xi^\varepsilon(g, t)\}$ is a fluctuation field. Since $\varrho^\varepsilon \simeq \varepsilon^{-2}z$, ε is the usual, central-limit type of prefactor. Physically, one would expect that as $\varepsilon \to 0$ the $\{\xi^\varepsilon(g, t)\}$ have a jointly Gaussian distribution. Only the convergence of the covariance has been proved, however.

Theorem 2 [11]. Let $0 \leqslant t < (1/e)\, t_0(z, \beta)$. Then

$$\lim_{\varepsilon\to 0} \langle \xi^\varepsilon(g, t)\, \xi^\varepsilon(f, 0)\rangle_\varepsilon = \int \mathrm{d}q\,\mathrm{d}p\, z\, h_\beta(p) f(q, p) \exp[Lt] g(q, p)\,. \tag{2.10}$$

Here L is the linearized Boltzmann operator, *i.e.* (2.8) linearized as $h_\beta(1 + g)$ around global equilibrium.

At least for short times (2.10) proves the behaviour of time correlations as expected for low density. It constitutes the microscopic basis for the computation of transport coefficients, as defined through the Green-Kubo formulae, at low density from the linearized Boltzmann equation.

Theorem 2 has been extended to nonequilibrium states [12, 13].

3. – The motion of a tagged particle (self-diffusion).

We want to study the motion of a tagged particle in a hard-sphere fluid at low density. The scaling is as before. The hard-sphere diameter is $\varepsilon\sigma$. The hard-sphere fluid is in thermal equilibrium at inverse temperature β and fugacity $\varepsilon^{-2}z$. The position of the tagged particle is denoted by $q^\varepsilon(t)$, its velocity by $(1/m)p^\varepsilon(t)$. (In fact, the tagged particle could have a mass and a diameter different from those of the fluid particles.) Initially $q^\varepsilon(0) = q$, $p^\varepsilon(0) = p$, and the hard-sphere system is in equilibrium under the influence of the external potential due to the tagged particle at q. Since the initial data of the fluid particles are random, $(q^\varepsilon(t), p^\varepsilon(t))$ is a random process. We are interested in its behaviour as $\varepsilon \to 0$, *i.e.* at low density. Physically, we expect the collisions to become uncorrelated. Therefore, the limit $(q(t), p(t)) = \lim_{\varepsilon\to 0} (q^\varepsilon(t), p^\varepsilon(t))$ is

expected to be the following stochastic process: The tagged particle starts at q with momentum p. It travels freely. After a random time with an exponential distribution the tagged particle collides with a fluid particle, which has an incoming momentum with a Maxwellian distribution. The outgoing momentum of a tagged particle is determined by the hard-sphere collision rule. After the collision the tagged particle travels freely, etc. The successive collisions and times of free travel are uncorrelated. On a formal level, the distribution of $(q(t), p(t))$, $\varrho_t(q, p)$, is governed by the linear Boltzmann equation

$$\frac{\partial}{\partial t}\varrho_t(q,p) + \frac{1}{m}p\frac{\partial}{\partial q}\varrho_t(q,p)\cdot \tag{3.1}$$
$$\cdot\sigma^2 \int\limits_{\hat{\omega}\cdot(p-p_1)\geqslant 0} \mathrm{d}p_1\,\mathrm{d}\hat{\omega}\,\frac{1}{m}\hat{\omega}\cdot(p-p_1)[zh_\beta(p_1')\varrho_t(q,p') - zh_\beta(p_1)\varrho_t(q,p)]\,.$$

All multitime correlations of $(q(t), p(t))$ are computed from (3.1) according to the standard rules for Markov processes.

Theorem 3 [14]. Let $(q^\varepsilon(t), p^\varepsilon(t))$ and $(q(t), p(t))$ be defined as above. Then

$$\lim_{\varepsilon\to 0}(q^\varepsilon(t), p^\varepsilon(t)) = (q(t), p(t))\,, \tag{3.2}$$

where $\lim\limits_{\varepsilon\to 0}$ means convergence of all multitime correlations.

This result is applicable to a nonequilibrium steady state. We consider a binary mixture of hard spheres. The hard spheres are mechanically identical and distinguished only through their colour, say black and white. Mechanically the binary mixture is in equilibrium. It is confined to a slab with colour-changing boundary conditions: Outgoing hard spheres at the left (right) boundary exit always white (black). As $t \to \infty$ the binary mixture establishes a stationary colour profile. An extension of theorem 3 proves that in the limit $\varepsilon \to 0$ this colour profile is obtained from the linear Boltzmann equation (3.1) with the appropriate boundary conditions.

Let me mention two other results which are only loosely connected to the foregoing one. The connection is that the motion of the tagged particle is studied in a situation where a physical parameter becomes small. Before we considered the limit of low density for the fluid; now we take 1) the mass ratio and 2) the interaction strength to become small. The model of the introduction is distinguished by the fact that the motion of the tagged particle is followed over long times with the physical parameters being kept fixed.

For the heavy particle we consider a hard sphere of diameter σ and mass M (both fixed) immersed in an ideal gas of light point particles. Their mass is $m^\varepsilon = \varepsilon m$. The only interactions are elastic collisions between the heavy par-

ticle and the gas particles. Initially the heavy particle is at the origin with velocity $v^\varepsilon(0) = v$ and the ideal gas is in equilibrium with density $\varrho^\varepsilon = \varepsilon^{-\frac{1}{2}}\varrho$ and with velocity distribution $f^\varepsilon(v) = \varepsilon^{\frac{3}{2}} f(\varepsilon^{\frac{1}{2}} v)$. In a unit time interval the heavy particle suffers of the order of ε^{-1} collisions each one of which changes the velocity by an amount of order $\varepsilon^{\frac{1}{2}}$. Because the light particles move so fast, recollisions become negligible.

Theorem 4 [15]. Let $v^\varepsilon(t)$ be the velocity of the heavy particle at time t. Let $f(v)$ be radial with at least four moments. Then, in the sense of joint distributions (multitime correlations),

$$\lim_{\varepsilon\to 0} v^\varepsilon(t) = v(t)\,. \tag{3.3}$$

$v(t)$ is the Ornstein-Uhlenbeck process governed by

$$\frac{\mathrm{d}}{\mathrm{d}t} v(t) = -\gamma v(t) + D^{\frac{1}{2}}\xi(t)\,, \tag{3.4}$$

$v(0) = v$. Here $\xi(t)$ is Gaussian white noise, $\gamma = (2\pi/3)(m/M)\varrho\sigma^2\int \mathrm{d}^3v|v|f(v)$ is the friction constant and $D = (2\pi/3)(m/M)\varrho\sigma^2\int \mathrm{d}^3v|v|^3 f(v)$ is the diffusion constant in velocity space.

For the weak-coupling limit we consider the motion of a particle through a random distribution of soft scatterers. The techniques developed by now are powerful enough to handle also other cases, but let us stick to published results. The centres of the scatterers are randomly (Poisson) distributed throughout space. Their density is $\varepsilon^{-3}\varrho$. At each centre we place a spherical potential $V^\varepsilon(q) = \varepsilon^{\frac{1}{2}} V(q/\varepsilon)$. V is of finite range and smooth. Note that the volume fraction filled by the potentials is independent of ε. We now let a particle of mass m move through the random configuration of scatterers. Its velocity is denoted by $v^\varepsilon(t)$. Of course, the position of the moving particle is $q^\varepsilon(t) = q(0) + \int_0^t \mathrm{d}s\, v^\varepsilon(s)$. By conservation of energy $\lim_{\varepsilon\to 0} |v^\varepsilon(t)| = \lim_{\varepsilon\to 0} |v^\varepsilon(0)| = |v|$. Per unit time $v^\varepsilon(t)$ suffers ε^{-1} changes of the order $\varepsilon^{\frac{1}{2}}$.

Theorem 5 [16, 17]. Let $v^\varepsilon(t)$ be the velocity of a moving particle. Then, in the sense of joint distributions,

$$\lim_{\varepsilon\to 0} v^\varepsilon(t) = v(t)\,, \tag{3.5}$$

$v(0) = v$. $v(t)$ is diffusion on the sphere with radius $|v|$. The diffusion coefficient is $\varrho(1/m^2|v|)(1/2\pi)\int \mathrm{d}^3k\,|k|\,|\hat{V}(k)|^2$.

4. – Some results for systems at finite density.

Very few rigorous results have been obtained for systems at finite density. The open problems are the existence of transport coefficients, the validity of linearized (around global equilibrium) hydrodynamics and the derivation of the nonlinear hydrodynamic equations. There is only one nontrivial model system for which at least some faint reflection of these general problems can be investigated, namely hard rods. This is a system of point particles on the line, all of equal mass. They have a hard-core diameter σ and interact through elastic collisions. A somewhat unusual feature of hard rods is the infinite number of conserved fields. In a collision the number of particles with a given velocity does not change. Therefore, it is conserved in the course of time. This also implies that there are many equilibrium (steady) states. As for the ideal gas we are free to choose the velocity distribution $h(v)$. The dynamical quantity of interest is $n(\mathrm{d}q, t; v)$, the actual number of particles with velocity v in the interval $\mathrm{d}q$ at time t. v should be thought of as a label for the conserved field. For a real fluid it would run only from 1 to 5 (mass, momentum and energy). By the conservation law to each $n(\mathrm{d}q, t; v)$ there is a corresponding microscopic current $j(\mathrm{d}q, t; v)$. It turns out [18] that the total current-current correlation function in equilibrium is given by

$$\begin{aligned}(4.1)\qquad &\int\{\langle j(\mathrm{d}q, t; v)\, j(0, t'; v')\rangle - \langle j(\mathrm{d}q, t; v)\rangle\langle j(0, t'; v')\rangle\} = \\ &= \delta(t-t')\,\frac{\sigma^2\varrho^2}{1-\sigma\varrho}\, h(v)\,h(v')\,|v-v'|\,\big(\delta(v-v')-1\big) + \frac{\varrho}{(1-\sigma\varrho)^2}\, h(v)\, v^2\,\delta(v-v') + \\ &\qquad + \frac{\sigma\varrho^2}{1-\sigma\varrho}\, h(v)\,h(v')\left[\frac{\sigma\varrho}{1-\sigma\varrho}\int \mathrm{d}w\, h(w)\, w^2 - \frac{1}{1-\sigma\varrho}\,(v^2+v'^2)\right].\end{aligned}$$

Note that the current-current correlation does not cluster in time. For the Green-Kubo formula the constant part has to be truncated. One checks the validity of the usual picture of linearized hydrodynamics. To my knowledge, this is the only mechanical system for which a nontrivial current-current correlation has been established.

The hard rods are so simple that also the validity of the Euler equations can be proved. For this a continuum limit has to be carried through. We assume that the hard-rod diameter is $\sigma^\varepsilon = \varepsilon\sigma$ and that the density increases as ε^{-1}. On the chosen macroscale each volume element contains many (*i.e.* ε^{-1}) rather short (*i.e.* ε) hard rods. Note that the mass density is independent of ε. $n^\varepsilon(\mathrm{d}q, t; v)$ is again the actual number of particles with velocity v in the interval $\mathrm{d}q$ at time t. The ε-dependence comes from both the dynamics and the initial state.

Theorem 6 [19]. Let the initial state, $\langle\cdot\rangle$, satisfy some reasonable cluster properties in space and let

$$\lim_{\varepsilon\to 0}\langle \varepsilon n^{\varepsilon}(\mathrm{d}q, 0; v)\rangle = n(q; v)\,\mathrm{d}q\,, \tag{4.2}$$

$$\lim_{\varepsilon\to 0}\left\langle\left(\varepsilon n^{\varepsilon}(\mathrm{d}q, 0; v)\right)^2\right\rangle - \langle \varepsilon n^{\varepsilon}(\mathrm{d}q, 0; v)\rangle^2 = 0\,. \tag{4.3}$$

Then

$$\lim_{\varepsilon\to 0} n^{\varepsilon}(\mathrm{d}q, t; v) = n(q, t; v)\,\mathrm{d}v \tag{4.4}$$

and $n(q, t; v)$ is the solution of

$$\begin{aligned}\frac{\partial}{\partial t}n(q, t; v) + \frac{\partial}{\partial q}\Big[vn(q, t; v) + \\ + \sigma n(q, t; v)\Big(1 - \sigma\int \mathrm{d}v'\, n(q, t; v')\Big)^{-1}\int \mathrm{d}w(v - w)n(q, t; w)\Big] = 0\end{aligned} \tag{4.5}$$

with initial condition $n(q, 0; v) = n(q; v)$.

(4.5) is the Euler equation for the system of hard rods.

The motion of a tracer particle in an ideal gas is presently under active investigation. If we assume that the gas particles are very heavy, then the system degenerates into the Lorentz gas. This is the motion of a point particle through randomly distributed, infinitely heavy scatterers. Physically, the Lorentz gas has been studied extensively. (See the lecture by B. J. ALDER.) It provides an interesting test case for both theory and molecular dynamics. On a rigorous level, diffusive behaviour has not been established so far. The system simplifies if the scatterers are arranged periodically. Then it suffices to study the motion in one unit cell. For two-dimensional systems this looks then like a billiard table (without friction) with periodic boundary conditions and some obstacles inside. This is known as the Sinai billiard. Its dynamical properties have been studied in great detail (cf., *e.g.*, [20, 21]). We assume a finite horizon for the periodic Lorentz gas, *i.e.* no path can extend out to infinity without hitting a scatterer. (This assumption would not be satisfied for circular scatterers arranged as a square lattice.) The particle starts initially, say, with a uniform distribution in the cell next to the origin. Let $q(t)$ denote the position of the particle at time t.

Theorem 7 [22]. For the periodic Lorentz gas in two dimensions with a finite horizon

$$\lim_{\varepsilon\to 0}\varepsilon q(\varepsilon^{-2}t) = D^{\frac{1}{2}}b(t) \tag{4.6}$$

in the sense of joint distributions. D is the 2×2 diffusion matrix, $0 < D < \infty$, and $b(t)$ is two-dimensional Brownian motion.

This establishes transport and diffusive behaviour for the periodic Lorentz gas. The decay of the velocity autocorrelation function is estimated to be subexponential as $\exp[-\alpha|t|^\gamma]$. Numerically $\gamma = 0.7$ [23]. More detailed information is available, in particular for the triangular lattice at the two thresholds—bounded motion to finite horizon and finite horizon to infinite horizon (cf. [24]).

Let us return to the tracer particle in the ideal gas. SINAI and SOLOVEICHIK [25] establish

$$\lim_{t\to\infty} \frac{1}{t^2} \langle q(t)^2 \rangle = 0 \,. \tag{4.7}$$

This might look like a trivial result—it is not. In particular, it implies that the velocity autocorrelation function has to decay as $t \to \infty$. In one dimension stronger results are available. We assume that the tracer particle, mass M, interacts with the ideal-gas particles, mass m, through elastic collisions. The gas has uniform density and a Maxwellian velocity distribution. If $m = M$, then the velocity autocorrelation function can be computed explicitly [26]. It yields a finite diffusivity. By a somewhat more elaborate argument convergence to Brownian motion, as in (4.6), can be established [27]. If $m \neq M$, the collisions become hard to follow and no computional tool is available. Still

Theorem 8 [28, 29]. For the tracer particle in one dimension

$$\frac{\sqrt{\pi}}{2\sqrt{2}} \frac{1}{\varrho\sqrt{\beta m}} \leqslant \frac{1}{t} \langle q(t)^2 \rangle \leqslant \frac{\sqrt{2}}{\sqrt{\pi}} \frac{1}{\varrho\sqrt{\beta m}}$$

for large t, where β is the inverse temperature and ϱ the density of the gas.

The upper bound coincides with the known value of the diffusion coefficient for $M = m$. This suggests the conjecture that the diffusion coefficient may be independent of M. Recent molecular-dynamics simulations [30] indicate that this is not the case.

Let me finally turn to a somewhat loosely connected topic. As before, the tracer particle is immersed in an ideal gas. But now it is confined by some external potential V which grows sufficiently fast such that $\int dq \cdot \exp[-\beta V(q)] < \infty$. Initially the ideal gas is in equilibrium with a Maxwellian velocity distribution and the tracer particle starts at a given position with some velocity. We would expect then that, as $t \to \infty$, the distribution of the tracer particle tends to its equilibrium distribution. This has been called a « return to equilibrium », since the joint system ideal gas plus tracer particle is only locally perturbed away from equilibrium. In [31] methods are developed which are powerful enough to establish such a return to equilibrium. If the potential V confines the tracer particle to some finite region, return to equilibrium is proved in [32].

REFERENCES

[1] M. KROOK and T. T. WU: *Phys. Rev. Lett.*, **36**, 1107 (1976).

[2] A. V. BOBYLEV: *Sov. Phys. Dokl.*, **20**, 822 (1976).

[3] M. ERNST: *Phys. Rep.*, **78**, 1 (1981).

[4] F. KING: *BBGKY hierarchy for positive potentials*, Ph. D. Thesis, Department of Mathematics, University of California at Berkeley (1975).

[5] H. GRAD: *Principles of the kinetic theory of gases*, in *Handbuch der Physik*, Band 12, edited by S. FLÜGGE (Springer, Berlin, 1958), p. 205.

[6] H. SPOHN: *Boltzmann hierarchy and Boltzmann equation*, in *Kinetic Theories and the Boltzmann Equation*, edited by C. CERCIGNANI, *Lecture Notes in Mathematics*, Vol. **1048** (Springer, Berlin, 1984), p. 207.

[7] O. E. LANFORD: *Time evolution of large classical systems*, in *Dynamical Systems and Applications*, edited by J. MOSER, *Lecture Notes in Physics*, Vol. **38** (Springer, Berlin, 1975), p. 1.

[8] O. E. LANFORD: *Astérisque*, **40**, 117 (1976).

[9] R. ILLNER and M. PULVIRENTI: *Global validity of the Boltzmann equation for a two-dimensional rare gas in vacuum*, preprint.

[10] K. UCHIYAMA: *Derivation of the Boltzmann equation from dynamical systems*, preprint.

[11] H. VAN BEIJEREN, O. E. LANFORD, J. L. LEBOWITZ and H. SPOHN: *J. Stat. Phys.*, **22**, 237 (1980).

[12] H. SPOHN: *J. Stat. Phys.*, **26**, 285 (1981).

[13] H. SPOHN: *Fluctuation theory for the Boltzmann equation*, in *Nonequilibrium Phenomena*, Vol. **1**, edited by J. L. LEBOWITZ and E. W. MONTROLL (North-Holland, Amsterdam, 1983), p. 225.

[14] J. L. LEBOWITZ and H. SPOHN: *J. Stat. Phys.*, **29**, 39 (1982).

[15] D. DÜRR, S. GOLDSTEIN and J. L. LEBOWITZ: *Commun. Math. Phys.*, **78**, 507 (1981).

[16] H. KESTEN and G. C. PAPANICALAOU: *Commun. Math. Phys.*, **78**, 19 (1980).

[17] D. DÜRR, S. GOLDSTEIN and J. L. LEBOWITZ: preprint.

[18] H. SPOHN: *Ann. Phys.* (*N.Y.*), **141**, 353 (1982).

[19] C. BOLDRIGHINI, R. L. DOBRUSHIN and YA. SUKHOV: *J. Stat. Phys.*, **31**, 577 (1983).

[20] G. GALLAVOTTI: *Lectures on the billiard*, in *Dynamical Systems, Theory and Applications*, edited by J. MOSER, *Lecture Notes in Physics*, Vol. **38** (Springer, Berlin, 1975), p. 236.

[21] L. A. BUNIMOVICH: *Commun. Math. Phys.*, **65**, 295 (1979).

[22] L. A. BUNIMOVICH and YA. G. SINAI: *Commun. Math. Phys.*, **78**, 479 (1980).

[23] J. P. BOUCHAUD and P. LE DOUSSAL: *J. Stat. Phys.*, **41**, 225 (1985).

[24] L. A. BUNIMOVICH: *On the diffusion in dynamical systems*, in *Statistical Physics and Dynamical Systems*, edited by J. FRITZ, A. JAFFE and D. SZÁSZ, *Progress in Physics*, Vol. **10** (Birkhäuser, Boston, Mass., 1985), p. 127.

[25] Private communication.

[26] D. W. JESPEN: *J. Math. Phys.* (*N.Y.*), **6**, 405 (1965).

[27] F. SPITZER: *J. Math. Mech.*, **18**, 973 (1969).
[28] YA. G. SINAI and M. R. SOLOVEICHIK: *Commun. Math. Phys.*, **104**, 423 (1986).
[29] D. SZÁSZ and B. TÓTH: *Commun. Math. Phys.*, **104**, 445 (1986).
[30] D. DÜRR, E. OMERTI and M. RONCHETTI: *Numerical evidence for mass dependence in the diffusive behaviour of the « heavy particle » on the line*, preprint.
[31] E. PRESUTTI, YA. G. SINAI and M. R. SOLOVEICHIK: *Hyperbolicity and Möller-morphism for a model of classical statistical mechanics*, in *Statistical Physics and Dynamical Systems*, edited by J. FRITZ, A. JAFFE and D. SZÁSZ, *Progress in Physics*, Vol. **10** (Birkhäuser, Boston, Mass., 1985), p. 253.
[32] S. GOLDSTEIN, J. L. LEBOWITZ and K. RAVISHANKAR: *Commun. Math. Phys.*, **85**, 419 (1982).

Round-Table: Perspectives in Nonequilibrium Molecular Dynamics.

Chairman: H. J. M. HANLEY

Secretary: D. HEYES

The panel opened with remarks by HANLEY who summarized his opinions on the status and results of nonequilibrium molecular dynamics (NEMD) and raised some issues touched upon by the lectures. He requested comments on the issues by the panelists. He also invited the panelists to make further comments if they wished and invited contributions from the audience. A summary of the material is as follows.

General remarks (H. J. M. HANLEY)

Since NEMD is a rapidly developing topic, it is appropriate to recall concepts, list some references that discuss the techniques, and outline some of the results that have been obtained so far.

Nonequilibrium molecular dynamics refers to simulation techniques that introduce directly nonequilibrium behaviour into a system through such mechanisms as external forces or gradients. The philosophy thus differs from conventional molecular dynamics in which one studies nonequilibrium behaviour via fluctuations around the equilibrium state. The advantage of NEMD is that it is direct, flexible and applicable to systems far from equilibrium.

Early efforts used special boundary conditions or external fields to introduce the spatial variations in the system. Pioneers include LEES and EDWARDS [1], GOSLING, MCDONALD and SINGER [2], ASHURST and HOOVER [3] and CICCOTTI and JACUCCI [4]. Later methods were based on adjustments to the periodic imaging and *ad hoc* modifications to the Newtonian equations of motion [5-7]. Recently, much of the approximate nature of the early work has been removed by constructing equations of motion that can constrain variables other than mass, momentum and energy. (See EVANS in this volume, for example.) This freedom, coupled as always with advances in computer technology, has

opened up the field of computer simulation in general. The potential of NEMD has yet to be fully appreciated.

General references on the modern techniques include [8, 9]. As an aside it turns out that NEMD simulations seem very forgiving and there is good agreement among the approaches, including some that are obviously crude, by today's standard.

Objectives. As noted, NEMD can be applied in principle to any phenomenon. In particular, I shall discuss an example close to my own experience. Much work to date has concentrated on investigating a liquid subjected to a shear rate, γ, and thus has impacted on the field of rheology. Rheology is the study of fluid flow and deformation. The flow of all fluids falls under this heading, but the topic has evolved as a study of complex molecules, polymeric solutions, or polymer melts because such materials display exotic non-Newtonian, non-linear phenomena. Reference [10] gives a pictorial summary of many of them. They result largely because the viscosity is shear rate dependent, $\eta = \eta(\gamma)$, and normal pressure differences among P_{xx}, P_{yy} and P_{zz} exist.

A goal of NEMD is to connect the macroscopic rheological laws and constitutive relations with the atomistic microscopic behaviour of a liquid. It turns out that this approach indicates that rheological non-Newtonian behaviour is not restricted in principle to fluids of complex structure.

Output. For computational convenience most of the NEMD simulations model a liquid undergoing planar Couette flow. The temperature is usually fixed by removing the viscous heat with a thermostat. Key outputs from the simulations are:

The kinetic temperature, T,

$$T = \frac{m}{3Nk}\left\langle \sum_{i=1}^{N} [v_i - u(r_i)]^2 \right\rangle,$$

where v_i is the velocity of particle i and u the streaming velocity at position r_i; the energy per particle, E,

$$E = \frac{1}{N}\left\langle \sum_i \left\{ \frac{m}{2}[v_i - u(r_i)]^2 + \sum_{j\neq i} \varphi_{ij} \right\} \right\rangle,$$

where $\varphi_{ij} \equiv \varphi(R_{ij})$ with $R_{ij} = |\boldsymbol{r}_i - \boldsymbol{r}_j|$ and the elements of the pressure tensor $\boldsymbol{P}$,

$$\boldsymbol{P} = \frac{1}{V}\left\{ \sum_i \left[m(\boldsymbol{v}_i - \boldsymbol{u}(r_i))(\boldsymbol{v}_i - \boldsymbol{u}(r_i)) + \sum_{j\neq i} R_{ij} \frac{\partial \varphi}{\partial R_{ij}} \right] \right\}.$$

The viscosity and pressure p follow from $\boldsymbol{P}$, since

$$\boldsymbol{P} = p\boldsymbol{I} + \boldsymbol{\Pi},$$

where $\boldsymbol{I}$ in the unit tensor and $\boldsymbol{\Pi}$ is the traceless friction pressure tensor. (Bulk viscosity can be ignored in Couette flow.) We have

$$\Pi_{xy}(\gamma) = -\eta(\gamma)\gamma\,,$$

where $\gamma = \mathrm{d}u_x/\mathrm{d}y + \mathrm{d}u_y/\mathrm{d}x$. Note that $\eta = \eta(\gamma)$ and that p is one-third the trace of $\boldsymbol{P}$; we define this as a mechanical pressure and in general

$$p = p(N/V, T, \gamma)\,,$$

where N/V is the number of particles in volume V.

An extremely instructive quantity to extract from the simulation in the pair correlation function $g(\boldsymbol{r}, \gamma)$ which represents the distribution of particles around a central particle and hence is a measure of the structure of the liquid. For a system under shear one can write [10]

$$g(\boldsymbol{r}, \gamma) = g_s + g_+\hat{x}\hat{y} + g_-(\hat{x}^2 - \hat{y}^2) + g_0(\hat{z}^2 - \tfrac{1}{3}) + \dots\,,$$

where $\hat{x} = r_x/r$, etc. The expansion coefficient g_+ is related to the shear viscosity η and g_-, g_0 relate to normal pressure differences in the fluid. For a Newtonian liquid, $g_s = g(r)$ the usual radial distribution function and g_+, g_-, g_0 vanish.

Results. I would like to mention two general results. The first is that NEMD simulations were ahead and are still ahead of kinetic theory and nonequilibrium statistical mechanics: ahead in the sense that they are experimental data that need an explanation. They have thus provided a stimulus even if they are subject to reservations.

The second general result is that the simulations give one a feel and often a quantitative picture of the concept of response and relaxation in a fluid that is perturbed. Related to this they have caused one to take a fresh look at rheology. We have mentioned the result that the simulations indicate that even the simplest liquids—hard spheres, soft spheres, or Lennard-Jones—will display behaviour normally only associated with molecules of complex structure. This being the case, one has first to look at the basic physics of a non-Newtonian phenomenon rather than to discuss it in terms of molecular complexity.

In more detail the simulations (reinforced by experimental data from suspensions, colloids and macromolecules) suggest that, if the product $\tau\gamma \gtrsim 10^{-2}$, then non-Newtonian behaviour can be expected. τ is Maxwell's relaxation time. It can be defined as the ratio η/G, where G is the shear modulus.

Furthermore, one has a chance for the first time to address a complex flow problem given some *a priori* microscopic information on non-Newtonian parameters of the system.

Some specific results from NEMD include:

1) Direct calculations of the transport coefficients of a liquid: the viscosity, thermal conductivity and diffusion coefficients.

2) The shear rate—or its equivalent—has to be included in the thermodynamic description of the fluid. Thus for a fluid under shear

$$E = E(N/V, T, \gamma), \quad p = p(N/V, T, \gamma).$$

This result has lead to a heuristic thermodynamic description [11] for a system in the steady state:

$$\mathrm{d}E = T\,\mathrm{d}S - p\,\mathrm{d}V + \xi\,\mathrm{d}\gamma,$$

where S is defined as the entropy and ξ is a state function analogous to a chemical potential. The consequences of this formalism are quite far-reaching. For example, the stability and hence the phase behaviour of a system under shear is affected by the shear rate.

3) As discussed above, if p is the trace of $\boldsymbol{P}$, then

$$P_{xx} \neq P_{yy} \neq P_{zz}.$$

4) The asymptotic behaviour of some properties has been evaluated. For instance:

For a 2-dimensional liquid,

$$\eta = -A \log(B\gamma), \quad p = p(0) + A\gamma \log(B\gamma).$$

For 3 dimensions

$$\eta = \eta(0) - A\gamma^{\frac{1}{2}}, \quad p = p(0) + A\gamma^{\frac{3}{2}}, \quad \eta(\omega) = \eta(0) + A(i\omega)^{\frac{1}{2}}.$$

A and B are constants unique to each equation, ω is the frequency.

Some problems and questions. The results of NEMD, issues and problems are discussed in ref. [8, 9] and, in particular, in ref. [10-13]. Reference [10] is a special issue of *Physics Today* and ref. [13] reports on a conference on nonlinear phenomena held in Boulder, Colorado.

We also refer to the lectures of Dufty, Holian and Evans in this volume.

It seems the most significant problems arise because NEMD simulations, by their nature, deliberately put the system out of equilibrium. Consequently any phenomena observed are irreversible and dissipative. How does one define the properties of a system out of equilibrium? Especially, how does one define the properties if the concept of a Newtonian fluid appears invalid, and perturbations away from equilibrium or steady states appear nonanalytic under certain conditions?

Following this, what support can one expect from statistical mechanics? How does one provide a thermodynamic description? I refer to the lectures of Dufty and of Dorfman in this volume for discussions of the former questions and appropriate references. See also the work of Evans and Hoover and co-workers. As noted, HANLEY and EVANS [12] have discussed the thermodynamics and parts of their arguments have been expounded on and presented independently by KEIZER [14]. Other authors interested in this problem include NETTLETON [15] and PEREZ-GARCIA, JOU and their colleagues [16].

Another basic question that has arisen and was first discussed at length in ref. [3] is to what extent the NEMD simulations correspond to physical reality. A related question is how artificial is the thermostatting? These points are raised again by DUFTY and by EVANS in their remarks as panelists.

Some more mechanical questions include:

Now does the behaviour of a dilute gas (in which the contributions are kinetic and the nonlinear results are analytic) transfer to that of the dense liquid (in which the contributions are potential and the nonlinear results seem to be nonanalytic)? In other words, what are the density dependences of the nonlinear coefficients?

Do we have adequate simulation data for $\eta = \eta(\gamma)$ at low values of the shear rate, γ, and at the high values of γ? Similarly for $\eta = \eta(\omega)$ at low frequency, ω.

The future. The future emphasis of NEMD will be less on the techniques —although they will continue to be developed, of course—and more on applications. For the first time, one can tackle a flow problem given some information on the microscopic behaviour of the system. More workers will simulate molecules of increasing complexity and the link with traditional rheology will become stronger.

Attention will be given to nonlinear phenomena, such as shear-induced phase transitions, and we speculate that NEMD will indicate phenomena of a sheared fluid that have yet to be discovered in the laboratory.

NEMD will be applied to « unusual » systems: suspensions, films, granular materials, emulsions, membranes and the like.

Finally, NEMD will follow the path of equilibrium molecular dynamics and become a general, even an essential, tool to test statistical mechanics. The results that one observes from such tests will point to further theoretical work.

Remarks (J. W. DUFTY)

Dufty remarks are summarized as follows:

The field of nonequilibrium computer simulations is a rapidly developing one, and there remain many unsettled questions regarding both the inter-

pretation and limitations of methods used. In addition, much of the data obtained from such simulations have not yet been given an adequate theoretical explanation. In this context I limit my remarks to simulations of shear flow and address two distinct questions: 1) What are the properties of a Lees-Edwards fluid?, and 2) Do these properties represent those of real fluids?

The first question refers to the predictions of a specific model using Lees-Edwards boundary conditions. The main complication here is to relate models with and without thermostats. The kinetic-theory analysis I presented earlier this week shows that in general it should be expected that transport properties of a fluid held at constant temperature are different from those for a fluid allowed to heat. The difference is fundamental, and remains even after the temperature has been scaled out of the transport properties. A further question is the characterization of thermostats. Several choices are currently employed, but their justification at this stage is empirical. It would be useful to formulate the criteria for selecting a good thermostat, beyond simply preserving the Green-Kubo results at asymptotically small shear rates. More importantly, detailed calculations on a given model would be useful to see if there are any qualitative changes induced by a thermostat. Generally, the nonconservative forces are nonlocal and imply long-range correlations over the entire system, even at low density. What are the implications of such correlations? For example, is the transition to an ordered phase seen at large shear rates possible without a thermostat? In the context of a given model, with or without thermostat, there are many other interesting and open theoretical problems. These include mode-coupling anomalies in 3 dimensions, instabilities in 2 dimensions at small shear rates, and large wave vector hydrodynamic fluctuations around uniform shear flow.

To answer the second question above, the properties of the Lees-Edwards fluid should be known in more detail. It is clear that they are unrealistic in many ways. The boundary conditions do not represent real fluid-surface interactions even qualitatively. They are nonlocal and do not lead to the usual boundary layer found in all real fluids. Even far from the boundaries the hydrodynamic fields differ—the temperature for the Lees-Edwards fluid is uniform, while for real fluids it has a spatial variation. As a consequence of this difference, the pressure tensors as a function of the shear rate are not related in any simple way. These and related considerations suggest that in the domain of nonlinear transport there is no well-defined experiment that could be performed to test the predictions of the computer simulations. My own view is that the Lees-Edwards boundary conditions define an interesting theoretical model for a special nonequilibrium state, and that future short-term emphasis should be placed on establishing more precisely the relationship of simulation methods to appropriate theoretical calculations. The current status of nonequilibrium statistical mechanics is such that much can be learned from these idealized but somewhat unrealistic models.

Remarks (D. J. EVANS)

EVANS addressed the concept that thermostatting a model system may be an artifact. He argued that many thermostatting procedures give effectively the same results for a model system under equivalent conditions. Specifically he presented new results, calculated with Brad HOLIAN [17], which showed that within statistical uncertainties the Gaussian isothermal method, the Nosé-Hoover, the Berendsen and isoenergetic MD produce the same shear viscosities at high shear rates in a dense liquid at the same density and temperature (see table I).

TABLE I. – *This table compares viscosities obtained using six different thermostats to maintain steady states very far from equilibrium.* The results are for 32 soft spheres under shear $\gamma\sigma(m/\varepsilon)^{\frac{1}{2}} = 1.0$, $kT/\varepsilon = 1.0$, $\varrho\sigma^3 = 0.7$. At this shear rate the viscosity has decreased to 70% of its Newtonian ($\gamma = \mathrm{d}u_x/\mathrm{d}y \to 0$) value. The columns are from left to right: temperature, internal energy, shear viscosity, second moments of the internal energy and kinetic energy, run length in thousands of time steps and the integration time step. (The inverse-twelve potential was cut off for particle separations larger than half the periodic cube edge.) Note the agreement, within statistical uncertainties of all the results. Note also that even with the optimum choice of time constant for the Nosé-Hoover method it is still more than twice as inefficient as the Gaussian isothermal method. The data are from ref. [17].

Method	kT/ε	E/ε	$n\sigma^2(m\varepsilon)^{-\frac{1}{2}}$
Gaussian isothermal	1.0	147.6 + 0.1	1.524 + 0.007
Gaussian isoenergetic	0.996 + 0.002	147.38	1.537 + 0.008
$NH\tau(\varepsilon/m\sigma^2)^{\frac{1}{2}} = 1$	1.0001 + 0.0002	147.4 + 0.2	1.55 + 0.02
$NH = 0.096\,22$	0.998 + 0.001	147.2 + 0.2	1.56 + 0.02
$= 0.033\,3$	0.998 + 0.001	147.7 + 0.4	1.56 + 0.04
BERENDSEN: $T_s = 0.78$	0.996 + 0.003	148.4 + 0.05	1.56 + 0.03

Method	$(\Delta E/\varepsilon)^2$	$(\Delta KE/\varepsilon)^2$	kts	$\Delta(\varepsilon/m\sigma^2)^{\frac{1}{2}}$
Gaussian isothermal	49.3 + 10	0.0	50	0.003
Gaussian isoenergetic	0.0	27.6 + 2	40	0.003
$NH\tau(\varepsilon/m\sigma^2)^{\frac{1}{2}} = 1$	108.9 + 2	60 + 3	50	0.003
$NH = 0.096\,22$	110 + 4	52 + 1	40	0.003
$= 0.033\,3$	83 + 3	43 + 1	73	0.001
BERENDSEN: $T_s = 0.78$	62 + 30	30 + 10	60	0.003

Remarks (J. P. RYCKAERT)

RYCKAERT described the interest in NEMD for obtaining the transport properties of molecular systems. He emphasized that the difference-in-trajec-

tory approach coupled with the Doll or Sllod tensor is successful for the molecular case, permits one to apply very small perturbations, *i.e.* to work in the linear region, and to avoid the use of a thermostat. Moreover he suggested that a comparison between Green-Kubo, difference-in-trajectory [4-6] and large-gradient methods [7-9] (the last requires an extrapolation to zero shear rate) is timely. He pointed out that work is in progress to test the relative efficiency of these methods, *e.g.*, in the Lennard-Jones fluid far from the melting line, already considered by HOLIAN and EVANS [18].

Denis EVANS pointed out that the Green-Kubo approach has a greater N-dependence and larger statistical uncertainties than the NEMD method, which obtains the zero-shear-rate limiting viscosity by extrapolating from finite to zero shear rate. Berni ALDER questioned the ability of NEMD to reproduce the long-time decay of the correlation functions. He commented that a divergence of trajectories limits the use of NEMD in the vicinity of the molasses tail, when a difference-in-trajectory approach is adopted. Giovanni CICCOTTI remarked that the only serious problem with the last approach can come from correlations decaying with a power law. He suggested that an exponential decay can always be obtained.

Contribution from the floor.

A number of short contributions finished the session. Gary MORRISS considered a solution to two bodies under isothermal shear. This problem can be reduced to one of 3 degrees of freedom which is amenable to analytic solution. This produces expressions for the normal pressure differences and the shear thinning behaviour. The ratio of shear viscosity at finite shear rate, γ, divided by its value at zero shear rate decreases as γ^2 as $\gamma \to 0$ and $(\ln \gamma)/\gamma^2$ as $\gamma \to \infty$.

Bill HOOVER continued the theme of the rheology of two- and three-body systems ($N = 2$ or 3) by presenting the results of simulations of them. Two particles are sufficient for simulating diffusive and viscous flows. Three particles are required for heat flow. Interestingly much of their transport behaviour is only approximately a factor of 2 different from the infinite-N limit! Giovanni CICCOTTI questioned the criticisms raised against NEMD. He observed that in the limit of zero perturbation one has the theoretical Green-Kubo result. For nonzero perturbation this result is no longer rigorous nor of special value. However, for small perturbations (in the linear region) the linear-response theory, without thermostat, can be checked by the subtraction method [4-6]. This method can be applied also when using a thermostat and one would still find agreement with Green-Kubo. For larger perturbations, in the nonlinear region the thermostatted subtraction method or Hoover and Evans [7-9] NEMD can be applied. This has permitted many interesting and unexpected discoveries in the behaviour of simple fluids [10, 13]. These two last methods, whenever a test has been attempted, turned out to be equivalent.

Moreover, if doubts remain on the validity of the results so obtained for « real » fluids, one can refer to any of « natural » NEMD methods available (*e.g.*, Hoover [3] or Tenenbaum, Trozzi and Ciccotti [19, 20]). Again the agreement with results obtained with previous « bulk » methods is very good. Michel MARESCHAL reported: It is worthwhile to study nonequilibrium systems by simulation with stochastic boundary conditions [19, 20] for, at least, two reasons: first, large simulations are now possible where the inhomogeneity is the object of the study and one expects that, despite the small sizes of the systems, a macroscopic behaviour will show up. Second, many nonequilibrium methods have been developed and a comparison between these various methods is necessary, in particular in the case of temperature gradient.

We want to address the question of low large should a system be in order to distinguish between bulk properties and boundary effects.

We studied a moderately dense, two-dimensional hard-disk fluid. The system was periodic in the y-direction, but enclosed between two mathematical lines in the x-direction. The interaction with the lines was such that incident particles were reemitted with an equilibrium velocity distribution corresponding to a given temperature. We made several runs for different geometries with plate distances ranging from ten to forty mean free paths, Λ, and temperature differences ranging from one to ten times the left-boundary temperature.

We looked at density and temperature profiles and compared them with the solution of a nonlinear BGK model equation. We also looked at time-dependent local correlation functions.

The temperature profile is nearly linear, except in the Knudsen region which extends over one mean free path. Measuring the moments of the velocity distribution function, we found an agreement with the Chapman-Enskog solution in the bulk but a different behaviour at the boundary. That behaviour is accounted for by a moment method of solution of the kinetic equation where one allows for a different solution depending on the sign of V_x. This solution predicts then a temperature slip $T_s(0)/\Delta T \approx \Lambda/d$, where d is the width of the system. The measured slips agree closely with that prediction.

The heat flux in the x-direction being constant, and $\mathrm{d}T/\mathrm{d}x$ being constant in the bulk, their ratio is a nonequilibrium transport coefficient, λ, which depends on plate distance, d, and temperature difference, ΔT. Theory predicts that $\lambda(T, d, \Delta T) \approx \tilde{\lambda}(T, \Delta T) \times (1 + \Lambda/d)^{-1}$ and, therefore, the plate distance dependence reduces to 2 % for $d/\Lambda \approx 50$. Simulations permit us to measure λ as function of ΔT.

We also performed measurements on heat flux correlation functions. Here also, the boundary effects seem to be limited to the Knudsen region.

In conclusion, we can say that boundary effects are well separated from bulk properties in moderately dense fluid systems, and such simulations will prove useful with study of nonequilibrium systems.

The last contribution came from David HEYES who reported the results of some Sllod NEMD calculations of shear thinning and shear thickening of the Lennard-Jones liquid close to the triple point. In common with many dense suspensions this simple liquid exhibits first and second Newtonian regions of viscosity, shear thinning and shear thickening. States beyond extreme shear thinning are characterized by a « string » phase. The structure of the liquid consists of lines of molecules packed along the streaming lines of shear into a trigonal lattice when viewed in cross-section. Consequences of this for molecular dynamics were alluded to.

REFERENCES

[1] A. W. LEES and S. F. EDWARDS: *J. Phys. C*, **5**, 1921 (1972).
[2] E. M. GOSLING, I. R. MCDONALD and K. SINGER: *Mol. Phys.*, **26**, 1475 (1973).
[3] W. G. HOOVER and W. T. ASHURST: *Adv. Theor. Chem.*, **1**, 1 (1975).
[4] G. CICCOTTI and G. JACUCCI: *Phys. Rev. Lett.*, **35**, 789 (1975).
[5] G. CICCOTTI, G. JACUCCI and I. R. MCDONALD: *Phys. Rev. A*, **13**, 426 (1976).
[6] G. CICCOTTI, G. JACUCCI and I. R. MCDONALD: *J. Stat. Phys.*, **21**, 1 (1979).
[7] W. G. HOOVER, D. J. EVANS, R. B. HICKMAN, A. J. LADD, W. T. ASHURST and B. MORAN: *Phys. Rev. A*, **22**, 1690 (1980).
[8] D. J. EVANS and G. P. MORRISS: *Comput. Phys. Rep.*, **1**, 2999 (1984).
[9] W. G. HOOVER: *Annu. Rev. Phys. Chem.*, **34**, 103 (1983).
[10] *Physics Today* (January, 1984), see the article by R. B. BIRD and C. F. CURTISS, p. 36.
[11] S. HESS and H. J. M. HANLEY: *Int. J. Thermophys.*, **4**, 97 (1983).
[12] H. J. M. HANLEY and D. J. EVANS: *J. Chem. Phys.*, **76**, 3225 (1982).
[13] *Physica (Utrecht) A*, **118** (1983).
[14] J. KEIZER: *Physica (Utrecht) A*, **118**, 350 (1983); *J. Chem. Phys.*, **82**, 2751 (1985).
[15] R. E. NETTLETON: *J. Chem. Phys.*, **81**, 2458 (1984); *J. Phys. A*, **12**, 2357 (1985).
[16] C. PEREZ-GARCIA and D. JOU: *Phys. Lett. A*, **95**, 23 (1983).
[17] D. J. EVANS and B. L. HOLIAN: *J. Chem. Phys.*, **83**, 4069 (1985).
[18] B. L. HOLIAN and D. J. EVANS: *J. Chem. Phys.*, **78**, 5147 (1983).
[19] A. TENENBAUM, G. CICCOTTI and R. GALLICO: *Phys. Rev. A*, **25**, 2778 (1982).
[20] C. TROZZI and G. CICCOTTI: *Phys. Rev. A*, **29**, 916 (1984).

Part V

MOLECULAR SYSTEMS

The Method of Constraints in Molecular Dynamics. General Aspects and Application to Chain Molecules.

J. P. RYCKAERT

Université Libre de Bruxelles, Pool de Physique
CP 223 Campus Plaine, Boulevard du Triomphe, 1050 *Brussels, Belgium*

1. – Introduction.

Molecular-dynamics (M.D.) simulations at an atomistic level are performed nowadays on various systems ranging from a monoatomic fluid or solid to biological systems like membranes or proteins. Following a classical-mechanics description, atoms are modelled by point particles interacting according to a prescribed potential energy which is conveniently split into an intermolecular and an intramolecular part. The potential acting between molecules is most often taken to be a sum of pair interactions between centres of forces located at the nuclei positions. When an analytical intramolecular potential is adopted, it is usually written as a sum of individual contributions corresponding to the various bond, bending, torsional energies, with in addition pair interactions between nonbonded atoms.

However, a survey of the literature on M.D. simulations of polyatomic systems [1] reveals that, in a great number (a majority) of cases, the intramolecular structure is taken to be totally or partially rigid. Geometrical constraints are imposed to force some structural quantities like bond lengths, bending angles, ..., to remain constant during the dynamics. The essential motivation for imposing these constraints lies in the possibility to eliminate some fast vibrational modes which would, otherwise, affect the efficiency of the M.D. simulation by reducing considerably the numerical-integration time step. In the classical example of the diatomic molecule, the period of vibration is 10 to 100 times shorter than typical correlation times for translational or rotational velocities. In chain molecules like alkanes, intramolecular frequencies range from 300 to more than 3000 cm^{-1}. In sect. **2**, we discuss a full atomic model of paraffins which is partially rigid. We deliberately freeze all vibrations above 300 cm^{-1} and so leave explicit only the torsional and bending modes of the carbon skeleton. These internal motions are then treated as soft modes, together with the translational and rotational motions of the chain as a whole.

There are still additional comments to be made on the use of rigid constraints in M.D. « Hard » degrees of freedom, as they are usually rather well decoupled from the slow modes, are difficult to thermalize by standard M.D. Their freezing, therefore, reduces considerably the time needed for achieving an equilibrium situation. On the other hand, rigid models simplify the description of the intramolecular potential in the sense that they require less parameters. However, partially rigid models are sometimes criticized [2] for the unwanted effects of the imposition of geometrical constraints on the slow variable statistics and dynamics. The modification of the equilibrium distribution function of the internal angle of the flexible trimer when one goes from harmonic to rigid bonds is a typical example [2]. This fundamental problem must be appreciated in each case. In alkanes, it has been shown [3] that these effects are negligible on torsional-angle statistics provided the bending vibrations of the carbon skeleton are not frozen.

Now, once a (partially) rigid model is adopted, two different kinds of variables can be used to express the dynamical equations of motion of the system. A set of generalized co-ordinates may be defined and used with corresponding generalized velocities to write down the Lagrangian function of the whole system from which Lagrange equations (of the second kind) are derived by the standard procedure. For strictly rigid bodies, such a scheme is well known and, in principle, simple to apply. In practice, numerical difficulties are encountered with Euler angle variables specifying the orientation of the body, so that more complicated schemes are usually followed [4]. For partially rigid bodies, the derivation of the equation of motion in generalized co-ordinates becomes rapidly fastidious, if not unmanageable, as the number of intramolecular degrees of freedom increases.

The use of atomic Cartesian co-ordinates provides a simpler alternative in the present case where, anyway, the equations must be integrated numerically. The Cartesian equations of motion are Newton-like equations of motion in which the total force on an individual atom contains contributions from all constraints implying this particle. These forces of constraint, in turn, depend upon a set of Lagrange multipliers to be evaluated from the constraints themselves by an auxiliary calculation.

The method of constraints [5], based on this Cartesian co-ordinate approach, was originally developed in the case of partially rigid molecules with bond constraints to perform standard M.D. simulations at fixed energy, fixed volume and fixed number of molecules. The generalization of this method towards other forms of constraints [6, 7], or towards other statistical-mechanics ensemble M.D. [8, 9] is more recent.

In the present lecture, we briefly review the basic aspects of the method of constraints and give more emphasis to its latest developments. In sect. **2**, we discuss the imposition of rigid constraints in polyatomic molecules, first in the somewhat pedagogical cases of the flexible trimer and the rigid linear

triatomic, and then in chain molecules like n-alkanes. Section **3** is devoted to the derivation of the equations of motion and to some general aspects regarding the evaluation of Lagrange multipliers and the numerical integration of the Cartesian equations of motion. In sect. **4**, we outline a very general iterative technique to compute these Lagrange parameters and, at the same time, their effect on the particle trajectory. As an illustration for potential applications, we describe in the last section some technical aspects of a M.D. simulation of a crystal of paraffins, the aim of which is to analyse the nature of the so-called rotator phases observed experimentally between the crystalline and the liquid phases for these chain molecules.

2. – The imposition of geometrical constraints.

The most common form of geometrical constraint is the bond constraint where the distance between two atoms i and j, d_{ij}, is kept constant and equal to the experimental average bond length, *i.e.*

$$(\boldsymbol{r}_i - \boldsymbol{r}_j)^2 - d_{ij}^2 = 0 \,. \tag{1}$$

In the particular example of a semi-rigid model of water, the imposition of two bond constraints (1) freezes the O—H stretches. The intramolecular analytical potential is then only a function of the bending angle and should reproduce its experimental average value and the bending frequency. This model of water is rather academic as all stretch frequencies ($\simeq 3500\ \mathrm{cm}^{-1}$) are only twice as large than the bending one. For our purpose, this model is a convenient one as it corresponds to the simplest case of a partially rigid molecule for which the derivation of the Cartesian equations of motion is particularly simple to present explicitly (see the next section).

That bond constraints are not sufficient to ensure the rigidity of all molecules is best seen in the case of a linear triatomic molecule like CS_2. The number of degrees of freedom has to be reduced in this case from 9 to 5 by constraints, whilst the number of atomic pairs is only three. The rigidity is obtained by considering only one bond constraint (between the two sulphur atoms $S^{(1)}$ and $S^{(2)}$, say) and a vectorial linear constraint expressing that the third atom lies along the axis defined by the vector $\boldsymbol{r}_{S^{(2)}} - \boldsymbol{r}_{S^{(1)}}$, *i.e.*

$$\boldsymbol{r}_c = \boldsymbol{r}_{S^{(1)}} + \tfrac{1}{2}(\boldsymbol{r}_{S^{(2)}} - \boldsymbol{r}_{S^{(1)}}) \,. \tag{2}$$

Similar linear constraints can be considered for fully rigid planar molecules with more than 3 atoms or 3-dimensional bodies with more than 4 atoms. For

linear, planar or 3-dimensional molecules, we need to consider a set of respectively $n_b = 2, 3$ (noncollinear) or 4 (noncoplanar) atoms as basic and to connect them by $\frac{1}{2} n_b(n_b - 1)$ rigid bond constraints. Then, as in (2), we write quite generally for any additional atom $k > n_b$

$$\boldsymbol{r}_k = \boldsymbol{r}_1 + \sum_{i=2}^{n_b} a_{ik}(\boldsymbol{r}_i - \boldsymbol{r}_1) \tag{3}$$

using vectors $\boldsymbol{r}_i - \boldsymbol{r}_1$ as basic vectors of the 1-, 2- or 3-dimensional space, the coefficients a_{ik} being fixed by the molecular geometry. If we note that the forces of constraint are proportional to the gradient of the constraints with respect to the atomic co-ordinates (see the next section), it can be seen that, in the specific case of linear and planar molecules, the forces of constraint corresponding to (3) have components orthogonal to the molecular axis or plane and are, therefore, able to compensate any external force tending to break the linear or planar character of the body. As the forces of constraint associated to bond constraint act along the bonds, a bond constraint network cannot, therefore, be a good choice anyway for these special cases [6].

By going now to a partially rigid model of a n-alkane chain, we will now show that geometrical constraints are not limited to the above-mentioned usual ones but can still take other forms. The n-alkane molecular geometry is depicted in fig. 1 for the particular all-trans conformation in which all C atoms are lying in the plane chosen here to be the plane of the paper. Only 4 successive C atoms of the chain skeleton are represented together with the H atoms connected

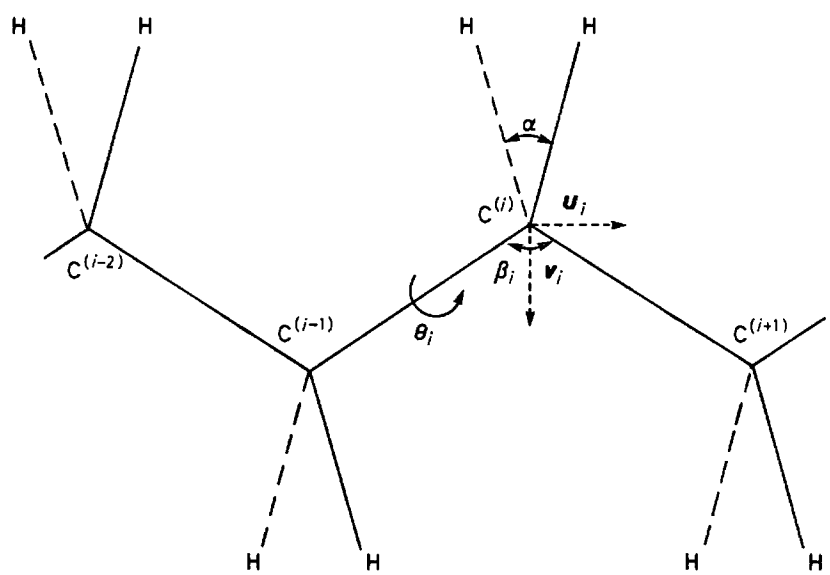

Fig. 1. – Schematic representation of a portion of n-alkane in an all-trans configuration. Carbon atoms are in the plane of the paper, whilst the hydrogens are shown in perspective to distinguish those lying above and below the plane. β_i and θ_i are bending and torsional angle variables.

to them by chemical bonds. α is the angle between the two C—H bonds relative to C^i while β_i is the bending angle between two adjacent C—C bonds. The backbone torsional angle θ_i is the dihedral angle between 2 successive planes defined by 3 adjacent C atoms. All n-alkane conformations correspond essentially to the various combinations obtained when θ_i takes the values 0 (local trans conformation), or $\pm 2\pi/3$ (local gauche conformations) corresponding to the staggered conformations of the substituents of adjacent C atoms.

Without entering here into details about potentials, we now discuss the imposition of rigid constraints in such chain molecules characterized by vibrational frequencies ranging from 300 cm^{-1} to more than 3000 cm^{-1}. Exploiting the gap in frequency between the C backbone bending and torsional vibrations ($\simeq$ 300 cm^{-1}) and all other vibrations around or above the C—C stretch ($\simeq$ 700 cm^{-1}), it is adequate to freeze all modes at $\simeq$ 700 cm^{-1} and above, in order to keep a reasonable time step to study conformational dynamics by M.D.

In the present case, we consider a full atomic chain model, where C and H atoms are all represented by point particles with associated centres of forces. More simple models using a single bead to represent a CH_2 or CH_3 unit were first employed in M.D., but here we are interested by a more realistic model required to study crystal phases of paraffins for which the « united atoms » model does not work [7]. In the bead model, all fast vibrations implying H atoms were automatically eliminated by construction.

If we first consider separately the carbon backbone, we need only to freeze the C—C stretch by bond constraints (1), as all its other degrees of freedom (bendings and torsions) will be left unconstrained, subject to an adequate intramolecular potential. Except for the methyl terminal groups, the presence of explicit H atoms will not ultimately introduce extra degrees of freedom as we decided to freeze all the corresponding vibrations. For a CH_2 group, it implies that 6 constraints have to be added to the model. This can be achieved by expressing the H atomic co-ordinates in terms of the C ones using the following symmetrical geometrical conditions. The $HC^{(i)}H$ triangle is rigid and the planes defined by the two triangles $HC^{(i)}H$ and $C^{(i-1)}C^{(i)}C^{(i+1)}$ are orthogonal to each other. Moreover, the bisectors of the angles α and β_i point along a common axis. Therefore, consider a local Cartesian reference frame with $C^{(i)}$ as origin and unit vectors $\boldsymbol{u}_i$, $\boldsymbol{v}_i$ and $\boldsymbol{w}_i$ defined by choosing $\boldsymbol{u}_i$ along $\boldsymbol{r}_{C^{(i+1)}} - \boldsymbol{r}_{C^{(i-1)}}$ and $\boldsymbol{v}_i$ along the bisector of the bending angle β_i (see fig. 1). If d_{CH} is the C—H bond length, the hydrogen co-ordinates given by

$$\boldsymbol{r}_H = \boldsymbol{r}_{C^{(i)}} - d_{CH} \cos\left(\frac{\alpha}{2}\right) \boldsymbol{v}_i \pm d_{CH} \sin\left(\frac{\alpha}{2}\right) \boldsymbol{w}_i \tag{4}$$

satisfy all mentioned geometrical requirements.

Expression (4) gives exactly 3 constraints per H atom. It is a nonlinear

function of the C co-ordinates which appear through the unit vectors $\boldsymbol{v}_i$ and $\boldsymbol{w}_i$ defined by

$$\boldsymbol{u}_i = (\boldsymbol{r}_{C^{(i+1)}} - \boldsymbol{r}_{C^{(i-1)}})/|\boldsymbol{r}_{C^{(i+1)}} - \boldsymbol{r}_{C^{(i-1)}}| ,$$

$$\boldsymbol{v}_i = (\boldsymbol{r}_{C^{(i+1)}} + \boldsymbol{r}_{C^{(i-1)}} - 2\boldsymbol{r}_{C^{(i)}})/|\boldsymbol{r}_{C^{(i+1)}} + \boldsymbol{r}_{C^{(i-1)}} - 2\boldsymbol{r}_{C^{(i)}}| ,$$

$$\boldsymbol{w}_i = \boldsymbol{u}_i \wedge \boldsymbol{v}_i .$$

Note that no alternative scheme based on 6 bond constraints is possible here given the flexibility of the C—C—C bending angles. Concerning the H atoms belonging to the terminal methyl groups, they define an additional torsional angle (left unconstrained) around the terminal C—C bonds. Therefore, we need to incorporate 8 constraints for each group of three H atoms. This can be achieved by bond constraints only. If $C^{(1)}$ and $C^{(2)}$ are the two first C atoms of the chain already connected by a bond constraint, it is sufficient to join by rigid bonds any set of 8 pairs among the H—H, $C^{(1)}$—H and $C^{(2)}$—H pairs implying the H atoms of the terminal methyl groups. The $C^{(1)}H_3$—$C^{(2)}$ body is rigid but rotates around the $C^{(1)}$—$C^{(2)}$ bond.

In this section, we have seen that the constraint relations can take various forms. Therefore the M.D. method in Cartesian co-ordinates for (partially), rigid molecules will be presented in the next section using a general formulation valid for arbitrary constraints.

3. – The equations of motion.

Formally, the equations of motion in Cartesian co-ordinates for a set of particles subject to holonomic constraints can be obtained from Hamilton's principle [10]. They are usually known as the Lagrange equations of the first kind. In the particular case of a polyatomic molecule of n atoms connected by l geometrical constraints that can be denoted formally as

$$\sigma_k(\boldsymbol{r}) = 0 , \qquad k = 1, l, \tag{5}$$

these equations have the general form

$$m_i \ddot{\boldsymbol{r}}_i = \boldsymbol{F}_i - \sum_{k=1}^{l} \lambda_k \frac{\partial \sigma_k}{\partial \boldsymbol{r}_i} , \qquad i = 1, n, \tag{6}$$

where F_i is the force acting on atom i deriving from the potential (both inter and intramolecular) and $\{\lambda_k\}_{k=1,l}$ is a set of l time-dependent Lagrange multipliers to be fixed by the constraint relations themselves.

The normal route to proceed would be to first take the second time derivative

of the constraint relations, *i.e.*

$$\ddot{\sigma}_k = \sum_{i=1}^{n} \sum_{\alpha=1}^{3} \left\{ \sum_{j=1}^{n} \sum_{\beta=1}^{3} \frac{\partial^2 \sigma_k}{\partial r_{i\alpha} \partial r_{j\beta}} \dot{r}_{i\alpha} \dot{r}_{j\beta} + \frac{\partial \sigma_k}{\partial r_{i\alpha}} \ddot{r}_{i\alpha} \right\} = 0 , \tag{7}$$

where α, β indices refer to the three Cartesian components. Substitution of (6) into (7) yields a set of l linear equations in λ_k the solution of which are reincorporated into (6). Explicit equations of motion for the n atoms

$$\ddot{\boldsymbol{r}}_i = \mathscr{F}_i(\{\boldsymbol{r}, \dot{\boldsymbol{r}}\}) \tag{8}$$

would be obtained and could then be integrated numerically to perform the M.D. simulation. Actually, we do not adopt such a route for the following reasons. Equations (6) are not independent. Their exact solution, starting from an initial configuration satisfying the constraints, will by construction still satisfy the constraints at later times $0 < t < \infty$. However, the solution obtained by numerical integration will satisfy the constraints only approximately because of algorithm and round-off errors. What could be anticipated and has been observed in preliminary calculations is that constraint relations deviate from 0 in a diverging way at a rate depending of the time step.

Therefore, to integrate eq. (6) numerically, the λ_k are no longer evaluated « exactly » but are treated as parameters γ_k determined by the requirement that the numerical trajectory satisfies the constraint at each time step. This technique depends on the specific algorithm used. We now take the particular case of the Verlet algorithm [11] as it is at the same time very simple to be combined with the present method and also very efficient for practical applications.

Using eq. (6), the Verlet algorithm evaluates the positions at the next time step according to

$$\boldsymbol{r}_i(t + \Delta t) = -\boldsymbol{r}_i(t - \Delta t) + 2\boldsymbol{r}_i(t) + \frac{\boldsymbol{F}_i(t)}{m_i} \Delta t^2 - \sum_{k=1}^{l} \frac{\gamma_k}{m_i} \left(\frac{\partial \sigma_k}{\partial \boldsymbol{r}_i} \right)_{r(t)} \Delta t^2 , \tag{9}$$

where $\{\gamma_k\}$ are determined by substituting (9) into the constraints (5). Formally this yields a set of l algebraic equations with l unknowns $\{\gamma_k\}$ that we write

$$T_k(\{\gamma_{k'}\}_{k'=1,l}) = 0 . \qquad k = 1, l. \tag{10}$$

Solving for $\{\gamma_k\}$, we get an estimate of $\{\lambda_k\}$ which does not affect the order of error of the Cartesian trajectory. (For an « exact » algorithm γ_k and λ_k would be strictly equal, whilst, in the present case, the deviation is of order Δt^4 on σ_k, so that $\gamma_k = \lambda_k + O(\Delta t^2)$.)

In practice the set of equations (10) is not linear, so that iterative techniques

must be used. Such a method, very general and simple to implement, is developed in the next section.

We now derive eqs. (9) and (10) explicitly in the particular case of the semirigid triatomic model of water mentioned in sect. **2**.

The constraints σ_1 and σ_2 between hydrogen $H^{(1)}$ and $H^{(2)}$ and oxygen coordinates are

$$\sigma_i \equiv (\boldsymbol{r}_{H^{(i)}} - \boldsymbol{r}_O)^2 - d_{OH}^2 = 0 \qquad (i = 1, 2). \tag{11}$$

The resulting eqs. (9) are simply

$$\begin{cases} m_H \ddot{\boldsymbol{r}}_{H^{(1)}} = \boldsymbol{F}_{H^{(1)}} - 2\lambda_1(\boldsymbol{r}_{H^{(1)}} - \boldsymbol{r}_O)\,, \\ m_H \ddot{\boldsymbol{r}}_{H^{(2)}} = \boldsymbol{F}_{H^{(2)}} - 2\lambda_2(\boldsymbol{r}_{H^{(2)}} - \boldsymbol{r}_O)\,, \\ m_O \ddot{\boldsymbol{r}}_O = \boldsymbol{F}_O + 2\lambda_1(\boldsymbol{r}_{H^{(1)}} - \boldsymbol{r}_O) + 2\lambda_2(\boldsymbol{r}_{H^{(2)}} - \boldsymbol{r}_O)\,. \end{cases} \tag{12}$$

Simplifying the notation

$$\boldsymbol{r}'(t + \Delta t) = -\boldsymbol{r}(t - \Delta t) + 2\boldsymbol{r}(t) + \frac{\boldsymbol{F}(t)}{m}\Delta t^2\,, \tag{13}$$

the positions at the next step become with Verlet algorithm

$$\begin{cases} \boldsymbol{r}_{H^{(1)}}(t + \Delta t) = \boldsymbol{r}'_{H^{(1)}}(t + \Delta t) - 2\,\dfrac{\gamma_1}{m_H}\big(\boldsymbol{r}_{H^{(1)}}(t) - \boldsymbol{r}_O(t)\big)\Delta t^2\,, \\ \boldsymbol{r}_{H^{(2)}}(t + \Delta t) = \boldsymbol{r}'_{H^{(2)}}(t + \Delta t) - 2\,\dfrac{\gamma_2}{m_H}\big(\boldsymbol{r}_{H^{(2)}}(t) - \boldsymbol{r}_O(t)\big)\Delta t^2\,, \\ \boldsymbol{r}_O(t + \Delta t) = \boldsymbol{r}'_O(t + \Delta t) + \\ \qquad\qquad + 2\left\{\dfrac{\gamma_1}{m_O}\big(\boldsymbol{r}_{H^{(1)}}(t) - \boldsymbol{r}_O(t)\big) + \dfrac{\gamma_2}{m_O}\big(\boldsymbol{r}_{H^{(2)}}(t) - \boldsymbol{r}_O(t)\big)\right\}\Delta t^2\,. \end{cases} \tag{14}$$

Substitution of (14) into (9) leads to two quadratic equation in γ which can be written in a matricial form as

$$\boldsymbol{A}\begin{pmatrix}\gamma_1\\ \gamma_2\end{pmatrix} = \Delta t^{-2}\boldsymbol{B}(\gamma)\,, \tag{15}$$

(16) $\boldsymbol{A} =$

$$= \left[\begin{array}{c:c} -4(m_H^{-1} + m_O^{-1})(\boldsymbol{r}'_{H^{(1)}} - \boldsymbol{r}'_O)(\boldsymbol{r}_{H^{(1)}} - \boldsymbol{r}_O) & -4m_O^{-1}(\boldsymbol{r}'_{H^{(1)}} - \boldsymbol{r}'_O)(\boldsymbol{r}_{H^{(2)}} - \boldsymbol{r}_O) \\ \hdashline -4m_O^{-1}(\boldsymbol{r}'_{H^{(2)}} - \boldsymbol{r}'_O)(\boldsymbol{r}_{H^{(1)}} - \boldsymbol{r}_O) & -4(m_H^{-1} + m_O^{-1})(\boldsymbol{r}'_{H^{(2)}} - \boldsymbol{r}'_O)(\boldsymbol{r}_{H^{(2)}} - \boldsymbol{r}_O) \end{array}\right],$$

$$\boldsymbol{B} = \begin{bmatrix} d_{OH}^2 - (\boldsymbol{r}^1_{H^{(1)}} - \boldsymbol{r}'_O)^2 - (\boldsymbol{r}''_{H^{(1)}} - \boldsymbol{r}''_O)^2 \\ d_{OH}^2 - (\boldsymbol{r}'_{H^{(2)}} - \boldsymbol{r}'_O)^2 - (\boldsymbol{r}''_{H^{(2)}} - \boldsymbol{r}''_O)^2 \end{bmatrix}. \tag{17}$$

In $\boldsymbol{A}$, $\boldsymbol{r}$ and $\boldsymbol{r}'$ are short symbols for $\boldsymbol{r}(t)$ and $\boldsymbol{r}'(t+\Delta t)$, respectively. $\boldsymbol{r}''$, in $\boldsymbol{B}$, denotes the total constraint force contribution to the displacement, made explicit in the r.h.s. of (14). Equation (15) can be solved iteratively starting with $\gamma_1^{(0)} = \gamma_2^{(0)} = 0$, according to the formula

$$\begin{pmatrix} \gamma_1^{(n)} \\ \gamma_2^{(n)} \end{pmatrix} = \Delta t^{-2}\, \boldsymbol{A}^{-1} \boldsymbol{B}(\gamma^{(n-1)})\,. \tag{18}$$

Such a procedure was found to converge rapidly for partially rigid chains [5].

4. – An iterative method treating individual constraints in succession.

In sect. 3, the basic formulae to perform a M.D. step were given for a molecule of n atoms subjet to l constraints of arbitrary functional form. In practice, the explicit substitution of (9) into the constraint relations and the resolution of the resulting eqs. (10) may become rapidly tedious as the number of constraints increases or as their dependence on the Cartesian co-ordinates gets more complicated like in example (4).

It is possible to follow a much simpler alternative method in which constraints are always treated individually in a sequential order from the first to the last with an iterative loop over the whole sequence. In the original paper about the method of constraints [5], such a method called SHAKE was proposed in the particular case of a set of bond constraints only. We now indicate how this method works for arbitrary constraints [7].

Let us focus on a given constraint k and the N-th iteration loop over the whole sequence $k' = 1, l$ of constraints $\sigma_{k'} = 0$. We denote by $\{\{\boldsymbol{r}_i^{\text{old}}\}\}$ the subset of atomic positions involved in σ_k at this stage of the iterative process. We determine the new positions of these atoms $\{\{\boldsymbol{r}_j^{\text{new}}\}\}$ using the formula

$$\boldsymbol{r}_j^{\text{new}} = \boldsymbol{r}_j^{\text{old}} - \Delta t^2 \frac{\mathscr{E}_k^N}{m_j} \left(\frac{\partial \sigma_k}{\partial \boldsymbol{r}_j}\right)_{\boldsymbol{r}(t)}, \tag{19}$$

where $\mathscr{E}_k^N$ is evaluated as the first-order solution of the equation obtained in substituting (19) in the constraint relation $\sigma_k = 0$ itself.

We have

$$0 = \sigma_k(\{\{\boldsymbol{r}^{\text{new}}\}\}) = \sigma_k(\{\{\boldsymbol{r}^{\text{old}}\}\}) + \left(\frac{\partial \sigma_k}{\partial \mathscr{E}_k^N}\right)_{\mathscr{E}_k^N=0} \mathscr{E}_k^N + O(\Delta t^4 \mathscr{E}_k^{N^2}) \simeq \sigma_k(\{\{\boldsymbol{r}^{\text{old}}\}\}) +$$

$$+ \mathscr{E}_k^N \sum_j \left(\frac{\partial \sigma_k}{\partial \boldsymbol{r}_j}\right)_{\boldsymbol{r}^{\text{old}}} \left(\frac{\partial \boldsymbol{r}_j^{\text{new}}}{\partial \mathscr{E}_k^N}\right) \simeq \sigma_k(\{\{\boldsymbol{r}^{\text{old}}\}\}) - \Delta t^2 \mathscr{E}_k^N \sum_j m_j^{-1} \left(\frac{\partial \sigma_k}{\partial \boldsymbol{r}_j}\right)_{\boldsymbol{r}^{\text{old}}} \left(\frac{\partial \sigma_k}{\partial \boldsymbol{r}_j}\right)_{\boldsymbol{r}(t)},$$

so, to first order, we get

$$\mathscr{E}_k^N = \Delta t^{-2} \frac{\sigma_k(\{\{\boldsymbol{r}^{\text{old}}\}\})}{\sum_j m_j^{-1} [(\partial \sigma_k/\partial \boldsymbol{r}_j)_{\boldsymbol{r}^{\text{old}}} (\partial \sigma_k/\partial \boldsymbol{r}_j)_{\boldsymbol{r}(t)}]}, \tag{20}$$

in which the sum in the denominator runs only over atoms involved in σ_k.

The iterative procedure proceeds as follows. Let us identify, at the beginning, $\{\boldsymbol{r}^{\text{old}}\}$ with the « unconstrained » positions $\boldsymbol{r}'(t+\Delta t)$ (13). One starts the first loop using sequentially (20) and (19) for all constraints producing at each step refined co-ordinates $\{\{\boldsymbol{r}^{\text{new}}\}\}$ to be substituted to the set $\{\{\boldsymbol{r}^{\text{old}}\}\}$. The same process is repeated for the next loops. In this way, the co-ordinates of all atoms $i=1, n$, after completion of the treatment of the k-th constraint at the N-th loop, are given by

$$\boldsymbol{r}_i^{\text{new}} = \boldsymbol{r}'(t+\Delta t) - \frac{\Delta t^2}{m_i} \sum_{k'=1}^{l} \gamma_{k'}^{(kN)} \left(\frac{\partial \sigma_{k'}}{\partial \boldsymbol{r}_i}\right)_{\boldsymbol{r}(t)}$$

with

$$\gamma_{k'}^{(kN)} = \sum_{N'=1}^{N} \mathscr{E}_{k'}^{N'}, \qquad k' \leqslant k,$$

$$\gamma_{k'}^{(kN)} = \sum_{N'=1}^{N-1} \mathscr{E}_{k'}^{N'}, \qquad k' > k.$$

The convergence of the iterative process is controlled by X_N, the maximum deviation of $|\sigma_k(\{\{\boldsymbol{r}_j^{\text{old}}\}\})|$ from 0 for all constraints $k=1, l$ within the N-th cycle. If X_N gets smaller than some tolerance value at cycle M, the final positions

$$\boldsymbol{r}_i^{\text{new}} = \boldsymbol{r}_i'(t+\Delta t) - \frac{\Delta t^2}{m_i} \sum_{k=1}^{l} \gamma_k^{(lM)} \left(\frac{\partial \sigma_k}{\partial \boldsymbol{r}_i}\right)_{\boldsymbol{r}(t)} \tag{21}$$

are accepted as the new configuration $\{\boldsymbol{r}_i(t+\Delta t)\}$. The choice of $\{\boldsymbol{r}_i'(t+\Delta t)\}$ to start the iterative procedure should guarantee that the numerical process converges to the physical solution among the different solutions of the set of nonlinear algebraic equations (10).

This method is very easy to program as it is based on the two formulae (19) and (20) only, to be applied to all constraints in succession. In practice the method has proved to work very satisfactorily even for very complex networks of bond constraints like in small proteins [12]. The same is true for more complex constraint schemes, as will be illustrated in the next section.

5. – Application to a crystal of partially rigid paraffins.

In order to illustrate the contents of this lecture and the wide flexibility of the method of constraints, we now briefly report some aspects of a molecular-dynamics experiment on a crystal of paraffins, a work presently in progress. The aim of this work, done in collaboration with Dr. M. KLEIN, is to better understand the nature and the dynamics of so-called « rotator » phases observed in n-alkanes (with 9 to $\simeq 40$ C per chain) between the crystalline and

the liquid phases [13]. In solid phases, both crystalline and rotator, the chains are essentially in an all-trans (elongated) configuration with their long axes parallel to each other. In the rotator phases, observed around 300 K, the chains have much more internal flexibility, as is suggested by the experimental observation of « defects » corresponding to intramolecular conformational trans → → gauche modifications. This situation suggested us to adopt the « realistic » partially flexible model of n-alkane developed in sect. **2** [7].

The preliminary model considered so far is an infinite-chain model in which each chain is modelled by a 16 CH_2 unit portion repeated periodically along the longitudinal axis of the chain. A set of 30 chains are disposed perpendicularly to the XY basal plane in agreement with the subcell structure of polyethylene and odd-numbered C chains at low temperature. All chains are free to translate in the three directions of space but rotate only around their longitudinal (z) axis, while the length of the portion of 16 units is fixed by the periodic conditions in the z direction. In this system, each chain consists of 48 atoms (16 C and 32 H). Out of the corresponding 144 degrees of freedom per chain, 112 are frozen by constraints, *i.e.* 16 C—C bond constraints (1) and 6 constraints equivalent to the vectorial constraints (4) per CH_2 unit [7]. The intermolecular potential is a sum of atom-atom interactions (Williams potential [14]) and the intramolecular part contains harmonic C—C—C bendings and C—C—C—C torsional potential with 3 minima corresponding to the trans and the two gauche local conformations. The time step is $3.3 \cdot 10^{-15}$ s, which gives total-energy fluctuations less than 1 percent of the kinetic-energy fluctuations. The constraint part was solved using the method of sect. **4** with a tolerance value of $5 \cdot 10^{-7}$ on the constraint satisfaction, a value which gives the order of the absolute discrepancy in Å of the atomic Cartesian co-ordinates with respect to those obtained with the Lagrange parameters, solution of eq. (10). On average, at 300 K, 25 iterations over the whole sequence of 112 constraints are necessary to be within the tolerance. The CPU time required by the constraints amounts 25 % of the total time step.

It is then clear that, as far as the computer time per step is concerned, M.D. simulations with vibrations frozen by constraints, or with explicit vibrations will never differ appreciably. The gain on the time step size is thus a real gain in efficiency.

REFERENCES

[1] D. Levesque, J. J. Weis and J. P. Hansen: *Top. Curr. Phys.*, **36**, 37 (1984) (see table 2.1).
[2] N. G. Van Kampen and J. J. Lodder: *Am. J. Phys.*, **52**, 419 (1984).
[3] W. F. Van Gunsteren: *Mol. Phys.*, **40**, 1015 (1980).
[4] D. J. Evans: *Mol. Phys.*, **34**, 317 (1977).

[5] J. P. RYCKAERT, G. CICCOTTI and H. J. C. BERENDSEN: *J. Comput. Phys.*, **23**, 327 (1977).
[6] G. CICCOTTI, M. FERRARIO and J. P. RYCKAERT: *Mol. Phys.*, **47**, 1253 (1982),
[7] J. P. RYCKAERT: *Mol. Phys.*, **55**, 549 (1985).
[8] J. P. RYCKAERT and G. CICCOTTI: *J. Chem. Phys.*, **78**, 7368 (1983).
[9] M. FERRARIO and J. P. RYCKAERT: *Mol. Phys.*, **54**, 587 (1985).
[10] T. C. BRADBURY: *Theoretical Mechanics* (Wiley, New York, N. Y., 1968), p. 499.
[11] L. VERLET: *Phys. Rev.*, **159**, 98 (1967).
[12] W. F. VAN GUNSTEREN and H. J. C. BERENDSEN: *Mol. Phys.*, **34**, 1311 (1977).
[13] R. G. SNYDER, M. MARONCELLI and S. P. QI: *Science*, **214**, 188 (1981).
[14] D. E. WILLIAMS: *J. Chem. Phys.*, **47**, 4680 (1967).

Molecular Liquids: Orientational Order and Dielectric Properties.

I. R. McDonald

Department of Physical Chemistry, University of Cambridge - Cambridge, U.K.

1. – Introduction.

It is clearly hopeless to attempt in three lectures to cover the full range of problems encountered in the simulation of molecular fluids. I am, therefore, going to limit myself largely to just two topics: the characterization of the order found in molecular liquids, particularly of the angular correlations; and the calculation and interpretation of dielectric properties. These topics are, in fact, closely related, since the dielectric behaviour of polar liquids is linked to the existence in the fluid of a degree of orientational order of a particular type. I want to begin, however, by saying a little about the history of simulation of molecular systems and follow that with some brief remarks about the models and algorithms used in the calculations.

1·1. *A little history.* – Everybody here will know that computer simulation is now a widely used technique for the study of molecular liquids (and solids also), and the number of papers on the subject increases rapidly each year. In speaking of « computer simulation » I do not find it helpful to make too sharp a division between molecular-dynamics and Monte Carlo calculations. For example, our understanding of how to treat the dielectric problem correctly has developed in large part as a result of Monte Carlo work. However, just to keep the material within bounds, I shall mention only the key early papers based on the molecular-dynamics method.

The distinction of publishing the first article in which molecular dynamics was used for a molecular rather than an atomic system belongs to Harp and Berne [1], whose paper entitled « Time-correlation functions, memory functions and molecular dynamics » appeared in *The Physical Review* in September, 1970. (A review article covering similar ground was published in *Advances in Chemical Physics* in the same year [2].) It, therefore, required about fifteen years from the publication of the pioneering work of Alder and Wainwright [3]

before molecular dynamics became truly « molecular », though, of course, there had been much important work carried out on atomic fluids in the interim. HARP and BERNE used a Stockmayer potential (and a modified form thereof), with parameters roughly appropriate to carbon monoxide. In the event, they did not claim any great realism for their models, and made little effort to compare their results with experiment. Their interest lay instead in discussing the nature of the rotational and translational motion in a simple molecular fluid from a general theoretical point of view. Their paper, therefore, fell firmly into the pattern of most earlier work on atomic systems, namely that of careful studies of phenomena which should be common to all liquids of a certain class rather than of attempts to model any specific liquid. Of course, the paper was only a first step in this direction, and many important questions remained unanswered and even unasked. In retrospect, it is surprising that nobody felt inclined to pursue this type of program in a systematic way. For example, it was not until ten years later that a complete study of the dielectric properties of the Stockmayer fluid was published [4]. Instead, matters took a very different turn, because the next paper to appear was the famous article on the simulation of water published by RAHMAN and STILLINGER in 1971 [5]. The philosophy behind this work was not at all the same as that of Harp and Berne. Instead of using a simple model to study general problems, RAHMAN and STILLINGER took a rather complicated model in an effort to mimic and ultimately to understand the behaviour of a particular substance, and moreover a substance whose properties are in many respects anomalous. Their goal was to some extent achieved, particularly insofar as structural properties were concerned. The Rahman-Stillinger paper made a very large impact. It is important historically not only for what it contained (which was a great deal) but for the new audience it attracted. Physical chemists, biologists, materials scientists and others were able to see that molecular dynamics was potentially a very powerful tool for unravelling the microscopic behaviour of complex liquids and solids that exist in nature. In the summer of 1972, there was a two-month workshop held at CECAM, in Orsay, near Paris, organized by Herman BERENDSEN [6] and essentially built around the paper of Rahman and Stillinger. The workshop was very influential in promoting activity of a similar type in Europe. RAHMAN and STILLINGER themselves continued with a series of papers devoted to other models and other properties of water [7].

Following closely on the work of Rahman and Stillinger came a number of studies of liquid nitrogen. Water, of course, is one of the most complicated of liquids. Liquid nitrogen, by comparison, is a very simple substance; the nitrogen molecule has no dipole moment and only a modest quadrupole moment, its length-to-breadth ratio is smaller than that of other homonuclear diatomics such as the halogens, etc. The first molecular-dynamics study of liquid nitrogen was published by the Orsay group—BAROJAS, LEVESQUE and QUENTREC—in 1973 [8]. Two years later, a much more detailed paper was

published by CHEUNG and POWLES [9]. The latter contained by far the most complete comparison between simulation and experiment that had been attempted up until that time. Indeed, there are not many later papers that excel it in that respect. Finally, in the same year as the paper of Cheung and Powles, the first account appeared of the simulation of a fluid of flexible molecules; this was the work of Ryckaert and Bellemans [10] on liquid butane.

All the papers listed above were published in the period up to 1975. Although they are few in number, they are concerned with a wide range of topics and contain the groundwork for much of the later development of the subject.

1·2. *Models.* – All the work that I am going to describe is based on two classes of intermolecular-potential models. The first consists of the frankly simplistic, in particular of dipolar hard spheres and Stockmayer particles, for which the potential between polar molecules 1 and 2 is given by

$$v(1,2) = v_0(R) - \frac{\mu^2}{R^3} D(1,2)\,, \tag{1.1}$$

where $v_0(R)$ is a spherically symmetric interaction (hard sphere or Lennard-Jones), $R \equiv |\boldsymbol{R}_{12}| = |\boldsymbol{R}_2 - \boldsymbol{R}_1|$, μ is the dipole moment and the term in $D(1,2)$ is the ideal dipole-dipole term. The angular dependence of the interaction is, therefore, wholly contained in the function $D(1,2)$, given by

$$D(1,2) = 3(\boldsymbol{u}_1\cdot\boldsymbol{s})(\boldsymbol{u}_2\cdot\boldsymbol{s}) - \boldsymbol{u}_1\cdot\boldsymbol{u}_2\,, \tag{1.2}$$

where $\boldsymbol{u}_i$ is a unit vector parallel to the dipole moment of molecule i and $\boldsymbol{s}$ is a unit vector parallel to $\boldsymbol{R}_{12}$. Potentials of the form of (1.1) provide the simplest possible model of a polar fluid, but not one that is adequate to describe any real, strongly polar liquid. In particular, they lead to dielectric constants that are unrealistically high. For example, if we were to represent the acetonitrile molecule as a dipolar hard sphere, the dielectric constant at room temperature would be roughly 200, very much larger than the experimental value ($\varepsilon = 36$).

The inadequacies of the dipolar hard-sphere and Stockmayer potentials are linked to their neglect of molecular « shape » and possibly also of higher-order electrostatic moments. Both deficiencies may in some measure be remedied by the use of *interaction site models*. In the interaction site approach, a molecule is conceived as consisting of a number of interaction sites that are commonly but not necessarily coincident with the positions of the atoms. The total intermolecular potential energy is then obtained as the sum of site-site potentials, usually assumed to be spherically symmetric, *i.e.*

$$v(1,2) = \sum_\alpha \sum_\beta v_{\alpha\beta}(|\boldsymbol{r}_{1\alpha} - \boldsymbol{r}_{2\beta}|)\,, \tag{1.3}$$

where $\boldsymbol{r}_{1\alpha}$, $\boldsymbol{r}_{2\beta}$ are the co-ordinates, respectively, of site α on molecule 1 and site β on molecule 2, and the sum runs over all sites on each molecule. The site-site potential is frequently written as the sum of a short-range (SR) part, typically hard sphere, Lennard-Jones or exp-6 in form, and a Coulomb interaction between point charges q_α and q_β:

$$v_{\alpha\beta}(r) = v_{\alpha\beta}^{\mathrm{SR}}(r) + \frac{q_\alpha q_\beta}{r}. \tag{1.4}$$

A large number of molecular fluids have been successfully modelled in this way.

Since the principles underlying the choice of potential model will be familiar to everyone here, I shall make only two general comments. Firstly, in most simulations, the molecules are treated as rigid, and polarization and other many-body effects are ignored. Both restrictions can be lifted, but only at considerable cost, not least in computing time. Secondly, interaction site models may be made substantially more realistic by allowing for an angle dependence of the site-site potentials. Elaborations of this type could rather easily be incorporated into a Monte Carlo program.

1·3. *Algorithms.* – The conventional approach to the solution of the equations of motion of a rigid body involves a separation of internal and centre-of-mass co-ordinates; the former may then be expressed in terms of Euler angles (or polar angles, if the molecule is linear). In its simplest form, this method is useless for molecular-dynamics calculations because the equations that describe the time evolution of the angular variables have a singularity at $\theta = 0$ or π, where θ, for a linear molecule, would be the usual polar angle. Any attempt to solve the equations of motion numerically, therefore, runs into difficulty whenever θ_i (for any molecule) approaches within a few degrees of either $\theta_i = 0$ or $\theta_i = \pi$. The problem can be circumvented in rather neat fashion by referring the orientation of each molecule to its own set of axes and redefining the z-direction whenever a singularity threatens. It is sufficient to rotate the axes in such a way, say, that the z-axis becomes what previously was the x-axis. This is the method used by RAHMAN and STILLINGER [5] and also by the Orsay group in the original work on nitrogen [8] and, more recently, on hydrogen chloride [11].

Several alternative methods have been devised in which the singularity is avoided from the outset. CHEUNG and POWLES [9] and SINGER, TAYLOR and SINGER [12] have developed singularity-free algorithms that are specific to linear molecules, while EVANS and MURAD [13] have described a general method based a rewriting of the Eulerian equations in terms of quaternions. There is, in addition, a completely different approach, namely the method of « constraint dynamics » due to RYCKAERT, CICCOTTI and BERENDSEN [14],

VAN GUNSTEREN and BERENDSEN [15] and CICCOTTI, FERRARIO and RYCKAERT [16]. This method is very simple in conception and is also very easy to program, at least for small molecules. The atoms of the molecule are assumed to be held together by infinitely stiff springs and the integration of the equations of motion takes place in two stages. In the first stage, the atoms move solely under the influence of the external (intermolecular) forces, no account being taken of the intramolecular springs. In the second stage, the co-ordinates of the atoms are reset in such a way as to satisfy the assumed bond length (or bond angle) constraints. Since the resetting is a consequence solely of the intramolecular forces, the centre-of-mass co-ordinates remain unaltered in the second stage. The latest version of the method can be used for any type of molecule and remains efficient even when the number of constraints is very large [16]. The atoms of a molecule are divided into two sets: « basic » particles and « secondary » particles. The number of basic particles is the number required to specify the orientation of the molecule—two if the molecule is linear, three if it is planar, and four if it is nonplanar. It is only the motion of the basic particles that needs to be followed, the positions of the remainder being determined by the geometry of the molecule. RYCKAERT (this volume, p. 329) will give a more detailed account in his seminar.

It is a curious fact that, despite the huge expenditure on computer time that molecular-dynamics calculations entail, the amount of published information on the efficiency of different algorithms is very small. As far as one can judge, however, the Eulerian-angle, quaternion and constraint methods are of comparable efficiency in terms of the total computing time required to do a specific task. There are some harsh things said in the literature about the supposed inefficiency of the original, Eulerian-angle method, but I am not aware of any firm evidence to support these claims. The special feature of constraint dynamics that gives it an advantage over other methods is that it is as easy to apply to flexible as to rigid molecules.

2. – Structure and orientational order.

2·1. *The molecular-pair distribution function.* – The most important quality in the equilibrium statistical mechanics of molecular liquids is the *molecular-pair distribution function*, which we shall write as $g(1, 2)$. For the sake of notational simplicity, we use the symbol i to denote both the translational and orientational co-ordinates of molecule i (assumed to be rigid). Thus $i \equiv (\boldsymbol{R}_i, \boldsymbol{\Omega}_i)$, where $\boldsymbol{\Omega}_i \equiv (\theta_i, \varphi_i)$ (the polar angles) if the molecule is linear and $\boldsymbol{\Omega}_i \equiv (\theta_i, \varphi_i, \chi_i)$ (the Euler angles) if it is nonlinear. In either case, the orientation is defined relative to a laboratory-fixed frame of reference.

The pair distribution function may usefully be written as the ensemble

average of a product of delta-functions. We first define a *pair density* as

$$(2.1)\qquad \varrho^{(2)}(\boldsymbol{R}, \boldsymbol{\Omega}; \boldsymbol{R}', \boldsymbol{\Omega}') = \Big\langle \sum_{i \neq j}^{N}\sum \delta(\boldsymbol{R}_i - \boldsymbol{R})\, \delta(\boldsymbol{R}_j - \boldsymbol{R}')\, \delta(\boldsymbol{\Omega}_i - \boldsymbol{\Omega})\, \delta(\boldsymbol{\Omega}_j - \boldsymbol{\Omega}') \Big\rangle .$$

The pair density gives the probability of finding a molecule at $\boldsymbol{R}'$ with orientation $\boldsymbol{\Omega}'$ given that there is a molecule at $\boldsymbol{R}$ with orientation $\boldsymbol{\Omega}$, where $\boldsymbol{R}$, $\boldsymbol{R}'$ denote the co-ordinates of arbitrarily chosen molecular « centres ». In a homogeneous fluid, the pair density is a function only of $\boldsymbol{R} - \boldsymbol{R}'$, $\boldsymbol{\Omega}$ and $\boldsymbol{\Omega}'$, and the pair distribution is defined as

$$(2.2)\qquad g(1, 2) = (\Omega/\varrho)^2\, \varrho^{(2)}(\boldsymbol{R}_{12}, \boldsymbol{\Omega}_1, \boldsymbol{\Omega}_2) ,$$

where ϱ is the molecular number density, $\Omega \equiv \int \mathrm{d}\boldsymbol{\Omega}_i = 4\pi$ (linear) or $8\pi^2$ (nonlinear).

The analogue of $g(1, 2)$ in the atomic case is the radial distribution function $g(r)$, but $g(1, 2)$ is a much more complicated object because of the dependence on orientations. Unlike $g(r)$, $g(1, 2)$ is impossible (for most of us) even to visualize. The importance of $g(1, 2)$ stems from the fact that it contains all the information about the pair structure of the fluid, and thermodynamic properties such as internal energy and pressure can, therefore, be written as integrals over $g(1, 2)$ by a generalization of results well known in the theory of atomic liquids (assuming that the forces are pairwise additive). The problem is that $g(1, 2)$ contains too much information; if we wish to discuss the structure of a molecular fluid intelligently, some of the unwanted information must be removed. Two possibilities suggest themselves: a harmonic decomposition of $g(1, 2)$ or an analysis in terms of site-site distribution functions. We shall discuss each of these in turn, but, before doing so, we make note of two useful results.

First, if we integrate $g(1, 2)$ over all angles, we obtain a function $g_c(R)$ say, which describes the radial distribution of molecular centres:

$$(2.3)\qquad g_c(R) = (1/\Omega^2) \iint g(\boldsymbol{R}_{12}, \boldsymbol{\Omega}_1, \boldsymbol{\Omega}_2)\, \mathrm{d}\boldsymbol{\Omega}_1\, \mathrm{d}\boldsymbol{\Omega}_2 = \langle g(1, 2) \rangle_{\boldsymbol{\Omega}_1 \boldsymbol{\Omega}_2} ,$$

where the angular brackets with subscripts denote an unweighted average over the subscript angles. There is often an obvious choice of molecular centre, such as the midpoint of the internuclear bond in a homonuclear molecule. Depending on the choice of centre, $g_c(R)$ may or may not be measurable experimentally (in the example just given, it would not), but it is easily calculable by simulation and often resembles the radial distribution function of an atomic liquid.

The second result of interest is relevant to molecules having an axis of symmetry (linear molecules, for example, or spherical tops). Let $\boldsymbol{u}_i$ be a unit

vector along the symmetry axis of molecule i. Then we define a set of angular correlation parameters $G_l(R)$ ($l = 1, 2, \ldots$) by multiplying $g(1, 2)$ by a Legendre polynomial $P_l(\boldsymbol{u}_1 \cdot \boldsymbol{u}_2)$ and then integrating over all co-ordinates:

$$(2.4) \qquad G_l = \varrho \int g(\boldsymbol{R}_{12}, \boldsymbol{\Omega}_1, \boldsymbol{\Omega}_2)\, P_l(\boldsymbol{u}_1 \cdot \boldsymbol{u}_2)\, \mathrm{d}\boldsymbol{R}_{12}\, \mathrm{d}\boldsymbol{\Omega}_1\, \mathrm{d}\boldsymbol{\Omega}_2 = \\ = \varrho \int \langle g(1, 2)\, P_l(\boldsymbol{u}_1 \cdot \boldsymbol{u}_2) \rangle_{\boldsymbol{\Omega}_1 \boldsymbol{\Omega}_2}\, \mathrm{d}\boldsymbol{R}_{12} = \langle (N-1)\, P_l(\boldsymbol{u}_1 \cdot \boldsymbol{u}_2) \rangle .$$

The value of the first-rank order parameter G_1 of a polar fluid is related to its dielectric constant, while G_2 enters the theoretical expressions for a number of observable properties including, in particular, the integrated intensity of depolarized scattered light [17]. Both G_1 and G_2 are, therefore, measurable experimentally, but only with difficulty (especially G_2), and can also be calculated in simulations, but again only with difficulty, as we shall see below.

2·2. *Expansions of* $g(1, 2)$. – In order to simplify matters, we restrict discussion in this section to the case of linear molecules, for which the natural expansion functions are the normalized spherical harmonics $Y_{lm}(\theta, \varphi)$. We choose a system of polar co-ordinates with the z-axis lying along the vector $\boldsymbol{R}_{12}$ and expand $g(1, 2)$ as

$$(2.5) \qquad g(1, 2) = 4\pi \sum_{l_1 l_2 m} g_{l_1 l_2 m}(R)\, Y_{l_1 m}(\boldsymbol{\Omega}_1)\, Y_{l_2 \bar{m}}(\boldsymbol{\Omega}_2) ,$$

where $\bar{m} \equiv -m$; the sum on m in (2.5) runs from $-l$ to l, where l is the smaller of l_1 and l_2. We need three properties of the spherical harmonics:

$$(2.6) \qquad \int Y^*_{lm}(\boldsymbol{\Omega})\, Y_{l'm'}(\boldsymbol{\Omega})\, \mathrm{d}\boldsymbol{\Omega} = \delta_{ll'}\, \delta_{mm'} ,$$

$$(2.7) \qquad Y_{l\bar{m}}(\boldsymbol{\Omega}) = (-1)^m\, Y^*_{lm}(\boldsymbol{\Omega}) ,$$

$$(2.8) \qquad P_l(\boldsymbol{u}_1 \cdot \boldsymbol{u}_2) = \frac{4\pi}{2l+1} \sum_m Y^*_{lm}(\boldsymbol{\Omega}_1)\, Y_{lm}(\boldsymbol{\Omega}_2) ,$$

where $\boldsymbol{u}_1$, $\boldsymbol{u}_2$ are defined as in subsect. **2·1**. An expression for $g_{l_1 l_2 m}(R)$ can now be obtained by multiplying through (2.5) by $Y^*_{l_1 m}(\boldsymbol{\Omega}_1)\, Y^*_{l_2 \bar{m}}(\boldsymbol{\Omega}_2)$ and integrating over angles:

$$(2.9) \qquad g_{l_1 l_2 m}(R) = \frac{1}{4\pi} \iint g(1, 2)\, Y_{l_1 \bar{m}}(\boldsymbol{\Omega}_1)\, Y_{l_2 m}(\boldsymbol{\Omega}_2)\, \mathrm{d}\boldsymbol{\Omega}_1\, \mathrm{d}\boldsymbol{\Omega}_2 = \\ = 4\pi \langle g(1, 2)\, Y_{l_1 \bar{m}}(\boldsymbol{\Omega}_1)\, Y_{l_2 m}(\boldsymbol{\Omega}_2) \rangle_{\boldsymbol{\Omega}_1 \boldsymbol{\Omega}_2} .$$

The harmonic expansion coefficient $g_{l_1 l_2 m}(R)$ is called the « projection » of $g(1, 2)$ onto the angular function labelled by the indices $(l_1 l_2 m)$. Because $Y_{00}(\boldsymbol{\Omega}) = (1/4\pi)^{\frac{1}{2}}$, we see immediately from (2.3) and (2.9) that $g_c(R) =$

$= g_{000}(R)$; all other coefficients tend to zero as $R \to \infty$. In addition, it follows from the property (2.8) that the order parameters G_l may be expressed as

$$G_l = \frac{\varrho}{2l+1} \sum_m (-1)^m \int g_{llm}(R)\, \mathrm{d}\boldsymbol{R}\,. \tag{2.10}$$

An expansion similar to (2.5) can be made of the molecular-pair correlation function $h(1, 2) = g(1, 2) - 1$. The two sets of expansion coefficients differ only trivially: $h_{l_1 l_2 m}(R) = g_{l_1 l_2 m}(R)$ for $(l_1 l_2 m) \neq (000)$ and $h_{000}(R) = g_{000}(R) - 1$.

The expansion coefficients $g_{l_1 l_2 m}(R)$ are easy to calculate in a simulation and provide one means of characterizing the nature and range of any orientational order that exists in the fluid. Particularly detailed studies of the spherical harmonic expansion have been carried out by STREETT and TILDESLEY [18, 19] for hard dumbbells (two fused hard spheres of equal diameters) and Lennard-Jones diatomics with and without a quadrupole, and by SINGER, TAYLOR and SINGER [12], also for Lennard-Jones diatomics. Their conclusions may be summarized as follows (note that all molecules discussed in [12, 18, 19] are homonuclear). *a*) Orientational order in these fluids is short ranged. Whereas $g_{000}(R)$ has oscillations extending to several atomic diameters ($= \sigma$), higher-order expansion coefficients are all very small in magnitude beyond $R \simeq 2$ to $2.5\,\sigma$. *b*) The range of orientational correlations increases both with density and with elongation of the molecule. *c*) Results for hard dumbbells resemble those for Lennard-Jones diatomics; the attractive part of the Lennard-Jones potential is almost irrelevant to the degree of angular ordering. *d*) The main effect of adding a quadrupole moment is to increase the magnitude of the expansion coefficients corresponding to those harmonics that are present in the quadrupole-quadrupole interaction, most noticeably the coefficient $g_{220}(R)$. *e*) The magnitude of the expansion coefficients decreases rapidly with increasing l_1 and l_2.

The appeal of this type of analysis is largely a question of taste. Its strength is that it is systematic in nature. The difficulty (at least for me) lies in attaching a physical significance to the expansion coefficients: it is not easy to extract from the results a feeling for how neighbouring molecules pack together.

Where harmonic expansions have without doubt proved to be very useful is in the study (both theory and simulation) of polar fluids. The type of expansion most commonly used differs from (2.5) insofar as the orientations $\boldsymbol{\Omega}_1$ and $\boldsymbol{\Omega}_2$ are referred to a laboratory-fixed frame of reference rather than one in which the z-axis lies along the intermolecular vector. The expansion functions are now products of three spherical harmonics, the third one being a function of the angle $\boldsymbol{\Omega}_R \equiv (\theta_R, \varphi_R)$ between $\boldsymbol{R}_{12}$ and the z-axis in the laboratory-fixed frame. The pair distribution function is now written as

$$g(1, 2) = \sum_{l_1 l_2 l} g(l_1 l_2 l;\, R) \sum_{m_1 m_2 m} C(l_1 l_2 l;\, m_1 m_2 m)\, Y_{l_1 m_1}(\boldsymbol{\Omega}_1)\, Y_{l_2 m_2}(\boldsymbol{\Omega}_2)\, Y^*_{lm}(\boldsymbol{\Omega}_R)\,, \tag{2.11}$$

where $C(\quad)$ is a Clebsch-Gordan coefficient, familiar from the theory of angular momentum. Equation (2.11) reduces to (2.5) (apart from the factor 4π in the latter, which is introduced in order to make $g_{000}(R) = g_c(R)$) when the z-axis of the laboratory frame is parallel to $\boldsymbol{R}_{12}$. In general, of course, the two expansions are different, but the projections $g(l_1 l_2 l; R)$ can always be expressed as linear combinations of the coefficients $g_{l_1 l_2 m}(R)$, and *vice versa*. Equation (2.11) is often written in the form

$$g(1, 2) = \sum_{l_1 l_2 l} g(l_1 l_2 l; R)\, \Phi^{l_1 l_2 l}(\boldsymbol{\Omega}_1, \boldsymbol{\Omega}_2, \boldsymbol{\Omega}_R)\,, \tag{2.12}$$

where the angular functions $\Phi^{l_1 l_2 l}(\boldsymbol{\Omega}_1, \boldsymbol{\Omega}_2, \boldsymbol{\Omega}_R)$ are called *rotational invariants*. The « laboratory frame » expansion (2.11) may appear more complicated than its « intermolecular-frame » counterpart (2.5), but in practice it has simpler mathematical properties, particularly with respect to Fourier transformation [20].

Many theories of simple polar fluids (dipolar hard spheres, for example) begin by writing the pair correlation function $h(1, 2)$ as

$$h(1, 2) = h_S(R) + h_\Delta(R)\, \Delta(1, 2) + h_D(R)\, D(1, 2) \tag{2.13}$$

plus higher-order terms that are often ignored. The function $D(1, 2)$ is the one defined in (1.2), and

$$\Delta(1, 2) = \boldsymbol{u}_1 \cdot \boldsymbol{u}_2 = P_1(\boldsymbol{u}_1 \cdot \boldsymbol{u}_2) \tag{2.14}$$

is the cosine of the angle between the dipole-moment orientations of molecules 1 and 2. Equation (2.13) is nothing more than the expansion (2.12) truncated after three terms, because $\Delta(1, 2) = \Phi^{110}$, $D(1, 2) = \Phi^{112}$ and $h_S(R) \equiv \equiv h_{000}(R) = g_c(R) - 1$. The notation Δ and D (due to WERTHEIM [21]) has the advantage of greater compactness.

The truncated expansion (2.13) is important theoretically because it contains the minimum information needed to discuss the structure, thermodynamics and dielectric properties of a polar fluid. Thus $h_S(R)$ describes the radial distribution of the spheres in which the dipoles are embedded (restricting ourselves here to the case of dipolar hard-sphere and Stockmayer fluids); the projection $h_D(R)$ determines the dipole-dipole contribution to thermodynamic properties; and $h_\Delta(R)$ yields the dielectric constant of the fluid, as we shall show later. The function $h_\Delta(R)$, although defined in a laboratory-fixed frame, also provides information about the relative orientation of molecules that is very easy to interpret. Apart from a normalizing factor, $h_\Delta(R)$ is the mean value of $\boldsymbol{u}_1 \cdot \boldsymbol{u}_2$ for molecules separated by distances in the range R to $R + \mathrm{d}R$, weighted by the number of molecules lying in that range. If we multiply

through (2.13) by $\Delta(1,2)$, integrate over angles, and use the fact that $\langle\Delta^2\rangle_{\Omega_1\Omega_2} = \frac{1}{3}$, we find that

$$h_\Delta(R) = 3\langle h(1,2)\,\Delta(1,2)\rangle_{\Omega_1\Omega_2}\,. \tag{2.15}$$

If we compare this result with (2.4), we see that

$$G_1 = \tfrac{1}{3}\varrho\int h_\Delta(R)\,\mathrm{d}\boldsymbol{R} = \tfrac{1}{3}\varrho\hat{h}_\Delta(0)\,, \tag{2.16}$$

where $\hat{h}_\Delta(k)$ is the Fourier transform of $h_\Delta(R)$:

$$\hat{h}_\Delta(k) = \int \exp\left[-i\boldsymbol{k}\cdot\boldsymbol{R}\right] h_\Delta(R)\,\mathrm{d}\boldsymbol{R}\,. \tag{2.17}$$

For strongly polar fluids of the dipolar hard-sphere or Stockmayer type, $h_\Delta(R)$ is significantly nonzero out to ten or more molecular diameters and is positive nearly everywhere, showing that dipoles tend to align themselves parallel to the dipole at the origin. In a real polar fluid, there will always be other, competing angle-dependent forces. The effect of such forces will frequently be to disrupt dipolar correlations, and the range of $h_\Delta(R)$ will, therefore, be greatly reduced. The pronounced positive tail in $h_\Delta(R)$ is the origin of the unrealistically high dielectric constants characteristic of these models (see subsect. **3**·1).

2·3. *Site-site distribution functions.* – When dealing with an interaction site model, the natural way to discuss the structure of the fluid is in terms of the site-site distribution functions $g_{\alpha\beta}(r)$. The meaning of these functions is a very simple one. If α, β are two sites in a molecule, $g_{\alpha\beta}(r)$ describes the radial distribution of sites α in molecule j with respect to an origin located at site β in molecule i, i and j being different. The formal definition of $g_{\alpha\beta}(r)$ in terms of delta-functions is

$$\varrho^2\, g_{\alpha\beta}(r) = \left\langle \sum_{i\neq j}^{N}\sum \delta(\boldsymbol{r}_{i\alpha})\,\delta(\boldsymbol{r}_{j\beta} - \boldsymbol{r})\right\rangle\,. \tag{2.18}$$

This reduces to the definition of $g(r)$ in an atomic fluid when each molecule consists of only one site. Note that all reference to molecular orientations has disappeared from the definition (2.18). In real liquids, the most important site-site distribution functions are those that describe the distribution of atomic sites. Information on the atomic-pair distribution functions can be obtained from X-ray and neutron scattering experiments.

Because the site-site distribution functions are not explicitly dependent

on the angular variables, they can provide information on orientational correlations only if a model of the local structure is first assumed. In practice, useful results can be obtained if a study of the site-site distribution functions is combined with calculations of the harmonic expansion coefficients of subsect. 2·3 or of quantities closely related to those coefficients. Consider the case of liquid acetonitrile, for which an analysis of this type has been carried out on data obtained by molecular-dynamics simulation [22]. Acetonitrile has four inequivalent atomic sites and consequently there are ten independent atomic-pair distribution functions. For each pair of atomic sites we may define quantities $\overline{P}^{(1)}(r_{\alpha\beta})$ and $\overline{P}^{(2)}(r_{\alpha\beta})$, where $\overline{P}^{(l)}(r_{\alpha\beta})$ is the mean value of $P_l(\boldsymbol{u}_1\cdot\boldsymbol{u}_2)$ for molecules 1, 2 having atoms α, β that are separated by distances in the range $r_{\alpha\beta}+\mathrm{d}r_{\alpha\beta}$. On combining all these results, together with calculations of running co-ordination numbers based on integration of $g_c(R)$, *i.e.*

$$n(R) = 4\pi\varrho\int_0^R g(\boldsymbol{R}')\,R'^2\,\mathrm{d}R'\,, \tag{2.19}$$

the following picture emerges of the local order in the liquid. *a*) The first « shell » of neighbours (defined *via* (2.19), with R taken at the first minimum in $g_c(R)$) contains 10 to 11 molecules. The overall packing is, therefore, similar to that in a close-packed atomic liquid, such as argon. *b*) The three nearest neighbours are oriented antiparallel to the central molecule, but shifted relative to it in such a way as roughly to equalize the C-C and N-N separations of the cyanide group. *c*) Five or six molecules are loosely packed around the methyl group of the central molecule, arranged in such a way as to maximize the number of N-H contacts but with a wide span of angles. *d*) The range of strong angular correlations is restricted to centre-of-mass separations less than about 4.5 Å.

Given the large amount of information that is available, these are rather meagre results. This, however, reflects the reality of the situation. Even for a molecule such as acetonitrile, which has a large dipole moment ($\mu \simeq 4D$) and a shape that would apparently favour a compact arrangement of near neighbours, orientational correlations are confined to short distances and, therefore, necessarily involve only a few molecules. One must expect the same to be true in all cases where there are no strong and highly directional intermolecular forces. On the other hand, the angular correlations that do exist may well have a significant effect on experimental observables. This is certainly true of scattering experiments, as we shall now show.

As a simple example, consider a homonuclear diatomic molecule. If l is the bond length, the atomic co-ordinates of molecule i are

$$\boldsymbol{r}_\alpha = \boldsymbol{R}_i + \tfrac{1}{2}\boldsymbol{u}_i l\,, \qquad \boldsymbol{r}_{i\beta} = \boldsymbol{R}_i - \tfrac{1}{2}\boldsymbol{u}_i l\,. \tag{2.20}$$

The total intensity at a given momentum transfer $\hbar \boldsymbol{k}$ is determined by the fluctuations in atomic density as described by the structure factor $S(k)$. We may define the latter as

$$S(k) = \frac{1}{4N} \langle \varrho_{\boldsymbol{k}} \varrho_{-\boldsymbol{k}} \rangle , \tag{2.21}$$

where $\varrho_{\boldsymbol{k}}$ is a Fourier component of the atomic density:

$$\varrho_{\boldsymbol{k}} = \sum_{i=1}^{N} [\exp[-i\boldsymbol{k}\cdot\boldsymbol{r}_{i\alpha}] + \exp[-i\boldsymbol{k}\cdot\boldsymbol{r}_{i\beta}]] . \tag{2.22}$$

Equation (2.21) reduces to the usual definition of $S(k)$ for an atomic system in the limit $l \to 0$ (which is the reason for including the factor $\frac{1}{4}$ in the definition).

The structure factor can be related either to $g_{\alpha\beta}(r)$ or to $g(1, 2)$. In the first case, we use the fact that α and β are equivalent in order to rewrite (2.21) as

$$S(k) = \frac{1}{2} + \frac{1}{2N} \sum_{i=1}^{N} \langle \cos \boldsymbol{k}\cdot\boldsymbol{u}_i\, l \rangle + \frac{1}{4N} \left\langle \sum_{i\neq j}^{N}\sum \exp[-i\boldsymbol{k}\cdot(\boldsymbol{r}_{i\alpha} - \boldsymbol{r}_{j\beta})] \right\rangle . \tag{2.23}$$

The second term on the right-hand side of (2.23) represents the perfect correlation that exists between the two atoms on a given molecule; the third term is a Fourier transform of $g_{\alpha\beta}(r)$ (see (2.18)—note that all four atomic-pair distribution functions are identical). Thus

$$S(k) = S_{\text{intra}}(k) + S_{\text{inter}}(k) , \tag{2.24}$$

where the intramolecular contribution to the scattering is

$$S_{\text{intra}}(k) = \frac{1}{2} \left(1 + \langle \cos \boldsymbol{k}\cdot\boldsymbol{u}_1\, l \rangle_{\Omega_1}\right) = \frac{1}{2}\left(1 + \frac{\sin kl}{kl}\right) \tag{2.25}$$

and the intermolecular part is

$$S_{\text{inter}}(k) = \varrho \int \exp[-i\boldsymbol{k}\cdot\boldsymbol{r}]\, [g_{\alpha\beta}(r) - 1]\, \mathrm{d}\boldsymbol{r} = S_{\alpha\beta}(k) - 1 , \tag{2.26}$$

where $S_{\alpha\beta}(k)$ is the atomic structure factor and we have dropped a physically unimportant term in $\delta(\boldsymbol{k})$.

In order to relate $S(k)$ to $g(1,2)$, we proceed as follows:

$$(2.27)\qquad S(k) = \frac{1}{4N}\langle \varrho_{\boldsymbol{k}}\varrho_{-\boldsymbol{k}}\rangle =$$
$$= \frac{1}{N}\left\langle \sum_{i=1}^{N}\sum_{j=1}^{N}\exp[-i\boldsymbol{k}\cdot\boldsymbol{R}_{ij}]\cos(\tfrac{1}{2}\boldsymbol{k}\cdot\boldsymbol{u}_i\, l)\cos(\tfrac{1}{2}\boldsymbol{k}\cdot\boldsymbol{u}_j\, l)\right\rangle = \frac{1}{2}\left(1+\frac{\sin kl}{kl}\right)+$$
$$+\frac{1}{N}\left\langle \sum_{i\neq j}^{N}\sum\exp[-i\boldsymbol{k}\cdot\boldsymbol{R}_{ij}]\cos(\tfrac{1}{2}\boldsymbol{k}\cdot\boldsymbol{u}_i\, l)\cos(\tfrac{1}{2}\boldsymbol{k}\cdot\boldsymbol{u}_j\, l)\right\rangle = S_{\text{intra}}(k)+$$
$$+(\varrho/\Omega^2)\iiint \exp[-i\boldsymbol{k}\cdot\boldsymbol{R}_{12}][g(1,2)-1]\cos(\tfrac{1}{2}\boldsymbol{k}\cdot\boldsymbol{u}l)\cos(\tfrac{1}{2}\boldsymbol{k}\cdot\boldsymbol{u}_2\, l)\,\mathrm{d}\boldsymbol{R}_{12}\,\mathrm{d}\boldsymbol{\Omega}_1\,\mathrm{d}\boldsymbol{\Omega}_2\,.$$

We now substitute the expansion (2.5) of $g(1,2)$ and obtain

$$(2.28)\qquad S(k) = S_{\text{intra}}(k) + f(k)\,[S_{\text{c}}(k)-1] + S_{\text{aniso}}(k)\,,$$

where $S_{\text{c}}(k)$ is the Fourier transform of $g_{\text{c}}(R)-1$, $f(k)$ is given by

$$(2.29)\qquad f(k) = \langle\cos(\tfrac{1}{2}\boldsymbol{k}\cdot\boldsymbol{u}_1 l)\cos(\tfrac{1}{2}\boldsymbol{k}\cdot\boldsymbol{u}_2 l)\rangle_{\boldsymbol{\Omega}_1\boldsymbol{\Omega}_2} = \left(\frac{\sin\frac{1}{2}kl}{\frac{1}{2}kl}\right)^2$$

and $S_{\text{aniso}}(k)$ contains all spherical harmonic components of $g(1,2)$ beyond $(l_1 l_2 m) = (000)$. If we compare (2.24), (2.26) and (2.29), we find that

$$(2.30)\qquad S_{\alpha\beta}(k) = 1 + f(k)\,[S_{\text{c}}(k)-1] + S_{\text{aniso}}(k)\,.$$

Equation (2.30) can be generalized to more complicated molecules and provides a useful way of analysing the results of simulations. It partitions the intermolecular contribution to the structure factor (and hence to the predicted scattering) into a part arising from the packing of the molecular centres and a part arising from angular correlations in the fluid. If $S_{\text{aniso}}(k)$ is small enough to be ignored, we obtain what is called the « free-rotation » approximation to $S(k)$. As an illustration, it is useful to contrast the results obtained for two molecules of the same symmetry, namely methane and carbon tetrachloride. In simulated liquid methane [23], the free-rotation approximation is almost exact. Orientational correlations are, therefore, scarcely worth looking for, since they are clearly extremely weak. For carbon tetrachloride, the situation is very different [24]. At small k, the free-rotation approximation works very well, but it fails badly beyond $k \geqslant 1.8$ Å^{-1}. There is, for example, a pronounced peak in $S_{\text{inter}}(k)$ at $k \simeq 2.2$ Å that is seen both experimentally and in simulations but is completely absent in the free-rotation approximation. Orientational order in carbon tetrachloride is, therefore, strong but short ranged. The example shows that this type of calculation is valuable in two ways: *a*) in yielding a global measure of the importance of angular

correlations and *b*) in identifying features in the experimental structure factor that are associated with orientational order in the liquid. In carbon tetrachloride, the angular order arises, at least in part, from an interlocking of neighbouring molecules.

2·4. *The calculation of* G_2. – We now consider the question of the calculation of the order parameters G_l defined by (2.4), focussing on the parameter G_2; G_1 will be considered in detail in subsect. 2·5. The quantity G_2 is of importance for the interpretation of a variety of experiments. On the face of it, it would seem an easy matter to calculate G_2 by simulation. Alas! this is not the case.

There are two numerical problems in determining G_2. The first is the fact that the calculated value converges only very slowly with the length of the molecular-dynamics or Monte Carlo run. STREETT and TILDESLEY [18], for example, calculated G_2 by the Monte Carlo method for a fused hard-sphere model of carbon disulphide. Working with a system of 500 molecules, they found that G_2 approached a steady value only after about 5 million configurations, which is perhaps an order of magnitude longer than is necessary to obtain acceptable estimates of thermodymanic properties. The second difficulty is linked to the question of what range of intermolacular separations make a significant contributions to G_2, and to the possible distorting effect of the periodic boundary condition. Although the harmonic expansion coefficients that contribute to G_2 *via* (2.10) may be short ranged, G_2 itself is determined by an integral in which the coefficients are weighted by R^2. The precise rate at which the coefficients $g_{l_1 l_2 m}(R)$ approach zero is, therefore, a crucial matter. Let $\overline{P}^{(l)}(R)$ be the mean value of $P_l(\boldsymbol{u}_1 \cdot \boldsymbol{u}_2)$ for molecules whose centres are separated by distances in the interval R to $R + \mathrm{d}R$. Then the contribution to G_2 from molecules lying in a sphere (superscript s) of radius R centred on a given molecule is

$$G_2^s(R) = 4\pi\varrho \int_0^R g_c(R')\, R'^2\, \overline{P}^{(2)}(R')\, \mathrm{d}R' \tag{2.31}$$

and $G_2 = \lim_{R\to\infty} G_2^s(R)$.

IMPEY, MADDEN and TILDESLEY [25] have computed G_2 *via* (2.31) for a Lennard-Jones triatomic model of carbon disulphide. They find *a*) that $\overline{P}^{(2)}(R)$ oscillates in sign as a function of R and is very small in magnitude for $R \geqslant 2.5\,\sigma$ (where σ is the C-C Lennard-Jones length parameter), but *b*) the integrand in (2.31) is a strongly oscillatory function that decays only slowly towards zero, with the consequence *c*) that $G_2^s(R)$ is also oscillatory. Under triple-point conditions, $G_2^s(R)$ oscillates about a mean value of approximately 0.37, with a displacement, even at half the length of the periodic box ($R \simeq 4.5\,\sigma$), of $\pm\,0.2$. The mean value itself is reasonably steady as a function of R, and the oscillations in the integrand of (2.31) beyond $R \geqslant 2.5\,\sigma$ appear to make no net contribution to the integral. IMPEY, MADDEN and TILDESLEY, there-

fore, suggest that the oscillations in $G_2^s(R)$ are an artifact of averaging over spherical shells and are irrelevant to the final value of G_2. In support of their claim, they give the results of a different calculation in which G_2 is obtained by integrating over cubic (superscript c) shells to give

$$G_2^c(R) = 4\pi\varrho \int_{-R}^{R} dx \int_{-R}^{R} dy \int_{-R}^{R} dz\, g_c(R')\, R'^2\, \overline{P}^{(2)}(R') \,, \tag{2.32}$$

where $R' = (x^2 + y^2 + z^2)^{\frac{1}{2}}$ and $G_2 = \lim_{R\to\infty} G_2^c(R)$. As anticipated, the function $G_2^c(R)$ is not oscillatory and appears to be approaching a plateau value at $R \simeq 2.5\,\sigma$. This seems encouraging. Unfortunately, for larger R, the value of $G_2^c(R)$ begins to change rapidly and monotonically—but in a direction dependent on the state conditions. IMPEY, MADDEN and TILDESLEY ascribe this behaviour to the influence of the periodic boundary conditions. That the periodicity plays a role is certainly plausible. As a simple example, consider a linear arrangement of four molecules of the form (1, 2, 3, cube edge, 4, 1′), where 1′ is the image of 1 in a neighbouring cell and molecules 3 and 4 are separated by the boundary of the cube but are not too far apart. The orientation of 3 will be correlated with that of 1 *via* mutual correlations with the intermediate molecule 2, but it will also be correlated with the orientation of 1′ *via* molecule 4. But 1 and 1′ are images and their orientations are, therefore, the same. Hence molecule 3 experiences the effect of 1 in two ways, one of which (*via* 4 and 1′) is spurious in the sense that it would not occur in an infinite system. According to IMPEY, MADDEN and TILDESLEY, the best estimate of G_2 is that given by the plateau value of $G_2^c(R)$, *i.e.* that obtained by cubic averaging over a volume that is only about one-eigth that of the molecular-dynamics cell. The value calculated by averaging over the whole cube, which is the natural way to obtain maximum statistics, is almost certainly wrong, since it behaves erratically with changes in state conditions. Unfortunately, the « plateau » value is very narrow. The authors end their article on a note of optimism, but the main lesson to be drawn from their work is surely that accurate calculation of a property such as G_2 requires use of a much larger sample than would otherwise be needed.

3. – Dielectric properties.

The theory of dielectrics is well known to be a very complicated subject. Most of the difficulties can be traced to the fact that the dipolar interaction is long ranged: the integral of R^{-3} over a volume V diverges logarithmically. The slow decay of the dipole-dipole potential has as a corollary the fact that $h(1, 2)$ is also long ranged: the projection $h_D(R)$ also decays as R^{-3} at large R.

A detailed calculation shows that

$$\lim_{R\to\infty} h_D(R) = \frac{(\varepsilon-1)^2}{4\pi y\varrho\varepsilon}\frac{1}{R^3}, \tag{3.1}$$

where $y = 4\pi\beta\varrho\mu^2/9$ and ε is the static dielectric constant. A practical consequence of the long-range correlations is the fact that the structure of a simulated polar fluid is dependent on the assumed geometry, *i.e.* the boundary conditions or, more precisely, on the way in which the dipolar term in the pair potential is treated. It also turns out that the dynamical evolution of the system is strongly dependent on the choice of boundary conditions. We shall discuss these two problems in turn: firstly, the question of structure and the calculation of the dielectric constant and, secondly, the dynamics and the difficulties associated with the study of dielectric relaxation.

3·1. *The static dielectric constant.* – In order to provide a framework in which to discuss the simulation of polar fluids, it is useful first to derive some results appropriate to an infinite system; we may then consider the significance of these results for particular computational schemes. In deriving the infinite-system results, we follow in outline a recent review article by MADDEN and KIVELSON [26].

Consider an infinite sample of dielectric material (a polar fluid) placed in an external field $\boldsymbol{E}^0(\boldsymbol{R})$. The field $\boldsymbol{E}^0(\boldsymbol{R})$ is the field that would exist at the point $\boldsymbol{R}$ in the absence of the sample. As a result of applying the field, a polarization $\boldsymbol{P}(\boldsymbol{R})$ (dipole moment per unit volume) appears in the sample. The field $\boldsymbol{E}(\boldsymbol{R})$ within the sample (the Maxwell field), therefore, differs from $\boldsymbol{E}^0(\boldsymbol{R})$ by an amount determined by the polarization $\boldsymbol{P}(\boldsymbol{R}')$ at all other points $\boldsymbol{R}'$. The relation between the two fields is

$$\boldsymbol{E}(\boldsymbol{R}) = \boldsymbol{E}^0(\boldsymbol{R}) + \int \mathrm{d}\boldsymbol{R}'\, \boldsymbol{T}(\boldsymbol{R}-\boldsymbol{R}')\cdot\boldsymbol{P}(\boldsymbol{R}'), \tag{3.2}$$

where $\boldsymbol{T}(\boldsymbol{R}-\boldsymbol{R}')$ is the dipole-dipole interaction tensor:

$$\boldsymbol{T}(\boldsymbol{R}-\boldsymbol{R}') = \frac{3(\boldsymbol{R}-\boldsymbol{R}')(\boldsymbol{R}-\boldsymbol{R}')}{|\boldsymbol{R}-\boldsymbol{R}'|^5} - \frac{\boldsymbol{I}}{|\boldsymbol{R}-\boldsymbol{R}'|^3}, \tag{3.3}$$

where $\boldsymbol{I}$ is the unit tensor. Equation (3.2) is more conveniently written in terms of Fourier components in the form

$$\hat{\boldsymbol{E}}(\boldsymbol{k}) = \hat{\boldsymbol{E}}^0(\boldsymbol{k}) - \frac{4\pi}{k^2}\boldsymbol{k}\boldsymbol{k}\cdot\hat{\boldsymbol{P}}(\boldsymbol{k}), \tag{3.4}$$

where the caret denotes a spatial Fourier transform.

The polarization is determined by the Maxwell field through the expression

$$\boldsymbol{P}(\boldsymbol{R}) = \int \mathrm{d}\boldsymbol{R}'\, \chi(\boldsymbol{R} - \boldsymbol{R}') \cdot \boldsymbol{E}(\boldsymbol{R}) \tag{3.5}$$

or, in $\boldsymbol{k}$-space,

$$\hat{\boldsymbol{P}}(\boldsymbol{k}) = \hat{\chi}(\boldsymbol{k}) \cdot \hat{\boldsymbol{E}}(\boldsymbol{k}) \,. \tag{3.6}$$

The susceptibility $\hat{\chi}(\boldsymbol{k})$ (a tensor) is related to the dielectric permittivity $\boldsymbol{\varepsilon}(\boldsymbol{k})$ (also a tensor) by

$$4\pi\hat{\chi}(\boldsymbol{k}) = \boldsymbol{\varepsilon}(\boldsymbol{k}) - \boldsymbol{I} \,. \tag{3.7}$$

Equations (3.6) and (3.7) together yield the « constitutive » relation of electrostatics, *i.e.* (ignoring the k-dependence) $4\pi\boldsymbol{P} = (\varepsilon - 1)\boldsymbol{E}$. The susceptibility $\hat{\chi}(k)$ provides the link between the polarization and the Maxwell field. In a similar way, we may write

$$\hat{\boldsymbol{P}}(\boldsymbol{k}) = \hat{\chi}^0(\boldsymbol{k}) \cdot \hat{\boldsymbol{E}}^0(\boldsymbol{k}) \,, \tag{3.8}$$

where the susceptibility $\hat{\chi}^0(\boldsymbol{k})$ measures the response to the external field. The relation between $\hat{\chi}(\boldsymbol{k})$ and $\hat{\chi}^0(\boldsymbol{k})$ follows from (3.4), (3.6) and (3.8):

$$\hat{\chi}^0(\boldsymbol{k}) = [\boldsymbol{I} + (4\pi/k^2)\, \boldsymbol{k}\boldsymbol{k} \cdot \hat{\chi}(\boldsymbol{k})]^{-1} \cdot \hat{\chi}(\boldsymbol{k}) \,. \tag{3.9}$$

The dielectric permittivity is an intensive property of the fluid, independent of both the size and shape of the sample. The same is, therefore, true of $\hat{\chi}(\boldsymbol{k})$, since $\hat{\chi}(\boldsymbol{k})$ and $\boldsymbol{\varepsilon}(\boldsymbol{k})$ are trivially related by (3.7). Therefore, $\hat{\chi}(\boldsymbol{k})$ and $\boldsymbol{\varepsilon}(\boldsymbol{k})$ are independent of $\boldsymbol{k}$ in the limit $\boldsymbol{k} \to 0$. Thus

$$\lim_{\boldsymbol{k}\to 0} \hat{\chi}(\boldsymbol{k}) = \chi \boldsymbol{I} \,, \tag{3.10}$$

$$\lim_{\boldsymbol{k}\to 0} \boldsymbol{\varepsilon}(\boldsymbol{k}) = \varepsilon \boldsymbol{I} \,, \tag{3.11}$$

where χ and ε are scalars; ε is the dielectric constant. On the other hand, the relation between $\hat{\chi}(\boldsymbol{k})$ and $\hat{\chi}^0(\boldsymbol{k})$ is shape dependent: (3.9) has been derived for an infinite sample. Different components of $\hat{\chi}^0(\boldsymbol{k})$ will, therefore, behave differently in the long-wavelength limit. In particular, the behaviour of the « transverse » (perpendicular to $\boldsymbol{k}$) and « longitudinal » (parallel to $\boldsymbol{k}$) components will differ. If we take the z-axis along $\boldsymbol{k}$, we find from (3.9) to (3.11) that

$$4\pi \lim_{\boldsymbol{k}\to 0} \hat{\chi}^0_{xx}(\boldsymbol{k}) = \varepsilon - 1 \qquad \text{(or } y\text{) (transverse)} \,, \tag{3.12}$$

$$4\pi \lim_{\boldsymbol{k}\to 0} \hat{\chi}^0_{zz}(\boldsymbol{k}) = \frac{\varepsilon - 1}{\varepsilon} \qquad \text{(longitudinal)} \tag{3.13}$$

and

$$4\pi \lim_{k\to 0} \operatorname{Tr} \hat{\chi}^0(k) = \frac{(\varepsilon-1)(2\varepsilon+1)}{\varepsilon} . \tag{3.14}$$

From the general theory of linear response, we know that the polarization induced by a weak external field is related to the fluctuations in polarization in the absence of the field. The polarization induced by the field is given microscopically by the dipole-moment density, *i.e.*

$$\boldsymbol{P}(\boldsymbol{R}) = \langle \boldsymbol{M}(\boldsymbol{R}) \rangle_{\boldsymbol{E}^0} = \langle \mu \sum_i \boldsymbol{u}_i \, \delta(\boldsymbol{R} - \boldsymbol{R}_i) \rangle_{\boldsymbol{E}^0} , \tag{3.15}$$

where $\langle \ldots \rangle_{\boldsymbol{E}^0}$ denotes a statistical average in the presence of the field and $\boldsymbol{u}_i$ has the same meaning as in (1.2). The susceptibility $\hat{\chi}^0(\boldsymbol{k})$ is given in terms of Fourier components of $\boldsymbol{M}(\boldsymbol{R})$ by

$$\hat{\chi}^0(\boldsymbol{k}) = \frac{\beta}{V} \langle \hat{\boldsymbol{M}}(\boldsymbol{k}) \hat{\boldsymbol{M}}(-\boldsymbol{k}) \rangle , \tag{3.16}$$

where the statistical average is now computed in the absence of the field and

$$\hat{\boldsymbol{M}}(\boldsymbol{k}) = \mu \sum_{i=1}^{N} \boldsymbol{u}_i \exp[-i\boldsymbol{k}\cdot\boldsymbol{R}_i] . \tag{3.17}$$

It follows from (3.12) to (3.14) that

$$\lim_{k\to 0} \langle \hat{M}_x(\boldsymbol{k}) \hat{M}_x(-\boldsymbol{k}) \rangle = \frac{V}{4\pi\beta} (\varepsilon - 1) , \tag{3.18}$$

$$\lim_{k\to 0} \langle \hat{M}_z(\boldsymbol{k}) \hat{M}_z(-\boldsymbol{k}) \rangle = \frac{V}{4\pi\beta} \frac{\varepsilon - 1}{\varepsilon} \tag{3.19}$$

and

$$\lim_{k\to 0} \langle |\boldsymbol{M}|^2 \rangle = \frac{V}{4\pi\beta} \frac{(\varepsilon-1)(2\varepsilon+1)}{\varepsilon} . \tag{3.20}$$

In the limit $\boldsymbol{k} = 0$, (3.20) becomes

$$\frac{(\varepsilon-1)(2\varepsilon+1)}{9\varepsilon} = g_{\mathrm{K}} y , \tag{3.21}$$

where y is the molecular parameter introduced in (3.1) and g_{K} is the Kirkwood g-factor:

$$g_{\mathrm{K}} = \frac{\langle |\boldsymbol{M}(0)|^2 \rangle}{N\mu^2} . \tag{3.22}$$

From (2.16) and (3.22) we see that

$$(3.23)\qquad g_{\mathrm{K}} = \frac{1}{N}\left\langle \sum_{i=1}^{N}\sum_{j=1}^{N} \boldsymbol{u}_i\cdot\boldsymbol{u}_j \right\rangle = 1 + \langle (N-1)\,\boldsymbol{u}_1\cdot\boldsymbol{u}_2\rangle = \\ = 1 + G_1 = 1 + \frac{1}{3}\,\varrho\int h_{\Delta}(R)\,\mathrm{d}\boldsymbol{R}\,.$$

We may also define a k-dependent generalization of (3.23) by

$$(3.24)\qquad g(k) = 1 + \tfrac{1}{3}\varrho\hat{h}_{\Delta}(\boldsymbol{k})\,.$$

The important point to carry away from this calculation is that different components of the microscopic polarization fluctuate differently for $k > 0$. In particular, for an infinite system, the fluctuations in the longitudinal component at small k are suppressed relative to fluctuations in the transverse component by a factor ε^{-1}.

Let us see how these considerations work out when applied to the results of simulations. The only system that has been studied in the detail we require is the Stockmayer fluid. POLLOCK and ALDER [4] have calculated the function $g(k)$ by molecular dynamics for a range of values of μ at fixed density and temperature and compared their results with the so-called QHNC theory of Patey [27]. More accurate theories of simple polar fluids are now available [28], but at moderate values of the parameter $\mu^{*2} = \mu^2\sigma^3/\varepsilon$ (where ε, σ characterize the Lennard-Jones part of the interaction), the QHNC results provide a fair guide to what the infinite-system results should be. POLLOCK and ALDER have made two series of calculations, one by the Ewald or, as applied to point dipoles, the Ewald-Kornfeld (EK) method, and a less complete set by the usual method involving spherical cut-off (SC) of the potential; the Ewald method will be discussed in the lectures of Hansen (this volume, p. 89). The main features of the results of Pollock and Alder for the case $\mu^* = 1$, $\varrho^* = N\sigma^3/V = 0.8$ and $T^* = k_{\mathrm{B}}T/\varepsilon = 1.35$ may be summarized as follows. *a*) For large k ($k\sigma \geqslant 3$), the EK and SC methods yield almost identical curves of $g(k)$ *vs.* k. *b*) In the EK calculations, $g(k)$ varies smoothly with k down to the smallest accessible wave number in the periodic system ($k_{\min} = 2\pi/L$, where L is the length of the molecular-dynamics cell). At small k, the curve rises so as to approach, by extrapolation to $k = 0$, a value $g(k \to 0) \simeq 1.4$. Good agreement is maintained with the infinite-system (QHNC) results down to $k = k_{\min}$. *c*) In the SC calculations, the curve of $g(k)$ rises slightly above the EK results for $2 \leqslant k\sigma \leqslant 3$, and then falls sharply to approach a value at $k = 0$ of $g(k \to 0) \simeq 0.8$. *d*) The value obtained for $g_{\mathrm{SC}} = \langle |\boldsymbol{M}(0)|^2\rangle/N\mu^2$ agrees with that derived by extrapolation of the finite-wavelength results, but that for g_{EK} does not; $g_{\mathrm{EK}} \simeq 2.0$ is much larger than $\lim_{k\to 0} g(k)$. Clearly g_{K} in (3.21) cannot be identified with either g_{SC} or g_{EK}.

How are we to explain these results? The key to the problem is the fact that, although the permittivity is independent of geometry, its relation to the polarization (expressed by $g(k)$) is not; (3.18) and (3.19), for example, apply to an infinite system and other relations would be obtained if a different geometry were assumed. At large k, however, the boundary conditions become irrelevant. The results for $g(k)$ should, therefore, be independent of whether the SC or EK method is used, as indeed they are. By the same rule, it is not unexpected to find differences appearing when the wavelength $\lambda = 2\pi/k$ of the fluctuation is comparable with the length of the simulation cell. For the 256-molecule system studied by POLLOCK and ALDER, L at $\varrho^* = 0.8$ is approximately equal to $6.8\,\sigma$. Thus the results of the simulation show that the differences between the two methods have appreciable consequences when $\lambda \geqslant 3L$ (or six times the range of a potential truncated at $R = \frac{1}{2}L$).

What dictates the behaviour of the SC results at small k? We can answer this question in the following way. Equation (3.21) was originally derived by KIRKWOOD [29] by considering the fluctuations in dipole moment in a sphere embedded in a dielectric continuum of the same dielectric constant as the sphere. Kirkwood's result can be generalized [30] to the case when the continuum has a dielectric constant ε', say, with $\varepsilon' \neq \varepsilon$. Then

$$\frac{(\varepsilon - 1)(2\varepsilon' + 1)}{\varepsilon + 2\varepsilon'} = 3yg(\varepsilon')\,. \tag{3.25}$$

The SC method, since it neglects interactions beyond the cut-off distance, corresponds approximately to the situation where $\varepsilon' = 1$ (a sphere *in vacuo*). Thus

$$g_{\text{SC}} = g(\varepsilon' = 1) = \frac{\varepsilon - 1}{y(\varepsilon + 2)}\,, \tag{3.26}$$

from which we see that

$$\frac{g_{\text{SC}}}{g_{\text{K}}} = \frac{9\varepsilon}{(2\varepsilon + 1)(\varepsilon + 2)} \simeq \frac{9}{2\varepsilon} \qquad \text{if } \varepsilon \gg 1\,. \tag{3.27}$$

Consequently, when the SC method is used, long-wavelength fluctuations are strongly suppressed by comparison with those appropriate to the infinite-system limit (represented by g_{K}). For the case in hand, $\varepsilon \simeq 6$ and we, therefore, expect to find $g_{\text{SC}}/g_{\text{K}} \simeq 0.5$, in fair agreement with the results of Pollock and Alder. This demonstrates the internal consistency of the two calculations, but there are strong arguments against the use of the SC method. Firstly, (3.26) does not provide a practical route to the calculation of ε when ε is large; it requires a much higher precision in the determination of g_{SC} than is normally achievable. Secondly, the pair structure of the fluid is severely distorted by

truncation of the dipolar potential. This fact is apparent from (3.27), because g_{SC} and g_K are each determined by the integral over the corresponding $h_\Delta(R)$. The SC results for $h_\Delta(R)$ deviate markedly from their infinite-system values for $R \geqslant 1.2\,\sigma$ [4] and are, therefore, of little physical interest.

We now have to explain the behaviour of the EK results at $\boldsymbol{k} = 0$. In contrast to the SC method, the Ewald sum corresponds to an infinite system, albeit an infinitely periodic one. We, therefore, expect (and find) that agreement with infinite-system results is maintained for all nonzero wave vectors. At $\boldsymbol{k} = 0$, however, there is a discontinuity. We can understand this if we recognize that it is necessary, even for an infinite system, to distinguish carefully between $\lim_{k \to 0} \boldsymbol{k}$ and $\boldsymbol{k} = 0$. Consider (3.18) and (3.19). For $k > 0$, fluctuations in the z-component of the polarization are a factor ε^{-1} times smaller than those in the x and y directions. But at $\boldsymbol{k} = 0$, the distinction between x, y and z is lost, and all components of the polarization fluctuations must, therefore, change discontinuously to a value given by one-third of the right-hand side of (3.20). (Note that the sum of the three components varies continuously down to and including $\boldsymbol{k} = 0$.)

In the EK method, the discontinuity at $\boldsymbol{k} = 0$ manifests itself in a different way. The reason for this is a simple one: the $\boldsymbol{k} = 0$ term in the Ewald sum is treated differently from all other contributions. The source of the $\boldsymbol{k} = 0$ term is the fact that the system will, in general, have a uniform polarization because the periodic cells will each have a net dipole moment that is nonzero. The value of the $\boldsymbol{k} = 0$ term is shape dependent; in conventional applications of the EK method, the $\boldsymbol{k} = 0$ term is simply ignored. So far as fluctuations are concerned, neglect of the $\boldsymbol{k} = 0$ term is equivalent to supposing that the infinitely periodic lattice of cells is embedded in a conducting medium [30]. We may, therefore, deduce the appropriate fluctuation formula by setting $\varepsilon' = \infty$ in (3.25) to give

$$g_{EK} = g(\varepsilon' = \infty) = \frac{\varepsilon - 1}{3y}. \tag{3.28}$$

The analogy with conducting boundary conditions is a useful conceptual prop, but its significance has occasionally been overemphasized. That (3.28) is the correct formula to use follows rigorously from neglect of the $\boldsymbol{k} = 0$ term in the Ewald sum [31]; the derivation is independent of any assumption concerning the surroundings. Comparison of (3.18), (3.19) and (3.28) shows that the fluctuations in the transverse components of the polarization are now continuous for all $\boldsymbol{k}$ and the discontinuity in the g-factor arises from the loss of the special character of the longitudinal fluctuations at $\boldsymbol{k} = 0$.

There is another way besides the EK method of taking account of the long range of the dipole-dipole interaction. This is the reaction field (RF) method of Barker and Watts [32], which amounts to a realization of the idea underlying Kirkwood's derivation of (3.21). The dipolar potential is truncated at a

separation R_c (as in the SC method), but the region beyond R_c is now treated as a dielectric continuum. Consider a truncation sphere centred on molecule i and let $\boldsymbol{M}_i$ be the total moment of the sphere. The potential energy of a configuration of molecules is taken as

$$V_N = \tfrac{1}{2}\sum_{i\neq j}^{N}\sum v(i,j) - \tfrac{1}{2}\mu\sum_{i=1}^{N}\boldsymbol{E}_R(i)\cdot\boldsymbol{u}_i\,, \tag{3.29}$$

where $v(i,j) = 0$ for $|\boldsymbol{R}_i - \boldsymbol{R}_j| > R_c$, and $\boldsymbol{E}_R(i)$ is the *reaction field* acting on molecule i due to the polarization of the continuum by the dipole moment $\boldsymbol{M}_i$. The reaction field is given by

$$\boldsymbol{E}_R(i) = \frac{1}{R_c^3}\frac{2(\varepsilon'-1)}{2\varepsilon'+1}\boldsymbol{M}_i\,, \tag{3.30}$$

where ε' is the dielectric constant of the continuum. The natural choice is $\varepsilon' = \varepsilon$, a scheme that we shall refer to as RF(ε). This requires a prior knowledge of the dielectric constant of the fluid of interest, but in practice the reaction field (3.30) is insensitive to the precise choice of ε'. The RF method has been used in molecular-dynamics calculations by ADAMS [33] and by NEUMANN, STEINHAUSER and PAWLEY [34]. The correct fluctuation formula to use at $\boldsymbol{k} = 0$ is now (3.25), with the appropriate choice of ε'; if $\varepsilon' = \varepsilon$, the fluctuations are proportional to g_K. The choice $\varepsilon' = \infty$ in (3.30)—the RF(∞) scheme—is similar in spirit to the EK method and yields almost identical results, but the two are not completely equivalent. If we choose $\varepsilon' = 1$, the RF method reduces to the SC convention. A unified treatment of all the boundary conditions we have discussed can be found in papers of Neumann and Steinhauser quoted in [34].

The main conclusion to be drawn from this long discussion is that the dielectric constant can be calculated in a variety of ways that are mutually consistent, but the fluctuations in dipole moment must be related to ε in a manner determined by practical details of the simulations. Provided the correct formula is used in each case, all methods should give the same result for ε. In practice, there are serious objections to the use of the SC method, and the EK, RF(ε) and RF(∞) schemes are all much more satisfactory. Comparison of (3.21) and (3.28) shows that

$$\frac{g_{EK}}{g_K} = \frac{3\varepsilon}{2\varepsilon+1} \simeq \frac{3}{2} \qquad \text{if } \varepsilon \gg 1\,. \tag{3.31}$$

This result raises again the possibility that a simulation (this time by the EK method) might give results for $h_\Delta(R)$ that are significantly different from those expected in the infinite-system limit. In fact, the curves obtained in EK (or RF(∞)) geometries are qualitatively similar for all R, and the difference

between g_{EK} and g_K is the result of an accumulation of small differences at large R. In principle, the RF(ε) method should mimic most closely the properties of an infinite system, but it has been suggested that equilibrium is attained more rapidly when the EK method is used [35]. Whatever method is used, it is clear from published results that long runs ($\sim 50\,000$ molecular-dynamics time steps) and large systems ($N \geqslant 250$) are needed if accurate values of ε are to be obtained. It should be noted, finally, that in all cases the dipole moment $\boldsymbol{M}(0)$ that enters the fluctuation formula for $\boldsymbol{k} = 0$ is always the dipole moment of the complete molecular-dynamics cube and not, for example, that of some spherical region within the cell. This result, about which there had previously been some confusion, is now rigorously established [34, 36]. The way in which the integral over $h_\Delta(R)$ reaches its asymptotic value for the cube differs dramatically for SC as compared with other methods [34].

3·2. *Dielectric relaxation.* – We want now to look at the way in which the considerations of subsect. **3·1** must be extended in order to deal with the dynamics of polar fluids, particularly with the problem of *dielectric relaxation.* Dielectric-relaxation processes may be discussed in terms of four distinct time correlation functions. These consist of *a*) the single-molecule, dipole-dipole correlation function $C_1(t)$, defined as

$$C_1(t) = \frac{1}{N} \sum_{i=1}^{N} \langle \boldsymbol{u}_i(t) \cdot \boldsymbol{u}_i(0) \rangle \,, \tag{3.32}$$

where the subscript 1 denotes the fact that we are dealing with a first-order Legendre polynomial; *b*) the collective analogue of $C_1(t)$, which we shall denote by $C_1^{\text{coll}}(t)$:

$$C_1^{\text{coll}}(t) = \frac{1}{\langle |\boldsymbol{M}(0)|^2 \rangle} \langle \boldsymbol{M}(t) \cdot \boldsymbol{M}(0) \rangle \,, \tag{3.33}$$

where $\boldsymbol{M}(t)$ is the total dipole moment of the region of interest—in our case, the molecular-dynamics cell; *c*) the correlation function of the transverse components of the polarization density, *i.e.*

$$C_\perp(\boldsymbol{k}, t) = \frac{1}{\langle |\boldsymbol{M}_x(\boldsymbol{k})|^2 \rangle} \langle \hat{\boldsymbol{M}}_x(\boldsymbol{k}, t)\, \hat{\boldsymbol{M}}_x(-\boldsymbol{k}) \rangle \qquad (\text{or } y) \,, \tag{3.34}$$

where $\hat{\boldsymbol{M}}_x(\boldsymbol{k}) \equiv \hat{\boldsymbol{M}}_x(\boldsymbol{k}, t = 0)$; and *d*) the longitudinal equivalent of (3.34):

$$C_\parallel(\boldsymbol{k}, t) = \frac{1}{\langle |\hat{\boldsymbol{M}}_z(\boldsymbol{k})|^2 \rangle} \langle \hat{\boldsymbol{M}}_z(\boldsymbol{k}, t)\, \hat{\boldsymbol{M}}_z(-\boldsymbol{k}) \rangle \,. \tag{3.35}$$

As before, the z-direction is parallel to $\boldsymbol{k}$.

The single-molecule function (3.32) can be determined experimentally from infra-red spectroscopic measurements, and the collective function (3.33) is related to the complex dielectric permittivity $\varepsilon(\omega)$. The relationship between $C_\perp(\boldsymbol{k}, t)$, $C_\parallel(\boldsymbol{k}, t)$ and the components of a generalized frequency and wave-vector–dependent susceptibility $\hat{\chi}^0(k, \omega)$ is given by linear-response theory [26] as

$$\hat{\chi}^0(\boldsymbol{k}, \omega) = \frac{\beta}{V}\left(\langle \boldsymbol{M}(\boldsymbol{k})\, \boldsymbol{M}(-\boldsymbol{k})\rangle + i\omega \int_0^\infty \mathrm{d}t \exp[i\omega t] \langle \boldsymbol{M}(\boldsymbol{k}, t)\, \boldsymbol{M}(-\boldsymbol{k})\rangle\right) \tag{3.36}$$

which is a generalization of the static result (3.16). In the limit $\boldsymbol{k} \to 0$, the right-hand side of (3.36) is linked to $\varepsilon(\omega)$ in a manner that is shape dependent but involves the same functional of the permittivity $\varepsilon(\omega)$ that occurs in the static case (see (3.18) and (3.19)). Thus

$$\lim_{\boldsymbol{k}\to 0} \langle |\hat{M}_x(\boldsymbol{k})|^2\rangle [1 + i\omega \tilde{C}_\perp(\boldsymbol{k}, \omega)] = \frac{V}{4\pi\beta}[\varepsilon(\omega) - 1] \qquad (\text{or } y)\,, \tag{3.37}$$

$$\lim_{\boldsymbol{k}\to 0} \langle |\hat{M}_z(\boldsymbol{k})|^2\rangle [1 + i\omega \tilde{C}_\parallel(\boldsymbol{k}, \omega)] = \frac{V}{4\pi\beta}\frac{\varepsilon(\omega) - 1}{\varepsilon(\omega)}\,, \tag{3.38}$$

where a tilde is used to denote a Laplace transform with respect to time:

$$\tilde{f}(\omega) = \int_0^\infty \exp[i\omega t] f(t)\, \mathrm{d}t\,. \tag{3.39}$$

The functions $C_1(t)$, $C_1^{\text{coll}}(t)$, $C_\perp(\boldsymbol{k}, t)$ and $C_\parallel(\boldsymbol{k}, t)$ are all calculable by simulation. The form of the collective functions, particularly $C_1^{\text{coll}}(t)$, is influenced by the choice of boundary conditions, but $\varepsilon(\omega)$ (like ε in the static case) should always be the same.

Some useful, qualitative information on the behaviour of the collective functions can be obtained by assuming that $\varepsilon(\omega)$ is describable in terms of a single relaxation time [26]. This is the Debye approximation, or « diffusion limit », in which $\varepsilon(\omega)$ behaves as

$$\frac{\varepsilon(\omega) - 1}{\varepsilon(0) - 1} = \frac{1}{1 - i\omega\tau_{\text{D}}}\,, \tag{3.40}$$

where $\varepsilon(0) \equiv \varepsilon$ and τ_{D} is the Debye relaxation time. In the Debye approximation, a plot of the real *vs.* the imaginary part of $\varepsilon(\omega)$ (a Cole-Cole plot) is a semicircle, irrespective of the choice of τ_{D}, and many real liquids have Cole-Cole plots that are approximately semicircular. If we compare (3.40) with (3.37) and (3.38), we find that the corresponding approximations to $\tilde{C}_\perp(\boldsymbol{k}, \omega)$

and $\tilde{C}_{\parallel}(\boldsymbol{k}, \omega)$ are, respectively,

$$\lim_{k\to 0} \tilde{C}_{\perp}(\boldsymbol{k}, \omega) = \frac{1}{-i\omega + 1/\tau_{\mathrm{D}}}, \tag{3.41}$$

$$\lim_{k\to 0} \tilde{C}_{\parallel}(\boldsymbol{k}, \omega) = \frac{1}{-i\omega + \varepsilon/\tau_{\mathrm{D}}}. \tag{3.42}$$

These results imply that both $C_{\perp}(\boldsymbol{k}, t)$ and $C_{\parallel}(\boldsymbol{k}, t)$ decay exponentially, but with characteristic times that differ by a factor ε:

$$C_{\perp}(\boldsymbol{k}, t) = \exp\left[-t/\tau_{\mathrm{D}}\right], \tag{3.43}$$

$$C_{\parallel}(\boldsymbol{k}, t) = \exp\left[-\varepsilon t/\tau_{\mathrm{D}}\right]. \tag{3.44}$$

The qualitative predictions contained in (3.43) and (3.44) are well borne out by the simulations reported in [37] (for the Stockmayer fluid) and [38] (for a model of liquid acetonitrile). The calculations for acetonitrile yield a static dielectric constant $\varepsilon \simeq 30$, while the ratio of the correlation times for transverse and longitudinal functions (obtained by integration) for the three smallest wave vectors are $\tau_{\perp}/\tau_{\parallel} = 20$ ($k = 0.18\,\text{Å}^{-1}$), 26 ($k = 0.25\,\text{Å}^{-1}$) and 31 ($k = 0.31\,\text{Å}^{-1}$). However, the correlation functions are certainly not exponential at all times. In particular, the longitudinal function has an oscillatory behaviour; the same effect, in more pronounced form, is seen in the results for the Stockmayer fluid [37]. We shall have more to say later about this interesting phenomenon.

Within the limits imposed by use of the Debye approximation, we may expect (see subsect. 3·1) (3.43) and (3.44) to describe equally well results obtained by the EK and RF methods, and also those obtained with the SC convention if k is not too small. At $\boldsymbol{k} = 0$, however, the various methods will yield different dynamical properties; the form of $C_1^{\mathrm{coll}}(t)$ (the $\boldsymbol{k} = 0$ collective function) will, therefore, be dependent on the assumed boundary conditions. It follows that the relation between the collective (τ_1^{coll}) and single-molecule (τ_1) integral correlation times will also vary with boundary conditions, since there is no reason to expect $C_1(t)$ to be appreciably shape dependent. The clarification of the relation between the two correlation times is one of the main themes of dielectric-relaxation theory.

Use of the Debye approximation makes it possible to predict the qualitative behaviour of $C_1^{\mathrm{coll}}(t)$ for different assumed geometries by constructing the appropriate functional of the permittivity (3.40). The functional is always the same as the one that relates ε to static fluctuations in $\langle|\boldsymbol{M}|^2\rangle$. In the EK method, the functional of interest is $\varepsilon(\omega) - 1$. Thus

$$C_1^{\mathrm{coll}}(t) = \exp\left[-t/\tau_{\mathrm{D}}\right] \qquad \text{(EK)} \tag{3.45}$$

which is just the extrapolation to $\boldsymbol{k} = 0$ of the behaviour of the transverse function at finite wavelenghts. The results of Pollock and Alder [37] for the Stockmayer fluid do indeed show that $C_1^{\text{coll}}(t)$ is approximately exponential at long times, and a value of τ_D can be derived from the slope of ln $C_1^{\text{coll}}(t)$ *vs.* t at large t. The correlation time $\tau_1^{\text{coll}}(\text{EK})$ is invariably larger than τ_1. Not unexpectedly, the ratio $\tau_1^{\text{coll}}(\text{EK})/\tau_1$ increases with dipole moment; this trend reflects the growing importance of cross-correlations between dipoles. An approximate relation, derived in the appendix, expresses τ_D in terms of τ_1 in the form

$$\tau_D = \frac{3\varepsilon g_K}{2\varepsilon + 1}\tau_1 . \tag{3.46}$$

From the observed dependence of g_K on μ, we may expect the ratio $\tau_1^{\text{coll}}/\tau_1$ to increase as μ^2 or faster.

In SC geometry, the $\boldsymbol{k} = 0$ correlation function is related to the so-called Glarum functional, obtained by replacing ε by $\varepsilon(\omega)$ on the right-hand side of (3.26). A simple calculation shows that the Debye approximation to $C_1^{\text{coll}}(t)$ is now

$$C_1^{\text{coll}}(t) = \exp\left[-(2+\varepsilon)\,t/3\tau_D\right] \qquad \text{(SC)} \tag{3.47}$$

and $\tau_1^{\text{coll}}(\text{SC}) = 3\tau_D/(2+\varepsilon)$. The rate of decay for large t is, therefore, dramatically faster than when the same function is calculated *via* the EK method: (3.45) and (3.47) show that $\tau_1^{\text{coll}}(\text{SC})/\tau_1^{\text{coll}}(\text{EK}) \simeq 3/\varepsilon$. This result is consistent with some calculations of Adams [33] for a Stockmayer-like potential. If we approximate τ_1 by the expression (3.46), it follows that $\tau_1^{\text{coll}}(\text{SC}) \simeq (9g_K/2\varepsilon)\tau_1$ when ε is large. From the results for g_K and ε given by POLLOCK and ALDER [4] we may expect $\tau_1^{\text{coll}}(\text{SC})$ to be smaller than τ_1 for strongly polar fluids. Moreover, since ε is found to increase faster than either τ_D or g_K, we must also expect both the absolute value of $\tau_1^{\text{coll}}(\text{SC})$ and the ratio $\tau_1^{\text{coll}}(\text{SC})/\tau_1$ to decrease with increasing dipole moment. This behaviour is wholly unphysical and an artifact of the use of a truncated potential.

Finally, the functional associated with a sphere cut out of an infinite system, called the Fatuzzo-Mason functional, is obtained by replacing ε by $\varepsilon(\omega)$ on the left-hand side of (3.21). In the Debye approximation, $C_1^{\text{coll}}(t)$ decays as the sum of two exponentials, combining the time scales of the transverse and longitudinal components of the dipole-moment density:

$$C_1^{\text{coll}}(t) = \frac{1}{2\varepsilon + 1}\left(2\varepsilon \exp\left[-t/\tau_D\right] + \exp\left[-\varepsilon t/\tau_D\right]\right) \qquad \text{(infinite system).} \tag{3.48}$$

The earlier discussion might lead us to think that (3.48) is the result appro-

priate to the RF method. This is not the case, because, in the usual application of the RF method, the surroundings are characterized by a frequency-independent dielectric constant. In this case, the decay of $C_1^{\text{coll}}(t)$ (within the Debye approximation) is given [34] (with $\varepsilon' = \varepsilon$) by

$$C_1^{\text{coll}}(t) = \exp\left[-3\varepsilon t/(2\varepsilon + 1)\,\tau_{\text{D}}\right] \quad (\text{« instantaneous » RF}). \tag{3.49}$$

It is interesting and slightly unexpected that (3.45) is a better approximation than (3.49) to the infinite-system result (3.48).

What conclusions may we draw from this discussion? *a*) Since $\varepsilon(\omega)$ is independent of geometry, it is in principle irrelevant which method is used to calculate it. *b*) Once $\varepsilon(\omega)$ is known, $C_1^{\text{coll}}(t)$ can be predicted for any assumed geometry: the expressions that relate $C_1^{\text{coll}}(t)$ in different geometries are valid in general and not only (as we have used them) in the Debye approximation. *c*) In practice, use of the SC method is not a sensible way to proceed. *d*) There is little to choose between RF and EK boundary conditions, but *e*) use of the EK method does have certain advantages. Firstly, the function $C_\perp(\boldsymbol{k}, t)$ reduces to $C_1^{\text{coll}}(t)$ without a discontinuity at $\boldsymbol{k} = 0$. This is helpful if we want to use finite-wavelength results in an effort to improve the statistics of the calculation. Secondly, the truncation of the dipolar interaction at $R = R_c$ leads to problems of energy drift in the RF calculations. To avoid this it is necessary either to rescale the velocities at frequent intervals or to smooth the discontinuity by means of a « tapering » function [34]. Neither solution is ideal. In the EK method, the difficulty does not arise, because the real-space part of the Ewald-Kornfeld potential is short ranged.

We end by briefly reviewing some of the scientific (rather than methodological) conclusions that have been reached. One particularly interesting question concerns the nature of the oscillations seen in the function $C_\parallel(\boldsymbol{k}, t)$ at small $\boldsymbol{k}$. As we mentioned earlier, oscillations have been observed both for the Stockmayer fluid [37] and for a model of acetonitrile [38], but the physical origin of the effect is believed to be different in the two systems. In both cases, the oscillations may be viewed as arising from a coherent superposition of single-molecule motions. For the Stockmayer fluid, the oscillations are considered to be « inertial » in character; at long wavelength, the frequency of the oscillations is accurately given by a calculation based on free-rotor behaviour (which itself is oscillatory). The collective mode is called a « dipolaron », by analogy with the plasmon mode of ionic fluids. For acetonitrile, the oscillations are characterized as « librational », *i.e.* they correspond to a trapped reorientational motion that is strongly dependent on the intermolecular torques rather than on the inertial properties of the molecule.

A second question of interest concerns the relation between τ_{D} and τ_1. If we identify τ_{D} with $\tau_1^{\text{coll}}(\text{EK})$, all published results to date show that (3.46) overestimates τ_{D} by a factor of between one and two. Equation (3.46) is some-

times written in the modified from

$$\tau_D = \frac{3\varepsilon g_K}{2\varepsilon + 1} \frac{\tau_1}{1 + f}, \tag{3.50}$$

in which g_K includes the known effects of static cross-correlations between dipoles, while f describes the (unknown) effects of dynamical cross-correlations; the significance of f is discussed in the appendix. The available results show that f is always positive, with a typical numerical value of about one-half. Dynamical cross-correlations, therefore, partly offset the purely static effects.

We must remember, finally, that real molecules are polarizable. This fact makes a fully realistic simulation of dielectric response a truly formidable problem, but one that is certain to attract increasing attention in the future.

Appendix

Derivation of eq. (3.50).

We may write a memory function equation [39] for $C_\perp(\boldsymbol{k}, t)$ in the form

$$\lim_{\boldsymbol{k}\to 0} \tilde{C}_\perp(\boldsymbol{k}, \omega) = \frac{1}{-i\omega + \tilde{N}_\perp(\boldsymbol{k}, \omega)} \tag{A.1}$$

with

$$N_\perp(\boldsymbol{k}, t = 0) = \lim_{\boldsymbol{k}\to 0} \frac{\langle \hat{M}_x(\boldsymbol{k})\, \hat{M}_x(-\boldsymbol{k})\rangle}{\langle \hat{M}_x(\boldsymbol{k})\, \hat{M}_x(-\boldsymbol{k})\rangle} = \frac{4\pi\beta}{3V} \frac{\langle |\dot{\boldsymbol{M}}(0)|^2\rangle}{\varepsilon - 1}, \tag{A.2}$$

where we have used (3.18) and the fact that the components of $\dot{\boldsymbol{M}}$ are all equivalent. If the time dependence of $N_\perp(k, t)$ is approximated by a delta-function, (A.1) reduces to (3.41), with the Debye relaxation time identified as

$$\tau_D = \frac{3V}{4\pi\beta} \frac{\varepsilon - 1}{\langle |\dot{\boldsymbol{M}}(0)|^2\rangle}. \tag{A.3}$$

For $C_1(t)$, we may similarly write

$$\tilde{C}_1(\omega) = \frac{1}{-i\omega + \tilde{N}_1(\omega)} \tag{A.4}$$

with (remembering that $\boldsymbol{u}$ is a unit vector)

$$N_1(t = 0) = \langle |\dot{\boldsymbol{u}}|^2\rangle = \frac{1}{3N\mu^2} \langle |\dot{\boldsymbol{M}}(0)|^2\rangle. \tag{A.5}$$

If we suppose that $N_1(t)$ is also a delta-function in time, (A.4) becomes

$$C_1(t) = \frac{1}{-i\omega + 1/\tau_1} \tag{A.6}$$

with τ_1, the integral correlation time of subsect. 3·2, given by

$$\tau_1 = \frac{N\mu^2}{\langle |\dot{\boldsymbol{M}}(0)|^2 \rangle} . \tag{A.7}$$

Equation (3.46) now follows immediately from (A.3) and (A.7) if we substitute for g_K from (3.21).

The key approximation made above is that the time dependence of the two memory functions is the same; apart from the neglect of any $\boldsymbol{k}$-dependence in $C_1(t)$, this is completely analogous to an approximation used by KIM and NELKIN [40] in a study of density fluctuations in liquids. Equation (3.46) relies additionally on the assumption that both memory functions are delta-functions. Some allowance for the fact that the two memory functions will, in general, evolve differently in time can be made in *ad hoc* fashion by introducing the factor $(1 + f)^{-1}$ on the right-hand side of (3.50). There is an inconsistency here, since the fact that all quantities in (3.50) are independent of frequency implies that the memory functions are equal apart from a constant, multiplicative factor. The role of the dynamical correlations, therefore, appears as a scaling of the static correlations (in practice, as a reduction, because f turns out to be positive).

REFERENCES

[1] G. D. HARP and B. J. BERNE: *Phys. Rev. A*, **2**, 975 (1970).
[2] B. J. BERNE and G. D. HARP: *Adv. Chem. Phys.*, **17**, 63 (1970).
[3] B. J. ALDER and T. E. WAINWRIGHT: *J. Chem. Phys.*, **27**, 1208 (1957).
[4] E. L. POLLOCK and B. J. ALDER: *Physica (Utrecht) A*, **102**, 1 (1980).
[5] A. RAHMAN and F. H. STILLINGER: *J. Chem. Phys.*, **55**, 3336 (1971).
[6] H. J. C. BERENDSEN: *Molecular Dynamics and Monte Carlo Calculations on Water* (CECAM Report, 1972).
[7] F. H. STILLINGER: *Adv. Chem. Phys.*, **31**, 1 (1975).
[8] J. BAROJAS, D. LEVESQUE and B. QUENTREC: *Phys. Rev. A*, **7**, 1092 (1973).
[9] P. S. Y. CHEUNG and J. S. POWLES: *Mol. Phys.*, **30**, 921 (1975).
[10] J. P. RYCKAERT and A. BELLEMANS: *Chem. Phys. Lett.*, **30**, 123 (1975).
[11] D. LEVESQUE, J. J. WEIS and D. W. OXTOBY: *J. Chem. Phys.*, **79**, 917 (1983).
[12] K. SINGER, A. J. TAYLOR and J. V. L. SINGER: *Mol. Phys.*, **33**, 1957 (1977).
[13] D. J. EVANS and S. MURAD: *Mol. Phys.*, **34**, 327 (1977).
[14] J. P. RYCKAERT, G. CICCOTTI and H. J. C. BERENDSEN: *J. Comput. Phys.*, **23**, 327 (1977).
[15] W. F. VAN GUNSTEREN and H. J. C. BERENDSEN: *Mol. Phys.*, **34**, 1311 (1977).
[16] G. CICCOTTI, M. FERRARIO and J. P. RYCKAERT: *Mol. Phys.*, **47**, 1253 (1982).

[17] M. R. BATTAGLIA, T. I. COX and P. A. MADDEN: *Mol. Phys.*, **37**, 1413 (1979).
[18] W. B. STREETT and D. J. TILDESLEY: *Proc. R. Soc. London, Ser. A*, **348**, 485 (1976).
[19] W. B. STREETT and D. J. TILDESLEY: *Proc. R. Soc. London, Ser. A*, **355**, 239 (1977).
[20] C. G. GRAY and K. E. GUBBINS: *Theory of Molecular Fluids*, Vol. **1** (Oxford, 1984), appendix A.
[21] M. S. WERTHEIM: *J. Chem. Phys.*, **55**, 4291 (1971).
[22] H. J. BOHM, P. A. MADDEN and I. R. MCDONALD: *Mol. Phys.*, **49**, 347 (1983).
[23] S. MURAD, D. J. EVANS, K. E. GUBBINS, W. B. STREETT and D. J. TILDESLEY: *Mol. Phys.*, **37**, 725 (1979).
[24] I. R. MCDONALD, D. G. BOUNDS and M. L. KLEIN: *Mol. Phys.*, **45**, 521 (1982).
[25] R. W. IMPEY, P. A. MADDEN and D. J. TILDESLEY: *Mol. Phys.*, **44**, 1319 (1981).
[26] P. A. MADDEN and D. KIVELSON: *Adv. Chem. Phys.*, **56**, 467 (1984).
[27] G. N. PATEY: *Mol. Phys.*, **35**, 1413 (1978).
[28] P. H. FRIES and G. N. PATEY: *J. Chem. Phys.*, **82**, 429 (1985).
[29] J. G. KIRKWOOD: *J. Chem. Phys.*, **7**, 911 (1939).
[30] S. W. DELEEUW, J. W. PERRAM and E. R. SMITH: *Proc. R. Soc. London, Ser. A*, **373**, 27 (1980).
[31] B. U. FELDERHOF: *Physica (Utrecht) A*, **101**, 275 (1980).
[32] J. A. BARKER and R. O. WATTS: *Mol. Phys.*, **26**, 789 (1973).
[33] D. J. ADAMS: *Proc. R. Soc. London, Ser. A*, **394**, 137 (1984).
[34] M. NEUMANN, O. STEINHAUSER and G. S. PAWLEY: *Mol. Phys.*, **52**, 97 (1984).
[35] S. W. DELEEUW, J. W. PERRAM and E. R. SMITH: *Proc. R. Soc. London, Ser. A*, **388**, 177 (1983).
[36] G. N. PATEY, D. LEVESQUE and J. J. WEIS: *Mol. Phys.*, **45**, 733 (1982).
[37] E. L. POLLOCK and B. J. ALDER: *Phys. Rev. Lett.*, **46**, 950 (1981).
[38] D. M. F. EDWARDS, P. A. MADDEN and I. R. MCDONALD: *Mol. Phys.*, **51**, 1141 (1984).
[39] J. P. HANSEN and I. R. MCDONALD: *Theory of Simple Liquids* (London, 1976), Chapt. 9.
[40] K. KIM and M. NELKIN: *Phys. Rev. A*, **4**, 2065 (1971).

Simulation of Properties of Spectroscopic Interest.

P. A. MADDEN

Physical Chemistry Laboratory,
University of Oxford, South Parks Road, Oxford OX13 QZ, *U. K.*

1. – Introduction.

Spectroscopic studies of liquids are undertaken in order to build detailed pictures of molecular motion and to understand, at a microscopic level, the interaction of radiation with matter. Computer simulations have proven invaluable aids to these goals and, in addition, provide a route by which the ideas derived from spectroscopic studies can be linked to the interpretation of other measured quantities, such as transport coefficients. In describing the relationship I will not be concerned with questions of simulation technique, most of the studies made to date have used standard molecular-dynamics methods. Instead I shall attempt to explain why the application of simulation methods to interpret spectroscopic data is necessary and to illustrate the kind of information which has been gained. The principles involved here are very general, though I will only be able to demonstrate them with a limited number of examples.

All the experimental quantities with which I shall be concerned may be regarded as some functional of a two-point correlation function of a collective, dynamical property of the system [1]. For example, an infra-red absorption lineshape $(I(\omega))$ may be related to the symmetrized correlation function of the total dipole density $(\boldsymbol{M})$ of the sample

$$I(\omega) \leftrightarrow \int_0^\infty \mathrm{d}t \exp[-i\omega t] \tfrac{1}{2} \{\langle M_z(t) M_z(0)\rangle + \langle M_z(0) M_z(t)\rangle\} . \tag{1}$$

Notice that I have not written « proportional to », the actual relationship is more complex than that [1, 2]. Such relationships may be derived for spectroscopic lineshapes and relaxation times by linear-response theory [1-3]: non-linear-optics experiments which give dynamical information may be also be expressed in the same general way [4]. In standard computer simulations correlation functions are calculated classically (though quantum techniques are under

development [5]); the most appropriate way to connect such functions with experiment is to regard them as an approximation to the symmetrized correlation function above. In this way detailed-balance effects should come out correctly though, of course, any specifically quantum effect on the dynamics (*e.g.*, tunnelling) will not be described. Quantum effects on dynamical experiments have been estimated from classical simulations [6] and quantum simulations are under development [7]. Having issued these sketchy warnings and suggested some useful references, I will now introduce these macroscopic relationships between observables and classical correlation functions out of a hat as the need arises!

Since correlation functions may be determined from experiment, where does the need for simulations arise? I suggest there are two central reasons. The first is that even the ideal experiment does not give enough information to form a good picture of the molecular motion. The perfect n.m.r. relaxation time gives only the integral of a time correlation function; even a full orientational correlation function, from an idealized Raman spectrum, tells us relatively little about the intermolecular encounters (as we shall see). With simulations many properties which are not experimentally observable may be calculated. These may be used to *enhance* the specificity of the information which may be obtained from experiment, by providing better windows on the microscopic world. The earliest simulations of spectroscopic quantities were undertaken for this reason [3, 8] and had a considerable impact.

The second reason is that the relationships between observables and correlation functions involve only collective variables of the whole system. These correlation functions must be related to molecular behaviour and, at a quantitative level, this is a far from trivial process. Consider the infra-red absorption. At frequencies near to a vibrational transition the important part of the dipole density will be that which is modulated by the relevant molecular vibrational normal co-ordinate (q^i)

$$\boldsymbol{M}(t) = \sum_{\substack{i \\ (\mathrm{mol})}} \boldsymbol{m}^i q^i , \tag{2}$$

where

$$\boldsymbol{m}^i = \frac{\partial \boldsymbol{M}}{\partial q^i} . \tag{3}$$

In a conventional view infra-red bandshapes give orientational correlation functions, this arises when $\boldsymbol{M}$ is taken to be just the sum of the molecular dipoles ($\boldsymbol{M} = \sum \boldsymbol{\mu}^i$) so that

$$\boldsymbol{m}^i = \frac{\partial \boldsymbol{\mu}^i}{\partial q^i} = \left(\frac{\partial \mu}{\partial q}\right) \boldsymbol{e}^i , \tag{4}$$

where $\boldsymbol{e}^i$ is a unit vector along the dipole direction. Following the conventional

line further gives

$$(5)\qquad I(\omega) \leftrightarrow \int_0^\infty \mathrm{d}t \exp[-i\omega t] \sum_{ij} \langle m_z^i(t) m_z^j \rangle =$$

$$= \int_0^\infty \mathrm{d}t \exp[-i\omega t] \left(\frac{\partial \mu}{\partial q}\right)^2 N \langle e_z^1(t) e_z^1(0) q^1(t) q^1(0) \rangle =$$

$$= \int_0^\infty \mathrm{d}t \exp[-i\omega t] \left(\frac{\partial \mu}{\partial q}\right)^2 N \langle e_z^1(t) e_z^1(0) \rangle \langle q^1(t) q^1(0) \rangle .$$

Between the 1st and 2nd lines the correlation between the normal co-ordinates on different molecules is ignored and between the 2nd and 3rd the correlation between the vibrational and rotational degrees of freedom is neglected. Both of these approximations *may* be appropriate for some vibrations of some liquids. The vibrational correlation function is measurable, from the isotropic Raman lineshape, so that it appears that the 1st-rank orientational correlation function

$$(6)\qquad C_1(t) = \langle P_1(\boldsymbol{e}^1(t) \cdot \boldsymbol{e}^1(0)) \rangle$$

(where P_l is an l-th order Legendre function) is also measurable. However, there is a still more pernicious approximation undermining the conventional view; this is that the total dipole density is the sum of molecular dipoles, calculated as if the molecules were isolated (*i.e.* eq. (4)). In fact, there are additional dipoles due to the intermolecular interactions (« interaction-induced » dipoles), *i.e.* in fact

$$(7)\qquad \boldsymbol{m}^i(t) = {}^0\boldsymbol{m}^i(t) + {}^1\boldsymbol{m}^i(t) ,$$

where ${}^0\boldsymbol{m}^i$ is the isolated molecule dipole and ${}^1\boldsymbol{m}^i$ the interaction-induced one. For example, the dipoles induced by the electric fields due to the permanent dipoles of neighbouring molecules (dipole-induced dipoles) are given by

$$(8)\qquad {}^1\boldsymbol{m}^i = \sum_{j \neq i} \frac{\partial \boldsymbol{\alpha}^i}{\partial q^i} \cdot \boldsymbol{T}(\boldsymbol{r}^{ij}) \cdot \bar{\boldsymbol{\mu}}^j + \boldsymbol{\alpha}^j \cdot \boldsymbol{T}(\boldsymbol{r}^{ij}) \cdot \left(\frac{\partial \boldsymbol{\mu}^i}{\partial q^i}\right),$$

where $\boldsymbol{\alpha}^i$ and $\bar{\boldsymbol{\mu}}^i$ are the molecular polarizability and dipole moment and $\boldsymbol{T}(\boldsymbol{r})$ is the dipole-dipole tensor

$$(9)\qquad \boldsymbol{T}(\boldsymbol{r}) = (4\pi\varepsilon_0)^{-1} (3\boldsymbol{r}\,\boldsymbol{r} - \boldsymbol{r}^2 \boldsymbol{I}) r^{-5} .$$

Consequently, instead of eq. (5) we now have

$$(10)\qquad I(\omega) \leftrightarrow \int_0^\infty \mathrm{d}t \exp[-i\omega t] N \{ \langle {}^0m_z^1(t) {}^0m_z^1(0) \rangle + 2 \langle {}^0m_z^1(t) {}^1m_z^1(0) \rangle + \langle {}^1m_z^1(t) {}^1m_z(0) \rangle \} \langle q^1(t) q^1(0) \rangle$$

and the spectrum reflects not just the relaxation of the molecular orientation (now in the first term of the curly brackets) but also that of the induced dipole, which is due to the relative motion of molecules, and of the interference between the two processes.

Although this point has been worked through here for the specific case of i.r. absorption, the principle is quite general: observations tend to be influenced by more than one dynamical process, one of which is often intermolecular. The i.r. lineshape is influenced by orientational relaxation, vibrational relaxation and by intermolecular motion, but they cannot be separated by experimental considerations alone. Simulation can be of great value in *unravelling* the influence of the various processes. The earliest simulation study undertaken for this reason was probably that of Frenkel and McTague [9]. If we take an optimistic (rather than conventional) view, we could claim that simulations may restore the status of observable to quantities such as the orientational correlation function. Whilst the point is general, the extent of the problem varies from one experimental technique to another. Neutron scattering and n.m.r. suffer least from interaction-induced effects, whereas nonlinear-optics measurements are probably worst.

The central principle to be adopted in comparing experiments and simulation is that the experimental observations can be extremely good, *i.e.* quantities such as the i.r. lineshape can be measured with high precision. The problem arises in breaking down the observation into a picture of molecular behaviour. Consequently the simulation should be refined and tested by direct comparison with the experimentally measured quantity. We should ideally calculate $I(\omega)$ (or an analogous measured quantity) with as good a representation for $\boldsymbol{M}$ (and as good a potential) as we can devise, rather than compare some easy to calculate quantity like a relaxation time with something deduced by interpreting an experiment. If the simulation can reproduce such direct observations, we may then interrogate it with a detail not available to the experimentalist with some confidence that the picture, so obtained, has something to do with reality.

In order to illustrate the application of simulation methods, I shall focus in some detail on properties of carbon disulphide and contrast, relatively briefly in sect. **5**, the behaviour of other liquids with it. CS_2 has a long liquid range and I shall be concerned with its behaviour below the boiling point, where it is a rather dense liquid. The attractive intermolecular interactions in CS_2 are fairly weak and nonspecific, so that packing effects and the repulsive forces are most important in determining the structure and dynamics. The potential which has been used in the simulations was devised to give an extremely good representation of the thermodynamic and structural properties of the liquid [10] and the dynamical properties were found to be very good too [11].

The properties with which I shall be concerned are associated with the reorientation and translation of single molecules, as these are probably of the most general interest. I shall briefly discuss spectra of other motions in sect. **6**.

2. – On relating experimental and simulation results.

2·1. *Interaction-induced effects in the Raman spectrum.* – Although this may seem a somewhat technical subject with which to start, I have chosen it (and the subject of the next section) so as to emphasize from the beginning the importance of the correct approach to experimental data.

A problem arises with interaction-induced effects in trying to extract information on reorientation from depolarized Raman spectra which is entirely analogous to that described for i.r. in the introduction. The expressions for the correlation functions which determine the Raman spectrum are the same as for the i.r. case, except that molecular dipoles ($\boldsymbol{\mu}$) are replaced by laser-induced dipoles ($\boldsymbol{\alpha}\cdot\boldsymbol{E}$).

For the depolarized spectrum we need to calculate [9]

$$V^{-1}\langle M_z(t)\,M_z\rangle = \varrho\,\{\langle {}^0m_z^1(t)\,{}^0m_z^1\rangle + 2\,\langle {}^0m_z^1(t)\,{}^{\mathrm{I}}m_z^1\rangle + \langle {}^{\mathrm{I}}m_z^1(t)\,{}^{\mathrm{I}}m_z^1\rangle\} \tag{11}$$

with the laser polarized along the x-direction. This gives (for a linear molecule, like CS_2)

$$ {}^0m_z^1 = \frac{\partial\alpha_{zx}^1}{\partial q^1}E = \gamma e_z^1 e_x^1 E\,, \tag{12}$$

where γ is the vibrationally modulated molecular-polarizability anisotropy. If we use only the dipole-induced dipole (DID) term analogous to eq. (8),

$$ {}^{\mathrm{I}}m_z^1 = \sum_{j\neq 1}\left\{\frac{\partial\boldsymbol{\alpha}^1}{\partial q^1}\cdot\boldsymbol{T}(\boldsymbol{r}^{ij})\cdot\boldsymbol{\alpha}^j + \boldsymbol{\alpha}^j\cdot\boldsymbol{T}(\boldsymbol{r}^{j1})\cdot\frac{\partial\boldsymbol{\alpha}^1}{\partial q^1}\right\}_{zx}. \tag{13}$$

The DID expression is only the leading term [12] in expansions of the induced dipole in a multiple-scattering series and also treats the molecular polarizability as if concentrated at a point, overlap effects may also give induced moments. It is diffucult to represent these extra terms in a simulation.

For N_2, which is not very polarizable and not far from spherical, the extra terms are very small and the simple DID expression gives a very good representation of the interaction-induced effects. Thus in the case of N_2 the ideal of faithfully simulating the observed Raman lineshape is a realistic goal. This has been done by SAMPOLI and co-workers [13] (following pioneering studies of this type by FRENKEL and MCTAGUE [9]) and essentially perfect agreement between experimental and calculated lineshapes obtained. The agreement is so good that the simulated correlation functions can be regarded as those of the real fluid; such functions will be discussed below.

For more anisotropic and polarizable molecules, like CS_2, the importance of both higher-order DID terms [14] and of the distribution of polarizable matter [15] has been demonstrated. In such cases we must settle for rather less

than an *a priori* realistic simulation. Experimentalists have always approached the issue of separating interaction-induced and reorientational effects with the idea that the latter dominate the low-frequency region of the spectrum. This idea may be justified (*v.i.*) if there is a time scale separation between the slow relaxation of the molecular orientation and the rapid relaxation of the intermolecular co-ordinates; it is stimulated by the shape of the observed spectra in dense fluids, which show a pronounced low-frequency peak (see fig. 1). This idea has been investigated in a simulation of CS_2 using the DID model as a representative of the induced dipole [14].

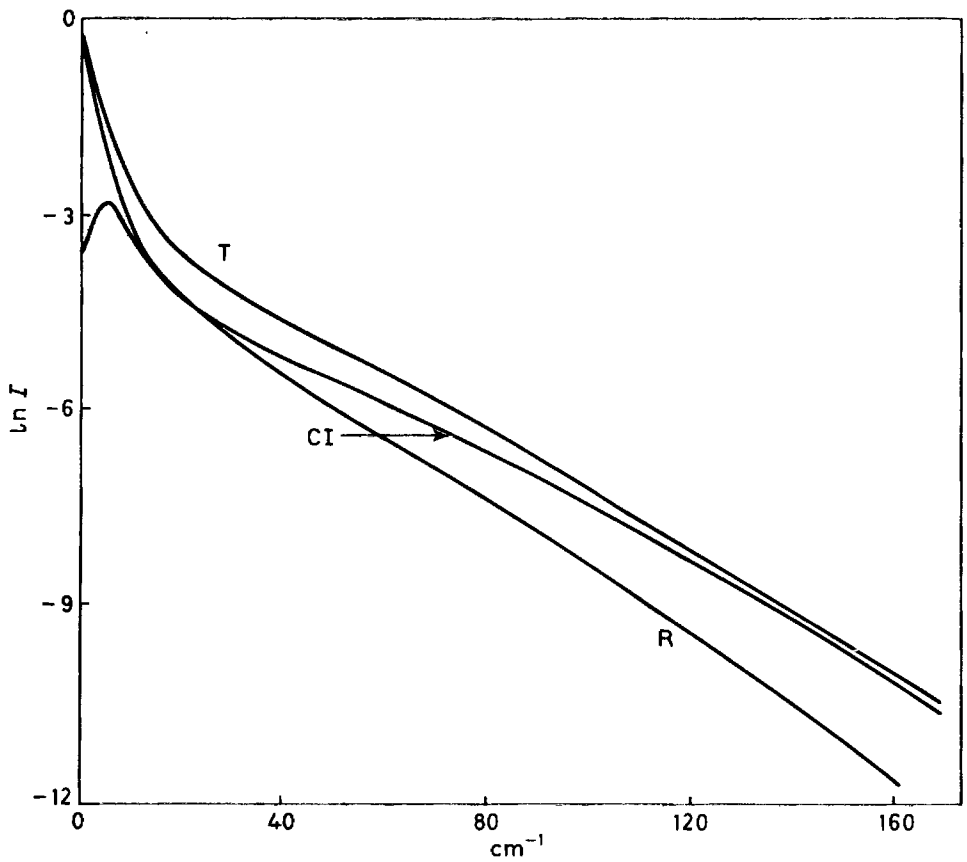

Fig. 1. – Simulated Raman spectrum of CS_2 at 244 K (ref. [14]). T gives the total spectrum, which is very similar to the observed one. R and CI give the reorientational and collision-induced components (eq. (17)).

The three correlation functions of eq. (11), the a.c.f.'s of ${}^0\boldsymbol{m}^1$ and ${}^1\boldsymbol{m}^1$ and the interference term, are shown in fig. 2. The correlation between the induced and molecular dipole is large. There is no obvious difference in time scales and the prospect for recognizing the three functions in a spectrum by their distinctive frequency signature is bleak.

An alternative basis for unravelling the spectrum is obtained through a different decomposition of the total dipole; rather than eq. (7) write

$$m_z^1(t) = (1+f)\,{}^0m_z^1(t) + \delta m^1(t)\,, \tag{14}$$

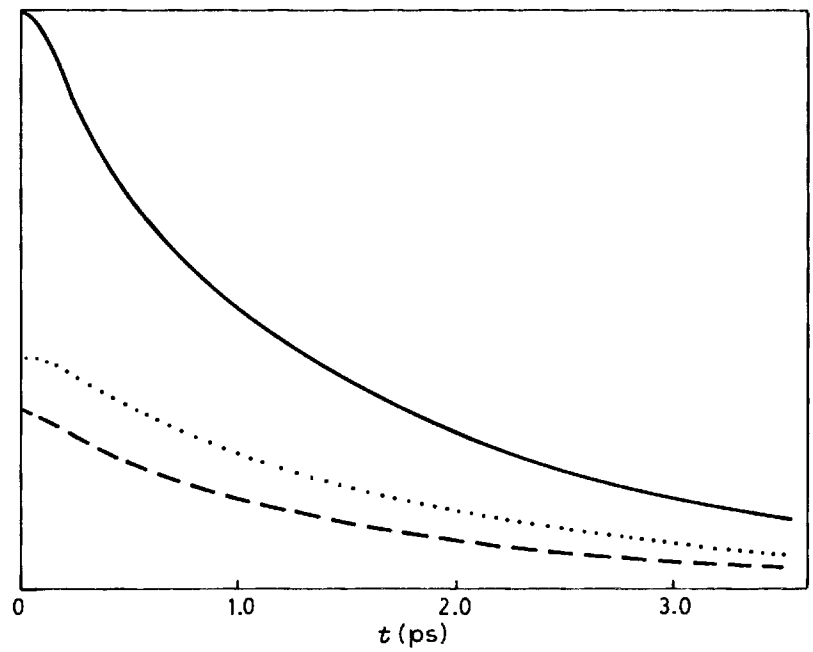

Fig. 2. – The three correlation functions of eq. (11) for the Raman spectrum of CS_2 at 244 K: — — ${}^0\boldsymbol{m}$, ··· interference term, — — — ${}^I\boldsymbol{m}$.

where

$$\delta m_z^1 = {}^I m_z^1 - f\,{}^0 m_z^1 \tag{15}$$

and

$$f = \langle {}^I m_z^1\, {}^0 m_z^1 \rangle / \langle {}^0 m_z^1\, {}^0 m_z^1 \rangle \,. \tag{16}$$

f is called the *projection* of the induced dipole along the molecular one. It may be thought of as the average induced dipole for a given molecular orientation. The dipole-induced dipole of a nonspherical molecule with its neighbours in their average position is nonzero, due to the closer proximity of the equatorial neighbours [12]. $f\,{}^0 m_z^1$ represents this nonzero average and δm_z^1 is the remaining part of the instantaneous induced dipole, due to fluctuations in the positions of the neighbours. In this representation the idea of the time scale separation is that the relaxation of the neighbours to their equilibrium position following a change in the orientation of the central molecule is rapid compared to the overall rate of molecular reorientation. The *mean* induced dipole will then follow the reorientation of the central molecule and the remaining fluctuating part relax rapidly. The total correlation function, now written

$$\langle M_z(t)\, M_z \rangle = \varrho(1+f)^2 \langle {}^0 m_z^1(t)\, {}^0 m_z^1 \rangle + \\ + \varrho\,[\langle \delta m_z^1(t)\, \delta m^1 \rangle + 2(1+f)\langle \delta m_z^1(t)\, {}^0 m_z^1 \rangle]\,, \tag{17}$$

should then contain a slow, reorientational part (given by the first term in

eq. (17)) and a rapidly relaxing part given by the square-bracketed term, which may be called fluctuation- or collision-induced. Note that the amplitude of the reorientational contribution to the spectrum is modified by a «local-field factor» given by $(1+f)^2$ [16].

The three correlation functions in eq. (17) are shown in fig. 3. While $\langle \delta m_z(t)\, \delta m_z \rangle$ is appreciably faster than $\langle {}^0m_z(t)\, {}^0m_z \rangle$, it still contains a slowly relaxing tail—as does the cross term. However, as the figure shows, these tails are of opposite sign and their combination, in the square-bracketed term of eq. (17), is rapidly relaxing. The spectrum calculated in the simulation is

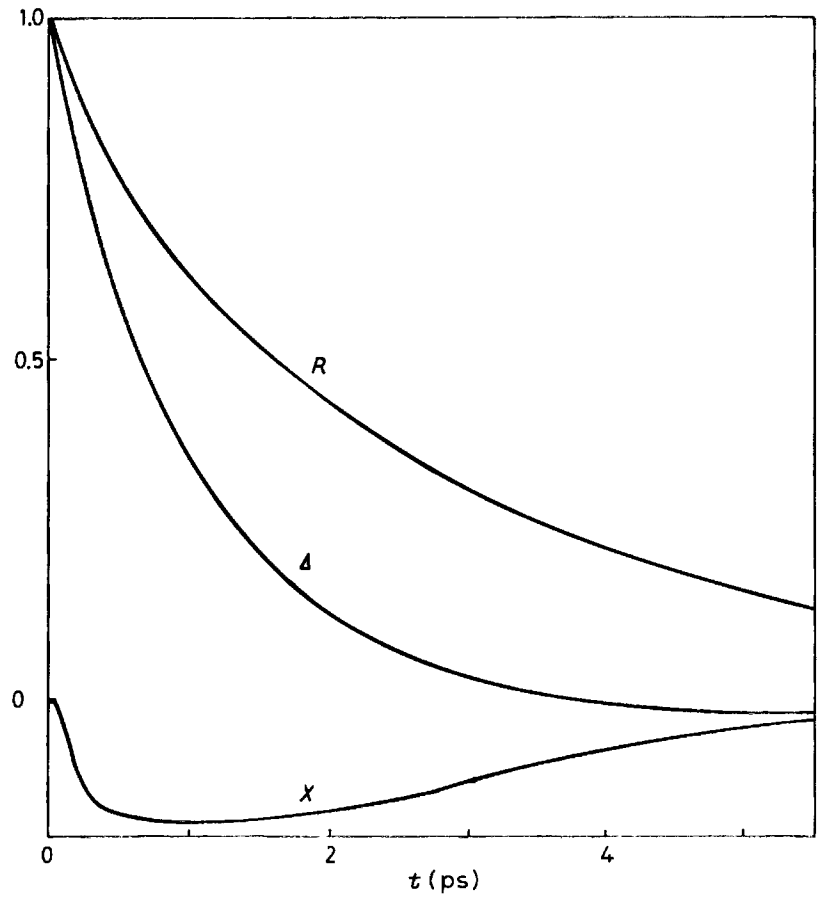

Fig. 3. – The three correlation functions of eq. (17) for the Raman spectrum of CS_2 at 244 K.

shown in fig. 1. Its shape is very similar to the experimental one. The shapes of the reorientational and collision-induced contributions to the spectrum are also shown. The reorientational term dominates the low-frequency spectrum and the collision-induced one the high-frequency wings.

This implies that we can obtain only a limited amount of information from the experimental spectrum. The low-frequency feature is well described by a Lorentzian, the width of which we can identify as a molecular reorientation time (discussed below). Its amplitude is modified by the $(1+f)^2$ local-field

factor which is calculable in the simulation [13-16]. However, since the spectrum beyond about 20 cm^{-1} is strongly influenced by the collision-induced effects, we cannot really learn anything about the reorientational correlation function for times less than ~ 0.25 ps. Unfortunately, this is the regime in which any interesting information on intermolecular events is likely to be contained.

In closing this section I should like to re-emphasize the generality of the phenomenon I have discussed. The problem arises whenever a molecular property (here a polarizability) is affected by intermolecular interactions. The result is to limit in a specific way the amount of microscopic information which can be obtained directly from the experiment. The time scale separation is not general—it is a property of the liquid and was not found in similar studies of N_2 and CO_2 [13, 15]. It is consistent with a stable cage of neighbours around a CS_2 molecule. Finally simulation studies have been made to clarify the role of interaction-induced effects in other experiments, in particular dielectric absorption [17] and transient nonlinear-optics [18] measurements.

2·2. *The Raman and* n.m.r. *reorientation times.* – Having established that some information on molecular reorientation can be obtained from the Raman spectrum in CS_2, we now consider the orientational correlation function calculated in the simulation.

The orientation correlation functions, $C_1(t)$, $C_2(t)$ and $C_3(t)\big(C_l = \langle P_l(\boldsymbol{e}^1(t)\cdot\boldsymbol{e}^1)\rangle\big)$, are shown plotted in fig. 4 as $[l(l+1)]^{-1}\times\ln C_l(t)$. The reason for choosing

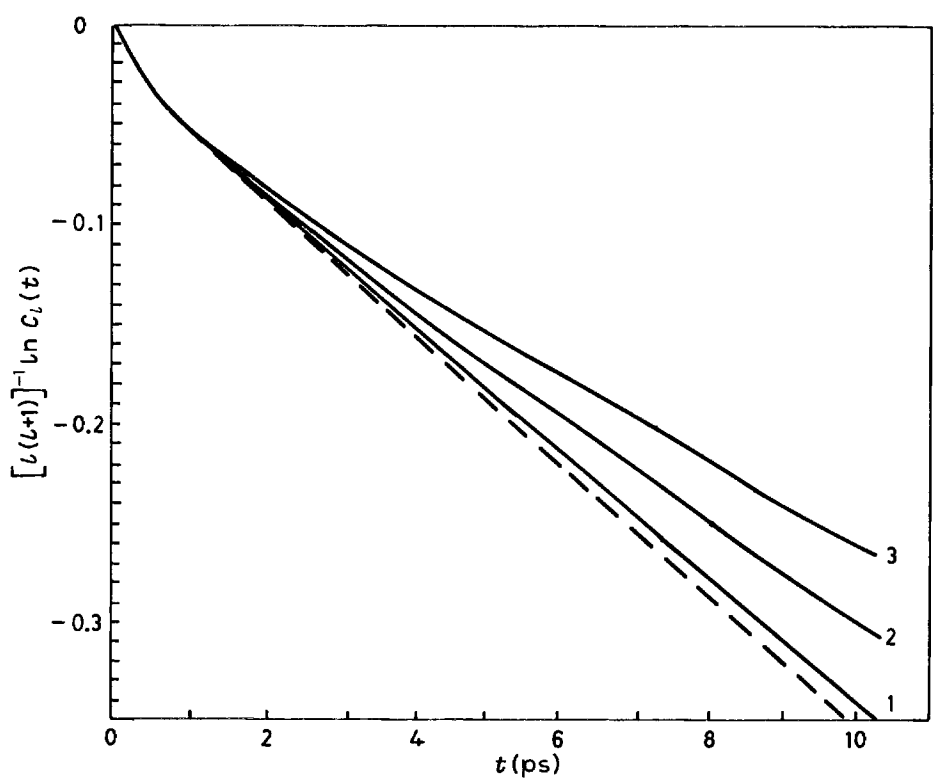

Fig. 4. – The orientational correlation functions for CS_2 at 191 K, plotted as $(l(l+1))^{-1}\ln C_l(t)$ for $l = 1, 2, 3$. The dashed line shows the cumulant approximant.

this representation will become clear later. We note that after about 0.7 ps the decay of these functions is exponential, showing that on this time scale the reorientation is Markovian, as the result of many uncorrelated steps. In this regime the relaxation is characterized by a simple linear decay law

$$\frac{\partial C_l}{\partial t} = -\tau_{l,\mathrm{SI}}^{-1} C_l(t) \tag{18}$$

and all information on the nature of individual elementary encounters has been lost. For example, N_2 and H_2O also show such long-time exponential decay. At earlier times nonexponential decay is seen and the shape of the correlation function does vary from one fluid to another. This non-Markovian behaviour is a result of the discrete nature of the intermolecular encounters and an understanding of it should give us some insight into the molecular motion; at least, this is the reason for pursuing these spectroscopic studies.

$C_1(t)$ (in part) determines the shape of an i.r. spectrum and we have seen that the reorientational correlation function $C_2(t)$ dominates the low-frequency part of the Raman spectrum. C_3 cannot be measured. To what extent can the experimentally available information on $C_2(t)$ be used to verify that the simulated functions are a good representation of reality? Since the low-frequency Raman spectrum is characterized by a Lorentzian, only the exponential region of C_2 is determined. The Lorentzian half-width may be compared with the decay time $\tau_{2,\mathrm{SI}}$ characterizing the slope of the linear region of $\ln C_2(t)$ in fig. 4. The interesting short-time behaviour produces non-Lorentzian features in the reorientational spectrum at such high frequencies that it is obscured by the collision-induced spectrum. The correspondence between the exponential slopes of the simulation and the Lorentzian widths of the experiment is very good [11], but this hardly serves to confirm the veracity of the short-time behaviour.

Information on the reorientation of a CS_2 molecule is also obtained from the ^{13}C n.m.r. relaxation times [19]; a contribution due to chemical shift anisotropy relaxation can be separated [20] which (as the chemical shift anisotropy is well known) gives the time integral of C_2

$$\tau_{2,\mathrm{n.m.r.}} = \int_0^\infty \mathrm{d}t\, C_2(t)\,. \tag{19}$$

If $C_2(t)$ were perfectly exponential, then $\tau_{2,\mathrm{SI}}$ (from Raman) and $\tau_{2,\mathrm{n.m.r.}}$ would agree. However, a bump at short times in the real $C_2(t)$ of the type and amplitude seen in the simulated $C_2(t)$ would lead to $\tau_{2,\mathrm{n.m.r.}}$ being about 10 % larger than $\tau_{2,\mathrm{SI}}$. This is exactly the behaviour found experimentally [21].

Of course, this corroboration of the short-time, nonexponential character exhibited by the simulated correlation function will not convince the real sceptic as it involves taking the experimental results very seriously. My view

is that in favourable cases (like CS_2) the experimental measurements are potentially very accurate. In these cases precision is lost when the experiments are not properly interpreted. In this case precision has been retained by carefully simulating what is actually measured.

From here on I shall be concerned rather less with closely tying experimental and simulation results and more with exploring how simulations have been used to build up a picture of molecular motion, beginning with more detailed studies of the nonexponential behaviour of time correlation functions at short times.

3. – Detailed studies of short-time effects.

3·1. *The diffusion coefficient and the velocity correlation function.* – The diffusion coefficient is obtained experimentally (and in a simulation) from the mean square displacement of a molecule

$$\lim_{t\to\infty} \frac{\partial}{\partial t} \langle (\Delta r^i(t))^2 \rangle = 6D\,. \tag{20}$$

However, it is more interesting, from a molecular viewpoint, to regard it as the time integral of the velocity autocorrelation function (VACF). In a fixed co-ordinate system a component of the displacement vector obeys

$$\Delta r^i_\alpha(t) = \int_0^t \mathrm{d}\tau\, V^i_\alpha(t)\,, \tag{21}$$

where $\boldsymbol{V}^i$ is the molecular velocity. It can then be shown that

$$\frac{\partial}{\partial t} \langle (\Delta r^i_\alpha(t))^2 \rangle = 2\int_0^t \mathrm{d}\tau\, \langle V^i_\alpha(\tau)\, V^i_\alpha(0) \rangle + \lim_{\delta\to 0} \frac{1}{\delta} \int_{t-\delta}^{t+\delta} \mathrm{d}t\, (t-\tau) \langle V^i_\alpha(\tau)\, V^i_\alpha(0) \rangle \tag{22}$$

and, when t is larger than the relaxation time of the velocity, the second term vanishes, leaving

$$D = (1/3) \int_0^\infty \mathrm{d}\tau\, \langle \boldsymbol{V}^i(\tau) \cdot \boldsymbol{V}^i \rangle\,; \tag{23}$$

the relationship of D to the VACF is, therefore, the same as that of the n.m.r. relaxation time to C_2.

The diffusion coefficients found in the CS_2 simulations agree well with experiment. The velocity a.c.f. at 191 K (approaching the triple point) is shown in fig. 5 [11] The negative portion shows that, on average, molecules have a

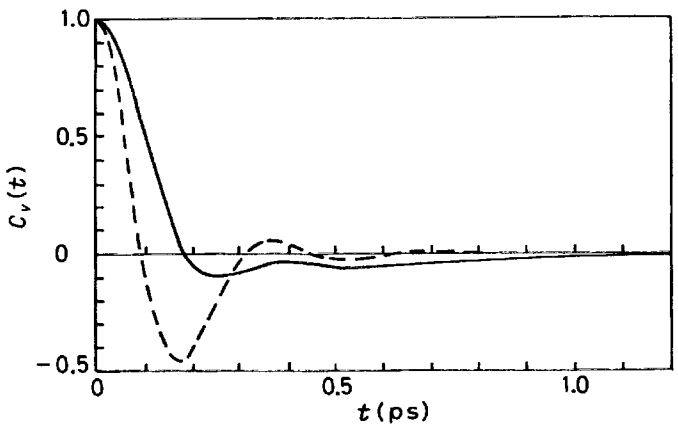

Fig. 5. – The velocity a.c.f. for CS_2 at 191 K. The dashed line shows the force a.c.f.

tendency to have a component of velocity in the reverse direction after about 0.2 ps. This shape is typical of that seen in many simulations of dense fluids; the reversal is interpreted as a rebound from a cage of neighbours [22]. The depth of the minimum increases as the fluid becomes denser and leads to a rapid decrease in the value of the diffusion coefficient.

The nature of the rebound becomes clearer when we resolve the velocity [22, 23] into its components parallel and perpendicular to the molecular axis at time zero. We can define two a.c.f.'s which monitor this resolved motion

$$C_v^{\parallel}(t) = \frac{\langle (\boldsymbol{V}^i(0)\cdot \boldsymbol{e}^i(0))(\boldsymbol{V}^i(t)\cdot \boldsymbol{e}^i(0))\rangle}{\langle (\boldsymbol{V}^i(0)\cdot \boldsymbol{e}^i(0))^2\rangle} \tag{24}$$

and

$$C_v^{\perp}(t) = \frac{\langle (\boldsymbol{V}^i(0)\times \boldsymbol{e}^i(0))\cdot(\boldsymbol{V}^i(t)\times \boldsymbol{e}^i(0))\rangle}{\langle (\boldsymbol{V}^i(0)\times \boldsymbol{e}^i(0))^2\rangle}\,; \tag{25}$$

they are shown for the 191 K run on CS_2 in fig. 6. The perpendicular motion is much more strongly hindered than the parallel one. The structure of the cage must persist for quite a long time otherwise the forces would become

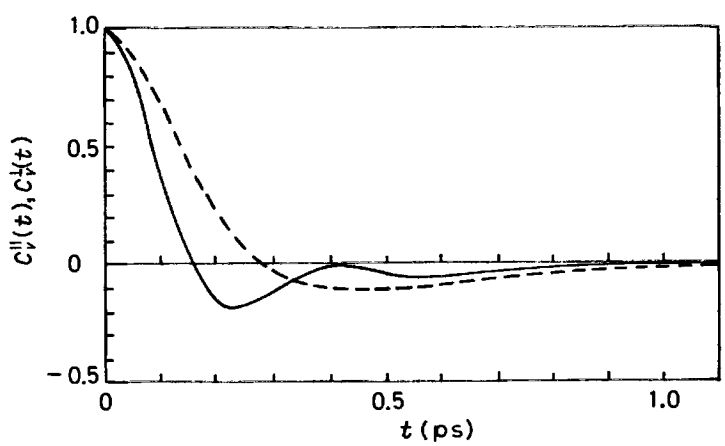

Fig. 6. – The resolved VACFS for CS_2 at 191 K: dashed, parallel; solid, perpendicular.

uncorrelated and the velocity correlation function would decay exponentially.

At first sight $C_v^{\parallel}$ and $C_v^{\perp}$ appear dead at about 1 ps; however, this view is quite erroneous, as the following argument shows. According to eq. (22) we may define the diffusion coefficient from either $C_v^{\parallel}$ or $C_v^{\perp}$, *i.e.*

$$\int_0^\infty \mathrm{d}\tau\, C_v^{\parallel}(\tau) = \int_0^\infty \mathrm{d}\tau\, C_v^{\perp}(\tau) \tag{26}$$

(that is, the molecule must eventually forget its initial orientation and diffuse isotropically in space). Further, the ∞ may be replaced by a finite time after which the VACFs are zero. However, the « by eye » integral of $C_v^{\parallel}$ out to 1 ps is clearly larger than that of $C_v^{\perp}$, in fact they are in the ratio of about two to one. This implies that the molecule remembers its initial orientation and that the VACFs persist out to much longer times than 1 ps. Just how long this persistence is can be made clear by plotting the components of the molecular displacement in the initial molecular frame, *i.e.*

$$\langle(\Delta r_{\parallel}^i)^2(t)\rangle = \langle[(\boldsymbol{r}^i(t) - \boldsymbol{r}^i(0))\cdot \boldsymbol{e}^i(0)]^2\rangle \tag{27}$$

and

$$\langle(\Delta r_{\perp}^i)^2(t)\rangle = \langle[(\boldsymbol{r}^i(t) - \boldsymbol{r}^i(0))\times \boldsymbol{e}^i(0)]^2\rangle\,, \tag{28}$$

as shown in fig. 7.

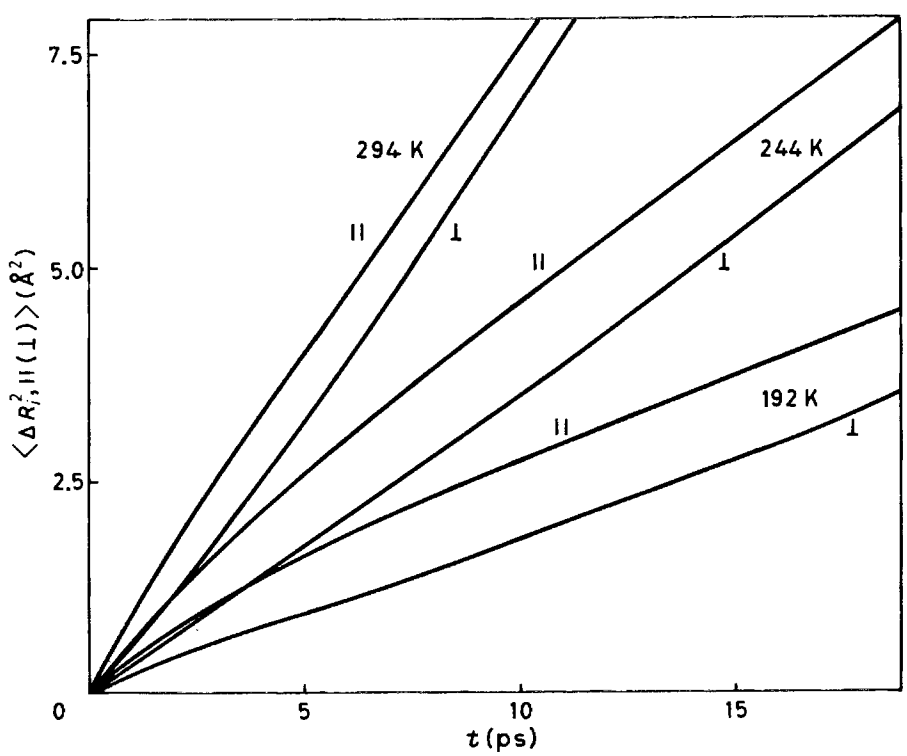

Fig. 7. – The resolved mean-square displacements for CS_2.

At long times

$$\frac{\partial}{\partial t}\langle(\Delta r^i_{\parallel\,\perp})^2(t)\rangle = \frac{2k_{\mathrm{B}}T}{m}\int_0^t C_v^{\parallel(\perp)}(\tau)\,\mathrm{d}\tau \tag{29}$$

and, also at long times,

$$\frac{\partial}{\partial t}\langle(\Delta r^i_{\parallel})^2(t)\rangle = \frac{\partial}{\partial t}\langle(\Delta r^i_{\perp})^2(t)\rangle\,. \tag{30}$$

The simulation data show that these slopes do not become equal out to very long times. One must conclude that the existence of the cage produces an intermediate-time tail in the velocity correlation. It is clear that great care must be taken in obtaining a diffusion coefficient by integrating the VACF.

This preferential displacement of molecules parallel to their initial orientation has no effect on macroscopic measurements of diffusion. However, it has implications for the interpretation of spectroscopic measurements which probe intermolecular interactions at short times, for example, interaction-induced spectra, and for quasi-elastic neutron scattering measurements. It is a rather simple rotation-translation coupling effect.

3·2. *The orientational and angular-velocity correlation functions.* – Unfortunately the relationship between the observed measure of angular displacement (*i.e.* the orientational c.f.) and the relevant velocity (the angular velocity) is less straightforward than in the translational case. In many studies orientational correlation functions have been analysed using the memory function formalism [24]; there is some resemblance between the first memory function and the angular-velocity correlation function when the reorientation is strongly hindered. The memory function formalism is very useful for tying together the results of diverse experiments. However, I now believe that a more informative way to analyse the simulation data is via a cumulant expansion; this approach has been developed by LYNDEN-BELL [25].

The rate of change of some function of the orientation of a particular molecule is given by

$$\frac{\partial}{\partial t}f(Q^i(t)) = i\boldsymbol{\omega}^i(t)\cdot\hat{\mathscr{L}}f(Q^i(t))\,, \tag{31}$$

where $\boldsymbol{\omega}$ is the angular velocity and $\hat{\mathscr{L}}$ is an infinitesimal rotation operator (familiar from quantum mechanics as the angular-momentum operator). Integrating gives

$$f(Q^i(t)) = \exp_0\left[i\int_0^t \boldsymbol{\omega}^i(t')\cdot\mathscr{L}\,\mathrm{d}t'\right]f(Q^i(0))\,, \tag{32}$$

where $\exp_0$ denotes a time-ordered exponential. Now consider an *isotropic* ensemble of molecules. To get the average *change* in f we may take an axis system for each molecule which coincides with the molecular axis system at $t = 0$, so that $f(Q(0))$ is the same for each molecule. It follows that the average effect of orientation is described by the reorientation propagator

$$\hat{R}(t) = \left\langle \exp_0 \left[i \int_0^t \boldsymbol{\omega}^1(t') \cdot \hat{\mathscr{L}} \, \mathrm{d}t' \right] \right\rangle . \tag{33}$$

A standard way of approximating the average of a time-ordered exponential is to express it in the cumulant averages of $\boldsymbol{\omega}$ [26], *i.e.*

$$\hat{R}(t) = \exp \left[\sum_n \hat{K}_n(t) \right] . \tag{34}$$

If we take the case of a linear molecule for simplicity, then the first few cumulants are

$$\hat{K}_1(t) = \int_0^t \mathrm{d}t_1 \langle \omega_\alpha(t_1) \rangle \hat{\mathscr{L}}_\alpha = 0 , \tag{35a}$$

$$\hat{K}_2(t) = \int_0^t \mathrm{d}t_1 \int_0^t \mathrm{d}t_2 \{ \langle \omega_\alpha(t_1) \omega_\beta(t_2) \rangle - \langle \omega_\alpha(t_1) \rangle \langle \omega_\beta(t_2) \} \hat{\mathscr{L}}_\alpha \hat{\mathscr{L}}_\beta = \\ = \int_0^t \mathrm{d}t_1 \, (t - t_1) \langle \boldsymbol{\omega}(t_1) \cdot \boldsymbol{\omega}(0) \rangle \hat{\mathscr{L}}^2 , \tag{35b}$$

$$\hat{K}_3(t) = \ldots = 0 , \tag{35c}$$

$$\hat{K}_4(t) = \ldots = \int_0^t \mathrm{d}t_1 \int_0^t \mathrm{d}t_2 \int_0^t \mathrm{d}t_3 [\langle \omega_\alpha(t_1) \omega_\beta(t_2) \omega_\gamma(t_3) \omega_\delta(t_4) \rangle - \\ - \langle \omega_\alpha(t_1) \omega_\beta(t_2) \rangle \langle \omega_\gamma(t_3) \omega_\delta(t_4) \rangle - \langle \omega_\alpha(t_1) \omega_\gamma(t_3) \rangle \langle \omega_\beta(t_2) \omega_\delta(t_4) \rangle - \\ - \langle \omega_\alpha(t_1) \omega_\delta(t_4) \rangle \langle \omega_\beta(t_2) \omega_\gamma(t_4) \rangle] \hat{\mathscr{L}}_\alpha \hat{\mathscr{L}}_\beta \hat{\mathscr{L}}_\gamma \hat{\mathscr{L}}_\delta . \tag{35d}$$

By virtue of the time ordering $t_1 > t_2 > t_3 > t_4$. In the second equality in each case we have neglected those terms which vanish because they involve averages in an odd power of a component of $\boldsymbol{\omega}$.

The particular combination of correlation functions which make up the cumulant averages has the following very important properties:

i) If any pair of factors within a cumulant is uncorrelated, then the cumulant vanishes. Suppose the angular velocity of a molecule loses its memory on a time scale of τ_ω, then any $\langle \ldots \rangle_c$ in which two times differ by more than τ_ω will vanish (*e.g.*, in the $\hat{K}_4$ term if $t_1 - t_4 > \tau_\omega$). This means that at long times ($t > \tau_\omega$) all the cumulants simply become proportional to t.

ii) At short times the integral can be expanded as a series in even powers of t, the $2n$-th cumulant is proportional to t^{2n}. Thus the higher-order cumulants are unimportant at short times.

iii) All cumulants except $\hat{K}_2$ vanish if $\boldsymbol{\omega}(t)$ is a Gaussian process; that is, if a time series of values of $\boldsymbol{\omega}$ ($\boldsymbol{\omega}(t_1)$, $\boldsymbol{\omega}(t_2)$, etc.) appears as if selected from a Gaussian probability distribution. This behaviour is characteristic of a process to which many independent degrees of freedom contribute simultaneously and weakly. Since the angular velocity is linearly related to the torques, it is sufficient that the torques have this property. The Gaussian limit is an important case in theories of molecular motion as it corresponds to Brownian motion.

To evaluate the correlation function [25] $C_l(t)$ we take the matrix elements of $R(t)$ between spherical harmonics of rank l. For a linear molecule

$$C_l(t) = (2l+1)\int \mathrm{d}Q P_l(\cos Q)\hat{R}(t)P_l(\cos Q)\,. \tag{36}$$

Notice that, by virtue of i) above, $C_l(t)$ has to be exponential at sufficiently long times ($t > \tau_\omega$). The simplest approximation is to retain only the $\hat{K}_2$ term in the cumulant expansion. From ii) above this will be valid at short times and from iii) it will be valid at long times to the extent that $\boldsymbol{\omega}(t)$ is Gaussian. The $\hat{K}_2$ term is proportional to $\hat{\mathscr{L}}^2$ and, therefore,

$$C_l(t) = \exp\left[-l(l+1)\int_0^t \mathrm{d}\tau\,(t-\tau)\langle\boldsymbol{\omega}(\tau)\boldsymbol{\omega}\rangle\right]. \tag{37}$$

This establishes a relationship between C_l and the AVACF and makes clear the limits of its applicability.

We can test the validity of the lower cumulant approximation rather easily by plotting the functions $[l(l+1)]^{-1}\ln C_l(t)$ *vs.* t for several values of l. As eq. (37) shows, these plots will coincide if the approximations is accurate. Higher-order cumulants are proportional to higher powers of $\hat{\mathscr{L}}^2$ and, therefore, give contributions of higher powers in $l(l+1)$ to the decay rate, causing the plots to fan out. In the CS_2 data (fig. 4) the non-Gaussian effects are discernible, but overall the truncated cumulant expansion works remarkably well. In particular, it works over the region in which the C_l are nonexponential. This shows that we can account for the non-Markovian behaviour from the properties of the AVACF.

The AVACF for CS_2 is shown in fig. 8. Its shape is very similar to that of the VACF and may be described with the same rebound/caging concept. Since the second derivative of the AVACF is the torque CF and that of the VACF is the force CF, this implies a close similarity for the relaxation of the force and torque, which is again consistent with the cage idea.

The dashed line in fig. 4 shows the orientational CF predicted by the truncated

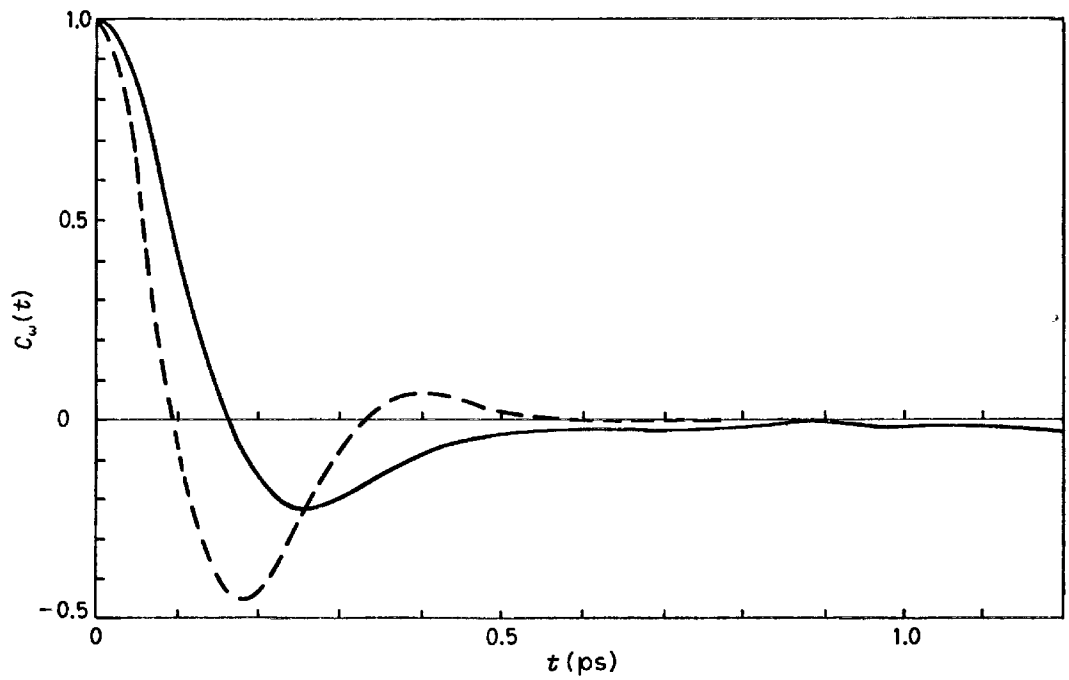

Fig. 8. – The angular-velocity a.c.f. for CS_2 at 191 K. The dashed line shows the torque a.c.f.

cumulant scheme, *i.e.* eq. (37). To see how the shape of the AVACF determines the form of the short-time behaviour of C_l, we note that ln $C_l(t)$ is (roughly) proportional to t times the integral of the AVACF up to time t. If the AVACF decayed monotonically (no rebounds), the integral would continually increase until $t > \tau_\omega$ when it would become constant and ln C_l *vs.* t would be concave downwards. In the rebound case when the motion is strongly hindered the integral passes through a maximum when the AVACF passes through zero and approaches the asymptotic value from below, consequently ln $C_l(t)$ shows a point of inflexion—as observed in CS_2. This shape is thus characterisitc of a molecule undergoing strongly hindered motion.

4. – Probing the intermolecular encounters.

So far we have seen how several (almost) observable properties of CS_2 show characteristics which indicate the existence of a well-packed cage of neighbours which persists for an appreciable time. Despite this, these characteristics have not really helped us understand the nature of the cage nor brought us closer to formulating a description of its influence at even a semi-quantitative level. By following the relationship of one correlation function to another and analysing these functions using theories which attempt to bypass the description of molecular interactions (*e.g.*, memory function analysis) most simulation studies have simply copied the approach that experimentalists have pursued over the last twenty years (though probably to greater effect). In so doing a

great deal has been learnt about the way certain experiments probe the liquid, but very little has been been done to establish a conceptual framework from which a unifying, theoretical description of molecular motion in a dense liquid might emerge.

4·1. *Cages, rebounds, etc.* – Since cages and rebounds do seem to be useful ideas in describing motion in a dense liquid, it seems appropriate to try to observe them *per se*. Some work has been done along these lines. Since the full phase-space distribution function contains too much information, some significant projection of it must be identified. Unfortunately, once one departs from the well-trodden path of interrelated correlation functions, the choice of an interesting measure of a concept, such as a cage, becomes very subjective. Consequently these studies tend to have been conducted in isolation and have had little impact; however, there are signs that this is changing with the growing realization that the traditional measures have not yielded much insight.

Among the interesting measures which have been studied are the distribution of times and distances between successive reversals of the velocity [22, 27], the velocity of a particle relative to that of a neighbour and the momentum transferred between them [28, 29] and the rate of change of the occupants of

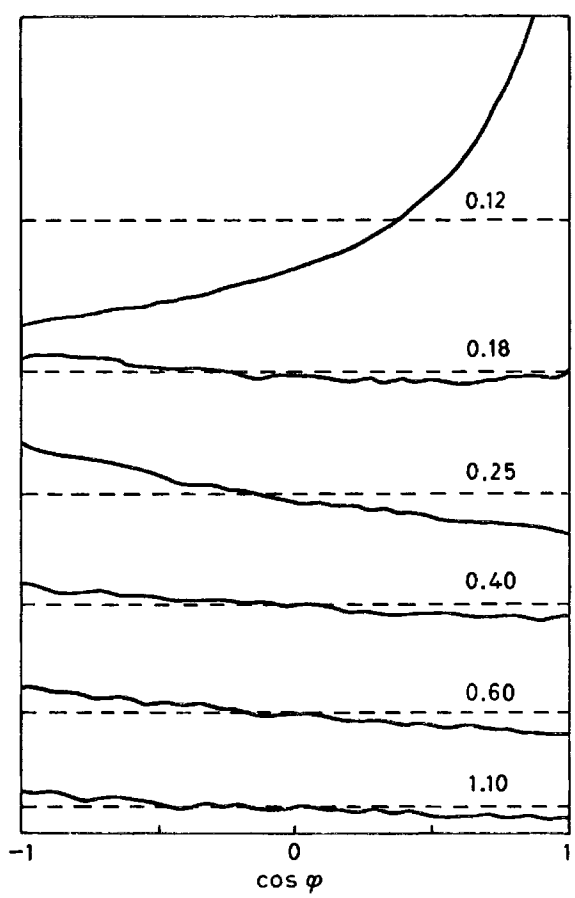

Fig. 9. – Plots of $\cos\varphi$ (eq. (38)) *vs.* φ at various time delays for CS_2 at 191 K. From ref. [30].

the nearest-neighbour shell and the velocity CF of the shell with respect to the central particle [31]. Here I shall just describe some results of Hutchinson and Lynden-Bell [30] on CS_2 and CF_4 (for which the results are very similar).

These authors have calculated for each particle trajectory

$$\cos\varphi(\Delta t) = \hat{V}(t_1 + \Delta t)\cdot\hat{V}(t_1) \tag{38}$$

(where $\hat{V}$ is a unit vector along the istantaneous velocity) and assigned the results to a series of bins in $\cos\varphi$, averaging over t_1. The result is shown in fig. 9 for several values of Δt. It shows that the distribution of $\cos\varphi$ at about the first zero of the VACF is almost uniform, but at later times it builds up in the reverse direction—the velocity appears to recover its memory! More insight is gained by slicing the distribution in the other direction. Figure 10 shows

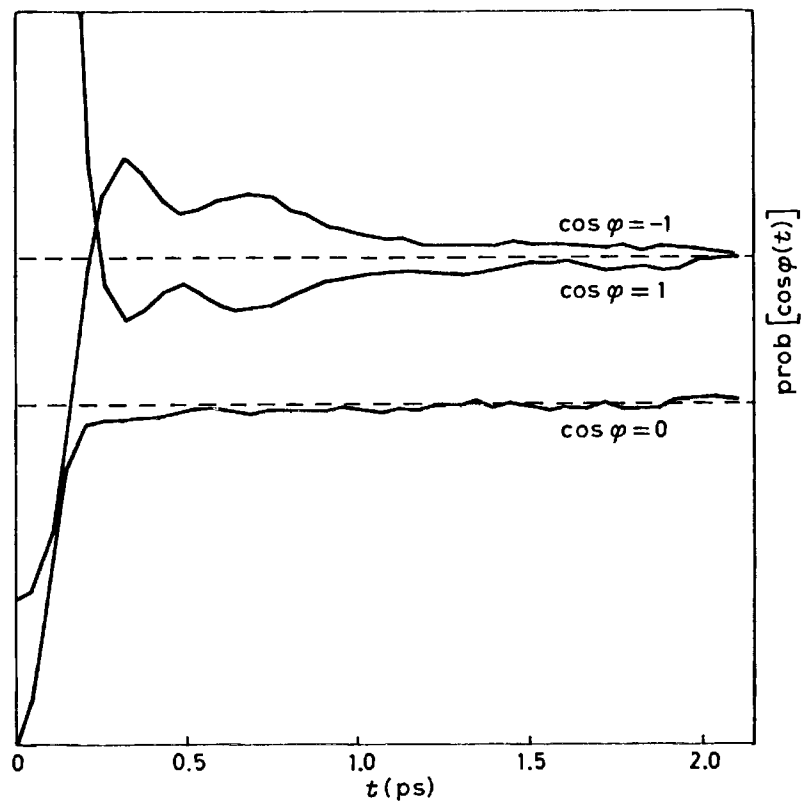

Fig. 10. – The probability *vs.* delay time, that the molecular velocity is parallel, anti-parallel and perpendicular to its original direction, for CS_2 at 191 K. From ref. [30].

the probability as a function of time in forward ($\cos\varphi = 1$), backward ($\cos\varphi = -1$) and sideways ($\cos\varphi = 0$) directions. Both the forward and backward probabilities show extrema which are very similar to those which occur in the VACF; the sideways distribution is featureless. This suggests the possibility that the structure in the VACF is due to a small number of molecules rattling backwards and forwards with the majority being involved in more serious impacts with more rapid loss of memory.

LYNDEN-BELL and co-workers also examined the nature of the cage in CF_4. They showed that, in the dense liquid, the identity of the molecules in the cage changed rather slowly (87 % were still in the same shell after 7 ps). However, this is about the decay rate expected from diffusion out of a spherical region with the radius of the cage so that specific « bonds » are not involved. This contrasts with the finding of similar studies on the water cage around an ion in solution [31].

4·2. *Why do the torques appear Gaussian?* – As we have seen, the truncated cumulant expansion appears to give a good description of the orientational correlation function in CS_2 (and many other liquids [25]). This implies that the angular velocity and the underlying torques are behaving as if they are Gaussian, especially at short times. This finding is somewhat surprising as the more direct monitors of the intermolecular events (subsect. 4·1) point to the importance of some rather strong collisional events, which might have been expected to lend a Poisson character to the torques. It is not surprising that in the Markov regime, where linear transport laws describe the correlation function, we should have lost the information on the individual intermolecular events and see only their cumulative effect [32] (as in Brownian motion, which is typically Gaussian). What is disappointing is that, having gone to great lengths to find the non-Markovian, short-time behaviour in CS_2, we find that it too is Gaussian and therefore, by implication, also carries little information about molecular encounters. One response to this problem would be to invent experiments which probe other than two-point time correlation functions; so far this has not been done in studies of molecular liquids (though it has for macromolecular solutions [33]). We also note that non-Gaussian effects lead at long times (cf. fig. 4) to a breakdown of the Debye relationships between relaxation times (*e.g.*, $\tau_1/\tau_2 = 3$); this phenomenon has been known for many years [34] but has produced little detailed insight. Here I would simply like to investigate the circumstances under which strong non-Gaussian effects can be seen in orientational correlation functions.

As noted earlier (subsect. 3·2) the initial decay of the correlation function is dominated by the second cumulant, the higher-order terms grow (if the angular velocity is non-Gaussian) and reach their asymptotic values at a time of order τ_ω. The relative size of these asymptotic terms is [35]

$$\hat{K}_{2n} \Rightarrow \frac{t}{\tau_\omega}\left(\frac{kT}{I}\tau_\omega^2\right)^n (\hat{\mathscr{L}}^2)^n . \tag{39}$$

$(kT/I)^{\frac{1}{2}}$ is the mean angular speed, so that $(kT/I)^{\frac{1}{2}}\tau_\omega$ is, roughly, the mean angular displacement before the angular velocity loses memory. If this is very small, the second cumulant will dominate at all times and only apparent Gaussian behaviour will be observed *irrespective* of the true statistics of the inter-

molecular torques. If, on the other hand, $(kT/I)^{\frac{1}{2}}\tau_\omega$ approaches unity, then any non-Gaussian effects will show up in the orientational correlation function.

A very good illustration of this prediction occurs in methyl cyanide (CH_3CN) when the orientational correlation functions which describe the motion of the symmetry axis (tumbling) are contrasted [35] with those which describe the reorientation about the symmetry axis (spinning): they are denoted $C_l(t)$ and $S_m(t)$ respectively. The C_l and S_m correlation functions determine the shapes of i.r. and Raman lines of parallel and perpendicular vibrations and their time integrals determine n.m.r. correlation times.

The tumbling and spinning motions are generated by the components of the angular velocity perpendicular and parallel to the molecular axis, respectively. The correlation functions of these components of the angular velocity are shown in fig. 11. They decay on similar time scales ($\tau_\omega \sim 0.6$ ps); the perpendicular term shows a rebound, but the parallel does not, probably because the end-over-end motion has to displace a larger volume of the surrounding fluid. Despite the fact that τ_ω for the two motions is about equal, the angular distance travelled in this time is very different, due to the small moment of inertia about the molecular axis. For the tumbling motion $(KT/I_\perp)^{\frac{1}{2}}\tau_\omega$ is 0.085, whereas for spinning $(kT/I_\parallel)^{\frac{1}{2}}\tau_\omega$ is 0.58 (at 291 K). The low value for the

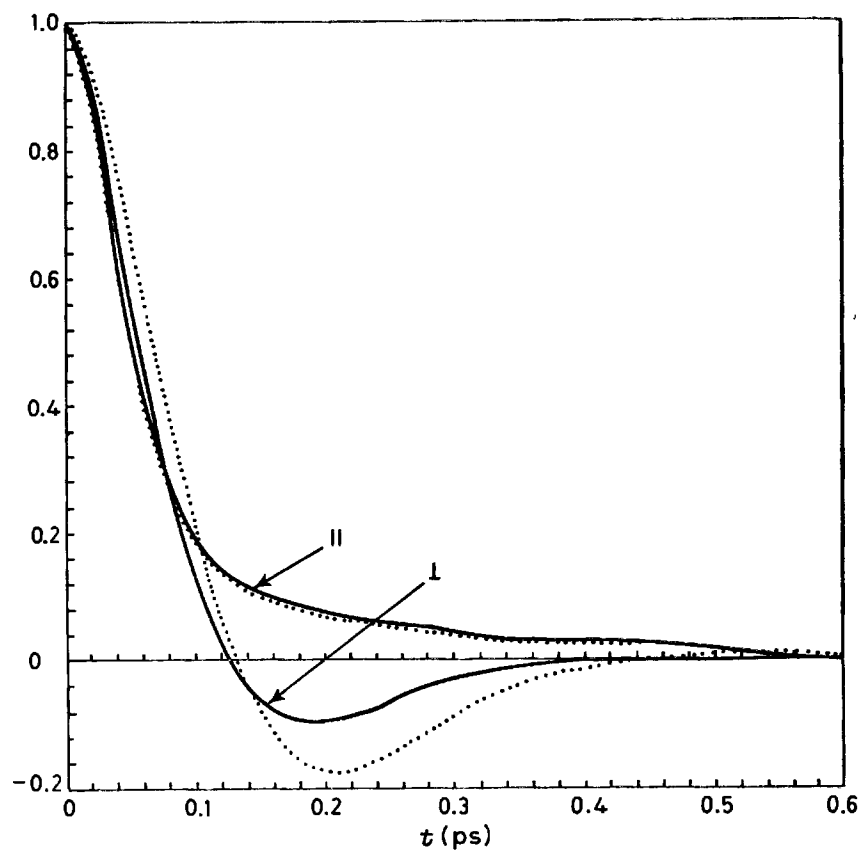

Fig. 11. – The a.c.f.'s of the parallel and perpendicular components of the angular velocity of CH_3CN (with respect to the molecular axis) are shown by the solid lines (ref. [35, 36]).

tumbling motion means that spinning motion is almost planar and that the lowest cumulant is a good approximation to $C_l(t)$ (which is found to be very similar in shape to the C_l functions for CS_2, fig. 4).

Figure 12 shows the S_m functions plotted as $m^{-2} \ln S_m(t)$, which should be m independent if the truncated cumulant were accurate. The spinning correlation function is seen to be strongly non-Markovian and non-Gaussian. The form of S_m predicted by the lowest cumulant is shown by the dashed line;

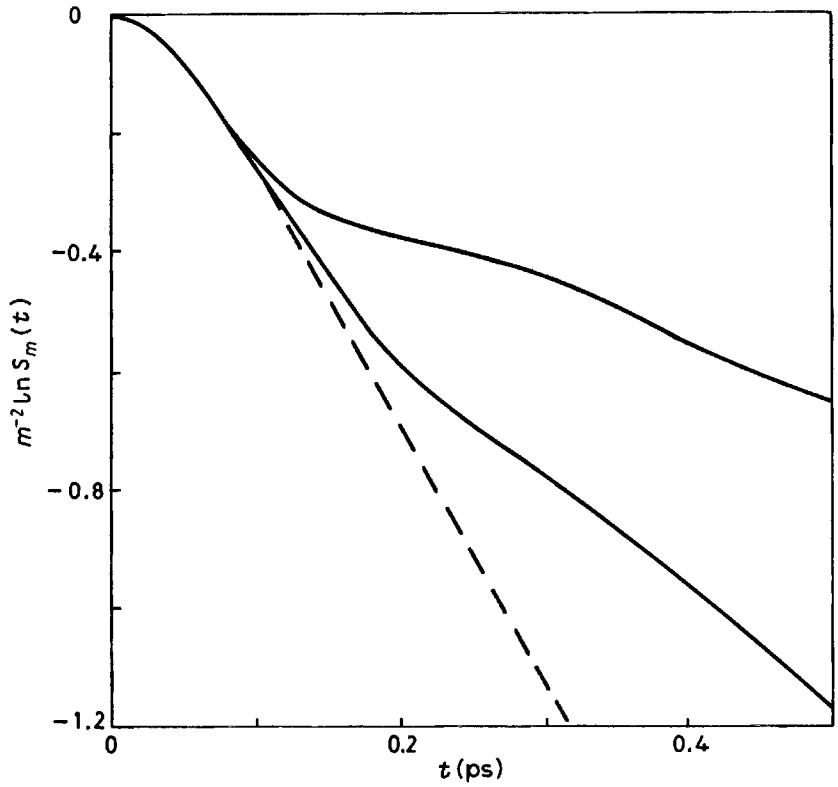

Fig. 12. – The correlation functions for the spinning motion of CH_3CN (ref. [35]) plotted as $m^{-2} \ln S_m(t)$. The dashed line is the cumulant approximant.

it exhibits none of the interesting features, consistent with the structureless form for the relevant AVACF (fig. 11). The non-Markovian nature of the spinning correlation functions is directly observable in the i.r. and Raman perpendicular bandshapes in CH_3CN—which are strongly non-Lorentzian [36, 37].

The type of process responsible for the origin of the non-Markovian, non-Gaussian features may be illustrated by comparing them with those predicted by suitably chosen stochastic equations. This type of work has been pursued by several workers in different contexts [38]. The stochastic equations may be studied by stochastic simulation methods [39] which are easy to apply. This does not give a theory of the lineshape. The stochastic simulation represents another system whose properties may be compared with those of the molecular system; in particular, the choice of stochastic equation is far from unique.

The non-Gaussian behaviour is indicative of the importance of strong, nonharmonic torques. Recalling that the spinning motion is planar, on the time scale of interest, a plausible way to mimic such effects is to consider the planar rotation in a static three-well cosine potential [35] (the average potential seen by the methyl group must have threefold symmetry). Fluctuations in the potential give rise to a drag term and a random torque which is Gaussian and relaxes instantly in time. The equations of motion are thus

$$\dot{\varphi} = \omega\,, \tag{40a}$$

$$\dot{\omega} = -\gamma\omega - \frac{V_0}{I}\cos 3\varphi + f(t)\,, \tag{40b}$$

where

$$\langle f(t)f(t')\rangle = \frac{\gamma kT}{I}\,\delta(t-t')\,. \tag{40c}$$

In the absence of the static potential these would be the (linear) equations of ordinary Brownian motion theory for which the correlation functions

$$S_m(t) = \langle \cos m\Delta\varphi(t)\rangle \tag{41}$$

would be given exactly by the lowest cumulant approximation. The background potential introduces strong nonlinear (in φ) fluctuations in the torques as the methyl group makes excursions from one minimum to another. In each minimum the torques are approximately harmonic.

The stochastically simulated $S_m(t)$ [35] are shown in fig. 13 for $V_0/kT = 1$

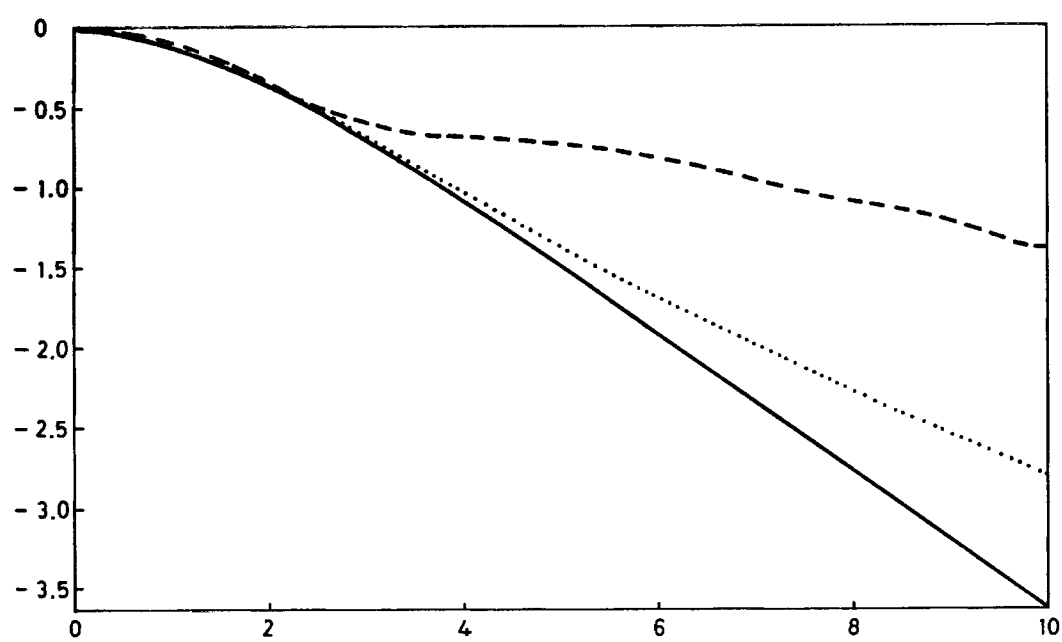

Fig. 13. – The correlation functions for the spinning motion predicted by the stochastic model of eq. (40): — — — $m = 2$, · · · $m = 1$, ——— cumulant. From ref. [35].

and $(I/kT)^{\frac{1}{2}}\gamma = 1$; the general features are very similar to those shown by the spinning correlation functions of the molecular-dynamics simulation. The cumulants of the angular velocity may also be calculated in the simulation and the second-cumulant prediction is shown by the dashed line in the figure. The idea that the departure from Gaussian behaviour is due to strong fluctuations during excursions between adjacent minima is well supported by the fact that the time at which the S_m break away from the cumulant prediction agrees with the most probable pausing time between barrier hops. Higher cumulants may also be calculated. As expected, from the discussion of subsect. 3·2, the fourth cumulant is zero at short times and becomes linear after a time which corresponds rather well with the time at which the AVACF is insignificantly different from zero.

This stochastic simulation, therefore, enables us to formulate some ideas about the local interactions felt by the methyl group. Whilst giving a reasonable representation of the orientational CF, it has other shortcomings; hopefully these can be remedied by a further dip into the brain-tub of stochastic models.

5. – Other liquids.

It would not be appropriate to end these lectures, which have almost exclusively been illustrated with work on CS_2, without contrasting the behaviour of this liquid with others which have been studied in simulations for the purpose of extracting information of spectroscopic significance.

The most extensively studied liquids have been model diatomics with or without added multipoles. SINGER and co-workers [22, 40] have made very detailed studies of two-site Lennard-Jones models which were chosen to model various real diatomics ranging from N_2, with the smallest elongation, to Br_2 and CO_2. The single-particle motion in CS_2 is very similar to that of the denser more elongated diatomics. Such characteristics as the rebounds in the AVACF and VACF and the preferential displacement along the long axis are found. For the lighter, less dense molecules, like N_2 [8, 22, 23], the motion is less strongly hindered and the orientational correlation functions show structure which is closely related to that seen in the correlation function of a free rotor [41]. STEELE and co-workers [42, 43] have followed a somewhat different line and systematically varied the potential in diatomic simulations, at the expense of comparing with real liquids, keeping the liquid density and temperature the same. In one piece of work [42] they show how varying the potential from purely repulsive site-site interactions to site-site Lennard-Jones and then adding quadrupoles changes the character of the VACF ans AVACF from weakly hindered (no rebounds) to the strong hindered situation we have examined above. They have also compared the VACF and AVACF in the liquid and solid

phases [43]. Similar work has been done by LYNDEN-BELL and MCDONALD [44], who studied the reorientational motion in tetrahedral molecules with site-site Lennard-Jones potentials which were varied so as to make the molecules increasingly « knobby ». The behaviour of the orientational correlation functions ranged from quasi-free to strongy hindered as the potential was changed. It was rationalized with the truncated cumulant scheme and various theoretical models were examined.

In the few cases in which they have been included in the potential, dipoles seem to have produced no new characteristic effects on the orientational correlation function. As we have seen, the orientational correlation functions of the tumbling motion of methyl cyanide, which has a very large dipole, were very similar to those of CS_2 [36].

In the above-mentioned fluids the attractive intermolecular forces are relatively weak and repulsions exert the strongest influence on the structure of the fluid. In simulations of water this is not so. There are strong specific forces which represent the effect of hydrogen bonds. The spectroscopic properties of water [45, 46] (and ice [47]) have been simulated to only a modest extent, probably because of worries about the quality of the available potentials. Nevertheless the simulations have proved remarkably successful in reproducing the exceptional spectroscopic phenomena normally associated with the hydrogen bond. The orientational correlation functions [45, 46] show an extraordinarily strong short-time feature, which looks like one cycle of an oscillation. The transform of these functions shows reasonable agreement with librational peaks found in the i.r., Raman and inelastic neutron spectra of water which occur at quite high frequencies. Surprisingly the usual representation (subsect. 3·2) shows that the lowest cumulant approximation describes this behaviour [46], so that it may be traced to very deep rebounds in the angular velocity. The velocity a.c.f. shows similar deep minima, which correspond to different frequencies to those which occur in the AVACF. These also have spectroscopic signatures, they occur in infra-red and Raman spectra by virtue of interaction-induced effects [48].

6. – Other topics.

So far I have confined my attention to the single-particle orientation and translation motions, for the purpose of best illustrating my theme in a limited amount of time. However, there are many other aspects of molecular dynamics which are relevant to the spectroscopy of liquids and to which simulation studies have been addressed.

6·1. *Collective vs. single-particle motion.* – Most spectroscopic experiments actually give a collective correlation function which is at least partially coherent.

For example, as McDONALD has shown, dielectric spectra give the CF of a Fourier component of the dipole density, *e.g.*

$$M_{\mathrm{T}}(\boldsymbol{k}) = \sum_i {}^{\mathrm{T}}\boldsymbol{\mu}^i e^{i\boldsymbol{k}\cdot\boldsymbol{r}^i}, \tag{42}$$

where ${}^{\mathrm{T}}\boldsymbol{u}^i$ is the transverse part of the instantaneous molecular dipole and

$$\langle \boldsymbol{M}_{\mathrm{T}}(\boldsymbol{k}, t)\cdot\boldsymbol{M}_{\mathrm{T}}(\boldsymbol{k}, 0)\rangle = \sum_{ij} \langle {}^{\mathrm{T}}\boldsymbol{\mu}^i(t)\,{}^{\mathrm{T}}\boldsymbol{\mu}^j(0)\times\exp\left[i\boldsymbol{k}\cdot\left(\boldsymbol{r}^i(t)-\boldsymbol{r}^j(0)\right)\right]\rangle \tag{43}$$

which involves the cross-correlation between the dipoles on different molecules. The same basic expression gives the vibrational infra-red spectrum (see introduction), but now the correlation function becomes incoherent (*i.e.* involves only self-terms) because it is the vibrationally modulated part of the dipole which is required and the vibrational co-ordinates on different molecules are uncorrelated. Other examples are coherent neutron scattering, Rayleigh scattering and the correlation function of interest in dynamical nonlinear-optics experiments. It can be seen that collective functions are involved in the experiments which are of the greatest technological relevance.

Theoretical considerations often lead to relationships between the relaxation times of collective and single-particle correlation functions of the form

$$\tau_{\mathrm{coll}} = \frac{g}{1+j}\,\tau_{\mathrm{sing}}, \tag{44}$$

where g is the static value of the collective CF and j measures the correlation between the time derivatives of the variables on different molecules [49]. For example, McDONALD has already discussed relationships of this form in the context of dielectric relaxation, where g is related to the Kirkwood parameter and j to the correlation between the angular velocities on different molecules. The j parameter is often neglected; for example, in the de Gennes expression relating the coherent and incoherent neutron scattering times

$$\tau_{\mathrm{coh}}(k) = S(k)\,\tau_{\mathrm{inc}}(k)\,. \tag{45}$$

Relationships of the form of eq. (44) have proven quite useful, especially when the g parameter is greater than or close to unity (for example, (44) predicts pre-nematic slowing-down in a mesogenic substance, where $G_2 \to \infty$). In these cases neglect of j has given good predictions. One must be careful when the intermolecular correlations are long-ranged, as in the dielectric problem [50], and when g is small, when the choice of slow variables in the derivation of (44) is nontrivial. (In the neutron case when $k \to 0$ $S(k)$ becomes small and (45) fails to predict Rayleigh-Brillouin structure. In the *longitudinal* dipole density case, $g \propto 1/\varepsilon$ and (44) does not predict the short-time effects, briefly discussed

by McDONALD, see also [50].) More input from simulations on the way the relationship fails in these cases would be very valuable.

Simulating collective correlation functions is much more difficult than single-particle ones. The statistical properties are much worse [51]. Various methods have been suggested for improving the information. NEMD methods should be useful [52]. Other authors [11, 17] have extolled the merits of working at finite $\boldsymbol{k}$. If a spectrum is required, maximum-entropy methods have been found useful in effecting Fourier transforms [11, 53].

6·2. *Interaction-induced spectra.* – In the introduction and subsect. **2·1** I discussed interaction-induced (I-I) effects as if they were a nuisance, limiting the experimentally available information on reorientation, etc. An alternative view is that I-I spectra are of intrinisic interest as they *directly* reflect intermolecular dynamics. Spectra which are purely interaction-induced may be observed in cases where some symmetry-based selection rule forbids the appearance of the spectrum of a single molecule (for example, the infra-red spectrum of N_2, or the depolarized Rayleigh scattering from argon). Simulations have played an important role in the formation of ideas about the interpretation of these spectra.

The literature on the depolarized spectrum of argon is very extensive [54, 55] and there have been a number of studies of molecular liquids, amongst them N_2, Cl_2, CS_2 [56-58]. There have been some attempts to link the kind of information obtainable from these spectra with other quantities which are affected by intermolecular motions, such as the force correlations function [12] and the pair diffusion [59], which influences chemical reactions.

6·3. *Vibrational dynamics.* – Spectroscopic studies of vibrational dynamics fall into two classes. One may study either the relaxation of the phase of the vibration, which determines the isotropic Raman lineshape (« vibrational dephasing »), or the way in which the energy in the vibrational mode relaxes (« energy or T_1 relaxation »), this requires some kind of pump and probe experiment. The distinction between these processes and the way in which they are measured has been explained by OXTOBY [60].

The difficulties of studying the relaxation of an internal degree of freedom in a simulation are twofold. Firstly, a proper description of the internal coordinate must almost always be quantum mechanical. Secondly, internal modes exchange energy with external modes slowly (compared with the frequency of the internal motion) so that if an internal mode is included in a simulation it may not behave ergodically on an affordable time scale. These difficulties have been addressed in different ways in the two major studies of vibrational relaxation which have taken place to date.

In the first, due to OXTOBY and co-workers [61, 62], the vibrational mode is not explicitly included in the calculation. Rather the fluctuations in the

vibrational frequency, due to the intermolecular interactions, are calculated and these are used to evaluate theoretical expressions for the normal co-ordinate correlation function (just as the orientational correlation function could be calculated from trajectories of the angular velocity via (31) and (33)). This technique is most useful for studying fundamental bands. More recently, WILSON and his collaborators have attacked the simultaneous description of vibrational and molecular position variables head on [63]. This approach gives the possibility not only of studying simple spectroscopic processes involving low-lying states but also of directly simulating events which involve highly excited molecules.

REFERENCES

[1] The book *Molecular Liquids*, edited by A. J. BARNES, W. J. ORVILLE-THOMAS and J. YARWOOD (Reidel, Dordrecht, 1984), provides a good background on spectroscopic studies of liquids. The article by STEELE (p. 111) reviews the relationship of correlation functions and experiment.

[2] R. G. GORDON: *Adv. Magn. Reson.*, **3**, 1 (1965).

[3] B. J. BERNE and G. D. HARP: *Adv. Chem. Phys.*, **17**, 63 (1970).

[4] G. J. KENNEY-WALLACE: in *Molecular Liquids*, edited by A. J. BARNES, W. J. ORVILLE-THOMAS and J. YARWOOD (Reidel, Dordrecht, 1984), p. 331.

[5] D. THIRUMALAI and B. J. BERNE: *J. Chem. Phys.*, **81**, 2512 (1984).

[6] F. BAROCCHI, M. ZOPPI and M. NEUMAN: *Phys. Rev. A*, **27**, 1584 (1983).

[7] N. CORBIN and K. SINGER: *Mol. Phys.*, **46**, 671 (1983); D. THIRUMALAI, R. W. HALL and B. J. BERNE: *J. Chem. Phys.*, **81**, 2523 (1984).

[8] P. S. Y. CHEUNG and J. S. POWLES: *Mol. Phys.*, **30**, 921 (1975); **32**, 1383 (1976).

[9] D. FRENKEL and J. P. MCTAGUE: *J. Chem. Phys.*, **72**, 2801 (1980).

[10] D. J. TILDESLEY and P. A. MADDEN: *Mol. Phys.*, **42**, 1137 (1981).

[11] D. J. TILDESLEY and P. A. MADDEN: *Mol. Phys.*, **48**, 129 (1983).

[12] P. A. MADDEN: in *Molecular Liquids*, edited by A. J. BARNES, W. J. ORVILLE-THOMAS and J. YARWOOD (Reidel, Dordrecht, 1984), p. 431, for an introductory account of interaction-induced effects.

[13] A. DE SANTIS, M. SAMPOLI and R. VALLAURI: *Mol. Phys.*, **53**, 695 (1984).

[14] P. A. MADDEN and D. J. TILDESLEY: *Mol. Phys.*, **55**, 969 (1985).

[15] B. M. LADANYI: *J. Chem. Phys.*, **78**, 2189 (1983).

[16] B. M. LADANYI and T. F. KEYES: *Mol. Phys.*, **33**, 1063 (1977).

[17] D. M. F. EDWARDS and P. A. MADDEN: *Mol. Phys.*, **51**, 1163 (1984).

[18] P. A. MADDEN: in *Ultrafast Phenomena*, Vol. **4**, edited by D. H. AUSTON and K. B. EISENTHAL (Springer, Heidelberg, 1984), p. 244.

[19] H. VERSMOLD: in *Molecular Liquids*, edited by A. J. BARNES, W. J. ORVILLE-THOMAS and J. YARWOOD (Reidel, Dordrecht, 1984), p. 309.

[20] H. W. SPIESS, D. SCHWEITZER, U. HAEBERLEIN and K. H. HAUSSER: *J. Magn. Reson.*, **5**, 101 (1971).

[21] T. I. COX, M. R. BATTAGLIA and P. A. MADDEN: *Mol. Phys.*, **38**, 1539 (1979).

[22] K. SINGER, J. V. L. SINGER and A. J. TAYLOR: *Mol. Phys.*, **37**, 1239 (1977).

[23] J. BAROJAS, D. LEVESQUE and B. QUENTREC: *Phys. Rev. A*, **2**, 1092 (1973).

[24] W. A. STEELE: in *Molecular Liquids*, edited by A. J. BARNES, W. J. ORVILLE-THOMAS and J. YARWOOD (Reidel, Dordrecht, 1984), p. 111.
[25] R. M. LYNDEN-BELL: in *Molecular Liquids*, edited by A. J. BARNES, W. J. ORVILLE-THOMAS and J. YARWOOD (Reidel, Dordrecht, 1984), p. 501; see also R. M. LYNDEN-BELL and I. R. MCDONALD: *Mol. Phys.*, **43**, 1429 (1981).
[26] R. KUBO: *J. Phys. Soc. Jpn.*, **17**, 1100 (1967).
[27] C. S. MURTHY and K. SINGER: *Proc. R. Soc. London, Ser. A*, **389**, 299 (1983). See also K. SINGER, J. V. L. SINGER and A. J. TAYLOR: *Mol. Phys.*, **37**, 1239 (1977).
[28] V. BALUCANI, R. VALLAURI and C. S. MURTHY: *J. Chem. Phys.*, **77**, 3233 (1982).
[29] H. A. POSCH, V. BALUCANI and R. VALLAURI: *Physica (Utrecht) A*, **123**, 516 (1984).
[30] R. M. LYNDEN-BELL, D. J. C. HUTCHINSON and M. J. DOYLE: *Mol. Phys.*, **58**, 307 (1986).
[31] R. W. IMPEY, P. A. MADDEN and I. R. MCDONALD: *J. Phys. Chem.*, **87**, 5071 (1983).
[32] R. ZWANZIG: in *Systems far from Equilibrium*, edited by L. GARRIDO (Springer, Berlin, 1980), p. 34.
[33] W. G. GRIFFIN and P. N. PUSEY: *Phys. Rev. Lett.*, **43**, 1100 (1979).
[34] M. S. BEEVERS, J. CROSSLEY, D. C. GARRINGTON and G. WILLIAMS: *J. Chem. Soc., Faraday Trans. II*, **73**, 458 (1977).
[35] R. M. LYNDEN-BELL, P. A. MADDEN and R. J. TOUGH: *Mol. Phys.*, **58**, 193 (1986).
[36] H. J. BÖHM, R. M. LYNDEN-BELL, P. A. MADDEN and I. R. MCDONALD: *Mol. Phys.*, **51**, 761 (1984).
[37] J. GOMPF, H. VERSMOLD and H. LANGER: *Ber. Bunsenges. Phys. Chem.*, **86**, 1114 (1982).
[38] M. FERRARIO, P. GRIGOLINI, M. LEONCINI, L. PARDI and A. TANI: *Mol. Phys.*, **53**, 1251 (1984), and references therein.
[39] W. F. VAN GUNSTEREN, H. J. C. BERENDSEN and J. A. C. RULLMAN: *Mol. Phys.*, **44**, 69 (1981).
[40] E. DETYNA, K. SINGER, J. V. L. SINGER and A. J. TAYLOR: *Mol. Phys.*, **41**, 31 (1980).
[41] W. A. STEELE: *Mol. Phys.*, **43**, 141 (1981).
[42] W. A. STEELE and W. B. STREETT: *Mol. Phys.*, **39**, 279 (1980).
[43] V. N. KABADI and W. A. STEELE: *J. Phys. Chem.*, **89**, 1467 (1985).
[44] R. M. LYNDEN-BELL and I. R. MCDONALD: *Mol. Phys.*, **43**, 1429 (1981).
[45] A. RAHMAN and F. H. STILLINGER: *J. Chem. Phys.*, **55**, 3336 (1971); **57**, 1281 (1972).
[46] R. W. IMPEY, P. A. MADDEN and I. R. MCDONALD: *Mol. Phys.*, **46**, 513 (1982).
[47] J. S. TSE, M. L. KLEIN and I. R. MCDONALD: *J. Chem. Phys.*, **81**, 6124 (1984).
[48] P. A. MADDEN and R. W. IMPEY: *Chem. Phys. Lett.*, **123**, 502 (1986).
[49] T. F. KEYES and D. KIVELSON: *J. Chem. Phys.*, **56**, 1057 (1972).
[50] P. A. MADDEN and D. KIVELSON: *Adv. Chem. Phys.*, **56**, 469 (1984).
[51] D. FRENKEL: *Proc. S.I.F.*, Course LXXV (North-Holland, Amsterdam, 1980), p. 156.
[52] D. J. EVANS and K. GAYLOR: *Mol. Phys.*, **49**, 963 (1983).
[53] D. J. TILDESLEY: in *Molecular Liquids*, edited by A. J. BARNES, W. J. ORVILLE-THOMAS and J. YARWOOD (Reidel, Dordrecht, 1984), p. 519.
[54] A. J. C. LADD, T. A. LITOVITZ and C. J. MONTROSE: *J. Chem. Phys.*, **71**, 4242 (1979).
[55] B. J. ALDER and E. L. POLLOCK: *Annu. Rev. Phys. Chem.*, **32**, 311 (1981).

[56] D. LEVESQUE, J. J. WEIS, P. MARTEAU, J. OBRIOT and F. FONDERE: *Mol. Phys.*, **54**, 1161 (1985).
[57] R. VALLAURI: in *Phenomena Induced by Intermolecular Interactions*, edited by G. BIRNBAUM (Plenum Press, New York, N. Y., 1985), p. 457.
[58] P. A. MADDEN and D. J. TILDESLEY: *Mol. Phys.*, **49**, 193 (1983).
[59] U. BALUCANI and R. VALLAURI: *Can. J. Phys.*, **53**, 1504 (1981).
[60] D. OXTOBY: *Adv. Chem. Phys.*, **40**, 1 (1979).
[61] D. LEVESQUE, J.-J. WEIS and D. W. OXTOBY: *J. Chem. Phys.*, **79**, 917 (1983).
[62] D. W. OXTOBY, D. LEVESQUE and J.-J. WEIS: *J. Chem. Phys.*, **72**, 2744 (1980).
[63] J. P. BERGSMA, P. H. BERENS, K. R. WILSON, D. R. FREDKIN and E. J. HELLER: *J. Phys. Chem.*, **88**, 612 (1984), and references therein.

Computer Simulation of Water and Ionic Solutions: What Can We Learn?

R. W. IMPEY

Chemistry Division, National Research Council of Canada
100 *Sussex Drive, Ottawa, Ont., Canada,* K1A OR6

1. – Introduction.

The way in which the structure of bulk water is modified by the introduction of ions and the extent to which this determines the dynamical properties of the solution are classic problems of electrochemistry [1, 2].

Until recently the progress towards a complete understanding of the structure of aqueous solutions at a microscopic level has been slow. Water itself is a strongly polar hydrogen-bonded liquid. The introduction of ions carrying localized charges of $|e|$ will produce a major perturbation in the hydrogen-bonded network. This perturbation may be so strong as to produce a « hydrated » ion, that is, the water surrounding the ion is strongly oriented by the ion and tends to be carried by it as the ion moves through the solution. This is the familiar picture of a hydrated ion; the number of molecules which contribute to the hydration is called the hydration number of the ion.

Much experimental effort has been devoted to determining the hydration numbers of different ions. The traditional methods are largely indirect: the value of the hydration number is inferred from measurements of properties such as mobility, compressibility, dielectric constants, etc. [3]. The most striking feature of the compiled data is that different experimental techniques can lead to vastly different estimates of the hydration number. For example, Na^+ values ranging from 1 to 71 have been reported [2]. The main reason for the wide spread in results in undoubtedly the fact that different types of measurements are sensitive to ion-solvent correlation over different ranges of both distance and time. For the concept of hydration number to be useful, a definition at the microscopic level is needed.

Following BOCKRIS and REDDY [2], we shall interpret the hydration number of an ion as being number of water molecules which are bound to the ion for times sufficiently long that they participate in the diffusive motion of the ion. Such a quantity may be termed a dynamic hydration number.

It is also possible to speak of co-ordination number, which is equal to the mean number of water molecules in the first co-ordination shell of the ion. The terms co-ordination and hydration are sometimes used interchangeably, but it is precisely the difference between them which is of interest here. The co-ordination number is determined solely by the static structure of the solution and is measurable by X-ray and neutron diffraction methods. The concept of hydration number is a wider one, since it involves the adoption of a suitable time scale.

In recent years, our knowledge of the microscopic structure and dynamics of aqueous solution has grown substantially. There are general reasons for this progress. The technique of neutron diffraction has been improved to the point where it is possible to determine both ion-solvent and ion-ion correlations [4-7]. Also, much is now known about ion-water interaction from *ab initio* potential-energy calculation [8-11]. The availability of realistic models of the water-water and ion-water interaction has encouraged the application of both molecular-dynamics and Monte Carlo methods to the study of ions in water. Finally, there has been significant progress in both the equilibrium and nonequilibrium statistical mechanics of ionic solutions [12-14].

The purpose of this lecture is to present the results of a series of molecular-dynamics calculations of aqueous solutions containing monoatomic ions at effectively infinite dilution. The specific systems considered are $[Li^+]_{aq}$ and $[Cl^-]_{aq}$. For these two systems detailed comparison can be made with experimental results; both structural (obtained from a neutron differencing technique) and dynamical (obtained from quasi-elastic scattering) information being available.

The outline of the lecture is as follows.

In the next section we give some details of the simulations and of the potential-energy functions used to describe the water-water and ion-water interactions; in sect. **3**, we discuss the structure of the solution in terms of partial radial distribution function, co-ordination numbers and functions relevant to neutron diffraction experiments; in sect. **4** we discuss the related concepts of residence time and hydration number and suggest definitions of each in terms of quantities which are easily measurable in the simulations; and finally in sect. **5**, we summarize the main results of the lecture.

2. – Molecular-dynamics calculations.

For the most part, the technical details of the molecular-dynamics calculations were the same as in our earlier work on pure water [15]. The primitive molecular-dynamics cube contained one ion and either 64 or 125 water molecules, and the usual periodic boundary conditions were imposed. The water molecules were treated as rigid objects and the equations of motion were

solved by the method of constraints developed by RYCKAERT *et al.* [16]; the standard finite-difference algorithm [17] was used for both the water molecules and the ion, with an integration time step of 0.005 ps. Approximately 2000 time steps were allowed for equilibration, and static and dynamic properties of the system were calculated averaging, typically, over a further 6000 time steps, covering a total real time of order 30 ps. All electrostatic interactions (ion-solvent and solvent-solvent) were computed by the Ewald method. To the extent that no account was taken of any counterion, the calculations correspond to conditions of infinite dilution, though the use of the periodic boundary condition means that this interpretation is not strictly correct. The density of the system was taken to be that of pure water at the temperature of interest.

The interactions between water molecules were modeled by the analytical potential-energy function of Matsuoka, Clementi and Yoshimine (MCY), obtained by fitting to the results of *ad initio* quantum-mechanical calculations on the water dimer [18, 19]. A large number of potential models have been used in the simulation of liquid water, the best known of which is the ST2 potential of Stillinger and Rahman [20]. Our choice of the MCY potential was dictated in part by a desire to maintain consistency with our previous work on pure water, but more importantly by the fact that the model is known to yield a fair description of many of the static and dynamic properties of real water [15, 19]. In the MCY model the short-range interactions between molecules are described by atom-atom potentials of the Born-Mayer type, and the charge distribution of the monomer is represented by three fractional point charges corresponding to a dipole moment of $2.19D$ (the measured gas-phase value is $1.85D$).

To describe the interactions between ions and water molecules, we have used the potentials of Kistenmacher *et al.* [10] (their « simple » models), which are also based on *ab initio* calculations at the dimer level. The short-range ion-molecule forces are again described by Born-Mayer type potentials, but the charge distribution of the water molecules is now modeled by six fractional charges. The fact that the water molecule presents a different charge distribution to an ion than to another water molecule is physically reasonable; an enhancement of the effective dipole moment is necessary in the ion-water case if account is to be taken of the polarizing effect of the ion.

3 – Structure.

The structure of the water molecules about an ion I is described by the two partial distribution functions $g_{IO}(r)$ and $g_{IH}(r)$ ($I \equiv Li^+, Cl^-$). The local order to which the forms of the calculated functions correspond is discussed in terms of the two idealized models of the ion-water complex which are shown

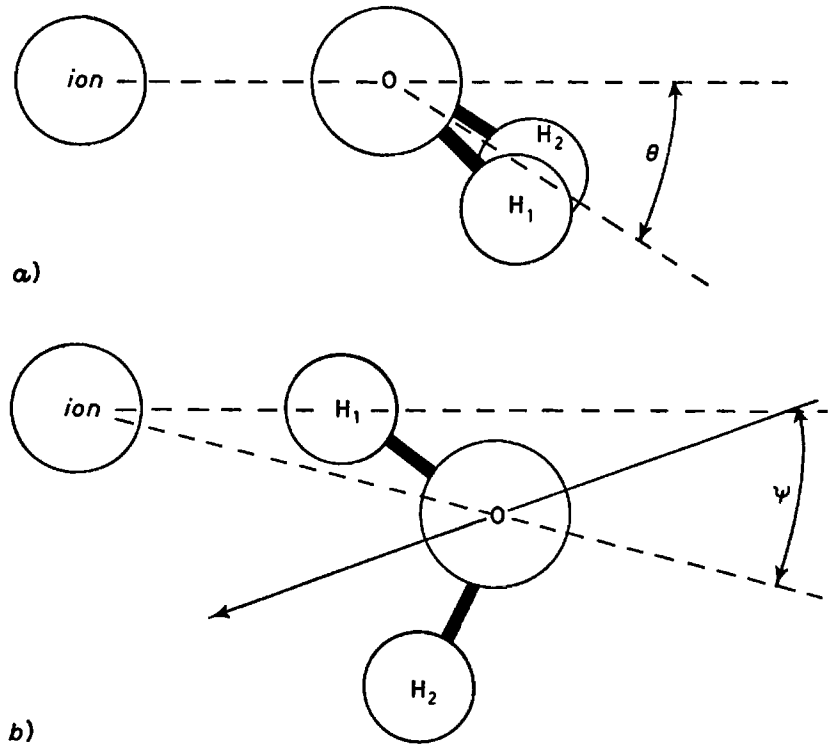

Fig. 1. – Possible structures of the ion-water complex for *a*) a cation and *b*) an anion.

TABLE I. – *Molecular-dynamics and experimental results.*

	$[Li^+]_{aq}$	$[Cl^-]_{aq}$
T (K)	278	287
$r(I\text{-O})$ (Å)	1.98 (1.95 + 0.02) ([a])	3.29 (3.34 + 0.02) ([a])
$r(I\text{-H})$ (Å)	2.57 (2.55 + 0.02) ([a])	3.35 (3.25 + 0.02) ([a])
$r(I\text{-H})$ (Å)	—	3.73
n_{ion}	5.3 (5.5 + 0.3) ([a])	7.2 (5.9 + 0.2) ([a])
θ (degrees)	40 (40 + 10) ([a])	—
ψ (degrees)	—	17 (< 7) ([a])
τ^s_{ion} (ps)	33.3	4.5
n_{hyd}	4.6 (5 + 1) ([b])	2.6 (2 + 1) ([b])

(*a*) Quantities in parentheses are experimental results [21] for a 3.57 mol solution of LiCl.
(*b*) Quantities in parentheses are « most probable » experimental values from table 2.20 of ref. [2].

in fig. 1; these are the same models used by ENDERBY, NEILSON and co-workers [4-7] in analyzing their results of neutron diffraction experiments on a number of electrolyte solutions. In the context of the suggested structures, the quantities of principal interest are the angle θ, which measures the deviation from planarity of the M^+-H_2O complex, and the angle ψ, which measures the deviation from linearity of the X^--H_2O bond in the anion-water complex.

3·1. *Partial radial distribution functions.* – The functions $g_{IO}(r)$ and $g_{IH}(r)$ for the two ions are plotted in fig. 2-5. The positions of the peaks are broadly consistent with the structures of fig. 1, as we shall see below. The separations at which the main peaks occur are summarized in table I, there is good agreement with the peak positions obtained in the neutron scattering experiments on a 3.57 mol solution of LiCl [21].

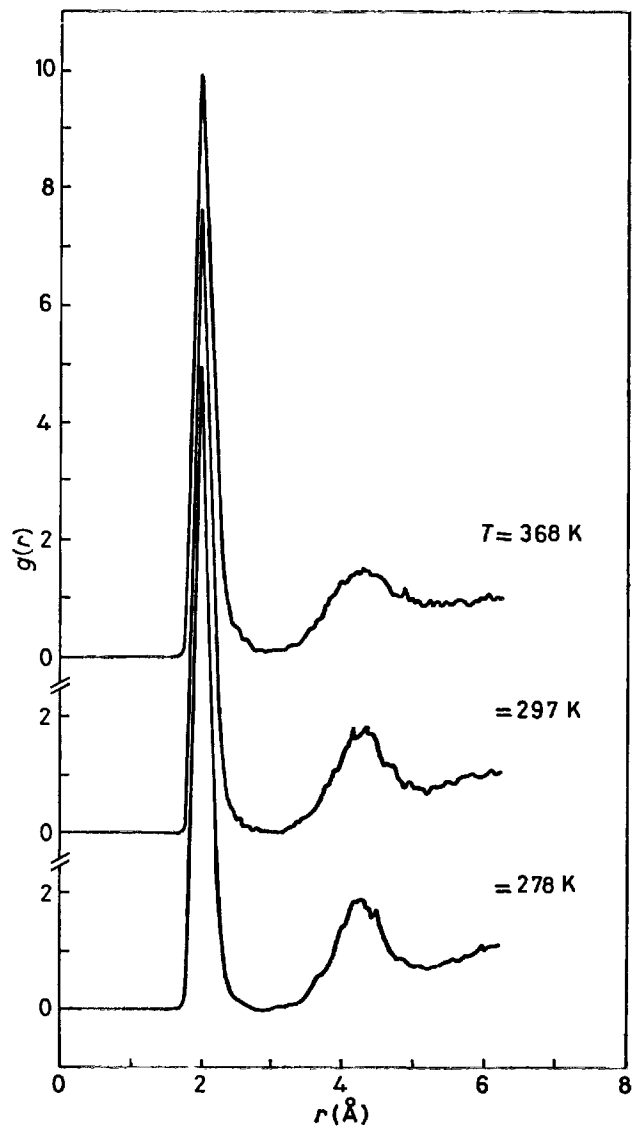

Fig. 2. – Radial distribution function $g_{IO}(r)$ for Li^+ as a function of temperature.

The results of fig. 2 and 3 indicate that the structure for the positive ion is characterized by a very pronounced main peak in $g_{IO}(r)$, which falls almost to zero between the first peaks. Also the structure around the Li^+ ion is only slightly relaxed as the result of an increase in temperature of 100 K (see below).

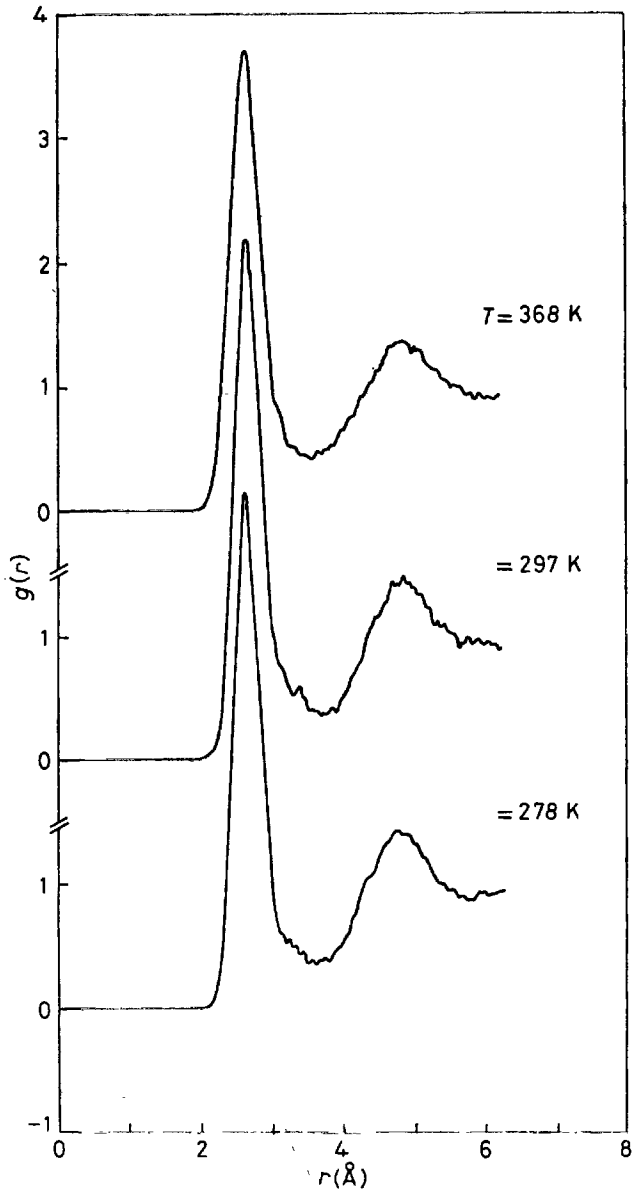

Fig. 3. – Radial distribution function $g_{IH}(r)$ for Li^+ as a function of temperature.

In the case of the negative ion, the main peak in $g_{XO}(r)$ and $g_{XH}(r)$ are roughly equal height. The two peaks seen in $g_{XH}(r)$ are closely spaced and correspond to the two nonequivalent hydrogen atoms H_1, H_2 of fig. 1*b*); in the lithium ion case, the second peak in $g_{MX}(r)$ derives from a different, more distant shell of water molecules.

3·2. *Co-ordination numbers.* – The separation $r = r_{min}$ at which the function $g_{IO}(r)$ has its first minimum may be used to define the first co-ordination shell of the ion, and integration of $r^2 g_{IO}(r)$ up to this point yields a value for the co-ordination number N_{ion}. For the Li^+ ion, the latter is a well-defined quantity, since the integral plateau as a function of its upper limit and the precise choice of outer radius of the co-ordination is unimportant. In the case of Cl^-, the co-ordination number is larger, but also has a less clear-cut physical significance, since $g_{IO}(r)$ has a much shallower first minimum. For the sharply defined co-ordination shell of the Li^+ ion, integration of $g_{IH}(r)$ up to its first minimum yields a co-ordination number equal to $2N_{ion}$, but for Cl^- there are deviations which suggest that there is some penetration by molecules belonging to the second shell of neighbours.

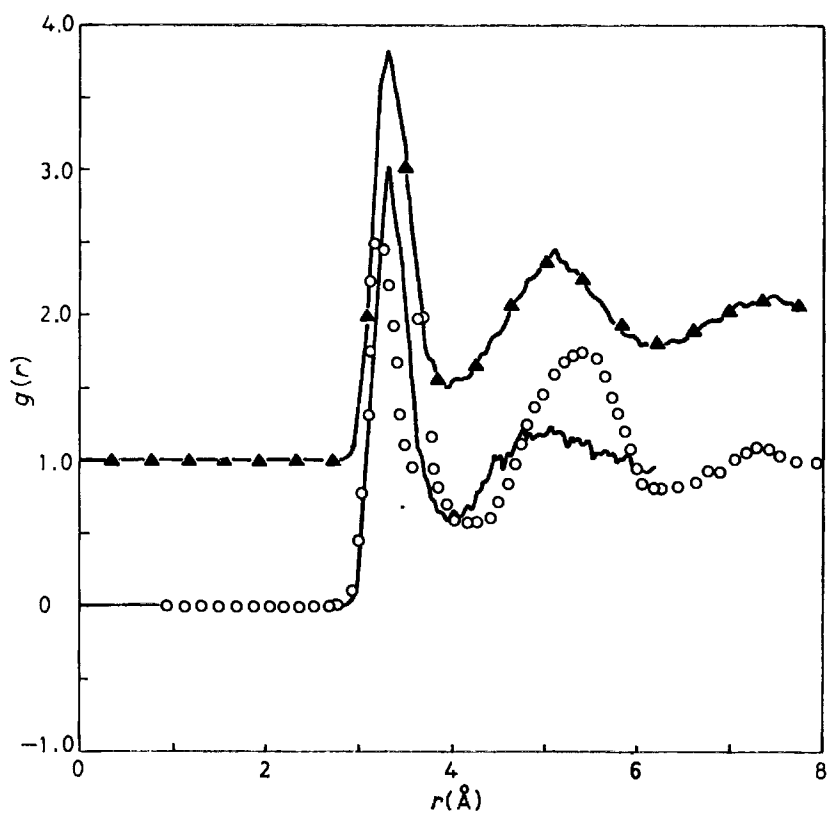

Fig. 4. – Radial distribution functions for Cl^- at 287 K. Plain curve: $g_{IO}(r)$ for a system of 64 water molecules. Curve with triangles: $g_{IO}(r)$ for a system of 125 water molecules.

The calculated co-ordination numbers are gathered together in table I, together with the neutron diffraction results for the 3.57 mol solution of LiCl studies by NEWSOME *et al.* [21]. Agreement with the present results is excellent for Li^+ not as good for Cl^-.

3·3. *Conformation of the ion-water complex.* – From the characteristic distances listed in table I and the bond lengths of the water molecule, the average values of the angles θ and ψ can be deduced. The results are listed in table I. For the cation, it is clear that on average there is a significant deviation from

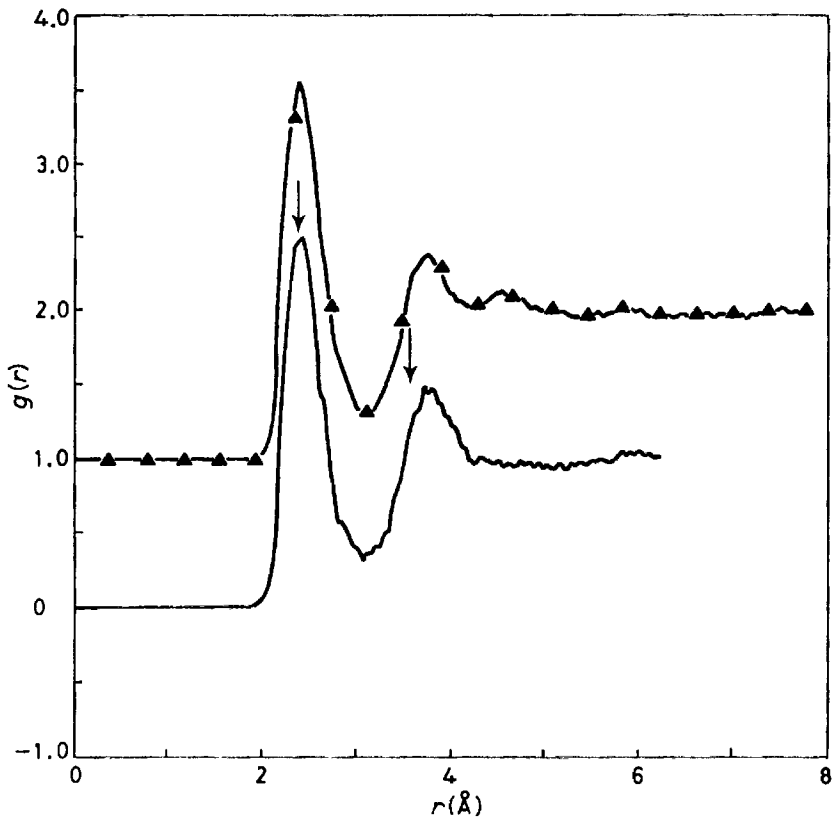

Fig. 5. – Radial distribution function $g_{IH}(r)$ for Cl^- at 287 K. Plain curve: results for a 64 water molecule system. Curve with triangles: results for a 125 water molecule system. The arrows mark the expected peak position for a linear Cl^--H-O bond.

planarity. The value θ is in excellent agreement with the experimental result [21] for 3.57 mol LiCl, though the comparison is complicated by the fact that the experiments show that θ is concentration dependent. The orientation of the water molecules is intermediate between the « dipole » and the « lone-pair » ($\theta = 55$) configuration. However, little physical meaning can be attached to the value of θ, particularly since the width of the main peak in $g_{IO}(r)$ makes it possible for many structures to contribute. The results do show that there is no marked tendency to adopt the cation-water geometry appropriate to the dimer. *Ab initio* results [11] predict that the minimum-energy configuration is planar, with C_{2v} symmetry, *i.e.* $\theta = 0$.

In the case of the anion, the situation is different. For Cl^-, the values of r(X-O) and r(X-H_1) are consistent with a nearly linear X^--H-O bond, which is

the geometry favoured at the dimer level. This is in agreement with the neutron scattering results [21]. The value of ψ quoted in table I appears to contradict this statement, but a shift of only 0.01 Å in the positions of the peaks in $g_{IO}(r)$ and $g_{XH}(r)$ would be sufficient to reduce the calculated angle to zero. In contrast to the results for Li^+, the experiments show that the geometry

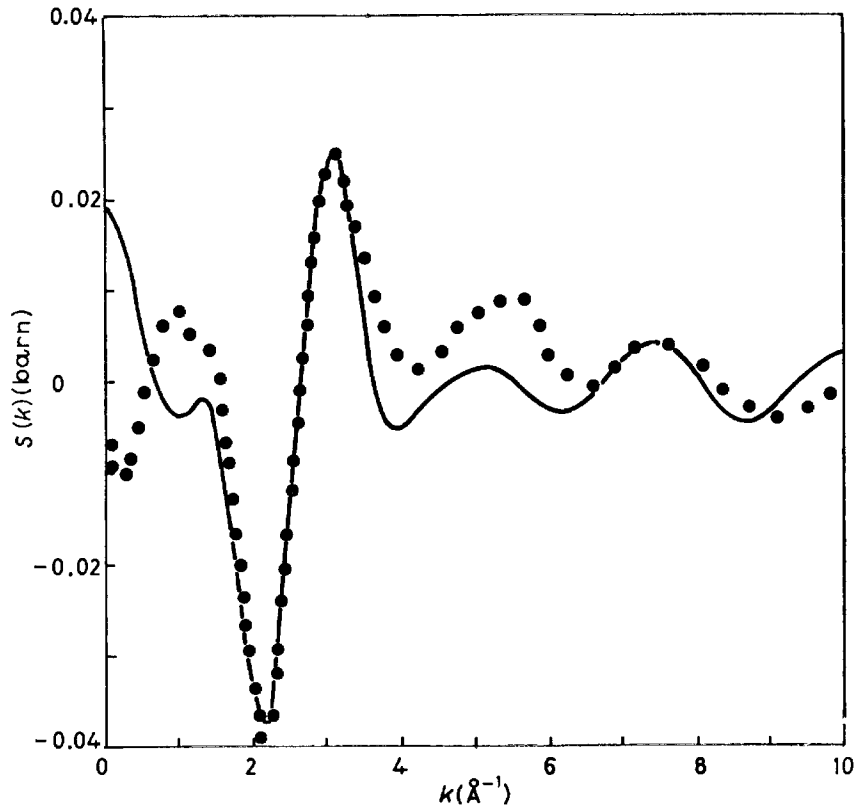

Fig. 6. – First-order difference scattering function $S_M(k)$ for Li^+. Curve: molecular-dynamics results at 278 K. Points: experimental results of Newsome *et al.* [21] for a 3.57 mol solution of LiCl.

of the anion-water complex is almost independent of concentration. In fig. 4 and 5, the arrows denote the positions at which the peaks would occur if the X^--H_1-O bond were strictly linear; the position of the second peak is very sensitive to small deviations from the ideal geometry.

3·4. *Neutron-weighted distribution functions.* – The neutron scattering pattern for an alkali halide-water system is the sum of ten partial structure factors $S_{\alpha\beta}(k)$, where k is the wave number. A complete microscopic understanding of ionic hydration requires detailed knowledge of all ten. At first sight the formidable problems of unravelling this large number of correlation

functions appear to make a real understanding of aqueous solution at a microscopic level almost impossible. However, if the experiment is repeated following isotopic substitution of the ions and the difference between the two scattering patterns is taken, the contribution from water-water correlations disappears. For example, isotopic substitution of a cation leads to the so-called first-order difference scattering function $S_M(k)$, with a Fourier transform $G_M(r)$ given by

$$G_M(r) = Ag_{MO}(r) + Bg_{MX}(r) + Cg_{MX}(r) + Dg_{MM}(r) + E \tag{1}$$

with a similar expression for $G_X(r)$. In practice, because of the large incoherent scattering cross-section of the proton, experiments are made on D_2O. The

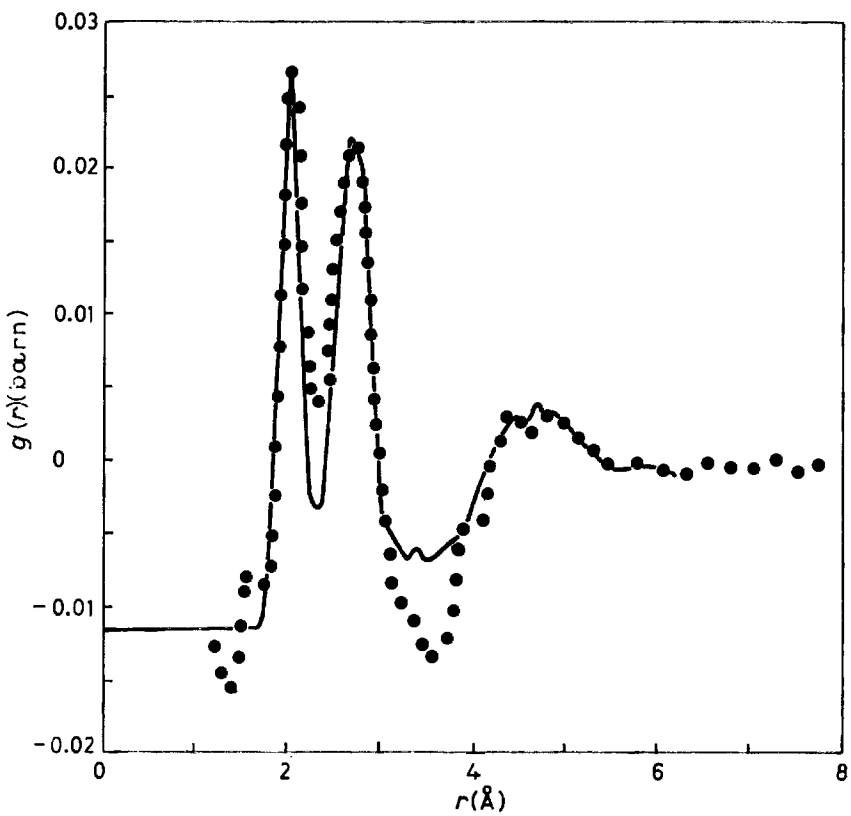

Fig. 7. – Fourier transform $G_M(r)$ of the first-order difference scattering for Li^+. Curve: molecular-dynamics results at 278 K. Points: experimental results of Newsome *et al.* [21] for a 3.57 mol solution of LiCl.

coefficients A, B, C and D are determined by the scattering lengths of the nuclei and the concentration of the solution and E is chosen to make $G_M(r)$ vanish as $r \to \infty$. Since C and D (the ion-ion correlations) will, in general, be much

smaller than A and B, the functions $G_M(r)$ and $G_X(r)$ provide a direct measure of the distribution of water molecules around the ion. This differencing technique was developed by ENDERBY, NEILSON and co-workers and several reviews of both the method and its applications have recently appeared [4-7]. The present results may again be compared with the experimental results for a 3.57 mol solution of LiCl in D_2O. The comparison is shown in fig. 6-9.

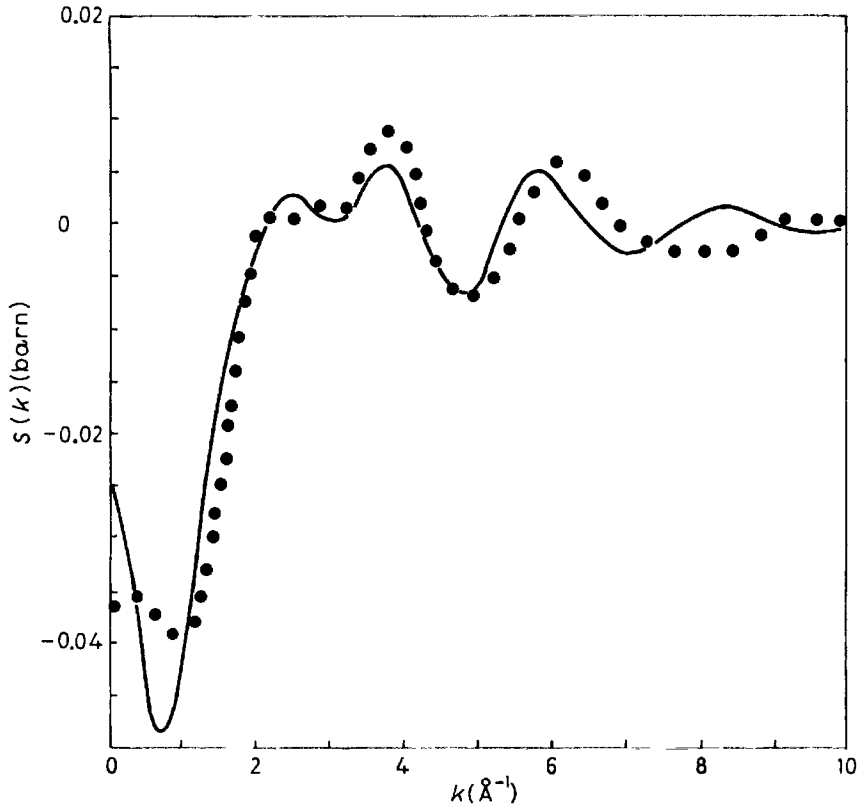

Fig. 8. – First-order difference scattering function $S_X(k)$ for Cl^-. Curve: molecular-dynamics results at 287 K. Points: experimental results of Newsome *et al.* [21] for a 3.57 mol solution of LiCl.

Overall, the agreement with experiment is very good, particularly in the real-space functions. The agreement for Li^+ would be worse if the comparisons were made with experimental results for a more concentrated (9.95 mol) solution. Experimentally the results are strongly concentration dependent; for example, the hydration number increases from less than 4 (3.3) at 9.95 mol to 5.5 at 3.57 mol, showing the importance of the counterion in such conditions. However, results of Cl^- with a range of concentrations and counterions show an apparent lack of sensitivity of anionic hydration to the nature of the counterion.

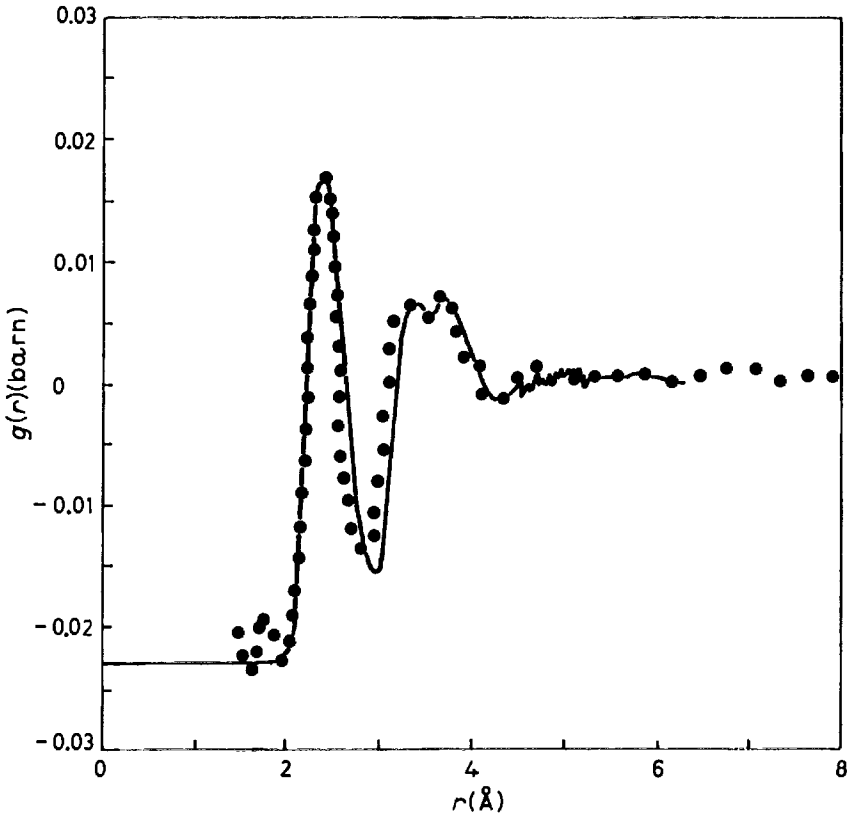

Fig. 9. – Fourier transform $G_X(r)$ of the first-order difference scattering function for Cl^-. Curve: molecular-dynamics results at 287 K. Points: experimental results of Newsome *et al.* [21] for a 3.57 mol solution of LiCl.

4. – Residence times and hydration numbers.

The structure of the different solutions was discussed in sect. **3** in terms of co-ordination numbers. As we pointed out in the introduction, the co-ordination number is defined solely in terms of static quantities. The concept of hydration is a more complex one, which we shall identify with that of persisting co-ordination. However, this interpretation becomes complete only when a choice of time scale is made. This time scale must be related in some way to the residence time of water molecules in the first co-ordination shell of the ion.

To obtain a precise definition of residence time, we introduce a function $P_j(t, t_n; t^*)$. This is a property of the water molecule j and is equal either to 0 or to 1. It takes the value 1 if molecule j lies within the first co-ordination shell of the ion at both time steps t_n and $t + t_n$ and in the interim does not leave the co-ordination shell for any continuous period longer than t^*. Under all other circumstances, it takes the value 0. We may now define an average quantity $n_{\text{ion}}(t)$, charateristic of the ion, by the expression

$$n_{\text{ion}}(t) = \frac{1}{N_t} \sum_{n=1} \sum_{j}^{N_t} P_j(t, t_n; t^*) \,. \tag{2}$$

It follows immediately from this definition that $n_{\text{ion}}(0) = n_{\text{ion}}$, the co-ordination number introduced in sect. 3, whereas $n_{\text{ion}}(t)$ measures the number of molecules which lie initially within the first co-ordination shell and are still there after a time t has elapsed. The parameter t^* is introduced to take account of molecules which leave the first co-ordination shell only temporarily and return to it without ever having properly entered the bulk. The use of the parameter t^* is only a crude device for dealing with this situation, but it avoids the necessity for any elaborate bookkeeping. For reasons which will become apparent shortly, we have set t^* equal to 2 ps.

The function $n_{\text{ion}}(t)$ turns out to have the same general form for all the ions that we have studied. Except at short times, it decays in an accurately exponential fashion with a characteristic time τ^s_{ion}, *i.e.* $n_{\text{ion}}(t) \sim n_{\text{ion}} \exp[-t/\tau^s_{\text{ion}}]$ for large t. The quantity τ^s_{ion} is a correlation time for the persistence of the first co-ordination shell around the ion; it provides a simple definition of the residence time of water molecules in that shell.

The results obtained for τ^s_{ion} are listed in table I. In the case of Li^+, the only ion for which we have made the necessary calculations, there is also a strong dependence on temperature. It is clear from the results that over a temperature range of 90 K the co-ordination shell of the Li^+ ion becomes markedly less stable. This feature is not apparent from studies of the structure alone (see fig. 2 and 3). The other point to note about the results for Li^+ is that at the lowest temperature studied the residence time is comparable with the length of the molecular-dynamics run used in its determination. Residence times have been measured by NMR for ions with unpaired spins, but studies of monovalent ions (Li^+ and F^-) have not so far yielded numerical estimates for the quantities of interest here [22]. For divalent ions, the residence times are found to be of order 10^{-9} s or longer.

The same calculation can be made for bulk water, yielding a function $n_{\text{bulk}}(t)$ which decays with a characteristic time t^s_{bulk}. For this purpose, the co-ordination shell is defined by the positon of the first minimum in the oxygen-oxygen distribution function $g_{\text{OO}}(r)$; we recall [15] that, for MCY water at 286 K, the first minimum in $g_{\text{OO}}(r)$ occurs at 3.34 Å and the corresponding co-ordination number is $n_{\text{bulk}} = 4.8$. Under the same state conditions, the calculated residence time is $\tau^s_{\text{bulk}} = 4.5$ ps.

If in the definition of $P_j(t, t_n; t^*)$ we set $t^* = 0$, we obtain a function $\tilde{n}_{\text{ion}}(t)$ which again decays exponentially but with a characteristic time $\tilde{\tau}^s_{\text{ion}}$ which is obviously shorter than τ^s_{ion}. In the case of Li^+, for which τ^s_{ion} is considerably longer than 2 ps, the difference between the two characteristic times is only small; the same would be true of the divalent ions which have been studied by NMR. The choice of $t^* = 2$ ps in the definition of $n_{\text{ion}}(t)$ was dictated by the fact that this is roughly the value obtained for the characteristic time $\tilde{\tau}^s_{\text{bulk}}$; for pure water at 286 K we find that $\tilde{\tau}^s_{\text{bulk}} = 1.8$ ps.

The quantity $\tilde{\tau}^s_{\text{ion}}$ bears a close relation to the residence time discussed by

HERTZ [22]. For pure water, HERTZ gives an estimate of 8 ps for the residence time calculated as the time required for a water molecule to difuse over one molecular diameter, *i.e.* from the first to the second peak in the oxygen-oxygen distribution function. Our definition of $\tilde{\tau}^s_{\text{bulk}}$ is more closely linked to the time required to diffuse over a molecular radius, *i.e.* from the first peak to the first minimum in the distribution function. Accordingly, we should expect our value for $\tilde{\tau}^s_{\text{bulk}}$ to be about one-quarter of the estimate given by HERTZ [22], which indeed is true.

The physical significance of τ^s_{ion} is that of a characteristic time over which the molecules in the first co-ordination shell exchange identity with molecules in the bulk and hence for any correlation between the ion and a particular water molecule to be lost. It is interesting to note that, in the case of pure water, the characteristic time τ^s_{bulk} is approximately equal to the mean of the three correlation times describing the reorientation of the principal axes of the water molecule (3.1, 5.7 and 3.7 ps, at 286 K). This is consistent with our earlier suggestion [15] that the break-up of the first co-ordination shell is initiated by molecular reorientation rather than translation.

With the significance of τ^s_{ion} and τ^s_{bulk} in mind, we choose to define the dynamic hydration number n_{hyd} of an ion in aqueous solution as the mean number of water molecules which remain within the first co-ordination shell over the period of time in which the co-ordination shell in bulk water is renewed. Because of the exponential character of the functions $n_{\text{ion}}(t)$ and $n_{\text{bulk}}(t)$, this number is given by

$$n_{\text{hyd}} = n_{\text{ion}} \exp\left[\tau^s_{\text{bulk}}/\tau^s_{\text{ion}}\right]. \tag{3}$$

Values of n_{hyd} obtained in this way are listed in table I. They show a relatively wider variation, from 2.6 (for Cl^-) to 4.6 (for Li^+), than do the co-ordination numbers discussed earlier.

The dynamical aspect of the hydration number concept has played an important role in recent work of Enderby and co-workers [4-7]. These authors have shown how quasi-elastic neutron scattering techniques may be used to study the hydration of an ion. Hydrated water molecules are identified as those which translate with the ionic diffusion coefficient on the time scale of the neutron experiment ((30÷100) ps). They may, therefore, be detected only if the residence time exceeds the neutron time scale, which is true for divalent ions. Our estimate of the residence time for Li^+ is consistent with the upper band established in the neutron work. For those ions for which the hydrated water is sufficiently tightly held that it may be detected in the neutron experiment, the hydration and co-ordination numbers are the same. This would also be true of the hydration number defined above since in such a case $\tau^s_{\text{ion}} \gg \tau^s_{\text{bulk}}$.

The hydration number measured in a neutron experiment and the defini-

tion offered here have as a common feature the fact that they provide estimates of the number of water molecules which are bound to an ion on a time scale relevant to the microscopic dynamics. Since our values are computed from the ratio of two numbers, we may hope that inadequacies in the potentials and other defects in the simulation will have been minimized and that the numbers obtained will, therefore, be realistic estimates of the hydration numbers in real aqueous solutions. As we have seen in the introduction, the experimental situation is confused since different types of experiments do not measure the same quantity. In table 2.20 of ref. [2], BOCKRIS and REDDY have compiled a list of the « most probable » values of what they term the primary hydration number, a quantity which is closely related to the hydration number defined by eq. (3). Their results for the ions of interest here are reproduced in table I. The agreement with the present work is very good, but this may be partly fortuitous, since BOCKRIS and REDDY [2] rely to a large extent on thermodynamic measurements. In view of the sharp distinction that we have drawn between a static co-ordination number and a dynamic hydration number, it would be more appropriate to limit the comparison to experimental estimates based solely on the measurement of ionic mobilities. The relevant data from ref. [2] (tables 2.19 and 2.20) are 3.57 for Li^+ and 0.9 for Cl^-. The agreement with our results is now less striking, but it should be emphasized that there is no reason to suppose that the quantity defined by eq. (3) is identical with that measured by any particular experimental method.

5. – Conclusions.

The results of our work may be summarized as follows. Firstly, computer simulations requiring only modest computing facilities are able to give quantitative information on the statics and dynamics of dilute aqueous solutions of weakly hydrated, spherical ions. The information obtained is useful in the interpretation of experimental data, and the comparison with experiment shows that currently available potentials provide a satisfactory description of the ion-water interactions in solution. There are few difficulties associated with the calculation of either the structure around the ion or the dynamics of the water molecules in the first shell of the ion. Secondly, the calculated structural properties are in very good agreement with the experimentally determined radial distribution functions. Finally, a definition of hydration number in terms of a time scale defined by the relative rates of break-up of the local order in the solution and in pure water leads to results which are in reasonable accord with estimates based on electrochemical measurements.

Under the combined pressure of theory and experiment many of the long-standing problems of classical electrochemistry are finally being understood

at the molecular level. Experimentally, the first-order differencing technique is yielding the detailed features of the ion-water co-ordination, while computer simulations are able to help elucidate and clarify the interpretation of the experimental data. Once the structural data are understood, the local dynamics of the co-ordination shell may be probed both by inelastic neutron scattering and molecular dynamics.

This close interplay between theory and experiment will continue to aid our knowledge of the properties of aqueous solutions at the molecular level.

* * *

This paper is based on the recent feature article by R. W. IMPEY, P. A. MADDEN and I. R. MCDONALD: *J. Phys. Chem.*, **87**, 5071 (1983).

I thank my Ph. D. supervisor Dr. P. A. MADDEN for his support and guidance while this work was being carried out. I am also indebted to Dr. I. R. MCDONALD.

I would like to thank Prof. G. CICCOTTI and W. G. HOOVER for inviting me to attend the Summer School and I am grateful for the financial support provided by the Società Italiana di Fisica.

REFERENCES

[1] R. A. ROBINSON and R. H. STOKES: *Electrolyte Solutions* (London, 1955).
[2] J. O'M. BOCKRIS and A. K. N. REDDY: *Modern Electrochemistry* (New York, N. Y., 1973).
[3] J. R. HINTON and E. S. AMIS: *Chem. Rev.*, **67**, 367 (1967).
[4] J. E. ENDERBY and G. W. NEILSON: *Adv. Phys.*, **29**, 323 (1980).
[5] J. E. ENDERBY and G. W. NEILSON: *Rep. Prog. Phys.*, **44**, 593 (1981).
[6] J. E. ENDERBY and G. W. NEILSON: *Water, a Comprehensive Treatise*, edited by F. FRANKS, Vol. **6** (New York, N. Y., 1979), p. 1.
[7] J. E. ENDERBY: *Annu. Rev. Phys. Chem.*, **34**, 155 (1983).
[8] E. CLEMENTI and H. POPKIE: *J. Chem. Phys.*, **57**, 1077 (1972).
[9] H. KISTENMACHER, H. POPKIE and E. CLEMENT: *J. Chem. Phys.*, **58**, 5627 (1973).
[10] H. KISTENMACHER, H. POPKIE and E. CLEMENT: *J. Chem. Phys.*, **58**, 5842 (1973).
[11] P. SCHUSTER, W. JAKVBUTZ and W. MARIUS: *Top. Curr. Chem.*, **60**, 1 (1975).
[12] H. C. ANDERSEN: in *Modern Aspects of Electrochemistry*, edited by B. E. CONWAY and J. O'M. BOCKRIS (New York, N. Y., 1975).
[13] H. L. FIEDMAN and W. D. T. DALE: in *Statistical Mechanics*, Part A, edited by B. J. BERNE (New York, N. Y., 1977).
[14] P. G. WOLYNES: *Annu. Rev. Phys. Chem.*, **31**, 345 (1980).
[15] R. W. IMPEY, P. A. MADDEN and I. R. MCDONALD: *Mol. Phys.*, **46**, 513 (1982).

[16] J. P. RYCKAERT, G. CICCOTTI and H. J. C. BERENDSEN: *J. Comput. Phys.*, **23**, 327 (1977).
[17] L. VERLET: *Phys. Rev.*, **159**, 98 (1967).
[18] O. MATSUOKA, E. CLEMENTI and M. J. YOSHIMINE: *J. Chem. Phys.*, **64**, 1351 (1976).
[19] G. C. LIE, E. CLEMENTI and M. J. YOSHIMINE: *J. Chem. Phys.*, **64**, 2314 (1976).
[20] F. H. STILLINGER and A. RAHMAN: *J. Chem. Phys.*, **68**, 666 (1978).
[21] J. R. NEWSOME, G. W. NEILSON and J. E. ENDERBY: *J. Phys. C*, **13**, L923 (1980).
[22] H. G. HERTZ: in *Water, a Comprehensive Treatise*, edited by F. FRANKS, Vol. **3** (New York, N. Y., 1983), p. 301.

Molecular-Dynamics Study of Several Atomic Solutes in Water (*).

K. WATANABE (**) and H. C. ANDERSEN

Department of Chemistry, Stanford University - Stanford, CA 94305

1. – Introduction.

The term « hydrophobic interaction » refers to the supposed tendency for nonpolar solutes and groups dissolved in water to be associated with one another. It is usually assumed to be a major factor influencing the immiscibility of water and nonpolar substances, the thermodynamic properties of aqueous solutions, the conformations of proteins and nucleic acids in solution, association equilibria in aqueous solution, micelle formation by amphiphilic molecules and the stability of lipid bilayers and biological membranes.

Computer simulation studies have been used to study two or more nonpolar solutes in water to learn about hydrophobic interaction. Calculations of the potential of mean force between two solutes in water at infinite dilution [1-3] and molecular-dynamics simulation of a pair of solutes in water [4] indicated the existence of two relatively stable configurations for the solute atoms, in agreement with the earlier semi-empirical theory of Pratt and Chandler [5]. One of these configurations is two solutes in contact, *i.e.* a near-neighbor pair. The other is two solute atoms separated by a water molecule, *i.e.* a solvent-separated pair of solutes.

There has been one reported simulation of more than two atomic solutes in water. RAPOPORT and SCHERAGA [6] calculated the motions in a system composed of 4 solute atoms and 339 water molecules. The simulation was run for 70 ps, which was considerably longer than any previously reported for aqueous systems. This simulation failed to reveal any tendency for the initially well-separated solutes to associate. As pointed out by RAPAPORT and SCHERAGA, however, there is a possibility that the duration of their simulation was insufficient to permit observation of the association of solutes.

(*) Work supported by the National Science Foundation, Grants CHE81-07165 and CHE84-10701.

(**) Natural Sciences and Engineering Research Council of Canada postdoctoral fellow.

This lecture reports the result of molecular-dynamics computer simulation studies of an aqueous solution of Kr at finite concentrations of about 0.8 and 1.4 mol/l. These calculations are similar to those of Rapoport and Scheraga, except that they were much longer runs and the potentials used were chosen to be appropriate for those of a real system, Kr in water. The systems simulated exhibited no tendency for the solutes to associate. When compared with randomly distributed particles, the nonpolar atoms dissolved in water were found to be correlated in such a way that they stayed away from each other. These results are in conflict with the usual notions of hydrophobic association of nonpolar solutes. A new analysis of published data on the solubility of nonpolar gases in water gives support to these results.

2. – Intermolecular forces and simulation method.

The water-water intermolecular potential used in this work is that of Swope and Andersen [7], which is a slight modification of the revised central-force model of Stillinger and Rahman [8]. The water intramolecular potential was a set of atom-atom harmonic potentials as used by ANDREA *et al.* [9].

The water-solute potential was assumed to be a Lennard-Jones interaction between the solute atom and the oxygen of the water molecule. SWOPE and ANDERSEN [7] have calculated the solubility of such solutes in this model of water as a function of temperature for a range of values of the Lennard-Jones parameters for the atom-water interaction. The ε and σ values chosen for the present work, namely 0.395 kcal/mol and 3.44 Å, led to a solubility with about the same magnitude and temperature dependence as that observed experimentally for Kr.

The solute-solute potential was assumed to be a Lennard-Jones interaction with ε and σ values of 0.401 kcal/mol and 3.6 Å. These parameters were chosen to make the potential similar to the Kr-Kr potential of Barker *et al.* [10].

The molecular-dynamics calculations were performed for a cubic system of constant volume using periodic boundary conditions. The velocity form of the Verlet algorithm [11] was used to integrate Newton's equations of motion with a time step of 0.6 fs. The calculations used the constant-temperature molecular-dynamics method [12]; stochastic collisions corresponding to a bath temperature of 298 K were applied to all the atoms and molecules every 0.3 or 0.6 ps.

We performed calculations of the mean force between two solutes at infinite dilution using the molecular-dynamics method. This was done by keeping the two solutes fixed at various separations and averaging the fluctuating force exerted on them by the solvent. The results confirmed previous simulations [1-4] and the theory of Pratt and Chandler [5] that showed the presence of a near-neighbor peak and a solvent-separated peak in the pair correlation function at infinite dilution.

3. – Simulation of several solutes in water.

Hydrophobic association of several nonpolar solutes was studied by simulating a system of 5 solute atoms and 195 water molecules. The initial configuration was generated from an equilibrated system of 200 water molecules, in a volume corresponding to a density of 1.0 g/cm^3, by randomly selecting 5 water molecules and replacing them by solute atoms located at the former positions of the oxygen atoms. Equilibration was carried out for 30 ps with long-ranged purely repulsive interactions acting between the solutes, while the water-water and solute-water intermolecular forces remained as described in sect. **2**. This part of the simulation permits the solute atoms to separate from each other and allows the water molecules to reorganize around each solute atom. At the end of the equilibration time, the solute-solute intermolecular force was changed to the Lennard-Jones form. This corresponds to $t = 0$. The simulation was continued until $t = 1.5$ ns, which was a very long computer run.

In describing the configuration of a pair of solute atoms, the following conventions will be used: i) Two solutes will be referred to as a near-neighbor pair if the intersolute distance is less than 5.2 Å, the separation distance corresponding to the first minimum in the solute-solute pair correlation function at infinite dilution. ii) Solute pairs with separation distances in the 5.2 Å to 8.6 Å range will be referred to as solvent-separated pairs. iii) Solute pairs separated by more than 8.6 Å, an estimated intersolute distance for the second minimum in the solute-solute pair correlation function at infinite dilution, will be considered unassociated.

At $t = 0$, the minimum-image interatomic distances for the five solutes ranged from 8.9 Å to 12.9 Å. There were no near-neighbor pairs or solvent-separated pairs. At $t = 12$ ps, a cluster of four particles containing no near-neighbor pairs had formed. During the first 480 ps of the simulation, the solutes formed a fluctuating cluster of four or five particles most of the time. Sometimes the cluster spanned the periodic cell, and sometimes it was compact. There were few near-neighbor pairs in the cluster; most adjacent pairs were solvent-separated.

The cluster started to break down at $t = 492$ ps. A significant decrease in the degree of association among the solute atoms was observed around this time. The simulation was continued for approximately one more nanosecond. During this period there was no tendency for the development of the relatively strong solute associations that were observed during the initial 0.5 ns of the simulation. The solute atoms formed compact clusters involving two to five atoms, with clusters extending across the periodic cell appearing only transiently, and with predominantly solvent-separated rather than near-neighbor pairs of atoms.

The results of this simulation give no support to the conventional wisdom of hydrophobic interaction that suggests that the solutes should want to aggregate and form primarily near-neighbor pairs. It is still possible, however, that given a sufficiently long time they might form such a stable cluster and that the simulation was not long enough for this to happen. To test whether a compact cluster with many near-neighbor pairs is actually favored in water, we performed a second simulation in which the solutes initially formed such a compact cluster and we observed whether the structure was stable and persisted. The five solutes remained closely associated for approximately 180 ps with some configurational rearrangements. The cluster had 5-8 near-neighbor pairs, and every solute formed a near-neighbor pair or a solvent-separated pair with every other solute most of the time. After $t = 180$ ps, the cluster became less closely associated. For $t > 180$ ps, there were at most 4 near-neighbor pairs, and for $t > 252$ ps there were at most two. In the last part of the simulation, from $t = 228$ ps to 348 ps, the structure was similar to that observed in the last nanosecond of the simulation in which the solute atoms were well separated initially. We conclude that the initial compact cluster is unstable in water.

Thus, starting from both an initial condition in which the atoms in water are well separated and an initial condition in which they form a cluster with several near-neighbor pairs, we found the system evolved toward states in which the atoms are not highly associated and in which the association is primarily through solvent-separated pairs. Since the same sorts of final configurations were achieved in both cases, we conclude that the runs were long enough to give a true indication of the equilibrium states.

The systems in the two previous simulations were small. They contained 195 water molecules, and when the five atoms formed a cluster containing primarily solvent-separated intersolute distances the cluster could span the periodic simulation cell. The small system size and periodic boundary conditions might be creating artifacts. To check this we performed a third simulation for a larger system containing 6 solute atoms and 394 water molecules (nominal solute concentration of about 0.8 mol/l). The results of this simulation confirm those for the smaller system.

Table I summarizes some of the results for the first and third simulations. Here n_{nn} is the time-averaged number of near-neighbor pairs of atoms and n_{ss} is the time-averaged number of solvent-separated pairs. The numbers given in table I are averages over the latter parts of each simulation, after the system had thoroughly equilibrated. For comparison, the table gives the numbers for a completely random distribution of the solutes in the volume. For both concentrations, n_{nn} is slightily greater than for a random distribution, but the excess is of the order of the statistical noise of the calculation. On the other hand, for both concentrations, n_{ss} is less than that for a random distribution and the difference appears to be significant. The sum of n_{nn} and n_{ss} for

TABLE I. – *Time average number of near-neighbor pairs and solvent-separated pairs.*

Simulation	n_{nn}	n_{ss}
5 Kr + 195 H_2O ([a])	0.90 ± 0.14	2.85 ± 0.26
(random distribution of 5 atoms) ([b])	0.679	3.441
6 Kr + 394 H_2O ([c])	0.66 ± 0.19	2.02 ± 0.12
(random distribution of 6 atoms) ([b])	0.509	2.580

(*a*) Calculated for the last nanosecond of the 1.5 ns molecular-dynamics run.
(*b*) Analytic calculation.
(*c*) Calculated for the last 0.6 ns of the 1.1 ns molecular-dynamics run.

both concentrations is significantly less than for a random distribution.

A striking consequence of these results is that on the average the solutes in solution tend to stay away from each other. They exhibit what might be called « hydrophobic repulsion » rather than hydrophobic attraction. This suggests that, although they do not want to go into the water (*i.e.* the solubility is low) and hence they are in a sense hydrophobic, once they are in solution they prefer to be surrounded by water and in that sense they are hydrophilic. This tendency to avoid one another in solution is described quantitatively by the osmotic second virial coefficient, given by

$$B_2 = \frac{1}{2}\int_0^\infty [1 - g_{ss}(r)]\, 4\pi r^2\, \mathrm{d}r\,. \tag{1}$$

In evaluating the integral, the $g_{ss}(r)$ was assumed to be unity for r greater than 11.4 Å. We obtained a large positive value, 502 Å^3. The correlation function to be used in this equation should be the solute-solute correlation function at infinite dilution. We used our finite-concentration results, but a comparison of the correlation functions for the two simulations shows that they are independent of concentration and are hence probably close to the infinite-dilution results.

A more complete account of this research will be published later [13].

4. – Summary and discussion.

In this lecture we have used intermolecular potentials that are consistent with some of the known properties of water and aqueous solution of krypton. The water-water potential is a slight modification of the revised central-force model, which was constructed to fit many of the properties of pure water. The solute-water interaction was one that has been shown to give temperature-dependent solubilities in agreement with experiment for Kr. The solute-solute potential is similar to an accurate Kr-Kr potential. It is important to use potentials that have some degree of quantitative validity as well as quali-

tative validity when investigating hydrophobic effects, because the work of Pratt and Chandler [5, 14] indicates that such effects are sensitive to the relative strengths of the various interactions in the solution.

We find that krypton atoms in water tend to stay away from each other rather than to aggregate, *i.e.* they have a large positive value of the second osmotic virial coefficient. When they are close together, they tend to form near-neighbor or solvent-separated pairs, with the latter being more favored than the former, as has been found by previous computer simulations, but the total number of such close encounters is less than for a random distribution of solutes.

These results are consistent with the theory of Pratt and Chandler [14]. This theory predicts that, if solute-solute attractions are much more important than solute-solvent attractions, then solutes will tend to cluster together in water. If, on the other hand, solute-solvent attractions are more important, the solutes will tend to be surrounded by water and will not want to cluster together. For our model of Kr, the latter situation appears to be the case.

There are no experimental data on Kr solutions with which to compare these results. However, a recent analysis [13] of deviations from Henry's law in aqueous solutions of He, N_2, H_2, CH_4 and Ar shows that, although the smaller less soluble gases have negative values of B_2, the value of B_2 is larger (*i.e.* less negative) for the more soluble gases. This correlation suggests that the most soluble noble gases, *i.e.* Kr and Xe, might have large positive values of B_2 at room temperature, which is consistent with the results of the present calculation for Kr.

REFERENCES

[1] C. Pangali, M. Rao and B. J. Berne: *J. Chem. Phys.*, **71**, 2975 (1979).
[2] C. S. Pangali, M. Rao and B. J. Berne: in *Computer Modeling of Matter*, edited by P. Lykos (Washington, D.C., 1978), p. 32.
[3] S. Swaminathan and D. L. Beveridge: *J. Am. Chem. Soc.*, **101**, 5832 (1979).
[4] A. Geiger, A. Rahman and F. H. Stillinger: *J. Chem. Phys.*, **70**, 263 (1979).
[5] R. L. Pratt and D. Chandler: *J. Chem. Phys.*, **67**, 3683 (1977).
[6] D. C. Rapoport and H. A. Scheraga: *J. Phys. Chem.*, **86**, 873 (1982).
[7] W. C. Swope and H. C. Andersen: *J. Phys. Chem.*, **88**, 6548 (1984).
[8] F. H. Stillinger and A. Rahman: *J. Chem. Phys.*, **68**, 666 (1978).
[9] T. A. Andrea, W. C. Swope and H. C. Andersen: *J. Chem. Phys.*, **79**, 4576 (1983).
[10] J. A. Barker, R. O. Watts, J. K. Lee, T. P. Schafer and Y. T. Lee: *J. Chem. Phys.*, **61**, 3081 (1974).
[11] W. C. Swope, H. C. Andersen, P. H. Berens and K. R. Wilson: *J. Chem. Phys.*, **76**, 637 (1982).
[12] H. C. Andersen: *J. Chem. Phys.*, **72**, 2384 (1980).
[13] K. Watanabe and H. C. Andersen: *J. Phys. Chem.*, **90**, 795 (1986).
[14] L. R. Pratt and D. Chandler: *J. Chem. Phys.*, **73**, 3434 (1980).

Structure and Dynamics of Molecular Crystals.

M. L. KLEIN

Chemistry Division, National Research Council of Canada
100 *Sussex Drive, Ottawa, Ont., Canada,* K1A 0R6

Molecular crystals and ionic salts with molecular ions often exist in several different structures. At sufficiently high temperatures the molecules can even undergo rotational diffusion. Such phases occur commonly and are referred to as plastic crystal or rotator phases. The characterization of the orientational disorder in rotator phases is dealt with in part I.

The nature of translational and reorientational dynamics in molecular crystals is explored in part II. Time correlation functions which probe both single-particle and collective motions are discussed. Depending upon the particular crystal, molecular reorientation may lead to anomalies in either the acoustic or optic phonon branches. Examples are presented which illustrate such phenomena.

Computer simulation techniques have recently been generalized to allow for variations in the size and shape of the replicated cell. These developments enable the relationship between crystal structures and potentials to be pursued at high temperatures. The basic ideas underlying the isothermal and isobaric MD methods are outlined in part III and examples of structural transformations are presented. Such investigations provide a valuable probe of potentials in the solid state.

PART I

Structure of Rotator Phases.

1. – Introduction.

In the case of molecules, the classification of the states of condensed matter as either solid or liquid is too simplistic since quenching of a liquid or vapour deposition can yield amorphous or glassy structures as well as an ordered

solid. In a system of N *rigid* molecules the configuration can be described by the $3N$-component vectors $\mathbf{X}$ and $\mathbf{\Omega}$ which specify respectively the centre-of-mass positions and the orientations. If we denote the presence of long-range translational order by brackets $\langle\ \rangle$, quasi-static irregular (glassy) order by braces $\{\ \}$, and the presence of diffusive motion by a circle $\circ$, then we can imagine the nine distinct states of condensed matter illustrated in fig. 1. The

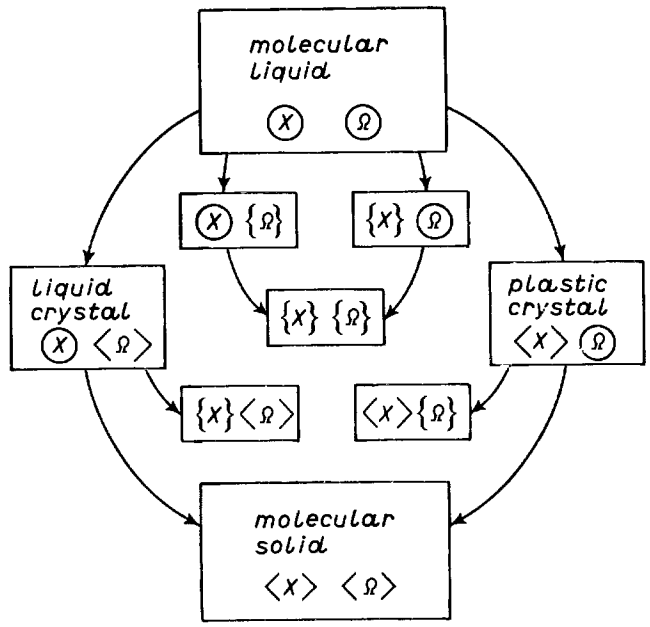

Fig. 1. – Schematic illustration of possible phases for molecular systems. The circles denote the presence of diffusion, brackets long-range order and the braces irregular or glassy order. X and Ω stand for the centre-of-mass positions and molecular orientation, respectively.

low-temperature molecular solid usually exhibits long-ranged order of both the centres of mass and the orientations and this is denoted by $\langle\mathbf{X}\rangle\ \langle\mathbf{\Omega}\rangle$. Liquid crystals have translational diffusion but well-ordered orientations. The complementary plastic crystal (rotator phase) has translational centre-of-mass order, but the molecules are undergoing rotational diffusion. A glassy plastic crystal obtained from quenching a plastic crystal is denoted by $\langle\mathbf{X}\rangle\ \{\mathbf{\Omega}\}$. Even fig. 1 is an oversimplification since we have made no mention of phase- or amplitude-modulated incommensurate structures.

Plastic crystals are characterized by relatively low shear elastic constants and a small entropy change when the crystal melts. In such crystals the molecules are reorienting in some complicated way which depends upon the intermolecular correlations (interactions), and cases of genuinely free rotation are rare. Part I of these lectures is concerned with the general understanding of such rotator phases [1] and the use of molecular-dynamics calculations to characterize this particular kind of structural disorder. Experimentally, a wide variety of techniques are used to probe this behaviour but perhaps the

most powerful is neutron scattering. Accordingly, in the next section we outline the theory of neutron scattering from orientationally disordered molecular crystals [2]. Then in sect. **3** we introduce the various order parameters which are used to characterize the disorder [3-6]. Finally, in sect. **4** we give some specific examples taken from published molecular-dynamics simulations [7-12].

2. – Characterization of orientational disorder by neutron scattering.

The Van Hove function $S(\boldsymbol{Q}, \omega)$ determines the cross-section for neutron scattering from a condensed system [13]

$$S(\boldsymbol{Q}, \omega) = N^{-1}\int_{-\infty}^{\infty} \mathrm{d}t \exp[i\omega t] \langle \varrho(\boldsymbol{Q}, 0)\, \varrho(-\boldsymbol{Q}, t)\rangle\,, \tag{1}$$

where $\hbar\boldsymbol{Q}$ and $\hbar\omega$ are the momentum and energy transferred to the sample in the scattering event. The formal derivation of $S(\boldsymbol{Q}, \omega)$ and its relationship to the scattering cross-section is given in many standard texts and so is not repeated here.

The density operator in eq. (1) is defined as

$$\varrho(\boldsymbol{Q}, t) = \sum_j b_j \exp[-i\boldsymbol{Q}\cdot\boldsymbol{r}_j(t)]\,, \tag{2}$$

where b_j is the scattering length of the j-th nucleus and the summation runs over all the nuclei in the sample. The brackets in (1) denote and average over time origins or equivalently an ensemble average. The peaks in $S(\boldsymbol{Q}, \omega)$ for a given value of the wave vector $\boldsymbol{Q}$ determine the frequencies of collective modes such as phonons, librons, etc. This function is discussed further in part II. However, before going into details concerning the dynamics, we will discuss the *static* structure factor $S(\boldsymbol{Q})$ which is the total scattering at a given value of $\boldsymbol{Q}$ and represents the summation over all inelastic processes with this value of $\boldsymbol{Q}$. In particular, we define

$$S(\boldsymbol{Q}) = \frac{1}{2\pi}\int_{-\infty}^{\infty} \mathrm{d}\omega\, S(\boldsymbol{Q}, \omega) = \langle|\varrho(\boldsymbol{Q})|^2\rangle/N\,. \tag{3}$$

The quantity $S(\boldsymbol{Q})$ can be partitioned into a contribution from coherent (Bragg) scattering

$$S_c(\boldsymbol{Q}) = |\langle\varrho(\boldsymbol{Q})\rangle|^2/N \tag{4}$$

which is the square modulus of a structure amplitude $\langle \varrho(\boldsymbol{Q}) \rangle$ and a remainder, the diffuse scattering

$$S_{\mathrm{d}}(\boldsymbol{Q}) = \langle |\varrho(\boldsymbol{Q})|^2 \rangle - |\langle \varrho(\boldsymbol{Q}) \rangle|^2 = \langle |\delta\varrho(\boldsymbol{Q})|^2 \rangle . \tag{5}$$

The above expressions are valid for atoms, molecules, etc. in all states of matter. The diffuse contribution contains information on the disorder that arises from thermal vibrations, orientational correlations, etc., but, as the name implies, this is not highly structured as a function of $\boldsymbol{Q}$. The coherent scattering, however, has peaks at specific values of $\boldsymbol{Q}$—the Bragg vectors $\boldsymbol{\tau}$. The *positions* of these peaks, which only arise for ordered solids, contain information on the arrangement of the molecules (*i.e.* lattice constants, etc.). In a plastic crystal, the *intensities* of the Bragg peaks yield information on the orientational probability distribution. To demonstrate this explicitly, we rewrite the density operator using the position vector of the molecular centre of mass $\boldsymbol{r}_m$ and the atomic position vectors relative to this origin, $\boldsymbol{x}_{ma}$. Thus

$$\varrho(\boldsymbol{Q}) = \sum_m \beta_m(\boldsymbol{Q}) \exp[-i\boldsymbol{Q}\cdot\boldsymbol{r}_m] , \tag{6}$$

where

$$\beta_m(\boldsymbol{Q}) = \sum_a \boldsymbol{b}_{ma} \exp[-i\boldsymbol{Q}\cdot\boldsymbol{x}_{ma}] . \tag{7}$$

In terms of this *molecular* scattering amplitude, $S_{\mathrm{c}}(\boldsymbol{Q})$ takes the form

$$S_{\mathrm{c}}(\boldsymbol{Q}) = \left| \sum_m \langle \beta_m(\boldsymbol{Q}) \exp[i\boldsymbol{Q}\cdot\boldsymbol{r}_m] \rangle \right|^2 \Big/ N ; \tag{8}$$

an analogous expression can be obtained for $S_{\mathrm{d}}(\boldsymbol{Q})$.

To proceed further, approximations must be introduced [2]. The usual starting point is to assume that translational and rotational motions can be decoupled. This allows the amplitude to be written as

$$\langle \varrho(\boldsymbol{Q}) \rangle \simeq \sum_m \langle \beta_m(\boldsymbol{Q}) \rangle \langle \exp[i\boldsymbol{Q}\cdot\boldsymbol{r}_m] \rangle . \tag{9}$$

Next, if we assume that all molecules in the system are the same, we can drop subscript m in the expression for $\langle \beta_m \rangle$. In addition, we make the usual Debye-Waller factorization to obtain

$$\langle \varrho(\boldsymbol{Q}) \rangle \simeq \langle \beta(\boldsymbol{Q}) \rangle \exp[-W_Q] \sum_m \exp[i\boldsymbol{Q}\cdot\langle \boldsymbol{r}_m \rangle] , \tag{10}$$

where

$$\exp[-W_Q] = \langle \exp[i\boldsymbol{Q}\cdot\delta\boldsymbol{r}_m] \rangle \simeq \exp[-Q^2\langle u^2 \rangle/6] , \tag{11}$$

and the displacement of the centre of mass

$$\boldsymbol{u} = \delta \boldsymbol{r}_m = \boldsymbol{r}_m - \langle \boldsymbol{r}_m \rangle \,. \tag{12}$$

The Bragg intensities now take a particularly simple form

$$S_c(\boldsymbol{Q}) = |\langle \beta(\boldsymbol{Q}) \rangle|^2 \exp[-2W_Q]\, N\Delta(\boldsymbol{Q} - \boldsymbol{\tau}) \,, \tag{13}$$

where Δ is the crystal delta-function and $\boldsymbol{\tau}$ the Bragg vector introduced previously. Apart from the modulation due to the rotational form factor, this expression is the same as for scattering from an atomic solid. We will not dwell on the diffuse scattering but note that it too can be simplified and when combined with (13) yields

$$S(\boldsymbol{Q}) = \langle |\delta\beta(\boldsymbol{Q})|^2 \rangle + |\langle \beta(\boldsymbol{Q}) \rangle|^2 S_m(\boldsymbol{Q}) \,, \tag{14}$$

where the centre-of-mass structure factor for the *solid* is given by

$$S_m(\boldsymbol{Q}) = [1 - \exp[-2W_Q]] + \exp[-2W_Q]\, N\Delta(\boldsymbol{Q} - \boldsymbol{\tau}) \,. \tag{15}$$

It should be recalled that for a molecular *liquid*

$$S_m(\boldsymbol{Q}) - 1 = \varrho \int \mathrm{d}\boldsymbol{r} \exp[i\boldsymbol{Q}\cdot\boldsymbol{r}][g_m(r) - 1] \,, \tag{16}$$

where ϱ is the molecular number density and $g_m(r)$ the radial distribution function for the centres of mass.

Additional simplification of the expression for $S(\boldsymbol{Q})$ follows if we assume that the molecules are rigid rotors and that there are no effects due to nuclear spin correlations, etc., in which case

$$\langle \beta(\boldsymbol{Q}) \rangle = \sum_a \langle b_a \rangle \langle \exp[i\boldsymbol{Q}\cdot\boldsymbol{x}_a] \rangle \,, \tag{17}$$

$$\langle |\beta(\boldsymbol{Q})|^2 \rangle = \sum_{ab} \langle b_a \rangle^* \langle b_b \rangle \langle \exp[i\boldsymbol{Q}\cdot\boldsymbol{x}_{ab}] \rangle \,. \tag{18}$$

The orientational averages implicit in (17) and (18) contain information on the orientational disorder in the system. If the molecular orientations are randomly distributed in space, one obtains

$$\langle \beta(\boldsymbol{Q}) \rangle = \sum_a \langle b_a \rangle j_0(Qx_a) \,, \tag{19}$$

$$\langle |\beta(\boldsymbol{Q})|^2 \rangle \sum_{ab} \langle b_a \rangle^* \langle b_b \rangle j_0(Qx_{ab}) \,, \tag{20}$$

where $j_0(x) = (\sin x)/x$ is the zeroth-order spherical Bessel function. With these simplifications the total scattered intensity is given by

$$S(\boldsymbol{Q}) = \sum_{ab} \langle b_a \rangle^* \langle b_b \rangle j_0(Qx_{ab}) + \Big| \sum_a \langle b_a \rangle j_0(Qx_a) \Big|^2 [S_m(\boldsymbol{Q}) - 1] . \tag{21}$$

Depending on whether (15) or (16) is used for $S_m(\boldsymbol{Q})$ eq. (21) is valid for a solid or a liquid. The first term in (21) is due to intramolecular correlations and gives rise to the periodic variation characteristic of high-Q scattering. In fact, this is how bond lengths are determined in condensed phases. The second term is due to intermolecular correlations; the rotational form factor giving rise to a severe damping of the centre-of-mass scattering. The presence of relatively few Bragg vectors is a characteristic feature of plastic (or rotator-phase) crystals. We see from the above analysis that this arises from the orientational « averaging » rather than enhanced centre-of-mass vibrations. While eq. (21) explains qualitatively the scattering from both molecular liquids and rotator-phase solids, the assumption of random or « free » rotation is not particularly good, even for the liquid.

A very useful higher-order approximation for solids is to expand $\langle \beta(\boldsymbol{Q}) \rangle$ in terms of symmetry-adapted functions [4]. For a cubic crystal Kubic harmonics are employed [14]

$$\langle \beta(\boldsymbol{Q}) \rangle = \langle b_A \rangle + n \langle b_B \rangle \sum_l i^l C_l j_l(Qd) K_l(\Omega) , \tag{22}$$

where C_l is the expansion coefficient, $K_l(\Omega)$ the Kubic harmonic, Ω the polar angles of $\boldsymbol{Q}$ and d is the bond length of the molecule which for simplicity is assumed to be AB_n (*e.g.*, CBr_4, SF_6, etc.). The normalized probability that an AB bond is in the solid angle $d\Omega$ is given by $f(\Omega)\,d\Omega$, where

$$4\pi f(\Omega) = 1 + \sum_{l=2}^{\infty} C_{2l} K_{2l}(\Omega) , \qquad C_{2l} = \langle K_{2l} \rangle . \tag{23}$$

In the case of a tetrahedral molecule or ion in a cubic rotator phase

$$\langle \beta \rangle = \langle b_A \rangle + 4 \langle b_B \rangle [j_0(Qd) + C_4 j_4(Qd) K_4 + \ldots] , \tag{24}$$

where

$$K_4 = (21/16)^{\frac{1}{2}} [5(x^4 + y^4 + z^4) - 3] . \tag{25}$$

Here (x, y, z) are the components of the unit vector in the direction of Q. To this level of approximation, the orientational distribution function is not isotropic but is peaked in specific directions which are indicated by the value of C_4 which in turn can be derived from fitting experimental Bragg intensities [2, 15]. This approach has been successfully exploited to analyse dif-

fraction data from a variety of solids such as CBr_4, SF_6, CD_4, C_2D_4, NH_4Br, KCN, etc. The interpretation of C_4 will be explored in more detail in sect. **3** where we also discuss other orientational order parameters. Raman scattering can also be used to probe the orientational distribution function [16]. Unfortunately, we have neither the time nor the space to go into details.

TABLE I. – *Experimental values for* $C_4 = \langle K_4(\Omega)\rangle$ *for various cubic rotator phase crystals.*

Crystal	Bond vector	C_4
CD_4	C-D	0.25 [5]
SF_6	S-F	1.47 [2]
NaCN	C-N	0.19 [15]
KCN	C-N	– 0.13 [15]

A few experimental values of the expansion coefficient C_4 are quoted in table I. To put the experimental values in perspective it should be noted that for pure [111] ordering a bond vector $C_4 = -1.53$, while for pure [100] ordering $C_4 = 2.29$. Such large values are never observed in practice because of thermal librational motion of the bond vectors in their pockets and because of the

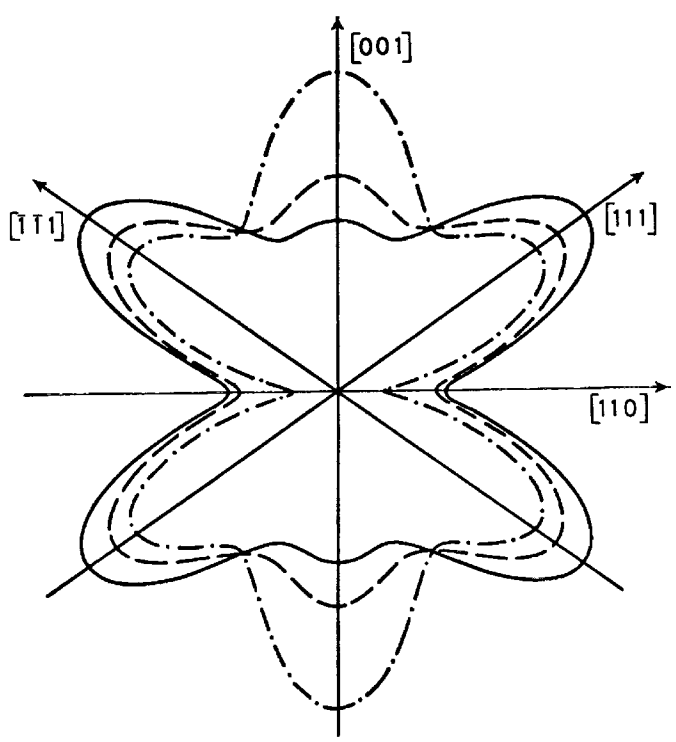

Fig. 2. – Orientational probability distribution $f(\Omega)$ for CN^- ions in NaCN and KCN viewed in the [110] plane: — · · KCN at 295 K, – – – KCN at 180 K, —·—·— NaCN at 295 K. The results (see ref. [15]) were obtained from a fit to Bragg intensities using the form $4\pi f(\Omega) = 1 + C_4 K_4(\Omega) + C_6 K_6(\Omega)$.

rotational diffusion. Nevertheless, the positive value for C_4 for the C-D bond vector has been interpreted to indicate a preference for [100] orientation, while the negative value for CN^- ion in KCN suggests that [111] orientations are preferred. Experiments on NaCN suggest that [100] orientations are favoured. The reason for the difference in behaviour between KCN and NaCN has been the subject of intense investigation and much speculation. The experimentally determined [15] orientational probability distribution for the CN^- ions in NaCN and KCN are shown in fig. 2. There is a marked difference in behaviour between the two crystals and this difference is also reflected in their polarized Raman spectra [16]. The effect on $f(\Omega)$ of cooling the KCN crystal should also be noted.

3. – Order parameters.

The expansion coefficients C_4, C_6, etc. introduced above arose naturally out of the experimental work as a way to characterize the orientational disorder in rotator phases. However, depending upon the symmetry of the molecule or molecular ion in question, other order parameters can also be useful, particularly from the point of view of theoretical analysis [6].

For simplicity consider a linear dipolar molecule (or ion) AB in a cubic crystal. Since we are dealing with a solid, it is convenient to use the crystal (X, Y, Z) axes as a reference frame for μ_α, the α component of the molecular dipole $\boldsymbol{\mu}$. In a rotator phase $\langle\mu_\alpha\rangle = 0$, whereas in general, for an ordered solid, $\langle\mu_s\rangle \neq 0$. However, this brings us to a crucial point: we should distinguish between site averages $\langle\mu_\alpha\rangle_s$ and system or ensemble averages

$$[\langle\mu_\alpha\rangle_s] = (1/N_s) \sum_s \langle\mu_\alpha\rangle_s . \tag{26}$$

If the averages are performed over times which are long with respect to τ, the characteristic reorientation time, then in a rotator phase $\langle\mu_\alpha\rangle_s = 0$ *and* $[\langle\mu_\alpha\rangle_s] = 0$. In a glassy phase (recall fig. 1) $\langle\mu_\alpha\rangle_s \neq 0$ but $[\langle\mu_\alpha\rangle_s] = 0$. This consideration applies equally to other order parameters and is relevant to both experiments and simulations since each has its own particular time « window » which may be greater than or less than τ.

The characterization of orientational order in quenched molecular systems borrows from the ideas developed to treat magnetic impurities in alloys (spin glasses), namely, we use the fluctuation in the ensemble-averaged order parameter [6]

$$[\langle\mu_\alpha\rangle_s^2] = (1/N_s) \sum_s \langle\mu_\alpha\rangle_s^2 . \tag{27}$$

It is usual to employ combinations of spherical harmonics as order pa-

rameters. Thus, to study the dipolar order, we could equally have used the three quantities

$$Y_1^{(1)} = (3/4\pi)^{\frac{1}{2}} x\,, \qquad Y_2^{(1)} = (3/4\pi)^{\frac{1}{2}} y\,, \qquad Y_3^{(1)} = (3/4\pi)^{\frac{1}{2}} z\,. \tag{28}$$

For quadrupolar order there are five quantities, two with E_g symmetry

$$Y_1^{(2)} = (5/16\pi)^{\frac{1}{2}} (3z^2 - 1)\,, \qquad Y_2^{(2)} = (5/16\pi)^{\frac{1}{2}} (x^2 - y^2) \tag{29}$$

and three functions with T_{2g} symmetry

$$Y_3^{(2)} = (15/4\pi)^{\frac{1}{2}} xy\,, \qquad Y_4^{(2)} = (15/4\pi)^{\frac{1}{2}} yz\,, \qquad Y_5^{(2)} = (15/4\pi)^{\frac{1}{2}} zx\,. \tag{30}$$

Because of the normalization condition on the components of the bond vector, *i.e.* $(x^2 + y^2 + z^2)^2 = 1$, the order parameters $[\langle Y^{(2)}\rangle_s^2]$ are not really independent of the quantity $C_4 = [\langle K_4\rangle_s]$.

For tetrahedral molecules or ions there are seven function $Y_n^{(3)}$, $n = 1, 7$. It is more usual to use quantities which are referred to as tetrahedral rotor functions $M_n(\Omega)$, $n = 1$ to 7. In a cubic crystal field these split into three groups M_1; M_2, M_3, M_4; M_5, M_6, M_7. We consider only one representative from each group

$$M_1 = (27/16)^{\frac{1}{2}} \sum xyz\,, \tag{31}$$

$$M_2 = (9/320)^{\frac{1}{2}} \sum (5x^3 - 3xr^2)\,, \tag{32}$$

$$M_5 = (27/64)^{\frac{1}{2}} \sum x(y^2 - z^2)\,, \tag{33}$$

where $\boldsymbol{r} = (x, y, z)$ is a unit vector directed along a bond vector and the summation runs over all arms of the tetrahedron [11]. The normalization has been fixed by

$$\sum_{n=1}^{7} \langle M_n^2\rangle = 1\,. \tag{34}$$

To appreciate the significance of the quantities M_n consider the four ideal orientations of a tetrahedron in a cubic field shown in fig. 3. In the T_d configuration shown $M_1 = +1$ with the definition of axes which is used here. A φ rotation through 90° generates another T_d configuration, for which $M_1 = -1$. Further rotations through 90° generate other T_d orientations, divided equally between those with $M_1 = +1$ and those for which $M_1 = -1$. Thus, in a disordered phase in which only T_d orientations are present, $\langle M_1\rangle = 0$ but $\langle M_1^2\rangle = 1$. Similar considerations to those just sketched show that, if orientations are exclusively of T_d type, then $\langle M_2^2\rangle = 0$ and $\langle M_5^2\rangle = 0$. We may repeat this argument for other orientations and thereby determine the order

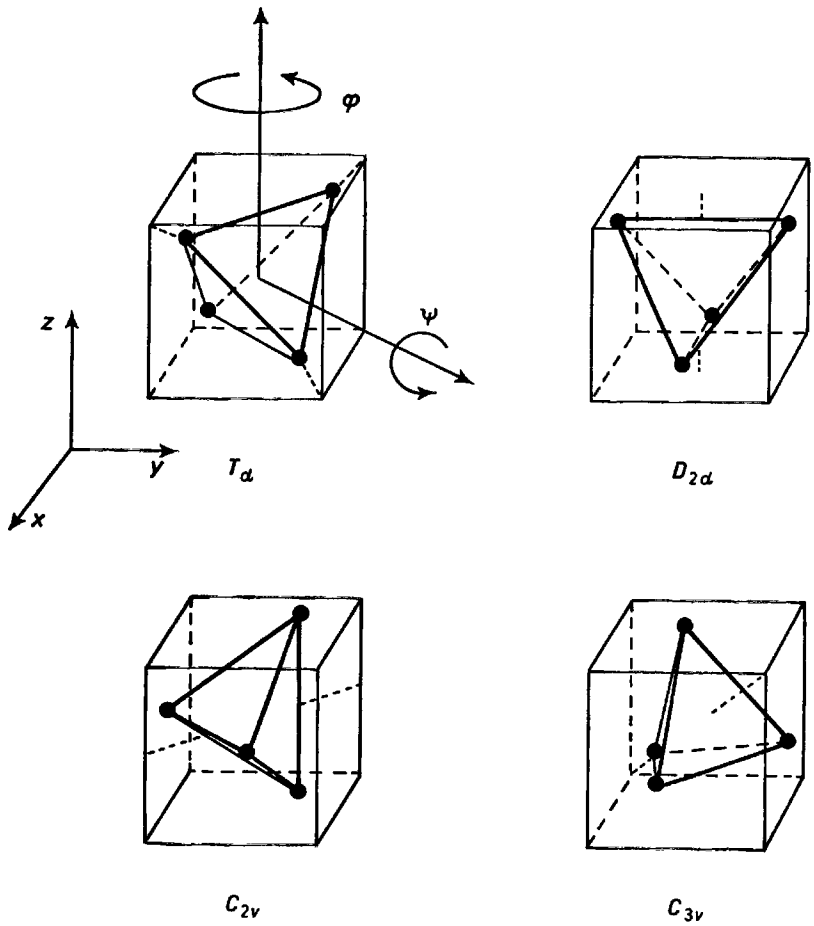

Fig. 3. – Ideal orientations of a tetrahedron in a cubic field (see text).

TABLE II. – *Order parameters for ideal orientations of a tetrahedron* (*).

	$\langle M_1^2 \rangle$	$\langle M_2^2 \rangle$	$\langle M_5^2 \rangle$	$\langle K_4 \rangle \equiv C_4$
T_d	1	0	0	−1.53
D_{2d}	0	0	(1/3)	−0.26
C_{3v}	(1/81)	(80/243)	0	0.74
C_{2v}	0	(5/16)	(1/48)	0.70

(*) These are averages over all symmetry-related orientations. Also $\langle M_n \rangle = 0$ for all n; $\langle M_1^2 \rangle = \langle M_2^2 \rangle = \langle M_4^2 \rangle$; $\langle M_5^2 \rangle = \langle M_6^2 \rangle = \langle M_7^2 \rangle$, where $\sum_n \langle M_n^2 \rangle = 1$.

parameters characterizing structures of T_d, D_{2d}, C_{2v} and C_{3v} type. The results are collected in table II, it is difficult to distinguish C_{2v} from C_{3v} order.

The use of the fluctuations in the order parameters M_n is an alternative to the expansion in Kubic harmonics. The Kubic harmonic values for standard configurations (T_d, D_{2d}, C_{2v} and C_{3v}) are also listed in table II. For T_d, all four bonds lie along [111] directions; for D_{2d} and C_{2v} all four bonds are equivalent but not oriented along the main symmetry axes; while for C_{3v}, one arm

lies along a $\langle 111 \rangle$ orientation and the other three lie nearly along $\langle 100 \rangle$ axes. Note that in evaluating $\langle K_4 \rangle$ an average is taken over all arms of the tetrahedron.

Chemists will recognize that the order parameters $Y^{(1)}$, $Y^{(2)}$, $Y^{(3)}$ or equivalently M_n have the symmetry of p, d and f atomic orbitals and in cubic rotator phases these separate into groups analogous to orbital splittings induced by a cubic crystal field.

4. – Molecular-dynamics calculations.

The order parameters introduced above have all been used to characterize the structure of rotator-phase solids generated in computer simulations [7-12]. A wide range of molecular crystals and ionic salts have now been investigated and from the many possible examples we have chosen three. We omit any discussion of how MD calculations are actually carried out for molecular solids or how to handle the long-range interionic forces in salts. It is assumed that these important prerequisites were dealt with in other lectures.

4·1. *Mixed crystal* $(KCN)_x(KBr)_{1-x}$. – The mixed crystal systems $(KCN)_x$-$(KBr)_{1-x}$ with $x < 0.58$, in contrast to pure KCN, show no evidence of structural phase transitions and appear to be cubic at all temperatures. Various experiments indicate that cooling produces an orientational glass state [6]. MD results on the cooling of the system $(KCN)_{0.5}(KBr)_{0.5}$ have been published [9]. In view of the fact the MD calculations were run for only about 10 ps at each temperature, it is not possible to make other than qualitative remarks on the experimentally observed orientational glass state [6].

Nevertheless, we will use these data to illustrate the value of the order parameters introduced above. The MD sample was equilibrated at 360 K at which temperature $C_4 = -0.36$. This is typical of a rotator-phase crystal with a preference for [111] order. On sequential cooling to 189 K, 116 K and 65 K the value of C_4 decreased to -0.63, -0.86 and -1.11, respectively, which indicated increased [111] order as the temperature is lowered, *i.e.* freezing into [111] pockets.

The dipolar and quadrupole order parameters $Y^{(1)}$ and $Y^{(2)}$ introduced above were also evaluated. At the higher temperatures $\langle Y \rangle_s = 0$ and $[\langle Y \rangle_s] = 0$ for all Y's. However, in view of the results for C_4 which showed a preference for [111] orientations, it is not surprising that it is the T_{2g} order parameter rather than the corresponding E_g function which rises rapidly at low temperature (see fig. 4). More unexpectedly, the dipole order parameter followed the T_{2g} curve. Typically, the quantities $[\langle Y \rangle_s]^2$ were two orders of magnitude smaller than the corresponding $[\langle Y \rangle_s^2]$. These results also suggest freezing into [111] pockets. To establish with greater certainty the existence

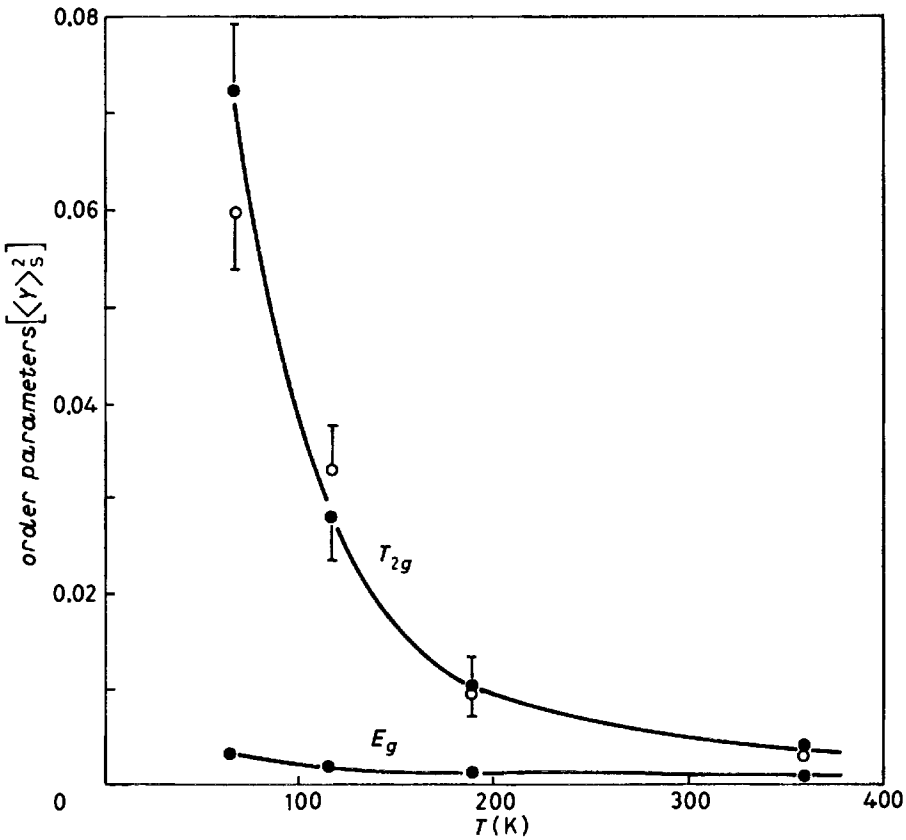

Fig. 4. – Temperature dependence of the order parameters for $(KCN)_{0.5}(KBr)_{0.5}$ defined in the text. The dots show the quadrupolar E_g and T_{2g} order parameters and the open circles the dipolar order parameter.

of a glasslike state would require very much longer calculations on very large systems.

4·2. *Lithium sulphate.* – The high-temperature cubic phase of solid lithium sulphate (Li_2SO_4) exhibits extreme disorder of two types: orientational disorder of the molecular anions and a high-mobility diffusive motion of the lithium cations. This rotator phase, which also behaves as a solid electrolyte, is an excellent system to illustrate how MD calculations can provide complementary information to that of real experiments. As before we are not concerned here with the details of the MD calculations [12] which were carried out using atom-atom potentials of the exp-6 type and two different approximations for the charge distribution of the $SO_4^=$ ion. In the first model the oxygen atoms carried a charge of $Q_0 = -0.8e$, while in the second $Q_0 = -0.5e$.

Atom-atom radial distribution functions for these two models are shown in fig. 5 and 6. The curves for the $SO_4^=$ ions are remarkably similar, in both cases the O-O structure is washed out due to the rotational motion of the anion. In fact, the O-O distribution resembles the H-H distribution calculated for the rotator phase of methane [8]. For the two models atom-atom distributions

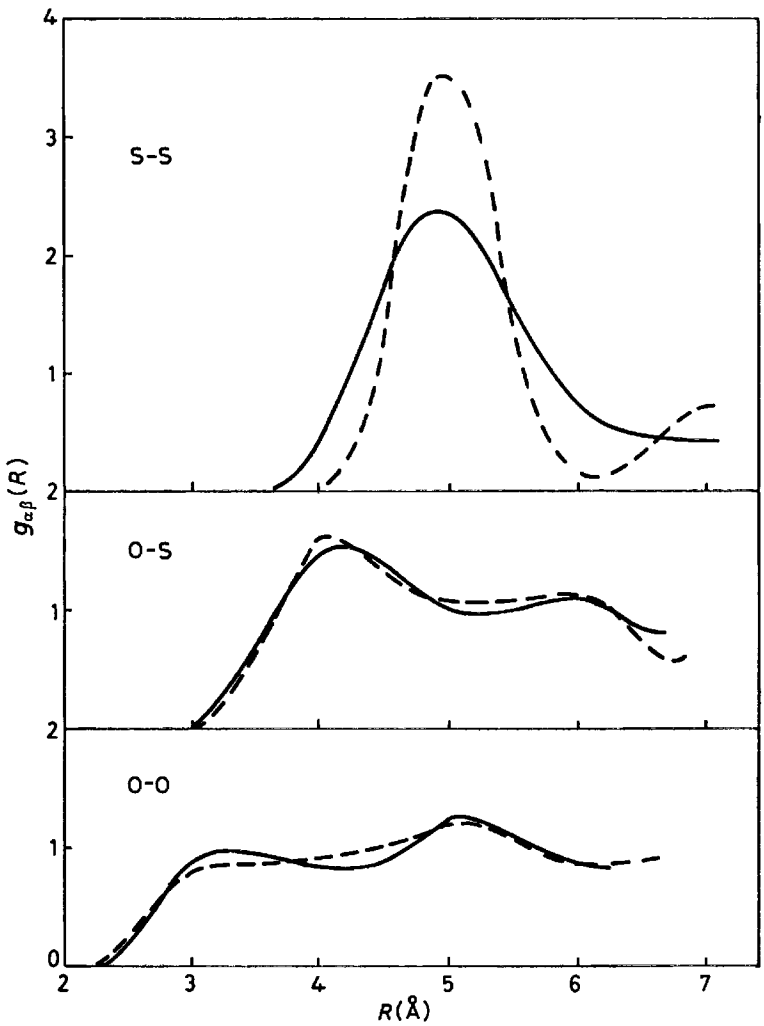

Fig. 5. – Atom-atom radial distribution functions for $SO_4^=$ ions in the cubic phase of lithium sulphate. The full and dashed curves refer to models with $Q_0 = -0.8e$ and $-0.5e$, respectively.

involving the lithium ions are very different and this difference in the spatial distribution of atoms is also reflected in the structure factor $S(\boldsymbol{Q})$. Figure 7 compares the $S(\boldsymbol{Q})$ calculated from the MD simulations with the experimental neutron scattering data. Clearly, the model with $Q_0 = -0.8e$ is more representative of the real crystal. The experimental diffraction data were interpreted in terms of an isotropic distribution of the O-atoms [17]. In this case the order parameters based on the tetrahedral rotor functions should have the values $\langle M_n \rangle = 0$ and $\langle M_n^2 \rangle = 1/7 = 0.143$ for $n = 1, 7$. Table III shows the MD results for both models of the $SO_4^=$ charge distribution. The model with $Q_0 = -0.8e$ shows a more isotropic distribution, in better agreement with experiment. In contrast, the model with $Q_0 = -0.5e$ displays a definite preference for C_{3v} or C_{2v} order. The improved description of the rotator phase provided by the model with $Q_0 = -0.8e$ comes about precisely because of the increased amount of D_{2d} order. Neither model seems to favour the T_d orientation.

TABLE III. – *Orientational order parameters* $\langle M_n^2 \rangle$ *for the rotator phase of lithium sulphate* [12].

Q_0	$\langle M_1^2 \rangle$	$\langle M_2^2 \rangle$	$\langle M_5^2 \rangle$
$-0.5e$	0.06	0.20	0.11
$-0.8e$	0.09	0.14	0.17

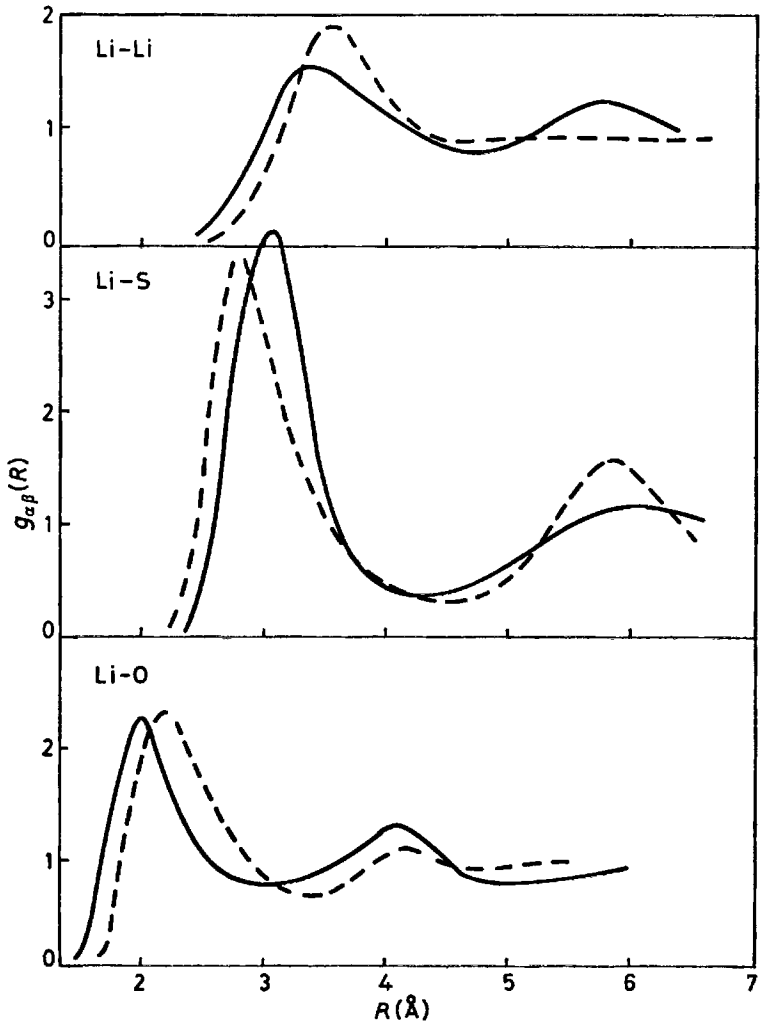

Fig. 6. – Atom-atom radial distribution functions for the cubic phase of lithium sulphate. The full and dashed curves refer to models with $Q_0 = -0.8e$ and $-0.5e$, respectively.

4·3. *Solid nitrogen.* – When liquid nitrogen freezes, the molecular centres of mass adopt an hexagonal close-packed structure (h.c.p.), but the molecules are orientationally disordered. The nature of this disordered phase has been widely discussed in the literature. Diffraction experiments [18] and Raman scattering [19] were first interpreted as indicating that the N_2 molecule precesses around the crystal c-axis with a fixed tilt angle θ, such that

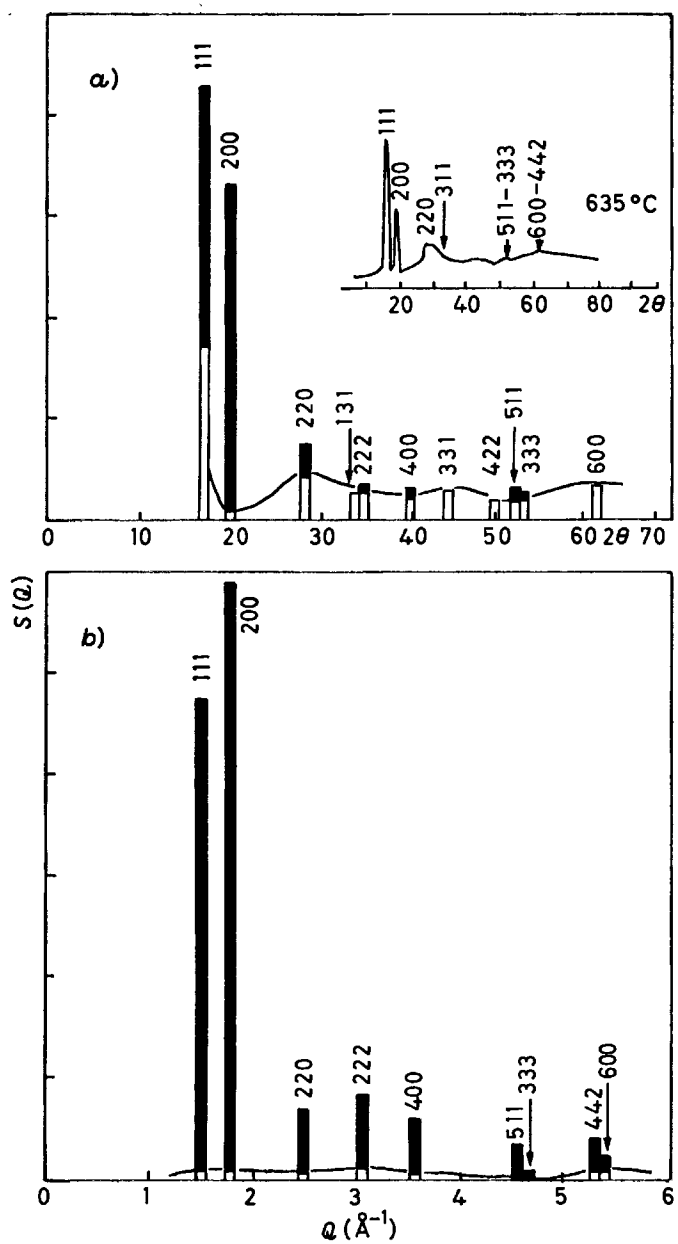

Fig. 7. – Neutron diffraction structure factor $S(Q)$ for lithium sulphate in its cubic rotator phase for the models with *a*) $Q_0 = -0.8e$ ($T = 861$ K) and *b*) $-0.5e$ ($T = 1153$ K), respectively. The Bragg vectors are labelled by the integers (lmn), the Bragg and diffuse contributions are indicated by filled and open regions. Inset is the experimental neutron diffraction pattern from ref. [17].

$\langle P_2(\cos\theta)\rangle = 0$. Molecular-dynamics calculations based on a simple atom-atom potential were shown to generate a stable h.c.p. rotator phase [7]. Figure 8 shows the time evolution of $\cos\theta$ for three randomly chosen molecules from the 288 used in the sample. These results show clearly that the molecules make frequent head-to-tail flips and that precession at a constant tilt angle is certainly not dominant. Subsequent reanalysis of the diffraction data in terms of the appropriate symmetry-adapted functions clarified this question [20]. The ap-

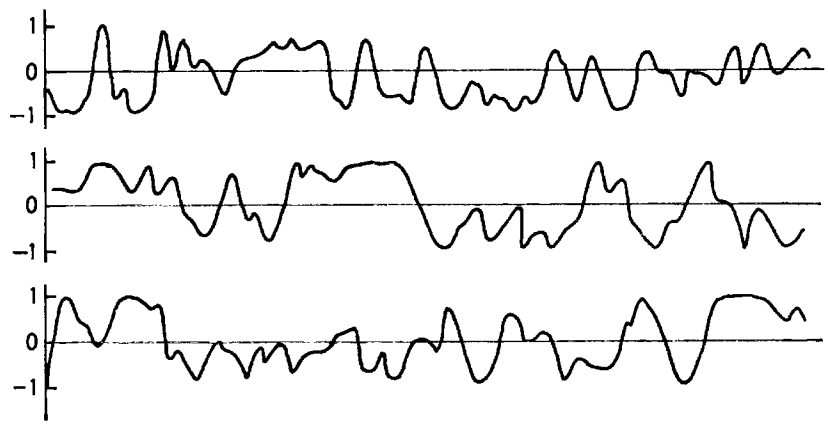

Fig. 8. – Time variation of $\cos\theta$ for three arbitrary nitrogen molecules, where θ is the angle between the molecular axis and the crystal c-axis. The time period covers about 27 ps.

propriate order parameter for this h.c.p. crystal is $a_2 = \langle P_2(\cos\theta)\rangle$. It turns out that $a_2 \approx 0$ which can arise from random orientations or precession at a fixed angle given by $\cos\theta = (1/3)^{\frac{1}{2}}$. In view of the MD calculations the former interpretation would seem to be more appropriate.

PART II

Dynamical Properties of Rotator Phases.

1. – Introduction.

As the name implies, molecular dynamics can be used to calculate the autocorrelation function (a.c.f.) of a dynamical variable $A(t)$. Such functions have the form

$$R(t) = \langle A(t)A(0)\rangle\,, \tag{35}$$

where the brackets denote an average of time origins. The Fourier transform of $R(t)$ is the power spectrum

$$R(\omega) = \int_{-\infty}^{\infty} \mathrm{d}t \exp\left[-i\omega t\right] R(t)\,. \tag{36}$$

Information on the dynamical behaviour of a system is contained in such power spectra. The a.c.f. in eq. (35) expresses only temporal relaxation, but spatial correlations may also be important. An example of such a correlation function is provided by the Van Hove function $S(\boldsymbol{Q}, \omega)$ in part I. However,

before going into details we enter a caveat concerning the time and frequency domain that can be probed using MD calculations. Typically, phase-space trajectories are followed for about $10^4 \Delta t$, where the time step $\Delta t \approx 10$ fs. The total MD run time is usually less than 100 ps, which in turn implies that one cannot easily probe phenomena with characteristic relaxation times longer than about 10 ps. Thus very slow relaxation phenomena are excluded. There is consequently also a lower limit to the frequency of phonons (sound waves) that can be followed, namely a few cm^{-1}. The system size, which usually contains less than 1000 molecules, places limits on the wavelength of collective modes. The longest wavelength allowed by the periodic boundary conditions in a given direction is L, the simulation cell edge length. Thus the minimum wave vector that can be probed is $Q = 2\pi/L \approx 0.15\,\text{Å}^{-1}$. This range of frequency and wave vector is precisely the domain of thermal-neutron scattering. It is normally not possible to examine the response of a solid in the frequency range of Brillouin experiments (GHz). However, as we shall see below, Raman scattering spectra can be calculated.

2. – Relaxation of the order parameters.

2·1. *Potassium cyanide.* – The order parameters introduced in part I were used to identify possible preferred orientations. For example, the CN^- ion favoured a [100] orientation in NaCN but a [111] orientation in KCN (recall table I). It is clearly also of interest to examine the relaxation of the order parameter as well as its mean or static value. Thus the integral of the appropriate normalized a.c.f. yields a reorientation time which in turn can be measured in NMR experiments. In the case of the alkali cyanides the a.c.f.'s of interest are

$$R^s_{11}(t) = \langle Y^{(2)}_1(t)\, Y^{(2)}_1(0)\rangle\,, \qquad E_g\,, \tag{37}$$

$$R^s_{33}(t) = \langle Y^{(2)}_3(t)\, Y^{(2)}_3(0)\rangle\,, \qquad T_{2g}\,, \tag{38}$$

and

$$\tau^s_{11} = \int \mathrm{d}t\, R^s_{11}(t)/R^s_{11}(0) \tag{39}$$

with an analogous expression for τ^s_{33}. For a polycrystalline sample the NMR reorientation time is given by [10]

$$\tau_2(\text{NMR}) = (2/5)[1 + 3C_4/21^{\frac{1}{2}}]\tau^s_{11} + (3/5)[1 - 2C_4/21^{\frac{1}{2}}]\tau^s_{33}\,. \tag{40}$$

The interpretation of this expresson is that the $\tau_2(\text{NMR})$ is the sum of the individual correlation times τ^s_{11} and τ^s_{33} weighted by the probability of finding the CN^- ion in an orientation, respectively, of either E_g (*i.e.* [100]) or T_{2g} (*i.e.* [111]) symmetry.

The dashed curves in fig. 9 show the single-ion a.c.f.'s of E_g and T_{2g} symmetry calculated for a model of KCN. These curves are featureless, with roughly equal lifetimes $\tau^s_{11} \approx \tau^s_{33} = 0.18$ ps. The value of τ_2(NMR) derived from the MD calculations corresponded rather well with experimental data [21]. The above discussion was based upon the dynamics of individual molecular ions. It turns out that polarized Raman spectra for alkali cyanides can be calculated from the Fourier transform of *collective* correlation functions defined by [16]

$$R_{11}(t) = \sum_k \sum_l \langle Y_1^{(2)}(k, t)\, Y_1^{(2)}(l, t)\rangle\,, \qquad E_g, \tag{41}$$

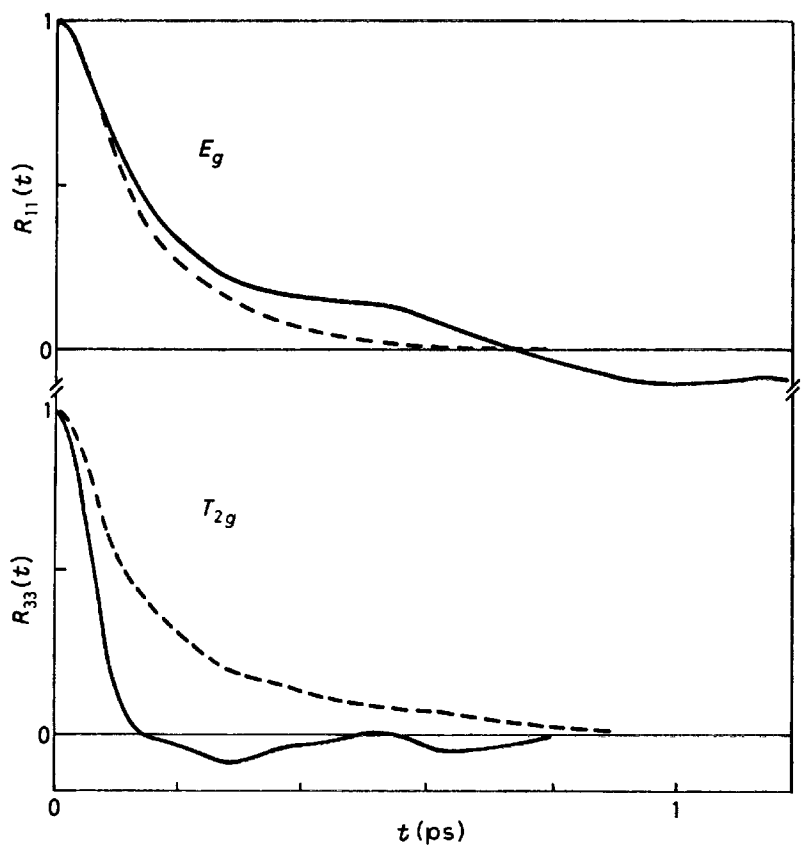

Fig. 9. – Reorientational correlation functions for CN^- ion in KCN at room temperature. The dashed curves are the single-ion functions and the full curves the collective functions (see text).

where the sums run over all pairs of anions k, l. When the summation is restricted to self-terms, we recover the single-ion correlation function $R^s_{11}(t)$. The collective reorientation functions shown in fig. 9 differ between themselves rather more than the corresponding single-particle quantities. In KCN, the E_g function decays much more slowly than the T_{2g} function which implies a considerable difference between the two Raman spectra. The Fourier transforms of these collective functions are shown in fig. 10. There are large errors

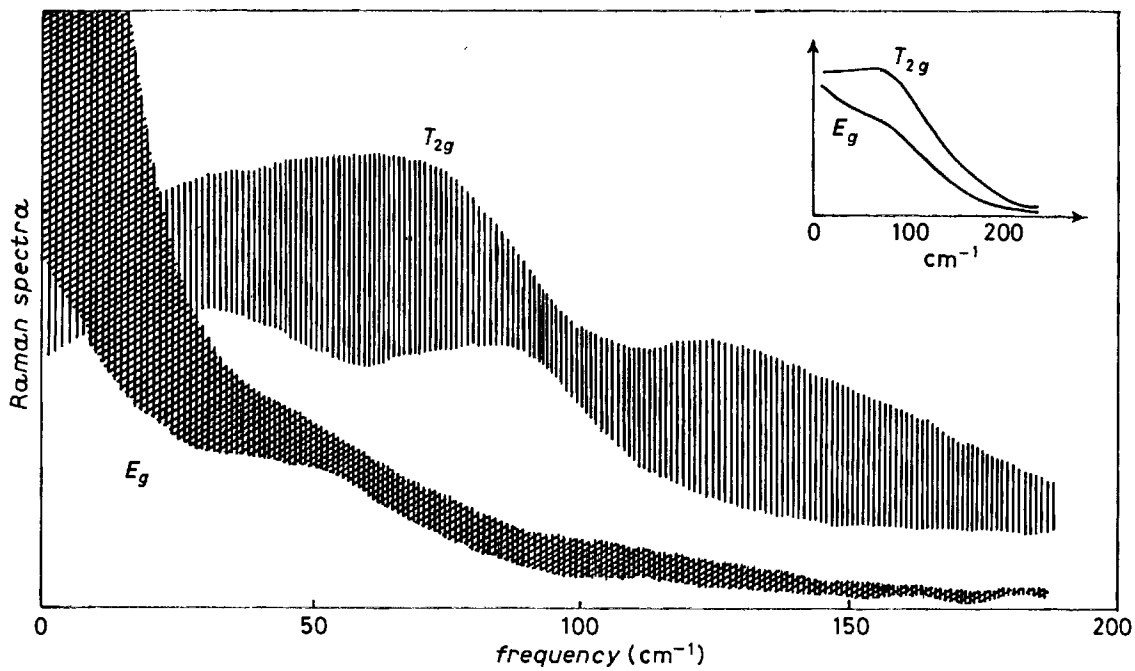

Fig. 10. – Raman spectra for KCN at room temperature. Inset is the experimental result of ref. [16]. The calculated spectra are derived from the collective time correlation functions shown in fig. 9. The shaded areas indicate likely uncertainties in the Fourier transform.

associated with calculating these spectra due to the inevitable loss of statistical information inherent in evaluating collective correlation functions. Nevertheless, there is qualitative accord with the experimental data [16] which are shown inset in fig. 10. The implication is that collective reorientation effects make an important contribution to the Raman spectrum in alkali cyanides.

2·2. *Lithium sulphate.* – The relaxation of the order parameter has also been examined for certain tetrahedral ions. In the case of $SO_4^=$ ion in the rotator phase of Li_2SO_4 the following single-ion a.c.f.'s

$$R_n(t) = \langle M_n(t) M_n(0) \rangle , \qquad n = 1, 7 , \tag{42}$$

were examined for the two models with different $SO_4^=$ charge distributions discussed in part I. It was found that (see fig. 11) in the more realistic model the D_{2d}-type order persisted for much longer times. It should be noted that the local environment of a given $SO_4^=$ ion in the low-temperature ordered solid corresponds closely to a D_{2d}-type configuration. The relaxation time of the order parameters in the rotator phase is in the picosecond range. These can be related to the line width of intramolecular (in this case $SO_4^=$ ion) vibrations, but unfortunately there is not time to pursue this question.

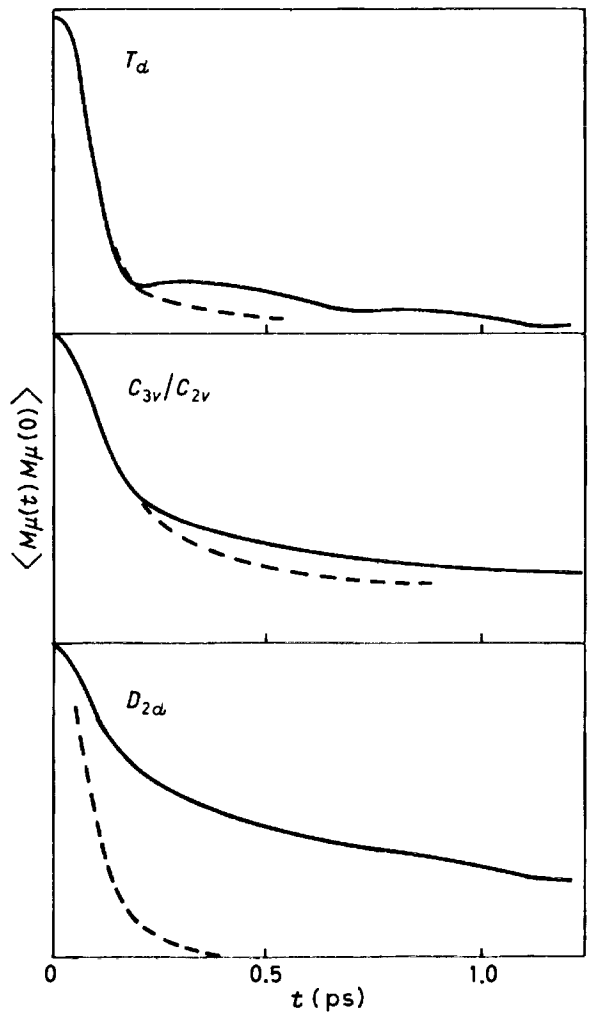

Fig. 11. – Relaxation of the single-ion orientational order parameters for $SO_4^=$ ions in the cubic rotator phase of lithium sulphate. The full and dashed curves refer to the models with $Q_0 = -0.8e$ ($T = 861$ K) and $-0.5e$ ($T = 1164$ K), respectively.

2·3. *Ammonium bromide.* – As a final example of order parameter relaxation we consider NH_4Br which exists in two cubic rotator phases. In the high-temperature α phase, NH_4Br has the NaCl-like structure with the NH_4^+ ion octahedrally co-ordinated but also orientationally disordered. Little is known experimentally about the nature of the disorder in the α phase [4]. On cooling at atmospheric pressure there is a transition at 411 K to a CsCl-like, eightfold co-ordinated β phase. Neutron diffraction has shown that there is flipping between orientations in which the NH bond vectors lie along [111] directions. At still lower temperatures ordered structures arise. For example, at 235 K the NH_4^+ tetrahedra order in an antiferro-type arrangement, with a weak tetragonal distortion (γ phase). Molecular-dynamics calculations have been carried out for both rotator phases using rigid-ion atom-atom potentials [11]. The resulting order parameters $\langle M_n^2\rangle$, $n = 1, 2, 5$, are shown in table IV.

TABLE IV. – *Order parameters for* NH_4Br *based upon* MD *calculations.*

Phase	T (K)	$\langle M_1^2 \rangle$	$\langle M_2^2 \rangle$	$\langle M_5^2 \rangle$	$\langle K_4 \rangle$
α	419	0.02	0.25	0.08	0.37
β	417	0.53	0.05	0.11	– 0.79
	344	0.65	0.02	0.09	– 1.00

It is apparent that the α phase shows a significant degree of C_{3v} order. This preference is revealed by the large value of $\langle M_2^2 \rangle$ and also by the large positive value for $\langle K_4 \rangle$; we recall that in a C_{3v} orientation the arms of the tetrahedron are aligned predominantly along the [100] crystal axes. On transforming to the β phase the arms of the tetrahedra shift to [111] orientations, as evidenced by the large negative value of $\langle K_4 \rangle$ and the large positive value of $\langle M_1^2 \rangle$. The behaviour of the static order parameters is in fair agreement with experimental data [4].

A question of particular interest is the persistence of orientational order of

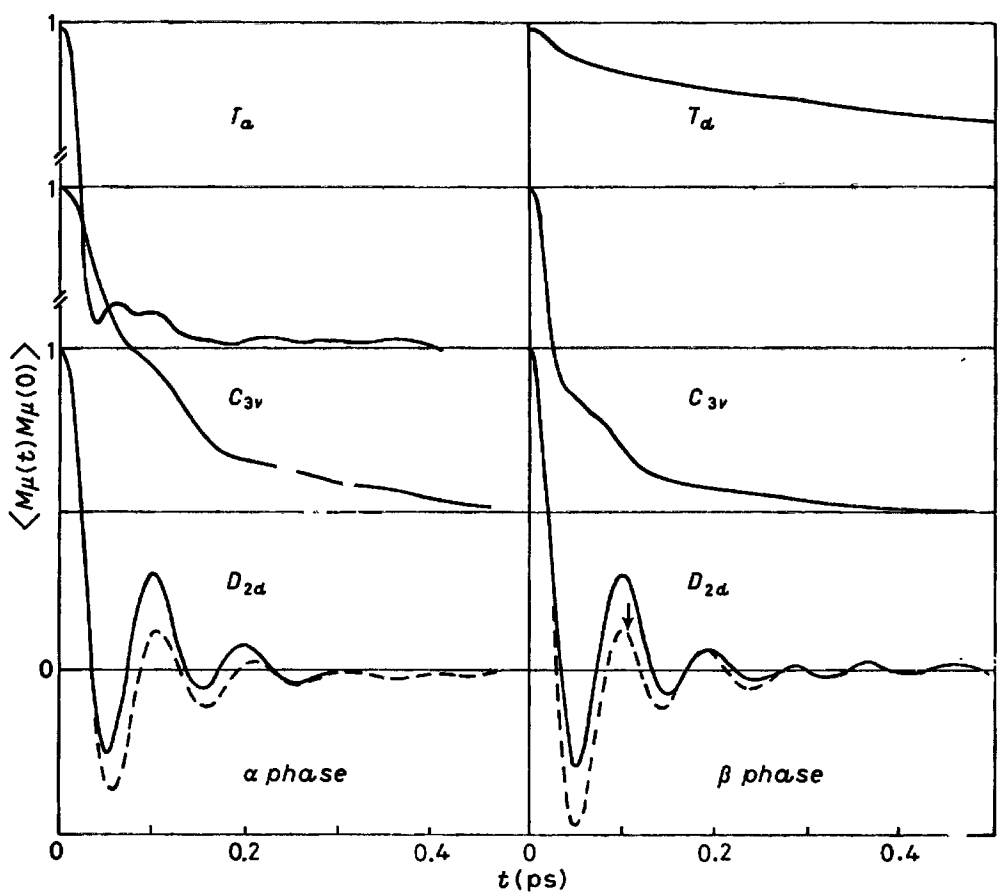

Fig. 12. – Relaxation of the single-ion orientational order parameters for NH_4^+ ions in the two cubic rotator phases of ammonium bromide. The dashed curves are the velocity a.c.f.'s for protons and the arrow indicates the experimentally observed oscillation period for the NH_4^+ ion.

a given type. Figure 12 shows the correlation functions $R_n(t)$, $n = 1, 2, 5$. In the α phase, it is clear that there is no strongly persistent order of any type, though the C_{3v} order is the longest lived. On passing to the β phase, the D_{2d} ($n = 5$) and C_{3v} ($n = 2$) curves are unaltered, but there is a dramatic change in the lifetime of T_d ($n = 1$) function, whose relaxation is now in the picosecond range. The D_{2d}-type function is strongly oscillatory in both phases and is suggestive of a libration about the C_2 axis of the tetrahedron. The decay of the C_{3v} order parameter is likewise suggestive of a more heavily damped torsional motion about the C_{3v} axis.

Table IV reveals that cooling of the β phase leads to increased localization

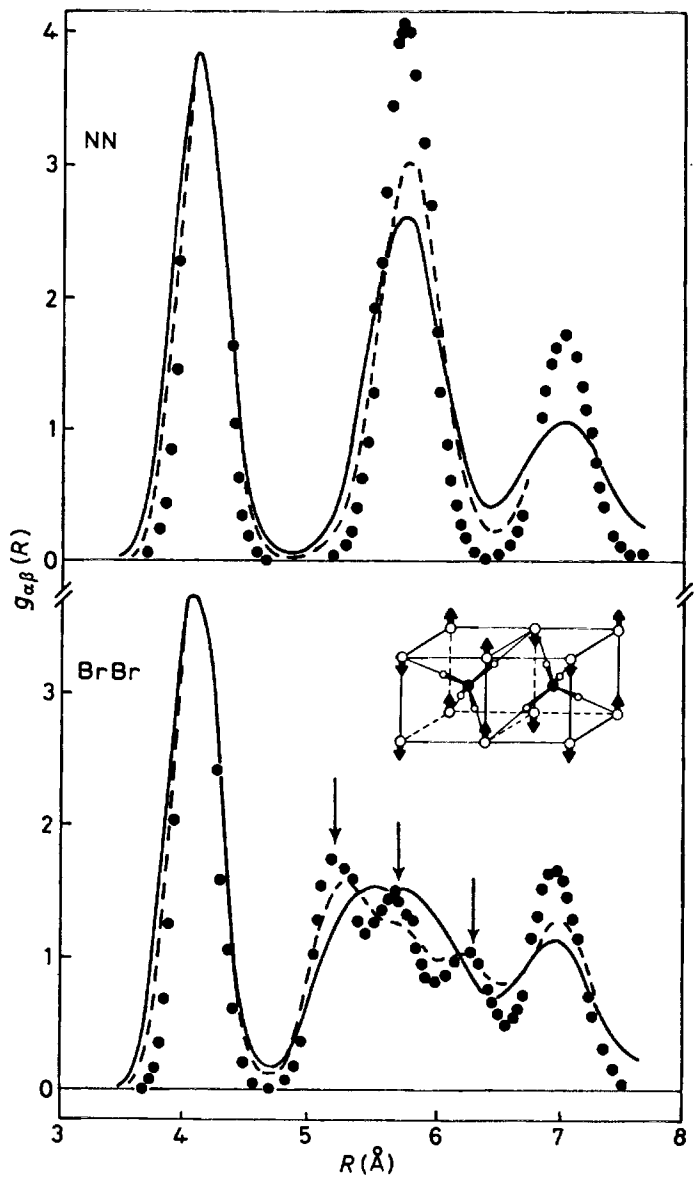

Fig. 13. – Atom-atom radial distribution functions for the β phase of NH_4Br. The full and dashed curves are for 410 K and 344 K, respectively, and the dots for 235 K. The inset shows the halide ion displacement pattern for the Brillouin zone transverse acoustic M-point phonon (see text).

of bond vectors in the [111] directions. Further cooling of the β phase to 235 K caused orientational ordering with an accompanying distortion of the Br^- sublattice (see fig. 13). The spontaneous formation of the γ phase provides us with an example of a solid $\rightarrow$ solid phase transition generated via conventional constant-volume MD calculations [11].

3. – Single-particle dynamics.

3·1. *Velocity autocorrelation functions.* – There are two ways to investigate the lattice vibrations via computer simulation. The first consists of examining the velocity a.c.f., defined as

$$Z_i(t) = \langle \boldsymbol{v}_i(t) \cdot \boldsymbol{v}_i(0) \rangle / \langle \boldsymbol{v}_i(0) \cdot \boldsymbol{v}_i(0) \rangle \,, \tag{43}$$

where $\boldsymbol{v}_i$ is the velocity of species i (this could be the centre-of-mass velocity or the velocity of an atom). The significance of $Z_i(t)$ is that its power spectrum is essentially the phonon density of states $Z_i(\omega)$. We will demonstrate this by using as an example an oscillator with amplitude A, frequency ω and phase φ. The displacement is given by

$$x(t) = A \cos(\omega t + \varphi) \,. \tag{44}$$

Differentiation of the above expression with respect to time yields the velocity $\dot{x}(t) = v_x(t)$ from which it follows that the average energy of a classical oscillator is constant

$$\langle E \rangle = \langle m\omega^2 x^2/2 + m v_x^2/2 \rangle = m\omega^2 A^2/2 = k_B T \,. \tag{45}$$

The last equality enables us to simplify the expression for $Z(t)$ which becomes

$$Z(t) = \langle \sum \sin(\omega t + \varphi) \sin \varphi \rangle / \langle \sum \sin^2 \varphi \rangle \,. \tag{46}$$

We now average over an ensemble of random phases and obtain

$$Z(t) = N^{-1} \sum \cos \omega t \,. \tag{47}$$

It then follows that

$$Z(t) = \int \mathrm{d}\omega \, Z(\omega) \cos \omega t \,, \tag{48}$$

where $Z(\omega)$ is the normalized phonon density of states, *i.e.* the number of oscillators with frequency ω, but normalized to 1 rather than $3N$.

We have just seen that information on the lattice vibrations has been obtained via the single-particle velocity a.c.f. and not from a collective a.c.f. This is not really a paradoxical result since single-particle displacements are nothing more than a superposition of *all* normal-mode oscillations and the single-particle (diffusive) motions. It is not surprising, therefore, that Fourier decomposition of the displacements yields information on the phonon density of states. Examples of the velocity a.c.f. for CF_4 molecules are given in fig. 14 for three phases:

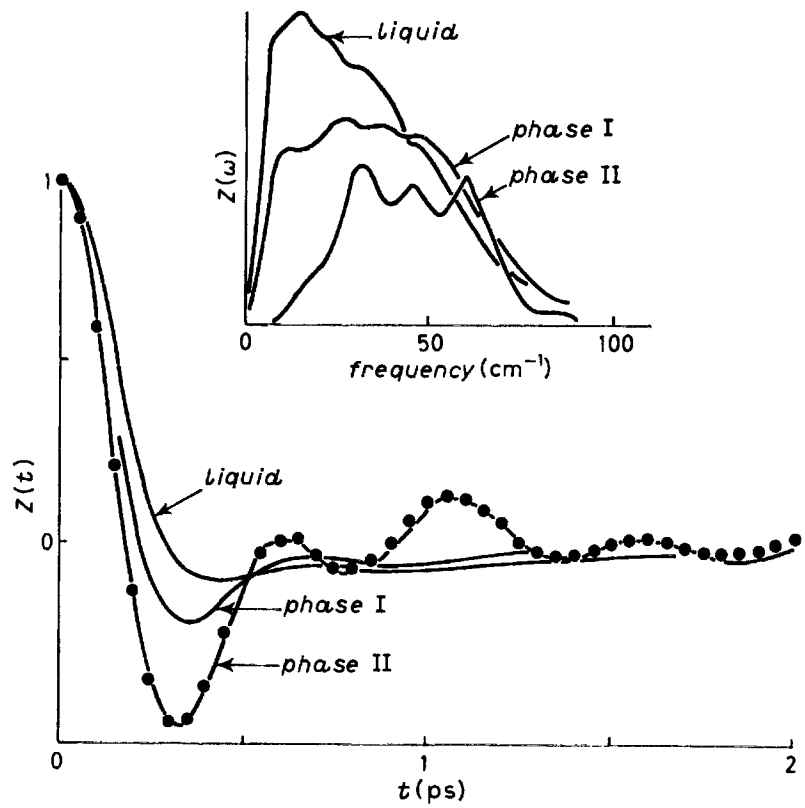

Fig. 14. – Velocity a.c.f. $Z(t)$ and its associated power spectrum $Z(\omega)$ for three phases of CF_4. The full curves were obtained from conventional constant-volume MD calculations and the dots from constant-pressure MD calculations.

the ordered low-temperature monoclinic solid (phase II), the orientationally disordered phase I and the liquid. The associated power spectra $Z(\omega)$ are shown inset. The velocity a.c.f. develops increased structure at low temperatures which is reflected in peaks (critical points) in the density of states.

A corresponding analysis can be carried out for rotational (librational) motions. In this case the appropriate a.c.f. is

$$C(t) = \langle \boldsymbol{\omega}(t)\cdot\boldsymbol{\omega}(0)\rangle / \langle \boldsymbol{\omega}(0)\cdot\boldsymbol{\omega}(0)\rangle\,, \tag{49}$$

where $\boldsymbol{\omega}$ is the angular velocity. The Fourier transform of $C(t)$ yields the density of librational states. Figure 15 shows $C(t)$ and $C(\omega)$ for the three phases of CF_4.

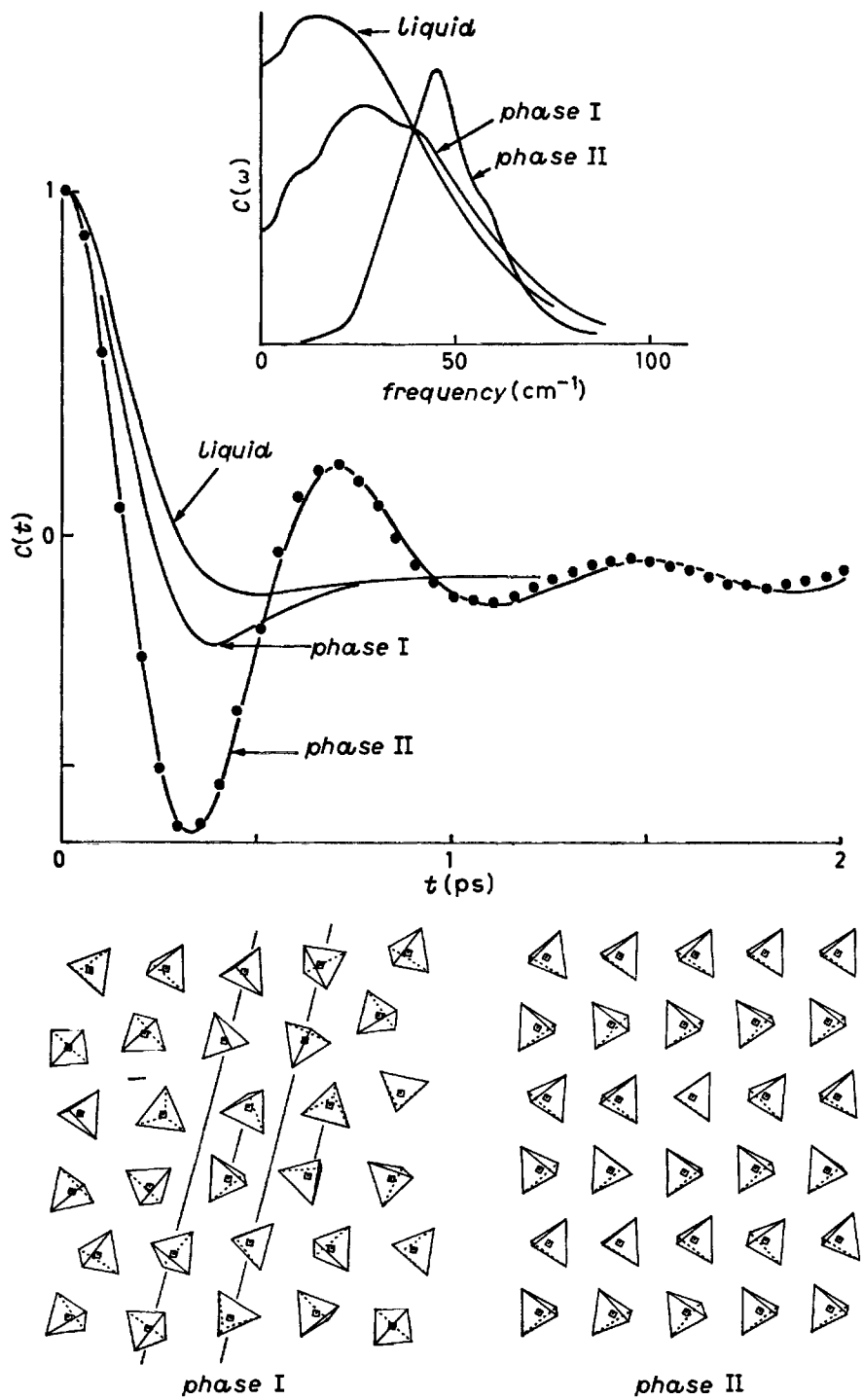

Fig. 15. – Angular velocity a.c.f. $C(t)$ and its associated power spectrum for three phases of CF_4. The full curves were obtained from conventional constant-volume MD calculations and the dots from constant-pressure calculations. The lower part of the figure shows instantaneous configurations from the two solid phases.

A sharp peak in $C(\omega)$ only arises in the low-temperature ordered solid (phase II). Instantaneous configurations from the MD simulation of the two solid phases are also shown in fig. 15.

4. – Collective modes. The dynamical structure factor.

Coherent inelastic neutron scattering has been widely used to study phonons propagating in solids. The most common method consists of scanning the energy (ω) response for a fixed value of the wave vector $\boldsymbol{Q}$. Peaks in the measured spectra are usually identified with phonon frequencies. The neutron response can be related to a time correlation function via the Van Hove function $S(\boldsymbol{Q}, \omega)$ already introduced in part I. Two methods have been used to evaluate the a.c.f. of the density operator $\varrho(\boldsymbol{Q}, t)$ which is implicit in eq. (1). In the most common method MD trajectories are used to evaluate $\varrho(\boldsymbol{Q}, t)$ which in turn is autocorrelated to yield the so-called intermediate scattering function

$$F(\boldsymbol{Q}, t) = \langle \varrho(\boldsymbol{Q}, t)\, \varrho(-\boldsymbol{Q}, 0)\rangle / N\,. \tag{50}$$

The allowed values of $\boldsymbol{Q}$ are determined completely by the size of the MD

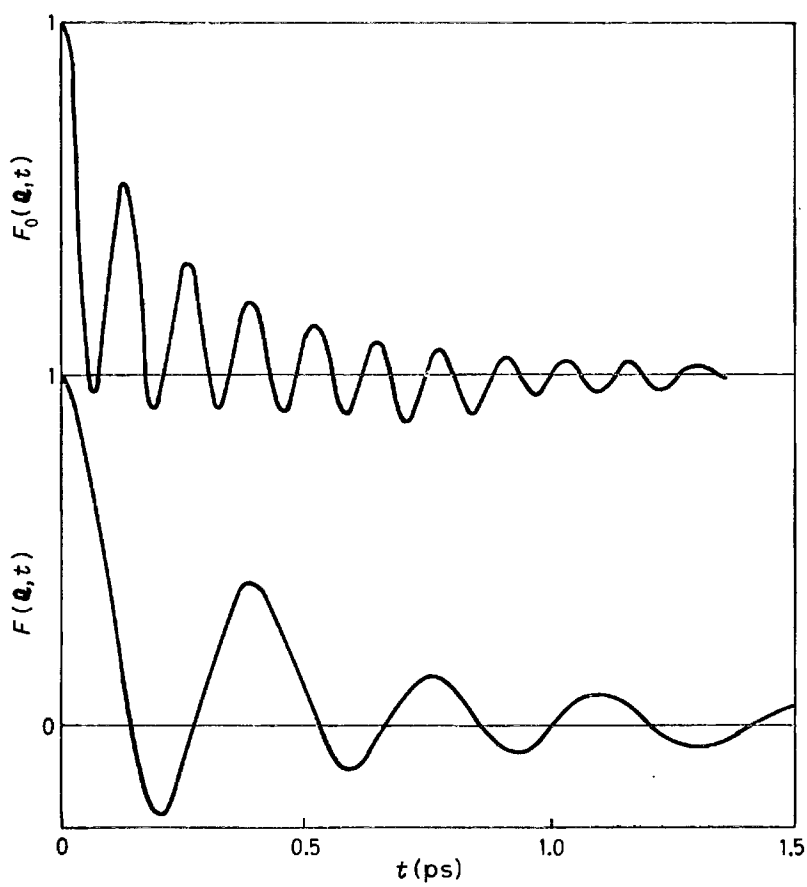

Fig. 16. – The functions $F(\boldsymbol{Q}, t)$ and $F_0(\boldsymbol{Q}, t)$ for KCN at room temperature; the curves are appropriate to longitudinal phonons propagating along the [100] direction. Top: optic branch; bottom: acoustic branch. The value of $\boldsymbol{Q} = 2\pi(0.33, 0, 0)/a$ corresponds to the smallest accessible wave vector in a system with 108 anions and cations.

simulation cell (box quantization)

$$Q = 2\pi(k, l, m)/L\,, \tag{51}$$

where k, l, m are integers and L is the box length. In cases where the function $F(\boldsymbol{Q}, t)$ decays into noise on the picosecond time scale the Fourier transformation to obtain $S(\boldsymbol{Q}, \omega)$ is reasonably straightforward. However, in cases where the phonon response is sharply peaked, especially in atomic systems, it is convenient to employ the so-called direct method to calculate $S(\boldsymbol{Q}, \omega)$. The Van Hove function is rewritten in the form

$$S(\boldsymbol{Q}, \omega) = \lim_{\tau\to\infty} \int_0^\tau \exp[i\omega t]\varrho(\boldsymbol{Q}, t)\,\mathrm{d}t \int_0^\tau \exp[-i\omega t']\varrho(-\boldsymbol{Q}, t')\,\mathrm{d}t'/\tau = \\ = \lim_{\tau\to\infty} |\varrho(\boldsymbol{Q}, \omega)|^2/\tau\,. \tag{52}$$

This method consists of evaluating the Fourier transform of the density operator directly and the spectral resolution increases on accumulating statistics.

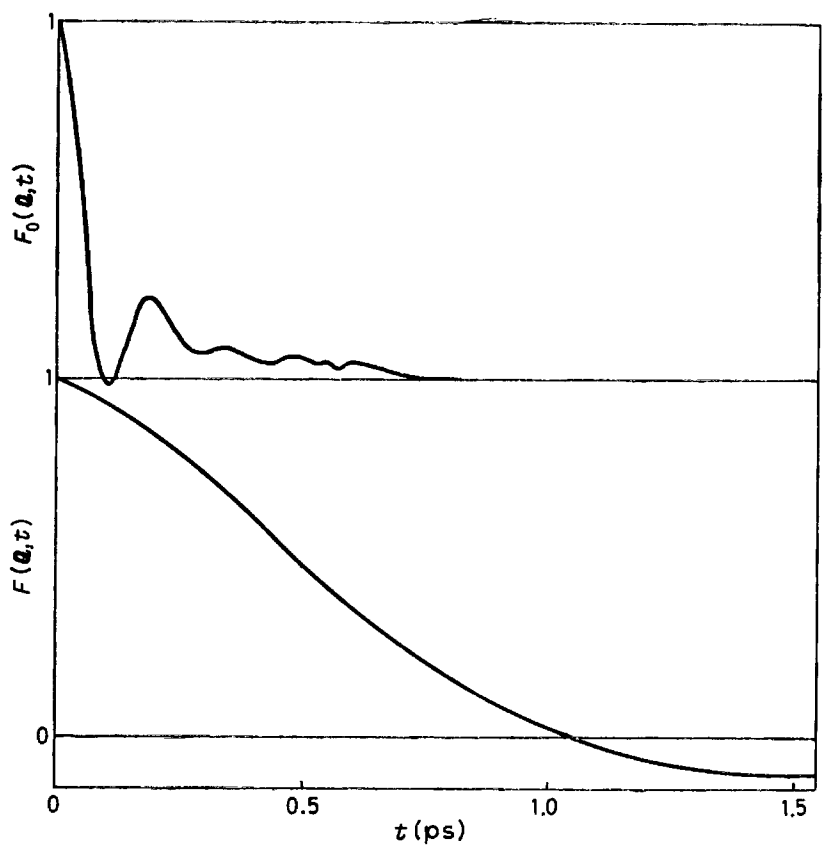

Fig. 17. – The functions $F(\boldsymbol{Q}, t)$ and $F_0(\boldsymbol{Q}, t)$ for KCN at room temperature; the curves are appropriate to transverse phonons propagating along the crystal [100] direction. Top: optic branch; bottom: acoustic branch. The value of $\boldsymbol{Q} = 2\pi(2, 0.33, 0)/a$ corresponds to the smallest wave vector accessible in a system with 108 anions and cations.

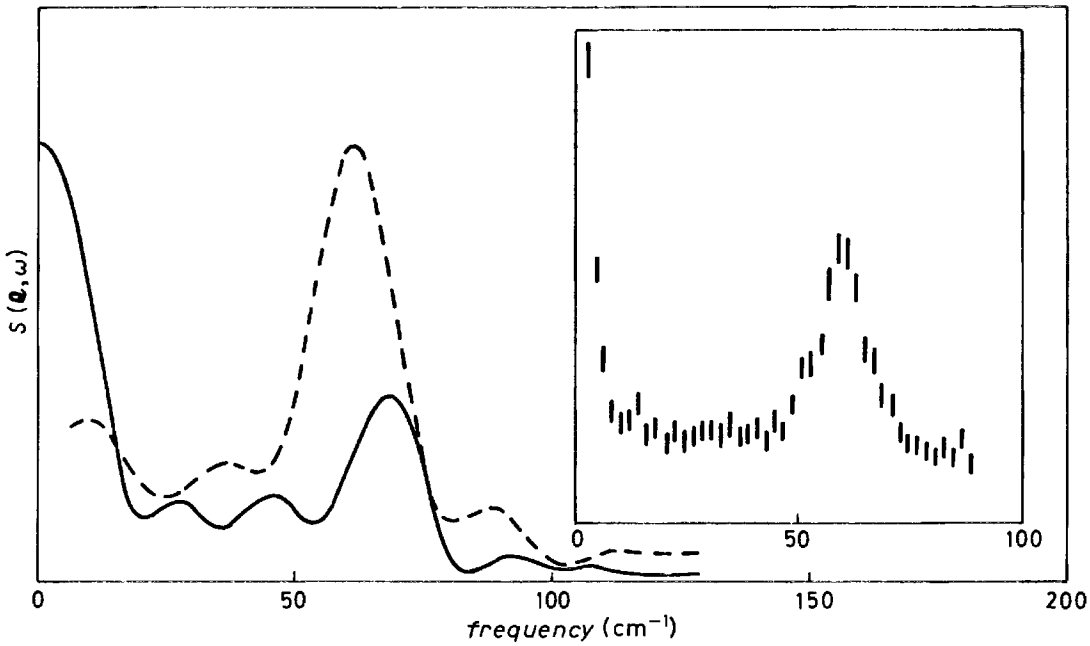

Fig. 18. – The Van Hove function $S(\boldsymbol{Q}, \omega)$ for a transverse acoustic zone boundary phonon, $\boldsymbol{Q} = 2\pi(1, 2, 0)/a$. Main figure gives results for KCN at two temperatures: ——— 184 K, — — — 493 K; inset are experimental data of neutron scattering at 175 K.

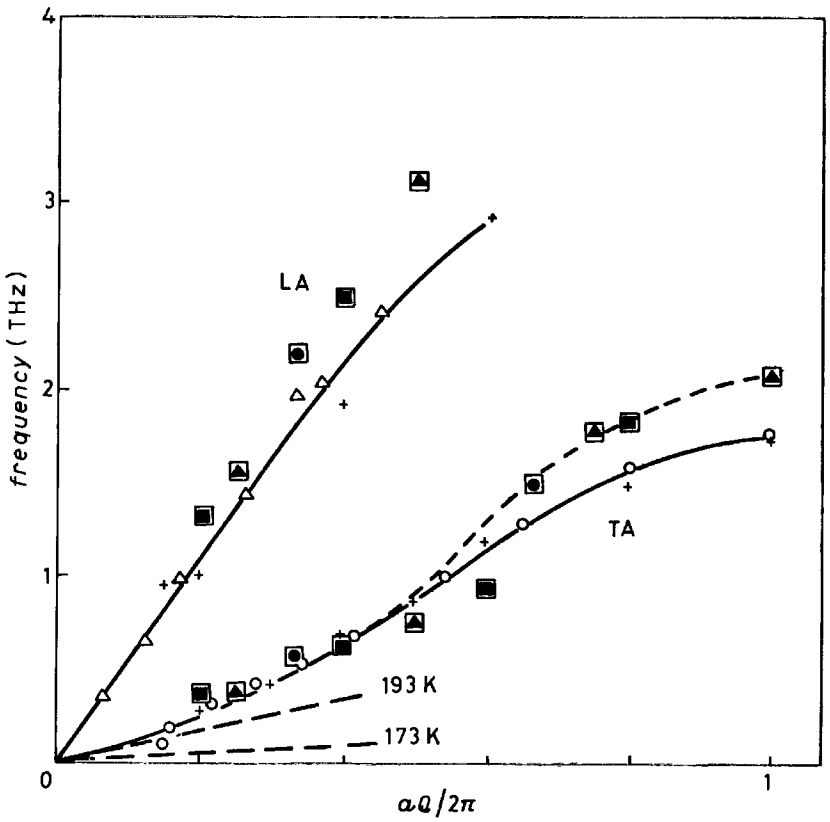

Fig. 19. – Phonon dispersion curves for phonons propagating along the [100] direction in KCN in its cubic rotator phase at 182 K. Experimental results are shown as open circles, open triangles and crosses. Molecular-dynamics results for different system sizes are indicated by the symbols enclosed in squares: • 108, ▲ 256, ■ 500. The dashed curves at low Q are derived from elastic-constant data at the indicated temperatures.

4·1. *Potassium cyanide.* – Figures 16 and 17 show typical examples of the intermediate scattering function $F(\boldsymbol{Q}, t)$. Both longitudinal acoustic (LA) and transverse acoustic (TA) modes are shown for a realistic model of KCN [10]. The oscillations in the LA curve are of considerably higher frequency than in the corresponding TA curve, the latter being anomalously low due to translation-rotation coupling [22]. In favourable case the function $F(\boldsymbol{Q}, t)$ can be transformed to yield $S(\boldsymbol{Q}, \omega)$ and an example is given in fig. 18. The particular $\boldsymbol{Q}$-vector shown corresponds to a zone boundary TA phonon propagating along the crystal [100] direction. Inset is the experimental response which is in fairly good agreement with the MD result [10]. A series of calculations of

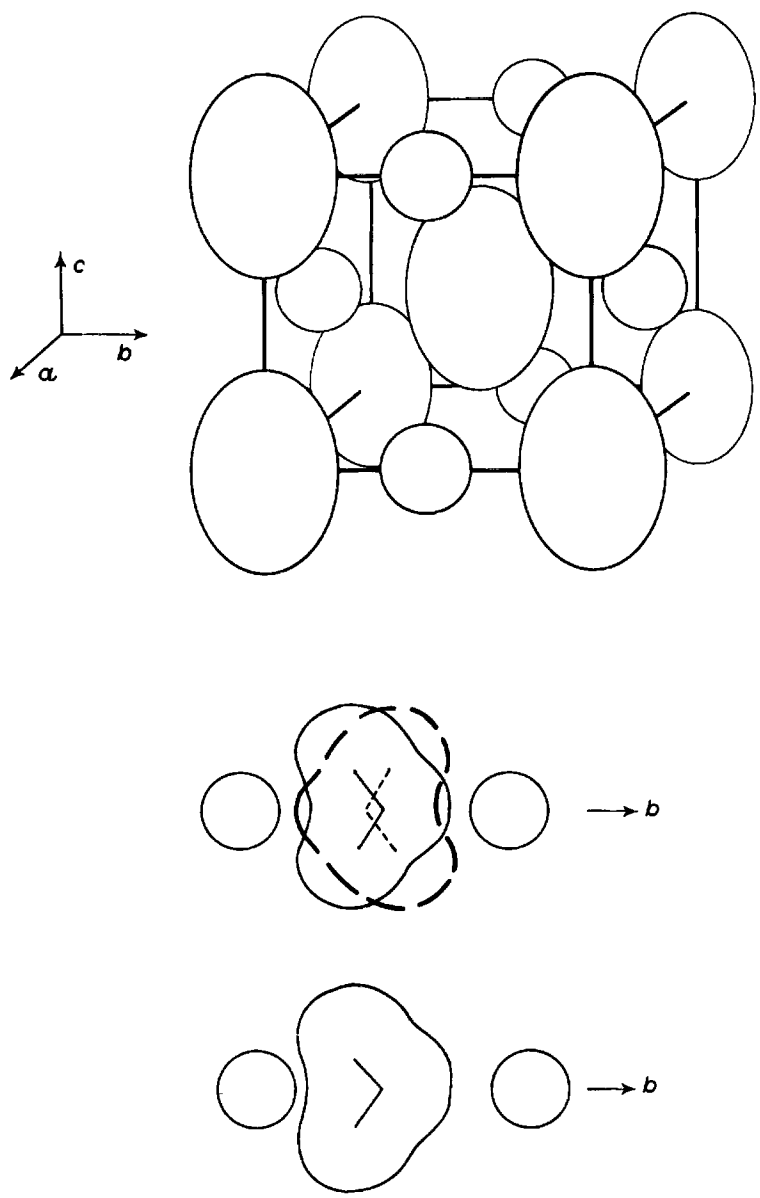

Fig. 20. – Schematic illustration of the structure of $NaNO_2$ in its high-temperature paraelectric phase. The ellipsoids indicate rotational disorder of the NO_2^- ions. Rotation about the c-axis is coupled to a b-axis translation.

this type can be used to construct a complete dispersion curve for phonons propagating in a given direction. Such a composite curve for KCN is presented in fig. 19 but based upon a different rigid-ion potential model. Again, there is fairly good accord with the experimental results which show an anomalous (nonsinusoidal) dispersion of the TA branch but not of the LA one. (Differences between the MD results and experiment at high Q-values can be attributed to neglect of polarization effects.) Optic modes of vibration can also be studied using MD calculations. These modes usually have high frequencies and their intensity is weaker than that of acoustic modes. In addition, there are many ways for such phonons to decay into lower-frequency translational and/or rotational modes. The possibility can lead to optic modes being less well defined. In order to pick out the frequency of optic modes, it is convenient to examine a function $F_0(\boldsymbol{Q}, t)$, defined in a manner analogous to $F(\boldsymbol{Q}, t)$ but with the nuclear co-ordinates replaced by the co-ordinates of the centres of mass and the ions given the fictitious scattering lengths. Thus in the case of KCN we use $b(K^+)=1$ and $b(CN^-) = -1$. The LO and TO functions are shown in fig. 15 and 16. The TO mode appears to be heavily damped and in fact such modes are barely seen in neutron scattering experiments.

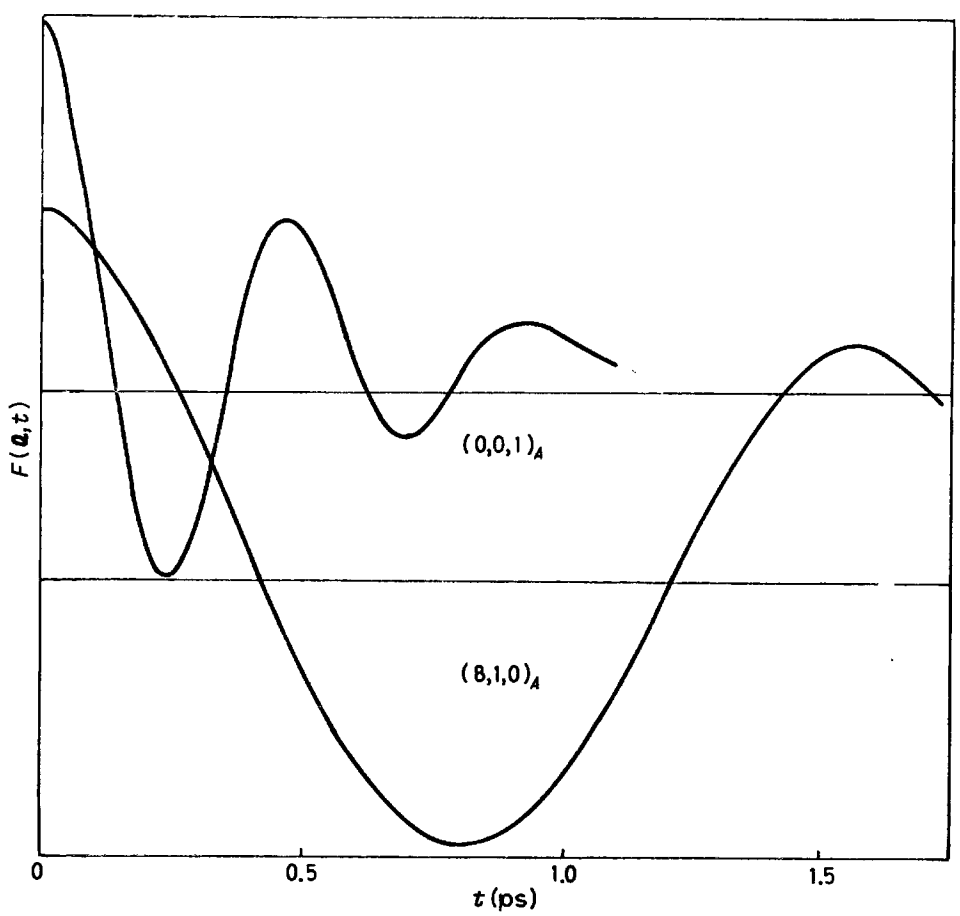

Fig. 21. – The function $F(\boldsymbol{Q}, t)$ for acoustic phonons propagating in the paraelectric phase of $NaNO_2$.

4·2. *Sodium nitrite.* – We have just seen that KCN shows evidence for translation-rotation coupling in the TA phonon branch in its rotator phase which has the rocksalt structure. We now turn to the example of $NaNO_2$ whose high-temperature rotator phase is noncubic (orthorhombic). A sketch of the structure is shown in fig. 20, the ellipsoids indicating orientationally disordered NO_2^- ions. In this paraelectric solid the dipoles of the NO_2^- ions are preferentially aligned parallel to the crystal b-axis. Molecular-dynamics simulations [11] have confirmed that rotation occurs predominantly around the c-axis and there

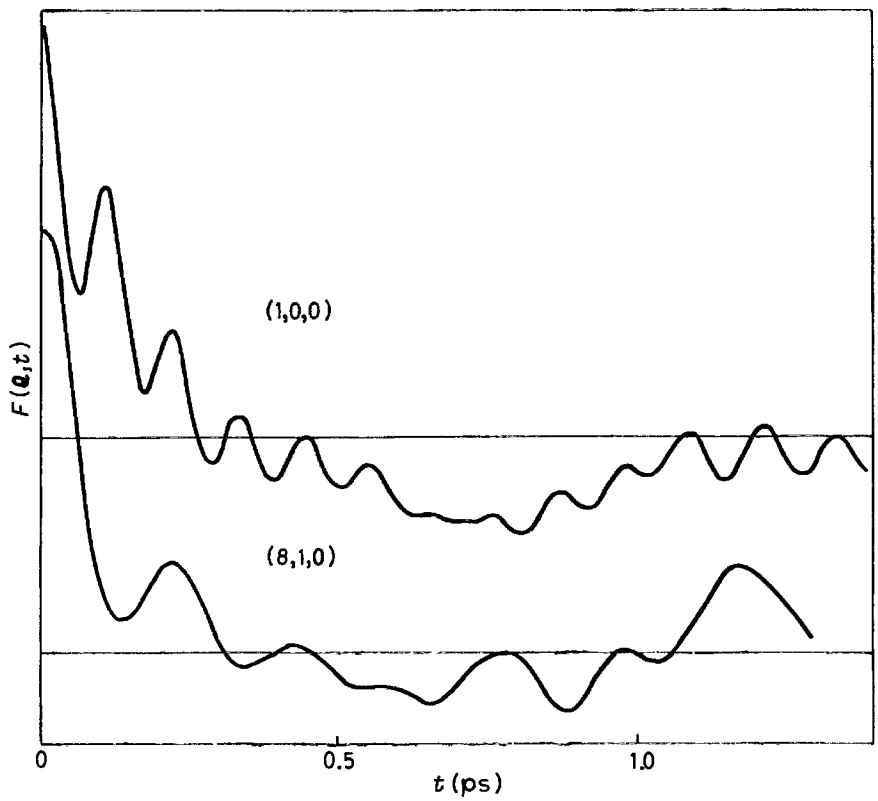

Fig. 22. – The function $F_0(Q, t)$ for optic phonons propagating in the paraelectric phase of $NaNO_2$. The slow modulation of the curves is due to anion reorientation.

is strong coupling of this reorientation to the centre-of-mass displacement of the ion. As a consequence, in contrast to KCN, the acoustic phonons are well behaved (fig. 21) and translation-rotation coupling manifests itself as a modulation of the optic response functions (fig. 22). Unfortunately, we cannot go into details except to state that it is the symmetry of the molecular ion which determines whether or not optic or acoustic branches couple to reorientations [22].

4·3. *Ammonium bromide.* – Finally, we return to the case of NH_4Br in its β phase. We noted above that cooling leads to a distortion of the Br^- sublattice and that this was consistent with a transition to the γ phase. The distortion,

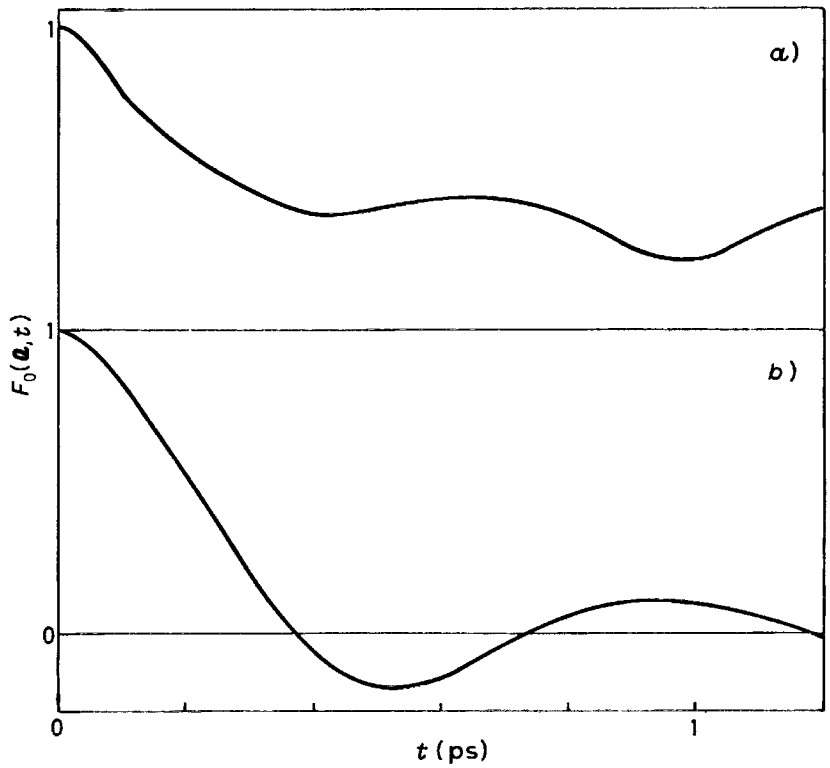

Fig. 23. – The function $F(\boldsymbol{Q}, t)$ for two phonons propagating along the crystal [110] direction in the β phase of NH_4Br (see text): *a*) $\boldsymbol{Q} = 2\pi(0.5, 0.5, 1)/a$, *b*) $\boldsymbol{Q} = 2\pi(0.25, 0.25, 1)/a$.

which is shown in fig. 13, is nothing more than a frozen phonon. (The appropriate wave vector turns out to be $\boldsymbol{Q} = (2\pi/a)(\frac{1}{2}, \frac{1}{2}, 1)$.) The corresponding response function $F(\boldsymbol{Q}, t)$ is expected to show a slow decay which in turn yields a central peak in $S(\boldsymbol{Q}, \omega)$. In effect, this $\boldsymbol{Q}$-vector becomes a Bragg vector of the γ phase. Figure 23 contrasts the behaviour of this phonon (Brillouin zone M-point) with a phonon on the same branch but only half-way to the zone boundary. The latter behaviour is clearly more normal.

PART III

Structural Transformations.

1. – Introduction.

We have seen in part II that conventional MD calculations can be used to study phase transitions and the $\beta \to \gamma$ ordering transition in NH_4Br was used as a specific example. This transition involved a coupling of the NH_4^+ ion rotation to the Br^- ion translation but no massive ionic displacements occurred, the basic arrangement of the ions being essentially unchanged. Although

phase transitions of this general type are quite common, rearrangements of the centre-of-mass packing can also occur [1]. Figure 24 illustrates how close-packed hexagonal (h.c.p.) or cubic (f.c.c.) crystals can transform to a body centred (b.c.c.) arrangement via a purely displacive transition. In the case of the f.c.c. crystal the [100] face becomes a [110] plane of the b.c.c. lattice if the cell vectors ($L_x:L_y:L_z$) transform from the ratios (1:1:1) to ($1:2^{\frac{1}{2}}:2^{\frac{1}{2}}$). The

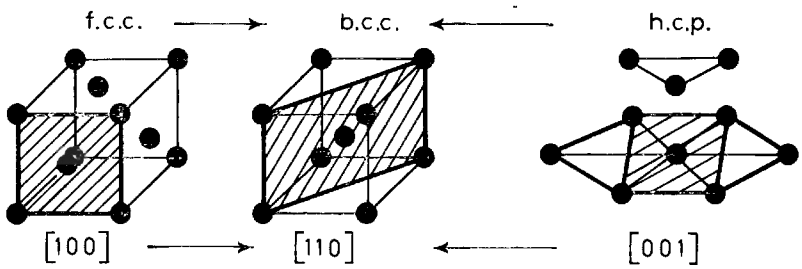

Fig. 24. – Possible transition pathways between f.c.c., b.c.c. and h.c.p. crystal structures (see text).

analogous transition for the h.c.p. crystal involves the basal plane becoming a [110] plane of the b.c.c. lattice. However, this time relative displacements of alternate basal planes are also required. Such motions may be the origin of the hysteresis and/or sluggish behaviour that seems to accompany transitions involving h.c.p. solids. Unfortunately, we do not have the space to dwell on the fundamental question of phase transition mechanisms which may involve a combination of kinetic and energetic considerations. However, transformations of the type illustrated in fig. 24 can now be studied using new and elegant methods which greatly enhance the power of traditional molecular-dynamics (MD) and Monte Carlo (MC) simulation techniques [23]. These new methods, which are discussed in sect. **2**, are not the only way to observe phase transitions. Indeed MD simulations have been reported on large systems (4096 molecules) which on cooling have spontaneously broken up into single crystal grains. The most thoroughly studied example is that of SF_6, whose low-temperature phase turned out to be triclinic [24]. This brute-force approach will likely yield the correct low-temperature crystal structure provided that the sample is big enough to releave the stresses built up at the grain boundaries. Our understanding of the effects of crystal surfaces and grain boundaries on structure is still at an embryonic stage [25]. Simulations on truly massive quasi-two-dimensional systems have revealed just how subtle such effects can be [26]. Accordingly, there is still a need for simulation techniques in which the basic cell can spontaneously transform its shape in response to changes in temperature and/or pressure. We will, therefore, outline the new methods which allow simulations to have this added flexibility [27-29]. The question of the influence of the periodic boundaries, which are present in virtually all simulations, is an important unresolved issue.

2. – Extended-system methods.

Historically it was ANDERSEN who first proposed the idea of carrying out MD calculations using the constraint of constant pressure, constant temperature and a combination of both [27]. The theory of Andersen only dealt with an isotropic system (*e.g.*, fluid) and was, therefore, not applicable to transformation of the type discussed above. It was PARRINELLO and RAHMAN who generalized the constant-pressure MD technique to deal with atomic solids [28]. The further generalization to handle molecules occurred later [30-32]. Since the basic theory for the isotropic atomic system requires only minor (but tedious) extensions to handle the full anisotropic molecular case, we will restrict most of our formal presentation to the simpler example.

The idea of using an extended-system approach is implicit in the work of Andersen but was formulated in an elegant fashion by NOSÉ. As an illustration of the method we reproduce Nosé's derivation of the dynamical equations for generating phase-space trajectories which yield canonical ensemble averages [29]. Then in subsect. **2**·2 we outline Andersen's scheme for constant-pressure MD calculations, again using the isotropic system as our pedagogical example. The general theory is now well documented in the literature and so is only sketched here. The two examples given below are not the only ways to control temperature and pressure in simulations [33-35]. Other methods have been proposed, each of which has its own particular band of aficionados. We have neither the time, nor the space or even the inclination to enter into a discussion on the relative merits of each scheme. We note simply that the methods we outline below have been successfully employed to study molecular solids and specific examples will be discussed in sect. **3**.

2·1. *Canonical-ensemble molecular dynamics.* The physical system of interest is composed of N atoms with co-ordinates $\boldsymbol{q}_i'$, masses m_i and potential energy $U(\boldsymbol{q}')$. The Hamiltonian written in terms of *real* variables is

$$H_0 = \sum (\boldsymbol{p}_i')^2/2m_i + U(\boldsymbol{q}') \tag{53}$$

and the Lagrangian is

$$L_0 = \sum m_i(\dot{\boldsymbol{q}}_i')^2/2 - U(\boldsymbol{q}_i') = K(\dot{\boldsymbol{q}}_i') - U(\boldsymbol{q}_i')\,, \tag{54}$$

the real velocity is simply

$$\dot{\boldsymbol{q}}_i' = \mathrm{d}\boldsymbol{q}_i'/\mathrm{d}t'\,, \tag{55}$$

where the primes denote *real* variables.

Application of the usual Lagrangian equation

$$\frac{\mathrm{d}}{\mathrm{d}t}\left(\frac{\partial L}{\partial \dot{A}}\right) = \frac{\partial L}{\partial A} \tag{56}$$

yields the standard equation of motion

$$m_i \ddot{q}_i' = -\,\partial U/\partial \boldsymbol{q}_i' \,. \tag{57}$$

The idea behind the extended-system method is to imagine that the system of interest is coupled to a heat bath to control the temperature [29]. Following NOSÉ this coupling is expressed via a variable s. The extended system (*i.e.* system of interest plus the heat bath) is described by *virtual* variables, co-ordinates $\boldsymbol{q}_i$, momenta $\boldsymbol{p}_i$, time t and the coupling parameter s. The interaction between the physical system and the heat bath is expressed through the scaling of the particle velocities

$$\mathrm{d}\boldsymbol{q}_i'/\mathrm{d}t' = s(\mathrm{d}\boldsymbol{q}_i/\mathrm{d}t) \,. \tag{58}$$

If $\boldsymbol{q}_i' = \boldsymbol{q}_i$, then s can be interpreted as a time dilation variable, since it then follows that

$$\mathrm{d}t' = \mathrm{d}t/s \,. \tag{59}$$

The Lagrangian of the extended system is written as

$$L_{\mathrm{N}} = L_0 + K_s - U_s \,, \tag{60}$$

where K_s and U_s are the kinetic and potential energies associated with the variable s. The former is assumed to have the form

$$K_s = Q\dot{s}^2/2 \,. \tag{61}$$

We interpret Q as the « mass » for the variable s, but it has the dimension energy·(time)^2. We have yet to determine the functional form for U_s. In terms of *virtual* variables, the Lagrangian is

$$L_{\mathrm{N}} = \sum m s^2 \dot{\boldsymbol{q}}_i^2/2 - U(\boldsymbol{q}) + Q\dot{s}^2/2 - U_s \,. \tag{62}$$

To obtain the equations of motion for the virtual variables we apply eq. (56) to eq. (62) with $A \equiv \boldsymbol{q}_i$, from which it follows that

$$\frac{\mathrm{d}}{\mathrm{d}t}(m_i s^2 \dot{\boldsymbol{q}}_i) = -\,\partial U/\partial \boldsymbol{q}_i \quad \text{or} \quad m_i s^2 \ddot{\boldsymbol{q}}_i = -\,\partial U/\partial \boldsymbol{q}_i - 2 m_i s \dot{s} \dot{\boldsymbol{q}}_i \,. \tag{63}$$

Similarly, the substitution $A \equiv s$ yields

$$Q\ddot{s} = \sum m_i s \dot{\boldsymbol{q}}_i^2 - \partial U_s/\partial s \,. \tag{64}$$

As they stand, these dynamical equations are not of any obvious use. However, the fact that the time average of $Q\ddot{s}$ vanishes enables us to guess the required functional form for U_s. From (64) we obtain

$$\langle \sum m s \dot{\boldsymbol{q}}_i^2 \rangle = \langle \partial U_s/\partial s \rangle \,. \tag{65}$$

Equation (65) suggests how to relate the kinetic energy, and hence the temperature, to the potential U_s. Namely,

$$g k_{\mathrm{B}} T \approx \partial U_s/\partial \ln s \,, \tag{66}$$

where g is the number of degrees of freedom in the extended system, T the temperature of the heat bath and k_{B} Boltzmann's constant. The Hamiltonian postulated by NOSÉ to describe the extended system based on the above arguments was, therefore [29],

$$\boldsymbol{H}_{\mathrm{N}} = \sum \boldsymbol{p}_i^2/2m_i s^2 + U(\boldsymbol{q}) + p_s^2/2Q + g k_{\mathrm{B}} T \ln s \,. \tag{67}$$

If the Hamiltonian formalism is applied to the virtual variables, it follows that the equations of motion are

$$\mathrm{d}\boldsymbol{q}_i/\mathrm{d}t = \partial \boldsymbol{H}_{\mathrm{N}}/\partial \boldsymbol{p}_i = \boldsymbol{p}_i/m_i s^2 \,, \tag{68}$$

$$\mathrm{d}\boldsymbol{p}_i/\mathrm{d}t = -\partial \boldsymbol{H}_{\mathrm{N}}/\partial \boldsymbol{q}_i = -\partial U/\partial \boldsymbol{q}_i \,, \tag{69}$$

$$\mathrm{d}s/\mathrm{d}t = \partial \boldsymbol{H}_{\mathrm{N}}/\partial p_s = p_s/Q \,, \tag{70}$$

$$\mathrm{d}p_s/\mathrm{d}t = -\partial \boldsymbol{H}_{\mathrm{N}}/\partial s = \sum \boldsymbol{p}_i^2/m_i s^3 - g k_{\mathrm{B}} T/s \,. \tag{71}$$

Analogous Lagrangian equations can be readily derived. The important point to note is that eqs. (58) and (68) imply

$$\boldsymbol{p}_i' = \boldsymbol{p}_i/s \,, \tag{72}$$

which, together with the relations $\boldsymbol{q}_i = \boldsymbol{q}_i'$ and $\mathrm{d}t' = \mathrm{d}t/s$, enable the Lagrangian equation to be written in terms of real variables. After some algebra one obtains

$$\frac{\mathrm{d}}{\mathrm{d}t'} (m_i s \, \mathrm{d}\boldsymbol{q}_i'/\mathrm{d}t') = -s(\partial U/\partial \boldsymbol{q}_i') \tag{73}$$

and

$$\frac{\mathrm{d}}{\mathrm{d}t'}(Q\,\mathrm{d}\ln s/\mathrm{d}t') = \sum m_i(\mathrm{d}\boldsymbol{q}_i'/\mathrm{d}t')^2 - gk_\mathrm{B}T\,. \tag{74}$$

HOOVER has shown how these dynamical equations can be expressed in a more compact form using friction coefficients [36].

NOSÉ obtained [29] the distribution function for the physical system by integrating the expression for the extended system over the phase space of the variable s. The particular choice of U_s given in eq. (67) ensures that the partition function has the form

$$Z = C\int \mathrm{d}\boldsymbol{p}'\int \mathrm{d}\boldsymbol{q}'\,\exp\left[-H_0(\boldsymbol{p}',\boldsymbol{q}')/k_\mathrm{B}T\right] \tag{75}$$

and hence the distribution function is

$$\varrho(\boldsymbol{p}',\boldsymbol{q}') = \exp\left[-H_0(\boldsymbol{p}',\boldsymbol{q}')/k_\mathrm{B}T\right]. \tag{76}$$

With the ergodic hypothesis, which relates the time average along a trajectory to the ensemble average, the average of any *static* quantity expressed as a function of $\boldsymbol{p}_i/s$, $\boldsymbol{q}_i$ along the trajectory determined by eqs. (68)-(71) is exactly that in the canonical ensemble. Hence, the above equations provide a scheme for carrying out constant-temperature MD calculations. The relationship of Nosé's method to other approaches has been discussed in a recent review [37].

2·2. *Constant-pressure molecular dynamics.* – In the case of constant-pressure MD simulations, following ANDERSEN [27], we imagine the system of interest to be coupled to a « piston » which can homogeneously dilate the system if the externally set pressure P is not compensated by the pressure generated within the system of interest. The volume of the system is $V = L^3$, where L is the box length, and the position of a particle is written

$$\boldsymbol{q}_i' = L\boldsymbol{q}_i \qquad (0 \leqslant \boldsymbol{q}_i \leqslant 1). \tag{77}$$

The extended-system Lagrangian has the form

$$L_\mathrm{A} = \sum m_i L^2\dot{\boldsymbol{q}}_i^2/2 - U(L\boldsymbol{q}) + W\dot{V}^2/2 - PV\,. \tag{78}$$

Here W is the « mass » of the piston. The equations of motion are

$$\boldsymbol{p}_i = \partial L_\mathrm{A}/\partial\dot{\boldsymbol{q}}_i = m_i L^2\dot{\boldsymbol{q}}_i\,, \qquad p_V = \partial L_\mathrm{A}/\partial\dot{V} = W\dot{V}\,, \tag{79}$$

from which it follows that the Hamiltonian is

$$H_{\Lambda} = \sum \boldsymbol{p}_i^2/m_i L^2 + U(L\boldsymbol{q}) + p_V^2/2W + PV\,. \tag{80}$$

The Hamiltonian equations of motion are

$$\partial \boldsymbol{p}_i/\partial t = -\,\partial H_{\Lambda}/\partial \boldsymbol{q}_i = -\,\partial U/\partial \boldsymbol{q}_i \tag{81}$$

and

$$\partial p_V/\partial t = -\,\partial H_{\Lambda}/\partial V\,. \tag{82}$$

The dynamical equations follow from eqs. (79)-(82)

$$\ddot{\boldsymbol{q}}_i = -\,(\partial U/\partial \boldsymbol{q}_i)/m_i L^2 - (2\dot{V}/3V)\,\dot{\boldsymbol{q}}_i \tag{83}$$

and

$$3VW\ddot{V} = \sum m_i L^2 \dot{\boldsymbol{q}}_i^2 - \sum \boldsymbol{q}_i \cdot (\partial U/\partial \boldsymbol{q}_i) - 3PV\,. \tag{84}$$

ANDERSEN showed that averages calculated using the phase-space trajectories derived from eqs. (83) and (84) correspond to the (N, P, H) ensemble in which the *enthalpy* is conserved [27].

2·3. *Constant-temperature and constant-pressure molecular dynamics.* – The two methods outlined above can be combined to treat the case of constant temperature *and* pressure. The appropriate extended-system Hamiltonian in terms of the Nosé virtual variables is [29]

$$H_{\mathrm{N}} = \sum \boldsymbol{p}_i^2/2m_i L^2 s^2 + U(L\boldsymbol{q}) + p_s^2/2Q + p_V^2/2W + PV + gk_{\mathrm{B}}T \ln s\,. \tag{85}$$

The relationship between the virtual variables and real (primed) variables is

$$\boldsymbol{q}_i' = L\boldsymbol{q}_i\,, \qquad \boldsymbol{p}_i' = \boldsymbol{p}_i/Ls \qquad \text{and} \qquad \mathrm{d}t' = \mathrm{d}t/s\,. \tag{86}$$

Dynamical equations for the variables $\boldsymbol{q}_i$, V and s can be derived in the same fashion as those in subsect. **2**·1 and **2**·2.

Before giving some examples of the extended-system technique we note that the method introduces parameters Q and W. The original articles give some discussion about the appropriate values to use [27-29]. If Q and W are too large, the coupling will be sluggish and, if they are too small, the system will be unable to respond.

3. – Phase transitions in molecular solids.

The equations derived in sect. **2** refer to an isotropic system. As mentioned in the introduction to part III, this is not sufficiently general to deal with solids. The method for extending the theory to anisotropic systems was given by PARRINELLO and RAHMAN [28] and, unfortunately, lack of space prohibits us from going into subtle details [38]. We note that the applications described below allow for the MD cell to change its size and *shape* in response to any net imbalance between an externally set pressure P and the internal pressure calculated from the trace of the stress tensor $\underline{\Pi}$. The equations of motion for carrying out constant-pressure MD calculations for a molecular system (the only type of calculations reported here) follow from the Lagrangian formulation of Parrinello and Rahman [28] suitably augmented to allow for rotational motion [30]. In particular, if $\underline{h}$ is the matrix formed by three time-dependent vectors $\boldsymbol{L}_1$, $\boldsymbol{L}_2$, $\boldsymbol{L}_3$ that specify the periodically replicated MD cell, then its volume is $V = \det \underline{h} \equiv \boldsymbol{L}_1 \cdot \boldsymbol{L}_2 \times \boldsymbol{L}_3$. The position of molecule i in the cell is given by

$$\boldsymbol{r}_i = \underline{h}\boldsymbol{s}_i\,, \tag{87}$$

where the components of $\boldsymbol{s}_i$ range from 0 to 1. It then follows that

$$\boldsymbol{r}_i^2 = \boldsymbol{s}_i^{\mathrm{t}} G \boldsymbol{s}_i\,, \qquad G = \underline{h}^{\mathrm{t}}\underline{h}, \tag{88}$$

where t denotes a transpose. The Lagrangian for rigid molecules is

$$L_{\mathrm{PR}} = \sum m_i \dot{\boldsymbol{s}}_i^{\mathrm{t}} G \dot{\boldsymbol{s}}_i - U + \tfrac{1}{2} W \operatorname{Tr}(\dot{\underline{h}}^{\mathrm{t}}\dot{\underline{h}}) + \tfrac{1}{2}\sum \boldsymbol{\omega}_i I \boldsymbol{\omega}_i - PV\,. \tag{89}$$

Here $\boldsymbol{\omega}_i$ and I are the angular velocity and inertia tensor of molecule i with mass m_i. The potential energy U depends upon the molecular orientations as well as upon their positions. The equations of motion for the scaled centre-of-mass co-ordinates are identical to those of Parrinello and Rahman, namely [28]

$$\ddot{\boldsymbol{s}}_i = \underline{h}^{-1}\boldsymbol{f}_i/m_i - G^{-1}\dot{\underline{G}}\dot{\boldsymbol{s}}_i\,, \tag{90}$$

where $\boldsymbol{f}_i$ is the net force on molecule i. The equations of motion for angular motion are not given here but follow simply by relating the time rate of change of the angular momentum to the torque [39]. Finally, the equation governing the dynamics of the MD cell is

$$W\ddot{\underline{h}} = (\underline{\Pi} - P)\,\underline{\sigma}\,, \tag{91}$$

where the matrix $\underline{\sigma} \equiv V(\underline{h}^{\mathrm{t}})^{-1}$.

Some care is needed in implementing the Parrinello-Rahman equations

for molecules [30] due to the fact that the MD cell may rotate, essentially because the equations of motion of the cell have been formulated in terms of the 3×3 matrix $\underline{h}$. In the applications to be described below the angular equations have been solved using quarternions [40]. Other formulations have appeared recently which offer certain advantages [31] and the theory has also been extended to nonrigid molecules [41]. Again, there is no space to go into details.

4. – Examples of simulated transitions.

4·1. *Solid carbon tetrafluoride.* – The constant-pressure MD technique was first applied to the condensed phases of CF_4 using an atom-atom potential which

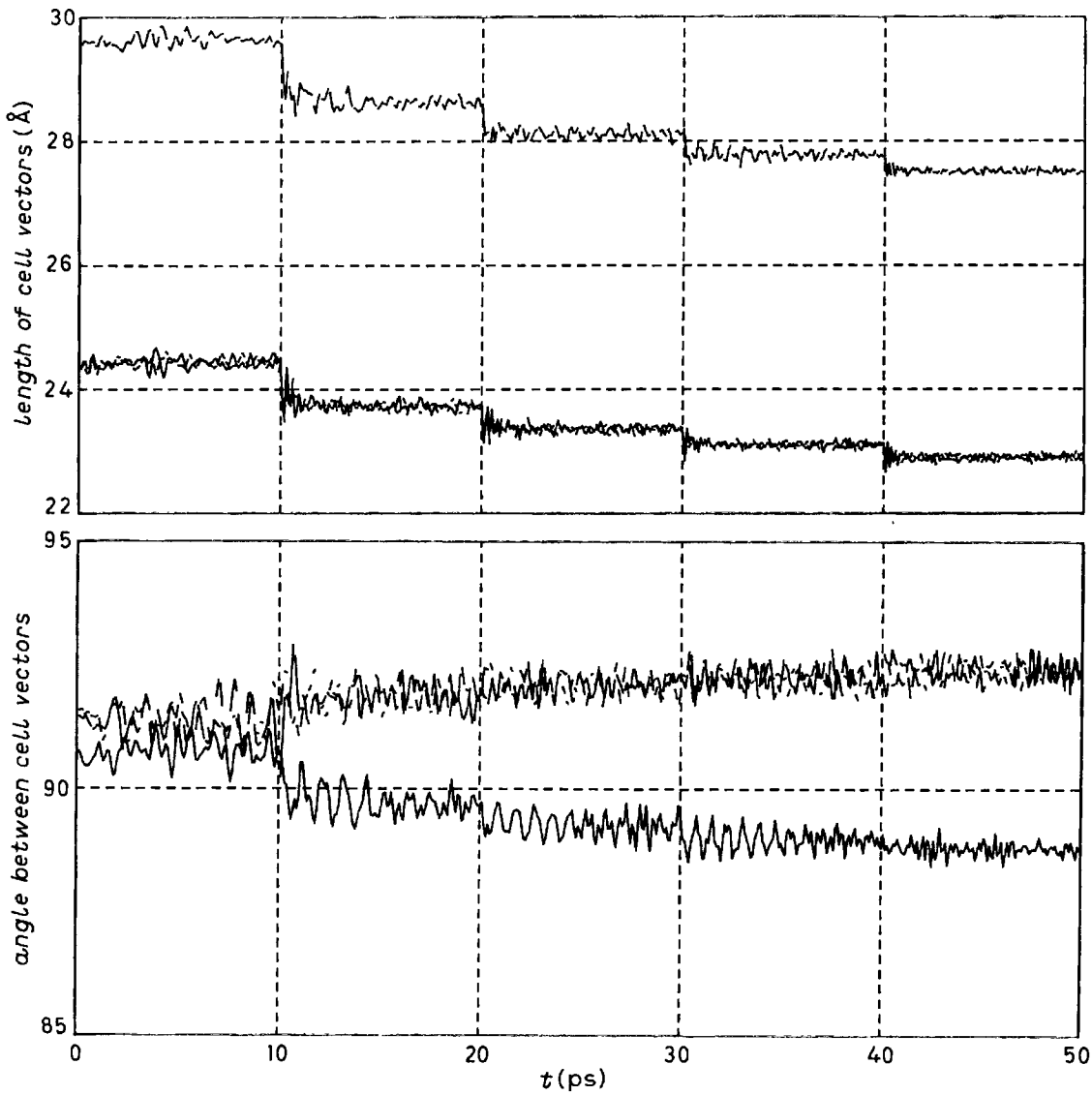

Fig. 25. – Time evolution of the parameters characterizing the pseudo-tetragonal MD cell of CF_4 in its monoclinic (phase II) structure at $T = 70$ K. At the end of each 10 ps MD run the pressure was increased by 5 kbar to a final value of 22 kbar.

gave essentially the correct crystal density [39]. At low temperature and $P \approx 0$ the crystal structure is monoclinic (phase II) but calculations can be carried out using a pseudo-tetragonal MD cell. Figure 15 shows a view of the phase-II structure, which reveals a rather efficient packing of the CF_4 tetrahedra. As a pedagogical example we show the effect of pressure on the pseudo-tetragonal cell as calculated by the generalized Parrinello-Rahman method. A sequence of 10 ps MD runs was used to pressurize CF_4 in 5 kbar steps, the final pressure being 22 kbar. In these calculations, performed in the (N, P, H) ensemble, the temperature was scaled to the desired value (70 K) as in traditional MD calculations. Once this is achieved, the system is left free to evolve. The effect of increased pressure is to dramatically reduce the volume of the crystal. However, the shape of the pseudo-tetragonal cell (and hence the monoclinic-cell parameters) also changes and this is illustrated in fig. 25. Thus the new MD methods can be used to test potentials if suitable structural data are available. Unfortunately, no such data exist for CF_4.

At higher temperatures CF_4 forms a rotator phase (phase I). The (N, P, H) ensemble MD calculations generated such a phase spontaneously [39]. The interested reader is referred to the original article for a full discussion of this system.

4·2. *Solid nitrogen at high pressure.* – The Andersen-Parrinello-Rahman constant-pressure MD technique was applied to solid nitrogen at high pressure [30]. The cubic rotator phase structure at room temperature is isomorphous with the high-temperature low-pressure structure of solid oxygen [42]. It consists of two types of orientationally disordered molecules. Disklike disordered (D_{2d}) molecules which form chains running along the cube directions and more spherically disordered (T_d) molecules which occupy the sites of an interpenetrating b.c.c. lattice. There are eight molecules in the unit cell, six D_{2d} and two T_d. The structure is illustrated in fig. 26. An atom-atom potential was

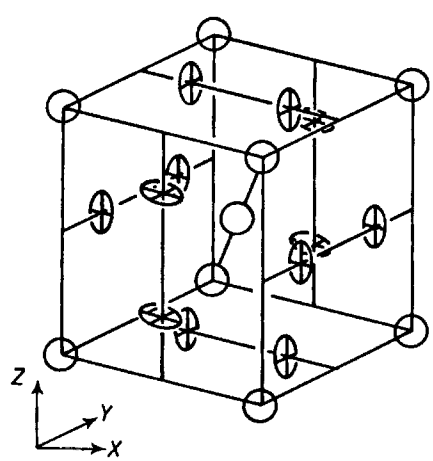

Fig. 26. – High-pressure $Pm3n$ rotator phase of solid nitrogen. The presence of disklike (D_{2d}) and spherical (T_d) molecules should be noted.

used to examine the effect of cooling this $Pm3n$ crystal at high pressure. After a brief MD run to test whether or not the orientationally disordered crystal was stable, the constant-volume constraint was replaced by one of constant pressure, in this case $P = 70$ kbar, and the calculation continued. The MD cell was then free to undergo volume and shear fluctuations. The leftmost panel in fig. 27 shows the evolution of the room temperature high-pressure MD run for 2500 time steps. Although there are evidently large volume and shear fluctuations, the MD cell is clearly cubic. A detailed study of individual molecules confirmed that the disklike and spherical molecules retained their identities.

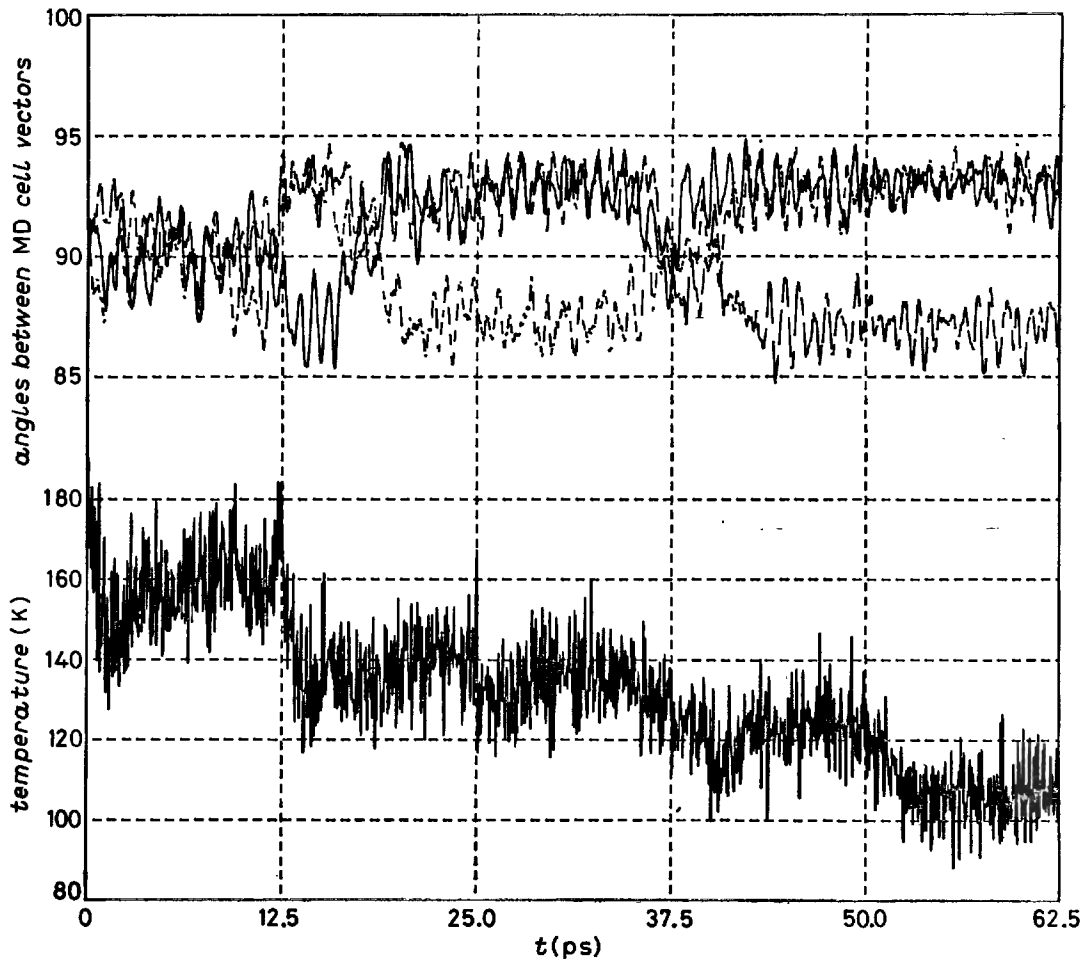

Fig. 27. – Time evolution of quantities characterizing the MD cell of solid N_2 in its $Pm3n$ rotator phase at $P = 70$ kbar. Each panel displays the results for 2500 time steps, the first 500 of which are used to scale the temperature. The low-temperature trigonal distortion should be noted.

The next panels in fig. 27 show the effect of sequentially quenching the room temperature solid-nitrogen structure in steps of 50 K, while maintaining $P = 70$ kbar. The volume is seen to decrease steadily and the three MD vectors remain equal in length. However, below 150 K the MD cell angles are no longer 90°; the system has undergone a spontaneous shear distortion of about 3°.

An inspection of the resulting structure reveals that the spherically disordered molecules are now all aligned along the trigonal direction, the crystal having $R3C$ symmetry. This prediction [30] of an ordering transition involving a trigonal distortion of about 3° at a temperature below 150 K seems to be in accord with recent X-ray work [43]. The exact nature of the transition in the real crystal has not yet been elucidated, but in this MD calculation the transition actually proceeds in two stages. The disklike D_{2d} molecules order around 230 K and then at around 140 K the T_d molecules align along a common direction. Figure 28 shows the behaviour of the molar volume as a function of temperature, the arrows indicating the two transitions discussed above.

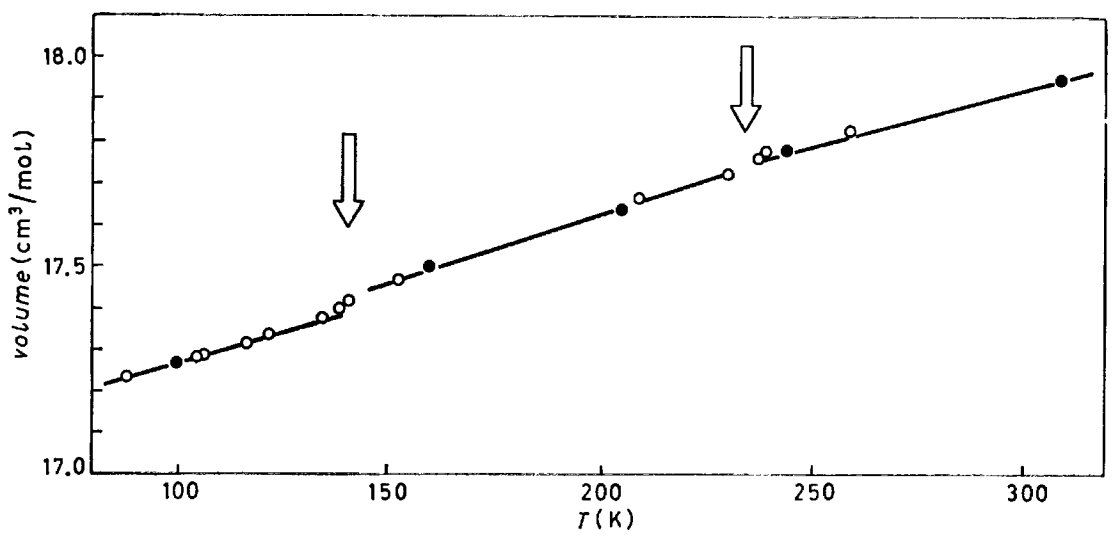

Fig. 28. – Isobaric ($P = 70$ kbar) thermal expansion of solid N_2 in its $Pm3n$ rotator phase based upon (N, P, H) molecule dynamics calculations. The arrows indicate possible structural transitions (see text).

All of the above calculations were based on a rather crude potential and hence the structural transitions shown in fig. 27 and 28 should be regarded as suggestive of the real system. Further calculations of the type mentioned here using realistic potentials would be very worthwhile.

4·3. *Bicyclo octane.* – Bicyclo (2.2.2) octane is a cage-shaped molecule that at room temperature is a cubic orientationally disordered solid. In this rotator phase the C_3 symmetry axes of the molecule point predominantly along one of the four possible [111] orientations. At low temperatures the C_3 axes point along a unique axis. Under its own vapour pressure an order-disorder transition occurs at 164 K and the solid melts at 447 K.

Molecular-dynamics calculations have been carried out using atom-atom and site-site potentials starting from an assumed trigonal structure. Figure 29 shows the results of an (N, P, H) calculation based on an eight-site model

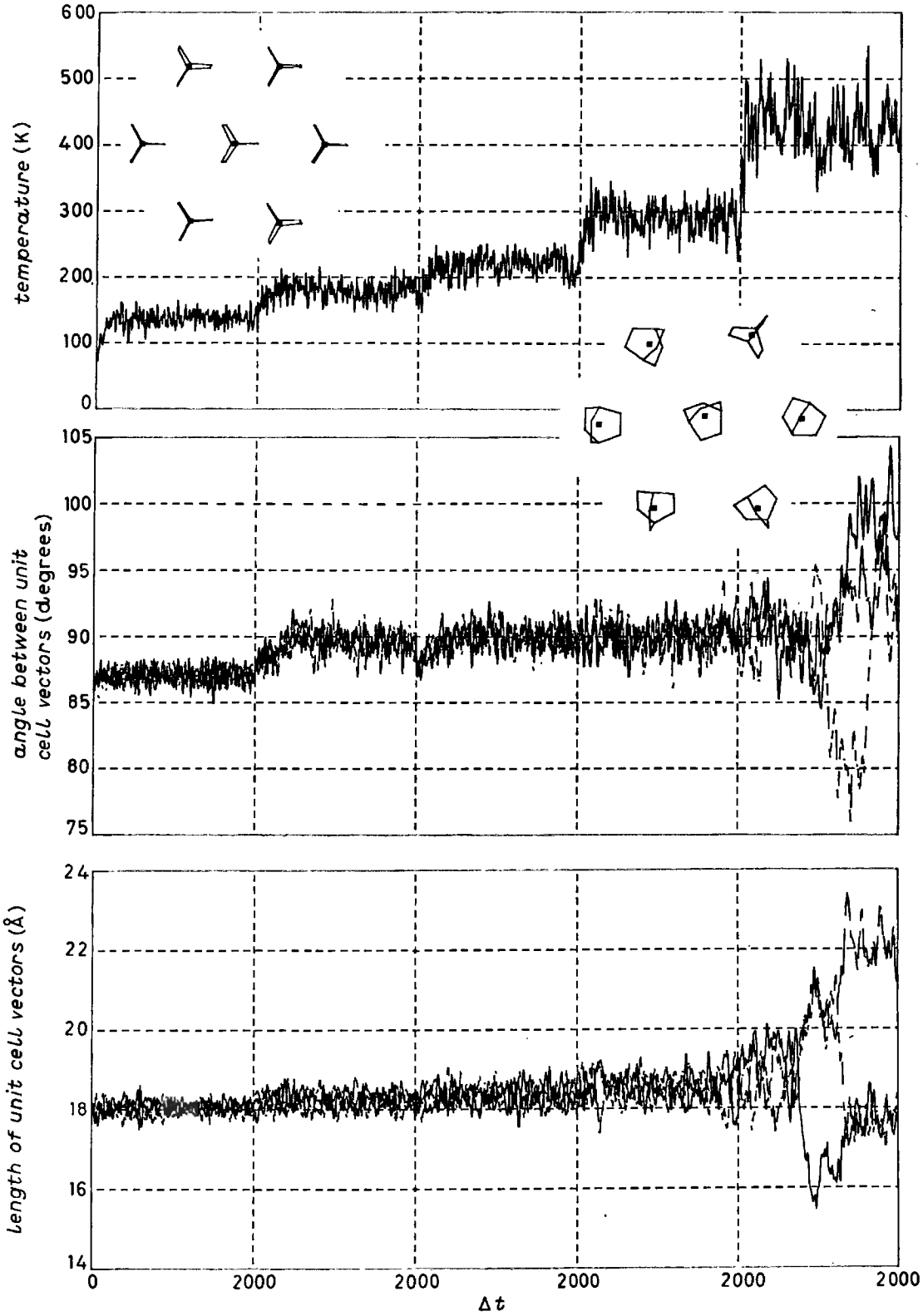

Fig. 29. – Evolution of quantities characterizing the MD cell of bicyclo octane. The rotator transition occurs at about 170 K and melting at about 425 K (see text).

which gave a fair account of the thermodynamic properties [44]. The low-temperature trigonal structure was stable up to about 170 K when it transformed to a cubic rotator phase. The latter was quite stable at room temperature. Further heating to 425 K led to erratic behaviour of the MD simulation cell (see fig. 29). This behaviour is associated with the onset of translational diffusion and is indicative of proximity to melting. This example illustrates that the (N, P, H) method is able to give a semi-quantitative modelling of a large globular molecule even with a very simple potential model.

4·4. *Phase diagram of potassium cyanide.* – The phase diagram of KCN is shown in fig. 30. Two rotator phases exist at high temperature. The *Fm3m* phase is isomorphous with common rocksalt and consists of interpenetrated f.c.c. lattices of anions and cations. The high-pressure *Pm3m* phase has the

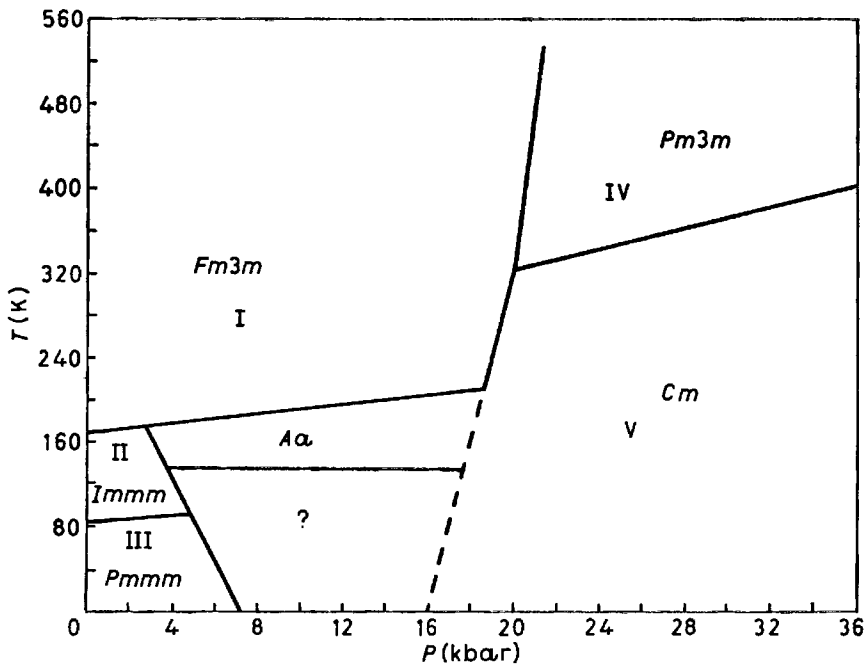

Fig. 30. – Phase diagram of KCN (see text).

CsCl structure and consists of interpenetrated simple cubic lattices. In the *Fm3m* structure each CN^- ion is octahedrally co-ordinated by K^+ ions, whereas in the *Pm3m* structure the CN^- ion has eight neighbouring K^+ ions. On cooling the high-pressure rotator phase the CN^- ions align along one of the [111] directions and the crystal undergoes a trigonal distortion [1]. The transition will not concern us here, but it is not unrelated to the type of transitions discussed in the previous section, *i.e.* no massive displacements are required. By contrast, cooling of the *Fm3m* rotator phase yields rather different structures depending on the pressure. The phase labelled *Aa* will not concern us further, but it appears to be ferroelectric. The phase *Immm* is orthorhombic with the CN^- ions aligned predominantly along the crystal *b*-axis but with

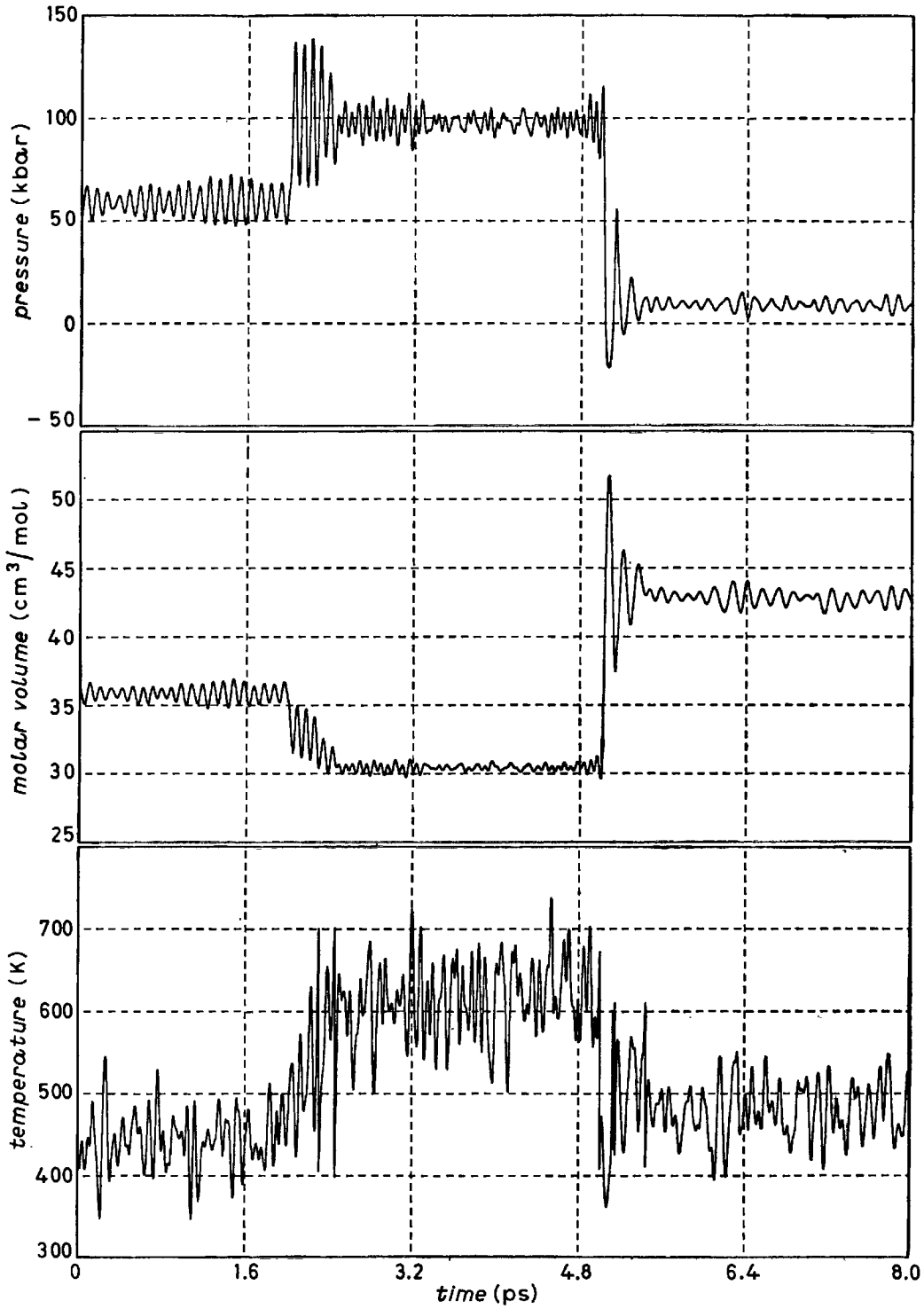

Fig. 31. – Evolution of the pressure, temperature and molar volume of KCN in an (N, P, H) ensemble MD run.

head-to-tail disorder, *i.e.* there is rotational disorder in the *ab* plane. Below about 83 K the fully antiferro ordered *Pmmm* structure forms. The rationalization of this phase diagram in terms of interionic-potential models clearly presents a challenge.

The first calculations using the (N, P, H) method [45] employed a three-charge site model for the CN^- ion. The $Fm3m$ phase was quite stable at 450 K. (In view of our previous discussion of the properties of KCN given in parts I and II this is no surprise!) The pressure was then brutally increased in stages and at 50 kbar the molar volume settled down at 36 cm^3/mol (see fig. 31) and the crystal appeared to be stable. The pressure was then brutally increased to 100 kbar. This shock caused the temperature to rise to over 600 K and the molar volume decreased to about 31 cm^3/mol. After a reasonable time period the pressure was instantly set to 10 kbar. This generated an expansion to about 43 cm^3/mol and the temperature fell to below 500 K. The behaviour of the MD cell param-

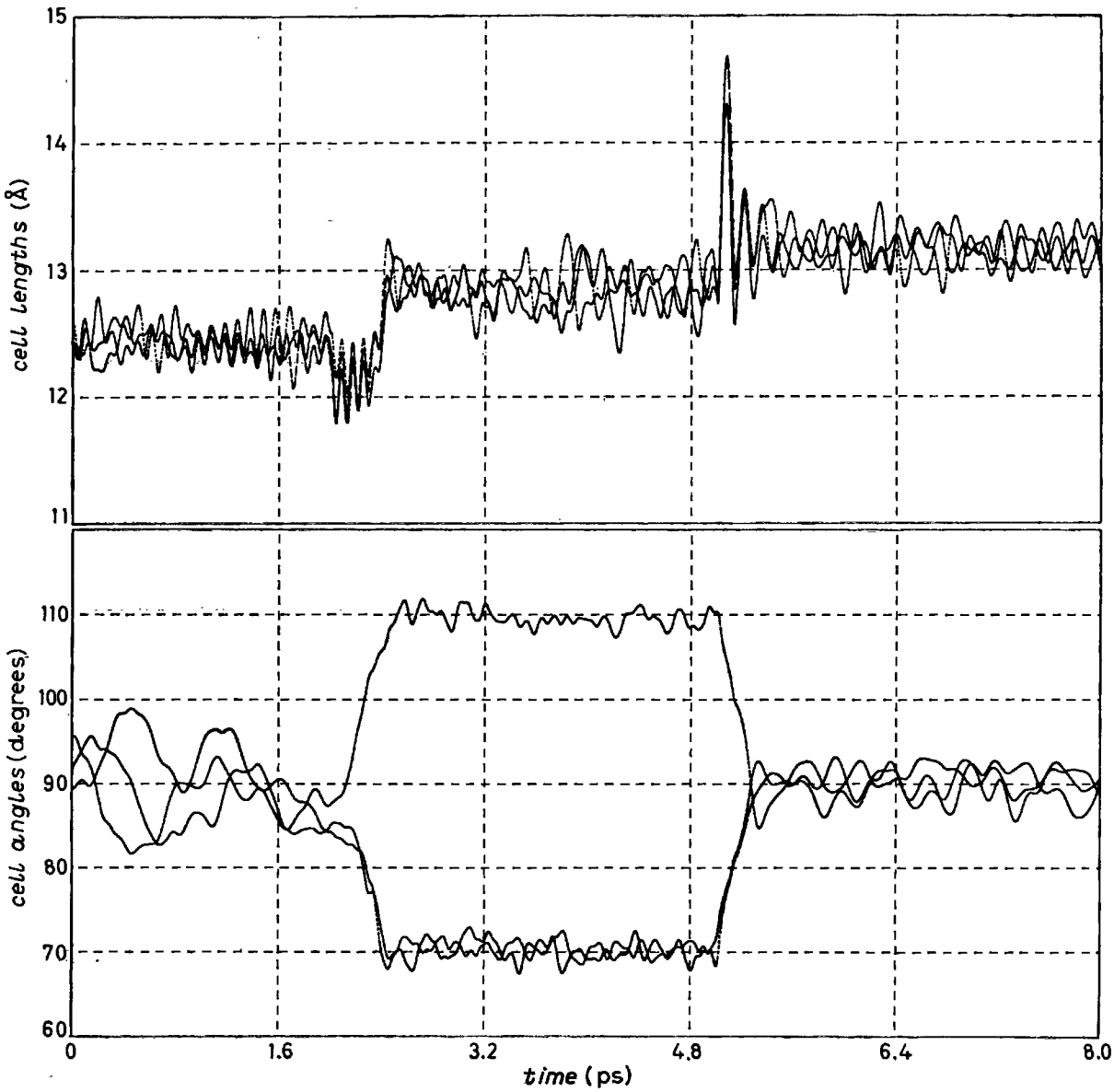

Fig. 32. – Evolution of MD cell parameters for KCN for the run shown in fig. 31. The transition from the $Fm3m$ (NaCl-like) to $Pm3m$ (CsCl-like) structure is indicated by the dramatic change in cell angles.

eters during this pressure cycle is shown in fig. 32. While the sample is cubic at 50 kbar, the cell angles are undergoing large fluctuations which suggest an instability. The brutal application of an additional 50 kbar pressure causes the MD cell to undergo a massive *shear*, the cell angles changing from $\sim 90°$ to the tetrahedral angle (109°) and its complement (71°). Inspection of the ionic radial distribution functions before and after the transition (fig. 33 and 34)

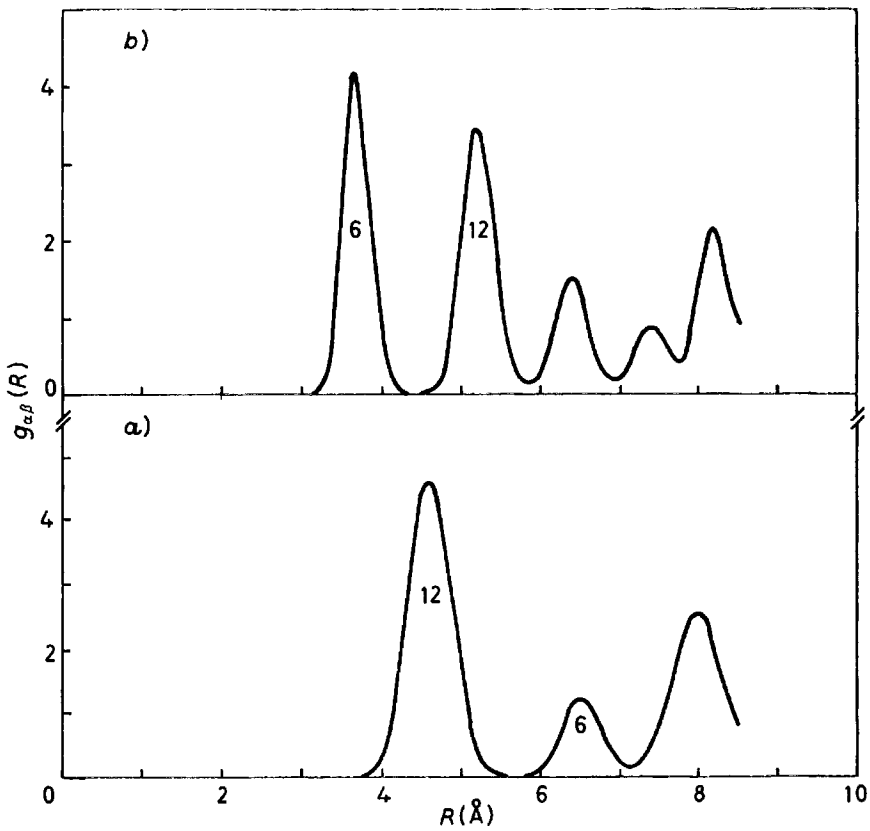

Fig. 33. – Atom-atom (potassium-potassium) radial distribution functions for the *a*) *Fm3m* (NaCl-like) and *b*) *Pm3m* (CsCl-like) phases of KCN from the MD runs shown in fig. 31 and 32.

clearly shows that the six co-ordinated NaCl-like structure has transformed to an eight co-ordinated CsCl structure. The mechanism of the transition, involving as it does a massive shearing of the whole MD cell, is unlikely to be the true mechanism. Rather, we should be content that the (N, P, H) method has found a pathway to the correct structure. We recall that the extended-system method was only constructed to give correct *static* properties. There is also the question of whether or not a transition pathway depends upon the choice of the mass parameter W.

Notwithstanding these unresolved questions concerning the transition mechanism, a detailed study was carried out of the cubic-to-orthorhombic transition in KCN using (N, P, H) calculations [46]. The results of such a

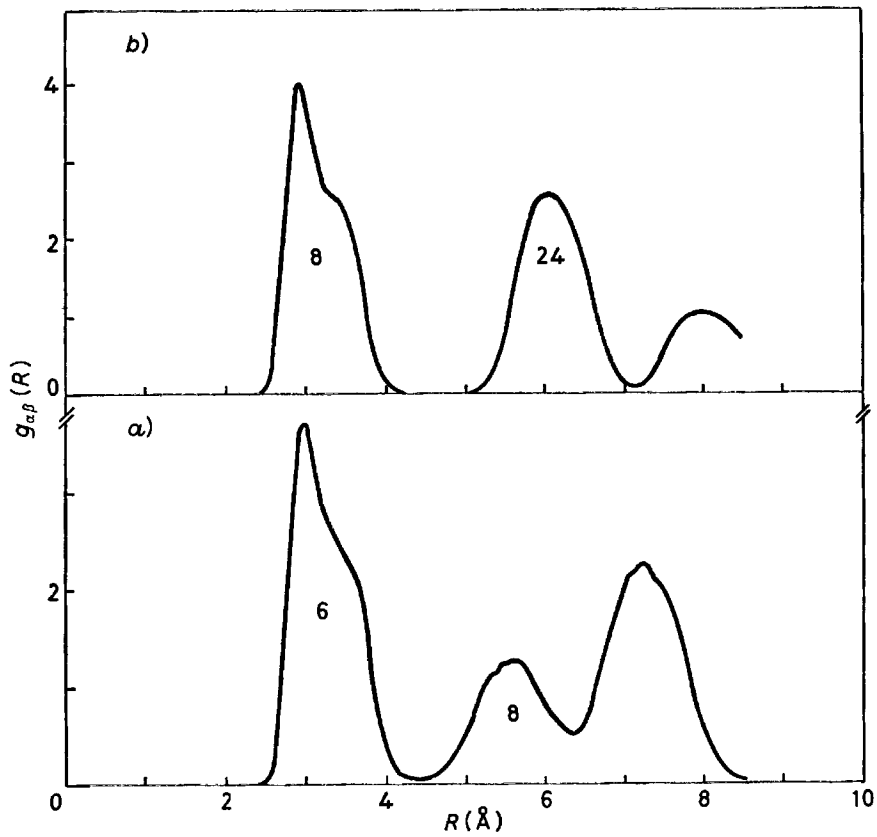

Fig. 34. – Atom-atom (carbon-potassium) radial distribution functions for the *a*) *Fm*3*m* (NaCl-like) and *b*) *Pm*3*m* (CsCl-like) phases of KCN from the MD run shown in fig. 31 and 32.

calculation are shown in fig. 35. These results were based on a similar potential to that used in the high-pressure transition. It was found that cooling of the orientationally disordered *Fm*3*m* phase at low pressure under isobaric-isoenthalpic conditions does indeed yield an orthorhombic crystal with essentially the correct cell constants. The CN^- ions align along what was the [110] direction of the parent phase. The resulting orthorhombic structure has head-to-tail disorder, but there was no indication of the transition to a fully antiferro ordered structure. This latter problem is likely due to the slow reorientation rate in the orthorhombic phase. The transition is at about 150 K in the simulation which compares favourably with the experimental value [47] of 168 K.

While we appear to have successfully simulated the transition, it is of interest to follow the approach to the transition to look for possible precursors. Experimentally [48], the shear elastic constant C_{44} shows a dramatic softening as the transition is approached, falling an order of magnitude from room temperature to 168 K. This effect is related to the anomalous dispersion of transverse acoustic phonons propagating along the crystal [100] direction (recall fig. 19), since the limiting slope is determined by C_{44}.

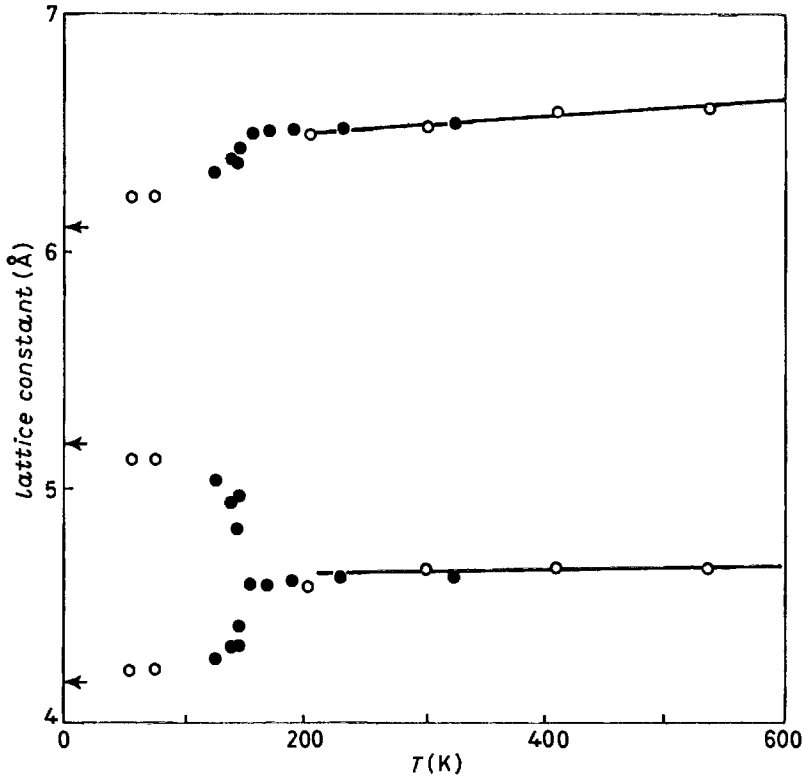

Fig. 35. – Calculated temperature dependence of the lattice constants of KCN expressed in a body-centred tetragonal reference frame. In the high-temperature rotator phase the cell constants were in the ratio $1:\sqrt{2}$. The bifurcation at low temperature signals the cubic-to-orthorhombic transition. The arrows indicate the experimental low-temperature cell constants from ref. [47].

Figure 36 shows the shear constant C_{44} calculated from the strain fluctuations in the (N, P, H) ensemble [49]. Although the calculated values have a large error, the anomalous softening is observed in the calculations [46]. It should be remarked that normally cooling a crystal causes the elastic constants to increase, whereas just the contrary behaviour is observed here. Below the transition, in the orthorhombic structure, the shear constants rapidly stiffen as the temperature falls. The rationalization of the anomalous softening of C_{44} and the anomalous dispersion of the transverse acoustic phonons have been the subject of numerous theoretical articles. The observed behaviour is due to effects of translation-rotation coupling [50, 51].

Lastly we comment on the behaviour of the orientational order parameter C_4. At room temperature the experimental value for KCN is -0.13 (table I), whereas just above the transition the value is -0.02. That is, the orientational distribution function (recall fig. 2) is more isotropic as the transition is approached. This phenomenon was not found in the (N, P, H) ensemble simulations [46]. There the value of C_4 was -0.13 at 207 K and -0.25 at 147 K. The latter value is more indicative of incipient [110] order rather than the observed isotropic results [15]. The origin of this last discrepancy may

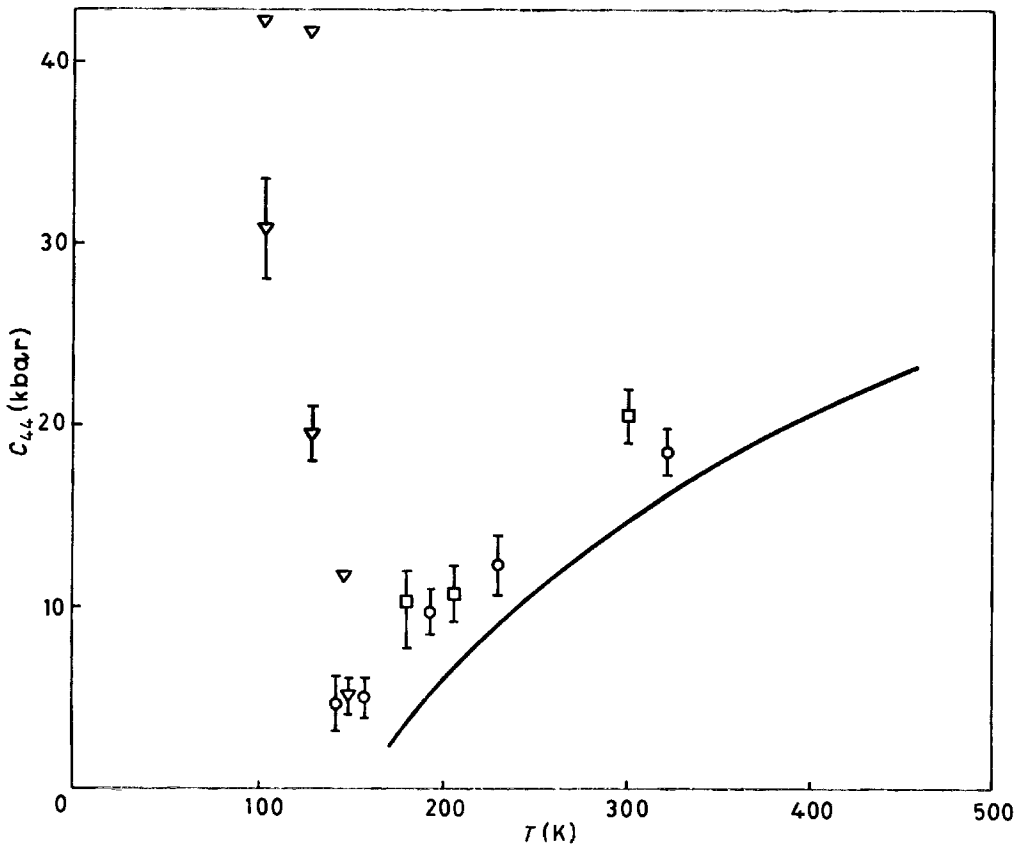

Fig. 36. – Temperature dependence of the elastic constant C_{44} of KCN for two models (circles and squares) based on (N, P, H) MD calculations. The experimental result (ref. [48]) is the full curve. The triangles refer to the orthorhombic phase.

again be related to the problem mentioned above. Namely, that the transition mechanism in the (N, P, H) calculations is not the real mechanism but simply one pathway. Another possibility is that the system size in too small to allow certain long-wavelength fluctuations, which not only lower the value of C_{44} but also influence the order parameter.

5. – Conclusions.

We have given a broad outline of three topics related to the structure and dynamics of orientationally disordered crystals. Great strides have been made in the past few years both in simulation techniques and the modelling of the interaction potentials (a subject not treated here). These important developments have taken us to the point where simulations based on MD and MC methods [52-55] have begun the challenge real experiments. The increased availability of supercomputers and specialized computing systems [24] can only mean that the kind of calculations outlined here will become routine. Hopefully, deeper questions can then be posed and even answered by molecular dynamics.

* * *

The work presented in this lecture would not have been possible without many fruitful collaborations. R. W. IMPEY, I. R. MCDONALD, S. NOSÉ, M. SPRIK and many others are thanked for their valuable contributions.

REFERENCES

[1] N. G. PARSONAGE and L. A. K. STAVELEY: *Disorder in Crystals* (Clarendon, Oxford, 1978).
[2] G. DOLLING, B. M. POWELL and V. F. SEARS: *Mol. Phys.*, **37**, 1859 (1979).
[3] H. M. JAMES and T. A. KEENAN: *J. Chem. Phys.*, **31**, 12 (1959).
[4] R. S. SEYMOUR and A. W. PRYOR: *Acta Crystallogr., Sect. B*, **26**, 1489 (1979).
[5] W. PRESS and A. HÜLLER: *Acta Crystallogr., Sect. A*, **29**, 252 (1973); W. PRESS: *Acta Crystallogr., Sect. A*, **29**, 257 (1973).
[6] K. M. MICHEL and J. M. ROWE: *Phys. Rev. B*, **22**, 1417 (1980).
[7] M. L. KLEIN and J.-J. WEIS: *J. Chem. Phys.*, **67**, 217 (1977).
[8] D. G. BOUNDS, M. L. KLEIN and G. N. PATEY: *J. Chem. Phys.*, **72**, 5348 (1980).
[9] D. G. BOUNDS, M. L. KLEIN, I. R. MCDONALD and Y. OZAKI: *Mol. Phys.*, **47**, 629 (1982).
[10] M. L. KLEIN and I. R. MCDONALD: *J. Chem. Phys.*, **79**, 2333 (1983).
[11] M. L. KLEIN, I. R. MCDONALD and Y. OZAKI: *J. Chem. Phys.*, **79**, 5579 (1983); *Phys. Rev. Lett.*, **48**, 1197 (1982).
[12] R. W. IMPEY, M. L. KLEIN and I. R. MCDONALD: *J. Chem. Phys.*, **82**, 4690 (1985).
[13] L. VAN HOVE: *Phys. Rev.*, **95**, 249 (1954).
[14] W. R. FEHLNER and S. H. VOSKO: *Can. J. Phys.*, **54**, 2149 (1976).
[15] J. M. ROWE, D. G. HINKS, D. L. PRICE, S. SUSMAN and J. J. RUSH: *J. Chem. Phys.*, **58**, 2039 (1973).
[16] D. FONTAINE and R. M. PICK: *J. Phys. (Paris)*, **40**, 1105 (1979).
[17] L. NILSSON, J. O. THOMAS and B. C. TOFIELD: *J. Phys. C*, **13**, 6441 (1980).
[18] T. A. SCOTT: *Phys. Rep.*, **27**, 89 (1976).
[19] F. D. MEDINA and W. B. DANIELS: *J. Chem. Phys.*, **64**, 150 (1976).
[20] W. PRESS and A. HÜLLER: *J. Chem. Phys.*, **68**, 4465 (1978).
[21] R. E. WASYLISHEN, B. A. PELTIT and K. R. JEFFREY: *J. Chem. Phys.*, **74**, 6022 (1981).
[22] K. H. MICHEL and J. M. ROWE: *Phys. Rev. B*, **32**, 5818, 5827 (1985).
[23] J. R. RAY and A. RAHMAN: *J. Chem. Phys.*, **80**, 4423 (1984); **82**, 4243 (1985).
[24] G. S. PAWLEY and G. W. THOMAS: *Phys. Rev. Lett.*, **48**, 410 (1980).
[25] G. CICCOTTI, M. GUILLOPÉ and V. PONTIKIS: *Phys. Rev. B*, **27**, 5576 (1983).
[26] F. F. ABRAHAM: *Phys. Rev. Lett.*, **50**, 978 (1983).
[27] H. C. ANDERSEN: *J. Chem. Phys.*, **72**, 2384 (1980).
[28] M. PARRINELLO and A. RAHAMN: *Phys. Rev. Lett.*, **45**, 1196 (1980); *J. Appl. Phys.*, **52**, 7182 (1981).
[29] S. NOSÉ: *Mol. Phys.*, **52**, 255 (1984); *J. Chem. Phys.*, **81**, 511 (1984).
[30] S. NOSÉ and M. L. KLEIN: *Phys. Rev. Lett.*, **50**, 1207 (1983); *Mol. Phys.*, **50**, 1055 (1983).
[31] M. FERRARIO and J.-P. RYCKAERT: *Mol. Phys.*, **54**, 587 (1985).
[32] J.-P. RYCKAERT and G. CICCOTTI: *J. Chem. Phys.*, **78**, 7368 (1983).

[33] W. G. HOOVER, A. J. C. LADD and B. MORAN: *Phys. Rev. Lett.*, **48**, 1818 (1982).
[34] D. J. EVANS: *J. Chem. Phys.*, **78**, 3297 (1983); D. J. EVANS, W. G. HOOVER, B. H. FAILOR, B. MORAN and A. J. C. LADD: *Phys. Rev. A*, **28**, 1016 (1983).
[35] H. J. C. BERENDSEN, J. P. M. POSTMA, W. F. VAN GUNSTEREN, A. DINOLA and J. R. HAAK: *J. Chem. Phys.*, **81**, 3684 (1984).
[36] W. G. HOOVER: *Phys. Rev. A*, **31**, 1695 (1985).
[37] H. C. ANDERSEN: CECAM report (1985).
[38] M. PARRINELLO, A. RAHMAN and P. VASHISHTA: *Phys. Rev. Lett.*, **50**, 1073 (1983).
[39] S. NOSÉ and M. L. KLEIN: *J. Chem. Phys.*, **78**, 6928 (1983).
[40] D. J. EVANS and S. MURAD: *Mol. Phys.*, **34**, 327 (1977).
[41] J.-P. RYCKAERT: *Mol. Phys.*, **55**, 549 (1985).
[42] D. T. CROMER, R. L. MILLS, D. SCHIFERL and L. A. SCHWALBE: *Acta Crystallogr., Sect. B*, **37**, 8 (1981).
[43] R. L. MILLS, B. OLINGER and D. T. CROMER: *J. Chem. Phys.*, **84**, 2837 (1986).
[44] E. NEUSY, S. NOSÉ and M. L. KLEIN: *Mol. Phys.*, **52**, 269 (1984).
[45] R. W. IMPEY, S. NOSÉ and M. L. KLEIN: *Mol. Phys.*, **50**, 243 (1983).
[46] R. W. IMPEY, M. L. KLEIN and M. SPRIK: *J. Chem. Phys.*, **83**, 3638 (1985).
[47] J. M. ROWE, J. J. RUSH and E. PRINCE: *J. Chem. Phys.*, **66**, 5147 (1977).
[48] S. HAUSÜHL: *Solid State Commun.*, **13**, 147 (1973).
[49] M. SPRIK, R. W. IMPEY and M. L. KLEIN: *Phys. Rev. B*, **29**, 4368 (1984).
[50] K. H. MICHEL and J. NAUDTS: *J. Chem. Phys.*, **67**, 547 (1977); **68**, 216 (1978).
[51] R. M. LYNDEN BELL, M. L. KLEIN and I. R. MCDONALD: *Mol. Phys.*, **48**, 1093 (1983).
[52] R. NAJAFABADI and S. YIP: *Scr. Metall.*, **17**, 1199 (1983).
[53] S. YASHONATH and C. N. R. RAO: *Mol. Phys.*, **54**, 245 (1985).
[54] D. LÉVESQUE, J.-J. WEIS and M. L. KLEIN: *Phys. Rev. Lett.*, **51**, 670 (1983).
[55] R. G. MUNRO and R. D. MOUNTAIN: *Phys. Rev. B*, **28**, 2261 (1983).

Molecular-Dynamics Study of Orientational Order in a Plastic Crystal.

High-Temperature Phase of Adamantane.

M. MEYER

Laboratoire de Physique des Matériaux, C.N.R.S.
1, *Place Aristide Briand,* 92195 *Meudon Cedex, France*

1. – Introduction.

Some molecular crystals undergo on heating a transition to a high-temperature plastic phase in which the molecules are dynamically orientationally disordered. The phase transition is associated with a rather important heat of transition. The crystalline structure of this orientationally disordered phase is highly symmetric. The amount of orientational disorder may vary significantly when we compare two different plastic crystals, *i.e.* the molecular orientations may change by rotational jumps between several equilibrium positions or vary continuously by rotational diffusion; moreover, some molecules exhibit intramolecular rotations while others are rigid [1].

The orientational order is an important part of the structural properties of plastic phases which are also called rotator phases.

Molecular-dynamics simulation is a suitable method to study temperature-dependent properties such as orientational order and dynamical properties such as rotational motion.

This method has already been used to characterize orientational order in molecular ionic crystals [2] and reorientational dynamics in bicyclooctane [3].

In this lecture, we explore by molecular-dynamics simulation the validity of the model of adamantane consisting of rigid molecules interacting via an exp-6 pairwise additive potential.

Adamantane or tricyclo (3, 3, 1, 1) decane is one of the best-known plastic crystals since it has been studied extensively over the past twenty years. The crystalline structure is now well established [4], the orientational order and the rotational motion have been characterized experimentally [5, 6].

We have investigated the temperature dependence of the structure, the

orientational probability density of the molecules (*). We have checked the validity of our calculations by comparing our results with the experimental values. The molecular-dynamics results show that the simulation technique is adequate to calculate the main physical properties of the plastic phase of hydrocarbon crystals with rigid molecules. Moreover, as it is typical of the molecular-dynamics approach, the simulation experiment gave a very accurate description of the structure. This type of information is difficult to extract without extra assumptions from the experimental data.

In sect. **2** we give some experimental data related to the structural analysis of adamantane. The computational model is described in sect. **3**. The different methods used to calculate the orientational probability density function are given in sect. **4**. The application to the determination of librational amplitude and the information about rotational motion deduced from this function are given in sect. **5**.

2. – Structural properties of adamantane.

The adamantane molecule (tricyclo (3, 3, 1, 1) decane; $C_{10}H_{16}$), shown in fig. 1*a*), contains 6 secondary carbon atoms bonded to 2 hydrogen atoms and 4 tertiary carbon atoms bonded to one hydrogen atom (fig. 1*a*)).

The molecular tetrahedral symmetry (T_d or $\bar{4}3m$) is represented by the regular tetrahedron built on the 4 tertiary carbons (fig. 1*b*)). The symmetry operations corresponding to this cubic point group are given in appendix A and some symmetry elements are shown in fig. 2.

In this lecture we are interested in the high-temperature phase of adamantane. This material undergoes at 208.6 K a transition [7] between a low-temperature ordered phase which is tetragonal [8] and a high-temperature plastic phase which is face-centred cubic [4].

The X-ray structural studies result in $Fm3m$ space group for the plastic phase with a lattice parameter $a = 9.445$ Å at room temperature (293 K) [4].

The comparison between the symmetry operations of the lattice and molecular point groups (appendix A) show that the molecule has a lower symmetry.

The cubic-harmonic analysis of the experimental results [9] gives the explanation of the higher symmetry of the average crystal structure. The molecules are randomly and equally distributed between two equilibrium orientations around which they undergo large librations. These orientations correspond to the maxima of the molecular orientational probability density func-

(*) This work has been made in collaboration with G. Ciccotti.

tion, they are characterized by the coincidence between all the symmetry elements of the molecule and the corresponding ones of the lattice site. As the ratio between the numbers of symmetry operations for the lattice site (48) and the molecular (24) point groups is equal to 2, there are two distinct orientations which are generally referred to as T_d orientations (fig. 2).

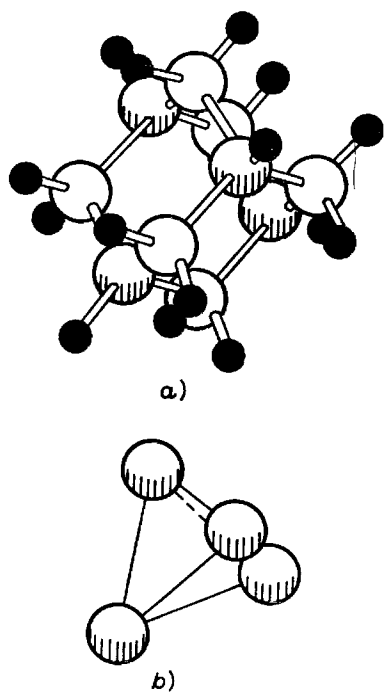

Fig. 1.

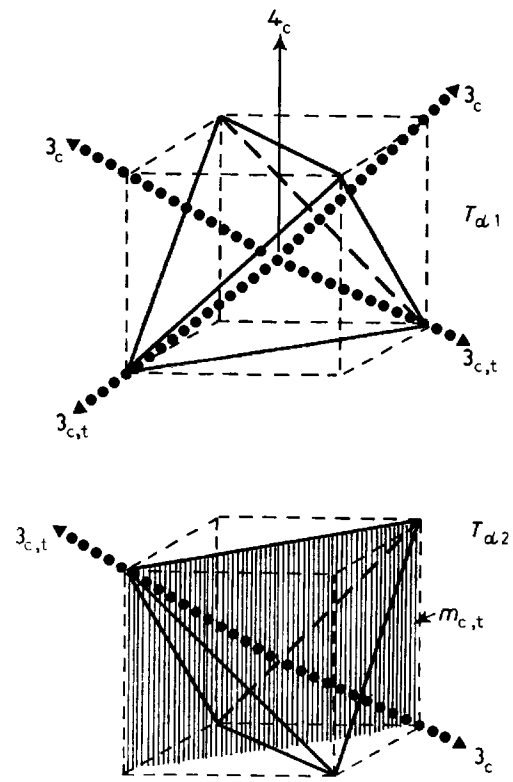

Fig. 2.

Fig. 1. – *a*) Schematic view of the adamantane molecule $C_{10}H_{16}$ with 4 tertiary carbons bonded to one hydrogen atom and 6 secondary carbons bonded to 2 hydrogen atoms, *b*) regular tetrahedron with vertices corresponding to the four tertiary carbons (the edges do not correspond to bonds; they are drawn to guide the eye). o carbon atoms, • hydrogen atoms.

Fig. 2. – Schematic view of the two T_d orientations of adamantane on a lattice site; the molecule is represented by a regular tetrahedron. Fourfold axes, $\bar{4}$ axes, threefold axes are indicated by the corresponding figures: 4, $\bar{4}$, 3. m is for a mirror and the indices c, t refer to cubic (lattice site) and tetrahedral (molecule).

Experimental results obtained by NMR techniques [10, 11] and neutron scattering [5, 6] point out the existence of a rotational motion of the molecules reorienting between their two equilibrium positions. Detailed analyses of these results assuming one or more types of rotations were performed. The conclusion was that the most probable reorientation mechanism is due to the $\pi/2$ rotations about the fourfold axes of the crystals [6, 10].

3. – Model and computation.

Molecular-dynamics computations were performed on systems containing $N = 108$ molecules with the usual periodic boundary conditions. Forces and energies were calculated with an atom-atom pair potential function of the form

$$V(r_{ij}) = -A_{\alpha\beta} r_{ij}^{-6} + B_{\alpha\beta} \exp[-C_{\alpha\beta}] r_{ij} ,$$

where α and β indicate the nature of the atoms i and j (α, β:C, H). r_{ij} is the distance between two atoms belonging to different molecules. Several sets of values for the potential parameters are available in the literature [12]. In the present calculation we have chosen those determined by WILLIAMS [13].

α β	$A_{\alpha\beta}$ (kJmol^{-1} Å^{-6})	$B_{\alpha\beta}$ (kJmol^{-1})	$C_{\alpha\beta}$ (Å^{-1})
C ... C	2376	349908	3.6
C ... H	523	36677	3.67
H ... H	114	11104	3.74

Due to the use of the minimum-image convention, the potential functions were truncated at $r_c = 14$ Å.

The adamantane molecule is assumed to be rigid. The equations of motion are integrated by using the recently developed method of constraints in Cartesian co-ordinates [14]. We chose as basic atoms the four tertiary carbons which form a regular tetrahedron centred on the centre of mass of the molecule (fig. 1*a*)), the six constraint lengths d between these atoms are equal to 2.483 Å. The coefficients C used to calculate the co-ordinates of secondary atoms are given in appendix B together with the Cartesian co-ordinates of the tertiary carbons for the two T_d orientations. The differential equations were integrated using Verlet's algorithm [15] with a time step $\Delta t = 9.87 \cdot 10^{-15}$ s. Our program was adapted to a vector computer with the method described by FINCHAM and RALSTON [16], the algorithm is given in appendix C and requires 6.5 s of CPU on a Cray 1S (*) for a time step. With our choice of Δt, the total energy has a relative accuracy of $4 \cdot 10^{-5}$. Two different temperatures have been investigated, 309 K and 403 K. The lattice parameter a for each temperature is obtained from the value of $a = 9.445$ Å at 293 K and atmospheric pressure given in ref. [4], by use of the thermal-expansion coefficient at constant pressure $\alpha_v = 4.7 \cdot 10^{-4}$ K^{-1} [17]. The initial configuration was chosen

(*) The CCVR is acknowledged for supplying Cray 1S computer time.

according to the experimental indication that the adamantane molecules are equally distributed between the two distinct equilibrium orientations.

The length of each run was 2500 time steps, *i.e.* $2.5 \cdot 10^{-11}$ s. Each run was preceded by 1500 steps of equilibration. The translational and rotational kinetic-energy equilibrium is reached in a few hundred steps, while, due to the existence of infrequent rotational jumps, the thermal equilibrium for orientations is reached in a time of the order of 1000 steps.

A description of the different runs including temperature T and the value of the lattice parameter a are listed in table I together with the potential energy U and the compressibility factor PV/NkT.

Mean square amplitudes are also given in table I.

TABLE I. – *Molecular-dynamics results for adamantane.*

Run	N	a (Å)	T (K)	$-U$ (kJmol^{-1})	$\frac{PV}{NkT}$	$\langle u_x^2\rangle_{\text{c.m.}}$ (Å^2)	$\langle \omega_x^2\rangle^{\frac{1}{2}}$ (degrees)	$\langle u_x^2\rangle_{\text{H}}$ (Å^2) (*)	$\langle u_x^2\rangle_{\text{H}}$ (Å^2) (**)
1	108	9.45	309	60.9	1	0.032	7.8	0.115	0.13
2	108	9.6	403	55.6	0.14	0.052	9.1	0.166	—

The following experimental values of the latent heat of sublimation H_S are given together with the corresponding temperatures and references where they are reported, all data were obtained at atmospheric pressure:

H_S (kJmol^{-1}) 59.3 [18] (at 198 K), 58.5 [19] (at 333 K), 53.5 [20] (in the temperature range (213÷366) K)

The two evaluations of the mean square amplitudes for hydrogen are indicated by

(*) $\langle u_x^2\rangle_{\text{c.m.}} + \frac{2}{3} r_{\text{H}}^2 \langle \omega_x^2\rangle$, where r_{H} is the vector joining an hydrogen atom to the centre of the molecule,

(**) the extrapolation to $t = 0$ of $\langle (R_{\text{H}}(0) - R_{\text{H}}(t)^2)\rangle$, where R_{H} is the radius vector of an hydrogen atom in the laboratory frame

Experimental results obtained at 300 K

$\langle u_x^2\rangle_{\text{c.m.}} = 0.048$ Å^2 [4], $\langle \omega_x^2\rangle^{\frac{1}{2}} = 8.6$ degrees [4] $\langle u_x^2\rangle_{\text{H}} = 0.14$ Å^2 [5]

The mean square vibrational amplitude of the centre of mass $\langle u_x^2\rangle_{\text{c.m.}}$ calculated at 309 K is in reasonably good agreement with the experimental value obtained by X-ray analysis.

The librational amplitudes $\langle \omega_x^2\rangle^{\frac{1}{2}}$ are calculated with the assumption of an isotropic motion, this is an application of orientational probability determination to be discussed later. The value obtained at the lower temperature is comparable to the experimental one.

The mean square displacements of the hydrogen atoms $\langle u_x^2\rangle_{\text{H}}$ calculated by two methods [21] are in good agreement with the experimental data obtained by incoherent quasi-elastic neutron scattering [5].

4. – Orientational order.

4·1. *Determination of the orientational probability density function.* – In the general case, the molecular orientations are described by the Euler angles of the molecule with respect to the crystal axes and the orientational order is described by the distribution function of these angles. This description, while complete, is heavy to handle. A simplified approach may be used in which one gives only the orientation of a molecular axis defined by its polar angles. We have chosen a molecular axis joining the centre of the molecule to one of the four tertiary carbons. This is a threefold one and there are four axes of this kind in the molecule (fig. 2). Therefore, each orientation of the molecule generates four (θ, φ) in the plane of polar angles.

The orientational order is then characterized by the orientational probability density function $P(\theta, \varphi)$ of the polar angles of the threefold molecular axes.

This function has been obtained for $T = 309$ K in the whole range of variation of θ and φ $(0 < \theta < \pi,\ 0 < \varphi < 2\pi)$, by calculating for each time step the set of values (θ, φ) for each tertiary carbon. The result is plotted in fig. 3 with contour lines corresponding to equal density probabilities. Eight equal maxima of the probability density are clearly visible, they correspomd to 2 molecular orientations (4 (θ, φ) per orientation) and the molecules are equally distributed between these two positions. The values of the polar angles for these maxima correspond to the T_d orientations (fig. 3). This result is the same as the experimental one showing that the preferential orientations of the threefold molecular axes coincide with the threefold crystal axes.

4·2. *Cubic-harmonics analysis.* – The molecular orientational probability density function $P(\theta, \varphi)$ can be expanded in terms of symmetry-adapted functions or surface harmonics. These functions are linear combinations of spherical harmonics which have been calculated and classified in sets belonging to the irreducible representations of the point groups [22]. In the case of the cubic point groups, the symmetry-adapted functions are the cubic harmonics [23] ${}_iK_l$ which are polynomials of degree l in terms of Cartesian co-ordinates. The index i labels independent functions belonging to the same irreducible representation for a given l [24]. The choice of ${}_iK_l$ necessary to obtain a complete basis of symmetry-adapted functions depends on the point group symmetry of the molecule and of the lattice site [25]. For a crystal structure F_{m3m} and a $\bar{4}3m$ molecular symmetry, the relevant symmetry-adapted functions belong respectively to the one-dimensional irreducible representations usually indicated by A_{1g}, A_{1u} and A_1, A_2 [25]. The probability density function $P(\theta, \varphi)$ is given by the following expression:

$$P(\theta, \varphi) = (1/4\pi)\Big(1 + \sum_{\substack{l \\ i}} \langle {}_iK_l \rangle\, {}_iK_l(\theta, \varphi)\Big) \tag{1}$$

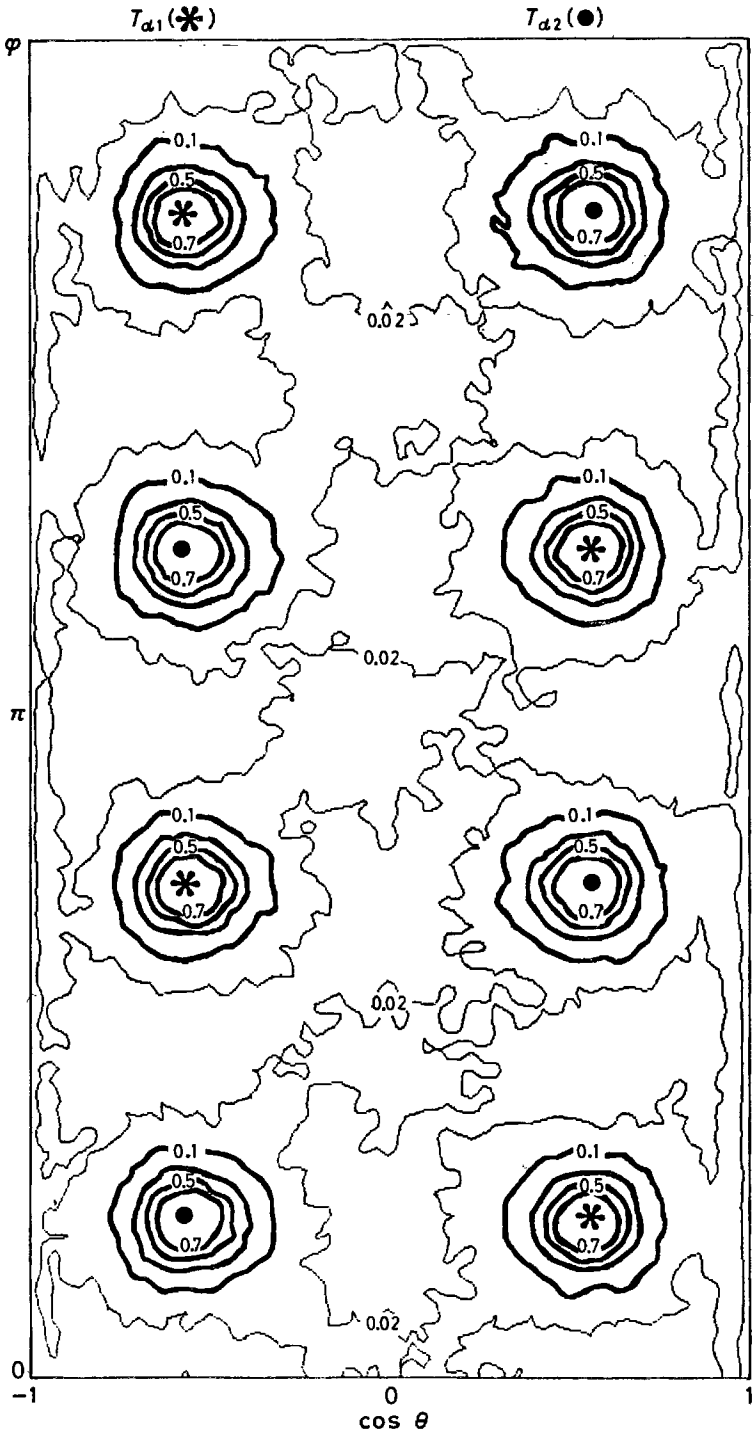

Fig. 3. – Orientational probability density function calculated at 309 K. $P(\theta, \varphi)$ is plotted in the plane $\cos\theta$, φ for the 4 tertiary carbons of the molecules. The location of the principal maxima ($P = 0.7$) corresponds to the T_d orientations of the molecules. The 8 positions of the threefold axes are plotted in plane $\cos\theta$, φ for the two T_d orientations.

with l values equal to 4, 6, 8, 9, 10, 12 when the expansion is limited to $l = 12$. The index i is always equal to 1 but for $l = 12$, where one has $i = 1, 2$. The polynomial expressions ${}_iK_l(\theta, \varphi)$ are given in appendix D. An example of cal-

TABLE II. – *Average values of cubic harmonics for adamantane.*

T (K)	Run	$\langle {}_1K_4 \rangle$	$\langle {}_1K_6 \rangle$	$\langle {}_1K_8 \rangle$	$\langle {}_1K_9 \rangle$	$\langle {}_1K_{10} \rangle$	$\langle {}_1K_{12} \rangle$	$\langle {}_2K_{12} \rangle$	$\langle {}_1K_3 \rangle$	$\langle {}_1K_7 \rangle$
309	1	– 0.992	1.353	0.396	– 0.011	– 0.996	0.065	– 0.517	0.036	0.022
403	2	– 0.681	0.974	0.245	0.009	– 0.561	0.034	– 0.278	0.026	– 0.009

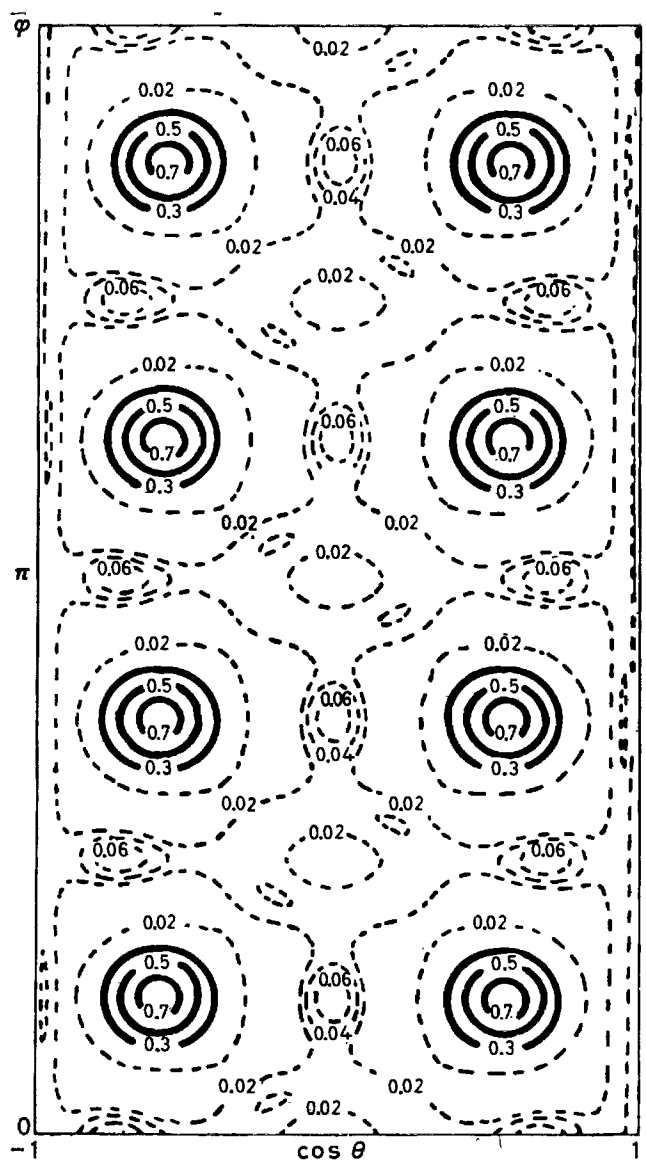

Fig. 4. – Orientational probability density function calculated at 309 K with cubic-harmonic expansion and plotted in the plane $\cos\theta$, φ. The locations of the maxima are quite comparable with those of fig. 3. The secondary maxima ($P = 0.06$) correspond to D_{2d} images.

culation of a cubic harmonic with the combination of spherical harmonics is detailed in appendix E.

To obtain $\langle {}_tK_l \rangle$ we compute ${}_tK_l(\theta, \varphi)$ for the orientation of a threefold molecular axis defined through the co-ordinates of a tertiary carbon with respect to the centre of the molecule. Then we average over time, molecules and all equivalent threefood axes in the molecule.

The results are listed in table II together with the average values of ${}_tK_l$ for the choices $l = 3$ and 7. $\langle {}_1K_3 \rangle$ and $\langle {}_1K_7 \rangle$ are not coefficients of the expansion, but their values can give useful information about the orientations of the molecules, as will be shown later.

The orientational probability density function has been calculated at two temperatures $T = 309$ and 403 K using eq. (1) and the values of $\langle {}_tK_l \rangle$ given in

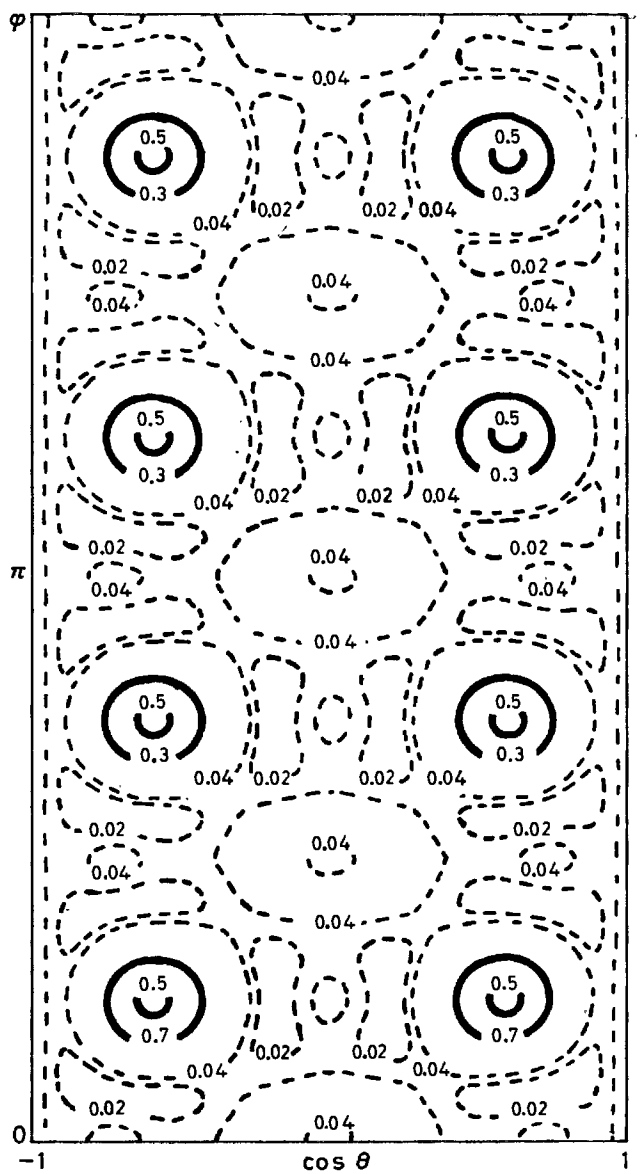

Fig. 5. – $P(\theta, \varphi)$ calculated at 403 K with cubic-harmonics expansion. The maxima ($P = 0.5$) correspond to T_d orientations.

table II. The contour lines corresponding to equal values of $P(\theta, \varphi)$ are given in fig. 4 and 5. Eight equal maxima of the probability density are clearly visible in these figures, they correspond to the two T_d orientations of the molecules.

The equipartition between the two T_d positions can also be deduced from the fact that $\langle {}_1K_3 \rangle$ and $\langle {}_1K_7 \rangle$ are equal to zero (cf. table II), since the values of the cubic harmonics ${}_1K_3$ and ${}_1K_7$ are, respectively, ± 1.972 and ± 2.37 for the two distinct positions corresponding to these orientations. A quantitative comparison between calculated values and experimental ones is made in fig. 6,

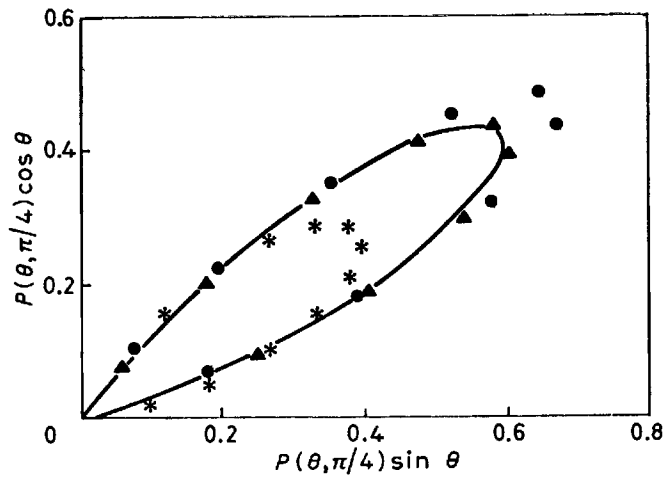

Fig. 6. – $P(\theta, \pi/4) \cos\theta$ *vs.* $P(\theta, \pi/4) \sin\theta$ calculated at 310 K in the range $0 < \theta < \pi/2$. Three sets of calculated values are represented, they correspond to the different expansions of $P(\theta, \varphi)$ in terms of K_l with l expansion limited respectively to 8, 10, 12: * calculated $\rightarrow K_8$, ▲ calculated $\rightarrow K_{10}$, • calculated $\rightarrow K_{12}$. The solid line corresponds to the experimental values determined at $T = 300$ K and analysed with l up to 10 [9].

where $P(\theta, \varphi)$ is plotted for $\varphi = \pi/4$ and $0 < \theta < \pi/2$ with three different upper limits in the expansion given by eq. (1). The orientational probability density function obtained from the analysis of experimental results with cubic harmonics limited to $l = 10$ is in very good agreement with the calculated values. The maximum values of $P(\theta, \varphi)$ differ significantly when the limit varies from 8 to 10 (fig. 6), when l increases the variation becomes negligible, this explains why the expansion of $P(\theta, \varphi)$ is limited to $l = 12$. The influence of the temperature on the orientational order has been investigated by comparing the orientational probability density functions calculated for $T = 309$ (fig. 4) and 403 K (fig. 5). The increase of the disorder is clearly visible, but the most probable orientations of the molecules remain the T_d ones. The maximum of $P(\theta, \varphi)$ has decreased, but it remains important when compared to 0.08 which is the value corresponding to a uniform probability density $(1/4\pi)$. If we consider now the secondary maxima, their positions do not vary with the temperature, they remain close to some particular orientations which are described hereafter.

4·3. *Ideal orientations.* – To describe the orientational order of the molecules with respect to the crystal axes, it is useful to define a certain number of configurations characterized by the coincidence of symmetry elements of the molecule and of the lattice site. These coincident configurations can be naturally classified by following the number of common symmetry elements. In a recent paper, KLEIN *et al.* [2], when discussing the characterization of orientational order, called these configurations « ideal ».

To define clearly the ideal configurations one has to consider all subgroups of both molecular and lattice site point groups (see chapt. II of ref. [26]) and to put in coincidence the symmetry elements of these various subgroups. In our case, the molecular point group is itself a subgroup of the site group. Therefore, the most symmetric of the ideal configurations is a T_d one. Next, we have D_{2d}, C_{3v} and C_{2v}. They are characterized as follows (fig. 7):

i) T_d orientations. All the symmetry elements of the molecular group coincide with some of the corresponding elements of the site point group. This

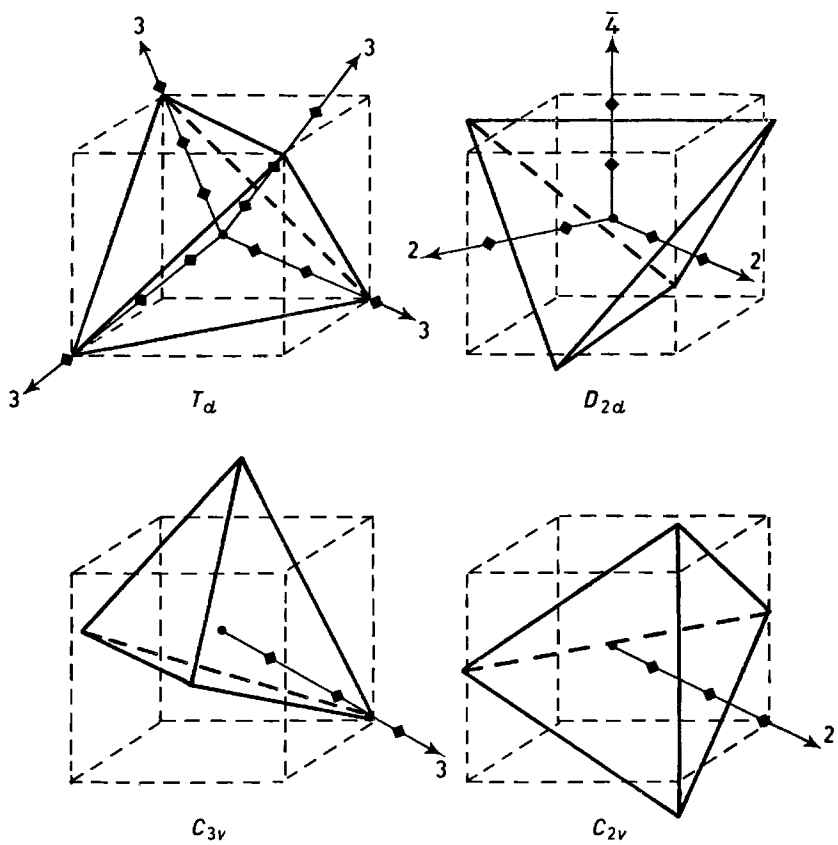

Fig. 7. – Schematic view of some « ideal orientations » of a tetrahedral molecule on a cubic site. There is only one distinct position represented for each orientation. All the coincident symmetry elements are not represented. Some axes are drawn: 4 threefold axes for T_d, the $\bar{4}$ axis and the twofold axes for D_{2d}, the threefold axis for C_{3v} and the twofold axis for C_{2v}. $\bar{4}$, 3, 2 indicate, respectively, $\bar{4}$ axis, threefold axis, twofold axis.

last has 48 symmetry operations, while the molecular group has 24. Therefore, there are two distinct T_d orientations.

ii) D_{2d} orientations. This subgroup contains one rotation reflection fourfold axis, three twofold axes and two mirrors. In all there are 8 symmetry operations and consequently this configuration has 6 distinct orientations.

iii) C_{3v} orientations. One threefold axis and three mirrors imply 6 symmetry operations and hence 8 distinct orientations.

iv) C_{2v} orientations. One twofold axis and two mirrors yield 4 symmetry operations and 12 distinct orientations.

There are 5 other common subgroups with a lower symmetry S_4, D_2, C_3, C_2, C_{1h}. For symmetry reason D_2 coincides with T_d and does not generate a new ideal configuration. The four other subgroups supplement the previous list, but they behave in a different way since they yield one-parameter families of configurations. The ideal orientations are not discrete because the coincidence of the symmetry elements is reduced to the coincidence of one element. There-

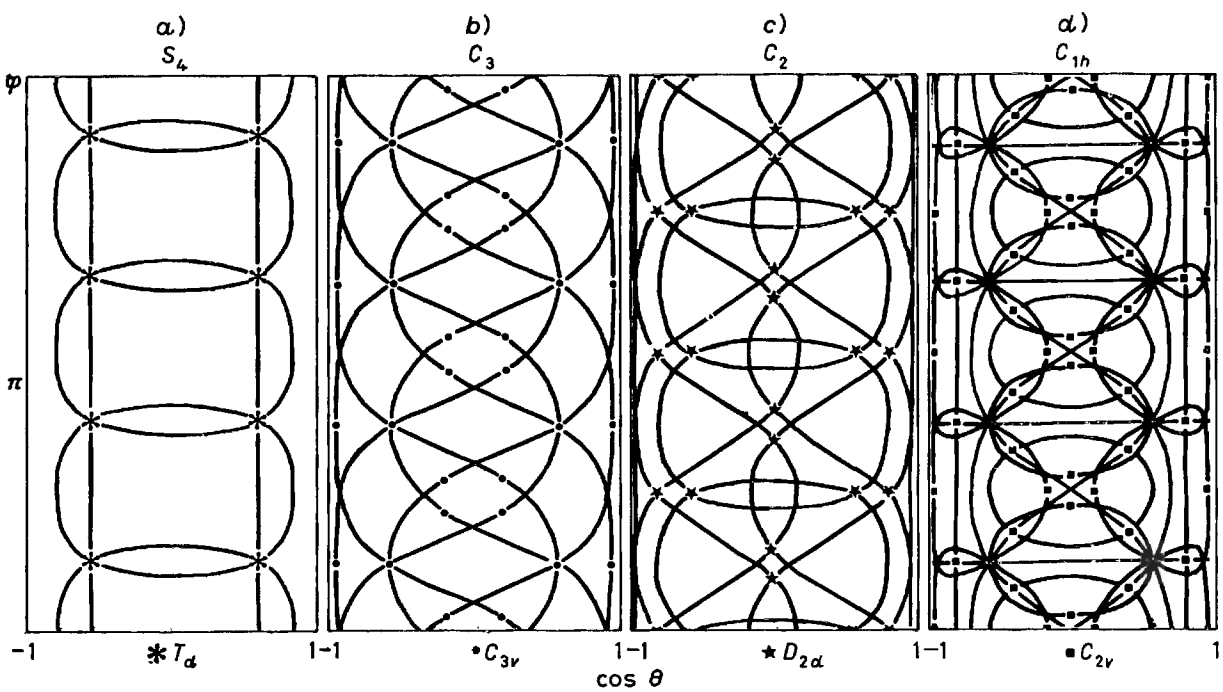

Fig. 8. – Images of the four families of ideal orientations. The polar co-ordinates of the four threefold molecular axes are given for each of the one-parameter families in their whole range of variation $0 < \varphi < 2\pi$, $-1 < \cos\theta < 1$: *a*) S_4 curves are obtained by the coincidence of one $\bar{4}$ axis, they intersect on the 8 images of the 2 T_d positions. *b*) C_3 curves are obtained by the coincidence of a threefold axis, they contain the 32 images of the 8 C_{3v} positions. *c*) C_2 curves are obtained by the coincidence of a twofold axis, they intersect on the 24 images of the 6 D_{2d} positions. *d*) C_{1h} curves are obtained by the coincidence of a mirror, they intersect on the 48 images of the 12 C_{2v} positions.

fore, any rotation leaving invariant this element changes one ideal orientation into another ideal orientation of the same family.

v) S_4 orientations. One $\bar{4}$ and twofold axis. This family contains T_d and D_{2d} orientations.

vi) C_3 orientations. One threefold axis. They contain T_d and C_{3v} orientations.

vii) C_2 orientations. One twofold axis. This family contains D_{2d} and C_{2v} orientations.

viii) C_{1h} orientations. One mirror. They contain T_d, D_{2d}, C_{3v}, C_{2v}.

To obtain the number of distinct one-parameter families of orientations for the last four classes, one can count the number of symmetry elements of the given class present in the cubic point group. For example, the existence, in the cubic symmetry, of 3 $\bar{4}$ axes, 4 threefold axes, 6 twofold axes and 9 mirrors implies 3 families of orientations for S_4, 4 for C_3, 6 for C_2 and 9 for C_{1h}: These families of ideal orientations are not represented in fig. 7, but their images are reported in fig. 8 as functions of θ and φ calculated for the four threefold molecular axes.

5. – Applications of the orientational probability density function.

5·1. *Librational amplitude.* – As already mentioned above, the orientational probability density function has been used to calculate the librational amplitude which cannot be evaluated directly because of the rotational diffusion.

If we assume that the librational motion is isotropic, we can relate its mean square amplitude $\langle\omega_x^2\rangle$ to the mean square amplitude $\langle\Delta\theta^2\rangle$ and $\langle\sin^2\theta\Delta\varphi^2\rangle$ of the threefold molecular axes [21]:

$$\langle\omega_x^2\rangle = \tfrac{1}{2}\big(\langle\Delta\theta^2\rangle + \langle\sin^2\theta\Delta\varphi^2\rangle\big)\,.$$

$\langle\Delta\theta^2\rangle$ and $\langle\sin^2\theta\Delta\varphi^2\rangle$ are calculated in a restricted region R around a maximum of $P(\theta, \varphi)$. R is chosen in order to circumscribe one and only one maximum.

The average values are defined as follows:

$$\Delta\varphi = \frac{\int_R P(\theta, \varphi)\varphi\,\mathrm{d}\theta\,\mathrm{d}\varphi}{\int_R P(\theta, \varphi)\,\mathrm{d}\theta\,\mathrm{d}\varphi}\,,$$

$$\Delta\varphi^2\sin^2\theta = \frac{\int_R P(\theta, \varphi)\sin^2\theta(\varphi - \langle\varphi\rangle)^2\,\mathrm{d}\theta\,\mathrm{d}\varphi}{\int_R P(\theta, \varphi)\,\mathrm{d}\theta\,\mathrm{d}\varphi}\,.$$

5·2. *Rotational motion.* – The secondary maxima of $P(\theta, \varphi)$ (fig. 4 and 5) are close to D_{2d}, C_{3v} and C_{2v} orientations (fig. 8). These secondary maxima could be related to the trajectories of the tertiary carbons obtained by rotations of the molecules. If the molecules rotate around fourfold, threefold or twofold crystal axes, the ideal families of configurations S_4, C_3, C_2, which contain T_d, D_{2d}, C_{3v} and C_{2v} orientations, represent the trajectories of the tertiary carbons in the plane (θ, φ).

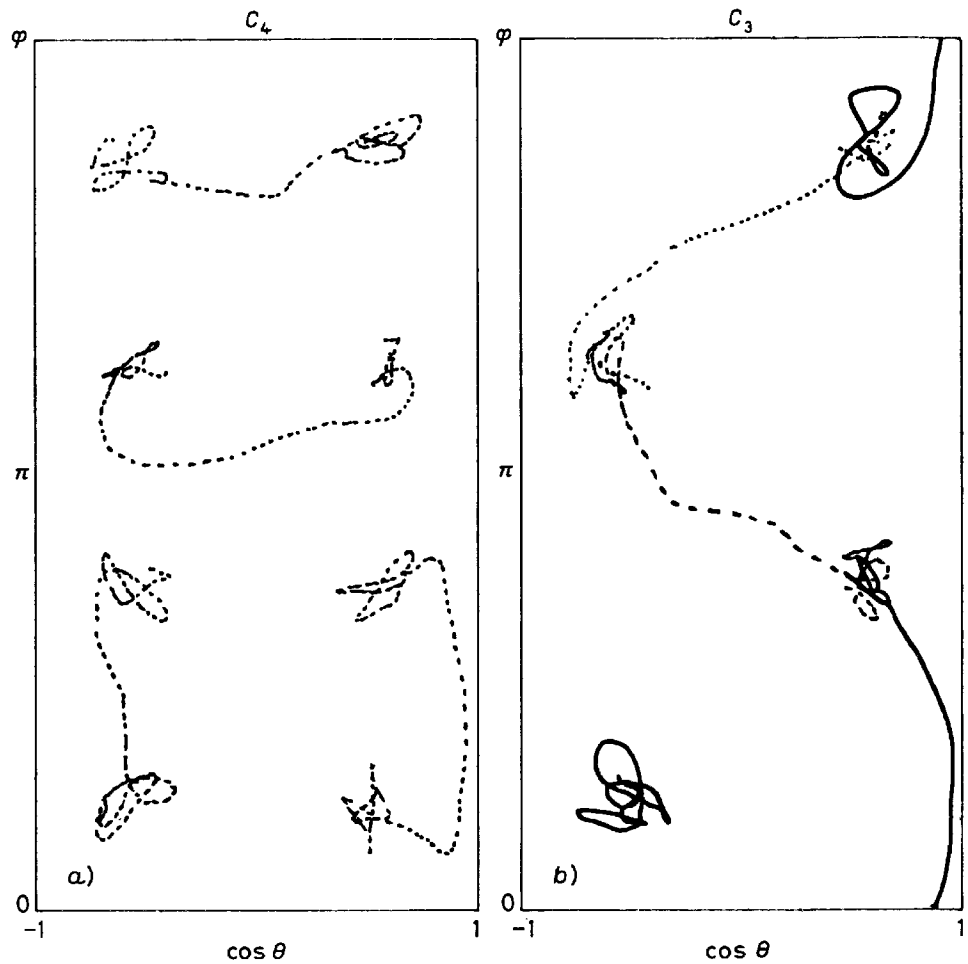

Fig. 9. – Trajectories of the tertiary carbons calculated at 309 K and plotted in the plane $\cos\theta$, φ. They correspond to different rotational jumps: *a*) C_4 rotational motion: $\pi/2$ about a fourfold crystal axis. *b*) C_3 rotational motion: $2\pi/3$ about a threefold crystal axis.

We have plotted in fig. 9 the trajectories of the tertiary carbons in the plane (θ, φ), they correspond to the rotational motion of two molecules observed at 309 K. The comparison between fig. 9*a*) and 8*a*) shows that the trajectories of the carbons are quite similar to a S_4 ideal family of configurations. The trajectories of fig. 9*b*) correspond to a C_3 ideal family of configurations.

These two molecular trajectories correspond to rotational jumps which have been characterized by comparing the molecular orientations before and after the rotation. They are, respectively, a $\pi/2$ rotation about a fourfold axis C_4 and a $2\pi/3$ rotation about a threefold axis C_3. A detailed analysis of rotational motion in adamantane will be given in a forthcoming paper. We found that the trajectories of the rotating molecules are close to the curves corresponding to the four families of configurations plotted in fig. 8. So the existence of secondary maxima related to ideal configurations corresponds to the rotational motion and the families of configurations give ideal trajectories followed by the rotating molecules.

6. – Conclusions.

Molecular-dynamics simulation using pairwise additive potential and constraint method for rigid molecules has proved suitable to calculate some properties of the plastic phase of adamantane. We have shown that the most probable orientations of the molecules are T_d ones and that they are equally distributed among the two possible T_d positions. We have calculated the orientational probability density function of the molecules and found good agreement with experimental results. The secondary maxima of this probability density function are related to the molecular rotations about fourfold and threefold axes.

APPENDIX A

Symmetry elements, symmetry operations of adamantane (high-temperature phase).

	Molecular symmetry $\bar{4}3m$					Lattice site symmetry $m3m$								
Elements		3	2	$\bar{4}$	m		4	3	2	2	C	$\bar{4}$	m	m	$\bar{3}$
Operations	E	$8C_3$	$3C_2$	$6S_4$	$6\sigma_d$	E	$6C_4$	$8C_3$	$3C_2$	$6C_2$	i	$6S_4$	$3\sigma_h$	$6\sigma_d$	$8S_6$
Total number of operations			24							48					

E identity;
C_4 $\pi/2$ rotation about a fourfold axis: 4;
C_3 $2\pi/3$ rotation about a threefold axis: 3;
C_2 π rotation about twofold axis: 2;
i inversion;
S_4 $\pi/2$ rotation about a fourfold rotation reflection axis $\bar{4}$;
S_6 $2\pi/3$ rotation about a threefold rotation reflection axis $\bar{3}$;
σ_d reflection on a diagonal mirror m;
σ_h reflection on a horizontal mirror m.

Appendix B

Cartesian co-ordinates of basic atoms R_i $(i = 1, 4)$
(with molecular centre of mass on origin).

	x_i (Å)	y_i (Å)	z_i (Å)
$T_d(1)$	0.878	0.878	0.878
	−0.878	−0.878	0.878
	−0.878	0.878	−0.878
	0.878	−0.878	−0.878
$T_d(2)$	−0.878	−0.878	0.878
	−0.878	0.878	0.878
	0.878	−0.878	0.878
	0.878	0.878	−0.878

Coefficients for secondary atoms $(\alpha = 1, 22)$ $R_\alpha = \sum_{i=1}^{4} C_{\alpha i} R_i$.

$C_{\alpha 1}$	$C_{\alpha 2}$	$C_{\alpha 3}$	$C_{\alpha 4}$
−0.253 986	−0.253 986	0.753 986	0.753 986
−0.253 986	0.753 986	−0.253 986	0.753 986
−0.253 986	0.753 986	0.753 986	−0.253 986
0.753 986	0.753 986	−0.253 986	−0.253 986
0.753 986	−0.253 986	0.753 986	−0.253 986
0.753 986	−0.253 986	−0.253 986	0.753 986
1.532 175	−0.177 392	−0.177 392	−0.177 392
−0.177 392	1.532 175	−0.177 392	−0.177 392
−0.177 392	−0.177 392	1.532 175	−0.177 392
−0.177 392	−0.177 392	−0.177 392	1.532 175
−0.786 162	0.931 378	0.931 378	−0.076 594
−0.786 162	−0.076 594	0.931 378	0.931 378
−0.786 162	0.931 378	−0.076 594	0.931 378
0.931 378	−0.786 162	−0.076 594	0.931 378
−0.076 594	−0.786 162	0.931 378	0.931 378
0.931 378	−0.786 162	0.931 378	−0.076 594
0.931 378	−0.076 594	−0.786 162	0.931 378
0.931 378	0.931 378	−0.786 162	−0.076 594
−0.076 594	0.931 378	−0.786 162	0.931 378
−0.076 594	0.931 378	0.931 378	−0.786 162
0.931 378	0.931 378	−0.076 594	−0.786 162
0.931 378	−0.076 594	0.931 378	−0.786 162

Appendix C

Subroutine of forces.

R (NM, NA) table of atomic co-ordinates
F(NM, NA) table of forces

```
FI  (NM * NA) intermediate table of forces
POT(NM * NA) intermediate table for potential energy
VIR(NM * NA) intermediate table for virial part of pressure
IPOTR (NA) table for the indices of potential indicating the atomic species
IPRET (IA, IA) table for indices of pair interaction
IA number of atomic species
BL      length of the simulated cell
CUT     cut-off radius

CUT2 = CUT*CUT
UBL = 1./BL
DO 1  I = 1, NM-1              loop on molecule I
DO 1  K = 1, NA                loop on atom K of molecule I
RT = R(I, K)                   atomic co-ordinate
IK = IPOTR (K)                 index of potential for atom K
M = 0
DO 2 L = 1, NA                 loop on atom L
IL = IPOTR (L)                 index of potential for atom L
IP = IPRET(IK, IL)             type of pair interaction
DO 2 J = I+1, NM               loop of molecule J
M = M+1
DR = RT-R(J,L)                 interatomic distance
DR = DR-AINT (DR*UBL+SIGN (0.5,DR)) *BL   minimum image
R2 = DR * DR
POT (M) = CVMGP (V (DR, IP), 0., CUT2-R2)      test on cut-off radius
FI(M) = CVMGP (FC (DR, IP), 0., CUT2-R2)       test on cut-off radius
VIR(M) = CVMGP (VR (DR, JP), 0., CUT2-R2)      test on cut-off radius
F(J,L) = FIJ,L) + FI(M)                force on atom L of molecule J
2     CONTINUE
F(I, K) = F(I, K) + SSUM(M, FI, 1) force on atom K of molecule I
EPOT = EPOT + SSUM (M, POT, 1) potential energy
PRES = PRES + SSUM (M, VIR, 1) virial
1     CONTINUE
```

Appendix D

Cubic harmonics [9].

$$ {}_1K_0 = 1 , $$

$$ {}_1K_3 = \sqrt{105}\, xyz , $$

$$ {}_1K_4 = \frac{5\sqrt{21}}{4}\,[x^4 + y^4 + z^4 - 0.6] , $$

$$ {}_1K_6 = \frac{231\sqrt{26}}{8}\left[x^2 y^2 z^2 + [{}_1K_4]/22 - \frac{1}{105}\right] , $$

$$ {}_1K_7 = \frac{11\sqrt{1365}}{4}\, xyz\left[x^4 + y^4 + z^4 - \frac{5}{11}\right] , $$

$$
\begin{aligned}
{}_1K_8 &= \frac{65\sqrt{561}}{16}\left[x^8+y^8+z^8-5.6[{}_1K_4]-\frac{210}{143}[{}_1K_6]-\frac{1}{3}\right],\\
{}_1K_9 &= {}_1N_9 xyz\left[x^2y^2z^2+\frac{3}{34}(x^4+y^4+z^4)-\frac{27}{442}\right],\\
{}_1K_{10} &= \frac{11\times17\times19\sqrt{227.5}}{80}\left[x^{10}+y^{10}+z^{10}-\frac{45}{19}[{}_1K_8]-\right.\\
&\qquad\left.-\frac{126}{17}[{}_1K_6]-\frac{210}{143}[{}_1K_4]-\frac{3}{11}\right],\\
{}_1K_{12} &= {}_1N_{12}\left[x^{12}+y^{12}+z^{12}-\frac{66}{23}[{}_1K_{10}]-\frac{495}{133}[{}_1K_8]-\right.\\
&\qquad\left.-\frac{2772}{323}[{}_1K_6]-\frac{315}{221}[{}_1K_4]-\frac{3}{12}\right],\\
{}_2K_{12} &= \frac{1}{30\sqrt{33}}[8\sqrt{145}\,\overset{c}{Y}_{12,4}-\sqrt{19}\,307\,\overset{c}{Y}_{1,28}+\sqrt{1113}\,\overset{c}{Y}_{12,12}],
\end{aligned}
$$

with

$$
\begin{aligned}
{}_1N_9 &= 2187.44\,, \qquad {}_1N_{12} = 1582.0556\,,\\
+\overset{c}{Y}_{12,4} &= \frac{15\sqrt{2002}}{2048}\sin^4\theta[7429z^8-9044z^6+3230z^4-340z^2+5]\cos 4\varphi\,,\\
+\overset{c}{Y}_{12,8} &= \frac{5\sqrt{143\times51\times19}}{1024}-\sin^8\theta[161z^4-42z^2+1]\cos 8\varphi\,,\\
+\overset{c}{Y}_{12,12} &= \frac{5\sqrt{13\times14\times17\times19\times23}}{2048}\sin^{12}\theta\cos^{12}\varphi\,;
\end{aligned}
$$

all the polynomials ${}_iK_l$ must be divided by a factor $\sqrt{4\pi}$.

$$+\overset{c}{Y}_{l,m} = (Y_{lm}+Y_{l-m})/\sqrt{2}\,,$$

$${}_iK_l = {}_iN_l[{}_iK_l]\,.$$

Appendix E

Calculation of ${}_1K_4$.

The coefficients for linear combinations of spherical harmonics $Y_{l,m}$ are given in ref. [22] for each value of l.

We select the table corresponding to A_{1g}, A_{1u} for $m3m$ and A_1, A_2 for $\bar{4}3m$.

In these representations there are symmetry-adapted functions for l values equal to 0, 4, 6, 8, 9, 10, 12.

Let us consider $l = 4$.

We have two coefficients with m values indicated in parentheses

$$0.763 \quad (0), \qquad 0.64 \quad (4),$$

$$_1K_4 = 0.763\,\overset{c}{Y}_{4,0} + 0.64\,\overset{c}{Y}_{4,4},$$

with $\overset{c}{Y}_{l,m} = (Y_{l,m} + Y_{l,-m})/\sqrt{2}$.

REFERENCES

[1] *The Plastically Crystalline State,* edited by J. N. SHERWOOD (Wiley and Sons, New York, N. Y., 1979).
[2] M. L. KLEIN, I. R. MCDONALD and Y. OZAKI: *J. Chem. Phys.*, **79**, 5579 (1983).
[3] E. NEUSY, S. NOSÉ and M. L. KLEIN: *Mol. Phys.*, **52**, 269 (1984).
[4] J. P. AMOUREUX, M. BEE and C. J. DAMIEN: *Acta Crystallogr. B*, **36**, 2633 (1980).
[5] R. E. LECHNER and A. HEIDEMANN: *Commun. Phys.*, **1**, 213 (1976).
[6] M. BEE, J. P. AMOUREUX and R. E. LECHNER: *Mol. Phys.*, **40**, 617 (1980).
[7] S. S. CHANG and E. F. WESTRUM: *J. Phys. Chem.*, **64**, 1547 (1960).
[8] C. E. NORDMAN and D. L. SCHMITTKONS: *Acta Crystallogr.*, **18**, 764 (1965).
[9] J. P. AMOUREUX and M. BEE: *Acta Crystallogr. B*, **36**, 2636 (1980).
[10] J. P. AMOUREUX, M. BEE and J. VIRLET: *Mol. Phys.*, **41**, 313 (1980).
[11] H. A. RESING: *Mol. Cryst. Liq. Cryst.*, **9**, 101 (1969).
[12] S. RAMDAS and J. M. THOMAS: in *Chemical Physics of Solids and their Surfaces*, edited by J. M. THOMAS and M. W. ROBERTS, Vol. 7 (The Chemical Society, London, 1978), p. 31.
[13] D. E. WILLIAMS: *J. Chem. Phys.*, **47**, 4680 (1967).
[14] G. CICCOTTI, M. FERRARIO and J. P. RYCKAERT: *Mol. Phys.*, **47**, 1253 (1982).
[15] L. VERLET: *Phys. Rev.*, **159**, 98 (1967).
[16] D. FINCHAM and B. J. RALSTON: *Comput. Phys. Commun.*, **23**, 127 (1981).
[17] S. M. BREITLING, A. D. JONES and R. M. BOYD: *J. Chem. Phys.*, **54**, 3959 (1971).
[18] M. MANSSON, N. RAPPORT and E. F. WESTRUM: *J. Am. Chem. Soc.*, **92**, 7296 (1970).
[19] W. K. BRATTON and I. SZILARD: *J. Org. Chem.*, **32**, 2019 (1967).
[20] P. J. WU, L. HSU and D. A. DOWS: *J. Chem. Phys.*, **54**, 2714 (1971).
[21] M. MEYER and G. CICCOTTI: *Mol. Phys.*, **56**, 1235 (1985).
[22] O. J. BRADLEY and A. P. CRACKNELL: *The Mathematical Theory of Symmetry in Solids* (Clarendon Press, Oxford, 1972), p. 51.
[23] F. C. VON DER LAAGE and H. A. BETHE: *Phys. Rev.*, **71**, 6171 (1947).
[24] F. M. MUELLER and M. G. PRIESTLEY: *Phys. Rev.*, **148**, 638 (1966).
[25] M. YVINEC and R. PICK: *J. Phys.*, **41**, 1045 (1980).
[26] E. PRINCE: *Mathematical Techniques in Crystallography and Material Science* (Springer-Verlag, New York, N. Y., 1982).

Biological Molecules and Membranes.

H. J. C. BERENDSEN

Laboratory of Physical Chemistry, University of Groningen
Nijenborgh 16 - 9747 *AG Groningen, The Netherlands*

1. – Introduction.

There is no difficulty in principle in applying molecular-dynamics (MD) techniques to large macromolecules including systems of biological interest [1-3]. In practice such systems have complex descriptions and parameters are not sufficiently accurate to provide at present a precision similar to that obtained on atoms and simple molecules. Refinements that will probably prove to be necessary, but that have not been worked out into standard procedures, concern the correct computation of long-range electrostatic interactions, taking the properties of the environment into account [4, 5], and the incorporation of atomic polarizabilities. Also the application of simulation techniques to reactive systems (such as enzymatic reactions) will require the construction of simplified potential fields in a reduced system of reactive co-ordinates, based on extensive quantum-mechanical calculations. Still, such developments are possible and will undoubtedly happen in due time.

The principal difficulty concerns the time scale on which interesting phenomena occur in large molecules. For example, a protein molecule, consisting of a specific sequence of amino acids, in a linear polypeptide chain, generally folds into a unique conformation which is thermodynamically stable. In physical time such a folding process takes seconds or minutes. Although along the folding pathway there are some events that are slow because they await sufficiently energetic fluctuations to cross an energy barrier, the main reason for the slow rate of the process is the vast dimensionality of configuration space and the huge sampling that has to be done in real time to find the thermodynamically stable region of configuration space. The problem resembles somewhat multidimensional global optimization, compared to annnealing processes that are very slow in physical time [6]. If no artificial short-cuts in this process can be found, brute-force simulation seems to be hopeless. One second real-time simulation of a small protein in solution with the present-day techniques

would require 10^{11} h of present-day supercomputer cpu time. No future improvements in computer capabilities can possibly cope with such problems.

Fortunately, there are very many problems of interest that occur on a much smaller time scale. The structural rearrangements in a macromolecule upon binding a small molecule, or upon changes in solvent or environment, occur on a time scale of 10 to 100 ps. Reactions are often slow ($\sim$1 ms), but this is so as a result of the presence of energy barriers. If these barriers can be found and the stochastic properties of the system can be described (based on simulation) in terms of a reduced system of low dimensionality, the reactive events can be computed. It may not always be necessary to simulate a system in all its degrees of freedom; if a suitable reduction can be formulated, the system may be studied by stochastic dynamics using potentials of mean force within the reduced system. Such methods are under development at present [7-10].

So, the future of macromolecular-dynamics simulation does not look grim, after all. In addition, the development of computer capabilities is so rapid [11, 12] that simulations which look impossible on present-day supercomputers will be standard jobs on desk-top special-purpose computional devices in ten years' time.

Large molecular systems of biological interest include proteins, nucleic acids (DNA and RNA), polysaccharides and membranes. Proteins have either a structural function or they act as catalysts for specific chemical reactions. In many cases they are membrane bound and they often act in co-operation with other proteins (or nucleic acids) in large macromolecular complexes. Nucleic acids are involved in the storage and transfer of chemical information and they generally act in conjunction with specific proteins. Polysaccharides have a structural, often lubricating role, in addition to being used for energy storage. They are often used in ill-understood recognition processes at cell surfaces. Membranes provide a fluid barrier between compartments and serve as localization for important catalytic processes that are often concerned with specific transport of small moleculess across the membrane, carried out by specialized membrane-bound protein molecules. In addition, voltage-dependent ion transport processes across membranes serve to transmit impulses in nerve cells.

Simulation techniques are being applied to these systems with the aim to understand and predict functional properties (related to dynamical events) on the basis of interactions on an atomic scale Thus understanding of biomolecular events is expected to reach far beyond the present level of phenomenological descriptions based on structural and kinetic data. In addition to this deeper level of understanding, prediction of properties will be possible, once the techniques have been sufficiently developed, the interaction potentials are sufficiently reliable, and the computing resources sufficiently available.

As envisaged now, computational predictions of material properties are expected to become very important in two applications: *drug design* and *protein*

design. Small molecules that bind to biomacromolecules and act as activator or inhibitor of specific functions could be computer-designed before they are synthesized and tested. In cases where the structure of the reception site is known, computational procedures, including molecular dynamics aided by advanced computer graphics, will undoubtedly become powerful tools in the process of drug design. For such applications it will be essential that reliable methods are available to predict the *free energy* of binding of small molecules to macromolecules, since it is the binding constant K, given by the standard Gibbs free energy of binding $\Delta G^0 = -RT \ln K$, that is important. Such methods will be discussed in subsect. 4·3. Computation of the effects of changing the amino acid composition of a protein on its structure, dynamical stability and binding or catalytic properties, will make the design of proteins for specific purposes possible. Present-day methods of genetic engineering make it possible to produce artificial proteins through genetically altered primitive organisms as bacteria or yeast cells, in industrial quantities if required. The impact of such techniques on pharmaceutical and chemical industrial processes is likely to become revolutionary. Existing enzymes may be made heat and solvent resistant; new catalysts may be designed. Also the design of structural polypeptides with properties superior to those of industrial polymers is possible. For all such applications predictions based on reliable simulation are essential.

From the vast field of biophysical applications [1-3] a few examples from our own laboratory will be singled out in the next sections. These are chosen so as to exemplify some specific applications, as well as to show the present limitations of the applications of MD to biomacromolecules. Section 2 describes two examples of the simulation of proteins: the difference between structure in solution and in the crystal, and the possible role of structural mobility. In sect. 3 methods to determine free energy will be reviewed for the purpose of computing binding constants, as well as for the purpose of finding the entropy of metastable configurational states. Section 4 describes simulations on models for biological membranes. These concern bilayer structures of amphiphilic molecules (having a hydrophilic head group and a hydrophobic hydrocarbon tail). The interest lies both in the dynamics and average structure of the hydrocarbon tail which exhibits a two-dimensional fluid behaviour, and in the charge distributions and interactions in the hydrophilic region.

2. – MD of proteins.

2·1. *Potentials and methods*. – Figure 1 shows a section of a typical protein, consisting of amino acids attached to each other by the almost rigid peptide bond —CO—NH—. Most proteins are built up from a linear chain 50 to 400 amino acids (there is a choice among 20 different types); often functional units are made up from several such subunit proteins. The interaction poten-

tial is usually described as a site-site potential without the use of virtual sites, with additional terms for bond stretching, bond angle deformation and dihedral angle rotation (see fig. 1). In most force fields only polar hydrogens (bound to oxygen or nitrogen) are explicitly taken into account, while —CH_2— and —CH_3 groups are taken as united atoms. The hydrogen bonds between polar hydrogens and lone-pair electrons of oxygen or nitrogen are represented by the combination of Coulomb and Van der Waals forces A simple water potential [13] consistent with the protein potential [14] is used.

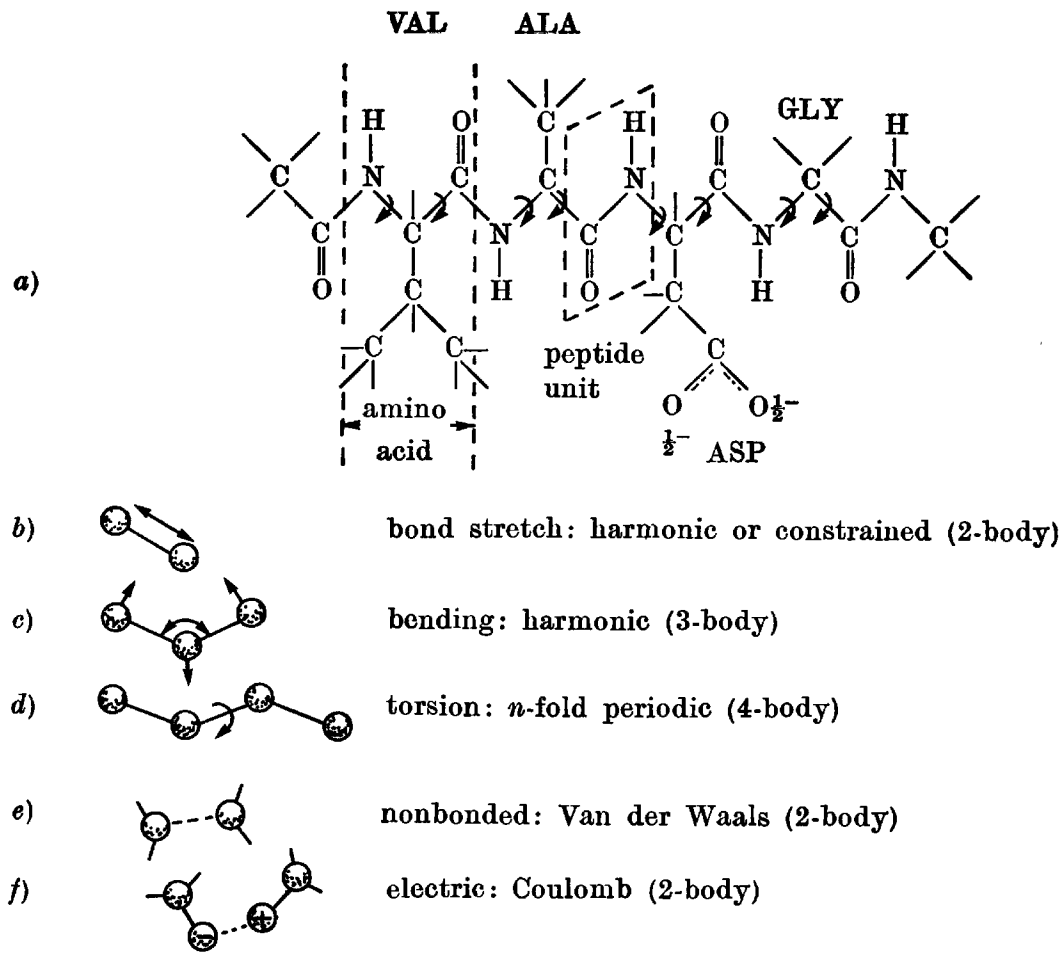

Fig. 1. – *a*) Portion of a polypeptide or protein chain, with the amino acid sequence valine-alanine-aspartic acid-glycine; *b*)-*f*) terms used in potential-energy description.

Simulations on proteins were first carried out in a CECAM Workshop in 1976 [15] by McCammon *et al.* [16]. See ref. [1, 2] for reviews. These simulations, as well as later ones [17, 18], were carried out without taking the solvent explicitly into account. In such « vacuum » simulations potentials of mean force should be used which should include a complete treatment of long-range electrostatic interaction in which the presence of a polarizable environment

(the solvent: water or an electrolyte solution) is taken into account by solution of the appropriate field equations [4, 5]. The proper solution of long-range electrostatic effects is quite essential because proteins ofter have helical segments in which the peptide dipole moments are aligned and exert a long-range electrostatic field, that appears to have a functional role in binding properties and catalytic function [4, 19, 20]. In practice the field equations are not properly solved because accessible methods have not been worked out for use in MD. Instead, *ad hoc* adjustments are commonly made: distance-dependent dielectric constants are being used or charges occurring at the outside of the protein are reduced to accommodate solvent screening. Such vacuum simulations are still very crude, although they may represent events inside the protein with sufficient accuracy.

The first question to ask concerns the reliability of MD simulations on proteins. An estimate of this reliability can be obtained by comparing the average MD structure of a crystalline protein (including water of hydration) to the structure as found by X-ray diffraction. In addition, the MD fluctuations can be compared with temperature factors found in the refinement procedure of X-ray data.

When the full unit cell of the crystal is simulated, as has been done [21] for the protein in BPTI (basic pancreatic trypsin inhibitor, consisting of 58 amino acids or 458 nonhydrogen atoms, with four protein molecules and 560 water molecules in the unit cell, totalling 7000 degrees of freedom), the accuracy of the average atom positions ranges from 0.08 to 0.17 nm. The backbone atoms (C-α atoms) remain more stable (0.08 nm) than the atoms of the flexible side chains. The average r.m.s. deviation of all atoms over a 20 ps simulation was found to be 0.12 nm. The X-ray structure is believed to be accurate to about 0.02 to 0.04 nm, although the resolution of the diffraction data is about 0.1 nm. The experimental temperature factors indicate a r.m.s. fluctuation of about 0.08 nm and this agrees roughly with r.m.s. fluctuations of atomic positions with respect to their averages in the MD simulation. So it can be concluded that the accuracy of atomic positions is of the same order as the structural fluctuations occurring in the crystalline state, with the potential field presently in use. This can be considered adequate for our purpose.

2·2. *Protein structure in solution.* – Although X-ray diffraction gives invaluable information about the detailed structure of a protein, it is necessarily restricted to the structure in the crystalline state. The crystals normally contain a high fraction of solvent (generally $\sim 50\,\%$) and the protein crystal contact areas are limited. Hence it is likely that in most cases the crystal structure does not deviate significantly from the structure in solution, and this is what biochemists generally assume. We performed a MD study of BPTI in solution [22], using a truncated octahedron as the periodic box [23] in order to reduce the number of water molecules required. The simulation contained one

BPTI molecule and 1500 water molecules, totalling 15 000 degrees of freedom, and was carried out at 300 K over 15 ps after equilibration. The r.m.s. positional differences between solution structure and X-ray structure now are 0.14 nm for the C-α backbone atoms and 0.22 nm for the average of all atoms. Some atomic positions deviate as much as 0.8 nm, but these invariably concern side chain atoms. The backbone structure remains stable. Figure 2 gives the

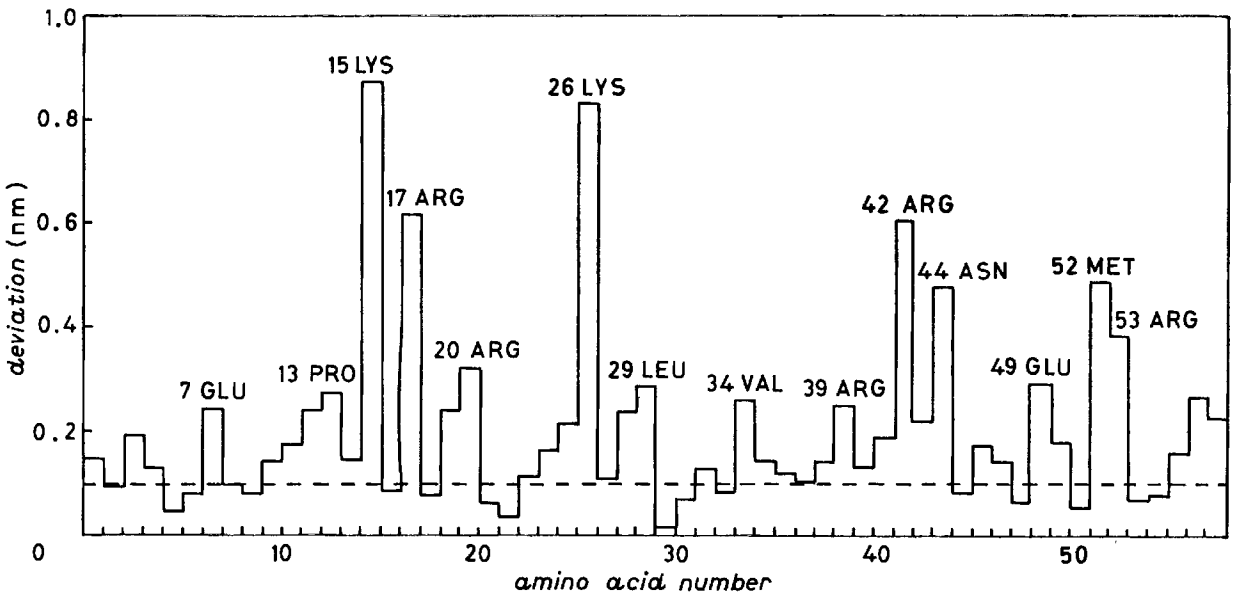

Fig. 2. – Differences in average structure between MD in solution and MD in crystal for the terminal atoms of side chains in BPTI. The dashed line gives the level of normal fluctuations.

deviations of the terminal atoms of side chains; the largest deviations are those of polar side chains (Lys, Arg, Asp, Asn, Glu) that are now free to move in solution. This result is to be expected. It turns out that crystal contacts inhibit the free motion of side chains in the crystal, which is possible in solution. Figure 3 gives an example of a side chain held in place by crystal contacts, but moving to a different position in solution.

It should be mentioned here that nuclear-magnetic-resonance techniques have recently been developed from which structural data on macromolecules in solution can be obtained. Two-dimensional NMR at 500 MHz resonance frequency gives cross-peaks for proton pairs that are either coupled by spin-spin coupling (allowing assignments of peaks and of local structure elements) or by dipolar coupling (NOE: nuclear Overhauser effect). The latter enables the identification of short through-space contacts, from which in principle the 3-D structure is resolvable. MD simulations have proved to be extremely useful in aiding the solution of the 3-D structure [24, 25]. This is accomplished by adding potentials to the potential field for those proton pairs for which experimental distance constraints are observed.

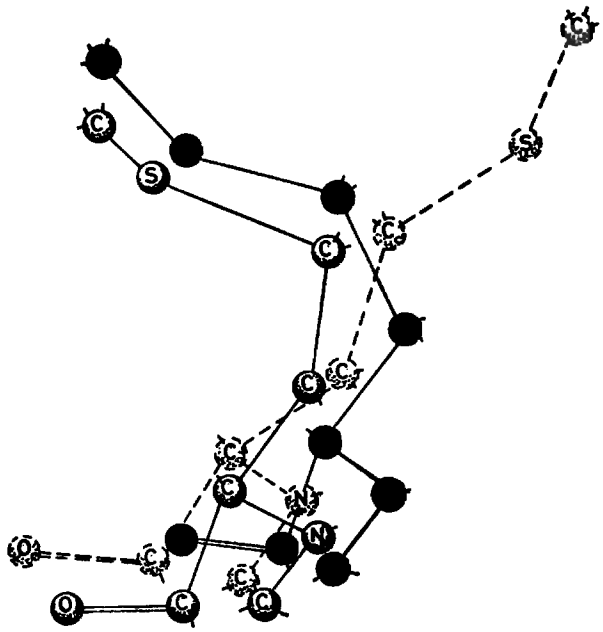

Fig. 3. – Methionine 52 side chain in crystal simulation (–•–), in X-ray structure (–o–) and in solution (– –o– –). In the crystal the side chain is held by crystal contacts.

2·3. *Functional role of protein dynamics.* – Certain regions of proteins have structural mobility, which often shows in X-ray diffraction of crystals by a lack of resolution in certain areas. It is likely that structural mobility is quite common in solution, also in cases that such a mobility is not seen in the crystal because it is inhibited by crystal contacts. Recently, in our laboratory M. MAKINEN of the University of Chicago has observed structural mobility in a helical part in a MD simulation of carboxypeptidase-*A* (an enzyme that chops off the carboxyterminal amino acid of proteins and peptides). Figure 4*a*) shows the mobility of α-C backbone atoms during a 20 ps MD run. The mobile region (identified as an α-helix) is not mobile at all in the crystal, according to X-ray data. A most interesting observation was made: if the simulation was carried out with a molecule bound in the active site, the mobility was inhibited (fig. 4*b*)). This points to a possible functional role of the structural mobility, the consequences of which are still to be analysed.

A protein should be viewed as a fluctuating structure that is able to accommodate the binding of small molecules (substrates, activators, inhibitors, coenzymes) by structural adaptation. Structural adaptations upon binding one molecule are often transmitted to influence the binding of another molecule at another site. There are several examples of proteins where a small molecule, which is known to bind specifically to the protein, does not fit into the structure as determined by X-ray diffraction. A clear and well-studied example of internal mobility is the ring-flipping of tyrosine rings, observed by NMR to occur on a millisecond time scale for some of the tyrosine rings in BPTI [26]. In the X-ray structure these rings cannot rotate since the energy barrier would

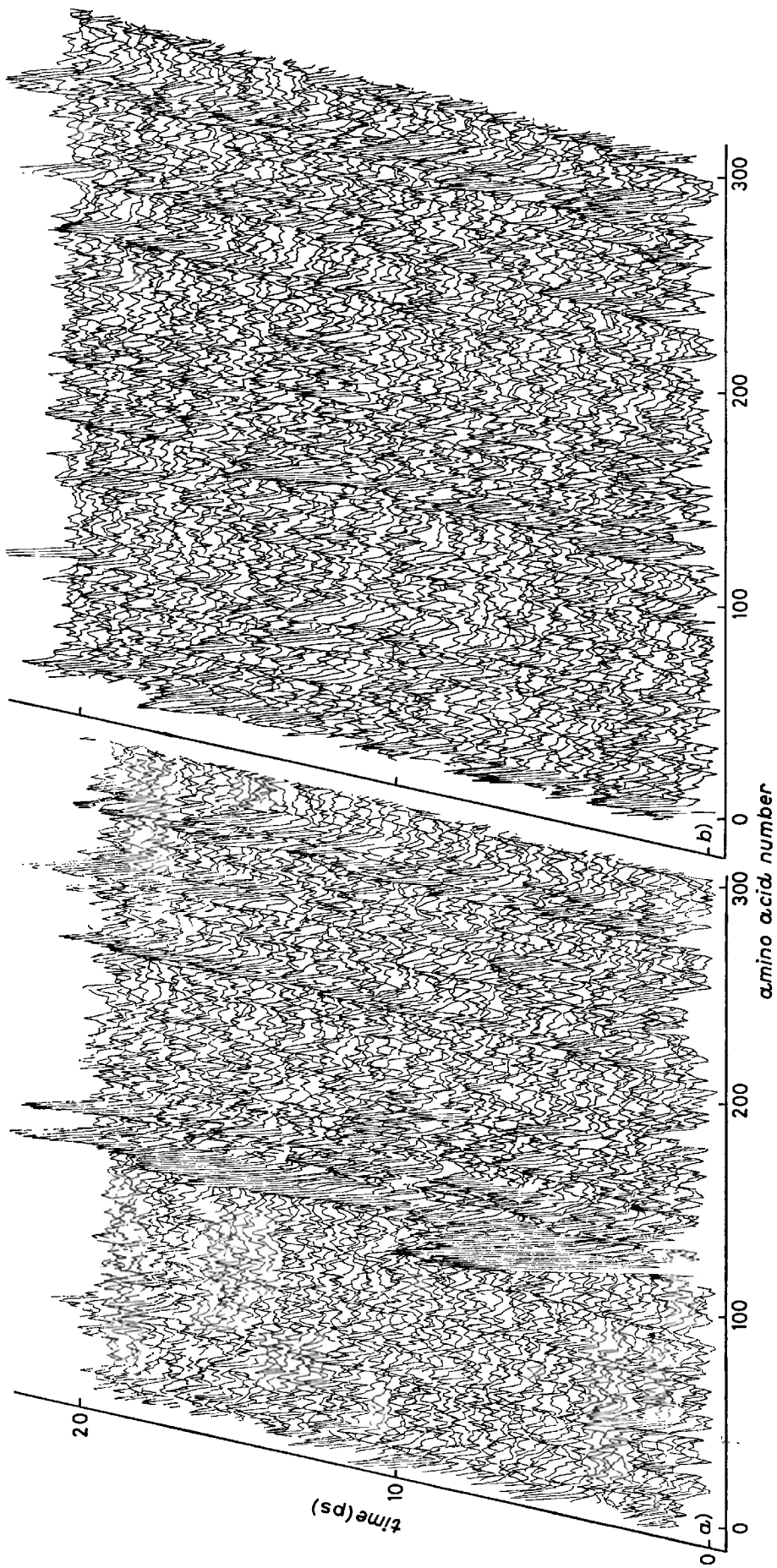

Fig. 4. – Fluctuation in structure of carboxypeptidase (M. MAKINEN): *a*) without, *b*) with inhibitor. The mobility of an α-helix around amino acid No. 120 is quenched by the inhibitor.

correspond to some 400 $kJ \cdot mol^{-1}$, but in reality they rotate over barriers one order of magnitude smaller. Internal fluctuations make such rotations possible. The free-energy barrier in the 300 K equilibrated structure is appreciably lower than the barrier in the X-ray structure [27].

The loss of mobility (and hence entropy) on binding of a substrate can also play a thermodynamic functional role [28]. An enzyme is confronted with an apparently conflicting double task: on the one hand, it must bind a substrate very specifically, and, on the other hand, it may not bind a substrate too tightly, because then either the substrate will not enter easily into a reaction or the reaction products will also be tightly bound and not be easily released. But specific binding needs specific favourable contacs involving large negative binding energies. In order to prevent an unfavourable large negative *free* energy of binding (corresponding to tight binding), a negative entropy of binding would be needed. This may be provided by a « tightening » of the protein structure on substrate binding. MD simulations are likely to be the only tool available to study such mobility-function relationships in detail.

3. – Free-energy considerations.

3·1. *The determination of binding constants* [29]. – As was mentioned in sect. **1**, an important quantity is the binding constant K of a small molecule S binding to an enzyme E:

$$E + S(\text{aq}) \rightleftharpoons ES\,, \qquad K = \frac{[ES]}{[E]\,[S]}\,. \tag{3.1}$$

(Biochemistry usually refer to the dissociation constant K^{-1}, expressed in molar units.) This K is related to the Gibbs free energy ΔG^0 of this process (using 1 molar concentration as reference state):

$$\Delta G^0 = -RT \ln K. \tag{3.2}$$

It is possible to determine ΔG^0 by simulation, breaking the process (3.1) up into two steps (fig. 5): First « grow » a substrate S slowly (or through a number of intermediate equilibrium states) onto the enzyme in a hypothetical process

$$E \to ES\,. \tag{3.3}$$

This can be done by letting the Hamiltonian H_0 of the enzyme in aqueous environment change slowly to the Hamiltonian H_1 of the enzyme-substrate complex:

$$H(\lambda) = (1-\lambda)H_0 + \lambda H_1\,. \tag{3.4}$$

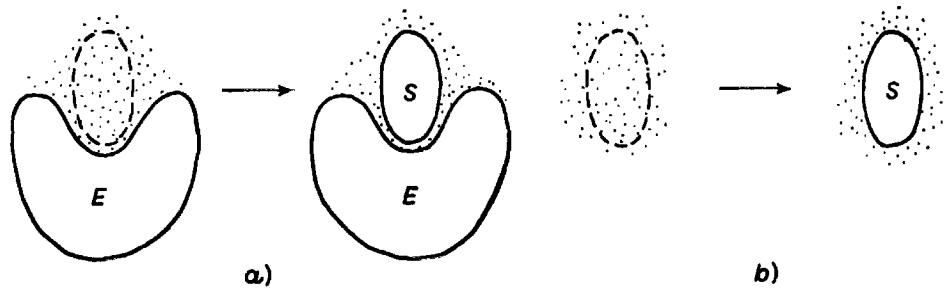

Fig. 5. – Computation of the binding constant of a substrate S to an enzyme E can be realized in two steps: *a*) slow growing of the substrate S onto the enzyme E and *b*) slow growing of the substrate S in aqueous solution. The difference in free energy of *a*)-*b*) yields the binding constant.

In this process of materializing the substrate onto the enzyme, the change in free energy F (which is practically equal to G) is found by (*)

$$F_2 - F_1 = \int_0^1 \left\langle \frac{\partial H(\lambda)}{\partial \lambda} \right\rangle_\lambda \mathrm{d}\lambda \,. \tag{3.5}$$

If we now substract ΔF for the related unphysical process of slowly materializing the substrate in water, we obtained ΔF for the binding process. The difference between ΔF and ΔG can be ignored.

Although this method has not been applied yet to protein-substrate complexes (it is computationally very demanding and requires accurate potential functions), similar processes have been applied to the free energy of solvation of small hydrophobic molecules in water. This was done by first computing the free energy of cavity formation in water by letting a repulsive cavity grow slowly [30]. It turns out [30, 31] that the integration according to eq. (3.5) can be carried out either by multistage simulation at intermediate values of λ, or by letting λ grow slowly during one long simulation, and integrating (3.5) in the process. The latter method is faster and extremely convenient to use.

Instead of calculating the complete binding constant, it may prove to be easier to compute ratios of binding constants of two similar substrates to the same protein or of one substrate to two different but similar proteins [29]. Such procedures may be the methods of choice for purposes of drug design and enzyme design.

3·2. *The determination of entropies of conformational states.* – Another free-energy problem that occurs frequently in the study of biopolymers is that many interesting polymers (specially smaller oligopeptides that act as hormones) have many conformational states. Such states are characterized by a specific

(*) See the contribution of D. FRENKEL in this volume, p. 151.

backbone structure, but rapidly fluctuating side chains, with lifetimes in the 10 ps to 1 ns range. In a limited MD simulation there are no transitions between such « conformers », although each conformer reaches a local equilibrium state. Although different conformers can be generated, their relative Boltzmann weight cannot be assessed directly from a simulation. Thus it is necessary to compute the free energy F (or, equivalently, the entropy S) of the α-th conformer to assess its statistical weight w_α:

$$w_\alpha = \exp[-\beta F_\alpha]/\sum_\alpha \exp[-\beta F_\alpha], \tag{3.6}$$

where

$$F_\alpha = E_\alpha - TS_\alpha. \tag{3.7}$$

In this special case where each conformer has a definite average structure, a direct method to compute the entropy has been proposed by KARPLUS and KUSHICK [32]. This method relies on statistical knowledge of the distribution function in multidimensional configuration space $P(\boldsymbol{q})$, that can be assembled during a simulation. The application of this method is only possible in so-called *nondiffusive* systems; if the system contains diffusing atoms, the distribution becomes unbounded.

It should be emphasized that the distribution $P(\boldsymbol{q})$ from a simulation is used rather than the $P(\boldsymbol{q})$ that can be derived from a normal-mode analysis of a conformer. The usual normal-mode analysis uses second derivatives of the potential function at a local minimum; it disregards anharmonic terms that allow the system to migrate into adjacent wells and cover a larger array of local minima within a region of the order of kT. Thus entropies based on normal-mode analysis will be too small (fig. 6).

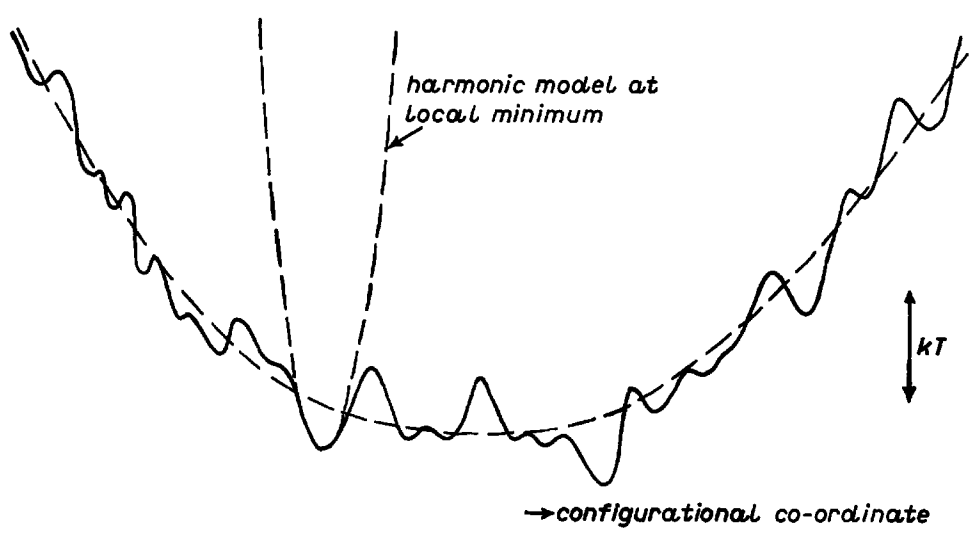

Fig. 6. – Region of configurational space, allowing a much wider distribution than does the harmonic model at the local minimum.

In the method of Karplus and Kushick [32] a Gaussian multivariate distribution of the co-ordinates is assumed. The method has been refined for non-Gaussian distributions [33]. For the Gaussian case all knowledge about the distribution is given by the configurational covariance matrix $\boldsymbol{\sigma}$:

$$\sigma_{ij} = \langle (q_i - \langle q_i \rangle)(q_j - \langle q_j \rangle) \rangle \,. \tag{3.8}$$

The entropy is given by

$$S = -k \iint \mathrm{d}\boldsymbol{p}\, \mathrm{d}\boldsymbol{q}\, P(\boldsymbol{p}, \boldsymbol{q}) \ln \{h^{3N} P(\boldsymbol{p}, \boldsymbol{q})\} \tag{3.9}$$

or, in Cartesian co-ordinates $\boldsymbol{x}$,

$$S = \frac{Nk}{2} + \frac{k}{2} \sum_{i=1}^{N} \ln \frac{2\pi m_i kT}{h^2} - k \int P(\boldsymbol{x}) \ln P(\boldsymbol{x})\, \mathrm{d}\boldsymbol{x} \,. \tag{3.10}$$

The latter integral (the configurational contribution to the entropy) is, in the case of a multivariate Gaussian distribution, given by

$$S_{\mathrm{conf}} = \frac{Nk}{2} + k \ln (2\pi)^N \det \boldsymbol{\sigma} \,, \tag{3.11}$$

as can be shown by an orthogonal transformation into a system of co-ordinates in which the correlation matrix becomes diagonal. The integral in (3.10) can then be evaluated, yielding the product of the diagonal elements. But since this product is equal to the determinant of the (now diagonal) matrix $\boldsymbol{\sigma}'$, and the determinant is invariant under an orthogonal transformation, it is sufficient to determine $\det \boldsymbol{\sigma}$ of the original covariance matrix without the need to find the eigenvalues of $\boldsymbol{\sigma}$.

We [34] have applied this method to a circular dodecapeptide

```
CH3CO—CYS—LYS—ASN—PHE—PHE
        |                |
        S               TRP
        |                |
        S               LYS
        |                |
       CYS—SER—THR—PHE—THR
```

which is the hormone *somatostatin* with two noncritical amino acids removed. Starting from an energy-minimized and subsequently MD-equilibrated structure (called B_1) a 20 ps MD run was carried out (in vacuum) at $T = 300$ K. The conformer retained a stable backbone structure during this run, but appeared to equilibrate more or less its other degress of freedom including side chain motions. Then another conformer was generated by artificial heating

to 1200 K (using a coupling to a heat bath [35]), quenching to a low temperature and equilibrating at 300 K. This structure, which had a different backbone configuration (called the D-conformer), was used for a 20 ps MD run at 300 K. From both the B_1 and the D conformer the entropy was calculated using (3.11).

The actual calculation is somewhat more involved than sketched above, because internal co-ordinates (angles and dihedral angles) were used. This is necessary because bond length constraints were used in the simulations; these have to be removed from the analysis because constraints will produce a zero determinant of the correlation matrix, while they correspond to zero eigenvalues (and so do translational degrees of freedom of the centre of mass and overall rotational degrees of freedom). But in the transformation of the integral in (3.10) to internal co-ordinates, the Jacobian of the transformation $J(\boldsymbol{q})$ appears:

$$-\int \mathrm{d}\boldsymbol{x}\, P(\boldsymbol{x}) \ln P(\boldsymbol{x}) = -\int \mathrm{d}\boldsymbol{q}\, P(\boldsymbol{q}) \ln P(\boldsymbol{q}) + \int \mathrm{d}\boldsymbol{q}\, P(\boldsymbol{q}) \ln J(\boldsymbol{q}) \,, \tag{3.12}$$

$$= \tfrac{1}{2} M + \tfrac{1}{2} \ln (2\pi)^M \det \boldsymbol{\sigma} + \int \mathrm{d}\boldsymbol{q}\, P(\boldsymbol{q}) \ln J(\boldsymbol{q}) \,, \tag{3.13}$$

where M is the number of degrees of freedom (in internal co-ordinates) and $\boldsymbol{\sigma}$ is given by (3.8).

The evaluation of $J(\boldsymbol{q})$ is quite involved [34], but it only gives a small correction. The covariance matrix was accumulated during the run and the determinant (of dimension 400) was evaluated at regular intervals.

In fig. 7 the configurational entropy is given for the two conformers, as a function of the length of the run. With entropy evaluations always great care

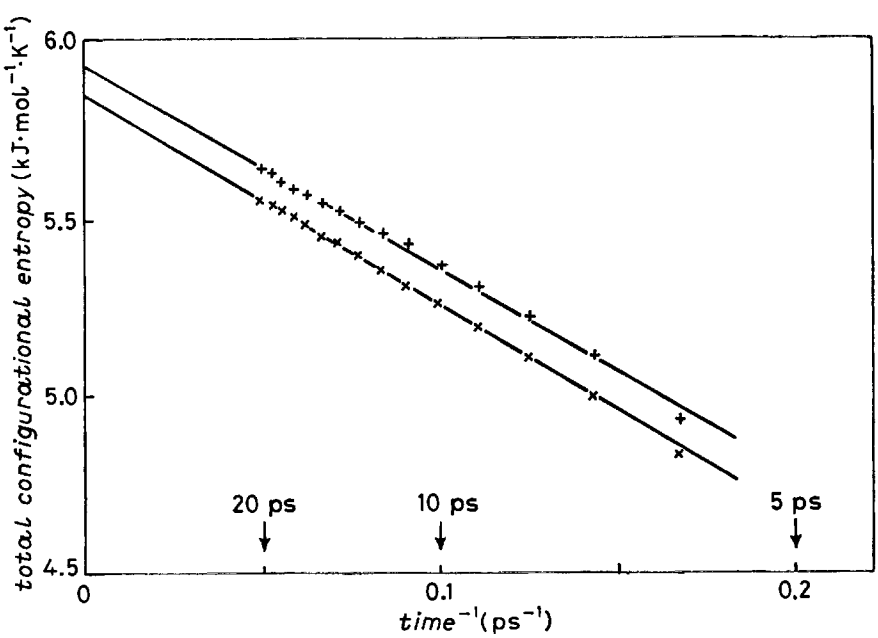

Fig. 7. – Configurational entropy of two conformers of somatostatin as a function of the inverse of the simulation time: +–+–+ D configuration, ×–×–× B configuration.

has to be taken, since statistical errors give a systematic contribution to the entropy due to the functional form of the entropy [33]. The systematic statistical error is expected to be linear in n^{-1}, where n is the number of independent samples. Despite the statistical insufficiency of a 20 ps MD run, extrapolation to infinite time is quite possible, yielding a difference in configurational entropy between the two conformers of 70 J mol^{-1} K^{-1}. With a correction for the Jacobian, the difference in absolute entropy becomes 60 J mol^{-1} K^{-1}, in (thermodynamic) favour of the D-conformer (see table I). This means that the entropy difference partly cancels the energy difference of the two conformers, such that the difference in free energy becomes insignificant. The energy difference alone would favour the B-conformer by about 10 kT!

TABLE I. – *Thermodynamic differences between two conformers of somatostatin* [34].

		B_1	D	$B_1 - D$
S_{config}	J mol^{-1} K^{-1}	5845	5911	-70 ± 20
S_{absolute}	J mol^{-1} K^{-1}	1876	1937	-60 ± 40
E_{pot}	kJ mol^{-1}	576	603	-27 ± 3
U (total)	kJ mol^{-1}	894	921	-27 ± 3
$-TS$	kJ mol^{-1}	-563	-581	$+18 \pm 12$
$F = U - TS$	kJ mol^{-1}	331	340	-9 ± 12

In conclusion it seems that entropy considerations are essential in comparing conformers. Unfortunately, the entropy calculation is not a trivial matter and requires a computational effort comparable with that of the MD run itself. It is not easily expanded to systems with many thousands degrees of freedom because of the size of the covariance matrix. If diffusive degrees of freedom are included (*e.g.*, if the simulation includes solvent), application of the method is no longer straightforward.

4. – Membrane simulations.

4·1. *Biological membranes and their models.* – A biological membrane consists of a bilayer of amphiphilic molecules (lipids) that have a hydrophilic head group and a hydrophobic tail, in which protein molecules are embedded (fig. 8). The most common amphiphilic molecule in biological membranes is lecithin, which is an ester of glycerol $CH_2OH—CHOH—CH_2OH$, having two hydrocarbon tails and one hydrophilic small tail containing a negatively charged phosphate group and a positively charged trimethylammonium group. The hydrocarbon tails are of mixed character: the length is predominantly 16 or 18 carbon atoms and many contain one more double bonds. In their physio-

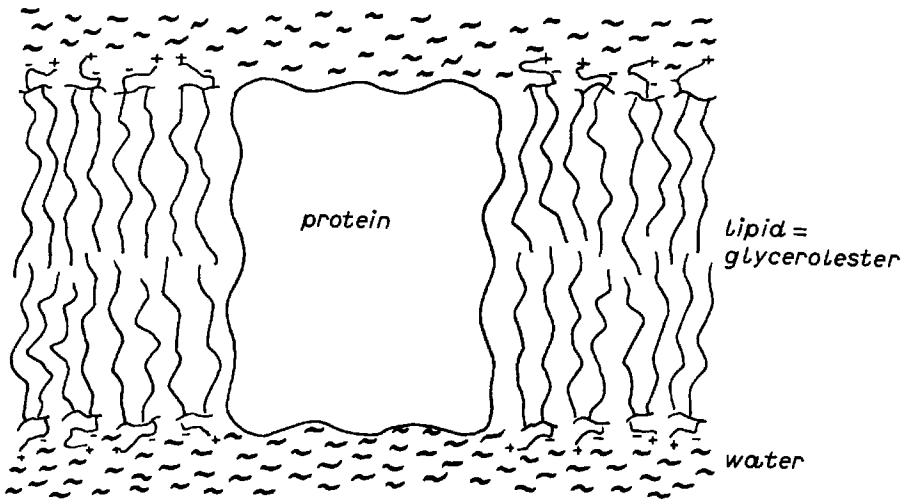

Fig. 8. – Schematic model of a biological membrane consisting of a bilayer of phospholipids (largely lecithin) in which proteins are embedded.

logical state they are in a two-dimensional fluid phase, with translational diffusion in the plane of the membrane. At lower temperatures such bilayers have a phase transition (smeared out because of the mixture of components) to a « gel » phase, in which the hydrocarbon tails cease to diffuse translationally, but still show rotational diffusion. The composition of the lipids in all biological organisms is such that they function above their phase transition at the temperature at which the organism is active. The biological membrane functions as a fluid confining matrix for many proteins with transport functions, while maintaining the separation between different compartments in the organism.

The complexity and variability of biological membranes is such that it is wise to start simulations on simpler « model » systems. Most soaps (fatty-acid solutions) have in their complicated phase diagrams a region where lamellar structures occur consisting of bilayers. Such phases are liquid crystals of the smectic type. However, the negative charges on the fatty-acid head groups (carboxylic acids) repel each other, this favours micellar structures above lamellar ones when the water content increases. Also intermediate structures, as hexagonal phases consisting of cylinders and cubic phases of ordered micelles, exist, while all these structures can also occur « inside out » like inverted micelles in lipid-rich phases. The multibilayer lamellar structures become more stable over a large range of composition if the head group charge density is diluted by mixing the fatty acid with long-chain alcohols.

A well-studied system is a mixture of decanol ($C_{10}H_{21}OH$), potassium or sodium decanoate ($K^+C_9H_{19}COO^-$) and water, which forms smectic liquid crystals consisting of multibilayers (fig. 9). The average structural order parameters of this system have been studied extensively by SEELIG [36] using deuterium magnetic resonance of specifically deuterated hydrocarbon tails. It is believed that this system forms a good model—be it crudely simplified—of

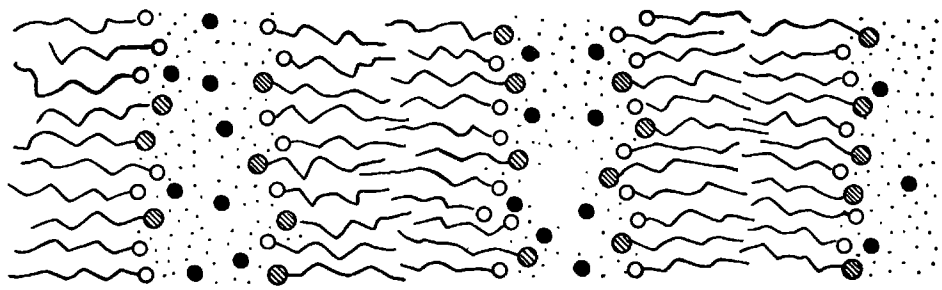

Fig. 9. – Smectic lamellar (multibilayer) structure of decanol (∿∿o), decanoate (∿∿●), Na^+ (•) and water (·).

a biological membrane. One difference still is that the decanoate/decanol/water system cannot exist as stable bilayers in infinite dilution (it then goes into a micellar structure), while lecithin bilayers do remain stable. The reason is that lecithin—although highly polar—bears no net charge.

4·2. *A simple membrane simulation* [37]. – A first study was undertaken using a small system of 2×16 decane molecules with modified head groups, but incorporating the detailed torsional potential function used by RYCKAERT and BELLEMANS in their pioneering study on liquid decane [38]. Head groups were taken as Lennard-Jones centres, with an additional harmonic restraining potential in the direction normal to the membrane plane. This is a very crude potential of mean force, meant to represent the average interactions of the head groups in the interface. The head groups are thus in a harmonic well with respect to the average of the positions of all head groups in a plane. The head group density was taken as the experimental density of 4 heads per nm^2. After equilibration (starting from a random configuration) an 80 ps run was performed at 300 K [37].

First the theoretical order parameters S_{CD}, defined as

$$S_{CD} = \langle \tfrac{1}{2}(3\cos^2\theta - 1)\rangle\,, \tag{4.1}$$

where θ is the time-varying angle between a C-D bond in a deuterated hydrocarbon and the normal to the plane, were compared with the experimental ones, for each carbon atom in the chain. The experimental results were exactly reproduced (fig. 10). The behaviour of these order parameters is quite remarkable: if the chains were perfectly ordered, the C-D bonds would be perpendicular to the bilayer normal and S_{CD} would be -0.5. The actual value around -0.3 indicates a certain degree of disorder. But one would expect the order to decrease progressively towards the ends of the chains as a result of the statistical occurrence of gauche conformations in the chains. Instead, a plateau region is observed for the first 6 or 7 carbon atoms, with progressive disorder only appearing near the end of the chain. This is a bit puzzling, and

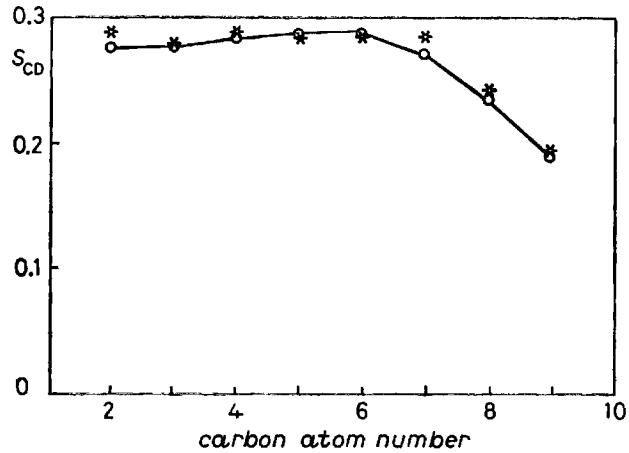

Fig. 10. – Order parameter for C-D bond in Na-decanoate-decanol-water bilayers at various carbon atoms (2 = near head, 9 = near tail): * experiment, o–o–o simulation.

the most common explanation adopted in the literature was that special defect structures called « kinks » (fig. 11) occur, consisting of a gauche$^{\pm}$-trans-gauche$^{\mp}$ sequence. These defects were supposed to run up and down the chains, reducing the order parameter homogeneously.

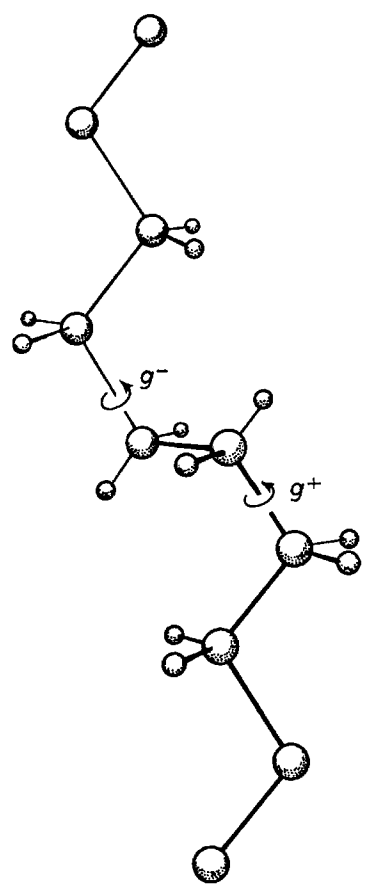

Fig. 11. – « Kink » structure characterized by g^-tg^+ (or g^+tg^-) sequence of rotational isomeric states.

Analysis of the MD run showed nothing of the kind. Kinks do occur, but not more than expected statistically among many other types of defects. They do not run up and down the chains. The reason for the observed plateau in the order parameters is an entirely different one: the chains show a collective *tilt*. When a molecule is tilted, the order parameters also decrease with respect to the ideal value of -0.5, and they do so homogeneously along the chain. The tilt turned out to be co-operative, in fact extending over the whole unit cell in this small system simulation. The collective tilt has a lifetime of the order of 10 ps and collectively tilted structures are temporally succeeded by

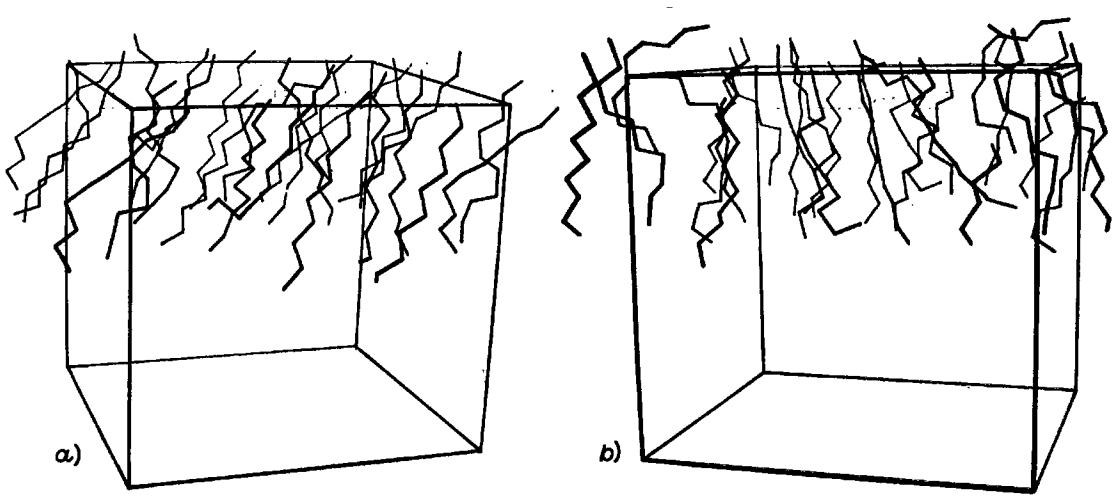

Fig. 12. – Two snapshots taken from an ordered (*a*)) and less ordered (*b*)) state of the bilayer. For clarity only the upper layer is shown (the lower layer was included in the simulation).

disordered structures (fig. 12). This behaviour fully explains the plateau region in the order parameters.

Since the tilt appeared to extend over the whole unit cell, it may be expected to be enhanced by the 2-D periodic boundary conditions used. Therefore, a new simulation was set up contemporaneously with the installation of a Cyber 170/760 at the Computer Centre of the University of Groningen with a $4\times$ large system, consisting of 2×64 decanoate molecules in a square unit cell of 4 nm$\times$4 nm. Four simulations of 80 ps each were carried out, at combinations of two temperatures (300 and 326 K) and two packing densities (0.25 and 0.276 nm^2 per head). The results have been fully described in [39]. They are in agreement with the results of the smaller simulation. The tilt now does not extend over the whole unit cell, but over about three neighbours (fig. 13). The autocorrelation function of the tilt, being a measure of its temporal persistence, is almost exponential with a decay constant of 8 ps (fig. 13*b*)).

For details of the results we refer to [39]. Two interesting features may be mentioned here: fig. 14 shows a *density dip* in the tail region of the chains,

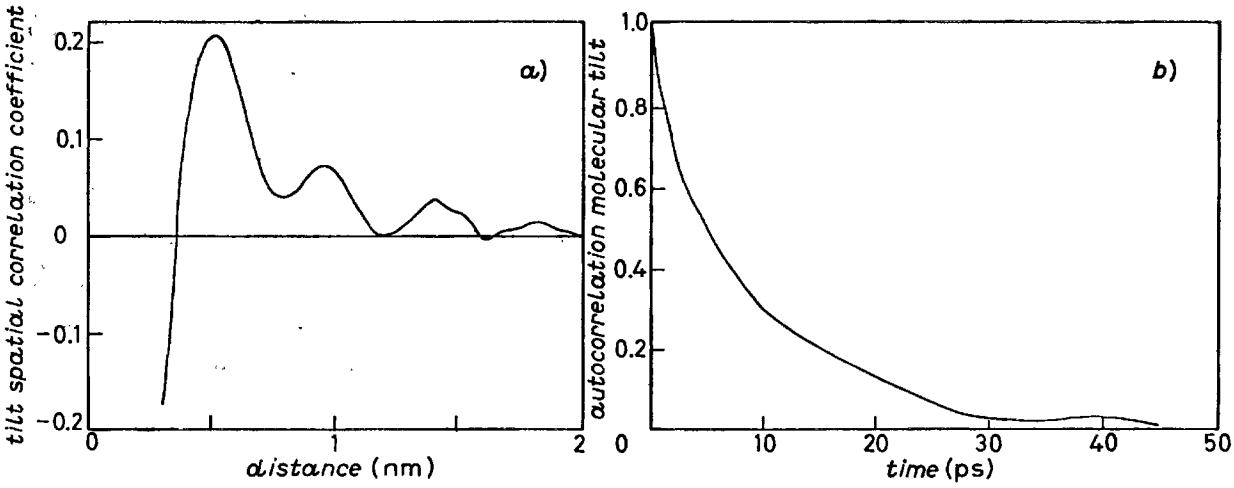

Fig. 13. – *a*) Tilt spatial correlation coefficient, *b*) molecular tilt autocorrelation.

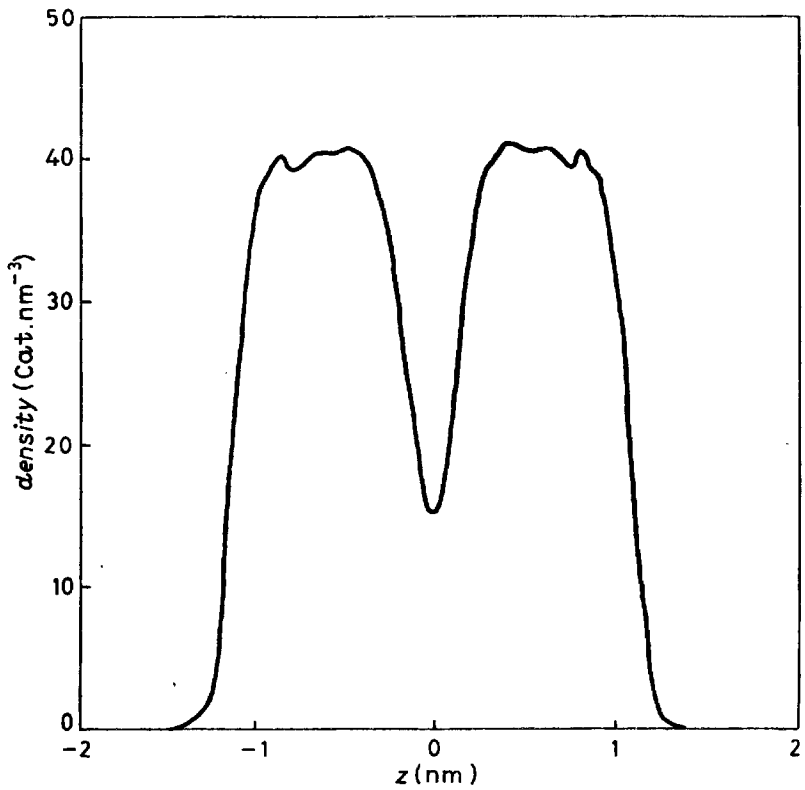

Fig. 14. – Density profile in *z*-direction (perpendicular to membrane plane).

due to the presence of the methyl groups. This density profile is very much like that observed by X-ray or electron diffraction in bilayer systems. Figure 15 shows the *lateral pressure* $P_\perp$ as a function of depth in the membrane. In anisotropic but square systems, the pressure is a cylindrically symmetric diagonal tensor, with a transverse component $P_\perp$ and a longitudinal component $P_\parallel$. The longitudinal component is independent of depth and equal to the external hydrostatic pressure (essentially zero in our case). The lateral

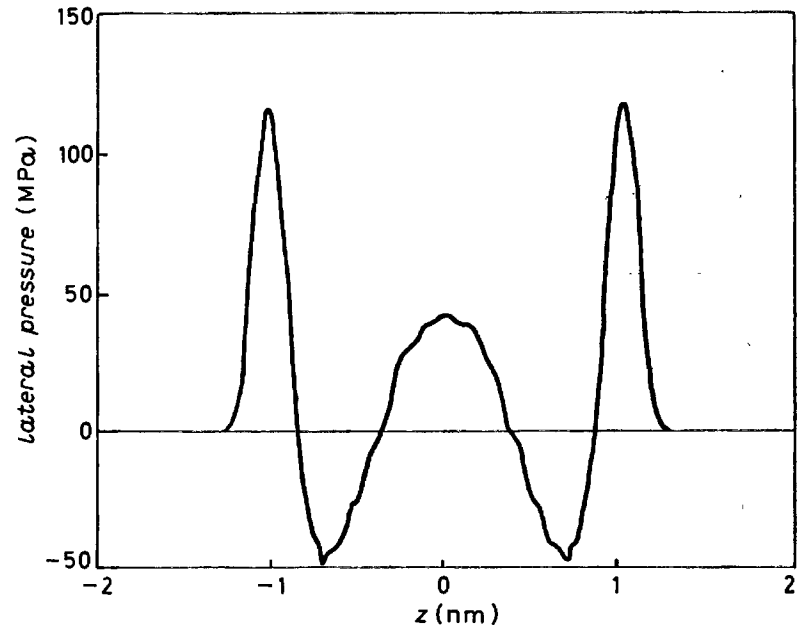

Fig. 15. – Profile of lateral component of the pressure tensor.

pressure depends on depth z and is related to the surface tension γ:

$$\gamma = \int [P_{\perp}(z) - P_{\parallel}]\, dz\,. \tag{4.2}$$

We see from fig. 15 that the lateral pressure is positive near the head groups (this is not essential but depends critically on the choice of head group interactions), negative in the chain region near the head groups and positive in the tail region. Thus, given a chance, each single layer would tend to curve with the head groups inwards and the tails outward, as far as the forces between the chains are concerned. In other words: the tails in a straight bilayer are compressed by the attractive forces between the better-ordered chain regions near the head groups.

4·3. *An all-atom membrane simulation.* – In order to refine the hydrophilic interactions, a simulation has been carried out on a decanoate/decanol/water multibilayer system including all atomic detail and long-range interactions (E. EGBERTS and H. J. C. BERENDSEN: ms in preparation). It consists of 52 Na^+ ions, 52 negatively charged decanoate, 76 decanol and 526 water molecules, totalling 8090 degrees of freedom. A constant-temperature and -pressure run was completed over 80 ps, after considerable equilibration had taken place. The long-range electrostatic interaction was modelled in three ranges: forces within a 0.7 nm cut-off were considered every step; forces between the 0.7 nm sphere and a cylinder of 1.7 nm radius were computed every time the short-range neighbour list was updated (every 10 steps) and kept between updates;

forces beyond the 1.7 nm cylinder were evaluated by numerical integration on the basis of the « measured » charge density distribution.

It turns out that the water-hydrocarbon interface develops a high degree of disorder. Ions and water penetrate in between the head groups, which themselves distribute over a range of some 0.5 to 0.8 nm. Figure 16 shows

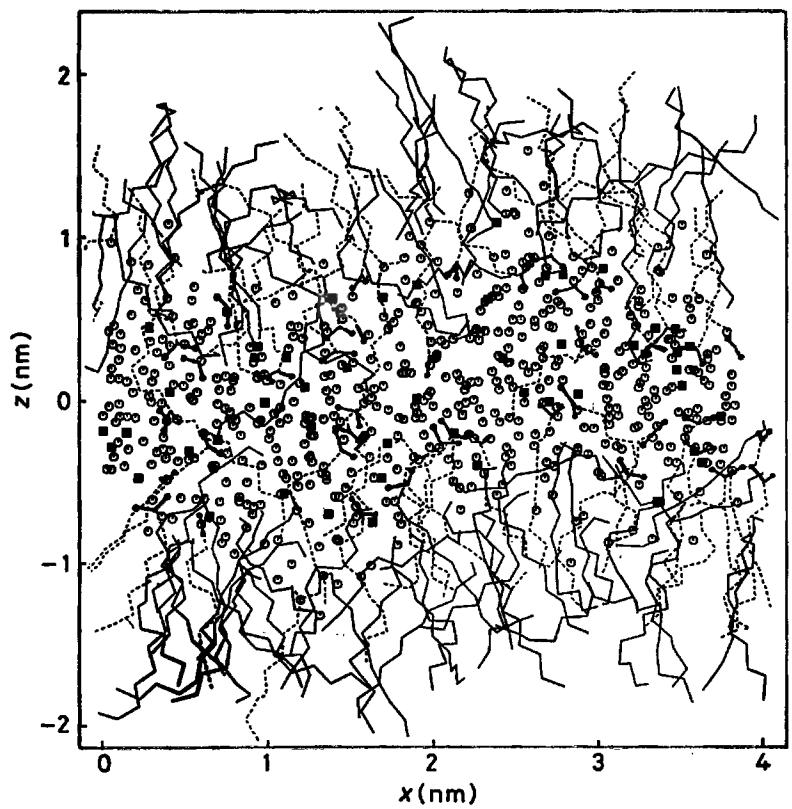

Fig. 16. – Projection in y-direction of simulation snapshot of Na-decanoate-decanol-water bilayer: ▪ Na^+, — — — decanoate, ——— decanol, ○ H_2O.

a projection of the structure. In fig. 17 the charge density of various components is shown in a cumulative fashion, plotting $\int_0^z \varrho(z')\,dz'$ (E. EGBERTS, preliminary results). The distribution of negatively charged ions (oxygens of the COO^- groups) is practically cancelled by the Na^+ ion distribution. Whatever net charge is left is again cancelled by the dipole-bound charge density ϱ', equal to the divergence of the water and alcoholic OH dipole density P:

$$\varrho' = \operatorname{div} P\,. \tag{4.3}$$

Thus the surprising observation is made that charge densities are almost completely cancelled, without giving rise to any appreciable long-range fields. Giving this a second thought, such a cancellation may not be so surprising.

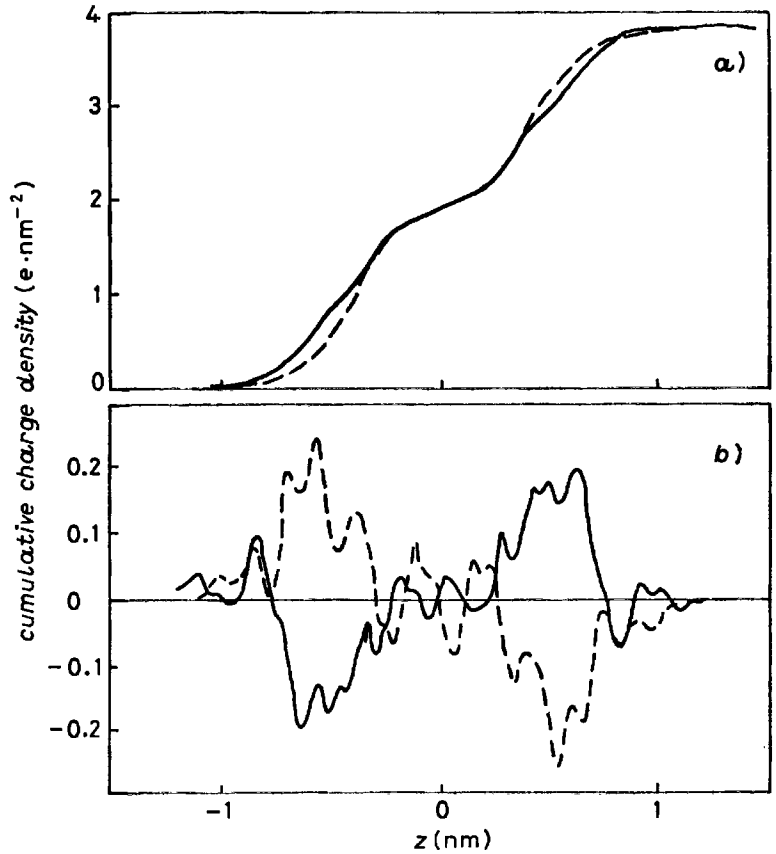

Fig. 17. – Cumulative charge distribution: *a*) decanoate negative charges (——) and Na^+ positive charges (– – –), *b*) net charge (——) and divergence of water (and OH) polarization (– – –).

It costs free energy to build up a long-range field:

$$\mathscr{E} = \frac{\varepsilon}{2} \int E^2(\boldsymbol{r})\, \mathrm{d}\boldsymbol{r} \tag{4.4}$$

and any molecular system with sufficient internal flexibility will tend to avoid such long-range fields by as much local charge cancellation as is possible. Apparently the head group flexibility in the presently studied system is such that this charge cancellation can take place to a considerable extent. This is quite in contrast to the generally accepted view of electrical double layers at membrane surfaces. It seems that MD simulations once more break through our conventional views that need constant modification.

* * *

The work described here was carried out by many collaborators to whom I am much indebted. Dr. W. F. VAN GUNSTEREN designed the GROningen MOle-

cular Simulation program package (*) that was used in all protein and some membrane simulations. Work on proteins in solution was largely his effort. Prof. M. MAKINEN (University of Chicago) simulated the enzyme carboxypeptidase. Dr. A. DINOLA (Rome) and Dr. O. EDHOLM (Stockholm) carried out simulations and computations on somatostatin. Dr. P. VAN DER PLOEG and drs. E. EGBERTS simulated membranes. Dr. J. P. M. POSTMA, Prof. J. HERMANS (Chapel Hill) and drs. H. ZWINDERMAN have contributed on devising water and protein potentials and on methods. Part of this work was supported by SON, the Foundation for Chemical Research, and by the Foundation for Biophysics, both under auspices of the Netherlands Organization for the Advancement of Pure Research (ZWO). Visitors were supported by the CNR of Italy (DINOLA), the NFR of Sweden (EDHOLM), ZWO of the Netherlands (HERMANS) and the Fogarty Foundation and EMBO (MAKINEN).

(*) GROMOS: For serious potential users the GROMOS package is available at nominal cost from Dr. W. F. VAN GUNSTEREN, Laboratory of Physical Chemistry, Nijenborgh 16, 9747 AG Groningen, The Netherlands. The package contains Fortran routines and vectorized versions of some routines for Cray as well as Cyber-205. It handles molecular dynamics and energy minimizations for any molecular system, with topologies and potential functions included for molecules of biological interest. A large number of analysis programs is included.

REFERENCES

[1] W. F. VAN GUNSTEREN and H. J. C. BERENDSEN: *Biochem. Soc. Trans.*, **10**, 301 (1982).
[2] J. A. MCCAMMON: *Rep. Prog. Phys.*, **47**, 1 (1984).
[3] W. F. VAN GUNSTEREN and H. J. C. BERENDSEN: *Molecular dynamics simulations*, in *Molecular Dynamics and Protein Structure*, Workshop at Chapel Hill, 1984, edited by J. HERMANS (Polycrystal Book Service, P.O. Box 27, Western Springs, Ill. 60558, 1985), p. 5.
[4] H. J. C. BERENDSEN: *Treatment of long-range forces in molecular dynamics*, in *Molecular Dynamics and Protein Structure*, see ref. [3].
[5] A. WARSHEL and S. T. RUSSELL: *Q. Rev. Biophys.*, **17**, 283 (1984).
[6] S. KIRKPATRICK, C. D. GELATT jr. and M. P. VECCHI: *Science*, **220**, 671 (1983).
[7] W. F. VAN GUNSTEREN, H. J. C. BERENDSEN and J. A. C. RULLMANN: *Mol. Phys.*, **44**, 69 (1984).
[8] A. BRUNGER, C. L. BROOKS III and M. KARPLUS: *Chem. Phys. Lett.*, **105**, 495 (1984).
[9] T. AKESSON and B. JÖNSSON: *Mol. Phys.*, **54**, 369 (1985).
[10] M. BERKOWITZ and J. A. MCCAMMON: *Chem. Phys. Lett.*, **90**, 215 (1982).
[11] H. J. C. BERENDSEN, W. F. VAN GUNSTEREN and J. P. M. POSTMA: in *High-Speed Computation*, edited by J. S. KOWALIK, NATO ASI Series F7 (1984), p. 425.
[12] H. J. C. BERENDSEN: in *Molecular Liquids—Dynamics and Interactions*, edited by A. J. BARNES, W. J. ORVILLE-THOMAS and J. YARWOOD, NATO ASI Series C135 (1984), p. 475.

[13] H. J. C. BERENDSEN, J. P. M. POSTMA, W. F. VAN GUNSTEREN and J. HERMANS: in *Intermolecular Forces*, edited by B. PULLMAN (Reidel Publ. Co., Dordrecht, 1981), p. 331.
[14] J. HERMANS, H. J. C. BERENDSEN, W. F. VAN GUNSTEREN and J. P. M. POSTMA: *Biopolymers*, **23**, 1513 (1984).
[15] CECAM Report on Workshop *Protein Dynamics*, edited by H. J. C. BERENDSEN (Centre Europeén de Calcul Atomique et Moléculaire, Orsay, 1976).
[16] J. A. MCCAMMON, B. R. GELIN and M. KARPLUS: *Nature (London)*, **267**, 585 (1977).
[17] M. LEVITT: *J. Mol. Biol.*, **168**, 595, 621 (1983).
[18] J. ÅQVIST, W. F. VAN GUNSTEREN, M. LEIJONMARCK and O. TAPIA: *J. Mol. Biol.*, **183**, 461 (1985).
[19] W. G. J. HOL, P. TH. VAN DUIJNEN and H. J. C. BERENDSEN: *Nature (London)*, **273**, 443 (1978).
[20] W. G. J. HOL: *Prog. Biophys. Molec. Biol.*, **45**, 149 (1985).
[21] W. F. VAN GUNSTEREN, H. J. C. BERENDSEN, J. HERMANS, W. G. J. HOL and J. P. M. POSTMA: *Proc. Natl. Acad. Sci. USA*, **80**, 4315 (1983).
[22] W. F. VAN GUNSTEREN and H. J. C. BERENDSEN: *J. Mol. Biol.*, **176**, 559 (1984).
[23] D. J. ADAMS: *Chem. Phys. Lett.*, **62**, 329 (1979).
[24] W. F. VAN GUNSTEREN, R. KAPTEIN and E. R. P. ZUIDERWEG: in *Nucleic Acid Conformation and Dynamics*, Report of NATO/CECAM Workshop, edited by W. K. OLSON (Orsay, 1983), p. 79.
[25] R. KAPTEIN, E. R. P. ZUIDERWEG, R. M. SCHEEK, R. BOELENS and W. F. VAN GUNSTEREN: *J. Mol. Biol.*, **182**, 179 (1985).
[26] K. WUTHRICH, A. DEMARCO and K. WUTHRICH: *Biophys. Struct. Mech.*, **2**, 139 (1976).
[27] J. A. MCCAMMON, C. Y. LEE and S. H. NORTHRUP: *J. Am. Chem. Soc.*, **105**, 2232 (1983).
[28] A. FERSHT: *Enzyme Structures and Mechanism* (Freeman, Reading, Mass., 1977).
[29] H. J. C. BERENDSEN, J. P. M. POSTMA and W. F. VAN GUNSTEREN: *Statistical mechanics and molecular dynamics: the calculation of free energy*, in *Molecular Dynamics and Protein Structure*, see ref. [3], p. 43.
[30] J. P. M. POSTMA, H. J. C. BERENDSEN and J. R. HAAK: *Faraday Symp. Chem. Soc.*, **17**, 55 (1982).
[31] J. P. M. POSTMA: Thesis, University of Groningen (1985).
[32] M. KARPLUS and J. N. KUSHICK: *Macromolecules*, **14**, 325 (1981).
[33] O. EDHOLM and H. J. C. BERENDSEN: *Mol. Phys.*, **51**, 1011 (1984).
[34] A. DINOLA, H. J. C. BERENDSEN and O. EDHOLM: *Macromolecules*, **17**, 2044 (1984),
[35] H. J. C. BERENDSEN, J. P. M. POSTMA, W. F. VAN GUNSTEREN, A. DINOLA and J. R. HAAK: *J. Chem. Phys.*, **81**, 3684 (1984).
[36] J. SEELIG and W. NIEDERBERGER: *J. Am. Chem. Soc.*, **96**, 2069 (1974).
[37] P. VAN DER PLOEG and H. J. C. BERENDSEN: *J. Chem. Phys.*, **76**, 3271 (1982).
[38] J.-P. RYCKAERT and A. BELLEMANS: *Faraday Disc. Chem. Soc.*, **66**, 95 (1978).
[39] P. VAN DER PLOEG and H. J. C. BERENDSEN: *Mol. Phys.*, **49**, 233 (1983).

Part VI

MATERIALS SCIENCE

Atomistic Simulations in Materials Science.

SIDNEY YIP

Department of Nuclear Engineering, Massachusetts Institute of Technology
Cambridge, MA 02139

1. – Introduction.

The use of atomistic-simulation models consisting of several hundred to several thousand interacting particles to study structural and dynamical properties of simple physical systems, such as a liquid or a solid, is by now quite well established in several areas of condensed-matter physics and theoretical chemistry. Yet it still remains to be demonstrated that such models can be usefully applied to problems in materials science where one is interested in the properties and behavior of solids with defects and the effects of extreme environmental conditions of high temperature, pressure, or external stress. The purpose of the present lectures is twofold, to show that atomistic simulations make possible a unified investigation of the many different properties of a model system, and to illustrate applications to materials science by considering selected studies of grain boundary models, thermal explosion processes and stress-induced crystal transformations.

We are concerned here specifically with the use of molecular-dynamics (MD) [1] and Monte Carlo (MC) [2] techniques to determine the behavior of an atomic system in a thermal environment. These methods have the advantage over other calculational techniques in that one can study essentially all the equilibrium and nonequilibrium properties at the atomic level without restriction to low temperatures, long times, or small amplitudes of deformation. MD and MC simulations are particularly effective in probing nonlinear processes that are difficult to analyze by analytical theories [3]; as examples of significant contributions one can point to studies of melting [4], crystal growth [5], diffusion kinetics [6] and crack propagation [7], to name just a few areas. In discussing these simulations one should keep in mind that they are intended to complement (but not replace) either theory or experiment. Their unique capability is that they can produce macroscopic behavior under precisely controlled conditions which can be varied by the investigator, and by so doing one can gain a great deal of physical insight into a complex

phenomenon where there may be several competing processes and no other way of separating one from the others.

We will begin by briefly recalling some of the basic elements of MD and MC simulation (sect. **2**) which are needed as background information. Then we proceed in sect. **3** with a fairly extensive discussion of studies of various physical properties of grain boundaries, sliding and migration, structural transition and melting, and vacancy migration and atomic diffusion. Taken together, these studies illustrate the rich variety of processes which can be modeled and how collectively they can lead to a more unified understanding of grain boundary systems. In sect. **4** we consider a quite different area of study, the thermal behavior of a fluid undergoing collision-induced exothermic reactions. Here one is interested in the conditions for criticality where the system temperature can show an instability by a sudden increase. This application also illustrates the interplay between simulation and continuum theory. In sect. **5** we discuss simulation of polymorphic transition in crystal lattices at finite temperatures which are also subjected to an external stress. Studies of this type should eventually greatly enhance our understanding of the effects of local environment and our ability to predict mechanical behavior of solids. As concluding remarks we take note of the importance of the interatomic-potential functions in planning a simulation study, and point out that incomplete knowledge of potentials is not an inherent limitation of the simulation methods themselves.

2. – Molecular-dynamics and Monte Carlo simulations.

The basic goal of MD and MC simulations is to observe the evolution of a model system through the determination of the movements of the individual particles. By virtue of the interactions among the particles the system is able to maintain mechanical as well as thermodynamic equilibrium, and, if an external perturbation were applied, the system will respond by relaxing toward a new equilibrium configuration. The essential difference between the two methods of simulation lies in the nature of system evolution. With MD the system trajectory in phase space is determined by *Hamiltonian* dynamics, whereas in MC the system evolves according to *stochastic* dynamics (the system energy is specified by the same Hamiltonian in both simulations). This distinction is immaterial so far as equilibrium properties are concerned, but different results may be obtained for dynamical properties. Compared to an energy minimization approach which we may call molecular statics [8], MD and MC have the advantage of taking thermal fluctuations into account; they are, therefore, uniquely well suited for the study of finite-temperature properties. This also means that both techniques may be used to determine the free energy

of the system, although this capability still mostly remains to be exploited [9].

The basic output of an MD simulation are the individual particle positions $\{\boldsymbol{r}_i\}$, $i = 1, \ldots, N$, of an N-particle model at various time steps during the simulation. These positions are the solutions to the Newton's equations of motion

$$m \frac{\mathrm{d}^2 \boldsymbol{r}_i}{\mathrm{d}t^2} = -\sum_{j \neq i} \frac{\partial V(\boldsymbol{r}_i - \boldsymbol{r}_j)}{\partial \boldsymbol{r}_i}, \tag{2.1}$$

where m is the particle mass and V is the two-body interatomic potential appropriate to the material of interest. The model system, therefore, evolves according to the interatomic forces which the particles exert on each other and to the prescribed initial and border conditions. (We use the term « border » instead of « boundary » to avoid confusion with « grain boundary ».) In simulating the system behavior at a particular thermodynamic state, it is not necessary to specify precisely the initial system configuration. In fact, the final results must be independent of such details, and, to ensure that this property is more or less satisfied, one should repeat the simulation using different starting configurations and average the results over several runs.

The proper border conditions to be specified depend on the system properties to be studied. For bulk properties in a homogeneous system it is usually appropriate and also convenient to impose periodic border conditions which have the effect of embedding the simulation model in an infinite system composed of periodic replicates of the finite-size model in all directions. The use of such border conditions for a simulation model containing a crystal defect may generate additional defect structure (see sect. **3**), which in turn could appreciably influence the system behavior. Other simple border conditions which one can consider are fixed borders, where stationary particles are placed beyond the borders of the simulation cell, and free borders, where the cell is treated as being embedded in vacuum.

The conventional implementation of periodic border condition results in a simulation cell with a fixed shape and size. This can be undesirable if the internal stress changes significantly during the simulation due to a temperature change or some local deformation. Recently, it was recognized that one can retain the simplicity of the periodic border condition but use a set of equations of motion which allow the cell borders to move in response to the imbalance between the internal stress and an externally prescribed stress [10]. Starting with a postulated Lagrangian, one can derive a system of equations like eq. (2.1) for the particle positions measured relative to a set of border vectors which themselves are dynamical variables and satisfy their own equations of motion. Using this approach, which we will refer to as the isostress method in contrast to the conventional isochoric method, one can study system behavior under a homogeneous external stress. As a special case simulations can be carried out at constant pressure.

In MC simulation one generally samples system configurations according to the canonical ensemble characterized by the distribution [11]

$$f(\{\boldsymbol{r}_i\}) \propto \exp\left[-\frac{1}{k_B T}\sum_{i<j} V(\boldsymbol{r}_i - \boldsymbol{r}_j)\right], \tag{2.2}$$

where T is the temperature. The extension to allow an arbitrary stress to be imposed also has been carried out recently [12, 13]. As the particle velocities are not considered, the system evolution is followed only in configuration space. Except for the velocity variables, the same simulation model, along with initial and border conditions specified for MD, can be used here. In the case where the pressure of a hard-sphere fluid has been calculated by both techniques, the results have been found to be the same [14]. While one can compare equilibrium properties given by the two simulations, various stages of transient behavior through which each model system evolves need not have any correspondence.

To be more specific, consider a property $A(\{\boldsymbol{r}_i\})$ which depends on the system configuration $\{\boldsymbol{r}_i\}$. The equilibrium value of A obtained by MD is defined as

$$\langle A\rangle_{\mathrm{MD}} = \frac{1}{K}\sum_{k=1}^{K} A(\{\boldsymbol{r}_i(t_k)\}), \tag{2.3}$$

where $\{\boldsymbol{r}_i(t_k)\}$ is the configuration at the k-th time step, and it is understood that the number of time steps K is sufficiently large that local fluctuations are averaged out. Clearly, the longer the interval of observation the more phase space the system can move through, and, therefore, the more accurate is the estimate of $\langle A\rangle_{\mathrm{MD}}$. For MC the equilibrium value is defined by

$$\langle A\rangle_{\mathrm{MC}} = \frac{1}{J}\sum_{j=1}^{J} A(\{\boldsymbol{r}_i\}_j), \tag{2.4}$$

where $\{\boldsymbol{r}_i\}_j$ denotes the j-th configuration sampled, and similarly the accuracy of $\langle A\rangle_{\mathrm{MC}}$ depends on how many configurations are taken into account. One expects that $\langle A\rangle_{\mathrm{MD}}$ and $\langle A\rangle_{\mathrm{MC}}$ should agree to within the combined uncertainty of the estimates, but there is no obvious correspondence between the « instantaneous » values $A(\{\boldsymbol{r}_i(t_k)\})$ and $A(\{\boldsymbol{r}_i\}_j)$.

3. – Structural and dynamical properties of grain boundary solids.

The development of materials for modern technological applications demands a fundamental understanding of the microstructure and kinetic processes underlying a variety of macroscopic behavior. A problem of long-standing

interest is the finite-temperature behavior of solids whose properties are controlled by processes occurring at or near grain boundaries; for example, in developing materials for fusion energy systems and for semiconductor devices carrying high currents, it is necessary to understand how temperature and stress affect the local structure and kinetics at interfaces.

In spite of the considerable interest in grain boundaries [15], our knowledge and understanding of their atomistic behavior at high temperatures are still quite limited. It is only recently that MD and MC results on bicrystal models have been reported. While simulations have not yet progressed to the point where they can be used directly in the interpretation of laboratory measurements, we will demonstrate in this section that the results are nevertheless useful in giving physical insight or providing information not available by other means.

3·1. *Bicrystal models.* – The grain boundary studies we will discuss all involve relatively simple bicrystal models. A bicrystal is formed by first joining together two identical perfect lattices which differ by a rotation of angle θ, the misorientation angle, about a chosen axis $\hat{n}_r$. Next one picks a plane, the boundary plane, as the interface between the two lattices. This plane is specified by choosing its normal to be along a unit vector $\hat{n}$. In addition to the 5 degrees of freedom in choosing $\hat{n}_r$, θ and $\hat{n}$, one can allow a rigid translation $\boldsymbol{T}$ of the two lattices relative to each other. Thus a grain boundary has in general 8 degrees of freedom. For certain values of θ there will be a number of lattice sites in either lattice where the two lattices, if they were interpenetrating, would coincide. These sites form a superlattice called the coincident site lattice, and one way to label a bicrystal is to give the value of Σ, where $1/\Sigma$ is the fraction of atoms in the two rotated lattices that are in coincidence. For cubic systems the value of Σ is determined by θ and the axis of rotation [16]. Notice, however, that by specifying Σ one does not fix the bicrystal since the grain boundary plane is not specified.

Another method of defining a bicrystal is to emphasize what is a grain boundary rather than how one constructs a grain boundary from a single crystal. In this method [17] one begins with the boundary plane with unit normal $\hat{n}_1$ in the upper half lattice and normal $\hat{n}_2$ in the lower half. A rotation by angle φ about one of the normals brings the number of degrees of freedom to 5, and adding $\boldsymbol{T}$ for rigid translation again gives a total of 8 degrees of freedom in defining a bicrystal. In this system of definition, a twist boundary would correspond to taking $\hat{n}_1 = \hat{n}_2$ with φ arbitrary, while a tilt boundary would correspond to taking $\varphi = 0$ with $\hat{n}_1 = -\hat{n}_2$ (symmetrical) or $\hat{n}_1 \neq -\hat{n}_2$ (asymmetrical). Notice that, if $\varphi = 0$ and $\hat{n}_1 = \hat{n}_2$, one has a stacking fault if $\boldsymbol{T} \neq 0$, or a single crystal if $\boldsymbol{T} = 0$.

We will be concerned with high-angle ($\theta > 15°$) symmetrical tilt boundaries in which the axis of rotation is perpendicular to the boundary plane. The construction of a $\Sigma = 7$ bicrystal in two dimension is shown in fig. 1 [18, 19].

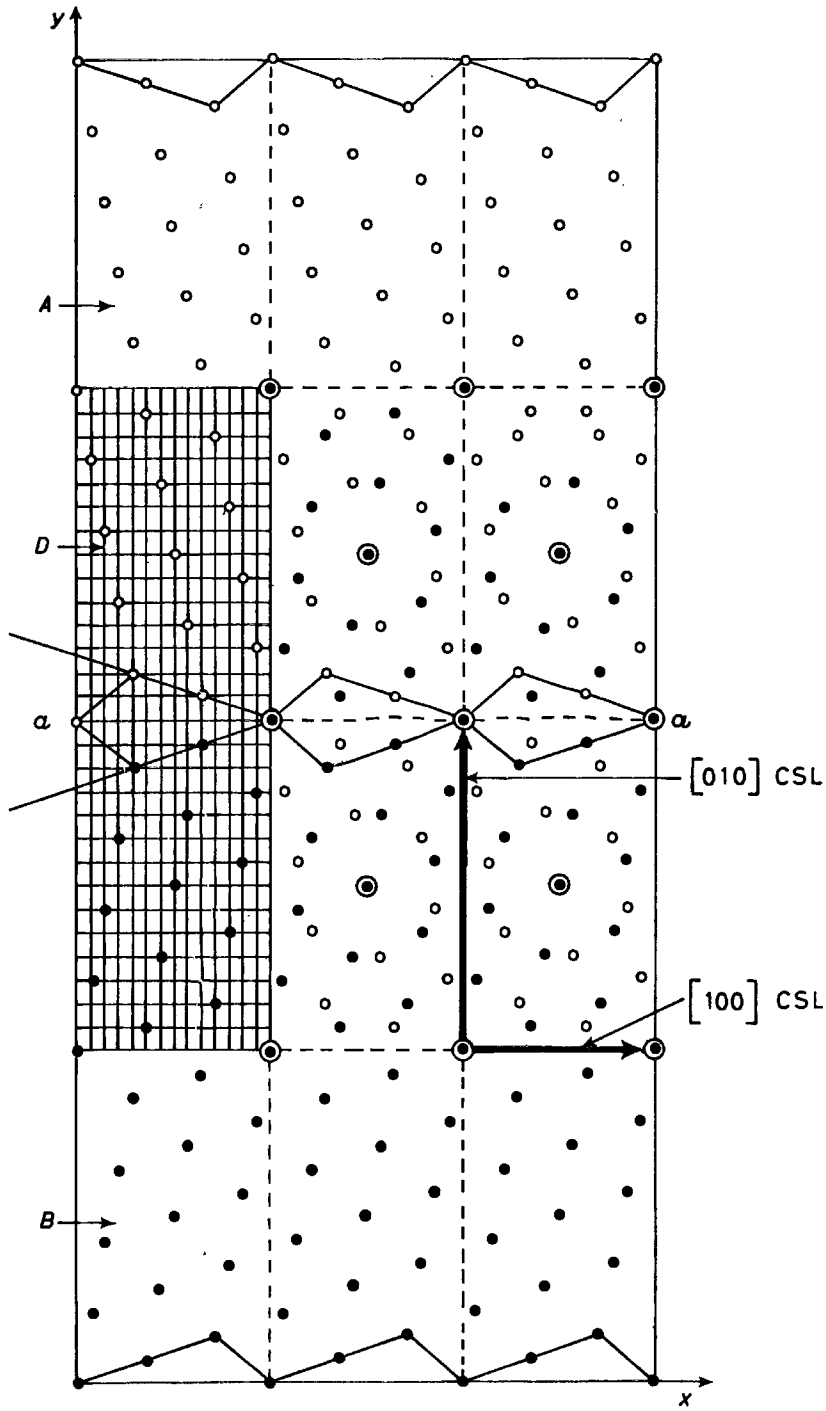

Fig. 1. – Construction of a $\Sigma = 7$ tilt grain boundary in a two-dimensional crystal [19]. Regions A and B show the upper and lower halves of a hexagonal bicrystal, the two regions differ by a rotation of $\theta = 38.21°$. Both lattices are shown in the middle region where several coincidence sites can be seen. Region D shows a portion of the simulation cell.

A simulation cell containing $N = 56$ atoms with periodic border conditions is shown in fig. 2*a*). Notice that it is natural to take the system to be periodic along the x-direction since this periodicity is an inherent property of the coincidence site lattice model. On the other hand, by assuming the system is also periodic along the y-direction we have introduced another boundary with an opposite rotational sense. It might be thought that the boundaries

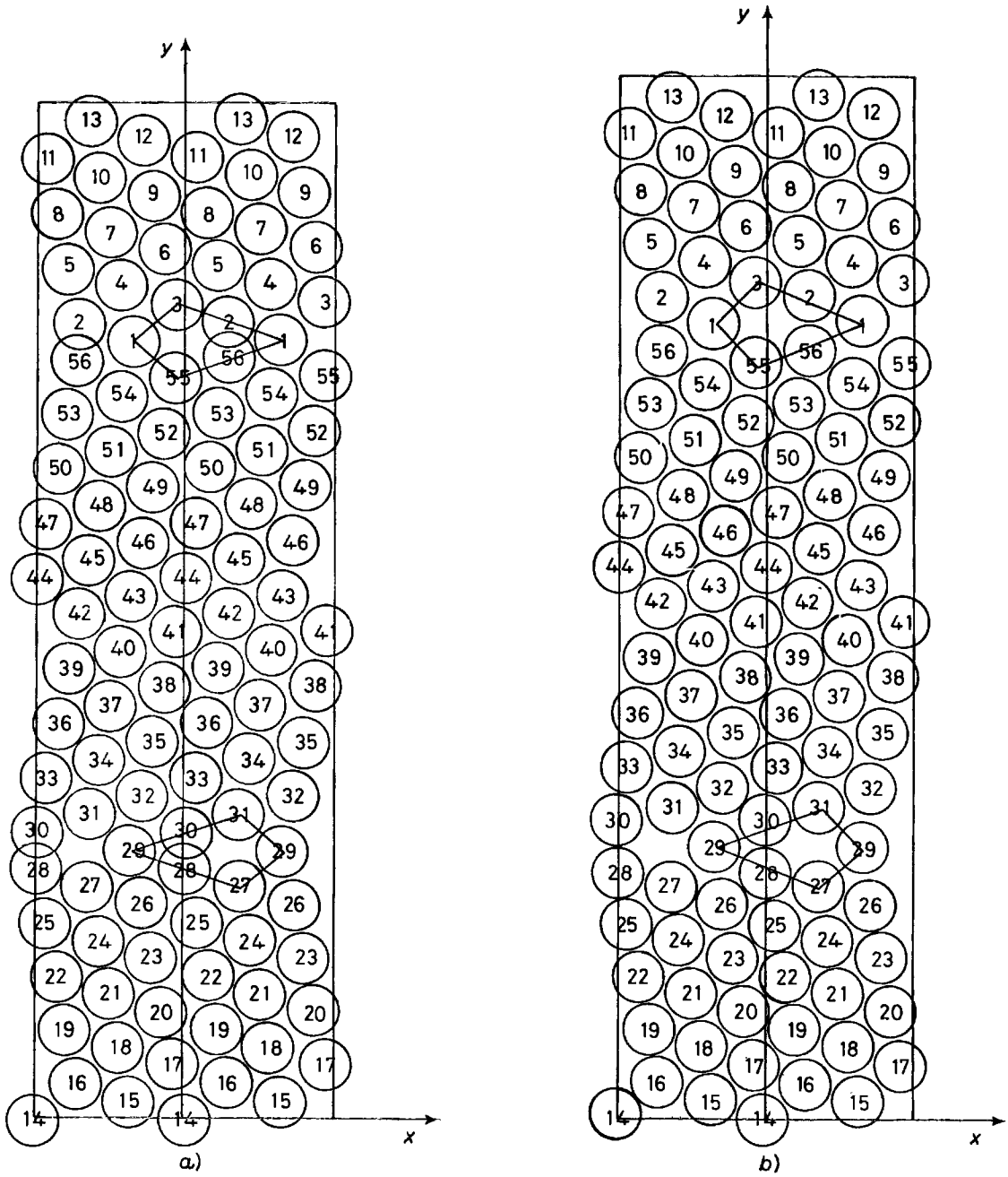

Fig. 2. – The $\Sigma = 7$ bicrystal model in two dimensions with $N = 56$ atoms and periodic border conditions, *a*) initial unrelaxed configuration showing two boundaries (kite-shaped configurations), each with a pair of atoms that are too closely packed; *b*) relaxed static configuration prior to dynamic simulation.

can move toward each other and eventually annihilate and leave behind a perfect lattice. This particular type of recrystallization indeed has been observed.

The $\Sigma = 7$ bicrystal in two dimensions has been studied using an interatomic potential of the Lennard-Jones form,

$$V(r) = 4\varepsilon\left[\left(\frac{\sigma}{r}\right)^{12} - \left(\frac{\sigma}{r}\right)^{6}\right], \tag{3.1}$$

where ε, σ are potential parameters. This interaction is appropriate to noble-gas elements and is probably adequate for illustration purposes. The relaxed configuration obtained using this potential is shown in fig. 2*b*). Relaxation is necessary because of the overcrowding in the boundary core region (kite-shaped configuration). There are different ways of allowing the relaxation to proceed [16, 18, 20]; in the present case relieving the strain resulted in an expansion of the cell dimension along the y-direction.

Bicrystal models in three dimensions have been used quite extensively in static calculations of grain boundary energies and structures in metals [21-23]. In these studies, as in all atomistic simulations of properties of real materials, the question of reliability of the potential function has become the central issue [23, 24]. Thus far, in dynamic simulations of grain boundaries a model potential such as eq. (3.1) [20, 25], Morse potentials [26, 27] and empirical potentials such as the Johnson I potential for iron [28] have been studied. One can expect that in future work the more sophisticated pseudopotentials [24, 29] will be considered as well. Static calculation on ceramic bicrystals such as MgO also have been reported recently [30]. The problem of obtaining adequate potentials for ionic systems is less severe than that for metals. This is a promising area of study for dynamic simulations.

3·2. *Coupled sliding and migration.* – The kite-shaped configurations shown in fig. 1 and 2 indicate a particular geometric arrangement of the atoms which is distinctly different from the bulk lattice arrangement away from the grain boundaries. When the system is brought into equilibrium at a finite temperature, the boundary core will deform as a result of the thermal motions of the atoms. If the deformations occur in a co-operative manner, then the boundary can undergo a displacement while maintaining its basic structure. One can readily imagine two different modes of boundary displacements, a relative translation along the boundary plane by the upper and lower lattices (sliding) and a movement of the boundary plane in a perpendicular direction (migration). If the individual atoms can move in a relatively small distance and yet collectively they cause the boundary to slide or migrate, then it is reasonable to expect that such displacements will be thermally activated and, therefore, observable in a dynamic simulation. Moreover, sliding and

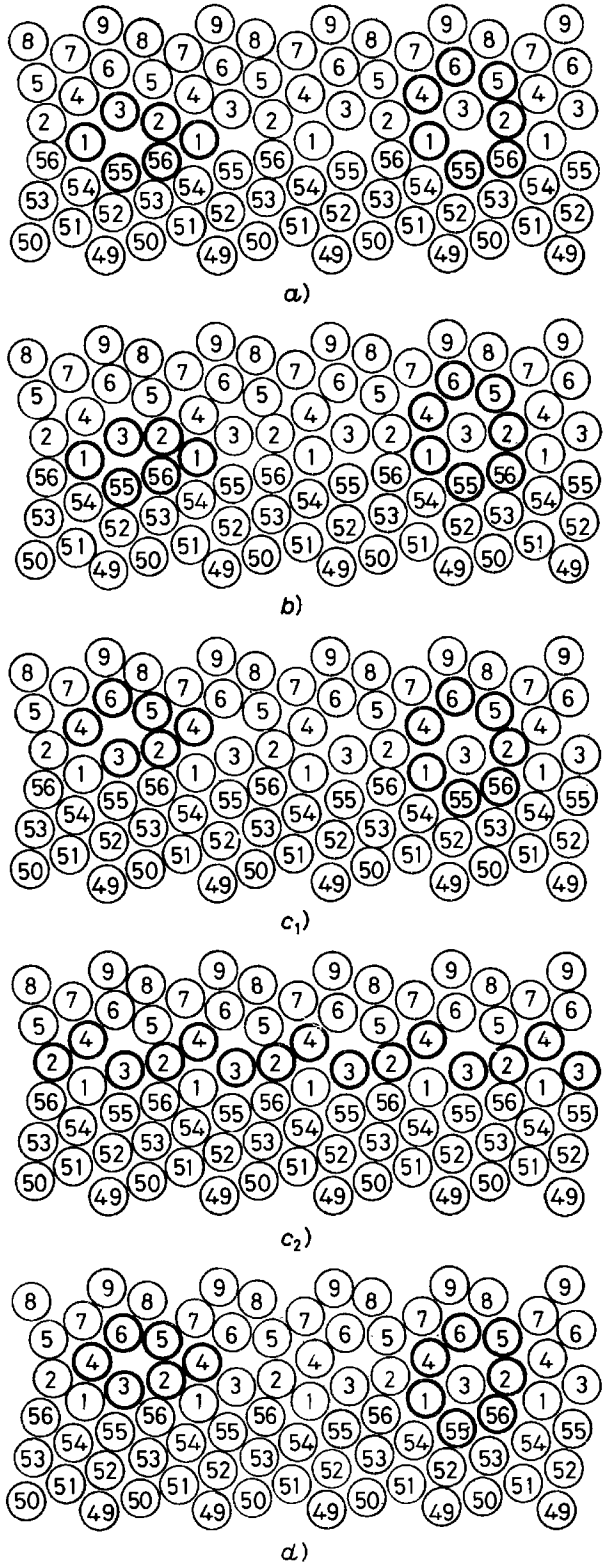

Fig. 3. – Sequence of upper grain boundary configurations (cf. fig. 2) showing the process of coupled sliding and migration [19]. Each configuration except *a*) is an average over an interval of 100 time steps starting at time step t, *a*) $t = 0$, *b*) $t = 1401$, *c*) $t = 1501$, *d*) $t = 1701$.

migration should be coupled if the boundary is to continually reconstitute itself during its movement [31].

The thermal activation of coupled boundary sliding and migration has been observed by MD simulation [18-20]. A series of time-averaged positions is shown in fig. 3 in the case of the $\Sigma = 7$ two-dimensional bicrystal model. The kite-shaped configurations outlined on the left illustrate how the boundary line, initially located at atom 1, migrates upward to the position of atom 4. The clusters outlined on the right show that during this process atom 3 changes from belonging to the upper crystal to being part of the lower crystal. Its position in fig. 3*b*) indicates a saddle point or activated-state configuration.

Coupled sliding and migration also has been observed in a three-dimensional bicrystal model, $\Sigma = 5$, with Lennard-Jones interaction and periodic borders [20]. In all cases the co-operative motions involved can be described using the DSC lattice [32] which can be constructed using every two divisions of the fine grid in region *D* of fig. 1. The relations between the basis vectors for the DSC and CSL lattices are, therefore, [100] DSC = [100] CSL/7 and [010] DSC = [010] CSL/7. The significance of the DSC lattice is that a relative translational displacement of the upper and lower parts of the bicrystal equal to a DSC lattice vector will leave the coincidence pattern unchanged while causing the boundary location to be shifted. Figure 4 shows an example of

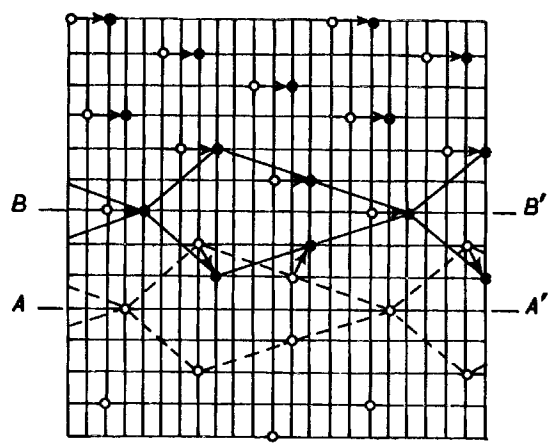

Fig. 4. – Observed atomic displacement in a $\Sigma = 7$ bicrystal model associated with coupled boundary sliding and migration from position *A* to position *B* [18]. These displacements occurred under either thermal or shear activation.

the atomic displacements that have been observed in the $\Sigma = 7$ bicrystal. One sees that relative to the lower crystal the atoms in the upper crystal undergo a lateral displacement equal to [100] DSC except for the atoms in the transition region. The displacements of the latter are more complicated because they have to change allegiance, from being part of the upper crystal to being part of the lower crystal.

There is some evidence from simulation results that as a grain boundary

starts to slide and migrate its movements have the characteristics of Brownian motion in that it may move for a while, stop, and either continue or reverse direction. Admittedly there is not a great deal of data to draw any general conclusions. We have noted previously that the use of periodic border condition (cf. fig. 2) creates another boundary which can lead to an annihilation of the two boundaries. Although annihilation is a process of some interest, its occurrence will prevent the study of unhindered boundary motion. The problem can be somewhat alleviated by using a very long simulation cell along the y-direction to keep the two boundaries as far separated as possible.

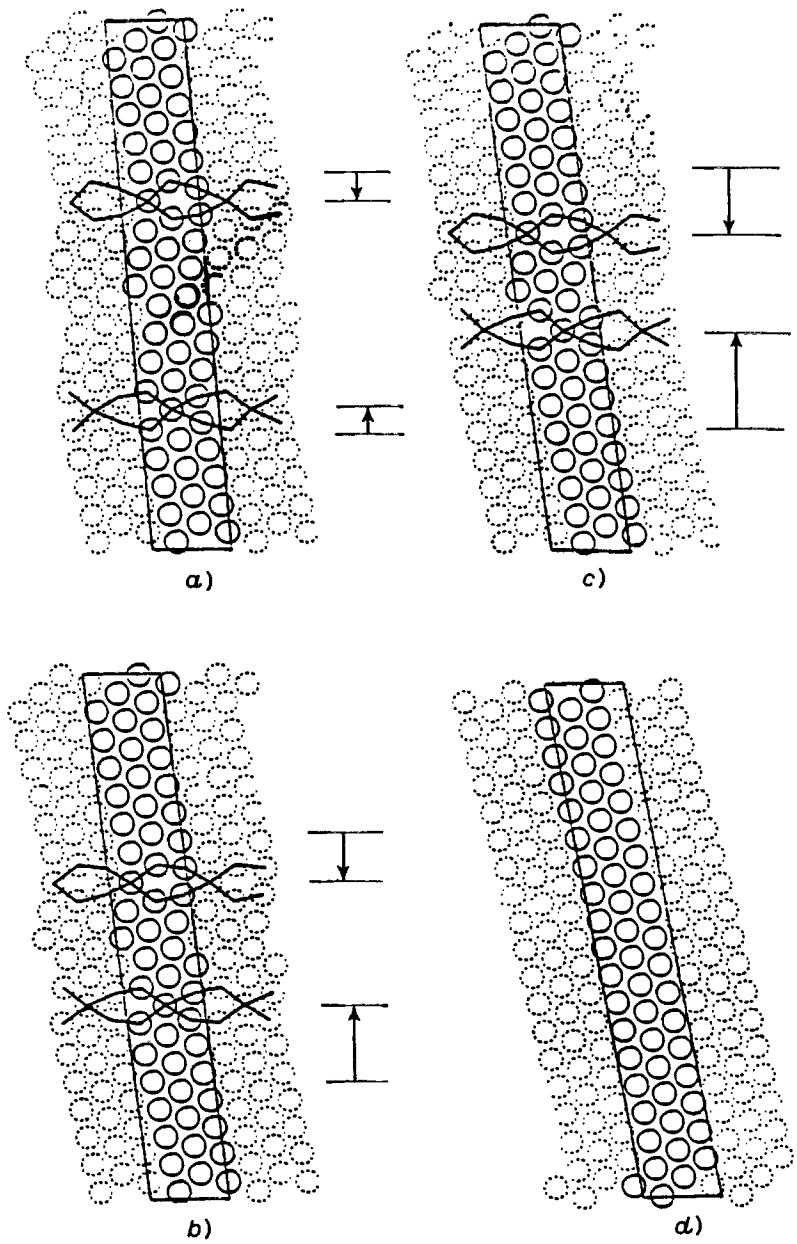

Fig. 5. – Snapshots of atomic configurations showing sliding and migration in a $\Sigma = 7$ bicrystal ($N = 56$) under shear at $\sigma_{xy}\,\sigma^2/\varepsilon = 1.6$ and $T = k_B T/\varepsilon = 0.044$ after sampling n configurations per particle, *a*) $n = 10^3$, *b*) $n = 2\cdot 10^3$, *c*) $n = 3\cdot 10^3$, *d*) $n = 4\cdot 10^3$ [33]. Arrows indicate the distances the boundaries have migrated.

In addition to thermal activation, boundary sliding and migration can be induced by external stress. This process has been observed in a MC study using the same $\Sigma = 7$ bicrystal model and the same initially relaxed configuration [33], and one finds the same mechanism of atomic displacements as shown in fig. 4. Figure 5 shows the sequence of instantaneous configurations induced by a shear stress. The final configuration is reached when the boundaries annihilate. With either thermal activation or stress activation, it was found that a threshold value exists below which boundary motion was not observed. The precise determination of this value would be difficult, however, because it will involve extrapolation to long runs and large number of particles. From results like those shown in fig. 5 one could in principle obtain an estimate of the effective interaction between the two boundaries by calculating the system potential energy at various interboundary separations. Using the available data thus far one can conclude only that the attractive interaction is rather strong and short ranged. Further work along this direction would be useful.

3·3. *Structural transition and melting.* – Melting is a basic physical process which should occur in any crystal lattice; it is most commonly described by a discontinuous change in the temperature variation of appropriate thermodynamic properties. In structural terms one anticipates that prior to melting there will be a significant increase in defect production and an onset of structural disorder; however, these are not quantitative measures that can be used to define whether or not melting has occurred. In the presence of a grain boundary, the melting point of a crystal will be lower than that of a perfect crystal because the system will be in a state of higher free energy. In addition, the boundary can undergo a melting transition while the bulk region remains a solid. If this occurs, then the system will exhibit two melting transitions.

The question of whether grain boundary melting can occur is of interest. Experimental evidence [34, 35] and theoretical calculations based on a two-dimensional lattice gas model [36] suggest that a distinct transition can occur at a temperature appreciably below bulk melting. MD simulations of a $\Sigma = 7$ two-dimensional bycrystal [37] indicate a structural transition occurring at approximately $0.7T_m$ to $0.8T_m$, where T_m is the melting temperature of the reference system [38], a perfect two-dimensional lattice in this case. This interpretation, that the transition is grain boundary melting, is based on the temperature variation of the enthalpy and on structure information in the form of instantaneous atomic configurations.

The simulation was carried out on a $\Sigma = 7$ bicrystal model ($N = 112$) which was identical to that shown in fig. 2 except the x-dimension was doubled. The isostress border condition (cf. sect. **2**) was employed with the system subjected to a hydrostatic pressure, $p^* = p\sigma^2/4\varepsilon = 0.494$ in reduced units. At the same pressure a reference system, a perfect crystal with $N = 56$, was also studied to determine the bulk melting temperature. Figure 6 shows the results

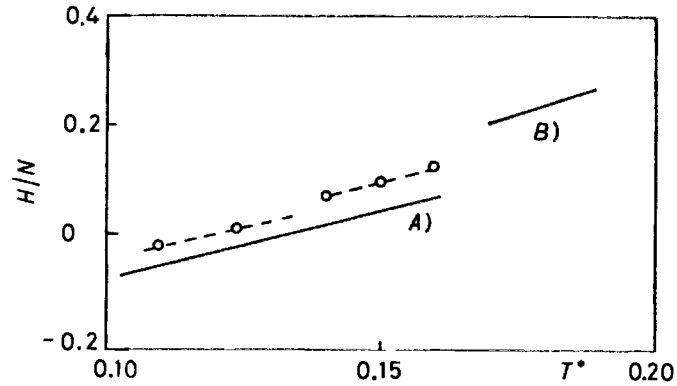

Fig. 6. – Variations of enthalpy per particle with temperature for the bicrystal [37] (circles) and a reference system [38] (single crystal, curve A), and liquid, curve B)). Dashed lines are drawn only for guiding the eye.

for the enthalpy

$$H = \tfrac{1}{2}\langle \sum_{i \neq j} V(\boldsymbol{r}_i - \boldsymbol{r}_j)\rangle + p^*\langle A\rangle , \tag{3.2}$$

where $\langle\,\rangle$ denotes a time average and A is the system area. One can see a discontinuous behavior in the bicrystal data in the vicinity of $T^* = 0.14$, while melting in the perfect crystal occurred at $T^* \sim 0.16$. The behavior in thermodynamic property can be correlated with structural behavior provided by the particle positions. Figure 7 shows the initial bicrystal structure and a snapshot of the instantaneous configuration at $T^* = 0.15$. It is evident that after sufficient time has elapsed for structural rearrangement there was considerable loss of order in the boundary regions, and this is consistent with the enthalpy behavior.

Detailed analysis of the bicrystal structure at elevated temperatures was difficult in this study because of the boundary mobility and the tendency for the system to recrystallize. For example, the regions of crystalline order and disorder in fig. 7 were not stationary in that a region of atoms remained crystalline for some time and then became disordered. While metastable behavior of this kind is not uncommon for a small system near a phase transition, it does create a problem in any attempt to characterize the structural properties of the bicrystal model.

There exist two MD investigations involving three-dimensional $\Sigma = 5$ f.c.c. bicrystals. One study where the potential used was that given by eq. (3.1) showed premelting transition in which the grain boundary region became highly defected though still remaining crystalline [25]. Another study in which a Morse potential and a pseudopotential were used to model aluminum also showed a gradual structural transition, at the onset of which the grain boundary core became significantly disordered and nonstationary [27]. At higher temperatures the disorder became more pronounced and the affected region

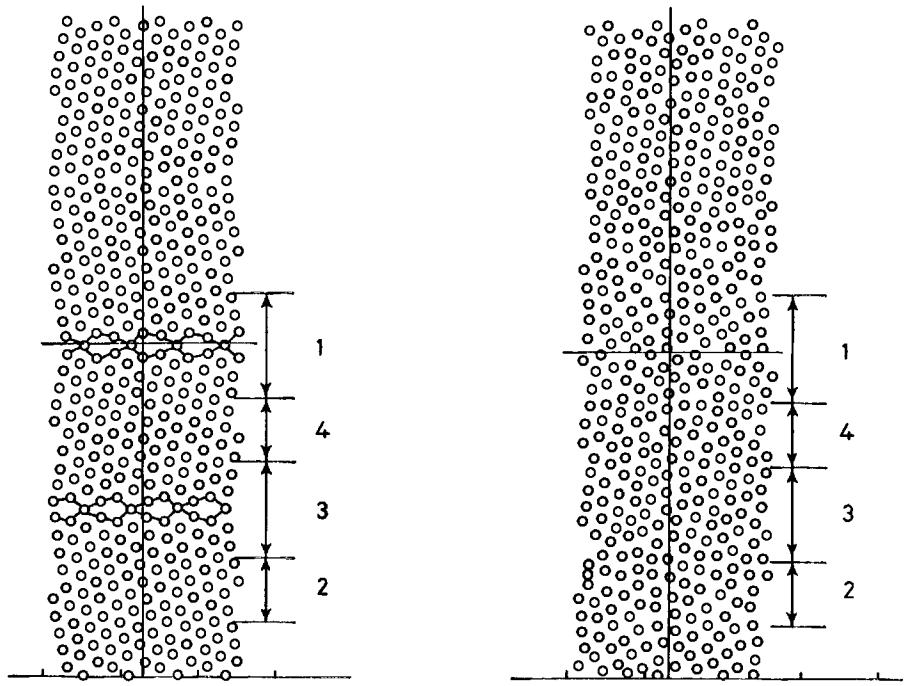

Fig. 7. – Instantaneous atomic positions in the $\Sigma = 7$ ($N = 112$) bicrystal, *a*) initial configuration with grain boundary and perfect-crystal regions approximately delineated as 1, 3 and 2, 4, respectively; *b*) configuration after 3000 time steps [37]. Note the increase of disorder in the initial grain boundary regions 1 and 3.

enlarged. At even higher temperatures, still below the bulk melting point, loss of crystalline order occurred in such a decisive manner as to signal a process of local melting. With reference to the melting point T_m of a corresponding model of a single crystal, the continuous transition began at about $0.5T_m$ with local melting setting in at about $0.75T_m$ [27].

Atomistic-simulation techniques are well suited for estimating interfacial free energies [39]. Gibbs free energies of two- and three-dimensional bicrystals ($\Sigma = 7$) with Lennard-Jones interactions have been recently obtained by means of molecular dynamics with the results indicating a grain boundary melting transition occurring at a temperature below $0.8T_m$ [40]. Although none of the conclusions based solely on simulation data can claim to be definitive, entirely independent calculations appear to give a consistent picture. It is also tempting to look for an analogy in surface melting [41]. On the other hand, there are still a number of effects to be investigated before any final conclusion can be reached [27].

3·4. *Vacancy migration and atomic diffusion.* – Atomic diffusion along grain boundaries (GB) is an important metallurgical process for matter transport. At temperatures not too close to melting it occurs much more rapidly than bulk diffusion. While it is generally believed that GB diffusion occurs by point defect exhange mechanisms, the details of the dominant mechanism and how

defect mobilities are influenced by the presence of a boundary are still not completely understood [42]. A related problem is the action of the grain boundary as a source or sink for defects which requires the understanding of how defects can be generated and once generated what are the defect-boundary interactions. Thus far experimental measurements have not been able to provide clear-cut answers to these fundamental questions. Some information has emerged from atomistic simulations, and it can be expected further progress is possible.

An extensive MD study of GB diffusion is an investigation of vacancy migration in a three-dimensional bicrystal model of a tilt boundary ($\Sigma = 5$) in b.c.c. iron [28, 43, 44]. In this work a vacancy was introduced into the boundary core and its migration trajectory was simulated over a time interval during which several hundred jumps were observed. By repeating this process at several temperatures one was able to determine an activation energy for vacancy migration. The simulation also produced other useful data. It was found that the thermal fluctuations could give rise to spontaneous Frenkel pair formation, and the motions of the resulting intersitial showed that this type of interstitial has low mobility and rather short lifetime. The availability of reasonably long vacancy trajectories made it feasible to construct a transition probability matrix, p_{ij}, for jumping from site i to site j. Although the statistics were not really adequate, there were nevertheless enough data to indicate a strong structure dependence and to suggest that p_{ij} may be the proper quantity with which to build a microscopic theory of diffusion in structured media.

The bicrystal model used in the simulation of vacancy migration was a stack of ten layers of (001) atomic planes, as shown in fig. 8*a*), with 40 atomic sites on each layer, as shown in fig. 8*b*). Periodic border conditions were applied along the y and z directions, but along the x-direction a fixed border condition was implemented to avoid creating another boundary. In fig. 8*b*) additional atoms located beyond the x borders are shown; these provided interactions with the atoms in the simulation model, but they were held rigid during the simulation. For the interatomic-potential function an empirical potential fitted to the elastic constant data of b.c.c. Fe(α) was used [45].

The bicrystal model thus constructed was allowed to relax after a vacancy was introduced into one of the sites in the boundary core. These sites are labeled as A, B, C, D in fig. 9. The need to distinguish one boundary site from another was already suggested by the vacancy formation energies which have been calculated by molecular statics [43] (see table I). One could, therefore, anticipate that the migration energy also will be site dependent.

After the vacancy was inserted (at site B) and the bicrystal allowed to equilibrate at a particular temperature, one observed from time to time the vacancy jumping into a neighboring site. Since this process depended on thermal activation, the frequency of jumps was temperature dependent. Also, the

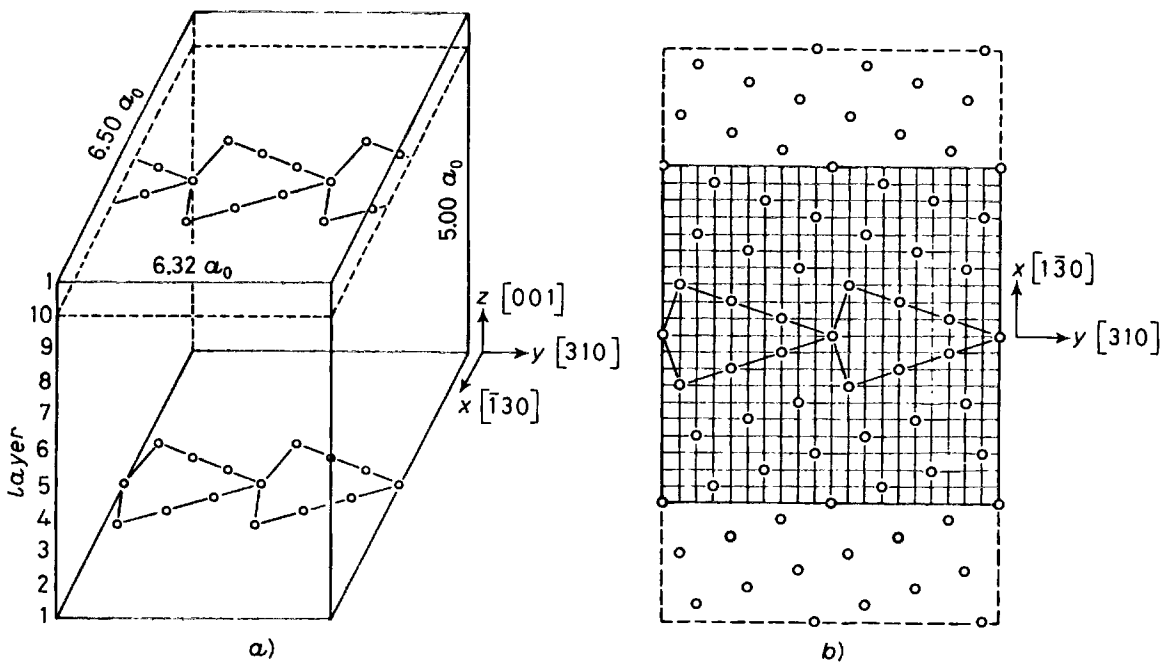

Fig. 8. – The bicrystal model of $\Sigma = 5$ tilt boundary ($N = 400$) for MD simulation of vacancy migration [28, 44], *a*) view showing the simulation cell, *b*) view of one of the (001) planes with 40 atoms and of the fixed atoms in the border regions enclosed by dashed lines.

TABLE I. – *Vacancy formation energies E_f and distribution of vacancy jumps observed at temperature T* [43, 44].

Site	E_f (eV)	$T = 1300$ K	$T = 1400$ K	$T = 1500$ K
A	1.33	3	5	9
B	0.94	126	153	197
C	1.26	20	34	49
D	1.17	32	46	62
bulk	1.35 (*)	14	26	36
total		195	264	353

(*) This value refers to the formation energy in a perfect lattice.

likelihood of the vacancy choosing one site over the other would be influenced by fluctuations in the local structure which in turn would vary with temperature. In the present study vacancy migration data were collected in long simulation runs at three temperatures, 1300, 1400 and 1500 K, where the melting point of iron is ~ 1800 K. Figure 9 shows a portion of the vacancy trajectory observed at $T = 1500$ K. From this kind of data one could determine the relative frequency of the vacancy jumping into a particular site. This distribution is shown in table I, along with the number of jumps into sites other

than the boundary core and the total number of vacancy jumps observed at each temperature. Although one cannot draw definitive conclusions from such small samples, it is satisfying to see that the qualitative features of the data are quite reasonable; for example, the jumps away from the boundary core

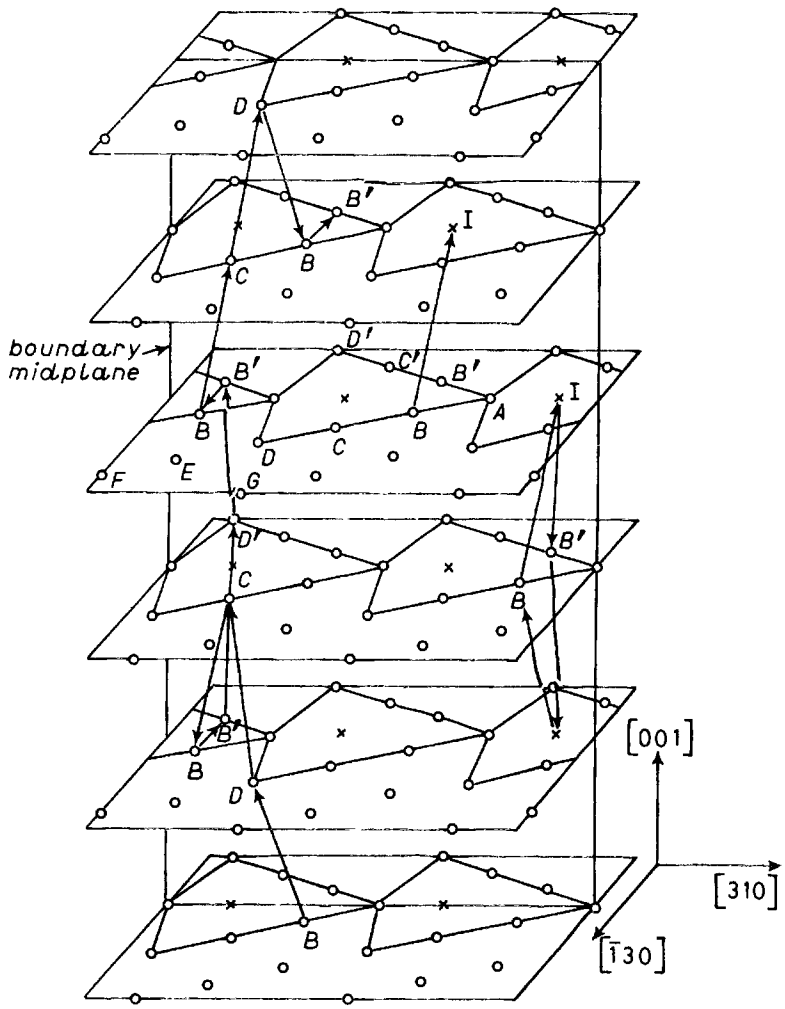

Fig. 9. – A portion of the vacancy migration trajectory observed during MD simulation at $T = 1500$ K [44]. Length scale along [001] has been magnified by a factor of 5. Sites in the boundary core are labelled A, B, C, D with the prime denoting equivalent site. I denotes the interstial site. Two such sites were involved in the exchange of atoms at sites B and B' (right sequence).

increased with temperature as they must, since the distinction between boundary and bulk should vanish as the system approaches melting.

One can extract an activation energy for vacancy migration from the data given in table I. Fitting the jump frequencies Γ to an Arrhenius behavior

$$\Gamma = \Gamma_0 \exp[-E_M/k_B T] \tag{3.3}$$

yields $E_M = 0.51$ eV and $\Gamma_0 = 4.8 \cdot 10^{13}$ s^{-1}. The activation energy value is reasonable since in the bulk E_M is ~ 1.0 eV. If one writes $\Gamma_0 = z\nu$, where $z = 8$ is the effective co-ordinate number, then the attempt frequency ν is $\sim 6 \cdot 10^{12}$, which is comparable to the vibrational frequency of $7.1 \cdot 10^{12}$ deduced from the Debye temperature of 470 K for b.c.c. iron.

To understand atomic diffusion it is necessary to look into the details of atom migration. A basic starting point in any description of diffusion is the time-dependent atomic mean square displacement

$$\langle \Delta^2 r(t) \rangle = \frac{1}{N} \left\langle \sum_{i=1}^{N} [\boldsymbol{r}_i(t) - \boldsymbol{r}_i(0)]^2 \right\rangle . \tag{3.4}$$

In a system where diffusion is taking place $\langle \Delta^2 r(t) \rangle$ will vary linearly with t at sufficiently long times and the self-diffusion coefficient is then given by the slope,

$$D = \frac{1}{6} \lim_{t \to \infty} [\langle \Delta^2 r(t) \rangle / t] . \tag{3.5}$$

This conventional interpretation is appropriate for homogeneous systems where all the atoms are equivalent, and it is implied that $\langle \Delta^2 r(t) \rangle$ will be independent of N, the number of atoms in the system, for sufficiently large N. For the bicrystal model where atoms located in the boundary core clearly behave differently from those in the bulk, the use of eq. (3.4) gives a result that will depend on the ratio of number of boundary core atoms to the number of bulk atoms. Figure 10 shows that during the simulation interval the bulk atoms make essentially no contribution to $\langle \Delta^2 r(t) \rangle$. This being the case, the diffusion coefficient extracted from such data will depend on how many bulk atoms are included in the computation of $\langle \Delta^2 r(t) \rangle$. One may argue that all the bulk atoms should be excluded in determining $\langle \Delta^2 r(t) \rangle$ for the bicrystal. This may be an acceptable working definition, but it does not take into account the situation at higher temperatures where neighboring sites to the boundary core become active in receiving vacancy jumps (cf. $T = 1500$ K in table I). Thus the definition of boundary core as a fixed region independent of temperature needs to be modified.

The MD study of vacancy migration has revealed a limitation of this simulation technique to directly observe atom jump trajectories. The difficulty is that, while the vacancy may jump several hundred times, these jumps involve many different atoms, such that the probability of having the same atom jumping more than once, aside from a reverse jump following shortly after a forward jump, is quite small. This means that despite the efforts of long simulation runs (by present standards) one still is not able to accumulate enough data on jumps of individual atoms to describe diffusion in terms of

the long-time behavior of an appropriate mean square displacement. The difference between vacancy migration and atom migration in solid-state diffusion has long been recognized [46]. Given the transition probability matrix for vacancy jump one can attempt to calculate the atom jump probability analytically. Alternatively one can use MC to generate many long vacancy migration trajectories from which an atom jump trajectory can be constructed [47]. This latter approach is currently being implemented in the

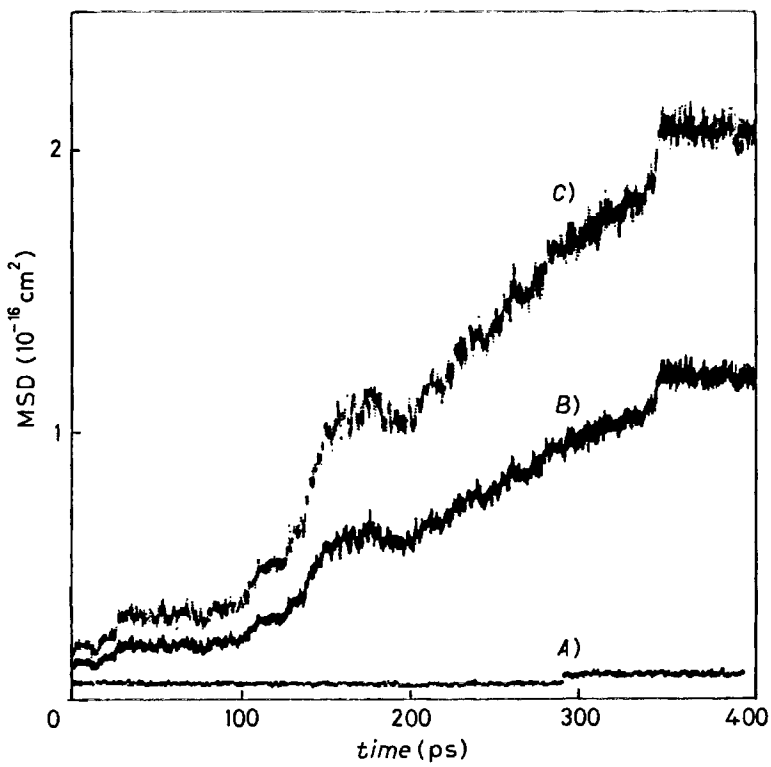

Fig. 10. – Mean square displacement of atoms in the bulk region (curve A)) and in the entire simulation cell (curve B)) at $T = 1300$ K [44]. Curve C) is the result for atoms in the grain boundary core (sites A, B, C, D in fig. 9).

case of grain boundary diffusion [48]. The advantage of MC is that each configuration sampled can be specified to be a configuration where a new jump has taken place, thus increasing enormously the efficiency of generating jump trajectory data. Of course, one gives up in the process the ability to treat fluctuations and correlations in p_{ij} from one jump to the next. At present it is not known whether this is a serious neglect.

It is possible that short-time data such as those shown in fig. 10 already contain the information about long-time diffusion. Recently it has been suggested that by examining the jump motions of only those atoms surrounding a vacancy one can obtain information about diffusion from simulation over a relatively short time that is normally obtained from simulation over much

longer times [49]. This intriguing idea needs to be validated in a test case where one can analyze diffusion in both ways.

4. – Thermal ignition in self-heating fluids.

The fundamental problem in thermal explosion phenomena is the critical behavior of a body of material which is capable of self-heating while being surrounded by a thermal reservoir held at a constant temperature [50-52]. As the system heats up, an instability will result if the heat generated within the body exceeds that removed by the reservoir, in which case the body temperature will show a sharp increase in its time evolution. The conditions relating the system size and material characteristics under which this behavior can occur are clearly of paramount interest, along with the induction period (time from initial heating to the onset of ignition) and the final temperature the system can reach.

In the continuum theory description thermal ignition is modeled by the time-dependent heat conduction equation with an Arrhenius reaction term. Criticality of the system is expressed by a dimensionless parameter δ, the Frank-Kamenetskii parameter, which is a measure of the relative importance of heat generation to heat removal by conduction. Much of the existing analysis has assumed constant reactant concentration, and one finds that not only is there a critical value of δ, but also the ratio of activation energy for reaction to the reservoir temperature must exceed a certain minimum value. Because the reaction term introduces exponential nonlinearities, only limited analysis of the time-dependent equation has been made [53]. Correspondingly, results for the induction period are quite incomplete [54].

With a few exceptions [55, 56] problems involving chemical reactions have not been investigated by atomistic simulations. In this section we will describe a molecular-dynamics study of thermal ignition in a slab of two-dimensional hard-sphere fluids bounded by heat-conducting walls [57]. The feasibility of simulating thermal explosion at the atomistic level will be demonstrated by direct observation of ignition behavior. The critical values of δ derived from the simulation are found to approach the continuum theory prediction as the system size increases. Because microscopic fluctuations are not averaged out in the molecular-dynamics output, it would appear that one can generate potentially valuable information on nonlinear fluctuations and instabilities in a chemical system.

4·1. *Continuum theory.* – A complete description of thermal explosion involves the consideration of both the system temperature and the reactant concentration. If one is concerned only with ignition, then it is reasonable to neglect reactant consumption. Moreover, for the analysis of critical conditions

it is sufficient to consider only the steady-state solution to the temperature equation. When cast in a dimensionless form, this equation reads

$$\frac{d^2\theta}{dx^2} = -\delta \exp\left[\frac{\theta}{1+\varepsilon\theta}\right], \tag{4.1}$$

where

$$\begin{cases} \theta = \dfrac{E}{RT_0^2}(T - T_0)\,, \\ x = r/r_0\,, \\ \delta = \dfrac{ZQEr_0^2}{kRT_0^2}\exp[-E/RT_0]\,, \\ \varepsilon = RT_0/E\,. \end{cases} \tag{4.2}$$

In these expressions we have defined activation energy E, wall temperature T_0, heat of reaction Q, collision frequency Z, slab half-thickness r_0, thermal conductivity k and gas constant R. Typical boundary conditions are $\theta(x=1)=0$ and $(d\theta/dx)_{x=0}=0$.

Equation (4.1) is simply a statement of balance between heat conduction and heat generation. The significance of the Frank-Kamenetskii parameter δ is that it is a measure of the relative importance of heat removal by conduction to heat production. We can expect that solutions will exist only for certain values of δ, and hence the condition for criticality. Notice that δ is not the only parameter in the problem, the ratio of wall temperature to activation energy, ε, also appears. Criticality, therefore, will depend on both ε and δ.

Although eq. (4.1) has no known analytic solutions, several approximations exist which enable one to examine essentially all the characteristic features of the problem [58-60]. In addition, numerical methods are available for obtaining very accurate results [61]. The basic approximation is to simplify the temperature dependence introduced by the Arrhenius factor. Setting the right-hand side of eq. (4.1) equal to $\delta f(\theta)$, one can write

$$f(\theta) = \exp\left[\frac{\theta}{1+\varepsilon\theta}\right] \simeq \exp[\theta]\,. \tag{4.3}$$

This approximation, valid when activation energy is high compared to ambient temperature, renders eq. (4.1) analytically tractable as originally shown by FRANK-KEMENETSKII [50-52]. The solution can be expressed as

$$\theta(x) = \theta_M - 2\ln(\cosh \alpha x)\,, \tag{4.4}$$

where $\alpha = (\delta \exp[\theta_M]/2)^{\frac{1}{2}}$, and $\theta_M = \theta(x=0)$ is the maximum temperature. The expression for θ_M is

$$\theta_M = \ln(2\sigma^2/\delta)\,, \tag{4.5}$$

where $\cosh \sigma = \sigma(2/\delta)^{\frac{1}{2}}$. From this one sees that for a given δ there will be either two solutions for θ_M or no solutions.

The variation of θ_M is illustrated by the dashed curve in fig. 11. In the region of double-valued solutions the system can exist in a low-temperature or a high-temperature steady state. As δ increases toward the critical value, the two solutions move toward each other and eventually merge at $\delta_c(\varepsilon = 0)$, a value which can be determined by differentiating eq. (4.1). (One finds $\delta_c = 0.878$ at which $\theta_M = 1.19$.) For $\delta > \delta_c$, the system will not have a steady-state solution because it is then in a supercritical state.

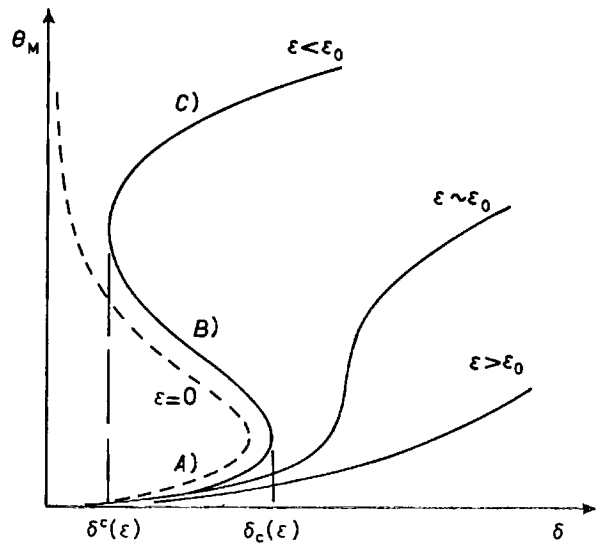

Fig. 11. – Dependence of θ_M on δ at various ε (schematic), region of multiple steady-state solutions is defined by $\delta^c(\varepsilon) < \delta < \delta_c(\varepsilon)$ with $\varepsilon < \varepsilon_0$. δ_c and δ^c are the critical values for ignition and extinction, respectively. For $\varepsilon < \varepsilon_0$, the solution does not show critical behavior in the sense of a jump condition, large change in θ_M for a small variation in δ.

The Frank-Kamenetskii approximation reduces the analysis to a one-parameter description; it is useful for showing that the competition between heat production and heat removal indeed leads to the existence of criticality. However, this approximation ignores another important aspect of chemical kinetics, that of finite activation energy.

The effect of nonzero ε in $f(\theta)$ can be analyzed using a number of different approximations [58-60]. By writing

$$f(\theta) \simeq \exp\left[\frac{\theta}{1+\varepsilon\theta_M}\right] \tag{4.6}$$

one can introduce a change of variables, $\theta' = \theta(1+\varepsilon\theta_M)$ and $\delta' = \delta(1+\varepsilon\theta_M)$, and again make use of the Frank-Kamenetskii solution, eqs. (4.4) and (4.5). Equation (4.6) is one of several approximations suggested which are all es-

sentially based on the idea of expanding the temperature about the maximum value.

The finite-ε analyses give a θ_M behavior qualitatively different from the Frank-Kamenetskii description. As shown in fig. 11, the system now has either a triple-valued or a single-valued solution depending on ε and δ. There exists a special value of ε, which we denote as ε_0, beyond which only single-valued solutions exist. (This value, which varies with geometry, has been estimated to be $\varepsilon_0 = 0.245$ in the case of a slab.) For $\varepsilon < \varepsilon_0$, one has triple-valued solutions provided $\delta^c(\varepsilon) < \delta < \delta_c(\varepsilon)$. Notice the appearance of two points of tangency, δ^c and δ_c. The significance of δ_c is similar to the critical δ in the Frank-Kamenetskii description. Suppose $\varepsilon < \varepsilon_0$ and δ is just slightly less than $\delta_c(\varepsilon)$, the system can reach a low-temperature steady state on curve A). Now, if δ is increased so that it is just slightly greater than $\delta_c(\varepsilon)$, the temperature will go to a much higher steady-state value on curve C). This sudden change in the steady-state temperature is the property that defines criticality; in other words, for a critical system there will be a temperature gap in which no steady-state solution is possible.

We will henceforth refer to $\delta_c(\varepsilon)$ as the critical value for ignition. A similar discussion can be given to the high-temperature branch, curve C), to show that $\delta^c(\varepsilon)$ is the critical point for extinction. One also can show that curve B), which lies between $\delta^c(\varepsilon)$ and $\delta_c(\varepsilon)$, is unstable, so that there are still only two steady-state temperatures for the system. For $\varepsilon > \varepsilon_0$, θ_M rises monotonically with δ as any steady-state value can be reached. In this case, there is no criticality and one expects no instabilities.

It is also interesting to compare the critical behavior deduced from eq. (4.1) with that derived from the equation describing the spatially uniform system, the Semenov model [62]. In the latter problem one can give a quite complete classification of the different regimes for criticality and ignition [63].

4·2. *Molecular-dynamics simulation.* – The objective of this study is to demonstrate the feasibility of simulating the temperature instability associated with thermal ignition [57]. To keep the simulation model as simple as possible, a two-dimensional hard-disk system in plane geometry is chosen. The use of hard-core interaction considerably facilitates the treatment of collision-induced exothermic reactions, while it is expected that the essential features of ignition behavior should not be affected by the details of interatomic collisions. For the present problem, two modifications of the standard molecular-dynamics techniques for hard-core systems [64] are needed. The first is that one must introduce reactions into the dynamics, and, secondly, one must provide for heat flow across the walls of the simulation system.

A simple way of simulating collision-induced reactions is to calculate the relative kinetic energy E_r of a pair of colliding hard disks at the instant of impact. If this value is greater than a prescribed threshold E, then the collision

will be treated as a reaction or inelastic collision, otherwise it will be treated as a normal elastic collision. In the event of a reaction, an amount of energy Q will be released through the outgoing velocities of the colliding disks. The fraction of Q given to each disk is governed by the laws of kinematics as expressed by the conservation of momentum and total energy. One could label the disks and distinguish between those capable of exothermic reaction (excited-state particles) and those incapable of reaction (ground-state particles). In the present simulation we have assumed no depletion of reactants, so in effect every particle is capable of reaction even if it has just reacted in the preceding collision.

In order to maintain close correspondence between simulation and the classical theory of thermal ignition, eq. (4.1), it is necessary to verify that our method of simulating reactions does give a reaction rate having an Arrhenius temperature dependence. From the simulation output one can determine the ratio of reaction rate to total collision rate. This ratio should have the behavior of $\exp[-E/RT]$. As shown in fig. 12, the data indeed follow this expected temperature variation. The same result also is obtained at a lower density $n^* = nd^2 = 0.157$, where n is the number density and d the hard-disk diameter.

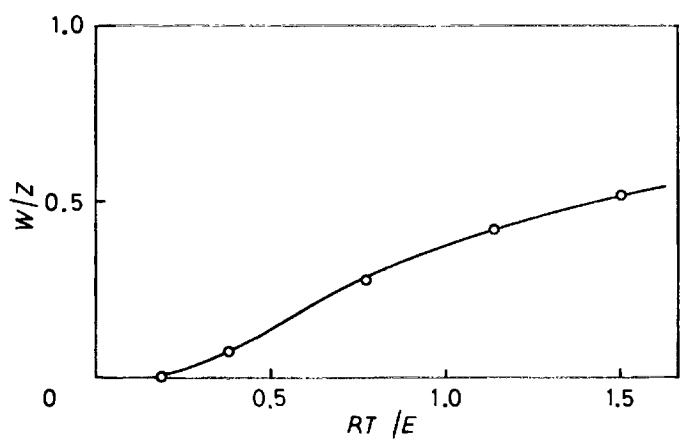

Fig. 12. – Temperature dependence of the ratio of reaction rate W to collision rate Z, molecular-dynamics data (circles) and the Arrhenius dependence $\exp[-E/RT]$ (curve).

The modification which allows heat transfer across the system walls consists of treating the boundaries of the square system along one direction (say the x-direction) to have fixed walls, while the boundaries along the other direction are periodic in the usual way. When a particle hits the fixed wall, it is reflected in one of two ways, specular or diffuse. In the case of specular reflection, $v_x' = -v_x$, $v_y' = v_y$, where the prime denotes the reflected velocity component and the unprimed components refer to the incident velocity. In the case of diffuse reflection, the reflected velocity is chosen from a Maxwellian distribution at the wall temperature consistent with detailed balance. The ratio of diffuse to specular reflection is chosen to be unity, since this choice leads

to results for the thermal conductivity, when the boundary condition is tested in a simulation of colliding hard-disk fluids without reactions, that are in agreement with the prediction of the Enskog theory for two-dimensional hard-sphere fluids [57].

4·3. *Results.* – The critical properties of reacting hard disks bounded by heat-conducting walls have been studied with the intention of determining the critical values of δ at a particular value of ε. A system of N disks, with N varying from 72 to 882, was placed in a square area with side dimension of $2r_0$. Each particle was assigned a velocity sampled from a Maxwellian distribution at the temperature of the fixed wall T_0. As the disks began to collide, the system temperature, defined as $RT = \langle K \rangle$, where $\langle K \rangle$ is the average kinetic energy of a particle, was monitored. In addition, the square was divided into ten strips along the x-direction, and a local temperature was calculated for each of the strips.

Two typical results for the temporal evolution of the temperature averaged over the entire system are shown in fig. 13. One sees that for condition *a*),

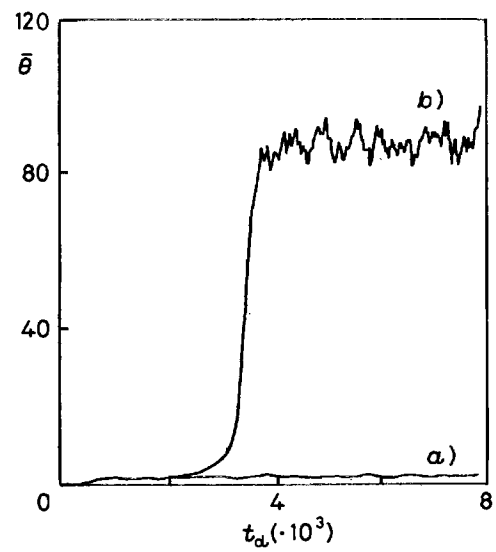

Fig. 13. – Temporal evolution of the reduced temperature θ at $\varepsilon = 0.175$ averaged over a slab of 648 disks, subcritical condition (*a*)) and supercritical condition (*b*)). One unit of simulation time interval is equivalent to $\sim 0.3t_c$, where t_c is the mean time between particle collisions.

which corresponds to a particular set of values, $\varepsilon = 0.175$, $n^* = 0.157$, $r_0 = 32.15\,d$ and Q, the temperature increased only slightly over a time interval of $\sim 8000\,t_d$, where $t_d \sim 0.3\,t_c$, t_c being the mean free time between particle collisions. The implication is that at this condition δ is less than δ_c. However, by increasing Q, one can increase δ (cf. eq. (4.2)) until it is greater than δ_c. This is the case with condition *b*). One sees that after a certain amount of incubation time (which we may call ignition time, $\sim 3600\,t_d$ in this case) the

temperature suddenly increases sharply by a factor of ~ 80. Having determined the δ values corresponding to conditions *a*) and *b*), one can then iterate between subcritical and supercritical conditions until a sufficiently precise value is determined for δ_c. This value is characteristic of the condition specified by n^*, r_0 and ε. Results of this type obtained for the same value of ε but different n^* and r_0 are summarized in table II.

TABLE II. – *Critical values of Frank-Kamenetskii parameter for a self-heating slab of hard disks* ($\varepsilon_0 = 0.175$).

nd^2	N	r_0/d	r_0/l (*)	δ_c	B
0.385	72	6.84	13.27	0.62	6.7
	128	9.12	17.70	1.04	9.0
0.157	72	10.72	5.84	0.48	4.9
	128	14.29	7.79	0.68	6.5
	200	17.86	9.74	1.02	8.1
	450	26.79	14.61	1.07	12.2
	648	32.15	17.53	1.12	14.6
0.116	450	31.21	11.84	1.08	10.5
0.077	450	38.23	9.18	0.83	8.6
	512	40.78	9.79	0.84	9.2
	648	45.87	11.02	0.94	10.3
	882	53.52	12.85	1.16	12.0

(*) l is the collision mean free path for hard disks, $l = 2\sqrt{2}\,nd g(d)$, where $g(d)$ is the equilibrium pair distribution at contact.

Examination of table II leads one immediately to two observations. The first is that, for a given density, δ_c increases with increasing system size and appears to reach an asymptotic value of 1.1. This is just the value predicted by a numerical solution of eq. (4.1). Thus we see that the present molecular-dynamics results can make contact with the continuum limit. Secondly, at fixed number of particles N, δ_c decreases with system density. This can be understood qualitatively by allowing surface heat transfer to take place at the wall boundary. Operationally, this means replacing the boundary condition $\theta(x = 1) = 0$ by $d\theta/dx = -B\theta$, where $B = Hr_0k$ is the Biot number with H the surface heat transfer coefficient. Now at a fixed ε_0, δ_c will depend on B. The variation of δ_c with B can be calculated using the approximation eq. (4.6) [58, 59]. The result is shown in fig. 14. At fixed N, r_0 is inversely proportional to $(n^*)^{\frac{1}{2}}$ and k is $\propto (n^*)^{-1}$. If we assume H is constant, then $B \propto (n^*)^{\frac{1}{2}}$ and fig. 14 shows δ_c decreasing with decreasing n^*. Figure 14 also shows that, at large B, δ_c eventually reaches a value corresponding

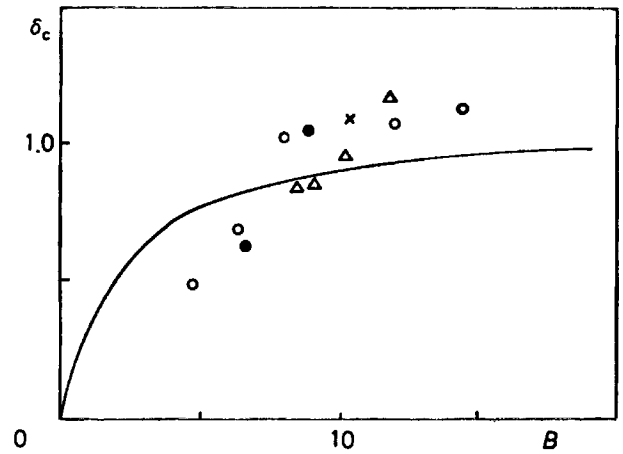

Fig. 14. – Variation of δ_c with Biot number B at $\varepsilon = 0.175$, molecular-dynamics results at several densities ($n^* = 0.077$ (△), 0.116 (×), 0.157 (○), 0.385 (●)) and continuum theory result using approximation eq. (4.6).

to the case of no surface heat transfer. At a given n^*, H and k are fixed, so B is proportional to r_0, the system size. Thus fig. 14 provides a qualitative explanation of the first observation as well.

The above arguments show that the molecular-dynamics results can be qualitatively understood on the basis of continuum theory. However, when the results are analyzed quantitatively, there is sufficient discrepancy remaining to justify further study of the observed size dependence of δ_c.

Other quantities which have been examined in this study are temperature profiles and the variation of ignition time with δ [57]. Comparison of a steady-state temperature distribution at subcritical condition with eq. (4.4) reveals a sharp temperature change at the wall boundary, implying that other boundary conditions [65] besides $\theta(x = 1) = 0$ should be used. Ignition times are expensive to simulate because a number of runs are required to average out the statistical fluctuations; they are also difficult to calculate from continuum theory [53, 66]. Consequently, only a preliminary comparison has been attempted [57]. Further study would be quite worthwhile since induction period is one of the most fundamental ignition properties.

The two basic variables in chemical reactions are species concentration and temperature. In the present work they are decoupled by the assumption of constant concentration. The results obtained are, therefore, relevant to only the initial phase of the system response. There is no intrinsic difficulty in simulating reactions involving species conversion [55], and it would be of considerable interest to study nonisothermal reactions with composition variation.

We have emphasized the comparison between molecular-dynamics results and continuum theory analysis. This is felt to be essential for demonstrating that the effects described by a macroscopic theory can be simulated in terms of particle dynamics. Once it is established that the basic phenomenon of

interest also can be properly described by a small system of discrete particles, then one can study the fluctuations in such a system and learn how the fluctuations are related to the macroscopic instabilities. Since fluctuations are beyond the scope of continuum theory, one has then the possibility of obtaining new information from simulation.

4·4. *Discussion.* – In concluding this section, we offer a few remarks on chemical-reaction models which involve significant energy releases. Compared to the isothermal models which exibit a rich variety of nonlinear behavior such as multiple steady states and associated hysteresis, complex self-generated oscillations and spatial instabilities [67], these models are relatively simple. On the other hand, the fact that exothermicity is explicitly treated makes them appropriate for studies of combustion phenomena. Generally speaking, one is interested in the temperature and concentration distributions which are intrinsically coupled but can be decoupled by assuming that consumption can be neglected. The Frank-Kamenetskii problem discussed here is an example of a nonisothermal model where only the temperature varies in space and time. A simpler model, one that is still of interest in thermal-ignition studies, is the Semenov problem where one further assumes that the temperature is spatially uniform [62, 63]. Another model which has received recent attention is one where all the heat release is assumed to go into heating up the system [68]. In this case, the coupling between temperature and concentration is treated explicitly, but then no spatial variation is allowed. We will now briefly consider both of these models.

The essence of the adiabatic collision model is the conservation condition

$$C_v T(t) + Q n(t) = \text{const}\,, \tag{4.7}$$

where C_v is the specific heat at constant volume, and $n(t)$ is the reactant concentration at time t. The assumption of this condition enables the reduction of the coupled rate equations

$$\begin{cases} \dfrac{\mathrm{d}n(t)}{\mathrm{d}t} = -\,k(T)n(t)\,, \\[2ex] C_v \dfrac{\mathrm{d}T(t)}{\mathrm{d}t} = Qk(T)n(t)\,, \end{cases} \tag{4.8}$$

where

$$k(T) = k_0 \exp\left[-\,E/RT(t)\right] \tag{4.9}$$

is the rate constant, to

$$\frac{\mathrm{d}n(t)}{\mathrm{d}r} = -\,k_0 n(t) \exp\left[-\,E/R\left[T_m - \frac{Q}{C_v}\,n(t)\right]\right]. \tag{4.10}$$

In (4.10) T_m is the maximum temperature, the temperature the system attains when the reactant is completely depleted, $n = 0$.

The deterministic rate equation (4.10) will show explosion behavior in the sense of a sudden increase in $T(t)$ (correspondingly, a decrease in $n(t)$), and from the inflection time we can define an ignition time. Alternatively, one can adopt a stochastic approach by formulating a master equation for the probability distribution $P(N, t)$, the probability that there are N reactant molecules at time t. Once $P(N, t)$ is known, one can calculate the average concentration

$$n(t) = \frac{1}{N_0} \sum_N NP(N, t) , \tag{4.11}$$

where N_0 is the initial number of reactant molecules, as well as the higher-order moments. These latter moments contain information about fluctuations, and one expects that fluctuation effects will be particularly enhanced in the vicinity of explosion. An interesting behavior of the model solution which is a manifestation of the strong nonlinear fluctuations is the bimodality property of $P(N, t)$. From the numerical solutions of the master equation, it has been found that, if the system started initially at a low temperature (relative to the activation energy E), then the concentration distribution $P(N, t)$ can have two well-separated peaks during an intermediate stage of time evolution. The implication is that depending on fluctuations the system concentration can have either a high value, corresponding to a situation where relatively few reactions have taken place, or a low value, signifying a significant depletion. This is an example of bifurcation phenomenon, and in the present context it may well be called « internal differentiation in time » [68].

In a limited way, the adiabatic explosion model has been studied by molecular dynamics using the two-dimensional hard-disk system described earlier [69]. The time variations of the concentration and the variance in concentration, along with $P(N, t)$, are found to agree well with the results of (4.10) and the corresponding master equation. Such comparisons are also useful for delimiting the number dependence of the simulation data. It has not been possible to observe bimodality by simulation because this behavior occurs under conditions where the time scale is beyond that directly accessible by molecular dynamics. On the other hand, Monte Carlo may be used to take advantage of the fact that one can introduce a renormalized time scale through an appropriate choice of the transition probability.

The Semenov model, like the Frank-Kamenetskii problem discussed here, treats only the temperature variation by assuming that reactant consumption is negligible. The governing equation is

$$\frac{\mathrm{d}u(s)}{\mathrm{d}s} = -\gamma u(s) + \varepsilon \exp\left[-\left[u(s) + \varepsilon\right]^{-1}\right] , \tag{4.12}$$

where $u = (T - T_0)/E$, T_0 being the temperature of the surrounding (wall), and time variable s and heat loss parameter γ are both dimensionless. In the steady state (4.12) can be compared to (4.1) and one sees that the diffusion term in the Frank-Kamenetskii model is now replaced by a surface heat loss which is simply proportional to the temperature difference between reactant and wall. Equation (4.12) can be analyzed analytically in a detailed discussion of criticality and ignition [63]. It would appear that a stochastic treatment of this model along with a simulation study would be interesting.

5. – Stress-induced structural transformations in crystalline solids.

The structural and mechanical behavior of solids under the combined effects of external stress and temperature are central issues in any comprehensive study of materials properties. Detailed understanding of such effects, particularly at the molecular level, is presently still lacking, even in the ideal case of a perfect crystal. Theoretical studies have been mostly confined to static calculations and a predetermined crystal structure [70], assumptions which may be valid at relatively low values of temperature and stress. On the other hand, it is clearly important to be able to study the behavior of solids at elevated temperatures and significant levels of stress without the constraints of prescribed deformations and taking into account all the possible consequences of fluctuations. For these purposes, the atomistic-simulation techniques being discussed here are very well suited.

Perhaps the most extensive simulation studies [7, 71] of stressed solids are the investigations of crack propagation. Other studies of mechanical behavior also exist [72]. More recently, there has been considerable interest in simulating polymorphic transitions in single crystals, which is made feasible by a method that allows the simulation cell to vary in size and shape [73]. Although the method of Parrinello and Rahman [10] was developed for molecular dynamics, the basic idea of treating the vectors defining the simulation cell as dynamical variables also may be applied in Monte Carlo simulation. Here we will briefly describe an implementation of this idea and some results on structural transformations in crystal lattices under uniaxial tension or compression [12, 13].

The essence of the Monte Carlo method generalized to allow the imposition of an arbitrary external stress is the ensemble distribution

$$f(\{\boldsymbol{r}_i\}, \boldsymbol{\varepsilon}, \boldsymbol{\sigma}) \propto \exp\left[-\left[U(\{\boldsymbol{r}_i\}) + \Omega_0 \operatorname{Tr} \boldsymbol{\sigma}:\boldsymbol{\varepsilon}\right]/k_B T\right], \tag{5.1}$$

where U is the internal energy, $\boldsymbol{\varepsilon}$ the strain tensor of the simulation cell, $\boldsymbol{\sigma}$ the external stress and Ω_0 the volume of the reference cell. If one samples this distribution instead of (2.2), then one generates an isostress-isothermal en-

semble. In (5.1) the strain is defined as

$$\boldsymbol{\varepsilon} = \boldsymbol{h}\boldsymbol{h}_0^{-1} - \mathbf{1}\,, \tag{5.2}$$

where $\boldsymbol{h}$ is a 3×3 matrix whose columns are the components of the three vectors defining the simulation cell [10] and subscript 0 refers to the reference cell. In the actual simulation, samplings of the particle movements and changes in the $h_{\alpha\beta}$ are carried out alternately, and in each case the Metropolis test [11] is used to decide whether to accept the configuration sampled.

The isostress Monte Carlo method has been applied to study structural transformations in a small ($N = 32$) simulation cell with periodic borders, where the interatomic potential was either of the Lennard-Jones type or the Johnson I potential empirically constructed for α-iron. In the former case a f.c.c. lattice of argon atoms was subjected to a uniform uniaxial load along [100] at 40 K. Under various loadings, the lattice deformed homogeneously and maintained its face-centered tetragonal symmetry. When a tensile load was applied, system failure or loss of cohesion was observed at 600 bar, as indicated by the increase in the components of $\boldsymbol{h}$ without limit. It is noteworthy that this critical value is considerably lower than the prediction of 3700 bar by static calculation [70]. In the case of compressive loading, it was found that beyond 350 bar the system transformed to an h.c.p. structure by a combination of large deformation and relative sliding of the (100) planes. This transformation is the same as that observed by PARRINELLO and RAHMAN in a molecular-dynamics simulation of Ni using a Morse potential [10].

The study of α-iron using the Johnson I potential had as its objective the observation of the Bain transformation (f.c.c. $\leftrightarrow$ b.c.c.) at finite temperatures [13]. There exists a class of structural transformations in solids, called the martensitic transformations, which are common in iron, iron alloys and many other materials [74]. This transformation, which occurs rapidly with a velocity approaching that of sound waves in the crystal, is believed to follow either a classical or a nonclassical path [75]. The distinction is that in the former case a nucleus having the product structure is created, while in the latter case the product is formed in a finite region through a continuous deformation of the parent structure. An example of a nonclassical martensitic transformation is that predicted by BAIN [76], who suggested that under a compressive load one should be able to observe a f.c.c. to b.c.c. transformation, as shown in fig. 15. Such a transformation has been observed when f.c.c. iron is quenched [77].

In a typical run, the simulation would begin with the system in the b.c.c. structure and a uniaxial tension would be applied along [001]. The system was allowed to relax at this fixed condition while being maintained at 70 K. Relaxation would consist of sampling a large number of configurations corresponding to various particle displacements as well as changes in $h_{\alpha\beta}$. During

this sampling the internal energy, the internal stress and the components of $\boldsymbol{h}$ were monitored. A set of such results at a fixed tensile loading is shown in fig. 16. The quantities $h_{\alpha\alpha}$, $\alpha = 1, 2, 3$, are the lengths of the simulation cell; it was found that in all cases the system remained tetragonal. One can see that during the relaxation the system showed a considerable expansion along [001] and contraction in the other two orthogonal directions. Equilibrium was achieved after about 2000 configurations sampled per particle.

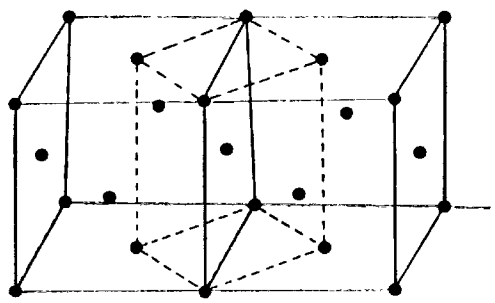

Fig. 15. – Crystallographic basis of the Bain transformation. The dashed lines delineate a body-centered tetragonal cell within two adjacent face-centered cubic unit cells. If the lattice is compressed along the [001] direction, the tetragonal cell can transform into a body-centered cubic cell at a certain stage of deformation. This relation is purely geometrical and does not involve any consideration of forces or energies.

The changes in the simulation cell dimensions in fig. 16 indicated a mechanical instability which, as we will see below, corresponded to a structural transformation. At the same time the potential energy was seen to increase and a balance was reached between the external stress σ, held constant throughout the simulation at $6 \cdot 10^9$ N/m^2, and the internal stress, calculated from the expression

$$\pi = \frac{1}{\Omega}\left[N k_B T \mathbf{1} - \sum_i \sum_{j>i} \left(\frac{V'}{r_{ij}}\right) \boldsymbol{r}_{ij} \boldsymbol{r}_{ij}\right], \tag{5.3}$$

where $\mathbf{1}$ is the unit tensor, V' is the derivative of the interatomic potential, and $\boldsymbol{r}_{ij}$ is the vector separation between particles i and j. The quantity shown is the component along [001], the stresses along [100] and [010] (not shown) fluctuated about an average value of zero, as expected.

The simulation data from a number of runs at 70 K and various uniaxial loadings are summarized in the stress-strain relation shown in fig. 17. Also indicated are the calculated results using the static method [78] with the same potential function. Going back to the b.c.c. starting structure (α phase), we see that under tension the lattice elongated continuously until the external stress increased to $6 \cdot 10^9$ N/m^2 at which level the system underwent a large deformation and reached a new stable structure. This structure appeared to have face-centered tetragonal symmetry. By reducing σ to zero we confirmed

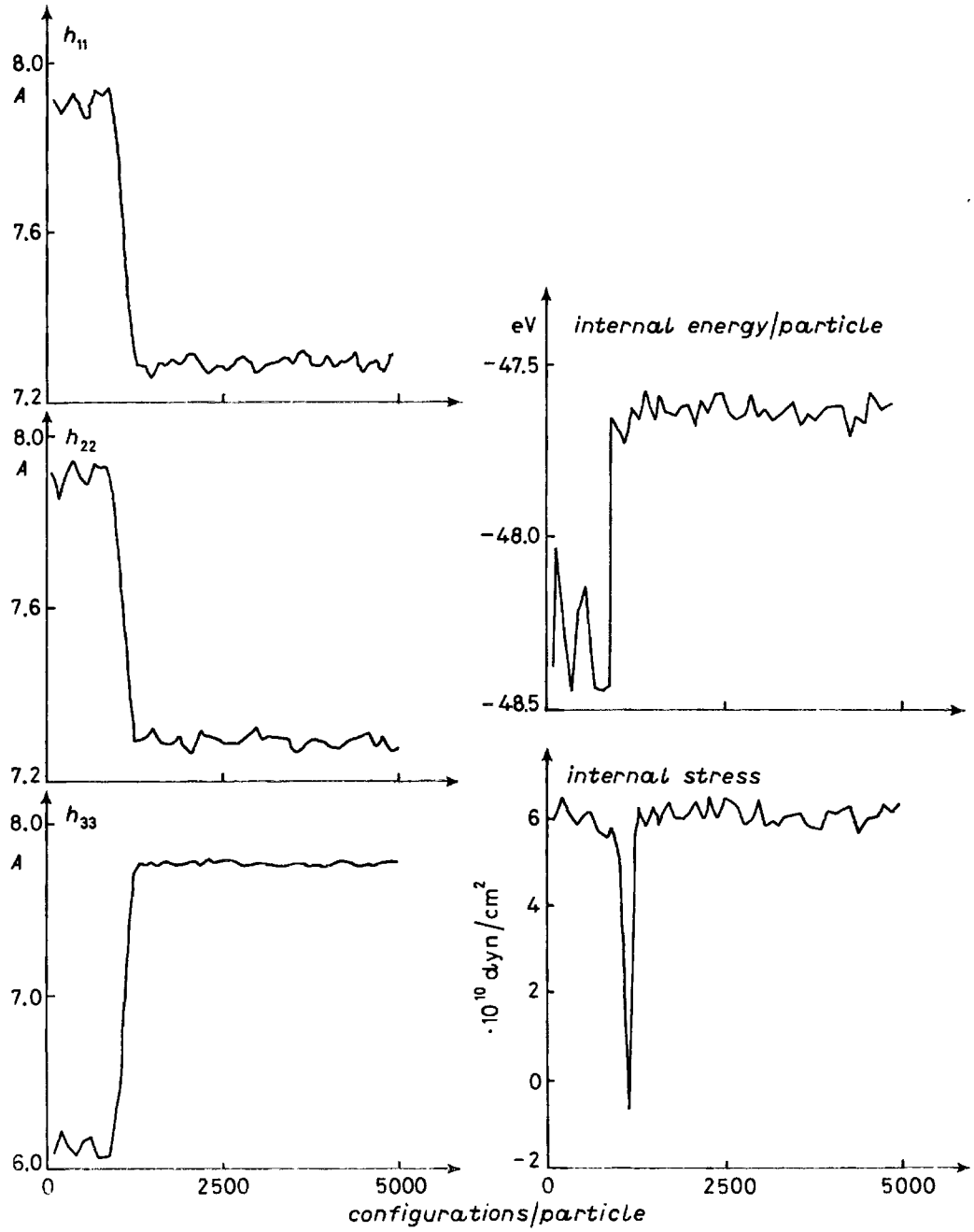

Fig. 16. – Response of simulation cell lengths, internal energy and internal stress of a 32-atom model of α-iron during relaxation under uniaxial tension of $6 \cdot 10^9$ N/m^2, Monte Carlo results showing the b.c.c. $\rightarrow$ f.c.c. transition at 70 K.

that indeed the system has transformed to the γ phase with f.c.c. structure, and that the instability observed at $\sigma = 6 \cdot 10^9$ N/m^2 corresponded to the α(b.c.c.) $\rightarrow \gamma$(f.c.c.) transformation. As shown in fig. 17, the reverse transition could be brought about by compression. It is not surprising that at finite temperature the critical values of σ turned out to be less than those predicted by static calculations. Repeating these simulations at higher temperatures, one finds still lower values of the critical stress; preliminary data indicate

that the $\alpha \to \gamma$ transformation could occur purely by thermal activation at temperatures greater than ~ 1200 K [79]. This result has, at best, only qualitative significance, since neither the potential function used is that reliable nor have the numerical effects like number dependence been studied carefully.

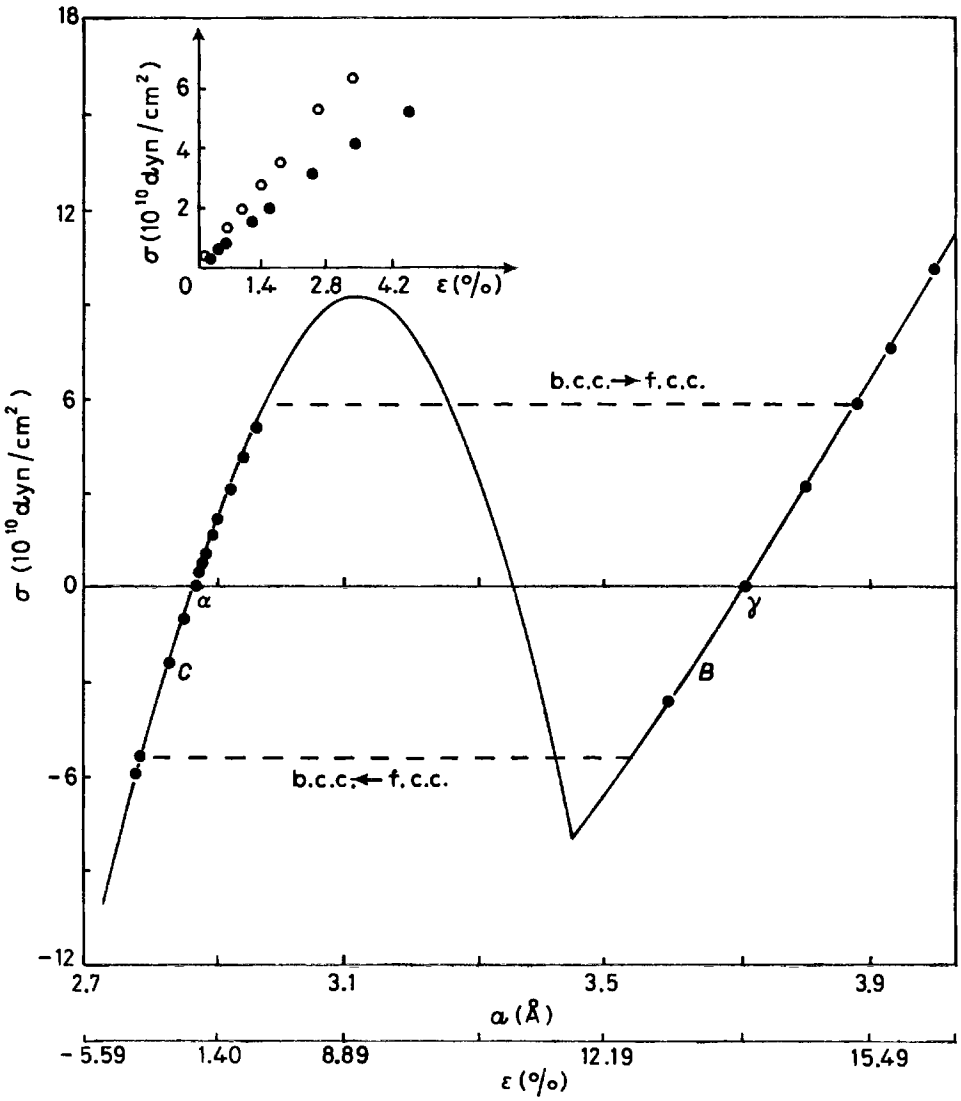

Fig. 17. – Stress-strain curve of iron obtained using the Johnson I potential showing the $\alpha \to \gamma$ transition under tension and the reverse transition under compression, Monte Carlo simulations at 70 K (closed circles) and static calculations (solid curve). Inset shows a comparison with experimental data on iron whiskers [80] (open circles) on an expanded scale.

6. – Concluding remarks.

In these lectures we have described three quite different applications of atomistic simulations. Our intent was to illustrate through a few relatively sim-

ple examples the wide range of problems that can be usefully studied using molecular-dynamics and Monte Carlo techniques. Despite the fact that several topics, such as potential function, boundary conditions, system size dependence and error analysis, were not addressed, it is hoped, nevertheless, that these discussions are sufficient to demonstrate the unique capabilities of MD and MC simulations for materials characterization at the microscopic level.

In any atomistic calculation of properties of real materials, an accurate interatomic potential is clearly an indispensable requirement. For metallic systems there exists no general solution to the problem of determining a reliable potential function [81]. Empirical potentials, fitted to various observed properties, have been constructed and used especially in the early studies. More recently the emphasis has shifted to the use of pseudopotentials which can be theoretically justified. However, even with pseudopotentials there are fundamental issues still to be resolved, for example, the validity of a pair potential representation for transition metals [82] and the justification for applying a potential function derived for bulk system to inhomogeneous structures such as cracks and interfaces [83]. On the other hand, for ionic systems such as ceramics, the potential is much better established. Here, the electrostatic interactions can be treated quite accurately and only the short-range repulsive forces are subject to uncertainties [84].

The limitation imposed by the lack of a realistic potential should be recognized but not construed as an argument against carrying out well-formulated simulation studies. We hold the view that quantitative results obtained from model calculations will be of value even though the potential function used is less than ideal. The reason is that the information and insight concerning microstructural details and local dynamics generated by MD or MC often are not obtainable by other means, thus even model results can be valuable if their implications are properly understood. Because sensitivity to potential function can vary greatly from one physical property to another, it is possible that acceptable results for certain properties can be obtained from idealized models or empirical potentials. On the other hand, it is certainly true that, without sufficiently realistic potentials, simulation studies of specific substances or certain physical phenomena should not be made. Even here one should not regard this limitation as an inherent deficiency of a simulation method itself. It is also worthwhile to note that simulation is an effective method of correlating different properties using a given potential function. Once a simulation program has been coded and tested, it is usually a straightforward matter to repeat the calculation for a different potential function. This means that, when more realistic potentials such as potentials taking into account noncentral forces or three-body interactions become available later, the earlier work can well serve as a reference for delineating those effects specific to the potential.

In conclusion, we note that many of the current problems in materials

research [85] tend to be highly interdisciplinary in nature and require fundamental understanding at the molecular level. Such problems are potentially well suited for simulation studies. The continued rapid growth of computer capabilities and the development of more powerful simulation techniques will further ensure that studies of the type discussed here become even more significant. Both the basic investigations of idealized model systems and the practical applications involving real materials will be of interest, the former to stimulate the development of theoretical models, and the latter to predict materials performance, guide the planning of experiments and aid in data interpretation.

* * *

This work was supported by a grant from the National Science Foundation, CHE-8415078.

REFERENCES

[1] For a description of the molecular-dynamics simulation technique, see J. R. BEELER: in *Advances in Materials Research*, edited by H. HERMAN, Vol. **5** (Wiley, New York, N. Y., 1970), p. 295; for a review and an extensive bibliography, see W. W. WOOD and J. J. ERPENBECK: *Annu. Rev. Phys. Chem.*, **27**, 319 (1976).

[2] For a description of Monte Carlo methods and applications, see *Monte Carlo Methods in Statistical Physics*, edited by K. BINDER (Springer-Verlag, Berlin, 1979).

[3] For a survey of applications in physical metallurgy, see the conference proceedings, *Interatomic Potentials and Crystalline Defects*, edited by J. K. LEE (Met. Soc. AIME, Warrendale, Penn., 1981), and the *Proceedings of the 1983* TMS-AIME *Meeting on Computer Simulation in the Study of Solid-Solid Interfaces*, which appeared as an issue of *Surf. Sci.*, **144**, No. 1 (1984).

[4] D. FRENKEL and J. P. MCTAGUE: *Annu. Rev. Phys. Chem.*, **31**, 491 (1980); *Ordering in Two Dimensions*, edited by S. K. SINHA (North-Holland, New York, N. Y., 1980); for a definitive study of melting in two dimensions, see F. F. ABRAHAM: *Phys. Rev. Lett.*, **50**, 978 (1983).

[5] See the many references given in G. H. GILMER: *Science*, **208**, 355 (1980).

[6] C. H. BENNETT: in *Diffusion in Solids: Recent Developments*, edited by A. S. NOWICK and J. J. BURTON (Academic Press, New York, N. Y., 1975), p. 73; *Diffusion in Solids* II, edited by G. E. MURCH and A. S. NOWICK (Academic Press, New York, N. Y., in press), chapters by G. E. MURCH and by G. JACUCCI.

[7] G. J. DIENES and A. PASKIN: in *Atomistics of Fracture*, edited by R. M. LATANISION and J. R. PICKENS (Plenum Press, New York, N. Y., 1983), p. 671; see also B. DECELIS, A. S. ARGON and S. YIP: *J. Appl. Phys.*, **54**, 4864 (1983), and references given therein.

[8] M. J. WEINS, H. GLEITER and B. CHALMERS: *J. Appl. Phys.*, **42**, 4639 (1971); G. HASSON, J.-Y. BOOS, I. HERBEURAL, M. BISCONDI and C. GOUX: *Surf. Sci.*, **31**, 115 (1972); R. E. DAHL, J. R. BEELER and R. D. BOURQUIN: *Comput. Phys. Commun.*, **2**, 301 (1971).

[9] C. H. BENNETT: *J. Comput. Phys.*, **22**, 245 (1976); G. JACUCCI and N. QUIRKE: in *Computer Simulation for Solids, Lecture Notes in Physics*, Vol. **166**, edited by C. R. A. CATLOW and W. C. MACKRODT (Springer-Verlag, Berlin, 1982), p. 38. For more recent discussions see D. FRENKEL and A. J. C. LADD: *J. Chem. Phys.*, **81**, 3188 (1984); A. RAHMAN and G. JACUCCI: *Nuovo Cimento D*, **4**, 357 (1984).

[10] A method for constant-pressure simulation was first discussed by H. C. ANDERSEN: *J. Chem. Phys.*, **72**, 2384 (1980), while extension to arbitrary stress was worked out by M. PARRINELLO and A. RAHMAN: *J. Appl. Phys.*, **52**, 7182 (1981); see also W. G. HOOVER: *Phys. Rev. A*, **118**, 111 (1983). For an extension to metallic systems see R. N. BARNETT, C. L. CLEVELAND and U. LANDMAN: *Phys. Rev. Lett.*, **54**, 1679 (1985).

[11] W. W. WOOD: in *Physics of Simple Liquids*, edited by H. N. V. TEMPERLY, J. S. ROWLINSON and G. S. RUSHBROOKE (North-Holland, Amsterdam, 1968), Chapt. 5.

[12] R. NAJAFADADI: Ph.D. Thesis, MIT (1983).

[13] R. NAJAFABADI and S. YIP: *Scr. Metall.*, **17**, 1199 (1983).

[14] W. G. HOOVER and B. J. ALDER: *J. Chem. Phys.*, **46**, 686 (1967).

[15] See, for example, the *Proceedings of Irsee Conference on Structure and Properties of Internal Interfaces, August 1984*, to appear in *J. Phys. (Paris) Colloq.* series.

[16] P. H. PUMPHREY: in *Grain Boundary Structure and Properties*, edited by G. A. CHADWICK and D. A. SMITH (Academic Press, New York, N. Y., 1976), p. 139.

[17] D. WOLF: in *Proceedings of Irsee Conference on Structure and Properties of Internal Interfaces, August 1984*, to appear in *J. Phys. (Paris) Colloq.* series.

[18] G. H. BISHOP, R. J. HARRISON, T. KWOK and S. YIP: in *Progress in Materials Science, Chalmers Anniversary Volume*, edited by J. W. CHRISTIAN, P. HAASEN and T. B. MASSALSKI (Pergamon Press, Oxford, 1981), p. 49.

[19] G. H. BISHOP, R. J. HARRISON, T. KWOK and S. YIP: *J. Appl. Phys.*, **53**, 5609 (1982). One of the first molecular-dynamics studies of bicrystals was carried out on a $\Sigma = 7$ two-dimensional model with Lennard-Jones potential, R. M. S. COTTERILL, T. LEFFERS and H. LILHOLT: *Philos. Mag.*, **30**, 265 (1974).

[20] G. H. BISHOP, R. J. HARRISON, T. KWOK and S. YIP: *J. Appl. Phys.*, **53**, 5596 (1982).

[21] For a review of early work see R. J. HARRISON, G. A. BRUGGEMAN and G. H. BISHOP: in *Grain Boundary Structure and Properties*, edited by G. A. CHADWICK and D. A. SMITH (Academic Press, New York, N. Y., 1976), p. 45.

[22] P. D. BRISTOWE: *J. Phys. (Paris) Colloq.*, **43**, C6-33 (1982).

[23] D. WOLF: *Acta Metall.*, **32**, 245 (1984).

[24] For a discussion of the availability of interatomic potentials for metals, see the first four contributions in *Interatomic Potentials and Crystalline Defects*, edited by J. K. LEE (Met. Soc. AIME, Warrendale, Penn., 1981).

[25] G. CICCOTTI, M. GUILLOPE and V. PONTIKIS: *Phys. Rev. B*, **27**, 5576 (1983); see also M. GUILLOPE, G. CICCOTTI and V. PONTIKIS: *Surf. Sci.*, **144**, 67 (1984).

[26] M. HASHIMOTO, Y. ISHIDA, R. YAMAMOTO and M. DOYAMA: *Acta Metall.*, **32**, 1 (1984), and references given therein.

[27] P. S. HO, T. KWOK, T. NGUYEN, C. NITTA and S. YIP: *Scr. Metall.*, **19**, 993 (1985).

[28] T. KWOK, P. S. HO, S. YIP, R. W. BALLUTTI, P. D. BRISTOWE and A. BROKMAN: *Phys. Rev. Lett.*, **47**, 1148 (1981).

[29] N. Q. LAM, L. DAGENS and N. V. DOAN: *J. Phys. F*, **13**, 1369, 2503 (1983).

[30] D. WOLF: *J. Am. Ceram. Soc.*, **67**, 1 (1984).

[31] M. F. ASHBY: *Surf. Sci.*, **31**, 498 (1972).

[32] W. BOLLMAN: *Crystal Defects and Crystal Interfaces* (Springer, New York, N. Y., 1970).

[33] R. NAJAFABADI and S. YIP: *Scr. Metall.*, **18**, 159 (1984).
[34] M. E. GLICKSMAN and C. L. VOLD: *Surf. Sci.*, **31**, 50 (1972).
[35] K. T. AUST: in *Progress in Materials Science, Chalmers Anniversary Volume*, edited by J. W. CHRISTIAN, P. HAASEN and T. B. MASSALSKI (Pergamon Press, Oxford, 1981), p. 27.
[36] R. KIKUCHI and J. W. CAHN: *Phys. Rev. B*, **21**, 1893 (1980).
[37] F. CARRION, G. KALONJI and S. YIP: *Scr. Metall.*, **17**, 915 (1983).
[38] K. TOUKAN, F. CARRION and S. YIP: *J. Appl. Phys.*, **56**, 1455 (1984).
[39] A. J. C. LADD, W. G. HOOVER, V. ROSATO, G. KALONJI, S. YIP and R. J. HARRISON: *Phys. Lett. A*, **100**, 195 (1984).
[40] P. DEYMIER: Ph. D. Thesis, MIT (1985); P. DEYMIER and G. KALONJI: *J. Chem. Phys.*, to be published.
[41] J. W. M. FRENKEN and J. F. VAN DER VEEN: *Phys. Rev. Lett.*, **54**, 134 (1985); for a molecular-dynamics study see J. Q. BROUGHTON and G. H. GILMER: *Acta Metall.*, **31**, 845 (1983).
[42] R. W. BALLUFFI: *Metall. Trans. B*, **13**, 527 (1982); N. L. PETERSON: *Int. Metall. Rev.*, **28**, 65 (1983).
[43] R. W. BALLUFFI, T. KWOK, P. D. BRISTOWE, A. BROKMAN, P. S. HO and S. YIP: *Scr. Metall.*, **15**, 951 (1981).
[44] T. KWOK, P. S. HO and S. YIP: *Phys. Rev. B*, **29**, 5354, 5363 (1984).
[45] R. A. JOHNSON: *Phys. Rev. A*, **134**, 1329 (1964).
[46] J. BARDEEN and C. HERRING: in *Imperfections in Nearly Perfect Crystals*, edited by W. SHOCKLEY (Wiley, New York, N. Y., 1952), p. 1.
[47] C. H. BENNETT and B. J. ALDER: *J. Phys. Chem. Solids*, **32**, 2111 (1971).
[48] C. NITTA: Ph. D. Thesis, MIT (1986); to be published.
[49] G. CICCOTTI: NATO-CECAM *Workshop on Solid State Diffusion, August 1983.*
[50] P. GRAY and P. R. LEE: *Combust. Oxid. Rev.*, **2**, 1 (1967).
[51] A. G. MARZHANOV and A. E. AVERSON: *Combust. Flame*, **16**, 89 (1971).
[52] D. A. FRANK-KAMENETSKII: *Diffusion and Heat Transfer in Chemical Kinetics*, 2nd edition (Plenum Press, New York, N. Y., 1969).
[53] J. W. BEBERNES and D. R. KASSOY: *SIAM (Soc. Ind. Appl. Math.) J. Appl. Math.*, **40**, 476 (1981); A. KAPILA: *SIAM (Soc. Ind. Appl. Math.) J. Appl. Math.*, **39**, 21 (1980).
[54] J. POLAND and D. R. KASSOY: *Combust. Flame*, **50**, 259 (1983); T. BODDINGTON, C.-G. FENG and P. GRAY: *Proc. R. Soc. London, Ser. A*, **385**, 289 (1983).
[55] J. PORTNOW: *Phys. Lett. A*, **51**, 370 (1975); P. ORTOLEVA and S. YIP: *J. Chem. Phys.*, **65**, 2045 (1976); J. S. TURNER: *J. Phys. Chem.*, **81**, 2379 (1977).
[56] H. W. HARRISON and W. C. SCHIEVE: *J. Chem. Phys.*, **58**, 3634 (1973); D. L. JOLLY, B. C. FREASIER and S. NORDHOLM: *Chem. Phys.*, **21**, 211 (1977); A. J. STACE and J. N. MURRELL: *Mol. Phys.*, **33**, 1 (1977); D. H. TSAI and S. TREVINO: *J. Chem. Phys.*, **79**, 1684 (1983).
[57] D. P. CHOU: Ph.D. Thesis, MIT (1981); D. P. CHOU and S. YIP: *Combust. Flame*, **47**, 215 (1982); **58**, 239 (1984).
[58] W. GILL, A. R. SHOUMAN and A. B. DONALDSON: *Combust. Flame*, **41**, 99 (1981).
[59] T. TAKENO: *Combust. Flame*, **29**, 209 (1977).
[60] N. W. BAZLEY and G. C. WAKE: *Combust. Flame*, **33**, 161 (1978).
[61] J. W. ENIG, D. SHANKS and R. W. SOUTHWORTH: *The numerical solution of the heat conduction equation occurring in the theory of thermal explosions*, NAVORD Report 4377, U.S. Ordnance Laboratory, November 7, 1956; A. R. SHOUMAN, A. B. DONALDSON and H. Y. TSAO: *Combust. Flame*, **23**, 17 (1974).
[62] N. N. SEMENOV: *Z. Phys.*, **48**, 571 (1928).
[63] J.-C. LERMANT and S. YIP: *Combust. Flame*, **57**, 41 (1984).

[64] M. L. PRUEITT: LASL Report LA-4696, Los Alamos Scientific Laboratory, New Mexico (1971).
[65] W. GILL, A. R. SHOUMAN and A. B. DONALDSON: *Combust. Flame*, **41**, 99 (1981).
[66] D. R. KASSOY and J. POLAND: *SIAM (Soc. Ind. Appl. Math.) J. Appl. Math.*, **39**, 412 (1980).
[67] See *Chemical Instabilities*, edited by G. NICOLIS and F. BARAS (Reidel, Dordrecht. 1984), for example, the contributions of P. GRAY and S. K. SCOTT and of R. A. A. SCHMITZ *et al.*
[68] G. NICOLIS, F. BARAS and M. MALEK MANSOUR: in *Chemical Instabilities*, edited by G. NICOLIS and F. BARAS (Reidel, Dordrecht, 1984), p. 171; F. BARAS, G. NICOLIS, M. MALEK MANSOUR and J. W. TURNER: *J. Stat. Phys.*, **32**, 1 (1983); F. BARAS and G. NICOLIS: to be published.
[69] D. P. CHOU, T. LACKNER and S. YIP: to be published.
[70] F. MILSTEIN and B. FARBER: *Phys. Rev. Lett.*, **44**, 277 (1980); N. H. MACMILLAN and A. KELLY: *Proc. R. Soc. London, Ser. A*, **330**, 291 (1972).
[71] P. C. GEHLAN, G. T. HAHN and M. F. KANNINEN: *Scr. Metall.*, **6**, 1087 (1972); W. T. ASHURST and W. G. HOOVER: *Phys. Rev. B*, **14**, 1465 (1976). For recent work other than ref. [7], see A. PASKIN, K. SIERADZKI, D. K. SOM and G. J. DIENES: *Acta Metall.*, **31**, 1253 (1983); M. MULLINS: *Acta Metall.*, **32**, 381 (1984); B. MORAN, W. G. HOOVER and D. M. NORRIS: report UCRL-91763 Lawrence Livermore Laboratory (October 1984).
[72] See, for example, E. D. SCHUKIN and V. S. YUSHCHENKO: *J. Mater. Sci.*, **16**, 313 (1981); B. W. DODSON and P. A. TAYLOR: *Phys. Rev. B*, **30**, 1679 (1984).
[73] M. PARRINELLO and A. RAHMAN: *J. Appl. Phys.*, **52**, 7182 (1981); see also J. R. RAY and A. RAHMAN: *J. Chem. Phys.*, **80**, 4423 (1984), and the references cited therein.
[74] J. W. CHRISTIAN: *The Theory of Transformations in Metals and Alloys* (Paragon Press, Oxford, 1965).
[75] G. B. OLSON and M. COHEN: *J. Phys. (Paris) Colloq.*, **43**, C4-75 (1982).
[76] E. C. BAIN: *Trans. Am. Inst. Min. Metall. Eng.*, **70**, 25 (1924).
[77] R. P. ZERWEKH and C. M. WAYMAN: *Acta Metall.*, **13**, 99 (1965).
[78] F. MILSTEIN: *Phys. Rev. B*, **3**, 1130 (1971).
[79] H. HSIEH, R. NAJAFADI and S. YIP: to be published.
[80] S. S. BRENNER: *J. Appl. Phys.*, **27**, 1484 (1956).
[81] See the first four chapters in ref. [3].
[82] D. G. PETTIFOR: in CECAM *Workshop on Interatomic Potentials in Transition Metals*, CECAM, Université Paris-Sud, Orsay (1983), p. 25.
[83] D. G. PETTIFOR: in *Atomistics of Fracture*, edited by R. M. LATANISION and J. R. PICKENS (Plenum Press, New York, N. Y., 1983), p. 281.
[84] C. R. A. CATLOW, I. D. FAUX and M. J. NORGETT: *J. Phys. C*, **9**, 447 (1976); C. R. A. CATLOW, K. M. DILLER and M. J. NORGETT: *Philos. Mag.*, **35**, 177 (1977).
[85] *Trends and Opportunities in Materials Research*, report of the Materials Research Advisory Committee, U.S. National Science Foundation (1984).

Round-Table: Perspectives in Materials Science.

Chairman: V. PONTIKIS

Session secretary: G. DE LORENZI

Introductory remarks.

The properties of simple liquids and solids have been studied extensively by molecular dynamics (MD), starting from the early 60's, but for systems of high complexity such as polymers or macromolecules this technique has been employed somewhat later. This situation is mainly due to the low speed of computers when MD began to be possible and also to the advanced developments achieved by analytical theories especially in the case of crystalline solids.

Many of the lectures given in this summer school investigated the properties of liquids, ionic systems, molecular solids, molecules and macromolecules. Therefore, it appears of interest to focus the discussion and talks during this round-table session on MD applications on crystalline solids and related problems. The properties of crystals (*e.g.*, mechanical, optical, mass transport, etc.) are greatly influenced by the presence of defects such as surfaces, grain boundaries, dislocations and inclusions. The study of defects in solids by MD is motivated by the following reasons:

a) Computer simulation is the only reliable way to get information at the atomic scale.

b) The temperature dependence of the thermodynamic quantities which are defect sensitive is easily obtained by MD, while it would be difficult or impossible to study by the traditional solid-state physics techniques. From this point of view MD appears as a valuable complementary tool to lattice dynamics.

For these reasons it is useful to translate the main limitations of MD, invoked frequently during this course, into the « language » of defects.

a) *Size limitations.*

The maximum size of a MD system, compatible with technical and/or financial limitations, is about $N \sim 100\,000$ particles; this corresponds for a f.c.c.

crystal to a cubic box with side length equal to thirty lattice cell parameters ($N = 108\,000$). Introducing in that system a point defect or a dislocation results in a concentration $C \sim 10^{-5}$ or a density $\varrho \sim 10^{12}$, respectively. These values are unrealistically high. They are reached only at the melting-point temperature for vacancies or in highly deformed crystals for dislocations.

As is usually done, periodic boundary conditions are often used in MD computations to avoid surface effects. For dislocations, the long-range stress-strain field generates some difficulties: though one wants to study the properties of an isolated dislocation, periodic images generate in fact a system containing two «infinite»-extension grain boundaries! To avoid such a problem a MD system embedded in an elastic continuum is sometimes used. The appropriate stress/strain conditions were imposed at the interfaces between the discrete medium and the continuum. However, such a solution is cumbersome for studying the dynamics of the defect. These two examples illustrate the kind of problems one has to deal with when investigating defect properties.

b) Time limitations.

The maximum trajectory length that can be generated for a small-size system ($N \sim 1000$ particles) by MD is about one nanosecond. Obviously, rare events with an occurrence frequency $f' < 10^8\ \mathrm{s}^{-1}$ cannot be investigated by MD simulation. For a thermally activated process, $f = f_0 \exp[-\delta H/k_B T]$ and the maximum barrier height corresponding to f' evaluated in the case of copper ($f_0 \sim 7$ THz, $T_{\mathrm{melting}} \sim 1356$ K) is $\delta H \sim 1.3$ eV. Consequently, MD cannot be used for the study of the mechanism of point defect creation from surfaces, grain boundaries or dislocations.

These examples are just an alternative way of presenting the usual limitations of MD in the low k and ω region. A possible way to bypass these limitations could be to couple MD simulation with intermediate-scale theory and/or finite-element analysis.

MD simulations can be used either as a means to test theoretical models or as a tool providing quantitative predictions of thermodynamic properties of materials. The latter approach is obviously highly potential dependent. For systems in which ionic interactions predominate, or alkali metals and rare gases, satisfactory models for the interatomic interactions exist and allow computations of thermodynamic bulk properties in good agreement with experiment. The situation is less simple for covalent systems, transition metals and in all cases for defects in solids.

Usually for such systems one uses semi-empirical or empirical potentials leading to somewhat doubtful results. Description of realistic systems by MD requires progress to be accomplished in the detailed knowledge of interatomic forces.

There is a variety of applications of MD simulations in Materials Science. The area covered is too large to review each of them. Therefore, the round-table

discussion will concentrate only on a few open problems and specific applications chosen from subjects of current interest to the participants.

Summary of contributed discussion.

1) *Presentation of a movie illustrating* MD *simulation of adatom and vacancy diffusion on low-index* f.c.c. *surfaces* (V. ROSATO).

The presented sequences concerned the (100), (110) and (111) surface of a Lennard-Jones (12-6) solid. This movie, which was made at the Section de Recherches de Métallurgie Physique, Centre d'Études Nucléaires de Saclay, resulted from work by DE LORENZI *et al.* [1] and ROSATO *et al.* [2] on surface diffusion mechanisms. It was clearly shown that defect migration on surfaces is highly co-operative. The movie emphasizes the importance of graphics in the analysis and the presentation of MD results.

2) *Comments on the potentials available for* MD *simulations* (M. KLEIN).

a) Atoms (rare-gas-like interactions). Lennard-Jones and other empirical or semi-empirical potentials are widely used despite important many-body contributions. For many cases pair interactions are a poor approximation to reality.

b) Ions. Induction effcts are important and pair potentials are not operative. Effective potentials are currently employed.

c) Molecules. The special feature here is that all of these are polar and polarizable. An important problem is to correctly take into account charge effects and the charge distribution. Effective site-site pair potentials are very attractive for MD simulations, but the agreement with experiment has to be investigated for each special case.

d) Metals and alloys. For many systems pseudopotentials have been derived and are satisfactory. However, these potentials are volume dependent and long ranged, so that problems arise by using them in MD simulations.

e) Covalent systems. For such systems three-body effects are predominant by definition. Empirical force constant models are actually used (Keating, Phillips, etc.).

3) *Presentation of a potential for silicon due to Stillinger and Weber* (F. ABRAHAM).

The present potential is similar to Keating's and reproduces nicely experimental liquid-state properties and two-particle static correlation functions.

HOOVER. The three-body interactions must vanish smoothly as triplets break up at the solid-liquid transition. How do you handle the potential discontinuity due to the breaking of the bonds?

ABRAHAM. The pair interaction $U(r_{12})$ that enters in the three-body potential $U^{(3)} = f(r_{13})\,U(r_{12})$ goes smoothly to zero at the distance at which the bond is broken, so there is no discontinuity.

4) *Studies of surfaces, grain boundaries and dislocations* (M. GUILLOPE).

The high-temperature structure of these defects investigated by MD simulations clarifies the results of experimental studies. Appropriate order parameters have to be used together with a detailed study of mass transport (see ref. [2] and [3]).

5) *Comments on the importance of characterizing materials by* MD *simulation* (S. YIP).

MD results on radiation-induced amorphous structures obtained by RAHMAN and LIMOGE [4] are presented. Emphasis is given to the problem of definition and the characterization of the defects in an amorphous system. Results of neutron scattering experiment in solid benzene at $T = 10$ K are compared with MD simulations by ANDERSON *et al.*

BERENDSEN. I thought that understanding was the main point rather than characterization of materials.

ABRAHAM. Are long-range correlations in solids a difficulty for simulations? What are the ranges in space and time necessary to study solid-state properties? One should characterize them precisely.

YIP. 30 Å for space ranges and 400 ps for time are usually enough.

PONTIKIS. It depends on what you are interested in. The self-diffusion coefficient for surface or grain boundary diffusion can be calculated to a good accuracy with a MD trajectory of 10 000 steps.

HOOVER. To prevent crystallization of the amorphous solid did you use the technique suggested by HANSEN, putting the system on a 4D sphere?

YIP. No.

GIOVANNELLA. Can the amorphous state be clearly identified?

YIP. There are some problems: the $S(k)$ shows large values (20 as opposed to 2) still in the amorphous state. Some local order persists in the amorphous state. Experimentally, on the diffraction diagrams, one observes well-defined spots within the ring patterns typical of the amorphous state.

6) *Presentation of recent work* [5] *on high-strain-rate plastic flow* (W. G. HOOVER).

The mechanisms for plastic flow depend on the scale of the model. At a microscopic level single-atom displacements account for deformations as dislocations predominate at the mesoscopic scale. The results obtained compare favourably with experiment. It is suggested that the future of such computer simulations lies in the combination of MD simulations with macroscopic finite-element calculations.

ABRAHAM. Can you define a dislocation by using just two atoms?

HOOVER. Obviously this is not possible.

ABRAHAM. Can you deduce the form of the interaction between dislocations?

HOOVER. Yes. We fitted the elastic-theory results to various configurations of 2, 3, 4 ... sets of dislocations as described in ref. [5*c*].

ABRAHAM. Did you apply this to the 2D melting problem?

HOOVER. No. By then your own work had already settled that problem.

HEYES. How large is the yield stress?

HOOVER. For an individual dislocation the value is a few percent of the shear modulus, but it is substantially reduced due to the co-operative behavior of many dislocations.

ABRAHAM. Are the results sensitive to the potential?

HOOVER. EVANS obtained similar results using an inverse 12th power potential.

PONTIKIS. Your logarithmic stress *vs.* strain rate plots are linear, while in general one finds experimentally a nonlinear region also.

HOOVER. In the plot I showed strain rates larger than 10^5. These are in a linear region. For smaller strain rates one would observe a very different behavior, creep, which is not so rate sensitive.

7) *Comments on the feasibility of producing new materials with prescribed properties using the computer, of replacing experiment by simulations and of predicting their properties at high pressure, temperature or under irradiation* (H. BERENDSEN).

The importance of MD simulations in pharmaceutical, medical and chemical industrial applications has been underlined. MD techniques can and are actually used in drug and vaccine design, and to investigate the properties of enzymes as industrial catalysts. This would be in the near future a valuable approach to study the structural stability of these molecules in different solvents, as a function of temperature and in different *p*H solutions. Emphasis was given to the difficulties one encounters in this area due to the lack of experimental data, the need of good potential functions and the poor performances of the actual computers (dedicated machines enhanced by a factor 100 are needed).

ABRAHAM. For molecular beam epitaxy (MBE), this approach seems close to feasible and it would be very useful.

HEYES. Are the times necessary for the simulation of such systems (reactions with enzymes) prohibitively long? Isn't this a problem?

BERENDSEN. What is really playing the dominant role is the structural conformation of the active site; this can be produced and studied by 100 ps MD simulation.

CACCAMO. Do you think really that a reliable description of the phenomena you mentioned will be possible using computer simulation in a near future?

BERENDSEN. I would be surprised if in 10 years this will not be possible!

8) MD *simulations in modeling electrolyte behavior, liquid-liquid extraction, corrosion, oxidation and catalysis* (P. TURQ).

The main problem here is the model one has to use for the solvent (water, CH_3CN, etc.). Discrete solvent models lead to long computations and, therefore, one uses preferentially, when possible, continuous rather than discrete models. MD simulations are necessary for the study of dynamic properties while the integral-equation approach (HNC) leads to good results for the static ones.

9) MD *simulation of water in minerals* (G. B. SUFFRITTI).

Some minerals contain water molecules which can move within microscopic layers in the structure (layer silicates) or along channels (zeolites). Due to the interest of such materials for mineralogy, chemistry and Earth sciences their study has been undertaken by MD simulations.

The results give a detailed description of quasi-free cation motion surrounded by water molecules within silicate layers [6]. Work is in progress to obtain information on IR spectra, transport and structural properties.

Similar calculations have been performed for water in a natural zeolite (natrolite) [7].

REFERENCES

[1] G. De Lorenzi, G. Jacucci and V. Pontikis: *Surf. Sci.*, **116**, 391 (1982).
[2] V. Rosato, G. Ciccotti and V. Pontikis: *Phys. Rev. B*, **33**, 1860 (1986).
[3] G. Ciccotti, M. Guillope and V. Pontikis: *Phys. Rev. B*, **27**, 5576 (1983).
[4] Y. Limoge and A. Rahman: unpublished work.
[5] *a*) W. G. Hoover, A. J. C. Ladd and B. Moran: *Phys. Rev. Lett.*, **48**, 1818 (1982); *b*) A. J. C. Ladd and W. G. Hoover: *Phys. Rev. B*, **26**, 5469 (1982); *c*) A. J. C. Ladd and W. G. Hoover: *Phys. Rev. B*, **28**, 1756 (1983).
[6] P. Demontis, E. S. Fois, A. Gamba, B. Manunza and G. B. Suffritti: *J. Mol. Struct.*, **93**, 245 (1983).
[7] P. Demontis, G. B. Suffritti, A. Alberti, S. Quartieri, E. S. Fois and A. Gamba: submitted to *Phys. Rev. B* (July 1985).

Part VII

QUANTUM PROBLEMS AND NEW COMPUTERS

The Simulation of Liquid Helium.

D. M. CEPERLEY

Lawrence Livermore National Laboratory - Livermore, CA 94550

1. – Introduction.

I am going to discuss a somewhat different topic than the main focus of this school, namely simulation methods for quantum-mechanical systems at finite temperatures. Recently it has been shown that static properties of some quantum systems can be obtained by simulation in a straightforward manner using path integrals, albeit with an order of magnitude more computing effort needed than for the corresponding classical systems. Some dynamical information can be gleaned from these simulations as will be discussed below. But this is very limited—there is no quantum version of the molecular-dynamics method.

The path integral method will be illustrated by discussing the application to liquid helium. This system was chosen because, firstly, the interaction potential between helium atoms is well understood, at least for temperatures of less than 10^4 K and pressures of less than 1 Mbar. Thus one can make an unambiguous comparison with the wealth of thermodynamic and scattering properties which have been measured. The Aziz [1] potential (HFDHE2) between all pairs of helium atoms was assumed. This is a short-ranged interaction and so only a minimum number of atoms are needed in the simulation to calculate most of the properties of bulk helium. Secondly, there has been a great deal of theoretical work on liquid helium. The picture directly related to the simulation method is that of Feynman [2]. Also there are simulation results at zero temperature [3] with which to compare. Finally there are still many interesting unresolved questions: the detailed form of the momentum distribution, the details of exchange in crystal helium 3, the form of the interface between liquid and solid helium. However, the simulations of liquid helium were primarily undertaken to establish confidence in the path integral method, to show that one can indeed obtain exact results at finite temperature for a strongly interacting quantum many-body system. Then one can proceed on to more complex and less understood systems.

2. – The density matrix.

Let us first review some of the basic properties of the density matrix, that operator which is needed to calculate any property of a quantum system at finite temperature. In operator notation the density matrix is $\exp[-\beta H]$, where $\beta = 1/kT$, T is the temperature and H is the Hamiltonian. Any observable O is obtained as

$$\langle O\rangle = \mathrm{tr}\,[O\exp[-\beta H]]/\mathrm{tr}\,[\exp[-\beta H]]\,. \tag{2.1}$$

If one can simulate the density matrix, that is sample co-ordinates R and R' (R refers to a point in the $3N$-dimensional co-ordinate space) for the density $\langle R\exp[-\beta H]R'\rangle$, then one can calculate any static property just as with classical systems. The brackets mean just to evaluate the density matrix between those points. The full density matrix in co-ordinate space is a function of $6N$ variables. The diagonal part of the density matrix is obtained when $R = R'$. Scalar properties such as the radial distribution function and the potential energy are determined only by the diagonal elements of the density matrix. Simulations off the diagonal are necessary to determine the momentum distribution.

One can obtain the density matrix at low temperatures by inserting a complete set of eigenstates $\varphi_n(R)$ with eigenvalues E_n:

$$\langle R\exp[-\beta H]R'\rangle = \sum_{n=1}^{\infty}\varphi_n^*(R)\exp[-\beta E_n]\varphi_n(R')\,. \tag{2.2}$$

Thus on the diagonal at low temperatures the density matrix goes to the square of the ground-state wave function.

On the other hand, at a sufficiently high temperature, the kinetic- and potential-energy operators can be allowed to commute and the density matrix can be evaluated as

$$\langle R\exp[-\beta H]R'\rangle = \langle R\exp[-\beta T]R'\rangle\exp[-\beta/2\{V(R)+V(R')\}]\,. \tag{2.3}$$

The first factor on the right-hand side is the density matrix for an ideal gas and has the explicit form of a Gaussian in $R - R'$:

$$\langle R\exp[-\beta T]R'\rangle = (4\pi D\beta)^{-3N/2}\exp[-(R-R')^2/4D\beta]\,, \tag{2.4}$$

where $D = \hbar^2/2m$. At high temperature the density matrix goes to the classical Boltzmann distribution, times a factor which keeps R and R' close and has the form of a harmonic spring potential. The spring constant gets tighter

and tighter as the temperature is increased. The thermal wavelength, equal to $(2D\beta)^{\frac{1}{2}}$, gives the spatial extent of quantum effects.

In order to simulate helium at low temperatures one uses the simple properties of an exponential operator:

$$\langle R_0 \exp[-\beta H] R_M\rangle = \langle R_0 \exp[-\tau H] R_1\rangle \langle \ldots \rangle \langle R_{M-1} \exp[-\tau H] R_M\rangle , \tag{2.5}$$

where the intermediate co-ordinates $R_1, \ldots, R_{M-1}$ are to be integrated over and $\tau = \beta/M$. Then, if M is large enough, one can use eq. (2.3) for the density matrix although in practice it is necessary to improve that approximation as will be discussed shortly. Equation (2.5) is the basis of the path integral method. One simply considers the expression on the right-hand side as a « classical » distribution to be sampled and $R_1, \ldots, R_{M-1}$ have an equal footing with R_0 and R_M. For the calculation of scalar observables, such as the potential energy, the diagonal part of the density matrix is needed and thus $R_0 = R_M$. Thus there are $3N \times M$ co-ordinates to sample instead of just $3N$ for a classical Monte Carlo simulation.

Such a « classical » distribution is very much like a system of N ring polymers at a temperature $T \times M$, made up from M « monomers ». The subscripts identify the monomer, they are also referred to as time slices (really imaginary time). Only monomers at the same time interact with each other with the potential $\tau V(r_{ij})$.

The other picture, due to FEYNMAN [1] and KAC [4], is of a random walk or path integral. If we take the limit as $M \to \infty$ of eq. (2.5), then the kinetic-energy operators describe a random walk starting at R_0, and ending at R_M and lasting a time β. The density matrix is equal to the average over all such walks of the free-particle density matrix times the exponential of the integrated potential along that walk:

$$\langle R_0 \exp[-\beta H] R_M\rangle = \langle R_0 \exp[-\beta T] R_M\rangle \overline{\left\langle \exp\left[-\int_0^\infty \mathrm{d}t \sum_{i<j} V(r_{ij}(t))\right]\right\rangle} . \tag{2.6}$$

The efficiency of the simulation will depend on the value of τ for which one can write down a good form for the density matrix. It turns out for helium the simple classical form of eq. (2.3) will be accurate enough only if $\tau < 0.001/\mathrm{K}$. This means for simulations in superfluid helium at 2 K that each polymer will have 500 monomers, which is very inefficient. One can do much better by solving the two-atom problem exactly and obtaining a pair product form [5] for the density matrix by assuming the average of the products in eq. (2.6) is equal to the product of the averages:

$$\langle R_0 \exp[-\beta H] R_M\rangle = \langle R_0 \exp[-\beta T] R_M\rangle \prod_{i<j} \overline{\left\langle \exp\left[-\int_0^\infty \mathrm{d}t V(r_{ij}(t))\right]\right\rangle} . \tag{2.7}$$

The error in this density matrix comes only from three- and higher-body scattering. It has been found that this pair product density matrix is sufficiently accurate for $\tau < 0.025/\mathrm{K}$ which leads to a substantially more efficient algorithm than one based on the semi-classical density matrix. The tabulation of the pair density matrices at a variety of temperatures is carried out by specialized numerical techniques [5].

The boson density matrix is defined by restricting the sum in eq. (2.2) to be only over fully symmetric states and can be obtained from the density matrix for distinguishable particles by symmetrizing with respect to particle co-ordinates

$$\langle R \exp[-\beta H] R' \rangle_{\text{boson}} = \sum_P \langle PR \exp[-\beta H] R' \rangle / N! \tag{2.8}$$

since all eigenfunctions which are not fully symmetric will disappear. In our classical analogy, the polymers can become cross-linked. To calculate properties on the diagonal, the random walks no longer must return to their starting places but to any other walk's starting place. It is like the game of musical chairs. The superfluid transition is driven by this indistinguishability which serves to connect superfluid helium macroscopically just as jello changes phase when it cools and its molecules cross-link. The transition happens when the thermal wavelength becomes approximately equal to the interparticle spacing. The task of the Monte Carlo algorithm is then plain, it is to effectively sample this combined space $\{R^{3NM} P_N\}$, where P_N is the permutation group. That is to sample all energetically favorable polymers and all the cross-linked possibilities.

3. – The Monte Carlo method.

The Metropolis algorithm [6] is almost universally used to evaluate ratios of integrals as in eq. (2.1). Let $\Pi(s)$ be the normalized distribution in eqs. (2.5)-(2.8), where s refers to all of the $3N \times M \times P$ co-ordinates. The Metropolis algorithm samples by setting up a Markov chain with the detailed-balance property

$$\Pi(s) P(s \to s') = \Pi(s') P(s' \to s) , \tag{3.1}$$

where P is the probability of making a transition from one state to another. A trial move to a nearby point s' is made based on some assumed probability function $\hat{P}(s')$. Then the trial move is accepted with probability equal to

$$a = \min\{1, \Pi(s') \hat{P}(s) / \Pi(s) \hat{P}(s')\} \tag{3.2}$$

which will guarantee that eq. (3.1) is obeyed for $P = a\hat{P}$. The algorithm is guaranteed to converge to Π, but the convergence time is governed by the

transition probabilities and it can be very slow, particularly for this type of distribution. After all, relaxation times for real polymers can be seconds, or days.

Now a naive scheme, taken over directly from the simulation of classical liquids, would be simply to take $\hat{P}$ uniform about s within a cube for only one monomer. While that would be effective for nearly classical systems, it would be excruciatingly slow at low temperatures, assuming M is large. The reason is that the springs from the nearby links of the polymer constrain any one link, so that motion of the ring as a whole would be very slow. For bosons one must make permutation moves as well as spatial moves, and those necessarily involve moving many links of at least 2 atoms together with the permutation move. In other words, an efficient algorithm for quantum systems at low temperatures must involve moving simultaneously many monomers.

The results to be discussed here were obtained by moving the co-ordinates of from 1 to 4 atoms in 4 to 8 time slices together with a permutation move to be discussed next. Now the conditional probability distribution of a point R, at time t, part way through a random walk of length t, which begins at R_1 and ends at R_2, is given by the conditional distribution

$$f(R) = \langle R_1 \exp[-tH]R\rangle \langle R \exp[-(\beta - t)H]R_2\rangle / \langle R_1 \exp[-\beta H]R_2\rangle \,. \tag{3.3}$$

Note that the integral over R of f is unity, so it is a probability distribution from which points R can be sampled. One can approximate f sufficiently accurately so that many co-ordinates may be sampled together with a high acceptance probability. But this means that an expression is needed for the density matrix, not just at the high temperature τ, but all the way down to the temperature appropriate to the size of moves to be made, which will equal something like twice the lambda temperature or 4 K, if permutation moves are to be accepted. However, only the density matrix at time τ will affect the converged results, the lower-temperature density matrices will affect only the rate of convergence of the random walk and hence the error bars. For the ideal gas, $f(R)$ is a Gaussian, one whose center moves in a straight line from R_1 to R_2, and whose width slowly spreads at the beginning of the walk and then contracts. Turning on the interaction in addition makes the regions where two monomers overlap forbidden. It is convenient to approximate f by a multivariate Gaussian (one with cross-correlations) since a Gaussian can be rapidly sampled. Again such an approximation only affects the error bars on the final answers, not the limiting results.

The basic principles of sampling permutations are the same as those for sampling spatial moves except permutations are in discrete space, not in continuous space. Again the move is constrained to be a local one. The new trial permutation is obtained from the old permutation by applying a pair, triplet, or quadruplet permutation, for example $P' = p_{ij}P$, where p_{ij} is a pair permu-

tation of particles i and j. There is some evidence that pair permutations are energetically not favored and the Markov chain converges faster if triplet and quadruplet moves are permitted. A new permutation connecting points R_1 and R_2 a time t apart is sampled with a frequency proportional to

$$\langle R_1 \exp[-tH] p_{ij} P R_2 \rangle \,. \tag{3.4}$$

Co-ordinate moves follow up on that permutation move. Until the co-ordinate moves are made, it is not known whether that permutation move will be accepted. Details will be given elsewhere [7].

4. – Results.

Figure 1 shows the energy *vs.* temperature for liquid helium in the low-temperature region at saturated-vapor pressure. The solid curve gives the experimental results [8], the crosses the Monte Carlo ones with error bars of about 0.10 K, for a run of about 1 h on the CRAY-1. The Bose statistics have

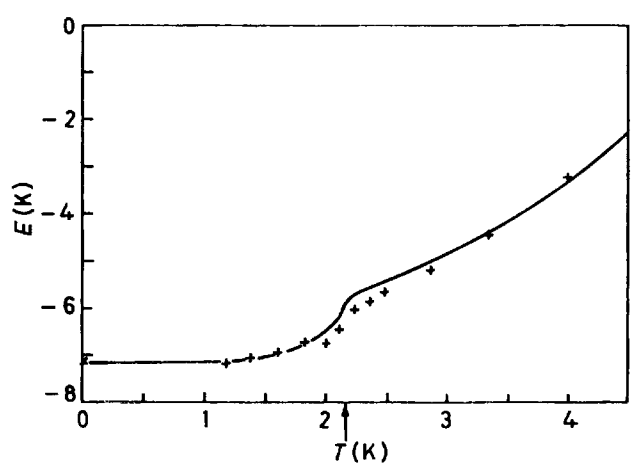

Fig. 1. – The internal energy in K/atom *vs.* the temperature at saturated-vapor pressure. The solid line is the experimental result [8]. The crosses are the results of the path integral Monte Carlo simulation with error bars of about 0.1 K. The × at zero temperature is the Green's function Monte Carlo result [3].

very little quantitative effect on the energy, less than 1 K. The point at zero temperature is the Green's function Monte Carlo result [3]. Except in the immediate vicinity of the transition, the path integral Monte Carlo results are accurate to 0.2 K, but lying systematically lower than the experimental results in the transition region. All of the simulations are performed with 64 atoms in periodic boundary conditions. There is numerical evidence that these boundary conditions favor permutations. The transition in the finite

system begins as soon as 2.5 K, whereas the experimental transition temperature is 2.17 K.

The comparison of the calculated specific heat with experiment at SVP is shown in fig. 2. The Monte Carlo results are obtained by taking finite differences of fig. 1. Thus the error bars are much larger. The results from using a fluctuation formula would have even larger error bars.

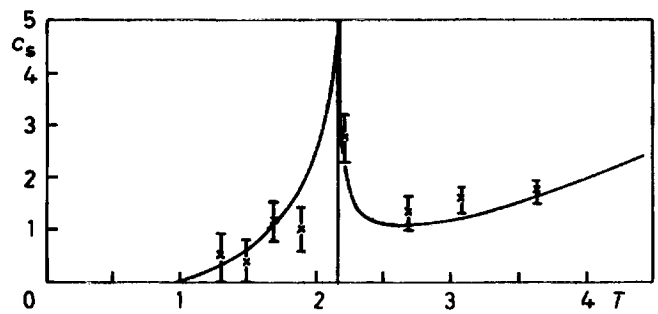

Fig. 2. – The specific heat per atom *vs.* the temperature. The curve is the experimental result [8]. The crosses with error bars are the finite differences of the Monte Carlo energies in fig. 1.

Figure 3 shows the pair correlation function at 2.08 K as obtained from X-ray scattering [9] at SVP, compared with the simulation results. They agree very well. Also shown is the effect of using Boltzmann statistics in the Monte Carlo calculation. This is obtained by not allowing permutation moves and increases the order in the liquid, raising the peak of the pair correlation

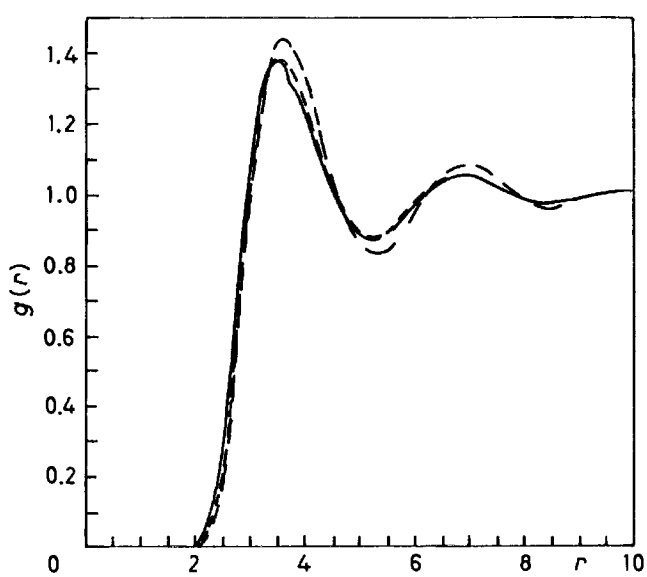

Fig. 3. – The pair correlation function for liquid helium at 2 K and SVP. The solid line is the X-ray scattering result [9]. The two dashed lines are the simulation results for bosons and for distinguishable atoms. The boson curve is the one lying very close to the experimental one.

function by 5%. There is similar agreement with scattering data at other densities and temperatures.

Although we have frequently referred to time slices, the simulation is actually in imaginary time, not real time. Nevertheless there is time-dependent information contained in the « dynamics » of these paths although it is smeared out because the motion is diffusive and not wavelike. Consider the dynamical structure factor $S(Q, w)$, measured by neutron scattering [10] and shown in fig. 4 at 1.2 K, for two wave vectors. There is a very large narrow peak cor-

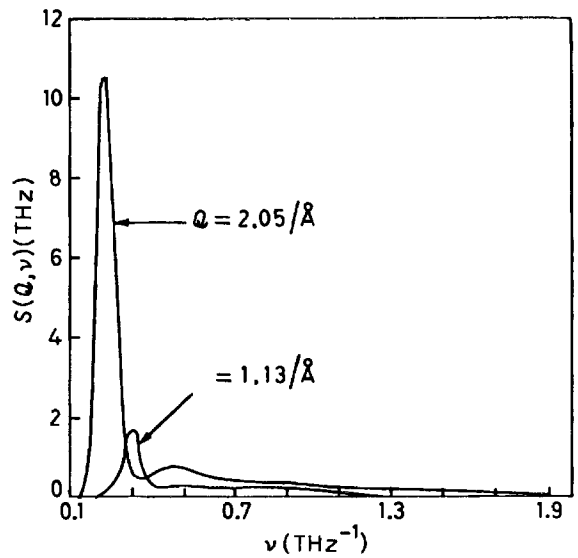

Fig. 4. – The dynamical structure factor at 1.2 K and SVP as measured by neutron scattering [10] for the two values of momentum transfer shown.

responding to single-phonon excitations, and a much broader multiphonon peak. Now in quantum Monte Carlo one can compute the imaginary-time density autocorrelation function

$$F(Q, t) = \mathrm{tr}\,[\varrho_Q \exp[-tH]\varrho_{-Q} \exp[-(\beta - t)H]]/\mathrm{tr}\,[\exp[-tH]]\,, \tag{4.1}$$

where

$$\varrho_Q = \sum_{i=1}^{N} \exp[-i\boldsymbol{Q}\boldsymbol{r}_i]/\sqrt{N}\,. \tag{4.2}$$

It can be shown by writing both $F(Q, t)$ and $S(Q, w)$ in their eigenfunction expansions that F is the Laplace transform of S:

$$F(Q, t) = \int_{-\infty}^{\infty} \mathrm{d}w \exp[-wt]S(Q, w)\,. \tag{4.3}$$

Inverse Laplace transforms are essentially impossible to perform with noisy

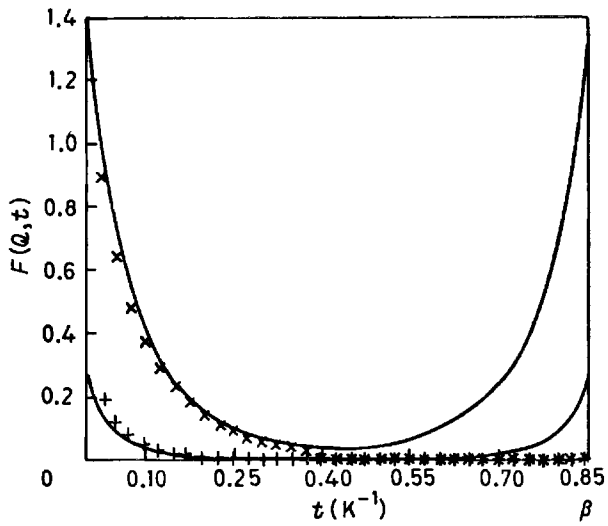

Fig. 5. – The Laplace transform of the experimental dynamical structure factor (× and +) in fig. 4 as compared with that calculated with path integral Monte Carlo (solid lines) for two values of momentum transfer.

data, thus we cannot go from F to S. The information has simply been lost with the Laplace transform. One could perform an inversion of F by assuming a functional form for $S(Q, w)$ with perhaps four unknown parameters, and using the values for $F(Q, t)$ to determine those parameters. It is very difficult to obtain more time-dependent information than this from the imaginary-time

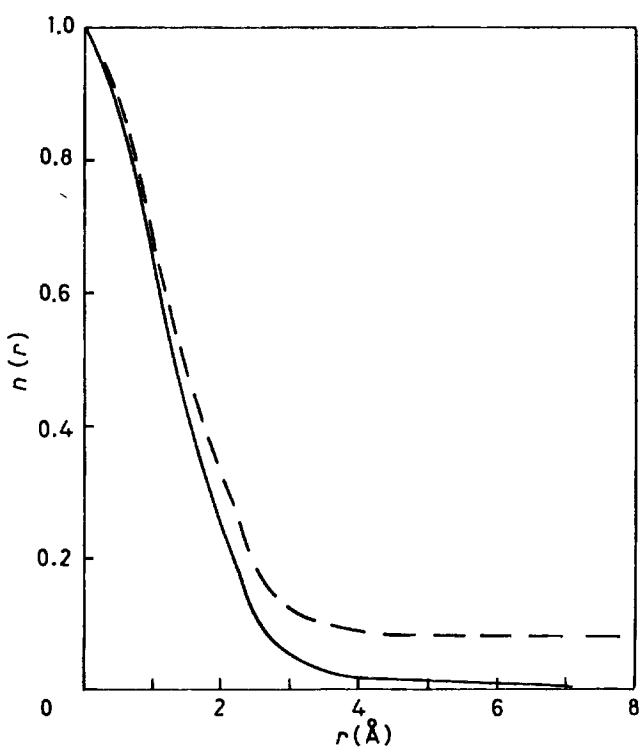

Fig. 6. – The single-particle density matrix at 2.86 K (solid line) and at 1.0 K (dashed line).

simulations. Since the experimental data are available, we can Laplace transform them and compare with the Monte Carlo results in imaginary time. This is done in fig. 5 with the data from fig. 4. The agreement is rather good both at this temperature and others where complete experimental data are available. The curves do differ at large values of t, because the experiments have not covered a wide enough range of energy transfers. The function F must be symmetric about $\beta/2$, and the Monte Carlo results are by definition.

The momentum distribution is of great interest since it is believed that many of the singular transport properties result from a finite fraction of the particles condensing into the zero-momentum state. Let $n(\boldsymbol{Q})$ be the probability of observing an atom with momentum $\boldsymbol{Q}$. It can be easily shown [11] that the Fourier transform of the momentum distribution is equal to the single-particle off-diagonal density matrix. Let

$$n(\boldsymbol{r}) = \int \mathrm{d}\boldsymbol{Q} \exp[i\boldsymbol{Q}\boldsymbol{r}] n(\boldsymbol{Q}) . \tag{4.4}$$

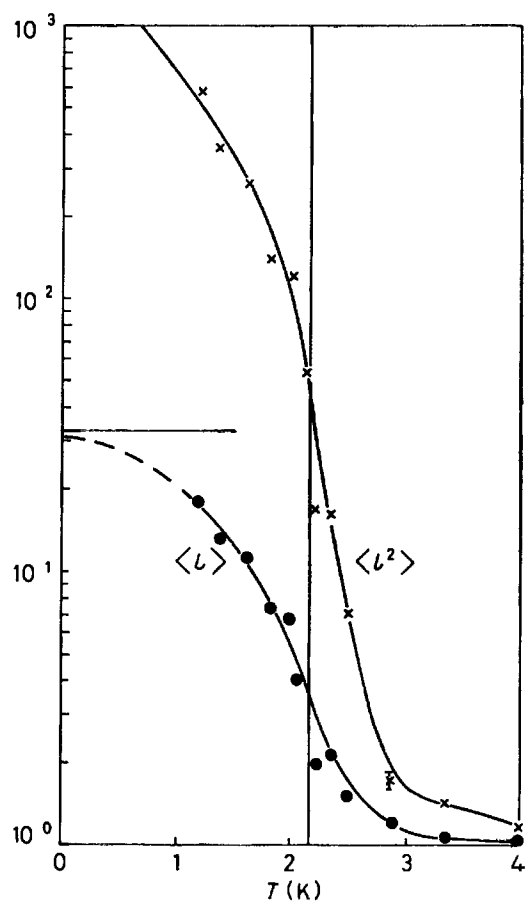

Fig. 7. – The average cycle length and squared cycle length of a permutation *vs.* the temperature at SVP. The vertical line at 2.17 K is the experimental transition temperature. For a random permutation of length N the average cycle length is $N/2$, marked for $N = 64$.

Then $n(\boldsymbol{r})$ is obtained as

$$(4.5) \qquad n(\boldsymbol{r}) = \mathrm{tr}\,[\boldsymbol{r}_1, \boldsymbol{r}_2, \ldots, \exp[-\beta H]\boldsymbol{r}_1 + \boldsymbol{r}, \boldsymbol{r}_2, \ldots]/\mathrm{tr}\,[\exp[-\beta H]]\,,$$

where $\boldsymbol{r}_i$ is the co-ordinate of atom i. Atom 1 is off the diagonal, it does not return to its starting place but to a point $\boldsymbol{r}$ displaced. In the polymer analogy, $n(\boldsymbol{r})$ is obtained by cutting one of the polymers, and measuring the resulting end-to-end distribution. The polymers can still cross-link and this is responsible for momentum condensation. By adding other polymers into the middle of the one linear polymer, the ends can become arbitrarily far apart. Otherwise they would be restricted to a distance on the order of a thermal wavelength. End-to-end distributions computed in this way at 2.9 K and 1.0 K are shown in fig. 6. The curves fall off to a constant value apparently by 5 A. This constant value is the number of particles which have exactly zero momentum, since the Fourier transform of a constant function n_0 is $n_0\delta(Q)$. The calculations are in agreement with experiment [12] giving a condensate at low temperatures

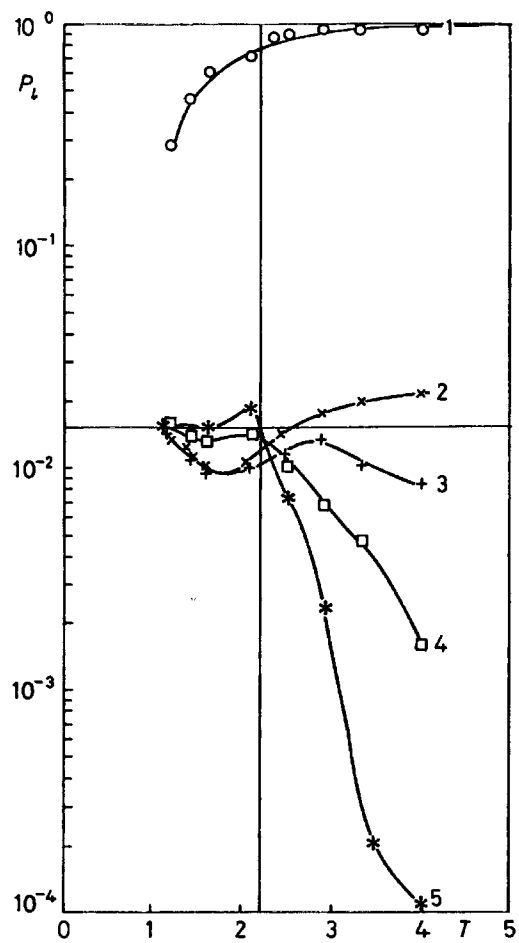

Fig. 8. – The distribution of cycles of length 1 to 5 as a function of temperature at SVP. The horizontal line shows the value expected for a random permutation of length 64.

of about 9 %, but in this case the Monte Carlo results are more accurate than the experiment, since measuring the momentum distribution by neutron scattering is extremely difficult.

Statistics on the distribution of various permutation cycle lengths and of the mean and the mean squared cycle length are given in fig. 7, 8. They show a rapid rise in the number of longer permutations between 2.5 K and 2.0 K, and then a saturation to the value appropriate to a random permutation below that temperature. In a random permutation all cycle lengths are equally probable. At 2.25 K cycles of lengths 2, 3, 4 and 5 have approximately the same probability which is perhaps the clearest indication that the transition is occurring there.

* * *

E. L. POLLOCK has collaborated with the author on the work reported here. Work performed under the auspices of the U.S. Department of Energy by the Lawrence Livermore National Laboratory under contract number W-7405-ENG-48.

REFERENCES

[1] R. A. AZIZ, V. P. S. NAIN, J. S. CARLEY, W. L. TAYLOR and G. T. MCCONVILLE: *J. Chem. Phys.*, **70**, 4330 (1979).
[2] R. P. FEYNMAN: *Statistical Mechanics* (Benjamin, Reading, Mass., 1972).
[3] M. H. KALOS, M. A. LEE, P. A. WHITLOCK and G. V. CHESTER: *Phys. Rev. B*, **24**, 115 (1981).
[4] M. KAC: *Probability and Related Topics in Physical Science* (Interscience, New York, N. Y., 1959), p. 165.
[5] E. L. POLLOCK and D. M. CEPERLEY: *Phys. Rev. B*, **30**, 2555 (1984).
[6] N. METROPOLIS, A. W. ROSENBLUTH, M. N. ROSENBLUTH, A. H. TELLER and E. TELLER: *J. Chem. Phys.*, **21**, 1087 (1953).
[7] D. M. CEPERLEY and E. L. POLLOCK: *Phys. Rev. Lett.*, **56**, 351 (1986).
[8] R. K. CRAWFORD: in *Rare Gas Solids*, Vol. II, edited by M. L. KLEIN and J. A. VENABLES (Academic Press, New York, N. Y., 1977), p. 663.
[9] H. N. ROBKOFF and R. B. HALLOCK: *Phys. Rev. B*, **24**, 159 (1981).
[10] E. C. SVENSSON, P. MARTEL, V. F. SEARS and A. D. WOODS: *Can. J. Phys.*, **54**, 2178 (1976).
[11] O, PENROSE and L. ONSAGER: *Phys. Rev.*, **104**, 576 (1956).
[12] V. F. SEARS, E. C. SVENSSON, P. MARTEL and A. D. B. WOODS: *Phys. Rev. Lett.*, **49**, 279 (1982).

A Numerical Approach to the Theory of Strong Interactions.

E. MARINARI

Dipartimento di Fisica, Università di Roma II (Tor Vergata)
Via Orazio Raimondo - 00173 *La Romanina (Roma), Italia*

1. – Introduction.

Lattice gauge theories [1] (LGT in the following) were introduced some years ago, and high-energy physics theoreticians immediately started getting useful results from this tool. LGT are borrowing much from statistical mechanics, and also from molecular dynamics. A talk about such a subject at the « Molecular Dynamics Simulation ... » School is an important one, since we really need to borrow new effective methods and algorithms, and we also hope to be able to give back some useful new ideas.

I will give here a very sketchy introduction to the subject, and try to communicate a bit of my interest. Understanding strong interactions is a fundamental step in trying to reconstruct the scheme of fundamental forces. Perturbation theory is not enough to succeed in such a goal, and one has to apply nonperturbative techniques, new for the high-energy physics.

Symmetries are the basic guide one uses in developing a description of fundamental forces. Gauge symmetries are the centre of the whole. The possibility of interpreting a gauge theory as a statistical mechanics is the new point, allowing an interchange of methods and techniques.

In sect. **2** I will underscore the importance of the gauge invariance (and its predictive power) already at the classical level. In sect. **3** I will underline the Feynman path integral formulation. In sect. **4** I will give some basic information about quantum chromodynamics (QCD). In sect. **6** I will define the lattice theory, and in sect. **5** I will explain what the continuum limit (the limit we are interested in) is. In sect. **7** I will illustrate the numerical methods one uses, and in sect. **8** I will define the correspondence between physical (interesting) observables and lattice operators. In sect. **9** I will discuss the problem of the statistical and systematic errors.

Reference [2] is a reprint collection, containing pioneering papers about the subject (mainly in the period 1974-1982). Reference [3] is a very detailed

and interesting review (1982). Reference [4] is a review mainly dedicated to the fermion problem (hadronic mass spectrum computation), while ref. [5] describes simulation algorithms and studies errors.

2. – The role of gauge invariance.

I want to underscore the essential role of gauge invariance in defining the form of the equations one needs in order to describe a given physical phenomenon. Symmetries play a central role in building up the theories of fundamental interactions. The importance of symmetry principles is stronger at the quantum level, but already at the classical level one can see how symmetry constraints minimize the number of free parameters of a theory. A theory with few inputs is exactly what one likes, getting in this way a large predictive power.

Let us start by the simple example of Maxwell equations, recalling what the property of gauge invariance is. Then, at the Lagrangian level, I will explain how the invariance properties fix the form of the motion equations.

Maxwell equations (with obvious notation) read

$$\nabla\cdot\boldsymbol{D} = 4\pi\varrho\,, \tag{2.1a}$$

$$\nabla\times\boldsymbol{H} = (4\pi/c)\boldsymbol{J} + (1/c)\frac{\partial\boldsymbol{D}}{\partial t}\,, \tag{2.1b}$$

$$\nabla\cdot\boldsymbol{B} = 0\,, \tag{2.1c}$$

$$\nabla\times\boldsymbol{E} + (1/c)\frac{\partial\boldsymbol{B}}{\partial t} = 0\,. \tag{2.1d}$$

From (2.1*c*)

$$\boldsymbol{B} = \nabla\times\boldsymbol{A}\,, \tag{2.2}$$

introducing the *vector potential* $\boldsymbol{A}$. Now (2.1*d*) reads

$$\nabla\times\left(\boldsymbol{E} + (1/c)\frac{\partial\boldsymbol{A}}{\partial t}\right) = 0\,, \tag{2.3}$$

and we can write the expression in brackets as minus the gradient of a *scalar potential* φ

$$\boldsymbol{E} = -\nabla\varphi - (1/c)\frac{\partial\boldsymbol{A}}{\partial t}\,. \tag{2.4}$$

$\boldsymbol{B}$ is invariant under the transformation

$$\boldsymbol{A} \to \boldsymbol{A}' = \boldsymbol{A} + \nabla\Lambda\,, \tag{2.5}$$

and in order to leave $\boldsymbol{E}$ invariant one has to transform

$$\varphi \to \varphi' = \varphi - (1/c)\frac{\partial \Lambda}{\partial t}\,. \tag{2.6}$$

This is a *local symmetry*, since Λ is a function of the point $\boldsymbol{x}$. The transformation (2.5), (2.6) does not affect the physics. All the following will be based on the idea of trying to describe fundamental interactions between elementary particles starting from invariance principles.

In order to explain our second point, we have to switch to the Lagrangian level. The equation of motion of a charged particle subject to an electromagnetic force

$$m\ddot{\boldsymbol{x}} = Q(\boldsymbol{E} + (\boldsymbol{v}/c)\times\boldsymbol{H}) \tag{2.7}$$

is obtained from the Lagrangian

$$\mathscr{L} = (m/2)\dot{\boldsymbol{x}}^2 + Q\big((\boldsymbol{v}/c)\cdot\boldsymbol{A}(\boldsymbol{x}, t) - q(\boldsymbol{x}, t)\big) = \mathscr{L}_0 + Q\mathscr{L}'\,, \tag{2.8}$$

where Q is the particle charge. Now the following theorem holds.

Let the motion of a particle be given by the Lagrangian

$$\mathscr{L}(q^i, \dot{q}^i, t;\, \boldsymbol{A}, \varphi)\,. \tag{2.9}$$

If one requires equations of motion invariant under gauge transformations, then necessarily

$$\mathscr{L} = \mathscr{L}_0 - Q(\varphi - \dot{q}^k A^k)\,. \tag{2.10}$$

The Lagrangian (2.8) is the most general form compatible with gauge invariance. The only free parameter left is Q, the particle charge. This is what is called the « minimal electromagnetic interaction ».

This is the kind of procedure one uses in order to define a so-called gauge theory, that is a theory based on a local invariance of the type of (2.5) and (2.6).

The construction of a gauge theory is analogous in the quantum case. A local invariance dictates, also in this case, the form of the interaction. By using as a premise the hypothesis that the fundamental fields transform under a given group, we will get definite Lagrangians. Different groups (different gauge theories, we will say) will give different Lagrangians, that turn out to describe different experimental phenomena. For example, in the Dirac equation, the case of electromagnetism,

$$(i\partial_\mu\gamma^\mu - eA_\mu\gamma^\mu - m)\psi = 0\,, \tag{2.11}$$

if ψ is a solution in the electromagnetic potential $A_\mu(x)$, then

$$\psi' = \exp\,[ie\alpha(x)]\,\psi \tag{2.12}$$

will be a solution in the gauge transformed potential

$$A'_\mu = A_\mu - \partial_\mu \alpha(x)\,. \tag{2.13}$$

In this case one gets a U_1 invariance (just a phase factor). A transformation of the wave function ψ by a x-dependent phase factor does not affect physics, and can be reabsorbed by a gauge transformation.

Some comments about the status of the understanding of fundamental interactions are in order. The electromagnetic interaction is well described by a simple gauge theory, in complete agreement with the present experimental knowledge. The unification with the weak interactions is achieved, and a gauge theory of electroweak interactions works very well. The most striking and beautiful success of such a theory has been given from the discovery of the Z^0 and $W^\pm$ particles at CERN, last year. Strong interactions are the most difficult part. The SU_3 gauge theory of strong interactions (see below) is in very good shape, but one needs to work out more predictions, that at the moment are hidden in the theory. That is what we are going to do, by using statistical mechanics, molecular dynamics and fast computers.

3. – Path integral quantization.

The basic tool one uses in order to write down a quantized field theory is the Feynman path integral [6]. I present here an introductory discussion of such a procedure, and of the way to make the path integral well defined, *i.e.* to discretize it. This is the first bridge between classical statistical mechanics and quantum mechanics.

One defines the quantum-mechanical amplitude for a particle going from x_i to x_f as

$$K(x_f, x_i) = \sum_{\text{paths}} \exp\,[iS_{cl}/\hbar]\,, \tag{3.1}$$

where S_{cl} is the classical action, and the sum runs over all possible paths of a particle going from the point x_i at the time $t = 0$ to x_f at the time t. In terms of the usual quantum-mechanical bras and kets K would be written as

$$\langle x_f, t_f | x_i, t_i \rangle\,.$$

An operative definition of such a sum can be given by going to imaginary

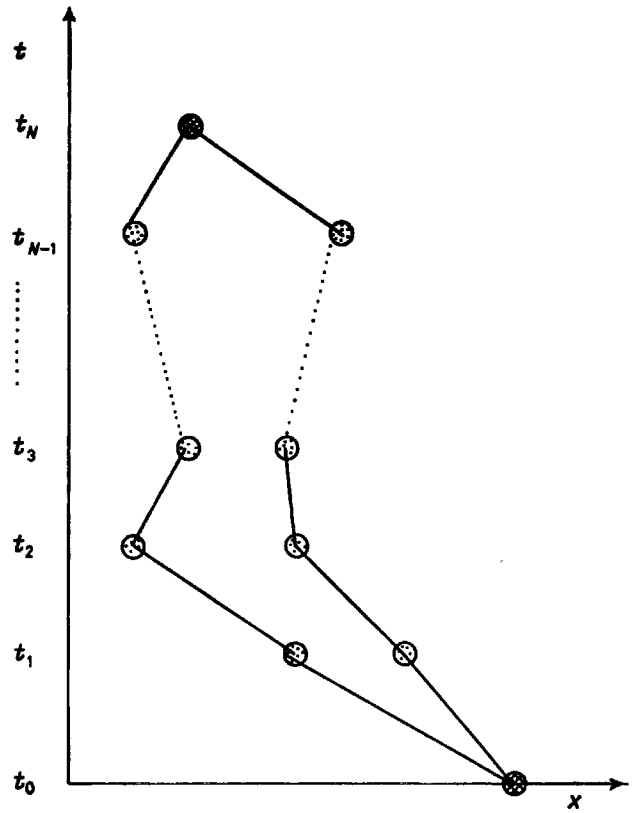

Fig. 3.1. – Discretization of the path integral.

time (in order to make the exponential behaviour decaying at large times), and by making the time discrete. First we go to imaginary time, by setting

$$t \to -it\,. \tag{3.2}$$

Now, following fig. 3.1,

$$t_{j+1} - t_j = \varepsilon\,, \tag{3.3}$$

$$x(t_j) \equiv x_j\,, \qquad \text{with } x(t_i) = x_0\,, \qquad x(t_f) = x_N \text{ fixed}\,, \tag{3.4}$$

$$K(x_f, x_i) \sim \int_{-\infty}^{+\infty} \left(\prod_{j=1}^{N-1} \mathrm{d}x_j\right) \exp\left[-S(x)/\hbar\right]\,, \tag{3.5}$$

where the limit $\varepsilon \to 0$ (small time steps) is understood. By discretizing the time we have transformed

$$S_{\text{continuum}} = \int_0^\tau \mathrm{d}\tau \left[(m_0/2)\left(\frac{\mathrm{d}x}{\mathrm{d}t}\right)^2 + V(x)\right] \tag{3.6}$$

into

$$S_{\text{lattice}} = \sum_{j=1}^{N} a[(m_0/2)(x_{j+1} - x_j)^2/a^2 + V(x_j)]\,, \tag{3.7}$$

where $a = i\varepsilon$.

To deepen our analogy with statistical mechanics we can define

$$Z = \int \mathrm{d}x_i \, \mathrm{d}x_f \, \delta(x_f - x_i) K(x_f, x_i) \tag{3.8}$$

to be the trace of the density matrix. We have a statistical mechanics with a Boltzmann factor

$$\exp[-S(x)/\hbar], \tag{3.9}$$

with the identification

$$\beta \equiv 1/\hbar . \tag{3.10}$$

The $\hbar \to 0$ limit selects classical physics (fluctuations are completely eliminated). We can compute quantum-mechanical expectation values by computing expectation values in the statistical mechanics we have defined.

4. – Quantum chromodynamics.

Consider the basic points about strong interactions. We know that hadrons are composed from constituents (*quarks*), 3 for baryons and 2 for mesons. Quarks, that are seen in experiments as constituents of the hadrons, are *confined*, *i.e.* they are permanently bound inside hadrons. Quarks move « freely » at short distances.

The SU_3 gauge theory (called colour invariance, and SU_3 is simply the group of unitary 3 times 3 complex matrices with determinant equal plus one) is capable in principle of explaining these facts. It is a quantum field theory of quarks (matter fields) and gluons (corresponding to the photon of the familiar electrodynamics), mediating the interaction. Baryons are constituted of 3 quarks of different colours, mesons from a quark and an antiquark. « Asymptotic freedom » (see ref. [3] for a detailed explanation) should guarantee the correct (and unusual) behaviour at short and long distances described in the former paragraph (one can look at it as to an antiscreening, *i.e.* the effective charge becoming weaker at shorter distances). The SU_3 field indices (the new degrees of freedom) are called *colour quantum numbers*. Colour is a new quantum number, absolutely conserved, like electric charge.

The Lagrangian (written in terms of the fundamental fields A and ψ) reads

$$\mathscr{L} = -\tfrac{1}{4} F^a_{\mu\nu} F^{a\mu\nu} - \sum_f \{ i\bar{\psi}^{if} \gamma_\mu D^{ij\mu} \psi^{jf} + m\bar{\psi}^{if} \psi^{if} \} , \tag{4.1}$$

where the ψ, $\bar{\psi}$ are quark matter fields, f is a flavour index (there are different copies of quarks: up, down, strange, ...), $F^a_{\mu\nu}$ is the gauge kinetic term (the action for the self-interacting gluonic fields, containing the simple free term

analogous to the one of electrodynamics and the constraint due to the gauge group),

$$F^a_{\mu\nu} \equiv \partial_\mu A^a_\nu - \partial_\nu A^a_\mu - g f^{abc} A^b_\mu A^c_\nu , \tag{4.2}$$

with f^{abc} being some given numbers, the structure constants of the gauge group (this is the added term). Moreover,

$$D^{ij}_\mu = \delta^{ij}\partial_\mu - igA^a_\mu T^{ij}_a , \tag{4.3}$$

where the T^{ij}_a are the group generators. The substitution we are doing in eq. (4.3) (the normal derivative ∂_μ is substituted by a covariant one) is analogous to the one we did in eq. (2.11) for electrodynamics.

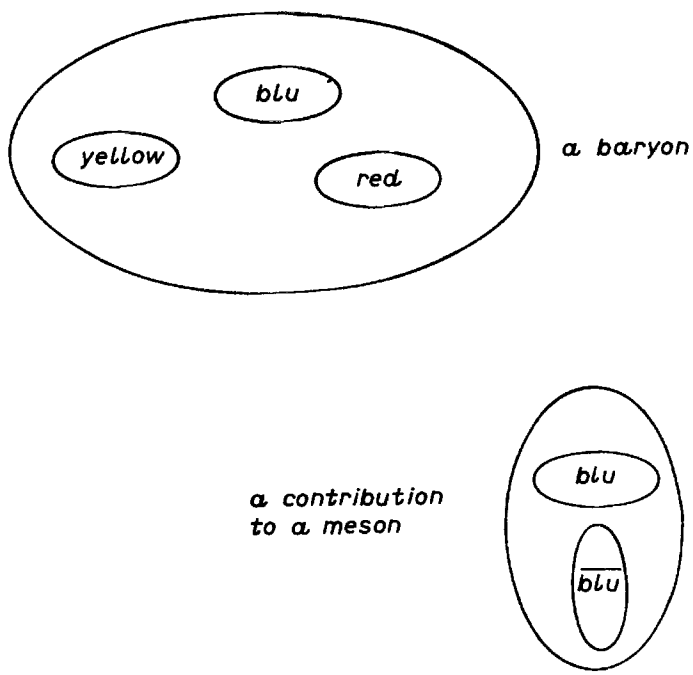

Fig. 4.1. – A baryon, made from 3 quarks in different colours, and a meson, made from a quark and an antiquark.

Using the path integral formulation, we can define now the quantized theory, given by the integration over all possible values of the fermionic and gauge fields. One will follow the same procedure used in order to build quantum mechanics, starting from the Lagrangian, getting the action and eventually constructing a partition function.

5. – Renormalization group and continuum limit.

Renormalization group (RG) is the key needed to extract physics from a theory such the one we are describing (strong-interaction physics). We will try to

compute masses of the particles (the energy of the bound state of 2 or 3 quarks), scattering lengths, etc. WILSON first established the crucial point that the physics one will get in such a theory just depends upon the *form* of the interaction (the fact that we have chosen SU_3 and not another group of invariance), and not upon minor details such as the values of the parameters (the coupling constant g) in the Lagrangian. There is just one single free parameter one has to fix, the scale of the theory (the definition of eV, more or less). Everything else is fixed.

Thanks to RG we know indeed how does the theory behave as a function of the coupling constant in the physically interesting zone.

Starting with different bare coupling constants (bare just means the parameter you put in your Lagrangian, or in your computer) g will give, if the g's are in the physically relevant region (*scaling region*), equivalent results, but for a rescaling you can compute from perturbation theory around $g = 0$ (asymptotic freedom implies this is the relevant limit for the short-distance regime, the relevant one in order to study bound states). Let us define

$$\beta \equiv 6/g^2 , \tag{5.1}$$

that is indeed the « inverse temperature » of the statistical mechanics defined from the path integral of (4.1). It has nothing to do with the physical temperature. The factor 6 is not very important. Now, as we said, we know from perturbation theory that, when varying β, as we do in a numerical experiment, any physical quantity (a mass, let us say) will behave as

$$m_{\text{computed}}(\beta) = m_{\text{physical}} \exp\left[-\beta A\right] (1/\beta)^B . \tag{5.2}$$

We know A and B from perturbation theory, but we need a computer if we want to compute by extrapolation m_{physical} (the interesting physical mass). The behaviour in β is known, and we will just have to check that g is small enough to reproduce the exponential behaviour given in (5.2). We will measure in this way the masses m_{physical} of different particles, or interparticle potentials, etc. (corresponding to different operators, some of which we will define in the following). One will be used in order to fix the unknown scale (that cannot be computed in the frame of the theory), and the other ones will be the outputs of the computation. They should match the ones existing in Nature.

Now we need a definition of the theory suitable for numerical studies. Following WILSON we will discretize the theory on a lattice, preserving gauge invariance in an exact manner and recovering the continuum theory in the physical limit ($g^2 \to 0$). In the next section we will end up with a lattice-model-like theory.

6. – The lattice theory.

Our goal is to discretize the theory. We are going to find a lattice theory that in the $g^2 \to 0$ limit will tend to the continuum one. The first role of the discretization is giving us a proper definition of the theory itself, in the same way we did with path integrals. Discretization will remove the unphysical infinities of the theory, and give « quantities » easy to handle on a computer.

It is very crucial to preserve the basic symmetries of the continuum theory in the lattice version. This is a serious problem in the fermion case, and the way to proceed is not yet completely understood [2-5, 7]. In our case the basic invariance is gauge invariance. In ref. [1] a lattice action preserving gauge invariance for all values of the lattice spacing a was proposed. This is just the simplest one of an infinite class of lattice actions with the good invariance properties one can write, and we are going to describe it in the following.

We write down in the following a simple action (something like a lattice model, as we said, but variables are not defined on sites but on links, and they are not constrained to be 1 or -1, but 3 times 3 complex matrices) which tends in the limit of interest to the continuum action implicitly defined in sect. **4**. All relevant quantities can be formulated in terms of the variables of the discrete theory, and computed numerically. Complexities of the continuum action can then be forgotten, and the theory of strong interactions can be thought in terms of the four-dimensional lattice with matrix variables we are going to define.

Let us recall, since it will be useful in the following, that the SU_3 group is represented from the 3 times 3 complex matrices U, obeying

$$U^\dagger U = \mathbf{1}\,,$$

$$\det(U) = +1\,.$$

One considers a 4-dimensional hypercubic lattice (of spacing a), and the matrices (see fig. 6.1)

$$U_\mu^{ab}(n) \in SU_3\,, \tag{6.1}$$

defined on the lattice links. Here a and b label the two « colour indices » of the 3 by 3 matrix (and they run from 1 to 3), n is the set of 4 labels (n_x, n_y, n_z, n_t) specifying a site, and μ is one of the 4 possible directions (3 spatial directions and the time one). n and μ, that is one site and one direction, specify a link. On a 4-dimensional lattice there are 4 links per site. The Dirac fields

$$\psi_\alpha^a(n) \tag{6.2}$$

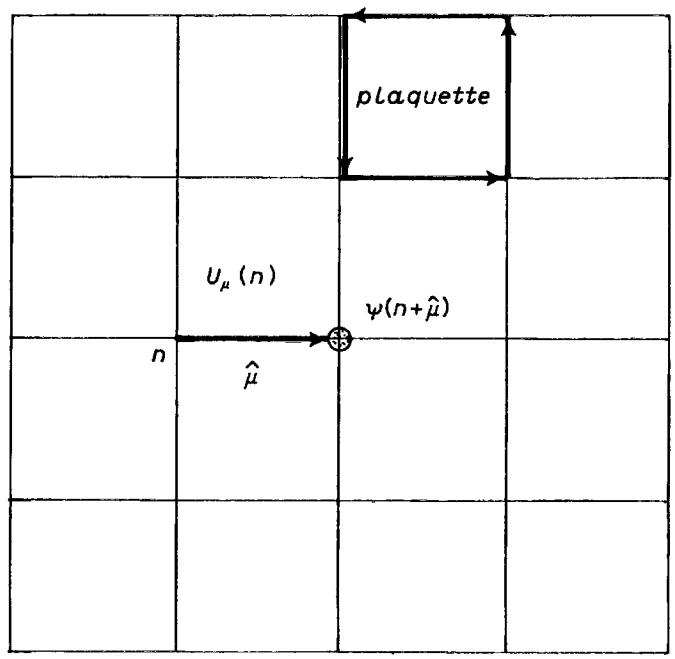

Fig. 6.1. – A $d = 2$ lattice. $U_\mu(n)$ is a gauge field (on the link joining the site n and the site $n + \hat{\mu}$). $\psi(n + \hat{\mu})$ is a fermionic matter field (on the site $n + \hat{\mu}$).

($a = 1, 2, 3$, α is the Dirac index, n the site label: in the following we will often drop the indices) are defined on sites.

In such a theory one can show that (see ref. [1]) the ordered products of the matrices found along a closed path are gauge invariant. The basic quantity of the theory is the product of matrices over the smallest possible closed path (a *plaquette*, see fig. 6.1):

$$U_p \equiv U_\mu(n)\, U_\nu(n + \hat{\mu})\, U_\mu^\dagger(n + \hat{\nu})\, U_\nu^\dagger(n)\,. \tag{6.3}$$

WILSON [1] defined the action as

$$S_{\text{lattice}} = c \sum_{\text{plaquettes}} (\text{Tr}\, U_p + \text{Tr}\, U_p^\dagger)\,. \tag{6.4}$$

The sum runs over all the squares with a side of one link that are on the finite lattice. Let me explain better the recipe. Consider a lattice with matrices defined on the links of the lattice. Consider an elementary square, that will be naturally associated to 4 of such matrices. Multiply, following (6.3), these 4 matrices in the correct order. You will get a matrix we called U_p. Take the trace. Do it for all the elementary circuits of the lattice. Sum all the contributions. This is the action of the configuration you are considering. It can be shown that in the continuum limit (the lattice spacing $a \to 0$) one recovers

$$S_{\text{lattice}} \to S = -\tfrac{1}{4}\int \mathrm{d}^4x\, F^a_{\mu\nu} F^{a\mu\nu}\,, \tag{6.5}$$

that is the pure gauge part of the action (4.1), since the group variables U are identified as

$$U_\mu(n) = \exp\,[igaA^a_\mu T^a]\,, \tag{6.6}$$

where g is the coupling constant and the T's are the group generators.

In the following we will just discuss the pure gauge part of the theory (eqs. (6.4) and (6.5)). The most part of the numerical simulations done up to now just consider this part.

Let us sum it up. We have defined a lattice theory, governed by the action (6.4), and we want to study it in the continuum limit. This theory is a 4-dimensional statistical mechanics, and we will be interested in computing expectation values of the field operators and correlation functions corresponding to physical observables. A dictionary of translations (see table 6.I) links the lattice operators to the continuum observables.

TABLE 6.I.

Continuum theory	Lattice theory
observables, that is gauge-invariant operators	closed Wilson loops
q-q potential	Wilson loop expectation values
glueball masses	correlation functions of Wilson loops
confinement deconfining transition	Polyakov loop behaviour
fermionic mass spectrum	fermionic lattice correlation function

7. – Numerical methods.

We will have to compute expectation values of the form

$$\langle\theta\rangle = \int[\prod \mathrm{d}U]\exp[-S\beta]\,\theta/[\prod \mathrm{d}U]\exp[-S\beta]\,, \tag{7.1}$$

where $\mathrm{d}U$ is the Haar measure over SU_3 (the invariant measure over the group, see ref. [2] for specific examples), and the products run over all the links of the lattice. We will better do the job by using an appropriate dynamics with the correct equilibrium properties, and computing

$$\langle\theta\rangle = \bar{\theta} \equiv \sum_i \theta_i(\{U_i\})/\sum_i \{1\}\,. \tag{7.2}$$

Here $\{U_i\}$ stands for (the i-th) configuration of U matrices distributed according to $\exp[-\beta S]$. Let us recall that our action is

$$S = \sum_{\text{plaquettes}} \mathrm{Re\,Tr}\, U_p\,. \tag{7.3}$$

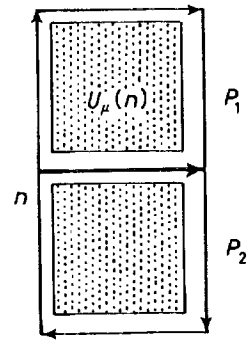

Fig. 7.1. – The contribution of a given link gauge field $U_\mu(n)$ to the action S. P_1 and P_2 are the two plaquettes containing $U_\mu(n)$.

The contribution of the field $U_\mu(n)$ to the action (in the 2-d case) is shown in fig. 7.1. We will update the $\{U\}$ configuration to the $\{U'\}$ one by using some suitable algorithm. We will illustrate here the *Metropolis algorithm*. We want to update the field $U_\mu(n)$. We pick up an SU_3 random matrix U_R, and compute

$$U_\mu^{\text{trial}}(n) = U_R \cdot U_\mu(n) \,. \tag{7.4}$$

We compute now the variation of the action due to substituting $U_\mu \to U_\mu^{\text{trial}}$,

$$\Delta S \equiv S' - S \,. \tag{7.5}$$

If $\Delta S < 0$, then we set $U' = U^{\text{trial}}$. Otherwise we pick up the random number x, uniformly distributed in the interval $(0, 1)$. If $\exp[-\Delta S] > x$, then we accept the update ($U'_\mu = U_\mu^{\text{trial}}$), else we reject it ($U'_\mu = U_\mu$). This dynamics reconstructs the Boltzmann distribution, proportional to $\exp[-\beta S]$.

8. – Observables and results.

We already said that physical observables (gauge-invariant operators) correspond to closed loops:

$$W(C) = \mathrm{Tr}\Big\{\prod_c U(n)\Big\} . \tag{8.1}$$

We call such a path a *Wilson loop* (see fig. 8.1). All the continuum observables will be represented, on the lattice, by products of matrices lying on closed paths. We will be computing

1) Wilson loop expectation values,

2) correlations between Wilson loops.

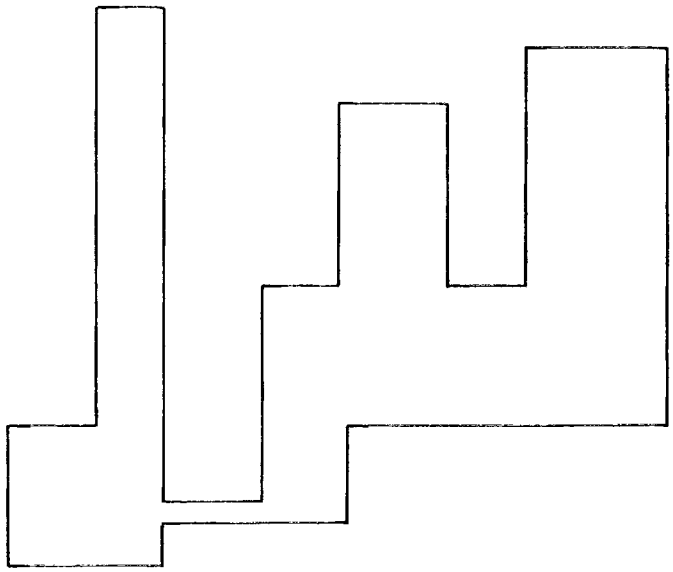

Fig. 8.1. – A (typical) Wilson loop.

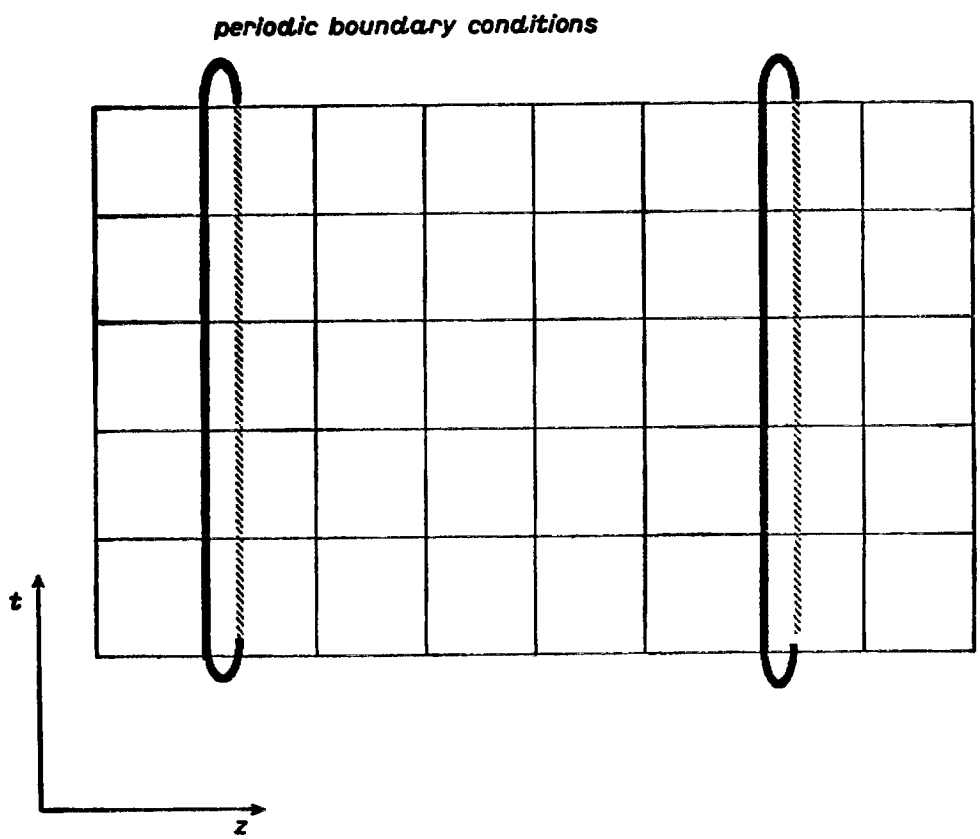

Fig. 8.2. – Correlation function between two Polyakov loops.

Let us say that, when selecting the correct quantum number,

$$\langle\theta(0)\,\theta(t)\rangle_c \xrightarrow[t\to\infty]{} \exp[-tm] + \dots . \tag{8.2}$$

Here t is the Euclidean time, one of the 4 dimensions of our lattice.

The time asymptotic behaviour of the connected part of the correlation function selects the smallest mass in the considered channel.

One crucial problem, as I already said, is the *confinement*. We want to decide if the theory describes a confined world or not. Do quarks of QCD move freely? That would be in contradiction with real world, and would discard QCD as a realistic theory.

In the respect one considers the so-called Polyakov loops (extended in the Euclidean time direction, and closed thanks to the periodic boundary conditions), and computes their connected correlation function (see fig. 8.2). We have that

$$\langle P(0)\,P(z)\rangle \underset{\substack{N_t\to\infty\\ z\to\infty}}{\sim} \exp[-KzN_t] \quad \text{(for confined quarks)}, \tag{8.3a}$$

$$\langle P(0)\,P(z)\rangle \sim \text{const} \quad \text{(for free quarks)}. \tag{8.3b}$$

Another problem is the one of the deconfining transition. If one considers an $N^3\cdot T$ lattice, in the limit of a large, fixed, finite T, $N\to\infty$, one gets a field configuration at a finite physical temperature (that has nothing to do with β,

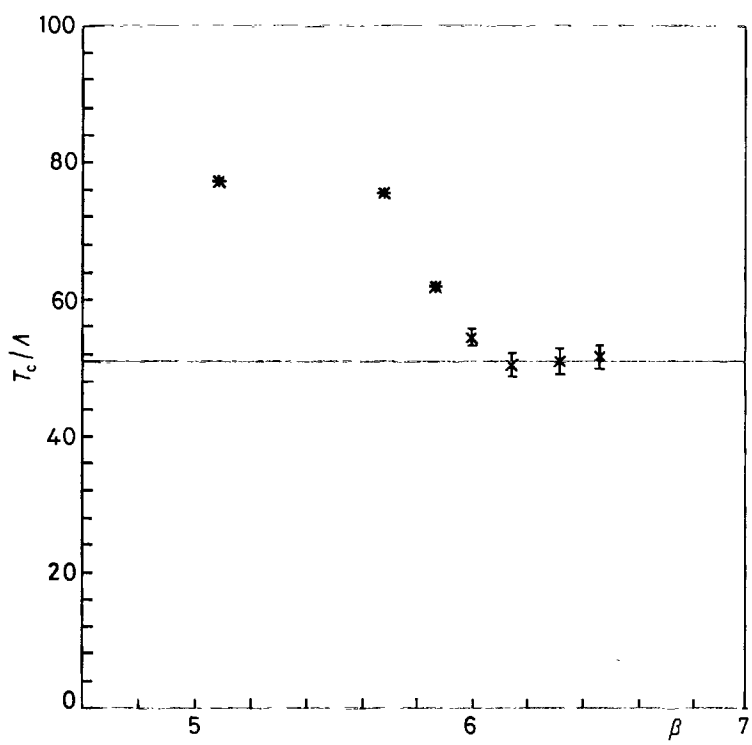

Fig. 8.3. – The deconfinement temperature over the square root of the string tension *vs.* β, from ref. [8].

the inverse temperature of the statistical mechanical theory). In this way one can monitor an expected phase transition and its order. The Polyakov loop acquires in this case a nonzero expectation value.

In fig. 8.3 I show a scaling picture of the deconfinement temperature, and in fig. 8.4 that of the QCD q-$\bar{q}$ potential *vs.* the q-$\bar{q}$ pair distance. These figures

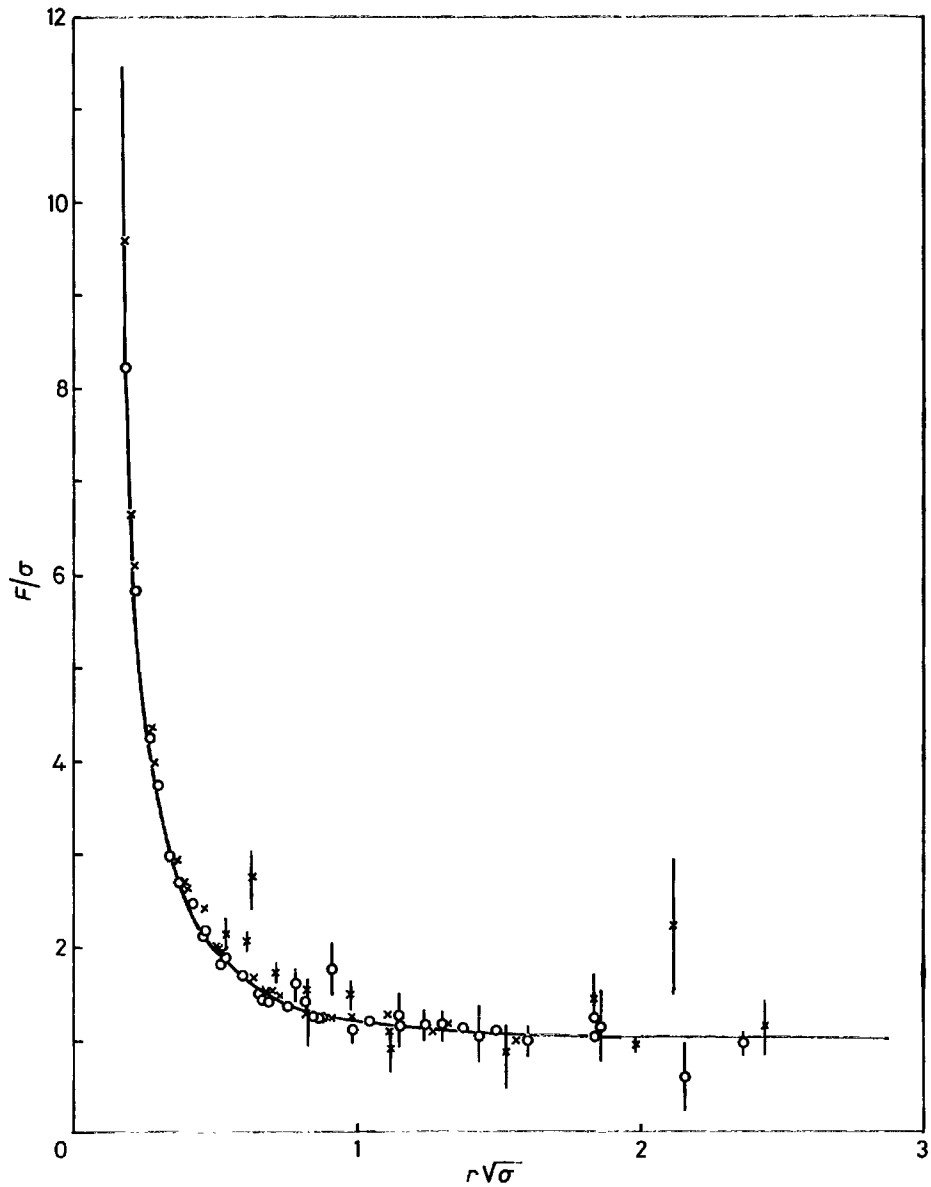

Fig. 8.4. – The q-$\bar{q}$ potential *vs.* the distance between q and $\bar{q}$ (in physical scale), from ref. [9].

are in physical units, and a continuum behaviour (see (5.2)) means that a plot *vs.* β should match with a horizontal line.

At last (for the pure gauge case) we recall the case of the computation of the *glueball masses*, a bound state that should exist in the theory.

For example, for the simplest possible state, we will use (8.1) for the

operator

$$\langle \{ \sum_{\text{plane}} \operatorname{Tr} U_p (t=0) \} \{ \sum_{\text{plane}} \operatorname{Tr} U_p (t) \} \rangle . \tag{8.4}$$

This is a difficult computation, since one needs measuring an exponentially small correlation function (at large time, in order to eliminate the unwanted contamination from the excited states) from a sum of numbers of order one ($\operatorname{Tr} U_p$). Many possible improvements to standard techniques have been suggested, some coming directly from the molecular-dynamics tradition (difference technique and source methods) and from statistical mechanics (for example, see ref. [5]).

9. – Statistical and systematic error.

The problem of the errors in such numerical computations is discussed in large detail in ref. [5]. I give here a short list of the main points.

Consider the *statistical error*. When we update a field configuration

$$\{U\} \to \{U'\} , \tag{9.1}$$

we can naively measure a « standard deviation » error on the observables. But one has to account also for the correlation between different measurements (corrected error). An algorithm can be more of less effective, but there will be a memory from the former configurations.

A second point is that the critical slowing-down one encounters when $\beta \to \infty$, implying that the correlation length $\xi \to \infty$ (since the $g = 0$ limit is a critical point of the theory, with diverging correlation length), makes the situation potentially difficult to control. There is a relevant danger of the system falling into metastable states, that could highly bias the estimated error.

The *systematic error* is very difficult to be estimated in a correct way (for example, a good control of the fitting procedures is essential). On a finite $N^3 \cdot T$ lattice one encounters two problems different in nature. Firstly a small volume size (N^3) can influence the measurement. Putting a proton in a too small box one will change its energy. Secondly a short time T can let excited states to survive. Problems of this kind in the pioneering simulations are becoming nowadays evident.

* * *

I wish to thank G. P. F. Ciccotti for the very fruitful discussions we had while I was preparing this text.

REFERENCES

[1] K. G. WILSON: *Phys. Rev. D*, **10**, 2445 (1974).
[2] C. REBBI, Editor: *Lattice Gauge Theories and Monte Carlo Simulations* (World Scientific Publishing, Singapore, 1983).
[3] J. B. KOGUT: in *Recent Advances in Field Theory and Statistical Mechanics*, edited by J. B. ZUBER and R. STORA (North-Holland, Amsterdam, 1984), p. 1.
[4] E. MARINARI: *Acta Phys. Pol. B*, **15**, 291 (1984), 23rd Cracow School, Zakopane.
[5] G. PARISI: *A Short Introduction to Numerical Simulations of Lattice Gauge Theories*, Cargese Summer School, 1984, to be published.
[6] R. P. FEYNMAN and A. R. HIBBS: *Quantum Mechanics and Path Integrals* (McGraw-Hill, New York, N. Y., 1965).
[7] H. B. NIELSEN and H. NINOMIYA: *Nucl. Phys. B*, **185**, 20 (1981).
[8] S. A. GOTTLIEB *et al.*: UCSD preprint (1985); S. MEYER: in the proceedings of the conference *High Energy Physics 1985* (Bari, July 1985).
[9] D. BARKAI, K. J. M. MORIARTY and C. REBBI: *Phys. Rev. D*, **30**, 2201 (1984).

Round-Table: Perspectives in Computations.

Chairman: Carl MOSER

Secretary: Richard LE SAR

New Computers for Molecular Dynamics.

C. MOSER

C.E.C.A.M., Université Paris-Sud - 91405 *Orsay, France*

In most cases, theoretical studies in physics use *models*. That is to say, the scientist develops an *ad hoc* mathematical framework to try to understand a particular physical phenomenon. The mathematical framework so devised may be further simplified so that an analytical solution is possible or it may be that only numerical solutions exist, in which case some use of computers may be necessary. Even so, in many cases, a few hours on a minicomputer like a VAX would be sufficient.

I suppose it would be justified to put most molecular-dynamics (MD) calculations in the category of *simulations* in that there is a general mathematical framework (or, more precisely, there are general mathematical frameworks) that we can write down, which we believe are the fundamental equations which govern the physics but are independent of the system and which, in principle, describe all observable thermodynamic properties. This picture of classical mechanical MD calculations is, of course, highly idealized; some aspects of modelization are frequently included in the calculations.

In principle, accurate quantum-mechanical simulations would give the same results as accurate experiments. In most practical cases, today when we talk about accurate measurements of some observable we refer to experiments. Perhaps one should have as one's goal to reserve elaborate MD calculations for « accurate » knowledge not easily obtainable from experiment.

If we wish to *simulate* the thermodynamic properties of physical systems, then there are three essential ingredients:

a) We must know the fundamental laws of physics which govern the time evolution of the physical system in question.

b) We must know with considerable accuracy the potential between the particles which make up the system. This potential, in principle, may be calculated from « first principles », but more often it takes an empirical form with some quantitative criteria providing the value of the parameters.

c) We must have *sufficient* particles in our systems to represent adequately the physical system. As thermodynamic properties are macroscopic observables, the number of particles which are *sufficient* is very much a function of the property and particular part of the phase diagram we wish to study. This is a complex problem which is usually simplified by imposing periodic boundary conditions (pbc). Often pbc are physically justified, but, as one becomes interested in more complex phenomena, then there may arise situations where pbc must be abandoned.

If pbc are not suitable for a given problem, then the number of particles in the system has to be considerably increased.

For long-range forces the computing time per step is proportional to N^2, where N is the number of particles in the system. To reduce computing needs one often does not compute all N^2 interactions but only some fraction of them which are less distant than an arbitrary cut-off in space from a given atom.

Computing power is needed not only for an adequate number of particles to simulate the system but also for an adequate number of time steps. Roughly speaking, time steps of the order of 10^{-14} s give stable energies. Computing time goes up linearly with the number of steps and the overall need for computing power is proportional to the characteristic time of the different physical phenomena in the problem under study.

If, futher, we wish to study the interaction of the given system with another system, say a liquid interface with a solid, or solute with solvent, etc., then an *adequate* number of particles and an *adequate* number of time steps is that much more consuming of computer power. In these cases the fundamental laws for simulation are not so well understood, so that then there will be much use of models.

For some of the model problems, studied in this school, a big slice of a minicomputer like a VAX or a few hours on a Cray or Cyber 205 super-computer is adequate (assuming a factor of about 50 to 75 between the two levels of computers).

But it is easy to see that, as we wish to carry out simulation for more and more complex problems, one needs the equivalent computing power of hundreds of Vaxs or several super-computers used full time for a given problem. But this power must cost very little, say of the order of a Micro-VAX.

Although it may seem impossible that such price/performance ratios could be available, in fact several laboratories in the world are now busy building computers which will bring all of this into the realm of real possibility.

The speakers at the round-table will be giving some more detailed information.

Computation for molecular dynamics.

BERENDSEN. The advances in molecular-dynamics simulations for studies of soft spheres, which make it possible at present to study systems with up to 1 000 000 degrees of freedom, have become practicable partly because of the increase in computer speed of a factor of 10 every 6 years or so. However, to study such problems as the dynamics of chemical reactions or protein folding would require perhaps 10^7 to 10^9 hours on current super-computers. We would need a quantum jump in computing speed to study such problems instead of the evolutionary increases of the past. Two of the possible ways to arrive at such a jump in speed would be through general-purpose parallel processors or special-purpose computers with the molecular-dynamics algorithm hard-wired into the memory. A computer built in Delft to carry out MD calculations calculates at about 10 times the speed of a Cray for atomic dynamics and costs only $ 30 000 for the hardware. While there will be improvements in parallel general-purpose machines, special-purpose machines will be the key element for spectacular advances in computing power in the future. Computational physicists should take a more active role in the development and use of their own computers; they should design them and make them particularly efficient for their own algorithm. These computers should be highly parallel and limited in applications, but it should be possible to reconfigure their structure. Finally, students must be trained to participate in this design work.

ABRAHAM. The computer is an essential tool in attempting to find solutions to problems. However, computers today are too slow, and they are unlikely to develop the necessary speed for some time to deal with some problems. One approach is to develop specialized computers. One such machine is the SPARK (Scientific Processing Array Kernel), which is a compact, parallel, pipelined processor. There are 128 processors in the array, giving 750 million floating-point operations per second (Mflops). This computer is not restricted to MD as long as the problem can be broken up into arrays.

MARINARI. A group in Rome has started building the APE (Array Processor with Emulator) project to develop a computer designed to do quantum chromodynamics (QCD). The architecture of the machine is designed such that the QCD problem is treated on a four-dimensional lattice. The problem then becomes a 32 times N^4-dimensional integral, calculated with a Monte Carlo integration and an inversion of a sparse $10^6 \times 10^6$ matrix. The essential feature of the architecture of the computer is to set up a simple network of processors with a synchronous controller. The software development includes that for the emulator and the simple, optimized vector compiler. The cost was about $ 300 000 for hardware. The construction time is estimated to be about one and one-half years.

After these three presentations, a discussion session took place.

G. M. VAN WAVEREN. Software development is lagging behind hardware development. For a multipurpose processor, will compilers be less complex and easier to program?

ABRAHAM. No. Historically, architecture drives compiler development, not *vice versa*.

BERENDSEN. I am very pessimistic about the development of software. It lags far behind hardware development. The problem is that a compiler cannot be defined for a general algorithm. If there were algorithm-oriented compilers, then it would be easier. Perhaps a better approach would be a box to hook on without development of a general compiler.

MARINARI. That is not quite true. We need a good compiler for even the small parallel processor we are building. We will put in a lot of effort for the vector part of the compiler.

R. W. IMPEY. To make these special-purpose machines useful to a general set of users will require development of subsidiary software, such as debuggers, editors, etc. It does not seem that those people developing these machines will bother to do this.

ABRAHAM. Like complex experimental equipment, some of these machines will be in only a few places. However, I am optimistic that the special-purpose machines will be general-purpose in that they will not be restricted to a single-type problem.

IMPEY. If there is no software, then they will not be general purpose.

ABRAHAM. The user will have to do more programming. But computer science is in its infancy. Parallelism brings a whole new aspect to the field and it will take a while to evolve.

IMPEY. Is software development a major part of computer manufacture?

ABRAHAM. More money is spent on software development than on hardware.

MOSER. Scientists cannot possibly be asked to solve the problems of generally useful software.

ABRAHAM. If we do not have reasonable software, then this development will fail since no one will use it.

B. PILLER. Most people who do MD use double precision, but the Delft machine is 24 bits and the IBM and APE machines are 32 bits. Do you need only 32-bit precision?

BERENDSEN. It depends on what you do. The « Verlet » algorithm needs more than 32 but the leapfrog is fine with 32 bits.

ABRAHAM. With a 32-bit machine you have to work harder and be more careful. The 64-bit machines are more expensive, but they are coming. People are developing algorithms that require single precision only.

BERENDSEN. Many physicists are not willing to think through the algorithm to make it more efficient.

W. L. MORGAN. I used to run MD calculations on a PDP 11/45 with an attached floating-point array processor and had speeds greater than a 7600. The array processors have improved so much, why not just move to super micros with array processors?

ABRAHAM. That is a pratical way for many people. Megaflop rates will be possible, but if you want gigaflop performance, then they are not enough.

MORGAN. By the time the Cray-2 is on line, the array processors will be at Cray-1 speed. In the future a lot will be gained by using micros and array processors. Since the 7600, nearly all speed gain came from memory speed and vectorization. Although parallel processors are nice, they will get faster linearly with processors. In the meantime, we need movement of software into hardware; *e.g.* hardware scatter/gather on the 205 *vs.* the Cray.

Part VIII

CONCLUSIONS

Synopsis of the School and Final Remarks.

A. BELLEMANS

Department of Physics, Université Libre de Bruxelles
C.P. 223, 1050 *Brussels, Belgium*

I am particularly grateful to the organizers, Giovanni CICCOTTI and Bill HOOVER, for inviting me to this School. Indeed, it is precisely in this same place, in 1957, that, as a young postdoc and a rather innocent bystander at that time, I witnessed the great breakthrough of computer simulations in statistical mechanics, by Berni ALDER and Bill WOOD. Many things have changed during the elapsed twenty-eight years: starting from simple models, *i.e.* hard spheres, Lennard-Jones atomic systems or even crude lattice systems, simulations have progressed tremendously, especially during the last ten years. However, as my direct personal involvement in simulations has decreased in the last couple of years, I feel myself again somewhat in the situation of a bystander, though not as innocent as I was in 1957!

The program of this School, carefully planned as it was by Giovanni CICCOTTI, Bill HOOVER and Paolo GIAQUINTA in order to survey many topics, was obviously very full and most of the speakers (twenty-nine altogether, a new record for Enrico Fermi Schools as I was told by the Administrative Secretary), starting from the educational level, ended their lectures by conveying to the audience the latest information concerning their respective line of research. In this way, a full up-to-date panorama has been given of tools, potentiality and achievements of simulations in statistical mechanics. I shall not attempt to make a systematic summary of the School, as this appears to me as a futile (and probably impossible) exercise, but I shall concentrate on some general problems and selected topics.

Computer simulations, within the field of statistical mechanics, have expanded amazingly since the pioneering work of the mid-fifties. Should we, *e.g.*, look at publications concerned with static and dynamic properties of liquids, then simulations have certainly reached a volume comparable to both theoretical and experimental works. Volume, however, is by no means a good criterion of respectability among the scientific community and the growing recourse to simulations (and numerical work in general), favoured by increasing computer facilities, has been sometimes criticized as endangering « creativity

of the mind ». The label of quality, presently acknowledged by many of our colleagues to simulations, follows essentially from the fact that they have been practised with care and good judgement, and it is, of course, absolutely necessary to continue that way. Hence:

1) We must choose the relevant questions, generated by theory or experiments, and we must provide theoreticians and experimentalists with significant answers, helping them in their future work.

2) Simulations of sophisticated models must aim to provide independent information at the atomic level, which is not available from experimental means.

3) Simulations must, by themselves, disclose new facts and address challenging questions to both theoreticians and experimentalists.

Many examples, given in the lectures, demonstrate that simulations can indeed meet these three requirements and I will briefly remind some of them to you:

Jean-Pierre HANSEN showed how the static and dynamic properties of a plasma (a rather unfamiliar state of matter at the terrestrial level) can be measured through simulations.

Ian MCDONALD, Paul MADDEN and Mike KLEIN showed how the information extracted from the simulations of models of liquids and solids, at various sophistication levels, is complementary to the generally raw experimental data and allows to sort out the different effects or mechanisms which are mixed and hidden in them.

Probably the most important basic fact, discovered by simulations, is the existence of long-time tails for various kinds of correlation functions, which shows that, even for simple liquids, chaos is generally not valid; the molasses tail, discussed by Berni ALDER and also by Robert DORFMAN, still constitutes a challenging problem.

Molecular-dynamics (MD) simulations generate their own theoretical problems, precisely those which theoreticians usually simply dismiss: there is no « infinitely weak coupling » between the system and its neighbourhood in simulations and neither is the system an infinite one! Lectures by Denis EVANS and James DUFTY showed how to tackle such problems.

I will now briefly review the tools specific to simulations, presented in several of the tutorial lectures, and comment on some recent progresses:

1) A standard technique, based upon the introduction of geometrical constraints, is available for simulating all types of polyatomic molecules; as Jean-Paul RYCKAERT explained it, selected kinds of internal modes (stretching,

bending, etc.) can be conveniently frozen, in so far as they are considered as irrelevant to the purpose of the simulation.

2) Periodic boundaries remain an essential ingredient of computer simulations as real walls would disastrously spoil the homogeneity of the system. We happily learned how the long-lived controversy (flourishing in the literature for more than ten years) on how to reconcile long-range (Coulomb) forces with periodicity has recently been resolved.

3) On the other hand, the usual conditions of constant volume and shape of the periodic cell have been relaxed by RAHMAN and PARRINELLO, leading to an extremely useful technique for studying structural phase transitions.

4) Various recipes have also been developed to free MD simulations from the microcanonical EVN ensemble and to generate other ensembles such as HpN or TpN; they fall into three different classes: extended-variable methods, stochastic methods or methods of strict constraints, each of which has its own advantages and defects.

5) As an alternative to the Green-Kubo method for calculating transport coefficients, nonequilibrium molecular-dynamics techniques (NEMD) have been developed: the system is constrained (or perturbed) by an appropriate generalized force and its response is measured. One may distinguish two different approaches:

the subtraction method of Ciccotti, Jacucci and McDonald, where the system is repeatedly weakly perturbed and one deduces transport coefficients by averaging over many responses along its trajectory in phase space;

the « gradient method », where a strong perturbation is applied to the system and its response recorded; careful use of fictitious forces, devised by EVANS, preserves homogeneity of the system, but one has to extrapolate the results to zero gradient.

Most of my comments have been directed towards the MD method, but let me recall that some nice applications of the Monte Carlo method (MC) were presented in Daan Frenkel's lectures and, while alluding to the MC method, let me point out that, in 1957, the very good agreement between MD and MC results for the equation of state of hard spheres was considered as a striking proof of ergodicity. This, of course, is not all the story as Giancarlo BENETTIN showed us and the questions he raised seem sufficiently important for devoting some of our time (and computer time) to them.

Last but not least of our tools, there is the computer itself. My own feeling, before the round-table chaired by Carl MOSER took place, was that not very many of us really care about it, as long it stands there, big, fast and accessible. The round-table has not altered this feeling very much. Obviously, in order to take full advantage of the new generation of computers, programs must be

rebuilt and sometimes different algorithms used, but the interest of most of us in software appears rather marginal and strictly special-purpose computers, built by their own users, will remain scarce, at least in the forthcoming years.

What about the future of computer simulations? I believe that the lecture of Sidney YIP and the round-table on material science, chaired by Vassili PONTIKIS, were highly significant: MD simulations have reached the point of touching the macroscopic level, *e.g.* to tackle a real polycrystal with its defects (and not just a single monocrystal). This means that we shall soon be able to attract a new class of customers, the engineering community. In a similar way, the drug industry will also become involved as drug conception may obviously get hints from simulations.

Yet, one should not be over-optimistic as there are still a few worrying points. The first one is the *size* of the systems which can be mimicked on computers. More than 10^4 degrees of freedom had to be considered by Herman BERENDSEN for modelling a protein in water and, in some of his simulations of noble gases adsorbed on graphite, Farid ABRAHAM included more than 10^5 atoms. With such a number, it seems that simulations could successfully cope with the static properties of the critical region, which would be a major achievement. More than size, the problem is *time* limitation, when one considers the dynamics of complex systems. Even a « simple » polyatomic liquid like *n*-butane is a problem: indeed, the shift from *gauche* to *trans* internal configurations, with an average period of 10 ps, constitutes already a relatively « rare event » on the scale of simulations which rarely exceed 100 ps. The situation gets worse if one wants to study the relaxation of proteins or chemical-reaction rates, although some relevant information can still be obtained by various tricks described, *e.g.*, in Herman Berendsen and Berni Alder's lectures.

On the whole then, and especially after the vivid historical account of the early beginnings given by Bill WOOD, the situation is far from distressing. We have learned to tackle many situations, our tools have considerably improved and the interaction with basic theory and experimental research is excellent. One black hole remains: strictly speaking, our world is governed by quantum mechanics, not by Newton's mechanics, and, although considerable progress has been made for static properties of quantum systems, exemplified by David Ceperley's work on liquid helium four, no efficient quantum molecular-dynamics method (QMD) has been devised yet, which would, *e.g.*, allow the computation of quantum transport coefficients. This problem is really hard, compared to all others which have been solved until now, but time helping, someday and somehow, it will be overcome.

PROCEEDINGS OF THE INTERNATIONAL SCHOOL OF PHYSICS « ENRICO FERMI »

Course I
Questioni relative alla rivelazione delle particelle elementari, con particolare riguardo alla radiazione cosmica
edited by G. PUPPI

Course II
Questioni relative alla rivelazione delle particelle elementari, e alle loro interazioni con particolare riguardo alle particelle artificialmente prodotte ed accelerate
edited by G. PUPPI

Course III
Questioni di struttura nucleare e dei processi nucleari alle basse energie
edited by C. SALVETTI

Course IV
Proprietà magnetiche della materia
edited by L. GIULOTTO

Course V
Fisica dello stato solido
edited by F. FUMI

Course VI
Fisica del plasma e applicazioni astrofisiche
edited by G. RIGHINI

Course VII
Teoria della informazione
edited by E. R. CAIANIELLO

Course VIII
Problemi matematici della teoria quantistica delle particelle e dei campi
edited by A. BORSELLINO

Course IX
Fisica dei pioni
edited by B. TOUSCHEK

Course X
Thermodynamics of Irreversible Processes
edited by S. R. DE GROOT

Course XI
Weak Interactions
edited by L. A. RADICATI

Course XII
Solar Radioastronomy
edited by G. RIGHINI

Course XIII
Physics of Plasma: Experiments and Techniques
edited by H. ALFVÉN

Course XIV
Ergodic Theories
edited by P. CALDIROLA

Course XV
Nuclear Spectroscopy
edited by G. RACAH

Course XVI
Physicomathematical Aspects of Biology
edited by N. RASHEVSKY

Course XVII
Topics of Radiofrequency Spectroscopy
edited by A. GOZZINI

Course XVIII
Physics of Solids (Radiation Damage in Solids)
edited by D. S. BILLINGTON

Course XIX
Cosmic Rays, Solar Particles and Space Research
edited by B. PETERS

Course XX
Evidence for Gravitational Theories
edited by C. MØLLER

Course XXI
Liquid Helium
edited by G. CARERI

Course XXII
Semiconductors
edited by R. A. SMITH

Course XXIII
Nuclear Physics
edited by V. F. WEISSKOPF

Course XXIV
Space Exploration and the Solar System
edited by B. ROSSI

Course XXV
Advanced Plasma Theory
edited by M. N. ROSENBLUTH

Course XXVI
Selected Topics on Elementary Particle Physics
edited by M. CONVERSI

Course XXVII
Dispersion and Absorption of Sound by Molecular Processes
edited by D. SETTE

Course XXVIII
Star Evolution
edited by L. GRATTON

Course XXIX
Dispersion Relations and Their Connection with Causality
edited by E. P. WIGNER

Course XXX
Radiation Dosimetry
edited by F. W. SPIERS and G. W. REED

Course XXXI
Quantum Electronics and Coherent Light
edited by C. H. TOWNES and P. A. MILES

Course XXXII
Weak Interactions and High-Energy Neutrino Physics
edited by T. D. LEE

Course XXXIII
Strong Interactions
edited by L. W. ALVAREZ

Course XXXIV
The Optical Properties of Solids
edited by J. TAUC

Course XXXV
High-Energy Astrophysics
edited by L. GRATTON

Course XXXVI
Many-Body Description of Nuclear Structure and Reactions
edited by C. BLOCH

Course XXXVII
Theory of Magnetism in Transition Metals
edited by W. MARSHALL

Course XXXVIII
Interaction of High-Energy Particles with Nuclei
edited by T. E. O. ERICSON

Course XXXIX
Plasma Astrophysics
edited by P. A. STURROCK

Course XL
Nuclear Structure and Nuclear Reactions
edited by M. JEAN and R. A. RICCI

Course XLI
Selected Topics in Particle Physics
edited by J. STEINBERGER

Course XLII
Quantum Optics
edited by R. J. GLAUBER

Course XLIII
Processing of Optical Data by Organisms and by Machines
edited by W. REICHARDT

Course XLIV
Molecular Beams and Reaction Kinetics
edited by CH. SCHLIER

Course XLV
Local Quantum Theory
edited by R. JOST

Course XLVI
Physics with Storage Rings
edited by B. TOUSCHEK

Course XLVII
General Relativity and Cosmology
edited by R. K. SACHS

Course XLVIII
Physics of High Energy Density
edited by P. CALDIROLA and H. KNOEPFEL

Course IL
Foundations of Quantum Mechanics
edited by B. D'ESPAGNAT

Course L
Mantle and Core in Planetary Physics
edited by J. COULOMB and M. CAPUTO

Course LI
Critical Phenomena
edited by M. S. GREEN

Course LII
Atomic Structure and Properties of Solids
edited by E. BURSTEIN

Course LIII
Developments and Borderlines of Nuclear Physics
edited by H. MORINAGA

Course LIV
Developments in High-Energy Physics
edited by R. R. GATTO

Course LV
Lattice Dynamics and Intermolecular Forces
edited by S. CALIFANO

Course LVI
Experimental Gravitation
edited by B. BERTOTTI

Course LVII
History of 20th Century Physics
edited by C. WEINER

Course LVIII
Dynamic Aspects of Surface Physics
edited by F. O. GOODMAN

Course LIX
Local Properties at Phase Transitions
edited by K. A. MÜLLER and A. RIGAMONTI

Course LX
C^*-Algebras and their Applications to Statistical Mechanics and Quantum Field Theory
edited by D. KASTLER

Course LXI
Atomic Structure and Mechanical Properties of Metals
edited by G. CAGLIOTI

Course LXII
Nuclear Spectroscopy and Nuclear Reactions with Heavy Ions
edited by H. FARAGGI and R. A. RICCI

Course LXIII
New Directions in Physical Acoustics
edited by D. SETTE

Course LXIV
Nonlinear Spectroscopy
edited by N. BLOEMBERGEN

Course LXV
Physics and Astrophysics of Neutron Stars and Black Holes
edited by R. GIACCONI and R. RUFFINI

Course LXVI
Health and Medical Physics
edited by J. BAARLI

Course LXVII
Isolated Gravitating Systems in General Relativity
edited by J. EHLERS

Course LXVIII
Metrology and Fundamental Constants
edited by A. FERRO MILONE, P. GIACOMO and S. LESCHIUTTA

Course LXIX
Elementary Modes of Excitation in Nuclei
edited by A. BOHR and R. A. BROGLIA

Course LXX
Physics of Magnetic Garnets
edited by A. PAOLETTI

Course LXXI
Weak Interactions
edited by M. BALDO CEOLIN

Course LXXII
Problems in the Foundations of Physics
edited by G. TORALDO DI FRANCIA

Course LXXIII
Early Solar System Processes and the Present Solar System
edited by D. LAL

Course LXXIV
Development of High-Power Lasers and their Applications
edited by C. PELLEGRINI

Course LXXV
Intermolecular Spectroscopy and Dynamical Properties of Dense Systems
edited by J. VAN KRANENDONK

Course LXXVI
Medical Physics
edited by J. R. GREENING

Course LXXVII
Nuclear Structure and Heavy-Ion Collisions
edited by R. A. BROGLIA, R. A. RICCI and C. H. DASSO

Course LXXVIII
Physics of the Earth's Interior
edited by A. M. DZIEWONSKI and E. BOSCHI

Course LXXIX
From Nuclei to Particles
edited by A. MOLINARI

Course LXXX
Topics in Ocean Physics
edited by A. R. OSBORNE and P. MALANOTTE RIZZOLI

Course LXXXI
Theory of Fundamental Interactions
edited by G. COSTA and R. R. GATTO

Course LXXXII
Mechanical and Thermal Behaviour of Metallic Materials
edited by G. CAGLIOTI and A. FERRO MILONE

Course LXXXIII
Positron Solid-State Physics
edited by W. BRANDT and A. DUPASQUIER

Course LXXXIV
Data Acquisition in High-Energy Physics
edited by G. BOLOGNA and M. VINCELLI

Course LXXXV
Earhquakes: Observation, Theory and Interpretation
edited by H. KANAMORI and E. BOSCHI

Course LXXXVI
Gamow Cosmology
edited by F. MELCHIORRI and R. RUFFINI

Course LXXXVII
Nuclear Structure and Heavy-Ion Dynamics
edited by L. MORETTO and R. A. RICCI

Course LXXXVIII
Turbulence and Predictability in Geophysical Fluid Dynamics and Climate Dynamics
edited by M. GHIL, R. BENZI and G. PARISI

Course LXXXIX
Highlights of Condensed-Matter Theory
edited by F. BASSANI, F. FUMI and M. P. TOSI

Course XC
Physics of Amphiphiles: Micelles, Vesicles and Microemulsions
edited by V. DEGIORGIO and M. CORTI

Course XCI
From Nuclei to Stars
edited by A. MOLINARI and R. A. RICCI

Course XCII
Elementary Particles
edited by N. CABIBBO

Course XCIII
Frontiers in Physical Acoustics
edited by D. SETTE

Course XCIV
Theory of Reliability
edited by A. SERRA and R. E. BARLOW

Course XCV
Solar-Terrestrial Relationship and the Earth Environment in the Last Millennia
edited by G. CINI CASTAGNOLI

Course XCVI
Excited-State Spectroscopy in Solids
edited by U. M. GRASSANO and N. TERZI